SYNTHESIS, CHARACTERIZATION, AND ELECTROCATALYTIC PROPERTIES OF NICKEL AND IRON THIOLATE COMPLEXES FOR HYDROGEN EVOLUTION CATALYSIS

by

BENJAMIN AARON YOSEN

(Under the Direction of Todd C. Harrop)

ABSTRACT

Development of cheap and efficient electrocatalyst is essential for realizing hydrogen gas as a clean alternative fuel source. Nature employs earth-abundant metals such as Ni and Fe in hydrogenases enzymes to reversibly catalyze proton reduction to H_2. Among the three classes of hydrogenases ([NiFe], [FeFe], and [Fe]-only), [NiFe]-hydrogenase is the most well-studied due to its ability to repair itself upon oxidative damage. Its active site features a pseudo-tetrahedral, see-saw like, $Ni(CysS)_4$ unit bridged to a low-spin Fe(II) coordinated by CO and CN^- ligands, forming a butterfly-like structure. Experimental and computational studies suggest Ni serves as the redox-active center mediating formation of the metal-hydride intermediate. Synthetic analogs of the Ni site have provided valuable insights but fail to capture the unique thiolate-rich tetrahedral Ni(II) center found in the native enzyme. To address this, we developed synthetic analogs utilizing aryl-thiolates to gain a deeper insight into the structure-to-function relationships that underpin hydrogenases activity using $[Ni(S\text{-}p\text{-}CF_3\text{-}Ph)_4]^{2-}$ as a model system. These complexes form putative $[Ni(SR)_3\text{-}solv]^-$ intermediates that result in the formation of higher ordered complexes under protic conditions. However, this behavior is suppressed by addition of

excess thiolate allowing the electrocatalytic activity to be assessed and its mechanism to be determined. To improve protic stability and catalytic activity of these systems, we incorporated *ortho*-carboxamide moieties to engage the coordinated thiolates in intramolecular hydrogen-bonding. Although we found improved protic stability, under electrocatalytic conditions the complex decomposes into active deposits on the electrode surface. Interestingly, this modification destabilizes the tetrahedral geometry resulting in a mixture of tetrahedral and square-planar homoleptic Ni(II) tetrathiolates in their solution-state. To increase the stability of these complexes under electrocatalytic conditions, we utilized a pentacoordinate PyPS-*p*-CF_3 ligand scaffold for a non-heme Fe-tetrathiolate complex which displays instability under protic conditions in MeCN resulting in active heterogenous deposits. However, in DMF deposition is mitigated, affording the activity of homogenous material to be assessed. Experimental and computational work suggests the important role the ligand platforms serve to catalyze proton reduction. This work provides a foundation for developing thiolate-rich Ni and Fe synthetic mimics that more accurately reflect the structural features of native enzyme active.

INDEX WORDS: Nickle, Thiolate, Electrocatalysis, Hydrogen Evolution, Nonheme, Iron

SYNTHESIS, CHARACTERIZATION, AND ELECTROCATALYTIC PROPERTIES OF NICKEL AND IRON THIOLATE COMPLEXES FOR HYDROGEN EVOLUTION CATALYSIS

by

BENJAMIN AARON YOSEN

A.A., Oxford College of Emory University, 2016

B.S., Emory University, 2018

A Dissertation Submitted to the Graduate Faculty of The University of Georgia in Partial Fulfillment of the Requirements for the Degree

DOCTOR OF PHILOSOPHY

ATHENS, GEORGIA

2025

© 2025

BENJAMIN AARON YOSEN

All Rights Reserved

SYNTHESIS, CHARACTERIZATION, AND ELECTROCATALYTIC PROPERTIES OF NICKEL AND IRON THIOLATE COMPLEXES FOR HYDROGEN EVOLUTION CATALYSIS

by

BENJAMIN AARON YOSEN

Major Professor:	Todd C. Harrop
Committee:	Jeffrey L. Urbauer
	Jason J. Locklin

Electronic Version Approved:

Ron Walcott
Vice Provost for Graduate Education and Dean of the Graduate School
The University of Georgia
August 2025

ACKNOWLEDGEMENTS

First, I would like to thank my advisor Dr. Todd Harrop for his unwavering support, mentorship, and guidance he has provided over the years. Thank you, Todd, for making me a better thinker, presenter, and scientist. Thank you for the countless hours you have spent pouring over my research reports, manuscript drafts, presentations, and time spent discussing my research. Beyond science, thank you for your compassion in dealing with the ups and downs life threw at me through graduate school. I would also like to thank Dr. Jeffrey Urbauer and Dr. Jason Locklin for serving on my committee and supporting me on my PhD career. I am grateful for the scientific expertise of the researchers at UGA including Dr. Earle Adams, Dr. Dongtao Cui, and Dr. Dennis Phillips. I am also thankful for those beyond our scientific community at UGA including the late Dr. Marylynn Olmstead from USC-Davis and Dr. Indranil Chakraborty at Florida International University for their help in collecting and solving crystal structures and to Dr. Timmothy Stemmler at the Medical University of South Carolina for his help in running and interpreting XAS data. Lastly, to the often-underappreciated staff and facility members at the old Chemistry building and at the new STEM-1 building, thank you for your hard work in creating a friendly, clean, and well managed working environment.

To my current group members, Jordan Ernst, Adrian Torres, and Amy Cheng, thank you for your friendship, support, and scientific minds. To Jordan thank you for keeping our lab safe and running smoothly. You are an awesome baker! To Adrian, thank you for your upbeat kindness that will be greatly missed. To Amy, thank you for your generosity and bright eagerness to learn. It has been awesome seeing everyone grow as both scientists and people. To the past members I

have been fortunate to work alongside, Dr. Yi Liu and Linsdey Howell, thank you equally for your friendship. Although you are deservedly Dr. Liu now, I am too used to calling you Yi. Thank you for setting such a great example for what a PhD student and scientist should be. I especially want to thank Lindsey for her dearly missed friendship. Thank you for the deep conversation about life and spirituality, the back-and-forth jokes, and the small but always fun pranks. It made coming to work a joy.

Dad and mom, thank you for raising me to become a man that is self-sufficient, determined, and hard working. These qualities, amongst others, have been instrumental in my pursuit of a PhD. You have never failed to be supportive throughout my time here and loved me well through it. To my siblings, Erica, Josh, and Shira, thank you for your support. To those friends I have made since starting my program, thank you for the many times of laughter, fruitful conversations, and pickleball that provided relief from the stresses of research.

To my wife and best friend, Annie, words cannot express how grateful I am for the unwavering support you have shown me from when we first started dating until I wrote the last word of this dissertation. You have been a steadfast source of joy in the midst of the stressful storm that is graduate school. Thank you for the countless uplifting and encouraging conversations. Thank you for unselfishly serving and supporting me every day. I love you. To Anna's family, thank you for making me feel welcome. For making me feel like your own son and your own brother.

TABLE OF CONTENTS

Page

CHAPTER

1 INTRODUCTION AND LITERATURE REVIEW 1

1.1 Viability of a Hydrogen Economy 1

1.2 Hydrogenase Overview 7

1.3 Ni Thiolate Complexes 25

1.4 NiS_4 HER Electrocatalysts 32

1.5 Mononuclear Ni-thiolate HER Electrocatalysts 44

1.6 Mononuclear NiP_4 HER Electrocatalysts 56

1.7 Heterobimetallic [NiFe] HER Electrocatalysts 63

1.8 Intent of Research 78

1.9 References 80

2 SYNTHESIS, PROPERTIES, AND ELECTROCHEMICAL PROTON REDUCTION OF A HOMOLEPTIC TETRATHIOLATO NI-SITE MODEL OF [NIFE]-HYDROGEASNE 92

2.1 Abstract 93

2.2 Introduction 94

2.3 Results and Discussion 99

2.4 Conclusion 129

2.5 Materials and Methods 131

2.6 Synthesis 132
2.7 Speciation Studies 137
2.8 Electrochemical Measurements 140
2.9 X-ray Diffraction/X-ray Absorption Measurements 143
2.10 Theoretical Studies 145
2.11 Supplementary Information 148
2.12 References 247
3 ASSESSSING THE IMPACT OF HYDROGEN BONDING ON STABILITY AND ELECTROCATALYTIC HYDROGEN EVOLUTION OF HOMOLEPTIC NICKEL-TETRATHIOLATE COMPLEXES 261
3.1 Abstract 262
3.2 Introduction 263
3.3 Results and Discussion 267
3.4 Conclusion 303
3.5 Materials and Methods 304
3.6 Synthesis and Characterization 306
3.7 Physical Measurements 352
3.8 Reactivity Studies 354
3.9 Supplementary Information 357
3.10 References 404
4 LIGAND-ASSISTED HYDROGEN EVOLUTION BY AN ELECTRON RICH NONHEME FE-THIOLATE COMPLEX 415
4.1 Abstract 416

4.2 Introduction....417
4.3 Results and Discussion....421
4.4 Conclusion....451
4.5 Materials and Methods....452
4.6 Synthesis and Characterization....454
4.7 X-ray Diffraction....498
4.8 Reactivity Studies....498
4.9 Electrochemical Measurements....500
4.10 Mechanism Computations....504
4.11 Supplementary Information....507
4.12 References....562
5 CONCLUSIONS....570
APPENDICES
A DIVERGENT BEHAIVOR OF NI(II) TETRATHIOALTE ORTHO-CARBOXAMIDO COMPLEXES IN EXCESS THIOALTE CONDITIONS....574

CHAPTER 1

INTRODUCTION AND LITERATURE REVIEW

1.1 Viability of a Hydrogen Economy

Although the industrial revolution propelled industrialized western civilization into the 20th century, it demanded an energy source to sustain it. This energy was provided by fossil fuels formed by remains of ancient organic matter that were subjected to intense heat and pressure over millions of years. The consumption of fossil fuels, including petroleum, coal, and natural gas, has only increased each decade since, as seen in Figure 1.1, as population size grows. Although this fuel is naturally occurring, produced from fossilized remains of organisms, the process to make it requires millions of years practically creating a non-renewable source of energy. Furthermore, the combustion of fossil fuels emit large amounts of greenhouse gases (GHGs) directly into the atmosphere with roughly 37.4 billion tons emitted in 2023.[1, 2] GHGs play a key role in maintaining the temperature of Earth's atmosphere by absorbing and remitting the heat given from Earth's crust when warmed by the sun. If GHGs were removed from the atmosphere, the fine balance that causes life to thrive would be severely disrupted as global temperatures would drop. On the other extreme, higher concentrations of GHGs would equally disrupt earth's ecosystems by increasing temperatures. Even a 2 ºC increase in global temperatures is proposed to cross several climate tipping points, resulting in an irreversible and self-perpetuating change in the climate.[3] Crossing this threshold is anticipated to have a deleterious impact on biomes, food supply, and increased

risk of coastal flooding.[4, 5] As more GHGs are emitted into the atmosphere from our reliance on fossil fuels, the scales are closer to be tipped over into these irreversible changes. This effect is exhibited by comparing CO_2 levels, the largest component of anthropogenic GHGs, between pre- and post- industrial revolution. Global concentrations of CO_2 pre-industrial revolution never exceeded 300.00 ppm; however, at the end of March 2024 it was measured at 423.16 ppm resulting in a 1.2 ºC increase in global temperatures since 1850.[6] If the current rate of CO_2 emissions is held, then concentrations are estimated to reach 500 ppm by 2080 leading to an increase of 3.0 ºC above pre-industrial revolution global temperatures.[7] The current unsustainable reliance of these fuel sources are spurring research to develop renewable alternatives capable of meeting growing energy demands without contributing to the increasing GHGs in the atmosphere.[8, 9]

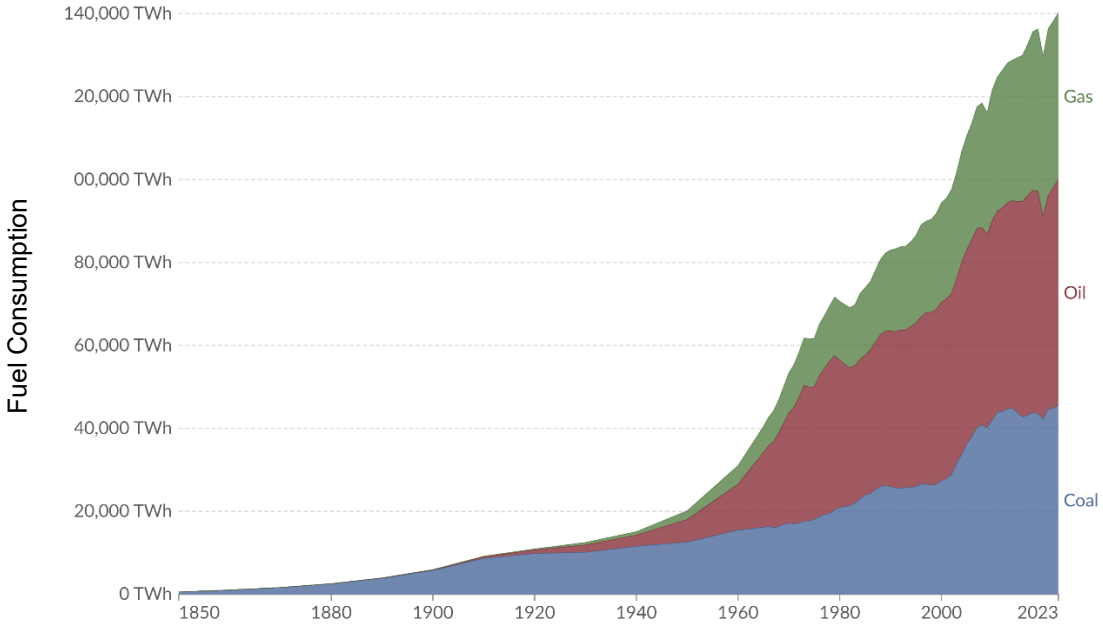

Figure 1.1. Amount of global fossil fuel consumption of coal (blue), oil (red), and gas (green) from 1850 to 2023. Graph generated from Our World in Data.[10]

One promising carbon-free energy carrier currently being explored is hydrogen gas (H_2), which is currently an essential building block for industrial and agriculture processes including petroleum refining and production of ammonia through the Haber-Bosch process.[11] Use of H_2 as a potential

fuel is being explored by the US Department of Energy (DOE) and European Union's Directorates-General for Energy with several research journals solely dedicated to publishing research into its development. Hydrogen is the simplest and most abundant element in the universe comprised of an electron and proton. It is a relatively inert molecule with a bond dissociation energy of 104 kcal/mol,[12] and the energy stored in its strong bond belies its promise as an alternative fuel. When combusted, H-atoms are produced and form strong bonds to oxygen forming water, leading to its classification as a clean source of energy.[13] Like combustion of fossil fuels, combustion of H_2 is spontaneous and exothermic, seen in Scheme 1.1, albeit with a lower heating value (H_2 = 286 kJ/mol; Gasolene = 5400 kJ/mol).[14] However, the energy stored in H_2 and its low molecular weight affords a higher energy density (142.0 kJ/g) compared to gasoline (45.6 kJ/g).[15] The high energy density and clean combustion of H_2 make this potential fuel source an attractive energy carrier. However, given its low density, H_2 comprises a very small part of the atmosphere due to its ability to escape Earth's gravitational force given. In turn, the most reliable avenue to gather H_2 for its use as a fuel source is to produce it.

$$H_2\,(g) + 1/2\,O_2\,(g) \longrightarrow H_2O\,(g) \qquad \Delta G^\circ = -60 \text{ kcal/mol}$$

$$C_8H_{18}\,(g) + 25/2\,O_2\,(g) \longrightarrow 8\,CO_2 + 9\,H_2O\,(g) \qquad \Delta G^\circ = -1180 \text{ kcal/mol}$$

Scheme 1.1. Standard free energies of the combustion of H_2 and isooctane, a major component of gasolene. ΔG^o values received from CRC Handbook of Chemistry and Physics.[16]

There are three predominant processes utilized to produce H_2: (i) steam methane reforming (SMR), (ii) biological hydrogen production, and (iii) electrocatalytic water splitting, reactions described in Table 1.1.[17] SMR produces H_2 from the combination of water and natural gas under high temperatures (700 – 1000 ºC) and pressures (25 atm). The CO that is produced from combustion further reacts with steam, in the water-gas shift reaction, to produce H_2 with CO_2

formed as a byproduct. Biological H_2 production takes advantage of the metabolic processes of algae and anaerobic bacteria that produce H_2 naturally.[18] Lastly, electrolysis, or electrocatalytic water splitting, utilizes electrical energy to split water into H_2 and O_2 in an electrochemical cell, shown in Figure 3.1. The anode of the electrochemical cell oxidizes water to O_2, known as the oxygen evolving reaction (OER, $2H_2O \rightarrow O_2(g) + 4H^+ + 4e^-$) or sometimes known as the water oxidation reaction (WOR). The protons produced from this reaction are reduced at the cathode to produce H_2, known as the hydrogen evolution reaction (HER, $4H^+ + 4e^- \rightarrow 2H_2\,(g)$).

Table 1.1. Current hydrogen production methods and metrics comparing their market viability.

H_2 Production Method		**Reaction**	**Conversion Efficiency**	**Production Cost ($/kg H_2)**	**Market Share**
Steam Methane Reforming (SMR)		$CH_4 + 2\,H_2O \xrightarrow{\Delta} CO_2 + 4\,H_2$	70-85%	0.09 – 0.18	95%
Biological	Bio Photolysis	$2\,H_2O \xrightarrow{h\nu} 2\,H_2 + O_2$	44%	*n.r.*	<1%
	Photo-decomposition	$CH_3COOH + 2\,H_2O \xrightarrow{h\nu} 4\,H_2 + 2\,CO_2$			
	Anaerobic Fermentation	$C_6H_{12}O_6 + 2\,H_2O \rightarrow 4\,H_2 + 2\,CO_2 + 2\,CH_3COOH$			
Electrolysis		(anode) $2\,H_2O \xrightarrow{1.23\ V} O_2 + 4\,H^+ + 4\,e^-$ (cathode) $4\,H^+ + 4\,e^- \xrightarrow{0.00\ V} 2\,H_2$	62-82%	1.47 – 2.95	4%

SMR currently dominates H_2 production, accounting for 95% of the market, due to its low cost and high conversion efficiency, defined as the relative ratio of energy output to input.[19] Although SMR is widely used, it is known as a grey H_2 source because of the formation of CO_2 as a byproduct. Alternatively, electrolysis produces H_2 from water without contributing GHGs to the atmosphere. The most common commercially used H_2O splitting cell, is a proton exchange membrane fuel cell that utilizes Pt nanoparticles as catalysts, commonly adsorbed on carbon, at

the cathode.[20] These metal based catalysts facilitate the one or two electron reduction of H^+ to form a bound hydrogen atom (H-atom) or hydride (H^-) on the metal. H_2 evolves either through homolytic coupling of two metal-bound H-atoms or coupling of the bound hydride with a free proton. Pt exhibits the highest electrocatalytic activity towards HER due to its ideal energetic trade-off between binding and releasing of H-atoms. This property can be represented by a volcano plot (Figure 1.2), showing activity of HER as a function of M-H bond strength, in which Pt sits at the peak.[21-23] Pt has proven to evolve H_2 at high efficiencies measured by overpotentials (η), defined as the voltage required for catalysis beyond the thermodynamic reduction potential of $2H^+/H_2$, of 20 - 50 mV. The rate of H_2 evolution, or turnover frequency (TOF), at these potentials are 30 - 60 s^{-1}.[21, 24, 25] Yet, the high price of Pt ($6200/mol) utilized in the electrocatalytic production of H_2 present an obstacle for electrolysis to carve out a large market share.[26]

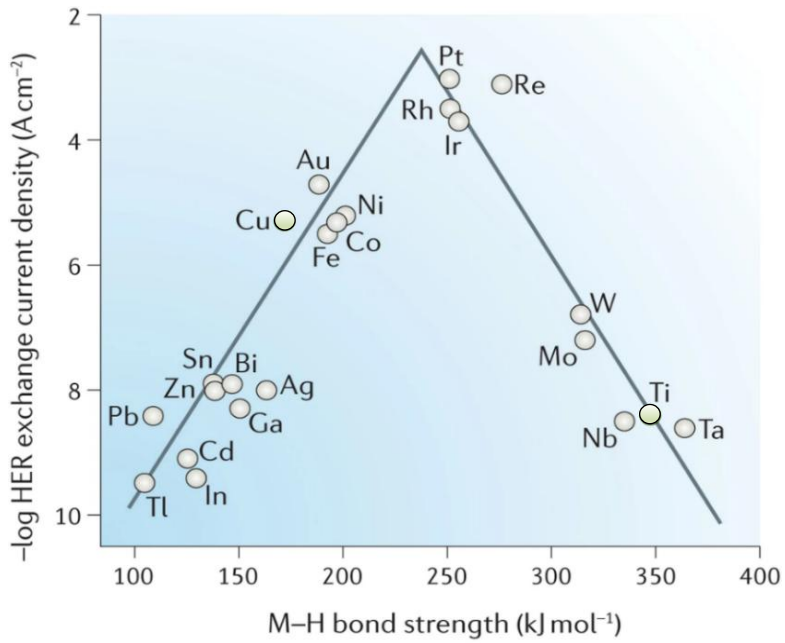

Figure 2.1. Volcano plot of the exchange current density (measure of electrodes performance) of HER versus the energy of the metal-hydrogen bond formed on the metal. Figure adapted from Symes et al.[27]

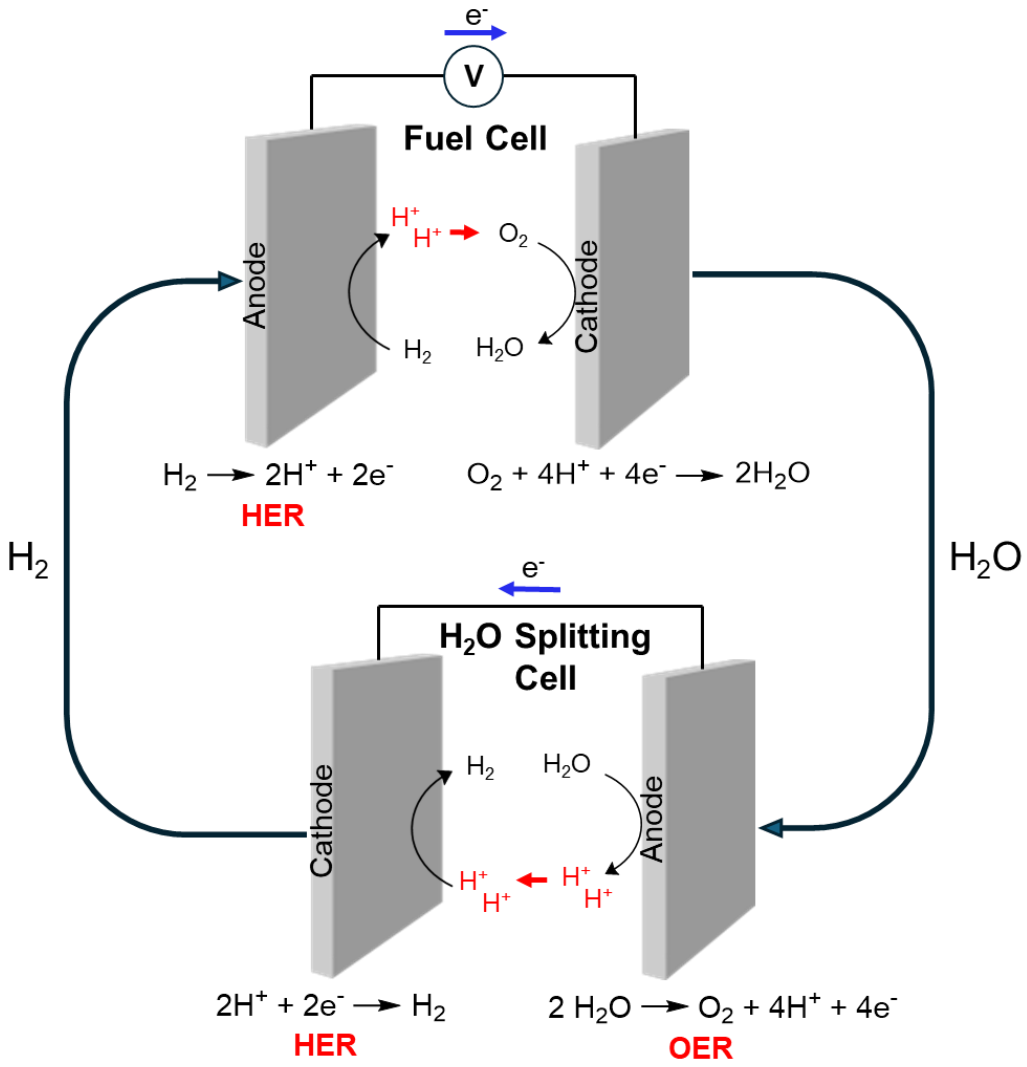

Figure 3.1. Simple representation of a renewable hydrogen fuel cell composed of a fuel cell (*top*), and a water splitting cell (*bottom*).

H_2 can be consumed to produce energy through its combustion, just as with gasolene or natural gas, however, only produces water vapor as a byproduct. For example, NASA utilizes combustion of H_2 to fuel the main engines of space shuttles. Another strategy to harness the energy of H_2 is to use a fuel cell depicted in Figure 1.3. Fuel cells produce electrical energy, like a battery, from the oxidation of H_2 without producing GHG like gasolene or diesel engines. Furthermore, current fuel cells are almost twice as efficient (40 – 80%) than gas/diesel engines (20 - 35 %), where efficiency

is defined as the amount of energy utilized in work over total energy produced.[28] This high efficiency highlights one reason to implement fuel cell in vehicles as the transportation sector accounts for more than a third of US CO_2 emissions.[29] However, currently there are only two H_2 fuel cell electric vehicles (FCEV) available, the Hyundai Nexo and Toyota Mirai.[30] Lack of FCEVs is largely due to two factors centered on the cost to generate and supply H_2 and harness its energy. The large cost, once again, is due to the use of expensive metals like Pt to catalyze production and consumption of H_2. This high cost is exemplified in a recent report from the DOE's hydrogen energy program comparing the cost-to-energy output ratios of H_2 fuel cells for long-range semi-trucks.[31] They found that the energy output ratio of a hydrogen fuel cell was $53/kW, roughly 80-fold more expensive than diesel engines ($0.70/kW). Ideally, fuel cells would be coupled to a water splitting cell to create a self-sustaining and clean energy source from H_2. However, to make this idea a reality, cheaper and more earth abundant materials are necessary to efficiently couple these reactions.

1.2 Hydrogenase Overview

Nature employs a class of metalloenzymes called hydrogenases (H_2ases) that catalyze the reversible reduction of protons to molecular hydrogen ($2H^+ + 2e^- \leftrightarrow H_2$). The capacity of microorganisms to metabolize H_2 was first discovered in the late 19th century, but it wasn't until 1931 that the enzyme responsible was termed 'hydrogenase' by Stephenson and Strickland.[32] They observed activity in anaerobically grown *Escherichia coli* cells that mediated the reversible reduction of organic dyes with H_2. Exposure of CO to the cells inhibited H_2 reduction indicating the involvement of a transition metal in the activation of H_2, later identified as Ni and Fe.[33] Since this discovery, H_2ases have been found in a wide array of organisms including bacteria, archaea, and some eukarya.[34-36] It has been estimated that 200 million tons of hydrogen are produced and

consumed by organisms in anoxic habitats. The anaerobic producing organism generates H_2 fermentatively by oxidation of carbohydrates and lipids with the H^+ being the terminal electron acceptor. The consumer organism utilize H_2 as an energy source and to balance the redox potential of the cell, through H_2 evolution or uptake.[37, 38] In addition, H_2ases can catalyze the conversion of para- to-ortho dihydrogen.[39] These reactions take place at a metal center containing earth-abundant metal Ni and Fe. H_2ases can be classified into three groups, according to the metal ion housed in their active site: (i) [NiFe]-, (ii) [FeFe]-, in which H_2 is the only substrate or product, and (iii) [Fe]-H_2ases, in which H_2 uptake is coupled to methenyltetrahydromethanopterin (methenyl-H_4MPT^+) reduction.[40-44] Research into understanding the structure and function of the H_2ases is spurred on by their ability to perform HER at TOFs close to 9000 s^{-1} and at overpotentials close to the thermodynamic minimum.[45, 46] In fact, a [NiFe]-H_2ase enzyme adsorbed on an electrode was shown to exhibit the same reversible behavior as a platinum electrode doing so with twice the efficiency for H_2 oxidation.[47] H_2ase make promising alternatives to expensive Pt ($6200/mol) based electrodes used in fuel cells given the cheaper, more earth-abundant metal, Ni ($0.93/mol) and Fe ($0.01/mol), utilized to perform HER.

1.2.1 [Fe]- and [FeFe]-Hydrogenase: Structure and Function

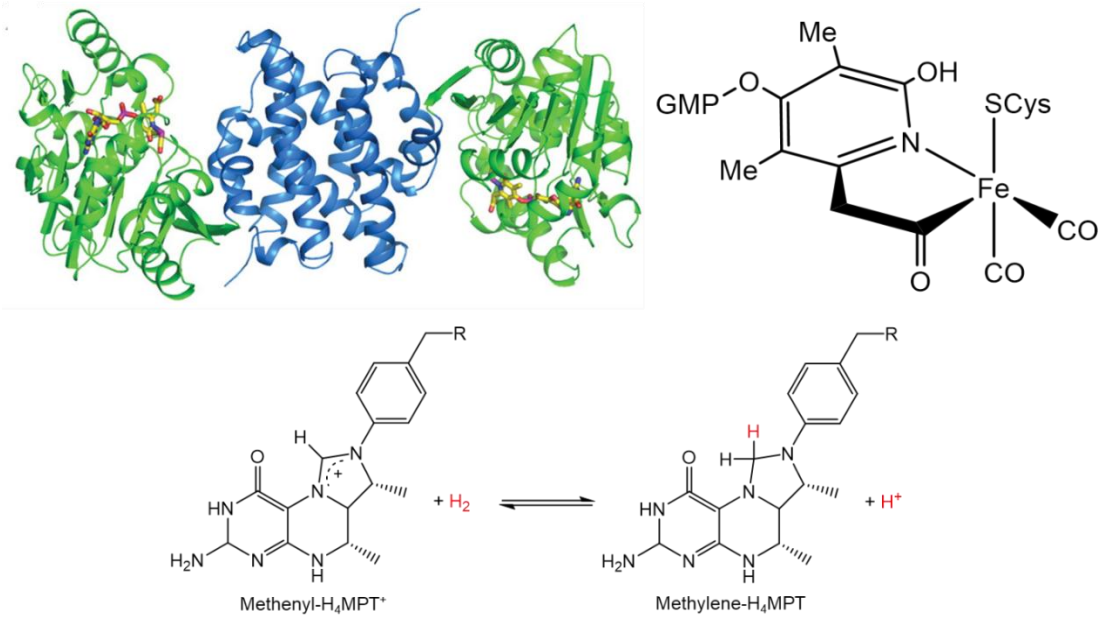

Figure 1.4. (*top left*) Crystal structure of [Fe]-H_2ase from *Methnocaldoccus jannaschii* (PDB: 3DAF).[29] (*top right*) Depiction of the active site in the catalytic ready state (GMP = guanosine monophophate). (*bottom*) Reaction catalyzed by [Fe]-H_2ase.

Among the three classes, [Fe]-H_2ase is the most recently discovered, and less studied, metalloenzyme. The crystal structure of the apoenzyme was solved in 2006, and the reconstituted holoenzyme was reported two years later, seen in Figure 1.4.[42, 48] Both the structure and catalytic mechanism differ from the other H_2ases but shows typical reactions of H_2ases (e.g., H^+/H_2 exchange). The crystal structure along with IR[49] and NRVS[50] analyses revealed the active site, depicted in Figure 1.4, to contain a $Fe(CO)_2(SCys)$ unit bound to a guanylylpyrodinol (GP) through its acyl and pyridyl donors. The catalytic cycle is still up for much debate, but one proposed mechanism, based on computations and crystallographic data, invokes formation of a Fe^{II}-H, upon H_2 binding and heterolytic splitting.[51, 52] The H^+ produced from this splitting is proposed to protonate the basic O-atom of pyridonate, and, finally, the hydride (H^-) is transferred to methenyl-H_4MPT^+.[51, 52] Fe remains in its 2^+ oxidation state throughout the catalyst cycle and any iron-sulfur

(Fe-S) cluster cofactors, unlike [NiFe]- and [FeFe]-H_2ase; therefore [Fe]-H_2ase is not considered a redox-active enzyme. Rather, the activity is dependent on the co-substrate, methenyl-H_4MPT^+, and in its absence, H_2 activation is not present.[49] The mononuclear structure and lack of redox activity sets [Fe]-H_2ase apart; however, consumption of H_2 is almost isoenergietic (ΔG = -1.3 kcal/mol) and H_2 splitting rates of 215 s^{-1} (pH 7.5) making its efficiency and rates of HER comparable to the other H_2ases.[53]

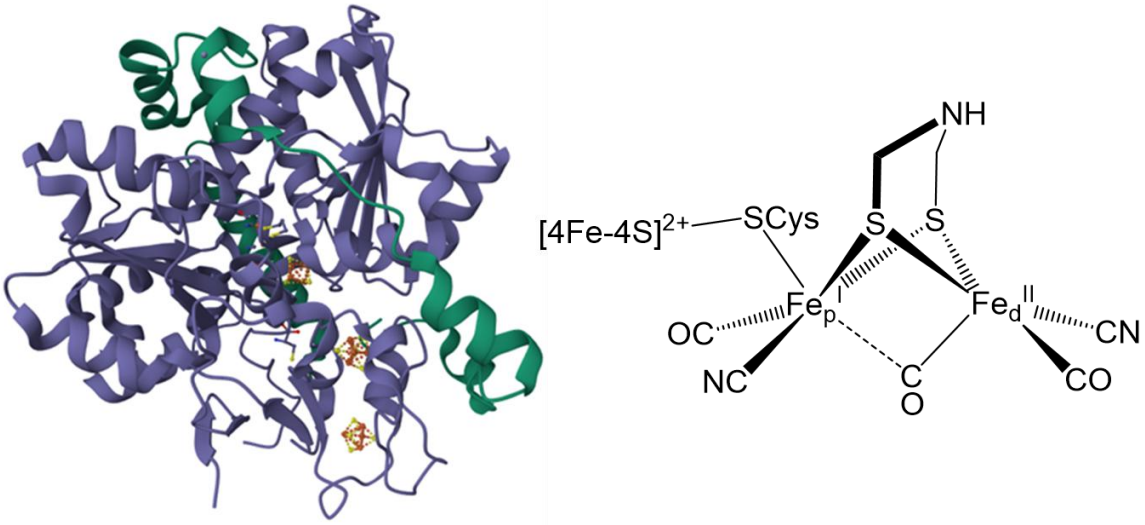

Figure 1.5. (*left*) Crystal structure of [FeFe]-H_2ase from *Desulfovibrio desulfuricans* (PDB: 1HFE).[54] (*right*) Depiction of the active site, known as the H-cluster, in the catalytic ready state (H_{ox}).

[FeFe]-H_2ase are monomeric proteins, structure shown in Figure 1.5, found in several lower eukaryotes and a wide range of bacteria.[55] The enzyme functions bidirectionally, catalyzing the reversible interconversion of protons and electrons to H_2, but it usually is committed to H_2 evolution approaching rates up to 9000 s^{-1} (H_2ase I from *Clostridium pasteurianum*).[46] [FeFe]-H_2ases vary in size (45-130 kDa) but each feature an active site known as the H-cluster. The H-cluster is buried deep within the protein and comprises a [4Fe-4S] metallocubane linked to an

apical CysS- amino acid residue. The two low-spin Fe centers are linked through S atoms of an azadithiolate (adt^{2-}) ligand. Each Fe contains bound CO and CN^-, with an additional μ-CO ligand completing the coordination sphere. The most unusual feature of the H-cluster is a covalently bound $[4Fe\text{-}4S]^{2+}$ at the proximal Fe (Fe_p). Although the unit is a common redox cofactor involved in electron transfer, it is not typically bound to the active site and is proposed to play a key role by storing and later providing electrons to the Fe centers during catalysis.

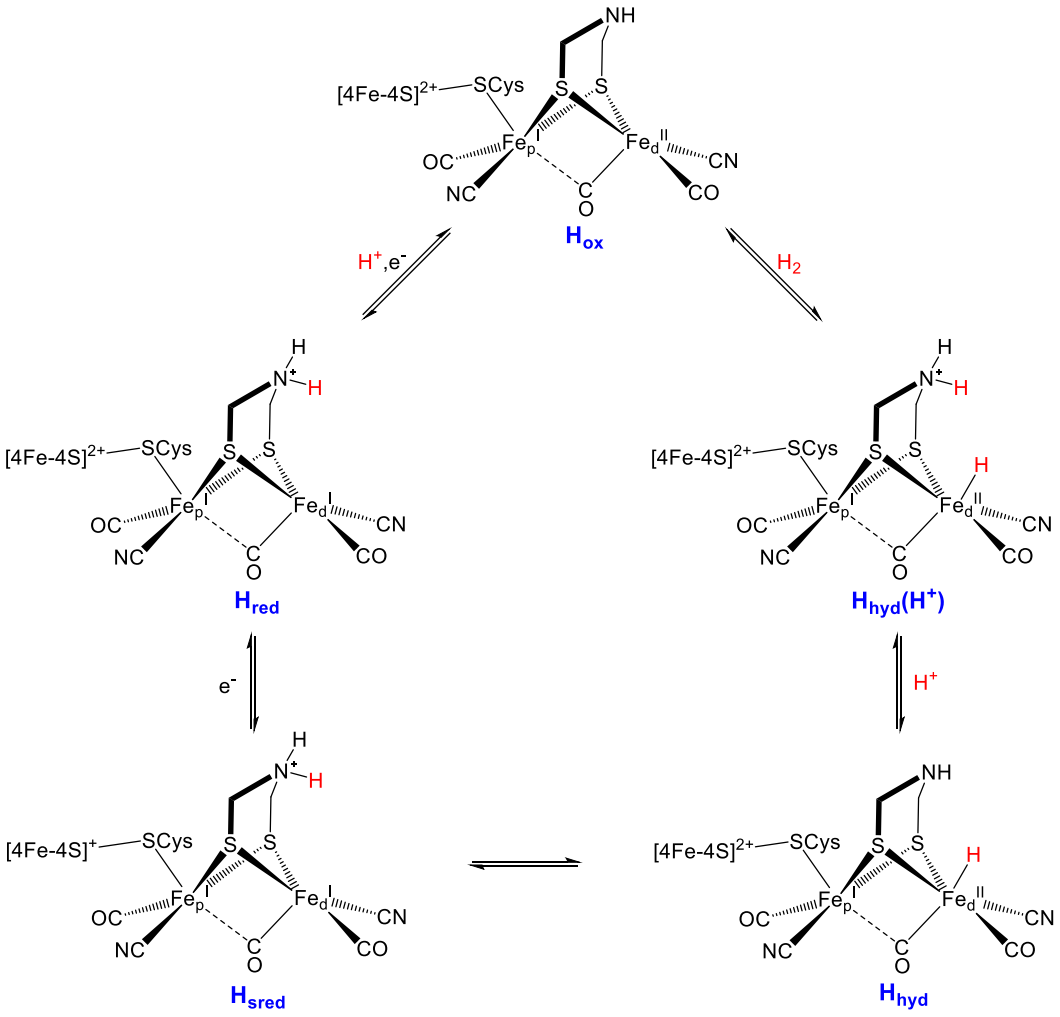

Scheme 1.2. Proposed catalytic cycle of [FeFe]-H_2ase.

Although the mechanism for HER is not as-well established as for [NiFe]-H_2ase, the catalytic cycle for [FeFe]-hydrogenase is proposed to go through five main states based on the number of electrons transferred to the active site, of which the first four have been spectroscopically probed. The catalytic cycle, shown in Scheme 1.2, begins in the enzyme's oxidized state (H_{ox}) that has been characterized by EPR and X-ray crystallography.[56, 57] If the enzyme is reducing H^+ then the next step involves a proton-coupled electron-transfer (PCET) that results in the protonation of the apical N of the adt^{2-} unit and reduction of the distal Fe (Fe_d; the Fe furthest from the covalently bound $[4Fe\text{-}4S]^{2+}$ unit) forming the reduced state (H_{red}; Fe_d^I-Fe_p^I). H_{red} is then further reduced at the $[4Fe\text{-}4S]^{2+}$ unit to form a super-reduced state (H_{sred}), identified by FTIR and EPR.[58] The super-reduced state is now poised to from a Fe^{II}-H (H_{hyd}) through intramolecular proton and electron transfer from the $adtH^-$ unit and Fe_p^I respectively. Lastly, protonation at the adt^{2-} unit triggers an electron transfer from the covalently bound $[4Fe\text{-}4S]^+$ cluster to Fe_p, $H_{hyd}(H^+)$. Protonation of the apical N atom of the adt^{2-} sets up a proton relay site to heterolytically coupling of the H^+ and Fe_d^{II}-H to evolve H_2 thus completing the cycle. This proton relay site is proposed to be a key factor for the high TOF values of [FeFe]-H_2ases.[59] Although this H_2ases possess the highest rates of TOF, it is irreversibly damaged by O_2 through its attack on the vacant site on Fe_d and is a key challenge for its use in industrial settings.[60, 61]

1.2.2 [NiFe]-Hydrogenase: Structure and Function

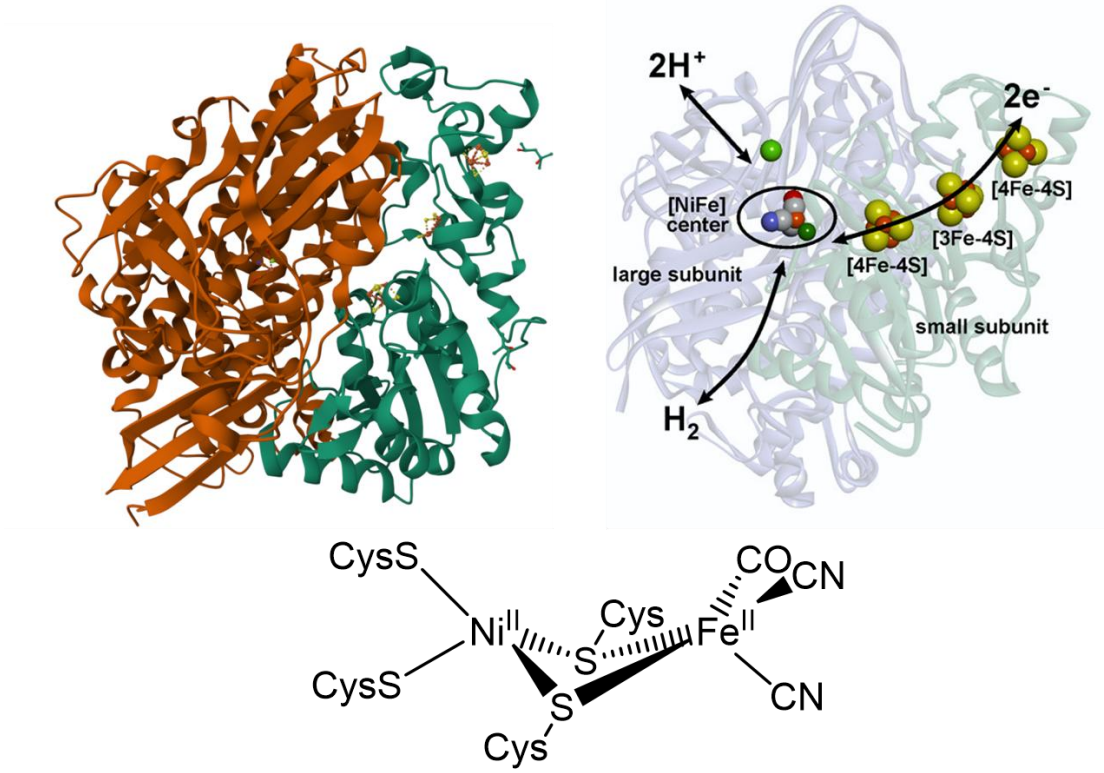

Figure 1.6. (*top left*) Crystal structure of oxidized form of [NiFe] hydrogenase from *Desulfovibrio gigas* (PDB: 1FRV).[62] (*top right*) Schematic representation of the ET chain and pathways for H_2 and H^+ transfer, figure taken from Lubitz et al.[63] (*bottom*) Depiction of the active site in its Ni-SI_a state.

The older and more abundant of the H_2ases is [NiFe]-H_2ase.[64] Like all hydrogenases, [NiFe]-H_2ase catalyzes the interconversion of molecular H_2 to protons and electrons, but most tend to catalyze the oxidation of H_2 at rates up to 6000 s^{-1}, and at overpotentials close to the thermodynamic minimum. This enzyme can be classified based on molecular phylogeny that divides them into four groups: (i) group 1 are membrane-bound H_2 uptake hydrogenases; (ii) group 2 contains uptake and sensory hydrogenases; (iii) group 3 contains F420-reducing, NAD(P)+ reducing, and methylviologen-reducing hydrogenases; and lastly (iv) group 4 contains energy-converting hydrogenases.[18] The most well studied [NiFe]-H_2ase belongs to group 1, O_2 sensitive

[NiFe]-H_2ase, also known as the "standard" H_2ase, isolated from sulfate-reducing bacteria.[63] Although H_2ases were discovered in the late 1800s, the first successful crystallization of a standard [NiFe]-H_2ase was in 1985 from *D. vulgaris* Miyazak and it wasn't until a decade later that Volbeda and coworkers reported the first crystal structure, from *D. gigas*, shown in Figure 1.6.[62, 65] Since then crystal structures of a variety of hydrogenases in all groups have been solved creating a large library of structures.

Standard [NiFe]-H_2ases are heterodimeric proteins composed of two subunits. The small subunit (~29 kDa) houses three Fe-S clusters that span from the exterior of the protein to the active site spaced at about 12 Å apart, labeled as proximal [4Fe-4S], medial [3Fe-4S], and distal [4Fe-4S] based on their proximity to the [Ni-Fe] active site. These clusters form a pathway for electrons to flow to and from the active site housed the large subunit (~63 kDa). The active site of the enzyme features a $\{Ni(\mu\text{-}SCys)_2Fe\}$-butterfly arrangement formed by two bridging cysteinyl ligands. In the H_2ase's catalytic ready state (Ni-SI_a, Scheme 1.3), Ni is coordinated by four cysteinyl ligands in a seesaw-like geometry and its geometry, of the $\{Ni(SCys)_4\}$ unit in the Ni-SI_a state, obtained upon incubation of as-isolated H_2ase with H_2, lies between the tetrahedral ($\tau_4 = 1$) and square planar ($\tau_4 = 0$) geometry with a τ_4 of 0.54.[66] This geometry is conserved throughout the catalytic cycle when only taking into account the $Ni(SCys)_4$ core, structural parameters of each state are shown in Table 1.2.[66, 67] On the other hand, the $\{Fe(CysS)_2(CO)(CN)_2\}$ unit takes on a distorted square pyramidal site with the CO ligand in the apical site with the metals separated by a distance (2.57 Å) close to sum of the Ni^{II} and Fe^{II} (2.56 Å) but not considered bound to each other.

Table 1.2. Average bond distances and τ_4 values of catalytically relevant states in [NiFe]-H_2ase shown in Scheme 1.3.

Catalytic State	Ni-S_{avg} (Å)	τ_4	Ni-H (Å)	Ref
Ni-SI_a[a]	2.33	0.54	*n.a*	[66]
Ni-R[b]	2.29	0.58	1.58	[68]
Ni-C*[c]	2.26	0.59	1.60	[69]
Ni-L*[d]	2.29	*n.r.*	*n.a.*	[70]

*Structural data obtained from geometry optimized structure, [a]*Desulfivirbio vulgaris* Miyazaki F (PDB: 1H2R), [b]*Desulfivirbio vulgaris* Miyazaki F (PDB: 4U9H), [c]DFT calculations from optimized structure of the active site from *Desulfivirbio vulgaris* Miyazaki F [NiFe]-H_2ase (PDB: 1H2R),[d]DFT calculations from *Desulfivirbio vulgaris* Miyazaki F [NiFe]-H_2ase (PDB: 1H2R), protonation of terminal Cys81.

The Ni-Fe active site is buried deep within the protein matrix requiring channels for substrates and products to transfer to and from the active site, approximated location in the enzyme is shown in Figure 1.6. One such channel, probed by the crystal structure of xenon-exposed enzymes, consist of hydrophobic amido acid residues proposed to make a narrow bottleneck for H_2 diffusion.[71, 72] Once H_2 reaches the active site and is oxidized, the protons exit through one of two pathways. One pathway, based on mutagenesis and theoretical studies, proposes that the H^+ first transfers from to a nearby glutamate residue, and is expelled to the molecular surface through several glutamate chains located near the proximal Fe-S cluster.[73, 74] The other proposed pathway begins with the H^+ transferring to an arginine residue and then reaching the surface through a His-rich tunnel.[75] All three channels lead to the [NiFe] active site thus allowing for the activation and production of H_2 by the redox active metals.

Early on, in the 1990's, it was suggested that Fe was responsible for the activation and metabolization of H_2. This proposal was based on well-established reaction between H_2 and Fe organometallic compounds and computations indicating a lower energetic pathway for H_2 to bind to Fe^{II} as opposed to Ni^{II}.[76] However, this proposal has been disputed based on more recent computations, done in the early 2000's, and later supported by the crystal structure of the Ni-C intermediate revealing the hydride forming at Ni.[69] It is now widely accepted that Ni, not Fe, is responsible for binding and cleaving H_2 in [NiFe]-H_2ase. The role of Ni as the metal responsible

for activating H_2 is further supported by its optimal position at the end of both the hydrophobic H_2 transport channel and ET chain. In addition, spectroscopic identification of mechanistic intermediates, including EPR, IR, Mössbauer, XRD, ect. *vide supra*, have indicated that Ni changes oxidation states ($Ni^{I,II,III}$) throughout turnover, whereas Fe remains in its low-spin Fe^{II} state.

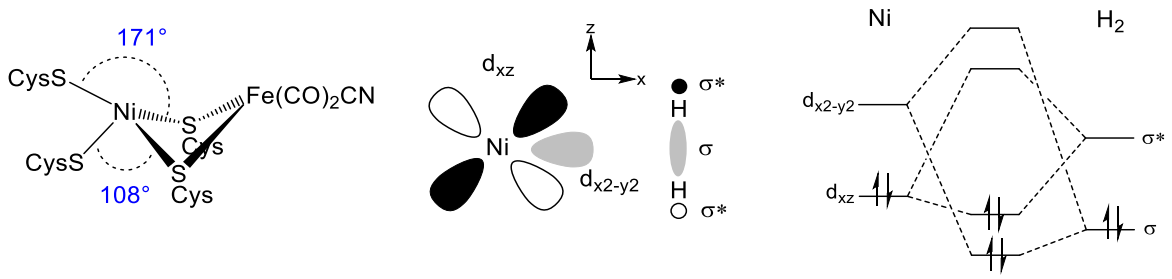

Figure 1.7. (*left*) Depiction of the active site [NiFe]-H_2ase in the Ni-SI_a state with select bond angles, (*middle*) proposed orbitals involved in H_2 oxidation, and (*right*) simplified orbital scheme associated with H_2 binding.[77]

The unusual psuedo-tetrahedral geometry of Ni^{II} is proposed to be a key factor in its ability to bind and activate H_2.[78, 79] The geometry of Ni^{II} in the Ni-SI_a state can be imagined as a "see-saw" in which there is almost a 180˚ angle between a terminal and bridging SCys, i.e, $<S_{term}$-Ni-S_{br}, seen in Figure 1.7. This 171º bend creates the "bench" and the other bend (108º) of the SCys residues makes up the "fulcrum". This unique geometry accomplishes two things, first it provides a vacant site for H_2 to bind at the "bench", and, second, is proposed to change the energy of the d-manifold of Ni^{II} (Figure 1.7) to have a fully occupied d_{xz} and an unoccupied d_{x2-y2} orbital.[80] When H_2 binds to the Ni^{II}, the bonding electrons in the σ-orbital of H_2 donates to the unoccupied d_{x2-y2} orbital of Ni. This binding mode allows the occupied d_{xz} orbital to back-donate to the vacant σ*-orbital of H_2, thus weakening the H-H bond and eventually leading to its scission. The interaction is consistent with the proposal that the distortion from square-planar Ni^{II} stabilizes the LUMO, thus

enhancing its hydride acceptor ability.[81, 82] Although Fe is not an active participant in H_2 oxidation, it most likely plays a role in attenuating electron density and acting as a Lewis acid to form a bridging hydride. Both metals play a vital role in catalyzing HER efficiently.

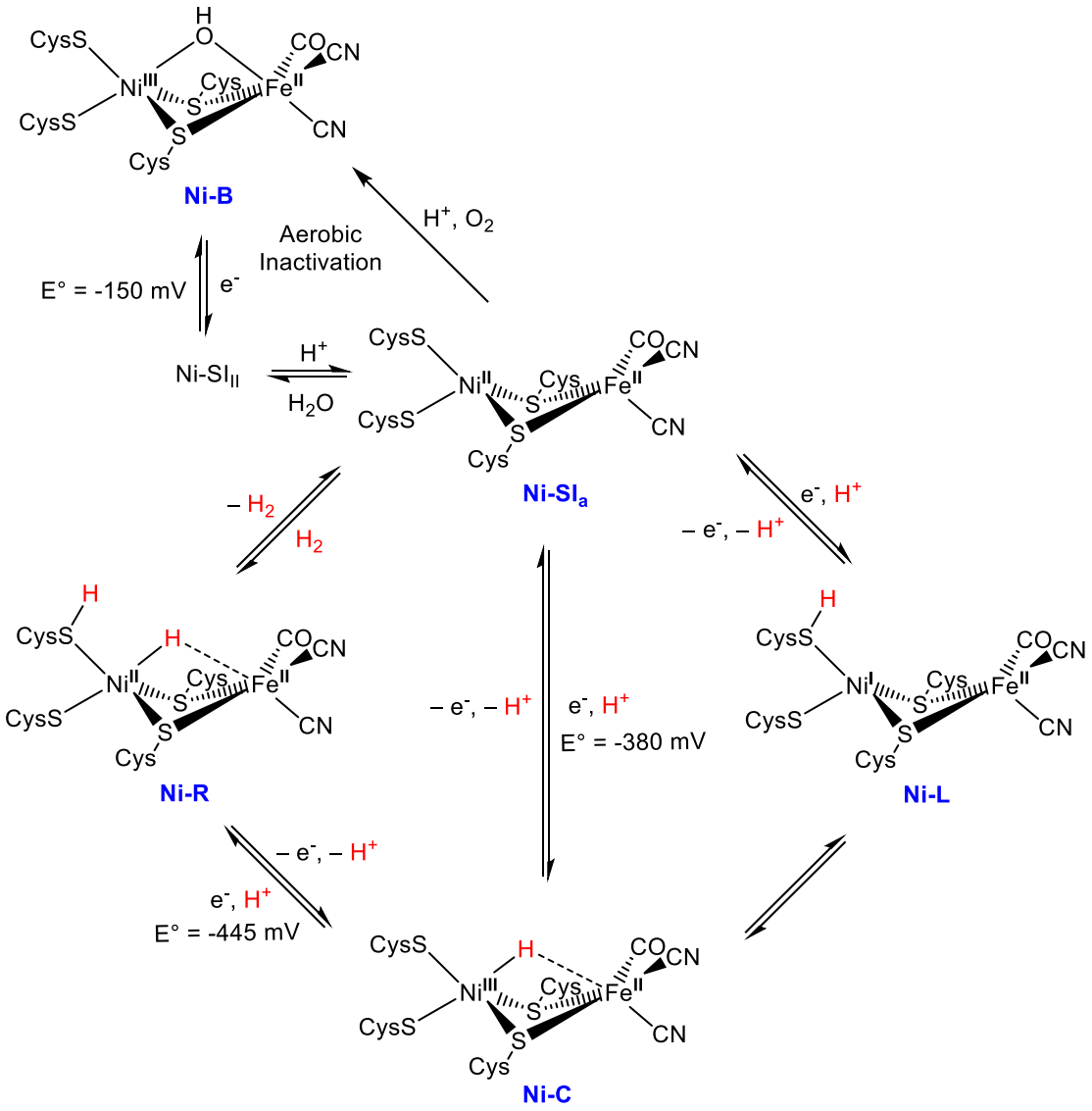

Scheme 1.3. Proposed catalytic cycle of [NiFe]-H_2ase. Standard potentials are vs NHE, at pH 8 and 30 ºC.[83] Ni-SI_a = silent-active state, Ni-L = light state, Ni-C = catalytic state, Ni-R = reduced state.

A combination of spectroscopic and crystallographic data has provided a clear picture of the proposed catalytic mechanism of H_2 activation by [NiFe]-H_2ase depicted in Scheme 1.3. In total

eleven states have been determined but only three, possibly four, are proposed states in the catalytic cycle, whereas the other states are a result of in-vitro isolation and processing. Although the minority of these states are proposed to be involved in catalysis, isolation of these aerobically modified states led to the discovery that [NiFe]-H_2ase can be reversibly inactivated by O_2 and CO. [84, 85] As isolated, the enzyme is in its aerobically inactive states composed of a mixture of its 'unready' (Ni-A) and 'ready' (Ni-B) state.[86] The Ni-A state is postulated to feature a bridging $^{-}$OOH ligand, requiring longer times of reactivation (> 1 hr).[86, 87] Whereas, the Ni-B state features a bridging $^{-}$OH, as determined by its crystallography, and can be activated back to its catalytic active state known as the silent-active state in a relatively short time (< 1 min.) through stepwise reduction to the Ni-SI_r state and protonation to form water. Once the Ni-SI_a state is generated, the enzyme is poised to activate H_2.

Although there is some debate about how [NiFe]-H_2ase performs H_2 oxidation, the widely accepted mechanism is shown in Scheme 1.3. The catalytic mechanism begins in the Ni-SI_a state ("Ni silent-active" due to the lack of EPR activity) consisting of a Ni^{II}-Fe^{II} core that has been characterized by FTIR and X-ray crystallography.[66] Although the low-spin (LS) configuration of Fe^{II} is well established, there is still some debate about the spin-state of Ni^{II} (LS, $S = 0$ or HS, $S = 1$) in the Ni-SI_a state. One would predict the Ni^{II} in the distorted tetrahedral to be HS, $S = 1$ based on crystal field theory. This predicted spin-state is in agreement with experimental data from Ni L-edge X-ray absorption spectroscopy[88] and computations showing that the HS Ni^{II} is more energetically favorable (20-30 kcal/mol) than LS Ni^{II}.[78, 89, 90] However, experimental results from magnetic circular dichroism[64] and saturation magnetization[91, 92] studies along with computations[93] have pointed to a low-spin (LS) ($S = 0$) Ni^{II}. It is important to note that the stability of the spin-state is dependent on the functional and basis-set used for the computations. Although the spin-

state of Ni^{II} in the Ni-SI_a state is still debated, the consensus is that this state is responsible for binding H_2 and initiating catalysis.

Upon binding to Ni^{II}, H_2 is heterolytically split resulting in the hydride binding to Ni and protonation of the terminal SCys from the EPR silent Ni-R ("most reduced") state, having the greatest number of electrons. High-resolution crystal structure of this state, solved in 2015 by Ogata and coworkers,[68] revealed a bridging hydride (μ-H^-), with a stronger bond to Ni (1.58 Å) than Fe (1.78 Å). Assignment of the bridging hydride between the Ni^{II} and Fe^{II} in the Ni-R state was further supported by nuclear resonance vibrational spectroscopy.[94] In addition, the crystal structure revealed residual electron density at one of the terminal Cys residues suggesting the presence of a proton, consistent with the initial proposed site of protonation. However, an argument has been made that the arginine residues proximal to Ni could act as a viable site of protonation after H_2 activation, *vide supra*.[95] The stepwise oxidation of Ni and deprotonation of the CysS state affords the Ni-C state ("catalytic intermediate"), featuring a Ni^{III}-(μ-H)-Fe^{II} core. This state results in an EPR active LS (S = 1/2) complex due to the oxidation of Ni^{II} to Ni^{III}. Although no crystal structure has been determined, the μ-H^- ligand has been confirmed by HYSCORE and ENDOR (pulse EPR techniques) that captured spin-coupling between the ^1H nucleus and Ni^{III} suggesting that the H^- is more closely bound to the Ni.[96, 97] The reductive elimination of the Ni^{III}-H reforms Ni-SI_a thus completing the catalytic cycle.

Despite the consensus that the catalytic mechanism goes through these three states, a fourth intermediate has been proposed, the Ni-L ("light") state. This intermediate is proposed to lie between the Ni-SI_a and Ni-C state, and forms from the tautomerization of the Ni-C state resulting in a Ni^{I}-Fe^{II} oxidation state and a proton on the terminal CysS.[98] Presence of the Ni-L state was originally proposed from the disappearance of the EPR and HYSCORE signals associated with

the Ni-C state upon low-temperature irradiation utilizing white light.[99-101] However, due to the enzymes activity in the dark, the formation of Ni-L was not immediately thought to be mechanistically viable. However, *in-situ* protein film IR electrochemistry revealed the formation of Ni-L in the absence of light indicating that it can be a possible pathway during catalysis.[102-104] The general consensus is that catalysis can follow two pathways; (i) directly to the Ni-SI_a state from the Ni-C state, through proton coupled electron transfer (PCET), or (ii) through its tautomerization to the Ni-L state and the reductive elimination of the proton.

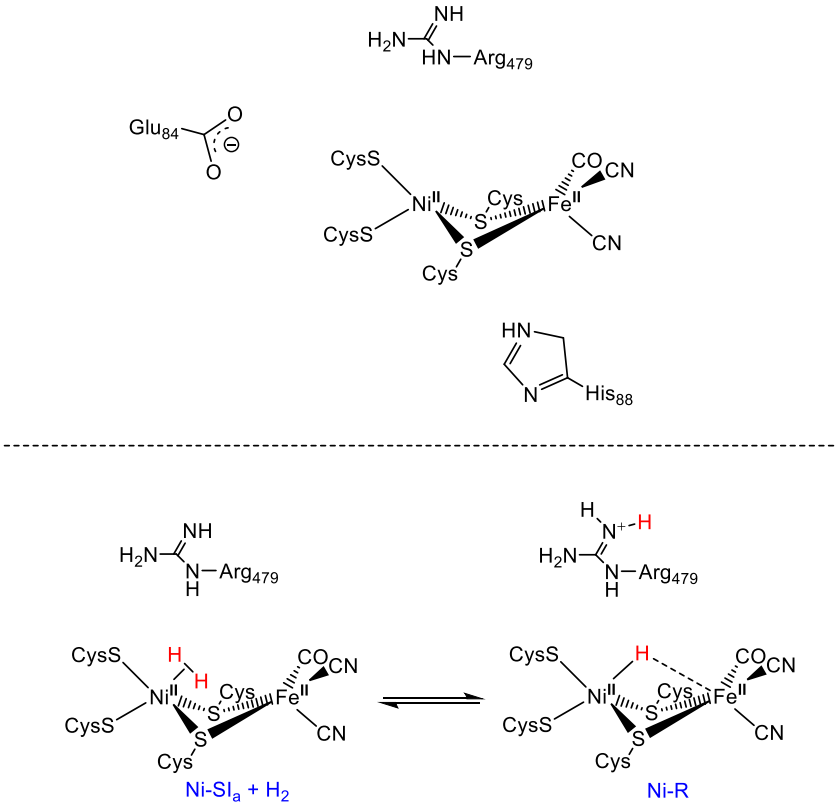

Figure 1.8. (*top*) Depiction of [NiFe]-H_2ase active site of *D. vulgaris* Miyazaki F with select amino acids and (*bottom*) proposed mechanism of Arg479 acting as a base upon H_2 scission by Ni-SI_a.

Three second coordination sphere residues are proposed to have a large impact on the activity of [NiFe]-H_2ase, as shown in Figure 1.8. A conserved histidine residue (His88, see Figure 1.8) resides ~3.4 Å from one of the bridging thiolates and is poised to act as a hydrogen bond (H-bond) donor, and is proposed to play a role in modulating the electronic structure of the active site.[37] Computations by Agrawal and coworkers reveal that the H-bond shifts 6-7% of the spin density from the bridging sulfur to Ni as a possible avenue to promote Ni centered oxidation rather than at the SCys.[105] An arginine residue (Arg479, see Figure 1.8) located above the Ni and Fe, ~4.5 Å away, has been implicated as the proton relay site (*vide supra*) in the Ni-R state in place of the terminal cysteine residue.[95] Mutation of this residue to a lysine significantly reduces the enzyme's H_2 oxidation efficiency and rate, observed by a 10-fold increase in the potential-dependent Michaelis constant, and suppresses H_2 production.[95, 106, 107] Lastly, a glutamate residue (Glu34, see Figure 1.8), is proposed to H-bond to one of the terminal Cys ligands, and has been implicated in the proton transfer (PT) during catalysis.[108] Mutation of this residue to glutamine, which acts a H-bond donor but does not allow PT, shows only 1% of the activity of wild-type H_2ases.[109] Mutagenesis studies of the Arg479 and Glu34 residues show that the ability to control H^+ transfer to and from the active site is important for the activity of [NiFe]-H_2ase.

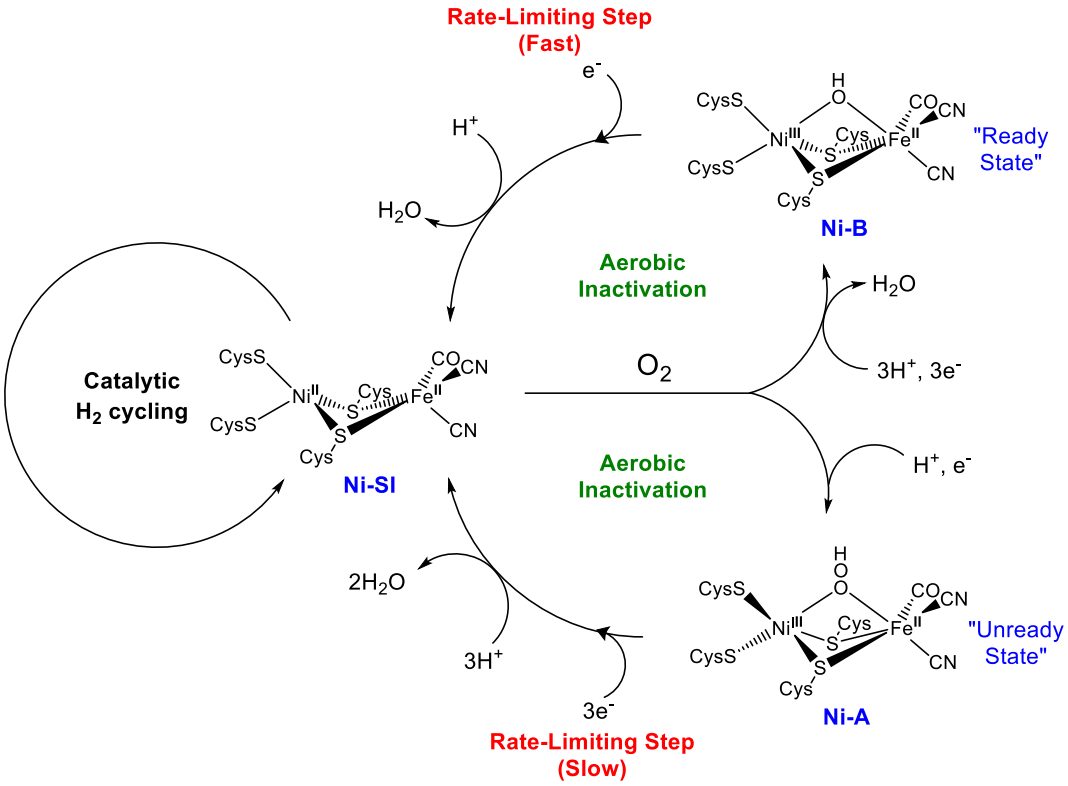

Figure 1.9. Simplified scheme showing the reparative mechanism from O_2 damage by membrane bound H_2ase. The Ni-B state is the 'Ready' state and Ni-A state (red) is the 'Unready' state.

One unique feature of [NiFe]-H_2ase is that it is the only H_2ase that shows O_2 tolerance, meaning that [NiFe]-H_2ase has mechanisms to repair itself upon oxidative deactivation and to sustain H_2 production in the presence of O_2.[110] O_2-tolerant membrane bound [NiFe]-H_2ases (MBHs) is the most well understood of these O_2-tolearant H_2ases. This class of [NiFe]-H_2ases is able to repair its self by reducing O_2 to H_2O, requiring $4e^-$ and $4H^+$ (O_2 + 4H+ 4e- → 2 H_2O), seen in Figure 1.9, and can be viewed like an oxidase, although a slow one (k_{cat} of 10^{-1} s^{-1}).[111] The prevailing proposal for the sustained activity of [NiFe]-H_2ase upon O_2 damage is the avoidance of forming the 'Unready' (Ni-A) state due to its slow activating times (~0.00025 s^{-1} at 10 °C) compared to the 'Ready' (Ni-B) state (~0.03 s^{-1} at 10 °C).[111] This circumvention requires rapid transfer of electrons and protons, proposed to be sequential, to form the Ni-B state before formation of the Ni-A state.

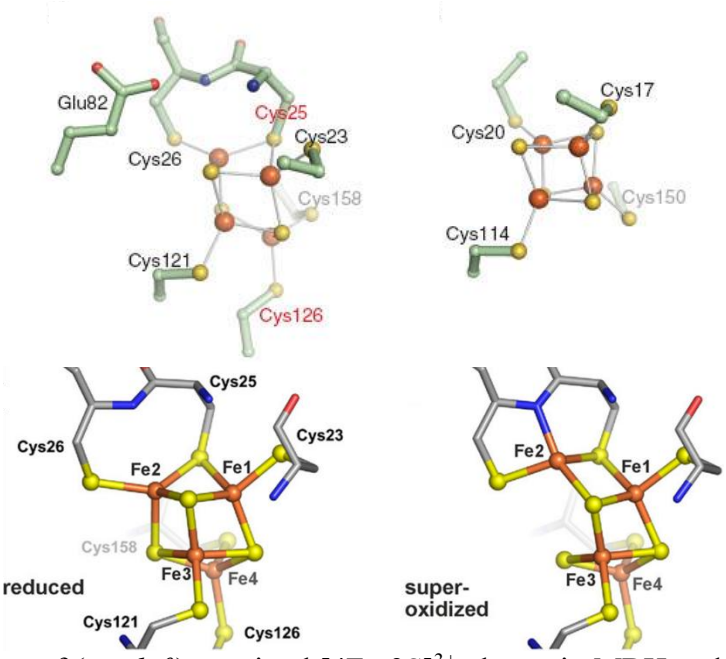

Figure 1.10. Structure of (*top left*) proximal $[4Fe\text{-}3S]^{3+}$ cluster in MBH and (*top right*) proximal $[4Fe\text{-}4S]^{2+}$ cluster in standard H_2ases. Fe = orange and S = yellow. Figure taken from Shormura, Y. et al.[112] Structure of (*bottom left*) reduced and (*bottom right*) super oxidized form of the proximal $[4Fe\text{-}3S]^{3+}$ cluster in MBH. Figure taken directly from Lubitz et al.[63]

This attribute of MBHs is proposed to be due to a unique conserved proximal $[4Fe\text{-}3S]^{3+}$ cluster that, when compared to standard [4Fe-4S] cluster, seen in Figure 1.10, has two 'extra' CysS residues, and substitution of one of the CysS residues for a sulfide.[113, 114] This substitution allows for the cluster to accommodate a super-oxidized state, $[4Fe\text{-}3S]^{3+/5+}$, through a conformational change that results in the breaking of a Fe-S bond and coordination of Fe to a deprotonated peptide N-atom on one of the 'extra' cysteine residues, shown in Figure 1.10.[112, 115] This conformational change is critical for facilitating an additional electron, that the $[4Fe\text{-}4S]^{3+/4+}$ cluster in standard H_2ases cannot provide, for the rapid reduction of O_2 to the bridged hydroxide in the Ni-B state. Once generated, the N-B state can reactivate to release H_2O enabling the enzyme to resume activity.

Although both [FeFe]- and [NiFe]-H_2ase reversibly catalyze the reduction of protons, they display some catalytic bias. Activity of these bidirectional enzymes varies, and several factors influence the direction in which H_2 is processed. One factor is the location of the H_2ase in the cell. H_2ases located in the cytoplasm often evolve H_2 whereas membrane-bound H_2ases oxidize H_2.[37] Another factor that controls directionality of HER is the strength at which the active site binds H_2. This binding strength is exhibited by the inhibitory effect of H_2, quantified by the multiple order of magnitude lower Michaelis-Menton constant for [NiFe] ($\sim 10^{-7}$ to 10^{-4} M) than [FeFe]-H_2ase ($\sim 10^{-4}$ to 10^{-3} M).[116] Therefore it follows that, [NiFe]-H_2ases tend to oxidize H_2 whereas [FeFe]-H_2ases tend to evolve H_2. [FeFe]-H_2ases are generally more active for both catalytic processes than their Ni counterpart, metrics of activity shown in Table 1.2. For example, those enzymes expressed for H_2 uptake, such as *Ralstonia* [NiFe] hydrogenase, bind H_2 strongly leading to modest HER reactivity, with TOF values of 70 s^{-1}.[110] Despite the difference in catalytic bias, H_2ases share similar features in their catalytic cycles. Both enzymes invoke a metal-bound hydride, terminal for [FeFe]-H_2ase and bridging for [NiFe]-H_2ase, and both utilize a base to serve as a proton relay site, the apical nitrogen in the adt^{2-} ligand of [FeFe]-H_2ase and the terminal cysteine of [NiFe]-H_2ase. However, what [NiFe]-H_2ases lack in their activity they make up for in their robustness making them attractive targets for industrial use in water splitting and fuel cells. Despite this desirable attribute, there are several factors hindering their use on an industrial scale: (i) the large size of the enzymes lowers the amount of catalyst sites that can cover the surface area of the electrode compared to the smaller Pt-nanoparticles, and (ii) low yields of expression and purification.[117] These limitations have spurred research into developing low-molecular weight HER electrocatalysts inspired by the native enzyme to use in place of Pt based electrodes.

Table 1.3. Catalytic bias and metrics for hydrogenases.

Hydrogenase Enzyme	Reaction Catalyzed	Turnover (s^{-1})[a]	Overpotential (mV)
[Fe]-only	H^+ reduction	555[b]	*n.a.*
	H_2 oxidation	215[c]	
[FeFe]	H^+ reduction	9000[d]	~0
	H_2 oxidation	28000[e]	
[NiFe]	H^+ reduction	640[f]	0 – 100[x]
	H_2 oxidation	6000[g]	

[a]Highest reported values. [b]*Metahnaobacterium thermoautotrophicum,* pH 6.5, [c]*Metahnaobacterium thermoautotrophicum,* pH 7.5, [d]*Desulfovibrio desulfuricans*, 30 ˚C, pH 8.0, methyl viologen. [e]*Desulfovibrio desulfuricans*, 30 ˚C, pH 8.0, benzyl viologen. [f]*Desulfovibiro gigas,* 30 ˚C, methyl viologen at -446 mV vs SHE. [g]*Allochromatium vinosum*, pH 7, 40 ˚C, at 200 mV vs SHE. [X]Depends on pH and hydrogenase. Higher overpotential correlates with higher pH and MBHs.[663]

1.3 Ni Thiolate Complexes

One way in which to gain a better understanding of the properties of an enzyme's active site and its reactivity is to develop low-molecular weight analogs. The power of these synthetic analogs of [NiFe]-H_2ase was exhibited by Yamamura and coworkers nearly 40 years ago.[118] Prior to the first reported crystal structure of [NiFe]-hydrogenase in 1995, it was clear from the EXAFS data of a F_{420}–reducing [NiFe]-H_2ase that Ni was coordinated by CysS ligands; however, it was unclear what the exact number of CysS ligands were.[119] To help determine the number, Yamamura reported a series of Ni- thiolate complexes with varying amounts of thiolates ligated to Ni.[118] By comparing the $Ni^{III/II}$ oxidation potential of the synthetic analogs to that of [NiFe]-H_2ase, Yamamura was able to predict the correct number of sulfur-atoms ligating Ni in the native enzyme. Since these Ni-thiolate models were reported in the 1980s, the synthesis and properties of many Ni tetrathiolato complexes have been reported, *infra vide*. These complexes utilize monomeric and bidentate ligands that incorporate both alkyl and aromatic thiolates. All complexes have the same goal, i.e, to mimic the pseudo-tetrahedral and thiolate-rich coordination sphere of the Ni site in [NiFe]-H_2ases.

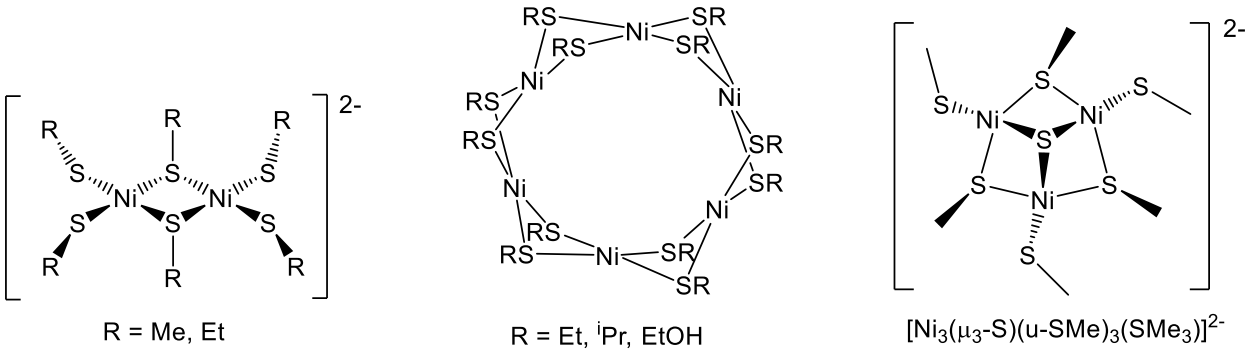

Figure 1.11. General structure of multinuclear Ni^{II} alkylthioaltes in a (*left*) open-chain, (*middle*) ring, and (*right*) capped structure.

The simplest of these models consist of homoleptic $[Ni(SR)_4]^{2-}$ complexes with monodentate alkyl and aromatic thiolates. Ni thiolates, and transition metal-thiolate complexes in general, have the tendency to aggregate creating oligomeric complexes featuring bridging thiolates.[120] Aggregation is exclusively the case for Ni alkyl thiolate complexes, which have no reported monomeric $[Ni(SR)_4]^{2-}$ analogs. Under low alkyl-thiolate/Ni ratios, isolable complexes take on the general form $[Ni_n(SR)_{2n+2}]^{2-}$ (n = 2, 3; R = Me, Et)[118, 121] or $[Ni_n(SR)_{2n}]$ (n = 4, 6, 8; R = Et, ^{i}Pr, EtOH, CyNMe, SCH_2COOEt)[122-127] depicted in Figure 1.11. Complexes of the general form $[Ni_n(SR)_{2n+2}]^{2-}$, shown in Figure 1.11, are open chain complexes with each Ni^{II} in a square-planar geometry possessing short Ni-S bond lengths (2.21 – 2.22 Å) that are generally described as covalent in nature. Complexes that take of the general form $[Ni_n(SR)_{2n}]$ are cyclic with Ni^{II} in a square-planar geometry possessing short Ni-S bond lengths (2.19 – 2.22 Å). Even increasing the ratio of alkyl thiolate to Ni (4.4:1) leads to the formation of unusual S-bridged trimeric complex $[Ni_3(\mu_3\text{-}S)(\mu\text{-}SMe)_3(SMe)]^{2-}$ complex with containing a capping sulfide with three square-planar NiS_4 units in a polycyclic system, shown in Figure 1.11.[128] Ni alkyl-thiolate complexes are known to further undergo oligomerization upon or exposure or synthesis in protic solvents.[122] In turn, use

of alkyl-thiolates are not ideal candidates for mimicking the pseudo-tetrahedral structure of the single Ni site in [NiFe]-H_2ase.

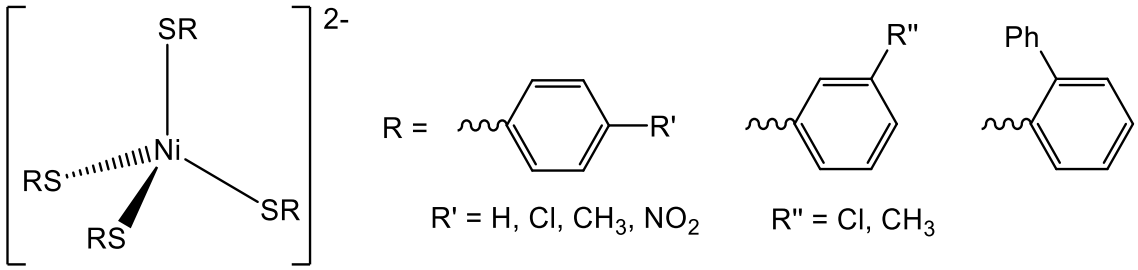

Figure 1.12. General structure of homoleptic Ni^{II} arylthioaltes that adopt a tetrahedral geometry.

On the other hand, the formation of Ni thiolate oligomers can be controlled utilizing aromatic thiolates, most likely due to the increase in steric bulk of the phenyl rings. These paramagnetic systems take on the general form $[Ni(SPh)_4]^{2-}$ ($S = 1$) in which the phenyl ring contains substituents in various positions, shown in Figure 1.12. The successful synthesis and isolation of these homoleptic mononuclear complexes requires excess thiolate conditions (> 4 PhS^-/Ni) in a polar, aprotic solvent. Similar to alkyl thiolates, depression of the ligand ratio or exposure to protic solvents (H_2O, MeOH) leads to intractable polymers.[118] However, the exact identity of these polymers and the process of formation remains ill-defined. In general, these complexes adopt a tetrahedral (τ_4 = 0.81 to 0.90) geometry with longer Ni-S bond lengths (2.27 – 2.33 Å) (Table 1.3). The driving force for tetrahedral geometry is proposed to be due to favorable overlap between the S-pπ orbitals and the C-pπ of the aryl when the Ni-S vector is coplanar with the aryl ring, depicted in Figure 1.13.[129] Distortions from ideal tetrahedral geometry is proposed to arise from the sterically unfavorable contacts between the *o*-H of the phenyl ring and the Ni and S atoms. In turn, these monomeric, tetrahedral $[Ni(SPh)_4]^{2-}$ complexes serve as reasonable structural models of the pseudo-tetrahedral Ni site in [NiFe]-H_2ase (τ_4 = 0.54).[66]

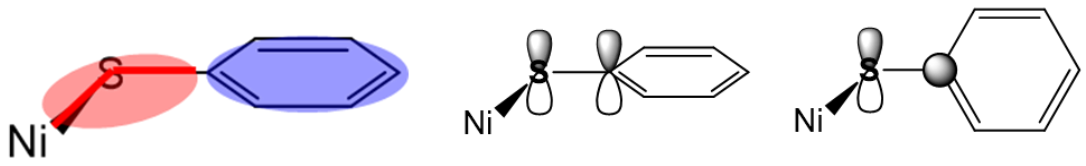

Figure 1.13. (*left*) Planes defined by the Ni-S vector (red) and aryl ring (blue), (*middle*) simplistic depiction of S-pπ and C-pπ when the Ni-S vector and aryl ring are coplanar, and (*right*) simplistic depiction of S-pπ and C-pπ when the Ni-S vector and aryl ring are perpendicular.

Although the solid-state structure of the Ni^{II} arylthiolate complexes indicate a monomeric and nearly tetrahedral structure, these systems exhibit interesting behavior in solution. Upon dissolution in polar, aprotic solvents (MeCN, DMSO) a small amount of diamagnetic (S = 0) material is observed by ^{1}H NMR.[129, 130] Furthermore, solution-state magnetic susceptibility values (μ_{eff} = 2.5 – 3.0 in CD_3CN, DMSO-d_6) are concentration and temperature dependent.[91, 129, 130] These solution-state properties point to an equilibrium between $S = 1 \leftrightarrow S = 0$ complexes. The S = 0 complex is ill-defined, but has been attributed to either a solvated $[Ni(SR)_3(solv)]^-$ complex or a bridging dimeric complex $[Ni(SR)_2(\mu\text{-}S)_2Ni(SR)_2]^{2-}$ complex.[131] Despite the multiple speciation, the monomeric complex is the predominate species upon dissolution based on solution-state μ_{eff}.

Given the speciation and thiolates susceptibility towards oxidation, it is not surprising that the electrochemistry of these $[Ni(SPh)_4]^{2-}$ complexes is convoluted. CV measurements showed irreversible $Ni^{III/II}$ couples [132, 133] possibly as a consequence of Ni^{III}-thiolate species undergoing auto redox decomposition (Ni^{III}-SR ↔ Ni^{II}--˙SR ↔ Ni^{II} + ½ RSSR) or oxidation of the bound thiolate.[134] In addition, the E_{red} features of the cyclic voltammetry (CV) are referred to as "complicated" suggesting some decomposition at the electrode. Despite the complications seen in the electrochemistry of these complexes, the electronic donating capacity of the coordinated thiolate ligands has an impact on the $Ni^{III/II}$ potentials. DPV measurements reported by Yamamura determined the $Ni^{III/II}$ potentials of $[Ni(SPh\text{-}X)_4]^{2-}$ (-0.05 to -0.40 V vs SCE) featuring a series of

electron-donating and withdrawing groups on the aryl ring (R = H, *p*-Cl, *p*-Me, *p*-NO_2, *m*-Me, see Fig 12). Although it is unclear if the potentials are correctly assigned to the $Ni^{III/II}$ couple of monomeric complexes, results suggest an inverse relationship between the oxidation potential and the Hammett parameter of the aryl ring consistent with the anticipated change of electron density at the thiolate.[118]

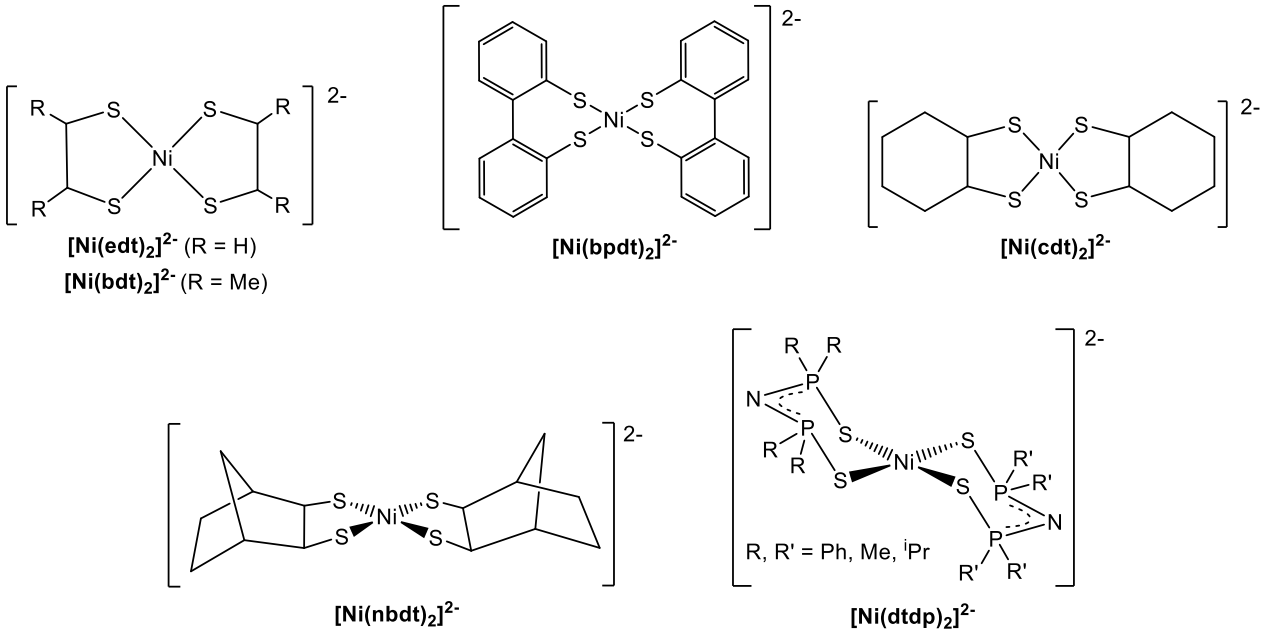

Figure 1.14. Mononuclear Ni^{II} tetrathiolates that contain chelating dithiolate ligands.

The problems presented by utilization of monomeric thiolates (protic instability, ill-defined equilibrium upon dissolution, and complex electrochemistry) inspired the synthesis of more robust Ni tetrathiolates utilizing chelating dithiolates, depictions of structures shown in Figure 1.14. The simplest of these models incorporate an ethane dithiolate (edt^{2-}), first reported by Holm.[135] Reacting edt^{2-} with $NiCl_2$ in a 2:1 ratio unexpectedly yielded a dimeric $[Ni_2(edt)_3]^{2-}$ complex with both Ni sites show a small deviation from ideal planarity with relatively short Ni-S bond lengths (Table 1.3). A similar fate is observed for Ni complexes containing butane dithiolate (bdt^{2-}), biphenyl dithiolate ($bpdt^{2-}$), and *o*-xyl dithiolate.[136, 137] However, the presence of the excess ligand to Ni (10:1 for edt^{2-} and 4:1 for $bpdt^{2-}$) leads to isolable and crystalline monomeric complexes

$[Ni(edt)_2]^{2-}$ and $[Ni(bpdt)_2]^{2-}$.[136-139] All the monomeric complexes are square-planar with short Ni-S bond lengths relative to the $[Ni(SPh)_4]^{2-}$ tetrahedral complexes, parameters shown in Table 1.4. Isolation of monomeric complexes enables the oxidation chemistry of synthetic models that better mimic the active site to be interrogated. Both $[Ni(edt)_2]^{2-}$ and $[Ni(bpdt)_2]^{2-}$ exhibit quasi-reversible $Ni^{III/II}$ couples at -0.69 V and -0.35 V (vs SCE, DMF), respectively with the quasi-reversibility most likely due to degradation of the complex at the electrode. Despite the successful isolation of the monomeric complexes, they convert to their dimeric counterparts in both aprotic and protic solvents over the course of several hours.

On the other hand, Ni complexes utilizing norbornane dithiolate ($nbdt^{2-}$) and cyclohexane dithiolate (cdt^{2-}), seen in Figure 1.14, were shown to be more stable in both protic and aprotic solutions, i.e. remaining in their monomeric form.[140-142] The increased stability is proposed to be due to the ligand's bulkiness and rigid conformation of the chelate. Unsurprisingly, use of chelating ligands results in square-planar complexes with Ni-S bonds close to other reported square-planar NiS_4 complexes, Table 1.4. Isolation of the more stable NiS_4 complexes facilitates the reversible $Ni^{III/II}$ couples at -0.75 V and -0.76 V (vs SCE, DMF) of $[Ni(cdt)_2]^{2-}$ and $[Ni(nbdt)_2]^{2-}$ respectively. In addition, reversibility is further enabled by the electron-rich ligands that can better stabilize the Ni^{III} formed at the electrode. Due to the reversibility of the $Ni^{III/II}$ couple, an attempt to isolate the Ni^{III} species was performed. Exposure of air to a solution of $[Ni(nbdt)_2]^{2-}$ in DMF yielded an immediate color change from green to red brown. The EPR spectrum of this solution exhibits an axial signal with $g_{x,y} = 2.14$ and $g_z = 2.05$, consistent with Ni^{III} (S = 1/2), and the same EPR spectrum is observed with chemical oxidation, using $[Cp_2Fe]^+$, and controlled potential electrolysis. These complexes best resemble the reversible oxidation of $Ni^{III/II}$ in [NiFe]-H_2ase; however, lack a pseudo-tetrahedral geometry that is so unique to the enzyme. Lastly, a group of

stable dithiolate Ni^{II} complexes utilizes dithioimidodiphosphinato ligands, $[Ni(dtdp)_2]^{2-}$.[141, 143-145] This family of complexes exhibits an equilibrium between the tetrahedral and square-planar isomers. The tetrahedral isomers are observed in the solid-state when the ligands are symmetric and at higher temperatures when in solution. It was computationally determined that the spin-state (S = 0 or 1) is dependent on the twist angle of the S-P-N-P-N chain with a low energetic barrier between the isomers.[146] The electrochemistry of $[Ni(dtdp)_2]^{2-}$ has not been assessed. $[Ni(cdt)_2]^{2-}$ and $[Ni(nbdt)_2]^{2-}$ best resemble the reversible oxidation of $Ni^{III/II}$ in [NiFe]-H_2ase; however, lack the pseudo-tetrahedral geometry that is so unique to the enzyme.

Table 1.4. Select Bond Distances (Å) and τ_4 values from select Ni thiolate complexes.

	Complex	**Ni–S_{avg} (Å)**	**τ_4**	**ref**
Multimeric Ni-thiolato Complexes	$(Ph_4P)_2[Ni_2(edt)_3]$	2.210	0.11	[147]
	$(Et_4N)_2[Ni_3(pdt)_6]$	2.172	0.01[a], 0.17[b], 0.21[b]	[148]
	$(Et_4N)_2[Ni_2(Et)_6]$	2.214	0.09	[121]
	$[Ni(Et)_2]_6$	2.201	0.03	[124]
	$[Ni(\mu\text{-}SPh)_2]_{11}$	2.211	0.00	[149]
	$(Et_4N)_2[Ni_2(S\text{-}p\text{-}Cl\text{-}Ph)_6]$	2.214	0.07	[131]
Monomeric Ni-arylthiolato Complexes	$(Et_4N)_2[Ni(SPh)_4]$	2.292	0.83	[118]
	$(Et_4N)_2[Ni(S\text{-}p\text{-}Cl\text{-}Ph)_4]$	2.281	0.81	[129]
	$(Et_4N)_2[Ni(S\text{-}o\text{-}Ph\text{-}Ph)_4]$	2.288	0.90	[150]
	$(Et_4N)_2[Ni(S\text{-}p\text{-}Cl\text{-}Ph)_4]$	2.281	0.81	[129]
Monomeric Ni-alkylthiolato Complexes	$(Ph_4P)_2[Ni(edt)_2]$	2.194	0.00	[136]
	$(Et_4N)_2[Ni(bpdt)_2]$	2.216	0.04	[137]
	$[Li(DMF)(MeOH)_2]_2[Ni(nbdt)_2]$	2.183	0.00	[140]

[a]Central Ni, [b]Terminal Ni

1.4 NiS_4 HER Electrocatalysts

The goal of the low-molecular weight analogs is to better understand the interplay of structure-to-function relationships between the $Ni(SCys)_4$ site in [NiFe]-H_2ase. The closest structural analog are the $[Ni(SPh)_4]^{2-}$ complexes, seen in Figure 1.12. However, their HER activity has not been assessed most likely dies to their instability under protic conditions and complicated electrochemistry. The HER activity of the homogenous analogs is assessed by scanning the voltammogram of the complex in the presence of an acid as the proton source, often in an organic medium. A typical HER electrocatalyst undergoes two electrochemical (reduction events) and two chemical transformations (protonation events), known as E and C steps, respectively, to produce H_2 during the catalytic cycle (Scheme 1.4). Hydrogen evolution is thought to proceed through a metal-bound hydride. The redox-active metal facilitates the two-electron reduction of H^+ to form the bound hydride (H^-). H_2 can be formed through the heterolytic coupling of the hydride and proton, like [NiFe]-H_2ase, or the homolytic coupling of two metal-hydrides, formally $H\cdot + H\cdot \rightarrow H_2$. Although there are many Ni-based heterogeneous HER electrocatalysts, this review will focus on homogeneous catalysis. Four metrics are commonly assessed to determine the HER activity of homogeneous electrocatalysts, in no particular order: (i) TOF, (ii) overpotential (η), (iii) turnover number (TON), and (iv) faradaic efficiency (FE). TOF and η were defined prior, *vide supra*. TON is defined as the number of times the catalyst converts substrate to product per unit time. FE represents how efficiently the catalyst utilizes the electrons provided to yield product, reported as a percentage. The ideal HER electrocatalyst remains stable during turnover, has high TOF, TON and FE, and a low overpotential.

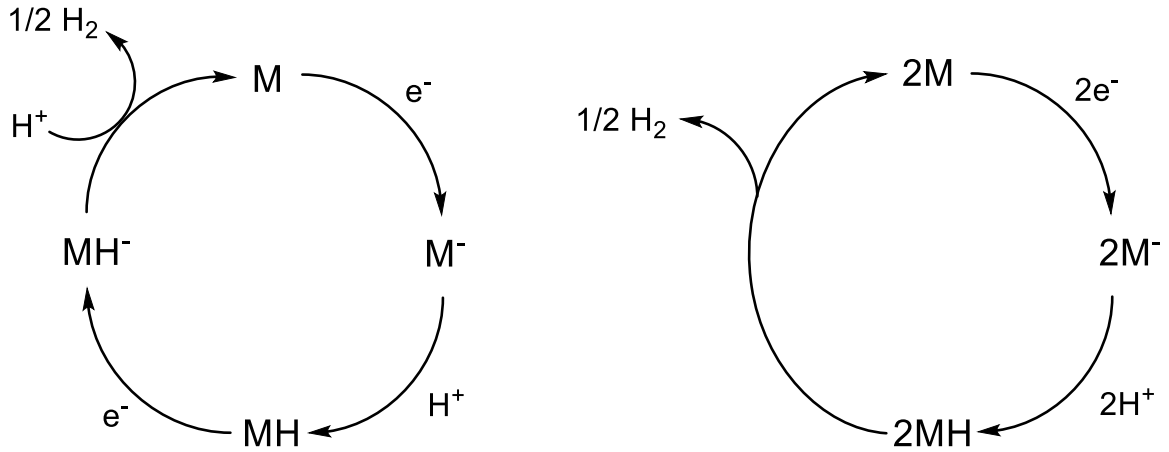

Scheme 1.4. General catalytic cycles for (*left*) heterolytic and (*right*) homolytic mechanism for HER.

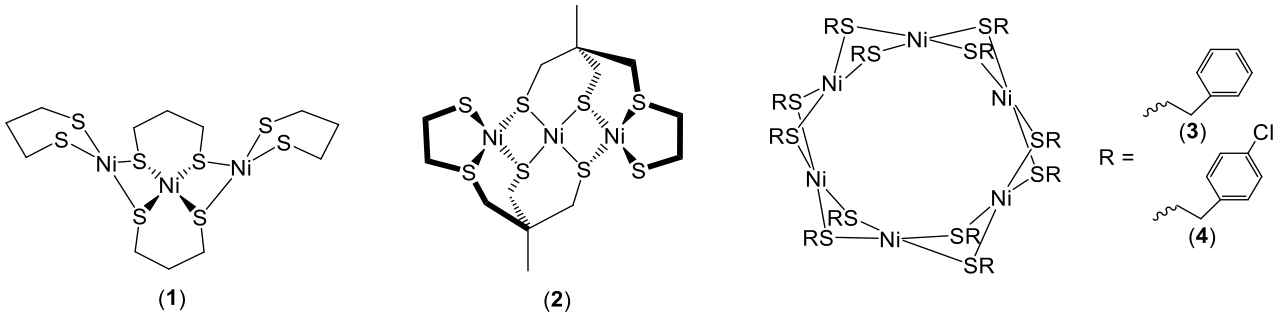

Figure 1.15. Ni thiolate cluster HER electrocatalysts.

A large number of mononuclear, homogenous Ni^{II} complexes have been reported as HER active electrocatalysts. Many reported HER electrocatalysts incorporate thiolate donors in a mixed donor set or completely lack thiolates all together due to the notable issue with $[Ni(SR)_4]^{2-}$, *vide supra*. In addition, some NiS_4 electrocatalysts have shown the propensity to deposit on the electrode giving rise to catalysis from the heterogeneous material.[151, 152] As such, it is important to ensure that the catalysis is not arising from heterogenous material deposited on the electrode during catalysis, commonly determined by a rinse test.[153] Deposition is mostly avoided for HER electrocatalysts that incorporate thiolate donors on mixed donor chelating ligands containing nitrogen, oxygen, and phosphorus. There are a handful reported HER electrocatalysts, shown in

Figure 1.15, that are Ni-thiolate multimers that square-planar Ni^{II} ions bridged by alkyl-thiolates, Ni-alkylthiolate trimers $(Ni_n(SR)_{3n+2})$[148, 154] (**1** and **2**) and hexanuclear metallacrowns $(Ni_6(SR)_{12})$[155, 156] (**3** and **4**). The only metrics that are reported for these multinuclear electrocatalysts are for **2** (TON = 5.0, FE = 30%).[154] Furthermore, the mechanisms of the multinuclear catalysts are not investigated in detail. In turn, the activity of these electrocatalysts will not be discussed.

1.4.1. Ni-Dithiolene HER Electrocatalysts

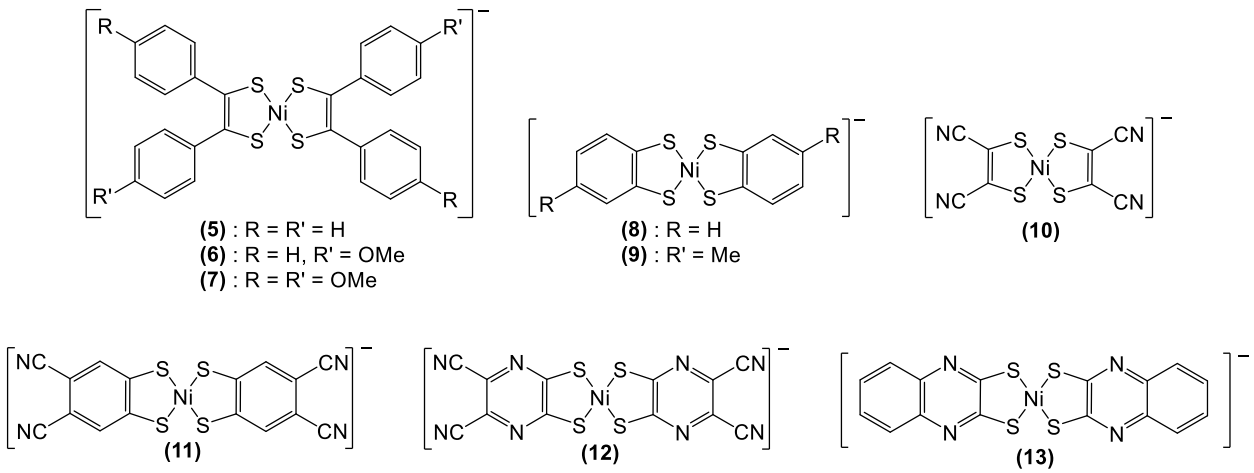

Figure 1.16. NiS_4 dithiolene HER electrocatalysts,

Table 1.5. Reported HER metrics and mechanisms of NiS_4 dithiolene electrocatalysts.

Catalyst	$^{-}/^{-2}$ (V)[a]	TOF (s^{-1})	η (V)	TON (h^{-1})	FE	Mechanism	H^+ Source	Ref
5[b]	-1.26 (r)	*n.r.*	*n.r.*	5	66%	ECCE	TFA	157
6[b]	-1.29 (r)	*n.r.*	0.96	8	83%	ECCE	TFA	157
7[b]	-1.33 (r)	*n.r.*	*n.r.*	4	74%	ECCE	TFA	157
8[d]	-0.92 (r)	*n.r.*	0.59	38	71%	ECCE	TFA	158
9[d]	-0.95 (r)	*n.r.*	0.47	53	88%	ECCE	TFA	158
10[d]	-0.08 (r)	*n.r.*	0.57	2	34%	ECCE	TFA	158
11[b]	-2.51 (r)	*n.r.*	1.10	*n.r.*	*n.r.*	ECCE	AcOH	159
12[e]	*n.r.*	*n.r.*	0.31	138	92%	C[ECEC]	H_2O (pH = 5)	160
13[g]	*n.r.*	*n.r.*	0.23	70	100%	C[ECEC]	H_2O (pH = 5)	160

[a]Potentials are vs Fc/Fc^+, [b]DMF, [d]MeCN, [e]Acetate buffer, [g]Borate buffer, (r) reversible couple, and *n.r.* (not reported).

The most common motif among mononuclear NiS_4 HER electrocatalysts, is the utilization of dithiolene ligands. Dithiolene ligands are termed 'non-innocent' because they are redox active and

can be viewed in a metal complex as either in the dianionic dithiolate, monoanionic radical, or neutral dithioketone state with a highly delocalized π-electron system over the ligand and metal.[161] In turn, the assignment of the electronic state of the metal is difficult and couples are reported as the overall charge of the complex. However, dithiolene ligands can stabilize low-valent metal oxidation states ($Ni^{I/0}$) due to the ligand's π-acidity making them attractive targets for reductive chemistry required for HER.

Mitsopoulou and Artero reported a series of HER catalysts, **5**-**11** in Figure 1.16, utilizing a dithiolene ligand with varying R-groups attached to the benzene ring.[157, 158] These catalysts in their neutral state are described two coordinated radical anionic thiolates a Ni^{II} ion, and all are proposed to go through an ECEC mechanism (Scheme 1.5) based on computations. Catalysis is initiated with the reduction to a di-anionic state (intermediate II) in which the added electron is delocalized across the S-S dithiolene and Ni. This E step causes a slight distortion away from the initial square-planar geometry. Next, two sequential protonation steps occur at the bound S-atoms in the cis-position (intermediate III, IV). A second reduction, again localized at the dithiolene-Ni orbitals, event yields a diprotonated monoanionic complex (intermediate V) setting up heterolytic coupling to evolve H_2. Coupling is proposed to go through the transition state (TS), shown in scheme 1.5, formed by intramolecular proton transfer from one -SH to Ni resulting in a further distortion of geometry. Although this distortion is necessary to evolve H_2, molecular rearrangement contributes to overpotentials. Given that **5**-**11** are proposed to go through a similar mechanism, one can see that the overpotential of these catalysts are directly related to the reduction potential needed to reach the di-anionic state. This relationship is best seen for **11** which possesses the highest overpotential and most negative reduction potential, Table 1.5. This relationship reveals that

overpotential of HER electrocatalysts can be modulated by the electronic donating capacity of the ligand.

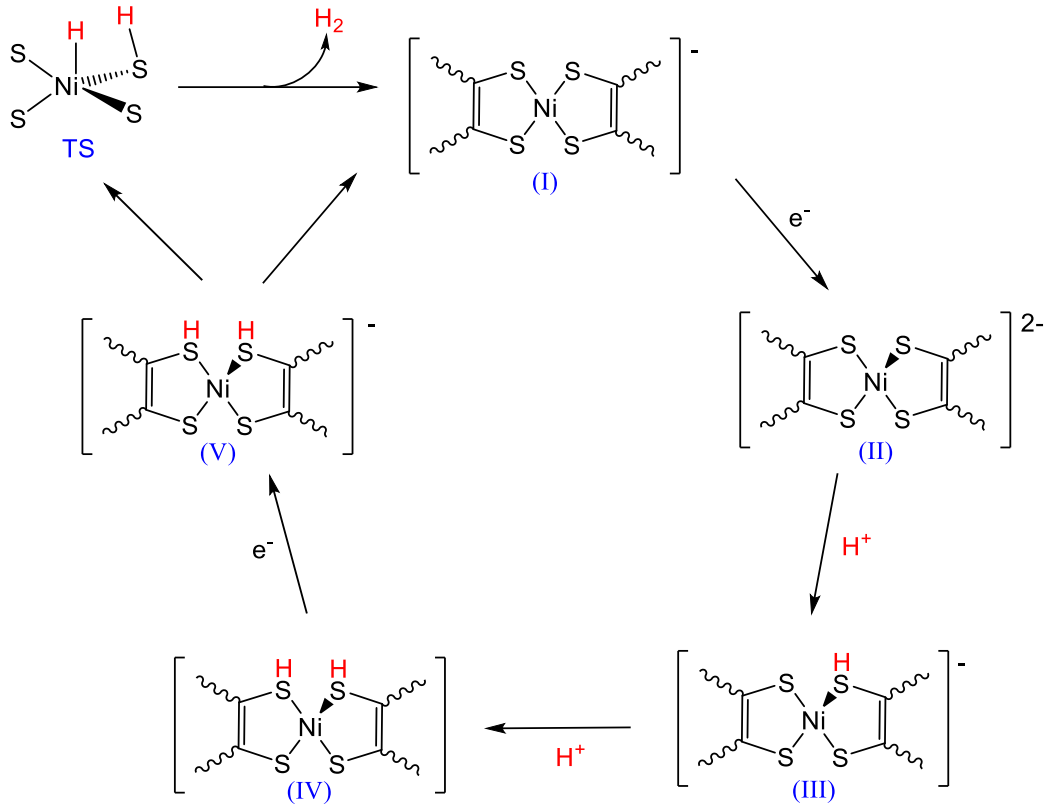

Scheme 1.5. Proposed mechanistic scheme for HER by **5** – **11** based on the relative energies of computed intermediates.

In an effort to reduce the overpotential Sakai and coworkers incorporated N-atoms of the aromatic dithiolene ligands to promote ligand-centered proton-coupled electron transfer (PCET) in HER electrocatalysis of **12** and **13**, seen in Figure 1.16.[160] As the name suggests PCET is broadly defiened as any process that involves the transfer of at least a single e^- and H^+ from one atom to another in a concerted or sequential manner, where sequential mechainsm involves a stable intermediate arising from a single e^- or H^+ transfer.[162] In a redox process, PCET occurs when the coupling of a H^+ and an e^- imparts an energietic advantage over solo e^- transfer by lowering the activation barrier. PCET can be determined by computing the energy of each step (H^+, e^-, H^+/e^-)

or by determining the redox potential dependency on pH known as Pourbaix diagrams (plotted as potential versus pH). Sakia and coworkers showed the PCET occurs in **12** and **13** utilizing Pourbaix diagrams; thus, leading the authors to propose two PCET steps on the pyrazine ligand during catalysis, mechanism shown in Scheme 1.6. PCET steps at pyrazine were also supported by the computed $SOMO_1$ of (**13** + e^-, H^+, intermediate II in Scheme 1.6) revealing significant orbital contribution from pyrazine and protonation of N, consistent with ligand centered PCET. Further investigation of these orbitals revealed a tautomer of $SOMO_1$, labeled $SOMO_2$ in Scheme 1.7, which contains a protonated S-atom with significant orbital contribution from the dithiolene, about ~30 kcal/mol less stable than $SOMO_1$. $SOMO_2$ represents the predicted SOMO for **5-11** upon reduction and protonation, intermediate (IV) in scheme 1.6. This result suggests that incorporation of a ligand to facilitate PCET decreases overpotential of HER electrocatalyst, seen by the almost ~0.8 V lower overpotential of **12** and **13** compared to **5-11**, see Table 1.. In addition, incorpration of more sites on the ligand frame of **12** and **13**, that can act as proton-relays, results in over double the TON for compared to **5-11**. These results suggest that (i) redox-active ligands can provide a more favorable, ie lower energetic, pathway for reductive chemistry to evolve H_2 and (ii) use of peripheral bases can be used to improve TON.

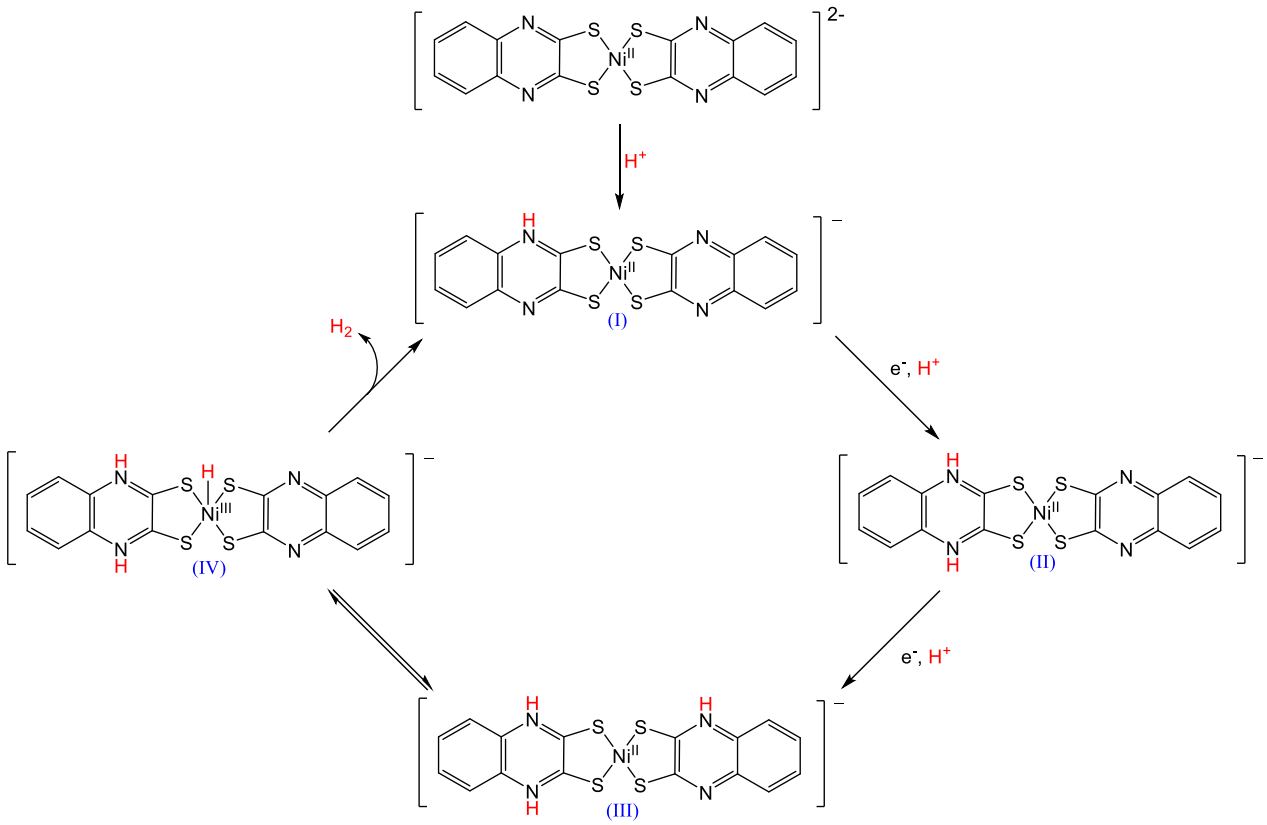

Scheme 1.6. Proposed mechanistic scheme for HER by **13** based on the relative energies of computed intermediates.

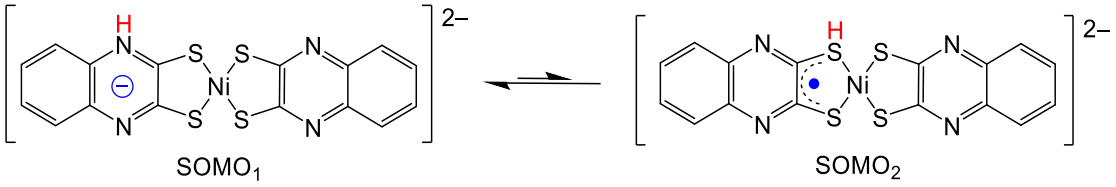

Scheme 1.7. Proposed tautomerization of the SOMO for **13** + H^+/e^-.

1.4.2. Ni-Thioether HER Electrocatalysts

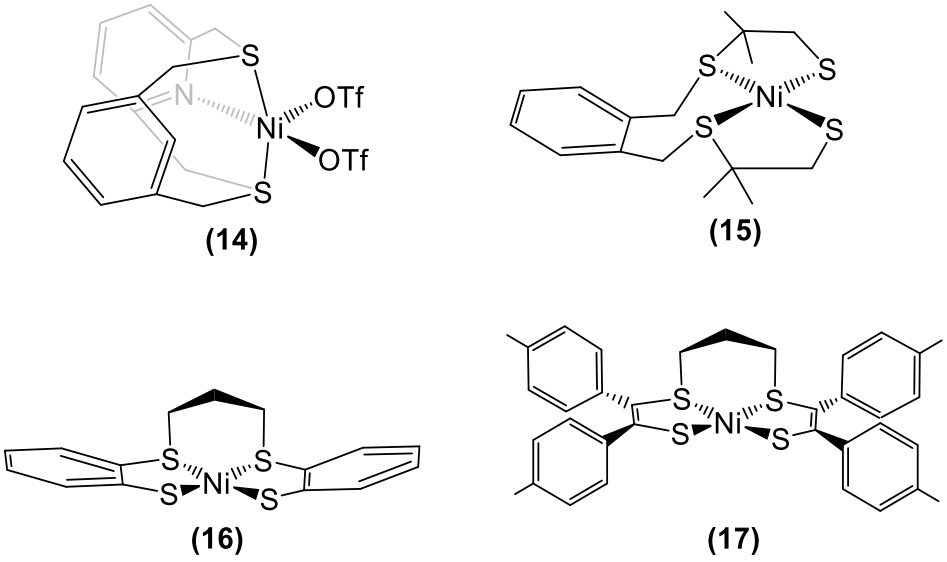

Figure 1.17. NiS_4 thioether containing HER electrocatalysts.

Table 1.6. Reported HER metrics and mechanisms of NiS_4 thioether electrocatalysts.

Catalyst	$Ni^{II/I}$ (V)[a]	TOF (s^{-1})	η (V)	TON (h^{-1})	FE	Mechanism	H^+ Source	Ref
15[b]	*n.r.*	2	*n.r.*	1.4	*n.r.*	*n.r.*	$Et_3NH{\cdot}Cl$	163
16[b]	-1.70 (q)	*n.r.*	0.76	*n.r.*	*n.r.*	ECEC	TFA	164
17[b]	-1.72 (q)	*n.r.*	0.82	*n.r.*	*n.r.*	ECEC	TFA	164

[a]Potentials are vs Fc/Fc^+, [b]DMF, (q) quasi-reversible couple, and *n.r.* (not reported).

Ligand sphere design is important to stabilize the multiple oxidations states ($Ni^{I/II/III}$) that Ni based HER electrocatalysts may go through. One such way is to utilize a donor sphere with mixed hard and soft bases in thiolate and thioether donor atoms. Thioethers are weaker σ-donors than the corresponding thiolates, and, generally, incorporate multidentate ligand constructs to stabilize their coordination to Ni^{II}. Although the tetradentate ligands predispose Ni^{II} to square-planar geometry, weaker Lewis basicity of thioethers, compared to thiolates, makes the Ni^{I} state more accessible by depressing the $Ni^{II/I}$ couple and stabilizing Ni^{I}, a soft acid. Incorporation of thioethers in the donor set of **14**, depicted in Figure 1.17, has aided in the isolation and *in-situ* spectroscopic identification (EPR, UV-vis) of a Ni^{I} state of a homogeneous Ni catalyst, albeit with no thiolates.[165, 166] Complex

15, see Figure 1.17, was initially used as a Ni precursor to form dinuclear models of the [NiFe] hydrogenase, however, it is active for HER albeit slowly and with no proposed mechanism.[163]

Although dithiolene based electrocatalysts involve the ligand in its redox activity, Mitsopolou and coworkers found that incorporation of an alkyl group in **16** and **17**, depicted in Figure 1.17, shifts the redox-activity to Ni.[164] This shift is due to (i) increased Ni character of the LUMO and (ii) increased nucleophilicity of the Ni, making the $Ni^{II/I}$ couple more positive. Due to the shift to Ni centered reduction, the computed mechanism proposes a Ni^{II}-H intermediate (III; Scheme 1.8) formed by an oxidative addition of Ni^0 through intramolecular proton transfer from a protonated S-atom of the bound ligand. Formation of Ni^{II}-H sets up heterolytic coupling to evolve H_2 going through a TS involving the protonation of a bound S-atom, cleaving the Ni-S bond, and finally coupling with the hydride. Cleavage and rebinding of one of the coordinated atoms from the metal during a chemical or catalytic prosses is commonly termed as hemilability and is a motif seen in other HER electrocatalysts, *vide infra*. Due to the Ni centered reduction in HER electrocatalysis of **16** and **17**, it is not surprising that the overpotential is directly correlated with the potential required to reduce $Ni^{II/I}$ (Table 1.6). Although increasing the basicity of the Ni through changing the electronic nature of the ligand promotes Ni centered activity, more akin to the native enzyme, it impacts the overpotential. The overpotential for **16** (Table 1.5) is ~0.3 V higher compared to its non-alkylated counterpart **8** (Table 1.4). The higher overpotential is due to a more negative potential, by ~0.8 V, required to induce catalysis for **16**. The dithiolene ligand in **8** provides a lower energetic pathway for reduction; thus, facilitating more efficient HER.

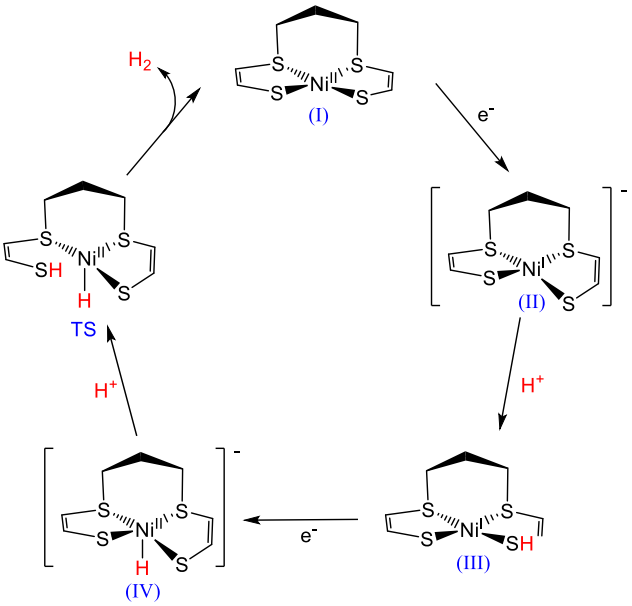

Scheme 1.8. Proposed mechanistic scheme for HER by **16** and **17** based on the relative energies of computed intermediates.

1.4.3. Ni-Substituted Rubredoxin as a HER Electrocatalyst

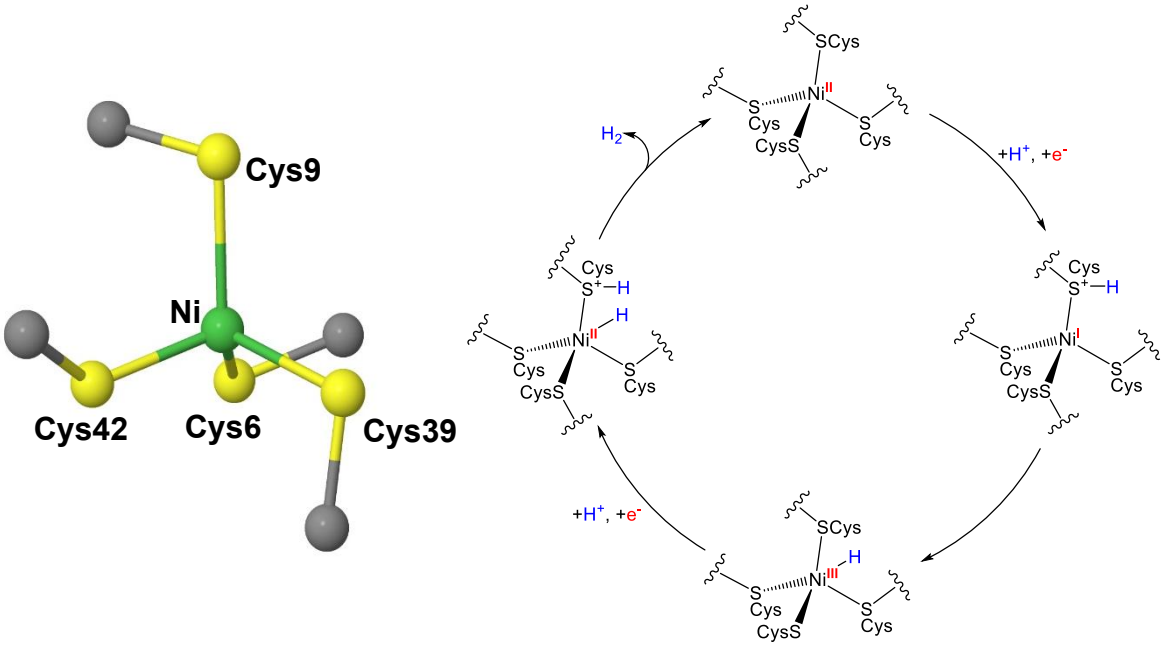

Figure 1.18. (*left*) Depiction of the Ni-substitute Rubredoxin active site from *Colstridium pasteurianum* (PDB: 1R0J) active site depicting coordinating ligands to Ni (green) and (*right*) its proposed catalytic mechanism for HER.

The repurposing of metalloproteins as mimics of natural metalloenzymes for small-molecule activation has provided another avenue to better understand the catalysts for enzymes such as Fe-superoxide reductase, acetyl-coenzyme A synthase, and O_2 and NO reducing enzymes.[167-170] The Moura and Shafaat groups have taken this approach utilizing rubredoxin (Rb) as a structural and functional mimic of [NiFe]-H_2ase. This small (5-6 kDa), electron-transfer protein coordinates Fe in a tetrahedral geometry by four cysteine residues. Fe in Rb, from *Desulfovibiro desulfruicans,* can be exchanged with Ni to maintain its $M(SCys)_4$ coordination sphere ($Ni\text{-}S_{avg}$ = 2.31 Å) and geometry (τ_4 = 0.84), active site shown in Figure 1.18.[66, 171-173] Ni-substituted Rb (NiRb) (PDB: 6NW1, 6RXN) is a close structural match to the Ni site in [NiFe]-H_2ase, Table 1.2. Use of the protein scaffold in NiRb affords several advantages over the synthetic systems, including, excluding multimeric speciation, decomposition in protic environments, and providing a secondary coordination sphere that can be modulated to see the impact on HER electrocatalysis.

HER activity of NiRb was first reported by Moura and coworkers in 1988, utilizing viologen assays, and more recently investigated for electrocatalysis by Shafaat through protein film electrochemistry.[171, 174] Shafaat reported the HER electrocatalysis of NiRb with a TOF value of 100 s^{-1} (acetate buffer, pH 4.5, 4 ˚C), which surpasses that of [NiFe]-H_2ase under similar conditions (TOF = 50 s^{-1}) but at higher overpotentials (η = 0.54 V).[174, 175] Higher overpotentials are, in part, due to the inefficient transfer of electrons to the active site of NiRb that lack [FeS]-clusters. Furthermore, the lack of the bridged Fe^{II}, that is proposed to modulate electron density, can also contribute to higher overpotentials. Interestingly, the native FeRb showed a lack of HER activity under the same conditions. Through spectroscopy and computations, it was proposed that NiRb follows a mechanism that mirrors [NiFe]-H_2ase, shown in Figure 1.18.[176] Computations suggest that formation of the Ni-L' and Ni-R' states of NiRb are generated through PCET involving the

reduction of the Ni and protonation of the bound SCys. Like in the native enzyme, H_2 evolves through the heterolytic coupling of Ni^{II}-H and a H^+ on the adjacent SCys. NiRd was also shown to perform HER in a solution of O_2-saturated buffer with minimal impact on the activity. O_2 was proposed to bind to the $Ni^{I}L$' state as opposed to the $Ni^{II}SI_a$, as in the native enzyme, and was computed to occur at a slower rate than H^+ reduction. NiRb is a good structural analog to the first coordination sphere of the Ni site in [NiFe]-H_2ase and catalysis HER at similar rates through a similar mechanism.

Several amnio acids near the active site in [NiFe]-H_2ase are proposed to impact the HER activity, *vide supra*. Considering the impact of these residues, Shafaat performed a series of mutations and studied the impact of HER activity.[173] Mutations of a valine to a glutamate residue, residing equidistance between the two coordinated CysS exhibits the largest impact on rate of HER. This mutation resulted in a 10-fold increase in the TOF from the wild type NiRb while only increasing the overpotential by ~20 mV. Magnetic dichroism simulations revealed that the mutation increases the solvent accessibility of the CysS ligand in the active site promoting better interaction with H^+. These mutation studies showcase the impact of secondary sphere can have on the performance of HER electrocatalysts. Chakraborty has also reported a bioengineered Cu storage protein featuring a square-planar $Ni(Cys)_4$ site but was only tested as a photocatalyst for HER.[177] NiRb is the closest structural mimics to the Ni-site in [NiFe]-H_2ase resulting in a mechanism that best parallels that of the native enzyme; thus, highlighting the importance in maintaining the thiolate-rich core about Ni^{II} in the pseudo tetrahedral geometry.

1.5. Mononuclear Ni-thiolate HER Electrocatalysts

1.5.1 NiS_2N_2 electrocatalysts.

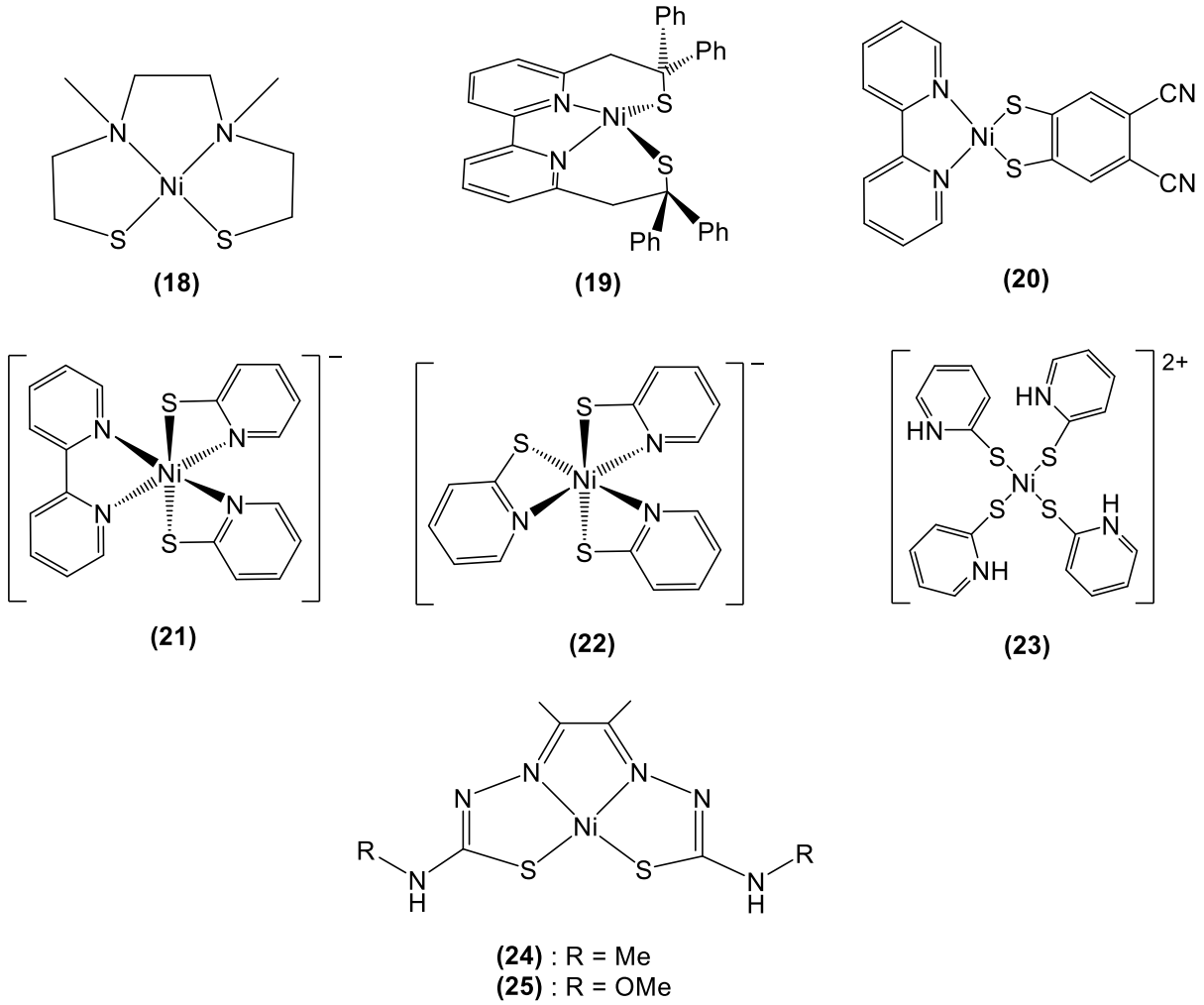

Figure 1.19. NiS_2N_2 HER electrocatalysts.

Table 1.7. Reported HER metrics and mechanisms of NiS_2N_2 electrocatalysts.

Catalyst	$Ni^{II/I}$ (V)[a]	TOF (s^{-1})	η (V)	TON (h^{-1})	FE	Mechanism	H^+ Source	Ref
18[b]	-1.52 (r)	1441, 5575	0.56, 0.67	*n.r.*	*n.r.*	ECCE	AcOH	178
19[b]	*n.r.*	22	*n.r.*	6	*n.r.*	*n.r.*	$Et_3NH{\cdot}BF_4$	179
20[d]	-1.54 (r)	*n.r.*	0.79	*n.r.*	*n.r.*	EECC	MCA[c]	159
24[b]	-2.31 (q)	4200	0.53	48	87%	ECEC	AcOH	162
25[d]	-2.20 (r)	3080	*n.r.*	21	80%	ECEC	$Et_3NH{\cdot}Cl$	163

[a]Potentials are vs Fc/Fc^+, [b]MeCN, [c]Chloroacetic acid, [d]DMF, (r) reversible couple, (q) quasi-reversible couple, and *n.r.* (not reported).

The use of mixed donor sets in Ni-thiolate containing HER electrocatalysts has become increasingly common. The most common donor sets employ tertiary amines N in donor sets resulting in NiS_nN_n (n = 2, 3) complexes **18**-**25** seen in Figure 1.19. The N/S donor sets tend to incorporate chelating or macrocyclic ligands in which the Ni is held in a square-planar geometry. As seen in NiS_4 HER electrocatalysts, redox-active ligands are commonly employed for NiS_nN_n (n = 2, 3) HER electrocatalysts except for **18**. Complex **18**, and other macrocyclic $Ni^{II}(N_2S_2)$ complexes, have been studied by Darensburg for their reactivity towards S-alkylation.[180] Upon alkylation of monomeric complexes, a S-bridged trimetallic $[(Ni^{II}N_2S_2)_2Ni^{II}]^{2+}$ complex forms, arising from the intermediate thioether complex, release of the Ni^{II} due to the more labile thioether, and its capture by the $Ni^{II}(N_2S_2)$ precursor. Wu and coworkers noted an absence of any investigation into their capability for H^+ reduction electrocatalysis and found that **18** catalyzes H^+ reduction at high rates (TOF of ~5000 s^{-1}) at modest overpotentials (~0.6 V).[178] Wu and coworkers suggest that the electrophilic thiolates play a vital role in proton transfer during catalysis seen in the proposed ECCE mechanism shown in Scheme 1.9. All reduction steps are proposed to take place at Ni, and, in turn, the first reduction step occurs at the $Ni^{II/I}$ (intermediate II). Next, two protonation events take place at each bound thiolate (intermediate II and IV). Protonation of the thiolates sets up a proton relay to form the Ni^{II}-H intermediate (V) through oxidative addition. To accommodate the bound-hydride, the other Ni-SH bond is cleaved, thus, positioning it to act as a proton relay site to evolve H_2 through heterolytic coupling. A similar mechanism is observed for **16** and **17**, scheme 1.8. These catalysts require two reductive steps to generate the hydride intermediate due the lower basicity of Ni, compared to NiRb and [NiFe]-H_2ase, as a consequence of the electron donating capacity of the donor set.

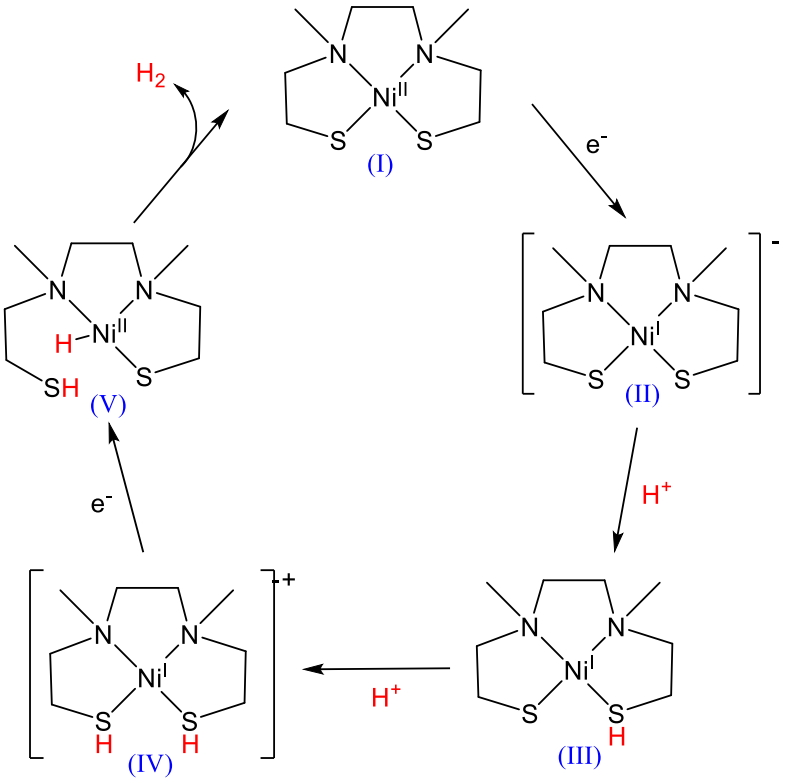

Scheme 1.9. Proposed mechanistic scheme for HER by **18** based on the relative energies of computed intermediates.

Redox-active ligands are common in NiS_nN_n (n = 2, 3) HER eletorcatalysts. One such redox active ligand used in Ni HER electrocatalysts is bipyridine (bpy) (see Figure 1.19, **19 - 21**). Like dithiolene ligands, incorporation of bpy in the coordination sphere around Ni presents an additional site of reduction during electrocatalysis. CV of **20** shows that two qausi-reversible peaks at -1.54 V (vs Fc/Fc^+) and -2.33 V (vs Fc/Fc^+) assigned to the $Ni^{II/I}$ couple and reduction of the bpy unit, respectively.[159] Upon addition of acid to the CV, catalysis was only initiated at the second reduction event implicating the reduction of bpy required for HER. Furthermore, this result suggests that the first two steps in the mechanism are EE, full mechanism shown in Scheme 1.10. To complete the mechanism, the authors determine the result of two sequential protonation steps (CC) utilizing computations after the EE steps (intermeidates II and III). Protonation of the doubly

reduced complex results in the formation of a Ni^{II}-H intermediate; however, they do not specify how the intermediate is formed. H_2 is proposed to evolve form the heterolytic coupling of the hydride and free H^+. Utilization of a bpy unit, like a dithiolene ligand, acts as an electron reservoir to facilitate the formation of the hydride without going through a putative Ni^0 state. This redox active ligand plays a synergetic role with Ni to provide a lower energetic pathway for H_2 evolution in comparison to a purely Ni based reductive catalysis.

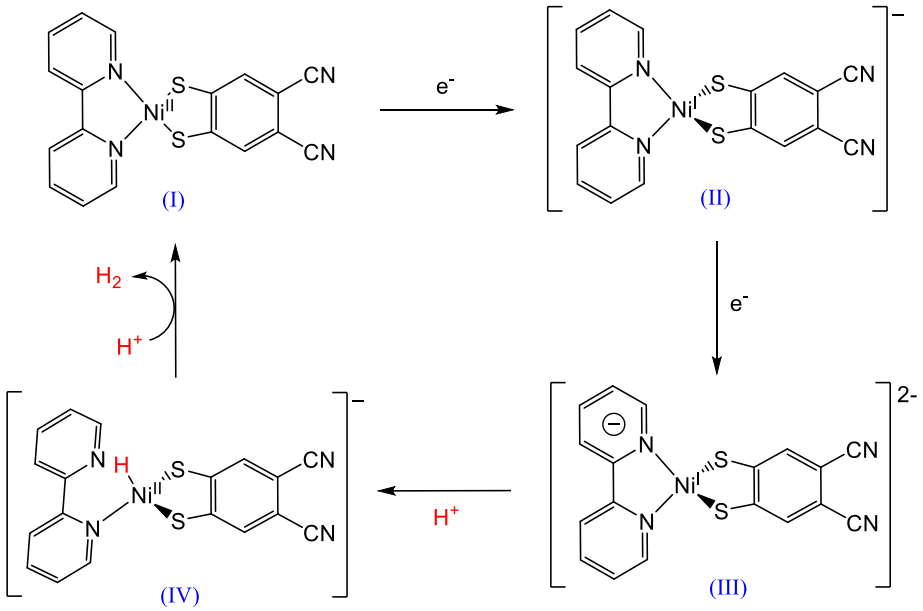

Scheme 1.10. Proposed mechanistic scheme for HER by **20** based experimental results and on the relative energies of computed intermediates.

The bpy unit has also been incorporated in a series of Ni pyridinethiolate HER catalysts reported by the Eisenberg group **21**-**23**, see Figure 1.19.[181] Eisenberg synthesized a series of 12 HER photo- and electrocatalysts through incorporation of electron withdrawing and donating groups at various positions on the pyridine ligand to study how tuning the electron donation capacity of ligands effects HER activity; however, catalysts **21**–**23** represent the unmodified complexes. These catalysts were primarily studied for their photocatalytic proton reduction giving large TONs, up to 5500. The authors did confirm HER electrocatalysis using AcOH, but no HER

metrics or mechanism was reported. Despite the lack of HER electrocatalytic figures of merit, the pH dependent UV-vis spectrum of the compounds suggested the pyridine ligand is hemilabile and plays a role as a proton relay site in place of the traditionally observed bound thioalte. This assessment was disputed by Cordones and coworkers, where they suggested, based on UV-vis and X-ray absorption studies, that addition of acid (TFA) protonates N of the pyridinethiolate ligand.[182] This protonation causes the dissociation of a pyS-H ligand resulting in Ni-solvato complexes: $[Ni(bpy)(DMF)_4]^{2+}$ upon protonation of **21** and $[Ni(DMF)_6]^{2+}$ upon protonation of **22**.[183] The authors tested the electrocatalytic activity of authentic solvato complex ($[Ni(bpy)(DMF)_4]^{2+}$) and protonated ligand (pyS-H), under similar conditions, but found that neither resulted in the HER activity seen for **21**. Based on this result they conclude that the electroactive species is most likely a Ni species with a partially bound pyS-H ligand that is stabilized under reducing conditions. This result implies that, under product conditions, there is an equilibrium between coordinated and uncoordinated ligand. This study highlights the importance of understanding the behavior of electrocatalysts under protic conditions.

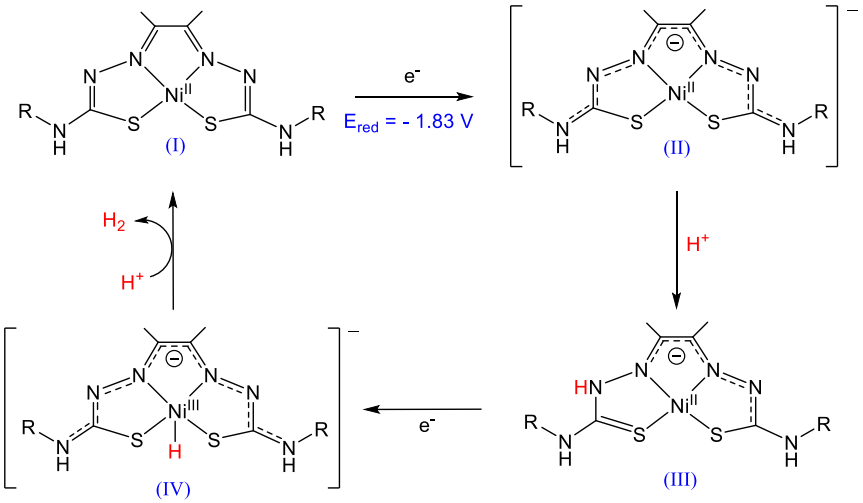

Scheme 1.11. Proposed mechanistic scheme for HER by **24** based on the relative energies of computed intermediates.

Another redox-active ligand utilized in NiS_nN_n (n = 2, 3) HER electrocatalysts is thiosemicarbazone possessing a soft donor set that can stabilize metals in low oxidation states making it an attractive target for reductive catalysis.[184, 185] Grapperhaus and Orio have utilized this redox-active ligand for a set of Ni^{II} complexes **24** and **25**, shown in Figure 1.19, that are HER active electrocatalysts for HER.[186, 187] The authors utilized relative energies of computed intermediates to propose an ECEC mechanism (Scheme 1.11) in which the first reduction takes place at the ligand (intermediate II), followed by protonated at the N-atom of hydrazine (intermediate III). A second reduction event occurs at Ni^{II} and an intramolecular proton transfer forms the Ni^{III}-H through an oxidative addition mechanism (intermediate IV). H_2 evolves from heterolytic coupling of the hydride with a H^+ relay on the N-atom of hydrazine. Although the free ligand of **24** also was found to be electrocatalytic towards HER (TOF = 1320 s^{-1}, η = 1.43 V, MeOH, AcOH)[188], incorporation of Ni^{II} (**24**) yields a more active (TOF of 4200 s^{-1}) and more efficient (η = 0.53) catalyst. This comparison highlights the important role of metals in HER, namely, to more efficiently form hydrides. Orio reported a similar complex (**25**) incorporating more electron rich methoxy groups that behaved similarly to **24** but with a higher TOF in ~2000 s^{-1} faster.[163] However, higher TOF is most likely a consequence of using stronger acids such as TFA. Another important factor is to consider the solvent utilized. For example, the TOF of **25** in DMF was considerably lower (1200 s^{-1}) due to the slower intramolecular proton transfer caused by hydrogen bonding from DMF. Regardless, both catalysts achieve high TOF values due to the proton relay groups provided by the hydrazine N-atoms. These catalysts break the relationship between overpotential, and the $Ni^{II/I}$ redox potential seen with prior electrocatalysts due to the more favorable (~0.5 V) reduction of the ligand. This result highlights the synergetic relationship between a ligand and metal that results in more efficient electrocatalytic HER.

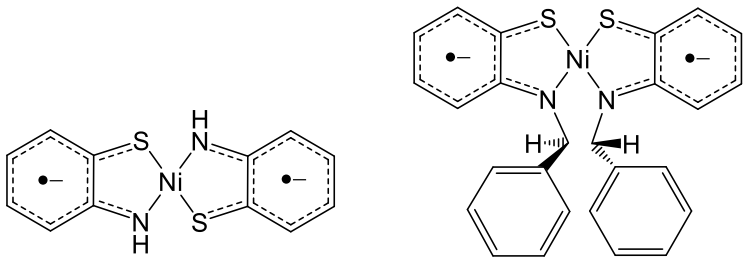

(26) (27)

Figure 1.20. NiS_2N_2 HER electrocatalysts containing semi(inmino)thioquinone ligands.

Table 1.8. Reported HER metrics and mechanisms of **18** and **19**.

Catalyst	-/2- (V)[a]	TOF (s^{-1})	η (V)	TON (h^{-1})	FE	Mechanism	H^+ Source	Ref
26[b]	-1.28 (r)	*n.r.*	~0.7	*n.r.*	*n.r.*	*n.r.*	AcOH	166
27[c]	-1.50 (r)	*n.r.*	~1.5	*n.r.*	*n.r.*	*n.r.*	AcOH	167

[a]Potentials are vs Fc/Fc^+, [b]MeCN, [c]THF, (r) reversible couple, (q) quasi-reversible couple, and *n.r.* (not reported).

Lastly, a set of NiS_nN_n (n = 2, 3) HER electrocatalysts feature a semi(imino)thioquinone ligand (Figure 1.20; **26** and **27**). These catalysts can be best described as a Ni^{II} complex with antiferromagnetically coupled radical ligands.[189] However, **26** and **27** have been primarily studied for their photocatalytic HER activity, and the electrocatalysis is not discussed thoroughly, with . **26** (TON =280,000) exhibiting higher photolytic activity than **27** (TON = 420).[190, 191] Electrocatalysis was tested utilizing AcOH in MeCN (for **26**) and THF (for **27**) but only overpotentials were reported. Close inspection of the CV with H^+ titrations, for **26** and **27**, reveal that catalysis is only initiated after two sequential reduction events. This result suggests that the active catalyst is the dianion of **26** and **27**; thus, catalysis is not initiated until a more negative reduction event is reached, ~ 0.5 V more negative than the -/2- couple. Electrocatalysts **26** and **27** possess large overpotentials (0.7 to 1.5 V) most likely due to the ligand acting as an electron hole that needs to be filled prior to the catalytic event. This result shows that redox-active ligands do not always provide lower energetic pathways for HER. Non-innocent ligands can act as electron

sinks without participating in the reduction of H^+ if their reduced state is sufficiently stable. One must carefully consider the redox activity of ligands employed in HER electrocatalysts.

1.5.2 NiS_2P_2 HER electrocatalysts.

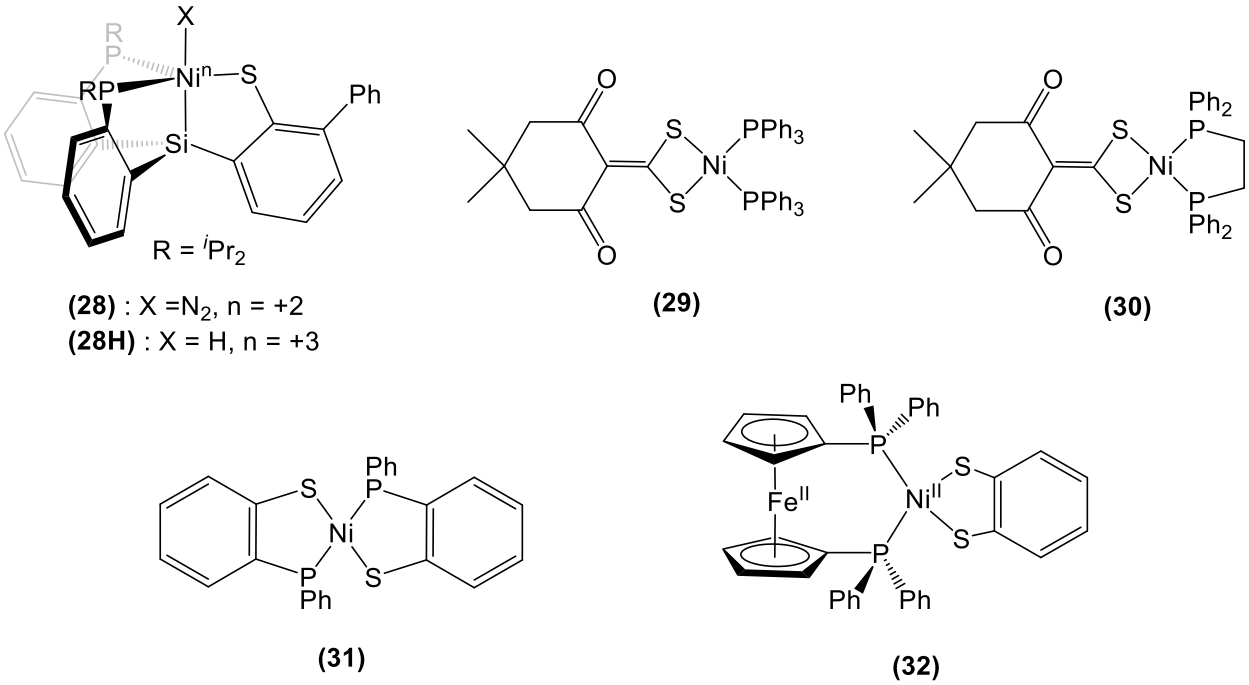

Figure 1.21. NiS_2P_2 and HER electrocatalysts.

Table 1.9. Reported HER metrics and mechanisms of NiS_2P_2 electrocatalysts.

Catalyst	$Ni^{II/I}$ (V)[a]	TOF (s^{-1})	η (V)	TON (h^{-1})	FE	Mechanism	H^+ Source	Ref
29[b]	-1.16 (q)	3280	0.45	*n.r.*	*n.r.*	ECEC	TFA	[192]
30[b]	-1.39 (q)	*n.r.*	1.01	*n.r.*	*n.r.*	*n.r.*	TFA	[192]
31[c]	-2.48 (q)	51	1.10	3.4	*n.r.*	ECEC	AcOH	[193]
32[d]	-1.76 (r)	1240	0.50	*n.r.*	99%	ECEC	AcOH	[194]

[a]Potentials are vs Fc/Fc^+, [b]MeCN, [c]DCM, [d]THF, (r) reversible couple, (q) quasi-reversible couple, and *n.r.* (not reported).

There are several Ni-thiolate containing HER electrocatalysts that incorporate phosphine groups in the coordination sphere, electrocatalysts **29-32** in Figure 1.21. Phosphine ligands, like thiolates, are soft σ-donors and their electron donating capacity can be modulated with various R groups directly bonded to the P-atom. Peters and coworkers utilized a mixed phosphine thiolate

coordination sphere (**28**, Figure 1.21) to *in-situ* generate a trigonal-bipyramidal Ni^{III}-H (**28H**) complex mimicking the Ni-C state in [NiFe]-H_2ase.[195] Complex **28H** was generated by low temperature chemical oxidation of a Ni^{II}-H and the hydride, of **28H**, was confirmed by IR ($\nu_{Ni\text{-}H}$ = 1728 cm^{-1}), NMR (δ_H = -6.90 ppm in C_6D_6), and EPR. UV-vis studies coupled with gas-chromatography revealed that upon warming of the *in-situ* generated **28H**, H_2 is generated by a bimolecular homolytic coupling mechanism yielding [Ni(SiP_2S)(μ-N_2)Ni(SiP_2S)], which is in equilibrium with its monomeric form. The electrocatalysis of [Ni(SiP_2S)(μ-N_2)Ni(SiP_2S)] was confirmed from bulk electrolysis of the complex with PhOH, only FE (~98%) was reported. Although an electrocatalytic HER mechanism was not proposed, insight is gleaned from protonation of the possible intermediates, Ni^{III}-H (**28H**) and its reduced form Ni^{II}-H ($\mathbf{28H^-}$) with PhOH. H_2 is only generated from the protonation of $\mathbf{28H^-}$ suggesting that if HER proceeds via a unimolecular mechanism then it likely requires a Ni^{II}-H intermediate to be generated. Complex **28** provides a valuable platform to establish spectroscopic assignments for a terminal Ni^{III}-H.

Minimization of molecular movement of a catalyst during turnover is one way in which overpotentials can be reduced; however, molecular rearrangement can be advantageous for catalysis. This advantage is seen in a set of heteroleptic square-planar HER electrocatalysts active **29** and **30** reported by Kumar and coworkers, structures depicted in Figure 1.20.[192] The authors showed that the activity of these catalysts correlated with the rigidity in the phosphine unit, the less rigid ligand results in a lower overpotential. They propose the flexibility afforded by the non-chelated phosphine ligand (**29**) decreases the strain required to couple the proton and Ni-hydride in the proposed transition state. Lowering the strain on the ligand lowers the activation energy for H_2 evolution, thus, decreasing overpotential. Another way to decrease overpotential, as seen for prior electrocatalysts, is to positively shift the potential of the electrochemical step needed to

initiate catalysis, usually the $Ni^{II/I}$ couple or, if present, the E_{red} of the redox-active ligand. For example, **31** possessing the highest overpotential amongst the phosphine containing complexes likely attributed to its very negative $Ni^{II/I}$ couple.[193, 196, 197]

The importance of ligand flexibility for reactivity is also seen in a rather unique electrocatalyst **32**, see Figure 1.21, reported by the Jones group.[194] Ni^{II} is held in a square-planar geometry with terminally bound thiolates and two phosphine atoms that bridge to ferrocene (Fc) via the C-atom of the cyclopentene. Although **32** is structurally classified as a bimetallic complex, the authors claim it is more analogous to a mononuclear HER electrocatalyst. This proposal was based on computations revealing that the frontier molecular orbitals had negligible contribution from Fe suggesting reactivity is entirely dependent on Ni. Despite this proposal, the Fe-free complex [Ni(dppe)(bdt)] (dppe = 1,2-bis(diphenylphosphino)ethane; bdt = 1,2-benzene dithiolate) did not display HER electrocatalysis, even when utilizing a stronger acid (*p*-TsOH), suggesting the Fe unit has a role in catalysis. The authors propose flexibility afforded by the larger P-Ni-P angle of **32** (101˚) compared to [Ni(dppe)(bdt)] (86˚) facilitates catalysis. The importance of a flexible ligand is seen in the proposed mechanism (see Scheme 1.12) obtained through DFT computations on a truncated model, containing non-chelating phosphine ligands to retain flexibility of the coordinating ligand. Catalysis is proposed to go through an ECEC mechanism with a $Ni^{II/I}$ E-step (intermediate II) causing a distortion of the geometry away from square-planar. Next, protonation occurs at Ni^{I} (intermediate III) to yield a Ni^{III}-H or a terminal thiolate (intermediate IV). Both pathways are accessible with a computed energy difference of ~4 kcal/mol with intermediate IV being slightly favored. Further reduction of Ni in both intermediates yields the Ni^{II}-H (intermediate V), and the second protonation event evolves H_2. Reduction of intermediate IV at Ni triggers formation of Ni^{II}-H though oxidative addition from intramolecular proton transfer. H_2 is proposed

to evolve through a transition state with both hydrogens bound to the Ni in a pseudo-octahedral geometry. In order to achieve this TS, the phosphine ligand needs to be sufficiently flexible to open the two adjacent vacant coordination sites for hydrogen to bind. The Fc unit provides more degrees of freedom than the dppe ligand accommodating the TS necessary for H_2 evolution.

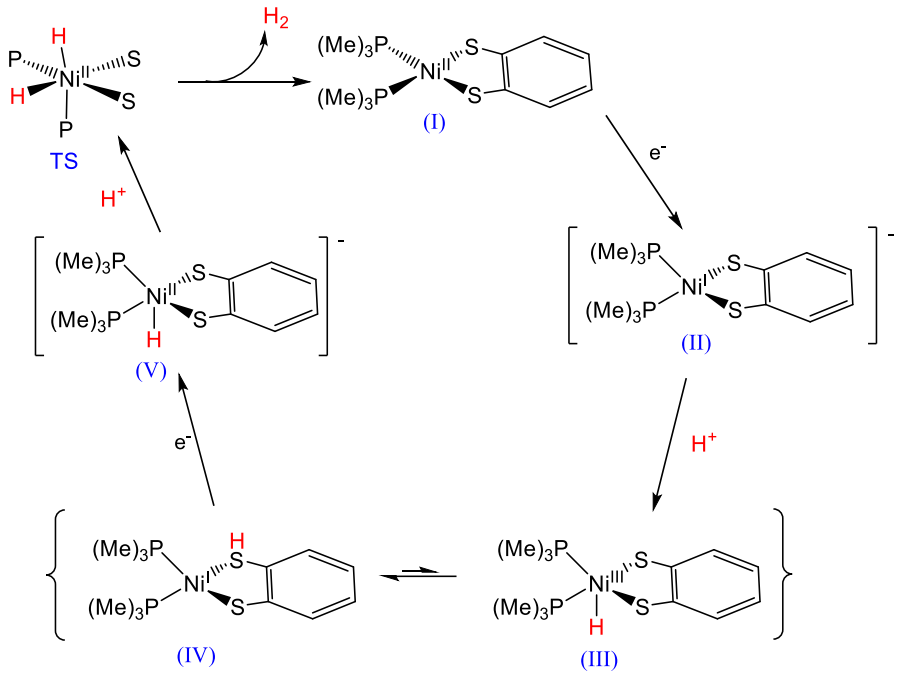

Scheme 1.12. Proposed mechanistic scheme for HER by a truncated model of **32** based on the relative energies of computed intermediates.

The role of thiolates in electrocatalysis becomes clear upon comparing the proposed mechanisms of the NiS_4 tod $NiS_2(L)_2$ (L = P, N, O). Overall, it appears that catalysts that lack a purely-thiolate rich core generally require two reduction steps to generate a Ni^{II}-H intermediate form the starting Ni^{II} complex, implying generation of the Ni^0 intermediate. This general observation reveals that thiolates, strong electron donors, sufficiently increase the basicity of Ni to generate Ni-H from oxidative addition of H^+ from Ni^I as opposed to Ni^0. Sequential reduction at the same site, ie Ni, is a thermodynamically expensive process. This unfavorable process is circumvented by incorporation of non-innocent redox active ligands that can an provide additional

source of electrons through its reduction. The reduced ligand can provide one or two electrons to form Ni-H without expending energy to reduce Ni multiple times. Another way to reduce the energy required to evolve H_2, is by protonation of the bound. From a purely electrostatic point of view, protonation decreases the overall charge of the catalyst resulting in a more positive reduction potential, thus decreasing overpotential. Additionally, bound thiolates can impact the kinetics of HER in two ways. First, the thiolate can act as a proton relay group, through its hemilability, to speed up coupling of a H^+ and H^- to evolve H_2. Furthermore, protonation of bound thiolate reduces the chance of a free H^+ to interact with Ni to form a Ni-H by facilitating intramolecular H^+ transfer.

Although it is hard to draw broad conclusions about the role of the ligand sphere on the metrics of HER, due to several factors, some common trends appear. First, the reduction event required to initiate the catalysis is directly related to overpotential, either the $Ni^{II/I}$ couple or the reduction of the ligand. Due to this relationship, overpotential can be tuned by the electronic nature of the donor atoms. Second, molecular rearrangement of the ligand, through distortion or hemilabile, is commonly proposed to take place during the catalytic mechanism. The molecular reorganization of the coordination-sphere may contribute to increased overpotentials. Lastly, in general, ligand frames that incorporate bases in the second coordination sphere tend to possess higher TOF values. These factors highlight the structural importance of the native enzyme that the synthetic mononuclear Ni electrocatalyst lack, namely the rigid tetrahedral geometry and redox-inactive, thiolate-rich donor-set of the Ni in the [NiFe]-H_2ase. Lack of these structural similarities results in larger overpotentials required to catalyze HER and fails to properly parallel the HER mechanism proposed for [NiFe]-H_2ase.

1.6 Mononuclear NiP_4 HER Electrocatalysts

1.6.1 H_2 oxidation complexes and electrocatalysts

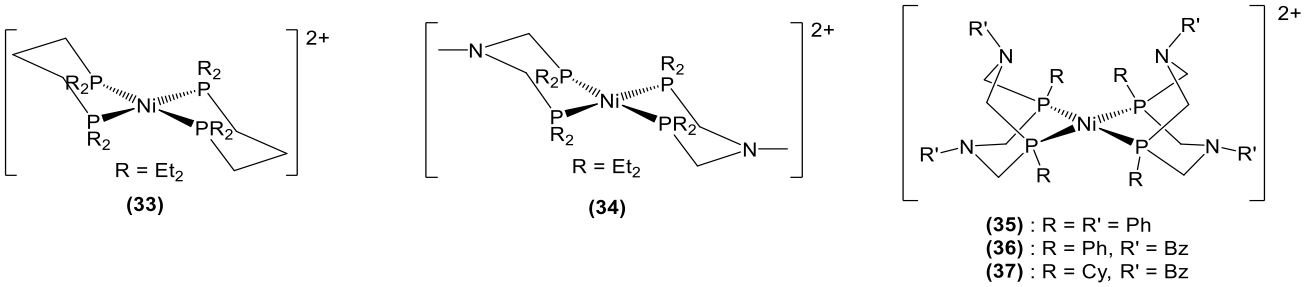

Figure 1.22. Ni tetraphosphine H_2 oxidation complexes and electrocatalysts.

Ni-tetraphosphines were pioneered by DuBois and coworkers as some of the first electrocatalysts to display reversible HER.[198, 199] Phosphine ligands are soft σ-donors with an ability to π-backbond, depending on attached substituents, making them able to stabilize low oxidation states of metal ions. This property makes phosphines attractive ligand frames to stabilize $Ni^{I,0}$. DuBois initially investigated Ni-tetraphosohine complexes for their ability to oxidize H_2. The first reported from these set of complexes, shown in Figure 1.22, was **33**. Dubois and coworkers found that **33** rapidly cleaves H_2, in the presence of an external base, to quantitatively yield Ni^{II}-H, confirmed by ^1H NMR (δ_{H-} = -15.69 ppm) suggesting a heterolytic cleavage mechanism.[198] Although **33** rapidly, within seconds, cleaves H_2 under synthetic conditions, it is a slow electrocatalyst for H_2 oxidation (< 0.5 s^{-1}) with large overpotentials of 0.8 V (MeCN, Et_3N, 1 atm H_2). Incorporation of pendant bases in the secondary coordination sphere for complex **34**, Figure 1.22, dramatically reduces the overpotential to 0.15 V with the TOF values remaining the same.[199] *In-situ* ^1H NMR, low temperature, of the reaction product of **34** purged with H_2 confirmed heterolytic H_2 splitting by the presence of a Ni^{II}-H species (δ_{H-} = -14.75 ppm) and resulting H^+ on the N-atom of the ligand (δ_{NH} = 7.38 ppm). This process is reversible evidence by the addition of triethylamine resulted in the disappearance of the NH peak by NMR. This result suggests that the

N-atom facilitates intramolecular heterolytic cleavage of H_2 and functions a proton relay to transfer H^+ away, and to, the metal site.

Due to the incorporation of the proton relay site in **34**, one would anticipate the rate of H_2 oxidation to faster than in **33**; however, the rates are comparable because the rate determining step is the initial H_2 binding. This putative intermediate, Ni-H_2, has not been observed experimentally but computations suggest that one of the 6-membered ligands isomerize from a chair to a boat conformation to facilitate the attractive interaction of bound H_2 and N-atom, as shown by the H_2 intermediate in Schem 13. This interaction asymmetrically polarizes the H-H bond facilitating its cleavage to yield a H^- on the Ni and a H^+ on the N-atom without a change to the oxidation state of Ni. CV of this product (Ni^{II}-H) for **33** and **34**, in the presence of triethylamine, revealed each possessed a two-electron oxidation proposed to be the oxidation of Ni^{II}-H to Ni^{II} with the loss of a H^+ and 2 e^-. However, the oxidation occurs 0.7 V more negative for **33**(Ni^{II}-H) suggesting that the pendant base reduces the thermodynamic requirement to oxidize the Ni^{II}-H to Ni^{III}-H resulting in a lower overpotential. Dubois ascribes this result to a PCET event that circumvents the large energy barrier associated with the formation of Ni^{III}-H facilitated by the presence of the pendant base.[200]

In light of the importance of incorporating bases to facilitate cleavage of H_2 upon binding, **35** - **37** were synthesized, structure shown in Figure 1.22.[201] This set of complexes were designed to position bases on the ligand frame near the binding pocket of Ni to avoid isomerization to the boat conformation necessary to stabilize a proposed Ni-(H-H) intermediate. Comparison of H_2 cleavage between **34** and **35** show that there was no reaction with **35** and appearance of low concentrations of the H_2 addition products in **36**, the Ni^{II}-H species. This result is further supported by the calculated ΔG^o_{H2} of **35** (9 kcal/mol) and **36** (3 kcal/mol), reflecting the higher basicity of the N-

atom of **36**. The more basic N-atom of **37** better polarizes the H_2 bond promoting the heterolytic cleavage.

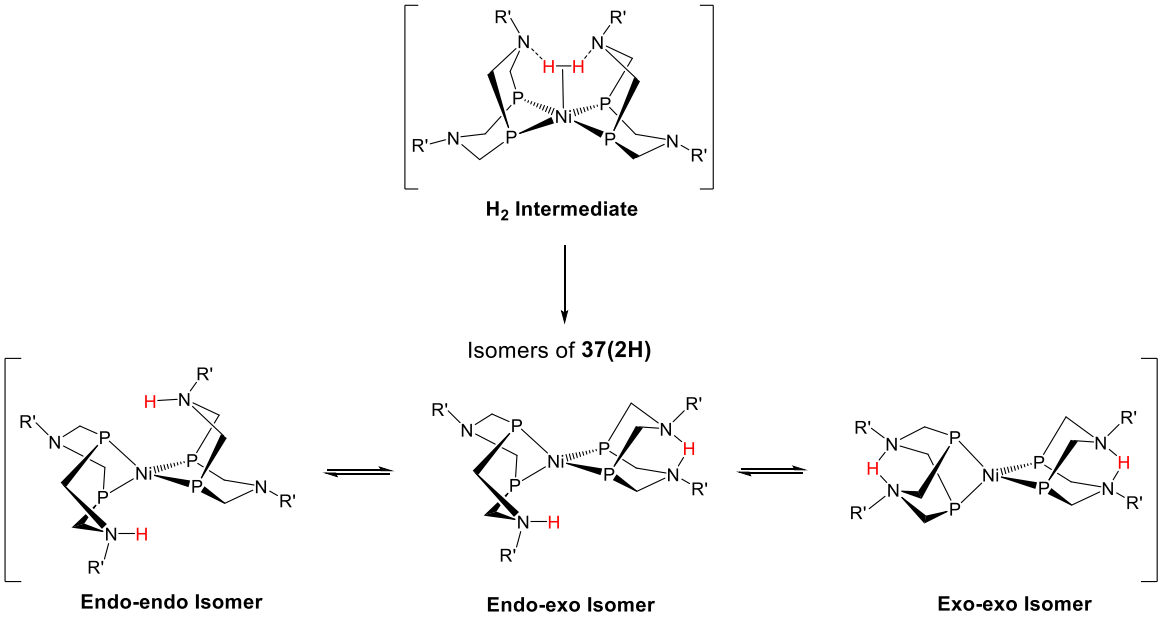

Scheme 1.13. Proposed binding and activation of H_2 in **37** and the subsequent equilibrium of the diprotonated Ni^0 complexes (**37(2H)**).

Despite this result, DuBois and coworkers showed that incorporation of bulkier substituents on the phosphine atom in **37**, compared to **36**, shifter the thermodynamic bias for H_2 oxidation, ΔG^o_{H2} of -3 kcal/mol.[201] This effect was attributed to distortion to a more tetrahedral geometry of **37** (τ_4 = 0.50), imposed by bulkier ligands, compared to **36** (τ_4 = 0.32); thus a greater hydride affinity at Ni. Distortion from a square-planar geometry is proposed to lower the energy of the LUMO, consisting of antibonding interactions between the $d(x^2\text{-}y^2)$ orbital of Ni and σ orbital of phosphine. This orbital is the acceptor orbital for two electrons upon addition of the hydride; therefore, the distortion to more tetrahedral geometry makes the formation of the hydride more favorable.[202] This effect results in the increased TOF of **37** (10 s^{-1}) relative to **35** and **36** (<0.5 s^{-1}). Given the affinity of **37** for H_2 binding, addition of H_2 to **37** was analyzed by variable temperature ^1H and ^{31}P NMR to better understand the nature of this binding and cleaving event.[203] These

experiments led to the discovery of **37(2H)**, shown in Scheme 1.13, in which one amine in each ligand is protonated in a tetrahedral Ni^0 complex. Although this result provides no direct evidence of how H_2 binds and cleaves, computations suggest the H_2 intermediate is stabilized by the favorable interactions of two pendant N-atom. The cleavage occurs by Ni^{II} providing two electrons to polarize the H-H bond. Importantly, DuBois and coworkers found that the **37(2H)** could exist as three isomers, shown in Scheme 1.13, suggesting that during turnover the position of the pendant bases are key to facilitating the interaction of the metal-bound hydride and the H^+, as seen only for the endo-endo isomer.[200]

1.6.2 Ni tetraphosphine HER electrocatalysts

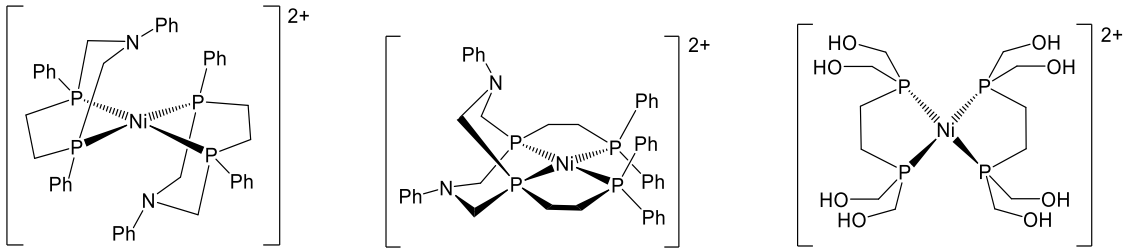

Figure 1.23. NiP_4 HER electrocatalysts.

Table 1.10. Reported HER metrics and mechanisms of NiP_4 electrocatalysts.

Catalyst	Ni(II/I) (V)[a]	TOF (s^{-1}) (H_2O)[b]	η (V) (H_2O)[b]	TON (h^{-1})	FE	Mechanism	H+ Source	Ref
35[c,d]	-0.83 (r)	590 (720)	0.30 (0.32)	*n.r.*	*n.r.*	ECEC	DMFH(OTf)	[204]
38[c,d]	-1.13 (r)	33,000 (106,000)	0.63 (*n.r.*)	11	99	ECEC	DMFH(OTf)	[205]
39[c,d]	-1.52 (ir)	200,000 ($1.6*10^6$)	*n.r.* (1.20)	*n.r.*	90	ECEC	DMFH(OTf)	[206]
40[e]	-1.23* (ir)	~10,000	0.48	*n.r.*	92	EECC	H_2SO_4	[207]

[a]Potentials are vs Fc/Fc^+, [b]Parentheses represent values obtained after water was added (0.1 M for **31**, 1.2 M for **34**, and 6.5 M for **35**), [c]MeCN, [e]0.1 M H_2SO_4, *$Ni^{II/0}$ couple, (r) reversible couple, (ir) irreversible couple, and *n.r.* (not reported).

Due to lack of H_2 activation from **35**, shown in Figure 1.22, the electrocatalytic activity for HER was investigated.[204] DuBois and coworkers found that **35** was active for HER and TOF was increased in the presence of H_2O resulting in rates comparable to [NiFe]-H_2ase. The authors proposed HER undergoes an ECEC mechanism, shown in scheme 1.14, involving the reduction of $Ni^{II/0}$ with two electrons and protonation of the N-atom (intermediate III), which forms the hydride containing intermediate V through oxidative addition. The last protonation step occurs at the N-atom to form the proposed TS. As suggested by the NMR studies of **37(2H)**, shown in Scheme 1.13, the TS is proposed to exist as two isomers and H_2 only evolved when exo isomer is formed. This proposal implies that only a fraction of the doubly protonated, doubly reduced catalyst results in turnover and higher rates would be achieved if the exo-exo isomer is avoided. In turn, DuBois and coworkers suggest that H_2O increases the TOF of **35** as a result of converting the exo-exo isomer to the active forms. Kinetic measurements suggest that H_2O enhances the rate of protonation of endo over exo isomers.[208]

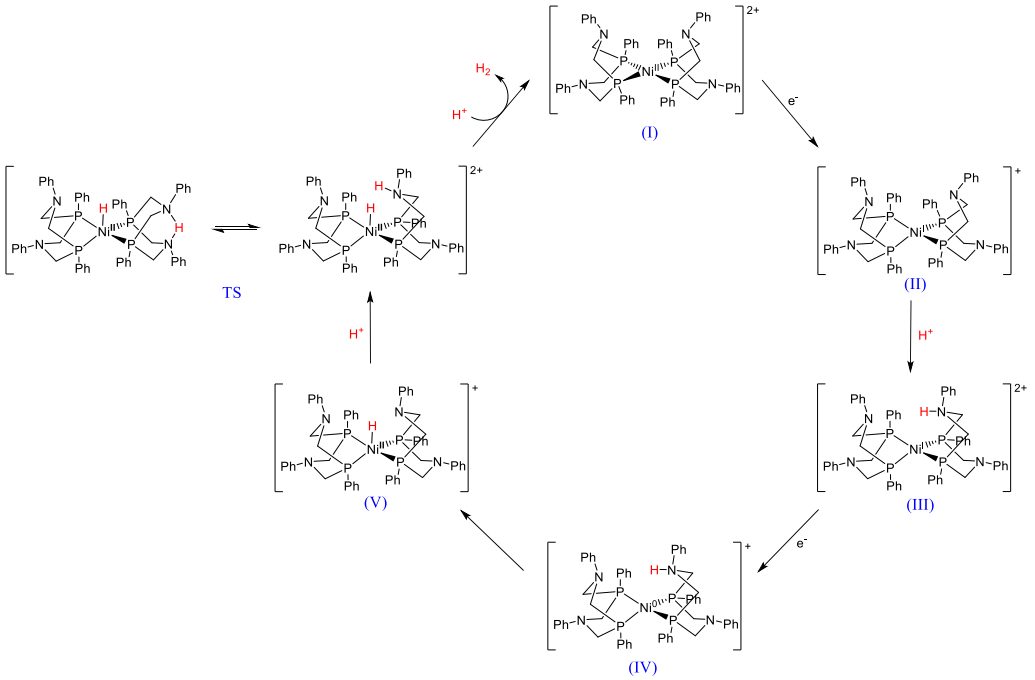

Scheme 1.14. Proposed mechanistic scheme for HER by **35** based on the relative energies of computed intermediates.

In order to circumvent the unfavorable isomerization, Dubois and coworkers developed catalyst **38**, shown in Figure 1.23, that positions the pendant bases in the endo geometry to better facilitate the coupling of a H^+ and Ni-H.[205] This predisposed geometry resulted in an exceptionally fast catalyst (TOF = 33,000 s^{-1}) surpassing that of the native hydrogenases (TOF values up to 9000 s^{-1}), and increases to 106,000 s^{-1} in the presence of H_2O. **38** is proposed to go through a similar mechanism as **34**, scheme 1.14, for H_2 evolution. Despite the increased TOF, **38** possesses a relatively larger overpotential (0.63 V) than **38** (0.30 V) proposed to be a result of the more negative $Ni^{II/I}$ couple of **38** (-1.13 V vs Fc/Fc^+) compared to **35** (-0.83 V vs Fc/Fc^+) responsible for initiating catalysis. This difference in $Ni^{II/I}$ couple is not a result of the donor set but rather arises from the difference in geometry. As suggested for $Ni^{II}P_4$ complexes that can cleave H_2, the energy of the LUMO can be lowered through distortion of geometry from square-planar to tetrahedral. Lowering the energy of the LUMO, the orbital responsible for accepting an electron upon reduction of Ni^{II}, should result in a more positive $Ni^{II/I}$ couple. This relationship is observed for **35** which possess a more distorted tetrahedral geometry (τ_4 = 0.32) than **38** (τ_4 = 0.01) and thus a ~0.3 V more positive $Ni^{II/I}$ couple.. Another way to reduce the number of exo-pinches that limit catlysis is to only include one P_2N_2 ligand as Wiender and coworkers did for **39**, depicted in Figure 1.22.[206] Electrocatalyst **39** utilizes a rigid tetra-phosphine ligand that incorporates pendant bases on one side holding Ni in a square-planar geometry. The catalyst possesses a very high TOF value ($1.6*10^6$ s^{-1}) but does so at a large overpotential (1.20 V) proposed to be due to the imposed rigidity by the tetradentate ligand. This rigidity hinders molecular rearrangement involved in coupling the pendant H^+ and the Ni-H, as seen in **35.** These complexes reveal incorporation and positioning of pendant bases as proton relay groups has a large impact catalytic rate of HER.

Lastly, the Yang group reported a water-soluble NiP_4 HER electrocatalyst **40**, shown in Figure 1.23, that is stable under highly acidic conditions, over 18 h of electrolysis at a pH of 1.0, with high rates of turnover, ~10,000 s^{-1}.[207] To gain insight into the HER mechanism, the authors investigated a stepwise mechanism under stoichiometric conditions. CV and DPV of **40** revealed an irreversible couple at -1.26 V (vs Fc/Fc+), responsible for initiating catalysis, corresponding to a 2e- reduction event. This result suggests the first two steps of the cycle involve two sequential reduction a Ni. The Ni^0 complex of **40** (**40^{2-}**) was independently synthesized by addition of 2 mol-equivalents of Co(Cp) (Cp = cyclopentadienyl). Addition of an excess of a weak acid ($HNEt_3$, pKa = 9.3) to **$(40)^{2-}$** yielded a Ni-H product, identified by ^1H NMR (δ_{H-} = -13.45 ppm, DMSO-d_6), that was stable for three days. Addition of an excess of a strong acid ($PhNH_3$, pKa = 3.6, DMSO-d_6) to **$(40)^{2-}$** afforded a mixture of products including **40** and H_2, identified by ^1H NMR (δ_{H2} = ~4.6 ppm, DMSO-d_6). These results suggest that the hydride is generated from the oxidative addition of Ni^0, yielding a Ni^{II}-H, and H_2 evolves from the heterolytic coupling of the H^+ and hydride.

All NiP_4 HER electrocatalysts presented here are possess a TOF that surpasses that of [NiFe]-H_2ase (700 s^{-1}) due to incorporation and, importantly, position of bases in the secondary coordination sphere to facilitate coupling between an external H^+ and hydride on the Ni acting as a proton relay. Proton relay sites are proposed to play similar roles in H_2ases such as the azadithiolate moiety of [FeFe]-H_2ase or the terminal Cys in [NiFe]-H_2ase. Additionally, NiP_4 electrocatalysts reveal that $Ni^{II/I}$ couples are not only influenced by the electronic nature of the ligand but also the geometry it imposes. Although a small sample size, NiP_4 catalysts poised in a more tetrahedral geometry result in more positive $Ni^{II/I}$ potentials. If the $Ni^{II/I}$ couple is the step required to initiate catalysis, then the overpotential is a function of geometry. This relationship may betray the importance of maintaining the pseudo-tetrahedral geometry of Ni(II) in [NiFe]-

H_2ase to minimize overpotential. Lastly, these electrocatalysts are proposed to generate a Ni^{II}-H complex via oxidative addition of a H^+ from the Ni^0 state due to insufficient basicity of the Ni^I state. In comparison to the native enzyme, the basicity of the Ni^I state, seen in the Ni-L state, is sufficient to generate a Ni^{III}-H. This result may be attributed to the higher donor capacity of thiolate compared to phosphine and highlights the importance of tetrathiolate donor sphere in [NiFe]-H_2ase.

1.7. Heterobimetallic [NiFe] HER Electrocatalysts

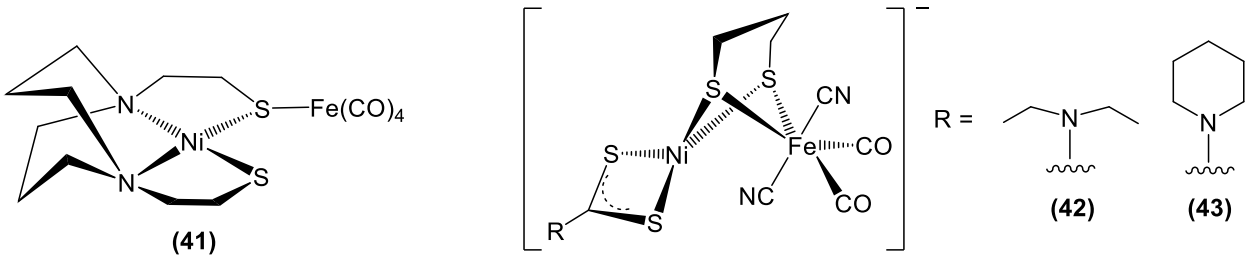

Figure 1.24. Select Ni-Fe bimetallic structural mimics of [NiFe]-H_2ase.

Ultimately to best capture the structure-to-function relationship of [NiFe]-H_2ase, synthetic electrocatalysts must incorporate Fe through bridging thiolates and maintain redox activity on Ni. However, centralizing activity on Ni presents a challenge because both metals are redox active and have similar affinities for formation of metal-hydrides, seen by the volcano plot shown in Figure 1.2. Furthermore, from a purely synthetic standpoint, controlled formation of discrete bimetallic complexes is challenging due to the propensity of thiolates to form multimetallic complexes through bridging thiolates. Despite these challenges, in 1996, only one year after the crystal structure of [NiFe]-H_2ase was solved, Darensbourg and coworkers reported the first thiolate bridged [NiFe] complex **41**, see in Figure 1.24, as a structural model of [NiFe]-H_2ase, synthesized by the S-metalation of the $Ni^{II}N_2S_2$ unit with $[Fe_2(CO)_9]$.[209] This complex represented the first

discrete bimetallic, Ni-Fe, complex with a bridging thiolate. However, **41** is not the most accurate structural mimic due to a mixed N_2S_2 coordination sphere, one bridging thiolate, a square-planar Ni, and lack of CN^- ligands bound to Fe. It wasn't until 10 years later the first bridging dithiolate [NiFe] complexes **42** and **43**) were reported by Tatsumi.[210] These complexes are still the closest structural match to [NiFe]-H_2ase, each possess a NiS_4 unit with two thiolates bridge to Fe coordinated by CO and CN^- ligands; however, they are thermally unstable in solution preventing the HER electrocatalytic activity from being tested.

There are quite a number of synthetic [NiFe]-H_2ase structural mimics that have been reported and reviewed in depth by others.[59, 211, 212] Synthetic [NiFe] complexes are generally isolated from a combining, through thiolate bridges, of independently synthesized Ni- and Fe-units. In general, these feature a dithiolate ligand bridging a square-planar Ni^{II} and a five-or six-coordinate $Fe^{II/I}$ featuring at least one CO ligand to ensure low-spin configuration. The coordination environment of the Ni^{II} incorporates a variety of atoms including N, S, and P coordination to Ni^{II} in a bidentate or tetradentate resulting a square-planar geometry. Two of the corresponding thiolates bridge to the Fe-unit in which Fe is coordinated by, most commonly, CO, CN^-, NO, Cp, and/or phosphine-based ligands resulting in a coordination number of five to six. Cp(CO) is a common ligand combination to replace the $CO(CN)_2$ ligand motif bound to Fe in the native enzyme. Although numerous [NiFe]-H_2ase structural mimics have been reported, only a handful are electrocatalytic, which is the focus of this section.

1.7.1 [NiFe] heterobimetallic HER electrocatalysts containing terminal thiolates or thioethers

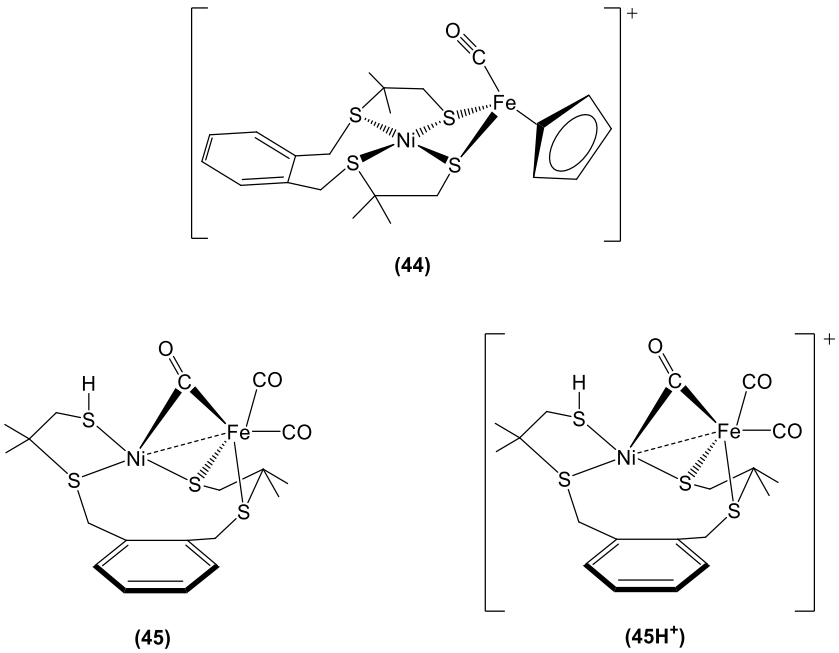

Figure 1.25. HER electrocatalysts containing the $\{S_2Ni(\mu\text{-}S)_2Fe\}$ motif.

Table 1.11. Reported HER metrics and mechanisms of electrocatalysts containing the $S_2Ni(\mu\text{-}S)_2Fe\}$ motif.

Catalyst	$(NiFe)^{+/0}$ (V)[a]	TOF (s^{-1})	η (V)	TON (h^{-1})	FE	Mechanism	H^+ Source	Ref
44[b]	-1.43 (r)	*n.r.*	0.73	5	72	*n.r.*	TFA	[213]
45[c]	-1.81 (r)	300	0.54	5	*n.r.*	*n.r.*	TFA	[214]
45H^{+}[c]	-1.73 (ir)	480	0.57	8	*n.r.*	*n.r.*	TFA	[214]

[a]Potentials are vs Fc/Fc^+,[b] DMF, [c]MeCN, (r) reversible, (ir) irreversible couple, and *n.r.* (not reported).

The HER electrocatalysts that most closely resemble the structure of [NiFe]-H_2ase utilize a $xbsms^{2-}$ unit (H_2xbsms = 1,2-bis(4-mercapto-3,3-dimethyl-2-thiabutyl)benzene] ligating Ni^{II} in a rigid square-planar geometry. The first of which was reported by Artero and coworkers complex **44**, shown in Figure 1.25.[213] This catalyst consists of $\{S_2Ni^{II}(\mu\text{-}S)_2Fe^{II}\}$ unit in which Ni is in a mixed thiolate-thioether ligand frame and Fe(CO)(Cp) is attached through two bridging thiolate. This complex is the only bimetallic to mimic a NiS_4 coordination sphere seen in the Ni site of

[NiFe]-H_2ase however, **44** is not an efficient HER electrocatalyst with overpotentials of 0.75 V. One possible reason for large overpotential is the proposed reductive elimination of CO to form $Ni^{II}(\mu\text{-H})Fe^{III}$ (intermediate IV) during the catalytic cycle, see scheme 1.15, proposed by computations. The reductive elimination of CO was computed to be ~20 kcal/mol and confirmed by loss of ν_{CO} in the IR upon addition of TFA and sodium amalgam (E° = -2.3 V Fc/Fc^+).[215] Formation of this $Ni^{II}(\mu\text{-H})Fe^{III}$ intermediate suggests that Fe is responsible for the redox activity, not Ni as seen in the native enzyme.

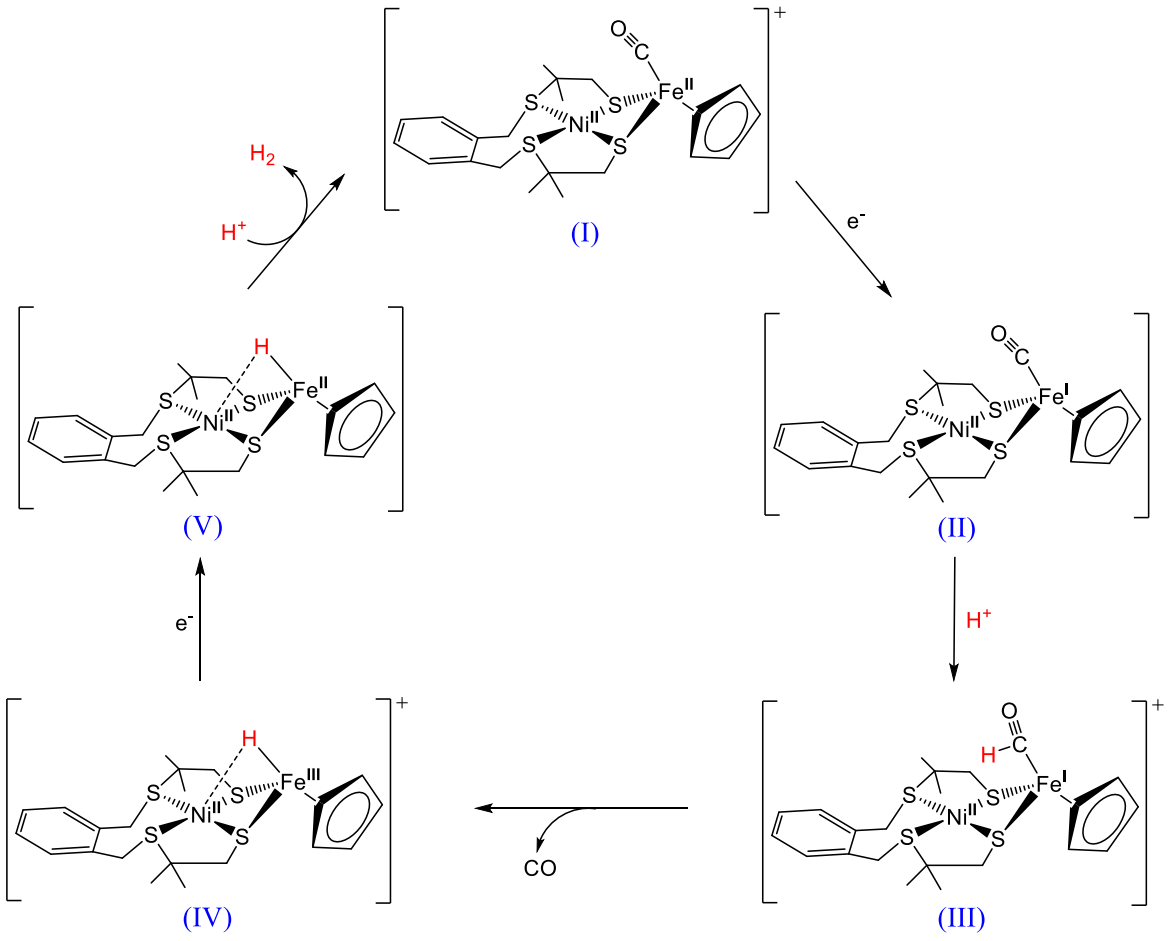

Scheme 1.15. Proposed mechanistic scheme for HER by **44** based on the relative energies of computed intermediates.

Lubitz and coworkers reported another bimetallic HER electrocatalyst **45**, seen in Figure 1.25, featuring an $xbsms^{2-}$ unit; however, utilization of $[Fe^0(BDA)(CO)_3]$ (BDA = benzylideneacetone) to generate these bimetallic species from $[Ni^{II}(xsbms)]$ results in a terminal bound thiolate coordinated **to** Ni.[214] This unique coordination sphere facilitates protonation of the terminal thiolate, shown utilizing $HBF_4{\cdot}Et_2O$, to form the isolable and crystalline complex $\mathbf{45H^+}$. Protonation of the terminal thiolate results in a ~0.06 Å elongation of the Ni-$S_{terminal}$ bond in **45** (2.1644 Å) with the Ni-SH remaining intact. Reversible protonation of **45** was confirmed by ^1H NMR (δ_{SH} = 4.80 ppm), and by comparing the IR of $\mathbf{45H^+}$ (ν_{SH} = 2512 cm^{-1}) with its deuterated analog (ν_{SD} = 1832 cm^{-1}), isolated from protonation of **45** with $DBF_4{\cdot}Et_2O$. Protonation at the terminal thiolate is analogous to the proposed protonation of a terminal CysS of in the Ni-R and Ni-L state of [NiFe]-H_2ase. Both complexes, **45** and $\mathbf{45H^+}$, are diamagnetic (S = 0) with their crystal structures revealing a short Ni-Fe bond, distances of 2.426 Å (**45**) and 2.433 Å ($\mathbf{45H^+}$) suggesting a bond between them. Given the net charge of these complexes, the metal ions are best described as Ni^I and Fe^I. Although both complexes are electrocatalytic for HER utilizing TFA, no mechanism is proposed. Furthermore, protonation of the terminal thiolate during turnover is eliminated due to lack of protonation utilizing TFA, a weaker acid than $HBF_4{\cdot}Et_2O$. Despite a lack of mechanistic insight, **45** is a rare example of a bimetallic NiFe complex that possess a terminal thiolate, thus allowing spectroscopic handles to be established for bound protonated thiolates.

1.7.2 $NiP_2(\mu\text{-}S)_2(\mu\text{-}H)Fe$ heterobimetallic electrocatalysts.

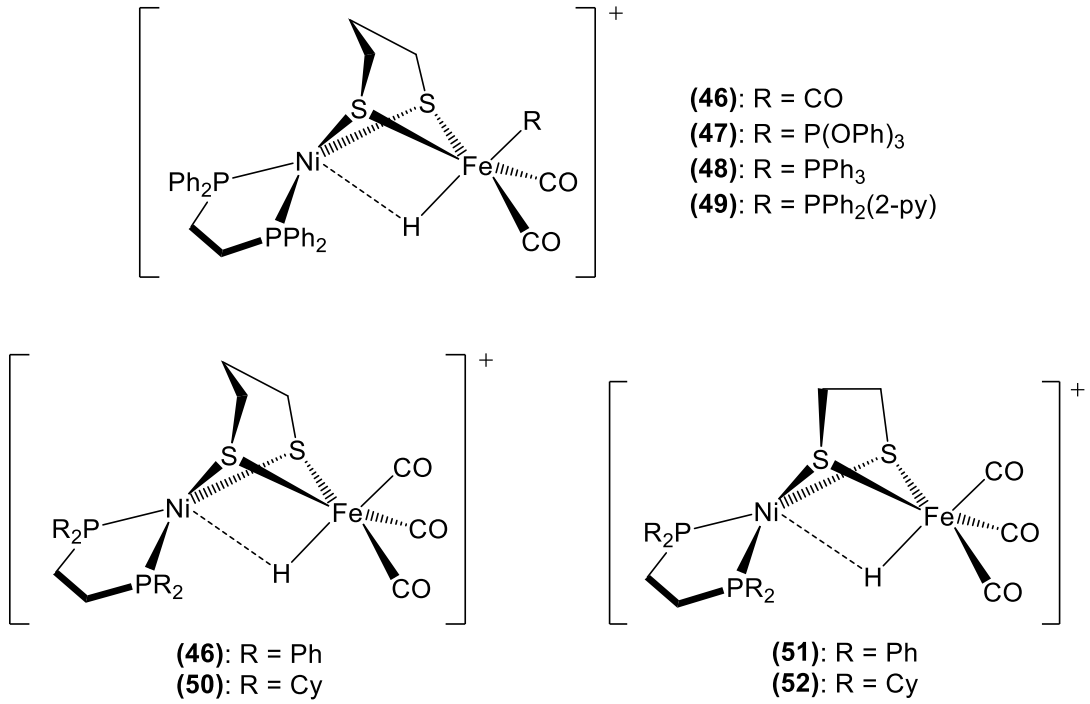

Figure 1.26. HER electrocatalysts reported by Rauchfuss and coworkers containing the $\{P_2Ni(\mu\text{-}S)_2Fe\}$ motif featuring a hydride.

Table 1.12. Reported HER metrics and mechanisms of Rauchfuss electrocatalysts containing the $\{P_2Ni(\mu\text{-}S)_2Fe\}$ motif.

Catalyst	$(NiFe)^{+/0a}$	TOF (s^{-1})	η (V)	TON (h^{-1})	FE	Mechanism	H^+ Source	Ref
46[b]	-1.34 (q)	20	0.50	*n.r.*	*n.r.*	ECEC	TFA	[194]
47[b]	-1.44 (q)	50	0.60	*n.r.*	*n.r.*	ECEC	TFA	[194]
48[b]	-1.49 (q)	50	0.62	*n.r.*	*n.r.*	ECEC	TFA	[194]
49[b]	-1.34 (q)	20	0.50	*n.r.*	*n.r.*	ECEC	TFA	[193]
50[b]	-1.56 (ir)	50	0.59	*n.r.*	*n.r.*	ECEC	MCA[c]	[193]
51[b]	-1.33 (ir)	240	0.49	*n.r.*	*n.r.*	ECEC	TFA	[193]
52[b]	-1.47 (ir)	20	0.59	*n.r.*	*n.r.*	ECEC	MCA[c]	[193]

[a]Potentials are vs Fc/Fc^+, [b]DCM, [c]Chloroacetic acid, (ir) irreversible couple, (q) quasi-reversible couple, and *n.r.* (not reported).

The most common structural motif in heterobimetallic [NiFe]-H_2ase HER electrocatalysts is the $\{P_2Ni^{II}(\mu\text{-}S)_2Fe^{II}\}$ coordination unit, electrocatalyst **46-59**, depicted in Figures 1.26 and 1.27.

These catalyst utilizes a bidentate phosphine ligand to chelate the terminal portion of Ni and an alkyl dithioalte to bridge to Fe, which is coordinated by a variety of ligands (L = CO, CN, P, Cp*), resulting in a square-planar geometry about Ni. Rauchfuss has reported a number of these catalysts with incorpration of a bridging hydride (**46-52**, Figure 1.26) modeling the Ni-C state in [NiFe]-H_2ase.[216, 217] The hydride free species can exist either in the reactive $Ni^{II}Fe^0$ form in which Ni is planar, or the unreactive $Ni^{I}Fe^{I}$ state in which Ni is tetrahedral, with an experimentally estimated barrier of ~10 kcal/mol between the geometric isomers for **46**.[218] Only protonation of a $Ni^{II}Fe^0$ state with $HBF_4{\cdot}Et_2O$ yields the desired $Ni^{II}(\mu\text{-H})Fe^{II}$ complexes, **46-52**. Crystal structures of these complexes reveal that the bridging hydride is bound more closely to Fe than Ni (Fe–H = 1.46 - 1.58 Å; Ni-H = 1.64 - 1.91 Å). However, the bridging hydride in the Ni-C state of [NiFe]-H_2ase is more closely bound to Ni (Ni-H = 1.57 Å, Fe-H 1.70 Å). Despite this discrepancy, Rauchfuss was able to isolate, characterize, and test electrocatalytic activity of a series of [Ni(μ-H)Fe] with varying donor sets around Fe and substituents on the P-atoms coordinated to Ni, **46-52**.

Rauchfuss and coworkers found that **46-52** catalytically reduce H^+ and utilizing both experimental and computational results leading them to propose an ECEC mechanism, seen in Scheme 1.16, starting from the neutral complex $Ni^{II}Fe^0$ (intermediate I). Protonation of this intermediate yields a $Ni^{II}(\mu\text{-H})Fe^{II}$ (intermediate II, isolated complexes **46-52**) through Fe-based oxidative addition confirmed by the presence of a hydride by ^{1}H NMR ($\delta_{H\text{-}}$ = -3 to -8.15 ppm), crystal structures, changes of ν_{CO}, and nuclear resonance vibrational spectroscopy (NRVS).[94] Although **46-52** possess hydrides, addition of acid does not induce H_2 release suggesting further reduction is required.[219] Reduction affords a mixed valent core, viz $Ni^{II}(\mu\text{-H})Fe^{I}$, $Ni^{I}(\mu\text{-H})Fe^{II}$, and $Ni^{1.5}(\mu\text{-H})Fe^{1.5}$ (intermediate III). Lastly, H_2 is liberated from heterolytic coupling of a free H^+. These catalysts show a small range of TOF values (20 – 50 s^{-1}), except for **51** (240 s^{-1}), and

overpotentials (0.49 – 0.62 V) with more electron donating yielding higher TOF values at the expense of higher overpotentials, see Table 1.11. This relationship is further exhibited by a similar electrocatalyst **53** reported by Wang and coworkers, shown in Figure 1.27).[220] This electrocatalyst incorporates a more electron rich ligand, pentamethylcyclopentadienyl (Cp*), bound to Fe. Incorporation of a more-electron donating group at Fe increases the TOF (760 s^{-1}) at the cost of increasing overpotential (~0.8 V). Increasing the electron density of Fe through its donor atoms necessitates a more negative potential needed to generate the $Ni^{II}Fe^{0}$ intermediate proposed to initiate H^{+} reduction. Although these electrocatalysts are active for HER, they mediate catalysis through Fe unlike the native enzyme.

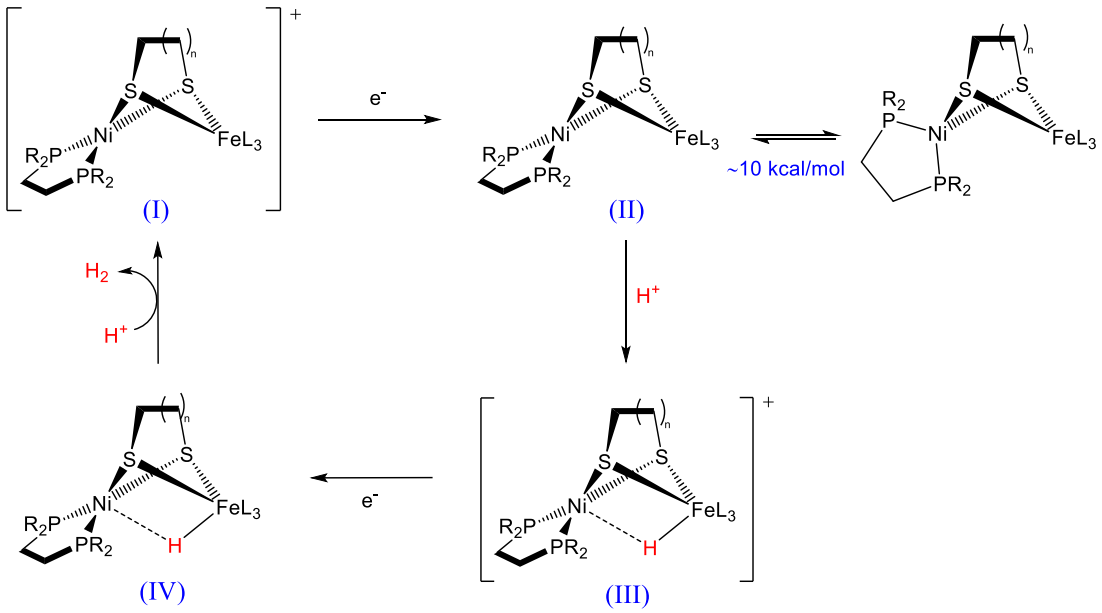

Scheme 1.16. General representation of the proposed mechanistic scheme for HER by hydride containing [NiFe] electrocatalysts, **46-52** based experimental results and on the relative energies of computed intermediates

1.7.3 $NiP_2(\mu\text{-}S)_2Fe$ heterobimetallic electrocatalysts.

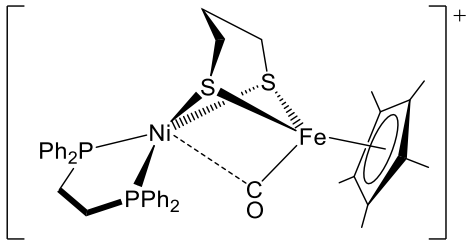

(53)

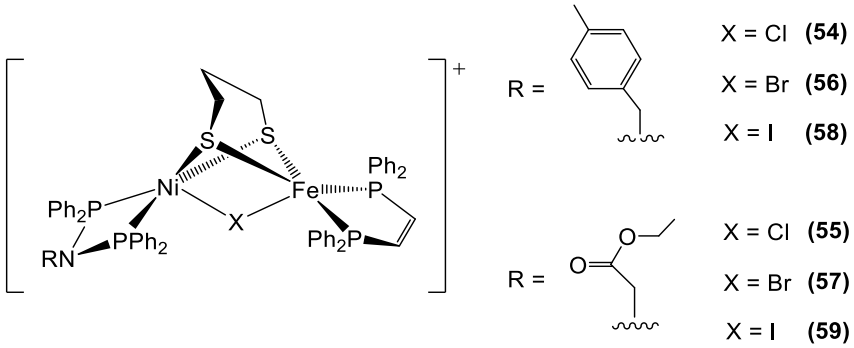

Figure 1.27. HER electrocatalysts reported containing the $\{P_2Ni(\mu\text{-}S)_2Fe\}$ motif.

Table 1.13. Reported HER metrics and mechanisms of electrocatalysts containing the $\{P_2Ni(\mu\text{-}S)_2Fe\}$ motif.

Catalyst	$(NiFe)^{+/0}$ [a]	TOF (s^{-1})	η (V)	TON (h^{-1})	FE	Mechanism	H^+ Source	Ref
53 [b]	-1.52 (ir)	760	~0.8	*n.r.*	*n.r.*	EECC	AcOH	[220]
54 [b]	-1.55 (ir)	10	0.57	*n.r.*	*n.r.*	*n.r.*	MCA[c]	[221]
55 [b]	-1.51 (ir)	17	0.53	*n.r.*	*n.r.*	*n.r.*	MCA[c]	[221]
56 [b]	-1.50 (ir)	7	0.55	*n.r.*	*n.r.*	*n.r.*	MCA[c]	[221]
57 [b]	-1.47 (ir)	13	0.51	*n.r.*	*n.r.*	*n.r.*	MCA[c]	[221]
58 [b]	-1.45 (ir)	6	0.52	*n.r.*	*n.r.*	*n.r.*	MCA[c]	[221]
59 [b]	-1.41 (ir)	12	0.48	*n.r.*	*n.r.*	*n.r.*	MCA[c]	[221]

[a]Potentials are vs Fc/Fc^+, [b]MeCN, [c]Chloroacetic acid, (r) reversible couple, and (ir) irreversible couple.

Wang and coworkers reported a series of HER-active electrocatalysts with a $\{P_2Ni^{II}(\mu\text{-}S)_2Fe^{II}\}$ core **54-59**, depicted in Figure 1.27, incorporating bridging halogens with their crystal structures revealing Ni^{II} in a distorted square-pyramidal geometry and Fe^{II} in an octahedral geometry.[221] These catalysts possess relatively low TOF values (6-17 s^{-1}) with modest overpotentials (0.48 - 0.57 V). Within this set of electrocatalysts (**54**-**59**), incorporation of electron-withdrawing

bridging halogens possess lower TOF values and lower overpotentials, correlated to more positive reduction potentials. The inverse is true for the substituted N-groups, but the reasoning is not clear, and no mechanism is proposed.

1.7.4 $NiN_2(\mu\text{-}S)_2Fe$ heterobimetallic electrocatalysts.

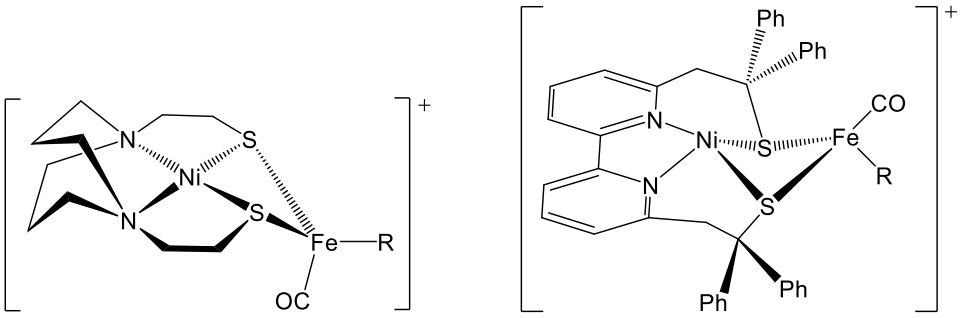

(60): R = Cp
(61): R = Cp*

(62): R = Cp
(63): R = Cp*

Figure 1.28. HER electrocatalysts reported containing the $\{N_2Ni(\mu\text{-}S)_2Fe\}$ motif.

Table 1.14. Reported HER metrics and mechanisms of electrocatalysts containing the $\{N_2Ni(\mu\text{-}S)_2Fe\}$ motif.

Catalyst	$(NiFe)^{+/0a}$	TOF (s^{-1})	η (V)	TON (h^{-1})	FE	Mechanism	H^+ Source	Ref
60[b]	-1.64 (ir)	52	0.94	0.3	77	ECEC/ E[CECE]	TFA	[222]
61[b]	-1.91 (ir)	32	1.31	0.6	88	*n.r.*	TFA	[223]
62[b]	-1.29 (r)	250	~0.5	11	70	EECC/ E[ECCE]	$Et_3NH{\cdot}BF_4$	[179]
63[b]	-1.46 (r)	*n.r.*	*n.r.*	11	72	E[CEEC]	$Et_3NH{\cdot}BF_4$	[224]

[a]Potentials are vs Fc/Fc^+, [b]MeCN, (r) reversible couple, (ir) irreversible couple, and *n.r.* (not reported).

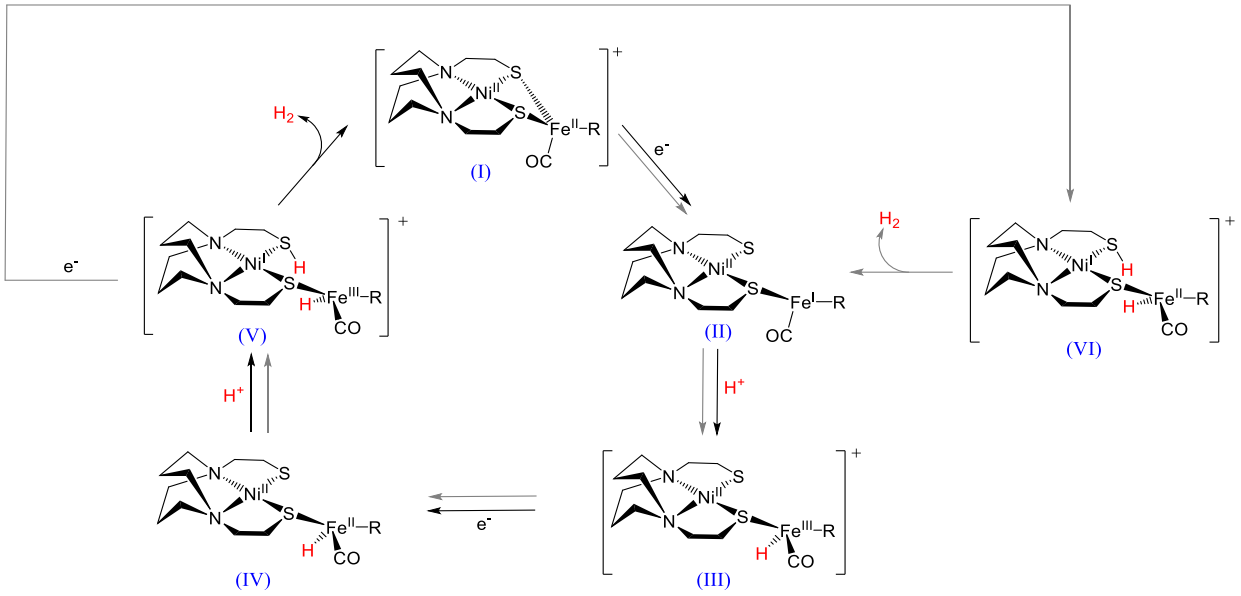

Scheme 1.17. Proposed mechanistic scheme for HER by **60** and **61** going through the ECEC (black) or E[CECE] (grey) mechanism based on the relative energies of computed intermediates.

The last set of bimetallic electrocatalysts feature a macrocyclic N_2S_2 ligand that holds Ni^{II} in a rigid square-planar geometry, with Ni slightly puckered above the plane, formed by the ligand, with two thiolates bridging to Fe^{II} that is coordinated by Cp/Cp* and CO. Darensbourg and coworkers reported the electrocatalytic HER activity of a set of {N_2S_2NiFe} electrocatalysts **60** and **61**, Figure 1.28, reminiscent of the first reported synthetic [NiFe] mimic, complex **41** in Figure 1.23.[222, 223] Although these catalysts are not the most active HER electrocatalysts, their proposed mechanism, shown in Scheme 1.17, offers insight into a potential role of bridging thiolates during HER turnover. Catalysis is first initiated by reduction of $Fe^{II/I}$ causing the cleavage of a bridging thiolates (intermediate II). This cleavage opens a coordination site necessary to form a terminal Fe^{III}-hydride (intermediate III) through oxidative addition. Intermediate III is further reduced at $Fe^{III/II}$ (intermediate IV), and a second protonation event at the free thiolate causes intramolecular reduction of Ni^{II} by Fe^{II}-H to generate a Ni^{I}(μ-S)Fe^{III}-H (intermediate V). The thiol can act as a proton shuttle to couple H^+ to the Fe^{III}-H to evolve H_2 resulting in rebinding of the deprotonated

thiol, completing a proposed [ECEC] mechanism. Alternatively, the authors propose a thermodynamically equivalent pathway in which the Fe of the $Ni^{I}(\mu\text{-}S)Fe^{III}$-H intermediate is further reduced (intermediate IV) before heterolytic coupling to evolve H_2, this presents an alternative E[ECEC] mechanism. Both proposed mechanisms suggest hemilability of a bridging thiolate can play a role as proton shuttles in other [NiFe] HER electrocatalysts. Furthermore, the calculated mechanism suggests that Fe is responsible for H^+ reduction. The Fe center reactivity is furtherer supported by the investigation of hydride formation in a derivative of **60**, $[Ni(N_2S_2)Fe(P(OEt_3)_3)]$. [225] $[Ni(N_2S_2)Fe(P(OEt_3)_3)]$ was found to heterolytically activate H_2. This reactivity was exhibited by reaction of $[Ni(N_2S_2)Fe(P(OEt_3)_3)]$ with H_2, in the presence of a strong base (MeONa), yielding the isolable hydride bound complex $[Ni^{II}(N_2S_2)Fe^{II}(H)(P(OEt_3)_3)]^+$. The X-ray structure of a deuteride labeled complex revealed the deuteride was bound more tightly to Fe (Fe-D = 1.58 Å, Ni-D = 2.18 Å). Although this complex was not tested for HER activity, it performs hydride transfer and evolves H_2 upon addition of a strong acid (HBF_4). Modification of **60** to incorporate a more electron-donating group (Cp*) at Fe in **61** results in a lower TOF, by almost a half, and at a higher overpotential, by ~0.3 V. Although it is unclear why TOF is affected by this modification, the modification decreases the potential required to generate the Fe^{I} intermediate needed to initiate catalysis, therefore, resulting in a higher overpotential.

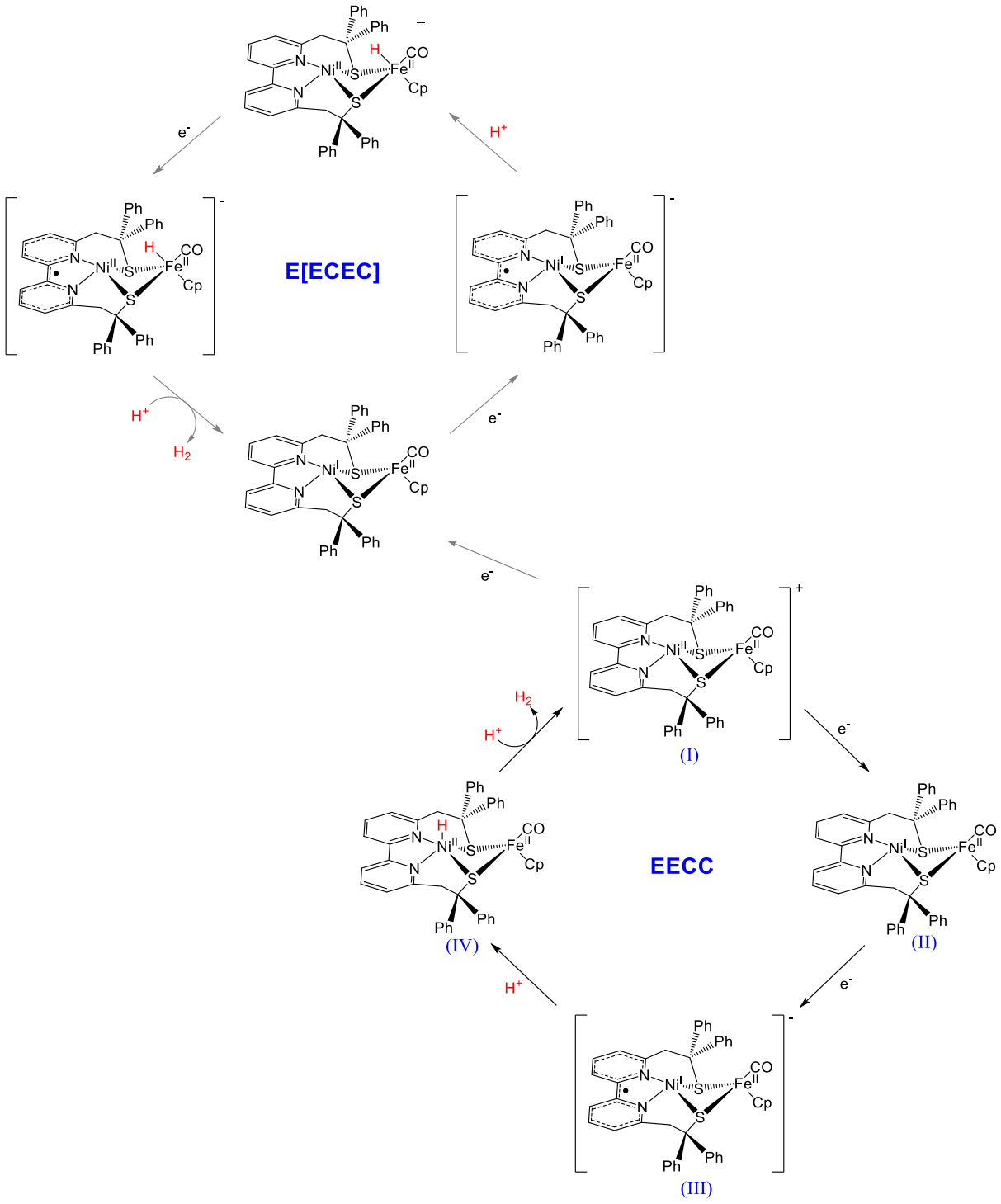

Scheme 1.18. Proposed mechanistic schemes for HER by **62** for both the EECC (black arrow) and E[ECEC] (grey arrows) pathways based on experimental results and the relative energies of computed intermediates.

All reported [NiFe] HER electrocatalysts with proposed mechanisms (**44**, **46-52**, **60**, **61**) utilize Fe, not Ni, in their redox activity with hydride proposed to be bound more tightly to Fe, if bridging, or solely on Fe. The only reported HER bimetallic catalyst that is not proposed to go through Fe is **62**, reported by Artero and Duboc, seen in Figure 1.28.[179] Complex **62** utilizes a tetradentate N_2S_2 unit incorporating a bpy unit to bind Ni^{II} in a square-planar geometry and two of the thiolates bridge to Fe^{II} coordinated by Cp and CO. The authors proposed an EECC mechanism based on experimental results, see Scheme 1.18. First, the authors observed that electrocatalysis was not initiated until the second reduction event of bpy, suggesting Ni and bpy unit are reduced as the first and second step of the cycle (intermediate II and III). Chemical reduction (*in-situ*) of **62** with one mol-equivalent of $CoCp_2$ generated a $Ni^{I}Fe^{II}$ complex (intermediate II), characterized by EPR, IR, and Mössbauer, as a synthetic model of Ni-L state of the native enzyme. After reduction of $Ni^{II/I}$ and bpy (EE steps), protonation is proposed to form a Ni^{II}-H (intermediate IV) through oxidative addition of a H^+ to form a putative Ni^{III}-H which is reduced by the bpy unit. In order to confirm a terminally bound hydride, a Ni^{II}-H complex was *in-situ* generated (*in-situ*) from addition of excess $NaBH_4$ to **62**. Characterization of this solution by ^1H NMR (δ_H = -6.80 ppm) confirms the Ni-R like intermediate. Although crystalline material could not be isolated, the optimized structure of the Ni-R like intermediate shows a terminally bound hydride to Ni (Ni-H = 1.55 Å) similar to the Ni-H bond length (Ni-H = 1.58 Å) in the Ni-R state of the native enzyme. Lastly, heterolytic coupling of a free H^+ from exogenous acid to intermediate IV generates H_2. **62** is the first reported example of a [NiFe] HER electrocatalyst in which H^+ reduction is proposed to be Ni centered. However, Tang and Hall disputed an EECC mechanism by computing a lower energy E[ECEC] mechanism for **62** that goes through an Fe^{II}-H centered intermediate, shown in Scheme 1.18.[226] Involvement of Fe in the catalytic cycle was later confirmed by Duboc and coworkers in

an analogous catalyst **63** featuring a Cp* in place of Cp in **62**.[224] In turn, both mechanisms may be possible for H_2 production by **62** and **63**; however, the lowest energy pathway most likely involves the formation of the hydride on Fe not Ni.

Comparison of all these synthetic [NiFe] electrocatalysts reveals that Fe is primarily responsible for H^+ reduction evidence by changes in the oxidation state of Fe and formation of Fe-H. The roles of the metals are reversed in [NiFe]-H_2ase. In the native enzyme, Ni is the only metal participating in redox activity and undergoes oxidative addition to form a Ni-H. Another key difference between these bimetallic models and the native enzyme lies in the donor set and geometry of Ni. These synthetic mimic lack of a thiolate rich coordination sphere and Ni held is in a rigid pseudo-tetrahedral geometry. All synthetic models use a mixed coordination sphere that either holds Ni^{II} in a rigid square-planar geometry or can reorganize adopting a more tetrahedral geometry. Lack of the thiolate-rich coordination sphere leads to a less electron-rich Ni and most likely contributes to the inability to stabilize a Ni^{III}-H intermediate. Furthermore, the pseudo-tetrahedral geometry may positively shift the reduction potential of Ni, as proposed by Dubois for the NiP_4 electrocatalysts, circumventing the redox involvement of Fe. However, incorporation of terminal thiolates and holding Ni^{II} in a pseudo-tetrahedral geometry poses challenges due to the propensity to form multinuclear bridging species with Ni^{II} preferring square-planar geometry, *vide infra*. The innovations required to achieve this unique geometry will deepen our understanding of the unusual structure-to-function relationship of [NiFe]-H_2ase.

1.8 Intent of Research

The driving force behind this research is the development of cheap and efficient electrocatalysts for hydrogen production. One such way to gain insight into developing cheaper catalysts is to understand how enzymes called H_2ases utilize cheap and earth-abundant Ni and Fe to evolve H_2 with high efficiency. In turn, the goal of this research is to elucidate the relationship between the unique coordination environment of Ni in [NiFe]-H_2ase and its reactivity utilizing a synthetic modeling approach. There are many reported Ni and [NiFe] electrocatalysts that surpass the TOF of the native enzyme; however, they fail to match the enzyme's efficiency. Furthermore, these electrocatalysts lack a purely thiolate coordination sphere around Ni nor capture its distorted-tetrahedral geometry. In turn, there is a gap of knowledge revealing how the unique structure of Ni facilitates the efficient electrocatalytic processing of H_2.

The Ni^{II}-tertraaryl thiolate complexes, Figure 1.12, are the best structural mimics of the native enzyme, however, they have several problematic characteristics for use as proton reducing electrocatalysts. First, maintaining the tetrahedral geometry about NiS_4 complexes is challenging as most reported complexes tend to hold square-planar geometries. Second, NiS_4 complexes tend to form multinuclear species under synthetic conditions and further degrade under protic conditions. Lastly, the NiS_4 complexes tend to have ill-defined electrochemistry. Unsurprisingly, there are no reported Ni^{II} homoleptic tetrathiolate electrocatalysts. There are two main goals of this research: (i) Synthesize and characterize homoleptic tetrathiolaonickelate(II) complexes that replicate the geometry of the native enzyme to understand the electronic properties that govern geometry preference and the behavior in solution; and (ii) determine the HER electrocatalysis and mechanism of said complexes to gain insight into the role of coordination sphere in the function of the enzyme.

This chemistry is investigated with three different platforms. The first platform involves homoleptic Ni^{II} complexes bearing (S-*p*-CF_3-Ph) ligands. This simple model is used to understand the factors that govern the preferred tetrahedral geometry of aryl-thiolates, their propensity to form multinuclear species upon dissolution, and the fate of the NiS_4 systems under protic conditions. Controlling these factors are key to circumventing their shortcomings as HER electrocatalysts. We show that under excess thiolate conditions nuclearity and protic stability can be improved therefore allowing the HER electrocatalysis to be assessed. However, this electrocatalyst still exhibits degradation in the presence of acid limiting its HER activity. The second generation of Ni^{II}-tetrathioaltes incorporates amido groups, of varying size, to engage the bound thiolates in H-bonding to improve HER activity. H-bonding affords more stability of the Ni^{II}-tetrathioaltes under protic condition; however, impacts the preferred geometry of these species. Furthermore, it was determined that HER activity resulted from heterogenous material deposited on the electrode. Lastly, a five-coordinate pyridine-diamide-dithiolate ligand was utilized to develop a mononuclear Fe based HER electrocatalyst to improve stability of complexes under protic conditions. It was found that the addition of acid resulted in protonation and cleavage of the Fe-N_{amide} bond leading to ligand rearrangement. The stability of the catalyst was improved utilizing different solvent conditions allowing the catalytic properties to be assessed. Ultimately, these electrocatalysts not only provide insight into the fundamental chemistry of Ni and Fe thiolates and H^+ reduction but also as potential alternatives for more cost efficient electrocatalyst for hydrogen evolution.

1.9 References

(1) Lacis, A. A.; Schmidt, G. A.; Rind, D.; Ruedy, R. A. *Science,* **2010**, *330*, 356.

(2) Friedlingstein, P.; Jones, M. W.; O'Sullivan, M.; Andrew, R. M.; Bakker, D. C. E.; Hauck, J.; Le Quéré, C.; Peters, G. P.; Peters, W.; Pongratz, J.; et al. *Earth Syst. Sci. Data Discuss.,* **2021**, *2021*, 1.

(3) Armstrong McKay, D. I.; Staal, A.; Abrams, J. F.; Winkelmann, R.; Sakschewski, B.; Loriani, S.; Fetzer, I.; Cornell, S. E.; Rockström, J.; Lenton, T. M. *Science,* **2022**, *377*, eabn7950.

(4) Warren, R.; Price, J.; Graham, E.; Forstenhaeusler, N.; VanDerWal, J. *Science,* **2018**, *360*, 791.

(5) Rasmussen, D. J.; Bittermann, K.; Buchanan, M. K.; Kulp, S.; Strauss, B. H.; Kopp, R. E.; Oppenheimer, M. *Environmental Research Letters,* **2018**, *13*, 034040.

(6) Administration, N. O. a. A. *Trends in Atmospheic Carbon Dioxide*. 2024. (accessed June 30, 2024).

(7) Fuss, S.; Canadell, J. G.; Peters, G. P.; Tavoni, M.; Andrew, R. M.; Ciais, P.; Jackson, R. B.; Jones, C. D.; Kraxner, F.; Nakicenovic, N.; et al. *Nature Climate Change,* **2014**, *4*, 850.

(8) Hoffert, M. I.; Caldeira, K.; Jain, A. K.; Haites, E. F.; Harvey, L. D. D.; Potter, S. D.; Schlesinger, M. E.; Schneider, S. H.; Watts, R. G.; Wigley, T. M. L.; et al. *Nature,* **1998**, *395*, 881.

(9) Lewis, N. S.; Nocera, D. G. *Proc. Natl. Acad. Sci. U.S.A.,* **2006**, *103*, 15729.

(10) *Global fossil fuel consumption*. 2023. https://ourworldindata.org/grapher/global-fossil-fuel-consumption?time=1850..latest&facet=none (accessed July 23, 2024).

(11) Smith, C.; Hill, A. K.; Torrente-Murciano, L. *Energy & Environmental Science,* **2020**, *13*, 331.

(12) Benson, S. W. *J. Chem. Educ.,* **1965**, *42*, 502.

(13) Vincent, K. A.; Parkin, A.; Armstrong, F. A. *Chem. Rev.,* **2007**, *107*, 4366.

(14) Sara, M. C., Jyn-Yuan; Carlos, Fernandez-Pello. *Fundamentals of Combustion Processes*; Springer Sciecne, 2011.

(15) Züttel, A.; Remhof, A.; Borgschulte, A.; Friedrichs, O. *Philosophical Transactions of the Royal Society A: Mathematical, Physical and Engineering Sciences,* **2010**, *368*, 3329.

(16) Lide, D. *CRC Handbook of Chemistry and Physics*; CRC press, 2003.

(17) Mahmood, N.; Yao, Y.; Zhang, J.-W.; Pan, L.; Zhang, X.; Zou, J.-J. *Adv. Sci.,* **2018**, *5*, 1700464.

(18) Das, D.; Veziroglu, T. N. *International Journal of Hydrogen Energy,* **2008**, *33*, 6046.

(19) Chen, Y.; Wang, Y.; Xu, H.; Xiong, G. *Applied Catalysis B: Environmental,* **2008**, *81*, 283.

(20) Zhao, J.; Liu, H.; Li, X. *Electrochemical Energy Reviews,* **2023**, *6*, 13.

(21) Trasatti, S. *J. Electroanal. Chem. Interfacial Electrochem.,* **1972**, *39*, 163.

(22) Nørskov, J. K.; Bligaard, T.; Logadottir, A.; Kitchin, J. R.; Chen, J. G.; Pandelov, S.; Stimming, U. *Journal of The Electrochemical Society,* **2005**, *152*, J23.

(23) Miles, M. H.; Thomason, M. A. *Journal of The Electrochemical Society,* **1976**, *123*, 1459.

(24) Chen, W.-F.; Muckerman, J. T.; Fujita, E. *Chem. Commun.,* **2013**, *49*, 8896.

(25) Chen, Y.; Ding, R.; Li, J.; Liu, J. *Applied Catalysis B: Environmental,* **2022**, *301*, 120830.

(26) Vault, B. *BullionVault's Platinum Price Live Chart*. (accessed June 30, 2024).

(27) Roger, I.; Shipman, M. A.; Symes, M. D. *Nat. Rev. Chem.,* **2017**, *1*, 0003.

(28) Mekhilef, S.; Saidur, R.; Safari, A. *Renewable and Sustainable Energy Reviews,* **2012**, *16*, 981.

(29) *Carbon Pollution from Transportation*. United States Enviornmental Protection Agency, 2021. (accessed June 06, 20204).

(30) *Fuel Cell Electric Vehicles*. US Department of Energy, 2024. (accessed.

(31) Cullen, D. A.; Neyerlin, K. C.; Ahluwalia, R. K.; Mukundan, R.; More, K. L.; Borup, R. L.; Weber, A. Z.; Myers, D. J.; Kusoglu, A. *Nature Energy,* **2021**, *6*, 462.

(32) Hoppe-Seyler., F. **1887**, *11*, 561.

(33) Stephenson, M.; Stickland, L. H. *Biochem J,* **1931**, *25*, 205.

(34) Tamagnini, P.; Leitão, E.; Oliveira, P.; Ferreira, D.; Pinto, F.; Harris, D. J.; Heidorn, T.; Lindblad, P. *FEMS Microbiol. Rev.,* **2007**, *31*, 692.

(35) Tamagnini, P.; Axelsson, R.; Lindberg, P.; Oxelfelt, F.; Wünschiers, R.; Lindblad, P. *Microbiol. Mol. Biol. Rev.,* **2002**, *66*, 1.

(36) Vignais, P. M.; Billoud, B. *Chem. Rev.,* **2007**, *107*, 4206.

(37) Vignais, P. M.; Billoud, B.; Meyer, J. *FEMS Microbiol. Rev.,* **2001**, *25*, 455.

(38) Wu, L.-F.; Mandrand, M. A. *FEMS Microbiol. Rev.,* **1993**, *10*, 243.

(39) YAGI, T.; TSUDA, M.; INOKUCHI, H. *J. Biochem.,* **1973**, *73*, 1069.

(40) Fontecilla-Camps, J. C.; Amara, P.; Cavazza, C.; Nicolet, Y.; Volbeda, A. *Nature,* **2009**, *460*, 814.

(41) Fontecilla-Camps, J. C.; Volbeda, A.; Cavazza, C.; Nicolet, Y. *Chem. Rev.,* **2007**, *107*, 4273.

(42) Shima, S.; Pilak, O.; Vogt, S.; Schick, M.; Stagni, M. S.; Meyer-Klaucke, W.; Warkentin, E.; Thauer, R. K.; Ermler, U. *Science,* **2008**, *321*, 572.

(43) Fontecilla-Camps, J. C.; Volbeda, A.; Cavazza, C.; Nicolet, Y. *Chem. Rev.,* **2007**, *107*, 5411.

(44) Darensbourg, M. Y.; Lyon, E. J.; Zhao, X.; Georgakaki, I. P. *Proc. Natl. Acad. Sci. U.S.A.,* **2003**, *100*, 3683.

(45) Hinnemann, B.; Moses, P. G.; Bonde, J.; Jørgensen, K. P.; Nielsen, J. H.; Horch, S.; Chorkendorff, I.; Nørskov, J. K. *J. Am. Chem. Soc.,* **2005**, *127*, 5308.

(46) Adams, M. W. W. *Biochimica et Biophysica Acta (BBA) - Bioenergetics,* **1990**, *1020*, 115.

(47) Morozov, S. V.; Karyakina, E. E.; Zorin, N. A.; Varfolomeyev, S. D.; Cosnier, S.; Karyakin, A. A. *Bioelectrochemistry,* **2002**, *55*, 169.

(48) Pilak, O.; Mamat, B.; Vogt, S.; Hagemeier, C. H.; Thauer, R. K.; Shima, S.; Vonrhein, C.; Warkentin, E.; Ermler, U. *J. Mol. Biol.,* **2006**, *358*, 798.

(49) Lyon, E. J.; Shima, S.; Boecher, R.; Thauer, R. K.; Grevels, F.-W.; Bill, E.; Roseboom, W.; Albracht, S. P. J. *J. Am. Chem. Soc.,* **2004**, *126*, 14239.

(50) Guo, Y.; Wang, H.; Xiao, Y.; Vogt, S.; Thauer, R. K.; Shima, S.; Volkers, P. I.; Rauchfuss, T. B.; Pelmenschikov, V.; Case, D. A.; et al. *Inorg. Chem.,* **2008**, *47*, 3969.

(51) Wang, C.; Lai, Z.; Huang, G.; Pan, H.-J. *Chem. Eur. J.,* **2022**, *28*, e202201499.

(52) Thauer, R. K.; Klein, A. R.; Hartmann, G. C. *Chem. Rev.,* **1996**, *96*, 3031.

(53) Zirngibl, C.; Hedderich, R.; Thauer, R. K. *FEBS Lett.,* **1990**, *261*, 112.

(54) Nicolet, Y.; Piras, C.; Legrand, P.; Hatchikian, C. E.; Fontecilla-Camps, J. C. *Structure,* **1999**, *7*, 13.

(55) Shepard, E. M.; Mus, F.; Betz, J. N.; Byer, A. S.; Duffus, B. R.; Peters, J. W.; Broderick, J. B. *Biochemistry,* **2014**, *53*, 4090.

(56) Pandey, A. S.; Harris, T. V.; Giles, L. J.; Peters, J. W.; Szilagyi, R. K. *J. Am. Chem. Soc.,* **2008**, *130*, 4533.

(57) Silakov, A.; Reijerse, E. J.; Albracht, S. P. J.; Hatchikian, E. C.; Lubitz, W. *J. Am. Chem. Soc.,* **2007**, *129*, 11447.

(58) Adamska, A.; Silakov, A.; Lambertz, C.; Rüdiger, O.; Happe, T.; Reijerse, E.; Lubitz, W. *Angew. Chem. Int. Ed.,* **2012**, *51*, 11458.

(59) Schilter, D.; Camara, J. M.; Huynh, M. T.; Hammes-Schiffer, S.; Rauchfuss, T. B. *Chem. Rev.,* **2016**, *116*, 8693.

(60) Ghirardi, M. L.; Dubini, A.; Yu, J.; Maness, P.-C. *Chem. Soc. Rev.,* **2009**, *38*, 52.

(61) Kubas, A.; Orain, C.; De Sancho, D.; Saujet, L.; Sensi, M.; Gauquelin, C.; Meynial-Salles, I.; Soucaille, P.; Bottin, H.; Baffert, C.; et al. *Nat. Chem.,* **2017**, *9*, 88.

(62) Volbeda, A.; Charon, M.-H.; Piras, C.; Hatchikian, E. C.; Frey, M.; Fontecilla-Camps, J. C. *Nature,* **1995**, *373*, 580.

(63) Lubitz, W.; Ogata, H.; Rüdiger, O.; Reijerse, E. *Chem. Rev.,* **2014**, *114*, 4081.

(64) Vignais, P. M.; Billoud, B.; Meyer, J. *FEMS Microbiol. Rev.,* **2001**, *25*, 455.

(65) Higuchi, Y.; Yasuoka, N.; Kakudo, M.; Katsube, Y.; Yagi, T.; Inokuchi, H. *J. Biol. Chem.,* **1987**, *262*, 2823.

(66) Higuchi, Y.; Ogata, H.; Miki, K.; Yasuoka, N.; Yagi, T. *Structure,* **1999**, *7*, 549.

(67) Alfano, M.; Cavazza, C. *Protein Sci,* **2020**, *29*, 1071.

(68) Ogata, H.; Nishikawa, K.; Lubitz, W. *Nature,* **2015**, *520*, 571.

(69) Krämer, T.; Kampa, M.; Lubitz, W.; van Gastel, M.; Neese, F. *ChemBioChem,* **2013**, *14*, 1898.

(70) Dong, G.; Ryde, U. *J. Biol. Inorg. Chem.,* **2016**, *21*, 383.

(71) Montet, Y.; Amara, P.; Volbeda, A.; Vernede, X.; Hatchikian, E. C.; Field, M. J.; Frey, M.; Fontecilla-Camps, J. C. *Nat. Struct. Biol.,* **1997**, *4*, 523.

(72) Topin, J.; Rousset, M.; Antonczak, S.; Golebiowski, J. *Proteins,* **2012**, *80*, 677.

(73) Fdez. Galván, I.; Volbeda, A.; Fontecilla-Camps, J. C.; Field, M. J. *Proteins,* **2008**, *73*, 195.

(74) Teixeira, V. H.; Soares, C. M.; Baptista, A. M. *Proteins,* **2008**, *70*, 1010.

(75) Szőri-Dorogházi, E.; Maróti, G.; Szőri, M.; Nyilasi, A.; Rákhely, G.; Kovács, K. L. *PLOS ONE,* **2012**, *7*, e34666.

(76) Pavlov, M.; Siegbahn, P. E. M.; Blomberg, M. R. A.; Crabtree, R. H. *J. Am. Chem. Soc.,* **1998**, *120*, 548.

(77) McGrady, G. S.; Guilera, G. *Chem. Soc. Rev.,* **2003**, *32*, 383.

(78) Yson, R. L.; Gilgor, J. L.; Guberman, B. A.; Varganov, S. A. *Chem. Phys. Lett.,* **2013**, *577*, 138.

(79) Bruschi, M.; Tiberti, M.; Guerra, A.; De Gioia, L. *J. Am. Chem. Soc.,* **2014**, *136*, 1803.

(80) Das, R.; Neese, F.; van Gastel, M. *Phys. Chem. Chem. Phys.,* **2016**, *18*, 24681.

(81) Raebiger, J. W.; Miedaner, A.; Curtis, C. J.; Miller, S. M.; Anderson, O. P.; DuBois, D. L. *J. Am. Chem. Soc.,* **2004**, *126*, 5502.

(82) DuBois, D. L.; Blake, D. M.; Miedaner, A.; Curtis, C. J.; DuBois, M. R.; Franz, J. A.; Linehan, J. C. *Organometallics,* **2006**, *25*, 4414.

(83) Bouwman, E.; Reedijk, J. *Coord. Chem. Rev.,* **2005**, *249*, 1555.

(84) Ogata, H.; Mizoguchi, Y.; Mizuno, N.; Miki, K.; Adachi, S.-i.; Yasuoka, N.; Yagi, T.; Yamauchi, O.; Hirota, S.; Higuchi, Y. *J. Am. Chem. Soc.,* **2002**, *124*, 11628.

(85) Bagley, K. A.; Van Garderen, C. J.; Chen, M.; Woodruff, W. H.; Duin, E. C.; Albracht, S. P. J. *Biochemistry,* **1994**, *33*, 9229.

(86) Volbeda, A.; Martin, L.; Cavazza, C.; Matho, M.; Faber, B. W.; Roseboom, W.; Albracht, S. P. J.; Garcin, E.; Rousset, M.; Fontecilla-Camps, J. C. *J. Biol. Inorg. Chem.,* **2005**, *10*, 239.

(87) Ogata, H.; Hirota, S.; Nakahara, A.; Komori, H.; Shibata, N.; Kato, T.; Kano, K.; Higuchi, Y. *Structure,* **2005**, *13*, 1635.

(88) Wang, H.; Ralston, C. Y.; Patil, D. S.; Jones, R. M.; Gu, W.; Verhagen, M.; Adams, M.; Ge, P.; Riordan, C.; Marganian, C. A.; et al. *J. Am. Chem. Soc.,* **2000**, *122*, 10544.

(89) Delcey, M. G.; Pierloot, K.; Phung, Q. M.; Vancoillie, S.; Lindh, R.; Ryde, U. *Phys. Chem. Chem. Phys.,* **2014**, *16*, 7927.

(90) Pardo, A.; De Lacey, A. L.; Fernández, V. M.; Fan, H.-J.; Fan, Y.; Hall, M. B. *J. Biol. Inorg. Chem.,* **2006**, *11*, 286.

(91) Kowal, A. T.; Zambrano, I. C.; Moura, I.; Moura, J. J. G.; LeGall, J.; Johnson, M. K. *Inorg. Chem.,* **1988**, *27*, 1162.

(92) Wang, C. P.; Franco, R.; Moura, J. J.; Moura, I.; Day, E. P. *J. Biol. Chem.,* **1992**, *267*, 7378.

(93) Li, S.; Hall, M. B. *Inorg. Chem.,* **2001**, *40*, 18.

(94) Ogata, H.; Krämer, T.; Wang, H.; Schilter, D.; Pelmenschikov, V.; van Gastel, M.; Neese, F.; Rauchfuss, T. B.; Gee, L. B.; Scott, A. D.; et al. *Nat. Commun.,* **2015**, *6*, 7890.

(95) Evans, R. M.; Brooke, E. J.; Wehlin, S. A. M.; Nomerotskaia, E.; Sargent, F.; Carr, S. B.; Phillips, S. E. V.; Armstrong, F. A. *Nat. Chem. Biol.,* **2016**, *12*, 46.

(96) Whitehead, J. P.; Gurbiel, R. J.; Bagyinka, C.; Hoffman, B. M.; Maroney, M. J. *J. Am. Chem. Soc.,* **1993**, *115*, 5629.

(97) Brecht, M.; van Gastel, M.; Buhrke, T.; Friedrich, B.; Lubitz, W. *J. Am. Chem. Soc.,* **2003**, *125*, 13075.

(98) Kampa, M.; Pandelia, M.-E.; Lubitz, W.; van Gastel, M.; Neese, F. *J. Am. Chem. Soc.,* **2013**, *135*, 3915.

(99) van der Zwaan, J. W.; Albracht, S. P. J.; Fontijn, R. D.; Slater, E. C. *FEBS Lett.,* **1985**, *179*, 271.

(100) Fichtner, C.; van Gastel, M.; Lubitz, W. *Phys. Chem. Chem. Phys.,* **2003**, *5*, 5507.

(101) Medina, M.; Claude Hatchikian, E.; Cammack, R. *Biochimica et Biophysica Acta (BBA) - Bioenergetics,* **1996**, *1275*, 227.

(102) Lill, S. O. N.; Siegbahn, P. E. M. *Biochemistry,* **2009**, *48*, 1056.

(103) Greene, B. L.; Wu, C.-H.; McTernan, P. M.; Adams, M. W. W.; Dyer, R. B. *J. Am. Chem. Soc.,* **2015**, *137*, 4558.

(104) Murphy, B. J.; Hidalgo, R.; Roessler, M. M.; Evans, R. M.; Ash, P. A.; Myers, W. K.; Vincent, K. A.; Armstrong, F. A. *J. Am. Chem. Soc.,* **2015**, *137*, 8484.

(105) Agrawal, A. G.; van Gastel, M.; Gärtner, W.; Lubitz, W. *J. Phys. Chem. B,* **2006**, *110*, 8142.

(106) Brooke, E. J.; Evans, R. M.; Islam, S. T. A.; Roberts, G. M.; Wehlin, S. A. M.; Carr, S. B.; Phillips, S. E. V.; Armstrong, F. A. *Biochemistry,* **2017**, *56*, 132.

(107) Evans, R. M.; Beaton, S. E.; Rodriguez Macia, P.; Pang, Y.; Wong, K. L.; Kertess, L.; Myers, W. K.; Bjornsson, R.; Ash, P. A.; Vincent, K. A.; et al. *Chem. Sci.,* **2023**, *14*, 8531.

(108) Dementin, S.; Burlat, B.; De Lacey, A. L.; Pardo, A.; Adryanczyk-Perrier, G.; Guigliarelli, B.; Fernandez, V. M.; Rousset, M. *J. Biol. Chem.,* **2004**, *279*, 10508.

(109) Evans, R. M.; Ash, P. A.; Beaton, S. E.; Brooke, E. J.; Vincent, K. A.; Carr, S. B.; Armstrong, F. A. *J. Am. Chem. Soc.,* **2018**, *140*, 10208.

(110) Goldet, G.; Wait, A. F.; Cracknell, J. A.; Vincent, K. A.; Ludwig, M.; Lenz, O.; Friedrich, B.; Armstrong, F. A. *J. Am. Chem. Soc.,* **2008**, *130*, 11106.

(111) Cracknell, J. A.; Wait, A. F.; Lenz, O.; Friedrich, B.; Armstrong, F. A. *Proc. Natl. Acad. Sci. U.S.A.,* **2009**, *106*, 20681.

(112) Shomura, Y.; Higuchi, Y. *Rev. Inorg. Chem.,* **2013**, *33*, 173.

(113) Fritsch, J.; Lenz, O.; Friedrich, B. *Nat. Rev. Microbiol.,* **2013**, *11*, 106.

(114) Goris, T.; Wait, A. F.; Saggu, M.; Fritsch, J.; Heidary, N.; Stein, M.; Zebger, I.; Lendzian, F.; Armstrong, F. A.; Friedrich, B.; et al. *Nat. Chem. Biol.,* **2011**, *7*, 310.

(115) Shomura, Y.; Yoon, K.-S.; Nishihara, H.; Higuchi, Y. *Nature,* **2011**, *479*, 253.

(116) Artero, V.; Fontecave, M. *Coord. Chem. Rev.,* **2005**, *249*, 1518.

(117) Leach, M. R.; Zamble, D. B. *Curr. Opin. Chem. Biol.,* **2007**, *11*, 159.

(118) Yamamura, T.; Miyamae, H.; Katayama, Y.; Sasaki, Y. *Chem. Lett.,* **1985**, *14*, 269.

(119) Lindahl, P. A.; Kojima, N.; Hausinger, R. P.; Fox, J. A.; Teo, B. K.; Walsh, C. T.; Orme-Johnson, W. H. *J. Am. Chem. Soc.,* **1984**, *106*, 3062.

(120) Halcrow, M. A.; Christou, G. *Chem. Rev.,* **1994**, *94*, 2421.

(121) Watson, A. D.; Rao, C. P.; Dorfman, J. R.; Holm, R. H. *Inorg. Chem.,* **1985**, *24*, 2820.

(122) Yamamura, T. *Bulletin of the Chemical Society of Japan,* **2006**, *61*, 1975.

(123) Gould, R. O.; Harding, M. M. *J. Chem. Soc., A,* **1970**, 875.

(124) Woodward, P.; Dahl, L. F.; Abel, E. W.; Crosse, B. C. *J. Am. Chem. Soc.,* **1965**, *87*, 5251.

(125) Dance, I. G.; Scudder, M. L.; Secomb, R. *Inorg. Chem.,* **1985**, *24*, 1201.

(126) Gaete, W.; Ros, J.; Solans, X.; Font-Altaba, M.; Brianso, J. L. *Inorg. Chem.,* **1984**, *23*, 39.

(127) Barrera, H.; Bayón, J. C.; Suades, J.; Germain, C.; Declerq, J. P. *Polyhedron,* **1984**, *3*, 969.

(128) Henkel, G.; Kriege, M.; Matsumoto, K. *J. Chem. Soc., Dalton Trans.,* **1988**, 657.

(129) Rosenfield, S. G.; Armstrong, W. H.; Mascharak, P. K. *Inorg. Chem.,* **1986**, *25*, 3014.

(130) Yamamura, T.; Arai, H. *Bull. Chem. Soc. Jpn.,* **1992**, *65*, 1799.

(131) Colpas, G. J.; Kumar, M.; Day, R. O.; Maroney, M. J. *Inorg. Chem.,* **1990**, *29*, 4779.

(132) Costa, T.; Dorfman, J. R.; Hagen, K. S.; Holm, R. H. *Inorg. Chem.,* **1983**, *22*, 4091.

(133) Christou, G.; Huffman, J. C. *J. Chem. Soc., Chem. Commun.,* **1983**, 558.

(134) Krueger, H. J.; Holm, R. H. *Inorg. Chem.,* **1987**, *26*, 3645.

(135) Rao, C. P.; Dorfman, J. R.; Holm, R. H. *Inorg. Chem.,* **1986**, *25*, 428.

(136) Baidya, N.; Mascharak, P. K.; Stephan, D. W.; Campagna, C. F. *Inorg. Chim. Acta,* **1990**, *177*, 233.

(137) Erkizia, E.; Conry, R. R. *Inorg. Chem.,* **2000**, *39*, 1674.

(138) Snyder, B.; Rao, C.; Holm, R. *Aust. J. Chem.,* **1986**, *39*, 963.

(139) Tremel, W.; Kriege, M.; Krebs, B.; Henkel, G. *Inorg. Chem.,* **1988**, *27*, 3886.

(140) Fox, S.; Wang, Y.; Silver, A.; Millar, M. *J. Am. Chem. Soc.,* **1990**, *112*, 3218.

(141) Davison, A.; Switkes, E. S. *Inorg. Chem.,* **1971**, *10*, 837.

(142) Yamamura, T.; Arai, H.; Kurihara, H.; Kuroda, R. *Chem. Lett.,* **1990**, *19*, 1975.

(143) Simón-Manso, E.; Valderrama, M.; Boys, D. *Inorg. Chem.,* **2001**, *40*, 3647.

(144) Rösler, R.; Silverstru, C.; Espinosa-Pérez, G.; Haiduc, I.; Cea-Olivares, R. *Inorg. Chim. Acta,* **1996**, *241*, 47.

(145) Churchill, M. R.; Cooke, J.; Fennessey, J. P.; Wormald, J. *Inorg. Chem.,* **1971**, *10*, 1031.

(146) Maganas, D.; Grigoropoulos, A.; Staniland, S. S.; Chatziefthimiou, S. D.; Harrison, A.; Robertson, N.; Kyritsis, P.; Neese, F. *Inorg. Chem.,* **2010**, *49*, 5079.

(147) Snyder, B.; Rao, C.; Holm, R. *Aust. J. Chem.,* **1986**, *39*, 963.

(148) Saha, P.; Amanullah, S.; Dey, A. *J. Am. Chem. Soc.,* **2020**, *142*, 17312.

(149) Ivanov, S. A.; Kozee, M. A.; Merrill, A. W.; Agarwal, S.; Dahl, L. F. *J. Chem. Soc., Dalton Trans.,* **2002**, 4105.

(150) Silver, A.; Koch, S. A.; Millar, M. *Inorg. Chim. Acta,* **1993**, *205*, 9.

(151) Wombwell, C.; Reisner, E. *Dalton Trans.,* **2014**, *43*, 4483.

(152) McCarthy, B. D.; Donley, C. L.; Dempsey, J. L. *Chem. Sci.,* **2015**, *6*, 2827.

(153) Lee, K. J.; McCarthy, B. D.; Dempsey, J. L. *Chem. Soc. Rev.,* **2019**, *48*, 2927.

(154) Pieri, C.; Bhattacharjee, A.; Barrozo, A.; Faure, B.; Giorgi, M.; Fize, J.; Réglier, M.; Field, M.; Orio, M.; Artero, V.; et al. *Chem. Commun.,* **2020**, *56*, 11106.

(155) Angamuthu, R.; Bouwman, E. *Phys. Chem. Chem. Phys.,* **2009**, *11*, 5578.

(156) Kagalwala, H. N.; Gottlieb, E.; Li, G.; Li, T.; Jin, R.; Bernhard, S. *Inorg. Chem.,* **2013**, *52*, 9094.

(157) Zarkadoulas, A.; Field, M. J.; Papatriantafyllopoulou, C.; Fize, J.; Artero, V.; Mitsopoulou, C. A. *Inorg. Chem.,* **2016**, *55*, 432.

(158) Zarkadoulas, A.; Field, M. J.; Artero, V.; Mitsopoulou, C. A. *ChemCatChem,* **2017**, *9*, 2308.

(159) Koshiba, K.; Yamauchi, K.; Sakai, K. *ChemElectroChem,* **2019**, *6*, 2273.

(160) Koshiba, K.; Yamauchi, K.; Sakai, K. *Angew. Chem. Int. Ed.,* **2017**, *56*, 4247.

(161) Periyasamy, G.; Burton, N. A.; Hillier, I. H.; Vincent, M. A.; Disley, H.; McMaster, J.; Garner, C. D. *Faraday Discussions,* **2007**, *135*, 469.

(162) Hammes-Schiffer, S. *J. Am. Chem. Soc.,* **2015**, *137*, 8860.

(163) Oudart, Y.; Artero, V.; Pécaut, J.; Lebrun, C.; Fontecave, M. *Eur. J. Inorg. Chem.,* **2007**, *2007*, 2613.

(164) Drosou, M.; Zarkadoulas, A.; Bethanis, K.; Mitsopoulou, C. A. *J. Coord. Chem.,* **2021**, *74*, 1425.

(165) James, T. L.; Cai, L.; Muetterties, M. C.; Holm, R. H. *Inorg. Chem.,* **1996**, *35*, 4148.

(166) Chakrabarti, S.; Sinha, S.; Tran, G. N.; Na, H.; Mirica, L. M. *Nat. Commun.,* **2023**, *14*, 905.

(167) Liu, J.; Meier, K. K.; Tian, S.; Zhang, J.-l.; Guo, H.; Schulz, C. E.; Robinson, H.; Nilges, M. J.; Münck, E.; Lu, Y. *J. Am. Chem. Soc.,* **2014**, *136*, 12337.

(168) Manesis, A. C.; Shafaat, H. S. *Inorg. Chem.,* **2015**, *54*, 7959.

(169) Sigman, J. A.; Kwok, B. C.; Lu, Y. *J. Am. Chem. Soc.,* **2000**, *122*, 8192.

(170) Yeung, N.; Lin, Y.-W.; Gao, Y.-G.; Zhao, X.; Russell, B. S.; Lei, L.; Miner, K. D.; Robinson, H.; Lu, Y. *Nature,* **2009**, *462*, 1079.

(171) Saint-Martin, P.; Lespinat, P. A.; Fauque, G.; Berlier, Y.; Legall, J.; Moura, I.; Teixeira, M.; Xavier, A. V.; Moura, J. J. *Proc. Natl. Acad. Sci. U.S.A.,* **1988**, *85*, 9378.

(172) Min, T.; Ergenekan, C. E.; Eidsness, M. K.; Ichiye, T.; Kang, C. *Protein Science,* **2001**, *10*, 613.

(173) Slater, J. W.; Marguet, S. C.; Gray, M. E.; Monaco, H. A.; Sotomayor, M.; Shafaat, H. S. *ACS Catal.,* **2019**, *9*, 8928.

(174) Slater, J. W.; Shafaat, H. S. *J. Phys. Chem. Lett.,* **2015**, *6*, 3731.

(175) Léger, C.; Jones, A. K.; Roseboom, W.; Albracht, S. P. J.; Armstrong, F. A. *Biochemistry,* **2002**, *41*, 15736.

(176) Slater, J. W.; Marguet, S. C.; Monaco, H. A.; Shafaat, H. S. *J. Am. Chem. Soc.,* **2018**, *140*, 10250.

(177) Selvan, D.; Prasad, P.; Farquhar, E. R.; Shi, Y.; Crane, S.; Zhang, Y.; Chakraborty, S. *ACS Catal.,* **2019**, *9*, 5847.

(178) Luo, G.-G.; Wang, Y.-H.; Wang, J.-H.; Wu, J.-H.; Wu, R.-B. *Chem. Commun.,* **2017**, *53*, 7007.

(179) Brazzolotto, D.; Gennari, M.; Queyriaux, N.; Simmons, T. R.; Pécaut, J.; Demeshko, S.; Meyer, F.; Orio, M.; Artero, V.; Duboc, C. *Nat. Chem.,* **2016**, *8*, 1054.

(180) Denny, J. A.; Darensbourg, M. Y. *Chem. Rev.,* **2015**, *115*, 5248.

(181) Han, Z.; Shen, L.; Brennessel, W. W.; Holland, P. L.; Eisenberg, R. *J. Am. Chem. Soc.,* **2013**, *135*, 14659.

(182) Han, Z.; McNamara, W. R.; Eum, M.-S.; Holland, P. L.; Eisenberg, R. *Angew. Chem. Int. Ed.,* **2012**, *51*, 1667.

(183) Ledbetter, K.; Larsen, C. B.; Lim, H.; Zoric, M. R.; Koroidov, S.; Pemmaraju, C. D.; Gaffney, K. J.; Cordones, A. A. *Inorg. Chem.,* **2022**, *61*, 9868.

(184) Blanchard, S.; Neese, F.; Bothe, E.; Bill, E.; Weyhermüller, T.; Wieghardt, K. *Inorg. Chem.,* **2005**, *44*, 3636.

(185) Ashfield, L. J.; Cowley, A. R.; Dilworth, J. R.; Donnelly, P. S. *Inorg. Chem.,* **2004**, *43*, 4121.

(186) Jain, R.; Mamun, A. A.; Buchanan, R. M.; Kozlowski, P. M.; Grapperhaus, C. A. *Inorg. Chem.,* **2018**, *57*, 13486.

(187) Straistari, T.; Fize, J.; Shova, S.; Réglier, M.; Artero, V.; Orio, M. *ChemCatChem,* **2017**, *9*, 2262.

(188) Haddad, A. Z.; Garabato, B. D.; Kozlowski, P. M.; Buchanan, R. M.; Grapperhaus, C. A. *J. Am. Chem. Soc.,* **2016**, *138*, 7844.

(189) Bhattacharya, S.; Gupta, P.; Basuli, F.; Pierpont, C. G. *Inorg. Chem.,* **2002**, *41*, 5810.

(190) Das, A.; Han, Z.; Brennessel, W. W.; Holland, P. L.; Eisenberg, R. *ACS Catal.,* **2015**, *5*, 1397.

(191) Inoue, S.; Mitsuhashi, M.; Ono, T.; Yan, Y.-N.; Kataoka, Y.; Handa, M.; Kawamoto, T. *Inorg. Chem.,* **2017**, *56*, 12129.

(192) Mishra, A.; Mishra, G. K.; Anamika; Singh, N.; Kant, R.; Kumar, K. *Dalton Trans.,* **2024**, *53*, 1680.

(193) Jain, R.; Mashuta, M. S.; Buchanan, R. M.; Grapperhaus, C. A. *Eur. J. Inorg. Chem.,* **2017**, *2017*, 3714.

(194) Gan, L.; Groy, T. L.; Tarakeshwar, P.; Mazinani, S. K. S.; Shearer, J.; Mujica, V.; Jones, A. K. *J. Am. Chem. Soc.,* **2015**, *137*, 1109.

(195) Gu, N. X.; Oyala, P. H.; Peters, J. C. *J. Am. Chem. Soc.,* **2020**, *142*, 7827.

(196) Kim, J. S.; Reibenspies, J. H.; Darensbourg, M. Y. *J. Am. Chem. Soc.,* **1996**, *118*, 4115.

(197) Block, E.; Ofori-Okai, G.; Kang, H.; Zubieta, J. *Inorg. Chim. Acta,* **1991**, *188*, 7.

(198) Curtis, C. J.; Miedaner, A.; Ellis, W. W.; DuBois, D. L. *J. Am. Chem. Soc.,* **2002**, *124*, 1918.

(199) Curtis, C. J.; Miedaner, A.; Ciancanelli, R.; Ellis, W. W.; Noll, B. C.; Rakowski DuBois, M.; DuBois, D. L. *Inorg. Chem.,* **2003**, *42*, 216.

(200) Rakowski DuBois, M.; DuBois, D. L. *Chem. Soc. Rev.,* **2009**, *38*, 62.

(201) Wilson, A. D.; Newell, R. H.; McNevin, M. J.; Muckerman, J. T.; Rakowski DuBois, M.; DuBois, D. L. *J. Am. Chem. Soc.,* **2006**, *128*, 358.

(202) Fraze, K.; Wilson, A. D.; Appel, A. M.; Rakowski DuBois, M.; DuBois, D. L. *Organometallics,* **2007**, *26*, 3918.

(203) Wilson, A. D.; Shoemaker, R. K.; Miedaner, A.; Muckerman, J. T.; DuBois, D. L.; DuBois, M. R. *Proc. Natl. Acad. Sci. U.S.A.,* **2007**, *104*, 6951.

(204) Kilgore, U. J.; Roberts, J. A. S.; Pool, D. H.; Appel, A. M.; Stewart, M. P.; DuBois, M. R.; Dougherty, W. G.; Kassel, W. S.; Bullock, R. M.; DuBois, D. L. *J. Am. Chem. Soc.,* **2011**, *133*, 5861.

(205) Helm, M. L.; Stewart, M. P.; Bullock, R. M.; DuBois, M. R.; DuBois, D. L. *Science,* **2011**, *333*, 863.

(206) Klug, C. M.; Dougherty, W. G.; Kassel, W. S.; Wiedner, E. S. *Organometallics,* **2019**, *38*, 1269.

(207) Tsay, C.; Yang, J. Y. *J. Am. Chem. Soc.,* **2016**, *138*, 14174.

(208) Ho, M.-H.; O'Hagan, M.; Dupuis, M.; DuBois, D. L.; Bullock, R. M.; Shaw, W. J.; Raugei, S. *Dalton Trans.,* **2015**, *44*, 10969.

(209) Lai, C.-H.; Reibenspies, J. H.; Darensbourg, M. Y. *Angew. Chem. Int. Ed.,* **1996**, *35*, 2390.

(210) Li, Z.; Ohki, Y.; Tatsumi, K. *J. Am. Chem. Soc.,* **2005**, *127*, 8950.

(211) Tard, C.; Pickett, C. J. *Chem. Rev.,* **2009**, *109*, 2245.

(212) Kaur-Ghumaan, S.; Stein, M. *Dalton Trans.,* **2014**, *43*, 9392.

(213) Canaguier, S.; Field, M.; Oudart, Y.; Pécaut, J.; Fontecave, M.; Artero, V. *Chem. Commun.,* **2010**, *46*, 5876.

(214) Weber, K.; Krämer, T.; Shafaat, H. S.; Weyhermüller, T.; Bill, E.; van Gastel, M.; Neese, F.; Lubitz, W. *J. Am. Chem. Soc.,* **2012**, *134*, 20745.

(215) Connelly, N. G.; Geiger, W. E. *Chem. Rev.,* **1996**, *96*, 877.

(216) Carroll, M. E.; Barton, B. E.; Gray, D. L.; Mack, A. E.; Rauchfuss, T. B. *Inorg. Chem.,* **2011**, *50*, 9554.

(217) Barton, B. E.; Rauchfuss, T. B. *J. Am. Chem. Soc.,* **2010**, *132*, 14877.

(218) Huynh, M. T.; Schilter, D.; Hammes-Schiffer, S.; Rauchfuss, T. B. *J. Am. Chem. Soc.,* **2014**, *136*, 12385.

(219) Ulloa, O. A.; Huynh, M. T.; Richers, C. P.; Bertke, J. A.; Nilges, M. J.; Hammes-Schiffer, S.; Rauchfuss, T. B. *J. Am. Chem. Soc.,* **2016**, *138*, 9234.

(220) Chu, X.; Yu, X.; Raje, S.; Angamuthu, R.; Ma, J.; Tung, C.-H.; Wang, W. *Dalton Trans.,* **2017**, *46*, 13681.

(221) Song, L.-C.; Han, X.-F.; Chen, W.; Li, J.-P.; Wang, X.-Y. *Dalton Trans.,* **2017**, *46*, 10003.

(222) Ding, S.; Ghosh, P.; Lunsford, A. M.; Wang, N.; Bhuvanesh, N.; Hall, M. B.; Darensbourg, M. Y. *J. Am. Chem. Soc.,* **2016**, *138*, 12920.

(223) Ghosh, P.; Quiroz, M.; Wang, N.; Bhuvanesh, N.; Darensbourg, M. Y. *Dalton Trans.,* **2017**, *46*, 5617.

(224) Brazzolotto, D.; Wang, L.; Tang, H.; Gennari, M.; Queyriaux, N.; Philouze, C.; Demeshko, S.; Meyer, F.; Orio, M.; Artero, V.; et al. *ACS Catal.,* **2018**, *8*, 10658.

(225) Ogo, S.; Ichikawa, K.; Kishima, T.; Matsumoto, T.; Nakai, H.; Kusaka, K.; Ohhara, T. *Science,* **2013**, *339*, 682.

(226) Tang, H.; Hall, M. B. *J. Am. Chem. Soc.,* **2017**, *139*, 18065.

CHAPTER 2

SYNTHESIS, PROPERTIES, AND ELECTROCHEMICAL PROTON REDUCTION OF A HOMOLEPTIC TETRATHIOLATO NI-SITE MODEL OF [NIFE]-HYDROGEANSE

Benjamin A. Yosen, Amelia G. Reid, Phan T. Troung, Tiara Hinton, Indranil Chakraborty, Marilyn M. Olmstead, Timothy Stemmler, and Todd C. Harrop. Submitted to *Inorganic Chemistry*

2.1 Abstract

[NiFe]-hydrogenase enzymes process H_2 at a non-planar tetracysteinato-Ni site, the sole participator in proton binding/redox chemistry during turnover. With the objective of assessing whether a simple tetrahedral/tetrathiolato-Ni^{2+} core could promote H_2 evolution reaction (HER), we synthesized $(Et_4N)_2[Ni(S\text{-}p\text{-}CF_3\text{-}Ph)_4]$ (**1**) employing *para*-trifluoromethylbenzenethiolate ($^{-}S\text{-}p\text{-}CF_3\text{-}Ph$) as a Ni-site analog of [NiFe]-hydrogenase. Spectroscopic measurements and X-ray crystallography confirm the distorted tetrahedral geometry of **1**. Dissolution of **1** results in partial thiolate dissociation and formation of *S*,*S*-bridged complexes such as $(Et_4N)_2[Ni_2(S\text{-}p\text{-}CF_3\text{-}Ph)_6]$ (**3**) among other ill-defined species. Dissociation is further accelerated in the presence of Brønsted acids, complicating the assessment of **1** for proton reduction. However, this dissociation/proton instability is suppressed in the presence of additional thiolate ligand to ensure tetrahedral/tetrathiolato **1** persists in solution. Electrochemical HER activity was evaluated by monitoring the current response of an MeCN solution of **1**/excess thiolate after sequential titration with a weak Brønsted acid (acetic acid). The results suggest that **1** is a modest electrocatalyst for the HER with a turnover frequency of $14.5 \pm 3.6\ s^{-1}$ and an overpotential of 0.72 ± 0.02 V. Control experiments and supplementary DFT computations indicate that **1**, or a species derived from **1**, is responsible for the HER and suggest an ECCE-type mechanism.

2.2 Introduction

Hydrogen gas (H_2) offers a potential solution for a clean, renewable, and energy-dense alternative to fossil fuels, a significant soure of anthropogenic CO_2 emissions.[1-3] Steam methane reforming (SMR) is predominately used to produce H_2; however, SMR is energy intensive and considered only a grey source of H_2 due to formation of CO/CO_2 as byproducts.[4] Electrocatalytic water splitting offers a cleaner option for H_2 production, but this method relies heavily on expensive noble metal catalysts, e.g., Pt and Pd, for proton reduction.[5, 6] In contrast, anaerobic bacteria have evolved H_2 processing hydrogenase (H_2ase) enzymes that utilize inexpensive/Earth-abundant metal-containing active sites ([M]-H_2ase; M = NiFe, FeFe, or Fe) that provide inspiration for the development of cost-effective H_2 evolving catalysts.[7, 8] [NiFe]-H_2ase contains a redox-active cofactor that relies on Ni (Figure 2.1) to catalyze the reversible oxidation of H_2 with turnover frequencies (TOFs) up to 6,000 s^{-1} for H_2 oxidation[9] and ~700 s^{-1} for H_2 production,[10, 11] performed at or near the thermodynamic equilibrium potential $E°(2H^+/H_2)$. Although Ni and Fe play important roles in [NiFe]-H_2ase activity, only Ni participates in redox catalysis by alternating through putative $Ni^{3+/2+/1+}$ oxidation states.[7] In the resting Ni-SI_a state, the Ni center is in a distorted tetrahedral/see-saw geometry coordinated to four cysteinates (CysS), two of which bridge to a low-spin Fe^{2+} center.[5] This S-rich anionic $Ni(SCys)_4$ core is proposed to depress the $Ni^{3+/2+}$ couple, with a terminal CysS serving as a base/proton relay site (see Ni-R structure in Figure 2.1) to facilitate H_2 evolution through the heterolytic coupling of the bridged hydride with a protonated CysSH.[5, 12-14]

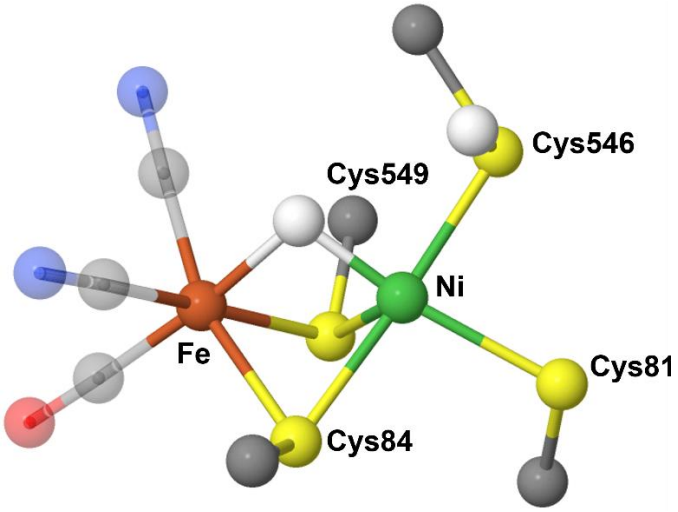

Figure 2.1. Active site of [NiFe]-H_2ase from *Desulfovibrio vulgaris* Miyazaki F (PDB: 4U9H) in the Ni-R state[14] depicting coordinating ligands to Ni (green) and Fe (red).

Since the first reported X-ray absorption spectroscopic[15] and X-ray diffraction[16] data on [NiFe]-H_2ase ~30 years ago, synthetic chemists have developed various low molecular weight (LMW) model complexes to explore the underlying principles governing H_2ase activity at the $Ni(SCys)_4$ active site.[17-26] Several mononuclear complexes focus on the generation of highly active electrocatalysts for the H_2 evolving reaction (HER) drawing inspiration from the structural and electronic features of the active site. For example, Ni complexes with soft P-rich coordination spheres have been reported to achieve TOFs up to 10^7 s^{-1}.[27] Indeed, these Ni-P_4 HER electrocatalysts have provided valuable information regarding factors that influence efficiency and turnover utilizing chelating diphosphine ligands. Their work highlights that selective positioning of pendant N-bases on the ligand serve as effective proton relays to increase HER rates (Chart 2.1).[27, 28] Drawing more parallels to the enzyme active site, the development of bimetallic mimics utilizing chelating diphosphine/dithiolate-P_2S_2[21, 29] and diamino/dithiolate-N_2S_2[30-34] ligands to hold Ni in a square-planar geometry with thiolate bridges to other first-row metals (Chart 2.1) have

also contributed to the development of key synthetic strategies and ligand design principles to generate active HER catalysts. For example, these models have shed light on the relationship between the electron richness of the catalyst and overpotential (η), the potential role of bridging thiolates as proton-binding sites, and the difficulty in centering redox activity solely on Ni.

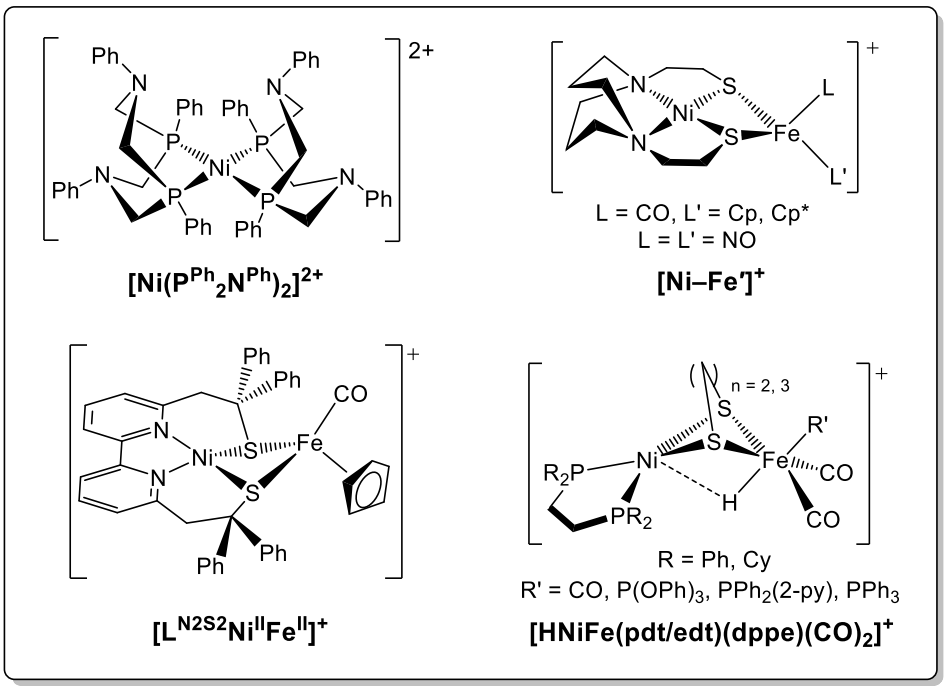

Chart 2.1. Structures of select functional models of [NiFe]-H_2ase featuring various donor types and coordination geometries about Ni^{2+}.

HER activity of Ni complexes in thiolate-only/non-planar coordination geometries are underexplored. Indeed, metal-thiolate coordination chemistry is associated with many challenges[35-38] including: (i) autoredox chemistry resulting in irreversible oxidation/deligation of the thiolate to generate disulfide with concomitant reduction of the metal center; (ii) instability under protic conditions; and (iii) the tendency to form higher nuclearity species, sometimes intractable, through bridging thiolates. These obstacles must be considered when constructing mononuclear Ni-thiolate systems as mimics of the $Ni(SCys)_4$ core in [NiFe]-H_2ase. Two classes

of mononuclear $[Ni(SR)_4]^{2-}$ are known containing either chelating dithiolates or homoleptic complexes with monodentate thiolates (select examples shown in Chart 2.2).[17, 39-50] Maintaining a mononuclear species is highly dependent on solvent, identity of the thiolate ligand, and the metal/thiolate ratio employed during synthesis. In addition, these complexes are generally in planar/distorted planar coordination geometries except for homoleptic Ni complexes featuring aryl-thiolates that almost exclusively exist in distorted tetrahedral geometries much like that in [NiFe]-H_2ase (Chart 2). The proposed driving force being the favorable π-overlap of the out-of-plane S-pπ orbitals (with respect to the benzene ring[51]) and the benzene-pπ system when the plane defined by Ni-S-C is coplanar with the phenyl ring.[48, 52, 53] Homoleptic Ni-aryl-thiolate, and even Ni-thiolate complexes with bidentate dithiolates,[42, 43, 49] are proposed to exist in equilibrium with S-bridged species (via thiolate dissociation) as reflected by their concentration-dependent NMR, UV-vis, and solution-state magnetic moment (μ_{eff}) values.[39, 54, 55] Although it has been postulated that the equilibrium is due to thiolate dissociation,[54, 55] it is unclear what the identity of this species is. Two proposed species are solvent-bound $[Ni(SR)_3(solv)]^-$,[55] or some higher order species, such as *S*,*S*-bridged dimers $[(RS)_2Ni(\mu\text{-}SR)_2Ni(SR)_2]^{2-}$.[56] Extensive studies for the latter have not been performed. For example, addition of H_2O or EtOH to MeCN solutions of $[Ni(SPh)_4]^{2-}$ leads to precipitation of intractable polymers, denoted as $[Ni(SPh)_2]_\infty$.[41] However, there is no strong evidence to suggest the identity of this species nor the mechanism of its formation. Issues associated with LMW Ni-thiolate complexes are nullified in [NiFe]-H_2ase and other Ni-enzymes due to the protection enabled by the protein scaffold. For example, Shafaat and coworkers utilize the protein scaffold in rubredoxin (Rd), a small electron-transfer protein whose native metal is Fe, to create a tetrahedral $Ni(SCys)_4$ site (NiRd) that exhibits H_2ase activity (TOF up to 100 s^{-1}, η = 540 mV).[57, 58] This work suggests that tetrahedral/tetrathiolato-Ni complexes, barring auto-redox

and protic stability/solubility issues, should also be functional models for the HER. However, the electrocatalytic HER activity of homoleptic Ni-aryl-thiolate complexes has not been reported. This absence is most likely due to their ill-defined solution speciation, instability in protic conditions, and irreversible redox events.

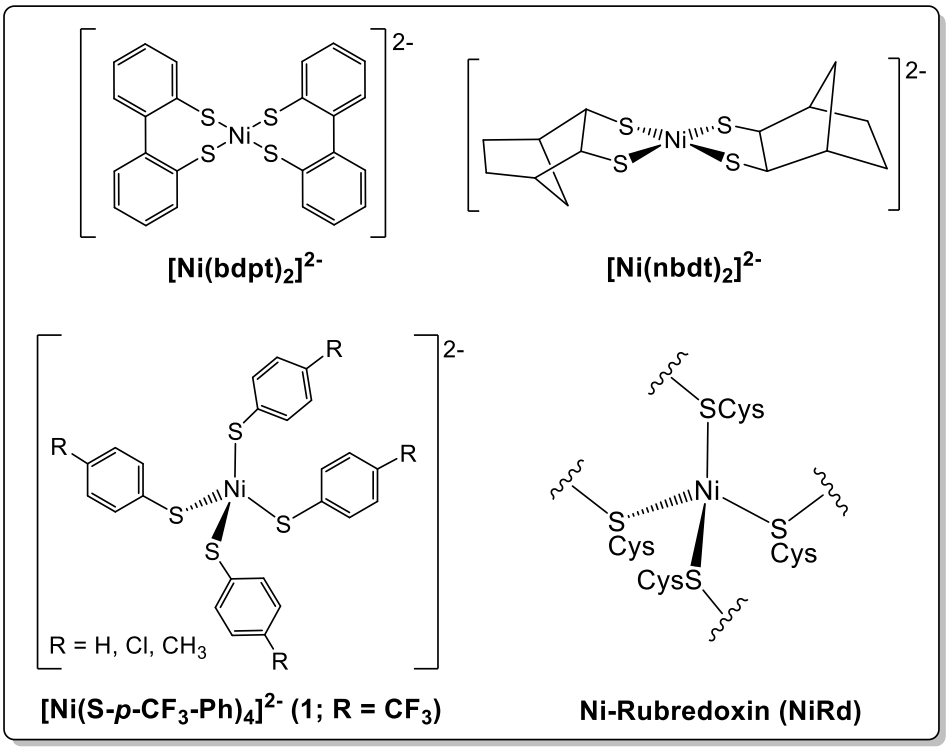

Chart 2.2. Structures of thiolate-rich monomeric Ni^{2+} complexes.

The objective of this work was to synthesize, characterize, and evaluate the capability of a tetrahedral Ni^{2+} complex in a thiolate-only ligand environment, a discrete model of the tetracysteinato-Ni site in [NiFe]-H_2ase, for electrochemical HER. With this goal in mind, we employed *para*-trifluoromethylbenzene thiolate to afford Ni-site model $(Et_4N)_2[Ni(S\text{-}p\text{-}CF_3\text{-}Ph)_4]$ (**1**) (Chart 2.2). As stated above, LMW homoleptic complexes featuring aryl-thiolates almost exclusively afford tetrahedral Ni^{2+} species; however, and despite their structural similarity to the Ni site in [NiFe]-H_2ase, none have been assessed for H_2 evolution. This absence is likely due to the noted speciation and protic solvent instability of such complexes.[41, 54, 55] We thus posited that

using the strong electron-withdrawing *p*-CF_3 group (σ_p = 0.54[59]) in **1** would diminish the nucleophilicity of the thiolate to prevent or depress such speciation while also providing an additional spectroscopic handle to monitor through ^{19}F NMR. Reported herein is the synthesis, structural/spectroscopic/electrochemical properties, solution speciation, and electrochemical HER activity of the homoleptic tetrathiolato Ni^{2+} complex **1** and its redox-inert Zn^{2+} analogue $(Et_4N)_2[Zn(S\text{-}p\text{-}CF_3\text{-}Ph)_4]$ (**2**). Despite incorporation of the *p*-CF_3 group, complex **1** affords thiolate-bridged species such as a proposed *S*,*S*-bridged dimer $(Et_4N)_2[(p\text{-}CF_3\text{-}PhS)_2Ni(\mu\text{-}S\text{-}p\text{-}CF_3\text{-}Ph)_2Ni(S\text{-}p\text{-}CF_3\text{-}Ph)_2]$ (**3**) even when dissolved in aprotic MeCN due to thiolate dissociation. Unsurprisingly, dimer/oligomerization is further accelerated in the presence of Brønsted acids. However, the equilibrium can be shifted back to mononuclear/tetrahedral complex **1** by adding excess thiolate equivalents to freshly dissolved solutions of **1**. With thiolate in excess, complex **1** was measured for HER in MeCN using acetic acid (AcOH; pK_a = 23.5[60]) as the proton source to result in a modest electrocatalyst. Electrochemical control measurements with free thiolate $(Et_4N)(S\text{-}p\text{-}CF_3\text{-}Ph)$ and Zn^{2+} complex **2** support that **1**, or a species derived from **1**, is responsible for the observed electrocatalysis. Kinetic isotope measurements with AcOD-d_4 and supporting theoretical computations from density functional theory (DFT) suggest that **1** operates via an ECCE (E = electrochemical; C = chemical step) type mechanism.

2.3 Results and Discussion

Synthesis. Preparation of the tetrahedral/tetrathiolato Ni^{2+} complex $(Et_4N)_2[Ni(S\text{-}p\text{-}CF_3\text{-}Ph)_4]$ (**1**) was adopted from Mascharak.[54] This method employs slightly high thiolate-to-Ni ratios and polar aprotic solvents to prevent formation of intractable thiolato-bridged polymers (vide infra).[41, 54] Dropwise addition of a blue MeCN slurry of $(Et_4N)_2[NiCl_4]$ into an MeCN solution containing upwards of 4.5 mol-equiv of the tetraethylammonium (Et_4N^+) salt of *para*-

trifluoromethylbenzenethiolate (Et_4N)(S-*p*-CF_3-Ph) produced a homogeneous dark maroon-red solution indicative of **1**.[41, 54, 61] After workup, **1** was isolated as a dark-red powder in 77% yield. The corresponding tetrahedral/tetrathiolato Zn^{2+} complex $(Et_4N)_2[Zn(S\text{-}p\text{-}CF_3\text{-}Ph)_4]$ (**2**) was isolated in 90% yield using near identical conditions.[62] Synthesis of the *S*,*S*-bridged planar complex $(Et_4N)_2[(p\text{-}CF_3\text{-}PhS)_2Ni(\mu\text{-}S\text{-}p\text{-}CF_3\text{-}Ph)_2Ni(S\text{-}p\text{-}CF_3\text{-}Ph)_2]$ (**3**) denoted as $(Et_4N)_2[Ni_2(S\text{-}p\text{-}CF_3\text{-}Ph)_6]$, a potential product during reactions with H^+, was also attempted. Combining complex **1** with a stoichiometric amount of a methylating (Me_3OBF_4) or an oxidizing (ferrocenium hexafluorophosphate = $FcPF_6$) agent, reagents that result in modification of a coordinated thiolate to methyl-thioether or disulfide, respectively, were employed to generate **3**.[38, 63] While **3** was produced (see Experimental section in the supporting information = SI), both syntheses afford product mixtures that were difficult to separate, thus isolation of **3** was not successful. The Ni-nitrosyl complex $(Et_4N)_2[Ni(S\text{-}p\text{-}CF_3\text{-}Ph)_3(NO)]$ (**4**) was also synthesized, a proxy for a putative Ni-H intermediate, in 53% yield by addition of Ph_3CSNO[64] to **1** (1:1) in MeCN. Standard characterization from UV-vis, FTIR, $^1H/^{19}F$ NMR, ESI-MS, XAS, magnetic moment, X-ray diffraction, and CHN elemental analysis support the formulation of the complexes (see below).

X-ray Crystallography, X-ray Absorption Spectroscopy, and Electronic Structures. X-ray diffraction of single crystals of **1**-**2** confirmed their monomeric nature and distorted tetrahedral coordination geometries. Thermal ellipsoid plots of **1**-**2** and all relevant structural data are provided in Figure 2.2 and Table 2.1 and S2.1-S2.2 of the supporting information (= SI; both structures contain disorder in one or more of the *p*-CF_3-Ph rings; see Figures S2.32-S2.33). The crystal structures of homoleptic **1** and **2** display four aryl-thiolato ligands coordinating M^{2+} in approximate tetrahedral geometry with average M–S bond distances of 2.282 and 2.350 Å for **1** and **2**, respectively (Table 2.1). Additional structural details, obtained by calculating the tetrahedral

distortion parameter τ_4 (1 for a perfect tetrahedron; 0 for a perfect square-plane[65]), reveal that the distortion for **1** (τ_4 = 0.79), indicating primarily, albeit distorted, tetrahedral is expectedly greater than in **2** (τ_4 = 1.00). Complex **2** crystallizes in the tetragonal $I4_1/a$ space group, with ¼th of the complex within the asymmetric unit and thus it is strictly tetrahedral. Apart from the predictable M–SPh elongation and more ideal tetrahedral geometry for the d^{10} Zn^{2+} complex, **1** and **2** are largely isostructural and approach D_{2d} point symmetry (ignoring the *p*-CF_3 groups). Comparing **1** to previously reported homoleptic tetrahedral/tetrathiolato complexes $[Ni(S\text{-}p\text{-}X\text{-}Ph)_4]^{2-}$ (X = H, Cl) suggest similar structures throughout with only subtle differences (Table 2.1).[40, 41, 47, 54] While these distances are similar amongst homoleptic $[Ni(SR)_4]^{2-}$, they are significantly elongated when comparing to neutral tetrahedral (S = 1) Ni^{2+} complexes with tripodal supporting ligands featuring a single Ni-SPh bond (avg = 2.21 Å), likely a consequence of overall complex charge.[66-68] There is a modest trend with respect to the *p*-X Hammett parameter, Ni–SPh distance and τ_4, i.e., electron-withdrawing *p*-X yields shorter Ni–SPh bonds and the more distorted tetrahedron. Furthermore, three of the four aryl-thiolate rings are nearly coplanar with the plane defined by Ni-S-C (Table S2.2), a consistent structural feature in other reported tetra-aryl-thiolato-Ni^{2+} complexes, one proposed driving force for tetrahedral coordination.[40, 48, 52, 54]

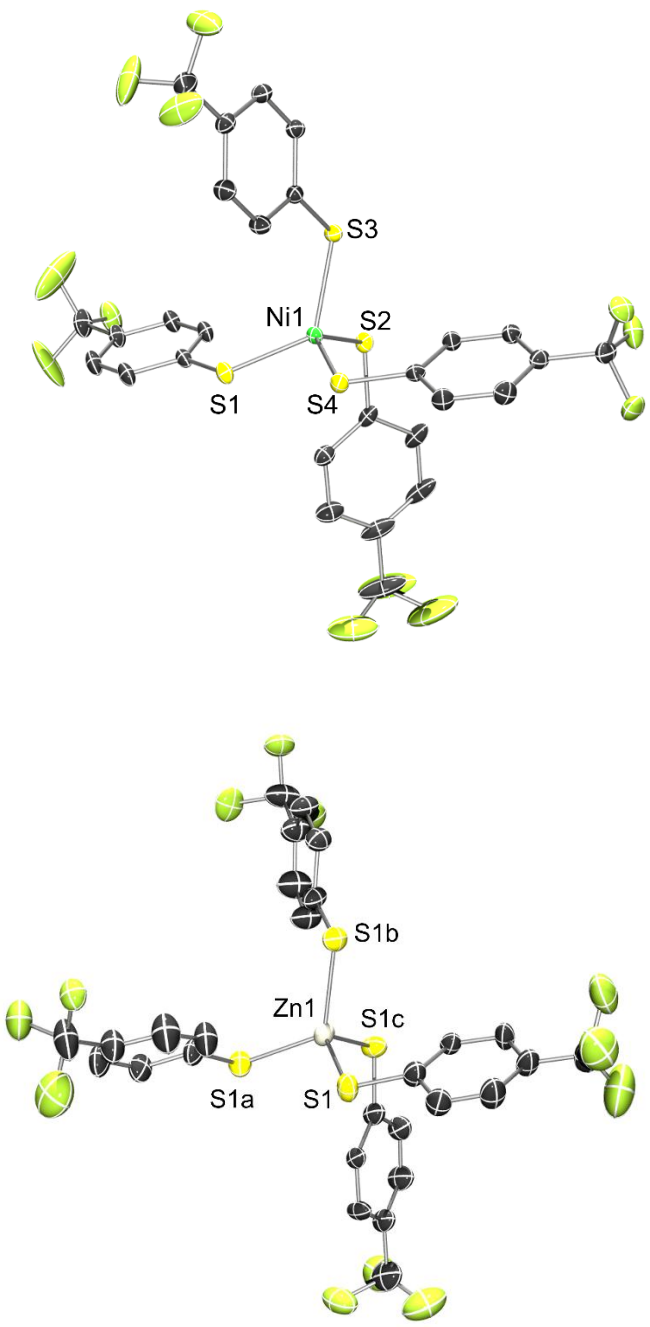

Figure 2.2. X-ray structures of the dianions of **1** (*top*) and **2** (*bottom*) at 50% thermal probability ellipsoids with the atom labeling scheme. H atoms and Et_4N^+ counterions are omitted for clarity.

Table 2.1. Select Bond Distances (Å) and τ_4 values[65] from XRD and DFT of Select Tetrathiolato Ni^{2+} and Zn^{2+} Complexes.TW = this work.[a]

Complex	Ni–S (Å)	Ni–S_{avg} (Å)	τ_4	ref
Tetrahedral Ni/Zn-thiolates				
$(Et_4N)_2[Ni(S\text{-}p\text{-}CF_3\text{-}Ph)_4]$ (**1**)	2.296, 2.290, 2.275, 2.266	2.282	0.79	TW
DFT-optimized **1** (S = 1, MeCN)	2.331, 2.349, 2.312, 2.336	2.332	0.82	TW
$(Et_4N)_2[Ni(S\text{-}p\text{-}Cl\text{-}Ph)_4]$	2.279, 2.281, 2.293, 2.269	2.281	0.81	54
$(Et_4N)_2[Ni(SPh)_4]$[b]	2.287, 2.306, 2.296, 2.279	2.292	0.83	41
$(Et_4N)_2[Ni(SPh)_4]$[c]	2.258, 2.331, 2.293, 2.302	2.296	0.81	47
$(Ph_4P)_2[Ni(SPh)_4]$	2.303, 2.289, 2.272, 2.287	2.288	0.83	40
$(Et_4N)_2[Ni(S\text{-}o\text{-}Ph\text{-}Ph)_4]$	2.288	2.288	0.90	48
NiRd[d]	2.254, 2.381, 2.477, 2.134	2.304	0.87	69
DFT-optimized NiRd[e]	2.345, 2.282, 2.332, 2.287	2.312	0.84	70
$(Et_4N)_2[Zn(S\text{-}p\text{-}CF_3\text{-}Ph)_4]$ (**2**)	2.350	2.350	1.00	TW
DFT-optimized **2** (S = 0, Gas)	2.392, 2.403, 2.385, 2.392	2.393	0.95	TW
$(Ph_4P)_2[Zn(SPh)_4]$	2.362, 2.363, 2.329, 2.357	2.352	0.87	40
Planar Ni-thiolates				
DFT-optimized **1** (S = 0, MeCN)	2.251, 2.252, 2.266, 2.254	2.255	0.08	TW
$[Ni(HPyS)_4](NO_3)_2$	2.213, 2.215, 2.214, 2.204	2.212	0.00	50
$[Li(DMF)(MeOH)]_2[Ni(nbdt)_2]$	2.185, 2.182	2.184	0.00	44
$(Ph_4P)_2[Ni(edt)_2]$[f]	2.201, 2.188	2.195	0.00	43
$(Ph_4P)_2[Ni_2(edt)_3]$[f]	2.211^{br}, 2.221^{br}, 2.174^{t}, 2.161^{t} 2.158^{br}, 2.166^{br}, 2.194^{t}, 2.181^{t}	2.183	0.11	42
$(Et_4N)_2[Ni(bpdt)_2]$	2.214, 2.219, 2.221, 2.209	2.216	0.04	49
$(Et_4N)_2[Ni_2(bpdt)_3]$[f]	2.201^{br}, 2.191^{br}, 2.204^{t}, 2.203^{t} 2.233^{br}, 2.224^{br} 2.195^{t}, 2.192^{t}	2.205	0.03, 0.15	49
$(Et_4N)_2[Ni_2(S\text{-}p\text{-}Cl\text{-}Ph)_6]$[f]	2.212^{br}, 2.220^{br}, 2.204^{t}, 2.219^{t}	2.214	0.07	56
DFT-optimized **3** (S = 0)[f]	2.246^{br}, 2.247^{br}, 2.211^{t}, 2.243^{t}	2.237	0.18	TW

[a]Abbreviations: S-*o*-Ph-Ph = 2-phenylbenzenethiolate; Rd = rubredoxin; HPyS = prydinium-2-thiolate; bpdt = biphenyl-2,2'-dithiolate; edt = ethane-1,2,-dithiolate; nbdt = norborane-1,2-dithiolate. [b]Crystallized in the monoclinic space group. [c]Crystallized in the orthorhombic space group. [d]From *C. pasteurianum*, pdb = 1R0J, see ref. 69. [e]Values taken from the 'full' model of NiRd, see ref. 70.[f]Ni-S distances defined as terminal (t) or bridging (br).

Additional structural information from Ni K-edge X-ray absorption spectroscopic (XAS) and magnetic moment (μ_{eff}) measurements support the tetrahedral geometry of **1** in the solid-state. X-ray absorption near edge spectroscopic (XANES) analysis reveals a relatively intense pre-edge

feature at 8331 eV (area = 0.165 eV^2) corresponding to a 1s→3d transition with a rising edge 1s→4p feature at 8345 eV, both features are consistent with tetrahedral coordination at Ni^{2+}.[71] Extended X-ray absorption fine structure (EXAFS) for **1** (Figure 2.3) indicates coordination of four S-scatterers at a Ni–S(avg) distance of 2.274 Å (Table S2.3), in-line with that obtained from XRD (2.282 Å) (Table 2.1; vide supra). In contrast, square-planar Ni^{2+} complexes generally display shorter Ni-SR distances, 2.17-2.21 Å,[17, 42-45, 72, 73] (Table 2.1) and weak intensity/symmetry-forbidden 1s→3d transitions in XAS.[74] The solid-state μ_{eff} was determined to be 3.47 BM (spin-only μ_{eff} = 2.83 BM) and further supports tetrahedral (S = 1) coordination. Collectively, all solid-state measurements are on-par with other monodentate tetrathiolato-Ni^{2+} complexes containing aryl-thiolate ligands that, with one exception (i.e., $[Ni(HPyS)_4]^{2+}$, $HPyS^-$ = N-protonated form of 2-pyridinethiolate; see Table 2.1), afford tetrahedral geometries. In contrast, $[Ni(SR)_4]^{2-}$ complexes with mono-/multidentate alkyl-thiolate or multidentate aryl-thiolate donors, are invariably square-planar (Table 2.1).[42-45, 49, 72]

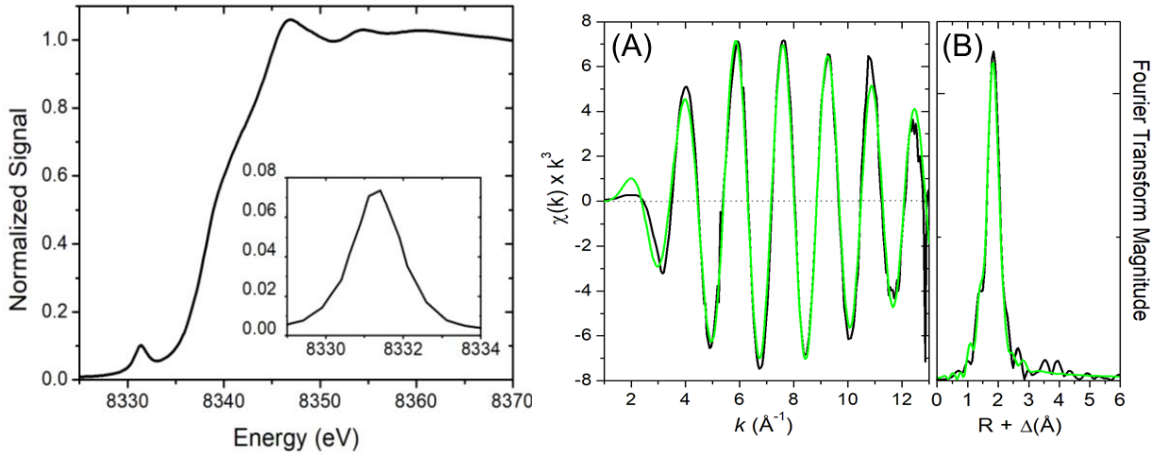

Figure 2.3. *Left*: Ni K-edge XANES for **1**. *Inset*: baseline subtracted expansion of pre-edge feature for **1**, offset for clarity (coding same as XANES). *Right*: Raw k^3-weighted EXAFS data (panel A; black) and phase shifted Fourier transform EXAFS (panel B; black) of **1** with best-fit simulation (green).

DFT computations (B3LYP/def2-TZVPP) were employed to gain insight on electronic structure. Input structures for the geometry optimization of **1** and **2** were taken from the crystallographic coordinates. For *S*,*S*-bridged dimeric complex **3**, initial coordinates were obtained from the crystal structure of the *p*-Cl-SPh analogue, *p*-Cl replaced with *p*-CF_3, published by Maroney.[56] The DFT-optimized structure of **1** (Figure S2.34) largely resembles that determined by XRD with a modest overestimation of the Ni-thiolate distances (Δ: +0.04 Å) from XRD and reasonable approximation of the distorted tetrahedral geometry (τ_4 = 0.75). Overestimation of the Zn-thiolate bonds from XRD (Δ: +0.04 Å) in geometry-optimized **2** (Figure S2.36) was also observed and appears to be a common outcome when employing hybrid functionals such as B3LYP.[75] The electronic structure of **1** indicates a lowest unoccupied spin-down MO (β-LUMO) that is mostly Ni-based (63%, Figure 2.4). A large Ni contribution in the β-LUMO, coupled with the Löwdin spin density of **1** (76% on Ni, Figure 2.4), suggests a Ni-centered redox process (vide infra). Expectedly, square-planar/dimeric **3** is structurally/electronically quite different from **1**. Shorter Ni-thiolate bonds (~2.2 Å) and significant Ni-*d*π and *S*-pπ contributions to the π* HOMO (23% Ni, 51% S) and HOMO-1 (15% Ni, 57% S; 0.05 eV from HOMO), suggest more covalent character (Figure S2.37).[38, 76, 77] Apart from a modest lengthening of the Ni-thiolate bonds and slight distortion in τ_4 (0.18; see Table 2.1), DFT-computed **3** is comparable to the structurally characterized *p*-Cl analogue. These small deviations may reflect the stronger electron-withdrawing effect, and hence weaker nucleophilicity, of the *p*-CF_3-substituted thiolate in **3**. The LUMO in **3** is a σ*-based MO with major contributions from Ni-d_{x2-y2} (42%) and S-*p*σ orbitals (21%).

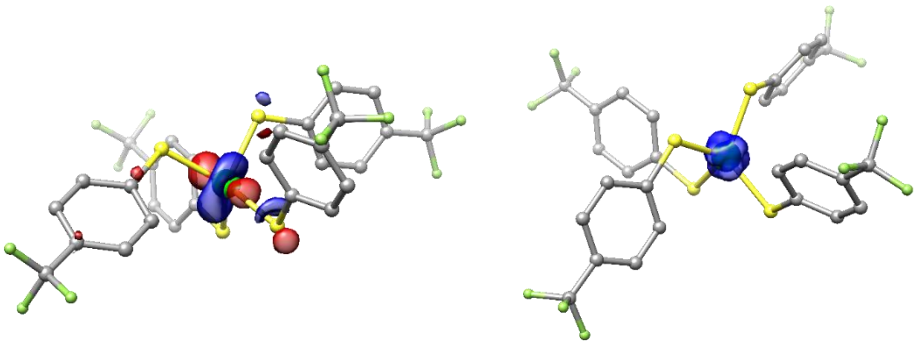

Figure 2.4. DFT-generated isosurface plots of the β-LUMO of **1** (l*eft*) and spin-density plot of **1** (*right*) (blue denotes positive spin). Color scheme: Ni, green; S, yellow; F, green-yellow; C, gray. H atoms are omitted for clarity.

Solution-state characterization. Solution studies of related homoleptic tetrahedral/tetra-aryl-thiolato Ni^{2+} complexes indicate thiolate loss is facile and results in putative and transient $[Ni(SPh)_3(L)]^-$ (L = donor solvent such as DMSO) planar complexes.[55] Thiolate dissociation is further accelerated in the presence of protic solvents (vide infra) resulting in intractable thiolato-bridged complexes labeled as $[Ni(SPh)_2]_\infty$.[41] An initial sign of the speciation of **1** was observed in its UV-vis spectrum, which exhibits a nearly featureless and flat profile in MeCN (Figure 2.5). Contrastingly, $(Ph_4P)_2[Ni(SPh)_4]$ displays two closely spaced charge-transfer (CT) bands at 460 and 510 nm (ε ~2500 M^{-1} cm^{-1}) with *d-d* transitions at 676 and 725 nm (ε ~300 M^{-1} cm^{-1}) in DMF/toluene (1:1) (Table 2.2).[78] Notably, this spectrum was acquired in the presence of an additional 10 mol-equiv of PhS^-. Examination of the literature indicates near identical features for $[Ni(S\text{-}p\text{-}X\text{-}Ph)_4]^{2-}$ (X = H, Cl) when spectra are recorded in polar aprotic solutions (MeCN, DMSO) containing ***excess thiolate***.[55, 79] The reported UV-vis of $(Et_4N)_2[Ni(S\text{-}p\text{-}Cl\text{-}Ph)_4]$ in MeCN, *in the absence of excess thiolate*, matches the featureless spectrum reported here for **1**.[54, 56] Clearly, dissolution of $[Ni(SPh)_4]^{2-}$ complexes, even in aprotic solvents, results in partial thiolate

dissociation. Additionally, thiolate dissociation, and in some cases further thiolate reactivity, is also observed in tetrahedral/charge neutral [(κ^3-L)Ni-SAr] (L = substituted tris(pyrazolyl)borate, phenyltris((tert-butylthio)-methyl)borate tripodal ligands) complexes and may be a general property for Ni-thiolates in a tetrahedral ligand field.[66, 67] Adding 20 mol-equiv of (Et_4N)(S-*p*-CF_3-Ph) to MeCN solutions of **1** converts the featureless spectrum to one that reproduces the tetrahedral complex, i.e., CT bands at 465 and 508 nm (ε = 3400 and 3800 M^{-1} cm^{-1}, respectively) and *d-d* transitions at 680 and 720 nm (ε ~600 M^{-1} cm^{-1}) (Figure 2.5; Table 2.2). The origin of these transitions align with those proposed for $(PPh_4)_2[Ni(SPh)_4]$[78] and NiRd.[70, 78] For example, the UV-vis for NiRd is comparable with two intense bands at 360 and 450 nm attributed to CysS-to-Ni^{2+} LMCT transitions, and *d-d* bands at 670 and 720 nm (Table 2.2).[70, 78, 79] Time-dependent DFT (TD-DFT) of **1** reproduce the experimental spectrum quite well and supports the proposed assignments (Figure 2.5), i.e., two CT bands (S-*p*π-to-Ni-*d*π) at 463 and 518 nm followed by *d-d* transitions between 640-700 nm. These absorption features thus represent general UV-vis signatures for tetrahedral/tetra-aryl-thiolato-Ni^{2+} complexes (Table 2.2).[78, 79] In contrast, the experimental and computed UV-vis of dimer/planar **3** comprises of an intense LMCT centered at 380 nm (λ_{sh}: 415 nm) and is largely featureless in the visible region with a broad band centered at 650 nm composed of several *d-d* bands (Figures S2.21 and S2.43).

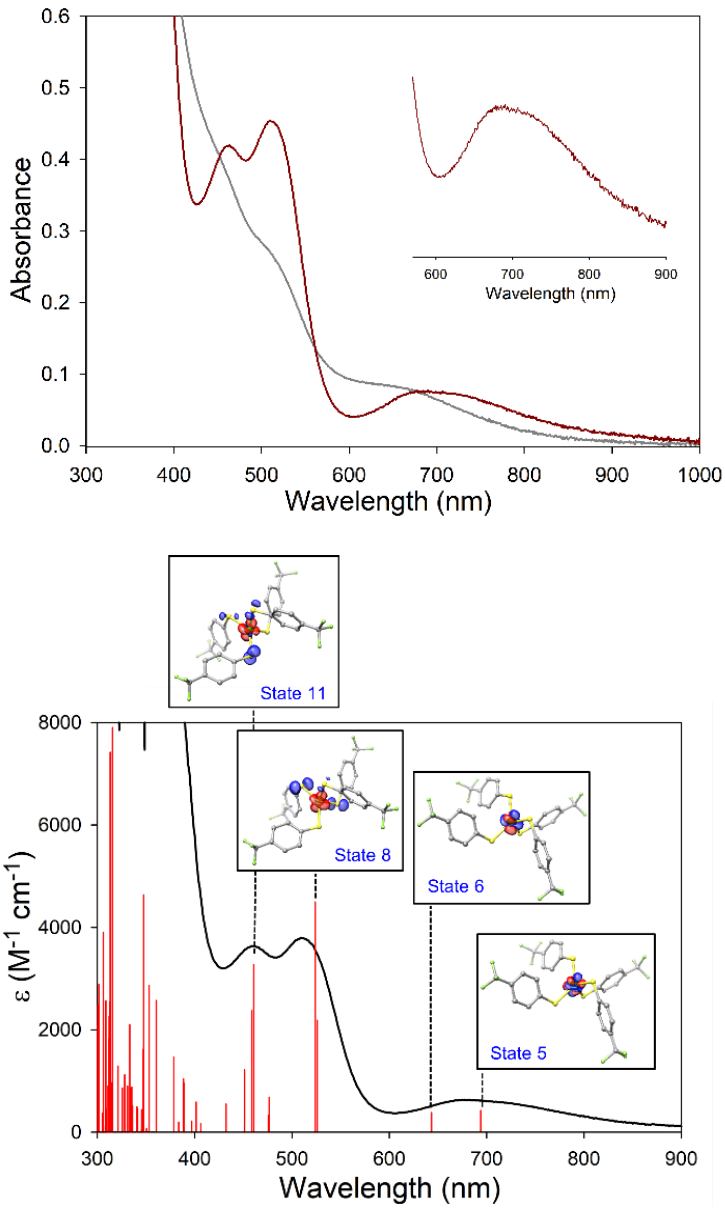

Figure 2.5. *Top*: UV-vis spectrum of an MeCN solution of **1** (0.13 mM; gray trace) and after the addition of 20 mol-equiv (Et_4N)(S-*p*-CF_3-Ph) (red trace). *Inset*: zoom-in of the ligand-field bands. *Bottom:* Experimental UV-vis of **1**/ 20 mol-equiv (Et_4N)(S-*p*-CF_3-Ph) in MeCN (black) with TD-DFT calculated optical transitions (red sticks). *Insets*: Electron difference density plots for select transitions: blue and red lobes reflect loss and gain of electron density, respectively.

Table 2.2. Select UV-vis and Electrochemical Properties (reported or converted[80] vs. Fc^+/Fc) of Tetrathiolato Ni^{2+} Complexes. TW = this work; NR = Not reported.[a]

Complex	λ (nm) (ε (M^{-1} cm^{-1}))	E_{ox} (V)[b]	E_{red} (V)[b]	ref
$(Et_4N)_2[Ni(S\text{-}p\text{-}CF_3\text{-}Ph)_4]$ (**1**)	720 (600), 680 (580), 508 (3800), 465 (3400)[c,d]	-0.20, -0.08[c]	-1.94[c, d]	TW
Computed **1**	694 (640), 643 (650), 518 (7200), 463 (8000)[c]	NR	-2.69 (r, $Ni^{2+/1+}$)	TW
$(Et_4N)_2[Ni(S\text{-}p\text{-}Cl\text{-}Ph)_4]$	660-680 (NR), 300-500 (NR)[c]	NR	NR	56
$(Et_4N)_2[Ni(SPh)_4]$	660 (780 sh), 430 (6000 sh)[c]	-0.44[c] -0.57[e]	NR	41, 81
$(Ph_4P)_2[Ni(SPh)_4]$	725 (~300), 676 (~300), 510 (~2500), 460 (~2400)[f]	NR	NR	78
NiRd[g]	720 (460), 670 (385), 450 (3200), 360 (5460)[h]	-0.20[i]	NR	70, 78
Computed NiRd	732 (640), 661 (70), 455 (1800), 351 (4700)[j]	-0.52[k]	-2.70[k]	58, 70
$[Ni(HPyS)_4](NO_3)_2$	634 (30), 371 (32,700), 291 (82,500)[c]	NR	-1.78[l]	50
$(Ph_4P)_2[Ni(edt)_2]$	NR	-1.06[c] (r, $Ni^{3+/2+}$)	NR	42
$(^nBu_4N)_2[Ni_3(pdt)_5]$	NR	NR	-2.20, -2.40[m]	82
$Ni_6(PET)_{12}$	~550 (br), ~420, ~340[m]	~+0.4[m]	~ -2.4[m]	83

[a]Abbreviations: sh = shoulder; Rd = rubredoxin; HPyS = pyridinium-2-thiolate; edt = ethane-1,2,-dithiolate; pdt = propane-1,2,-dithiolate; PET = 2-phenylethanethioalte' br = broad. [b]Unless indicated (r = reversible), all potentials represent irreversible couples; [c]MeCN. [d]Values obtained in the presence of excess thiolate (50 mol-equiv $(Et_4N)(S\text{-}p\text{-}CF_3\text{-}Ph)$ for **1**; 10 mol-equiv KSPh for $(Ph_4P)_2[Ni(SPh)_4]$).[e]DMSO. [f]DMF/Toluene 50% (v/v). [g]NiRd from *D. gigas*. [h]pH 7.4 Tris-HCl buffer, with 50% (v/v) ethylene glycol. [i]100 mM KCl, pH 4.5 acetate buffer. [j]Values taken from the vertical transition energies of the 'full' model of NiRd, see ref. 58. [k]H_2O. [l]DMF. [m]THF

^1H NMR spectra of $[Ni(SPh)_4]^{2-}$-derived complexes including **1**,[40, 41, 54, 55] exhibit paramagnetically-shifted peaks (Figure 2.6). Most indicative of tetrahedral **1** is the peak at ~20 ppm, assigned to the *meta*-H in $[S\text{-}p\text{-}CF_3\text{-}SPh]^-$ (Figure 2.6).[54, 55] The *ortho*-H resonance is obscured by Et_4N^+ peaks, but appears at ~1 ppm. A group of low intensity peaks at ~7 ppm

corresponding to a diamagnetic (S = 0) species is also present in all preparations of **1**. The ^{19}F NMR signal in **1** serves as an additional spectroscopic handle and confirms both S = 0 (δ = -62.0 ppm; compared to δ = -61.7 ppm for Zn^{2+} complex **2**, Figure S2.18), and S = 1 (δ = -19.0 ppm) complexes in solution (Figure 2.7). The ^{19}F peak (Figure 2.7) corresponding to tetrahedral **1** account for ~50% of the Ni species ([**1**] = 2.0 mM in CD_3CN; see Figure S2.46); however, adding 20 mol-equiv of (Et_4N)(S-*p*-CF_3-Ph) pushes the speciation back to tetrahedral/monomer **1** (~85%; Figure S2.46). Comparing the ^{1}H NMR of (Et_4N)(S-*p*-CF_3-Ph) to **1** eliminates free thiolate as the diamagnetic contributor (Figure S2.2). Comparable peaks at ~7 ppm are also described in the ^{1}H NMR spectra of previously reported $[Ni(S\text{-}p\text{-}X\text{-}Ph)_4]^{2-}$ (X = H, Cl, Me) and $[Ni(S\text{-}m\text{-}Cl\text{-}Ph)_4]^{2-}$ complexes.[54] In contrast to **1**, the ^{1}H NMR of **2** displays sharp/correctly integrated proton resonances, although the analogous Zn^{2+} complex $[Zn(SPh)_4]^{2-}$ exhibits broad NMR signals that suggests thiolate dissociation in the simpler unsubstituted benzenethiolate-ligated system, previously attributed to the overall dianionic charge of the complex.[84] The attenuated basicity of *p*-CF_3-PhSH (pK_a: 8.4, computed in DMSO[85]; cf. pK_a (*p*-Br-PhSH): 9.0 in DMSO[86]) versus PhSH (pK_a: 10.3 in DMSO)[86] likely alleviates electron density at the metal to suppress ligand dissociation by minimizing Zn-*d*/S-*p* electron/electron repulsion given their identical overall charge.

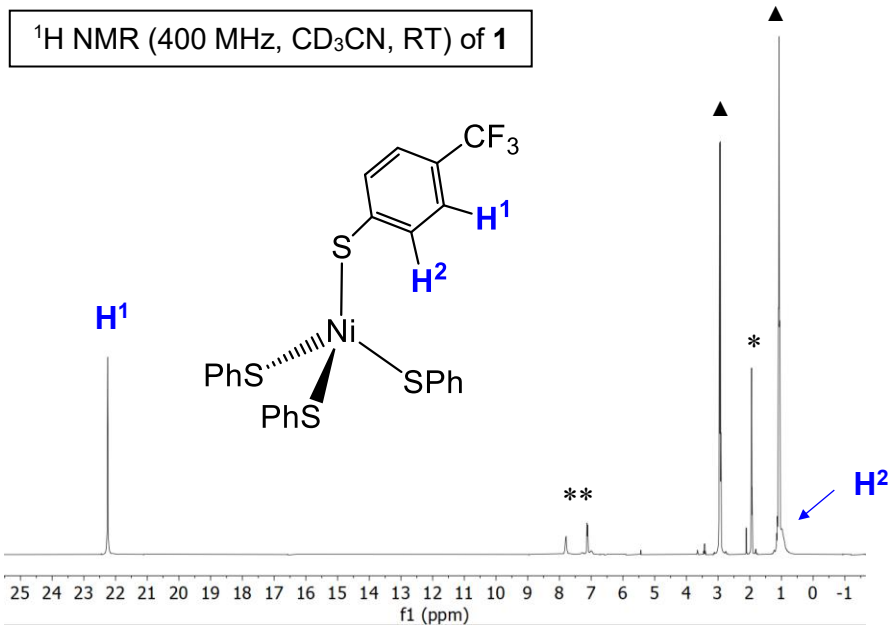

Figure 2.6. ^{1}H NMR spectrum of complex **1** in CD_3CN at RT (δ vs. residual protio solvent signal*). Peaks associated with $S = 0$ species indicated with **. *Note*: SPh = *p*-CF_3-SPh. ▲ = Et_4N^+ peaks.

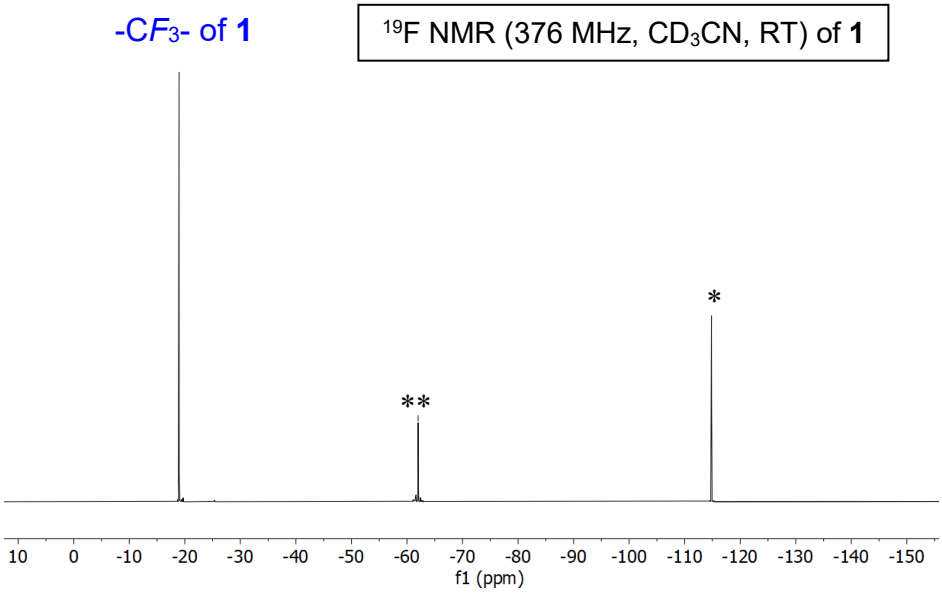

Figure 2.7. ^{19}F NMR spectrum of complex **1** in CD_3CN at RT (δ vs. $CFCl_3$). Peak at -114.81 ppm is from PhF (internal standard) as indicated with *. Peak associated with $S = 0$ species indicated with **.

Solution ESI-MS and μ_{eff} analyses further confirm the speciation described above. Unlike the solid-state μ_{eff} value of 3.47 BM, measurements for **1** in CD_3CN ([**1**] = 10.3 mM) yield μ_{eff} of 2.75 BM, characteristic of $[Ni(S\text{-}p\text{-}X\text{-}Ph)_4]^{2-}$ complexes (μ_{eff} = 2.7-2.9 BM in CD_3CN; 2.5-3.0 BM in DMSO-d_6).[39, 54] Addition of 20 mol-equiv thiolate to solutions of **1** increase μ_{eff} to 3.05 BM, suggesting more tetrahedral species. ESI-MS(-) analysis of MeCN solutions of **1** indicate charged complexes symptomatic of *S*,*S*-bridged species, e.g., $[Ni_2(S\text{-}p\text{-}CF_3\text{-}Ph)_5]^-$ (*m*/*z* = 1001.0; dimer **3** - thiolate; Figures S2.11- S2.12). However, various ligand substitution and redox reactions can happen in coordination complexes examined by ESI-MS.[87] Recording ESI-MS(-) of **1** with 20 mol-equiv $(Et_4N)(S\text{-}p\text{-}CF_3\text{-}Ph)$ resulted in disappearance of signals assigned to the bridged complex and enhancement of peaks associated with **1**, e.g., $(Et_4N)[Ni(S\text{-}p\text{-}CF_3\text{-}Ph)_4]^-$ (*m*/*z* = 896.1) and $[Ni(S\text{-}p\text{-}CF_3\text{-}Ph)_3]^-$ (*m*/*z* = 589.1) (Figure S2.13). Collectively, all solution measurements suggest **1** partially converts to a diamagnetic complex upon dissolution, likely thiolate-bridged complexes such as $[(RS)_2Ni(\mu\text{-}SR)_2Ni(SR)_2]^{2-}$ (dianion of **3**, R = S-*p*-CF_3-Ph); however (depending on concentration), the bulk speciation leans toward the paramagnetic tetrahedral Ni^{2+} species in the presence of excess thiolate.

To confirm that bridged complexes such as **3** contribute to the 'diamagnetic' NMR signals, we attempted to synthesize **3** by several routes, e.g., chemical oxidation, methylation, and protonation (vide supra), all of which should afford the suspected *S*,*S*-bridged dimer. However, each synthesis resulted in a spectroscopically identical mix of compounds where no single complex was readily isolated, although one species was observed that we tentatively identify as **3**. Ultimately, NMR analysis points to diamagnetic complexes (Figures S2.22 and S2.24), one of which indeed has signals identical to those observed in solutions of **1** (Figure S2.23). While this result does not undoubtedly confirm **3**, it points to the complexity of the speciation. We posit that multiple species

are observed due to varying types of soluble thiolate-bridged $[Ni(S\text{-}p\text{-}CF_3\text{-}Ph)_2]_n$ complexes with variable n ($\geq$ 2). For example, complexes featuring linked aryl-thiolato-bridges such as the oligomeric ring complexes $[Ni(SPh)_2]_n$ (n = 9, 11; all planar Ni^{2+}),[88] the face-sharing tetrahedral dimer $[(RS)Ni(\mu_2\text{-}SR)_3Ni(SR)]^-$ (R = 2,4,5-triisopropylbenzenethiolate),[89] and the *p*-Cl analogue of **3**[56] (vide infra) provide support for this proposal. Bridged complexes such as **3** being in equilibrium with monomer/tetrahedral **1** in solution may advocate against the presence, or sufficient lifetime, of a putative $[Ni(SPh)_3(solv)]^-$ (**I**) species.[55] Multimeric planar Ni-thiolate complexes form under low thiolate-to-Ni ratios employed in synthesis and can occur upon thiolate dissociation due to protonation (or spontaneously) and substitution with donor solvents.[36, 90, 91] Indeed, spontaneous thiolate dissociation readily occurs even with chelating alkyl-thiolato-bound Ni^{2+} complexes to afford bridged species.[92] Thus, intermediates such as **I** would be fleeting at best. Yamamura suggested that tetrahedral $[Ni(SPh)_4]^{2-}$ is in equilibrium with the planar version (*S* = 0) of complex **I** in DMSO, which is the source of the peaks at ~7 ppm in the ^1H NMR.[55] However, Maroney demonstrated that these peaks originate from a thiolate-bridged dimeric complex analogous to **3**, and were successful in growing crystals and obtaining ^1H NMR, albeit through an ill-defined reaction between $[Ni(Me_6tren)Cl_2]$ (Me_6tren = tris(2-(dimethylamino)ethyl)amine and $(Et_4N)(S\text{-}p\text{-}Cl\text{-}Ph)$.[56] Thus, spectral comparisons with this bridged species suggest that the peaks at ~7 ppm belong to complexes analogous to **3**. Based on the results presented here, it is possible, although difficult to verify, that the MeCN-solvated complex $[Ni(S\text{-}p\text{-}CF_3\text{-}Ph)_3(MeCN)]^-$ (**I** in eqs. 1-2; Scheme 1.1) is a common intermediate between **1** and **3** according to the following (DFT-estimated ΔG in blue):

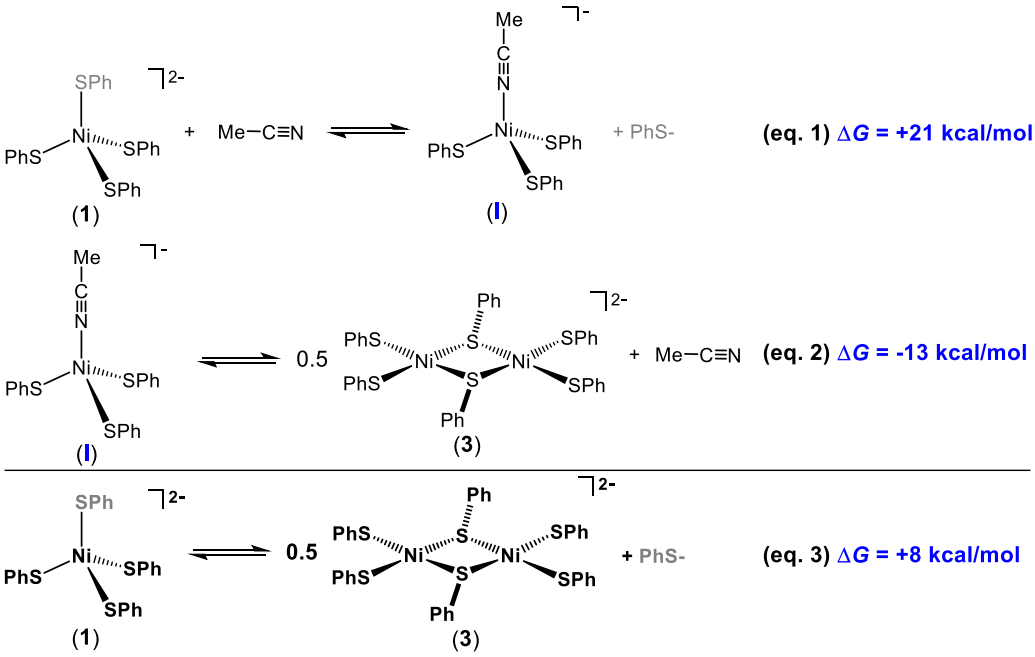

Scheme 2.1. Stepwise path to formation of *S*,*S*-bridged planar **3** from monomer/tetrahedral **1** via putative $[Ni(SPh)_3(MeCN)]^-$ intermediate **I**. *Note*: PhS designation is used for simplicity, complex **1** contains coordinated *p*-CF_3-PhS; MeCN was used for this work but can represent any donor solvent in **I**; square-planar **I** ($S = 0$), suggested in ref. 55 (where solv = DMSO) was computed to be 14 kcal/mol less stable than the tetrahedral ($S = 1$) geometry.

ESI-MS(-) measurements of **1** reveal that $[Ni(S\text{-}p\text{-}CF_3\text{-}Ph)_3]^-$, a likely dimer precursor/fragment, is the most intense ion detected (Figure S2.11) under electrospray conditions. Additionally, strong donor solvents favor the product side of eq. 1 of Scheme 2.1 that may eventually yield dimer. Furthermore, delivering excess thiolate equivalents to solutions of **1**, favor the tetrahedral $[Ni(S\text{-}p\text{-}CF_3\text{-}Ph)_4]^{2-}$ complex based on UV-vis (see Figure 2.5). As written in Scheme 2.1, excess thiolate (eq. 1, eq. 3) and suitable donor solvents (eq. 2) favor monomer; however, prior reports indicate that planar dimers featuring aryl-thiolates such as **3** are substitutionally-inert and do not readily convert back to monomeric/tetrahedral **1** even with additional thiolate.[54, 56] In contrast, adding

thiolate to solutions containing a mixture of thiolate-bridged complexes including **3** (reverse of eq. 3) indicates monomeric/paramagnetic **1**, evidenced by characteristic peaks in $^{1}H/^{19}F$ NMR (Figures S2.47-S2.49), and the appearance of the two adjacent CT bands in the UV-vis (Figure S2.50). Several groups also report using thiolates or neutral N-donors to readily cleave *S*,*S*-bridged square-planar Ni-dimers into their corresponding monomeric species.[63, 93-96] Thus, we assign the peaks at δ ~7 ppm in the ^{1}H NMR of freshly-dissolved monomer **1** to soluble thiolate-bridged complexes such as **3** or of higher nuclearity that can't be eliminated or identified at present. Both **1** and the bridged complex(es) are interconvertible, with **1** being predominant when thiolate is in excess.

DFT allowed us to gain further insight into the solution speciation represented by eqs. 1-3 (Scheme 2.1). To estimate the preference for each of the aforementioned species, we computed the Gibbs free energy difference (ΔG) of the reactions described by eqs. 1-3 using DFT at the B3LYP/def2-TZVPP level of theory with an MeCN solvent field (ε = 37.5). A clear preference for tetrahedral monomer **1** was indicated. For example, the ΔG of eq. 3, which describes the overall $S = 1$ monomer **1**/$S = 0$ dimer **3** conversion, computes as an endergonic reaction (8 kcal/mol) in favor of the reactant/monomer side, i.e., **1**. If one considers the stepwise path to **3** via eqs. 1-2, then **1** or **3** are favored by 21 and 13 kcal/mol, respectively, over a postulated $S = 1$ tetrahedral intermediate $[Ni(S\text{-}p\text{-}CF_3\text{-}Ph)_3(MeCN)]^-$ (**I**). The possibility of a planar intermediate **I** was also investigated but not included due to a high ΔG (26 kcal/mol) in favor of the reactant side of eq. 1. An optional proposal regarding the peaks in the ~7 ppm region of the ^{1}H NMR is an equilibrium between tetrahedral complex **1** and its $S = 0$ square-planar isomer. However, the computed ΔG between these geometric isomers is 14 kcal/mol in favor of tetrahedral **1**.

Solution behavior of 1 in the presence of Brønsted Acids. With the intent of utilizing **1** for HER electrocatalysis, we examined the behavior of **1** in the presence of strong and weak Brønsted acids such as HBF_4•Et_2O (pK_a = 1.6 in MeCN[97]) and AcOH (pK_a = 23.5 in MeCN[60]), respectively. Earlier studies indicate formation of insoluble complexes, represented as $[Ni(SPh)_2]_\infty$, when weak acids such as EtOH or H_2O are added to solutions of $[Ni(SPh)_4]^{2-}$.[41, 55] Consistent with prior reports, addition of either stoichiometric HBF_4•Et_2O or 25 mol-equiv AcOH to dark-red MeCN solutions of **1** resulted in precipitation of a fine purple powder and a nearly colorless solution. IR/NMR analysis of this precipitate and the bleached MeCN solution suggest a $[Ni(S\text{-}p\text{-}CF_3\text{-}Ph)_2]_n$-type complex and thiol HS-*p*-CF_3-Ph, respectively. Full characterization of the purple precipitate was limited due to poor solubility. A qualitative UV-vis spectrum of this solid in DMSO revealed an intense band at 510 nm (Figures S2.52-S2.53). Monitoring the NMR of **1** upon addition of AcOD-d_4 suggest loss of **1** even in the presence of low acid/**1** ratios (e.g., 5:1), indicated by the change in solution color to pale brown and attenuation of the NMR signals of **1** (Figure S2.56-S2.58). The fine purple precipitate is eventually observed when > 20 mol-equiv of AcOD-d_4 are added, as described above. Clearly, as-isolated **1**, even in the presence of weak acids, readily protonates a coordinated thiolate to yield intractable species. To impede polymerization and shift to tetrahedral/monomer **1**, excess (Et_4N)(S-*p*-CF_3-Ph) was added to CD_3CN solutions of **1** and the same NMR experiment with AcOD-d_4 was conducted. Titration of AcOD-d_4 up to 60 mol-equiv indicates 95% of tetrahedral/monomer **1** remains based on $^1H/^{19}F$ NMR (Figures S2.59-S2.61). Thus, undesired polynuclear Ni-thiolate complexes in acidic organic media can be suppressed by utilizing excess ligand.

Electrochemistry. Electrochemical experiments were completed in MeCN with 0.25 M $^n Bu_4NPF_6$ as supporting electrolyte using a GC working electrode; all potentials are reported

versus an externally referenced ferrocenium/ferrocene (Fc^+/Fc) couple. For comparative purposes, potentials for previously reported Ni-thiolate complexes are converted to the same reference potential.[98] The cyclic voltammogram (CV) of **1** is complex and displays several irreversible features (Figure S2.63). Scanning cathodically revealed one irreversible reduction at -1.98 V (E_{red}), assigned to the $Ni^{2+/1+}$ couple, along with several irreversible oxidation waves. Recording the CV with excess thiolate, to ensure only monomeric/tetrahedral species (vide supra), revealed the same E_{red} event at -1.94 V consistent with the $Ni^{2+/1+}$ assignment, and an irreversible oxidation (E_{ox}) at -0.38 V (Figure 2.8). The irreversibility of the reduction wave, even with excess thiolate, indicates a structural change accompanies this process, proposed to be thiolate dissociation to afford three-coordinate (3C) $[Ni(S\text{-}p\text{-}CF_3\text{-}Ph)_3]^{2-}$. Reversing the scan resulted in a similar current response at E_{ox} = -0.38 V and a new reduction event at -1.60 V in addition to the $Ni^{2+/1+}$ couple at ~-2 V (Figure 2.8). Comparing the CV of **1** to $(Et_4N)(S\text{-}p\text{-}CF_3\text{-}Ph)$ (E_{ox} = -0.33 V, E_{red} = -1.68 V; Figure S2.62) and other *p*-substituted aryl-thiols/disulfides[99] suggests these waves are due to free thiolate oxidation/disulfide reduction. The CV of Zn^{2+} complex **2** provides further justification for this assignment as E_{red} ~ -1.70 V only appears with scans initiated anodically, i.e., oxidation of the Zn-coordinated thiolate (E_{ox} = 0.11 V) is required to generate disulfide and enable E_{red} (Figure S2.64). Other waves in the CV of **1** without excess thiolate are difficult to assign due to the speciation. Expectedly, these oxidation events are minimized in the CV of **1** recorded with additional thiolate (Figure 2.8). Because Fc^+ oxidation of **1** affords disulfide and a mixture of thiolate-bridged complexes such as **3** (vide supra), we assign oxidation events more positive than -0.40 V (see Figure S2.63) to coordinated thiolates, i.e., no Ni^{3+} intermediate(s).

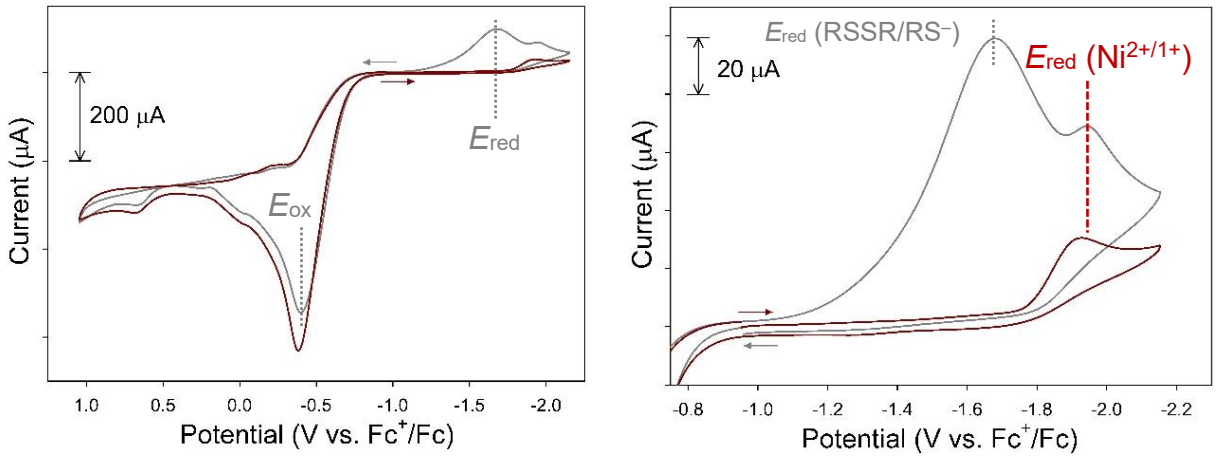

Figure 2.8. CV of complex **1** (1.89 mM) with 20 mol-equiv (Et_4N)(S-*p*-CF_3-Ph) in MeCN at RT (0.25 M $^nBuN_4PF_6$ supporting electrolyte, GC working electrode, 100 mV/s scan rate). *Left*: full CV window measured. *Right*: expansion of cathodic region to display the $Ni^{2+/1+}$ couple. Arrows display the scan direction (red = cathodic scan, gray = anodic scan). The E_{ox} (RS^-/RSSR) and E_{red} (RSSR/RS^-) of the thiolate are listed in gray (left); the $Ni^{2+/1+}$ couple is marked in red (right)

Making comparisons to analogous tetrahedral homoleptic Ni-aryl-thiolates is limited, but all propose primarily ***irreversible redox*** events. For example, voltammetric measurements on $[Ni(SPh)_4]^{2-}$ report E_{ox}, assigned as $Ni^{3+/2+}$, in different solvents (-0.57 V in DMSO[41]; -0.44 V in MeCN[81]; see Table 2.2). The close match to the E_{ox} of PhSH (-0.49 V in DMF[99]) suggests this oxidation is likely due to free thiolate and not a Ni^{3+} species. Notably, reversible $Ni^{3+/2+}$ couples have been reported for planar dicarboxamido/dithiolato-NiN_2S_2 complexes which are quite negative (E½ = -0.70 to -0.90 V in DMF or MeCN[100, 101]). Tetrathiolato/planar complexes containing chelating dithiolates also display rather low (quasi)reversible $Ni^{3+/2+}$ events that center around -1 V in DMF (Table 2.2).[42-45] Irreversible S-based redox have been reported in the CVs for planar/anionic Ni^{2+} complexes containing monodentate aryl-thiolates with supporting tridentate ancillary ligands such as the complex anions $[Ni(pdmt)(SPh)]^-$ (pdmt = pyridine-2,6-dimethanethiolate; E_{ox} = -0.47 V, E_{red} = -1.73 V in DMF[93]), $[Ni(L^S)(Mes^S)]^-$ (L^S = bis(2-

mercaptophenyl)sulfide, Mes^S = 2,4,6-trimethylthiophenolate; E_{ox} = -0.83 V, E_{red} = -2.03 V in MeCN[102]), and $[Ni(nmp)(S\text{-}p\text{-}CF_3\text{-}Ph)]^-$ (nmp = dianion of *N*-(2-mercaptoethyl)picolinamide; E_{ox} = -0.19 V, E_{red} = -1.64 V in DMF[96]). The latter complex contains the identical aryl-thiolate as in **1**, albeit in a planar geometry. Given that E_{ox} of Zn complex **2** is +0.11 V, coupled with the E_{ox} values of the aforementioned planar Ni-thiolate complexes, we assign the E_{ox} at -0.08 V to the coordinated thiolates of **1**, whereas the E_{ox} at -0.20 V may be due to Ni-bound thiolates of thiolate-bridged complexes such as **3** (see Figure S2.63). Indeed, the E_{ox} values (-0.20, +0.13 V in MeCN[56]) for the related *S,S*-bridged dimer $[Ni_2(S\text{-}p\text{-}Cl\text{-}Ph)_6]^{2-}$ are close to those reported here.

Although oxidative events have been described for homoleptic tetrahedral and planar Ni-thiolate complexes, descriptions of reductive events are scarce. The reversible $Ni^{2+/1+}$ couple for a related tetrahedral NiS_4 complex [$(PhTt^{tBu})$Ni-SPh] is -1.17 V vs. Fc^+/Fc in THF and provides one benchmark, but this complex is charge neutral with only one Ni-thiolate bond and hence the reduction is expectedly facile.[66] For the homoleptic/tetrahedral $Ni(SCys)_4$ site in NiRd, a direct analogue of **1**, Shafaat reports an estimated $Ni^{2+/1+}$ potential of -2.01 V vs. NHE[58] (~ -2.70 vs. Fc^+/Fc in MeCN[80]), considerably more negative than **1** due to coordination of alkyl- vs. aryl-thiolates. However, this value is in-line with what we compute for the reversible $E½$ ($Ni^{2+/1+}$) for **1** at -2.69 V (MeCN; vide infra), i.e., no thiolate dissociation during redox. Homoleptic/square-planar tetra-aryl-thiolato-Ni complex $[Ni(HPyS)_4]^{2+}$ (HPyS = N-protonated form of pyridine-2-thiolate) demonstrates an irreversible $Ni^{2+/1+}$ couple at -1.78 V in DMF, slightly more positive than **1**.[50] While this value may be contrary to that expected for a planar Ni complex, the more positive E_{ox} likely arises from the overall cationic charge on the complex. For comparison, the $E½$ ($Ni^{2+/1+}$) values for square-planar neutral diamino/dithiolato-NiN_2S_2 complexes are considerably more cathodic with potentials ~ -2.40 V in MeCN.[92, 103] More in-line with the expectation for a planar

tetrathiolato-Ni complex is the irreversible reduction of the *S*,*S*-bridged hexameric complex $[Ni_6(PET)_{12}]$ (PET = 2-phenylethanethiolate), which exhibits E_{red} around -2.40 V in THF.[83] Other planar and multimeric *S*,*S*-bridged Ni complexes with alkyl-thiolates show low $Ni^{2+/1+}$ couples,[82, 104-106] down to -2.40 V (Table 2.2), comparable to NiRd and more negative than the analogous couple in **1**.

HER Electrocatalysis. Complex **1** was investigated for its activity in electrocatalytic proton reduction to H_2(g) or HER. CV measurements were acquired after titrating proton equivalents of the weak Brønsted acid AcOH into MeCN solutions of **1** (0.25 M ^{n}Bu$_4$NPF$_6$ electrolyte, GC working electrode, scan rate = 100 mV/s). Addition of AcOH to solutions of **1** resulted in catalytic waves (E_{cat}) at -1.47 V and -1.92 V (Figure S2.65); however, only E_{cat} at -1.92 V produced significant current enhancement suggestive of electrocatalysis. Standard rinse tests indicate no deposition of catalytic nanomaterial on the working electrode (Figure S2.66).[107, 108] While these results suggest **1**, or a complex derived from **1**, is an electrocatalyst for HER, its speciation is complex under these specific conditions. For example, addition of only 4-6 mol-equiv AcOH resulted in a color change of the solution from dark maroon-red to brown with the appearance of a new peak at -1.47 V (Figure S2.65) that modestly increased with [AcOH]. Addition of >20 mol-equiv resulted in lightening of the solution color and a purple precipitate, likely insoluble $[Ni_n(S\text{-}p\text{-}CF_3\text{-}Ph)_{2n}]_n$ ($n \geq 2$) oligo/polymeric species[61] (vide supra) as suggested by Yamamura ~40 years ago.[41] Extrapolating valid figures of merit under these conditions was thus not possible.

To circumvent the formation of intractable species, HER activity was next evaluated in the presence of excess $(Et_4N)(S\text{-}p\text{-}CF_3\text{-}Ph)$. Adding 20 mol-equiv of thiolate to MeCN solutions of **1** ensures the presence of tetrahedral monomer as confirmed by UV-vis and NMR spectroscopy (vide supra; see Figures 2.5 and S2.46). As with **1** alone, titrating AcOH into MeCN solutions of **1**/20

mol-equiv thiolate resulted in an electrocatalytic current response (Figure 2.9) with one major event near the $Ni^{2+/1+}$ couple at E_{cat} = -2.23 V, and a minor response at -1.93 V. The primary difference with excess thiolate present is loss of E_{cat} ~-1.5 V (Figure S2.65), proposed to be due to formation of thiolate-bridged complexes upon increasing proton equivalents.[41, 92] The absence of this E_{cat} supports this hypothesis. From these results, the η of HER catalyzed by **1** was found to be 0.72 ± 0.02 V using a standard method that accounts for homoconjugation of AcOH (see eq. iii in the SI),[109] with a TOF of 14.5 ± 3.6 s^{-1}, see eq. iv in the SI, obtained from i_c/i_p ratios at saturating acid conditions (~20 mol-equiv AcOH). While the electrocatalytic activity of **1** is modest, it is comparable to TOFs reported for other [NiFe]-H_2ase models that employ two metal sites and/or more elaborate ligand constructs (see Chart 2.2, Scheme S2.1, and Table 2.3). [30, 105, 106, 110-113] Additionally, the solution color in the electrochemical cell remains red throughout the experiment with no precipitate, consistent with tetrahedral/monomer **1**. The presence of **1** under these conditions was further confirmed by the distinct double-humped UV-vis spectrum of the reaction mixture taken directly from the electrochemical cell at the end of acid titration (Figure S2.68). The amount of **1** remaining in solution, estimated from $^1H/^{19}F$ NMR and UV-vis experiments is >90% after addition of 20 mol-equiv of AcOH. Standard rinse tests indicate no deposition on the GC working electrode (Figure S2.67). Furthermore, CVs of AcOH in the presence of Zn^{2+} complex **2** and with (Et_4N)(S-*p*-CF_3-Ph) (Figure S2.69) under identical conditions reveal that the Ni^{2+} complex is solely responsible for the electrocatalysis displayed in Figure 2.9. The HER activity of dimer **3** was not measured in this work because it could not be obtained in pure form. However, insight on its HER capacity can be extrapolated from a series of analogous, albeit charge neutral, planar [L-Ni(μ-$SAr)_2$Ni-L] (L = substituted aminobis(thiophenolate) ligands) dimers constructed by Castillo and colleagues.[114-116] Among the reported series of complexes, only dimers with close

Ni---Ni separations (~2.7 Å) and relatively acute hinge angles (angle defined by the intersection of the two Ni square planes) were adequate HER electrocatalysts. The large Ni---Ni separation (~3.4 Å; Table S2.8) computed for **3**, along with coplanar NiS_4 planes (hinge angle ~ 180°) suggest **3** would be a poor H_2 evolving electrocatalyst.

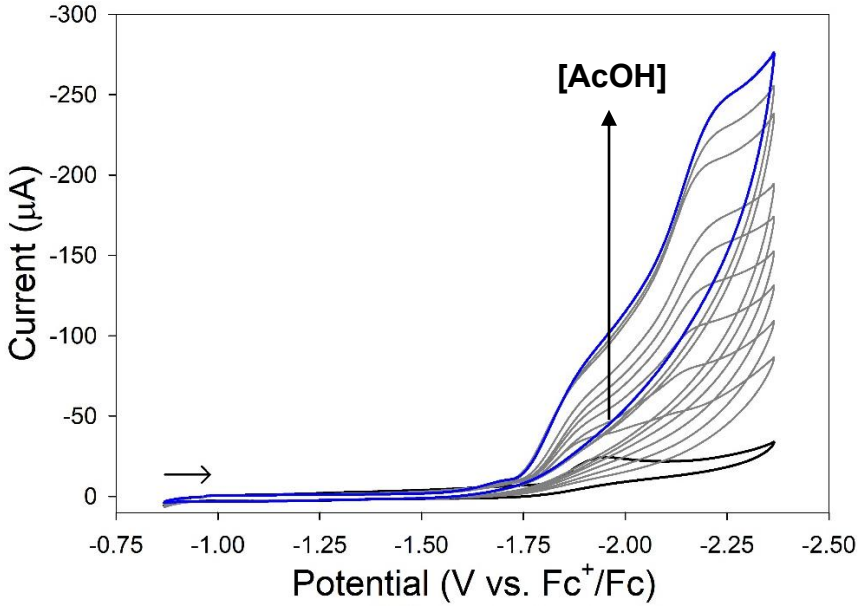

Figure 2.9. CV of complex **1** (1.89 mM) with 20 mol-equiv $(Et_4N)(S\text{-}p\text{-}CF_3\text{-}Ph)$ (black trace) and after the addition of AcOH in 2 mol-equiv increments (gray traces) up to a final of 18 mol-equiv (blue trace) in MeCN at RT. Conditions: 0.25 M $^n BuN_4PF_6$ supporting electrolyte, GC working electrode, 100 mV/s scan rate. Arrow displays the scan direction.

Additional kinetic parameters were obtained from plots of the catalytic current (i_c) or ratio of i_c to the reduction peak current of **1** in the absence of acid (i_p), i.e., i_c/i_p with respect to various conditions. For instance, i_c/i_p exhibits a linear dependence on $[H^+]$ until the acid-independent region is reached at ~30 mM (16 equiv) AcOH and a maximum i_c/i_p ratio of ~10 (Figure S2.70). The linear plot of i_c versus $[H^+]$ indicates a second-order dependence on $[H^+]$.[117] Similarly, i_c plotted against [**1**] (Figure S2.71) is also linear to indicate a first-order dependence of the catalytic rate on [**1**]. Hence, the results obtained correspond to the overall rate expression: rate = k[**1**]$[H^+]^2$,

using AcOH as the H^+ source. Further insight into the rate-limiting step and mechanism can be gleaned from the kinetic isotope effect (KIE, k_H/k_D). Utilizing AcOD-d_4, the KIE for HER was determined to be 1.62, obtained from the ratio of the TOF values under saturating conditions of the H^+ and D^+ sources (i_c/i_p values at 20 mol-equiv (40 mM) of AcOH or AcOD-d_4). This value falls within the so called 'normal' KIE regime, and contrasts with that expected for an inverse KIE (<1), generally attributed to rate-determining metal-hydride formation,[118-120] or large KIE values (>8), due to hydrogen tunneling.[121] The KIE determined here, to some degree, is comparable to the reported KIE of 2.6 for H_2 production by [NiFe]-H_2ase[122] and 3.81 for NiRd.[58] In the case of **1**, the rate-determining step is visualized by intramolecular coupling of a Ni-hydride to a proton on a coordinated thiol, viz. intramolecular H^+/H^- coupling toward H_2 evolution (vide infra) as suggested for other LMW Ni complexes.[31, 32, 106, 123]

Table 2.3. Select Parameters for Ni-thiolate HER Electrocatalysts (see Chart 2.1-2.2, Chart S2.1 in the SI for structures).

Complex	TOF (s^{-1})	η (V)	H^+ Source	Solvent	Ref
1	14.5	0.72	AcOH	MeCN	TW
[Ni(xsbms)][a]	<1.0	NR	Et_3N•HCl	DMF	104
[Ni('S_4')][b]	NR	0.76	TFA	DMF	106
$[Ni(PS)_2]$[c]	51	1.10	AcOH	CH_2Cl_2	112
$[NiN_2S_2]$[d]	1441, 5575	0.56, 0.67	AcOH	MeCN	113
$[Ni_3S_6]$[e]	NR	0.59	Et_3N•HCl	DMF	105
$[HNiFe(pdt)(dppe)(CO)_3]^+$[f]	20	0.50	TFA	CH_2Cl_2	111
$[HNiFe(edt)(dppe)(CO)_3]^+$[f]	240-310	0.49	TFA	CH_2Cl_2	111
$[Ni(xsbms)FeCpCO]^+$[a]	NR	0.73	TFA	DMF	110
$[L^{N2S2}Ni^{II}Fe^{II}]^+$[g]	250	0.69	Et_3N•HBF_4	MeCN	30, 124
$[Ni–Fe']^+$[h]	52	0.94	TFA	MeCN	31
NiRd[i]	100	0.54		H_2O[j]	57

[a]xsbms = 1,2-bis(4-mercapto-3,3-dimethyl-2-thiabutyl)benzene. [b]'S_4' = 1,3-bis(1,2-benzenedithiolate)propane. [c]PS = 2-(diphenylphosphanyl)benzenethiolate. [d]N_2S_2 = *N*,*N*′-dimethyl-*N*,*N*′-bis(2-sulfanylethyl)ethylenediamine. [e]S_6 = (tritylthio)ethylthio)methyl)-1,2-dithiolate. [f]dppe = diphenylphosphinoethane, pdt = propane dithiolate, edt = ethane dithiolate. [g]L^{N2S2} = (2,2′-(2,2′-bipyridine-6,6′-diyl)bis(1,1-diphenylethanethiolate)). [h]Ni–Fe′ = Ni(bismercaptoethane diazacycloheptane)-Fe(CO)(η^5-C_5H_5). [i]NiRd from *D. desulfuricans*. [j]Acetate buffer, pH = 4.5, 4 °C.

Proposed Mechanism of HER by 1. Mechanistic possibilities were investigated through DFT (B3LYP, def2-TZVPP) using CPCMC to model the MeCN solvent environment (details in the SI; see Figures S2.73-S2.77 and Tables S15-S19). Because $E_{red}(Ni^{2+/1+})$ at -1.94 V coincides with E_{cat} (see CV Figure 2.9), our working mechanism (Scheme 2.2) begins from the 3C trigonal planar (τ_3 = 0.04,[58]; $\sum Ni_\alpha$ = 359.9°; see Figure S2.74, Table S2.17) Ni^{1+} doublet dianion $^{2}\mathbf{1}^{\mathbf{R}}$, generated after reduction of **1**. Attempts to synthesize and characterize a Ni^{1+}-thiolate species derived from **1** via chemical reduction with strong reducing agents such as KC_8 or $CoCp^*_2$ were not successful and only led to ill-defined materials. However, experimental support for this probable structural change is indicated by the irreversible nature of the $Ni^{2+/1+}$ wave in the CV (see Figure 2.8). Additionally, dissociation of one aryl-thiolate from the putative 4C-tetrahedral (τ_4 = 0.81) Ni^{1+} species $[Ni(S\text{-}p\text{-}CF_3\text{-}Ph)_4]^{3-}$ is favorable and computed to be exergonic by 18 kcal/mol. To benchmark the method in estimating Ni reduction potentials (E½), the absolute potential of the Fc^+/Fc reference couple was calculated to be +5.009 V (Table S2.15 in the SI[125-129]). Utilizing known vales for the absolute potential of the SHE (+4.281 V[130]) coupled with its conversion against a common reference electrode (SHE = +0.244 V vs SCE in MeCN[80]) results in a computed E½(Fc^+/Fc) of +0.48 V vs. SCE in MeCN, comparable to the experimental value of +0.38 V.[98] The reversible, i.e., no thiolate loss during redox, $Ni^{2+/1+}$ potentials were then separately computed for the 4C and 3C complexes. E½(Ni^{2+}/Ni^{1+}) was estimated to be -2.69 V and -1.68 V (vs. Fc^+/Fc) for 4C-tetrahedral $[Ni(S\text{-}p\text{-}CF_3\text{-}Ph)_4]^{2-/3-}$ and 3C-trigonal $[Ni(S\text{-}p\text{-}CF_3\text{-}Ph)_3]^{1-/2-}$, respectively, bracketing a range where the experimental value (E_{red} = -1.94 V) falls close to the mean.

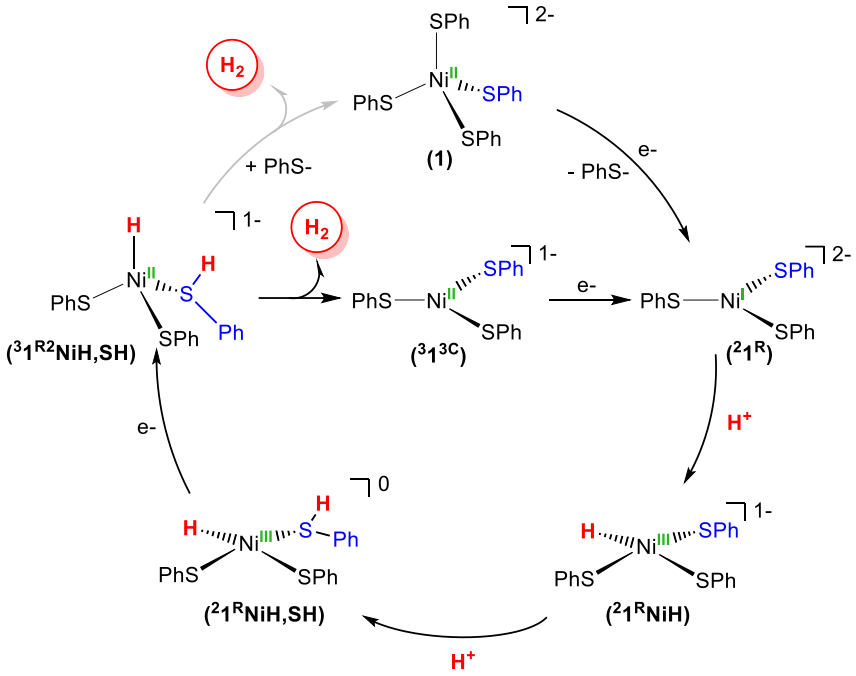

Scheme 2.2. Proposed ECCE mechanism (path i) for the HER catalyzed by complex **1**. After the first complete cycle, the following cycles begin with $^{3}\mathbf{1}^{\mathbf{3C}}$ following an ECCE mechanism.

Beginning with the doublet (S = ½)/3C species $^{2}\mathbf{1}^{\mathbf{R}}$ (Ni–S_{avg}: 2.296 Å), four plausible paths were considered: (i) ECCE (E = electrochemical step; C = chemical step), and (ii) ECEC mechanisms where a ***Ni-H intermediate*** is traversed after the first 'E' step (reduction of **1** to $^{2}\mathbf{1}^{\mathbf{R}}$); or (iii) ECCE, and (iv) ECEC paths where ***ligand protonation*** occurs after reduction. A second consecutive reduction step, or EECC mechanism, was also computed but not further considered because of the unfavorable barrier to access a Ni(0)-thiolate species (E½(Ni^{1+}/Ni^{0}) ~ -4 V; data not shown). Planar and tetrahedral intermediates for each path were also considered (see Scheme S2.3; Figures S2.73-S2.75). Paths iii and iv, involving a thiolate protonation second 'C' step, were eliminated due to large differences in ΔG, upwards of 50 to 70 kcal/mol. Focusing on mechanisms i and ii, the first 'C' step (second overall) results in a Ni-hydride (NiH) intermediate ($^{\mathbf{R}}$**NiH** = one-electron reduced from $^{3}\mathbf{1}^{\mathbf{3C}}$/Ni-hydride intermediate) that can either be square-planar (S = ½; $^{2}\mathbf{1}^{\mathbf{R}}$**NiH**) or

tetrahedral (S = 3/2; **^{4}1^{R}NiH**); however, computations suggest that the NiH intermediate is more stable by ~12 kcal/mol in square-planar geometries (ΔG values for both isomers depicted in Figure S2.73, ECCE pathway) and accordingly we concentrate the initial discussion on these species.

Protonation of **^{2}1^{R}** yields **^{2}1^{R}NiH** (ΔG = +14 kcal/mol; Scheme 2.2), formally a Ni^{3+}–H species, resulting in an intermediate four-coordinate complex with only a slight geometric bias towards planar geometry (τ_4 = 0.43; see Figure S2.75 and Table S2.18 for structural information). The calculated Ni–H length (1.46 Å) compares favorably to other DFT-estimated distances in thiolato-ligated Ni, including a tetrahedral Ni^{3+} complex from Peters (Ni–H: 1.550 Å)[131] and the five-coordinate Ni^{3+}–H in NiRd reported by Shafaat (Ni–H: 1.41 Å).[58] Experimentally, terminal Ni–H bond lengths appear over a broad range (1.32-1.65 Å), with planar systems at the lower end as observed here.[132] Two paths follow **^{2}1^{R}NiH**; mechanism i, ligand protonation (ECCE, vide infra), or mechanism ii, reduction (ECEC). Although both routes lead to the same common intermediate before H_2 evolves (**1^{R2}NiH,SH** = doubly-reduced from **1**/Ni-hydride, protonated/coordinated thiol intermediate), protonation (*path I*, Scheme 2.2) is favored by ~10 kcal/mol over reduction (*path ii).* Protonation of coordinated thiolate affords the distorted planar complex **^{2}1^{R}NiH,SH** (τ_4 = 0.40, +23 kcal/mol from **^{2}1^{R}NiH**). The diminished charge on the bound thiol results in elongation of the Ni–thiol bond by ~0.08 Å and contraction of the remaining Ni-thiolate bonds (~0.08 Å) from the **^{2}1^{R}NiH** precursor (Figure S2.75, Table S2.18). The final 'E' step computes E½($Ni^{3+/2+}$) = -0.58 V (ΔG = +13.4 kcal/mol; Figure S2.73) going from **^{2}1^{R}NiH,SH** to **^{1}1^{R2}NiH,SH** (S = 0). The anionic intermediate **^{1}1^{R2}NiH,SH** is more square-planar (τ_4 = 0.20; Figure S2.75, Table S2.18) than its precursor with the anticipated lengthening of all Ni-S bonds after reduction to Ni^{2+}. Notably, the analogous tetrahedral (S = 1) species **^{3}1^{R2}NiH,SH** is nearly isoenergetic ($\Delta\Delta G$: 1.6 kcal/mol) with planar **^{1}1^{R2}NiH,SH**, indicating that involvement of either coordination geometry is valid (vide

infra). Regardless of the exact geometry of the penultimate species in our working model, experimental support for such intermediates exists in the report of the tetrahedral Ni-nitrosyl species $[Ni(SPh)_3(NO)]^{2-}$ (**II**; $S = 0$) obtained from the reaction of $[Ni(SPh)_4]^{2-}$ with NO(g) or Ph_3CSNO.[63] Indeed, complexes such as **II** are isolable with the thiolate used in this work; $(Et_4N)_2[Ni(S\text{-}p\text{-}CF_3\text{-}Ph)_3(NO)]$ (**4**) has been synthesized in modest yield with characterization (Figures S2.27-S2.31) suggestive of a structure identical to **II**. Notably, IR indicates the N-O stretching frequency for **4** (ν_{NO}: 1683 cm^{-1} in KBr) is ~30 cm^{-1} upshifted from **II** because of the electron-withdrawing *p*-CF_3 group. Although H^+ is not exactly isolobal with NO, one can view both as redox-active (to some degree) small molecules that react with tetra-aryl-thiolato nickelates in a similar fashion to yield 4C $[Ni(SAr)_3(H/NO)]^{n-}$ analogous to intermediates such as $^3\mathbf{1^{R2}NiH,SH}$ in Scheme 2.2.

The formation of the $\mathbf{1^{R2}NiH,SH}$ intermediate regardless of geometry, i.e. square-planar or tetrahedral, sets up H_2 evolution via a heterolytic coupling pathway, consistent with other proposed mechanisms for transition metal hydride systems with adjacent thiol/M-H species[31, 33] and NiRd.[58] To assess a potential transition state involved in this pathway, a relaxed surface potential energy scan (PES) was performed by probing the potential energy landscape as the Ni-H^----H^+-SR unit is brought closer in space, in increments of 0.11 Å. The scan was performed by re-optimizing the structure at each point, while keeping the H---H bond distances fixed at each increment change with the remaining atoms remaining relaxed. Although the PES of both geometries were computed, only the PES of the tetrahedral intermediate $^3\mathbf{1^{R2}NiH,SH}$ (Scheme 2.2, Figure 2.10 and S2.76), revealed one clear transition state (TS_1), as confirmed by the presence of one imaginary frequency, with a modest barrier for heterolytic coupling ($\Delta E \sim 12$ kcal/mol; $\Delta G \sim 14$ kcal/mol), comparable in magnitude to the computed barrier for H_2 evolution from NiRd ($\Delta G \sim 10$ kcal/mol).[58] The

transition state results from the lengthening of Ni-H (Δ = +0.29 Å) and a slight contraction of S-H (Δ = -0.04 Å) bonds of $^{3}\mathbf{1}^{\mathbf{R2}}$**NiH,SH** with minimal distortion in the geometry (Figure 2.10). As the H---H distance approaches ~0.7 Å, H_2 is formed resulting in distorted trigonal-planar species $[Ni^{2+}(S\text{-}p\text{-}CF_3\text{-}Ph)_3]^-$ ($^{3}\mathbf{1}^{\mathbf{3C}}$; τ_3 = 0.12,[58]; $\sum Ni_\alpha$ = 353.3°; see Figure S2.77, Table S2.19). Under experimental conditions, i.e., excess free thiolate, it is feasible for thiolate to rebind and regenerate 4C **1** (top of Scheme 2.2); however, during turnover, and on the electrochemical timescale, we propose the path likely proceeds from the $^{3}\mathbf{1}^{\mathbf{3C}}$ intermediate as depicted in the center of Scheme 2.2 after one catalytic cycle.

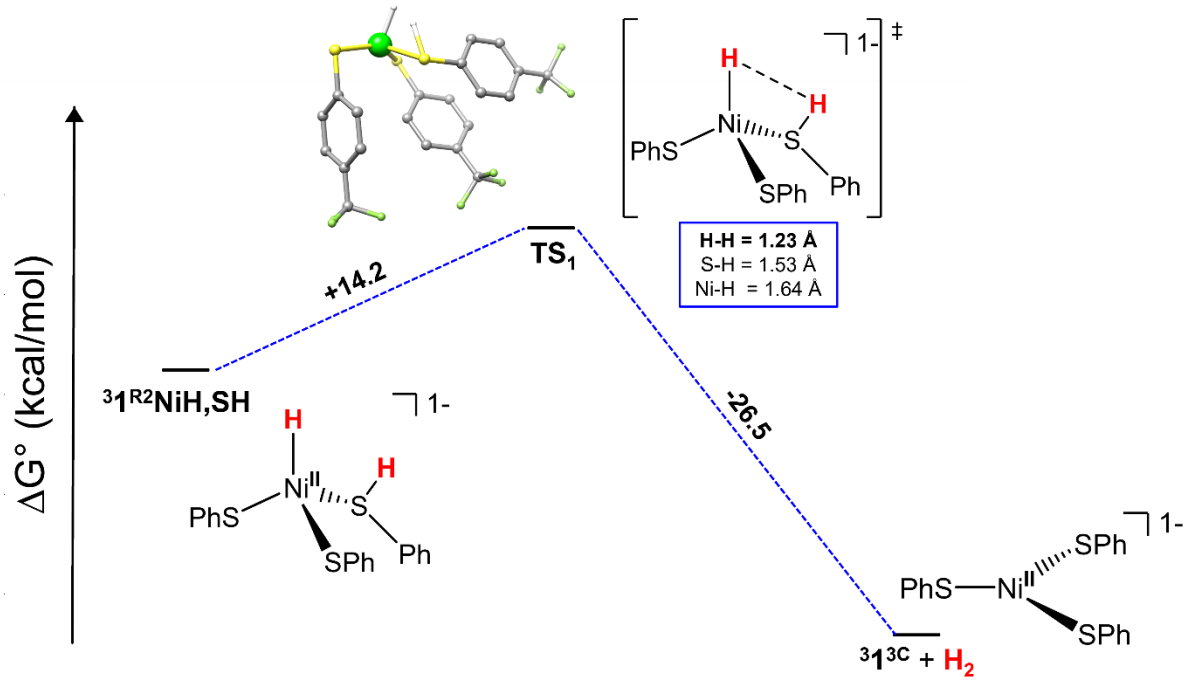

Figure 2.10. DFT-computed free energy profile (B3LYP/def2-TVZPP) of the transition state of the HER reaction (see Experimental section in the SI for details).

2.4 Conclusion

This work demonstrates, for the first time, that simple homoleptic LMW tetrathiolato/tetrahedral complexes such as **1** are reasonable structural and moderate functional analogues for the tetracysteinato-ligated Ni center housed in the active site of [NiFe]-H_2ase. While the activity of **1** for HER is rather modest (TOF ~14 s^{-1}, η ~ 0.70 V in MeCN, acid: AcOH), standard electrode rinse tests and control electrochemical measurements with tetrathiolato-Zn^{2+} complex **2** and free thiolate clearly establish that the Ni-thiolate complex is the active species. This result is not surprising given the previously reported, and superior, H_2ase activity of the $Ni(SCys)_4$ site in NiRd.[57] While these Ni-site models were initially reported ~40 years ago, their ability to perform HER was never evaluated likely due to issues regarding speciation to S-bridged complexes especially in protic solvents. As observed in prior reports of tetrahedral Ni-thiolate complexes,[54, 55] and even many square-planar Ni complexes with chelating dithiolates,[42, 43, 49] **1** converts to a new species when dissolved in MeCN consistent with thiolate dissociation and formation of S-bridged and diamagnetic entities such as **3**. Contrary to what has been reported,[54, 56] these bridged species are not substitutionally inert and readily revert back to tetrahedral monomer **1** upon addition of extra thiolate equivalents. The presence of excess thiolate further enhances the acid stability of **1**. However, and even in the presence of additional thiolate, complex **1** is only irreversibly reduced to a Ni^{1+} complex at -1.94 V (Figure 2.8), proposed to be the 3C trigonal planar complex anion $^{2}\mathbf{1}^{\mathbf{R}}$, which would alleviate buildup of negative charge at a putative 4C $[Ni^{1+}(SR)_4]^{3-}$ species. Nevertheless, **1** is the (pre)electrocatalyst for HER and is computed to go through an ECCE type mechanism with the Ni^{1+} complex $^{2}\mathbf{1}^{\mathbf{R}}$ being one of the first intermediates (Scheme 2.2). Despite being structurally different from H_2ase and NiRd due to thiolate loss after reduction to Ni^{1+}, similar intermediates are traversed (Scheme 2.2). Furthermore, **1** serves as the

'base model' to initiate further studies and improve upon stability/catalytic capability in a simple construct. Future work is focused on preventing dissociation without the need for additional thiolate, and the resulting multimeric speciation, by employing more rigid scaffold-like multidentate ligands to fix the coordination geometry about Ni. This strategy has been successful in H_2-activating mononuclear Fe models of the Fe-only H_2ase.[133] Dissociation can be further prevented by better abating the nucleophilicity of the Ni-bound thiolate, one reason for utilizing *p*-CF_3-PhSH, by appending suitable H-bond donor functionalities in future ligand frames.[134, 135] Lastly, installation of proton-relay units, widely successful in other mononuclear Ni-HER[27, 28] and Co-CO_2-reducing[136] electrocatalysts is also planned.

2.5 Materials and Methods

General Information. All reagents were procured from commercial suppliers and used as received unless otherwise noted. Acetonitrile (MeCN), tetrahydrofuran (THF), and diethyl ether (Et_2O) were purified by passage through activated alumina columns using an MBraun solvent purification system (MB-SPS). 2-methyltetrahydrofuran (2-MeTHF) was used as received and degassed by three freeze-pump-thaw cycles. All solvents were stored over 3 Å molecular sieves in an anaerobic glovebox before use. Methanol (MeOH) was degassed by at least three freeze-pump-thaw cycles and stored over 3 Å molecular sieves for a minimum of one week before use. The metal salts, $(Et_4N)_2[MCl_4]$ (M = Ni, Zn),[137] and triphenylmethyl-*S*-nitrosothiol (Ph_3CSNO)[138] were synthesized according to the published procedures. All reactions were performed under an inert atmosphere of N_2 using Schlenk-line techniques or in an MBraun Unilab glovebox.

Physical Methods. FTIR spectra were collected on a ThermoNicolet 6700 spectrophotometer running the OMNIC software. Solid-state samples were prepared as pressed KBr pellets. UV-vis spectra were recorded at 25 °C using a Cary-50 spectrophotometer containing a Quantum Northwest TC 125 temperature control unit. All UV-vis samples were prepared in gastight/screw-cap quartz cells with an optical pathlength of 1 cm. ^1H (400 MHz), ^{13}C (125 MHz), and ^{19}F NMR (376 MHz) spectra were recorded in the reported solvent on a 400 MHz Bruker BZH 400/52 NMR spectrometer with chemical shifts referenced to the residual protio signal of the deuterated solvent.[139] ^{19}F NMR spectra are referenced to $CFCl_3$ by employing a fluorobenzene internal standard (δ = -114.81 ppm in CD_3CN vs. $CFCl_3$[140]). Magnetic susceptibility measurements were performed in both the solid- and solution-state. Solid-state magnetic measurements were recorded with a Johnson Matthey Mark 1 magnetic susceptibility balance. Solution-state magnetic measurements (Evans method[141]) and NMR titration experiments with acetic acid-d_4 (CD_3CO_2D

= AcOD-d_4 from Cambridge Isotope Laboratories Inc., 99.5% D; 32 scans) were recorded in CD_3CN at 25 °C on a 600 MHz (^{19}F = 564 MHz) Varian Unity INOVA NMR spectrometer. Pascal's constants for diamagnetic corrections were taken from the literature.[142] Electrochemical measurements were performed with a Pine Research Inc. WaveDriver potentiostat; more details are provided in the stand alone electrochemistry section below. Low-resolution electrospray ionization mass spectrometry (LR-ESI-MS) data were collected using a Perkin-Elmer Sciex API I Plus quadrupole mass spectrometer or a Bruker Esquire 3000 plus ion trap mass spectrometer. Elemental microanalysis for C, H, and N was performed by Midwest Microlab in Indianapolis, IN.

2.6 Synthesis

(Et_4N)(S-*p*-CF_3-Ph). A batch of 4-(trifluoromethyl)benzenethiol (1.038 g, 5.826 mmol) and sodium metal (0.135 g, 5.87 mmol) were mixed in ~5 mL of MeOH to afford a gas-evolving, pale-yellow solution. The mixture was stirred for 10 min at RT while removing the headspace gas by applying an occasional vacuum. The heterogeneous mixture became homogeneous and pale-yellow in color after 10 min of stirring. To this solution was added a 3-4 mL MeOH solution of Et_4NCl (0.966 g, 5.83 mmol). After 30 min of stirring, the solvent was removed to afford a light-yellow oil. To this oil was added ~5 mL of THF and the mixture was stirred for 10 min. The white insoluble solid was removed by filtering over Celite and the bright yellow THF filtrate was concentrated to an oil. After 30 min of stirring in 5 mL of Et_2O at RT, a pale-yellow solid formed that was filtered off, washed with Et_2O (3 × 3 mL), and dried under vacuum to afford the product (1.084 g, 3.526 mmol, 61%). FTIR (KBr matrix), ν_{max} (cm^{-1}): 1328 (s, ν_{CF}), 1088 (s, ν_{CF}). ^1H NMR (400 MHz, CD_3CN, δ from protio solvent): 7.24 (d, 2H, J = 8.1 Hz), 6.93 (d, 2H, J = 8.2 Hz), 3.16 (q, 10H, J = 7.3 Hz), 1.17 (t, 15H, J = 7.3 Hz). $^{13}C\{^1H\}$ NMR (100 MHz, CD_3CN, δ from solvent signal): 169.3 (s), 134.2 (s), 127.4 (q, J = 268.1 Hz), 123.8 (q, J = 3.8 Hz), 117.9 (q, J = 31.3 Hz),

53.1 (s), 7.8 (s). ^{19}F NMR (376 MHz, CD_3CN, δ from $CFCl_3$): -60.86. LR-ESI-MS (*m/z*): [M-Et_4N]$^-$ calcd for $C_7H_4F_3S$ (relative abundance), 177.0 (100.0), 178.0 (8.4), 179.0 (4.8); found, 177.0 (100.0), 178.0 (8.8), 179.0 (5.3). Mp: 56-58 °C.

$(Et_4N)_2$[Ni(S-*p*-CF_3-Ph)$_4$] (1). A blue MeCN slurry (5 mL) of $(Et_4N)_2[NiCl_4]$ (0.097 g, 0.21 mmol) was added dropwise to a pale-yellow MeCN solution (2 mL) of (Et_4N)(S-*p*-CF_3-Ph) (0.269 g, 0.875 mmol). An immediate color change to dark-red occurred upon addition of the Ni^{2+} salt. After stirring at RT for 1 h, the solvent was removed in vacuo resulting in a sticky dark-red material. This residue was stirred in 10 mL of THF, and the solution immediately became dark-red in color with the appearance of a pale solid, determined to be Et_4NCl by ^{1}H NMR. After stirring for 30 min, the mixture was filtered over a pad of Celite, and the insoluble material was washed with ~10 mL of THF until the Celite remained colorless. The resulting dark-red filtrate was taken to dryness and ~5 mL of Et_2O was added. After 30 min of stirring, the dark-red insoluble solid was isolated by vacuum filtration on a glass-frit, washed with Et_2O (3 × 3 mL), and dried under vacuum to afford dark-red complex **1** (0.165 g, 0.161 mmol, 77%). FTIR (KBr matrix), ν_{max} (cm^{-1}): 1324 (s, ν_{CF}), 1059 (s, ν_{CF}). ^{1}H NMR (400 MHz, CD_3CN, δ from protio solvent): 22.25 (s, 6H), 2.94 (q, 16H, J = 7.2 Hz), 1.07 (m, 25H), 0.99 (br s, 4H); a minor amount of a diamagnetic species is evident from peaks at ~7.1 and 7.8 ppm, discussed in the main text. ^{19}F NMR (376 MHz, CD_3CN, δ from $CFCl_3$): -18.96 (complex **1** signal), -62.00 (diamagnetic species signal). UV-vis in the presence of 50 mol-equiv (Et_4N)(S-*p*-CF_3-Ph) (MeCN, 25 °C), λ_{max}, nm (ε, M^{-1} cm^{-1}): 720 (580), 680 (600), 508 (3800), 465 (3400). LR-ESI-MS (*m/z*): [M-SR-2Et_4N]$^-$ calcd for $C_{21}H_{12}F_9S_3Ni$ (relative abundance), 588.9 (100.0), 589.9 (25.3), 590.9 (55.1), 591.9 (15.0), 592.9 (13.2); found, 589.0 (100.0), 589.8 (25.1), 590.9 (58.8), 591.8 (14.7), 592.8 (14.9); [M-Et_4N]$^-$ calcd for $C_{36}H_{36}F_{12}S_4NNi$ (relative abundance), 896.1 (100.0), 897.1 (42.9), 898.1 (65.6), 899.1 (27.0),

900.1 (19.5), 901.1 (6.9); found, 895.9 (100.0), 896.9 (51.4), 897.9 (65.7), 898.9 (31.4), 899.8 (20.0), 900.6 (8.6); $[2M\text{-}SR\text{-}2Et_4N]^-$ calcd for $C_{35}H_{20}F_{15}S_6Ni_2$ (relative abundance), 1000.9 (92.4), 1001.9 (38.9), 1002.9 (100.0), 1003.9 (42.7), 1004.9 (50.9), 1005.9 (20.6), 1006.9 (17.7), 1007.9 (6.7), 1008.9 (4.6), 1009.9 (1.7); found, 1001.0 (98.7), 1001.9 (47.7), 1002.8 (100.0), 1003.8 (40.9), 1004.8 (52.3), 1005.8 (22.7), 1006.7 (15.9), 1007.7 (6.8), 1008.7 (4.5), 1009.7 (2.3). Solid-state μ_{eff} = 3.47 BM at 25 °C. Solution-state μ_{eff} = 2.75 BM; (+20 mol-equiv $(Et_4N)(S\text{-}p\text{-}CF_3\text{-}Ph)$) μ_{eff} = 3.05 BM; both recorded at 25 °C in MeCN. Anal. Calcd for $C_{44}H_{56}F_{12}N_2S_4Ni$: C, 51.42; H, 5.49; N, 2.73. Found: C, 51.04; H, 5.49; N, 2.69.

$(Et_4N)_2[Zn(S\text{-}p\text{-}CF_3\text{-}Ph)_4]$ (2). The synthesis of complex **2** was performed in a manner nearly identical to **1** with the exception of using the following reagents: $(Et_4N)(S\text{-}p\text{-}CF_3\text{-}Ph)$ (0.135 g, 0.439 mmol) in 5 mL of MeCN and $(Et_4N)_2[ZnCl_4]$ (0.049 g, 0.11 mmol) in 5 mL of MeCN. No significant color change was observed after the addition of the Zn^{2+} salt to the thiolate solution. Workup was similar to **1**, and complex **2** was isolated as a white solid (0.102 g, 0.0986 mmol, 90%). FTIR (KBr matrix), ν_{max} (cm^{-1}): 1323 (s, ν_{CF}), 1090 (vs, ν_{CF}). ^1H NMR (400 MHz, CD_3CN, δ from protio solvent): 7.64 (d, 8H, J = 8.0 Hz), 7.09 (d, 8H, J = 8.0 Hz), 3.13 (q, 20H, J = 7.3 Hz), 1.17 (m, 28H, J = 7.3 Hz). ^{19}F NMR (376 MHz, CD_3CN, δ from $CFCl_3$): -61.69. $^{13}C\{^1H\}$ NMR (100 MHz, CD_3CN, δ from solvent signal): 156.8 (s), 133.7 (s), 126.6 (q, J = 269.7 Hz), 124.3 (q, J = 3.9 Hz), 122.2 (q, J = 31.2 Hz), 53.1, 7.7 (s). LR-ESI-MS (*m/z*): $[M\text{-}SR\text{-}2Et_4N]^-$ calcd for $C_{21}H_{12}F_9S_3Zn$ (relative abundance), 594.9 (100.0), 595.9 (25.3), 596.9 (74.0), 597.9 (26.5), 598.9 (51.3), 599.9 (13.4), 600.9 (8.6); found, 595.2 (100.0), 596.1 (21.9), 597.0 (74.7), 597.9 (27.9), 598.9 (49.8), 599.9 (12.9), 600.9 (8.0). Anal. Calcd for $C_{44}H_{56}F_{12}N_2S_4Zn{\bullet}CH_3CN$: C, 51.37; H, 5.53; N, 3.91. Found: C, 52.17; H, 5.40; N, 3.90.

Attempted Synthesis of $(Et_4N)_2[Ni_2(S\text{-}p\text{-}CF_3\text{-}Ph)_6]$ (3). To a dark-red MeCN solution (3 mL) of **1** (0.090 g, 0.088 mmol) was added Me_3OBF_4 (0.013 g, 0.088 mmol) dropwise at RT. The initial addition of Me_3OBF_4 resulted in a solution color change to brown; this color became darker after complete addition of the reagent. No further changes were observed to the dark-brown solution after stirring for 2 h. Vacuum distillation of the solvent resulted in a dark-brown solid. To this solid was added ~3 mL of 2-MeTHF and the reaction flask was stored in a -20 °C freezer for 30 min. The solution was next filtered over a Celite-packed frit. The Celite retained a red-solid (0.054 g, 0.053 mmol) confirmed to be unreacted **1** by $^1H/^{19}F$ NMR. After taking the dark-brown filtrate to dryness, 5 mL of Et_2O was added, and the mixture was stirred for 1 h to yield a dark-brown solid suspended in solution. This solid was isolated by vacuum filtration, rinsed with Et_2O (3 × 3 mL), and dried under vacuum to afford 0.023 g of a mixture of *S*,*S*-bridged complexes. FTIR (KBr matrix), ν_{max} (cm^{-1}): 1324 (s, ν_{CF}), 1086 (s, ν_{CF}). UV-vis (MeCN, 25 °C), λ_{max}, nm: 630 (sh), 456 (br sh). ^1H NMR (400 MHz, CD_3CN, δ from protio solvent): 21.87 (s, 0.24H), 7.77 (d, 3H, J = 7.9 Hz), 7.64 (d, 6H, J = 8.0 Hz), 7.55 (br s, 4H), 7.12 (d, 3H, J = 8.0 Hz), 7.06 (d, 10H, J = 8.2 Hz), 6.82, (br, 1H), 3.15 (q, 16H, J = 7.3 Hz), 1.20 (m, 24 H, J = 7.3 Hz). ^{19}F NMR (376 MHz, CD_3CN, δ from $CFCl_3$): -19.93, -61.93, -62.35, -62.47, -63.30. LR-ESI-MS (*m/z*): $[M\text{-}SR\text{-}2Et_4N]^-$ calcd for $C_{35}H_{20}F_{15}S_5Ni_2$ (relative abundance), 1000.9 (92.4), 1001.9 (38.9), 1002.9 (100.0), 1003.9 (42.7), 1004.9 (50.9), 1005.9 (20.6), 1006.9 (17.7), 1007.9 (6.6); found, 1001.2 (91.1), 1002.2 (44.8), 1003.1 (100.0), 1004.1 (43.7), 1005.0 (45.2), 1006.0 (19.5), 1007.0 (14.3), 1008.0 (5.3); $[2M\text{-}2Et_4N+Ni]^-$ calcd for $C_{84}H_{48}F_{36}S_{12}Ni_5$ (relative abundance), 1206.6 (23.3), 1207.3 (23.5), 1207.8 (69.1), 1208.3 (63.1), 1208.8 (100.0), 1209.3 (83.4), 1209.8 (84.2), 1210.3 (71.3), 1201.8 (65.3), 1211.3 (45.4), 1211.8 (35.7), 1212.3 (22.9), 1212.8 (16.1), 1213.3 (9.6); found, 1206.0 (21.2), 1207.5 (21.9), 1208.0 (67.2), 1208.5 (61.7), 1209.0 (100.0), 1209.5 (86.5), 1210.0 (96.6), 1210.5

(71.7), 1211.0 (65.9), 1211.5 (48.1), 1212.0 (35.7), 1212.5 (25.6), 1213.0 (16.6), 1213.5 (10.9). Anal. Calcd for $C_{58}H_{64}F_{18}N_2S_6Ni_2$: C, 48.35; H, 4.48; N, 1.94. Found: C, 44.84; H, 3.54; N, 1.98. *Note*: The lack of a suitable fit to the CHN analysis is due to mixed and inseparable products.

$(Et_4N)_2$[Ni(S-*p*-CF_3-Ph)$_3$(NO)] (4). To a dark-red MeCN solution (4 mL) of **1** (0.062 g, 0.060 mmol) was slowly added a green MeCN solution (3 mL) of Ph_3CSNO (0.020 g, 0.065 mmol). Upon addition of Ph_3CSNO, the dark-red solution took on a green color and, as more was added, the solution became dark-green. After stirring the solution for 30 min at RT, 70 mL of Et_2O was added, and the mixture was placed in a -20 °C freezer. After cooling for 12 h, a dark-green solid appeared in solution, which was filtered off by vacuum filtration on a glass-frit, washed with Et_2O (3 × 3 mL), and dried under vacuum to afford **4** as a green powder (0.028 g, 0.032 mmol, 53%). FTIR (KBr matrix), ν_{max} (cm^{-1}): 1683 (m, ν_{NO}), 1322 (s, ν_{CF}), 1084 (s, ν_{CF}). FTIR (CaF_2 windows, MeCN), ν_{max} (cm^{-1}): 1772 (ν_{NO}), 1683 (ν_{NO}). UV-vis (MeCN, 25 °C), λ_{max}, nm (ε, M^{-1} cm^{-1}): 799 (br, 780), 425 (sh, 1300), 373 (sh, 4700). ^{1}H NMR (400 MHz, CD_3CN, δ from protio solvent): 7.73 (d, 6H, J = 8.1 Hz), 7.20 (d, 6H, J = 8.1 Hz), 3.15 (q, 19H, J = 7.3 Hz), 1.20 (t, 28H, J = 7.3 Hz). ^{19}F NMR (376 MHz, CD_3CN, δ from $CFCl_3$): -61.51 (s). LR-ESI-MS (*m*/*z*): $[M\text{-}SR\text{-}2Et_4N]^-$ calcd for $C_{14}H_8F_6S_2NONi$ (relative abundance), 441.9 (100.0), 442.9 (17.2), 443.9 (49.2), 444.9 (9.9), 445.9 (10.1); found, 442.1 (100.0), 443.1 (17.5), 444.0 (49.2), 445.0 (10.2), 446.0 (10.0). Anal. Calcd for $C_{37}H_{52}F_9N_3S_3ONi$: C, 50.46; H, 5.95; N, 4.77. Found: C, 46.85; H, 5.40; N, 4.68. *Note*: The lack of a suitable fit to the CHN analysis may be due to potential lability of the nitrosyl ligand.

2.7 Speciation Studies

Reaction of 1 with Stoichiometric HBF_4•Et_2O. To a 3 mL MeCN solution of **1** (0.076 g, 0.074 mmol) was added HBF_4•Et_2O (0.014 g, 0.086 mmol; 1.2 mol-equiv with respect to **1**; pK_a = 1.8 in MeCN[97]). Immediately upon addition of acid, the solution changed color from dark-red/brown, to brown, and finally to purple within 1 min, and a dark precipitate appeared. The mixture was stirred for 1 h at RT and then placed in a -20 °C freezer for 30 min. The dark-purple solid was isolated by vacuum filtration, washed with cold MeCN (3 × 3 mL), and dried on a vacuum line to afford 0.034 g of what is assigned as polymeric $[Ni(S\text{-}p\text{-}CF_3\text{-}Ph)_2]_n$ material. FTIR (KBr matrix), ν_{max} (cm^{-1}): 1327 (s, ν_{CF}), 1063 (s, ν_{CF}). UV-vis (MeCN, 25 °C), λ_{max}, nm: 510, 462 (sh). ^{1}H NMR (400 MHz, DMSO-d_6, δ from residual deuterated solvent): 22.08 (s), 7.69 (s), 7.51 (d), 7.40 (s), 7.10 (d), 7.03 (d), 3.24 (s), 2.07. ^{19}F NMR (376 MHz, DMSO-d_6): -14.37, -16.87, -60.14, -60.65, -61.76.

Reaction of 1 with Excess AcOH. To a 2 mL MeCN solution of **1** (0.073 g, 0.071 mmol) was added a 1 mL MeCN solution containing AcOH (0.106 g, 1.77 mmol; 25 mol-equiv with respect to **1**; pK_a = 23.5 in MeCN[60]). Similar to reaction with stoichiometric HBF_4•Et_2O, immediately upon addition of AcOH, the solution changed color from dark red-brown to brown to purple within 1 min, and a dark precipitate appeared. After 1 h of stirring, the precipitate was isolated by vacuum filtration, washed with cold MeCN (3 × 3 mL), and dried on a vacuum line to afford 0.032 g what is assigned as polymeric $[Ni(S\text{-}p\text{-}CF_3\text{-}Ph)_2]_n$ material. Spectroscopic characterization (IR, UV-vis, ^{1}H and ^{19}F NMR) of this product is nearly identical to the product isolated from the reaction of **1** and HBF_4•Et_2O (1:1).

Titration of 1 with AcOD-d_4 (NMR). <u>*Without added thiolate*</u>: A 56 mM solution of **1** (0.019 g, 0.018 mmol) in 0.32 mL of CD_3CN was prepared in a J-Young NMR tube that was sealed with a rubber septum and secured with (in this order) parafilm, electrical tape, and copper wire.

Separately, an 8.7 M solution of AcOD-d_4 was made in CD_3CN (total volume = 0.40 mL; 0.20 mL AcOD-d_4, 3.5 mmol; 0.20 mL CD_3CN) and stored in a septum-capped vial. After recording the ^1H and ^{19}F NMR of **1**, a 10 μL aliquot (0.087 mmol; 4.8 mol-equiv with respect to **1**) of the AcOD-d_4/CD_3CN solution was injected into the NMR tube via gas-tight syringe. The tube was gently shaken three times and sat undisturbed for 1 min, after which the NMR spectrum of the mixture was recorded. This procedure was repeated for each addition of AcOD-d_4/CD_3CN until no change was observed. The speciation of **1** with added AcOD-d_4 was assessed by comparing the integration of the peak at ~20 ppm (*m*-H of **1**) after each AcOD-d_4 addition to that of the Et_4N^+ counterion. *With added thiolate*: The same procedure was performed using a 34 mM solution of **1** (0.017 g, 0.017 mmol) containing 19 mol-equiv of (Et_4N)(S-*p*-CF_3-Ph) (0.098 g, 0.32 mmol) in 0.50 mL of CD_3CN. Aliquots of AcOD-d_4 (20 μL, 0.35 mmol; 21 mol-equiv with respect to **1**) were injected as described above. The speciation of **1** was measured in a manner similar to the experiments without thiolate (see above) considering integration of the Et_4N^+ counterion.

Quantification of 1/Excess Thiolate with AcOH (UV-vis). A 2.50 mM stock solution of **1** (0.010 g, 0.010 mmol) was prepared in 4.00 mL of MeCN; 0.12 mL of this stock was added to a vial containing 1.88 mL of MeCN to yield a final concentration of 0.15 mM for **1**. This solution was then used to dissolve a solid batch of (Et_4N)(S-*p*-CF_3-Ph) (0.002 g, 0.007 mmol, 23 mol-equiv with respect to **1**). This solution was transferred to a quartz cuvette and its UV-vis spectrum recorded. To the cuvette was next added 20 μL of a 0.30 M AcOH solution in MeCN (20 mol-equiv with respect to **1**) and the spectrum recorded. The amount of **1** remaining was calculated by taking the ratio of absorbance values at λ = 508 nm described by eq. i:

$$\frac{Abs_{508\ nm}\ (\mathbf{1}+23\ SR+20\ AcOH)}{Abs_{508\ nm}\ (\mathbf{1}+20\ SR)} \times 100\% \quad \text{(i)}$$

Speciation of 1 by ^{19}F NMR in CD_3CN. A 2.00 mM stock solution of **1** (0.004 g, 0.004 mmol) was prepared in 2.00 mL of CD_3CN containing PhF (10 μL). A 400 μL portion of the **1**/PhF (0.0008 mmol **1**) CD_3CN solution was placed in an NMR tube and the ^{19}F NMR spectrum was recorded. The relative concentrations of **1** and *S*,*S*-bridged complexes such as **3** were calculated by the ratio of the integrated peaks associated with **1** (δ = -19.22 ppm) and the bridged complexes (peaks centered at δ = -62.00 ppm), normalized to the PhF integration. To calculate the relative amounts of **1** and *S*,*S*-bridged complexes upon addition of thiolate, (Et_4N)(S-*p*-CF_3-Ph) (0.013 g, 0.042 mmol; 53 mol-equiv with respect to **1**) was added to the 400 μL CD_3CN solution of **1**/PhF in the NMR tube and the ^{19}F NMR spectrum was recorded, see Figure S46. To calculate the relative amounts of **1** and bridged complexes (e.g., **3**) integration of the ^{19}F peak of **1** was taken relative to the integration of the peak assigned to PhF and the percentage of **1** was determined by eq. ii:

$$\frac{\int \delta_{\mathbf{1}+SR}}{\int \delta_{\mathbf{1}} + \int \delta_{s,s-brg}} \times 100\% \quad \text{(ii)}$$

where $\int\delta_1$ + SR is the integration value of the peak at ~-19 ppm (**1**) in the presence of excess (Et_4N)(S-*p*-CF_3-Ph); $\int\delta_1$ and $\int\delta_{S,S\text{-}brg}$ are the integration values for the peaks of **1** (-19 ppm) and *S*,*S*-bridged complexes (~-62 ppm), respectively, in the absence of (Et_4N)(S-*p*-CF_3-Ph), i.e., as-isolated **1**.

Quantification of 1/Excess Thiolate by ^{19}F NMR in CD_3CN with AcOD-d_4. A 400 μL aliquot of the same CD_3CN stock of **1**/PhF described above was placed in an NMR tube and to this solution was added (Et_4N)(S-*p*-CF_3-Ph) (0.0050 g, 0.016 mmol; 20 mol-equiv with respect to **1**) and the ^{19}F NMR was recorded. Separately, a 1.57 M CD_3CN stock solution of AcOD-d_4 (0.09 mL, 1.57 mmol) in 0.91 mL of MeCN (total volume = 1.00 mL) was prepared. A 10 μL aliquot of the AcOD-d_4 stock (0.016 mmol, 20 mol-equiv with respect to **1**) was added to the NMR tube containing a

CD_3CN solution of **1**/PhF/(Et_4N)(S-*p*-CF_3-Ph) and the ^{19}F NMR spectrum measured. Integration of the ^{19}F peak of **1** (-19.0 ppm) was taken relative to the integration of the peak assigned to PhF and the percent of **1** was determined by eq. ii.

Speciation of *S*,*S*-bridged complexes by NMR in CD_3CN with (Et_4N)(S-*p*-CF_3-Ph). A mixture of *S*,*S*-bridged complexes including **3** (from isolated products of methylation reaction of **1**) (0.016 g) in 0.34 mL of CD_3CN was prepared in a J-Young NMR tube that was sealed with a rubber septum and secured with (in this order) parafilm, electrical tape, and copper wire. Separately, a 0.44 M solution of (Et_4N)(S-*p*-CF_3-Ph) (0.026 g, 0.085 mmol) was made in 0.2 mL of CD_3CN and stored in a septum-capped vial. After recording the ^1H and ^{19}F NMR of the thiolate-bridged complex mixture, a 10 μL aliquot (0.0044 mmol) of the CD_3CN solution containing (Et_4N)(S-*p*-CF_3-Ph) was added to the solution in the NMR tube. The tube was shaken, and the spectrum was recorded after 1 min.

2.8 Electrochemical Measurements

Electrochemistry. Cyclic voltammetry measurements were performed with a WaveDriver 40 bipotentiostat/galvanostat from Pine Research Instrumentation Inc. using an Ag/Ag^+ pseudo-reference electrode (Ag wire immersed in 0.25 M ^{n}Bu_4NPF_6 electrolyte in MeCN), Pt-wire counter electrode (directly submerged in solution), and a stationary glassy carbon working electrode (3 mm outer diameter). The potentiostat was interfaced with a PC using the Aftermath software. Measurements were collected at ambient temperature using ~2.0 mM analyte in MeCN containing 0.25 M ^{n}Bu_4NPF_6 as the supporting electrolyte under an N_2 atmosphere. Analyte potentials were referenced against an external ferrocene standard under identical conditions. Purity of the electrolyte in the solvent medium was confirmed over the available electrochemical window through scans taken prior to the addition of analyte or external reference. Acid titration

experiments for the HER were performed by addition of MeCN aliquots of a ~4.2 mM stock of AcOH in MeCN. AcOH was added in 10 μL aliquots (~2 mol-equiv with respect to complex). The solution was stirred for 20 s and sat undisturbed for an additional 10 s prior to measurement. The working electrode was cleaned between scans by washing with solvent, polishing on a felt cloth with a 0.3 μm alumina suspension from Allied High-Tech Products, and sonicating for 30 s in DI water. All CV are plotted according to the US convention.

Determination of Overpotential. The overpotential (η) was calculated using eq. iii, which was developed for homogenous electrocatalysis of the HER.[143]

$$\eta = |E^{\circ}_{H^+/H_2} - E_{cat/2}| \qquad \text{(iii)}$$

$E°_{H+/H2}$ is the standard reduction potential for the $2H^+/H_2$ couple of AcOH in MeCN taking into account homoconjugation.[109] $E°_{H+/H2}$ was calculated to be -1.27 V vs. Fc^+/Fc in MeCN. $E_{cat/2}$ is the potential for the HER catalyzed by the reported complexes at half the maximum of the catalytic current (i_c).[143]

Determination of k_{obs}. Observed rate constants (k_{obs}) for HER were calculated under pseudo first-order conditions where the $[H^+]$ is high enough that it is not depleted during catalysis, commonly designated as the acid-independent regime. For **1**/20 mol-equiv thiolate ([**1**] = 2.0 mM), this condition was reached at 18 mol-equiv (~36 mM) of AcOH. Under our experimental conditions, k_{obs} was defined as being equivalent to the maximum TOF or TOF_{max}; i_c/i_p value taken at 20 mol-equiv (~40 mM) of AcOH with k_{obs} estimated according to eq. iv.[117, 144]

$$\frac{i_c}{i_p} = \frac{n}{0.4463}\sqrt{\frac{RTk_{obs}}{Fv}} \qquad \text{(iv)}$$

In eq. iv i_c is the current under catalytic conditions, i_p is the current in the absence of acid, T is temperature (298 K), n is number of electrons in the catalytic process (n = 2 for HER), v is the scan rate (0.100 V/s), R is the gas constant, and F is the Faraday constant. We attempted to use foot-of-the-wave analysis (FOWA) to estimate k_{obs}, but FOWA was not suitable for **1** because of the deviations in i_c at the onset of the catalytic wave and irreversibility of the $Ni^{2+/1+}$ couple.

Quantifying amount of 1 remaining after CV titration. After completing an electrocatalytic HER experiment of **1**/20 mol-equiv (Et_4N)(S-*p*-CF_3-Ph) with AcOH, a 150 µL aliquot of the solution was taken from the electrochemical cell and placed in a quartz cuvette containing 2.00 mL MeCN and the UV-vis spectrum was recorded. Complex **1** was quantified using equation v:

$$\frac{Exp.\ Abs.}{[\mathbf{1}]\times\varepsilon_{508\ nm}} \times 100\% \quad \text{(v)}$$

where [**1**] = concentration of **1** (0.14 mM), ε_{508nm} = molar absorptivity value (3,800 M^{-1} cm^{-1}), and Exp. Abs. = experimental absorbance value obtained.

Determination of the Kinetic Isotope Effect (KIE). Using eq. iv, k_{obs} was calculated for HER experiments using CD_3COOD (AcOD-d_4) under the same conditions as described for AcOH (i_c/i_p values taken at 20 mol-equiv (~40 mM) of AcOD-d_4). The ratio of k_{obs} with AcOH to k_{obs} with AcOD-d_4 affords a KIE of 1.62.

Catalyst Concentration Dependence. A 100 mM stock solution of **1** (0.052 g, 0.051 mmol) containing 20 mol-equiv of (Et_4N)(S-*p*-CF_3-Ph) (0.310 g, 1.01 mmol) was prepared in 0.50 mL of MeCN. To this solution was added 60 µL of a 4.2 M solution of AcOH (prepared by adding 0.12 mL (2.1 mmol) of AcOH to 0.38 mL of MeCN; total volume = 0.50 mL) resulting in a new 90 mM (with respect to **1**) stock solution of **1**/20SR^-/5AcOH in 0.56 mL of total MeCN. A 62 µL aliquot of this solution was added to an electrochemical cell containing 10.00 mL of 0.25 M ^{n}Bu_4NPF_6 electrolyte in MeCN. The solution was stirred for 20 s and sat undisturbed for 10 s prior

to measurement. This procedure was repeated totaling five aliquots. The working electrode was cleaned between each scan as described prior. A linear relationship between i_c and [**1**] is indicative of a first-order dependence based on eq vi.[145]

$$i_c = nFA[cat]\sqrt{D(k[H^+])} \quad \text{(vi)}$$

AcOH Concentration Dependence. The order with respect to AcOH was calculated utilizing eq. vi. A linear relationship between i_c and √[AcOH] is indicative of a first-order dependence, and a linear relationship between i_c and [AcOH] indicates a second-order dependence,[145] Where i_c was taken at non-saturating conditions (less than ~30 mM AcOH) from the electrochemical AcOH titration experiments for the determination of k_{obs} (see above for details).

2.9 X-ray Diffraction/X-ray Absorption Measurements

X-ray Crystallographic Data Collection and Structure Solution and Refinement. Red crystals of **1** were obtained from slow diffusion of Et_2O into a saturated solution of **1** in MeCN at -20 °C. Colorless crystals of **2** were grown by slow diffusion of Et_2O into a saturated MeCN/THF (100:1) solution of **2** at -20 °C for 1 week. The crystals of **1** and **2** was mounted in a 100 K and 90 K nitrogen cold stream, respectively, (Cryo Industries low temperature apparatus) on the goniometer head of a Bruker D8 Quest equipped with a Bruker Photon II detector for **1**, and a Bruker D8 Venture Kappa DUO diffractometer equipped with a Bruker Photon 100 CMOS detector for **2**. Data were collected with the use of a Mo Kα (λ = 0.71073 Å) and Cu Kα (λ = 1.54178 Å) microsource for **1** and **2**, respectively. A multi-scan absorption correction was applied with the program SADABS.[146] The structure for **1** and **2** was solved by the dual space method, (SHELXT)[147] and refined by full-matrix least-squares on F2 (SHELXL-2017).[148] One fluorine atom (F8) of one CF_3 group in **1** were located in two positions with ratios of 68:32. The structure

for **2** is highly disordered and displays considerable diffuse scattering. The phenyl ring has two positions with two carbons shared; their occupancies are in the ratio of 48:52. The CF_3 groups were located in three positions with ratios of 48:30:22 and the Et_4N^+ is slightly positioned off of the two-fold axis of Wyckoff position e. A number of PART statements were employed to model the disorder. Further information on the structure determination is available in the deposited CIF, CCDC numbers 2443187 and 2443188 for **1** and **2**, respectively. These data can be obtained free of charge via http://www.ccdc.cam.ac.uk/conts/retrieving.html, or from the Cambridge Crystallographic Data Centre, 12 Union Road, Cambridge CB2 1EZ, UK; fax: (+44) 1223- 336-033; or e-mail: deposit@ccdc.cam.ac.uk.

X-ray Absorption Spectroscopy (XAS). XAS data were collected at the Stanford Synchrotron Radiation Lightsource (SSRL) beamline 9-3, which utilizes a Si[220] double-crystal monochromator with an inline mirror for X-ray focusing and for harmonic rejection. Duplicate independent samples were prepared anaerobically inside an MBraun glove box , with solid samples diluted 3:1 with inert Boron Nitride, then wrapped in Kapton tape. During data collection, samples were maintained at 12 K using a liquid He continuous flow cryostat. Transmission spectra were measured in 0.25 eV increments in the edge region (8325-8370 eV) and 0.05 $Å^{-1}$ increments in the extended X-ray absorption fine structure (EXAFS) region (out to k = 13.3 $Å^{-1}$), integrating from 1 to 25 s in a k^3-weighted manner for a total scan length of approximately 50 min. Data represent the average of three scans. X-ray energy scans were individually calibrated by collecting a Ni-foil absorption spectrum simultaneously with the compound; the first inflection point of the Ni-foil spectrum was assigned to 8,333 eV. The pre-edge features were investigated by normalizing the edge data using the EDG_FIT program (R-29). For analysis of the 1s→3d transition, data was fit with an arctan background + a pseudo-Voigt peak to model the rising edge and 1s→3d peak, XAS

spectra were processed using the Macintosh OSX version of the EXAFSPAK program suite[149] integrated with the Feff v8 software for theoretical model generation.[150] XAS simulations followed a pre-existing published strategy.[151]

2.10 Theoretical Studies

Computational Details. Density functional theory (DFT) calculations were performed with the ORCA electronic structure package, version 4.2.1. Geometry optimization and frequency analysis were performed using the B3LYP functional[75, 152] employing the RIJCOSX aproximation[153] and Grimme's D3(BJ) dispersion correction[154, 155] with coordinates from the crystal structures of **1** and **2** and the coordinates from the crystal structure of $(Et_4N)[Ni_2(S\text{-}p\text{-}Cl\text{-}Ph)_6]$[56] with the replacement of Cl with CF_3, referred to as complex **3**. The triple-ζ basis set def2-TZVPP[156, 157] was used for geometry optimization and frequency analysis with an automatically constructed auxiliary basis set on all atoms. No imaginary frequencies were found. Single point energy (SPE) calculations were performed on the optimized structures using the B3LYP functional[75, 152] employing the RIJCOSX approximation.[153] The triple-ζ basis set def2-TZVPP[156, 157] was used for all atoms with the matching auxiliary triple-ζ basis set def2-TZVPP/J. The conductor-like polarizable continuum model (CPCMC[158]) was utilized to model the solvent environment of MeCN (ε = 37.50). UCSF Chimera[159] was used to generate model structures and visualize isosurface plots of MOs with isodensity values of 0.05 a.u. Spin-density plots were visualized with isodensity values of 0.003 a.u.

Absorption spectra for geometry-optimized **1** and **3** were computed using time-dependent functional theory (TD-DFT).[160, 161] The Tamm-Dancoff approximation was performed for the first 80 roots using the B3LYP functional, D3(BJ) dispersion correction, and RIJCOSX

approximations. The def2-SVP basis set was used for all atoms except for Ni, S, and F for which the def2-TZVPP basis set was used. CPCMC[158] was utilized to model the solvent environment of MeCN (ε = 37.50). Vertical excitation energies and molar extinction coefficients for electronic transitions were calculated using the ORCA_MAPSPC module. The absorption spectrum was generated with a Gaussian linewidth of 2500 cm^{-1}. UCSF Chimera[159] was used to generate model structures and visualize isosurface plots of electron difference density maps with isodensity values of 0.005 a.u.

For mechanistic considerations, all intermediates were computed utilizing the same level of theory as previously described for **1**. The geometry optimizations were performed in the gas phase with FREQ and SPE calculated with CPCMC to model the solvent environment of MeCN. The Gibbs free energy of the protonation step ($\Delta G_{C\text{-}step}$) was calculated with eq. vii utilizing the Gibbs free energy of Et_3NH^+ as H^+ donor and its conjugate base Et_3N:

$$\Delta G_{C-step} = \Delta G(AH + Et_3N) - \Delta G(A^- + Et_3NH^+) \qquad \text{(vii)}$$

Both acid and conjugate base were optimized under the same level of theory as for **1** and frequency analysis was done with CPCMC (MeCN). DFT-calculated redox potentials are described elsewhere in the SI (see pgs. S82-S84) and the energy of each reduction step ($\Delta G°$) was calculated according to eq. viii:

$$\Delta G^\circ = -23.06(n)(E½) \qquad \text{(viii)}$$

where n is the number of electrons transferred (n = 1) and $E½$ is the compound reduction potential. Transition state calculations were performed utilizing a relaxed surface scan (ScanTS), under the same level of theory as for **1** utilizing CPCMC (MeCN), to scan the distances between hydride and proton on coordinated thiolate (2.614-to-0.400 Å in 20 steps). UCSF Chimera[159] was used to

generate model intermediates and transition states. Transition state structures for the intermediates yield only one imaginary frequency.

DFT-computed redox potentials. DFT methods were employed to provide an estimate of the reduction potentials for proposed intermediates in the HER catalytic cycle of **1** (Figure S73, Scheme S3). Further details are described in previously published work where DFT has been used to compute the one-electron potentials of several transition metal complexes.[125-129] The reduction potential ($E°$) is related to the Gibbs free energy difference in solution (ΔG_{soln}) given by eq. ix:

$$E^{\circ} = -\frac{\Delta G_{soln}}{nF} \qquad \text{(ix)}$$

Where F is Faraday's constant (23.06 kcal mol^{-1} V^{-1}) and n is the number of electrons transferred (n = 1). ΔG_{soln} can be determined from eq. x using the thermodynamic cycle depicted in Scheme S1 for the Ni(III/II) couple for the conversion of **^{4}1^{R}NiH,SH** to **^{3}1^{R2}NiH,SH**:

$$\Delta G_{soln} = \Delta G_{gas} + \Delta G(^{4}1^{R2}NiH,SH)_{solv} - \Delta G(^{3}1^{R2}NiH,SH)_{solv} \qquad \text{(x)}$$

where ΔG_{gas} is the Gibbs free energy difference in the gas phase, and the ΔG(***^{4}1^{R}NiH,SH ^{3}1^{R}NiH,SH***)$_{solv}$ and ΔG(***^{4}1^{R2}NiH,SH***)$_{solv}$ are the solvation energies in acetonitrile. The difference of the gas-phase Gibbs free energies of **^{4}1^{R}NiH,SH** and **^{3}1^{R2}NiH,SH** yields $\Delta G(red)_{gas}$, and the difference of the Gibbs free energies of **^{4}1^{R}NiH,SH** and **^{3}1^{R2}NiH,SH** using CPCMC(MeCN) yields $\Delta G(red)_{soln}$. Solvation energies (ΔG_{solv}) were obtained from the difference of single point energies, from single point energy calculations, of the intermediate in the absence and presence of solvent. The absolute potentials for the Fc^{+}/Fc couple was calculated at the same level of theory under an identical procedure to properly reference the redox couples. The results of the redox calculations for **^{4}1^{R}NiH,SH/^{3}1^{R2}NiH,SH** are presented in Table S15. *Note*: calculation of the potentials for other proposed intermediates were performed in an identical manner.

2.11 Supplementary Information

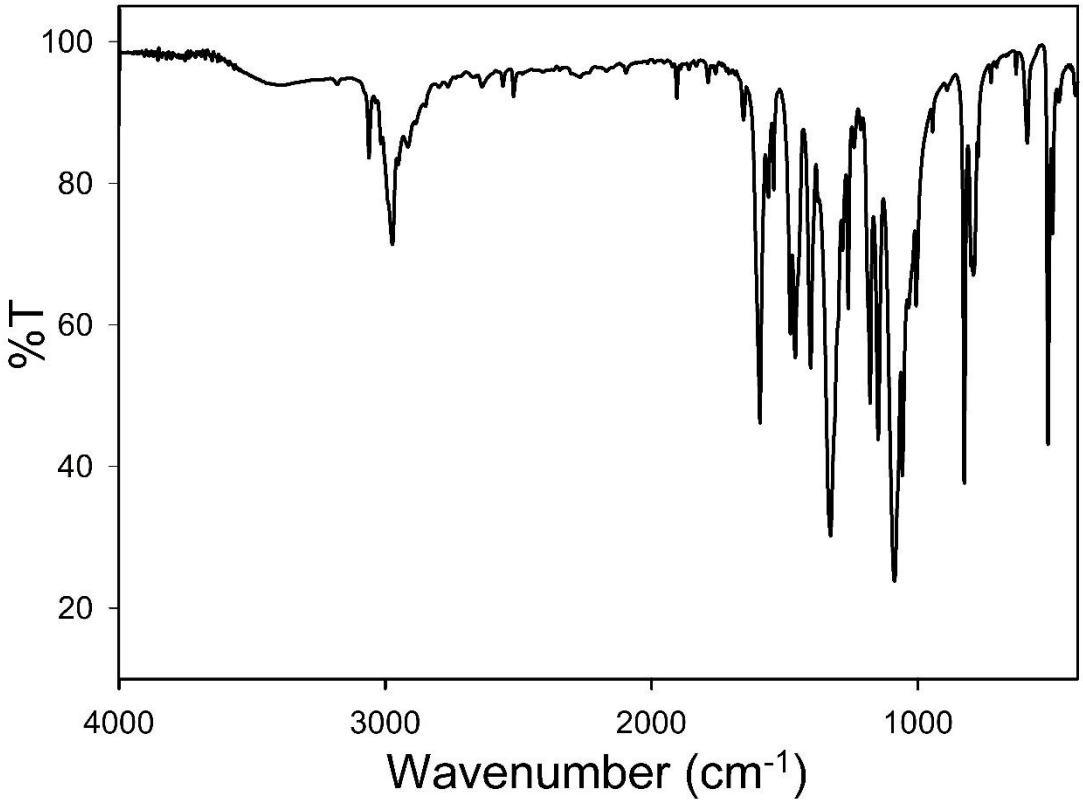

Figure S2.1. Solid-state FTIR spectrum of (Et_4N)(S-*p*-CF_3-Ph) in a KBr matrix at RT.

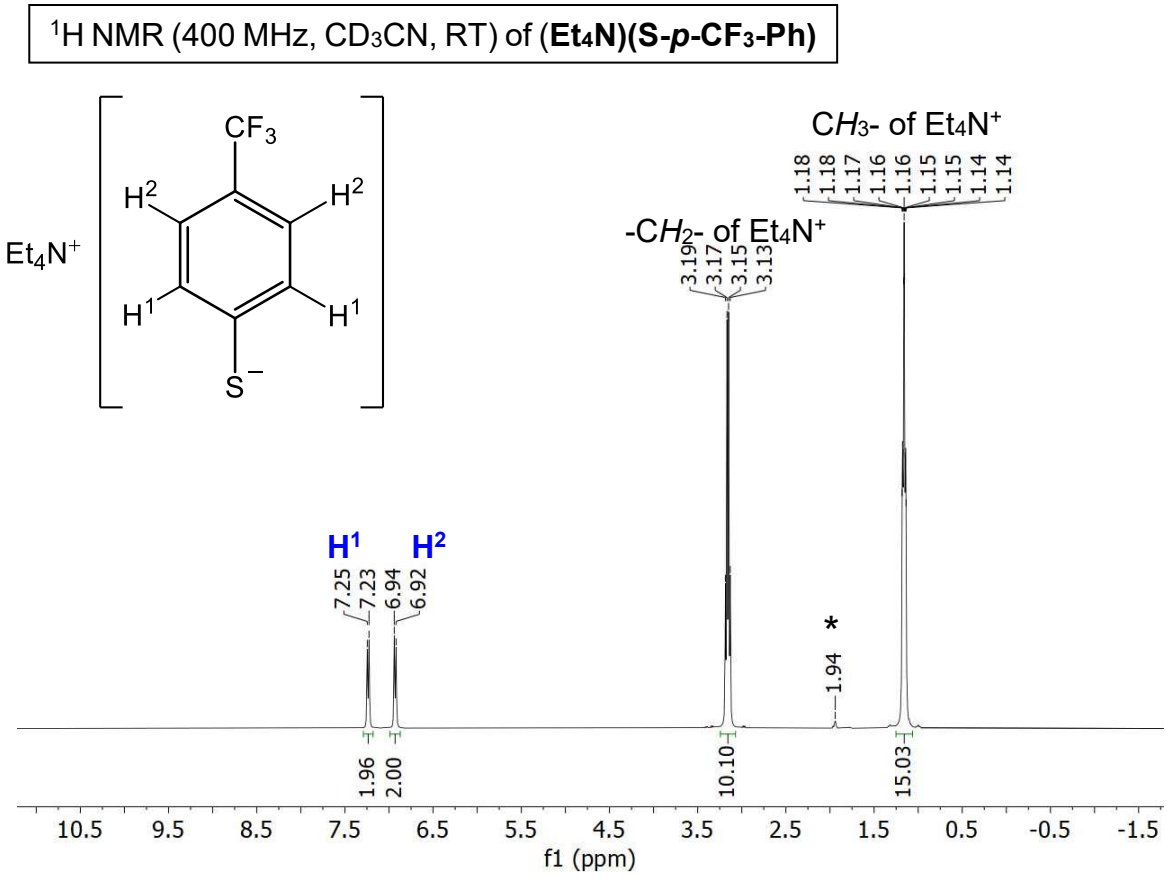

Figure S2.2. ^{1}H NMR spectrum of (Et$_4$N)(S-*p*-CF$_3$-Ph) in CD$_3$CN at RT (δ vs. protio signal (*) at 1.94 ppm).

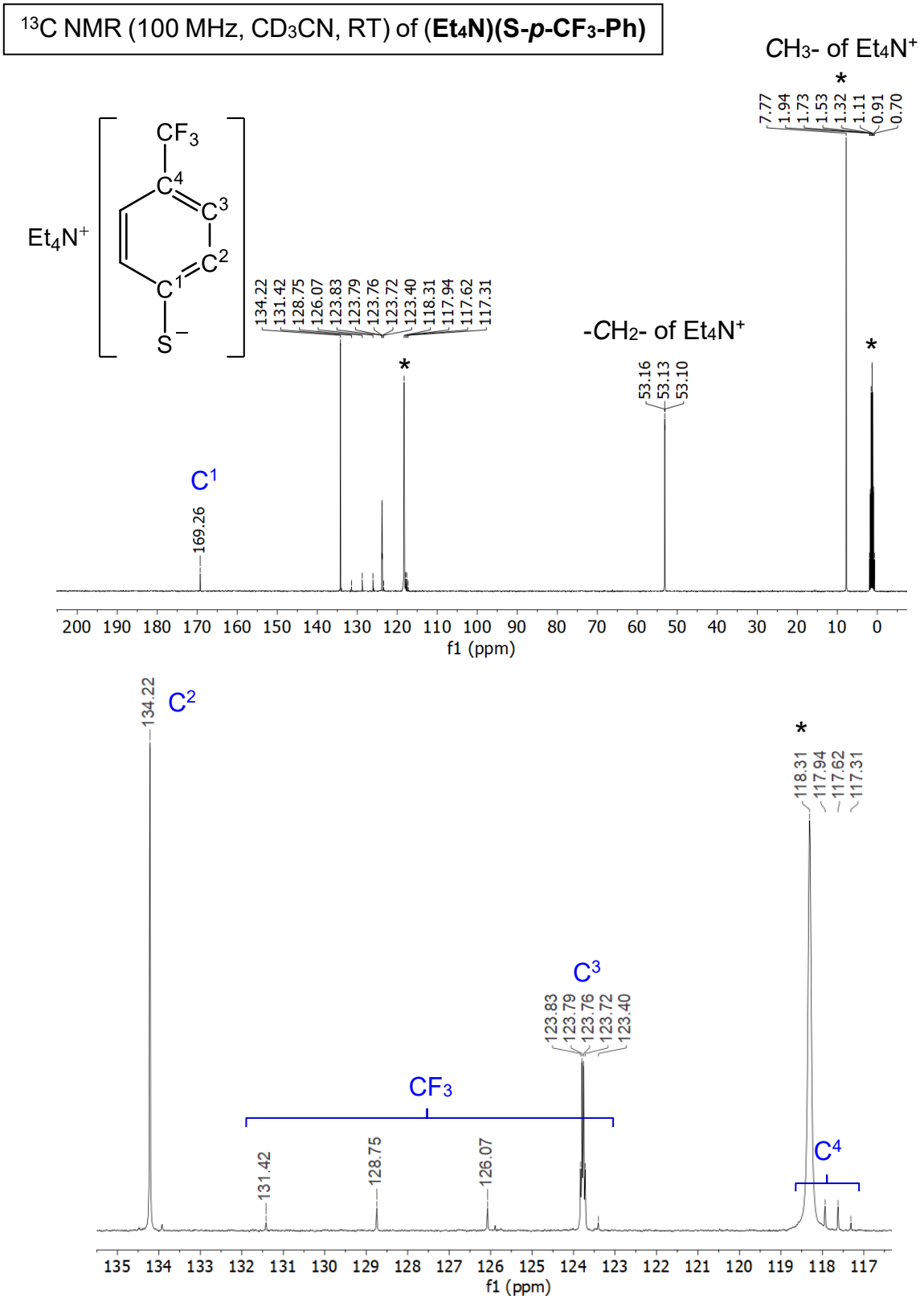

Figure S2.3. *Top*: ^{13}C NMR spectrum of (Et$_4$N)(S-*p*-CF$_3$-Ph) in CD$_3$CN at RT. *Bottom:* expansion of 117 – 135 ppm region. Solvent signal at 1.32 and 118.31 ppm are indicated with *.

^{19}F NMR (376 MHz, CD_3CN, RT) of (**Et_4N)(S-*p*-CF_3-Ph)**

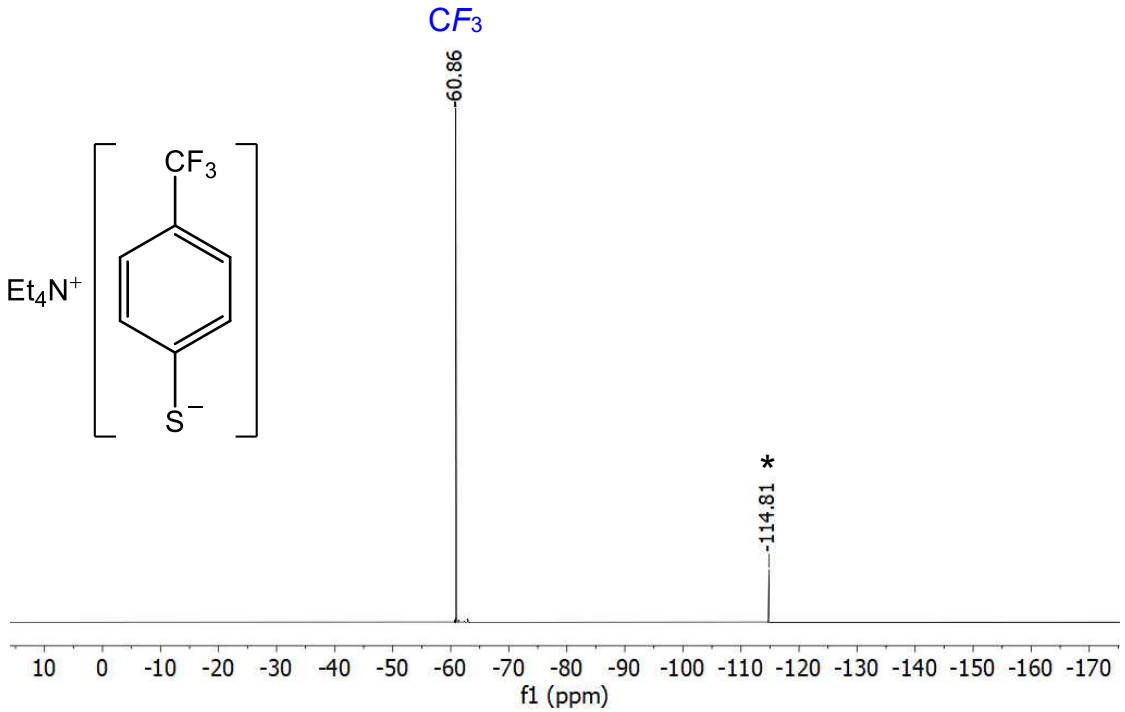

Figure S2.4. ^{19}F NMR spectrum of (Et_4N)(S-*p*-CF_3-Ph) in CD_3CN at RT. The peak at -114.81 ppm is from PhF added as an internal standard and indicated with *.

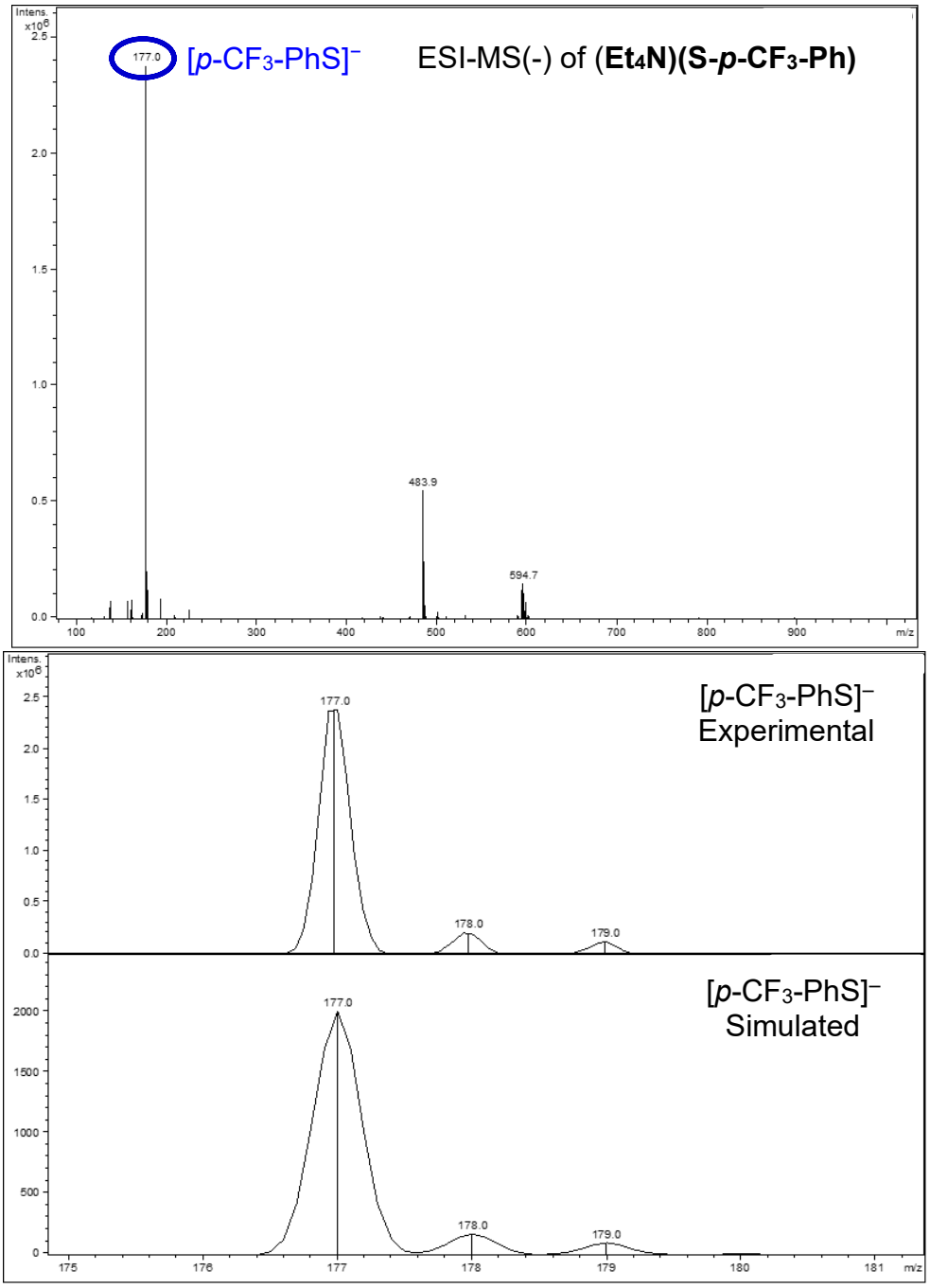

Figure S2.5. *Top*: Low-resolution ESI-MS(-) of (Et_4N)(S-*p*-CF_3-Ph) in MeCN. *Bottom*: experimental and simulated theoretical isotopic distribution for *m/z*: 177.0 Other peaks have not been identified as reaction products.

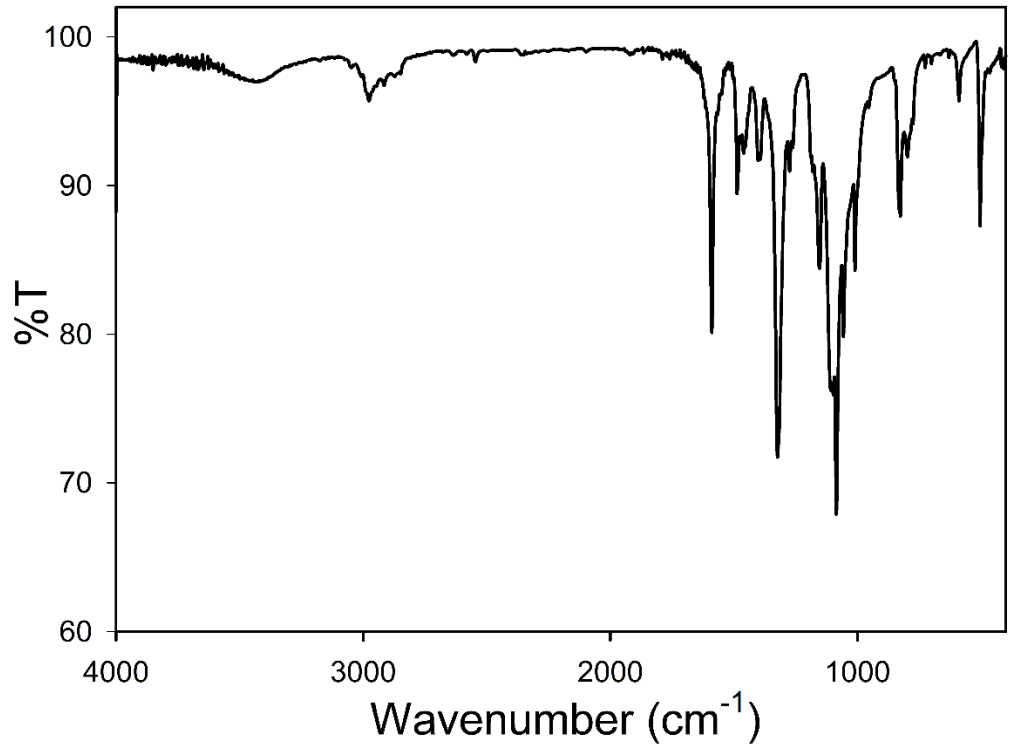

Figure S2.6. Solid-state FTIR spectrum of $(Et_4N)_2[Ni(S\text{-}p\text{-}CF_3\text{-}Ph)_4]$ (**1**) in a KBr matrix at RT.

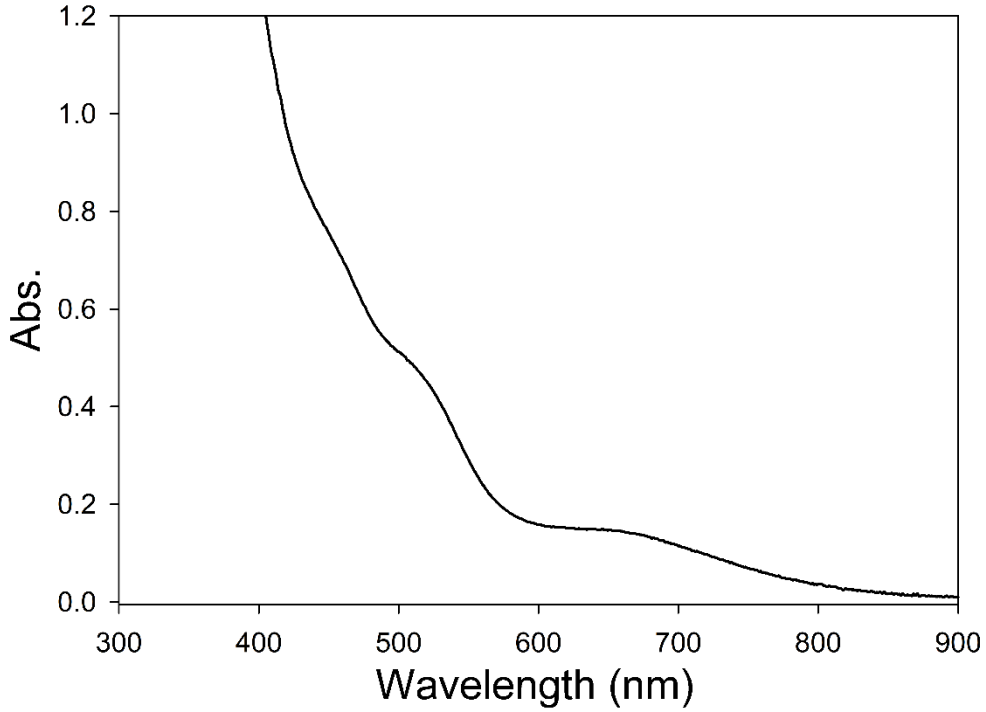

Figure S2.7. UV-vis spectrum of $(Et_4N)_2[Ni(S\text{-}p\text{-}CF_3\text{-}Ph)_4]$ (**1**) (0.15 mM) in MeCN at 25 °C.

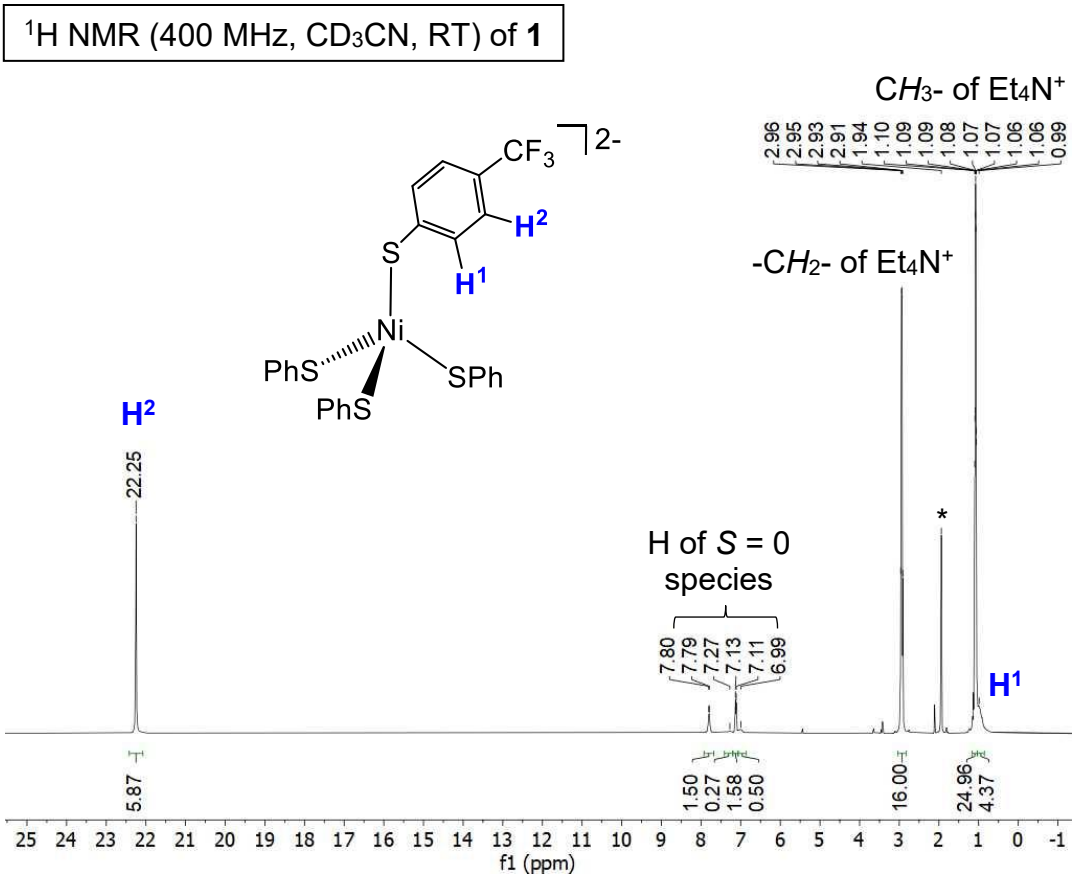

Figure S2.8. ^{1}H NMR spectrum of $(Et_4N)_2[Ni(S\text{-}p\text{-}CF_3\text{-}Ph)_4]$ (**1**) in CD_3CN at RT (δ vs. protio signal (*) at 1.94 ppm). Structure of **1** depicted in the inset displays one thiolate for clarity; all $PhS^- = p\text{-}CF_3\text{-}PhS^-$. Zoom-in views of the 1-3 ppm and 7-8 ppm regions are shown below in Figure S9.

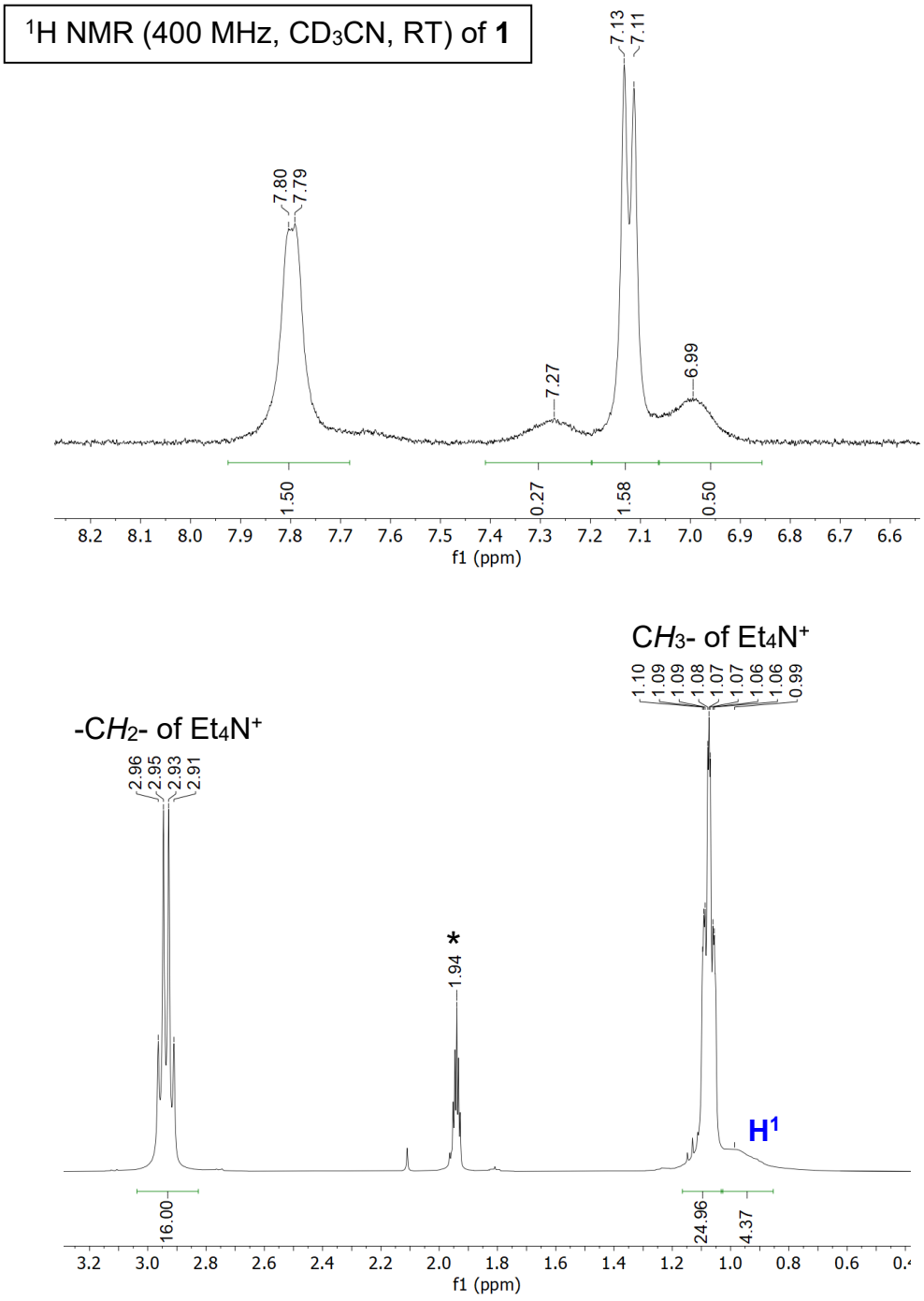

Figure S2.9. Magnified regions of the ^{1}H NMR spectrum of $(Et_4N)_2[Ni(S\text{-}p\text{-}CF_3\text{-}Ph)_4]$ (**1**) in CD_3CN at RT (δ vs. protio signal (*) at 1.94 ppm). Structure of **1** depicted in the inset displays one thiolate for clarity; all PhS^- = p-CF_3-PhS^-. *Top*: zoom-in of the 7-8 ppm region depicting H of the S = 0 species. *Bottom*: zoom-in of the 1-3 ppm region that contains Et_4N^+ and H^1. Full spectrum in Figure S8.

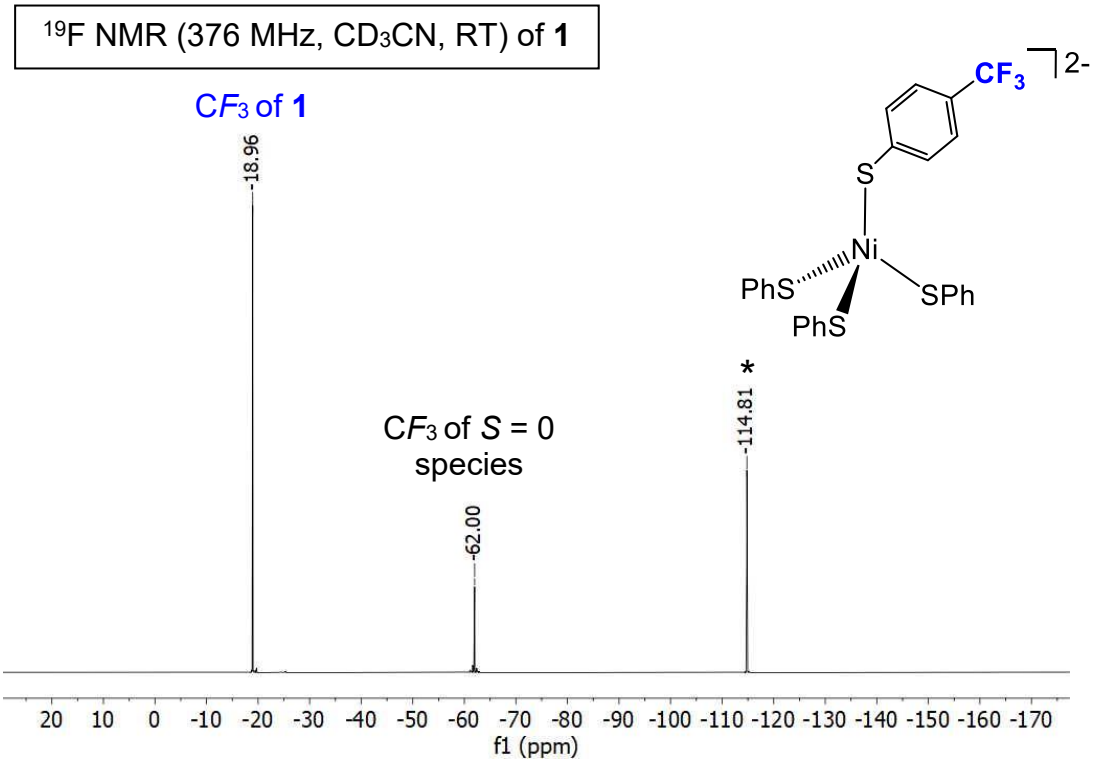

Figure S2.10. ^{19}F NMR spectrum of $(Et_4N)_2[Ni(S\text{-}p\text{-}CF_3\text{-}Ph)_4]$ (**1**) in CD_3CN at RT. Structure of **1** depicted in the inset displays one thiolate for clarity; all PhS^- = p-CF_3-PhS^-. Peak at -114.81 ppm is from PhF (internal standard) and indicated with *.

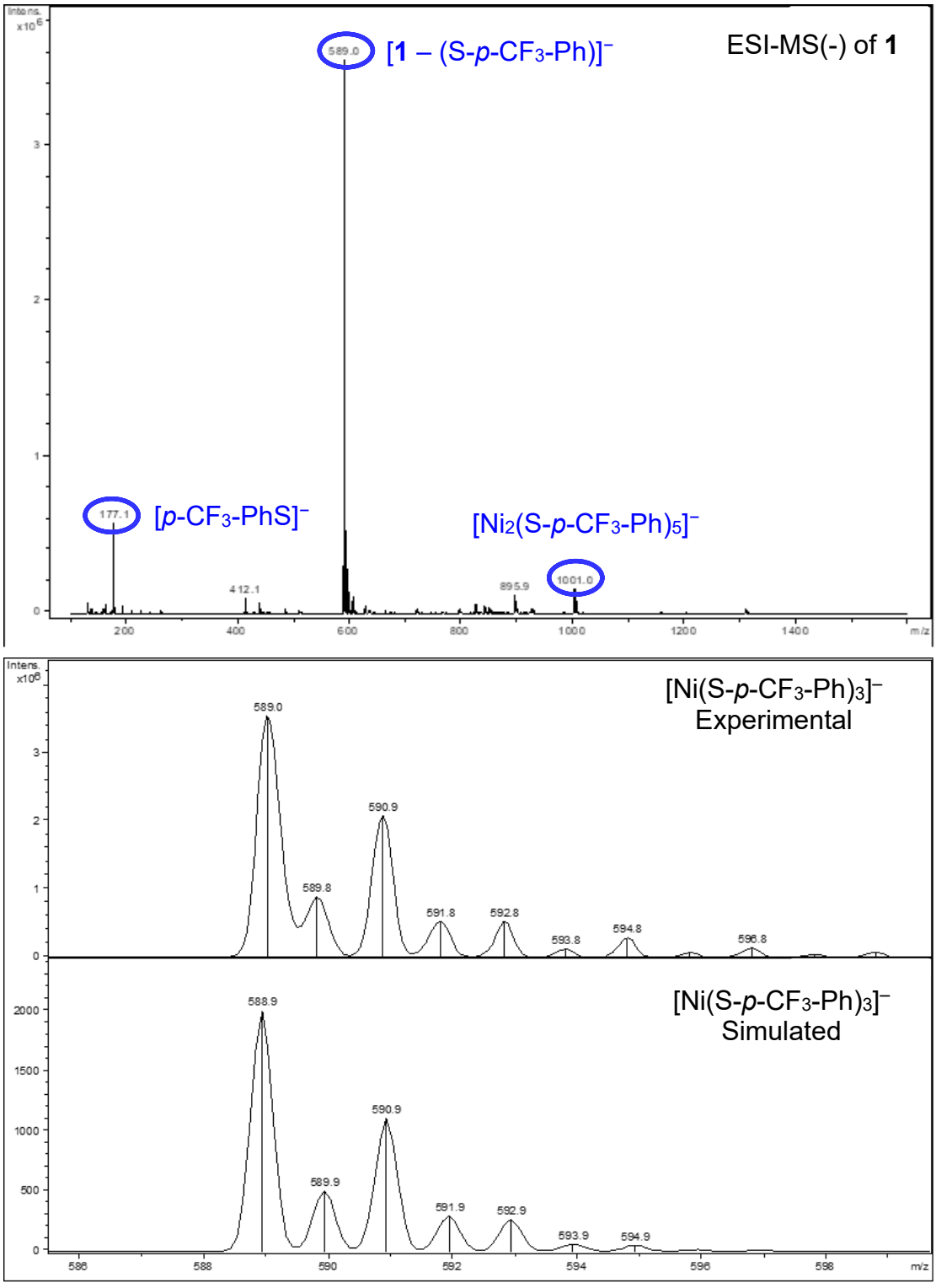

Figure S2.11. *Top*: Low-resolution ESI-MS(-) of **1** in MeCN. *Bottom*: experimental and simulated theoretical isotopic distribution of peak at *m/z*: 589.0.

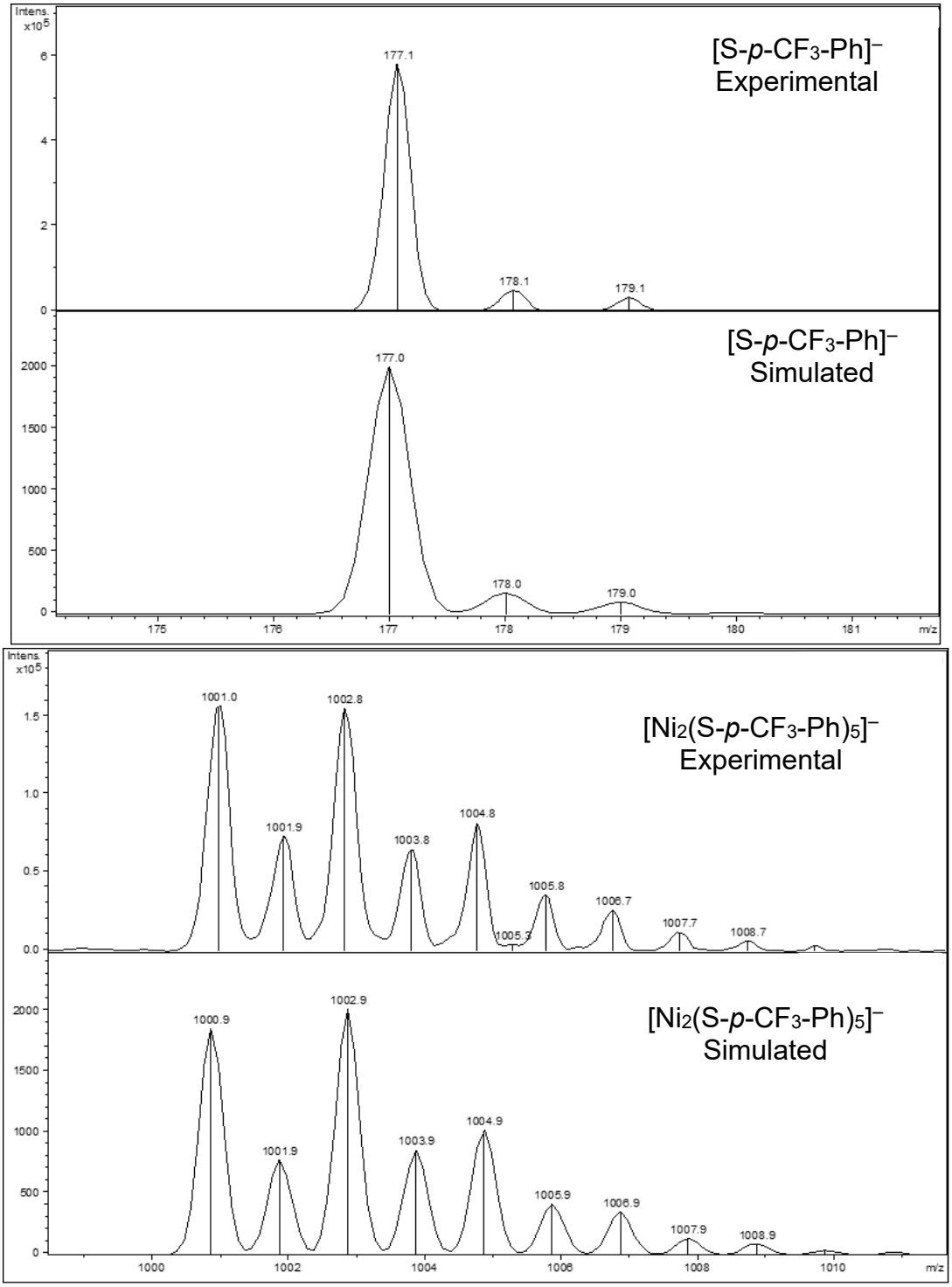

Figure S2.12. Zoom-in of low-resolution ESI-MS(-) of **1** in MeCN (full MS in Figure S11). *Top*: experimental and simulated theoretical isotopic distribution of peak at *m/z*: 177.1. *Bottom*: experimental and simulated theoretical isotopic distribution of peak at *m/z*: 1001.0.

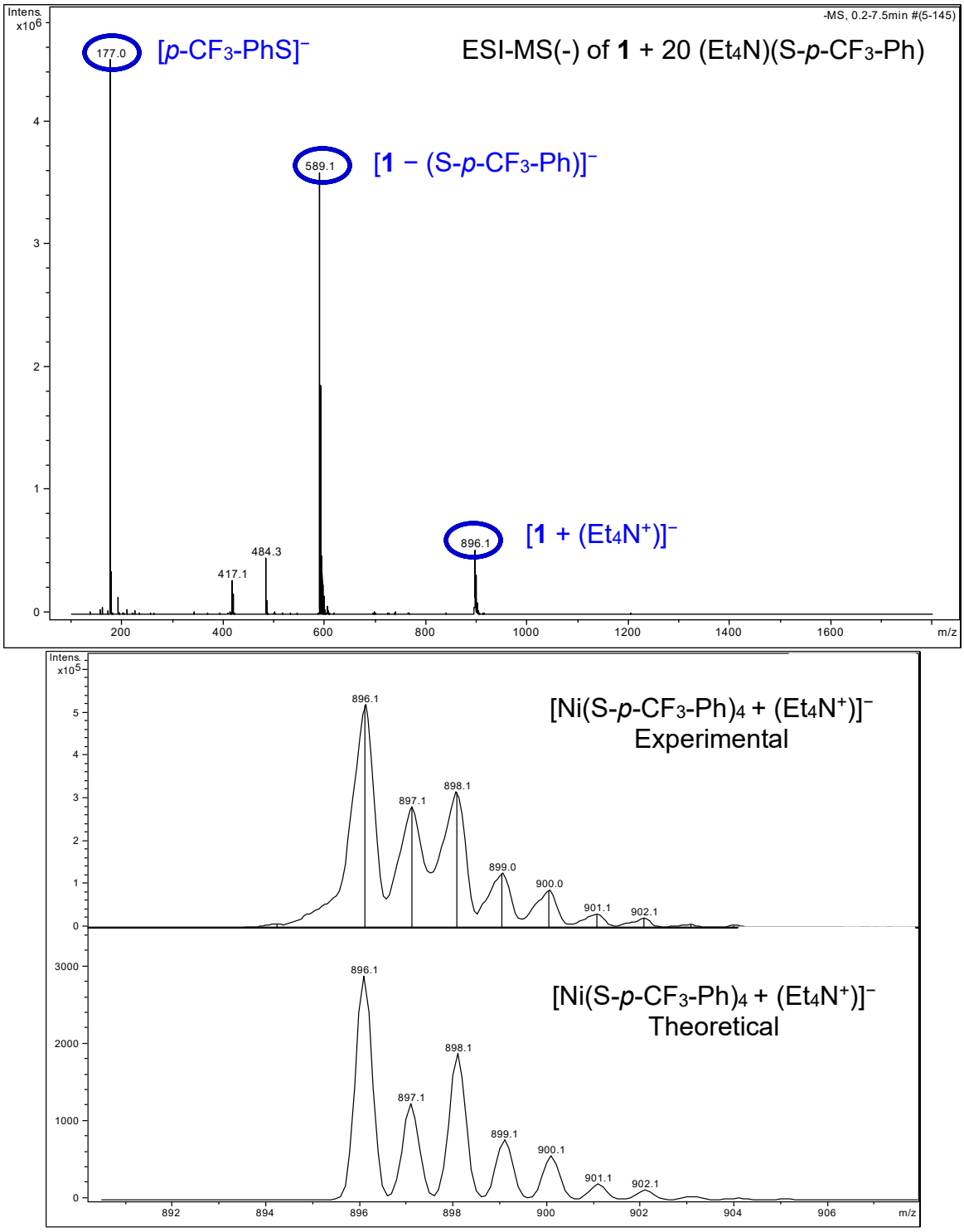

Figure S2.13. *Top*: Low-resolution ESI-MS(-) of $(Et_4N)_2[Ni(S\text{-}p\text{-}CF_3\text{-}Ph)_4]$ (**1**) with 20 mol-equiv. of $(Et_4N)(S\text{-}p\text{-}CF_3\text{-}Ph)$ in MeCN. *Bottom*: experimental and simulated theoretical isotopic distribution peak at *m/z*: 896.1.

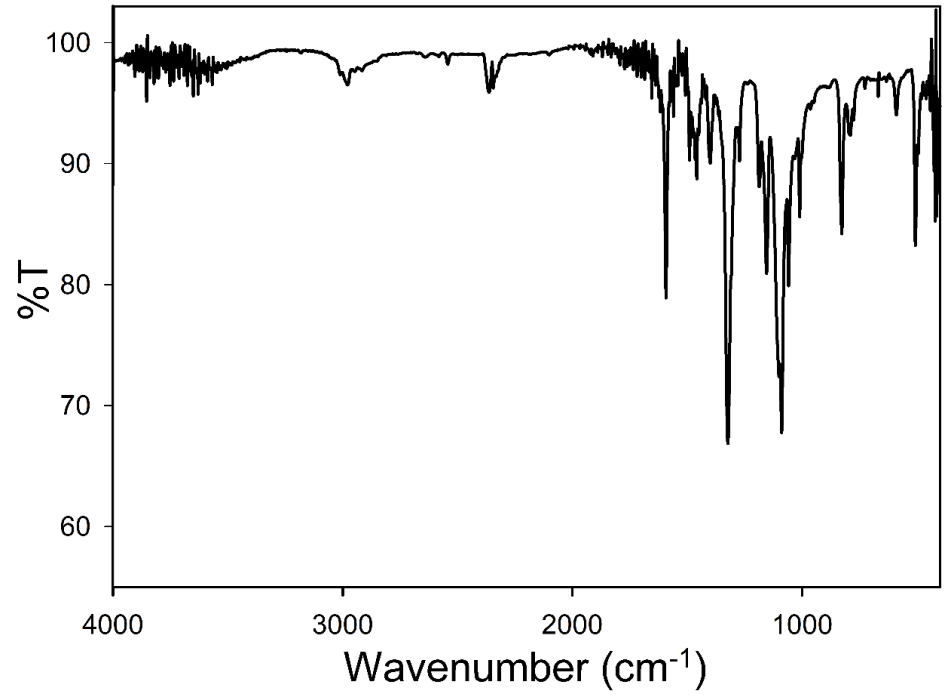

Figure S2.14. Solid-state FTIR spectrum of $(Et_4N)_2[Zn(S\text{-}p\text{-}CF_3\text{-}Ph)_4]$ (**2**) in a KBr matrix at RT.

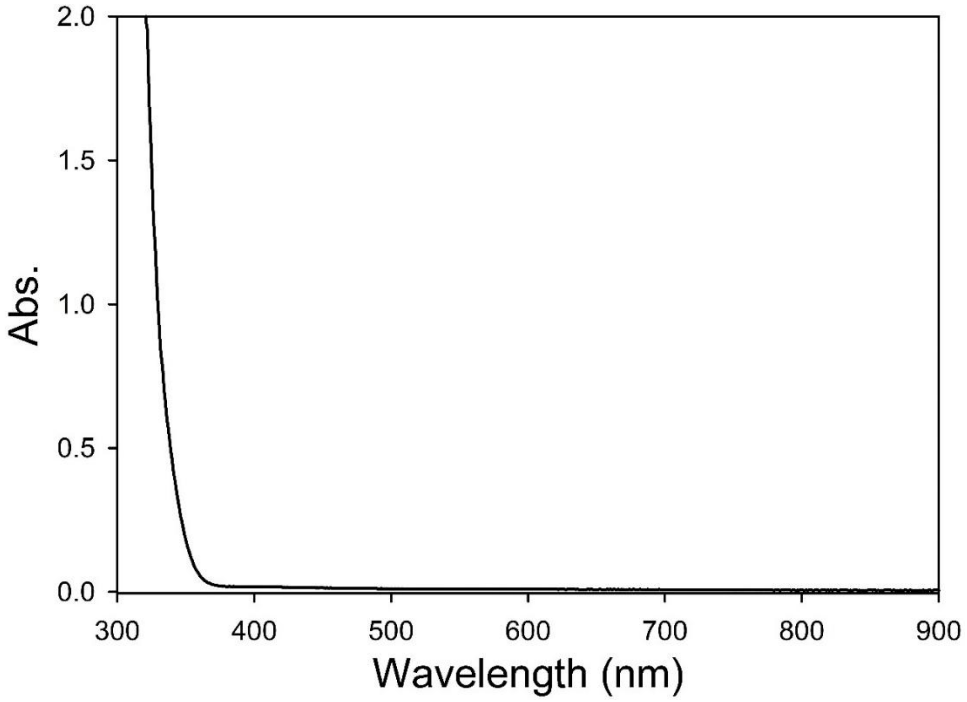

Figure S2.15. Qualitative UV-vis spectrum of $(Et_4N)_2[Zn(S\text{-}p\text{-}CF_3\text{-}Ph)_4]$ (**2**) in MeCN at 25 °C.

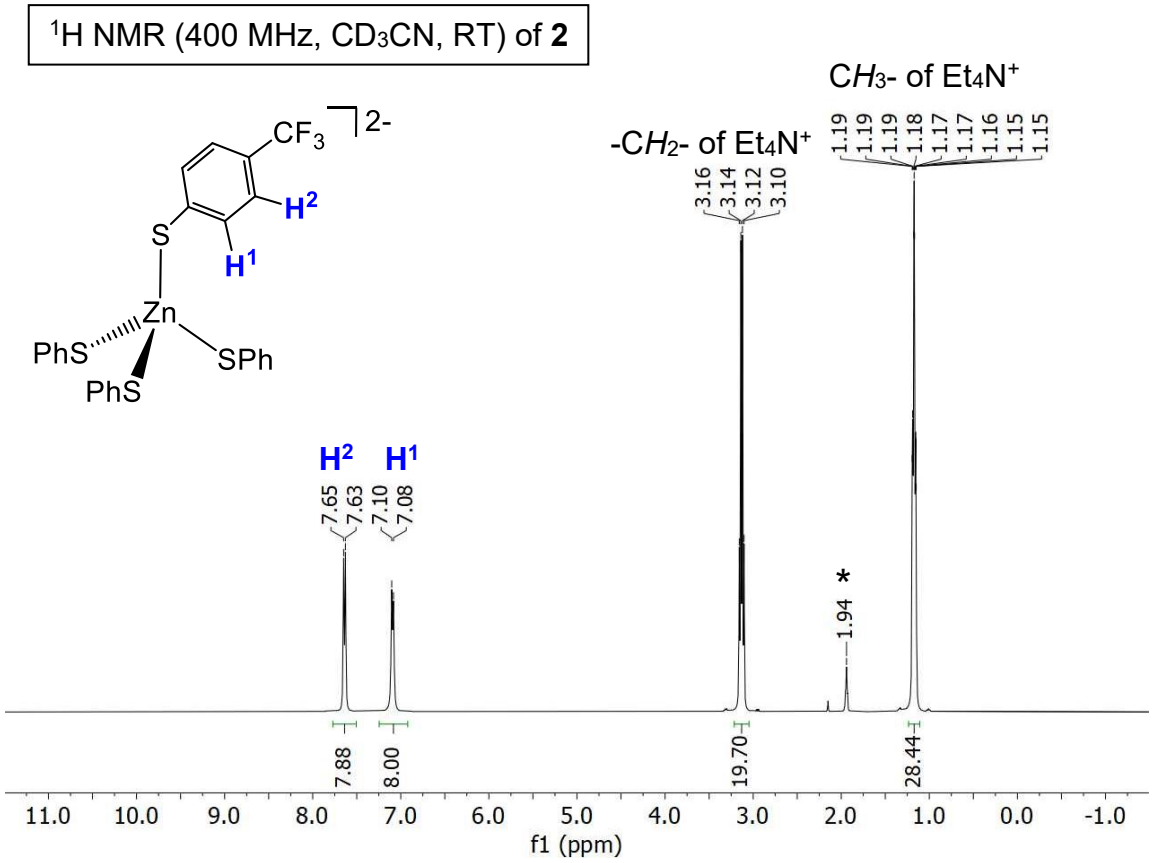

Figure S2.16. ^{1}H NMR spectrum of $(Et_4N)_2[Zn(S\text{-}p\text{-}CF_3\text{-}Ph)_4]$ (**2**) in CD_3CN at RT (δ vs. protio signal (*) at 1.94 ppm). Structure of **2** depicted in the inset displays one thiolate for clarity; all $PhS^- = p\text{-}CF_3\text{-}PhS^-$.

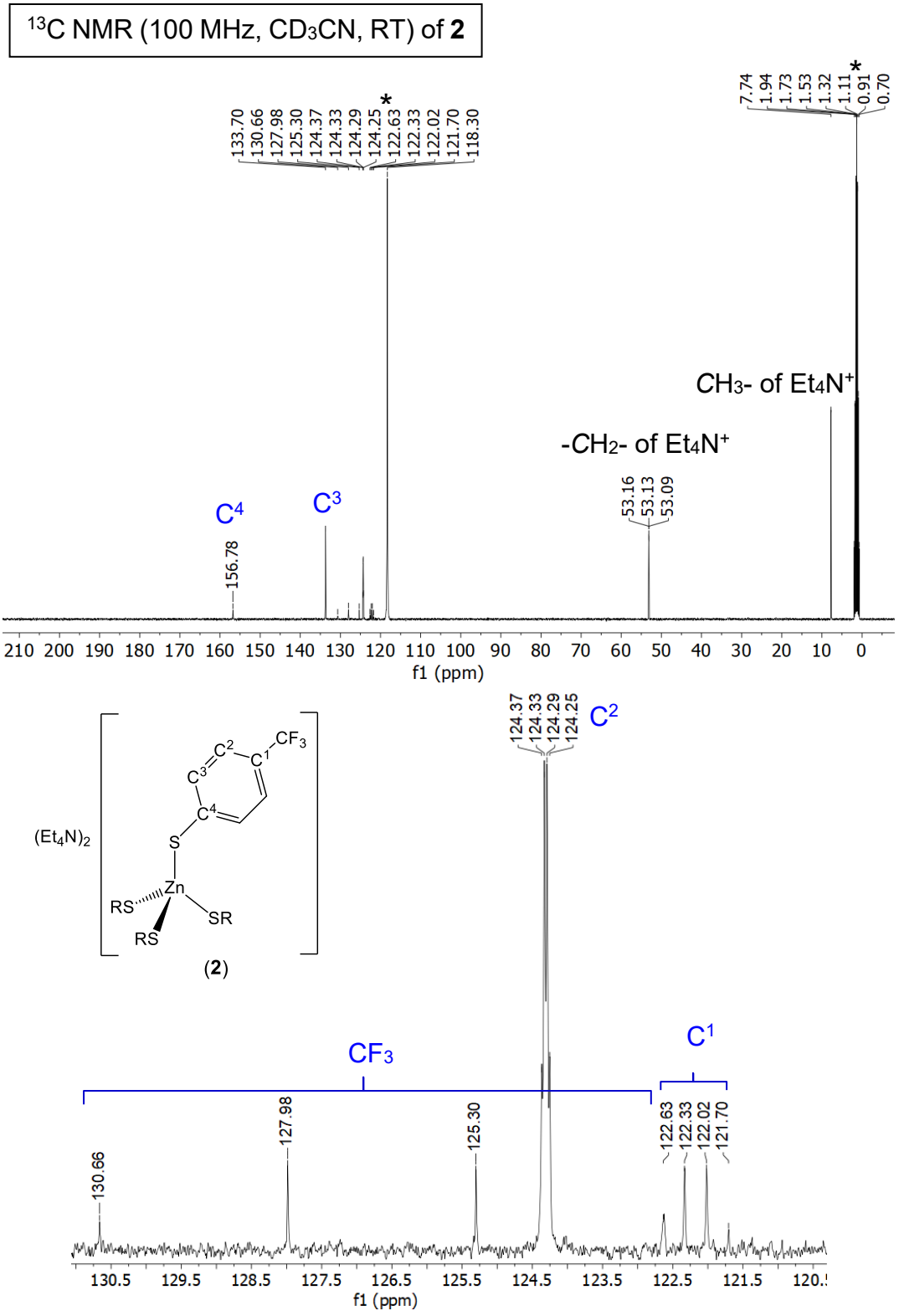

Figure S2.17. *Top*: ^{13}C NMR spectrum of $(Et_4N)_2[Zn(S\text{-}p\text{-}CF_3\text{-}Ph)_4]$ (**2**) in CD_3CN at RT. *Bottom:* expansion of 120-131 ppm region. Solvent signals at 1.32 and 118.31 ppm are indicated with *.

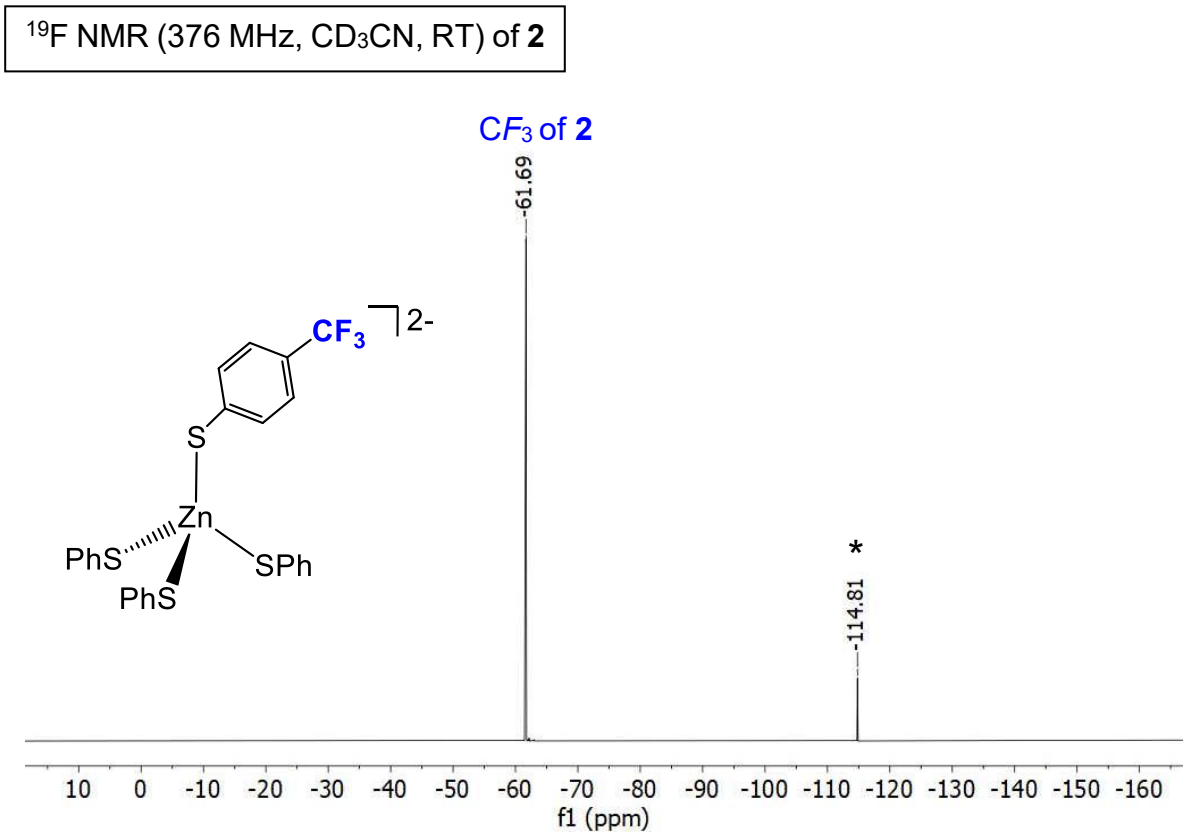

Figure S2.18. ^{19}F NMR spectrum of $(Et_4N)_2[Zn(S\text{-}p\text{-}CF_3\text{-}Ph)_4]$ (**2**) in CD_3CN at RT. Structure of **2** depicted in the inset displays one thiolate for clarity; all $PhS^- = p\text{-}CF_3\text{-}PhS^-$. Peak at -114.81 ppm is from PhF (internal standard) as indicated with *.

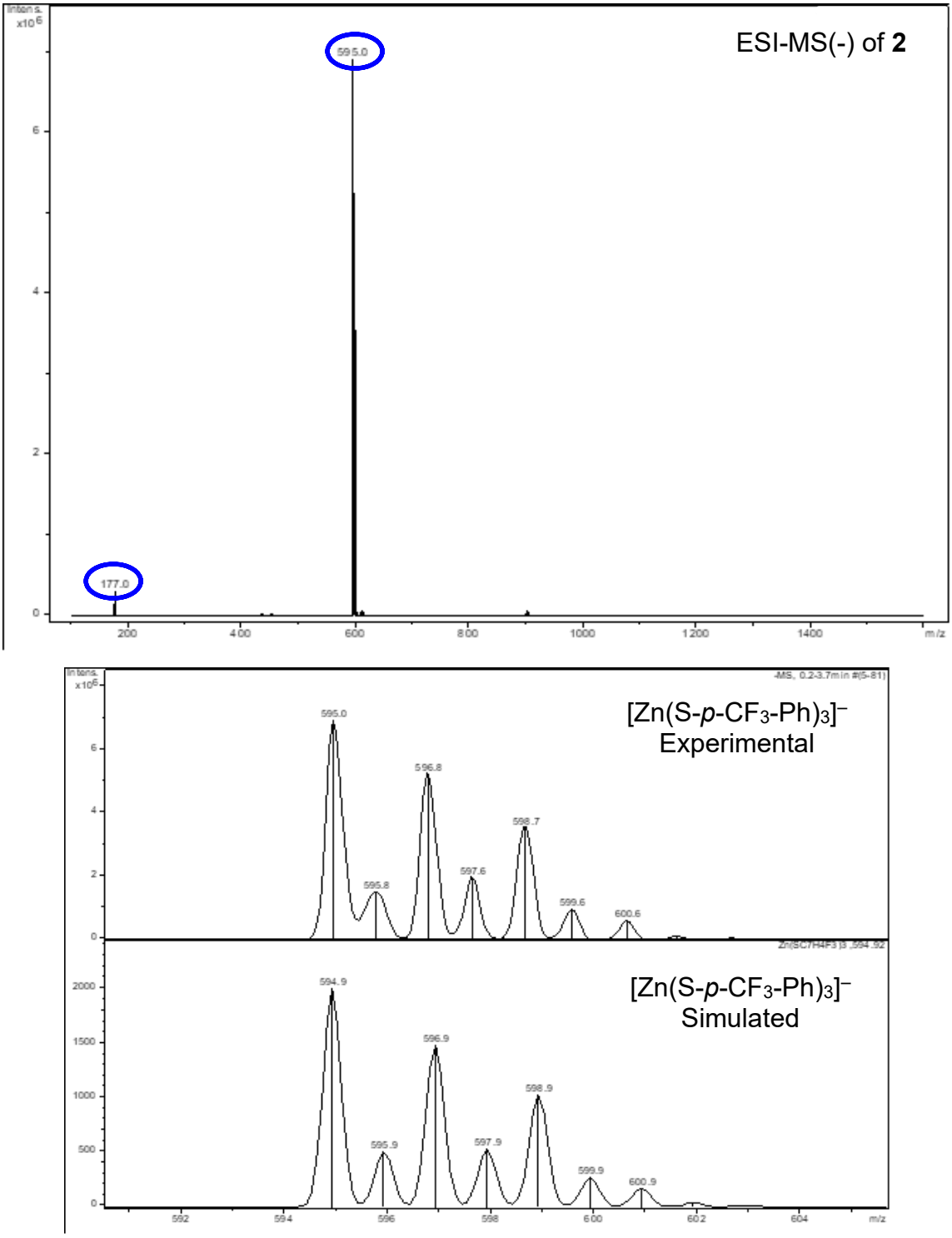

Figure S2.19. *Top*: Low-resolution ESI-MS(-) of $(Et_4N)_2[Zn(S\text{-}p\text{-}CF_3\text{-}Ph)_4]$ (**2**) in MeCN. *Bottom*: experimental and simulated theoretical isotopic distribution of peak at *m/z*: 595.0.

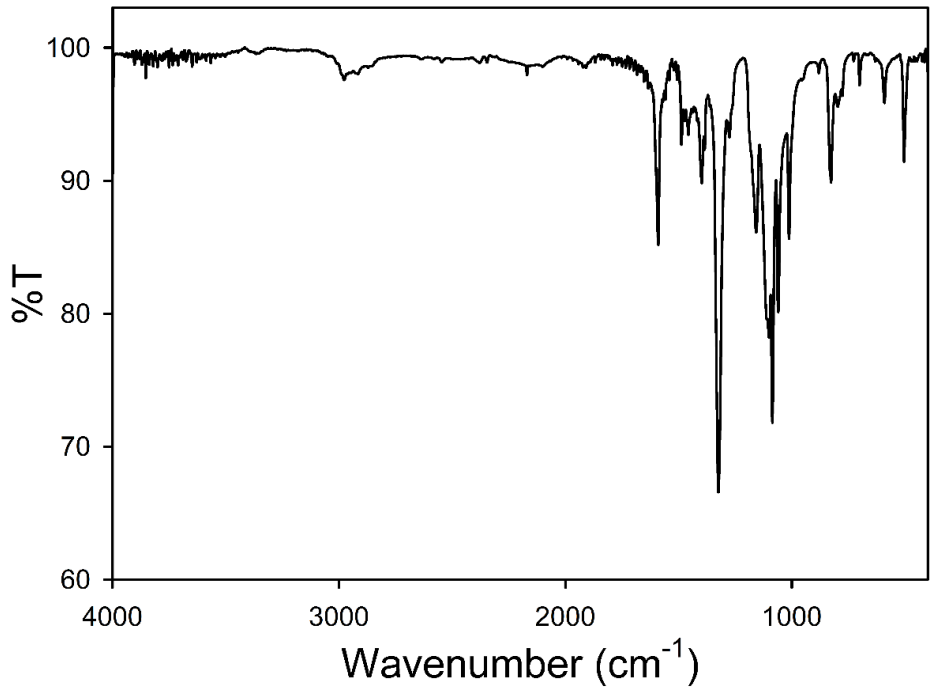

Figure S2.20. Solid-state FTIR spectrum of isolated product from the attempted synthesis of $(Et_4N)_2[Ni_2(S\text{-}p\text{-}CF_3\text{-}Ph)_6]$ (**3**) in a KBr matrix at RT.

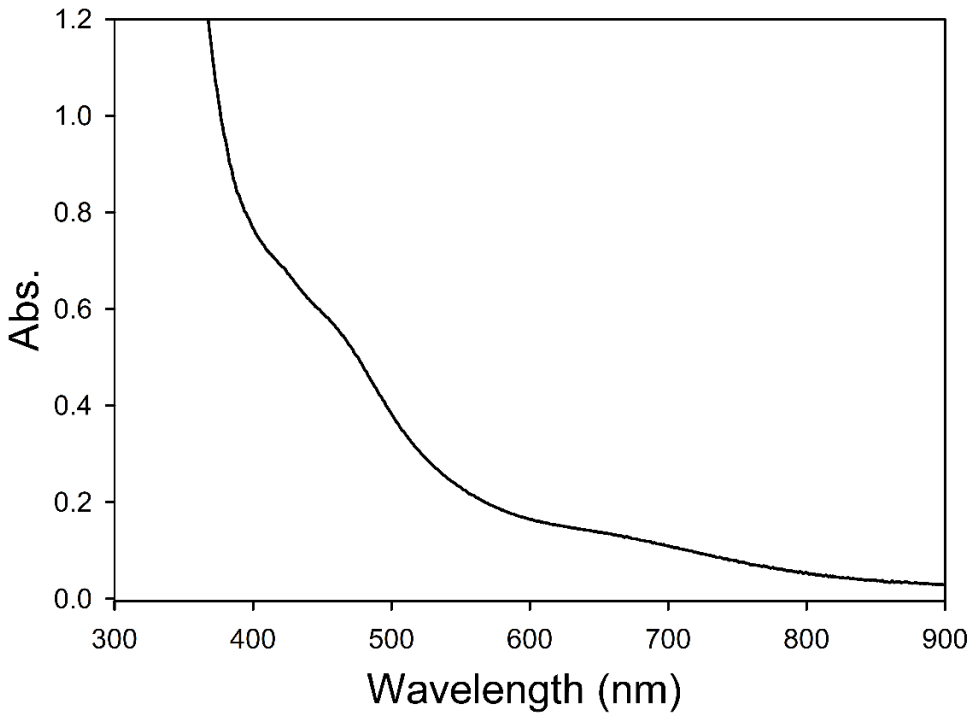

Figure S2.21. Qualitative UV-vis spectrum of isolated product from the attempted synthesis of $(Et_4N)_2[Ni_2(S\text{-}p\text{-}CF_3\text{-}Ph)_6]$ (**3**) in MeCN at 25 ˚C.

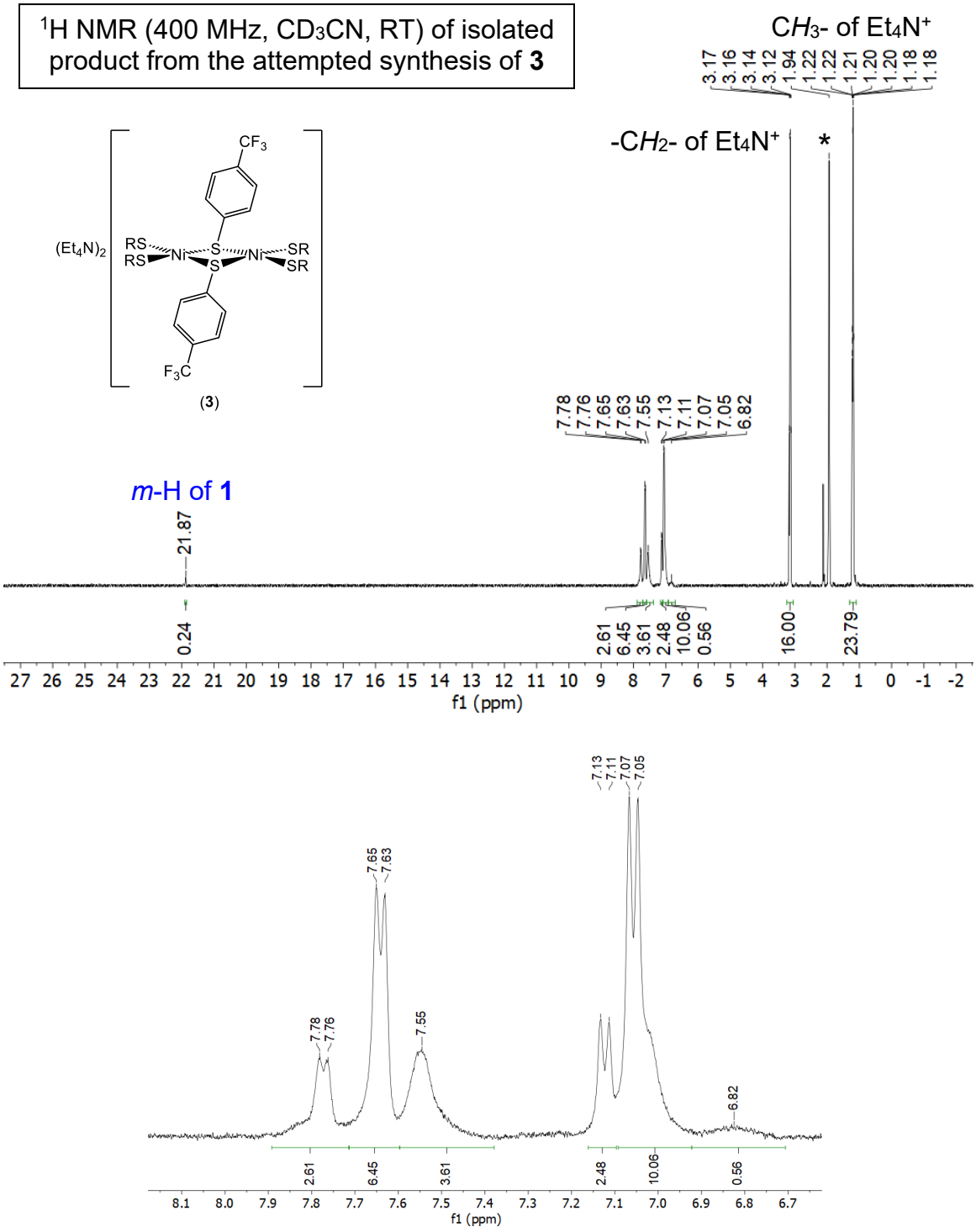

Figure S2.22. *Top*: ^{1}H NMR spectrum of isolated product from the attempted synthesis of $(Et_4N)_2[Ni_2(S\text{-}p\text{-}CF_3\text{-}Ph)_6]$ (**3**) in CD_3CN at RT (δ vs. protio signal (*) at 1.94 ppm). Proposed structure of **3** depicted in the inset displays only the bridging thiolate for clarity; all R = *p*-CF_3-PhS^-. *Bottom:* Zoom-in view of the 6-8 ppm region.

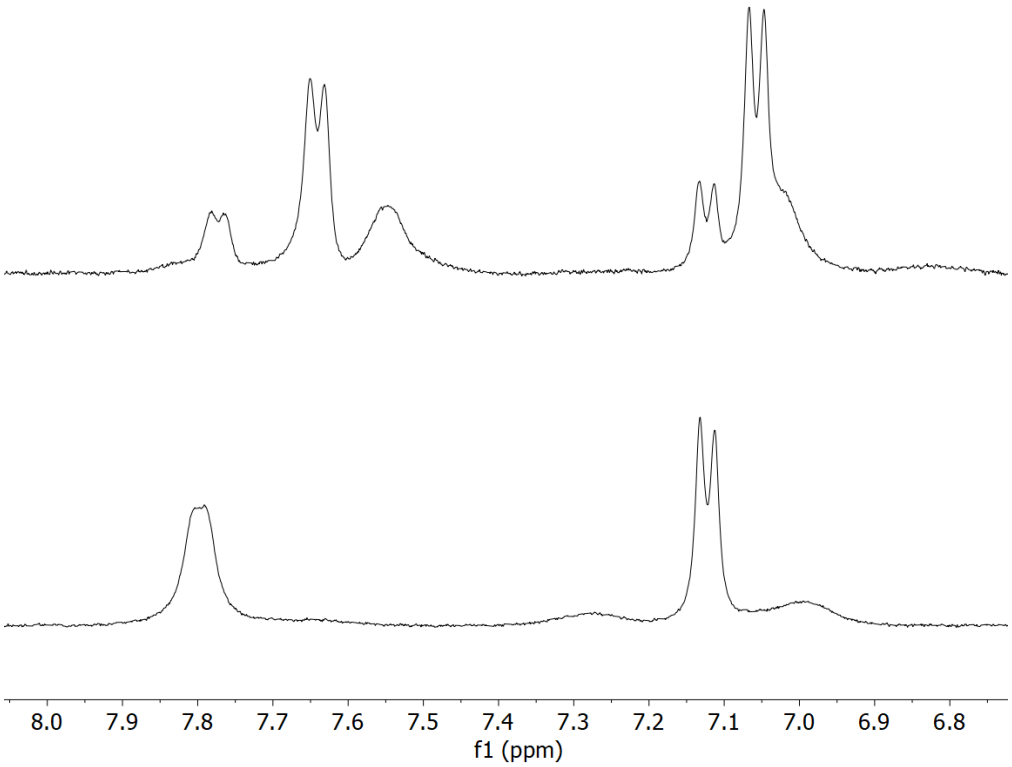

Figure S2.23. Comparison of the 6-8 ppm region in the ^{1}H NMR spectrum of the product from the attempted synthesis of **3** (top; see Figure S22 for full spectrum) and as-isolated **1** (bottom; see Figure S8 for full spectrum).

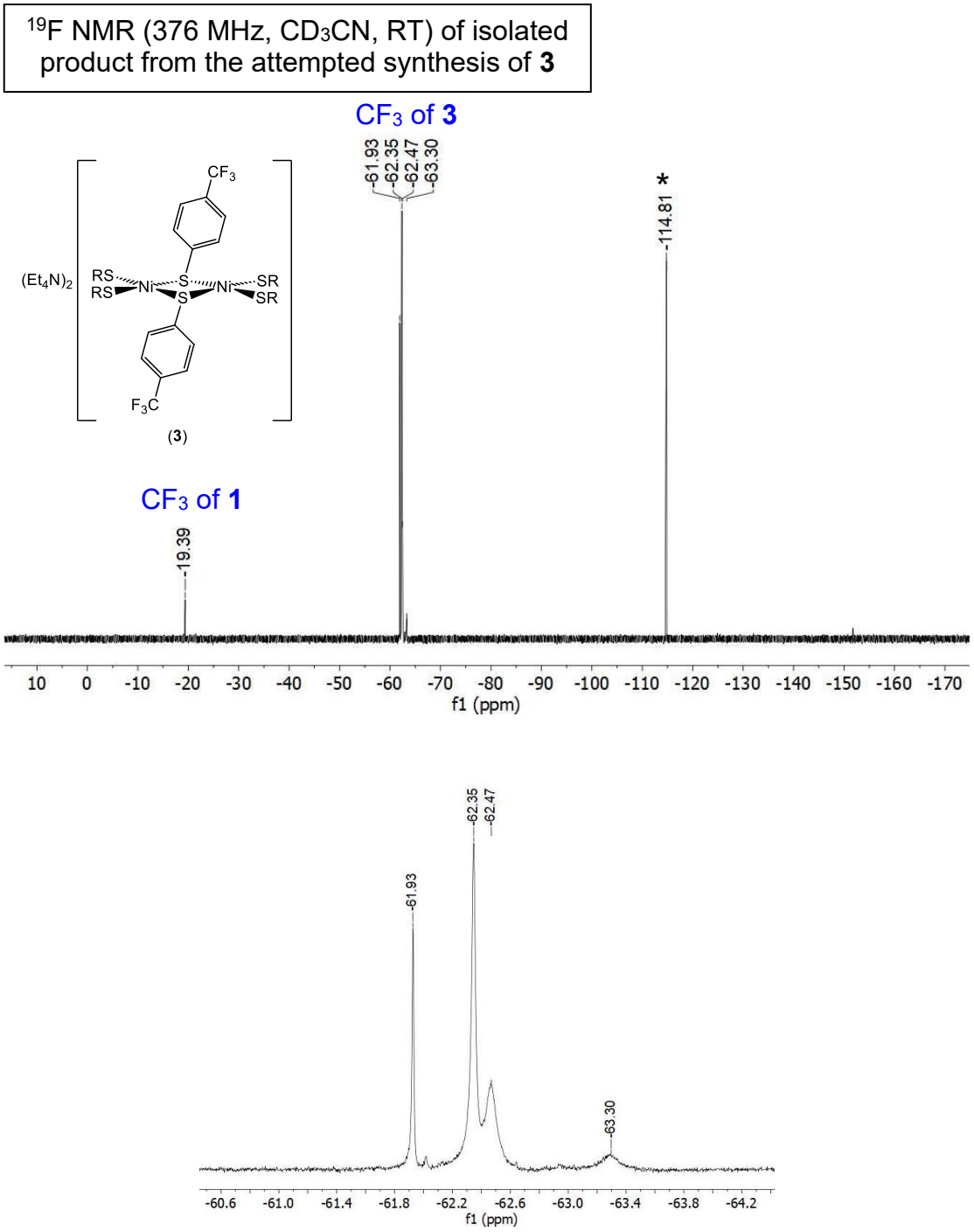

Figure S2.24. *Top*: ^{19}F NMR spectrum of isolated product from the attempted synthesis of $(Et_4N)_2[Ni_2(S\text{-}p\text{-}CF_3\text{-}Ph)_6]$ (**3**) in CD_3CN at RT. Proposed structure of **3** depicted in the inset displays only the bridging thiolate for clarity; all R = p-CF_3-PhS^-. *Bottom:* Zoom-in view of the -64 to -61 ppm region. Peak at -114.81 ppm is from PhF (internal standard) as indicated with *.

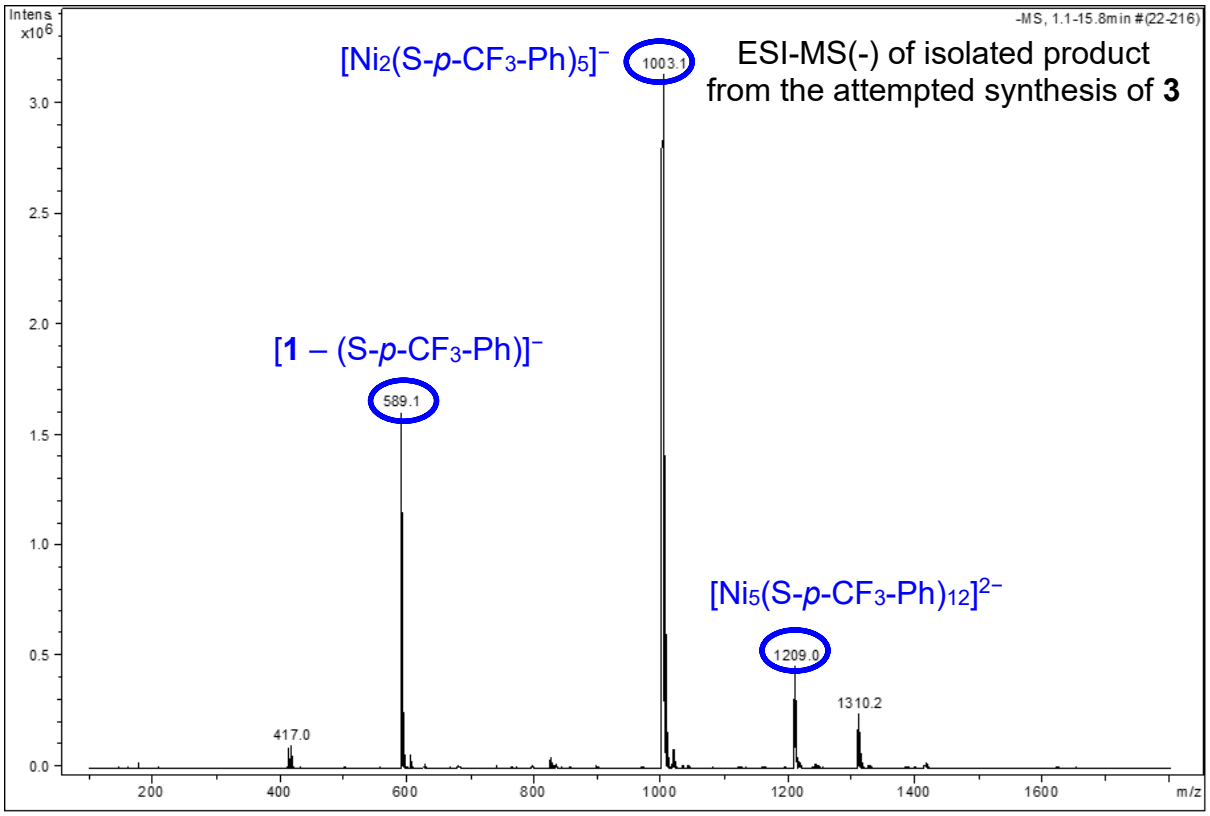

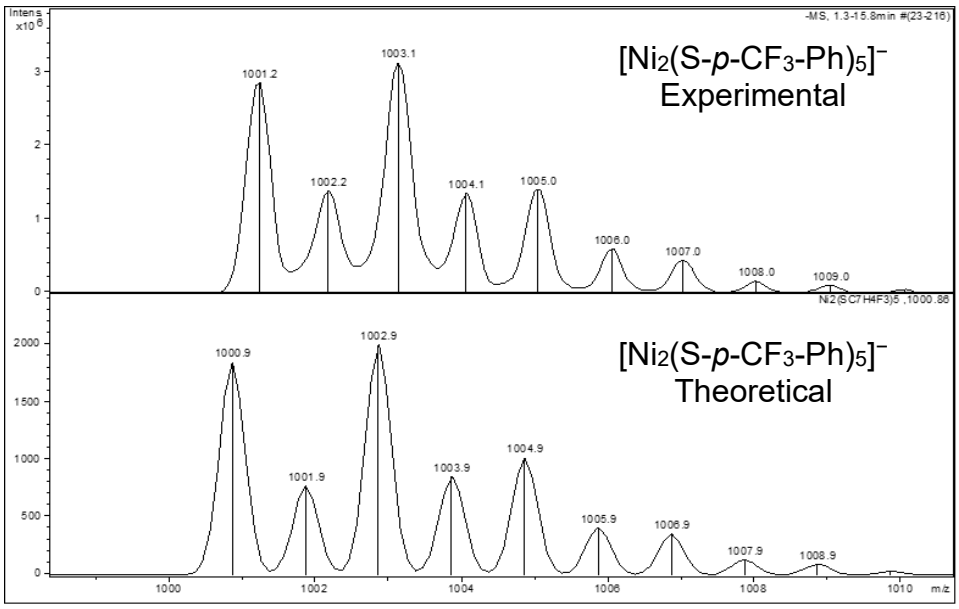

Figure S2.25. *Top*: Low-resolution ESI-MS(-) of product isolated from the attempted synthesis of **3** in MeCN. *Bottom*: experimental and simulated theoretical isotopic distribution of peak at *m/z*: 1001.2 peak.

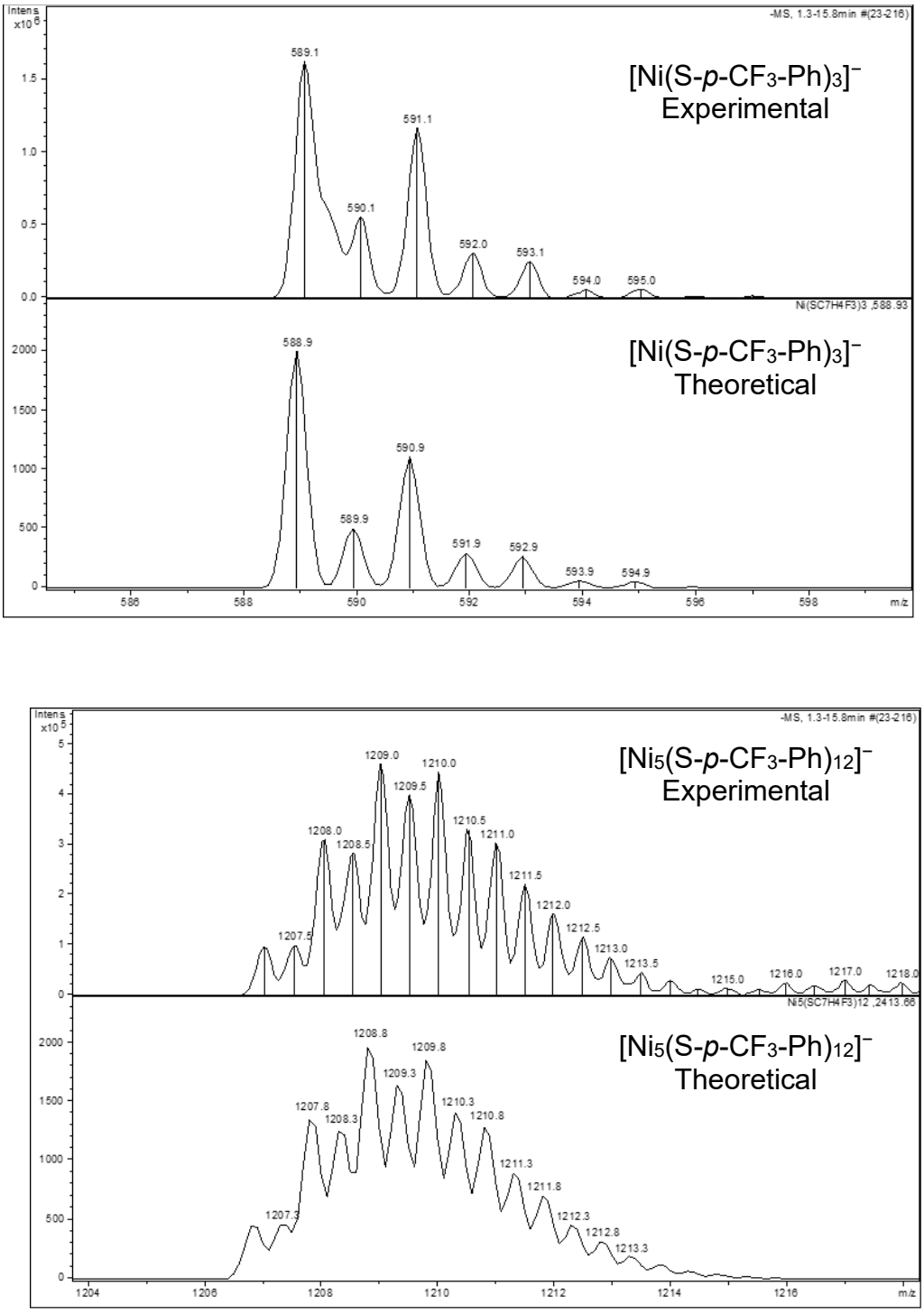

Figure S2.26. Low-resolution ESI-MS(-) of product isolated from the attempted synthesis of **3** in MeCN. *Top*: experimental and simulated theoretical isotopic distribution of peak at *m/z*: 589.1 peak. *Bottom*: experimental and simulated theoretical isotopic distribution of peak at *m/z*: 1209.0 peak.

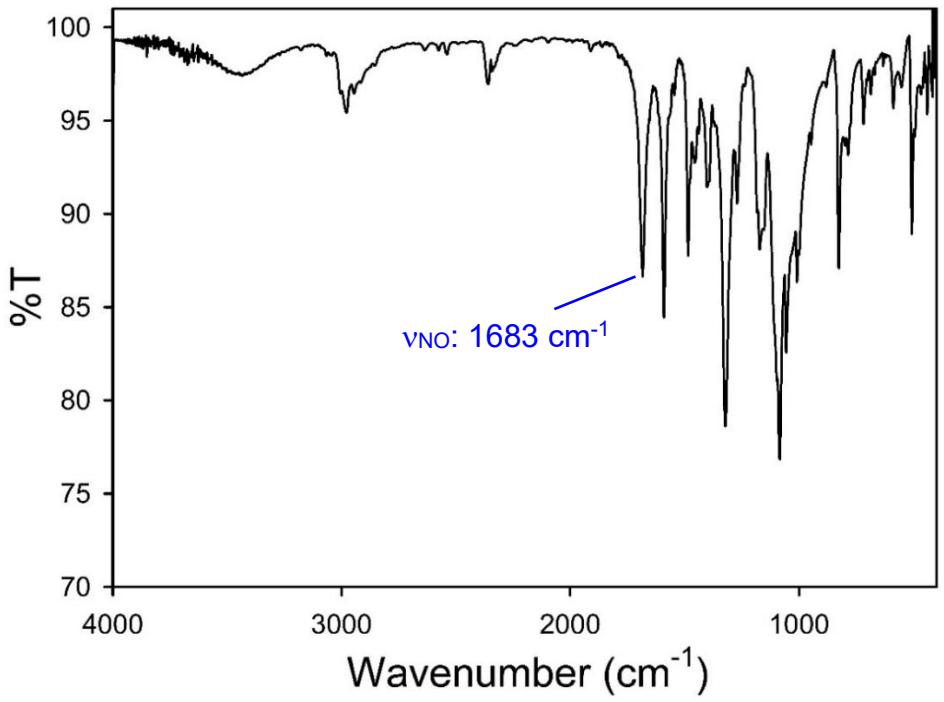

Figure S2.27. Solid-state FTIR spectrum of $(Et_4N)_2[Ni(S\text{-}p\text{-}CF_3\text{-}Ph)_3(NO)]$ (**4**) in a KBr matrix at RT.

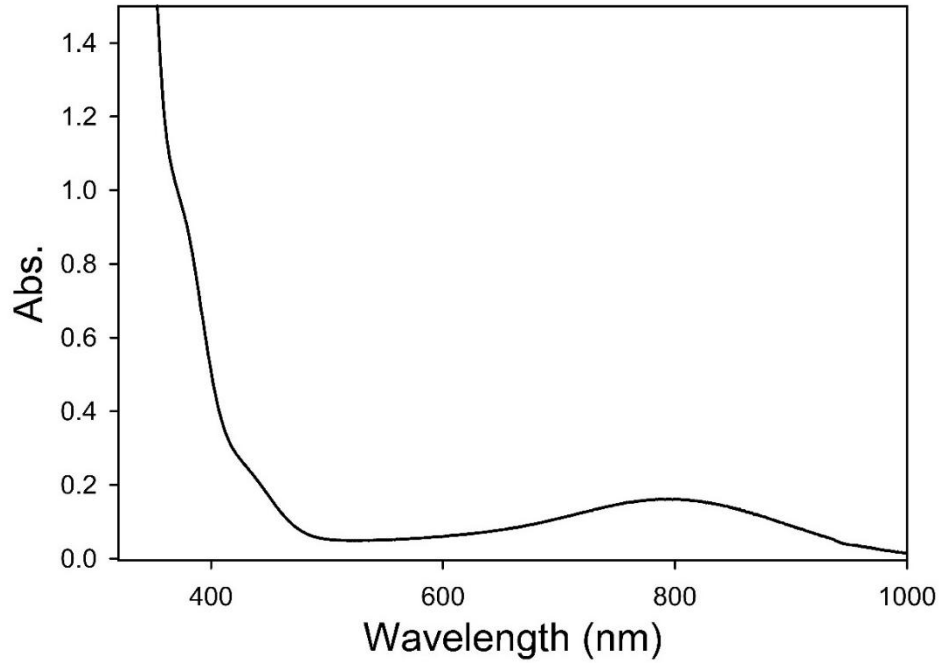

Figure S2.28. Qualitative UV-vis spectrum of $(Et_4N)_2[Ni(S\text{-}p\text{-}CF_3\text{-}Ph)_3(NO)]$ (**4**) in MeCN at 25 °C.

^{1}H NMR (400 MHz, CD_3CN, RT) of **4**

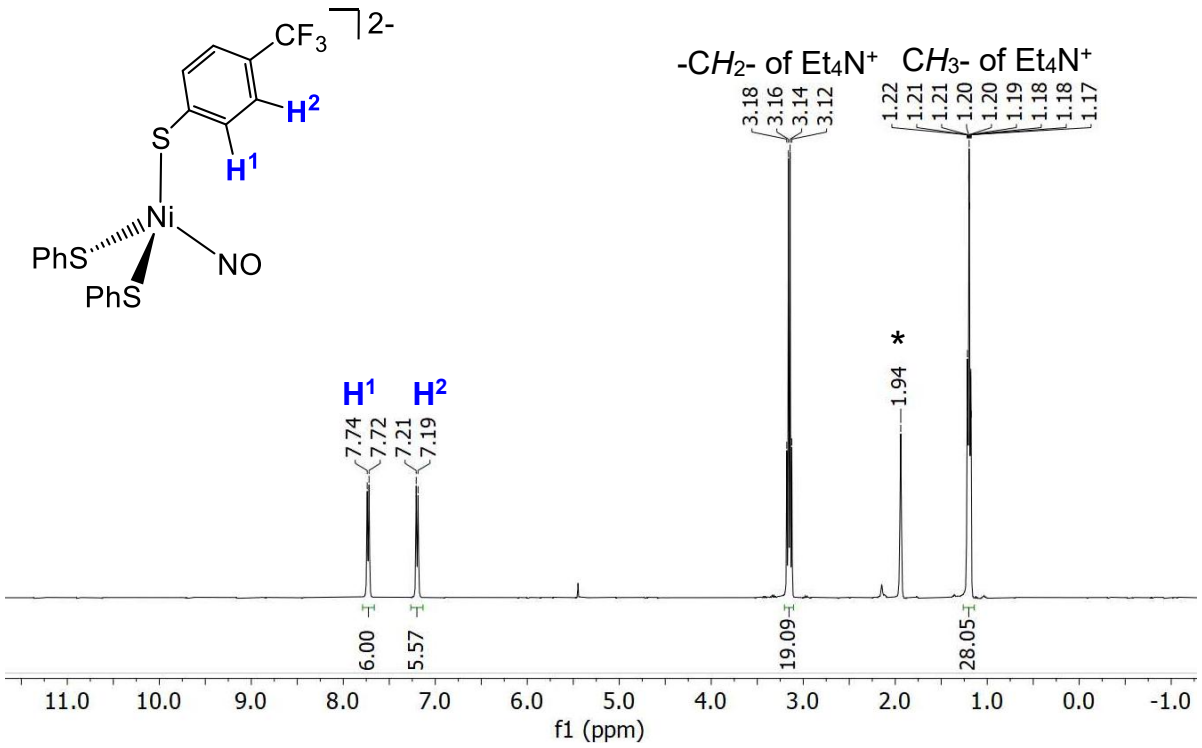

Figure S2.29. ^{1}H NMR spectrum of $(Et_4N)_2[Ni(S\text{-}p\text{-}CF_3\text{-}Ph)_3(NO)]$ (**4**) in CD_3CN at RT (δ vs. protio signal (*) at 1.94 ppm). Structure of **4** depicted in the inset displays one thiolate for clarity; all $PhS^- = p\text{-}CF_3\text{-}PhS^-$.

^{19}F NMR (376 MHz, CD_3CN, RT) of **4**

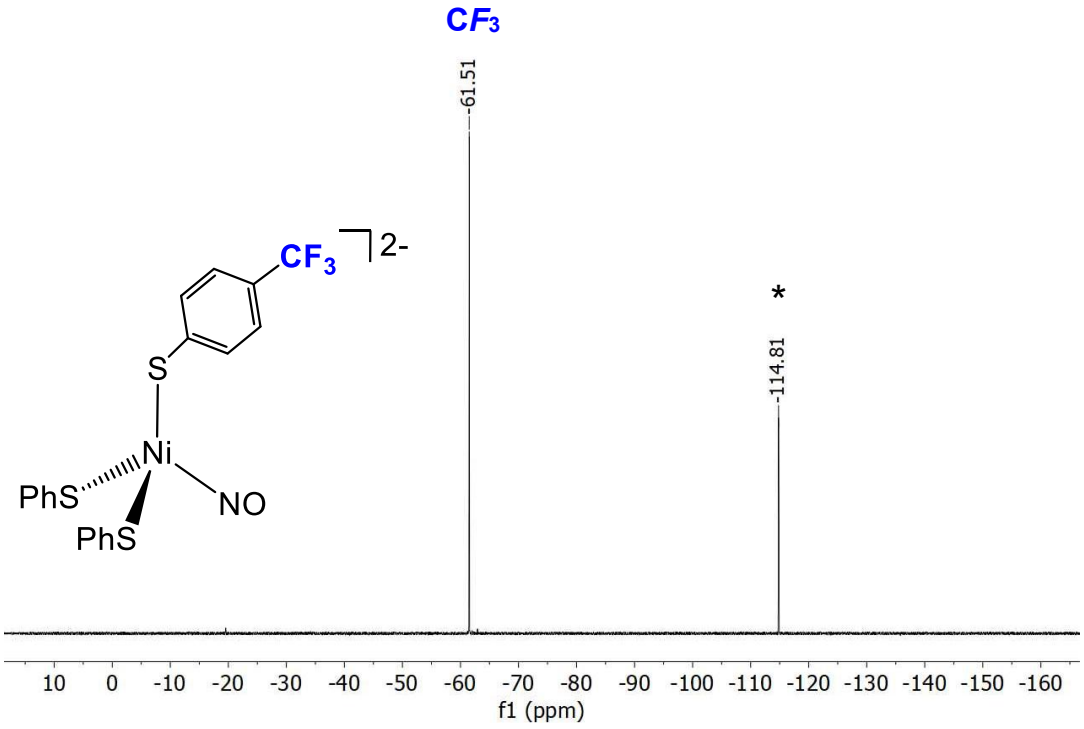

Figure S2.30. ^{19}F NMR spectrum of $(Et_4N)_2[Ni(S\text{-}p\text{-}CF_3\text{-}Ph)_3(NO)]$ (**4**) in CD_3CN at RT. Structure of **4** depicted in the inset displays one thiolate for clarity; all PhS^- = p-CF_3-PhS^-. Peak at -114.81 ppm is PhF (internal standard) as indicated with *.

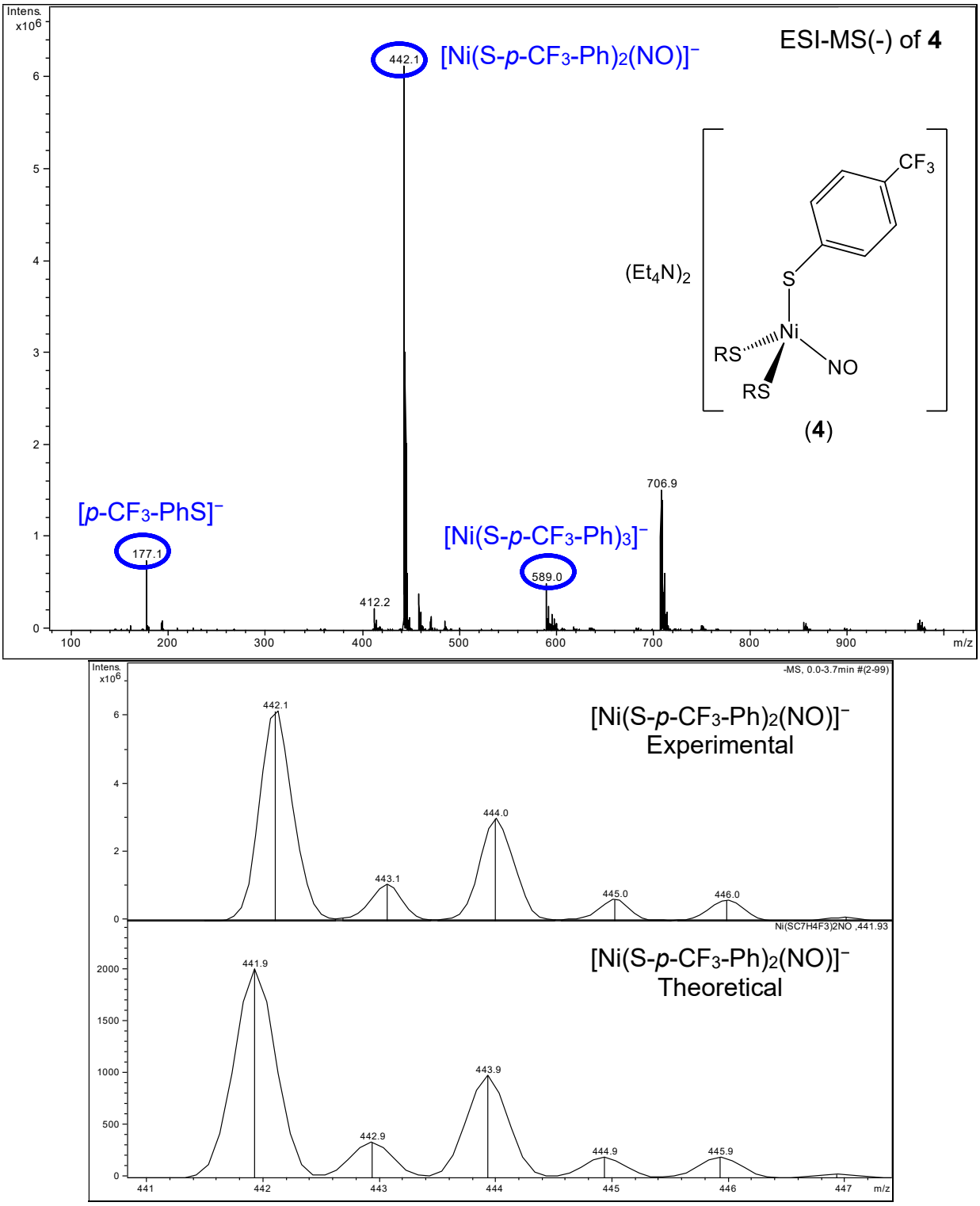

Figure S2.31. *Top*: Low-resolution ESI-MS(-) of $(Et_4N)_2[Ni(S\text{-}p\text{-}CF_3\text{-}Ph)_3(NO)]$ (**4**) in MeCN. *Bottom*: experimental and simulated theoretical isotopic distribution peak at *m/z*: 442.1.

Table S2.1. Summary of Crystal Data and Intensity Collection and Structure Refinement Parameters for $(Et_4N)_2[Ni(S\text{-}p\text{-}CF_3\text{-}Ph)_4]$ (**1**) and $(Et_4N)_2[Zn(S\text{-}p\text{-}CF_3\text{-}Ph)_4]$ (**2**).

Parameters	**1**	**2**
Formula	$C_{44}H_{56}F_{12}N_2NiS_4$	$C_{44}H_{56}F_{12}N_2ZnS_4$
MW	1027.85	1034.51
Crystal system	Monoclinic	Tetragonal
Space group	$P2_1/c$	$I4_1/a$
Crystal color, habit	dark, needle	colorless, prism
a, Å	16.3645(17)	13.4420(13)
b, Å	16.1498(17)	13.4420(13)
c, Å	19.206(2)	25.774(3)
α, deg	90	90
β, deg	110.128(3)	90
γ, deg	90	90
V, Å^3	4765.7(9)	4657.1(10)
Z	4	4
$\rho_{calcd,}$ g/cm^3	1.433	1.475
T, K	100(2)	90(2)
abs coeff, μ (Mo Kα), mm^{-1}	0.663	0.789
θ limits, deg	2.4-36.5	2.6-27.5
total no. of data	244656	30445
no. of unique data	23240	2682
no. of parameters	626	268
GOF of F^2	1.011	1.025
R_1,[a]	0.0482	0.0591
wR_2,[b]	0.1278	0.1801
max, min peaks, e/Å^3	1.45, -1.30	0.46, -0.34

[a] $R_1 = \Sigma| |F_o| - |F_c| | / \Sigma |F_o|$; [b] $wR_2 = \{\Sigma[w(F_o^2 - F_c^2)^2]/\Sigma[w(F_o^2)^2]\}^{1/2}$

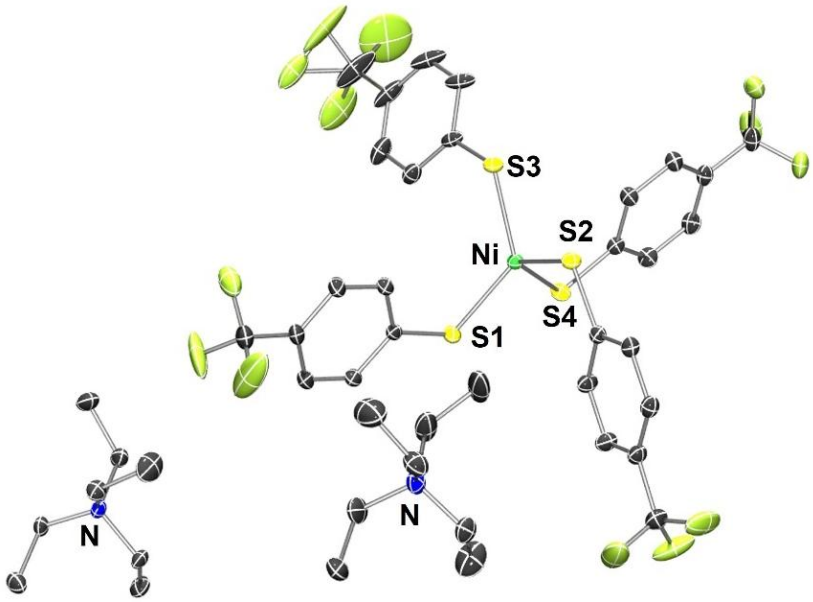

Figure S2.32. ORTEP diagram of $(Et_4N)_2[Ni(S\text{-}p\text{-}CF_3\text{-}Ph)_4]$ at 50% thermal probability ellipsoids for all non-hydrogen atoms. Disorder in one of the trifluoromethyl (CF_3) groups consisting of F7-F9 is shown.

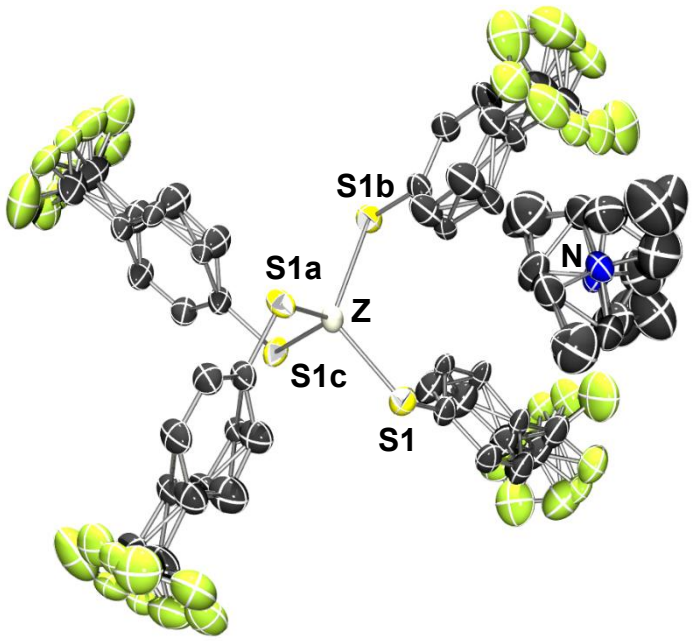

Figure S2.33. ORTEP diagram of $(Et_4N)_2[Zn(S\text{-}p\text{-}CF_3\text{-}Ph)_4]$ at 50% thermal probability ellipsoids for all non-hydrogen atoms. Disorder occurs in all trifluoromethyl-phenyl groups (Zn sits on a center of inversion) and in the C-atoms of the Et_4N^+ cations. These positions (% occupancy) have been effectively modeled as described in Experimental section 1.4 of the SI.

Table S2. Selected bond distances (Å) and bond angles (deg) for $(Et_4N)_2[Ni(S\text{-}p\text{-}CF_3\text{-}Ph)_4]$ (**1**) and $(Et_4N)_2[Zn(S\text{-}p\text{-}CF_3\text{-}Ph)_4]$ (**2**).

1		**2**	
Atoms	**Bond Distance (Å)**	**Atoms**	**Bond Distance (Å)**
$Ni\text{-}S_1$	2.290	$Zn\text{-}S_1$	2.3500
$Ni\text{-}S_2$	2.266		
$Ni\text{-}S_3$	2.275		
$Ni\text{-}S_4$	2.296		
Atoms	**Bond Angle (°)**	**Atoms**	**Bond Angle (°)**
$S_1\text{-}Ni\text{-}S_2$	87.8	$S_1\text{-}Zn\text{-}S_{1a}$	105.6
$S_1\text{-}Ni\text{-}S_3$	122.3	$S_1\text{-}Zn\text{-}S_{1b}$	117.5
$S_1\text{-}Ni\text{-}S_4$	113.5	$S_1\text{-}Zn\text{-}S_{1c}$	105.6
$S_2\text{-}Ni\text{-}S_3$	124.7		
$S_2\text{-}Ni\text{-}S_4$	124.5		
$S_3\text{-}Ni\text{-}S_4$	87.3		
∠Ar-(Ni-S-C)	**Angle (°)**		
$Ar_1\text{-}(Ni\text{-}S_1)$	1.2˚		
$Ar_2\text{-}(Ni\text{-}S_2)$	5.0˚		
$Ar_3\text{-}(Ni\text{-}S_3)$	38.0˚		
$Ar_4\text{-}(Ni\text{-}S_4)$	6.5˚		

Table S2.3. Summary of best fit simulation of EXAFS of **1**.

	Nearest-Neighbor Ligand Environment [a]				
Sample	**Atom [c]**	**R(Å) [d]**	**C.N. [e]**	**σ^2 [f]**	**F' [g]**
1	S	2.274	4	3.16	0.399

[a/b] - Independent metal-ligand scattering environments.
[c] - Scattering atoms: N (nitrogen), O (oxygen), C (carbon.
[d] - Metal-ligand bond length.
[e] - Metal-ligand coordination number.
[f] - Debye-Waller factor (Å x 10^3).
[g] - Number of degrees of freedom weighted mean square deviation between data and fit.

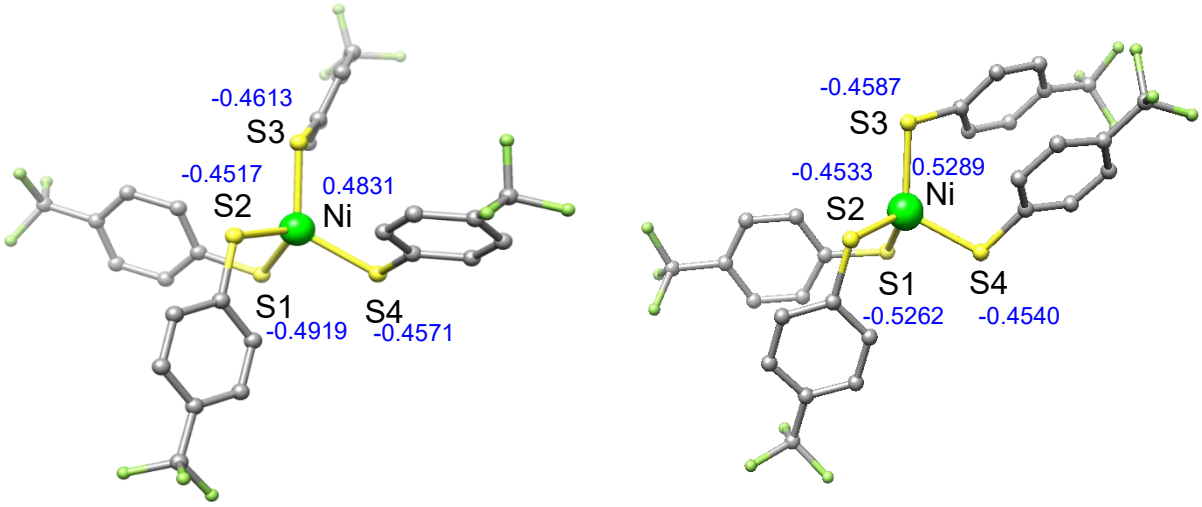

Figure S2.34. Geometry-optimized structures of the tetrahedral (S = 1) dianion of **1**. Gas-phase (left) and in MeCN (right). Input coordinates taken from the X-ray crystal structure of **1**. Mulliken atomic charges on Ni and S atoms are shown in blue.

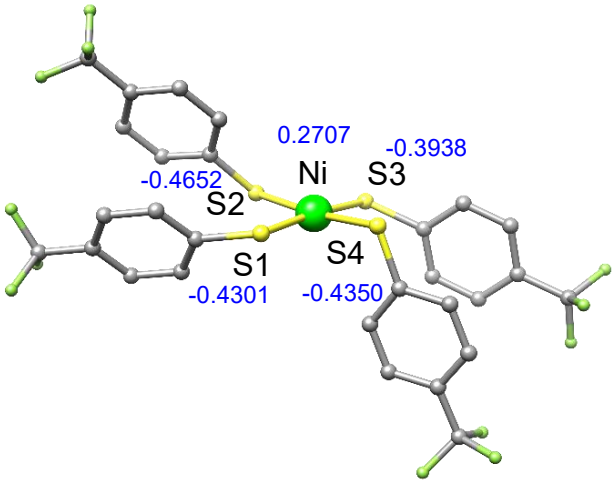

Figure S2.35. Geometry-optimized structure of the planar (S = 0) dianion of **1** in MeCN. Input coordinates taken from the crystal structure of **1** with the aryl-thiolato ligands positioned in an approximate square-planar geometry. Mulliken atomic charges on Ni and S atoms are shown in blue.

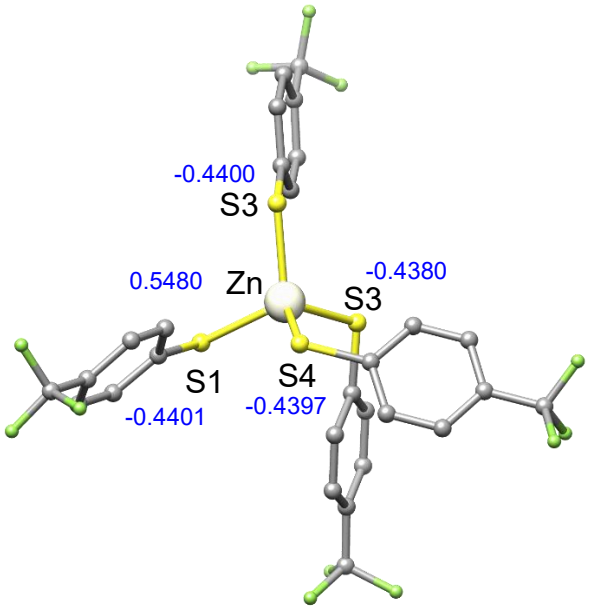

Figure S2.36. Geometry-optimized structure of the tetrahedral dianion of **2** in the gas-phase. Input coordinates taken from the X-ray crystal structure of **2**. Mulliken atomic charges on Zn and S atoms are shown in blue.

Table S2.4. Selected bond distances (Å) and bond angles (°) for geometry-optimized structures of the dianions of **1** ($S = 0$, $S = 1$) and **2**.

	1 ($S = 1$, Gas)	**1** ($S = 1$, MeCN)	**1** ($S = 0$, MeCN)	**2** ($S = 0$, Gas)
	Bond Distance (Å)			
	M = Ni			M = Zn
M-S_1	2.323	2.331	2.251	2.392
M-S_2	2.335	2.349	2.252	2.403
M-S_3	2.332	2.312	2.266	2.385
M-S_4	2.320	2.336	2.254	2.392
	Bond Angle (°)			
S_1-M-S_2	119.5	110.7	98.7	113.1
S_1-M-S_3	118.6	91.7	175.0	102.4
S_1-M-S_4	94.4	130.1	84.2	105.9
S_2-M-S_3	90.1	112.0	82.9	111.5
S_2-M-S_4	129.2	99.0	94.7	106.0
S_3-M-S_4	118.6	113.6	173.9	112.9
	τ_4			
	0.79	0.82	0.08	0.95
∠Ar-(Ni-S-C)	**Angle (°)**			
Ar_1-(Ni-S_1)	23.6	59.6		
Ar_2-(Ni-S_2)	11.2	30.3		
Ar_3-(Ni-S_3)	26.4	52.5		
Ar_4-(Ni-S_4)	23.6	30.2		

Table S2.5. Löwdin population analysis derived from the DFT computations (B3LYP/def2-TZVPP) for selected MOs of tetrahedral **1** (*S* = 1), with an MeCN solvent model. Only s and p contributions were tabulated for S-atoms.

α Orbitals	**MO#**	**Energy (eV)**	**%Ni**	**%S**
LUMO + 3	198	-0.5305	0.4	6.1
LUMO + 2	197	-0.6036	1.0	6.2
LUMO + 1	196	-0.6363	1.2	5.7
LUMO	195	-0.7468	2.1	3.5
HOMO	194	-4.9573	10.6	55.1
HOMO - 1	193	-5.0063	9.6	55.2
HOMO - 2	192	-5.2089	8.3	60.7
HOMO - 3	191	-5.2154	2.3	64.5

β Orbitals	**MO#**	**Energy (eV)**	**%Ni**	**%S**
LUMO + 3	196	-0.4938	1.1	9.3
LUMO + 2	195	-0.7033	16.2	4.8
LUMO + 1	194	-1.8772	70.2	18.0
LUMO	193	-1.9242	63.3	13.6
HOMO	192	-4.8433	11.9	51.5
HOMO - 1	191	-5.1047	1.4	60.4
HOMO - 2	190	-5.2702	24.5	51.9
HOMO - 3	189	-5.4739	7.3	45.8

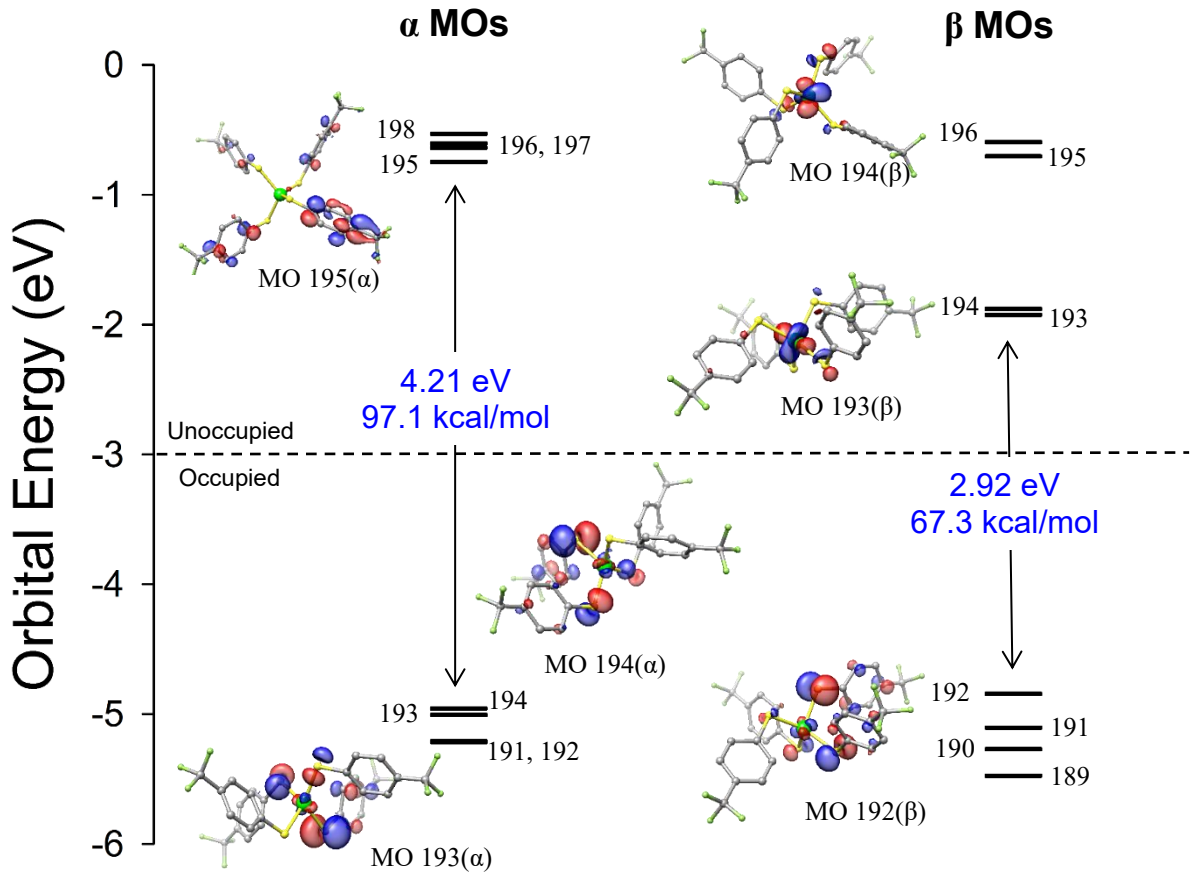

Figure S2.37. DFT-generated isosurface plots of the frontier MOs for tetrahedral (*S* = 1) **1** with an MeCN solvent model. Dashed line indicates the level below which MOs are occupied. Spin-up (α) MOs (*left*); spin-down (β) MOs (*right*). See Table S5 for contributions.

Table S2.6. Löwdin population analysis derived from the DFT computations (B3LYP/def2-TZVPP) for selected MOs of square-planar **1** ($S = 0$), with an MeCN solvent model. Only s and p contributions were tabulated for S-atoms.

Orbitals	MO#	Energy (eV)	%Ni	%S
LUMO + 3	197	-0.3373	1.2	5.3
LUMO + 2	196	-0.4232	0.8	4.5
LUMO + 1	195	-0.5161	3.2	5.0
LUMO	194	-1.2968	39.2	23.9
HOMO	193	-4.5471	34.7	52.2
HOMO - 1	192	-4.6915	17.7	52.9
HOMO - 2	191	-4.8444	8.6	65.4
HOMO - 3	190	-5.1671	83.8	12.8

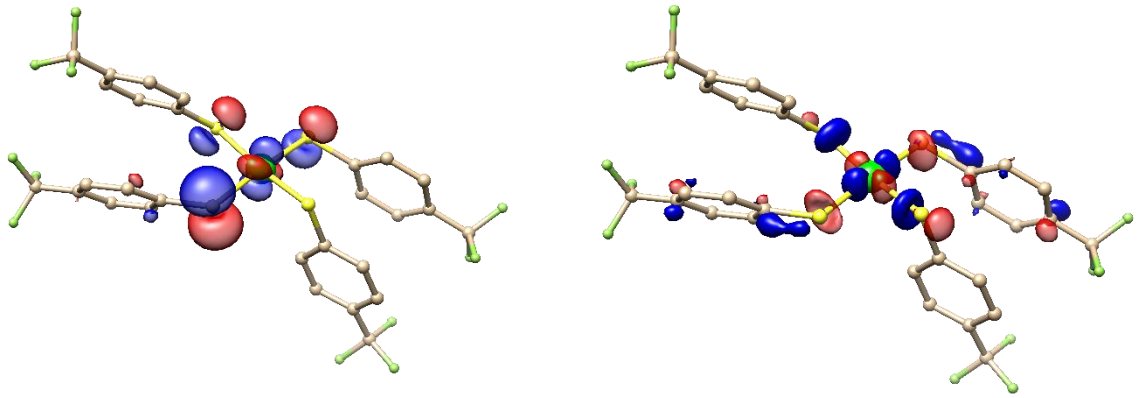

Figure S2.38. DFT-generated isosurface plots (B3LYP/def2-TZVPP) of the frontier MOs of planar ($S = 0$) **1**: MO 193 = HOMO (left) and MO 194 = LUMO (right). See Table S6 for contributions.

Table S2.7. Löwdin population analysis derived from the DFT computations (B3LYP/def2-TZVPP) for selected MOs of **2** (S = 0), with MeCN solvent model. Only s and p contributions were tabulated for S-atoms.

Orbitals	MO#	Energy (eV)	%Zn	%S
LUMO + 3	198	-0.5307	1.5	6.0
LUMO + 2	197	-0.5305	2.0	5.1
LUMO + 1	196	-0.5476	1.8	2.1
LUMO	195	-0.5622	2.5	4.8
HOMO	194	-5.0965	5.0	63.6
HOMO - 1	193	-5.1441	5.0	62.4
HOMO - 2	192	-5.1754	4.1	62.0
HOMO - 3	191	-5.2513	5.5	64.6

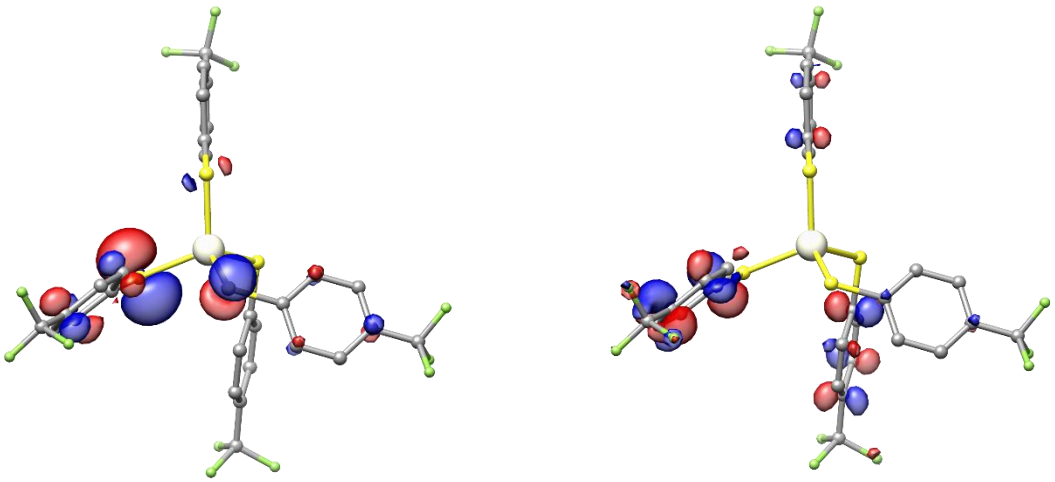

Figure S2.39. DFT-generated isosurface plots (B3LYP/def2-TZVPP) of the frontier MOs of **2**: MO 194 = HOMO (left) and MO 195 = LUMO (right). See Table S7 for contributions.

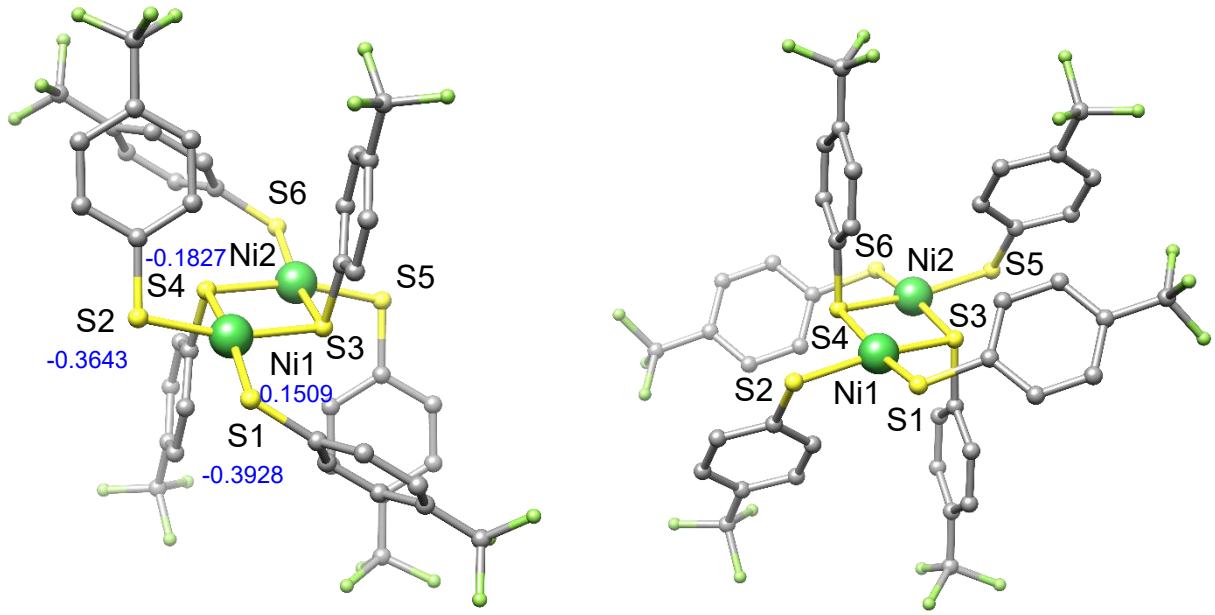

Figure S2.40. Geometry-optimized structure of the planar (S = 0) dianion of **3** in MeCN. Input coordinates taken from the X-ray crystal structure of the *p*-Cl-PhS^{-} analog of **3** (Maroney, M. J. and coworkers, *Inorg. Chem*. **1990**, *28*, 4779). Mulliken atomic charges on Ni and S atoms are shown in blue. Two different orientations are displayed.

Table S2.8. Selected bond distances (Å) and bond angles (deg) for geometry-optimized structure of the dianion of **3** (S = 0) in MeCN.

Atoms	Bond Distance	Atoms	Angle
Ni_1-S_1	2.211	S_1-Ni_1-S_2	90.1
Ni_1-S_2	2.243	S_1-Ni_1-S_3	99.2
Ni_1-S_3	2.246	S_1-Ni_1-S_4	169.7
Ni_1-S_4	2.247	S_2-Ni_1-S_3	164.5
Ni_2-S_3	2.247	S_2-Ni_1-S_4	89.9
Ni_2-S_4	2.246	S_3-Ni_1-S_4	83.1
Ni_2-S_5	2.211	S_3-Ni_2-S_4	83.1
Ni_2-S_6	2.243	S_3-Ni_2-S_5	89.9
$Ni_1\cdots Ni_2$	3.363	S_3-Ni_2-S_6	169.7
		S_4-Ni_2-S_5	164.4
		S_4-Ni_2-S_6	99.1
		S_5-Ni_2-S_6	90.3
	τ_4	Ni_1	0.18

Table S2.9. Löwdin population analysis derived from the DFT computations (B3LYP/def2-TZVPP) for selected MOs of **3** (S = 0), with MeCN solvent model. Only s and p contributions were tabulated for S-atoms.

Orbitals	MO#	Energy (eV)	%Ni	%S
LUMO + 3	299	-0.8315	4.8	5.7
LUMO + 2	298	-0.8782	8.2	10.1
LUMO + 1	297	-1.7137	35.0	23.2
LUMO	296	-1.8672	41.9	21.4
HOMO	295	-5.0963	22.8	54.1
HOMO - 1	294	-5.1292	15.3	55.4
HOMO - 2	293	-5.2043	15.2	58.2
HOMO - 3	292	-5.2129	26.1	53.7

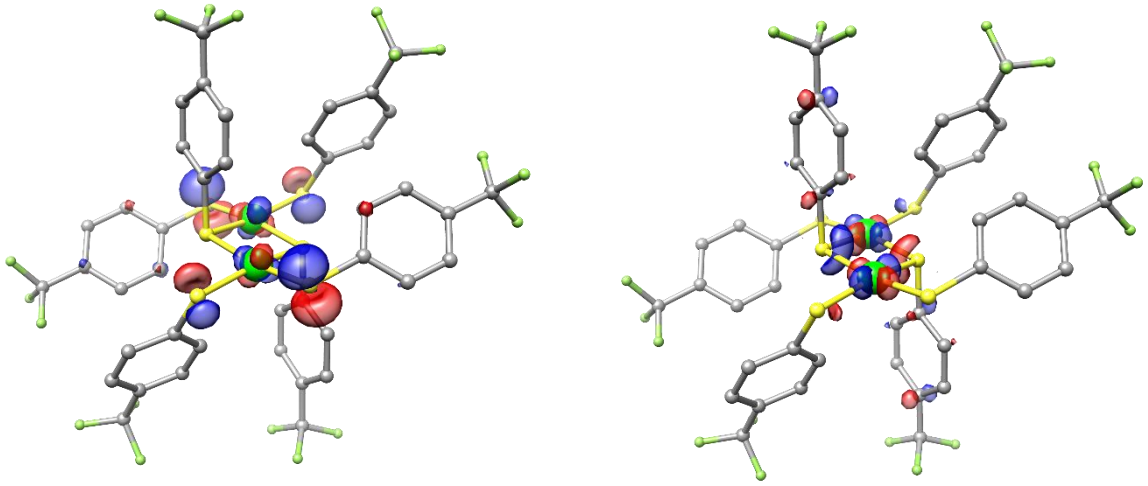

Figure S2.41. DFT-generated isosurface plots (B3LYP/def2-TZVPP) of the frontier MOs of **3**: MO 295 = HOMO (left) and MO 296 = LUMO (right). See Table S9 for contributions.

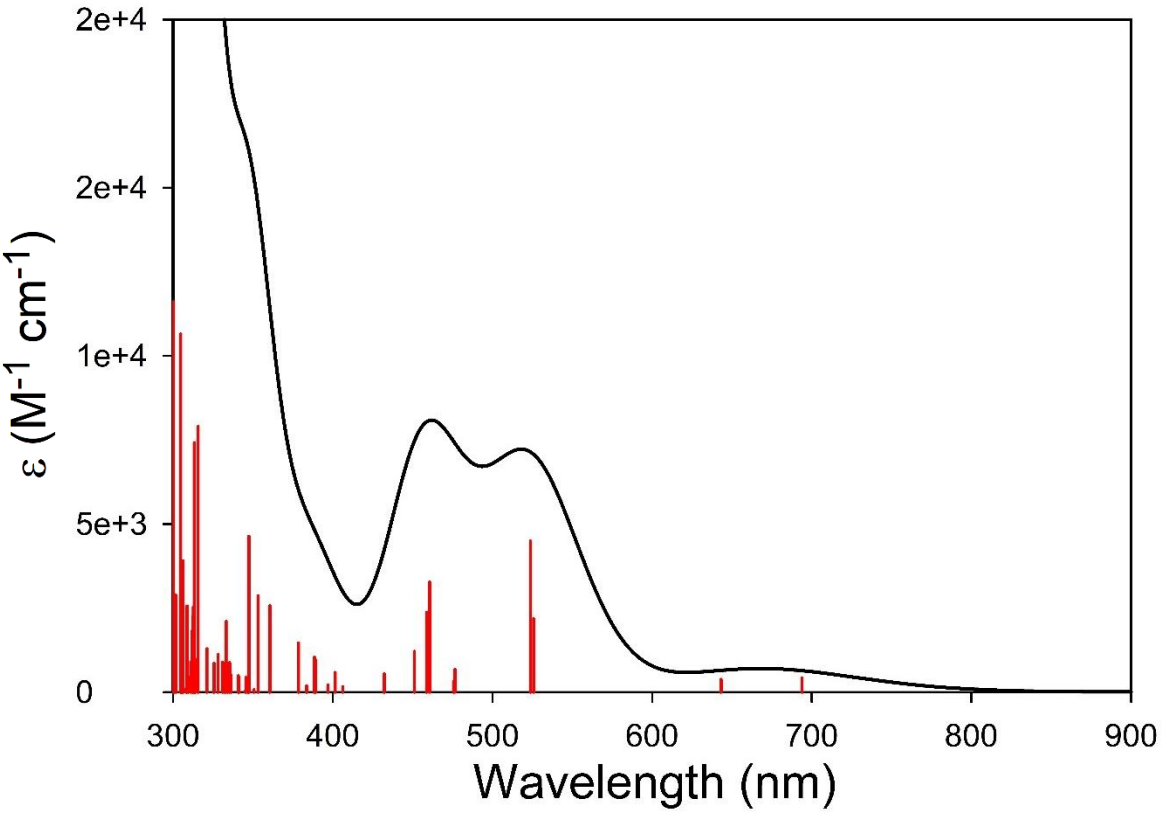

Figure S2.42. TD-DFT calculated optical absorption spectrum of **1*** with Gaussian (black) distribution (black line) and optical transitions (red sticks).

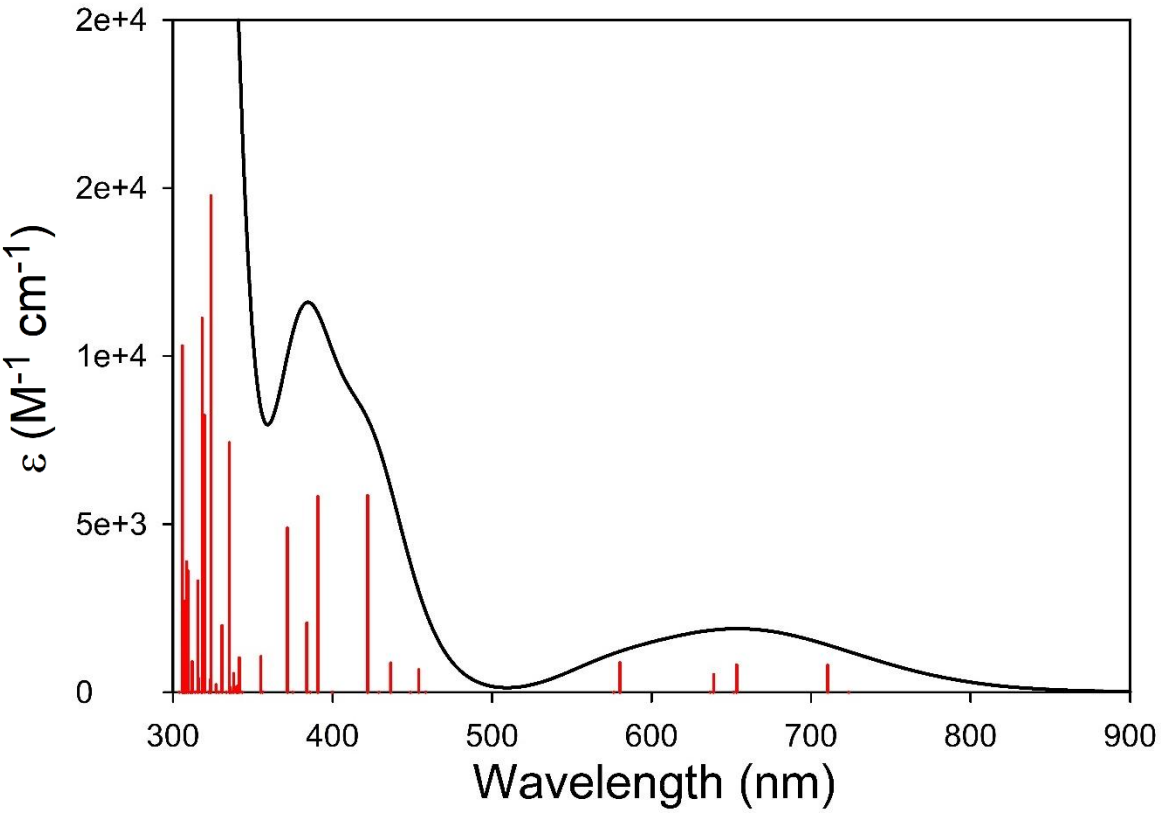

Figure S2.43. TD-DFT calculated optical absorption spectrum of **3*** with Gaussian (black) distribution (black line) and optical transitions (red ticks).

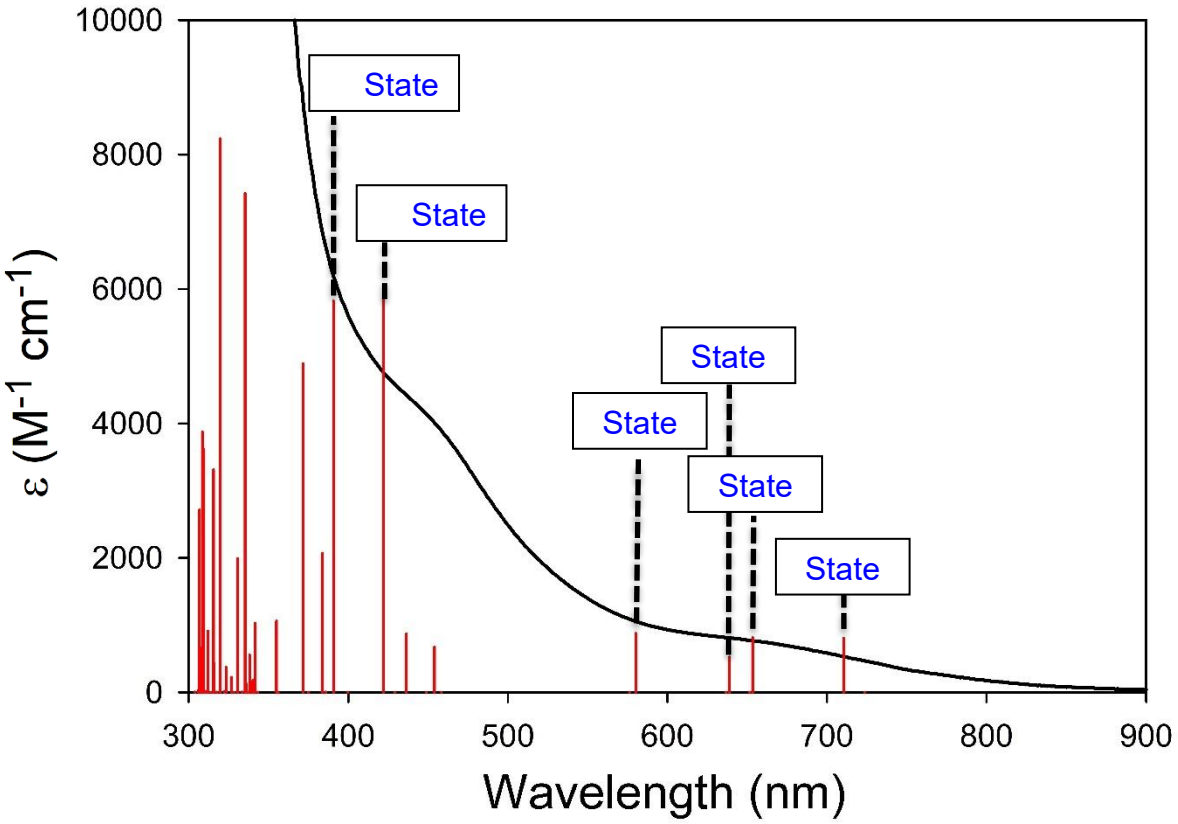

Figure S2.44. UV-vis spectrum of the thiolate-bridged mixture containing the dianion of **3** in MeCN (black trace) superimposed with TD-DFT computed optical transitions for **3*** (red sticks). Experimental ε for thiolate-bridged mixture containing **3** is estimated by assuming the isolated product is exclusively $[Ni_2(S\text{-}p\text{-}CF_3\text{-}Ph)_6]^{2-}$.

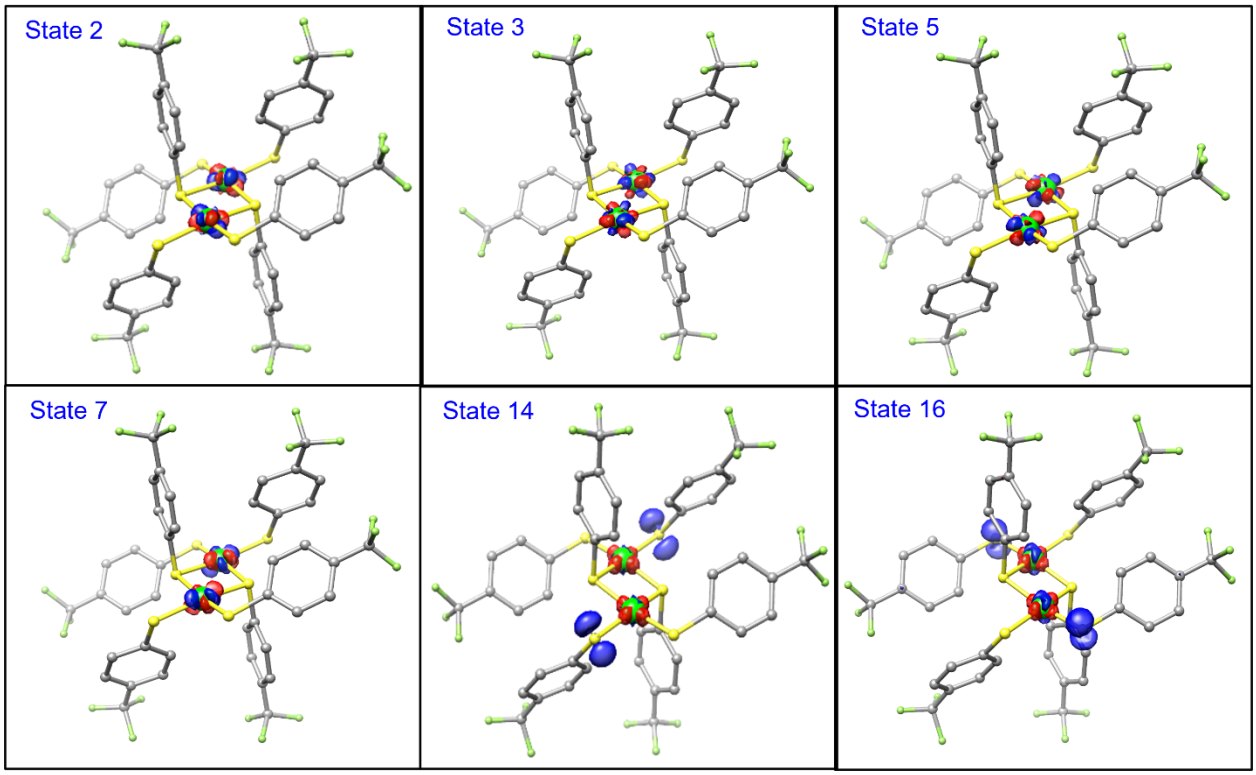

Figure S2.45. Electron difference densities for select transitions of **3***, shown in Figure S44, blue lobes reflect loss of electron density, while red lobes reflect increased electron density in the transitions.

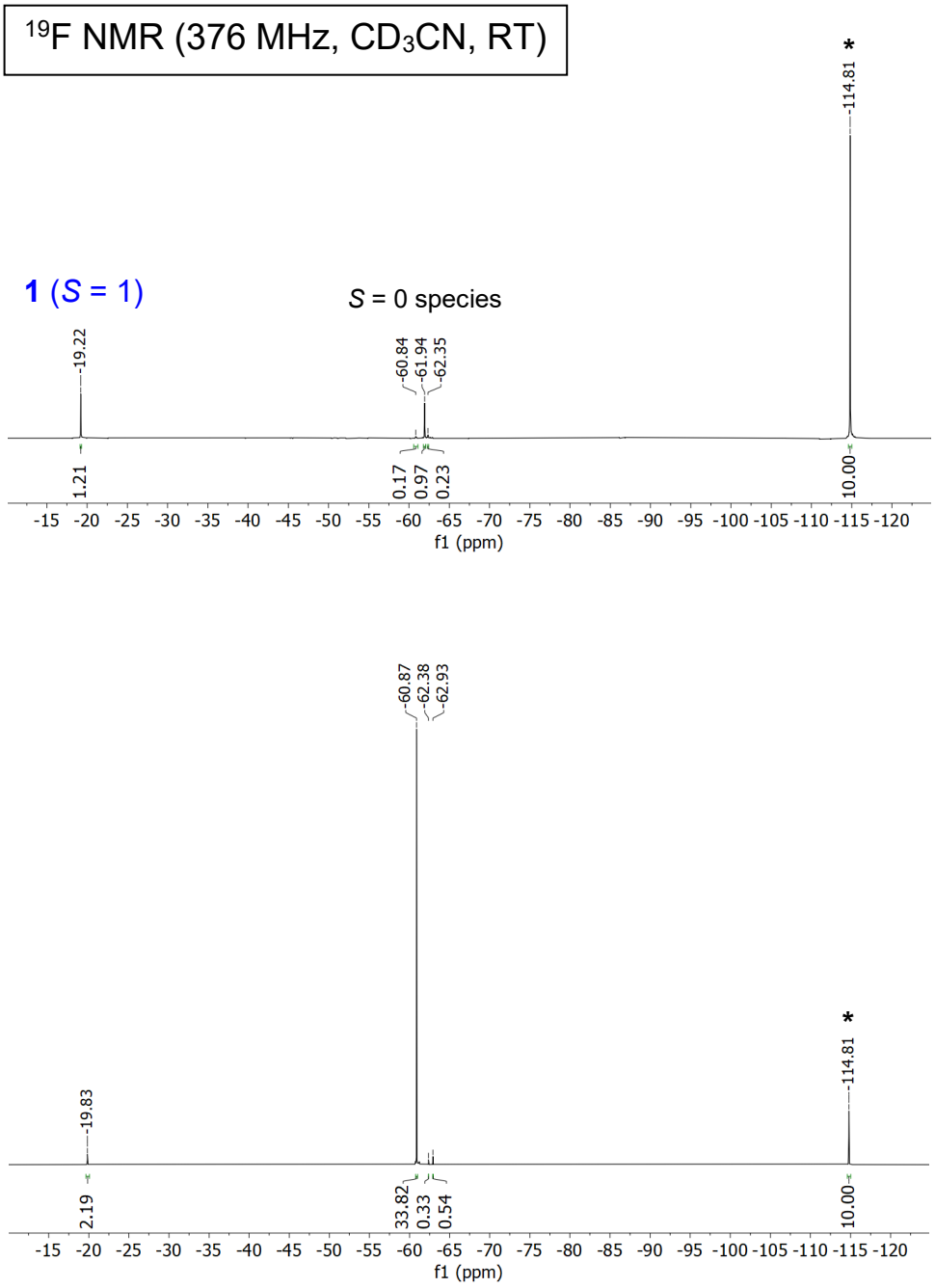

Figure S2.46. ^{19}F NMR of as-isolated **1** (2.0 mM) (*top*) and with 20 mol-equiv (Et_4N)(S-*p*-CF_3-Ph) (*bottom*) in CD_3CN (δ vs. $CFCl_3$). Mononuclear **1** is estimated based on the relative integration of the δ ~-19 ppm peak assigned to **1** (*S* = 1) before and after thiolate addition. Peak at -114.81 ppm is PhF (internal standard; assigned an arbitrary integration value) as indicated with *.

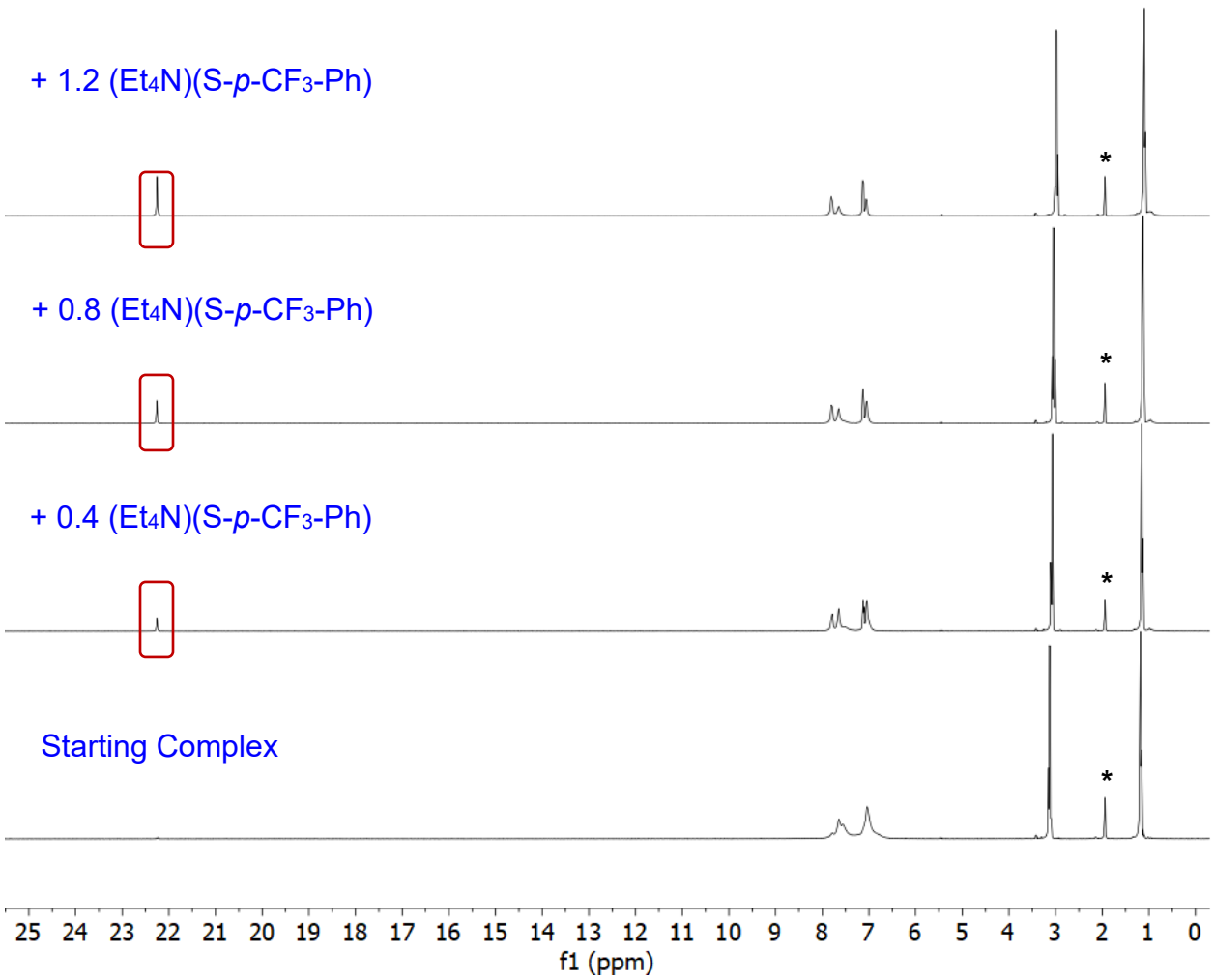

Figure S2.47. ^{1}H NMR of thiolate-bridged Ni complexes, including **3**, with various amounts of (Et_4N)(S-*p*-CF_3-Ph) in CD_3CN at RT (δ vs. protio signal (*) at 1.94 ppm; equiv estimated by assuming mixture is exclusively **3**). Zoom-in of ~7 ppm region is shown in Figure S2.48. *Note*: growth of peak at ~22 ppm (red box) is due to formation of tetrahedral complex **1**.

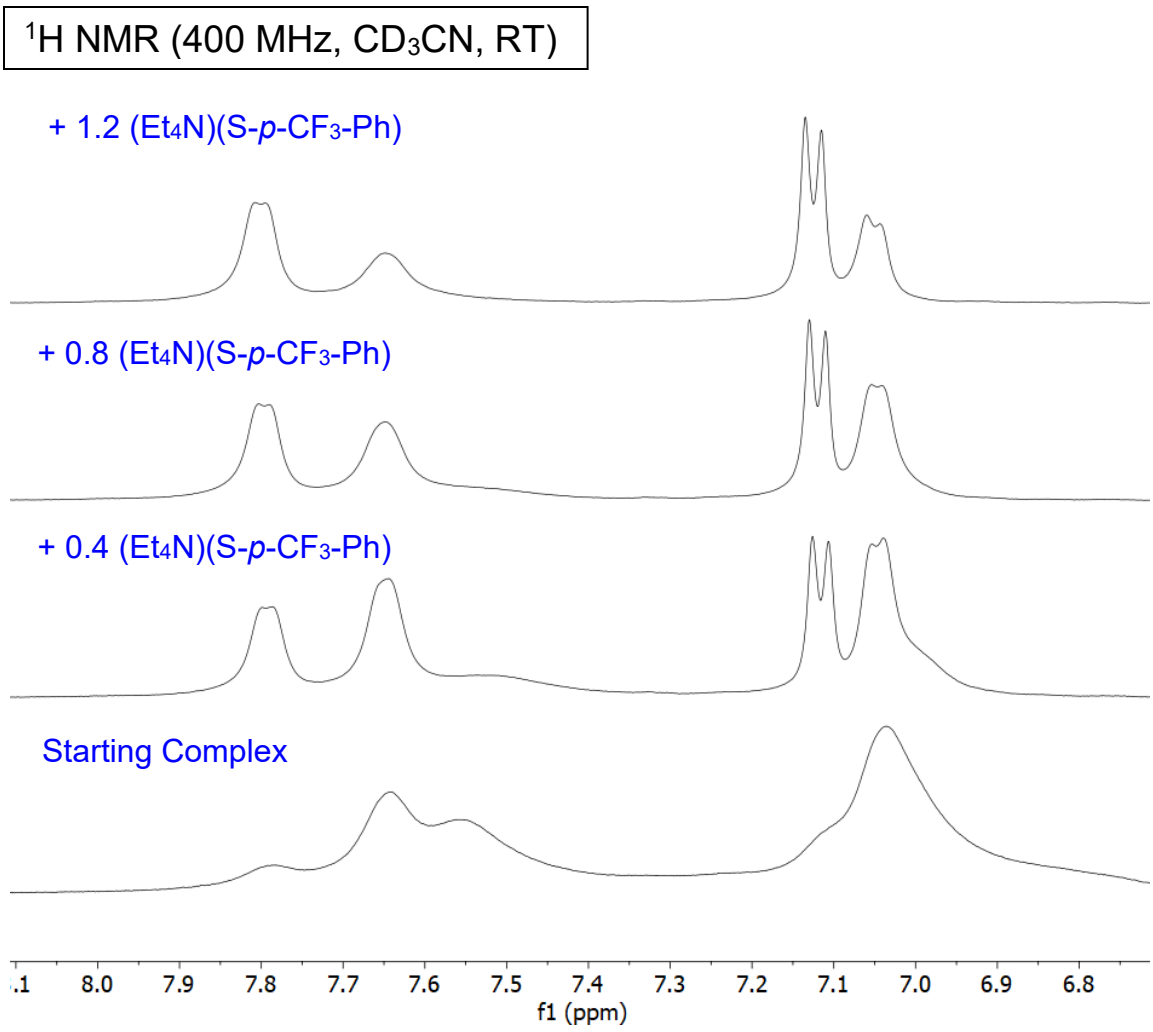

Figure S2.48. Zoom-in of the ~7 ppm region of the ^{1}H NMR of thiolate-bridged Ni complexes, including **3**, with various amounts of (Et_4N)(S-*p*-CF_3-Ph) in CD_3CN at RT (δ vs. protio signal (*) at 1.94 ppm; equiv estimated by assuming mixture is exclusively **3**). Full spectrum is shown in Figure S2.47.

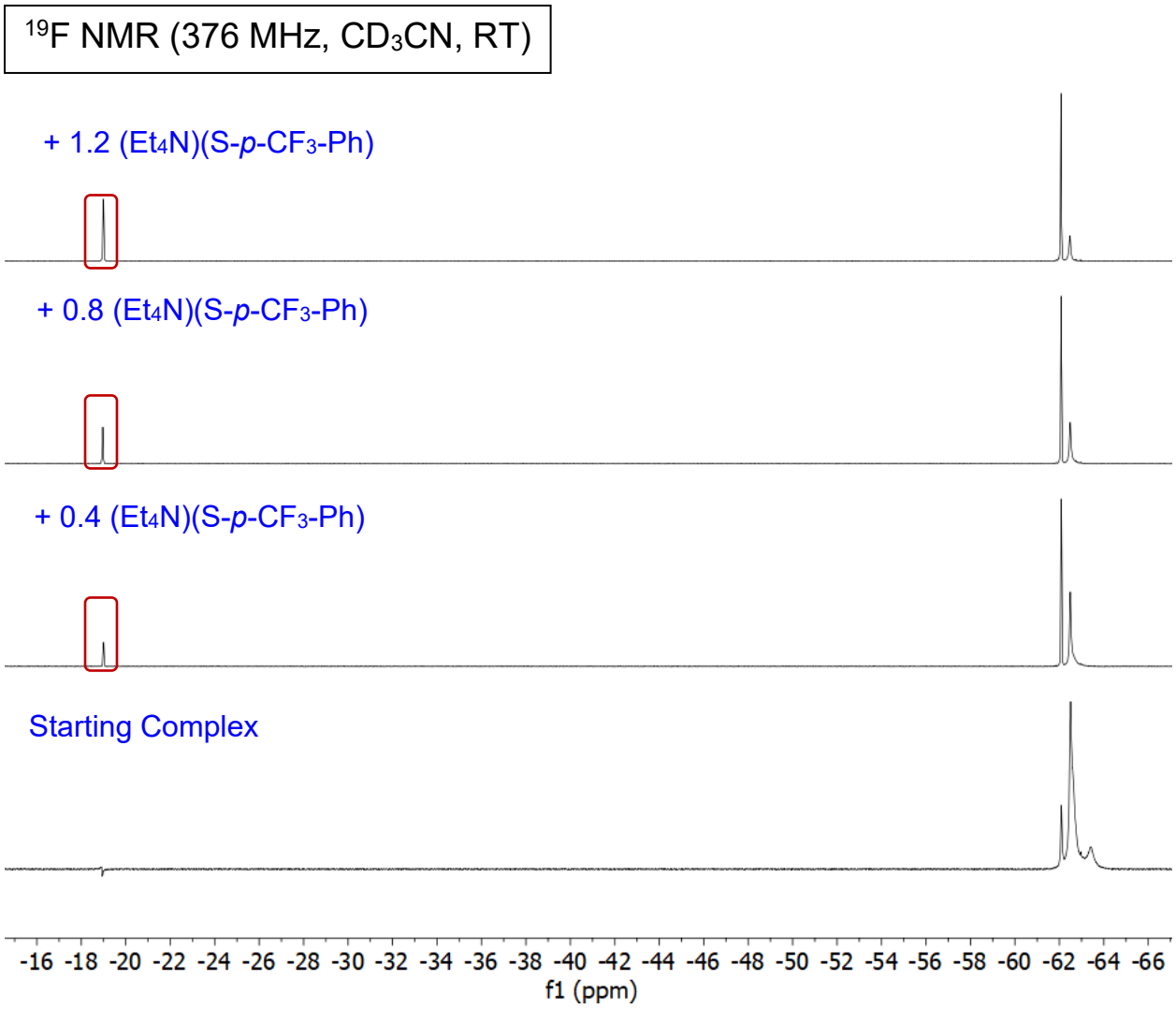

Figure S2.49. ^{19}F NMR of thiolate-bridged Ni complexes, including **3**, with various amounts of (Et_4N)(S-*p*-CF_3-Ph) in CD_3CN at RT (equiv estimated by assuming mixture is exclusively **3**). *Note*: growth of peak at -19 ppm (red box) is due to formation of tetrahedral complex **1**.

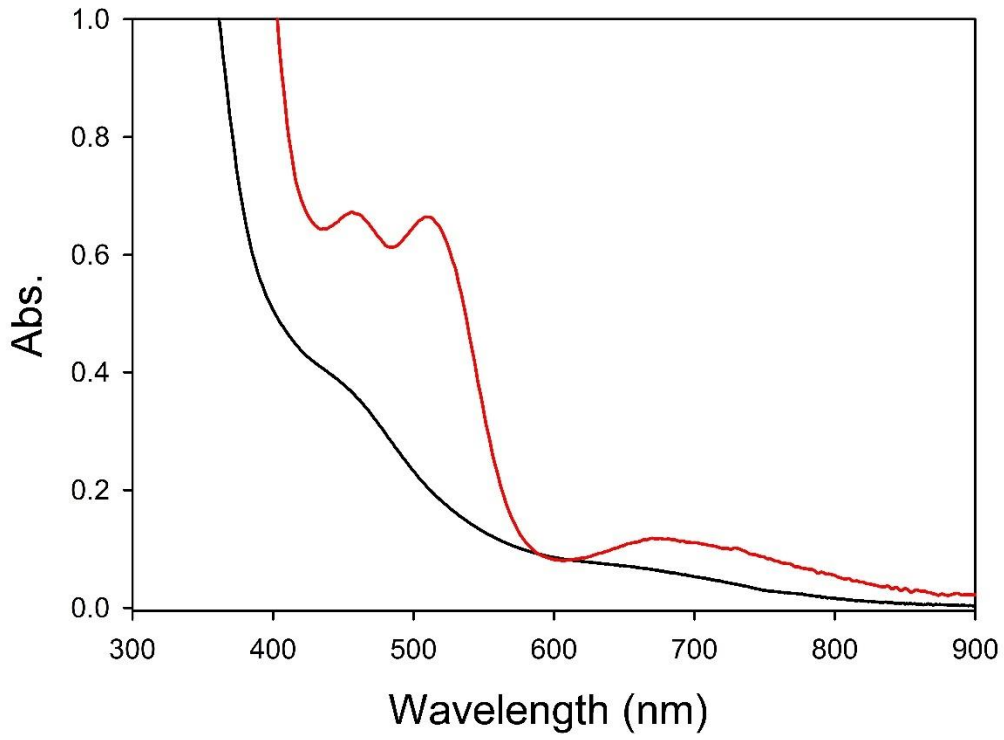

Figure S2.50. Qualitative UV-vis spectrum of thiolate-bridged Ni complexes, including **3** (black trace), and after adding 20 mol-equiv (Et_4N)(S-*p*-CF_3-Ph) (red trace; equiv estimated by assuming mixture is exclusively **3**) in MeCN at 25 °C. *Note*: appearance of CT bands at 460 and 510 nm is due to formation of tetrahedral complex **1**.

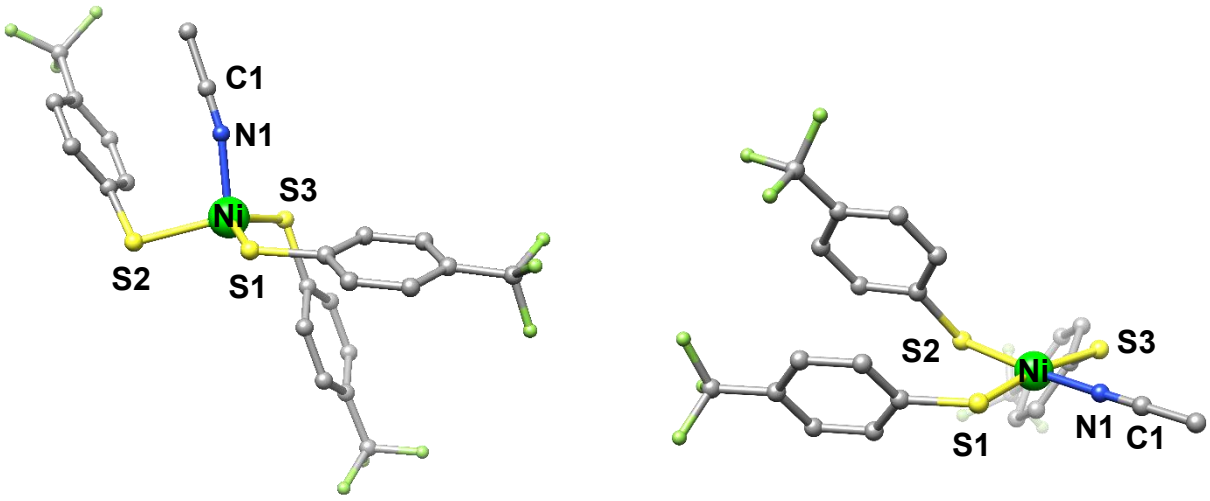

Figure S2.51. Geometry-optimized structures of putative Ni^{2+} intermediates with the general formula [Ni(S-*p*-CF_3-Ph)$_3$(MeCN)]$^-$ (**I**) as the tetrahedral complex anion (S = 1; *left*); and as the square-planar complex anion (S = 0; *right*). B3LYP/def2-TZVPP (CPMC to model MeCN).

Table S2.10. Selected bond distances (Å) and angles (deg) for geometry-optimized structures of putative Ni^{2+} intermediates with the general formula $[Ni(S\text{-}p\text{-}CF_3\text{-}Ph)_3(MeCN)]^-$ (**I**). B3LYP/def2-TZVPP (CPMC to model MeCN).

$[Ni(S\text{-}p\text{-}CF_3\text{-}Ph)_3(MeCN)]^-$	***S* = 1**	***S* = 0**
Atoms	**Bond Distance (Å)**	
$Ni\text{-}S_1$	2.289	2.261
$Ni\text{-}S_2$	2.335	2.208
$Ni\text{-}S_3$	2.289	2.262
$Ni\text{-}N_1$	2.003	1.900
$N_1\text{-}C_1$	1.147	1.148
	Bond Angle (deg)	
$S_1\text{-}Ni\text{-}S_2$	93.5	97.8
$S_1\text{-}Ni\text{-}S_3$	126.5	169.7
$S_1\text{-}Ni\text{-}N_1$	110.5	84.0
$S_2\text{-}Ni\text{-}S_3$	129.0	92.2
$S_2\text{-}Ni\text{-}N_1$	99.5	176.4
$S_3\text{-}Ni\text{-}N_1$	94.1	86.1
$Ni\text{-}N_1\text{-}C_1$	166.1	179.0
	τ_4	
	0.74	0.08

Table S2.11. Final single point energies from geometry-optimization (B3LYP/def2-TZVPP) with the CPCMC model for MeCN of selected complexes.

Compound	***S***	**Final Single Point Energy (E_h)**
MeCN	0	-132.657217321421
***p*-CF_3-PhS$^-$**	0	-966.696932471075
$[Ni(S\text{-}p\text{-}CF_3\text{-}Ph)_4]^{2-}$ (tetrahedral dianion of **1**)	1	-5374.96479120396
$[Ni(S\text{-}p\text{-}CF_3\text{-}Ph)_4]^{2-}$ (planar dianion of **1**)	0	-5374.9594861337
$[Ni(S\text{-}p\text{-}CF_3\text{-}Ph)_3(MeCN)]^-$ (tetrahedral anion of **I**)	1	-4540.90388629218
$[Ni(S\text{-}p\text{-}CF_3\text{-}Ph)_3(MeCN)]^-$ (planar anion of **I**)	0	-4540.89966773846
$[Ni_2(S\text{-}p\text{-}CF_3\text{-}Ph)_6]^{2-}$ (planar dianion of **3**)	0	-8816.5207723853

Table S2.12. Gibbs free energies from frequency calculations (B3LYP/def2-TZVPP) with the CPCMC model for MeCN of selected complexes.

Compound	*S*	Gibbs Free Energy (E_h)
MeCN	0	-132.7254553
***p*-CF_3-PhS^-**	0	-966.928222
$[Ni(S\text{-}p\text{-}CF_3\text{-}Ph)_4]^{2-}$ (tetrahedral dianion of **1**)	1	-5375.809771
$[Ni(S\text{-}p\text{-}CF_3\text{-}Ph)_4]^{2-}$ (planar dianion of **1**)	0	-5375.787262
$[Ni(S\text{-}p\text{-}CF_3\text{-}Ph)_3(MeCN)]^-$ (tetrahedral anion of **I**)	1	-4541.590423
$[Ni(S\text{-}p\text{-}CF_3\text{-}Ph)_3(MeCN)]^-$ (planar anion of **I**)	0	-4541.586544
$[Ni_2(S\text{-}p\text{-}CF_3\text{-}Ph)_6]^{2-}$ (planar dianion of **3**)	0	-8817.751314

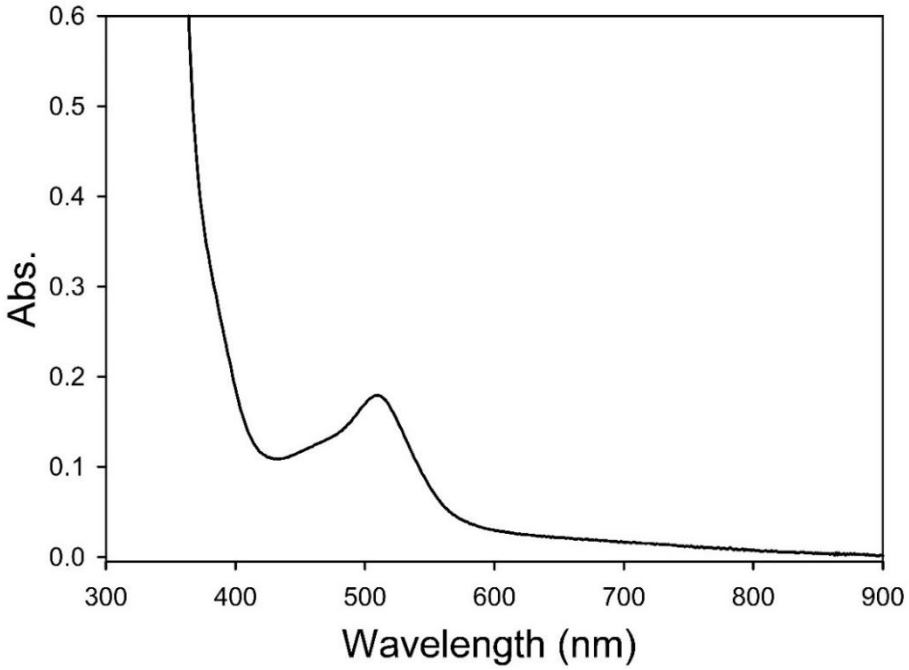

Figure S2.52. Qualitative UV-vis spectrum of the insoluble material isolated from the reaction of complex **1** with HBF_4•Et_2O (1:1) in MeCN. Spectrum recorded in DMSO at 25 °C.

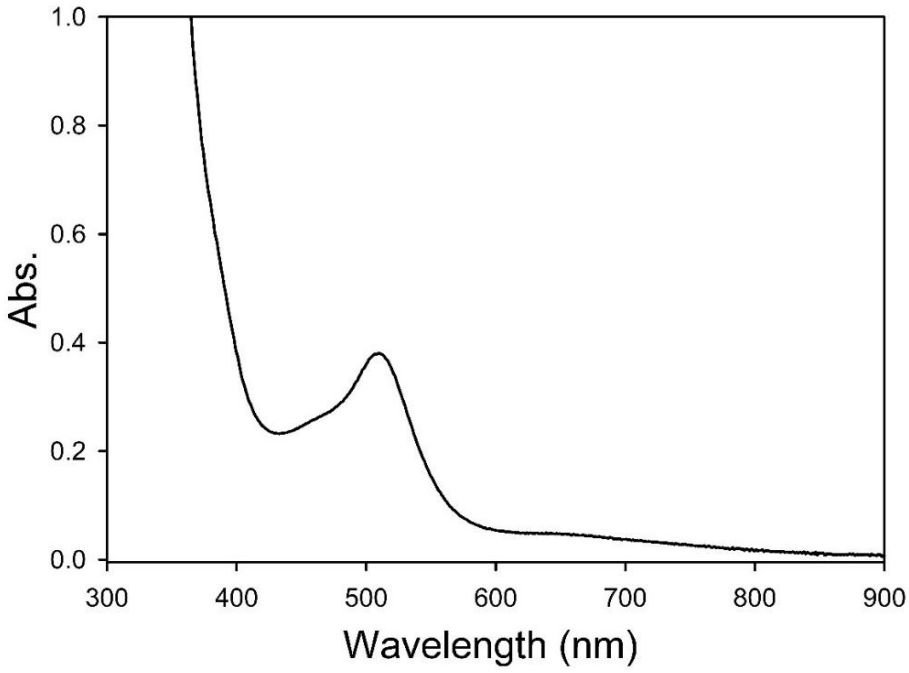

Figure S2.53. Qualitative UV-vis spectrum of the insoluble material isolated from the reaction of complex **1** with AcOH (1:25) in MeCN. Spectrum recorded in DMSO at 25 °C.

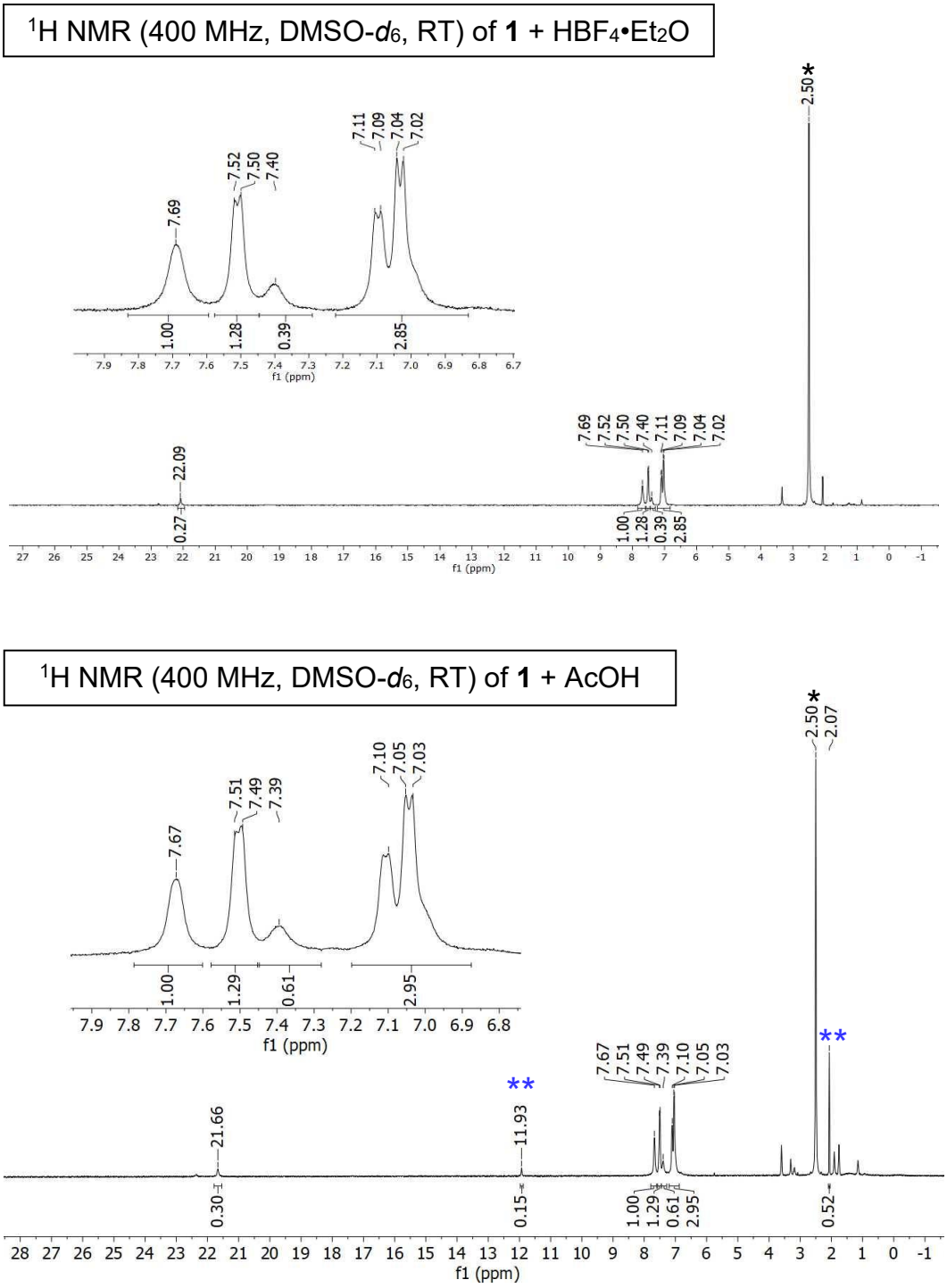

Figure S2.54. ^{1}H NMR spectrum of the insoluble material isolated from the reaction of complex **1** with HBF_4•Et_2O (1:1) (*top*) or **1** with AcOH (1:25) (*bottom*) in MeCN. Spectrum recorded in DMSO-d_6 at RT (δ vs. protio signal (*) at 2.50 ppm; residual protio acetic acid is observed (**) at 2.07 and 11.93 ppm in the bottom spectrum). *Insets*: Zoom-in of aromatic-H region.

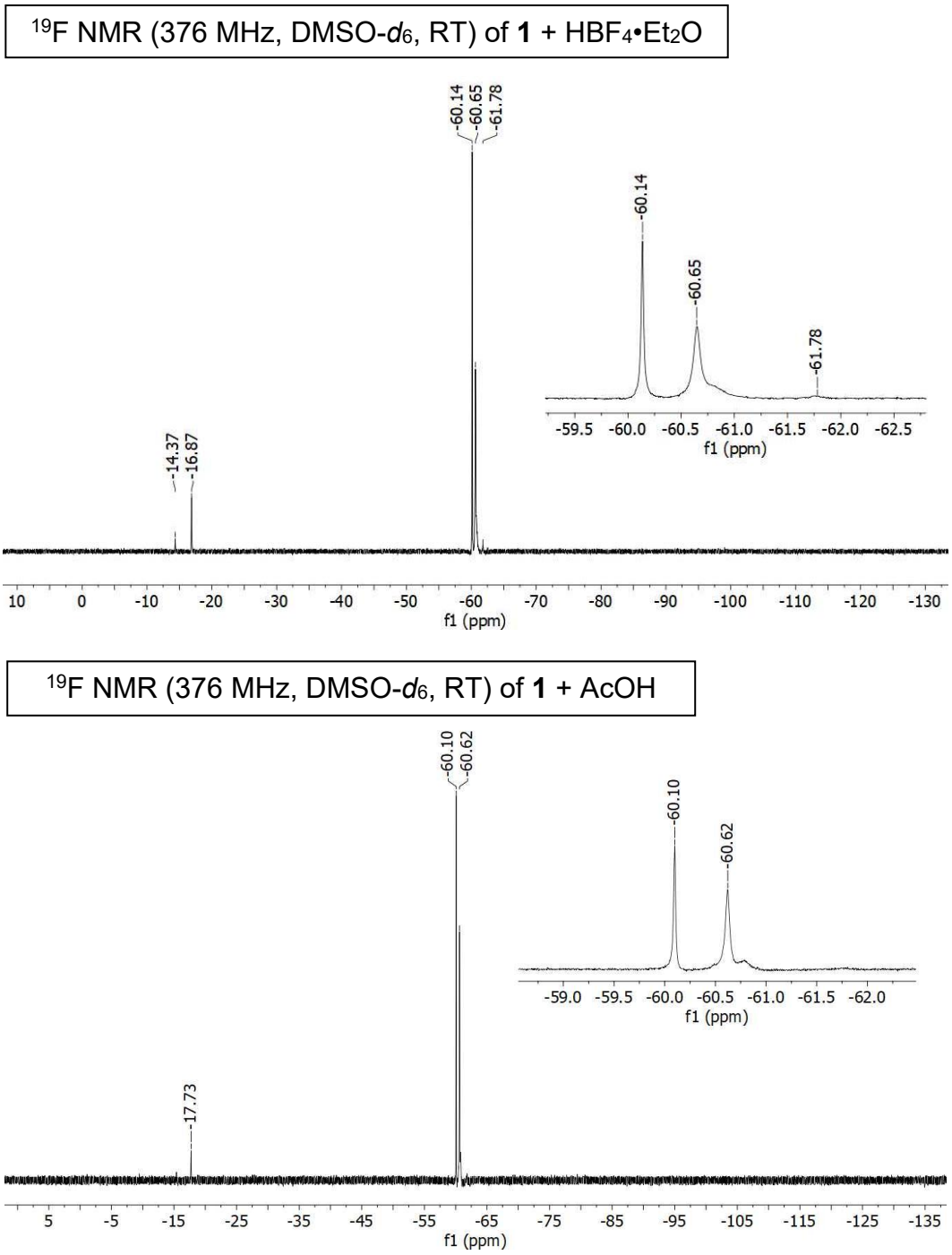

Figure S2.55. ^{19}F NMR spectrum of the insoluble material isolated from the reaction of complex **1** with HBF_4•Et_2O (1:1) (*top*) or **1** with AcOH (1:25) (*bottom*) in MeCN. Spectrum recorded in DMSO-d_6 at RT (δ vs. $CFCl_3$). *Insets*: Zoom-in of -60 ppm region.

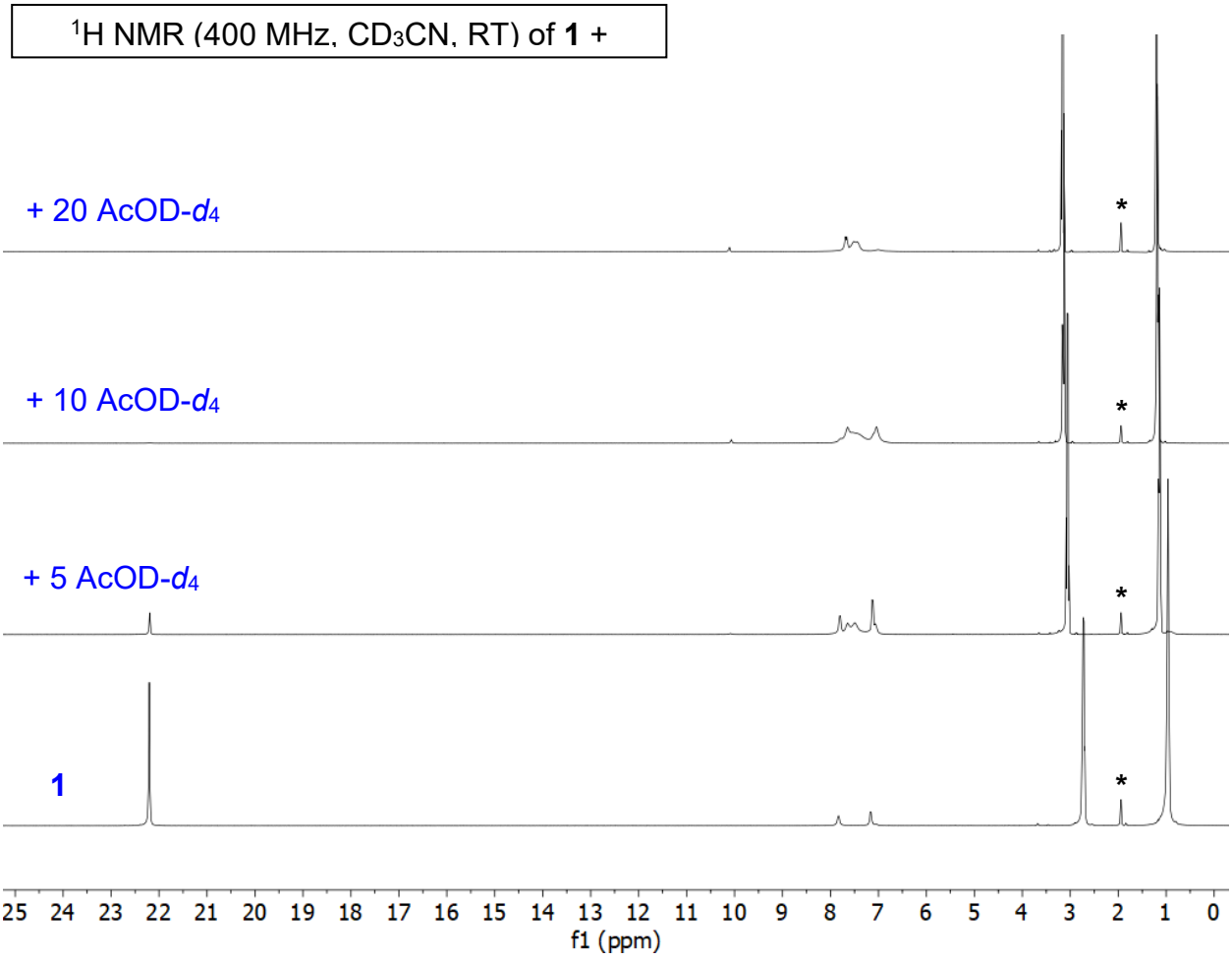

Figure S2.56. ^{1}H NMR monitor of the addition of AcOD-d_4 to complex **1** in CD_3CN at RT (δ vs. protio signal (*) at 1.94 ppm). Zoom-in of aromatic region shown in Figure S2.57.

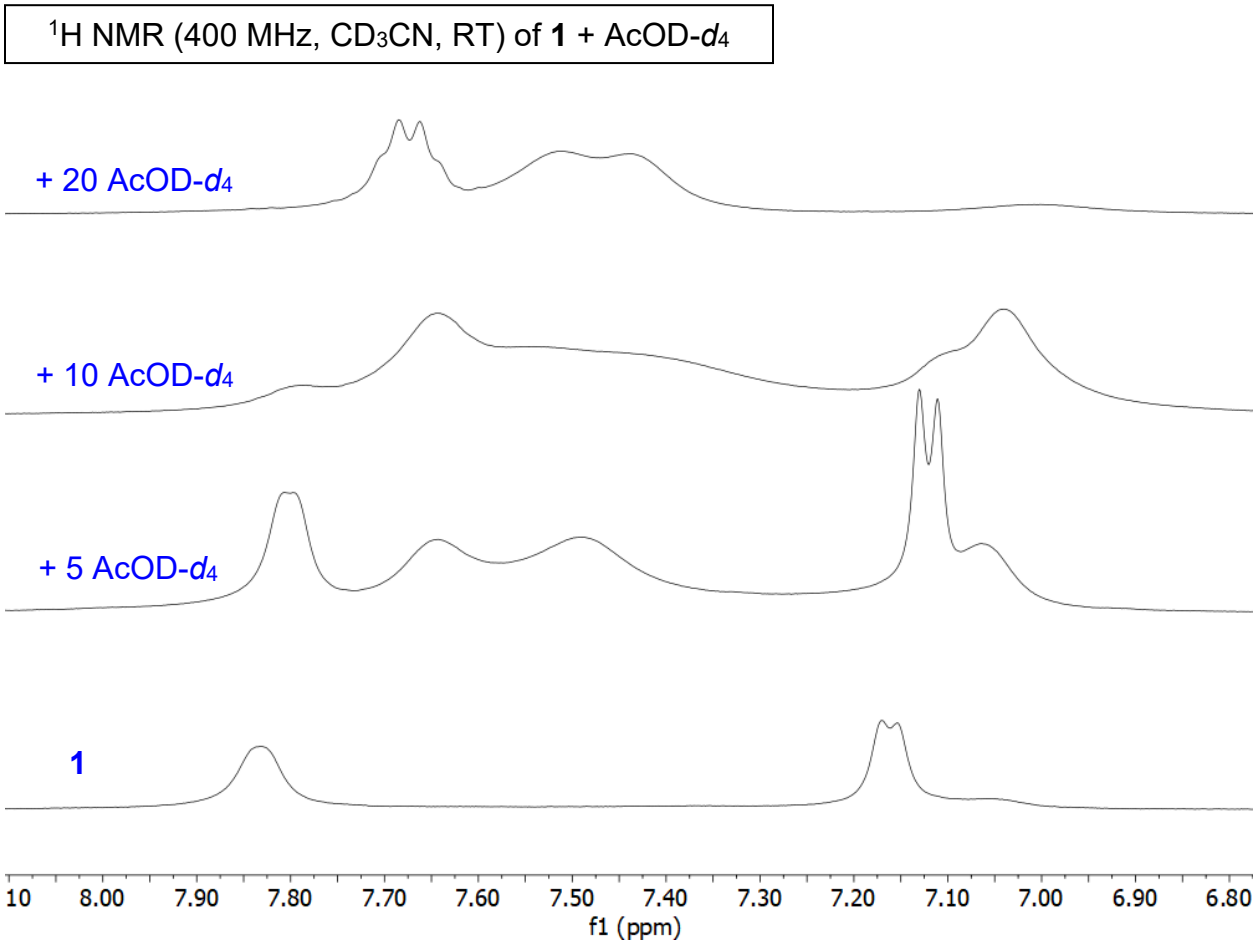

Figure S2.57. Zoom-in of the aromatic region of the ^{1}H NMR monitor of the addition of AcOD-d_4 to complex **1** in CD_3CN at RT (δ vs. protio signal (*) at 1.94 ppm). Full spectrum in Figure S2.56.

Table S2.13. Integration of peak for **1** at ~20 ppm and aromatic-H region obtained from the addition of AcOD-d_4 into CD_3CN solutions of **1** (see Figures S2.56-57). Integrations are relative to the -CH_2- peak at ~3 ppm from the Et_4N^+ counter ion.

Equivs AcOD-d_4	Integration (~20 ppm)	Integration (6 - 8 ppm)
0	6.08	2.52
5	3.98	7.67
10	1.09	13.99
20	0.05	16.06

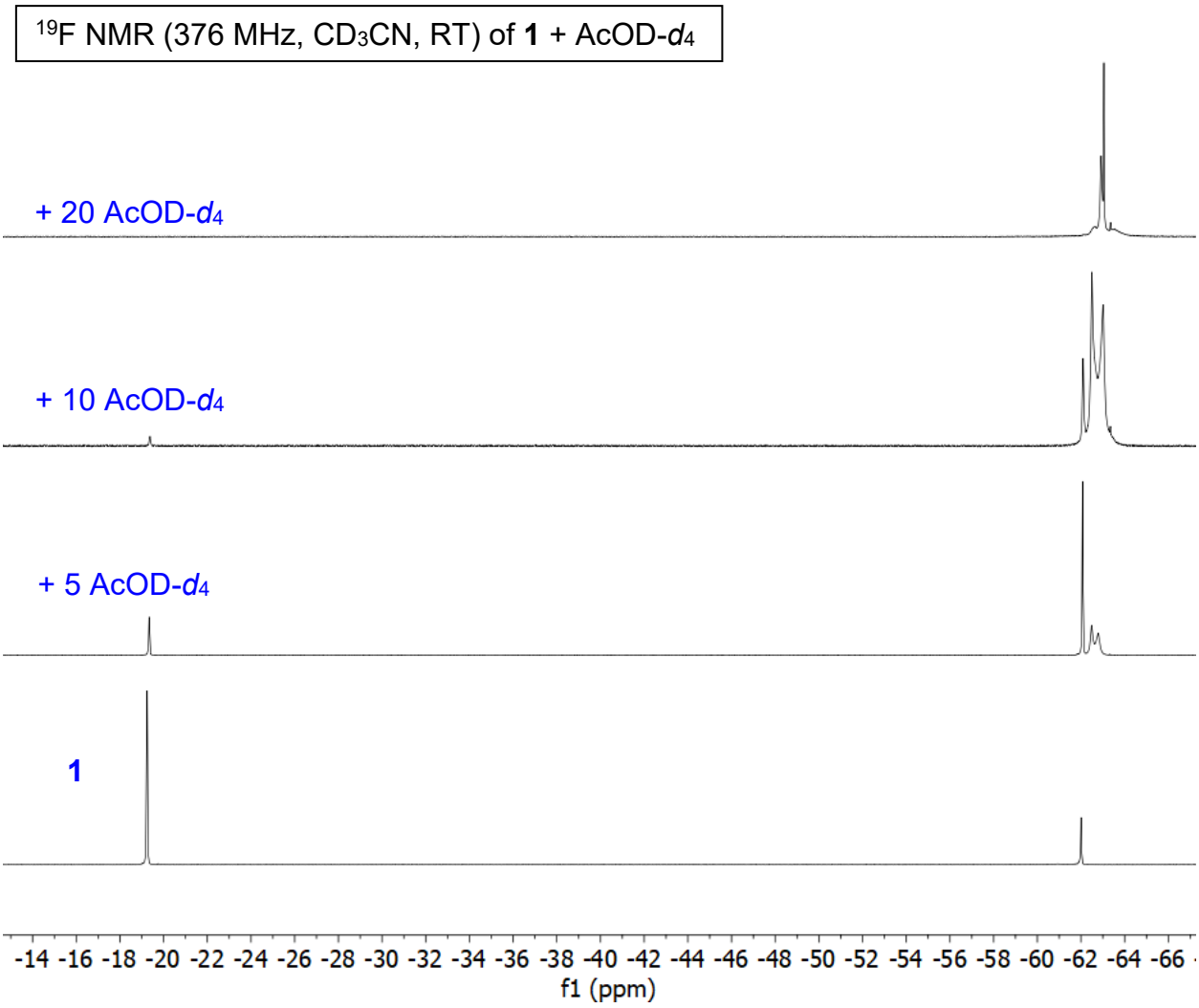

Figure S2.58. ^{19}F NMR monitor of the addition of AcOD-d_4 to complex **1** in CD_3CN at RT (δ vs. $CFCl_3$).

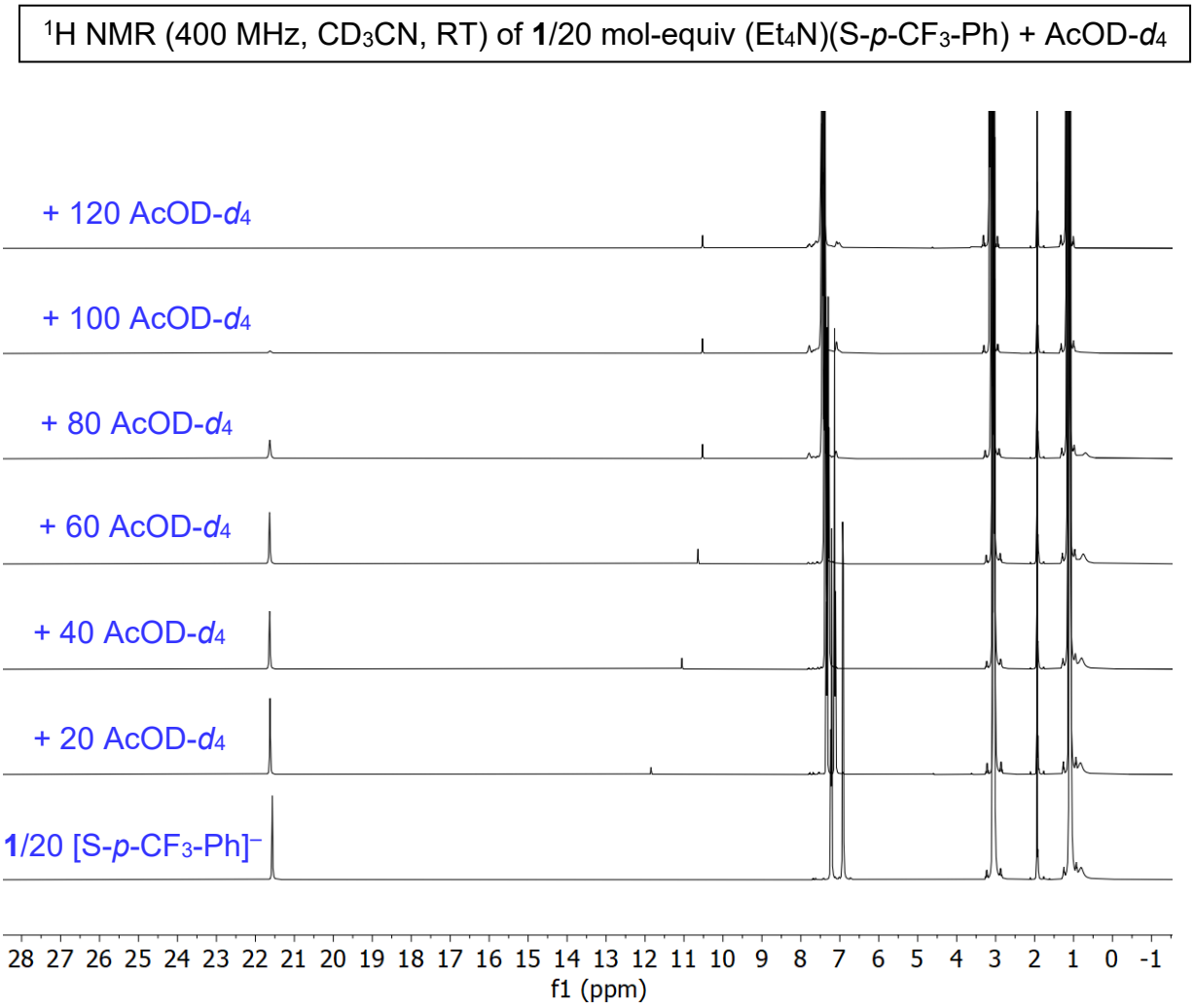

Figure S2.59. ^{1}H NMR monitor of the addition of AcOD-d_4 to complex **1**/20 mol-equiv (Et_4N)(S-*p*-CF_3-Ph) in CD_3CN at RT (δ vs. protio signal (*) at 1.94 ppm). *Note*: Peak at ~20 ppm, originating from **1**, remains even after addition of 20-80 equiv of AcOD-d_4. See Table S2.14 for quantification. Zoom-in of aromatic region shown in Figure S2.60.

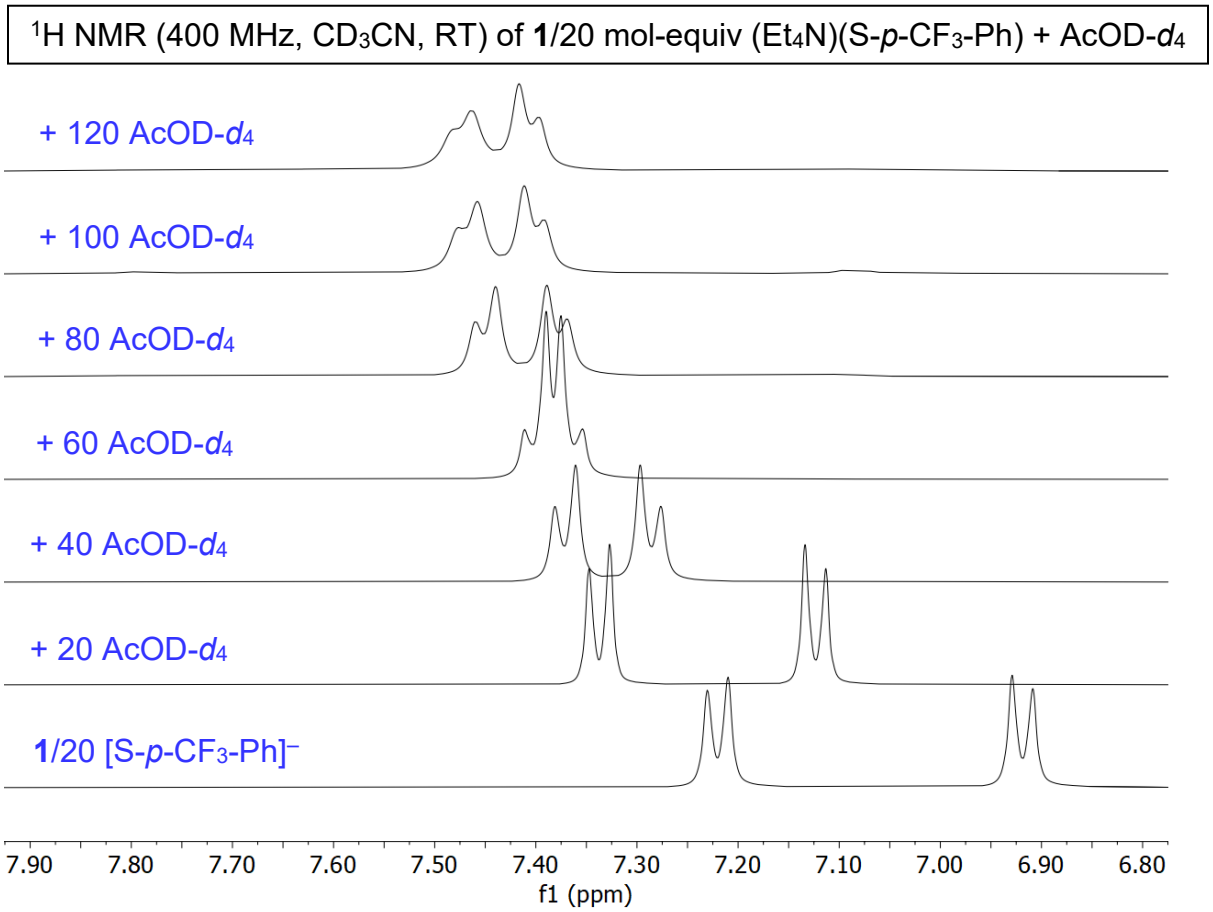

Figure S2.60. Zoom-in of the aromatic region of the ^{1}H NMR monitor of the addition of AcOD-d_4 to complex **1**/20 mol-equiv (Et_4N)(S-*p*-CF_3-Ph) in CD_3CN at RT. See Table S14 for quantification. Full spectrum in Figure S59.

Table S2.14. Integration of peak for **1** at ~20 ppm and aromatic-H region obtained from the addition of AcOD-d_4 into CD_3CN solutions of **1**/20 mol-equiv (Et_4N)(S-*p*-CF_3-Ph) (see Figures S59-S60). Integrations are relative to the -CH_2- peak at ~3 ppm from the Et_4N^+ counter ion.

Equivs AcOD-d_4	Integration (~20 ppm)	Integration (6-8 ppm)
0	7.59	69.46
20	7.57	67.09
40	7.56	71.92
60	7.18	73.24
80	4.62	75.31
100	1.32	78.64
120	0.19	80.36

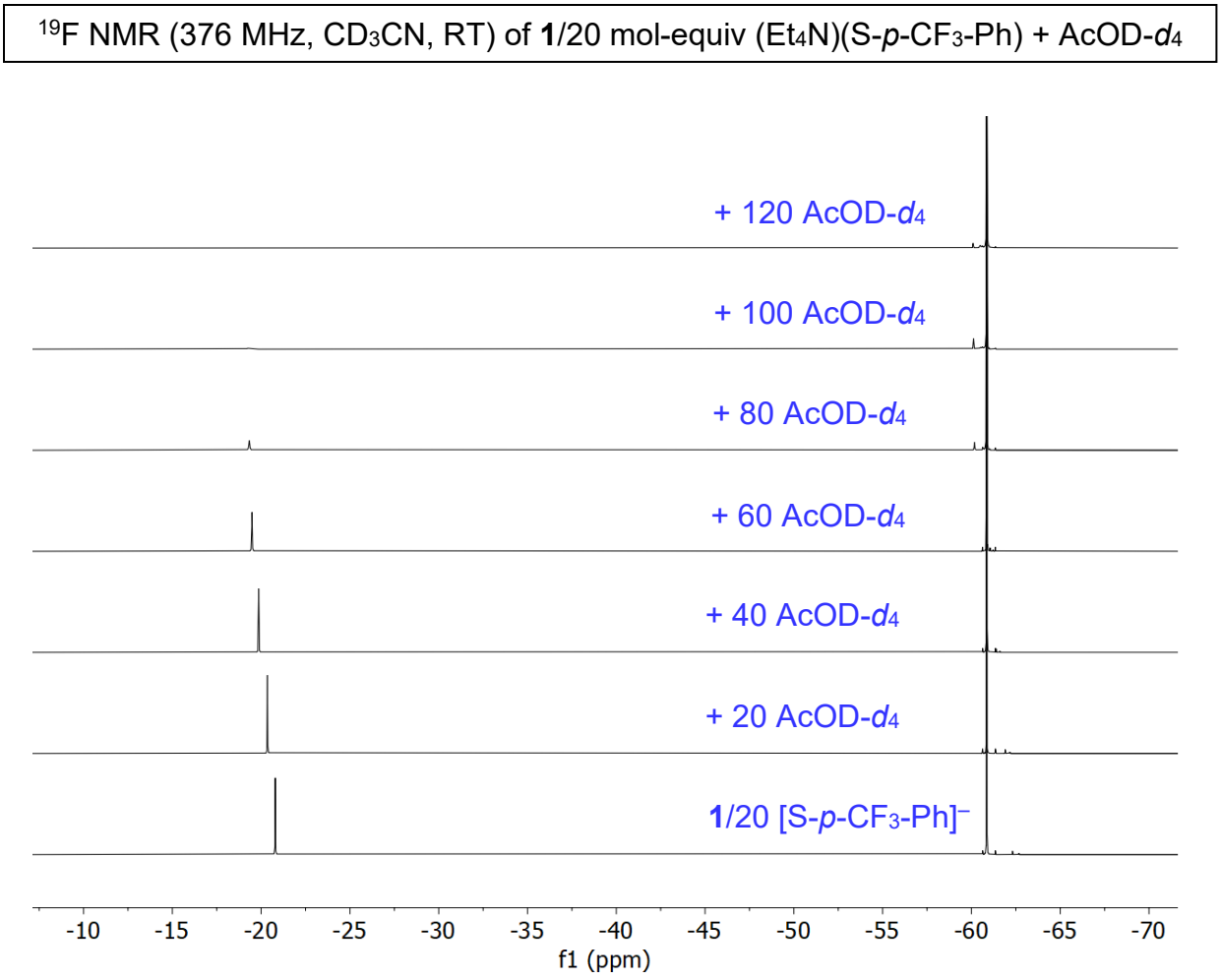

Figure S2.61. ^{19}F NMR monitor of the addition of AcOD-*d*$_4$ to complex **1**/20 mol-equiv (Et_4N)(S-*p*-CF_3-Ph) in CD_3CN at RT (δ vs. $CFCl_3$). *Note*: Peak at -20 ppm, originating from **1**, remains even after addition of 20-80 equiv of AcOD-*d*$_4$.

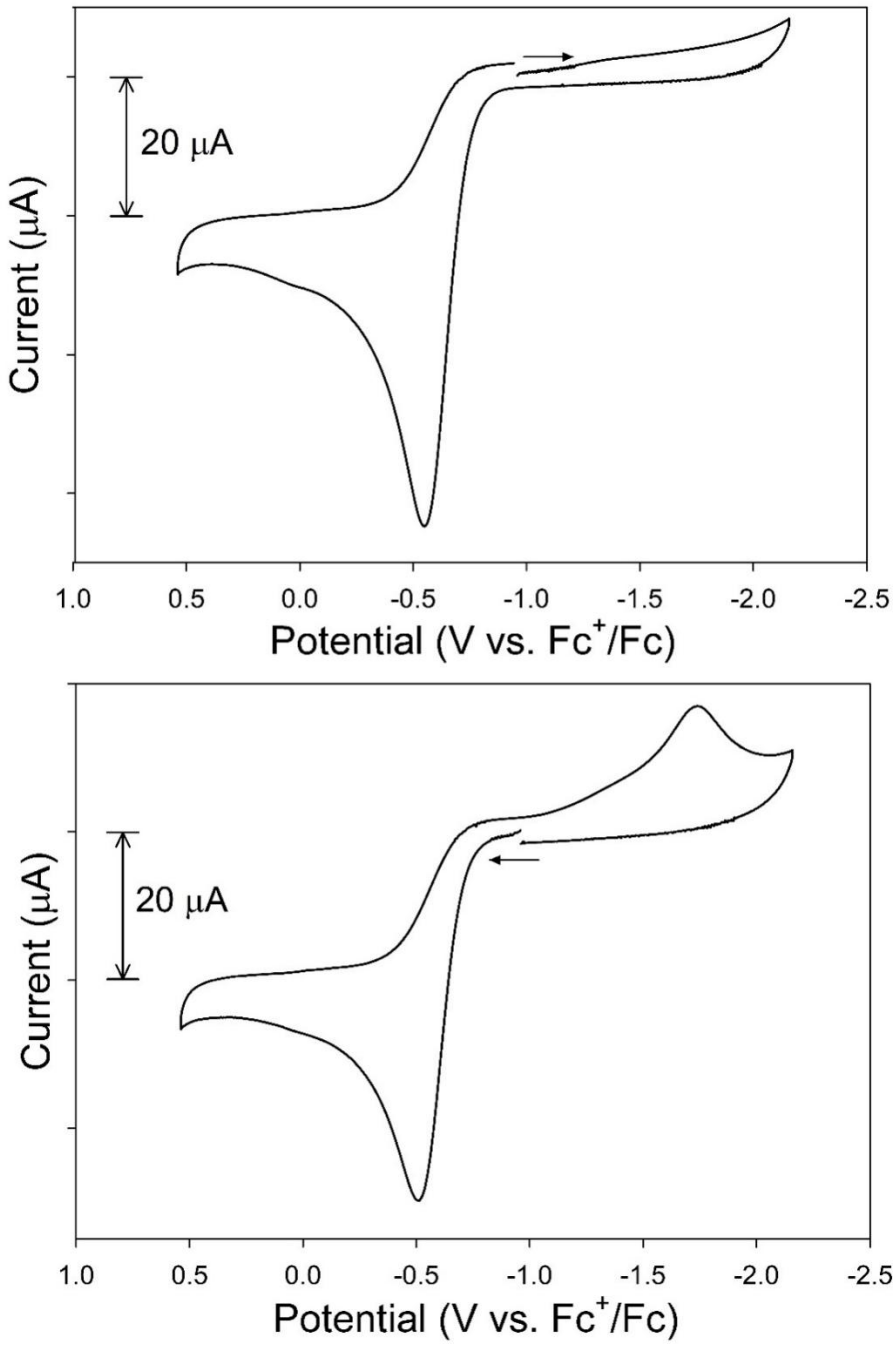

Figure S2.62. CV of $(Et_4N)(S\text{-}p\text{-}CF_3\text{-}Ph)$ in MeCN at RT (0.25 M $^nBu_4NPF_6$ supporting electrolyte, GC working electrode, 100 mV/s scan rate). Arrow shows direction of scan.

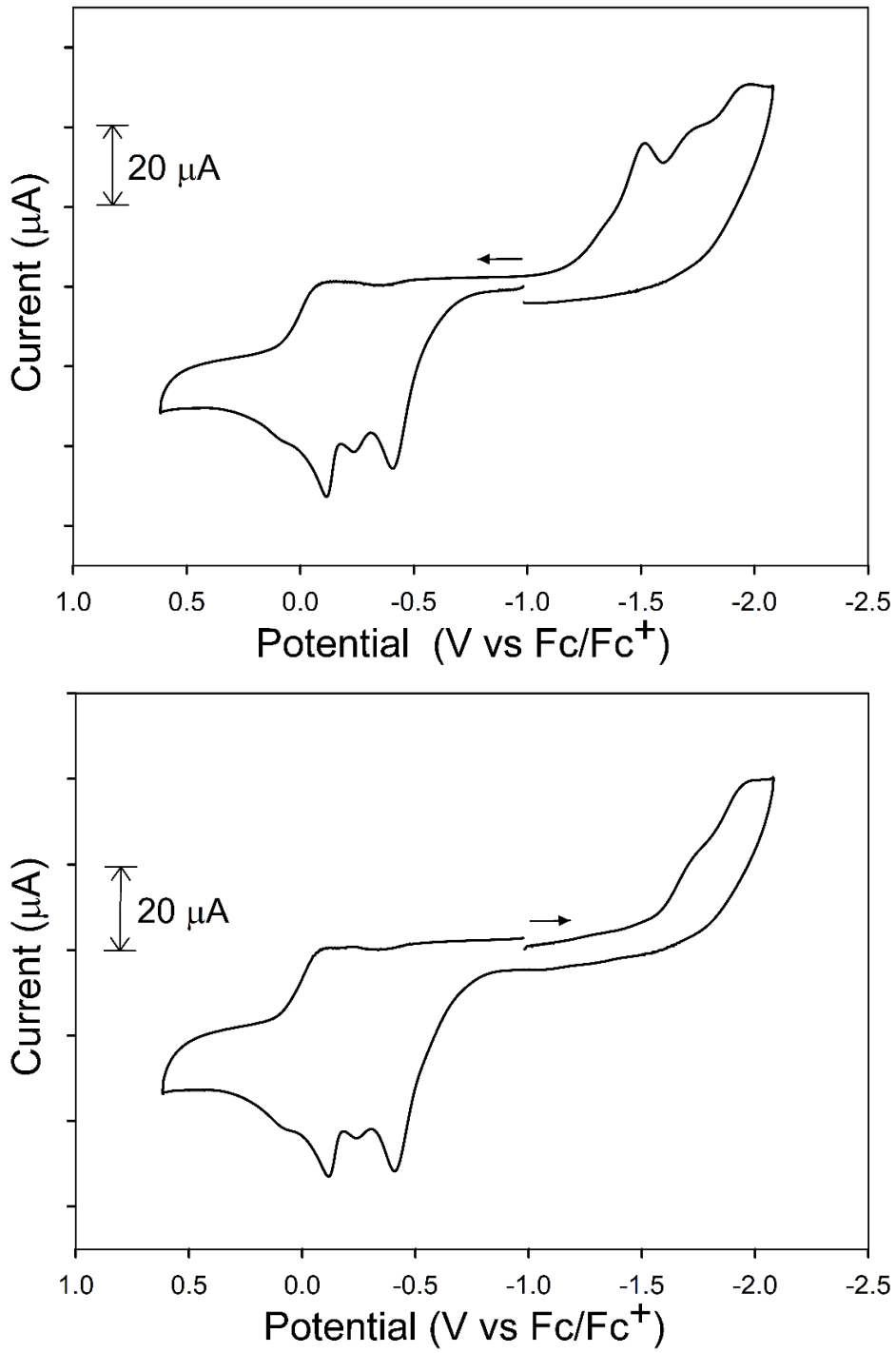

Figure S2.63. CV of $(Et_4N)_2[Ni(S\text{-}p\text{-}CF_3\text{-}Ph)_4]$ (**1**) in MeCN at RT (0.25 M $^nBu_4NPF_6$ supporting electrolyte, GC working electrode, 100 mV/s scan rate). Arrow shows direction of scan.

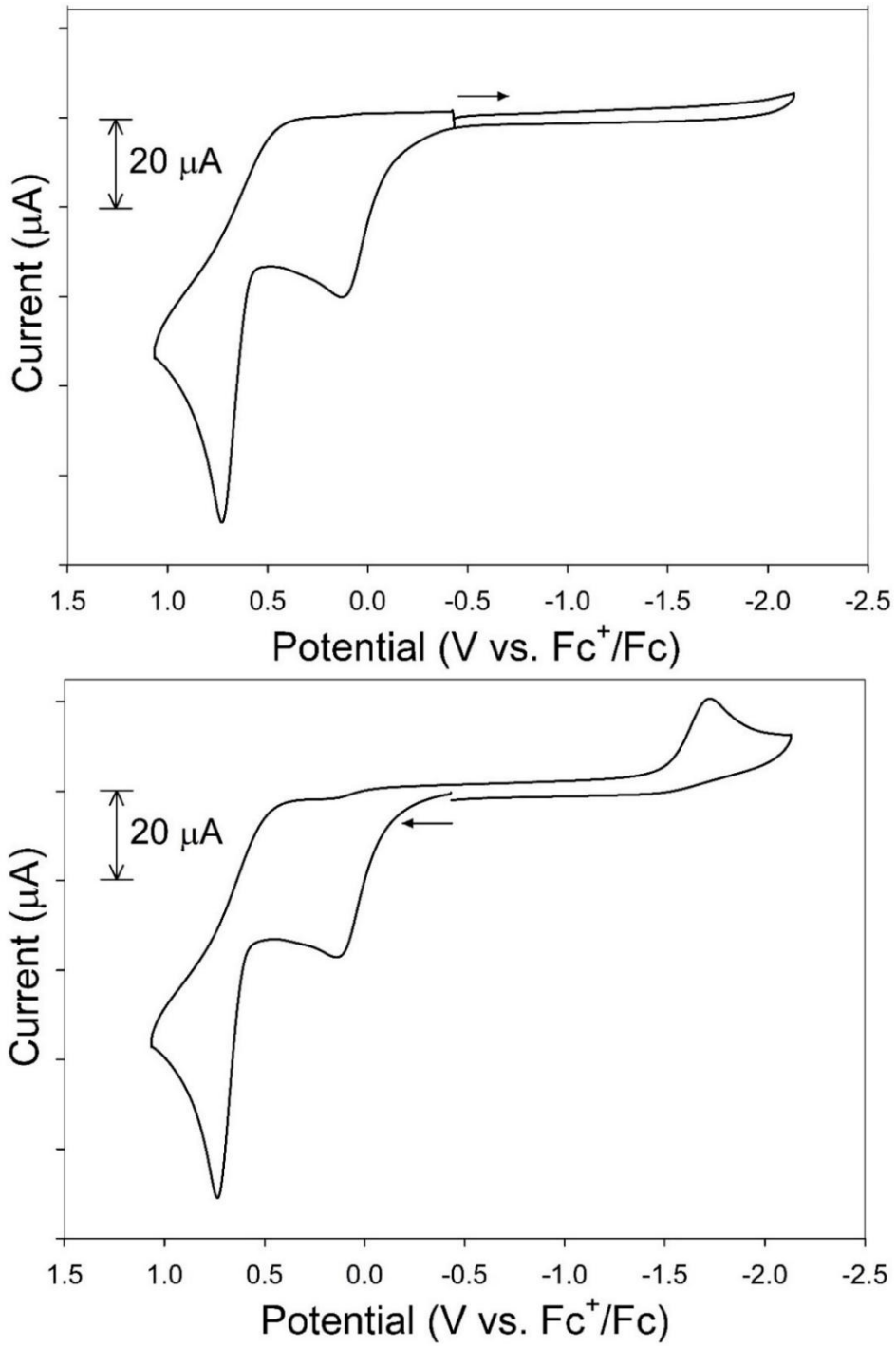

Figure S2.64. CV of $(Et_4N)_2[Zn(S\text{-}p\text{-}CF_3\text{-}Ph)_4]$ (**2**) in MeCN at RT (0.25 M $^nBu_4NPF_6$ supporting electrolyte, GC working electrode, 100 mV/s scan rate). Arrow shows direction of scan.

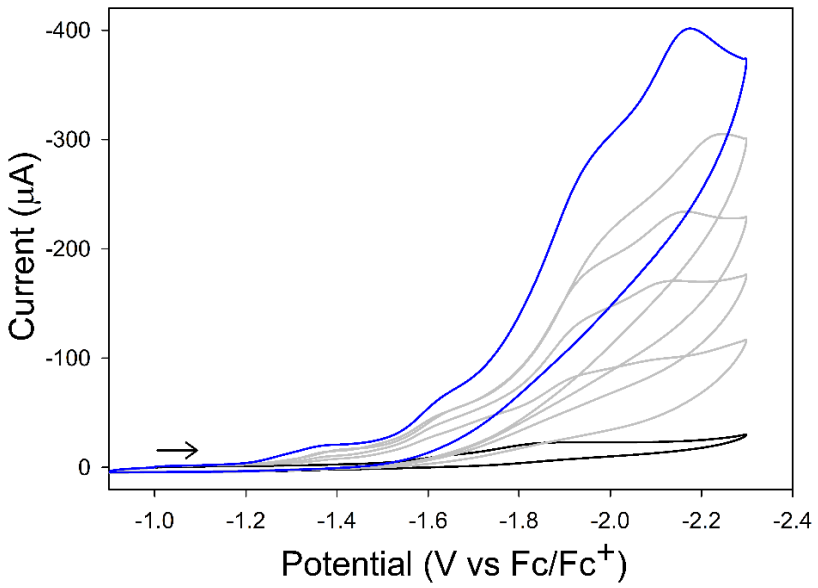

Figure S2.65. CV of complex **1** (1.87 mM; black trace) and after the addition of AcOH in 4 mol-equiv increments (gray traces) up to a final of 20 mol-equiv (blue trace) in MeCN at RT. Conditions: 0.25 M $^{n}Bu_4NPF_6$ supporting electrolyte, GC working electrode, 100 mV/s scan rate. Arrow displays the scan direction.

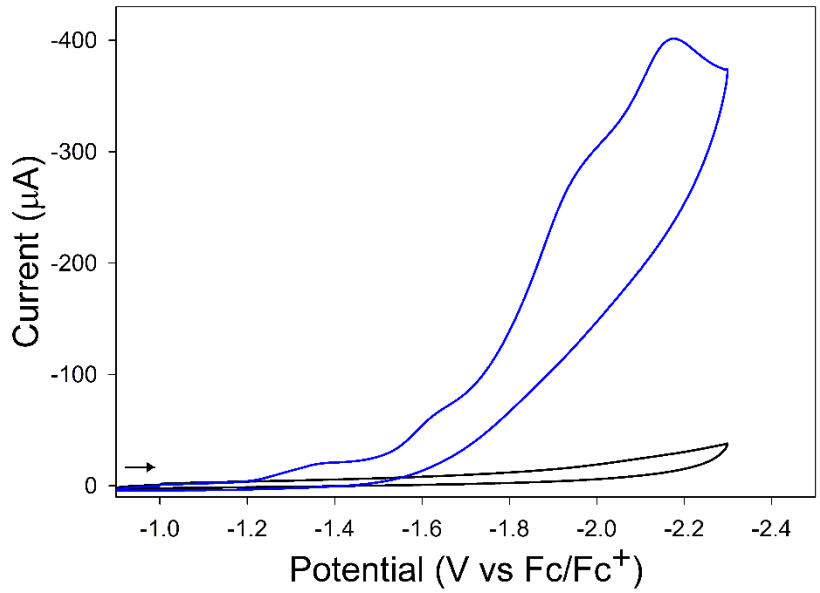

Figure S2.66. CV of complex **1** (1.87 mM) with 20 mol-equiv of AcOH (blue trace) in MeCN at RT, and subsequent CV after the rinse test of the working electrode and immersion into an electrochemical cell containing electrolyte/solvent and AcOH at identical concentrations (black trace). Conditions: 0.25 M $^{n}Bu_4NPF_6$ supporting electrolyte, GC working electrode, 100 mV/s scan rate. Arrow displays the scan direction.

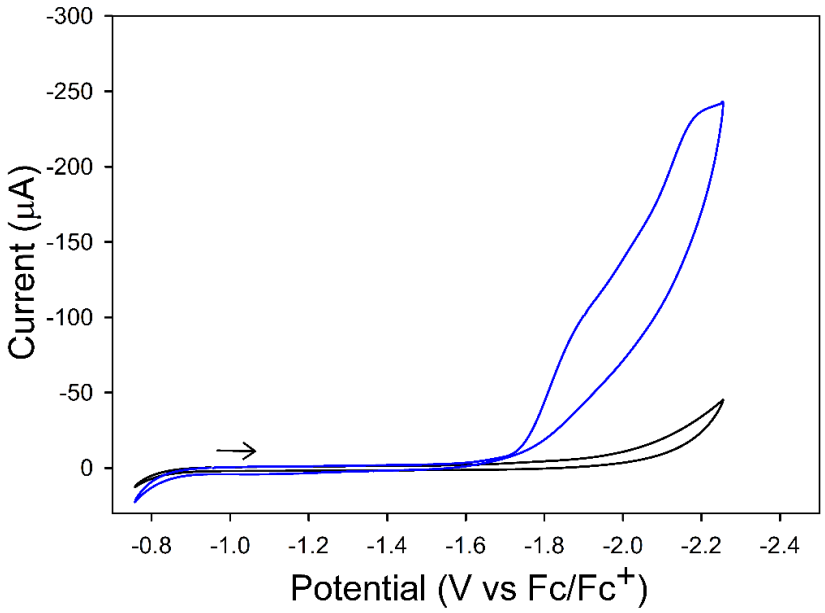

Figure S2.67. CV of complex **1** (1.89 mM) containing 20 mol-equiv of (Et_4N)(S-*p*-CF_3-Ph) and 20 mol-equiv of AcOH (blue trace) in MeCN at RT. Subsequent CV after rinse test of the working electrode and immersion into an electrochemical cell containing electrolyte/solvent and 20 mol-equiv each of (Et_4N)(S-*p*-CF_3-Ph) and AcOH (black trace). Conditions: 0.25 M ^{n}Bu$_4$NPF$_6$ supporting electrolyte, GC working electrode, 100 mV/s scan rate. Arrow displays the scan direction.

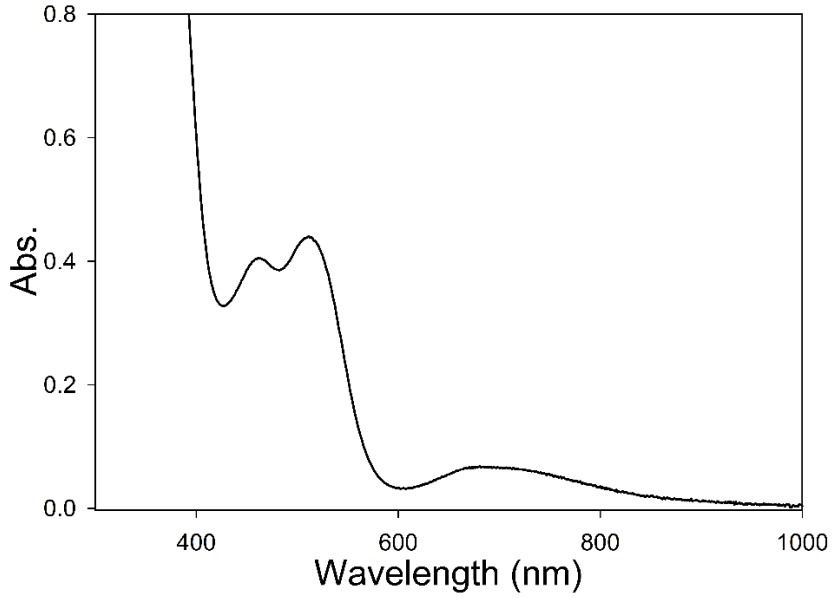

Figure S2.68. UV-vis spectrum of a 150 µL aliquot taken from the electrochemical cell containing **1**/20 mol-equiv (Et_4N)(S-*p*-CF_3-Ph) and 20 mol-equiv AcOH in MeCN at RT.

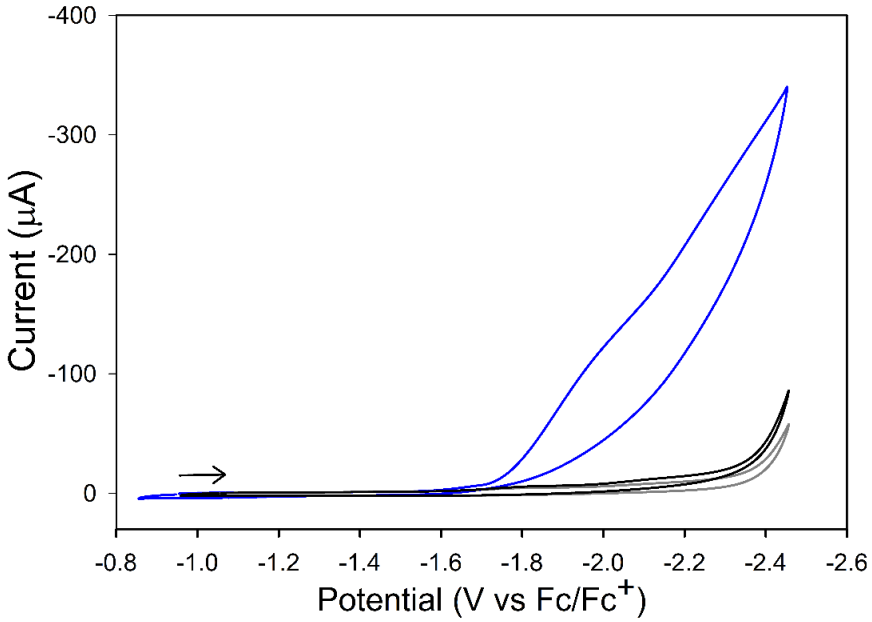

Figure S2.69. CV of compounds in the presence of 20 mol-equiv AcOH in MeCN at RT. Black trace = 38 mM solution of (Et_4N)(S-*p*-CF_3-Ph). Grey trace = 1.9 mM solution of Zn complex **2** with 20 mol-equiv of (Et_4N)(S-*p*-CF_3-Ph). Blue trace = 1.9 mM solution of Ni complex **1** with 20 mol-equiv of (Et_4N)(S-*p*-CF_3-Ph). Conditions: 0.25 M $^nBu_4NPF_6$ supporting electrolyte, GC working electrode, 100 mV/s scan rate. Arrow displays the scan direction.

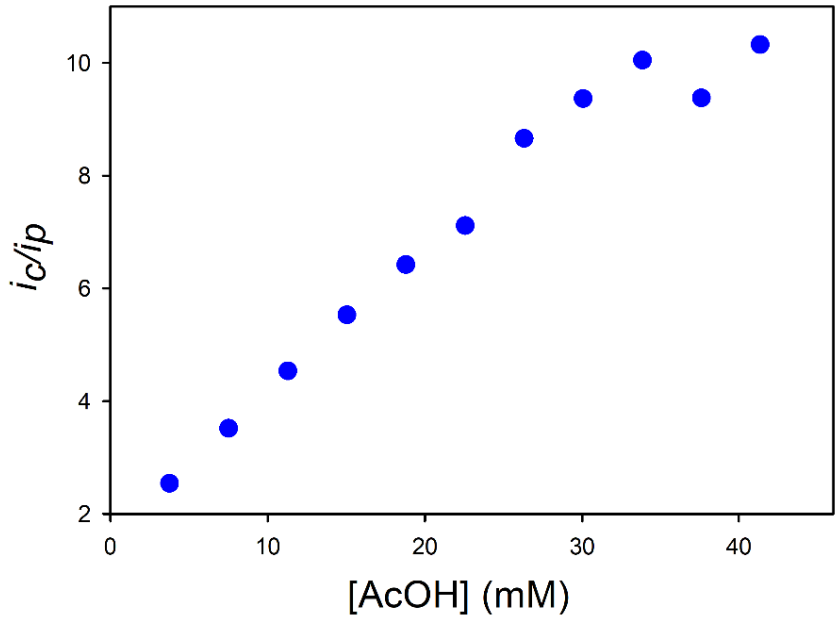

Figure S2.70. Normalized catalytic current response (i_c/i_p) versus [AcOH] taken from CV's of acid titrations of **1**/20 mol-equiv (Et_4N)(S-*p*-CF_3-Ph) in MeCN (see Figure 9 in the main paper).

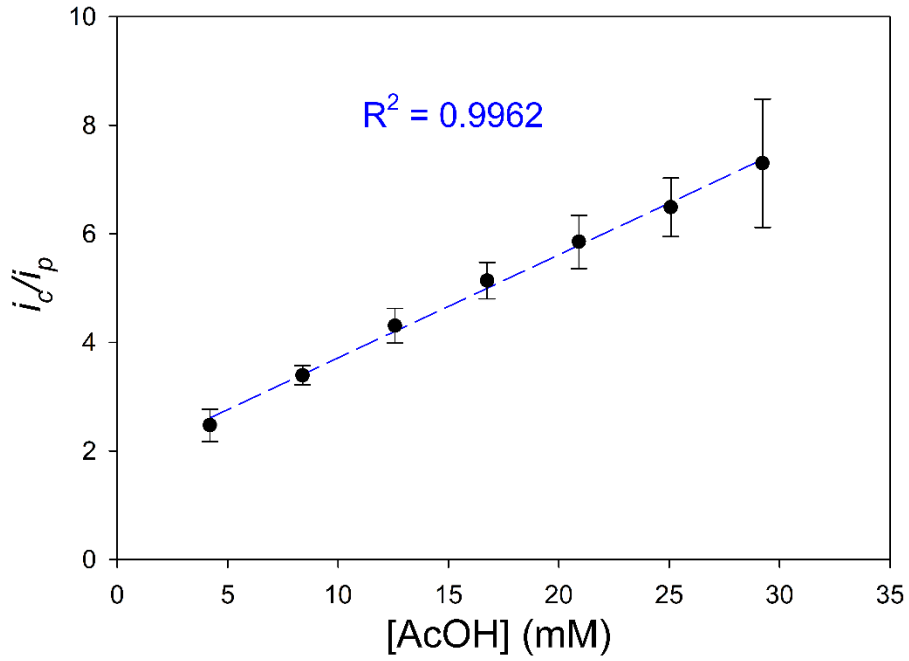

Figure S2.71. Ratio of catalytic current response (i_c/i_p) versus [AcOH] taken from CV's of AcOH titration to **1**/20 mol-equiv (Et_4N)(S-*p*-CF_3-Ph) prior to the acid-independent region, (18 mol-equiv AcOH, ~36 mM). Each point represents the average of three trials with error bars showing standard deviations.

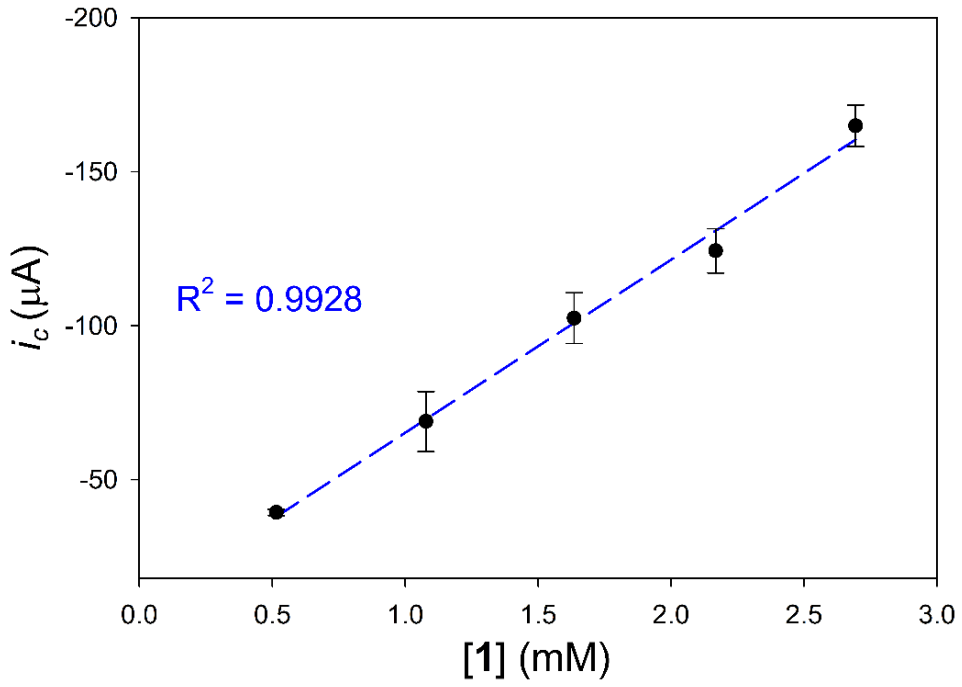

Figure S2.72. Catalytic current response (i_c) versus [**1**] in the presence of 20 mol-equiv of (Et_4N)(S-*p*-CF_3-Ph) and 5 mol-equiv AcOH. Each point represents the average of three trials with error bars showing standard deviations.

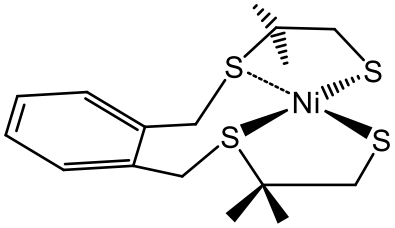

[Ni(xsbms)]

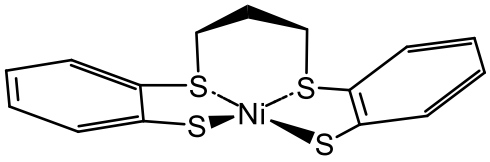

[Ni('S_4-C_3')]

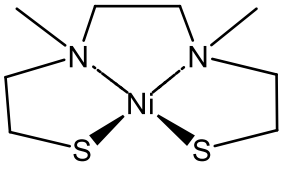

[NiN_2S_2]

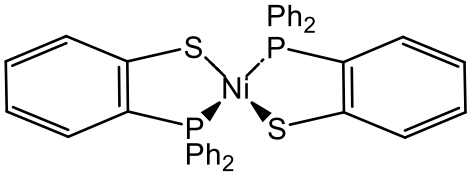

[$Ni(PS)_2$]

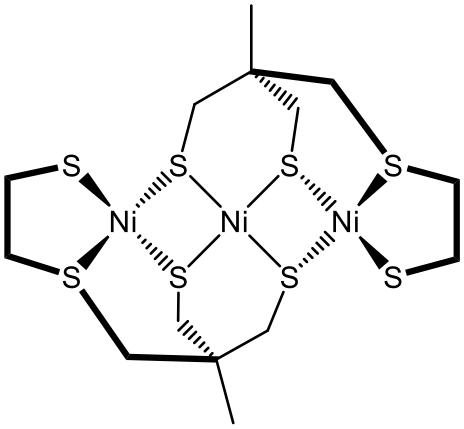

[Ni_3S_6]

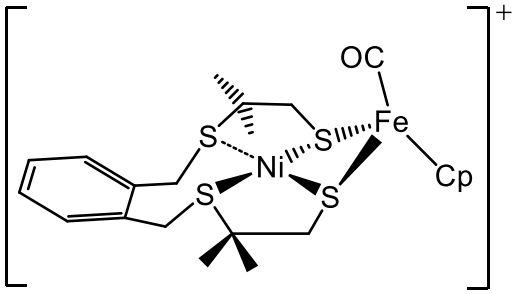

[Ni(xsbms)FeCpCO]$^+$

Chart S2.1. Structures of select Ni-thiolate HER electrocatalyst shown in Table 3 of the main paper.

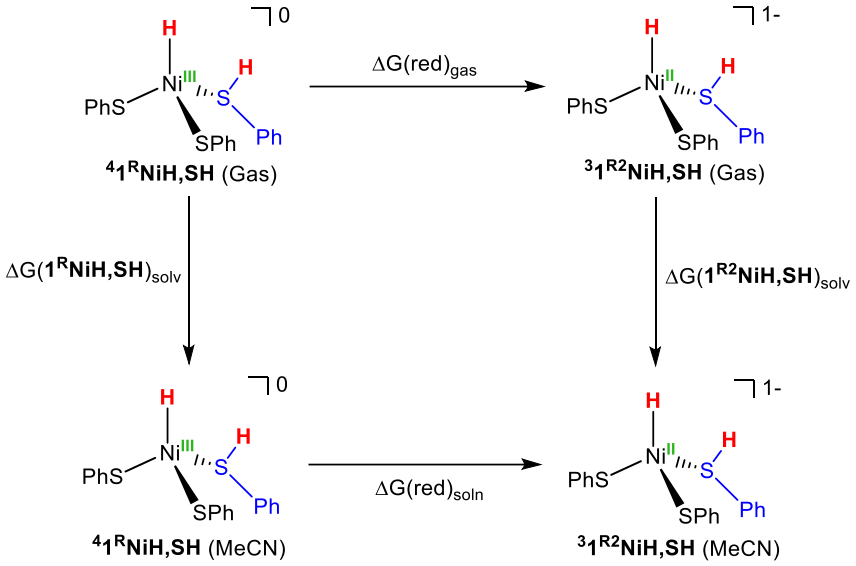

Scheme S2.1. Thermodynamic cycle used to calculate $E°$ for the $^{4}\mathbf{1}^{\mathbf{R}}$**NiH,SH**/$^{3}\mathbf{1}^{\mathbf{R2}}$**NiH,SH** conversion.

Table S15. Redox Potential calculations for $^{4}\mathbf{1}^{\mathbf{R}}$**NiH,SH**/$^{3}\mathbf{1}^{\mathbf{R2}}$**NiH,SH** and Fc^{+}/Fc in acetonitrile.

	Fc^{+}	**Fc**	**$^{4}\mathbf{1}^{\mathbf{R}}$NiH,SH**	**$^{3}\mathbf{1}^{\mathbf{R2}}$NiH,SH**
Gibbs free energy (G)	-1649.83178	-1650.08528	-4408.94134	-4409.07132
Δ*G* (gas)	-0.25350		-0.12997	
Single Point Energy (gas)	-1650.00833	-1650.26308	-4409.18475	-4409.31348
Single Point Energy (soln.)	-1650.08345	-1650.26876	-4409.20196	-4409.37955
Solvation Energy	-0.07512	-0.00567	-0.01721	-0.06606
Δ*G* (solv.)[b]	0.06944		-0.04885	
Δ*G* (soln.)[c]	-0.18406		-0.17883	
Δ*G* (soln.) (kcal/mol)	-115.501		-112.217	
E° (V)[d]	5.009		4.866	
E° (V) (vs. Fc^{+}/Fc)	**0.000**		**-0.142**	

[a] Energies are in hartrees (E_h) unless noted otherwise. [b] Difference in solvation energies. [c] Calculated according to eq. x. [d] Calculated according to eq. ix.

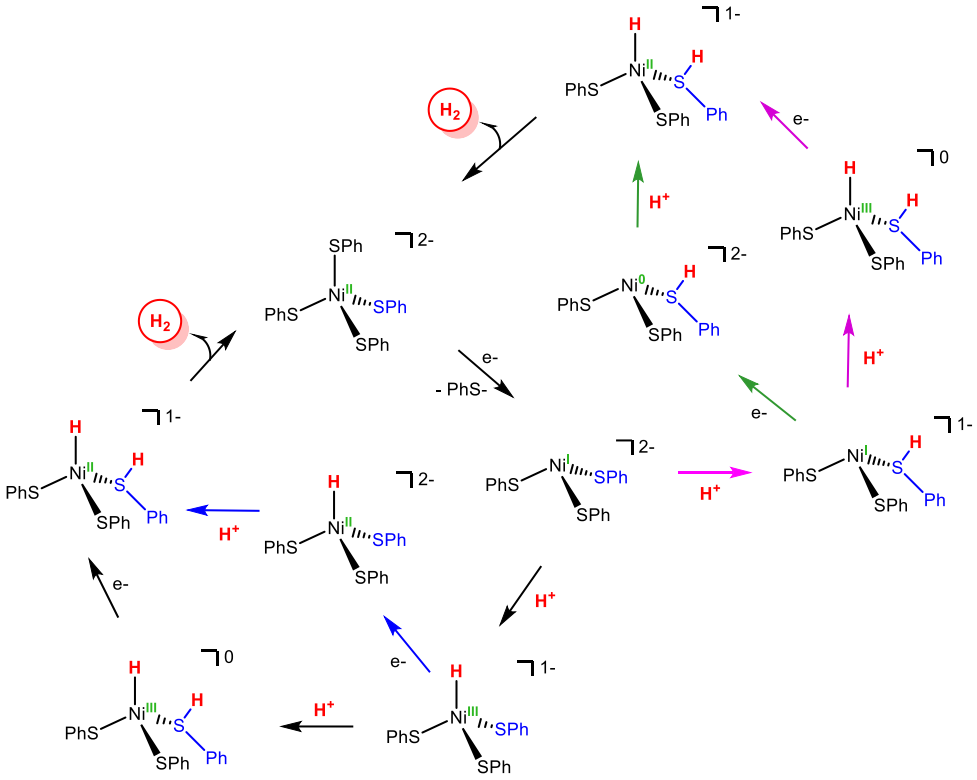

Scheme S2.2. All probable mechanistic paths for H_2 evolution from **1** starting from reduction of 1 to generate the 3C Ni^{1+} complex dianion $[Ni(SPh)_3]^{2-}$, i.e., $^{2}\mathbf{1}^{\mathbf{R}}$. *Note*: for simplicity, the general abbreviation PhS^- was used in this scheme to represent the *p*-CF_3 thiolate ligand of **1**.

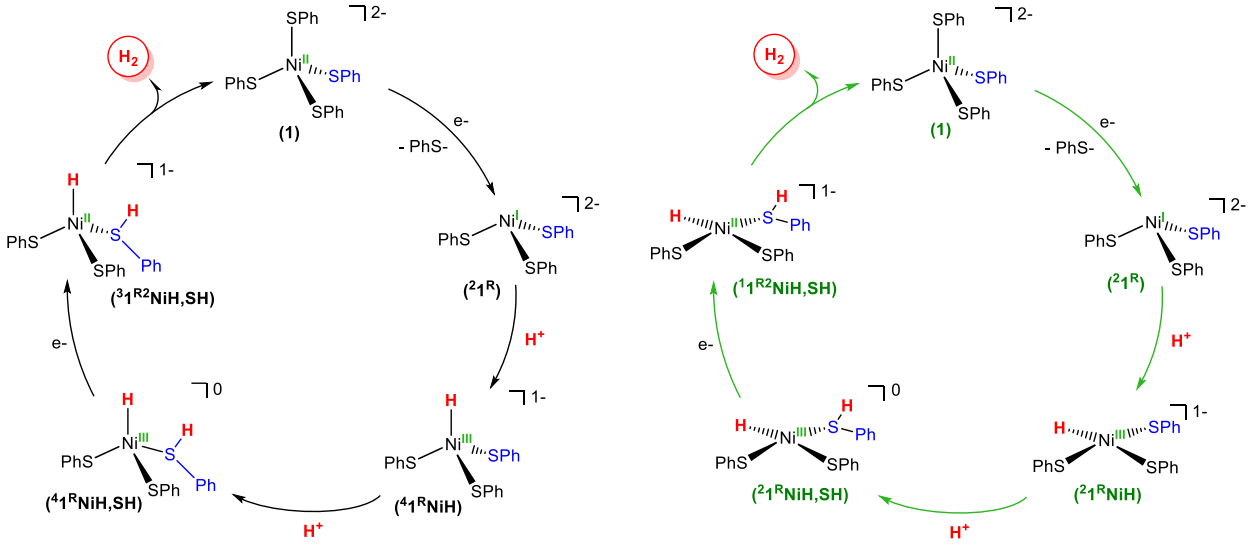

Scheme S2.3. Proposed ECCE mechanism of HER by **1** through tetrahedral (*left*) and square-planar intermediates (*right*).

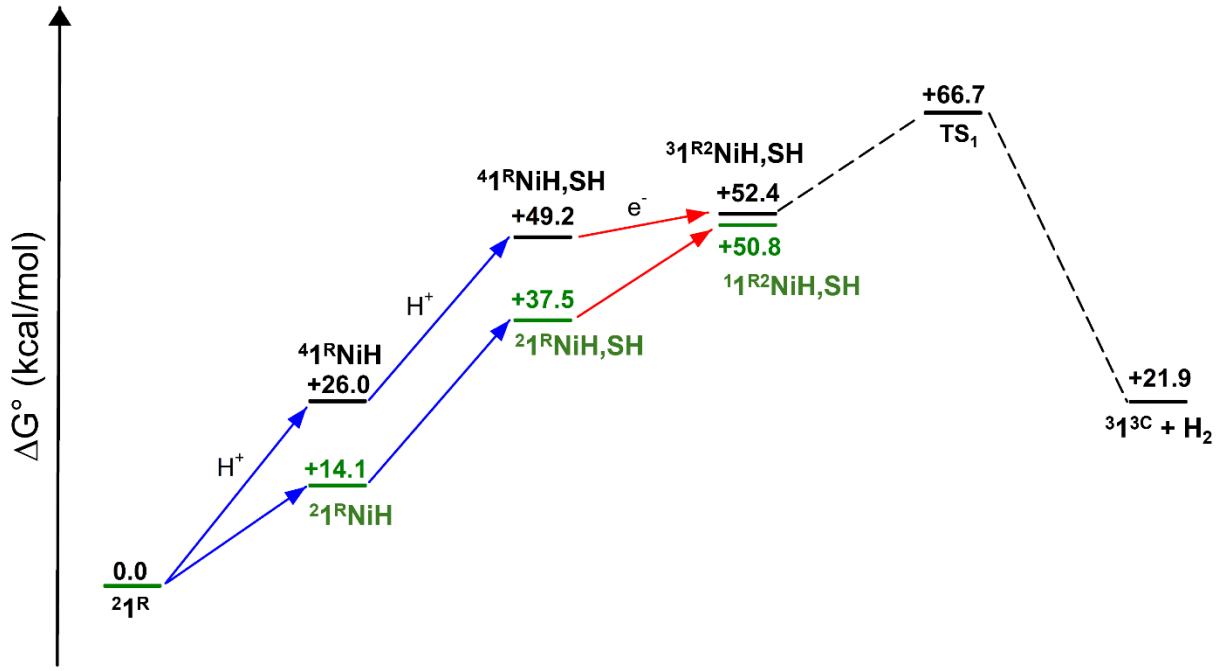

Figure S2.73. DFT-computed energy pathways for ECCE mechanism of HER by **1** through tetrahedral intermediates (*black*) and square-planar intermediates (*green*).

Table S2.16. Charge and Gibbs free energies from frequency calculations (B3LYP/def2-TZVPP, solution phase = MeCN) of intermediates in proposed mechanisms in Scheme S3, Figure S73.

Intermediate	Charge	Gibbs Free Energy (Eh)
$^{2}\mathbf{1}^{\mathbf{R}}$	2-	-4408.12685
$^{4}\mathbf{1}^{\mathbf{R}}\mathbf{NiH}^{a}$	1-	-4408.53953
$^{3}\mathbf{1}^{\mathbf{R2}}\mathbf{NiH}^{a}$	2-	-4408.69344
$^{4}\mathbf{1}^{\mathbf{R}}\mathbf{NiH,SH}^{a}$	0	-4408.95678
$^{3}\mathbf{1}^{\mathbf{R2}}\mathbf{NiH,SH}^{a}$	1-	-4409.13827
Et_3N	0	-291.91249
Et_3NH	1	-292.36662
$^{2}\mathbf{1}^{\mathbf{R}}\mathbf{NiH}^{b}$	1-	-4408.55845
$^{1}\mathbf{1}^{\mathbf{R2}}\mathbf{NiH}^{b}$	2-	-4408.69246
$^{2}\mathbf{1}^{\mathbf{R}}\mathbf{NiH,SH}^{b}$	0	-4408.97543
$^{1}\mathbf{1}^{\mathbf{R2}}\mathbf{NiH,SH}^{b}$	1-	-4409.14171
H_2	0	-1.17575
$^{3}\mathbf{1}^{\mathbf{3C}}$*c*	1-	-4408.00477

[a] Tetrahedral geometry. [b] Square planar geometry. [c] $[Ni(S\text{-}p\text{-}CF_3\text{-}Ph)_3]^-$

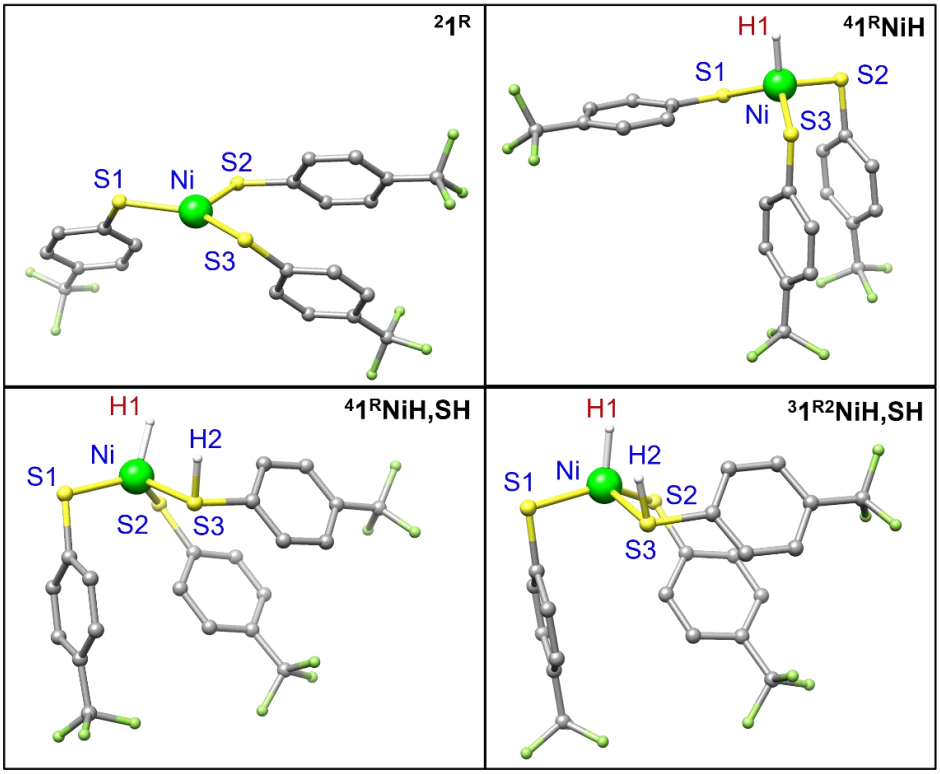

Figure S2.74. DFT-optimized structures (B3LYP/def2-TZVPP, gas-phase) for proposed *tetrahedral* intermediates for the ECCE mechanism of H_2 evolution from **1** (see Scheme S3, Figure S73).

Table S2.17. Select metric properties of the DFT-optimized structures of proposed *tetrahedral* intermediates for the ECCE mechanism of H_2 evolution from **1** (see Figure S74 for structures).

	$^{2}\mathbf{1}^{R}$	$^{4}\mathbf{1}^{R}$**NiH**	$^{4}\mathbf{1}^{R}$**NiH,SH**	$^{3}\mathbf{1}^{R2}$**NiH,SH**
Ni-S_1 (Å)	2.278	2.247	2.205	2.315
Ni-S_2 (Å)	2.311	2.232	2.193	2.311
Ni-S_3 (Å)	2.300	2.229	2.396	2.470
Ni-H_1 (Å)	---	1.578	1.574	1.572
S_3-H_2 (Å)	---	---	1.349	1.346
S_1-Ni-S_2 (°)	112.4	105.3	122.4	140.9
S_1-Ni-S_3 (°)	138.3	120.5	105.0	92.4
S_2-Ni-S_3 (°)	109.2	111.3	107.8	103.1
S_1-Ni-H_1 (°)	---	111.8	115.9	103.2
S_2-Ni-H_1 (°)	---	104.9	104.4	110.1
S_3-Ni-H_1 (°)	---	102.1	98.5	96.9
τ_3	0.04	---	---	---
τ_4	---	0.90	0.86	0.77

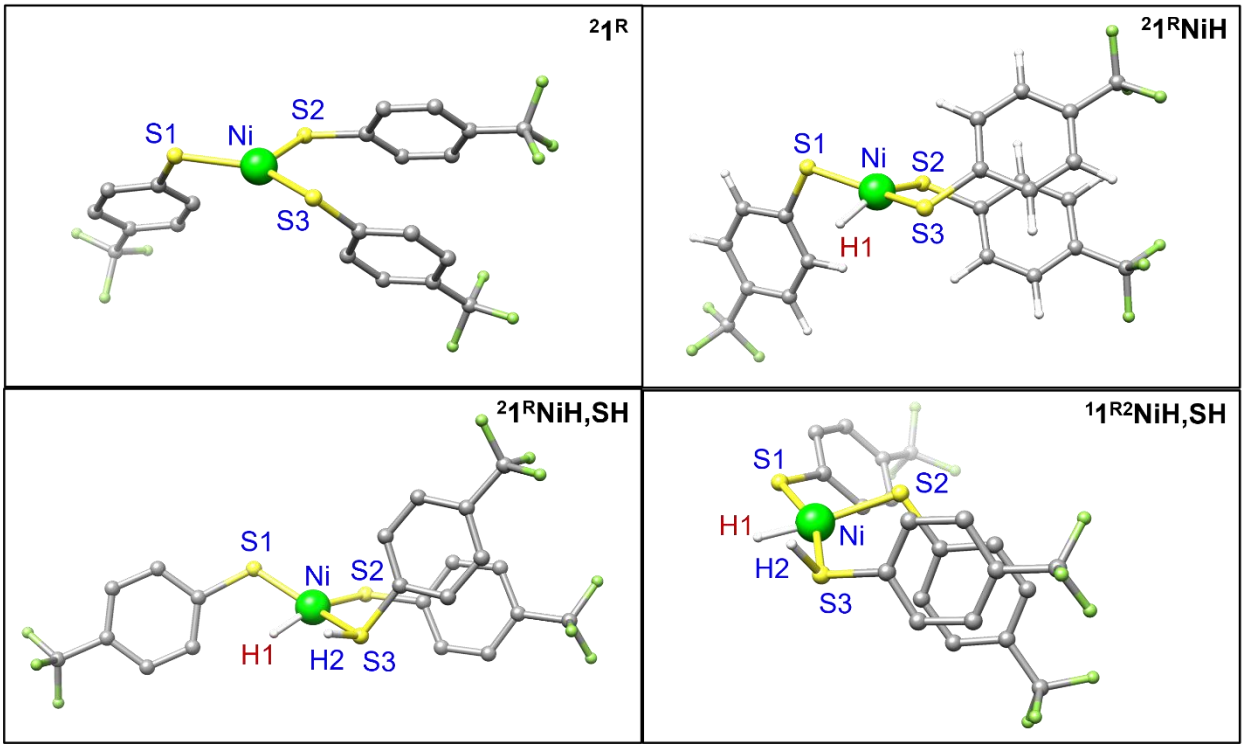

Figure S75. DFT-optimized structures (B3LYP/def2-TZVPP, gas-phase) for proposed *square-planar* intermediates for the ECCE mechanism of H_2 evolution from **1** (see Scheme S3, Figure S73).

Table S2.18. Select metric properties of the DFT-optimized structures of proposed *square-planar* intermediates for the ECCE mechanism of H_2 evolution from **1** (see Figure S75 for structures).

	$^{2}\mathbf{1}^{R}$	$^{2}\mathbf{1}^{R}$**NiH**	$^{2}\mathbf{1}^{R}$**NiH,SH**	$^{1}\mathbf{1}^{R2}$**NiH,SH**
Ni-S_1 (Å)	2.278	2.237	2.111	2.183
Ni-S_2 (Å)	2.311	2.219	2.194	2.272
Ni-S_3 (Å)	2.300	2.192	2.266	2.201
Ni-H_1 (Å)	---	1.458	1.457	1.484
S_3-H_2 (Å)	---	---	1.350	1.348
S_1-Ni-S_2 (°)	112.4	94.8	102.6	100.8
S_1-Ni-S_3 (°)	138.3	153.2	151.3	158.9
S_2-Ni-S_3 (°)	109.2	110.7	101.2	100.3
S_1-Ni-H_1 (°)	---	79.8	80.1	80.5
S_2-Ni-H_1 (°)	---	145.6	156.1	172.8
S_3-Ni-H_1 (°)	---	83.3	84.7	78.4
τ_3	0.04	---	---	---
τ_4	---	0.43	0.40	0.20

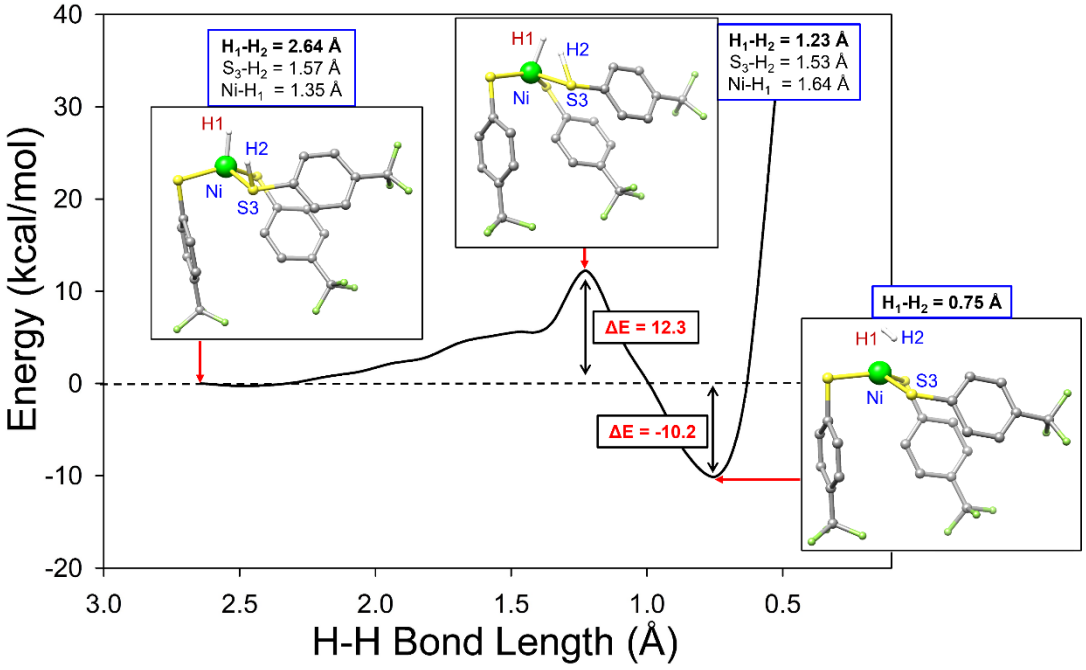

Figure S2.76. Relaxed surface potential energy scan of $^{3}\mathbf{1}^{R2}$**NiH,SH**. H---H (2.64 to 0.40 Å), distances were scanned in 0.11 Å increments. *Insets*: optimized structures of $^{3}\mathbf{1}^{R2}$**NiH,SH**, the transition state, and reaction well.

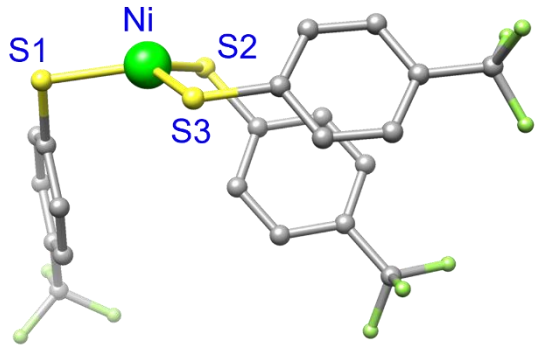

Figure S2.77. DFT-optimized structure (B3LYP/def2-TZVPP, gas-phase) of $^{3}\mathbf{1}^{3C}$ for the ECCE mechanism of H_2 evolution from **1** after heterolytic coupling to evolve H_2 (see Figure S76).

Table S2.19. Select metric properties of the DFT-optimized structure of $^{3}\mathbf{1}^{3C}$ for the ECCE mechanism of H_2 evolution from **1** (see Figure S77 for structures).

Atoms	**Bond Distances (Å)**
Ni-S_1	2.234
Ni-S_2	2.218
Ni-S_3	2.237
	Angles (°)
S_1-Ni-S_2	124.4
S_1-Ni-S_3	112.0
S_2-Ni-S_3	116.9
τ_3	0.12

Table S2.20. Cartesian coordinates for DFT-optimized structure of tetrahedral [Ni(S-*p*-CF_3-Ph)$_4$]$^{2-}$ (**1***, $S = 1$, B3LYP, def2-TZVPP, gas-phase).

Ni	0.46465529578580	-0.20143422215947	-0.04916990634501
S	-0.58184403872915	-1.12296462462491	-1.90315724370788
S	2.01431931367600	-1.92013521098563	0.15429566557847
S	1.13813005152755	2.00353942120657	0.32317853554982
S	-1.17904767294548	0.01742080072735	1.59034709393560
C	-5.28964333156493	2.37236410677879	-3.49110918101067
C	3.72172030496825	4.34968283327966	-4.63914116522548
C	-3.98455726032746	0.23995169635479	-3.58559140194731

C	-4.14481563079221	1.52989807866247	-3.05332724941286
C	-2.89678804597837	-0.53880259195763	-3.21913120756092
C	2.22416450600880	2.64366073349962	-3.54060615806805
C	-3.17845206646349	2.01493265184597	-2.15326681380428
C	3.11140761499444	3.72559523802001	-3.43450194816569
C	-1.91963428278885	-0.07615998918796	-2.30269048108518
C	-2.08992643548557	1.23242280144433	-1.78562493089247
C	1.65389099810031	2.07598544703933	-2.40660350818342
C	3.44989624168318	4.20490355340712	-2.15539091478997
C	1.94859751446931	2.57048456606994	-1.11358257905256
C	2.88041222042463	3.63754036286650	-1.02350765990853
C	-1.51535038270100	-2.73883258737955	1.32916076152213
C	-2.19662609853675	-3.92557367269026	1.56965463734696
C	2.78610239344400	-1.63116866739279	1.69479414321024
C	4.08063161196145	-2.14180057809536	1.95607502976137
C	-1.98047690892468	-1.50719478608651	1.84972943527410
C	-3.37429170337043	-3.93619375410584	2.33375872772639
C	-4.13052598202399	-5.18691986989997	2.59770092558447
C	2.15970063254318	-0.90204690689919	2.73520743754444
C	4.72072213150450	-1.92156436280794	3.17154454838283
C	-3.16601992615332	-1.53965182120776	2.63013450800485
C	-3.84477772245093	-2.72468418041290	2.87224372762015
C	2.79964597968751	-0.67140371246791	3.94204070678929
C	4.09102300241193	-1.17550450896157	4.17956637223463
C	4.76407608424307	-0.87041434383149	5.46903951839726
H	-4.72843699716033	-0.15557464777406	-4.28155155798106
H	1.94914678717836	2.25575203923376	-4.52464402964683
H	-2.78237300804639	-1.54277671127559	-3.63458213488761
H	-3.28337186754514	3.01623593599172	-1.72708236336305
H	0.95338638870162	1.24470700650014	-2.51502664903048
H	-1.35815030034026	1.63146432201882	-1.07903547310997
H	4.15052018055555	5.03854245367726	-2.05490308132659
H	3.13456725448621	4.02511508753655	-0.03380827935879
H	-0.60052534299331	-2.74881691876238	0.73559889267105
H	-1.81446576411174	-4.85553329315853	1.14305178045610
H	4.58333524518187	-2.71493439835040	1.17194531207409
H	1.14935110862718	-0.51926772384718	2.57981457165056
H	5.72052110658447	-2.32819753415986	3.34009604086010
H	-3.54752939155978	-0.59988832032518	3.03800831392246
H	-4.76221721444051	-2.71456650523020	3.46798757516556
H	2.28813741755491	-0.09508254680319	4.71797364221134
F	-5.05960529462144	3.05752292185870	-4.66098697171032
F	3.04391624584609	4.07522607736407	-5.78467044795965
F	-6.41524861068647	1.63833160359621	-3.73437439582070
F	3.78222038872094	5.71309513677835	-4.55580576140894
F	-5.64625390161354	3.32218857863732	-2.58471413609072

F	5.01974381430779	3.95949137527703	-4.86778817666046
F	-3.62688096081151	-6.27380022293331	1.95916304839497
F	-5.44570516261180	-5.10900115846959	2.22250126538024
F	-4.17669612747478	-5.52143926188720	3.93049568203505
F	5.09448440960713	0.45478908812772	5.60532214781806
F	5.92142595040723	-1.56676580243333	5.65113071928395
F	3.97939523806037	-1.13752848123544	6.55663504112891

Table S2.21. Cartesian coordinates for DFT-optimized structure of tetrahedral [Ni(S-*p*-CF_3-Ph)$_4$]$^{2-}$ (**1***, *S* = 1, B3LYP, def2-TZVPP, solvent phase = MeCN; modeled with CPCMC, see Experimental section).

Ni	-0.22834257833900	0.34864284298828	0.30655586806436
S	-0.86238675278502	-0.79889300755078	-1.64217565392277
S	1.45966509284979	-1.17235768659345	0.73576587390892
S	0.41994305293603	2.57323970047395	0.59959798457272
S	-1.92029145223096	0.24867959000539	1.90736399884406
C	-6.81456917504926	0.34438038990793	-2.01020700477911
C	5.90841023760651	2.01592385839983	-1.94979426014827
C	-4.84521182127140	-1.16274152950164	-2.29677904135298
C	-5.34520782549010	0.09300906361050	-1.91949877049663
C	-3.48192114292710	-1.42276618448046	-2.21910157501138
C	3.44165463478103	1.62721376813975	-1.96304044614238
C	-4.46172194621184	1.08673650245649	-1.47691637356286
C	4.54938608253032	2.25872006473781	-1.37678128713854
C	-2.57647207825079	-0.43691574083412	-1.77081508887647
C	-3.09686578162536	0.82412360774940	-1.41141476302532
C	2.17948442105843	1.75982929953038	-1.39533206983575
C	4.37051472548819	3.04379044103261	-0.23158805382390
C	1.98611042722072	2.50942139392005	-0.21303947424828
C	3.10412527602147	3.16848899098111	0.33661515487758
C	-2.05950495591466	-2.41113408519215	1.16474961636941
C	-2.71044926671291	-3.55002910186447	0.70725494545729
C	2.83400963561364	-0.31805971833080	1.43175301162367
C	4.13124384347981	-0.57786124819653	0.94167072681268
C	-2.76992042145450	-1.22354153137977	1.43768699647141
C	-4.10302012918938	-3.54559313119568	0.53643979765859
C	-4.78155638130925	-4.73406364632576	-0.06565587323736
C	2.70321102958909	0.61259910121418	2.48595771597773
C	5.25069374206508	0.04256887971268	1.48962519066599
C	-4.17153985627896	-1.24240047771121	1.28493220893478
C	-4.83154940600792	-2.38744464582367	0.84283086409055
C	3.81841352993646	1.24234298153662	3.03121394979952
C	5.10302607931305	0.95499405743132	2.54313204145709
C	6.29323753329436	1.66338043265846	3.10755281434252
H	-5.52835552866686	-1.94479455450269	-2.63539065354560
H	3.57027769957728	1.01817819586081	-2.86099460785217

H	-3.10341066725408	-2.41079471523977	-2.48626278806445
H	-4.83865664199354	2.06704817366482	-1.18032767864684
H	1.32902134034916	1.25374216307222	-1.85578325863693
H	-2.41598911898824	1.60480621512727	-1.06859733848298
H	5.22328270498534	3.53889473877437	0.23388877445435
H	2.97926527801375	3.75533366405615	1.24799517260618
H	-0.97704646016254	-2.41938044679065	1.29297720812837
H	-2.13143435702812	-4.44508033158578	0.47105830657930
H	4.25500828178393	-1.27351555491423	0.10944248772793
H	1.70905690176986	0.85058708247263	2.86582245054488
H	6.24041493781171	-0.18146364691584	1.08751496922959
H	-4.74287266338806	-0.33360035767130	1.48377020870868
H	-5.91491563053805	-2.36868080837845	0.70850492131765
H	3.69071883143146	1.96431004513727	3.84106384123913
F	-7.29689069853130	0.14123672604127	-3.27302530939884
F	5.95458710065832	2.20916371052393	-3.30018207432946
F	-7.54857697913667	-0.48443759891901	-1.20846049141088
F	6.86842096426878	2.80947901509669	-1.41735618659124
F	-7.16243129449722	1.60722375540308	-1.66681067566440
F	6.33070410346524	0.72907441737088	-1.75550017733964
F	-4.92366074884188	-4.62824028258901	-1.42376227512016
F	-6.04037772038358	-4.93518717622216	0.41090485243432
F	-4.09622189794126	-5.89029811773206	0.13701277905677
F	6.47473496815288	2.91214882771902	2.57442822437772
F	7.45708635297447	0.99712200590062	2.89133422452612
F	6.20469256937357	1.85808162373365	4.45096606982568

Table S2.22. Cartesian coordinates for DFT-optimized structure of square-planar [Ni(S-*p*-CF_3-Ph)$_4$]$^{2-}$ (**1$^{sq\text{-}pl}$**, $S = 0$, B3LYP, def2-TZVPP, solvent phase = MeCN).

Ni	-0.43713852231881	0.84878180407403	-0.56851254930192
S	-1.47057408875865	-0.44694800344615	-2.09356991453536
S	0.52980309777665	2.33259761739463	0.82559407980068
S	0.97422673369358	1.26447771513670	-2.29220708634518
S	-1.69519942334551	0.33038154190726	1.22459911832380
C	-7.50374722038645	-0.04226465931843	-1.60386652371075
C	6.24839314022332	3.56775336207544	-0.31226520508437
C	-5.41049575647920	-1.31214977838856	-2.18417012023376
C	-6.01764923382575	-0.13698996461881	-1.71971050439700
C	-4.02537354579377	-1.38361348597638	-2.29342035537484
C	4.82375234631892	1.60553878038187	-1.01492964923839
C	-5.21926689929580	0.97035720634579	-1.39060247976767
C	4.96856672529491	2.98326082668482	-0.82262551817045
C	-3.20690159733650	-0.29031500966802	-1.94403705772391
C	-3.83572949024605	0.89441563037458	-1.50320082873859
C	3.60289328304140	1.09485222073942	-1.45715654296389

C	3.88909098921409	3.84315871017418	-1.08100753056579
C	2.50750043899574	1.93748861355105	-1.71707664120524
C	2.67614995087572	3.32396528711146	-1.52364853341258
C	-2.26332822883231	-2.31640303608219	0.57459625263404
C	-3.11596884006841	-3.40436555246108	0.41196876041675
C	1.98578942804326	1.56612027152071	1.40428550005054
C	2.19729208797054	0.17137648295783	1.30234641511799
C	-2.75630729601145	-1.06246087151130	0.98906227157275
C	-4.48874827006923	-3.26562902513457	0.66788640272738
C	-5.40758776910215	-4.43386207707545	0.50504910523559
C	3.01403885120251	2.34947534468106	1.97610882665108
C	3.38672363501442	-0.40777200011144	1.72882746793565
C	-4.13359529726059	-0.94932908755494	1.26126375953232
C	-4.99256878351845	-2.03489081088596	1.10822866979528
C	4.20539039220138	1.77293922913314	2.39983868444712
C	4.40461383932532	0.38850176877603	2.27572648220548
C	5.71490140175827	-0.21907106889986	2.65242721724630
H	-6.01966168763407	-2.18335451840536	-2.43127143753883
H	5.65196006723234	0.92935004859010	-0.80109274148697
H	-3.55823498833945	-2.31466812125600	-2.61999999973280
H	-5.68338455609501	1.89149663282481	-1.03098780111843
H	3.48417945130375	0.01788415998680	-1.58638860562231
H	-3.21795193921961	1.74949452922327	-1.22632769494715
H	3.99758769676723	4.91991920244889	-0.92817923889605
H	1.83625781301915	3.99193790060475	-1.71726204550838
H	-1.19861755402921	-2.42286521940680	0.36521462141555
H	-2.71589607136433	-4.36268455140752	0.07416269732591
H	1.41149324585171	-0.44872044600498	0.86778343539539
H	2.88018393582323	3.43019820804900	2.05595067537651
H	3.52964104599943	-1.48574237593122	1.62613510174980
H	-4.53667806230047	0.01753758454259	1.56737877339086
H	-6.06037577920793	-1.91559165776859	1.30133916169246
H	4.99263651743547	2.40494769938050	2.81532228941281
F	-8.08625114217579	0.56314617907847	-2.68792117969111
F	7.23130640431961	2.65131486361376	-0.15415881387383
F	-8.10719602856556	-1.25175731234617	-1.49260882142715
F	6.74933684973307	4.53110948047611	-1.14152022902377
F	-7.90267958976302	0.69042930567228	-0.52864107613226
F	6.09909746874516	4.18147694265583	0.89791117358245
F	-4.97951830244951	-5.31599864622032	-0.43547669475411
F	-6.66659788726157	-4.06922666855858	0.14943258975370
F	-5.54787700167301	-5.16393539721911	1.65603640831749
F	6.60977141937749	-0.24370565481440	1.61406433292314
F	5.60297579824390	-1.51026579470346	3.06211079259314
F	6.34318679792631	0.45220564500843	3.65388235390098

Table S2.23. Cartesian coordinates for DFT-optimized structure of $[Zn(S\text{-}p\text{-}CF_3\text{-}Ph)_4]^{2-}$ (**2***, S = 0, B3LYP, def2-TZVPP, gas-phase).

Zn	0.21000067934407	-0.61211084926248	0.65743105602139
S	-1.45621138815940	-0.84232255182931	-1.03360492263609
S	2.34087441465657	-0.63359781983742	-0.42823185818092
S	0.08262236015401	1.47975651843498	1.81034541399942
S	-0.00518338185127	-2.31154254769474	2.34311818416609
C	-0.22042036092712	2.88528732722103	-5.64769314982496
C	-1.06522896454875	0.73998369539870	-4.71360291643909
C	-0.47796266276461	1.98791059418419	-4.49204304034747
C	-1.34341592982258	-0.09820324412117	-3.65226062022332
C	-0.18284652697533	2.36887842202148	-3.18055819625372
C	-1.05705684208518	0.27000451755056	-2.32127195160725
C	-0.45282405560607	1.52405831796969	-2.11663190365363
C	-0.76778064042853	-5.36816499263051	-0.23031454301746
C	4.65120516193941	0.74449484756110	0.09857011645537
C	-0.44881247841039	-4.11475741700104	0.25391466029556
C	3.43293021713711	0.25002852051980	0.61189552801162
C	-1.23622698429800	-7.79059208635648	0.08243455908666
C	-2.67347881186480	1.33142314217883	1.51509897703425
C	5.54145243858523	1.45253615206806	0.88928293689177
C	-0.94115035349971	-6.45046774408231	0.64081534915440
C	-3.92223289657316	1.89811526013942	1.34332457828770
C	-1.50394714826258	2.10950423394125	1.45580383619179
C	-0.30599017378342	-3.87682544565979	1.63729792611577
C	-4.05497396108683	3.26377388598871	1.09606808475952
C	-1.65667921166056	3.48184762182991	1.18002351291537
C	-5.39529753479704	3.86476763358691	0.89556584019124
C	-2.90352715737706	4.04803617447449	0.99656745400443
C	3.18849038814417	0.47675719123116	1.97987491408419
C	-0.75943036579048	-6.24591368864696	2.00643826761568
C	5.24804121980442	1.71784416051193	2.22991213376475
C	-0.44773350200093	-4.99005749454352	2.49093177884829
C	4.06011688876797	1.20840166187467	2.76289479490606
C	6.17602024865548	2.48941665875404	3.09947776419361
H	-1.28693098865708	0.41905652288104	-5.72304099560970
H	-1.77747289797510	-1.07199888607458	-3.83451923250682
H	0.27948631178877	3.32840164870573	-2.99058385369949
H	-0.18761439649294	1.82523481540002	-1.11283313076213
H	4.88141757992611	0.56798333484327	-0.94378330771854
H	-0.90071371077219	-5.50319801683266	-1.29600365730779
H	-0.34005623288512	-3.29668080638940	-0.44346832105137
H	-2.58764891679392	0.27444488630307	1.72008067276108
H	6.45633293686093	1.83140024897319	0.45437133588752
H	-4.80460590780757	1.27625824330958	1.41289481248560

H	-0.76750134673585	4.09454393837004	1.11571399348211
H	2.28555153500204	0.08354738089601	2.42605363982904
H	-2.98905284736606	5.10632652038666	0.78897489920036
H	-0.87572789264255	-7.07415910219042	2.69333297696356
H	-0.31695274808161	-4.84415697498408	3.55479095633179
H	3.80952895476917	1.39034843441117	3.80006698188678
F	0.12455202816354	2.19461410175192	-6.77413606349389
F	0.76828931793556	3.78666108367739	-5.43223142516849
F	-1.30865821113061	3.63259510263113	-6.01621103059398
F	-2.17315646700853	-7.74058882675015	-0.90181577669371
F	-5.82081535515014	3.83794203814264	-0.40238121243187
F	-0.14714649223935	-8.39437808764478	-0.48768077887206
F	-1.68900821513434	-8.69073428779149	0.99387196148511
F	-6.36747267768190	3.23264757415111	1.59869441866725
F	7.25531643215362	2.97799030953561	2.43698530344697
F	-5.45125780462539	5.17491663308863	1.26422460278649
F	6.69025472134395	1.75989678380081	4.13660161669937
F	5.58754060662200	3.56277473162343	3.70111604918588

Table S2.24. Cartesian coordinates for DFT-optimized structure of **[Ni^{I}(S-*p*-CF$_3$-Ph)$_4$]$^{3-}$** (*S* = 1/2, B3LYP, def2-TZVPP, gas-phase).

Ni	0.71918085167846	0.23770318813261	-0.00846471120726
S	-0.08974961837850	-0.48695347442595	-2.17437491048599
S	2.24339987774593	-1.59280306503486	0.19246281919626
S	1.35715816588236	2.51396351267405	0.15018443337440
S	-0.71816282486654	0.29120016092126	1.93398307616558
C	-6.01468261614079	0.66585535758132	-2.70955578310689
C	3.77200942164296	5.11256389548986	-4.77663187475883
C	-3.85062044446612	-0.22404412574230	-3.63660452040898
C	-4.57882222900346	0.35877235333144	-2.57647329686635
C	-2.49235569282514	-0.46860551720474	-3.50748154252747
C	2.24109879056461	3.39077688560864	-3.71929913147781
C	-3.88504157609840	0.68176139934437	-1.38865074971717
C	3.18110863504285	4.44383853395037	-3.60375567113686
C	-1.77018668772163	-0.14523259522222	-2.31790799749615
C	-2.52825343926297	0.44070905036929	-1.25997447890458
C	1.70012219359273	2.77791308873269	-2.59813996080367
C	3.54106482419091	4.86889481890695	-2.30427209639954
C	2.04704740554243	3.19413292524076	-1.27583775808812
C	2.99433346616052	4.26389482280385	-1.18576248073729
C	-1.57693107192574	-2.20208011524406	1.03063726510258
C	-2.45229473101275	-3.28106304388667	1.03707970249049
C	3.03821293495969	-1.60795717149356	1.71993525438191
C	4.06670653715831	-2.55864929473629	2.01402842695520
C	-1.75608669390960	-1.08991343753640	1.90418115736335
C	-3.56514969572476	-3.31518789707004	1.90686903724151

C	-4.50116819191954	-4.45780375526571	1.95869598483450
C	2.70880942408200	-0.70036088031123	2.77186529047307
C	4.70031205409076	-2.60279747097937	3.24579670413891
C	-2.88847167404317	-1.14803339497475	2.77551928844049
C	-3.76468081883652	-2.22062254860172	2.77862390940443
C	3.33307954546387	-0.75099052592645	4.00639798939148
C	4.34349040497585	-1.70264780177960	4.27597149777492
C	5.01945846244014	-1.78510252054975	5.58349058457400
H	-4.36513099247820	-0.49383129193884	-4.56390749324003
H	1.94398099694852	3.03628876300665	-4.71061929108361
H	-1.93861015757908	-0.92792259325374	-4.33142095334890
H	-4.43055383491634	1.12461296662730	-0.55087910830141
H	1.00103447845925	1.94154719064464	-2.70850014041570
H	-2.01056690789751	0.68515644250204	-0.32926518827738
H	4.26959303392232	5.67787692828016	-2.18571599960816
H	3.29136791378377	4.59760496570986	-0.18751487920867
H	-0.73027337360407	-2.18337828269850	0.34055035546383
H	-2.27254821249837	-4.11251335042025	0.35057926286718
H	4.34922958548009	-3.26479092911507	1.22735320577278
H	1.91573564799273	0.02486962488228	2.58589195380134
H	5.48559628112169	-3.34420129606315	3.42861898819939
H	-3.06430787459726	-0.30016110597833	3.44318308600355
H	-4.63105258133590	-2.21286779930315	3.44804203217891
H	3.02929174270890	-0.04540347183897	4.78418385214586
F	-6.29681989370737	1.98878710314173	-3.03899869781475
F	3.59508952446557	4.44066412422152	-5.94979262665489
F	-6.64356164591611	-0.06151306838542	-3.68702967078311
F	3.28108875428437	6.39372152978893	-5.02898603780157
F	-6.73369269326635	0.45509666912247	-1.56237963542110
F	5.13221070654487	5.32620556587211	-4.66934695646394
F	-4.26105887788562	-5.41508281620323	1.02288978703848
F	-5.82941777053851	-4.11345189940961	1.81338657702487
F	-4.49487462567778	-5.14335334468070	3.16920263885318
F	4.67362664275744	-0.79044736837352	6.44952683592831
F	6.40085041200236	-1.74004630579951	5.49698901642735
F	4.79085873234790	-2.96603830743950	6.28237362953819

Table S2.25. Cartesian coordinates for DFT-optimized structure of tetrahedral **[Ni^{II}(S-*p*-CF_3-Ph)$_3$(MeCN)]$^-$** (intermediate **I** in eq. 1 of Scheme 1 in the paper; *S* = 1, B3LYP, def2-TZVPP, solution-phase = MeCN).

Ni	2.37078006377514	-0.46570690128490	1.38076172437739
S	3.11919217971070	0.33244838019245	3.44397525131615
S	2.27572946517686	-2.63727432568984	2.09705986786120
S	0.98030027047729	0.52898646550847	-0.14094633198390
F	-4.91704423544791	-0.91000688830175	2.81481959721748
F	6.00371600807000	5.90267779038438	0.92788713930168

F	7.77596270702234	4.90812867349451	1.71038203399377
F	-5.37561980182362	-1.36142829702632	0.73988585394059
F	-5.55613883565934	0.67704833745088	1.46649511093313
F	6.96749428209748	4.33186454777355	-0.22252474250990
F	-0.44943397597335	-7.49490926631205	-1.67738372621178
F	-2.20936917931775	-6.29239231753105	-1.26631541221347
F	-0.92944930103063	-5.79411784251570	-2.95096436150676
C	5.51128350668381	1.64747106364983	3.01841337573002
C	6.31848035100775	2.64094960012418	2.46730677225494
C	4.11471280763768	1.65316751385200	2.82433899612684
C	5.74320077080055	3.67101700630384	1.70985031550527
C	-2.32406575500117	-0.93189290682779	1.75401968028089
C	6.61198127442171	4.69651936131455	1.04864250534036
C	3.55196998236069	2.70752866330437	2.07424290187171
C	-4.78131738552061	-0.43462280807149	1.55155075327904
C	-1.00226209626819	-0.72394816717969	1.36804596959580
C	4.35388170509828	3.70016651310641	1.51700666802292
C	1.09427621471698	-4.97643870666943	1.30996728049462
C	-3.35459268694174	-0.17586015374463	1.17810899935111
C	1.37221281274648	-3.63541743178068	0.95888751990402
C	0.37499983811444	-5.80863946766369	0.45839929328138
C	-0.67305074055264	0.24468569757021	0.39626509524661
C	-3.04626365026681	0.78709431179580	0.20522579029699
C	0.90120851703729	-3.16590709920025	-0.28407695446629
C	-1.72388449988776	0.99386107006978	-0.17722408855906
C	-0.08684806822991	-5.32397294993977	-0.77583776634205
C	0.17900041504472	-3.99682232026266	-1.13797563059791
C	-0.90208114138326	-6.21252666576068	-1.66197833956744
H	5.96626796524549	0.83823788850882	3.59312156819376
H	7.39901164073904	2.60874707388600	2.62033574882137
H	-2.55179642467873	-1.68825344017822	2.50780839622079
H	1.45006046969729	-5.36373969316728	2.26754011615976
H	-0.21338803967718	-1.32616269613972	1.82243663561187
H	2.47326820827614	2.72840956771954	1.91000752779314
H	0.17342939952825	-6.84087694128076	0.75351144692626
H	3.89750306211596	4.49892665636059	0.92874046624996
H	1.09387268155448	-2.13285626968683	-0.57752566868762
H	-3.84084883408231	1.38067024511620	-0.25154911574644
H	-1.49276583078548	1.74887436465810	-0.93199894899200
H	-0.17799405132777	-3.60561970986515	-2.09265162618734
N	4.02204972812882	-0.15754664889310	0.28997372699137
C	5.00123551653475	0.23439053118289	-0.16142467711800
C	6.23510785583738	0.75427832715404	-0.71707198968491
H	7.06561350936934	0.54740111943150	-0.02639239510879
H	6.14149682636230	1.84157508887064	-0.85451138029568
H	6.43800449846633	0.27904405619007	-1.68813097271307

Table S2.26. Cartesian coordinates for DFT-optimized structure of *square-planar* **[Ni^{II}(S-*p*-CF$_3$-Ph)$_3$(MeCN)]$^-$** (planar isomer of intermediate **I** in eq. 1 of Scheme 1 in the paper; $S = 0$, B3LYP, def2-TZVPP, solution-phase = MeCN).

Ni	0.17661408914478	1.12040001664692	0.63758832169368
S	-0.44104187589865	0.65729862723206	-1.43375310641602
N	0.52206547501065	1.79033338289611	2.39185344037359
S	1.65132091371311	2.71416363610268	-0.01020213861328
S	-0.87462822215790	-0.59001737654998	1.65568687957674
C	0.71205738379550	2.36705313123029	3.36660706406272
C	0.96543404948875	3.12940026218003	4.57451141090006
H	1.62507654297405	3.97733119933623	4.33588227616544
H	1.45036704382063	2.49099190419227	5.32755631727677
H	0.01685589895086	3.51462002909794	4.97895097355877
H	-5.01162579427159	1.76981610522192	0.09053723430345
C	-6.49406609201365	0.22865300903179	-1.58140319965244
C	3.76827351096907	1.65624059385061	-5.60119588964385
C	-4.21268882430375	-0.31124534504481	-2.49925694860399
C	-5.00883079770876	0.39265749705841	-1.58621822732544
C	-2.82652624889498	-0.20610350439246	-2.43951198615505
C	3.18418629992794	0.86259583920945	-3.28748608901963
C	-4.39897979047007	1.21157775289976	-0.62144180310300
C	3.20624806713909	1.89444128669081	-4.23491428158215
C	-2.19485336228815	0.58863931609185	-1.46001791245641
C	-3.01318271319828	1.31081690786784	-0.56293246070158
C	2.70413671353594	1.11003665656328	-2.00484060425060
C	2.74216474383631	3.17263300600173	-3.88993985764120
C	2.22459825833466	2.38448578769589	-1.64179252043765
C	2.25171211230778	3.41068039453540	-2.60788779497466
C	-1.19979835927054	-2.43449578931497	-0.40251360613331
C	-1.95133800071089	-3.31940279372741	-1.17329601740422
C	-1.80683031188559	-1.65296428007855	0.59792523767390
C	-3.32879589725554	-3.44761189565662	-0.95205233610014
C	-4.15067058626105	-4.40587818558443	-1.75967776717043
C	-3.19763143683229	-1.77267082263759	0.78763133379169
C	-3.95300565164481	-2.66274687326676	0.02849546922697
H	-4.67451246781448	-0.96292138705735	-3.24242908953634
H	3.54801645171235	-0.13169254028669	-3.55174885491480
H	-2.21473268677029	-0.77900774474137	-3.13807223245867
H	2.69160958575300	0.30646262380269	-1.26662473181396
H	-2.54552976196933	1.94035045704554	0.19512166116869
H	2.75406467683164	3.97923495168152	-4.62679008665458
H	1.86564377251686	4.39914590121846	-2.34825303923941
H	-0.12863358420544	-2.33769816562255	-0.57984076959761
H	-1.46053449679258	-3.91745272989149	-1.94224674046383
H	-3.68868081207959	-1.14782879776036	1.53539538049104

H	-5.02903846167985	-2.74083947401515	0.19965250159982
F	-6.95796791522419	-0.43329664535700	-2.66978093708386
F	3.81596006714834	0.34267435832025	-5.93194379970745
F	-6.93848259762377	-0.47136852602106	-0.49180767126712
F	3.05267562581854	2.28022426405646	-6.57201023147280
F	-7.16108420680093	1.41569052318622	-1.53806059901867
F	5.04698163100139	2.12345452291754	-5.72895663618484
F	-3.39691308992930	-5.22574061286486	-2.53252357768018
F	-5.02210764559794	-3.78129498307856	-2.60418850044926
F	-4.92314122217680	-5.21335547091200	-0.97651345693455

Table S2.27. Cartesian coordinates for DFT-optimized structure of *S*,*S*-bridged/planar **[Ni$_2$(S-*p*-CF$_3$-Ph)$_6$]$^{2-}$** (**3***, $S = 0$, B3LYP, def2-TZVPP, solution-phase = MeCN).

Ni	0.94022508022728	1.37444569182013	-0.26127765728738
C	1.63742537957748	-3.02052482297127	-5.53309261552756
C	-4.59055700434348	4.00393957415823	-3.92887485044358
C	3.47411967615451	0.31907806521691	6.11396198398259
S	1.21798810756215	-0.81693117842340	0.14866952144106
S	0.75395131629104	3.43514375828367	-1.03976078881884
S	3.10741695001585	1.73007567364639	0.19264243817923
C	-0.77918622280194	3.57851314243660	-1.90696734081130
C	-1.56748381031880	4.74647824128642	-1.74490524854961
C	-2.79828427254068	4.88277339011189	-2.39765916731302
C	-3.27936175418536	3.84184212331888	-3.21969708767040
C	-2.50269742974458	2.67917528770687	-3.40091540376793
C	-1.26666272398253	2.55623359028339	-2.76102908351022
C	3.19611736786553	1.29084845297177	1.89229978695183
C	4.45349525134007	1.01027927170513	2.49048789512645
C	4.55107068809973	0.68782237365702	3.84833989881831
C	3.39089844182301	0.62000969643791	4.64929756369117
C	2.13260481864997	0.88874861492399	4.06816773603594
C	2.03883788474687	1.22171420733002	2.71630930232360
C	1.40241125955708	-1.43186908700922	-1.52020794505439
C	1.52263562804041	-0.55787640677337	-2.62327588228210
C	1.59605698720288	-1.06385137124042	-3.92800090781199
C	1.55571826802434	-2.45397840509720	-4.14291996614222
C	1.47331676391437	-3.33599377835633	-3.04257465589399
C	1.40087146375926	-2.82948071243347	-1.74215255215397
H	-1.21036710609974	5.54793182051404	-1.08030028124333
H	-3.39722245350226	5.79404655651344	-2.25061766855682
H	-2.87208231468989	1.85745507249759	-4.02892687185659
H	-0.67160505284628	1.64366334814119	-2.90604071618704
H	5.36471805706357	1.04224891245118	1.87406567824582
H	5.53607507179252	0.47378042476052	4.28700546173289
H	1.21658784758497	0.84075820405954	4.67543153500004
H	1.05576854597401	1.44514186721967	2.27763164994777

H	1.53276597445320	0.53100408836929	-2.44881786699521
H	1.67206478228253	-0.37016817642148	-4.77733442592462
H	1.45048613596051	-4.42363748887576	-3.20510301007752
H	1.30203659695743	-3.51287635655267	-0.88735507675404
S	-1.23887631875049	0.84524871259174	-0.13032247319328
Ni	-0.96102454267469	-1.34810699065725	0.27202607978912
C	-1.40968042310397	1.45379849102616	1.54255374886894
S	-0.77928689307993	-3.41189994175485	1.04277522266142
S	-3.12813234117380	-1.70377191318552	-0.18510191342338
C	-1.53344016396560	0.57518280182840	2.64176427857756
C	-1.39091222580770	2.85005128932923	1.77156209576051
C	0.75982068268573	-3.56910760970920	1.89717745577714
C	-3.20693850957691	-1.27963427533736	-1.88903500971406
C	-1.59263143324301	1.07526102222917	3.94931934718446
H	-1.55655678411359	-0.51259958376306	2.46167685124772
C	-1.44969090881110	3.35062618914947	3.07518112766577
H	-1.28680571760784	3.53659366272395	0.91970025842757
C	1.54334534925598	-4.73750472404614	1.71683552023081
C	1.25706773256182	-2.55712785642833	2.75782118286507
C	-4.46095542886194	-1.00566374801622	-2.49737841096684
C	-2.04456728070336	-1.21662411570944	-2.70644154696089
C	-1.53469493218343	2.46387399551499	4.17127389946002
H	-1.67094104266948	0.37815697946216	4.79570843218697
H	-1.41285075687174	4.43694097381874	3.24335868062786
C	2.77915769432394	-4.88411505173428	2.35802898191305
H	1.17847739919969	-5.53120843423501	1.04715536265246
C	2.49795325078529	-2.69011211408440	3.38611763596495
H	0.66573009325040	-1.64453039134772	2.91711314841875
C	-4.55042337890235	-0.69614698004507	-3.85874331170055
H	-5.37591776850475	-1.03278438330294	-1.88630730241319
C	-2.13045589930065	-0.89685076013997	-4.06202840589199
H	-1.06391802841038	-1.43456864958412	-2.25937155692623
C	-1.60497062659794	3.02036666628287	5.56614733262545
C	3.26999423491143	-3.85292564342367	3.18630503628083
H	3.37408692729003	-5.79556018989383	2.19689086280304
H	2.87482871034855	-1.87576461803782	4.01936999469669
C	-3.38551030824511	-0.63508853291363	-4.65330003734269
H	-5.53292076107751	-0.48713617820241	-4.30531682085866
H	-1.21097169221185	-0.85362532346843	-4.66437174851215
C	4.58560846500018	-4.02488798364751	3.88513837703632
C	-3.46001175134028	-0.34759465200641	-6.12116179441937
F	-2.86186420300294	3.48928854344240	5.87970928478676
F	4.66860628406130	-0.22892370568191	6.48514833499453
F	2.49425458604362	-0.55139875444247	6.52979297075302
F	3.31293360187058	1.44625357679652	6.89742203659970
F	5.53017157865943	-4.63014896663157	3.09420723740023

F	4.48569521392191	-4.82069912306210	5.01093777580321
F	5.12500416006820	-2.84397929014723	4.30830830576457
F	-5.55051355273991	4.58779606730434	-3.13969408647425
F	-5.11052674105807	2.82116514257095	-4.37016003463224
F	-4.49131400802450	4.81436116273952	-5.04421997087303
F	-4.65378274247422	0.19335909527696	-6.50503079103019
F	-3.29034032727966	-1.48118253361499	-6.89336312245509
F	-2.48020672754837	0.52224407752927	-6.53838034809105
F	1.37885727707323	-2.09362120272552	-6.50170396727388
F	0.75578700340721	-4.05237018555710	-5.72834187154251
F	2.88329524725009	-3.53611830132084	-5.81517551687885
F	-0.75594448018879	4.08045071725723	5.74917072626793

Table S2.28. Cartesian coordinates for DFT-optimized structure of the free thiolate anion **[S-*p*-CF$_3$-Ph]$^-$** (*S* = 0, B3LYP, def2-TZVPP, solution-phase = MeCN).

C	2.61813412392873	-1.30103351376578	1.55638005440262
C	3.54703977502784	-2.30171815268448	1.95105313919301
C	2.49550788309998	-0.17797387232172	2.41779107561136
C	4.29588476159137	-2.19054915873939	3.11702847596228
C	3.24241912350424	-0.06094366416692	3.58541076472008
C	4.14896180443332	-1.06942442134354	3.95212867782471
C	4.99314142473830	-0.93059425687716	5.17325866600768
H	3.66901460736212	-3.18206017533455	1.31546651743240
H	1.79053863339885	0.61273087050649	2.15014493332672
H	4.99898458906031	-2.98295037713300	3.38539020254810
H	3.11749991462100	0.81915392989671	4.22035771164322
F	6.23114041451917	-0.39722001172427	4.91295398083050
F	5.24136591241202	-2.12136378891650	5.78464139214947
F	4.44138181759986	-0.12001329691243	6.11336867971990
S	1.67683521470289	-1.44607011048346	0.09193572862793

Table S2.29. Cartesian coordinates for DFT-optimized structure of MeCN (*S* = 0, B3LYP, def2-TZVPP, solution-phase = MeCN).

C	-0.97355336199766	1.37215539850376	2.75078980103774
C	-0.50054247043789	0.65981970791616	1.57241093473730
H	-0.12886835205264	1.37818326864975	0.82649113802045
H	-1.32410918106222	0.07760564864442	1.13285162828702
H	0.31500856726520	-0.02362401733246	1.85219924464511
N	-1.34779520171479	1.93588999361836	3.68384725327237

Table S2.30. Cartesian coordinates for DFT-optimized structure of intermediate **[Ni^{II}(S-*p*-CF$_3$-Ph)$_3$]$^-$** (**^{3}1^{3C}**, *S* = 1, B3LYP, def2-TZVPP, gas-phase).

Ni	-1.16524556046077	2.67696996037419	-1.96707863177391
S	-2.02815823974039	1.16903233488640	-3.37569033314263

S	0.70138124109232	3.60395945036456	-2.77203879636769
S	-1.59786414771335	2.39885717138189	0.19094086185531
C	-6.69589575104170	-1.10927895543471	-0.21843878038888
C	3.92562631405989	-0.67206119763381	0.13802353624600
C	-4.67611920448942	-1.40237130490547	-1.70212904688941
C	-5.56866601272607	-0.55917438240873	-1.03207326919457
C	-3.61847841907619	-0.85979795456264	-2.42932083968057
C	2.90368690153177	0.27417428250241	-1.96185971705865
C	-5.40620986735518	0.83200971766509	-1.12101922347045
C	3.22838183919751	0.42603946927801	-0.60839346021814
C	-3.42858497597924	0.53247255258712	-2.51407900374005
C	-4.36069125674372	1.36823007553983	-1.86150788469690
C	2.16583054022869	1.25660076534800	-2.62089526136988
C	2.80732292024732	1.57770997354964	0.07494513240032
C	1.72262877378422	2.40964283053038	-1.94651474417755
C	2.06868077225578	2.55422985433096	-0.58594090091889
C	-0.72602112940810	-0.19480675587930	-0.28004428807217
C	-0.86791078970192	-1.57615252137594	-0.23289041831449
C	-1.67893285327374	0.64445710513190	0.33533671520700
C	-1.95727931816312	-2.15525510458208	0.43619629210683
C	-2.16801844481433	-3.63301002428430	0.35542897237836
C	-2.74090820784631	0.04906261570439	1.04130082255499
C	-2.88462475314022	-1.33554354037448	1.08871689280830
H	-4.77296620820275	-2.48544237507642	-1.61428150976677
H	3.22433301863898	-0.61883950644696	-2.50158321420266
H	-2.89679422763580	-1.52111213569490	-2.91110841440136
H	-6.09324870350881	1.49510437458732	-0.59077966749456
H	1.88968145250594	1.12150770317008	-3.66809431248416
H	-4.23302092157823	2.44983751233441	-1.92195664046819
H	3.05431748476604	1.70509884333723	1.13115380792459
H	1.71787396313575	3.43231805283699	-0.04286218647208
H	0.11642661032922	0.24322817772925	-0.81680223377417
H	-0.13459917507951	-2.20976235980225	-0.73557870241281
H	-3.48792642888145	0.68734523535090	1.51498003682790
H	-3.74082709401628	-1.77861030938127	1.59995644380900
F	-7.91094689536071	-0.95795582768713	-0.82619718610681
F	4.72725092510299	-1.42168039747310	-0.66051095135894
F	-6.56784384195874	-2.43260244034096	0.03946476594941
F	4.70911180304790	-0.20661964295252	1.14757474884103
F	-6.81567143431881	-0.48734195511138	0.98840402103334
F	3.05195022063100	-1.54504879522977	0.71405682631792
F	-2.72679461491003	-4.01365434757350	-0.83766064584922
F	-2.99858473223512	-4.10760740261009	1.31492840460880
F	-1.00788157119485	-4.33402882169917	0.45261198339769

Table S2.31. Cartesian coordinates for DFT-optimized structure of intermediate **[Ni^{I}(S-*p*-CF$_3$-Ph)$_3$]$^{2-}$** (**^{2}1^R**, S = 1/2, B3LYP, def2-TZVPP, gas-phase).

Ni	0.40640505264361	-0.40532106384529	1.83984656987211
S	0.51269167878150	-0.96733222419871	-0.39882951277323
S	1.45020190628014	-1.93232340650363	3.17023620962001
S	-0.83505549917331	1.51625577623869	2.07955018628263
C	-3.34657146718590	2.62967348010081	-3.41146521102060
C	1.01698327639603	5.17804653823158	-2.39733590669956
C	-2.83560254117767	0.99109767794642	-1.59511405796312
C	-2.39391736713361	1.73773706995862	-2.70478541202235
C	-1.95719259904819	0.17984064175396	-0.89388008744412
C	1.47544716544733	3.42740075049522	-0.66420224618076
C	-1.04377993142136	1.65616449867275	-3.08107514526669
C	0.57209464957920	4.32234166173697	-1.26840641765918
C	-0.59092949700663	0.06748420041619	-1.26478406932215
C	-0.16865995974662	0.83627631585502	-2.37663834980651
C	1.05940788109876	2.58025162067441	0.35150125545823
C	-0.76211161504905	4.33526962414902	-0.82924795628562
C	-0.28158939996472	2.58254502180597	0.81942573313107
C	-1.17280191453679	3.48977802091223	0.19377661412304
C	3.12934214526513	-2.07790391064656	2.76174542877236
C	4.01304796911428	-2.79968492690499	3.61374783492721
C	3.69954615060097	-1.51787958376355	1.58450272195047
C	5.35979599943844	-2.94891897209015	3.31900190628312
C	5.04740728551869	-1.66730788540612	1.28922701811314
C	5.90279705149321	-2.38788405968494	2.14649838285474
C	7.35415314590657	-2.50232784473646	1.86868034864287
H	-3.88015798737314	1.05963362486486	-1.27813554144925
H	2.51378842867122	3.39270100031799	-1.00441460103334
H	-2.30012014212494	-0.37934519136366	-0.02320844297307
H	-0.67308432221751	2.25419242420492	-3.91557652331920
H	1.75995416492269	1.87344549683870	0.79836905250016
H	0.88429082397511	0.79513317153639	-2.66268514891119
H	-1.48651846061969	4.99812609994282	-1.30679948584825
H	-2.21734440045560	3.49192346204881	0.51164734922302
H	3.60125448242227	-3.24403560875453	4.52369514528976
H	3.04522368289524	-0.97272582963538	0.89970894843288
H	6.00654934267145	-3.51125219699704	3.99862826193983
H	5.44642357671590	-1.22616981764790	0.37242218719833
F	-3.73603166529113	3.72460166336848	-2.67756489790802
F	2.27669924731474	5.68812685603105	-2.22257965582400
F	-2.86136976262770	3.13081850924370	-4.57949160778248
F	1.07815844513701	4.52532529390567	-3.60556657019453
F	-4.53016047277392	2.00797221477082	-3.73487732461310
F	0.20533017196722	6.25209770334610	-2.61553486971088
F	7.66906334012377	-2.37248180417912	0.54997575279298

F	7.88976814447134	-3.69721449215176	2.27261511520192
F	8.12588379607548	-1.55371160085849	2.50988701940137

Table S2.32. Cartesian coordinates for DFT-optimized structure of the tetrahedral intermediate **[Ni^{III}H(S-*p*-CF$_3$-Ph)$_3$]$^-$** (**^{4}1^{R}NiH**, S = 3/2, B3LYP, def2-TZVPP, gas-phase).

Ni	1.26708713033881	-1.27751056447538	0.02755545940783
S	0.34617734476683	-1.86990720742594	-1.91340666441321
S	2.94571718351299	0.16092461606015	-0.27737711958210
S	0.00901342971834	-0.38199769384380	1.65947580085756
H	1.95951865366405	-2.61780601853962	0.48885896701667
C	-3.28455599866788	2.38106573673062	-4.28887809308165
C	-0.06230090379909	4.63695420194807	-3.08450050412426
C	-1.76128102805991	0.40437992496716	-4.49157124090774
C	-2.33987827945821	1.39027689213003	-3.67845484301485
C	-0.93687358411207	-0.56525270132124	-3.93333015709921
C	1.24281250161128	2.47993000215800	-3.15096805587101
C	-2.07532975244077	1.38941342594646	-2.30295537532902
C	0.63794638113815	3.49823513867520	-2.40438869731635
C	-0.67448851092567	-0.58715765511862	-2.54519444785144
C	-1.25652544942286	0.41293972071217	-1.74126916142560
C	1.94059264868563	1.46275803535655	-2.50446542325787
C	0.72666692908767	3.48201539826144	-1.00549183660625
C	2.04890244864213	1.43969203706575	-1.10060479384317
C	1.41882211303256	2.46122668718212	-0.36171752743434
C	-1.94730791321498	-2.26339392694710	0.98939853236755
C	-3.11998283291318	-2.96784956445620	1.24798284293485
C	-1.44221602848413	-1.33428114971738	1.92295606890324
C	-3.82752197260117	-2.76207204164058	2.44032717712799
C	-5.05956905433541	-3.55432459785922	2.74701814757253
C	-2.16396379739979	-1.13988088767062	3.12259755084197
C	-3.33719332318900	-1.84041287886691	3.37805618840953
H	-1.95569899604043	0.40346262303582	-5.56651699967309
H	1.14982443023696	2.47336993851909	-4.23795416720155
H	-0.47919734892196	-1.32647859861585	-4.56894215279941
H	-2.51035581257640	2.16001440453819	-1.66473242528030
H	2.39309185187738	0.65376188679486	-3.07975057297778
H	-1.05447876061596	0.42530255757407	-0.66930048229853
H	0.24019278148865	4.26545723002821	-0.42056421295855
H	1.47255159494682	2.43372746093767	0.72777664399094
H	-1.41346018369359	-2.42407245977672	0.05130481524018
H	-3.49370125223106	-3.67927882329788	0.50888218849138
H	-1.78562003452512	-0.42398911671007	3.85567223768888
H	-3.88050136317039	-1.67161318075278	4.31050077514417
F	-2.85232759506329	2.84168926966709	-5.49224765154809
F	-0.44782436179348	4.34117566577347	-4.34601640670410
F	-4.51542501380678	1.83367408260816	-4.53081007730920

F	-1.16834207731385	5.04273919500621	-2.41260603589010
F	-3.50130180800619	3.45990179485303	-3.50487188507529
F	0.73672283866318	5.74357873706449	-3.18251823452479
F	-5.68474233901706	-4.01056928802499	1.63342148790232
F	-5.98036763726095	-2.83901015233412	3.44793791792375
F	-4.79944724835070	-4.65956815619911	3.50865244357763

Table S2.33. Cartesian coordinates for DFT-optimized structure of the square-planar intermediate **[Ni^{III}H(S-*p*-CF$_3$-Ph)$_3$]$^-$** (**^{2}1^{R}NiH**, S = 1/2, B3LYP, def2-TZVPP, gas-phase).

Ni	-0.83031208185382	1.18608139918060	-0.17534993837112
S	-1.09414615413026	0.05352919689177	-2.03355596068749
S	-0.15605224140161	2.96727026212370	0.99768925539154
S	-2.18168870884776	0.42122097972698	1.41001594405410
H	0.55006153121232	1.28977559797189	-0.63384347324879
C	-7.03048645384843	-1.22538602816389	-2.35380203023541
C	-4.61286045116277	-1.84287883600403	-2.68022197456940
C	-5.57250062534267	-0.88579615089856	-2.32947120090086
C	-3.25736217486795	-1.53773884611363	-2.58406336146623
C	-5.15869426327473	0.37761653176165	-1.88236938133317
C	-2.82571417096617	-0.27689343478136	-2.13147229935701
C	-3.80434236726972	0.67872277489897	-1.79092449997785
C	-1.85055937096181	-2.20397426434452	0.55672531367782
C	-2.31836306061153	-3.46218448675309	0.19404460712510
C	1.05486385768088	2.46268023954098	2.14995896755097
C	1.48283529086593	1.12636946809454	2.31002334699469
C	-2.74380766522786	-1.18061585001565	0.93306091805497
C	-3.69455307533373	-3.73409128723998	0.20303133105778
C	-4.18988078988306	-5.06840792444181	-0.26009383629109
C	1.64366723261455	3.44616552430904	2.98023592666141
C	2.45581289366875	0.79306283073832	3.24703177273074
C	-4.12094724710420	-1.47084501865909	0.94240857657448
C	-4.59446639809760	-2.72890120868943	0.57722688131350
C	2.61265152112642	3.11171171003843	3.91729310376912
C	3.02981036398375	1.77863479775849	4.06226173813293
C	4.11378196709674	1.43698235873766	5.03276949692194
H	-4.92347031285267	-2.83604526575646	-3.00782252424580
H	-2.51182623052322	-2.29397422873053	-2.83488800579314
H	-5.90215418013774	1.12808997962250	-1.60561006278282
H	-3.48942994038665	1.66224958872991	-1.44060501850740
H	-0.78114208751414	-1.99263914867094	0.53880851482381
H	-1.61163175023785	-4.24072666361263	-0.10131846546885
H	1.02967332499207	0.34688605316842	1.69781874417601
H	1.32376118968617	4.48544955475819	2.87579723075921
H	2.76726035231768	-0.24814885689943	3.35219058071479
H	-4.82582109770510	-0.68479187804167	1.21837398669491
H	-5.66799626437706	-2.92304252500808	0.56709177958435

H	3.04992080688158	3.88931036343103	4.54776515679732
F	-7.80843578040723	-0.16649343555581	-2.70437304056446
F	-7.32460757204449	-2.22846211365608	-3.21724478848304
F	-7.49425318720274	-1.63252017906591	-1.13415619641994
F	-4.26921024667968	-5.15500793750210	-1.62302387374337
F	-5.42922864298046	-5.36280600566982	0.20328822196860
F	-3.37658035290925	-6.08995510694318	0.12076801242732
F	5.36695096150270	1.65167381473333	4.52607485375158
F	4.08991262522845	0.13562094203896	5.41635109612383
F	4.05322102728615	2.18147271296234	6.17059457461443

Table S2.34. Cartesian coordinates for DFT-optimized structure of the tetrahedral intermediate **[Ni^{II}H(S-*p*-CF$_3$-Ph)$_3$]$^{2-}$** (**^{3}1^{R2}NiH**, $S = 1$, B3LYP, def2-TZVPP, gas-phase).

Ni	1.53143816010691	-1.27852365879263	-0.06397297660396
S	0.42891992809182	-1.97268072463188	-2.04109273315201
S	3.22513785609028	0.39998749982947	-0.07338026662084
S	0.21929462868257	-0.47702251137111	1.70747070468442
H	2.20719474549221	-2.62830464047887	0.38271459709328
C	-3.52012812106627	2.20842968724323	-4.00109946383575
C	-0.10961569994359	4.53247033249970	-3.03730352325198
C	-2.02181339576411	0.24137297089447	-4.37690967600057
C	-2.50713223378237	1.23685329293764	-3.51043860837171
C	-1.12810724031637	-0.71598309101909	-3.91731874988174
C	1.25214249737605	2.41740014109053	-3.00480080140747
C	-2.06554626378545	1.24443816908150	-2.17637660113117
C	0.64138423310741	3.47309135819214	-2.30959229094555
C	-0.67583259416023	-0.73149509614614	-2.57132158579594
C	-1.17036594706658	0.28576214221760	-1.71730126270485
C	2.02240264165127	1.48130095985766	-2.32514022705938
C	0.80099714456176	3.55389637799689	-0.91587400250196
C	2.22141748682471	1.55844461660379	-0.92439941339281
C	1.56644807659895	2.61198828957979	-0.23958930900132
C	-1.78447125139994	-2.22923731117247	0.89155210346551
C	-3.01219170137099	-2.85868012414777	1.05011556719554
C	-1.30529591752204	-1.29407321725830	1.84701989330142
C	-3.82775143748785	-2.58771118168206	2.16495263073933
C	-5.10800283676328	-3.30668169262354	2.37660558288603
C	-2.14674590765652	-1.03137885303173	2.96383313621099
C	-3.37200232464546	-1.66161177576286	3.12270463969727
H	-2.34934293467251	0.22581930047424	-5.42025748867517
H	1.09842142850936	2.31698197224022	-4.08124939856810
H	-0.75114003459981	-1.48337967193099	-4.59828265458632
H	-2.41725312720408	2.01838065891438	-1.49150871775347
H	2.46919350528764	0.64388120433201	-2.86330632461890
H	-0.82801800288924	0.32033258615074	-0.68100300257320

H	0.30817563587245	4.35604154647421	-0.36060396239429
H	1.66800658428131	2.66099134444801	0.84615547046699
H	-1.16969141339979	-2.44190490837418	0.01371296848299
H	-3.35016951682209	-3.56829896454870	0.29098087933786
H	-1.80327573127937	-0.31013727098838	3.70993529172266
H	-3.99204904135281	-1.43528256560324	3.99472201898268
F	-3.27606293826207	2.64585005636271	-5.27372134624171
F	-0.62318124088339	4.11944227663461	-4.22126063400531
F	-4.79394174143205	1.67800764942874	-4.06530347276740
F	-1.14154556161938	5.05251228517952	-2.31810048024694
F	-3.63522537653190	3.31452516224664	-3.22711556699288
F	0.67856706482344	5.62567159748836	-3.35293667313771
F	-5.65675786436532	-3.79360798947428	1.23057151231552
F	-6.07271742068556	-2.53353084427125	2.96450362726598
F	-4.99990679862763	-4.40310738508932	3.20998059037202

Table S2.35. Cartesian coordinates for DFT-optimized structure of the square-planar intermediate **[Ni^{II}H(S-*p*-CF$_3$-Ph)$_3$]$^{2-}$** (**^{1}1^{R2}NiH**, *S* = 0, B3LYP, def2-TZVPP, gas-phase).

Ni	-0.51126073176139	1.56712137069049	-0.96312157913434
S	-1.30535636821387	0.35958529919978	-2.66043342905583
S	0.70541336054778	2.98164560576480	0.25169132253479
S	-1.99263525430285	0.98517161930968	0.73648024408954
H	0.36760651224684	2.05229325684374	-2.03663409636939
C	-7.05608267807069	-1.41892120417300	-1.83601396648637
C	-4.68553842728461	-1.87717622439502	-2.54717987291502
C	-5.65712834518208	-0.98056683295692	-2.07632850896946
C	-3.36940504257191	-1.45792774017062	-2.71160287798339
C	-5.27336412145198	0.33776615437521	-1.76439978230106
C	-2.96241974503484	-0.13766783331334	-2.40848051785714
C	-3.95856790971982	0.74903666830555	-1.92793093685008
C	-1.50283316269759	-1.67259767566587	0.12816236357257
C	-1.86249320231569	-3.00767057726107	0.02423948128272
C	1.28706738185088	2.31181163673183	1.73881193657685
C	1.18737360466085	0.93858441455702	2.09348086407975
C	-2.40971139628489	-0.69277836743236	0.61480678901411
C	-3.14860825362822	-3.43818361054378	0.40236208541915
C	-3.54528874617065	-4.85477500582179	0.21106668534204
C	1.96043096927161	3.16009245213183	2.66424914572362
C	1.72824238848828	0.45406313074015	3.27587476932635
C	-3.69723847105510	-1.15229265691001	0.99570859642208
C	-4.06358966868801	-2.48686593829915	0.88665821945488
C	2.50202357130749	2.67613415534766	3.84465913638601
C	2.39374912988358	1.31057500934968	4.17526808800918
C	3.03376796240075	0.79069020591347	5.40567922686417
H	-4.95600694820433	-2.91300733394529	-2.76108982176584

H	-2.61344082492435	-2.16814451037948	-3.05248940022462
H	-6.01790793903740	1.04281494890942	-1.38510128755709
H	-3.66359735774520	1.76585378377881	-1.67079630182219
H	-0.51528660395447	-1.34615281421946	-0.19883252316254
H	-1.14176551109820	-3.73191778172813	-0.36471296791047
H	0.65555252047423	0.26917865660266	1.41859224954371
H	2.04478580113670	4.22286846120426	2.42176598212054
H	1.62733834846746	-0.60761097735307	3.51421450496241
H	-4.42339521677274	-0.41825052799893	1.35085647947991
H	-5.07553464840878	-2.79446179124109	1.15869959185997
H	3.01113601966226	3.35968028038837	4.53019028494140
F	-7.98474432453899	-0.47955266549452	-2.20602266350673
F	-7.39072096833744	-2.55755271756973	-2.50543055610402
F	-7.34134906666239	-1.67865795330569	-0.51799897467930
F	-3.91995910917912	-5.16335590148741	-1.07771815378207
F	-4.60389319525231	-5.23190035362676	0.98391579190055
F	-2.53891499237757	-5.74096697126525	0.49131065983694
F	4.38527632921412	0.52901317603169	5.26871459778449
F	2.49867070287294	-0.37990925282588	5.84867922009423
F	2.97126362844191	1.66313493320757	6.46066990181495

Table S2.36. Cartesian coordinates for DFT-optimized structure of the tetrahedral intermediate **[Ni^{III}H(HS-*p*-CF$_3$-Ph)(S-*p*-CF$_3$-Ph)$_2$]** (**^{4}1^{R}NiH,SH**, S = 3/2, B3LYP, def2-TZVPP, gas-phase).

Ni	1.58359891053471	-0.65594093971223	0.71882044793857
S	0.91155416347343	-1.92209353001372	-0.94067156398958
S	3.19617474178923	0.83103504584775	0.49060548669161
S	-0.30519117165560	0.59306143531650	1.50054077170917
H	1.72723701307214	-1.64661133125539	1.93337930466300
H	-0.04067187194284	0.41190087306778	2.81095459848892
C	-4.12266763373992	0.75218481731617	-3.03231791744589
C	0.54330199935218	4.51945640700633	-3.54529349803870
C	-2.82568633839224	-1.29344610855990	-2.34003829892518
C	-2.84906766692244	0.08461378044129	-2.59045003209700
C	-1.67030277561843	-1.89383460204762	-1.84705710567201
C	2.14928625850870	2.65759661295980	-2.97547395232735
C	-1.70499245066999	0.85703497173528	-2.35631715599470
C	1.27176494446175	3.66048289612211	-2.54489311842431
C	-0.52042617061239	-1.12407617818390	-1.59034465315343
C	-0.54864500658772	0.25698088751058	-1.86243117871806
C	2.75542208307827	1.81563250684637	-2.04491855772978
C	1.01876046588795	3.82962576123443	-1.17717068327635
C	2.48445112441511	1.95718391848507	-0.67109577736500
C	1.62495906037749	2.98834133307511	-0.24758998198971
C	-2.91168093688891	0.07953854657031	0.86973850600869
C	-4.02933848144490	-0.73416672900452	0.68146531121539

C	-1.73396754460459	-0.47363128786564	1.37913958101418
C	-3.96270989803569	-2.08995674754832	1.01279695260116
C	-5.14220263800346	-2.98632919215764	0.72550779413365
C	-1.66166557537388	-1.83150088743636	1.71402625380709
C	-2.78348384438220	-2.63748487618048	1.53424693391701
H	-3.71640756448691	-1.89783143095368	-2.51854577709569
H	2.35125053949331	2.52992404386381	-4.04012729895620
H	-1.65843136609934	-2.96521009227156	-1.64010720690894
H	-1.71073841759005	1.92754568350707	-2.56853264055620
H	3.42424057924334	1.01991684317191	-2.37685579648854
H	0.34277429567604	0.85902925931021	-1.70078026913451
H	0.34581336055818	4.62076435827963	-0.84107446331274
H	1.42769283439530	3.11862508920351	0.81742067647706
H	-2.95299271769624	1.13573073579344	0.60119404504307
H	-4.94451855947203	-0.31073023008021	0.26634342106184
H	-0.72876669898800	-2.25537542470325	2.08752635285231
H	-2.73829057365430	-3.69770195118042	1.78813356149368
F	-4.94535422663628	-0.08820462334285	-3.69504101433444
F	1.18860578765025	4.59506466819742	-4.72790058490232
F	-4.83270054693551	1.21954338517576	-1.96083661528735
F	-0.69851664612334	4.02613508701470	-3.80811305237500
F	-3.89840727438448	1.81695237860861	-3.83010844595815
F	0.36542365637964	5.78326732522509	-3.09867085104774
F	-6.31727801109124	-2.33004387504069	0.81800040703691
F	-5.19859981452117	-4.04190261506151	1.56553682307876
F	-5.07336939579276	-3.49240599828619	-0.53482973772706

Table S2.37. Cartesian coordinates for DFT-optimized structure of the square-planar intermediate **[Ni^{III}H(HS-*p*-CF_3-Ph)(S-*p*-CF_3-Ph)$_2$]** (**^{2}1^{R}NiH,SH**, *S* = 1/2, B3LYP, def2-TZVPP, gas-phase).

Ni	-0.90186239164210	-0.22831680206489	1.42353980730155
S	-0.92397915597209	-1.29483508873511	-0.57557927474999
S	-0.64568983509967	1.51273156675135	2.59000434102760
S	-2.50230311169319	-1.28722546477987	2.48756885909227
H	0.47318228650178	0.10561727139888	1.07827786833591
H	-0.17505267751840	-0.44601910068866	-1.31082138914584
C	-6.38345287677983	-0.25090309345349	-3.02990632995229
C	-4.29137737895971	-1.62579438472014	-2.80113756802284
C	-4.99165000003782	-0.45932054281439	-2.48261441975697
C	-3.03980049077324	-1.86039859412935	-2.22983422767098
C	-4.44490479457329	0.48059691198369	-1.60006591931374
C	-2.50267821406533	-0.92477792632371	-1.34339584593090
C	-3.19755256961852	0.24802998108099	-1.02572295760913
C	-2.73171851026516	-3.58209134155100	0.95147130456433
C	-3.40397513042825	-4.44838579917044	0.09179608754609
C	1.02103401222363	1.98890615366417	2.92908017244666

C	2.11373866925069	1.10487963064123	2.92438812753716
C	-3.33706187705382	-2.38574906342437	1.38119641432198
C	-4.69692052528080	-4.13773170072438	-0.34750598927695
C	-5.37391202021871	-5.04809175557851	-1.33432522748444
C	1.23363005092493	3.33306500651393	3.29015117843252
C	3.38946277626751	1.55770779208624	3.25156585771924
C	-4.64203113979611	-2.09446383616050	0.94516024259596
C	-5.31675613287224	-2.95970170665234	0.08638068639992
C	2.50956676598752	3.78512052040879	3.61740624994396
C	3.59359364032260	2.89894095336110	3.59859655922950
C	4.98133380466052	3.40060762144495	3.89865976747453
H	-4.72514157945013	-2.36214020316775	-3.47843594301367
H	-2.49961798042694	-2.78049085808256	-2.45505738604973
H	-4.99786183864581	1.38863309961371	-1.35496437648793
H	-2.77561713364867	0.96391420877053	-0.31834639079972
H	-1.72910408253606	-3.82975097930390	1.30466948322174
H	-2.92397056581870	-5.37300390508877	-0.23598811810965
H	1.95700985462901	0.05562392016550	2.67104809990618
H	0.38910207984540	4.02517345411431	3.30792062731567
H	4.23067631123614	0.86235936801499	3.24686243151597
H	-5.12151574952838	-1.17267738571742	1.27827308297336
H	-6.32280073558288	-2.71314037382753	-0.25582238508288
H	2.66391161983368	4.83042023408238	3.89078289168398
F	-6.69010450066024	1.05833484515986	-3.15479721299371
F	-6.54619657967170	-0.82356587824486	-4.24031210613048
F	-7.31609165991260	-0.79592819271541	-2.20665912305811
F	-4.85514643248015	-4.89451716649073	-2.59065856935409
F	-6.69811515780825	-4.81503763886231	-1.43693142630720
F	-5.21366398108821	-6.35450877627130	-1.02323368325950
F	5.59928764001081	3.86779183753097	2.78163282608508
F	5.77855026345747	2.43125277306334	4.40283131125885
F	4.97493703475542	4.41931040889282	4.78872159163066

Table S2.38. Cartesian coordinates for DFT-optimized structure of the tetrahedral intermediate **[Ni^{II}H(HS-*p*-CF$_3$-Ph)(S-*p*-CF$_3$-Ph)$_2$]$^-$ (^{3}**1^{R2}NiH,SH**, S = 1, B3LYP, def2-TZVPP, gas-phase).

Ni	1.65347605860115	-0.58148009822371	0.63103258187285
S	0.80769179274423	-1.86281814171588	-1.09634774756919
S	3.02894619483429	1.24251737560068	1.00826292645948
S	-0.33960114736349	0.61618553544472	1.46513595029174
H	1.88369106558290	-1.47461026114189	1.90414892895071
H	0.06031768702081	0.26250732683751	2.70051895158428
C	-4.26267934011296	0.98210046182211	-2.86164603916959
C	0.74579428323165	4.20786486145384	-3.79885361532139
C	-2.95127216831223	-1.11166767955686	-2.39561092440707
C	-2.98792267942853	0.28708131759835	-2.51210952171861

C	-1.78870652077948	-1.75053656699442	-1.98187018256705
C	2.26943931262891	2.45049950698317	-2.80806345418237
C	-1.83463779915076	1.02964683623862	-2.21828356060296
C	1.32829471521547	3.47427176863117	-2.63231532771234
C	-0.62013517432006	-1.02116912916919	-1.65946998108436
C	-0.67248240450304	0.38573524340319	-1.80434067694835
C	2.80114847550707	1.79040418842283	-1.70331987693333
C	0.94130240497660	3.83573118477135	-1.33202527108226
C	2.41451228374226	2.12705042272910	-0.38615185886910
C	1.47857740467620	3.17687796426884	-0.23176831892217
C	-2.95706326987167	0.00014300451852	0.92088716188555
C	-4.03298423249545	-0.86497099314560	0.72456379253027
C	-1.72350744042141	-0.50323344261767	1.34517218675664
C	-3.87480177594084	-2.23278938182305	0.96880691679865
C	-5.01128380709019	-3.17566349510178	0.69115350053710
C	-1.55862561965603	-1.87621123703662	1.57739891531040
C	-2.63858536568964	-2.73637572015857	1.39642493129994
H	-3.84477245744456	-1.70020967374418	-2.61332318534673
H	2.57015040948295	2.15508697949973	-3.81467358873843
H	-1.77297581213602	-2.83673694427800	-1.87487449154655
H	-1.83889327111475	2.11672350181308	-2.32193743220445
H	3.51121689699720	0.97401517462284	-1.84515755290962
H	0.21989239941901	0.97393903974137	-1.60031720035179
H	0.20546467981453	4.63042789354852	-1.18597180262531
H	1.16411374228183	3.45066692414438	0.77693403145041
H	-3.07061427982251	1.06612234012250	0.72035491597667
H	-4.98696783844152	-0.47306602653951	0.37015962079725
H	-0.57727204585380	-2.25992405068905	1.86106170033380
H	-2.51418091048757	-3.80697569230186	1.56740521926479
F	-5.08535295095325	0.22566620561130	-3.63383111446112
F	0.99705266962793	3.60529657089625	-4.98515207823792
F	-5.00544163622890	1.30846573075139	-1.75141097525279
F	-0.60541255162960	4.34444094486143	-3.70576009796452
F	-4.06883837783384	2.15074249000089	-3.52067849856512
F	1.23034569874132	5.48266489343992	-3.91175886505275
F	-6.22370676060989	-2.60083251002512	0.88610407252515
F	-4.97185736913191	-4.28285745029162	1.47437540705569
F	-5.00565316830235	-3.62203719322299	-0.59506847133409

Table S2.39. Cartesian coordinates for DFT-optimized structure of the square-planar intermediate **[Ni^{II}H(HS-*p*-CF$_3$-Ph)(S-*p*-CF$_3$-Ph)$_2$]$^-$** (**^{1}1^{R2}NiH,SH**, $S = 0$, B3LYP, def2-TZVPP, gas-phase).

Ni	-0.23128697234424	1.33886358430726	-1.28042606020033
S	-1.34557583460609	0.43346371429762	-2.94879831215596
S	1.35901777152821	2.41130642098100	-0.23769311075370
S	-1.71736303630478	1.03489759192751	0.41095358105413

H	0.63305180657030	1.68171328730997	-2.43711776713863
H	-1.64498716008667	1.54528872131936	-3.65026078538394
C	-6.95633065845538	-1.35290844941597	-1.45567350642847
C	-4.65485785176874	-1.82075289958650	-2.35189174521784
C	-5.57616737568292	-0.89990046134165	-1.84255363154721
C	-3.38389920023974	-1.38377104996697	-2.72581343417207
C	-5.23008544232088	0.45095914249413	-1.71093379036600
C	-3.03364928549038	-0.03780298526871	-2.58700584909112
C	-3.95462703861792	0.88238289188115	-2.06927542154490
C	-1.30056058221884	-1.64342381406168	-0.16457997858335
C	-1.69256878674146	-2.97553718807690	-0.22439091881538
C	1.48516898683865	1.94070426951412	1.44968646306633
C	1.20431568869322	0.64357610477568	1.93313266577051
C	-2.14330617269104	-0.64603807965022	0.39226217794878
C	-2.94179004943754	-3.37260196272920	0.27560151799648
C	-3.39485107991348	-4.78504078576328	0.11779757449408
C	1.97641852963142	2.88885697577213	2.37603641421281
C	1.39755793460672	0.31496291006807	3.26977371155624
C	-3.38314343404457	-1.07914657715057	0.92800963700883
C	-3.77861654723001	-2.40743191130887	0.86299165555095
C	2.17777514757219	2.56180250227959	3.71296197677854
C	1.88378366052946	1.27067002235248	4.17633210106186
C	2.14970140036547	0.90124028159520	5.59826347398097
H	-4.91428669603010	-2.87654331944944	-2.43114211765866
H	-2.65134070217145	-2.09815264994421	-3.10398683349205
H	-5.94710277145422	1.15974443046386	-1.29332149290709
H	-3.65981138371328	1.92037806056279	-1.91726458752087
H	-0.32625818956383	-1.34612045306217	-0.55857550309917
H	-1.02417189324955	-3.71736223078961	-0.66798383357082
H	0.82744636131407	-0.10886950453759	1.24239490911703
H	2.19139960779188	3.90089747782100	2.02503890593864
H	1.16437665597113	-0.69414983246316	3.61630747086586
H	-4.04810979533626	-0.33460284613127	1.37033881573731
H	-4.75368690125458	-2.70361469669464	1.25530775833911
H	2.55203510441440	3.31671171260055	4.40826740313484
F	-7.84960021367448	-1.19925603647327	-2.47623889826729
F	-6.99878152184037	-2.65911456132396	-1.10915203841953
F	-7.45834937241486	-0.64913314500500	-0.41104122654879
F	-4.34405950728047	-5.14438179769018	1.01776486115144
F	-2.38036989193153	-5.68358274538084	0.23704172475115
F	-3.94685762345915	-5.03199692776559	-1.11658022595986
F	3.42438340595755	0.43823300151558	5.80101416430783
F	1.33139288736798	-0.08245327855928	6.05407971967554
F	2.00984802241657	1.95136708575178	6.45312238534373

Table S2.40. Cartesian coordinates for DFT-optimized structure of the tetrahedral transition state (**TS1**, *S* = 1, B3LYP, def2-TZVPP, gas-phase).

Ni	1.67682032317899	-0.59290947098857	0.56739353954460
S	0.95378441358562	-2.16703586451521	-0.91170944469944
S	3.10884831803472	1.18907748299694	0.77318889994626
S	-0.28982693546527	0.53294303811634	1.44388917522053
H	1.64686660959953	-1.14985955146401	2.10892225542136
H	0.63945661776941	-0.45307524895710	2.15122631623663
C	-3.96540395437772	0.89971868612827	-2.73994537772466
C	0.45069997859809	4.40705057907440	-3.67830623932687
C	-2.84379737422400	-1.25407461239349	-2.04575788652535
C	-2.75195196850144	0.10766459030134	-2.36461832344336
C	-1.70639790353128	-1.94908694121991	-1.63516853694386
C	2.13149922961799	2.69068129206264	-2.89582825554549
C	-1.51446184936890	0.75973130852177	-2.27657060718811
C	1.11416867293909	3.60596140344490	-2.59712172227289
C	-0.45655677066899	-1.30358542273134	-1.53424781101741
C	-0.38344911004718	0.06210765320463	-1.87072513729380
C	2.74347695272662	1.96518039215686	-1.87232520386221
C	0.71817825575481	3.79447407287041	-1.26342513392553
C	2.35397775534306	2.13381599524909	-0.52935555211352
C	1.33667948528540	3.07272531179373	-0.24581782354369
C	-2.83449826853205	0.03239544148177	0.59747386735617
C	-3.97218246174504	-0.74823928651757	0.41135082192041
C	-1.69073233710926	-0.51950242913739	1.19706715944123
C	-3.98230400621438	-2.07868466763692	0.85059012883526
C	-5.20496400505103	-2.91734666868998	0.63841848764608
C	-1.69321447386264	-1.86574757971399	1.59234665200672
C	-2.84040364098837	-2.63690620878618	1.43378944688497
H	-3.80522472853113	-1.77063158242770	-2.10090518911312
H	2.45030667504668	2.53920714621720	-3.92794168911909
H	-1.78754941700211	-3.00000968063624	-1.35609768252466
H	-1.43420418510325	1.81744954197485	-2.52835824159028
H	3.53017972685192	1.24830804923309	-2.11381471248139
H	0.57094242759687	0.58397025612561	-1.80264292626441
H	-0.07371356862064	4.50664551524908	-1.01879332677126
H	1.01993645815972	3.22640234002047	0.78726542947574
H	-2.83020058199831	1.07480590043256	0.27462525762830
H	-4.86104707220108	-0.31121739865056	-0.05047627046058
H	-0.80489206019806	-2.30581169932077	2.04445391899989
H	-2.84654468277317	-3.67524581234178	1.77026889022306
F	-4.99931814392438	0.13083817515180	-3.16333375674137
F	0.83888836576655	4.03639360551058	-4.92070162021549
F	-4.45048518625771	1.63902754410891	-1.69886978980721
F	-0.90845375602646	4.30803628386048	-3.64665719133932

F	-3.70848119453904	1.79879751396532	-3.72786285811618
F	0.71375064233623	5.74050662208370	-3.57692216753625
F	-6.34602632169274	-2.18299592088934	0.66611736038593
F	-5.34467183136482	-3.89499708769201	1.56718181541165
F	-5.18230311827062	-3.54824260662666	-0.57345894507782

2.12 References

(1) Turner, J. A. Sustainable Hydrogen Production. *Science* **2004**, *305*, 972. DOI: 10.1126/science.1103197.

(2) Gray, H. B. Powering the planet with solar fuel. *Nat. Chem.* **2009**, *1*, 7. DOI: 10.1038/nchem.141.

(3) Aslam, S.; Rani, S.; Lal, K.; Fatima, M.; Hardwick, T.; Shirinfar, B.; Ahmed, N. Electrochemical hydrogen production: sustainable hydrogen economy. *Green Chem.* **2023**, *25*, 9543. DOI: 10.1039/D3GC02849F.

(4) Szablowski, L.; Wojcik, M.; Dybinski, O. Review of steam methane reforming as a method of hydrogen production. *Energy* **2025**, *316*, 134540. DOI: 10.1016/j.energy.2025.134540.

(5) Vincent, K. A.; Parkin, A.; Armstrong, F. A. Investigating and Exploiting the Electrocatalytic Properties of Hydrogenases. *Chem. Rev.* **2007**, *107*, 4366. DOI: 10.1021/cr050191u.

(6) Liu, F.; Shi, C.; Guo, X.; He, Z.; Pan, L.; Huang, Z.-F.; Zhang, X.; Zou, J.-J. Rational Design of Better Hydrogen Evolution Electrocatalysts for Water Splitting: A Review. *Adv. Sci.* **2022**, *9*, 2200307. DOI: 10.1002/advs.202200307.

(7) Lubitz, W.; Ogata, H.; Rüdiger, O.; Reijerse, E. Hydrogenases. *Chem. Rev.* **2014**, *114*, 4081. DOI: 10.1021/cr4005814.

(8) Grinter, R.; Kropp, A.; Venugopal, H.; Senger, M.; Badley, J.; Cabotaje, P. R.; Jia, R.; Duan, Z.; Huang, P.; Stripp, S. T.; et al. Structural basis for bacterial energy extraction from atmospheric hydrogen. *Nature* **2023**, *615*, 541. DOI: 10.1038/s41586-023-05781-7.

(9) Jones, A. K.; Sillery, E.; Albracht, S. P. J.; Armstrong, F. A. Direct comparison of the electrocatalytic oxidation of hydrogen by an enzyme and a platinum catalyst. *Chem. Commun.* **2002**, 866. DOI: 10.1039/B201337A.

(10) Frey, M. Hydrogenases: Hydrogen-Activating Enzymes. *ChemBioChem* **2002**, *3*, 153. DOI: 10.1002/1439-7633(20020301)3:2/3<153::AID-CBIC153>3.0.CO;2-B.

(11) Fontecilla-Camps, J. C.; Volbeda, A.; Cavazza, C.; Nicolet, Y. Structure/Function Relationships of [NiFe]- and [FeFe]-Hydrogenases. *Chem. Rev.* **2007**, *107*, 4273. DOI: 10.1021/cr050195z.

(12) Dementin, S.; Burlat, B.; De Lacey, A. L.; Pardo, A.; Adryanczyk-Perrier, G.; Guigliarelli, B.; Fernandez, V. M.; Rousset, M. A Glutamate Is the Essential Proton Transfer Gate during the Catalytic Cycle of the [NiFe] Hydrogenase. *J. Biol. Chem.* **2004**, *279*, 10508. DOI: 10.1074/jbc.M312716200.

(13) De Lacey, A. L.; Fernández, V. M.; Rousset, M.; Cammack, R. Activation and Inactivation of Hydrogenase Function and the Catalytic Cycle: Spectroelectrochemical Studies. *Chem. Rev.* **2007**, *107*, 4304. DOI: 10.1021/cr0501947.

(14) Ogata, H.; Nishikawa, K.; Lubitz, W. Hydrogens detected by subatomic resolution protein crystallography in a [NiFe] hydrogenase. *Nature* **2015**, *520*, 571. DOI: 10.1038/nature14110.

(15) Scott, R. A.; Wallin, S. A.; Czechowski, M.; DerVartanian, D. V.; LeGall, J.; Peck, H. D., Jr.; Moura, I. X-ray Absorption Spectroscopy of Nickel in the Hydrogenase from *Desulfovibrio gigas*. *J. Am. Chem. Soc.* **1984**, *106*, 6864. DOI: 10.1021/ja00334a078.

(16) Volbeda, A.; Charon, M.-H.; Piras, C.; Hatchikian, E. C.; Frey, M.; Fontecilla-Camps, J. C. Crystal structure of the nickel–iron hydrogenase from *Desulfovibrio gigas*. *Nature* **1995**, *373*, 580. DOI: 10.1038/373580a0.

(17) Bouwman, E.; Reedijk, J. Structural and functional models related to the nickel hydrogenases. *Coord. Chem. Rev.* **2005**, *249*, 1555. DOI: 10.1016/j.ccr.2004.10.010.

(18) Thoi, V. S.; Sun, Y.; Long, J. R.; Chang, C. J. Complexes of Earth-Abundant Metals for Catalytic Electrochemical Hydrogen Generation under Aqueous Conditions. *Chem. Soc. Rev.* **2013**, *42*, 2388. DOI: 10.1039/C2CS35272A.

(19) McKone, J. R.; Marinescu, S. C.; Brunschwig, B. S.; Winkler, J. R.; Gray, H. B. Earth-abundant hydrogen evolution electrocatalysts. *Chem. Sci.* **2014**, *5*, 865. DOI: 10.1039/C3SC51711J.

(20) Behnke, S. L.; Shafaat, H. S. Heterobimetallic Models of the [NiFe] Hydrogenases: A Structural and Spectroscopic Comparison. *Comments Inorg. Chem.* **2016**, *36*, 123. DOI: 10.1080/02603594.2015.1108914.

(21) Schilter, D.; Camara, J. M.; Huynh, M. T.; Hammes-Schiffer, S.; Rauchfuss, T. B. Hydrogenase Enzymes and Their Synthetic Models: The Role of Metal Hydrides. *Chem. Rev.* **2016**, *116*, 8693. DOI: 10.1021/acs.chemrev.6b00180.

(22) Ahmed, M. E.; Dey, A. Recent developments in bioinspired modelling of [NiFe]- and [FeFe]-hydrogenases. *Curr. Opin. Electrochem.* **2019**, *15*, 155. DOI: 10.1016/j.coelec.2019.05.009.

(23) Dalle, K. E.; Warnan, J.; Leung, J. J.; Reuillard, B.; Karmel, I. S.; Reisner, E. Electro- and Solar-Driven Fuel Synthesis with First Row Transition Metal Complexes. *Chem. Rev.* **2019**, *119*, 2752. DOI: 10.1021/acs.chemrev.8b00392.

(24) Ogo, S. H_2 and O_2 activation by [NiFe]hydrogenases – Insights from model complexes. *Coord. Chem. Rev.* **2017**, *334*, 43. DOI: 10.1016/j.ccr.2016.07.001.

(25) Sun, L.; Duboc, C.; Shen, K. Bioinspired Molecular Electrocatalysts for H_2 Production: Chemical Strategies. *ACS Catal.* **2022**, *12*, 9159. DOI: 10.1021/acscatal.2c02171.

(26) Wiedner, E. S.; Appel, A. M.; Raugei, S.; Shaw, W. J.; Bullock, R. M. Molecular Catalysts with Diphosphine Ligands Containing Pendant Amines. *Chem. Rev.* **2022**, *122*, 12427. DOI: 10.1021/acs.chemrev.1c01001.

(27) Helm, M. L.; Stewart, M. P.; Bullock, R. M.; DuBois, M. R.; DuBois, D. L. A Synthetic Nickel Electrocatalyst with a Turnover Frequency Above 100,000 s^{-1} for H_2 Production. *Science* **2011**, *333*, 863. DOI: 10.1126/science.1205864.

(28) Tsay, C.; Yang, J. Y. Electrocatalytic Hydrogen Evolution under Acidic Aqueous Conditions and Mechanistic Studies of a Highly Stable Molecular Catalyst. *J. Am. Chem. Soc.* **2016**, *138*, 14174. DOI: 10.1021/jacs.6b05851.

(29) Barton, B. E.; Rauchfuss, T. B. Hydride-Containing Models for the Active Site of the Nickel−Iron Hydrogenases. *J. Am. Chem. Soc.* **2010**, *132*, 14877. DOI: 10.1021/ja105312p.

(30) Brazzolotto, D.; Gennari, M.; Queyriaux, N.; Simmons, T. R.; Pécaut, J.; Demeshko, S.; Meyer, F.; Orio, M.; Artero, V.; Duboc, C. Nickel-centred proton reduction catalysis in a model of [NiFe] hydrogenase. *Nat. Chem.* **2016**, *8*, 1054. DOI: 10.1038/nchem.2575.

(31) Ding, S.; Ghosh, P.; Lunsford, A. M.; Wang, N.; Bhuvanesh, N.; Hall, M. B.; Darensbourg, M. Y. Hemilabile Bridging Thiolates as Proton Shuttles in Bioinspired H_2 Production Electrocatalysts. *J. Am. Chem. Soc.* **2016**, *138*, 12920. DOI: 10.1021/jacs.6b06461.

(32) Ding, S.; Ghosh, P.; Darensbourg, M. Y.; Hall, M. B. Interplay of hemilability and redox activity in models of hydrogenase active sites. *Proc. Natl. Acad. Sci. U.S.A.* **2017**, *114*, E9775. DOI: 10.1073/pnas.1710475114.

(33) Tang, H.; Hall, M. B. Biomimetics of [NiFe]-Hydrogenase: Nickel- or Iron-Centered Proton Reduction Catalysis? *J. Am. Chem. Soc.* **2017**, *139*, 18065. DOI: 10.1021/jacs.7b10425.

(34) Ahmed, M. E.; Chattopadhyay, S.; Wang, L.; Brazzolotto, D.; Pramanik, D.; Aldakov, D.; Fize, J.; Morozan, A.; Gennari, M.; Duboc, C.; et al. Hydrogen Evolution from Aqueous Solutions Mediated by a Heterogenized [NiFe]-Hydrogenase Model: Low pH Enables Catalysis through an Enzyme-Relevant Mechanism. *Angew. Chem. Int. Ed.* **2018**, *57*, 16001. DOI: 10.1002/anie.201808215.

(35) Dance, I. G. The Strucutral Chemistry of Metal Thioalte Complexes. *Polyhedron* **1986**, *5*, 1037. DOI: 10.1016/S0277-5387(00)84307-7.

(36) Blower, P. J.; Dilworth, J. R. Thiolato-Complexes of the Transition Metals. *Coord. Chem. Rev.* **1987**, *76*, 121. DOI: 10.1016/0010-8545(87)85003-8.

(37) Krebs, B.; Henkel, G. Transition-Metal Thiolates: From Molecular Fragments of Sulfidic Solids to Models for Active Centers in Biomolecules. *Angew. Chem. Int. Ed.* **1991**, *30*, 769. DOI: 10.1002/anie.199107691.

(38) Grapperhaus, C. A.; Darensbourg, M. Y. Oxygen Capture by Sulfur in Nickel Thiolates. *Acc. Chem. Res.* **1998**, *31*, 451. DOI: 10.1021/ar950048v.

(39) Holah, D. G.; Coucouvanis, D. Synthesis and Characterization of a New Series of First Row Element Tetrahedral Mercaptide Complexes. *J. Am. Chem. Soc.* **1975**, *97*, 6917. DOI: 10.1021/ja00856a079.

(40) Swenson, D.; Baenziger, N. C.; Coucouvanis, D. Tetrahedral Mercaptide Complexes. Crystal and Molecular Structures of $[(C_6H_5)_4P]_2M(SC_6H_5)_4$ Complexes (M = Cd(II), Zn(II), Ni(II), Co(II), and Mn(II)). *J. Am. Chem. Soc.* **1978**, *100*, 1932. DOI: 10.1021/ja00474a053.

(41) Yamamura, T.; Miyamae, H.; Katayama, Y.; Sasaki, Y. Nickel Thiolates. Simple Synthesis, the Behaivor Upon Protolysis and Oxidation Potentials. *Chem. Lett.* **1985**, *14*, 269. DOI: 10.1246/cl.1985.269.

(42) Snyder, B.; Rao, C.; Holm, R. Mononuclear and Binuclear Metal(II) Complexes of Ethane-1,2-Dithiolate. Preparation, Equilibrium and Redox Properties of $[Ni(S_2C_2H_4)_2]^{2-}$ and $[Ni_2(S_2C_2H_4)_3]^{2-}$, and the Structures of $[Ni_2(S_2C_2H_4)_3]^{2-}$ and $[Pd(S_2C_2H_4)_2]^{2-}$. *Aust. J. Chem.* **1986**, *39*, 963. DOI: 10.1071/CH9860963.

(43) Baidya, N.; Mascharak, P. K.; Stephan, D. W.; Campagna, C. F. Mononuclear nickel(II) thiolates of square-planar geometry: syntheses, spectral and redox properties of $[Ni(SCH_2CH_2S)_2]^{2-}$ and $[Ni(SCH(CH_3)CH(CH_3)S)_2]^{2-}$ and the structure of $(Ph_4P)_2[Ni(SCH_2CH_2S)_2]\cdot 4H_2O$. *Inorg. Chim. Acta* **1990**, *177*, 233. DOI: 10.1016/S0020-1693(00)85981-2.

(44) Fox, S.; Wang, Y.; Silver, A.; Millar, M. Viability of the $[Ni^{III}(SR)_4]^-$ Unit in Classical Coordination Compounds and in the Nickel-Sulfur Center of Hydrogenases. *J. Am. Chem. Soc.* **1990**, *112*, 3218. DOI: 10.1021/ja00164a057.

(45) Yamamura, T.; Arai, H.; Kurihara, H.; Kuroda, R. Synthesis and the Structure of Bis(tetraphenylphosphonium) [Ni(1,2-trans-dimercaptocyclohexane)$_2$]. A New Addition to the Ni^{3+} Generating Thiolato Nickel Complexes. *Chem. Lett.* **1990**, *19*, 1975. DOI: 10.1246/cl.1990.1975.

(46) Sellmann, D.; Fünfgelder, S.; Knoch, F.; Moll, M. Transition Metal Complexes with Sulfur Ligands, LXXVI Redox and Addition Reactions of Nickel Complexes with Multidentate Thioether-Thiolato Ligands. X-Ray Structure Determinations of $(NMe4)_2[Ni('S_2')_2]$ and $[Ni('S_4–C_3')(PMe_3)]$. *Z. Naturforsch.* **1991**, *46*, 1601. DOI: 10.1515/znb-1991-1203.

(47) Rheingold, A. L.; Beall, K. S.; Riggs, P. J.; Groh, S. E. Bis(tetraethylammonium) Nickel Tetrakisthiophenolate: a New Polymorph. *Acta Cryst. C* **1993**, *49*, DOI: 10.1107/S0108270192007704.

(48) Silver, A.; Koch, S. A.; Millar, M. X-ray crystal structures of a series of $[M^{II}(SR)_4]^{2-}$ complexes (M - Mn, Fe, Co, Ni, Zn, Cd and Hg) with S_4 crystallographic symmetry. *Inorg. Chim. Acta* **1993**, *205*, 9. DOI: 10.1016/S0020-1693(00)87348-X.

(49) Erkizia, E.; Conry, R. R. Synthesis and Characterization of Square Planar Nickel(II)−Arylthiolate Complexes with the Biphenyl-2,2'-dithiolate Ligand. *Inorg. Chem.* **2000**, *39*, 1674. DOI: 10.1021/ic990931f.

(50) Han, Z.; Shen, L.; Brennessel, W. W.; Holland, P. L.; Eisenberg, R. Nickel Pyridinethiolate Complexes as Catalysts for the Light-Driven Production of Hydrogen from Aqueous Solutions in Noble-Metal-Free Systems. *J. Am. Chem. Soc.* **2013**, *135*, 14659. DOI: 10.1021/ja405257s.

(51) Fox, D. C.; Fiedler, A. T.; Halfen, H. L.; Brunold, T. C.; Halfen, J. A. Electronic Structure Control of the Nucleophilicity of Transition Metal−Thiolate Complexes: An Experimental and Theoretical Study. *J. Am. Chem. Soc.* **2004**, *126*, 7627. DOI: 10.1021/ja039419q.

(52) Williams, K. R.; Hedman, B.; Hodgson, K. O.; Solomon, E. I. Ligand K-edge X-ray absorption spectroscopic studies: metal-ligand covalency in transition metal tetrathiolates. *Inorg. Chim. Acta* **1997**, *263*, 315. DOI: 10.1016/S0020-1693(97)05663-6.

(53) Van Heuvelen, K. M.; Cho, J.; Dingee, T.; Riordan, C. G.; Brunold, T. C. Spectroscopic and Computational Studies of a Series of High-Spin Ni(II) Thiolate Complexes. *Inorg. Chem.* **2010**, *49*, 6535. DOI: 10.1021/ic100362q.

(54) Rosenfield, S. G.; Armstrong, W. H.; Mascharak, P. K. Convenient Synthesis and Properties of $(R_4N)_2[Ni(SAr)_4]$ (Ar = C_6H_5, *p*-C_6H_4Cl, *p*-$C_6H_4CH_3$, and *m*-C_6H_4Cl) and the Structure of Tetraethylammonium Tetrakis(*p*-chlorobenzenethiolato)nickelate(II). *Inorg. Chem.* **1986**, *25*, 3014. DOI: 10.1021/ic00237a018.

(55) Yamamura, T.; Arai, H. Tetrakis(thiolato)nickelate(II), $[Ni(RS)_4]^{2-}$; Ligand Dissociation and Electronic Spectra. *Bull. Chem. Soc. Jpn.* **1992**, *65*, 1799. DOI: 10.1246/bcsj.65.1799.

(56) Colpas, G. J.; Kumar, M.; Day, R. O.; Maroney, M. J. Structural Investigations of Nickel Complexes with Nitrogen and Sulfur Donor Ligands. *Inorg. Chem.* **1990**, *29*, 4779. DOI: 10.1021/ic00348a037.

(57) Slater, J. W.; Shafaat, H. S. Nickel-Substituted Rubredoxin as a Minimal Enzyme Model for Hydrogenase. *J. Phys. Chem. Lett.* **2015**, *6*, 3731. DOI: 10.1021/acs.jpclett.5b01750.

(58) Slater, J. W.; Marguet, S. C.; Monaco, H. A.; Shafaat, H. S. Going beyond Structure: Nickel-Substituted Rubredoxin as a Mechanistic Model for the [NiFe] Hydrogenases. *J. Am. Chem. Soc.* **2018**, *140*, 10250. DOI: 10.1021/jacs.8b05194.

(59) Hansch, C.; Leo, A.; Taft, R. W. A Survey of Hammett Substituent Constants and Resonance and Field Parameters. *Chem. Rev.* **1991**, *91*, 165. DOI: 10.1021/cr00002a004.

(60) Kütt, A.; Tshepelevitsh, S.; Saame, J.; Lõkov, M.; Kaljurand, I.; Selberg, S.; Leito, I. Strengths of Acids in Acetonitrile. *Eur. J. Org. Chem.* **2021**, *2021*, 1407. DOI: 10.1002/ejoc.202001649.

(61) Kashin, A. S.; Degtyareva, E. S.; Eremin, D. B.; Ananikov, V. P. Exploring the performance of nanostructured reagents with organic-group-defined morphology in cross-coupling reaction. *Nat. Commun.* **2018**, *9*, 2936. DOI: 10.1038/s41467-018-05350-x.

(62) Seo, W. T. M.; Riffel, M. N.; Oliver, A. G.; Tsui, E. Y. Metal-cation-induced shifts in thiolate redox and reduced sulfur speciation. *Chem. Sci.* **2024**, *15*, 7332. DOI: 10.1039/D4SC01025F.

(63) Tennyson, A. G.; Dhar, S.; Lippard, S. J. Synthesis and Characterization of $\{Ni(NO)\}^{10}$ and $\{Co(NO)_2\}^{10}$ Complexes Supported by Thiolate Ligands. *J. Am. Chem. Soc.* **2008**, *130*, 15087. DOI: 10.1021/ja803992y.

(64) Arulsamy, N.; Bohle, D. S.; Butt, J. A.; Irvine, G. J.; Jordan, P. A.; Sagan, E. Interrelationships between Conformational Dynamics and the Redox Chemistry of *S*-Nitrosothiols. *J. Am. Chem. Soc.* **1999**, *121*, 7115. DOI: 10.1021/ja9901314.

(65) Yang, L.; Powell, D. R.; Houser, R. P. Structural variation in copper(I) complexes with pyridylmethylamide ligands: structural analysis with a new four-coordinate geometry index, τ_4. *Dalton Trans.* **2007**, 955. DOI: 10.1039/B617136B.

(66) Cho, J.; Yap, G. P. A.; Riordan, C. G. Structural, Spectroscopic, and Electrochemical Properties of a Series of High-Spin Thiolatonickel(II) Complexes. *Inorg. Chem.* **2007**, *46*, 11308. DOI: 10.1021/ic701743z.

(67) Chattopadhyay, S.; Deb, T.; Ma, H.; Petersen, J. L.; Young, V. G., Jr.; Jensen, M. P. Arylthiolate Coordination and Reactivity at Pseudotetrahedral Nickel(II) Centers: Modulation by Noncovalent Interactions. *Inorg. Chem.* **2008**, *47*, 3384. DOI: 10.1021/ic702417w.

(68) Deb, T.; Anderson, C. M.; Chattopadhyay, S.; Ma, H.; Young, V. G.; Jensen, M. P. Steric and electronic effects on arylthiolate coordination in the pseudotetrahedral complexes $[(Tp^{Ph,Me})Ni–SAr]$ ($Tp^{Ph,Me}$ = hydrotris{3-phenyl-5-methyl-1-pyrazolyl}borate). *Dalton Trans.* **2014**, *43*, 17489. DOI: 10.1039/C4DT02726D.

(69) Maher, M.; Cross, M.; Wilce, M. C. J.; Guss, J. M.; Wedd, A. G. Metal-substituted derivatives of the rubredoxin from *Clostridium pasteurianum*. *Acta Cryst. D* **2004**, *60*, 298. DOI: 10.1107/S090744490302794X.

(70) Slater, J. W.; Marguet, S. C.; Cirino, S. L.; Maugeri, P. T.; Shafaat, H. S. Experimental and DFT Investigations Reveal the Influence of the Outer Coordination Sphere on the Vibrational Spectra of Nickel-Substituted Rubredoxin, a Model Hydrogenase Enzyme. *Inorg. Chem.* **2017**, *56*, 3926. DOI: 10.1021/acs.inorgchem.6b02934.

(71) Cramer, S. P.; Eidsness, M. K.; Pan, W. H.; Morton, T. A.; Ragsdale, S. W.; DerVartanian, D. V.; Ljungdahl, L. G.; Scott, R. A. X-ray Absorption Spectroscopic Evidence for a Unique

Nickel Site in *Clostridium thermoaceticum* Carbon Monoxide Dehydrogenase. *Inorg. Chem.* **1987**, *26*, 2477. DOI: 10.1021/ic00262a027.

(72) Yamamura, T.; Kurihara, H.; Nakamura, N.; Kuroda, R.; Asakura, K. Synthesis, X-Ray Analysis, EXAFS, and XANES of $[Ni(SCH_2CH_2S)_2]^{2-}$. An Evidence for the Mononuclear Square Planar $\{Ni(II)S_4^-\}$ Geometry in Nickel/Alkane Thiolate System. *Chem. Lett.* **1990**, *19*, 101. DOI: 10.1246/cl.1990.101.

(73) Halcrow, M. A.; Christou, G. Biomimetic Chemistry of Nickel. *Chem. Rev.* **1994**, *94*, 2421. DOI: 10.1021/cr00032a008.

(74) Yamamura, T.; Arai, H.; Nakamura, N.; Miyamae, H. Ni(1,4,8,11-tetrathiaundecane). Synthesis of a Square Planar $NiS_2S_2^-$ Complex in Terms of CO-dehydrogenase. *Chem. Lett.* **1990**, *19*, 2121. DOI: 10.1246/cl.1990.2121.

(75) Becke, A. D. Density-functional thermochemistry. III. The role of exact exchange. *J. Chem. Phys.* **1993**, *98*, 5648. DOI: 10.1063/1.464913.

(76) Broering, E. P.; Truong, P. T.; Gale, E. M.; Harrop, T. C. Synthetic Analogues of Nickel Superoxide Dismutase: A New Role for Nickel in Biology. *Biochemistry* **2013**, *52*, 4. DOI: 10.1021/bi3014533.

(77) Shearer, J. Insight into the Structure and Mechanism of Nickel-Containing Superoxide Dismutase Derived from Peptide-Based Mimics. *Acc. Chem. Res.* **2014**, *47*, 2332. DOI: 10.1021/ar500060s.

(78) Kowal, A. T.; Zambrano, I. C.; Moura, I.; Moura, J. J. G.; LeGall, J.; Johnson, M. K. Electronic and Magnetic Properties of Nickel-Substituted Rubredoxin: a Variable-Temperature Magnetic Circular Dichroism Study. *Inorg. Chem.* **1988**, *27*, 1162. DOI: 10.1021/ic00280a015.

(79) Huang, Y. H.; Moura, I.; Moura, J. J. G.; LeGall, J.; Park, J. B.; Adams, M. W. W.; Johnson, M. K. Resonance Raman Studies of Nickel Tetrathiolates and Nickel-Substituted Rubredoxins and Desulforedoxin. *Inorg. Chem.* **1993**, *32*, 406. DOI: 10.1021/ic00056a012.

(80) Pavlishchuk, V. V.; Addison, A. W. Conversion constants for redox potentials measured versus different reference electrodes in acetonitrile solutions at 25 °C. *Inorg. Chim. Acta* **2000**, *298*, 97. DOI: 10.1016/S0020-1693(99)00407-7.

(81) Fabre, P.-L.; Poliblanc, R. Lés tétraphénolates de métaux de transition, Mn, Fe, Co, Ni: étude électrochimique. *Bull. Soc. Chim. Fr.* **1986**, *5*, 704.

(82) Saha, P.; Amanullah, S.; Dey, A. Electrocatalytic Reduction of Nitrogen to Hydrazine Using a Trinuclear Nickel Complex. *J. Am. Chem. Soc.* **2020**, *142*, 17312. DOI: 10.1021/jacs.0c08785.

(83) Kagalwala, H. N.; Gottlieb, E.; Li, G.; Li, T.; Jin, R.; Bernhard, S. Photocatalytic Hydrogen Generation System Using a Nickel-Thiolate Hexameric Cluster. *Inorg. Chem.* **2013**, *52*, 9094. DOI: 10.1021/ic4013069.

(84) Wilker, J. J.; Lippard, S. J. Alkyl Transfer to Metal Thiolates: Kinetics, Active Species Identification, and Relevance to the DNA Methyl Phosphotriester Repair Center of *Escherichiacoli* Ada. *Inorg. Chem.* **1997**, *36*, 969. DOI: 10.1021/ic961082o.

(85) Yu, H.-Z.; Yang, Y.-M.; Zhang, L.; Dang, Z.-M.; Hu, G.-H. Quantum-Chemical Predictions of pK_a's of Thiols in DMSO. *J. Phys. Chem. A* **2014**, *118*, 606. DOI: 10.1021/jp410274n.

(86) Bordwell, F. G.; Hughes, D. L. Thiol Acidities and Thiolate Ion Reactivities Toward Butyl Chloride in Dimethyl Sulfoxide Solution. The Question of Curvature in Brønsted Plots. *J. Org. Chem.* **1982**, *47*, 3224. DOI: 10.1021/jo00138a005.

(87) Henderson, W.; McIndoe, J. S. *The ESI MS Behaviour of Coordination Complexes. In Mass Spectrometry of Inorganic and Organometallic Compounds*; John Wiley & Sons Ltd, 2005.

(88) Ivanov, S. A.; Kozee, M. A.; Merrill, A. W.; Agarwal, S.; Dahl, L. F. *Cyclo*-[Ni(μ_2-SPh)$_2$]$_9$ and *cyclo*-[Ni(μ_2-SPh)$_2$]$_{11}$: new oligomeric types of toroidal nickel(II) thiolates containing geometrically unprecedented 9- and 11-membered ring systems. *J. Chem. Soc., Dalton Trans.* **2002**, 4105. DOI: 10.1039/B204273H.

(89) Silver, A.; Millar, M. Synthesis and Structure of a Unique Nickel-thiolate Dimer, [(RS)Ni(μ_2-SR)$_3$Ni(SR)]$^{1-}$. An Example of Face-Sharing Bitetrahedra. *J. Chem. Soc., Chem. Commun.* **1992**, 948. DOI: 10.1039/C39920000948.

(90) Dance, I. G.; Scudder, M. L.; Secomb, R. *c*-Ni$_8$(SCH$_2$COOEt)$_{16}$, a Receptive Octagonal Toroid. *Inorg. Chem.* **1985**, *24*, 1201. DOI: 10.1021/ic00202a018.

(91) Tremel, W.; Kriege, M.; Krebs, B.; Henkel, G. Nickel-Thiolate Chemistry Based on Chelating Ligands: Controlling the Course of Self-Assembly Reactions via Ligand Bite Distances. Synthesis, Structures, and Properties of the Homoleptic Complexes [Ni$_3$(SCH$_2$C$_6$H$_4$CH$_2$S)$_4$]$^{2-}$, [Ni$_3$(SCH$_2$CH$_2$S)$_4$]$^{2-}$, and [Ni$_6$(SCH$_2$CH$_2$CH$_2$S)$_7$]$^{2-}$. *Inorg. Chem.* **1988**, *27*, 3886. DOI: 10.1021/ic00295a004.

(92) Arnet, N. A.; Bhuvanesh, N.; Darensbourg, M. Y. Proton affinity studies of nickel N_2S_2 complexes and control of aggregation. *J. Biol. Inorg. Chem.* **2019**, *24*, 909. DOI: 10.1007/s00775-019-01671-4.

(93) Krueger, H. J.; Holm, R. H. Chemical and Electrochemical Reactivity of Nickel(II,I) Thiolate Complexes: Examples of Ligand-Based Oxidation and Metal-Centered Oxidative Addition. *Inorg. Chem.* **1989**, *28*, 1148. DOI: 10.1021/ic00305a026.

(94) Cha, M.; Sletten, J.; Critchlow, S.; Kovacs, J. A. Synthesis and structure of a thiolate-ligated Ni cluster which contains an unusual thiolate bridging mode and an exposed Ni site. *Inorg. Chim. Acta* **1997**, *263*, 153. DOI: 10.1016/S0020-1693(97)05646-6.

(95) Jenkins, R. M.; Singleton, M. L.; Almaraz, E.; Reibenspies, J. H.; Darensbourg, M. Y. Imidazole-Containing (N_3S)-Ni^{II} Complexes Relating to Nickel Containing Biomolecules. *Inorg. Chem.* **2009**, *48*, 7280. DOI: 10.1021/ic900778k.

(96) Broering, E. P.; Dillon, S.; Gale, E. M.; Steiner, R. A.; Telser, J.; Brunold, T. C.; Harrop, T. C. Accessing Ni(III)-Thiolate Versus Ni(II)-Thiyl Bonding in a Family of Ni–N_2S_2 Synthetic Models of NiSOD. *Inorg. Chem.* **2015**, *54*, 3815. DOI: 10.1021/ic503124f.

(97) Kütt, A.; Rodima, T.; Saame, J.; Raamat, E.; Mäemets, V.; Kaljurand, I.; Koppel, I. A.; Garlyauskayte, R. Y.; Yagupolskii, Y. L.; Yagupolskii, L. M.; et al. Equilibrium Acidities of Superacids. *J. Org. Chem.* **2011**, *76*, 391. DOI: 10.1021/jo101409p.

(98) Connelly, N. G.; Geiger, W. E. Chemical Redox Agents for Organometallic Chemistry. *Chem. Rev.* **1996**, *96*, 877. DOI: 10.1021/cr940053x.

(99) Antonello, S.; Daasbjerg, K.; Jensen, H.; Taddei, F.; Maran, F. Formation and Cleavage of Aromatic Disulfide Radical Anions. *J. Am. Chem. Soc.* **2003**, *125*, 14905. DOI: 10.1021/ja036380g.

(100) Krüger, H. J.; Peng, G.; Holm, R. H. Low-Potential Nickel(III,II) Complexes: New Systems Based on Tetradentate Amidate-Thiolate Ligands and the Influence of Ligand Structure on Potentials in Relation to the Nickel Site in [NiFe]-Hydrogenases. *Inorg. Chem.* **1991**, *30*, 734. DOI: 10.1021/ic00004a025.

(101) Hanss, J.; Krüger, H.-J. First Isolation and Structural Characterization of a Nickel(III) Complex Containing Aliphatic Thiolate Donors. *Angew. Chem. Int. Ed.* **1998**, *37*, 360. DOI: 10.1002/(SICI)1521-3773(19980216)37:3<360::AID-ANIE360>3.0.CO;2-P.

(102) Wombwell, C.; Reisner, E. Synthesis, structure and reactivity of Ni site models of [NiFeSe] hydrogenases. *Dalton Trans.* **2014**, *43*, 4483. DOI: 10.1039/C3DT52967C.

(103) Farmer, P. J.; Reibenspies, J. H.; Lindahl, P. A.; Darensbourg, M. Y. Effects of Sulfur Site Modification on the Redox Potentials of Derivatives of [*N,N*'-Bis(2-mercaptoethyl)-1,5-diazacyclooctanato]nickel(II). *J. Am. Chem. Soc.* **1993**, *115*, 4665. DOI: 10.1021/ja00064a030.

(104) Oudart, Y.; Artero, V.; Pécaut, J.; Lebrun, C.; Fontecave, M. Dinuclear Nickel–Ruthenium Complexes as Functional Bio-Inspired Models of [NiFe] Hydrogenases. *Eur. J. Inorg. Chem.* **2007**, *2007*, 2613. DOI: 10.1002/ejic.200700067.

(105) Pieri, C.; Bhattacharjee, A.; Barrozo, A.; Faure, B.; Giorgi, M.; Fize, J.; Réglier, M.; Field, M.; Orio, M.; Artero, V.; et al. Hydrogen evolution reaction mediated by an all-sulfur trinuclear nickel complex. *Chem. Commun.* **2020**, *56*, 11106. DOI: 10.1039/D0CC04174B.

(106) Drosou, M.; Zarkadoulas, A.; Bethanis, K.; Mitsopoulou, C. A. Structural modifications on nickel dithiolene complexes lead to increased metal participation in the electrocatalytic hydrogen evolution mechanism. *J. Coord. Chem.* **2021**, *74*, 1425. DOI: 10.1080/00958972.2021.1918339.

(107) Artero, V.; Fontecave, M. Solar fuels generation and molecular systems: is it homogeneous or heterogeneous catalysis? *Chem. Soc. Rev.* **2013**, *42*, 2338. DOI: 10.1039/C2CS35334B.

(108) Fang, M.; Engelhard, M. H.; Zhu, Z.; Helm, M. L.; Roberts, J. A. S. Electrodeposition from Acidic Solutions of Nickel Bis(benzenedithiolate) Produces a Hydrogen-Evolving Ni–S Film on Glassy Carbon. *ACS Catal.* **2014**, *4*, 90. DOI: 10.1021/cs400675u.

(109) Fourmond, V.; Jacques, P.-A.; Fontecave, M.; Artero, V. H_2 Evolution and Molecular Electrocatalysts: Determination of Overpotentials and Effect of Homoconjugation. *Inorg. Chem.* **2010**, *49*, 10338. DOI: 10.1021/ic101187v.

(110) Canaguier, S.; Field, M.; Oudart, Y.; Pécaut, J.; Fontecave, M.; Artero, V. A structural and functional mimic of the active site of NiFe hydrogenases. *Chem. Commun.* **2010**, *46*, 5876. DOI: 10.1039/C001675F.

(111) Carroll, M. E.; Barton, B. E.; Gray, D. L.; Mack, A. E.; Rauchfuss, T. B. Active-Site Models for the Nickel–Iron Hydrogenases: Effects of Ligands on Reactivity and Catalytic Properties. *Inorg. Chem.* **2011**, *50*, 9554. DOI: 10.1021/ic2012759.

(112) Jain, R.; Mashuta, M. S.; Buchanan, R. M.; Grapperhaus, C. A. Electrocatalytic Hydrogen Evolution and Hydrogen Oxidation with a $Ni(PS)_2$ Complex. *Eur. J. Inorg. Chem.* **2017**, *2017*, 3714. DOI: 10.1002/ejic.201700590.

(113) Luo, G.-G.; Wang, Y.-H.; Wang, J.-H.; Wu, J.-H.; Wu, R.-B. A square-planar nickel dithiolate complex as an efficient molecular catalyst for the electro- and photoreduction of protons. *Chem. Commun.* **2017**, *53*, 7007. DOI: 10.1039/C7CC01942D.

(114) Mondragón, A.; Flores-Alamo, M.; Martínez-Alanis, P. R.; Aullón, G.; Ugalde-Saldívar, V. M.; Castillo, I. Electrocatalytic Proton Reduction by Dimeric Nickel Complex of a Sterically Demanding Pincer-type NS_2 Aminobis(thiophenolate) Ligand. *Inorg. Chem.* **2015**, *54*, 619. DOI: 10.1021/ic502547y.

(115) Mondragón-Díaz, A.; Robles-Marín, E.; Murueta-Cruz, B. A.; Aquite, J. C.; Martínez-Alanis, P. R.; Flores-Alamo, M.; Aullón, G.; Benítez, L. N.; Castillo, I. Conformational Effects of $[Ni_2(\mu\text{-}ArS)_2]$ Cores on Their Electrocatalytic Activity. *Chem. Asian J.* **2019**, *14*, 3301. DOI: 10.1002/asia.201901037.

(116) Murueta-Cruz, B. A.; Berlanga-Vázquez, A.; Martínez-Otero, D.; Benitez, L. N.; Castillo, I.; Mondragón-Díaz, A. Planar or Bent? Redox Modulation of Hydrogenase Bimetallic Models by the $[Ni_2(\mu\text{-}SAr)_2]$ Core Conformation. *Eur. J. Inorg. Chem.* **2021**, *2021*, 2089. DOI: 10.1002/ejic.202100105.

(117) Rountree, E. S.; McCarthy, B. D.; Eisenhart, T. T.; Dempsey, J. L. Evaluation of Homogeneous Electrocatalysts by Cyclic Voltammetry. *Inorg. Chem.* **2014**, *53*, 9983. DOI: 10.1021/ic500658x.

(118) Kotani, H.; Hanazaki, R.; Ohkubo, K.; Yamada, Y.; Fukuzumi, S. Size- and Shape-Dependent Activity of Metal Nanoparticles as Hydrogen-Evolution Catalysts: Mechanistic Insights into Photocatalytic Hydrogen Evolution. *Chem. Eur. J.* **2011**, *17*, 2777. DOI: 10.1002/chem.201002399.

(119) Marinescu, S. C.; Winkler, J. R.; Gray, H. B. Molecular mechanisms of cobalt-catalyzed hydrogen evolution. *Proc. Natl. Acad. Sci. U.S.A.* **2012**, *109*, 15127. DOI: 10.1073/pnas.1213442109.

(120) Chakrabarti, S.; Sinha, S.; Tran, G. N.; Na, H.; Mirica, L. M. Characterization of paramagnetic states in an organometallic nickel hydrogen evolution electrocatalyst. *Nat. Commun.* **2023**, *14*, 905. DOI: 10.1038/s41467-023-36609-7.

(121) Fukuzumi, S.; Kobayashi, T.; Suenobu, T. Unusually Large Tunneling Effect on Highly Efficient Generation of Hydrogen and Hydrogen Isotopes in pH-Selective Decomposition of Formic Acid Catalyzed by a Heterodinuclear Iridium−Ruthenium Complex in Water. *J. Am. Chem. Soc.* **2010**, *132*, 1496. DOI: 10.1021/ja910349w.

(122) Greene, B. L.; Wu, C.-H.; McTernan, P. M.; Adams, M. W. W.; Dyer, R. B. Proton-Coupled Electron Transfer Dynamics in the Catalytic Mechanism of a [NiFe]-Hydrogenase. *J. Am. Chem. Soc.* **2015**, *137*, 4558. DOI: 10.1021/jacs.5b01791.

(123) Brazzolotto, D.; Wang, L.; Tang, H.; Gennari, M.; Queyriaux, N.; Philouze, C.; Demeshko, S.; Meyer, F.; Orio, M.; Artero, V.; et al. Tuning Reactivity of Bioinspired [NiFe]-Hydrogenase Models by Ligand Design and Modeling the CO Inhibition Process. *ACS Catal.* **2018**, *8*, 10658. DOI: 10.1021/acscatal.8b02830.

(124) Wang, L.; Gennari, M.; Barrozo, A.; Fize, J.; Philouze, C.; Demeshko, S.; Meyer, F.; Orio, M.; Artero, V.; Duboc, C. Role of the Metal Ion in Bio-Inspired Hydrogenase Models: Investigation of a Homodinuclear FeFe Complex vs Its Heterodinuclear NiFe Analogue. *ACS Cat.* **2020**, *10*, 177. DOI: 10.1021/acscatal.9b03212.

(125) Namazian, M.; Lin, C. Y.; Coote, M. L. Benchmark Calculations of Absolute Reduction Potential of Ferricinium/Ferrocene Couple in Nonaqueous Solutions. *J. Chem. Theory Comput.* **2010**, *6*, 2721. DOI: 10.1021/ct1003252.

(126) Kim, H.; Park, J.; Lee, Y. S. A Protocol to Evaluate One Electron Redox Potential for Iron Complexes. *J. Comput. Chem.* **2013**, *34*, 2233. DOI: 10.1002/jcc.23380.

(127) Castro, L.; Bühl, M. Calculations of One-Electron Redox Potentials of Oxoiron(IV) Porphyrin Complexes. *J. Chem. Theory Comput.* **2014**, *10*, 243. DOI: 10.1021/ct400975w.

(128) Yan, L.; Lu, Y.; Li, X. A density functional theory protocol for the calculation of redox potentials of copper complexes. *Phys. Chem. Chem. Phys.* **2016**, *18*, 5529. DOI: 10.1039/C5CP06638G.

(129) Confer, A. M.; Sabuncu, S.; Siegler, M. A.; Moënne-Loccoz, P.; Goldberg, D. P. Mononuclear, Nonheme, High-Spin $\{FeNO\}^{7/8}$ Complexes Supported by a Sterically Encumbered N_4S-Thioether Ligand. *Inorg. Chem.* **2019**, *58*, 9576. DOI: 10.1021/acs.inorgchem.9b01475.

(130) Isse, A. A.; Gennaro, A. Absolute Potential of the Standard Hydrogen Electrode and the Problem of Interconversion of Potentials in Different Solvents. *J. Phys. Chem. B* **2010**, *114*, 7894. DOI: 10.1021/jp100402x.

(131) Gu, N. X.; Oyala, P. H.; Peters, J. C. H_2 Evolution from a Thiolate-Bound Ni(III) Hydride. *J. Am. Chem. Soc.* **2020**, *142*, 7827. DOI: 10.1021/jacs.0c00712.

(132) Eberhardt, N. A.; Guan, H. Nickel Hydride Complexes. *Chem. Rev.* **2016**, *116*, 8373. DOI: 10.1021/acs.chemrev.6b00259.

(133) Seo, J.; Manes, T. A.; Rose, M. J. Structural and functional synthetic model of mono-iron hydrogenase featuring an anthracene scaffold. *Nat. Chem.* **2017**, *9*, 552. DOI: 10.1038/nchem.2707.

(134) Gale, E. M.; Narendrapurapu, B. S.; Simmonett, A. C.; Schaefer, H. F., III; Harrop, T. C. Exploring the Effects of H-Bonding in Synthetic Analogues of Nickel Superoxide Dismutase (Ni-SOD): Experimental and Theoretical Implications for Protection of the Ni−SCys Bond. *Inorg. Chem.* **2010**, *49*, 7080. DOI: 10.1021/ic1009187.

(135) Dey, A.; Green, K. N.; Jenkins, R. M.; Jeffrey, S. P.; Darensbourg, M.; Hodgson, K. O.; Hedman, B.; Solomon, E. I. S K-Edge XAS and DFT Calculations on Square-Planar Ni^{II}–Thiolate Complexes: Effects of Active and Passive H-Bonding. *Inorg. Chem.* **2007**, *46*, 9655. DOI: 10.1021/ic7006292.

(136) Song, S.; Lee, W.; Lee, Y.; Cho, K. B.; Lee, J.; Seo, J. Two-Electron-Induced Reorganization of Cobalt Coordination and Metal–Ligand Cooperative Redox Shifting Co(I) Reactivity toward CO_2 Reduction. *Inorg. Chem.* **2023**, *62*, 2326. DOI: 10.1021/acs.inorgchem.2c04071.

(137) Gill, N. S. 680. Complex Halides of the Transition Metals. Part II. Tetrahedral Iron Complexes. *J. Am. Chem. Soc.* **1961**, 3512. DOI: 10.1039/JR9610003512.

(138) Harrop, T. C.; Tonzetich, Z. J.; Reisner, E.; Lippard, S. J. Reactions of Synthetic [2Fe-2S] and [4Fe-4S] Clusters with Nitric Oxide and Nitrosothiols. *J. Am. Chem. Soc.* **2008**, *130*, 15602. DOI: 10.1021/ja8054996.

(139) Fulmer, G. R.; Miller, A. J. M.; Sherden, N. H.; Gottlieb, H. E.; Nudelman, A.; Stoltz, B. M.; Bercaw, J. E.; Goldberg, K. I. NMR Chemical Shifts of Trace Impurities: Common Laboratory Solvents, Organics, and Gases in Deuterated Solvents Relevant to the Organometallic Chemist. *Organometallics* **2010**, *29*, 2176. DOI: 10.1021/om100106e.

(140) Rosenau, C. P.; Jelier, B. J.; Gossert, A. D.; Togni, A. Exposing the Origins of Irreproducibility in Fluorine NMR Spectroscopy. *Angew. Chem. Int. Ed.* **2018**, *57*, 9528. DOI: 10.1002/anie.201802620.

(141) Loliger, J.; Scheffold, R. Paramagnetic moment measurements by nmr. A micro technique. *J. Chem. Educ.* **1972**, *49*, 646. DOI: 10.1021/ed049p646.

(142) Bain, G. A.; Berry, J. F. Diamagnetic Corrections and Pascal's Constants. *J. Chem. Educ.* **2008**, *85*, 532. DOI: 10.1021/ed085p532.

(143) Appel, A. M.; Helm, M. L. Determining the Overpotential for a Molecular Electrocatalyst. *ACS Catal.* **2014**, *4*, 630. DOI: 10.1021/cs401013v.

(144) Lee, K. J.; Elgrishi, N.; Kandemir, B.; Dempsey, J. L. Electrochemical and spectroscopic methods for evaluating molecular electrocatalysts. *Nat. Rev. Chem.* **2017**, *1*, 0039. DOI: 10.1038/s41570-017-0039.

(145) Hu, X.; Brunschwig, B. S.; Peters, J. C. Electrocatalytic Hydrogen Evolution at Low Overpotentials by Cobalt Macrocyclic Glyoxime and Tetraimine Complexes. *J. Am. Chem. Soc.* **2007**, *129*, 8988. DOI: 10.1021/ja067876b.

(146) Krause, L.; Herbst-Irmer, R.; Sheldrick, G. M.; Stalke, D. Comparison of silver and molybdenum microfocus X-ray sources for single-crystal structure determination. *J. Appl. Cryst.* **2015**, *48*, 3. DOI: 10.1107/S1600576714022985.

(147) Sheldrick, G. SHELXT - Integrated space-group and crystal-structure determination. *Acta Cryst. A* **2015**, *71*, 3. DOI: 10.1107/S2053273314026370.

(148) Sheldrick, G. Crystal structure refinement with SHELXL. *Acta Cryst. C* **2015**, *71*, 3. DOI: 10.1107/S2053229614024218.

(149) *EXAFSPAK*; Stanford Synchotron Radiation Lightsource: Menlo Park, CA,, 2001. (accessed.

(150) Rehr, J. J.; Ankudinov, A. L. Progress and challenges in the theory and interpretation of X-ray spectra. *J. Synchrotron Rad.* **2001**, *8*, 61. DOI: 10.1107/S0909049500016423.

(151) Riggs-Gelasco, P. J.; Stemmler, T. L.; Penner-Hahn, J. E. XAFS of dinuclear metal sites in proteins and model compounds. *Coord. Chem. Rev.* **1995**, *144*, 245. DOI: 10.1016/0010-8545(95)01144-E.

(152) Lee, C.; Yang, W.; Parr, R. G. Development of the Colle-Salvetti correlation-energy formula into a functional of the electron density. *Phys. Rev. B* **1988**, *37*, 785. DOI: 10.1103/PhysRevB.37.785.

(153) Kossmann, S.; Neese, F. Efficient Structure Optimization with Second-Order Many-Body Perturbation Theory: The RIJCOSX-MP2 Method. *J. Chem. Theory Comput.* **2010**, *6*, 2325. DOI: 10.1021/ct100199k.

(154) Grimme, S.; Antony, J.; Ehrlich, S.; Krieg, H. A consistent and accurate ab initio parametrization of density functional dispersion correction (DFT-D) for the 94 elements H-Pu. *J. Chem. Phys.* **2010**, *132*, 154104. DOI: 10.1063/1.3382344.

(155) Grimme, S.; Ehrlich, S.; Goerigk, L. Effect of the damping function in dispersion corrected density functional theory. *J. Comput. Chem.* **2011**, *32*, 1456. DOI: 10.1002/jcc.21759.

(156) Weigend, F.; Ahlrichs, R. Balanced basis sets of split valence, triple zeta valence and quadruple zeta valence quality for H to Rn: Design and assessment of accuracy. *Phys. Chem. Chem. Phys.* **2005**, *7*, 3297. DOI: 10.1039/B508541A.

(157) Schäfer, A.; Horn, H.; Ahlrichs, R. Fully optimized contracted Gaussian basis sets for atoms Li to Kr. *J. Chem. Phys.* **1992**, *97*, 2571. DOI: 10.1063/1.463096.

(158) Klamt, A.; Schüürmann, G. COSMO: a new approach to dielectric screening in solvents with explicit expressions for the screening energy and its gradient. *J. Chem. Soc., Perkin Trans. 2* **1993**, 799. DOI: 10.1039/P29930000799.

(159) Pettersen, E. F.; Goddard, T. D.; Huang, C. C.; Couch, G. S.; Greenblatt, D. M.; Meng, E. C.; Ferrin, T. E. UCSF Chimera—A Visualization System for Exploratory Research and Analysis. *J. Comput. Chem.* **2004**, *25*, 1605. DOI: 10.1002/jcc.20084.

(160) Petrenko, T.; Kossmann, S.; Neese, F. Efficient time-dependent density functional theory approximations for hybrid density functionals: Analytical gradients and parallelization. *J. Chem. Phys.* **2011**, *134*, 054116. DOI: 10.1063/1.3533441.

(161) Neese, F.; Olbrich, G. Efficient use of the resolution of the identity approximation in time-dependent density functional calculations with hybrid density functionals. *Chem. Phys. Lett.* **2002**, *362*, 170. DOI: 10.1016/S0009-2614(02)01053-9.

CHAPTER 3

ASSESING THE IMPACT OF HYDROGEN BONDING ON STABILITY AND ELECTORCATALYTIC HYDROGEN EVOLUTION OF HOMOLEPTIC NICKEL-TETRATHIOLATE COMPLEXES

Benjamin A. Yosen, Tiara Hinton, Indranil Chakraborty, Timothy Stemmler, and Todd C. Harrop. To be submitted to *Dalton Transactions*.

3.1 Abstract

Studying the electrocatalytic properties of Ni(II) thiolates for production of hydrogen has been limited due to their instability to acid leading to the formation of polymers. This study investigates the impact of intramolecular hydrogen-bonding on the stability and performance of homoleptic Ni(II) tetrathiolate complexes for electrocatalytic hydrogen production through. By incorporating *ortho*-carboxamide groups to provide intramolecular H-bonding in $(Et_4N)_2$[Ni(S-*o*-^{i}PrCONH-*p*-CF_3-Ph)$_4$] (**1**) (where S-*o*-^{i}PrCONH-*p*-CF_3-Ph = thiolate of *o*-isopropylamide-*p*-trifluoromethyl-phenyl thiol) and $(Et_4N)_2$[Ni(S-*o*-OPhCONH-*p*-CF_3-Ph)$_4$] (**2**) (where S-*o*-OPhCONH-*p*-CF_3-Ph = thiolate of *o*-phenoxyacetamide-*p*-trifluoromethyl-phenyl thiol) we sought to improve protic stability, overpotential, and turnover frequency of Ni(II) tetrathiolate electrocatalysts. However, experimental evidence (XRD, XAS, UV-vis, NMR) reveals that this modification leads to a mixture of monomeric homoleptic Ni(II) tetathiolate complexes in either square-planar or tetrahedral geometries with a computed energy difference of ~5 kcal/mol. Despite geometric isomerization, these complexes exhibited greater stability under acidic conditions than their non-hydrogen bonding counterpart and cathodically shift the Ni(II/I) by ~0.20 V. By increasing the size of the organic substituents on the carboxamide moiety, i.e. in **2**, the protic stability increases without significantly impacting redox potentials. However, under electrocatalytic conditions it was found the activity arises from Ni/S containing heterogenous material.

3.2 Introduction

Reactions involving transfer of both protons and electrons are widespread in nature and play a vital role in the storage and generation of energy for the organism.[1, 2] One such reaction, the hydrogen evolution reaction (HER) has attracted significant interest in the pursuit of clean sources of energy.[3, 4] Enzymes, known as hydrogenases (H_2ases), have evolved to bidirectionally catalyze proton reduction efficiently, and are classified based on the metal housed in their active site: [NiFe]-, [FeFe]-, or [Fe]-only H_2ases.[5-9] These enzymes not only contain highly organized active sites but also intricate protein scaffolds to facilitate the coupling of protons and electrons. For example, the azadithiolate (adt^{2-}) unit in [FeFe]-H_2ase[10, 11] and the terminal SCys of [NiFe]-H_2ase are proposed to act as pendant bases, serving as proton relays during turnover.[12-14] Beyond the primary coordination sphere of the active site, secondary hydrogen-bonding interactions in these enzymes are proposed to play a crucial role in proton transfer. In [FeFe]-H_2ase, these interactions form a network between the bulk solvent and active site to facilitate H^+ transfer and modulate the redox potential of the covalently linked [4Fe-4S]-cluster, known as the H-cluster.[15, 16] Similarly, [NiFe]-H_2ase possesses several H-bonding interactions observed in the active site of [NiFe]-H_2ase, illustrated in Figure 3.1. This active site consists of a redox-active $Ni(CysS)_4$ unit in a see-saw geometry, coordinated to a $Fe(CO)(CN)_2$ unit through two bridging cysteines, adopting a distorted square-pyramidal geometry. Crystallographic studies reveal the presence of several hydrogen-bonds (H-bond) between the protein scaffold and active site of [NiFe]-H_2ase existing between a bridging SCys and a highly conserved His residue, and interaction between the cyano groups and a Ser and Arg residue.[14, 17, 18] Computational studies by Sun and coworkers suggests these H-bonding redistribute charge away from the active site, effectively acting as an electron 'pull', leading to a lower charge distribution. This redistribution of charge lowers the free energy of

proton-coupled-electron steps, thereby enhancing proton reduction efficeinecy.[19] Notably, in this work, the H-bond to the bridging SCys exerts the greatest influence in reducing the free energies of the H^+/e^- transfer steps.[19] This interaction, highlighted in Figure 3.1, is also proposed to alter the electronic structure of the [NiFe] center by shifting the spin density onto the Ni and away from sulfur to promote Ni centered oxidation.[20]

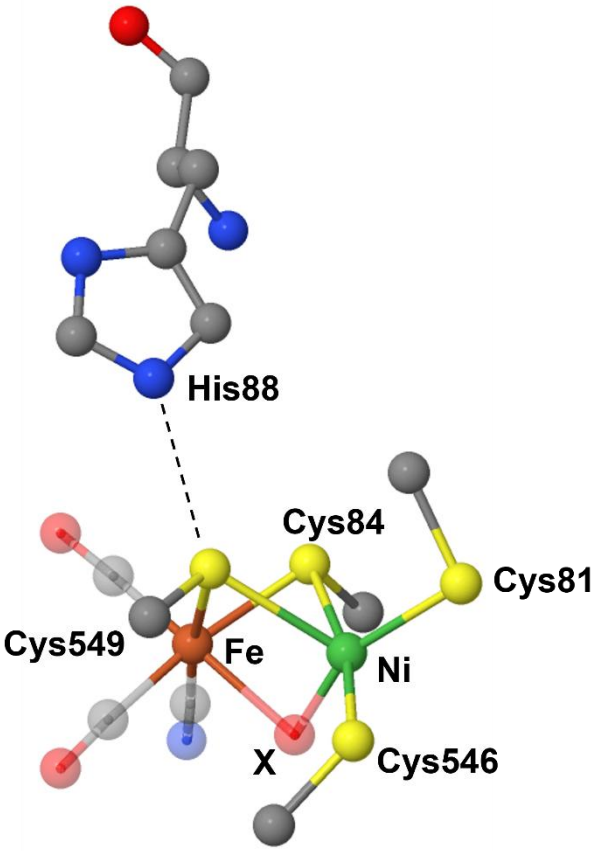

Figure 3.1. Active site of [NiFe]-H_2ase from *Desulfovibrio vulgaris* Miyazaki F. (PDB: 1WUI)[21] in the Ni-A state depicting coordinating ligands to Ni (green) and Fe (red) and a key secondary sphere interaction. Hydrogen atoms are omitted for clarity.

Secondary H-bond interactions to metal cysteine (M-SCys) motifs are commonly observed in other enzymes, such as Ni-SOD[22], rubredoxin[23, 24], and cytochrome-P450[25]. H-bonding to thiolate ligands can be categorized as active or passive depending on the involvement of the H-bond

acceptor orbital in thiolate-metal bonding.[26] Active H-bonding significantly alters the electronic structure and reactivity of the metal. For example, work by our group has demonstrated through synthetic models of Ni-SOD that intramolecular H-bonding can protect Ni-S bonds from oxidative damage by stabilizing S-based molecular orbitals and positively shifts redox potentials.[27, 28] However, more relevant for [NiFe]-H_2ase synthetic models is the impact of intramolecular H-bonding on redox potentials. For example, in the electron-transfer protein rubredoxin H-bond interactions with Fe-bound SCys residues was found to lower the Fe(III/II) couple by ~0.15 V.[29] A similar effect on redox potential is observed for Ni-substituted rubredoxin (NiRb), which contain a tetrahedral [Ni(SCys)$_4$] site,[30] as well as in synthetic models of cytochrome-P450.[31] The Shafaat group found, through mutagenesis studies, incorporation of H-bond donors in the secondary coordination sphere of NiRb increases TOF by three fold, compared to the wild type, but resulted in a ~0.2 V increase in overpotential.[32] They propose that the increase in TOF is due to better solvent accessibility afforded by the mutation.[30] Furthermore, H-bonding interaction is known to depress pK_a of coordinated thiolates,[33, 34] and reduce their nucleophilicity as shown by Carrano and coworker in Zn-thiolate complexes.[35-37]

The aim of this work is to improve the electrocatalytic activity of Ni(II) tetra-aryl thiolate complexes for electrochemical proton reduction. To achieve this, we modified $(Et_4N)_2$[Ni(S-*p*-CF_3-Ph)$_4$], introduced in Chapter 2, by incorporating *ortho*-carboxamide groups of varying steric bulk, namely $(Et_4N)_2$[Ni(S-*o*-^{i}PrCONH-*p*-CF_3-Ph)$_4$] (**1**) (where S-*o*-^{i}PrCONH-*p*-CF_3-Ph = thiolate of *o*-isopropylamide-*p*-trifluoromethyl-phenyl thiol) and $(Et_4N)_2$[Ni(S-*o*-OPhCONH-*p*-CF_3-Ph)$_4$] (**2**) (where S-*o*-OPhCONH-*p*-CF_3-Ph = thiolate of *o*-phenoxyacetamide-*p*-trifluoromethyl-phenyl thiol), Chart 3.1. As established prior, $[Ni(SPh)_4]^-$ complexes are unstable in protic solutions leading to precipitation of intractable polymers.[38] We proposed the instability is a result of

protonation and subsequent dissociation of the coordinate thiolate, thereby limiting the electrocatalytic activity of $(Et_4N)_2$[Ni(S-*p*-CF_3-Ph)$_4$] (**3**). In turn, the basicity of the coordination thiolates can be reduced via intramolecular H-bonding, while bulkier secondary R-groups, as in **2**, may further enhance protic stability through steric protection. By limiting decomposition upon exposure to acid sources, we anticipate the TOF values to increase for **1** and **2**. Furthermore, intramolecular H-bonding is proposed to depress the Ni(II/I) couple responsible for initiating catalysis, thus, improving overpotential. In turn, **1** and **2** are proposed to evolve hydrogen with higher TOF values and lower overpotentials compared to **3**.

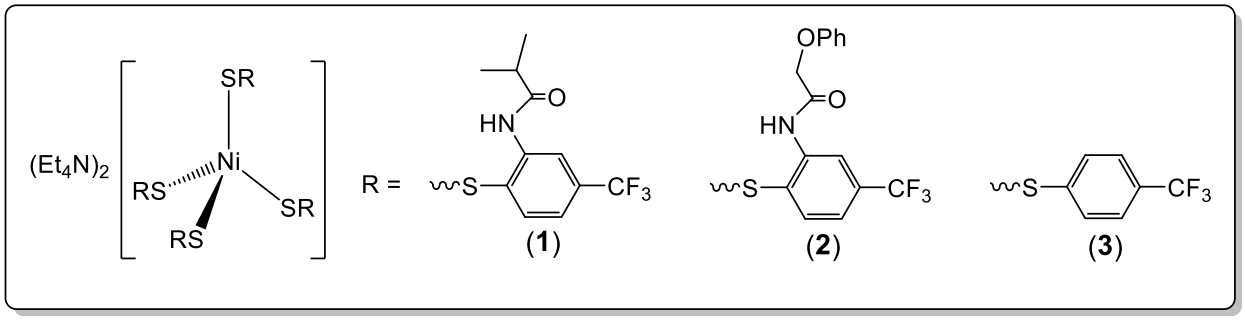

Chart 3.1. [NiFe]-hydrogenase model systems described in the present work. $(Et_4N)_2$[Ni(S-*o*-^{i}PrCONH-*p*-CF_3-Ph)$_4$] (**1**), and $(Et_4N)_2$[Ni(S-*o*-OPhCONH-*p*-CF_3-Ph)$_4$] (**2**), and $(Et_4N)_2$[Ni(S-*p*-CF_3-Ph)$_4$] (**3**).

Herein, we report the synthesis, structural/spectroscopic/electrochemical properties, speciation, electrochemical HER activities, and electronic structures of $(Et_4N)_2$[Ni(S-*o*-^{i}PrCONH-*p*-CF_3-Ph)$_4$] (**1**) and $(Et_4N)_2$[Ni(S-*o*-OPhCONH-*p*-CF_3-Ph)$_4$] (**2**) as models of the tetracysteinate-Ni(II) site in [NeFe]-H_2ase. X-ray diffraction analysis and X-ray absorption spectroscopy (XAS) reveal both complexes adopt a square-planar geometry in the solid-state. However, upon dissolution, ^{1}H/^{19}F NMR data suggests the presence of an S = 1 complex identified as the monomeric tetrahedral isomer. Computational studies suggest a low barrier to isomerization between the tetrahedral and

square-planar geometry indicating that both geometric isomers likely exist in solution. Furthermore, **1** and **2** appear to exist in an equilibrium with an *S,S*-bridged multimer, such as bridged trimer; however, this equilibrium can be shifted to monomer upon the addition of thiolate for **1**. Despite the complexity in their solution-state, incorporation of intramolecular H-bonding in **1** and **2** results in greater stability under acidic conditions and positively shifts the Ni(II/I) couple. However, the electrocatalytic activity observed for **1** and **2** stems from Ni-sulfide deposits on the electrode. These findings underscore the delicate balance of forces needed to maintain a tetrahedral geometry in $[Ni(SPh)_4]^{2-}$ systems and highlight the influence of intramolecular H-bonding on their protic stability and redox properties.

3.3 Results and Discussion

Synthesis. To improve the protic stability of $[Ni(SPh)_4]^{2-}$ complexes and depress their Ni(II/I) redox potentials, the simple $(S\text{-}p\text{-}CF_3\text{-}Ph)^-$ ligand, utilized in Chapter 2, was modified to incorporate *ortho*-carboxamide groups that can engage bound S-atoms in hydrogen-bonding. The monoanionic ligands were generated at high yields, ~85%, by acyl chloride coupling to the *ortho*-amine disulfide, $(S\text{-}o\text{-}NH_2\text{-}p\text{-}CF_3\text{-}Ph)_2$, followed by reduction with $NaBH_4$ and cation exchange with Et_4NCl. Preparation of the Ni(II) complexes $(Et_4N)_2[Ni(S\text{-}o\text{-}^i PrCONH\text{-}p\text{-}CF_3\text{-}Ph)_4]$ (**1**) and $(Et_4N)_2[Ni(S\text{-}o\text{-}OPhCONH\text{-}p\text{-}CF_3\text{-}Ph)_4]$ (**2**) were performed in a similar manner as previously reported complexes under higher thiolate/Ni ratios and polar aprotic solvents.[39] The dropwise addition of a blue MeCN slurry of $(Et_4N)_2[NiCl_4]$ into an MeCN solution containing 4.5 mol-equiv. of the tetraethylammonium (Et_4N^+) salt of the thiolate produced a homogeneous dark-red solution indicative of tetrathiolate Ni(II) complexes **1** and **2**. After work up, complexes were isolated as a green powder for **1**, at a 87% yield, and an red-orange powder for **2**, at a 91% yield. Complexes **1** and **2** can also be synthesized from disulfide/coordinated-thiolate exchange between

$(Et_4N)_2[Ni(S\text{-}p\text{-}CF_3\text{-}Ph)_4]$ (**3**) and the corresponding disulfide, as has been employed by others, albeit at lower yields at ~70%.[40-42] Standard characterization measurements such as UV-vis, FTIR, $^1H/^{19}F$ NMR, ESI-MS, XAS, magnetic moment, X-ray diffraction, and CHN combustion measurements support the homoleptic tetrathiolate formulation of **1** and **2** (see below).

X-ray Crystallography, X-ray Absorption Spectroscopy, and Electronic Structure. Diffraction quality crystals of **1**, using Me_4N^+ as the counterion, and **2**, seen in Figures 3.2 and 3.3, grew from pentane diffusion into an ethyl acetate solution of the resulting products at -20 ˚C, revealing their monomeric and homoleptic nature. Both complexes contain four aryl thiolate ligands coordinating Ni(II) in a square-planar geometry revealed by the tetrahedral distortion parameter (τ_4) of 0.01 and 0.00 for **1** and **2** (1 for a perfect tetrahedron; 0 for a perfect square-plane).[43] Additional structural information from Ni K-edge X-ray absorption spectroscopy (XAS) and magnetic moment (μ_{eff}) measurements support the square-planar geometry of **1** in the solid-state from as-isolated material. X-ray absorption near edge spectroscopic (XANES) analysis reveals a relatively intense rising edge 1s→4p feature at 8335 eV, suggestive of a Ni(II) oxidation state.[44] The a weak pre-edge feature at 8331 eV (area = 0.051 eV^2) is consistent with weak/symmetry-forbidden 1s→3d transitions in square-planar complexes.[44] EXAFS of **1** indicates four S-scatters at a $Ni\text{-}S_{avg}$ distance of 2.22 Å , in-line with values obtained from XRD, see Table 3.1. The lack of magnetic moment in the solid state of **1** further supports a square-planar ($S = 0$) geometry about the Ni(II) center. Adoption of a square-planar geometry is atypical for homoleptic tetra-aryl thiolate complexes $[Ni(S\text{-}p\text{-}X\text{-}Ph)_4]^{2-}$ (X = H, Cl, CF_3) which typically possess a slightly distorted tetrahedral geometry (τ_4 = 0.79 to 0.83).[38, 39, 45, 46] In turn, $Ni\text{-}S_{avg}$ bond lengths of **1** (2.222 Å) and **2** (2.224 Å) are expectedly shorter compared to the $NiS\text{-}_{avg}$ bond lengths of tetrahedral $[Ni(S\text{-}p\text{-}X\text{-}Ph)_4]^{2-}$ complexes ($Ni\text{-}S_{avg}$ = 2.281 – 2.296 Å) given the more covalent nature of the

Ni-S bond in square-planar copmlexes.[47] These results strongly point to exclusively square-planar geometries of **1** and **2** in their solid-state.

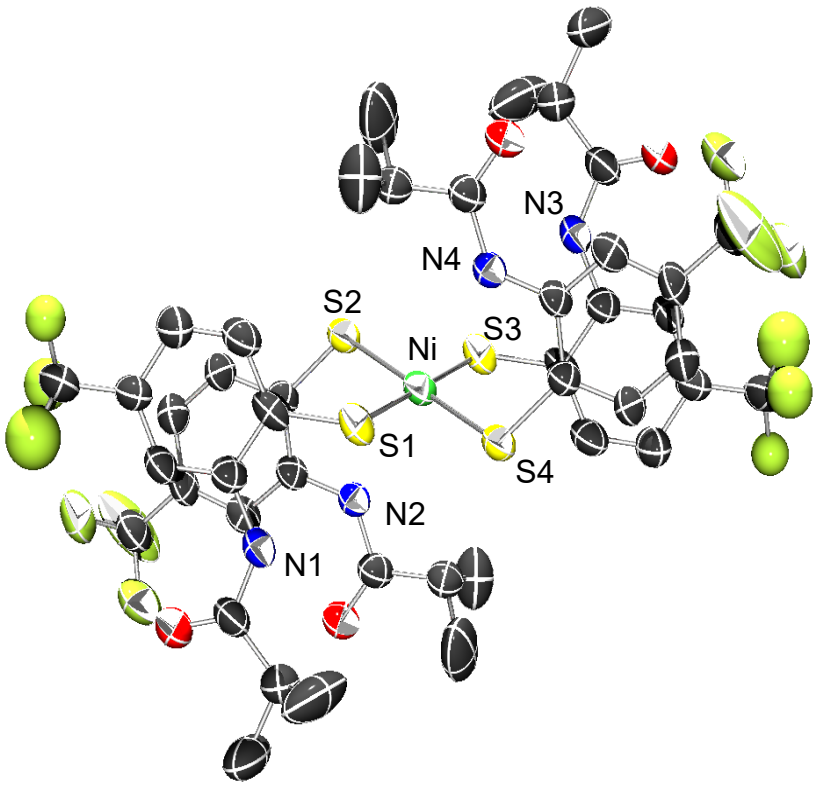

Figure 3.2. ORTEP diagram of the dianion of $(Et_4N)_2[Ni(S\text{-}o\text{-}^{i}PrCONH\text{-}p\text{-}CF_3\text{-}Ph)_4]$ (**1**) at 50% thermal probability ellipsoids. H atoms and counter anions are omitted for clarity. Color code: cyan, nickel; yellow, sulfur; nitrogen, blue; oxygen, red; gray, carbon; and green, fluorine.

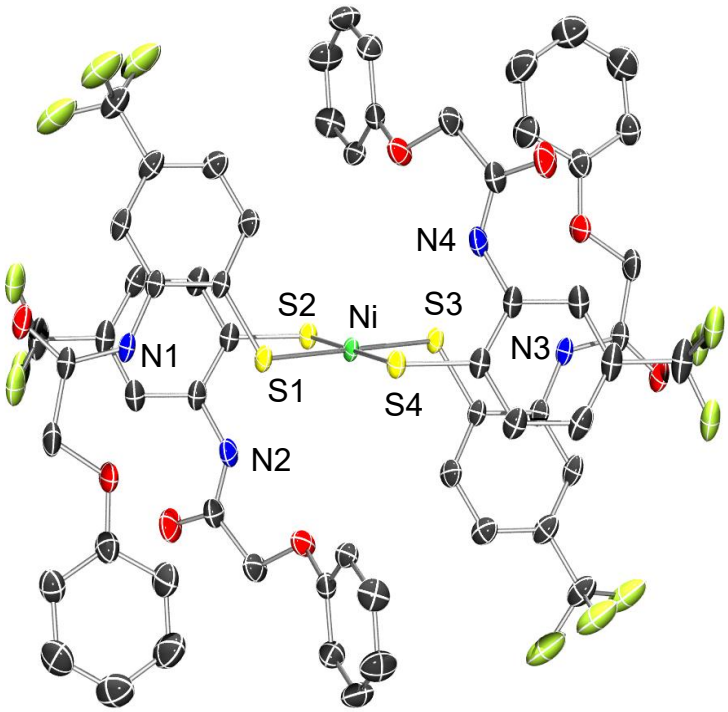

Figure 3.3. ORTEP diagram of the dianion of $(Et_4N)_2[Ni(S\text{-}o\text{-}OPhCONH\text{-}p\text{-}CF_3\text{-}Ph)_4]$ (**2**) at 50% thermal probability ellipsoids from *preliminary data*. H atoms and counter anions are omitted for clarity. Color code: cyan, nickel; yellow, sulfur; nitrogen, blue; oxygen, red; gray, carbon; and green, fluorine.

Despite this unexpected result, X-ray structures of **1** and **2** reveal the *ortho*-carboxamide groups are positioned to serve as intramolecular H-bond donors to the coordinated S-atoms. Solid-state intramolecular H-bonding interactions are confirmed by an average N_{amide}--S bond distance of 2.974 Å for both **1** and **2** that are well below the sum of the van der Waal's radii of N and S (3.55 Å).[41, 48] The similar N_{amide}--S bond distances suggest that the bulkier -OPh substituent in **2** does not impact intramolecular H-bonding. Compared to [NiFe]-hydrogenase, the N_{amide}---S distance of **1** and **2** are shorter than the H-bonding interaction of the bridging CysS and His residue (~3.4

Å).[6] However, these distances are comparable to those observed in other M-SR (M = Ni[27, 49], Zn[35], Fe[40, 50], Pt[41]) complexes with similarly positioned carboxamide-NH functionalities on aryl thiolate ligands. Furthermore, the amide groups are nearly coplanar with their respective benzene rings, possessing dihedral angles (<$C_{\alpha 1}$-$C_{\beta 1}$-N_1-C_1(O)) of ~160˚ for **1** and **2** which are preferable to spreading π-conjugation as observed in [Pt(bpy)(S-2-$PH_3CCONHPh)_2$] (bpy = 2,2-bipyridine) and $(Et_4N)_2$[M(S-o-^{t}BuCONHPh)$_4$] (M = Fe, Co).[40, 51] Although H-bonding is proposed to stabilize antibonding Ni(dπ)-S(pπ) orbital, resulting in shorter Ni-S bond lengths, the Ni-S bonds in **1** and **2** are slightly longer (by 0.01 to 0.03 Å) than observed in other square-planar Ni-tetra thiolate complexes, see Table S1.4. This elongation is likely due to more flexible monomeric aryl thiolate ligands of **1** and **2** compared to the more rigid dithiolate chelates of isolated monomeric Ni(II) tetrathiolate complexes. The closest structural analogue to **1** and **2** is [Ni(HpyS)$_4$]$(NO_3)_2$, reported by Eisenberg, which features four homoleptic pyridyl thiolate ligands coordinated to Ni(II) in a square-planar geometry possessing Ni-S_{avg} bond lengths of 2.212 Å.[52] Although the NH moieties are poised for intramolecular H-bonding to coordinated thiolate, as with **1** and **2**, the crystal structure instead reveals the NH is engaged in intermolecular H-bonding between two cis-pyridyl thiolate ligands and one counterion (NO_3^-). The Ni-S bond lengths of **1** and **2** are slightly longer than in [Ni(HpyS)$_4$]$(NO_3)_2$ likely due to withdrawing effect of the *p*-CF_3 groups reducing the covalency of the Ni-S bonds.

Table 3.1. Select bond distances (Å), angles, and τ_4 values from XRD and DFT of select monomeric tetrathiolate Ni(II) complexes.

Complex	Ni–S (Å)	Ni–S_{avg} (Å)	τ_4	<Ar-(Ni-S)	ref
1	2.236, 2.207, 2.214, 2.236	2.222	0.01	36.4˚, 74.1˚, 31.9˚, 81.8˚	TW
1*(SqPl)	2.213, 2.212, 2.230, 2.231	2.222	0.00	64.2˚, 24.8˚	TW
1*(T_d)	2.307, 2.307, 2.316, 2.334	2.316	0.82	85.5˚, 86.7˚, 76.0˚, 18.3˚	TW
2	2.224, 2.223	2.224	0.00	21.8˚, 69.4˚	TW
3	2.296, 2.290, 2.275, 2.266	2.282	0.79	1.2˚, 6.5˚, 5.0˚, 38.0˚	Ch. 2
3*(SqPl)	2.269, 2.248, 2.301, 2.280	2.276	0.06	42.8˚, 35.7˚, 27.8˚, 42.2˚	Ch. 2
3*(T_d)	2.323, 2.335, 2.332, 2.320	2.328	0.79	23.6˚, 11.2˚, 26.4˚, 23.6 ˚	Ch. 2
$[Ni(HpyS)_4](NO_3)_2$	2.213, 2.215, 2.214, 2.204	2.212	0.05	40.5˚, 13.3˚, 37.1˚, 33.5˚	[52]
$(PPh_4)_2[Ni(edt)_2]$[b]	2.201, 2.188	2.194	0.00	N/A	[53]
$(Et_4N)_2[Ni(bpdt)_2]$[c]	2.214, 2,215, 2.214, 2.204	2.216	0.04	N/A	[54]

[a]Abbreviations: TW = this work. [b]edt = ethane ditihoalte. [c]bpdt = 2,2-biphenyl dithiolate. *Computed complexes (B3LYP, def2-TZVPP, Gas Phase)

As noted prior, all structurally characterized $[Ni(SPh)_4]^{2-}$ complexes exhibit slightly distorted tetrahedral geometries. While the thermodynamic driving force for the adoption of tetrahedral geometries of Ni(II) tetra-aryl thiolate complexes has not been explicitly stated, previous groups have noted a *coplanarity* between the Ni-S bond vector and aryl ring.[39, 45, 55, 56] This arrangement maximizes orbital overlap between the out-of-plane 3p(π) S-orbital (referred to as S-3p(π,op)) with the α-C-3p(π) orbital of benzene, i.e., perpendicular to the plane formed by the ring). Spectroscopic and computational studies by Brunold et. al. on a series of tetrahedral Ni(II)-arlythiolate complexes

suggests this coplanar orientation facilitates delocalization of electron density over the S-Ph moiety.[57] This is evident by the diminished S-character in the HOMO, by ~10%, compared to an analogous alkyl thiolate complex, in which such delocalization is absent. Furthermore, the computations indicate that the S-3p(π,op) is involved in π-bonding with the Ni 3d(x^2-y^2) orbital. In turn, the delocalization of the S-3p(π,op) orbital, as a result of the overlap of the adjacent C-p(π) orbital, orbital results in a weakened π-donor. This overlap can be quantitatively assessed by measuring the angle between the Ni-S bond vector and the plane of the ring. An angle of 0˚ denoted maximal coplanarity, whereas 90˚ reflects an orthogonal orientation with minimal orbital overlap.

In previously reported Ni(II) tetra-aryl thiolate complexes, this angle is nearly 0˚ in three of the ligands, while the fourth deviates at ~35˚. In contrast, coplanarity in the aryl thiolate ligands are not achieved in the crystal structure of **1** and **2**, where this angle ranges from 20˚ – 80˚, Table 3.1. A similar distribution of angles is observed in the analogous complex $(Et_4N)_2$[Fe(S-*o*-^{t}BuCONH-Ph)$_4$] with angles of 16.2˚and 75.2˚.[40] Unlike **1** and **2**, this Fe complex adopts a distorted tetrahedral geometry (τ_4 = 0.89), suggesting the orbital overlap is not a thermodynamic driving force for tetrahedral coordination in first-row transition metal tetrathiolates. The disruption of ligand coplanarity observed in $[M(SPh\text{-}o\text{-amide})_4]^{2-}$ (M = Ni, Fe) complexes are likely a consequence of intramolecular H-bonding which fixes the orientation of the aryl ring. However, while the ferrous complex retains a distorted tetrahedral geometry, the incorporation of *ortho*-carboxamide substituents in Ni(II) tetrathiolates complexes **1** and **2** yields square-planar geometries. This behavior can be rationalized based on crystal-field theory. H-bonding further reduces the π-donor ability of S-R[31] resulting in a larger crystal field splitting parameter (Δ). This perturbation increases the ligand field strength of the aryl thiolate subtlety influencing the thermodynamic preference towards a square-planar geometry. This is further suggested by the computed energetic difference

between both geometries, discussed below. Although a weaker molecular force than H-bonding, intramolecular π-π stacking of aryl rings in **1** and **2** might provide further stabilization for the square-planar geometry. Both *cis*-aryl rings of **1** and **2** are nearly coplanar possessing a ~10˚ angle between the planes of benzene (0˚ is perfectly planar; 90˚ is perpendicular); however, only **2** shows intramolecular π-π stacking with a 3.665 Å distance between the centroids of the *cis*-benzene rings, within π-π stacking distances (less than 3.8 Å).[58] These results suggest that disruption of coplanarity due to intramolecular H-bonding, rather than π-π stacking, is the predominate factor that results in the atypical geometry for **1** and **2**.

To provide additional insight into how intramolecular H-bonding affects the metric parameters of Ni(II) tetrathiolate complexes and their stability in different geometries, density functional theory (DFT) was employed at the B3LYP/def2-TZVPP level of theory with solvent effects accounted for by utilizing the conductor-like polarizable continuum model (CPCMC) for MeCN (ε = 36.6).[59] DFT geometry-optimized complexes were generated using input coordinates from their respective X-ray crystal structures. The geometry-optimized structures of **1** and **2** are in close agreement with those determined from crystallography and are within the error of the DFT method, see Table 3.1 for structural comparisons; however, only **1** was computed in both geometric isomers, i.e. tetrahedral (**1*(T$_d$)**) and square-planar (**1*(SqPl)**). The tetrahedral isomer of **1** was optimized using coordinates of $(Et_4N)_2$[Fe(S-*o*-^{t}BuCONH-Ph)$_4$][40] by replacement of Fe with Ni, removal of -CH_3 from each ^{t}Bu group, and addition of *p*-CF_3 groups. Structural analysis of **1*(T$_d$)** shows Ni is coordinated in a tetrahedral geometry (τ_4 = 0.82) with a Ni-S_{avg} of 2.315 Å. These bond lengths are comparable to the analogous Fe(II) complex (Fe-S_{avg} = 2.329 Å) and expectedly longer than **1*(SqPl)** (2.222 Å). Intramolecular H-bonding from the carboxamide-NH is still present in **1*(T$_d$)** (N—S_{avg} = 2.936 Å) and only slightly elongated compared to **1*(SqPl)** (N—S_{avg}

= 2.926 Å), suggesting geometry does not significantly impact strength of this secondary interaction. Notably, the presence of H-bonding is reported to contract Ni-S bonds in square-planar complexes.[27, 28, 60] To determine if this holds for our system, the computed structures of **1*(T$_d$)**, **1*(SqPl)**, and the parallel geometric isomers of the non-hydrogen bonding counterpart [Ni(S-*p*-CF_3-Ph)$_4$]$^{2-}$ (**3**) (square-planar = **3*(SqPl)**; tetrahedral = **3*(T$_d$)**) can be compared at the same level of theory. Optimized structures of **1*(T$_d$)** and **1*(SqPl)** reveal a contraction of Ni-S_{avg} bond length by ~0.01 and ~0.05 Å, respectively, versus their non-hydrogen bonding counterparts, metrics seen in Table 3.1, consistent with the proposed decrease in the filled/filled repulsive interaction between Ni(dπ) and S(pπ) orbitals resulting from active H-bonding.[61, 62] Contraction of Ni-S bonds due to H-bonding is on a similar magnitude to [Ni(nmp)(SR)]$^{2-}$ (~0.03 Å), a square-planar model of NiSOD,[27] Zn(II)-aryl thiolate complexes (~0.005 Å) supported by a tripodal ligand,[35, 37] and tetrahedral Fe(II) (~0.02 Å) and Co(II) (~0.03 Å) tertraaryl thiolate complexes.[40] Thus, DFT suggests that intramolecular H-bonding is present regardless of geometry, and results in the contraction of the Ni-S bonds relative to its non-H-bonding counterpart, although only slightly for the theoretical tetrahedral isomer.

Not only does optimization of each isomer allow one to assess structural impacts of H-bonding but also the thermodynamic favorability of each geometry. For example, computed free energies for each geometric isomer of **3*** indicate a modest barrier for isomerization (~14 kcal/mol), favoring the tetrahedral geometry. The incorporation of intramolecular H-bonding in **1***, reduces the energetic barrier for isomerization between square-planar and tetrahedral geometries of Ni(II) tertathiolate complexes by ~10 kcal/mol resulting in a ΔG° of 5.1 kcal/mol, in favor of the tetrahedral geometry, Table S3.7. These computations suggest incorporation of *ortho*-carboxamide substituents onto Ni(II) tetra-aryl thiolate complexes reduces the thermodynamic driving force for

adoption of tetrahedral geometries, most likely due the enhanced field strength of the ligand, *vide supra*. This subtle change in driving force favors the exclusive formation of square-planar complexes observed in its solid-state, via XRD, XAS, and solid-state magnetic measurement.

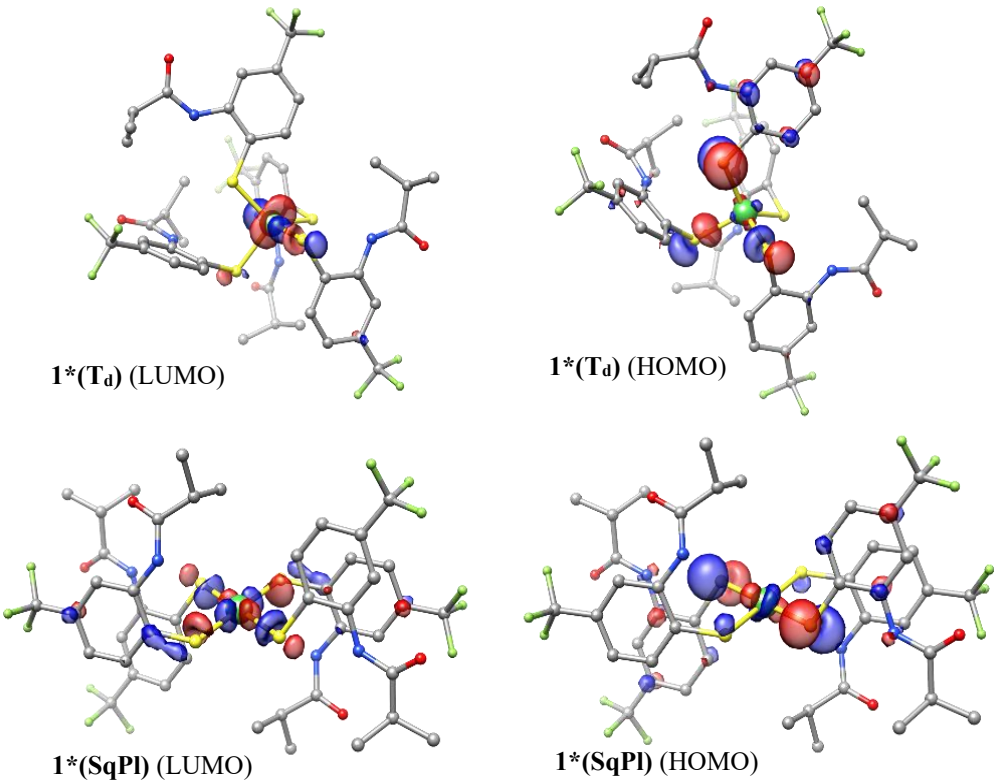

Figure 3.4. DFT-generated (B3LYP, def2-TZVPP, MeCN) isosurface plots of the frontier MO's of both isomers of **1***. Color scheme: Ni, green; S, yellow; F, green-yellow; C, gray. H-atoms are omitted for clarity.

The electronic structure of **1***, regardless of its geometry, involves large contributions from Ni and S-based orbitals, as seen in Table 3.2 and Figure 3.4. The HOMO (Ni/S% = 17.6/43.3%) and HOMO-1 (Ni/S% = 36.3/43.9%) of **1*(SqPl)** are primarily S-based and involve π-antibonding interactions between S-p(π) and Ni-d_{yz} orbitals reflecting the covalent nature of the bonds. When compared to the non-H-bonding analog (**3*(SqPl)**), in the same geometry, introduction of H-bonds leads to a decrease in the S-contributions of these frontier orbitals by ~17%, see Table 3.2, consistent with similar Ni-thiolate systems possessing intramolecular NH---S bonds.[27, 28, 63] As anticipated the LUMO of **1*(SqPl)** is primarily Ni-based (Ni/S% = 38.9/22.0%) with antibonding Ni-d_{x2-y2}(σ) and S-p(σ) interactions. In contrast, the HOMO(α) (Ni/S% = 7.8/51.1%) and HOMO(α)-1 (Ni/S% = 12.9/47.3%) of **1(T_d)*** feature *σ*-antibonding interactions between Ni-d_{xz}(σ) and S-p(σ), reflecting the more ionic character of the Ni-S bond in the tetrahedral geometry. Despite the difference in the Ni-S bond character between geometries, H-bonding decreases contributions from S in the HOMO by ~3%, see Table 3.2. The LUMO(β) of **1*(T_d)** shows significant Ni-d_{z2} character (~63%), that is σ-antibonding with S-p(σ) (~14%), comparable to the LUMO(β) of **3*** characterized as a σ-antibonding MO comprised of ~63% Ni-d(σ) and ~14% S-p(σ). However, the energy of the LUMO(β) is less for **1*(T_d)** (-2.11 eV) compared to **3*(T_d)** (-1.92 eV) consistent with the more positive Ni(II/I) couple of **1**, *vide infra*, in-line with Koopman's theorem.[64] The electronic structure of **1*** reveals that intramolecular H-bonding influences the Ni-S bonding interactions, reducing S-orbital contributions to the frontier MO's, though the extent varies depending on the nature of the Ni-S bond.

Table 3.2. Select metric parameters and Löwdin Orbital Compositions Derived from the DFT Calculations for Selected Molecular Orbitals of tetrahedral and square-planar isomers of **1*** and **3*** (B3LYP, def2-TVZPP, MeCN).

	1*(T$_d$)	**3*(T$_d$)**	**1*(SqPl)**	**3*(SqPl)**
Ni-S$_{avg}$ (Å)	2.316	2.328	2.222	2.256
τ_4	0.82	0.79	0.00	0.08
HOMO Ni(dπ)/S(pπ)%	7.8/51.1(α)	10.6/55.1(α)	17.6/43.3	34.7/52.2
HOMO − 1 Ni(dπ)/S(pπ)%	12.9/47.3(α)	9.6/55.2(α)	36.6/43.9	17.7/52.9

^{1}H NMR (400 MHz, CD$_3$CN, RT) of **1**

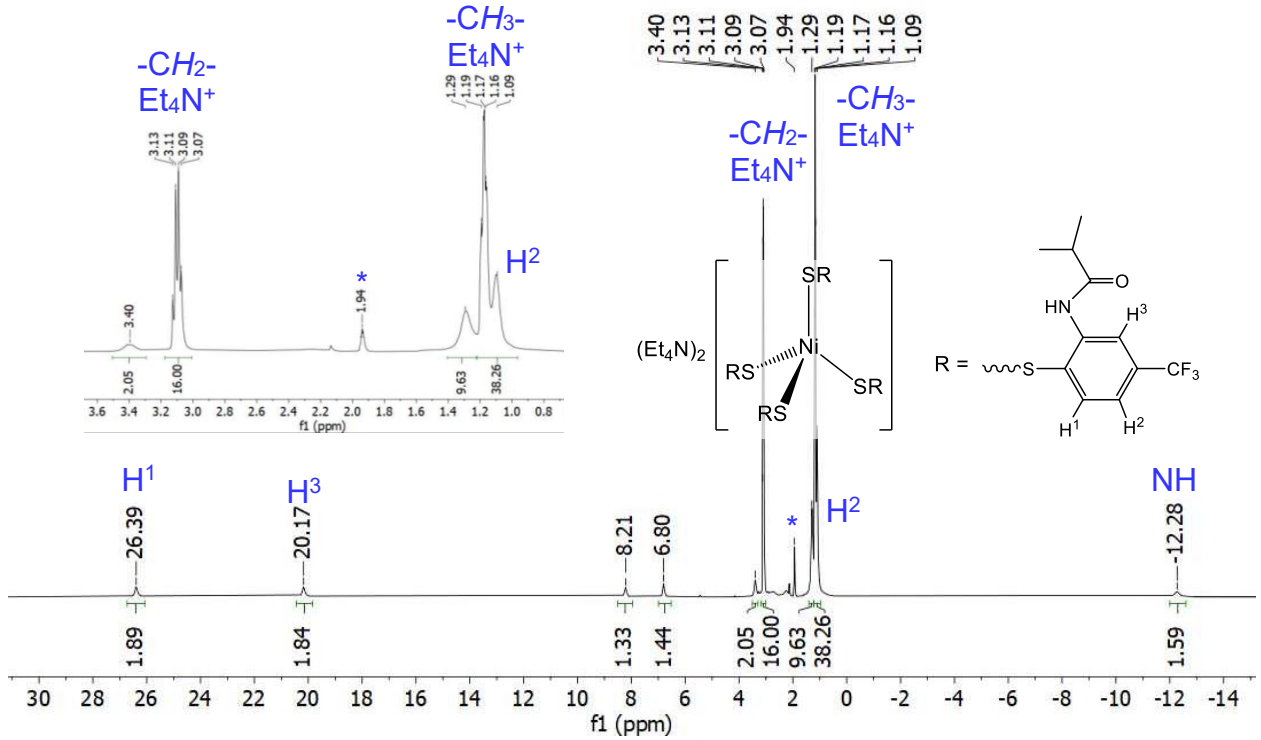

Figure 3.5. *Top:* ^{1}H NMR spectrum of (Et$_4$N)$_2$[Ni(S-*o*-^{i}PrCONH-*p*-CF$_3$-Ph)$_4$] (**1**) in CD$_3$CN at RT (δ vs. protio signal). *Inset:* expansion of 0.0 – 4.0 ppm region. Residual CH$_3$CN is observed at 1.94 ppm and is indicated with *.

Solution-sate characterization. To further investigate these atypical Ni-tetrathiolate complexes, their solution-state properties were assessed by $^{1}H/^{19}F$ NMR spectroscopy and magnetic measurements to determine whether the square-planar geometry is retained upon dissolution. Upon dissolution of **1** the ^{1}H NMR spectrum of crystalline material in CD_3CN, shown in Figure 3.5, reveals three contact shifted peaks: two downfield peaks at 26.39 ppm and 20.17 ppm and one upfield peak at −12.28 ppm, with **2** showing a similar distribution of proton resonances, shown in Figure S3.34. These contact shifted peaks are observed in all preparations of **1** and **2** from as-isolated and crystalline material, suggesting the presence of paramagnetic complex, likely the tetrahedral Ni(II)-tetrathiolate (S = 1) complex. This assignment is further supported by comparison to analogous tetrahedral complexes $(Et_4N)_2[M(S\text{-}o\text{-}^{t}BuCONHPh)_4]$ (M = Fe, Co; $S = 2$) [40, 65] which exhibit two downfield peaks (~20 ppm and ~14 ppm, assigned to *meta*-H^+) and an upfield peak (~−13 ppm, assigned to δ_{NH} of the carboxamide group). The up-field shift of δ_{NH} is further suggestive of intramolecular H-bond interaction with sulfur coordinated to a paramagnetic metal, Ni(II) (S = 1) for **1** and **2**, rather than solely through spin delocalization through the ring, as for *meta*-H^+.[40, 65] The ^{19}F NMR spectra of **1** ($\delta = -8.32$ ppm) and **2** ($\delta = -10.34$ ppm), shown in Figure 3.6 and Figure S3.35, also supports the presence of paramagnetic Ni(II) tetrathiolate complexes, e.g. (S = 1) δ = −18.96 ppm of freshly dissolved **3**, see Chapter 2. Further verification of paramagnetic material is found by their solution state magnetic moments: **1** ($\mu_{eff} = 1.86\ \mu_B$) and **2** ($\mu_{eff} = 1.96\ \mu_B$). Collectively, these results indicate that upon dissolution tetrahedral Ni(II) (S = 1) isomers of **1** and **2** are present, consistent with the low computed isomerization barrier.

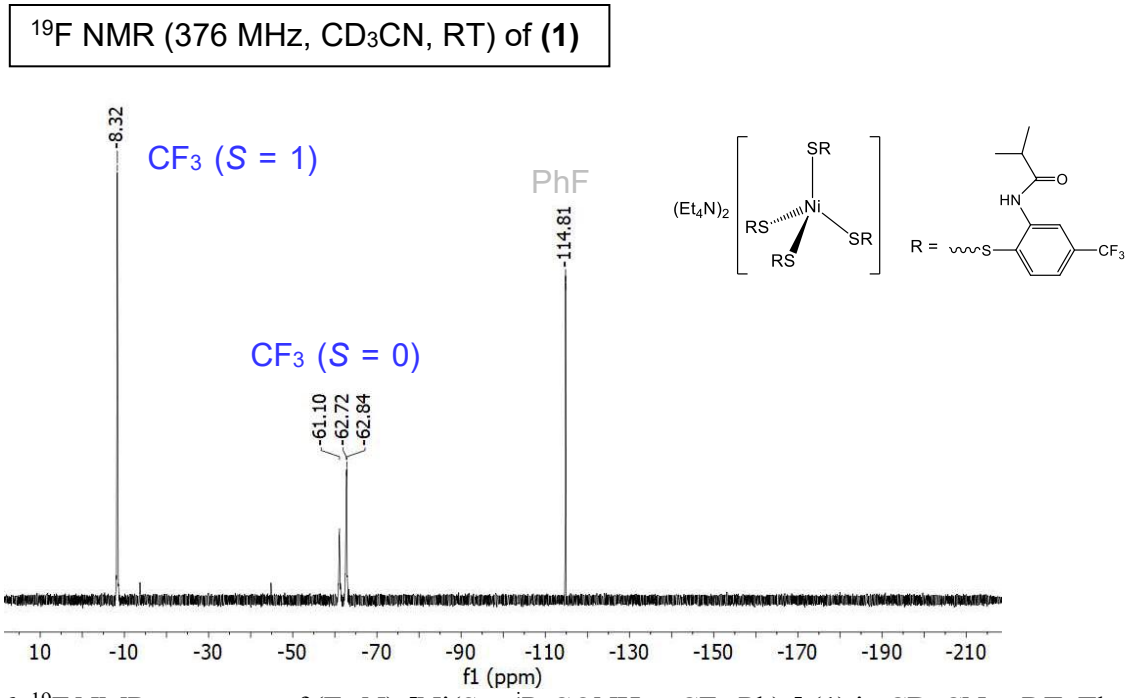

Figure 3.6. ^{19}F NMR spectrum of $(Et_4N)_2[Ni(S\text{-}o\text{-}^{i}PrCONH\text{-}p\text{-}CF_3\text{-}Ph)_4]$ (**1**) in CD_3CN at RT. The peak at -114.81 ppm is from PhF as an internal standard.

Despite the presence of tetrahedral isomer in the solution state, the low magnetic moment compared to other tetrahedral Ni(II) complexes (μ_{eff} = 3.5-4.2 μ_B)[66] suggests the presence of a diamagnetic complex. Solution-state NMR of related homoleptic tetrahedral/tetrathiolate complexes indicate facile thiolate loss results in transient, planar $[Ni(SPh)_3(L)]^-$ (L = donor solvent) complexes that subsequently from diamagnetic multimeric complexes of the general form $[Ni_n(\mu\text{-}SR)_n(SR)_{2n}]^{2-}$, depicted in Scheme 3.1, and suggested for **3**, as discussed in Chapter 2.[67, 68] Given this behavior, a similar equilibrium might be expected for the tetrahedral isomers of **1** and **2** upon dissolution. In all preparations of **1** and **2**, whether as-isolated or crystalline material, the ^{1}H NMR spectra contain a group of peaks in the aromatic region (~ 7 ppm) arising from a diamagnetic complex. Similar peaks in this region have been reported for previously studied tetrathiolate complexes, $[Ni(S\text{-}p\text{-}X\text{-}Ph)_4]^{2-}$ (X = H, Cl, Me, CF_3) and $[Ni(S\text{-}m\text{-}Cl\text{-}Ph)_4]^{2-}$.[39] Furthermore the ^{19}F NMR reveals the presence of S = 0 species, δ = ~−60 ppm for **1** and **2**

compared to δ = ~−62.01 ppm for the Zn(II) analog $(Et_4N)_2[Zn(S\text{-}o\text{-}^{i}PrCONH\text{-}p\text{-}CF_3\text{-}Ph)_4]$ (**4**), shown in Figure S3.39. The ^1H NMR and magnetic measurement data are consistent with a mixture of $S = 1$ (assigned to tetrahedral monomer) and $S = 0$ species in solutions of **1** and **2.** However the nature of the $S = 0$ complex is ambiguous, it may correspond to a multimeric complex resulting from thiolate dissociation a monomeric square-planar isomer, or a combination of both diamagnetic complexes, as shown in Scheme 3.1. Negative mode electrospray ionization mass spectra (ESI-MS) of MeCN solutions of **1**, shown in Figures S3.28-31, indicate charged complexes symptomatic of *S,S*-bridged species, e.g., $[Ni_3(S\text{-}o\text{-}^{i}PrCONH\text{-}p\text{-}CF_3\text{-}Ph)_8]^{2-}$ (m/z = 1136.3) and possible dimer $[Ni_2(S\text{-}o\text{-}^{i}PrCONH\text{-}p\text{-}CF_3\text{-}Ph)_6]^{2-}$ (m/z = 844.1). This result further suggested the formation of a *S,S*-bridged trimer and/or dimer via ligand dissociation of **1** upon dissolution.

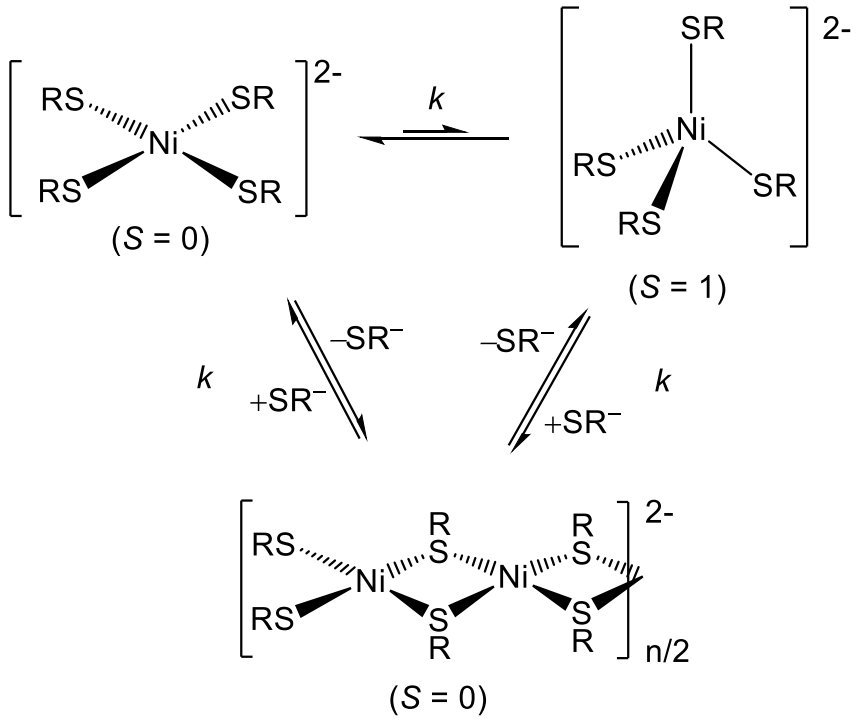

Scheme 3.1. Proposed ligand dissociation equilibrium between Ni-tetrathiolate monomer and *S,S*-bridged Ni multimer.

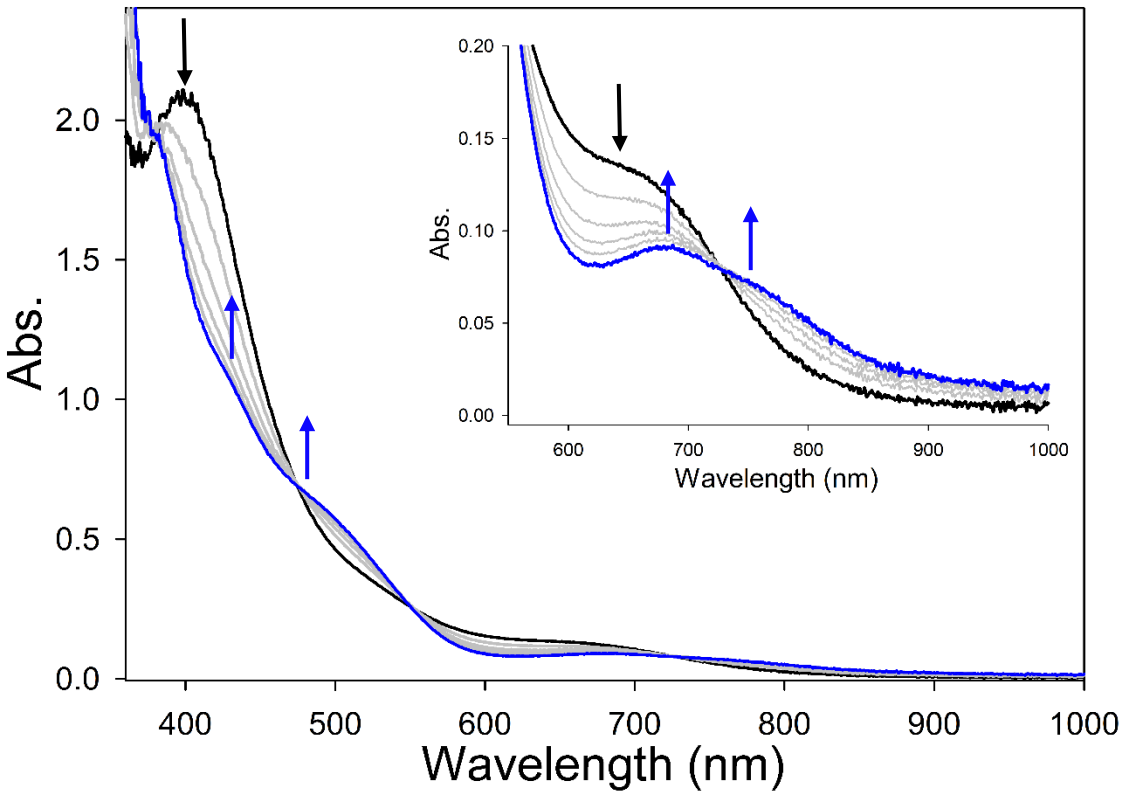

Figure 3.7. UV-vis of **1** (black) and addition of (Et_4N)(S-*o*-^{i}PrCONH-*p*-CF_3-Ph) up to 20 mol-equiv. (blue) with each scan in-between representing addition of 4 mol-equiv. of thiolate (grey) in MeCN at 25 °C. *Inset:* zoom-in of 600 -1000 nm region of spectra.

To assess whether ligand dissociation occurs upon dissolution of **1** to form the diamagnetic multimer, variable temperature ^{1}H NMR was performed as shown in Figure S3.49. As the temperature is lowered, the proton peaks associated with the S = 1 complex become sharper consistent with the proposed ligand dissociation equilibrium. A similar trend is reported by Nakamura for the disubstituted *ortho*-carboxamide $(Me_4N)_2[M(S\text{-}2,6\text{-}(CF_3CONH_2)Ph)_4]$[40] (M = Fe, Co), which also exhibits ligand dissociation.[40] To further investigate the proposed dissociation equilibrium, changes in electron absorption spectra and solution-state magnetic moment of **1** were assessed in the presence of excess thiolate. These studies aim to determine whether the addition of excess thiolate shifts the equilibrium toward tetrahedral monomer. The electronic absorption of

spectrum **1** in MeCN seen in Figure 3.7, exhibits almost a featureless absorbance profile with an intense band at 400 nm and a broad shoulder at ~680 nm. Broad absorbance bands in the UV-vis spectra are typical for monomeric Ni tetra-aryl thiolates such as $(Et_4N)_2[Ni(S\text{-}p\text{-}X\text{-}Ph)_4]$ (X = Cl, CF_3) in MeCN[68]; however, addition of excess thiolate to $(Et_4N)_2[Ni(S\text{-}p\text{-}X\text{-}Ph)_4]$ (X = H, CF_3) in MeCN and/or use of DMF:Tol (1:1) displays gives rise to distinct CT near ~460 and ~510 nm and two *d-d* bands ~670 and ~720 nm which are assigned to pure tetrahedral monomer.[69, 70] To determine whether **1** exhibits similar electronic transitions in the presence of excess thiolate, its UV-vis was monitored as increasing equivalents of ligand were added as shown in Figure 3.7. Upon addition of thiolate, the band at 400 nm and shoulder at ~680 nm decrease in intensity. Concurrently, three shoulders emerge at ~380, ~430 nm, and ~490 nm, along with the appearance of two broad peaks at 690 and 770 nm. No further changes in the spectrum were observed after the addition of 20 mol-equiv. of thiolate. Furthermore, the gradual transformation of the spectrum yields three distinct isosbestic points, indicating a clean conversion between complexes. Both variable temperature NMR and UV-vis titration experiments support an equilibrium governed by thiolate dissociation.

The absorption spectrum of **1** in MeCN with 50 mol-equivalents of thiolate, shown in Figure S3.27, yields the appearance of a similar absorbance spectrum with two broad LMCT bands at 430 nm (ε = 6300 M^{-1} cm^{-1}) and 490 nm (ε = 4100 M^{-1} cm^{-1}) and two *d-d* transitions at 690 (ε = 570 M^{-1} cm^{-1}) and 760 nm (ε = 460 M^{-1} cm^{-1}). This spectrum resembles those of previously reported for NiRb[69] and $[Ni(S\text{-}p\text{-}X\text{-}Ph)_4]^{2-}$ (X = H, CF_3)[67, 69, 70] complexes with excess thiolate, summarized in Table 3.2. Magnetic circular dichroism (MCD) studies on NiRd and $(PPh_4)_2[Ni(SPh)_4]$ assign the higher energy bands to ligand-to-metal charge transfer (LMCT) and the lower energy bands to *d-d* transitions.[40,69] The absence of more well-defined CT bands may be attributed their overlap

with intense transitions associated with the monomeric square-planar isomer of **1**, which remains unaffected under excess thiolate conditions. These electronic absorption features of **1** in the presence of excess thiolate are consistent with the authentic UV-vis signatures of tetrahedral/tetrathiolate-Ni(II) complexes. Blue shifting of LMCT bands has been observed in systems where hydrogen bonding engages metal bound thiolates, as this interaction reduces the electron density of the S-p(π) coordinated to the metal. For example, [Pt(bpy)(S-*o*-$PH_3CCONHPh)_2$] exhibits a blue-shift of 49 nm in its LMCT band compared to its non-hydrogen-bonded counterpart.[41] Similarly, incorporation of H-bonding moieties in **1** result in a blue shift of LMCT band (20 to 30 nm) and a red shift of *d*-*d* bands (~20 – ~40 nm) in comparison to $(Et_4N)_2$[Ni(S-*p*-X-Ph)$_4$] (X = H, CF_3)[67, 69, 70], values shown in Table 3.3. Lastly, solution-state μ_{eff} of **1** in the presence of 20 mol-equiv. of thiolate revealed an increase in magnetic susceptibility (μ_{eff} = 2.32 μ_B), consistent with increased population of monomeric *S* = 1 complex under these conditions. Even at these saturating conditions, in which the equilibrium is shifted towards monomeric complex, the magnetic moment of **1** is low compared to $(Et_4N)_2$[Ni(S-*p*-CF_3-Ph)$_4$] (**3**) under similar conditions (μ_{eff} = 3.05 μ_B; 20-mol equiv. of Et_4N(S-*p*-CF_3-Ph)). This is likely a result of the persistence of monomeric **1** (*S* = 0). Collectively, these solution-phase measurements suggest that **1** (*S* = 1) partly converts to a diamagnetic complex(es) upon dissolution, e.g., the *S*,*S*-bridged complex $(Et_4N)_2[(RS)_2Ni(\mu\text{-}SR)_2Ni(SR)_2]$; R = S-*o*-^{i}PrCONH-*p*-CF_3-Ph. However, the low magnetic moment observed, even under excess thiolate conditions, is proposed to be due to the presence of the square-planar isomer observed in their solid-state structures and XAS measurements. Although **1** exhibits formation of monomer under excess thiolate conditions, **2** does not behave similarly as indicated by UV-vis titration experiments. The addition of thiolate to solutions of **2**, results in the disappearance of all absorbance bands without the emergence of new

bands, see Appendix A for further discussion. These results indicate that both ligand dissociation and isomerization may contribute to the observed behavior of **1** upon dissolution.

Table 3.3. Select Electronic Absorption Transitions of Tetrathiolate Ni(II) Complexes[a].

Complex	λ (nm) (ε (M^{-1} cm^{-1}))	ref
$(Et_4N)_2[Ni(S\text{-}o\text{-}^{i}PrCONH\text{-}p\text{-}CF_3\text{-}Ph)_4]$ (**1**)	760 (460), 690 (570), 490 (4100), 430 (6900) [b, c]	TW
TD-DFT **1*(T$_d$)**	790 (sh, 771), 720 (1268), 505 (sh, 3066) 463 (11177)[b]	TW
TD-DFT **1*(SqPl)**	448 (3164), 383 (34785)[b]	TW
$[Ni(HpyS)_4](NO_3)_2$	634 (28), 371 (32700), 291 (82500) [b]	52
$(Et_4N)_2[Ni(S\text{-}p\text{-}CF_3\text{-}Ph)_4]$ (**3**)	720 (600), 680 (580), 508 (3800), 465 (3400)[b, c]	Ch 2
Computed **3**	694 (640), 643 (650), 518 (7200), 463 (8000)	Ch 2
$(Ph_4P)_2[Ni(SPh)_4]$	725 (~300), 676 (~300), 510 (~2500), 460 (~2400)[b, c]	40
NiRd[f]	720 (460), 670 (385), 450 (3200), 360 (5460)[g,h]	69
TD-DFT NiRd[h]	732 (636), 661 (70), 455 (2110), 351 (2330)[i]	71

[a]Abbreviations: NA = not available; Rd = rubredoxin; sh = shoulder; TW = this work. [b]MeCN. [c]Values obtained in the presence of excess thiolate (50 mol-equiv $(Et_4N)(S\text{-}o\text{-}^{i}PrCONH\text{-}p\text{-}CF_3\text{-}Ph)$ for **1**; 10 mol-equiv KSPh for $(Ph_4P)_2[Ni(SPh)_4]$). [f]Ni-substituted Rd from *D. gigas*., with 50% (v/v) ethylene glycol. [g]pH 7.6 Tris-HCl buffer. [h]Values taken from the 'full' model of NiRd, see ref. 64. [i]H_2O.

To increase the population of the ill-defined $S = 0$ complex in solution and aid in its identification, the equilibrium was shifted by removing free thiolate from solution. This was achieved by the addition of $FcBF_4$ ($E_{1/2}$ = 0.00 V vs Fc/Fc^+) to a solution of **1** in MeCN. Utilization of this chemical oxidant results in the selective oxidation of free thiolate (E_{ox} = −0.25 V) over coordinated thiolate (E_{ox} = 0.39 and 0.13 (sh) V), as detailed in the electrochemistry section below. Isolation of $(S\text{-}o\text{-}^{i}PrCONH\text{-}p\text{-}CF_3\text{-}Ph)_2$ from this reaction, identified by $^1H/^{19}F$ NMR, confirms the oxidation of thiolate. The ^1H NMR of the remaining oxidized product (**1^{ox}**), shown in Figure S3.52,

reveals several broad peaks in the aromatic region, with the most intense peaks at 8.20 and 6.82 ppm, which is almost superimposable with **1**, Figure S3.53. Although the $S = 1$ complex remains in isolated material, the $S = 0$ complex constitutes the majority of the material, comprising ~80% of the material in solution, as estimated by the relative integration of counterion-associated protons. The ^{19}F NMR spectrum of $\mathbf{1^{ox}}$, see Figure S3.54, similarly reflects a dominant diamagnetic component ($\delta_F = \sim -63$ ppm). Assignment of this diamagnetic material to free ligand is eliminated based on the ν_{CO} (3270 cm^{-1}) and ν_{NH} (1680 cm^{-1}) stretches of oxidized product which are consistent with coordinated ligand. Comparison of the negative mode electrospray ionization mass spectra (ESI-MS) between **1** and its oxidized product, see Figure S3.55, reveals the increased intensity of a peak at *m/z* of 1136.3, simulating well to $[Ni_3(S\text{-}o\text{-}^i PrCONH\text{-}p\text{-}CF_3\text{-}Ph)_8]^{2-}$. Isolation of this trinuclear complex, $[Ni_3(SR)_{n = 4, 8}]^{2-}$, is common for Ni-thiolate containing systems where R = ethanethiolate,[72] ethane dithiolate,[73] and S_2-*o*-xyl.[74] In these trimers, each NiS_4 fragment is held in a square-planar geometry, in which the central NiS_4 fragment shares an edge between the terminal NiS_2 fragments in a chair conformation. The diamagnetic nature of these complexes is confirmed by their ^1H NMR spectra. These results suggest the protons observed in the aromatic region of ^1H NMR arise, at least in part, from diamagnetic *S,S*-bridged multimers.

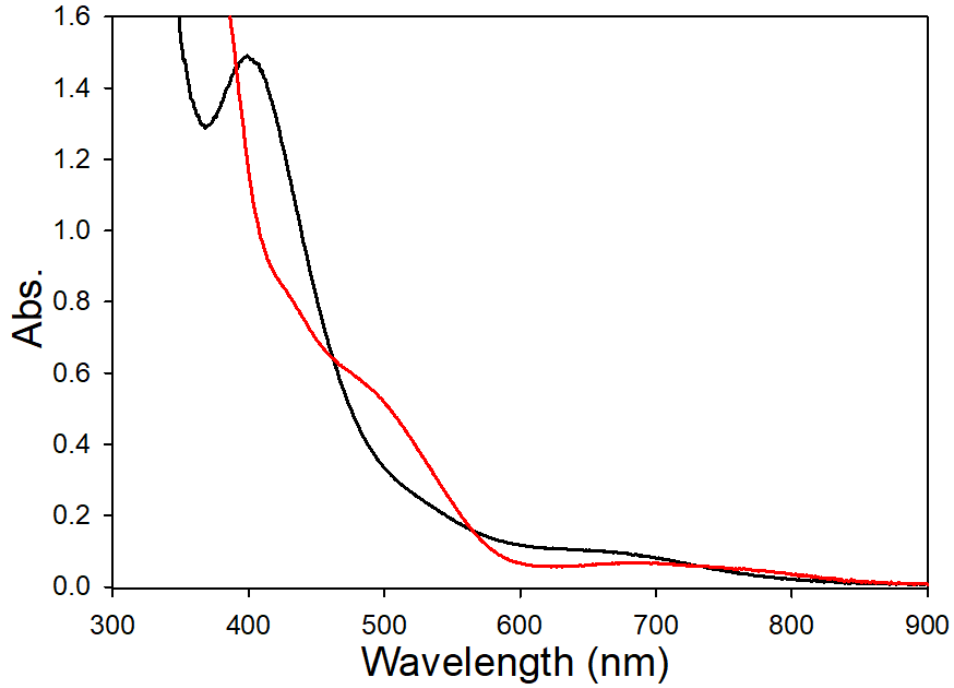

Figure 3.8. UV-vis spectrum of Et_2O insoluble product (black) from reaction of **1** with $FcBF_4$ and in the presence of excess thiolate (red) in MeCN at 25 ˚C.

The electronic absorption spectrum of the $\mathbf{1^{ox}}$, shown in Figure 3.8, exhibits an almost featureless spectrum with an intense band at 403 nm and a shoulder at ~680 nm possibly indicating formation of an analogous product. Notably, the near-featureless spectrum of the oxidized product is nearly identical with freshly dissolved **1** substantiating the presence of a multimetallic complex upon dissolution of **1**. This electronic absorption spectra is similar to the trimetallic $[Ni_3(S_2\text{-}o\text{-xyl})_4]^{2}$, which shows an intense charge-transfer band at 423 nm (8000 M^{-1} cm^{-1}, DMF) and a broad shoulder at ~520 nm.[74] To confirm whether the multimer is in equilibrium with monomer, thiolate was added to freshly dissolved oxidized product, resulting in an absorption profile resembling authentic **1,** Figure 3.8. The disappearance of the multimer is further corroborated by the absence of its corresponding peak in the ESI-MS(-) spectrum of **1** with 20 mol-equiv. of thiolate, see Figure S3.56. These results suggest the $S = 0$ complex observed upon dissolution of **1** can be attributed to a multimeric complex, such as $[Ni_3(S\text{-}o\text{-}^{i}PrCONH\text{-}p\text{-}CF_3\text{-}Ph)_8]^{2-}$, which can be converted back to

the monomeric form with the addition of thiolate. However, the presence of a square-planar monomer cannot be entirely ruled out as both isomeric forms of the monomer may coexist under excess thiolate conditions, as proposed in scheme 3.1.

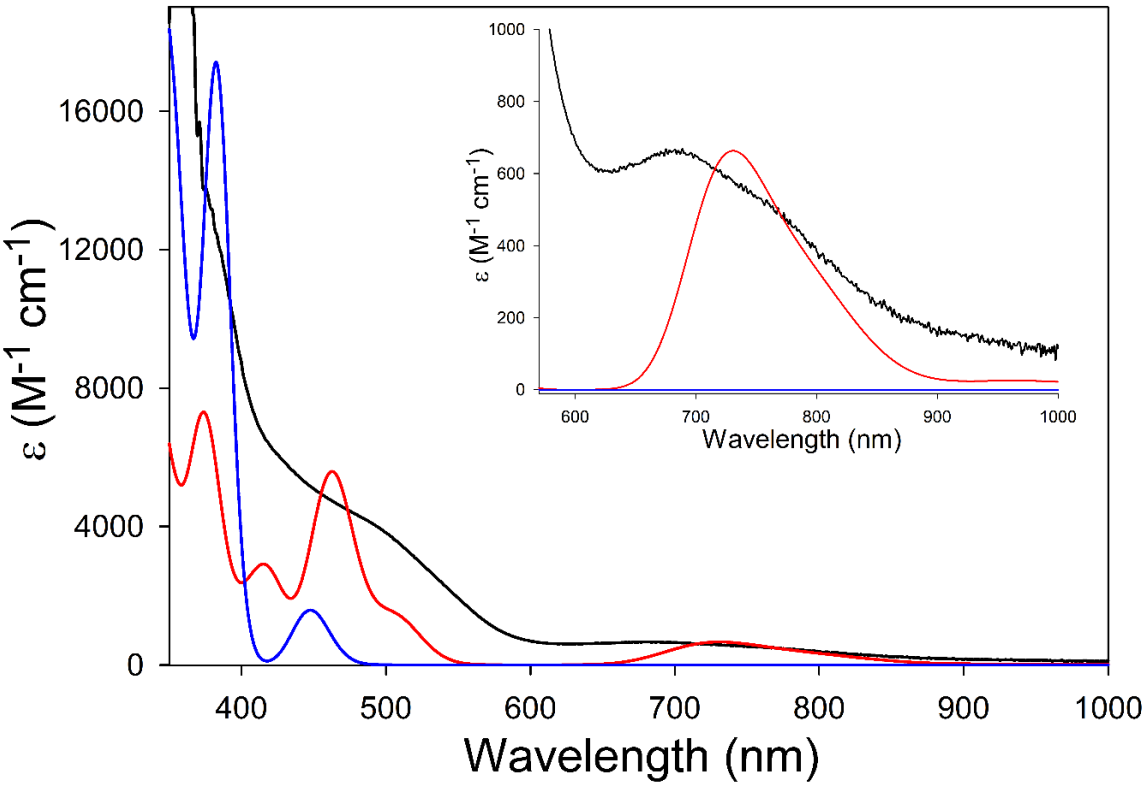

Figure 3.9. UV-vis of **1** with 50 mol-equiv. of (Et_4N)(S-*o*-^{i}PrCONH-*p*-CF_3-Ph) in MeCN at RT (black), TD-DFT calculated optical absorption spectrum of **1(T$_d$)*** (red) and **1(SqPl)*** (blue), computed molar absorptivity values for both were halved to plot on a similar scale as experimental values. *Inset*: zoom-in of 600 – 1000 nm region of spectra.

Next, time-dependent density functional theory (TD-DFT) was utilized to determine whether the monomeric square-planar isomer of **1**, or other isomers, could be readily identified by UV-vis. This computational technique was utilized to predict electronic absorption profile for both isomers, i.e., tetrahedral (**1*(T$_d$)**) or square-planar (**1*(SqPl)**), shown in Figures 3.8, S3.57 and S3.58. The

computed spectrum of **1*(T$_d$)**, shown in Figures 3.8 and S3.58, is comprised of two *d-d* transitions between 720 – 790 nm ($\varepsilon \sim 1000$ M^{-1} cm^{-1}), an intense band at 460 nm ($\varepsilon \sim 11000$ M^{-1} cm^{-1}), and a shoulder at 505 nm ($\varepsilon \sim 3100$ M^{-1} cm^{-1}), both identified as Sπ-to-Ni-*d*π CT transitions. The computed spectrum aligns reasonably well with the experimental spectrum of **1** with 50 mol-equiv. of thiolate, Figure 3.8, indicating that TD-DFT could be used to predict the electronic absorbance spectrum of **1*(SqPl)**. The computed spectrum of **1*(SqPl)**, shown in Figure S3.57, reveals two Sπ-to-Ni-d(x^2-y^2) CT transitions at 383 nm ($\varepsilon \sim 35000$ M^{-1} cm^{-1}) and 448 nm ($\varepsilon \sim 3200$ M^{-1} cm^{-1}) with some *d-d* transition present at 383 nm and is comparable to [Ni(HpyS)$_4$](NO$_3$)$_2$[52], a square-planar tetrathiolate complex, which exhibits an intense charge transfer band at 371 nm ($\varepsilon \sim 32700$ M^{-1} cm^{-1}) and a low intensity band at 630 nm, attributed to a small amount of pseudooctahedral Ni(II). Comparison of the computed spectrum with the experimental spectrum of **1** with excess thiolate, shown in Figure 3.9, suggests the shoulder observed at ~ 380 nm could arise from a square-planar isomer of **1**. The combination of experimental and computational suggests the coexistence of multiple complexes upon dissolution of **1**: (i) its tetrahedral and (ii) square-planar isomer, and (iii) a *S,S*-bridged multimeric complex, represented in Scheme 3.1.

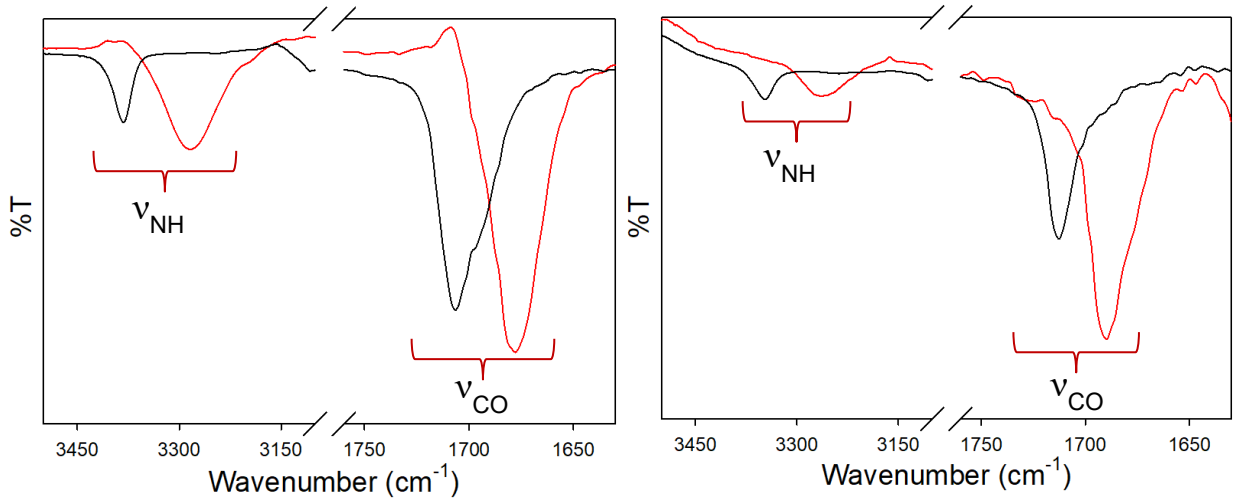

Figure 3.10. Liquid FTIR of (*left*) **1** (red) and (S-*o*-^{i}PrCONH-*p*-CF_3-Ph)$_2$ (black); (*right*) **2** (red) and (S-*o*-OPhCONH-*p*-CF_3-Ph)$_2$ (black). All FTIR spectra were recorded in THF at RT.

Intramolecular H-bonding in 1 and 2. FTIR spectral changes have been used as indicators for the presence of intramolecular H-bonds in several metal-thiolate complexes,[28, 41, 75] and is confirmed by monitoring changes in ν_{NH} and ν_{CO} of the carboxamide engaged in a H-bond versus free ligand, in which the extent of the shift correlates to the strength of the NH---S bond.[76] In order to confirm presence of intramolecular H-bonding in as-isolated material of **1** and **2**, in solid- and/or solution state, changes in the ν_{NH} and ν_{CO} stretching frequencies of complexed ligand to free, via disulfide, were monitored, shown in Figure 3.10. In THF, the ν_{NH} of (S-*o*-^{i}PrCONH-*p*-CF_3-Ph)$_2$ appears at 3382 cm^{-1} whereas the ν_{NH} of **1** appears red-shifted at 3284 cm^{-1} indicating H-bonding is intact in the solution state. This ~100 cm^{-1} shift in ν_{NH} ($\Delta\nu_{NH}$) is similar to shifts seen in H-bonded synthetic Fe-S clusters[42], square-planar [Pt(N_2S_2)][41], [Ni(N_2S_2)][27], and [Ni(dppe)(SPh)Me][49] (dppe = 1,2-bis(dipheylphosphino)ethane) complexes bearing *ortho*-carboxamide aryl thiolate donors, suggestive of intramolecular H-bonding, see Table S3.6. However, in its solid-state FTIR a blue-shift of ν_{NH} (−27 cm^{-1}) is observed. The ν_{NH} of (S-*o*-

^{i}PrCONH-*p*-CF_3-Ph)$_2$ appears at 3242 cm^{-1} and is ~100 cm^{-1} lower than similar *ortho*-carboxamide aryl disulfides.[50, 77] This unexpected shift is likely a result of intermolecular amide-amide H-bonding as seen in 2,3-(^{t}BuCOS)$_2$C$_6$H$_3$CONHPh (ν_{NH} at 3251 cm^{-1}).[78, 79] However, IR analysis for **2** in solution ($\Delta\nu_{NH}$ = 81 cm^{-1}) and solid state ($\Delta\nu_{NH}$ = 74 cm^{-1}) shows the anticipated downfield shift. Furthermore, H-bonding is evident by the red shifting of ν_{CO} for **1** ($\Delta\nu_{CO}$ = 29 cm^{-1}) and **2** ($\Delta\nu_{CO}$ = 25 cm^{-1}) between complexed ligand and disulfide. Despite their isomerization and ligand dissociation, FITR analysis of **1** and **2** reveals intramolecular H-bonding remains intact in both their solid- and solution-states.

Table 3.4. Changes in the IR Stretching Frequencies of ν_{CO} and ν_{NH} of the Carboxamide Group of Ligands upon Binding.

	RSSR[a]	**1**	RSSR[b]	**2**
$\nu_{NH\ (THF)}$	3382	3284	3345	3264
$\Delta\nu_{NH\ (THF)}$	---	**-98**	---	**-81**
$\nu_{CO\ (THF)}$	1707	1678	1715	1690
$\Delta\nu_{CO\ (THF)}$	---	**-29**	---	**-25**
$\nu_{NH\ (KBr)}$	3243	3269	3328	3254
$\Delta\nu_{NH\ (KBr)}$	---	**26**	---	**-74**
$\nu_{CO(KBr)}$	1666	1675	1705	1686
$\Delta\nu_{CO(KBr)}$	---	**9**	---	**-19**

$\Delta\nu_{NH/CO}$ = $\nu_{NH/CO}$ (metalated) – $\nu_{NH/CO}$ (disulfide); [a](S-*o*-^{i}PrCONH-*p*-CF_3-Ph)$_2$; [b](S-*o*-OPhCONH-*p*-CF_3-Ph)$_2$.

Stability in the presence of Brønsted Acids. The stability of **1** and **2** under protic conditions is critical for assessing their ability to catalytically reduce protons. Instability of these complexes was evaluated by their ^{1}H NMR upon incremental addition of AcOD-d$_4$ (pK_a = 22.3; MeCN)[80]. For example, titration experiments revealed **3** underwent complete degradation after the addition of 20 mol-equivalents of AcOD-d$_4$ (see Chapter 2) via protonation of coordinated thiolate. In contrast, engagement of thiolates with H-bonding is known to depress the pK_a of coordinated

thiolates[33, 34] and reduce their nucleophilicity.[35-37] Consequently, we anticipate that incorporation of H-bonding in **1** and **2** will enhance their protic stability. Monitoring the ^{1}H NMR spectrum of **1** reveals a gradual disappearance of the paramagnetically shifted peaks (δ_{H+} = ~26 and ~20 ppm) with increasing concentrations of AcOD-d_4, shown in Figure 3.11. Parallel to this change, there is an increase in the intensity of all broad peaks in the aromatic region, see Figures S3.60. Notably, a single distinguishable broad resonance emerges at δ_H = ~9.2 ppm upon addition of 10 mol-equiv. of deuterated acid. This new peak continuously shifts downfield as the titration progresses, reaching δ_H = ~9.8 ppm at 75 mol-equiv. of AcOD-d_4. Furthermore, at this point in the titration, no significant amount of (S = 1) remains. The disappearance of the paramagnetically shifted signals in parallel with the emergence of broad resonances in the aromatic region is consistent with conversion of monomeric (S = 1) complex to diamagnetic complex, which is tentatively assigned to a *S,S*-bridged multimeric complex. The singular δ_{NH} indicates uniformity in speciation and is ~0.4 ppm downfield from its corresponding disulfide (δ_{NH} = 8.80 ppm, Figure S3.39) indicating of intramolecular H-bonding. (ref) The progressive deshielding of δ_{NH} may be attributed to interactions between generated conjugated base ($^-$OAc) and the N-*H* proton of the *ortho*-carboxamide group. The stability of the monomeric square-planar isomer cannot be assessed due to the lack of unique resonances, i.e., the proton resonances of mono- and multimer (S = 0) complexes are indistinguishable. A similar titration experiment with **2**, shown in Figure S3.61, also demonstrated a gradual loss of monomeric (S = 1) complex as the acid concentration increased; however, analysis of aromatic region is challenging due to more complex spectra of **2**.

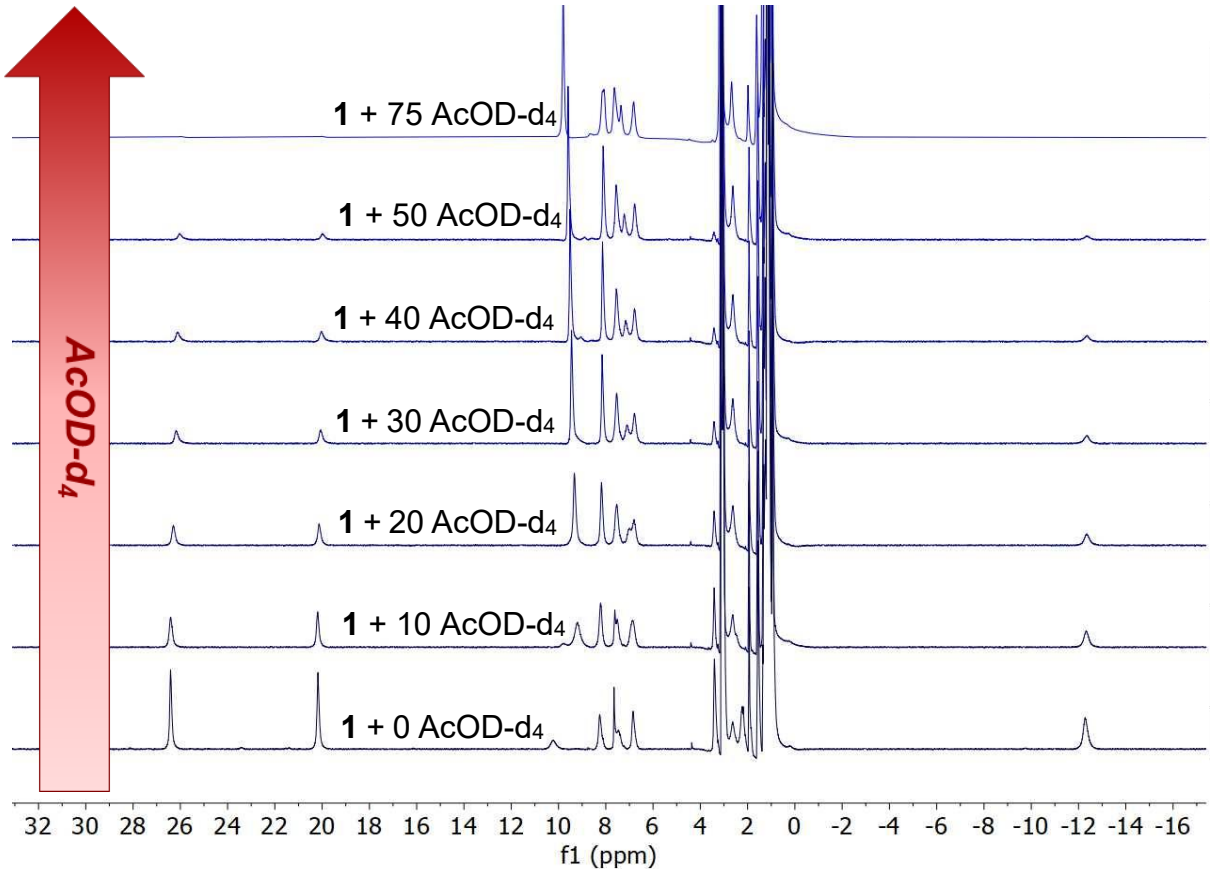

Figure 3.11. ^{1}H NMR (400 MHz, CD_3CN, RT) of **1** with the addition of various equivalents of AcOD-d_4. Residual CH_3CN is observed at 1.94 ppm.

The relative protic stability of complexes **1**-**3** was evaluated by determining the acid equivalents required to induce complete decomposition of each complex in solution. Complex **2** demonstrates the greatest protic stability, persisting up to 250 mol-equiv. of AcOD-d_4 followed by **1**, which persists up to 75 mol-equiv. and, lastly, **3**, which is completely gone after only 20 mol-equiv., see Chapter 2. The enhanced protic stability of **1** and **2** is attributed to the decreased basicity of the coordinated thiolates due to intramolecular H-bonding. The improved stability of **2** relative to **1** is proposed to arise from the steric bulk of the -OPh moiety of **2** which likely hinders access of the acid to the coordinated thiolates, as visualized by their space-filling models shown in Figure S3.62. The steric effect can be quantified by percentage of buried volume (%V_{Bur}), originally introduced

to quantify steric hinderance of N-heterocyclic carbenes,[81] which quantifies the fraction of the first coordination that is occupied by an organic ligand. The ($\%V_{Bur}$), is the fraction of the volume of the sphere centered on the metal occupied by a given ligand. By defining the x- and y-axis through the Ni-S bonds of **1** and **2**, see Figure 3.12, and z-axis through Ni the $\%V_{Bur}$ value we can compare the accessibility of the substrate to Ni. The increased $\%V_{Bur}$ of **2** (90.8%) compared to **1** (82.0%) indicates that **2** imposes a greater steric encumbrance around the Ni-center, thereby restricting access to its primary coordination sphere. The amount of exposed first-coordination sphere, i.e. coordinated thiolate, can be further visualized by the topographic steric maps which are analogous to physical maps in geography. Once the metal center is set at 'sea level' the whole complex is oriented to show the exposure of the metal from the top. The occupied space from the organic ligand elevated from the metal is depicted in red, whereas the ligand below is blue. By defining the z-axis through Ni and into free space, as shown in Figure 3.12, the topographical steric maps qualitatively show the coordinated thiolates of **1** are more accessible for a H^+. These results demonstrate that intramolecular H-bonding, along with incorporation of sterically bulky substituents, mitigates acid-induced decomposition of Ni(II)-tetrathioalte complexes, thereby, enhancing their suitability as proton reduction electrocatalysts.

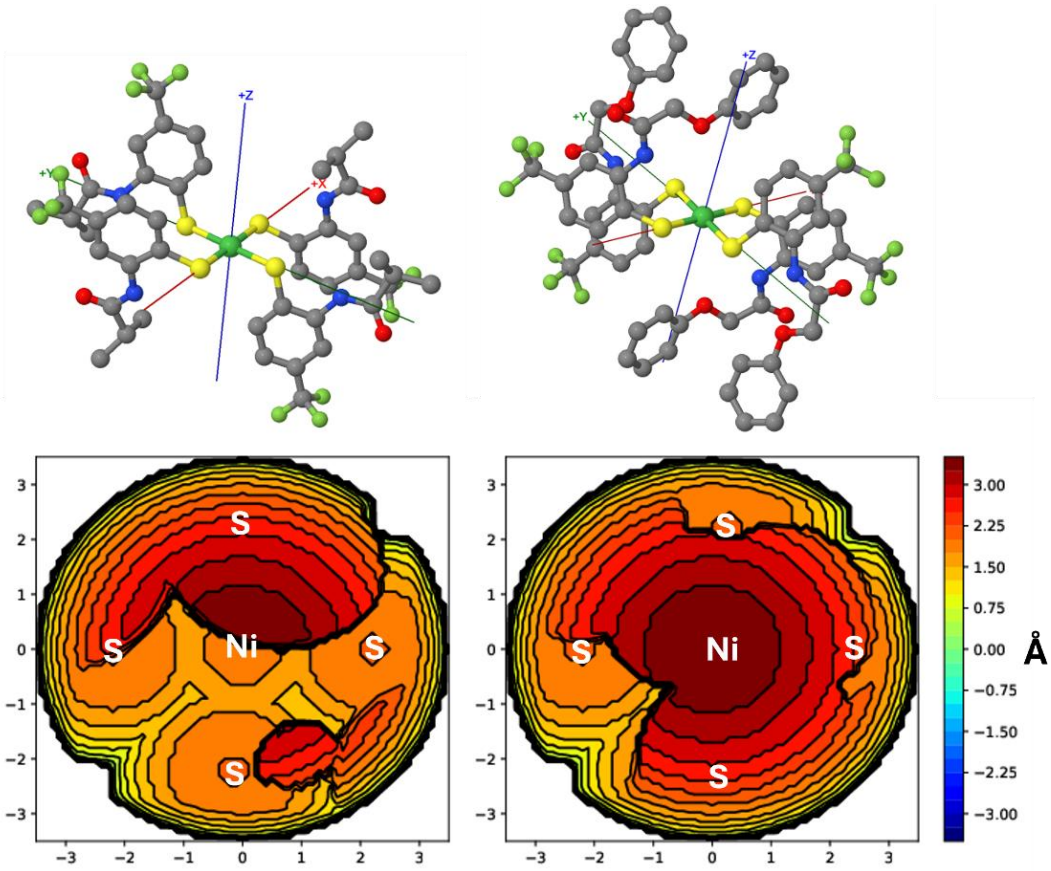

Figure 3.12. Ball-and-stick representations of **1** (*top, left*) and **2** (*top, right*) with their corresponding topographic steric maps directly beneath from the top-down view, H-atoms were omitted for calculation. The xyz-axis is defined as shown in the ball-and-stick representations. The SambVca 2.1 web application was used to create ball-and-stick and topographic map figures (sphere radius = 3.5 Å, mesh spacing = 0.10 Å).[82]

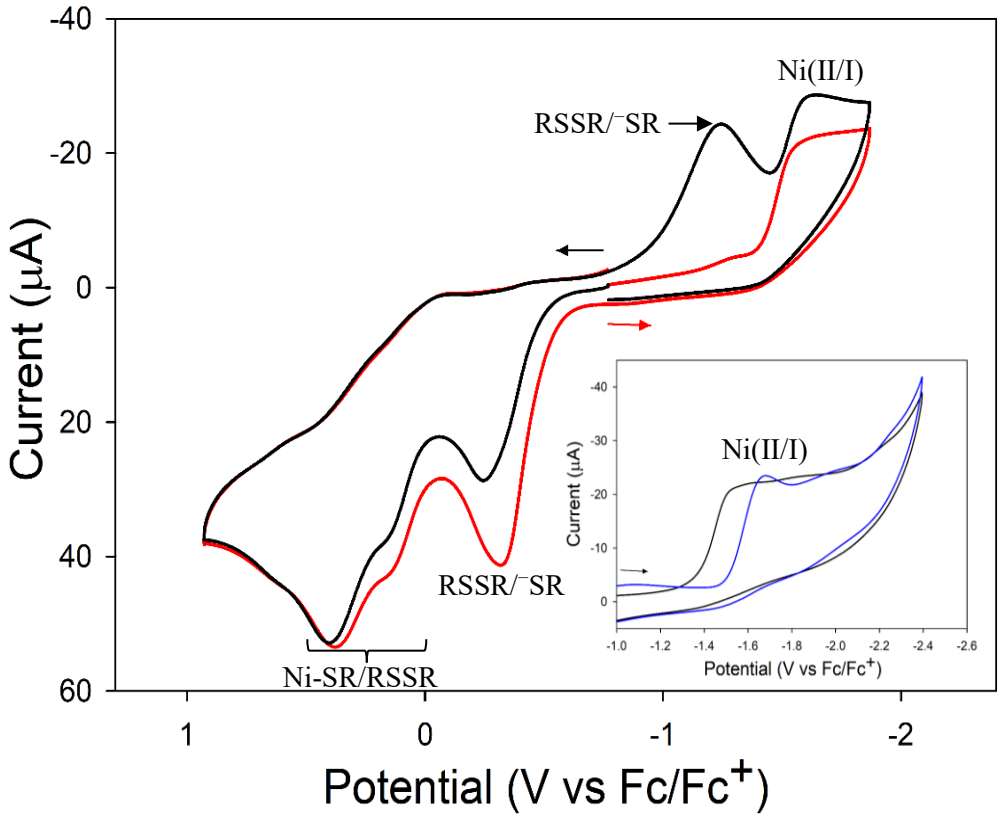

Figure 3.13. CVs' of $(Et_4N)_2[Ni(S\text{-}o\text{-}^{i}PrCONH\text{-}p\text{-}CF_3\text{-}Ph)_4]$ (**1**) in MeCN at RT (0.25 M $^{n}Bu_4NPF_6$ supporting electrolyte, glassy carbon working electrode, 100 mV/s scan rate). Arrow shows direction of scan. *Inset*: CVs' of **1** (black) and **1** with 20 mol-equiv. $(Et_4N)(S\text{-}o\text{-}^{i}PrCONH\text{-}p\text{-}CF_3\text{-}Ph)$ (blue) under the same conditions.

Electrochemistry. Intramolecular H-hydrogen has been shown to this secondary interaction positively shifts metal-based reduction potentials of metalloproteins[31, 48, 83] and model complexes.[40, 50] To determine whether intramolecular H-bonding exhibits the same effect for **1** and **2**, electrochemical measurements were performed in MeCN solutions of the complexes with 0.25 M $^{n}Bu_4NPF_6$ supporting electrolyte using a glassy carbon working electrode. These results are compared to **3** under similar conditions. All potentials are reported versus an externally referenced ferrocenium/ferrocene (Fc^{+}/Fc) couple. For the sake of simplicity, the discussion will focus primarily on the results for **1**. The cyclic voltammogram (CV) of **1**, sweeping negatively, shown

in Figure 3.13, displays a broad ill-defined irreversible reduction event (E_{red}) at ~ −1.55 V and two irreversible oxidation events at −0.33 and 0.39 V, the latter containing a shoulder at ~0.13 V. Reversing the direction of the scan results in a new E_{red} at −1.18 V with the increased definition of the broad reduction event at ~−1.5 V. The CV of **2**, see Figure S3.65, reveals a very similar voltammogram with a cathodic shift of the broad E_{red} event to ~−1.7 V. Comparison to (Et_4N)(S-*o*-^{i}PrCONH-*p*-CF_3-Ph) (E_{ox} = −0.25 V; E_{red} = −1.10 V), see Figure S3.63, suggests the irreversible waves in **1** (E_{red} = −0.33 V; E_{ox} = −1.18 V) correspond to thiolate oxidation and disulfide reduction, respectively. Further justification for this assignment is found in the CV of Zn^{2+} analog of **1**, $(Et_4N)_2[Zn(S\text{-}o\text{-}^{i}PrCONH\text{-}p\text{-}CF_3\text{-}Ph)_4]$ (**4**), shown in Figure S3.66, revealing an E_{red} ~ −1.19 V only when scans are initiated in the positive direction, i.e., oxidation of the Zn-coordinated thiolate transpires to generate disulfide at the working electrode surface. Although a single oxidation event might be expected for **4**, corresponding to oxidation of coordinated thiolate, several shoulders (E_{ox} = ~−0.3 and ~0.1 V) precede a well-defined irreversible E_{ox} at 0.60 V. The appearance of several broad and ill-defined oxidation events are observed for a similar complex $(Et_4N)_2[Zn(1,2\text{-}S_2\text{-}3,6\text{-}(RCONH)_2C_6H_2)_2]$ (R = ^{t}Bu, Me) possessing two broad oxidation peaks (0.0 to 0.4 V) and an irreversible E_{ox} = ~0.6 V; however, no assignments are made.[84] The ill-defined peaks for both **4** and $(Et_4N)_2[Zn(1,2\text{-}S_2\text{-}3,6\text{-}(RCONH)_2C_6H_2)_2]$ (R = ^{t}Bu, Me) peaks are most likely due to oxidation of coordinated thiolate of **4** and resulting multimeric Zn-aryl thiolate complexes. The only oxidation event that can be confidently assigned in **4** corresponds to the oxidation of free thiolate at −0.24 V, *vide supra*. Given the chemical oxidation of **1** in MeCN produces disulfide and a *S,S*-bridged complex, Ni-based oxidation does not occur under these conditions. Therefore, the remaining oxidation events of **1** (E_{ox} = 0.39 V and 0.13 V) are attributed to oxidation of coordinated thiolate but cannot be strictly assigned to monomeric or bridged complex. Assessing

the impact of H-bonding on the Ni(II/I) redox couple is difficult due to the complex speciation of **1** in solution. The presence of the tetrahedral monomer, square-planar isomer, and *S,S*-bridged multimeric species complicates the interpretation of electrochemical data.

Table 3.5. Redox potentials of tetrathiolate transition metal complexes with/without intra-molecular H-bonding to coordinated-thiolates. All redox potentials are reported in MeCN and referenced Fc/Fc^{+}.

Ni Complex[a]	**$Ni^{II/I}$ (V)**	**ΔE_{red} (V)**[b]	**ref**
1[c]	−1.68 (*irrev*)	+0.24	TW
3[c]	−1.92 (*irrev*)	0	TW
Fe Complexes	**$Fe^{III/II}$ (V)**		
$(Et_4N)_2[Fe(S\text{-}o\text{-}CH_3CONHPh)_4]$[c]	−0.68 (*rev*)	+0.25	40
$(Et_4N)_2[Fe(S\text{-}o\text{-}^tBuCONHPh)_4]$[c]	−0.69 (*rev*)	+0.24	40
$(Et_4N)_2[Fe(S\text{-}o\text{-}Ph_3CCONHPh)_4]$[c]	−0.72 (*rev*)	+0.21	40
$(Et_4N)_2[Fe(SPh)_4]$[b]	−0.93 (*rev*)	0	85
Mo/Pt Complexes	**$Mo^{V/IV}$ (V)**		
$(Et_4N)_2[Mo(O)(S\text{-}2\text{-}CH_3CONHPh)_4]$[c]	−0.76 (*rev*)	+0.45	78
$[Pt(bpy)(S\text{-}o\text{-}^tBuCCONHPh)_4]$[c]	−1.21 (*rev*)	0	78

[a]Presence of 20 mol-equivalent of their respective thiolate. [b]ΔE_{red} is difference in reduction potential of the substituted and non-substituted complexes. [c]MeCN.

Ambiguity in assigning redox couples arising from the ill-defined dissociation products can be eliminated by recording the CV of **1** in the presence of excess thiolate (20 mol-equiv). The addition of excess thiolates ensures that only the monomeric tetrathiolate species is present (*vide supra*). Under these conditions, the CV of **1**, inset of Figure 3.13, displays a more well-defined irreversible peak (E_{red} = −1.68 V) assigned to the Ni(II/I) couple. The irreversibility is likely due to structural changes, such as ligand loss, that occur upon reduction even in the presence of excess ligand. The impact of intramolecular H-bonding on the Ni(II/I) couple becomes apparent when

comparing these complexes to the H-bond-free analog (**3**) ($Ni^{II/I}$ = −1.92 V, MeCN, 20 mol-equiv (Et_4N)(S-*p*-CF_3-Ph)). Introduction of *ortho*-carboxamide groups in **1** result in a cathodic shift of +0.24 V, consistent with other metal-thiolate systems, detailed in Table 3.5. [40, 78, 85] These results highlight the role of active H-bonds in modulating redox properties of Ni(II) in tetrathiolate frameworks.

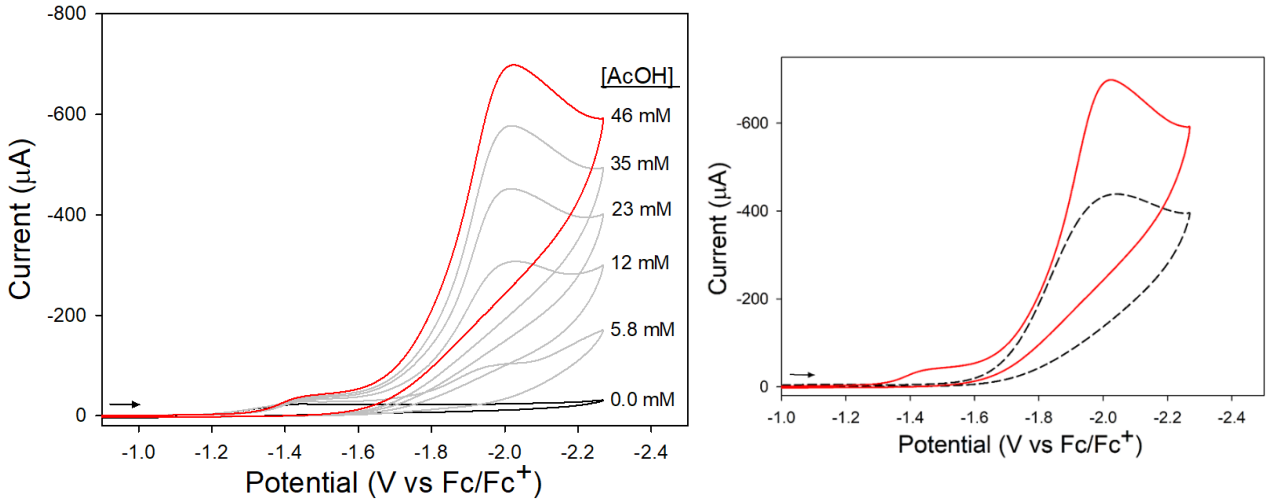

Figure 3.14. (*left*) CV of **1** after titrating with AcOH and (*right*) **1** (red) and rinse test experiment (black-dashed) both with AcOH (46 mM) in MeCN with 20 mol-equiv. (Et_4N)(S-*o*-^{i}PrCONH-*p*-CF_3-Ph) in MeCN at RT (0.25 M $^{n}Bu_4NPF_6$ supporting electrolyte, glassy carbon working electrode, 100 mV/s scan rate). Arrow shows direction of scan.

HER Electrocatalysis and Analysis of Deposited Material. Complexes **1** and **2** were subsequently investigated for their activity in electrocatalytic H^+ reduction to H_2 (g). CV measurements were acquired after titrating H^+ equivalents using the weak Brønsted acid acetic acid (AcOH; pK_a = 23.5 in MeCN[80]) into MeCN solutions of **1** (0.25 M $^{n}Bu_4NPF_6$ electrolyte, glassy carbon working electrode, scan rate = 100 mV/s). Upon the addition of AcOH, a significant current enhancement was observed at a catalytic potential (E_{cat}) of ~ −2.0 V (i_c/i_p ~ 30 at 20 mol-

equiv AcOH; i_c = catalytic current at E_{cat} ; i_p = current of Ni(II/I) couple), seen in Figure 3.14, accompanied by a minor enhancement at ~ −1.45 V prior to the beginning of the catalytic wave, known as a prewave. The presence of an irreversible prewave prior to catalysis indicates a precatalyst transformation, often associated with catalyst decomposition in HER electrocatalysts.[86-91] To assess whether catalytically active surface-adsorbed species were forming during the titration experiment, a standard rinse test was performed, shown in Figure 3.14.[92] The CV was performed in a solution of **1** and acid, and the potential was scanned from −0.8 to −2.3 V. Next the glassy carbon electrode was removed, rinsed with MeCN, and scanned over the same range in fresh electrolyte solution with only acid. This experiment resulted in a similar catalytic wave lacking the prewave feature, suggesting that electrocatalytic activity arises from surface-adsorbed material rather than a homogenous complex. Although **2** appears electrocatalytic, see Figure S3.68, it meets a similar fate as demonstrated by rinse test experiments, see Figure S3.69, confirming activity from deposited material. The composition of the deposited material derived from **1** was analyzed utilizing scanning electron microscopy (SEM) and electron dispersive spectroscopy (EDS) after 0.5 hours of electrolysis at ~−2.1 V in the presence of 25.0 mol-equiv of AcOH. SEM and EDS of the electrode surface, shown in Figures 3.15 and S3.72-S3.78, reveal the presence of a uniform Ni/S film interspersed with embedded Ni/S nanoparticles. Both the film and nanoparticles possess similar compositions of Ni:S (8:1) which might be described as sulfide doped Ni films/particles. This high Ni ratio composition of HER active deposits have been reported for purely Ni[93] and Ni:S (18:1)[89] deposits. Control experiments of ligand and Zn analog, shown in Figure S3.71, confirm that electrocatalysis and deposition arises from the Ni-S composition of **1**. Although a promising catalyst, under electrocatalytic conditions **1** transforms into an electrocatalytic adsorbed Ni/S film with embedded nanoparticles.

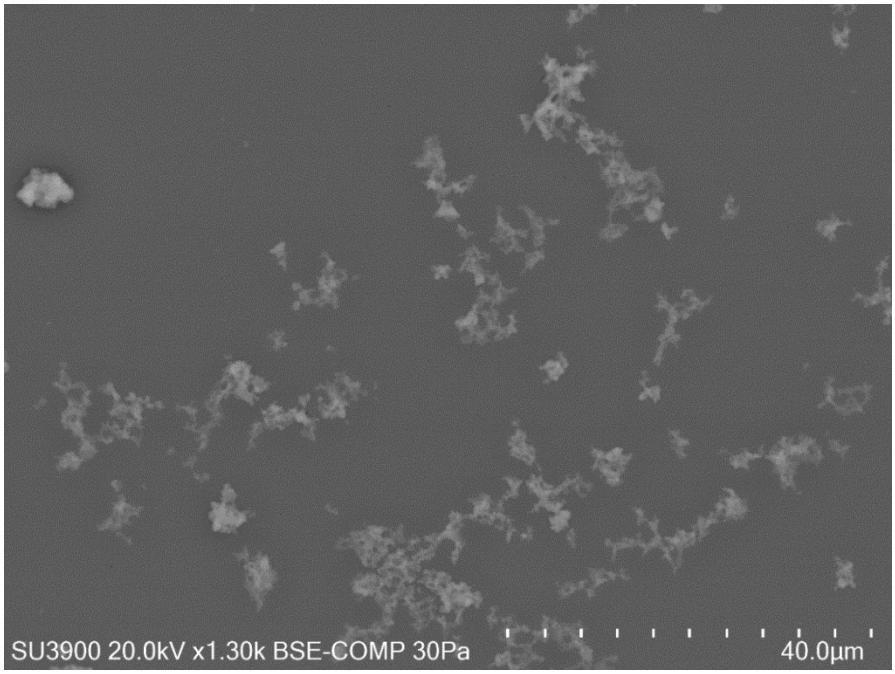

Figure 3.15. Zoom-in of SEM image of electrolyzed glassy carbon working from 1.7 mM solution of **1** and 24.6 mol-equiv. for 0.5 h.

While distinguishing between electrocatalysis originating from homogenous versus heterogenous material is important, the factors influencing the decomposition of dissolved complex remain poorly understood. Dempsey has observed that complexes prone to forming HER active deposits on electrodes typically feature ligands that can undergo electrochemical modification under both reducing and acidic conditions.[90] For example, complexes containing C=N or N-O bonds are susceptible to hydrogenation or hydrogenolysis, respectively, leading to their decomposition.[87, 93, 94] However, a growing number of Ni-S containing complexes have been reported to form HER active Ni/S films under HER electrocatalytic conditions, summarized in Table S3.16.[89-91, 95] Dempsey proposes that decomposition results from Ni inserting itself into the C-S bond of the thiolate ligand, degrading the ligand, and forming the deposited Ni/S material.[90] Although there is no direct evidence of electrochemical C-S cleavage by Ni, there are reports of

Ni-catalyzed desulfurization of C-S bonds if a hydride is present.[96-98] Unlike the 2:1 or 1:1 ratios, associated with C-S bond cleavage, EDS measurements of **1** suggest that the heterogenous material is primarily composed of Ni with an 8:1 Ni:S ratio. The difference in composition suggests an alternative decomposition pathway for **1**. Under electrocatalytic conditions, **1** most likely degrades by thiolate dissociation, resulting in deposition of metallic Ni with a minor sulfide incorporation. This proposed decomposition pathway is further suggested by the Ni-S anti-bonding character of the LUMOs of **1*(T$_d$)** and **1*(SqPl)**, *vide supra*, indicating reduction weakens the Ni-S bond thereby promoting ligand loss. The increased lability of the thiolate upon reduction of **1** offers insight into a decomposition mechanism under electrocatalytic conditions, i.e. ligand dissociation yielding primarily Ni deposits. Ligand-loss under catalytic conditions is consistent with its protic-instability and irreversible Ni(II/I) couple. To investigate whether free Ni could be minimized during CV acid titration experiments, the titration was repeated with 20-mol equiv. of thiolate for **1**, shown in Figure S3.70. The resulting CV reveals a similar waveform with a ~0.2 V cathodic shift of both the prewave (−1.60 V) and E_{cat} (−2.21 V) but excess thiolate does not appreciably inhibit formation of electrocatalytically active heterogenous material, as confirmed by rinse test experiments shown in Figure S3.71. Although an exact decomposition mechanism is unknown, **1** forms electrocatalytically active deposits under the acidic and reducing conditions employed here.

3.4 Conclusion

This study demonstrates that incorporation of intramolecular hydrogen bonding, via *ortho*-carboxamide substituents, in Ni(II) tetra-aryl thiolates influence their structural, electronic, and catalytic properties. Unexpectedly, this modification led to the presence of square-planar monomers of **1** and **2**, via XRD and XAS, attributed to the enhanced ligand field strength of the coordinated thiolates due to weakened π-donor capacity. However, upon dissolution NMR and magnetic measurements indicate both square-planar and tetrahedral isomers persist, consistent with the small difference in computed energy between the geometries (~5 kcal/mol). Additional solution-state measurements, UV-vis and NMR, indicate an equilibrium between monomeric **1** and **2** and *S,S*-bridged multimers through a ligand dissociation mechanism. The equilibrium, like **3**, be shifted back to monomer with the addition of thiolate. Incorporation of H-bonding, regardless of geometry, fine tunes the electronic structure of Ni(II) tetra-thiolates resulting in a diminished S-based character in the HOMO, creating more robust complexes. The impact on the robustness of these complexes is further exhibited by the increased stability in acidic conditions. We found that both H-bonding and increasing the steric bulk beyond the second-coordination sphere enhances the protic stability of Ni(II) tetrathiolates up to 10-fold. The decrease in electron density at the coordinated thiolates, provided by H-bonding, additionally results in a cathodic shift of the Ni(II/I) couple by ~200 mV. However, under electrocatalytic conditions these complexes decomposed to yield electroactive Ni/S films with embedded nanoparticles of the same composition. These findings highlight the role intramolecular hydrogen bonding has in tuning the ligand field strength of thiolates, modulating electronic structure, and behavior of Ni-tetrathiolate complexes under electrocatalytic conditions for hydrogen proton reduction.

3.5 Materials and Methods

General Information. All reagents were procured from commercial suppliers and used as received unless otherwise noted. Acetonitrile (MeCN), tetrahydrofuran (THF), and diethyl ether (Et_2O) were purified by passage through activated alumina columns using an MBraun solvent purification system (MB-SPS). All solvents were stored over 3 Å molecular sieves in an anaerobic glovebox before use. Methanol (MeOH) was degassed by at least three freeze-pump-thaw cycles and stored over 3 Å molecular sieves for a minimum of one week before use. The metal salts, $(Et_4N)_2[MCl_4]$ (M = Ni, Zn), were synthesized according to the published procedure.[99] $(Et_4N)_2[Ni(S\text{-}p\text{-}CF_3\text{-}Ph)_4]$ was synthesized according to prior published procedures, see Chapter 2. All reactions were performed under an inert atmosphere of N_2 using Schlenk-line techniques or in an MBraun Unilab glovebox.

Physical Methods. FTIR spectra were collected with a ThermoNicolet 6700 spectrophotometer running the OMNIC software. Solid-state and liquid-state FTIR spectra were collected with a ThermoNicolet 6700 spectrophotometer running the OMNIC software. Solid-state samples were prepared as KBr pellets in a glovebox under N_2 atmosphere and run in ambient conditions. Liquid FTIR samples were prepared in a glovebox under N_2 atmosphere from a ~10 mM solution of analyte. These samples were measured at ambient temperature using a Specac Omni-cell with CaF_2 windows and a 0.2 mm PTFE spacer. UV-vis spectra were recorded at 25 °C using a Cary-50 spectrophotometer containing a Quantum Northwest TC 125 temperature control unit. All UV-vis samples were prepared in gastight/screw-cap quartz cells with an optical pathlength of 1 cm. NMR spectra were recorded in the reported solvent on a 400 MHz Bruker BZH 400/52 NMR spectrometer and 600 MHz Varian Unity INOVA NMR RT with chemical shifts referenced to residual protio signal of the deuterated solvent.[100] ^{19}F NMR spectra are referenced to $CFCl_3$ by

employing a fluorobenzene internal standard (δ = -114.81 ppm vs. $CFCl_3$).[101] Magnetic susceptibility measurements were performed in both the solid- and solution-state. Solid-state magnetic measurements were recorded with a Johnson Matthey Mark 1 magnetic susceptibility balance. Solution state magnetic susceptibility measurements were recorded in CD_3CN at 25 °C using the Evans method on a 600 MHz NMR spectrometer.[102] Pascal's constants for diamagnetic corrections are taken from the literature.[103] Low resolution electrospray ionization mass spectrometry (LR-ESI-MS) data were collected using a PerkinElmer Sciex APII Plus quadrupole mass spectrometer or a Bruker Esquire 3000 plus ion trap mass spectrometer.

Computation Details. Density functional theory (DFT) calculations were performed with the ORCA electronic structure package, version 4.2.1. Geometry optimization and frequency of all models were performed using the B3LYP functional[104, 105] employing the RIJCOSX aproximation[106] and Grimme's D3(BJ) dispersion correction[107, 108] with coordinates from the crystal structures of **1** and **2**. The def2-SVP basis set was used for all atoms except for Ni, S, N, O, and F for which the triple-ζ basis set def2-TZVPP[109, 110] was used, for geometry optimization and frequency analysis with an automatically constructed auxiliary basis set on all atoms. No imaginary frequencies were found. Single point energy (SPE) calculations were performed on the optimized structures using B3LYP functional[104, 105] employing the RIJCOSX approximation.[106] The conductor-like polarizable continuum model (CPCMC)[59] was used with MeCN (ε = 37.5) for geometry optimization, frequency, and SPE unless otherwise noted. The triple-ζ basis set def2-TZVPP[109, 110] was used for all atoms with the matching auxiliary basis set triple-ζ basis set def2-TZVPP/J. UCSF Chimera[111] was used to generate model structure to visualize isosurface plots of MOs with isodensity values of 0.05 a.u.

The absorption spectra of the geometry-optimized **1(SqPl)*** and **1(T_d)*** was calculated using time-dependent functional theory (TD-DFT).[112, 113] The Tamm-Dancoff approximation was performed for the first 80 roots. The def2-SVP basis set was used for all atoms except for Ni, S, N, O, and F for which the def2-TZVPP bases set was used. In addition, the TD-DFT was using the B3LYP functional employing the RIJCOSX approximation using a solvent continuum model CPCMC(MeCN). Vertical excitation energies and molar extinction coefficients for transition were calculated using the ORCA_MAPSPC module to give transitions. The computed absorption spectrum was generated with a Gaussian linewidth of 1500 cm^{-1}. UCSF Chimera[111] was used to generate model structure to visualize isosurface plots of electron difference maps with isodensity values of 0.005 a.u.

3.6 Synthesis and Characterization:

(S-*o*-NH_2-*p*-CF_3-Ph)$_2$. A batch of 3-amino-4-(trifluoromethyl)benzenethiol hydrochloride (3.185 g, 13.87 mmol) was added to a 100 mL MeOH/H_2O (1:1) solution to result in a heterogenous mixture with a slight yellow color. To this solution was added NaOH (0.946 g, 23.7 mmol) generating a yellow homogenous solution. Compressed air was bubbled through the solution for 24 h while stirring. After ~4 h, a light-yellow precipitate began to appear. After 20 h, more solid formed and the solution was pale yellow in color. The solid was removed from the solution by filtration over a glass-frit and the isolated light-yellow solid was dissolved in 100 mL of CH_2Cl_2. The yellow CH_2Cl_2 solution was placed in a separatory funnel and washed with DI H_2O and K_2CO_3(aq) until the aqueous layer remained basic (pH ~9). Additional washes with saturated $NaHCO_3$(aq) (2×) and NaCl(aq) solutions were performed. The CH_2Cl_2 layer was dried with anhydrous $MgSO_4$, filtered, and the insoluble salt was washed with ~5 mL of CH_2Cl_2. The filtrate was then taken to dryness on a rotary evaporator to afford a light-yellow solid. To this solid was

added ~50 mL of pentane, the mixture was stirred for 1 h and placed in -20 °C freezer for 12 h. The resulting precipitate was isolated by vacuum filtration on a glass-frit, washed with pentane (3 × 5 mL), and dried on a vacuum line to afford the product as a light-yellow solid (1.710 g, 4.449 mmol, 64.2%). FTIR (KBr matrix), ν_{max} (cm^{-1}): 3456 (w, NH), 3416 (w, NH), 3352 (w, NH), 3312 (w, NH), 1339 (s, CF), 1120 (s, CF), 1080 (s, CF). ^{1}H NMR (400 MHz, $CDCl_3$, δ from protio solvent): 7.24 (d, 2H, J = 8.0 Hz), 6.95 (s, 2H), 6.83 (d, 2H, J = 8.0 Hz), 4.54 (s, 4H). $^{13}C\{^{1}H\}$ NMR (100 MHz, $CDCl_3$, δ from solvent signal): 148.6 (s), 136.9 (s), 133.7 (q, J = 32.3 Hz), 123.8 (q, J = 272.7 Hz), 121.8 (q, J = 1.5 Hz), 114.6 (q, J = 3.8 Hz), 111.8 (q, J = 3.9 Hz). ^{19}F NMR (376 MHz, $CDCl_3$, δ from $CFCl_3$): -65.00 (s). Mp: 71-73 °C.

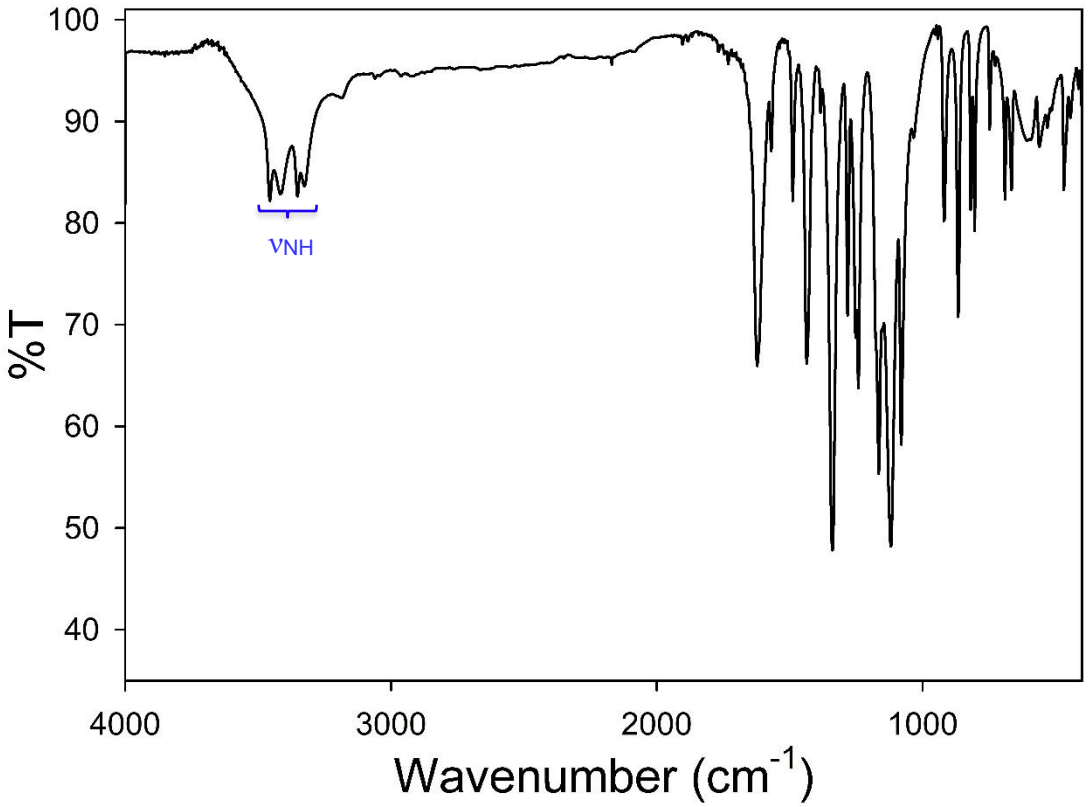

Figure S3.1. Solid-state FTIR spectrum of (S-*o*-NH_2-*p*-CF_3)$_2$ in a KBr matrix at RT.

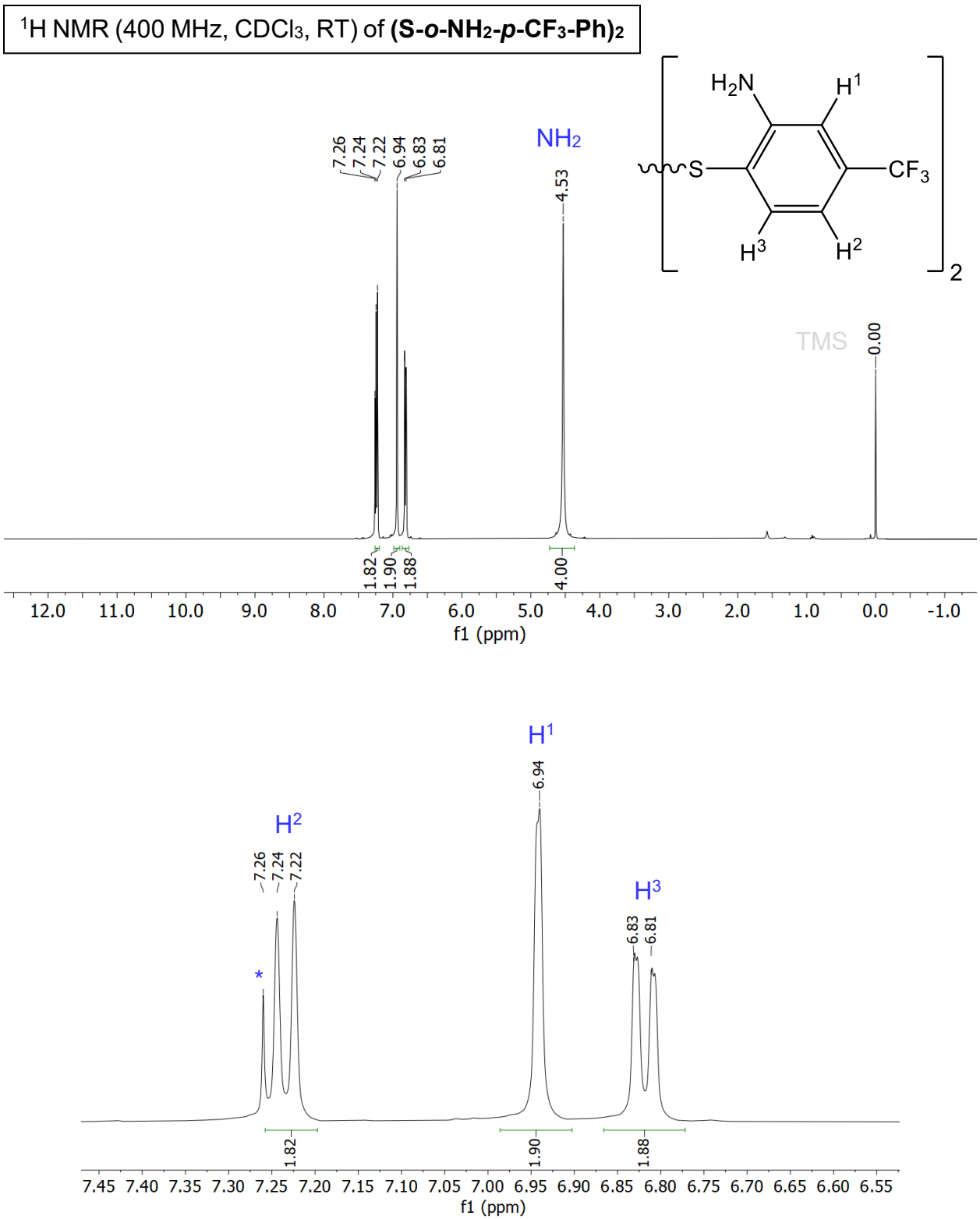

Figure S3.2. *Top:* ^{1}H NMR spectrum of (S-*o*-NH$_2$-*p*-CF$_3$-Ph)$_2$ in CDCl$_3$ at RT (δ vs. protio signal). *Bottom:* expansion of 6 – 8 ppm region. Residual CHCl$_3$ is observed at 7.26 ppm and is indicated with *.

^{13}C NMR (125 MHz, $CDCl_3$, RT) of **(S-*o*-NH_2-*p*-CF_3-Ph)$_2$**

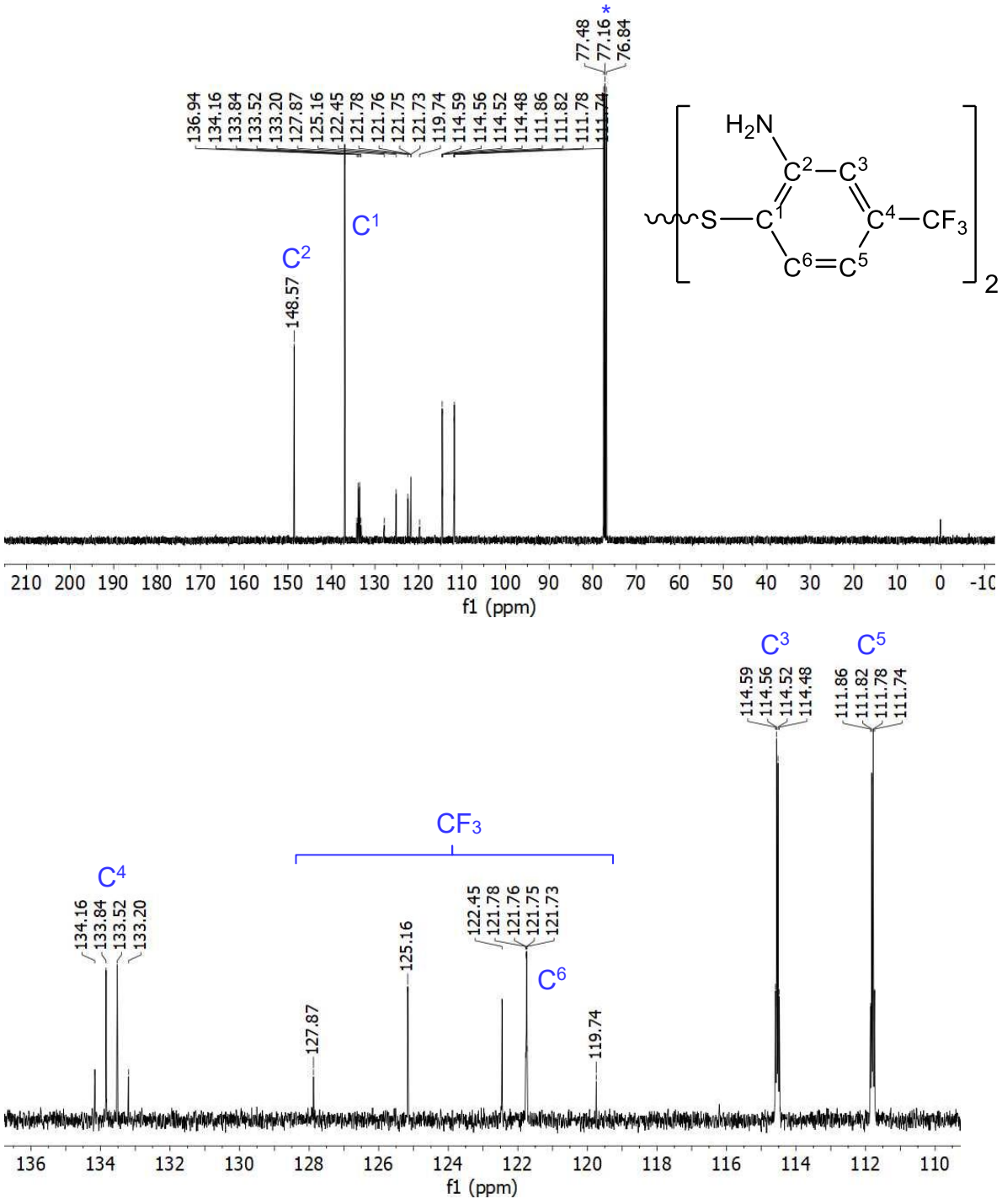

Figure S3.3. *Top:* ^{13}C NMR spectrum of (S-*o*-NH_2-*p*-CF_3-Ph)$_2$ in $CDCl_3$ at RT (δ vs. protio signal). *Bottom:* expansion of 110 - 136 ppm region. Residual $CHCl_3$ is observed at 7.26 ppm and is indicated with *.

^{19}F NMR (376 MHz, $CDCl_3$, RT) of **(S-*o*-NH_2-*p*-CF_3-Ph)$_2$**

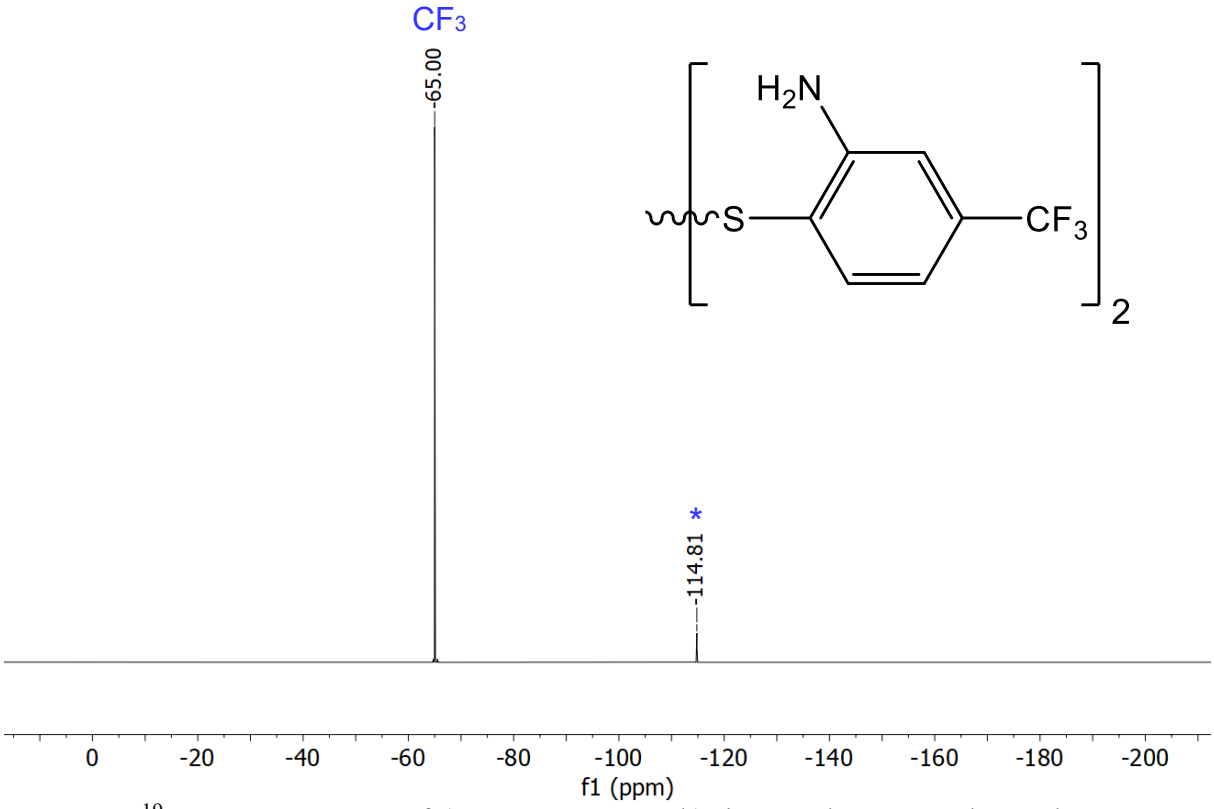

Figure S3.4. ^{19}F NMR spectrum of (S-*o*-NH_2-*p*-CF_3-Ph)$_2$ in $CDCl_3$ at RT. The peak at -114.81 ppm is from PhF as an internal standard and is indicated with *.

(S-*o*-^{i}PrCONH-*p*-CF_3-Ph)$_2$ To a dark yellow solution of (S-*o*-NH_2-*p*-CF_3-Ph)$_2$ (1.443 g, 3.754 mmol) in 20 mL of CH_2Cl_2 containing pyridine (0.743 g, 9.39 mmol) was added isobutyryl chloride (0.997 g, 9.36 mmol) under an N_2(g) stream to maintain anhydrous conditions. The solution took on a lighter color and an off-white precipitate appeared within ~5 min. CH_2Cl_2 was added to the reaction flask until the solution became a homogeneous light-yellow color and the solution was stirred at RT for ~3 h. After this time, the solution was placed in a separatory funnel and washed with DI H_2O and K_2CO_3 (aq) until the aqueous layer remained basic (pH ~9). Additional washes with saturated $NaHCO_3$ (aq) (2×) and NaCl (aq) solutions were performed. The

isolated CH_2Cl_2 layer was dried with anhydrous $MgSO_4$, filtered, and the insoluble salt was washed with ~10 mL of CH_2Cl_2. The filtrate was then taken to dryness on a rotary evaporator to afford an off-white solid. To this solid was added ~30 mL of pentane. The mixture was stirred for 1 h and the resulting precipitate was isolated by vacuum filtration on a glass-frit. The solid was washed with pentane (3 × 5 mL) and dried on a vacuum line to afford the product as an off-white solid (1.612 g, 3.073 mmol, 81.9%). FTIR (KBr matrix), ν_{max} (cm^{-1}): 3243 (m, NH), 1666 (s, CO), 1329 (s, CF), 1116 (s, CF), 1083 (s, CF). FTIR (THF, ~10 mM), ν_{max} (cm^{-1}): 3382 (m, NH), 1707 (s, CO). ^{1}H NMR (400 MHz, $CDCl_3$, δ from protio solvent): 8.80 (s, 2H), 8.12 (s, 2H), 7.43 (d, 2H, J = 8.0 Hz), 7.25 (d, 3H, J = 7.6 Hz, overlap with residual $CHCl_3$), 2.41 (septet, 2H, J = 6.9 Hz), 1.21 (d, 12H, J = 6.9 Hz). $^{13}C\{^1H\}$ NMR (100 MHz, $CDCl_3$, δ from solvent signal): 175.4 (s), 140.3 (s), 136.4 (s), 134.3 (q, J = 32.9 J = 273.2 Hz) . ^{19}F NMR (376 MHz, $CDCl_3$, δ from $CFCl_3$): -64.89 (s). LR-ESI-MS (*m/z*): [(S-*p*-CF_3-*o*-NHC(O)^{i}Pr-Ph)$_2$ − H^+]$^-$ calcd for $C_{22}H_{21}F_6S_2N_2O_2$ (relative abundance), 523.1 (100.0), 524.1 (26.5), 525.1 (12.8), 526.1 (2.7); found, 522.8 (100.0), 523.8 (24.8), 524.8 (12.4), 525.8 (2.2). [(S-*p*-CF_3-*o*-NHC(O)^{i}Pr-Ph)$_2$ + O_4 − $2H^+$]$^-$ calcd for $C_{22}H_{20}F_6S_2N_2O_6$ (relative abundance), 586.1 (100.0), 587.1 (26.), 588.1 (13.7), 589.1 (2.9); found, 586.0 (100.0), 586.8 (25.8), 587.9 (12.6), 588.9 (2.8). Decomposed at 168 °C.

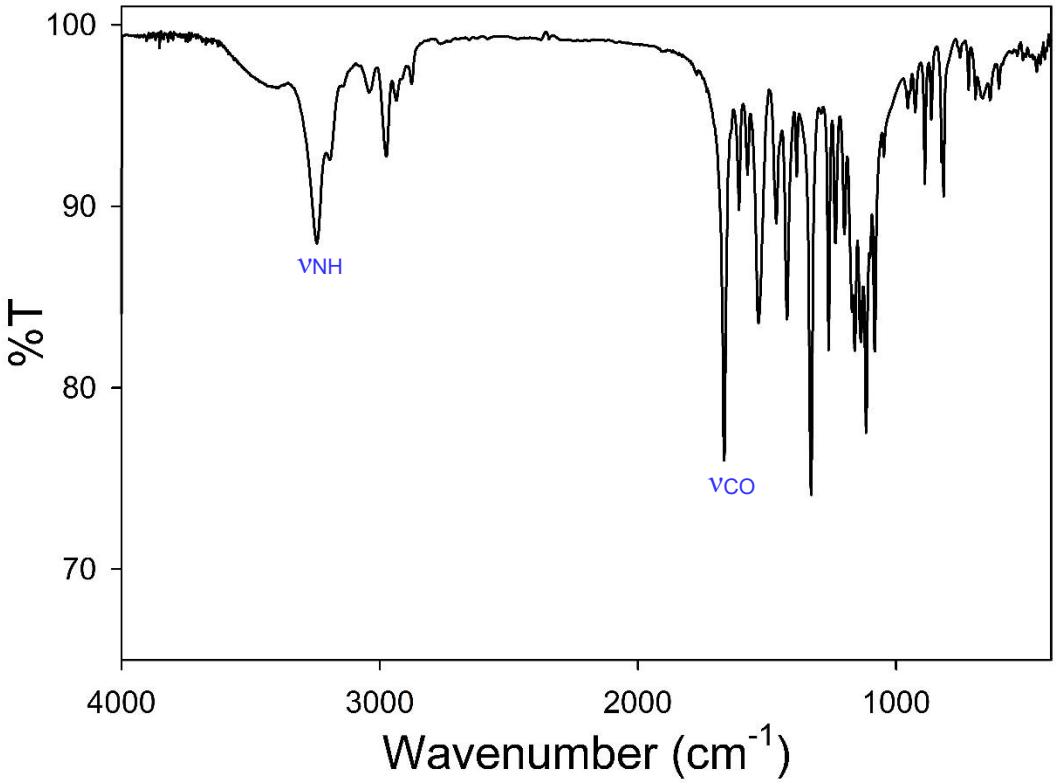

Figure S3.5. Solid-state FTIR spectrum of (S-*o*-^{i}PrCONH-*p*-CF_3-Ph)$_2$ in a KBr matrix at RT.

^{1}H NMR (400 MHz, $CDCl_3$, RT) of **(S-*o*-^{i}PrCONH-*p*-CF_3-Ph)$_2$**

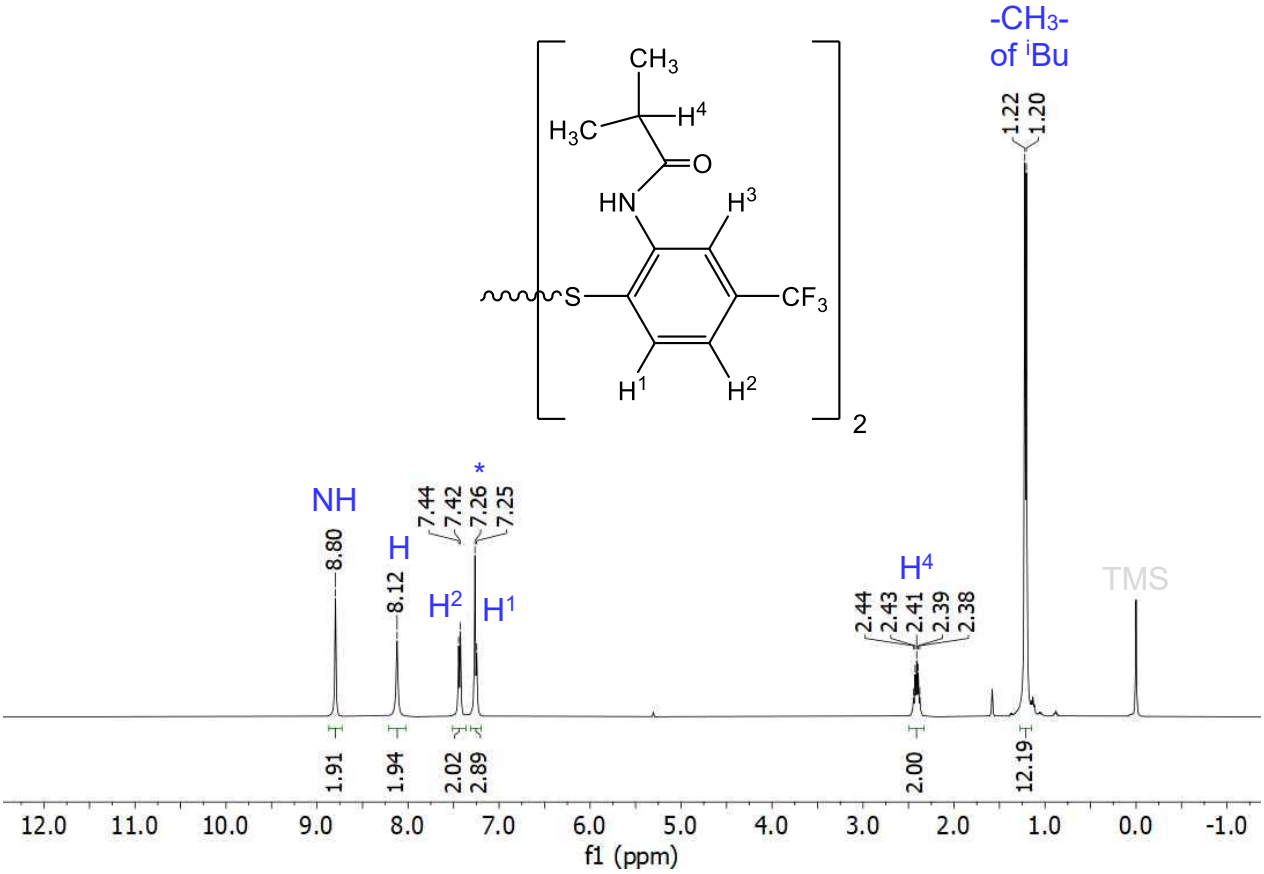

Figure S3.6. ^{1}H NMR spectrum of (S-*o*-^{i}PrCONH-*p*-CF_3-Ph)$_2$ in $CDCl_3$ at RT (δ vs. protio signal). Residual $CHCl_3$ is observed at 7.26 ppm and is indicated with *.

^{13}C NMR (100 MHz, $CDCl_3$, RT) of **(S-*o*-^{i}BrCONH-*p*-CF_3-Ph)$_2$**

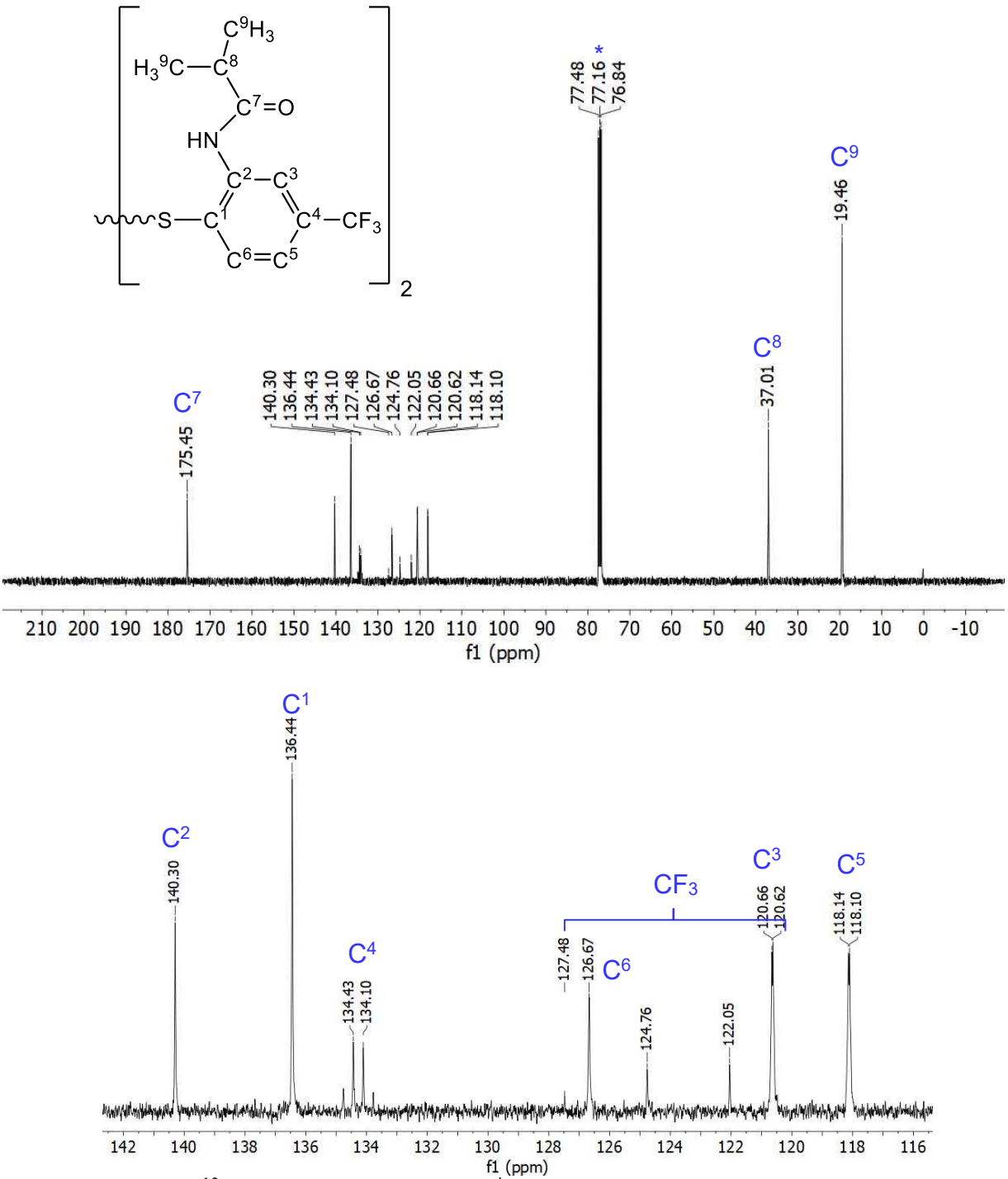

Figure S3.7. *Top:* ^{13}C NMR spectrum of (S-*o*-^{i}PrCONH-*p*-CF_3-Ph)$_2$ in $CDCl_3$ at RT (δ vs. protio signal). *Bottom:* expansion of 116 - 142 ppm region. Residual $CHCl_3$ is observed at 7.26 ppm and is indicated with *.

^{19}F NMR (376 MHz, $CDCl_3$, RT) of **(S-*o*-^{i}PrCONH-*p*-CF_3-Ph)$_2$**

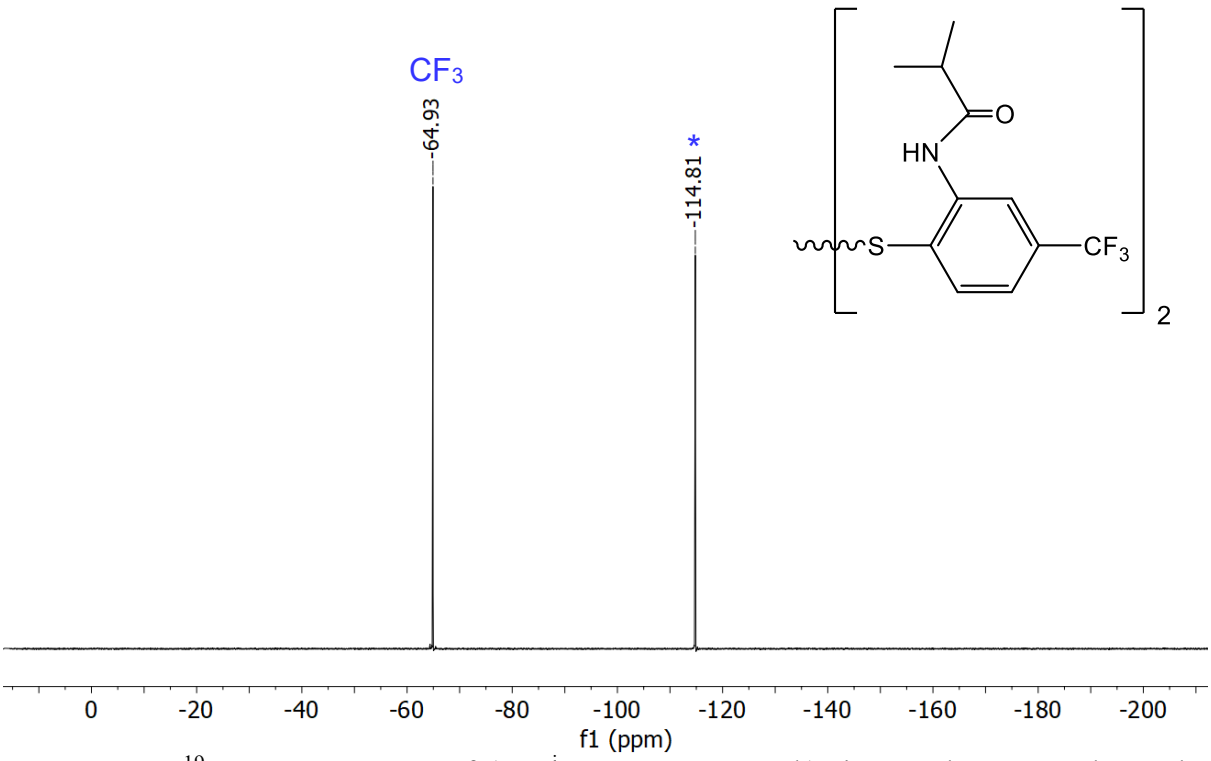

Figure S3.8. ^{19}F NMR spectrum of (S-*o*-^{i}PrCONH-*p*-CF_3-Ph)$_2$ in $CDCl_3$ at RT. The peak at -114.81 ppm is from PhF as an internal standard and is indicated with *.

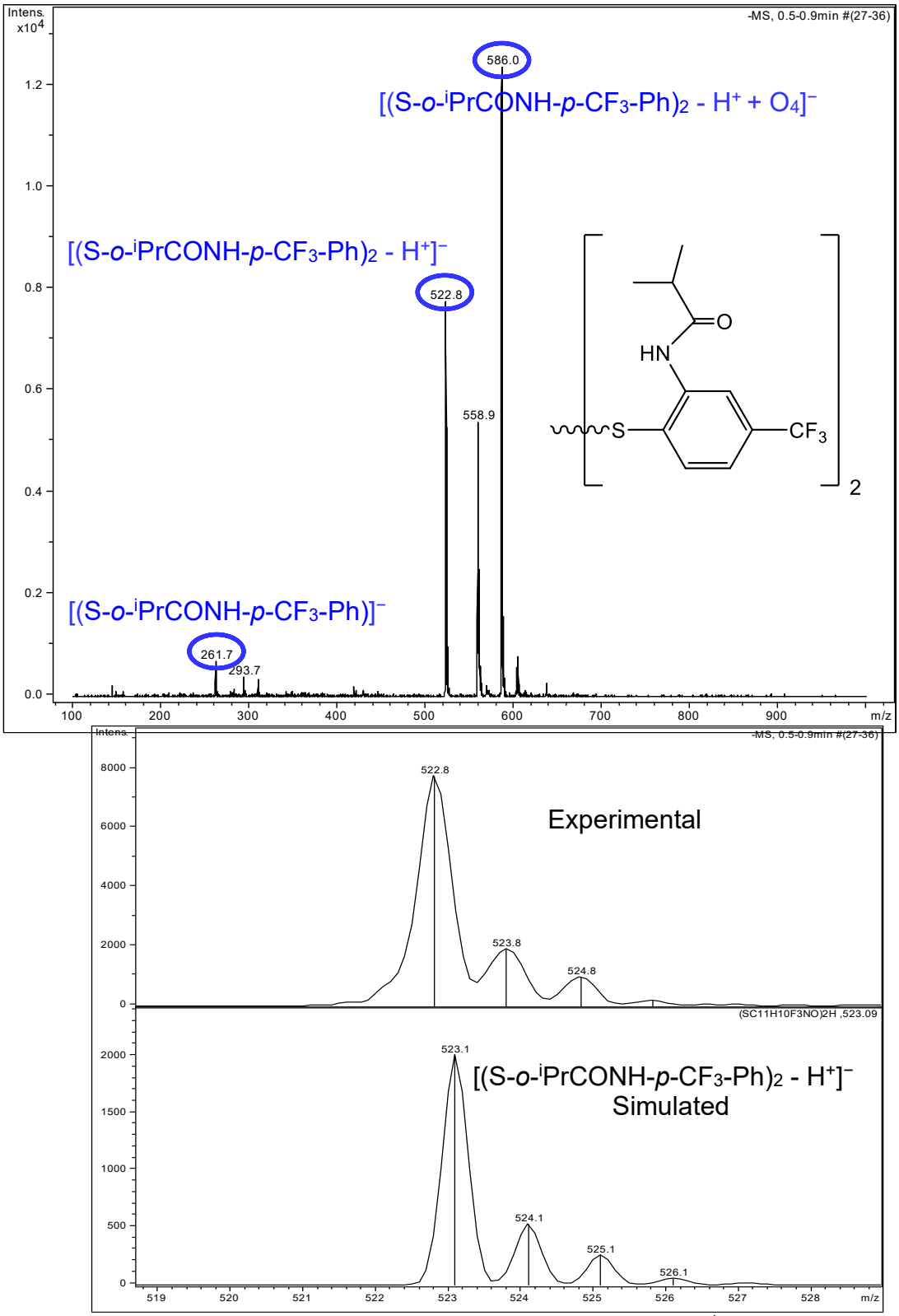

Figure S3.9. *Top:* Low-resolution ESI-MS(-) (negative mode) of (S-*o*-^{i}PrCONH-*p*-CF_3-Ph)$_2$ in MeCN/THF (1:1; v/v). *Bottom*: experimental and simulated theoretical isotopic distribution peak at *m/z*: 523.1 Other peaks not labeled have not been identified as reaction products.

(Et_4N)(S-*o*-^{i}PrCONH-*p*-CF_3-Ph) To a slurry of (S-*o*-^{i}PrCONH-*p*-CF_3-Ph)$_2$ (0.998 g, 1.90 mmol) in 4 mL of MeOH/THF (1:1; v/v), was added a ~2 mL MeOH solution containing $NaBH_4$ (0.159 g, 4.20 mmol). Gas evolution was observed upon initial addition of $NaBH_4$ that resulted in a yellow-colored solution and appearance of a fine white solid. After 1 h of stirring at RT, a ~2 mL MeOH solution containing Et_4NCl (0.661 g, 3.99 mmol) was added and resulted in a white precipitate. After stirring the mixture for ~30 min, the solution was filtered over a Celite packed frit and the yellow filtrate was taken to dryness. To the filtrate was added ~3 mL of THF resulting in a bright yellow-colored solution with a white solid suspended in solution. After the solution was stirred for 30 min, it was filtered over a Celite packed frit and rinsed with an additional ~3 mL of THF. The bright yellow THF filtrate was taken to dryness in vacuo and the residue was stirred for 30 min with ~3 mL of Et_2O. After this time, the insoluble was isolated by vacuum filtration on a glass-frit, washed with Et_2O (3 × 3 mL), and dried on a vacuum line to afford the product as a yellow solid (1.239 g, 3.156 mmol, 82.9%). FTIR (KBr matrix), ν_{max} (cm^{-1}): 3171 (m, NH), 1667 (vs, CO), 1324 (s, CF), 1102 (s, CF), 1074 (s, CF). ^{1}H NMR (400 MHz, CD_3CN, δ from protio solvent): 10.33 (s, 1H), 8.34 (s, 1H), 7.41 (d, 1H, J = 8.1 Hz), 6.88 (d, 1H, J = 8.1 Hz), 3.13 (q, 8H, J = 7.3 Hz), 2.59 (septet, 1H, J = 6.9 Hz), 1.22 (d, J = 6.9 Hz), 1.16 (tt, J = 7.3 (1.9) Hz) (peaks at 1.22 and 1.16 overlap integrating to 19H). ^{13}C{^{1}H} NMR (100 MHz, CD_3CN, δ from solvent signal): 176.0 (s), 154.0 (s), 139.7 (s), 133.2 (s), 126.9 (q, J = 269.4 ^{19}F NMR (376 MHz, CD_3CN, δ from C_6H_5F): -61.32 (s). LR-ESI-MS (*m/z*): [S-*p*-CF_3-*o*-NHC(O)^{i}Pr-Ph]$^-$ calcd for $C_{11}H_{11}F_3SNO$ (relative abundance), 262.1 (100.0), 263.1 (13.2), 264.0 (5.5); found, 261.8 (100.0), 262.8 (9.9), 263.8 (5.8). Mp 80 – 82 °C.

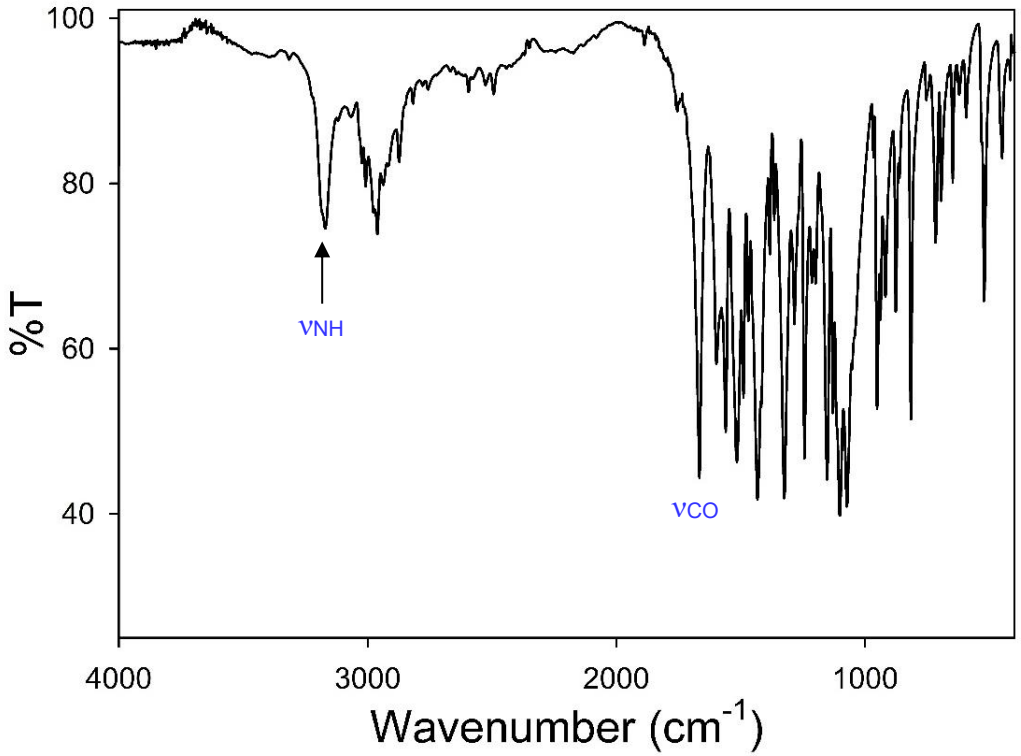

Figure S3.10. Solid-state FTIR spectrum of (Et_4N)(S-*o*-^{i}PrCONH-*p*-CF_3-Ph) in a KBr matrix at RT.

^{1}H NMR (400 MHz, CD_3CN, RT) of **(Et_4N)(S-*o*-^{i}PrCONH-*p*-CF_3-Ph)**

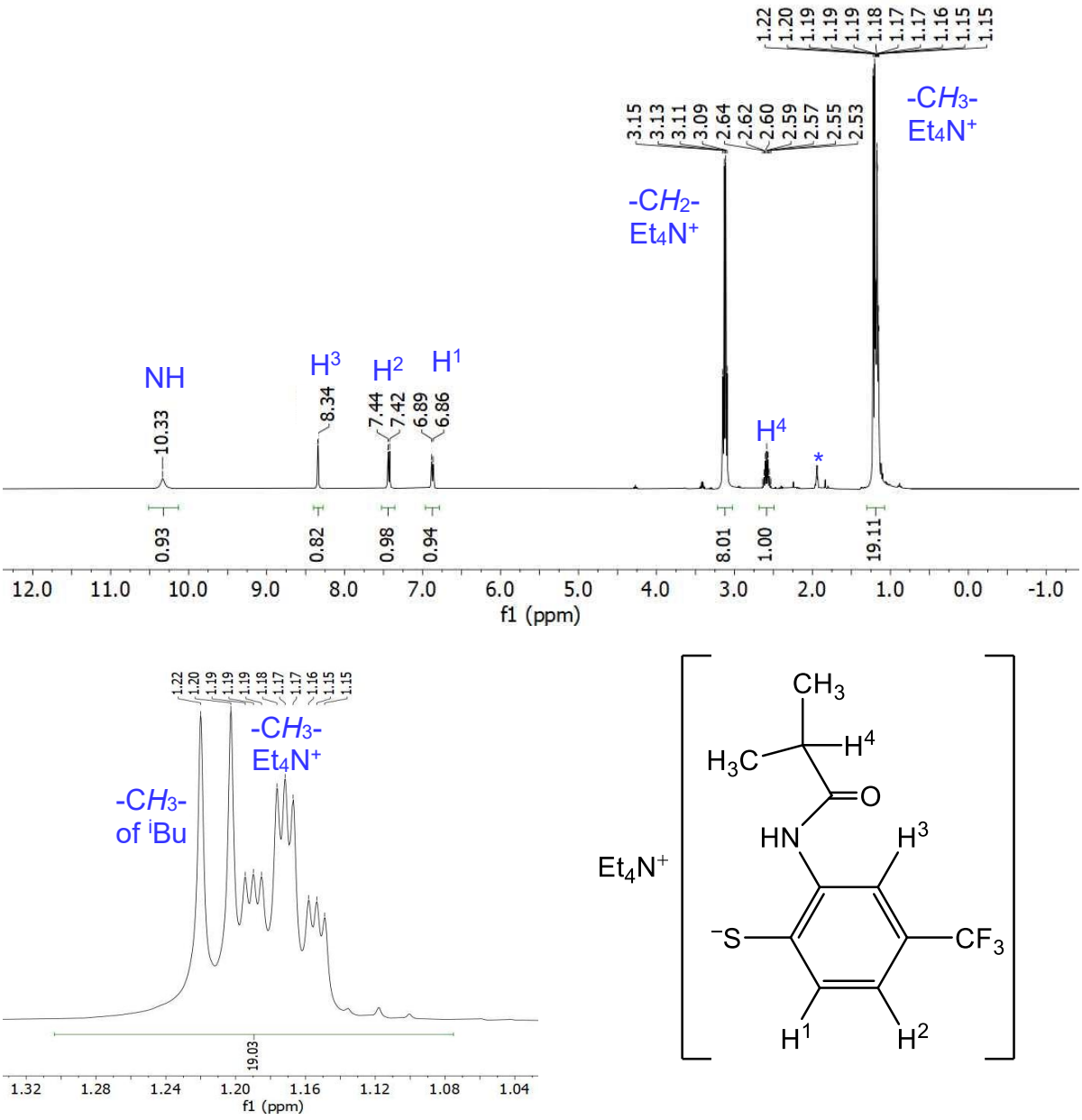

Figure S3.11. *Top:* ^{1}H NMR spectrum of (Et_4N)(S-*o*-^{i}PrCONH-*p*-CF_3-Ph) in CD_3CN at RT (δ vs. protio signal). *Bottom:* expansion of 1- 2 ppm region. Residual CH_3CN is observed at 1.94 ppm and is indicated with *.

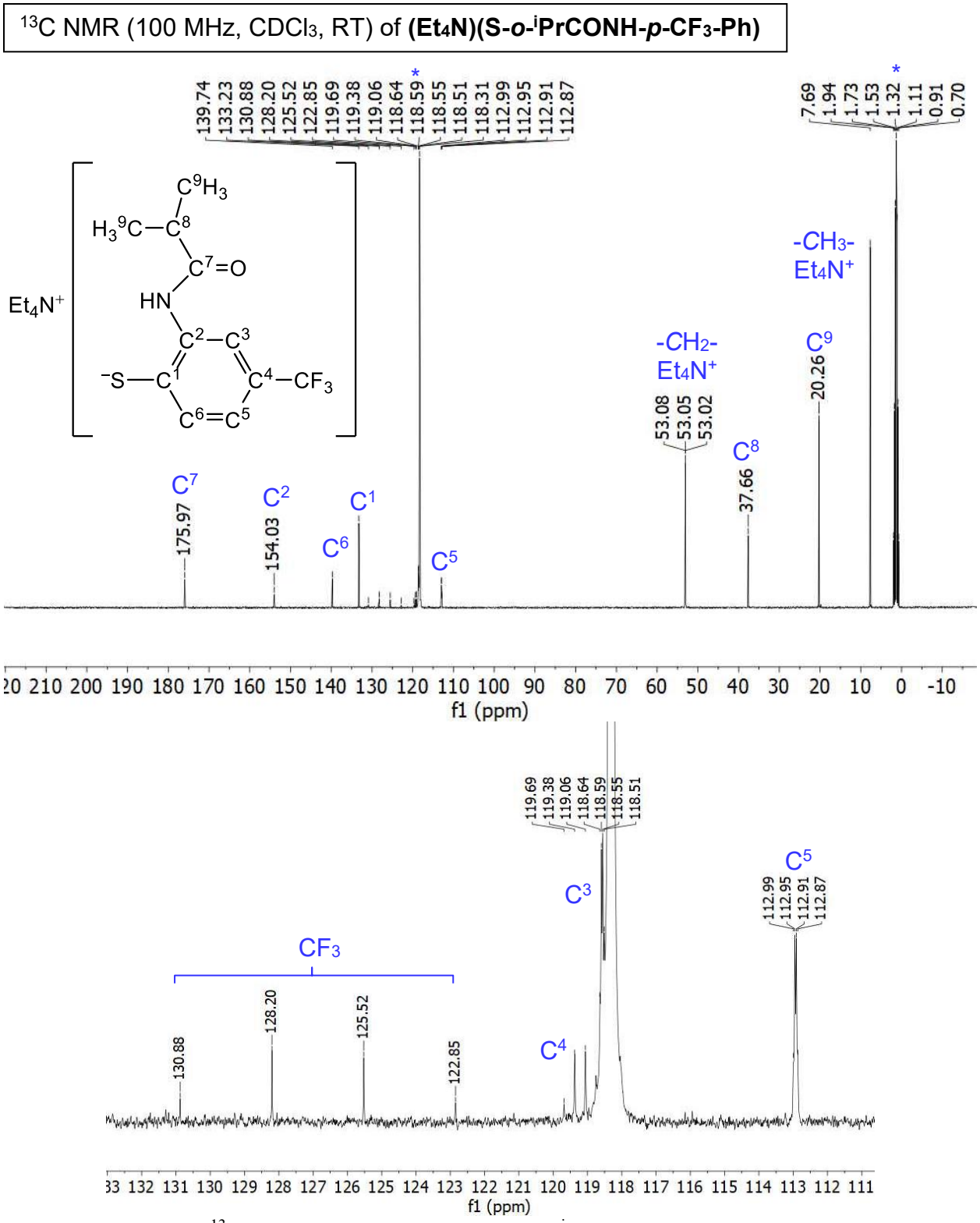

Figure S3.12. *Top:* ^{13}C NMR spectrum of (Et$_4$N)(S-*o*-^{i}PrCONH-*p*-CF$_3$-Ph) in CD$_3$CN at RT (δ vs. protio signal). *Bottom:* expansion of 111 - 133 ppm region. Residual CH$_3$CN is observed at 7.26 ppm and is indicated with *.

^{19}F NMR (376 MHz, $CDCl_3$, RT) of **(Et_4N)(S-*o*-^{i}PrCONH-*p*-CF_3-Ph)**

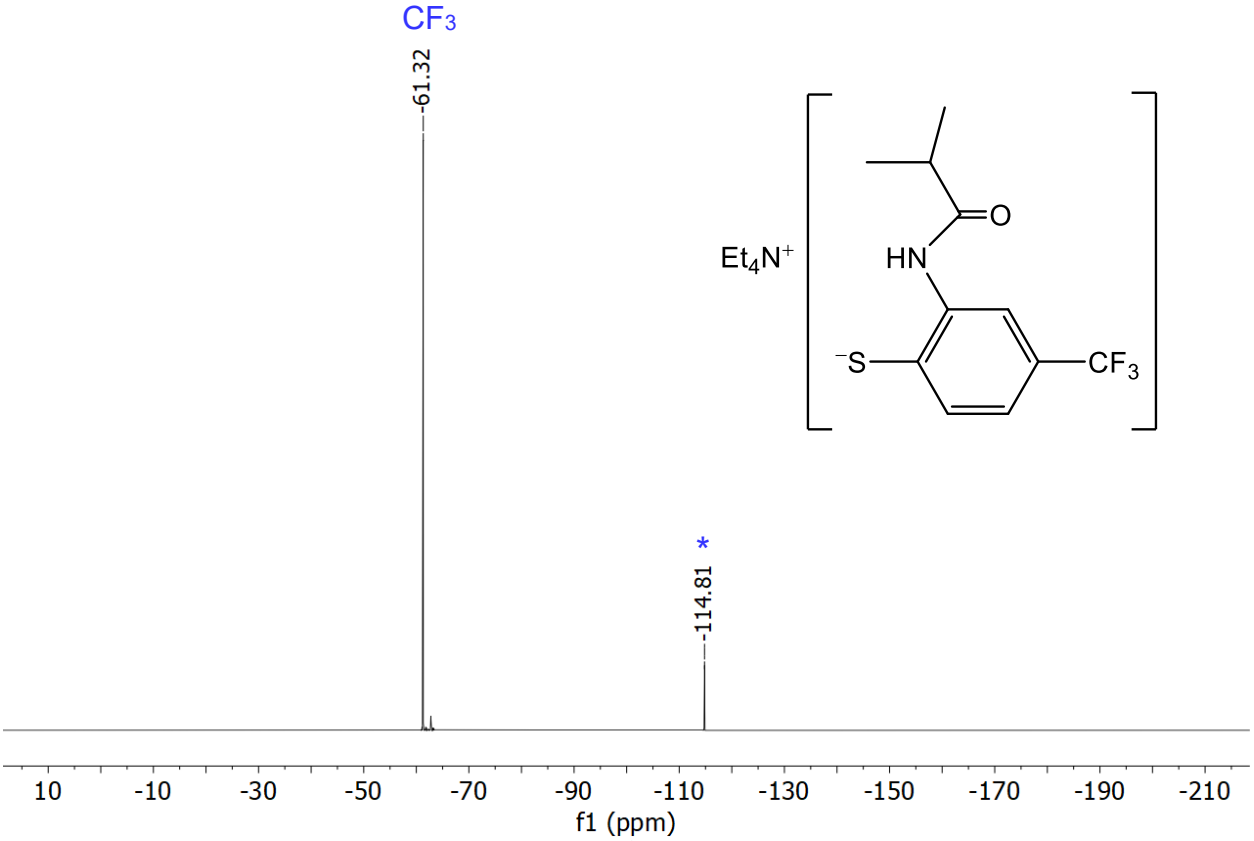

Figure S3.13. ^{19}F NMR spectrum of (Et_4N)(S-*o*-^{i}PrCONH-*p*-CF_3-Ph) in CD_3CN at RT. The peak at -114.81 ppm is from PhF as an internal standard and is indicated with *.

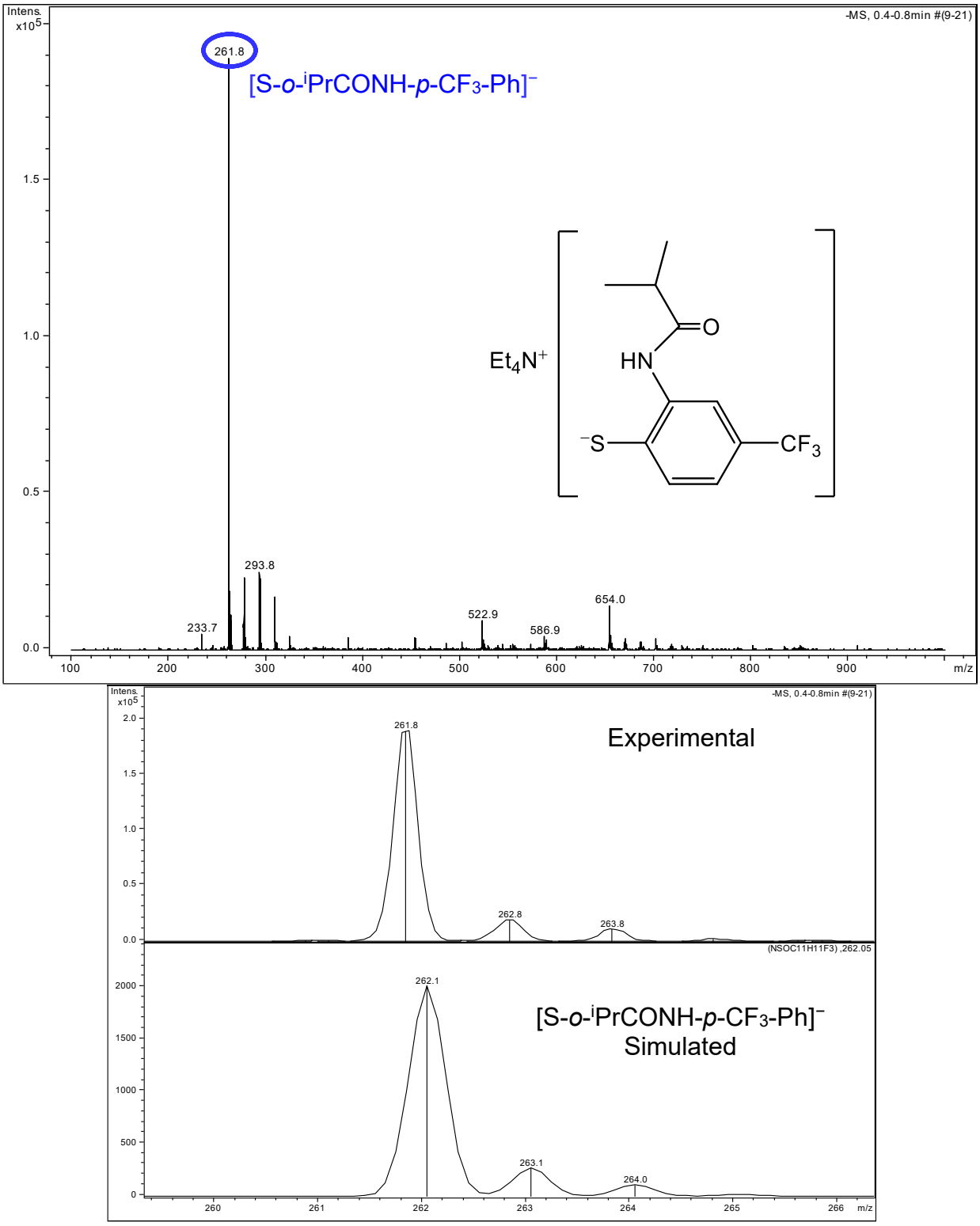

Figure S3.14. *Top:* Low-resolution ESI-MS(-) (negative mode) of (Et_4N)(S-*o*-^{i}PrCONH-*p*-CF_3-Ph) in MeCN. *Bottom*: experimental and simulated theoretical isotopic distribution peak at *m/z*: 261.8 Other peaks have not been identified as reaction products.

(S-*o*-OPhCONH-*p*-CF_3-Ph)$_2$ To a dark yellow solution of (S-*o*-NH_2-*p*-CF_3-Ph)$_2$ (1.281 g, 3.332 mmol) in 20 mL of CH_2Cl_2 containing pyridine (0.665 g, 8.41 mmol) was added phenoxyacetyl chloride (1.204 g, 7.058 mmol) under an N_2(g) stream to maintain anhydrous conditions. The solution took on a lighter color and an off-white precipitate appeared within ~5 min. An additional amount of CH_2Cl_2 (~60 mL) was added until the solution became a homogeneous light-yellow color and the solution was stirred for ~3 h at RT. After this time, the solution was placed in a separatory funnel and washed with DI H_2O and K_2CO_3(aq) until the aqueous layer remained basic (pH ~9). Additional washes wish saturated $NaHCO_3$ (2×) and NaCl(aq) solutions were performed. The isolated CH_2Cl_2 layer was then dried with anhydrous $MgSO_4$, filtered, and the insoluble salt was washed with ~10 mL of CH_2Cl_2. The filtrate was then taken to dryness on a rotary evaporator to afford an off-white solid and ~30 mL of pentane was added to the solid. The mixture was stirred for 1 h and the solid was isolated by vacuum filtration on a glass-frit. The solid was washed with pentane (3 × 5 mL) and dried on a vacuum line to afford the product as an off-white solid (1.857 g, 2.845 mmol, 85%). FTIR (KBr matrix), ν_{max} (cm^{-1}): 3328 (w, NH), 1705 (s, CO), 1331 (s, CF), 1126 (s, CF), 1083 (s, CF). FTIR (THF, ~10 mM), ν_{max} (cm^{-1}): 3345 (m, NH), 1715 (s, CO). ^{1}H NMR (400 MHz, $CDCl_3$, δ from protio solvent): 9.54 (s, 2H), 8.80 (s, 2H), 7.42 (d, 2H, *J* = 8.0 Hz), 7.34 (t, 4H, *J* = 7.8 Hz), 7.17 (d, 2H, *J* = 8.0 Hz), 7.08 (t, 2H, *J* = 7.2 Hz), 6.94 (d, 2H, *J* = 8.1 Hz), 4.49 (s, 4H). ^{13}C{^{1}H} NMR (100 MHz, $CDCl_3$, δ from solvent signal): 166.4 (s), 156.7 (s), 139.5 (s), 136.7 (s), 134.2 (q, *J* = 273.1 Hz), ^{19}F NMR (376 MHz, $CDCl_3$, δ from $CFCl_3$): -64.86 (s). LR-ESI-MS (*m/z*): [(S-*o*-OPhCONH-*p*-CF_3-Ph)$_2$ − H^+]$^-$ calcd for $C_{30}H_{22}F_6S_2N_2O_4$ (relative abundance), 651.1 (100.0), 652.1 (35.1), 653.1 (16.0), 654.1 (4.6); found, 651.0 (100.0), 651.7 (31.7), 652.8 (14.9), 653.8 (4.8). Decomposed at 173 °C.

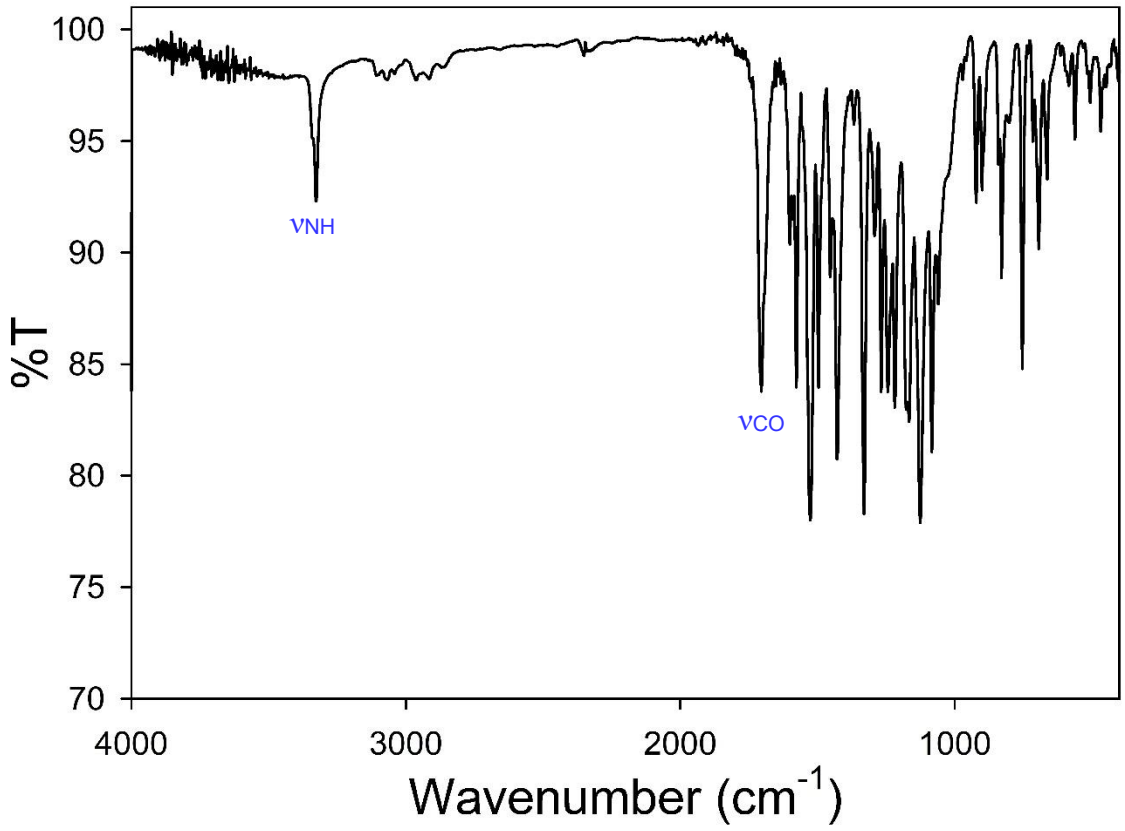

Figure S3.15. Solid-state FTIR spectrum of (S-*o*-OPhCONH-*p*-CF_3-Ph)$_2$ in a KBr matrix at RT.

^{1}H NMR (400 MHz, $CDCl_3$, RT) of **(S-*o*-OPhCONH-*p*-CF_3-Ph)$_2$**

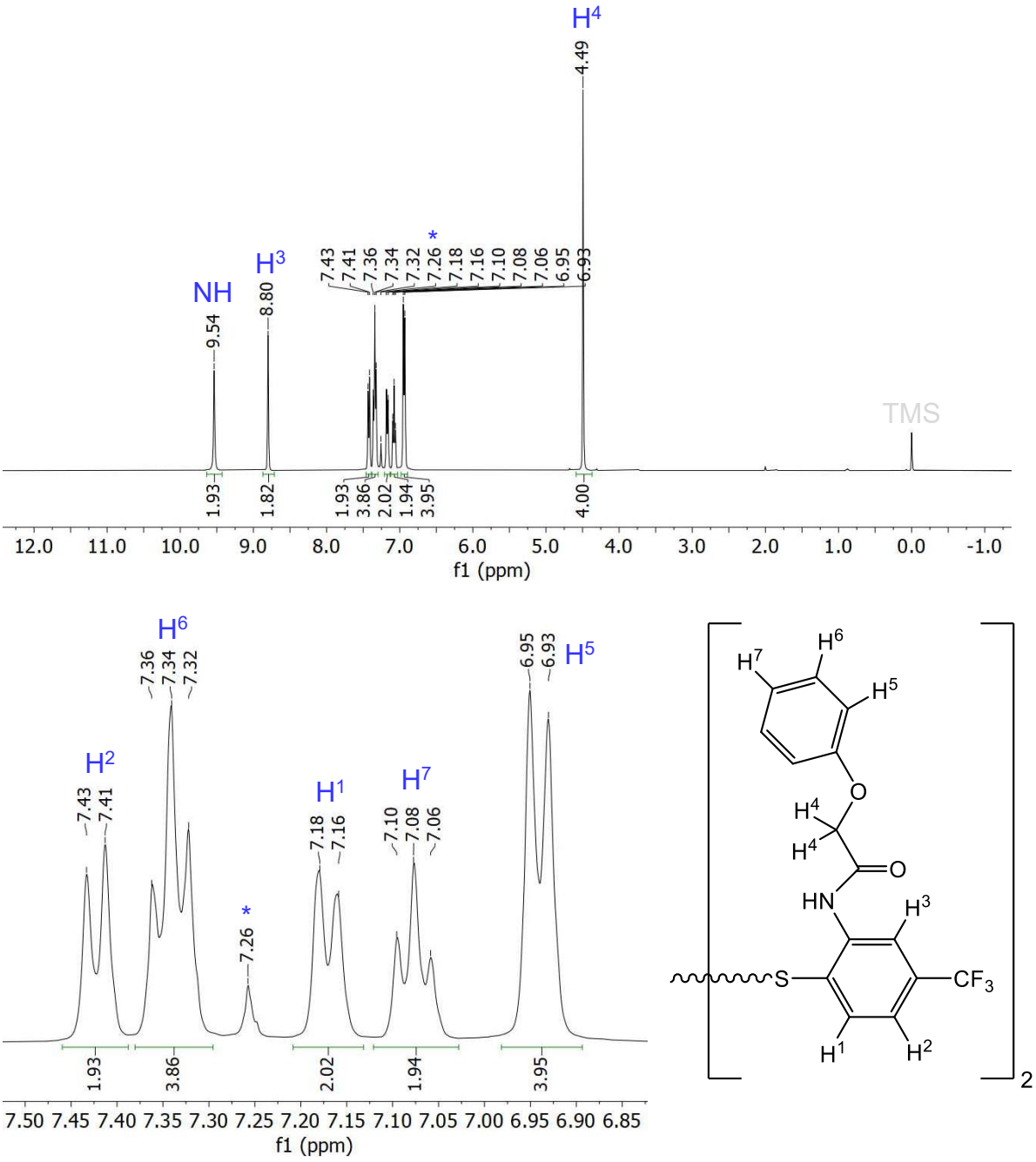

Figure S3.16. *Top:* ^{1}H NMR spectrum of (Et_4N)(S-*o*-OPhCONH-*p*-CF_3-Ph) in CD_3CN at RT (δ vs. protio signal). *Bottom:* expansion of 6 - 8 ppm region. Residual $CHCl_3$ is observed at 7.26 ppm and is indicated with *.

^{13}C NMR (100 MHz, $CDCl_3$, RT) of **(S-*o*-OPhCONH-*p*-CF_3-Ph)$_2$**

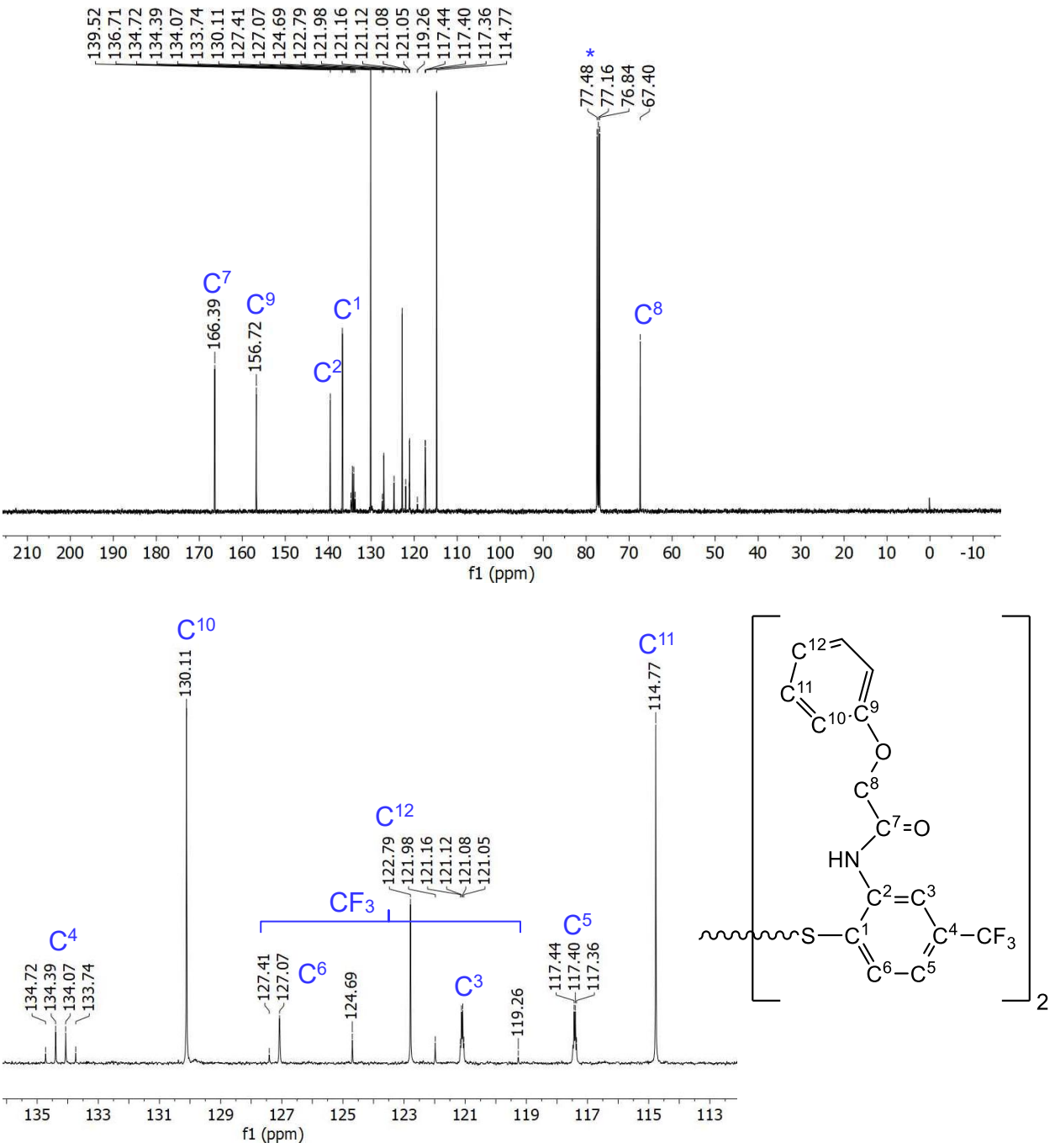

Figure S3.17. *Top:* ^{13}C NMR spectrum of (Et_4N)(S-*o*-OPhCONH-*p*-CF_3-Ph) in CD_3CN at RT (δ vs. protio signal). *Bottom:* expansion of 109 - 144 ppm region. Residual CH_3CN is indicated with *.

^{19}F NMR (376 MHz, $CDCl_3$, RT) of **(S-*o*-OPhCONH-*p*-CF_3-Ph)$_2$**

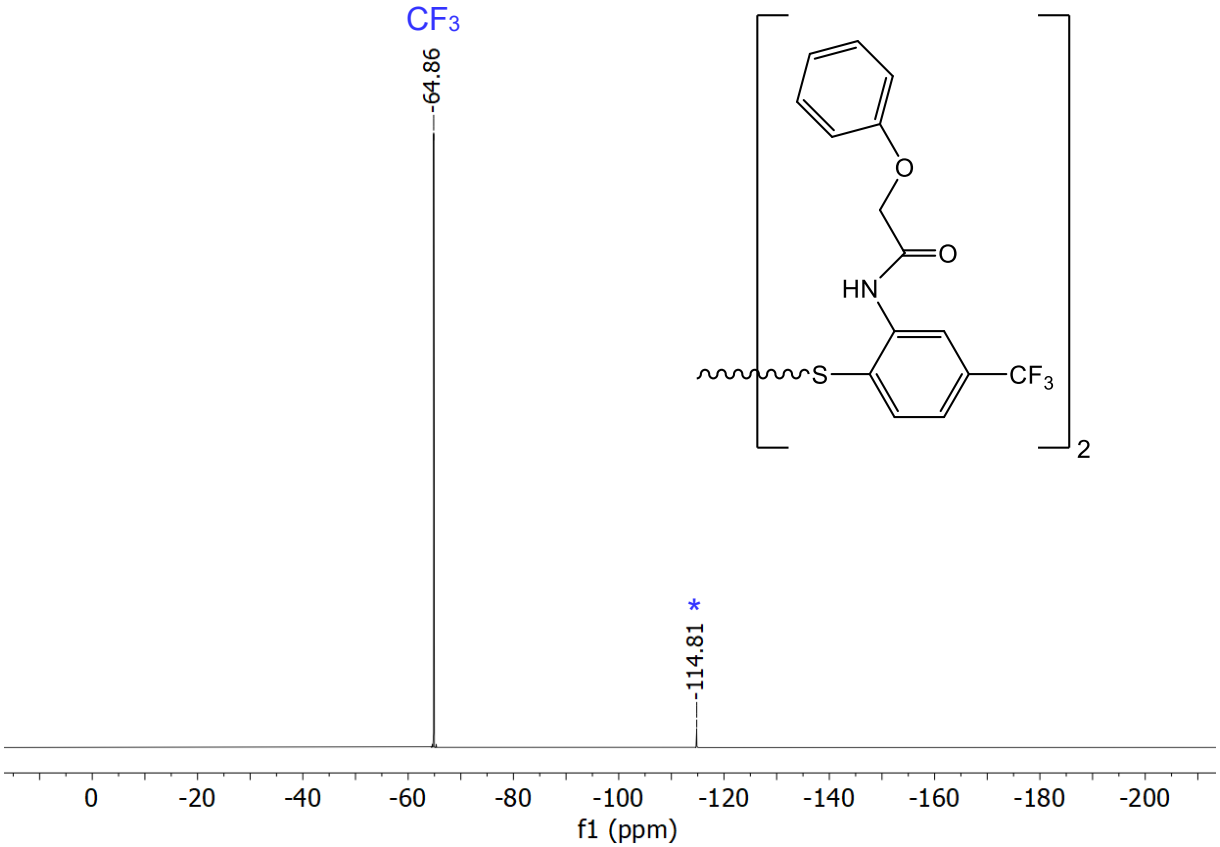

Figure S3.18. ^{19}F NMR spectrum of (S-*o*-OPhCONH-*p*-CF_3-Ph)$_2$ in $CDCl_3$ at RT. The peak at -114.81 ppm is from PhF as an internal standard and is indicated with *.

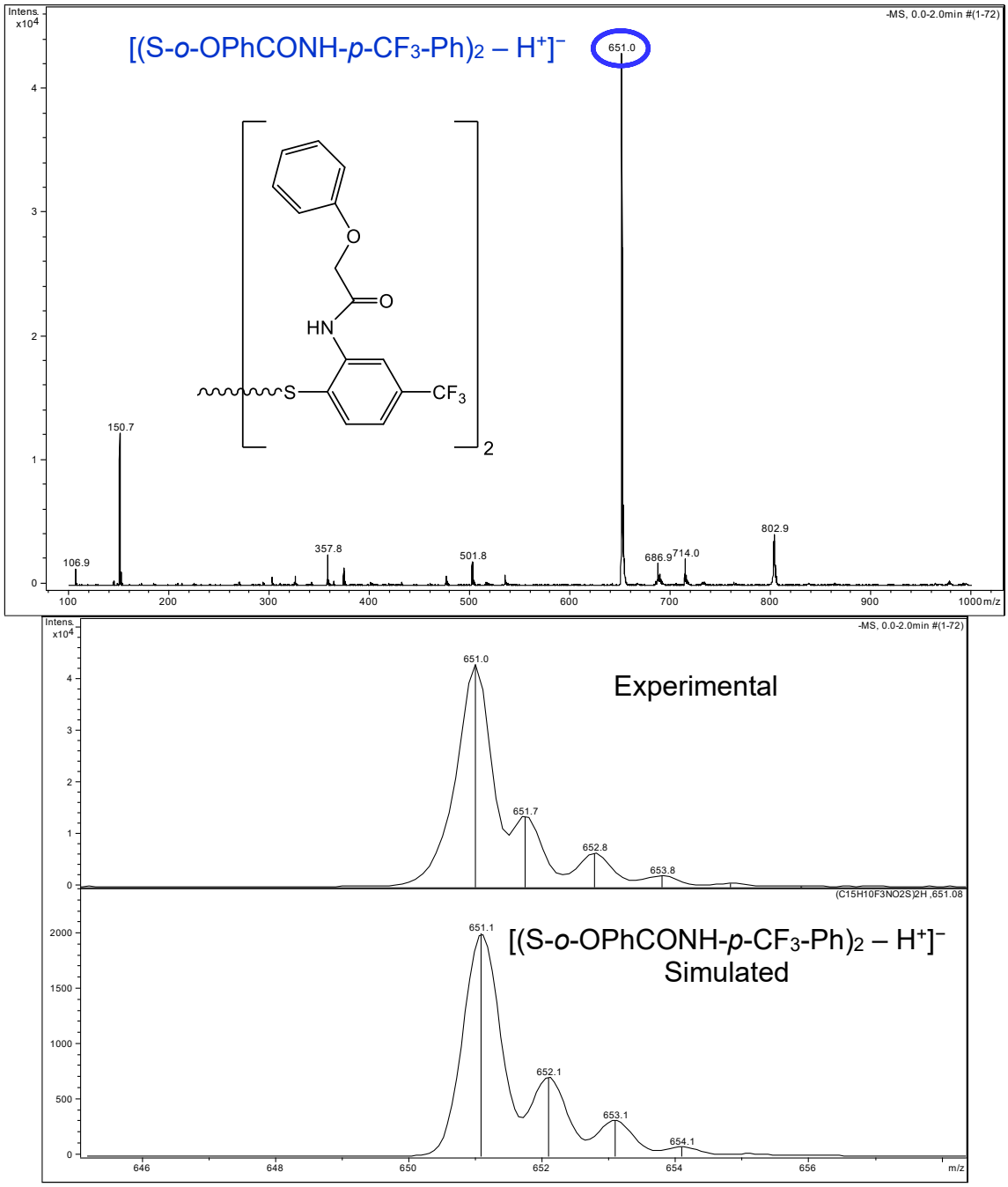

Figure S3.19. *Top:* Low-resolution ESI-MS(-) (negative mode) of (S-*o*-OPhCONH-*p*-CF_3-Ph)$_2$ in MeCN/THF (1:1; v/v). *Bottom*: experimental and simulated theoretical isotopic distribution peak at *m/z*: 651.1 Other peaks not labeled have not been identified as reaction products

(Et_4N)(S-*o*-OPhCONH-*p*-CF_3-Ph). To a yellow homogeneous solution of (S-*o*-OPhCONH-*p*-CF_3-Ph)$_2$ (0.107 g, 0.164 mmol) in ~2 mL of MeOH/THF (1:1; v/v), was added a ~2 mL MeOH solution containing $NaBH_4$ (0.019 g, 0.50 mmol). Gas evolution was observed upon initial addition of $NaBH_4$ that resulted in a solution that was dark-yellow in color. After 1 h of stirring at RT, the solution was taken to dryness with a short-path vacuum distillation apparatus and a ~2 mL MeCN solution containing Et_4NCl (0.054 g, 0.33 mmol) was added that resulted in a white precipitate. After stirring the mixture for ~30 min, the solution was filtered over a Celite packed frit and the yellow filtrate was taken to dryness. To the filtrate was added ~3 mL of THF resulting in a bright yellow-colored solution with a white solid suspended in solution. After the solution was stirred for 30 min, it was filtered over a Celite packed frit and rinsed with an additional ~3 mL of THF. The bright-yellow THF filtrate was taken to dryness in vacuo and the residue was stirred for 1 h with ~3 mL of Et_2O. After this time, the insoluble was isolated by vacuum filtration on a glass-frit, washed with Et_2O (3 × 3 mL), and dried on a vacuum line to afford the product as a yellow solid (0.126 g, 0.276 mmol, 84%). FTIR (KBr matrix), ν_{max} (cm^{-1}): 3101 (w, NH), 1676 (s, CO), 1319 (s, CF), 1090 (s, CF), 1068 (s, CF). ^1H NMR (400 MHz, CD_3CN, δ from protio solvent): 11.33 (s, 1H), 8.43 (s, 1H), 7.40 (d, 2H, *J* = 8.2 Hz), 7.32 (t, 2H, *J* = 8.0 Hz), 7.08 (d, 2H, *J* = 8.1 Hz), 6.99 (t, 1H, *J* = 7.4 Hz), 6.82 (d, 1H, *J* = 7.6 Hz), 4.61 (s, 2H), 3.08 (q, 9H, *J* = 7.3 Hz), 1.13 (t, 13H, *J* = 7.3 Hz). $^{13}C\{^1H\}$ NMR (100 MHz, $CDCl_3$, δ from solvent signal): 167.3 (s), 159.0 (s), 155.9 (s), 139.0 (s), 133.8 (s), 130.6 (s), 126.9 (q, *J* = 255.4 Hz), ^{19}F NMR (376 MHz, $CDCl_3$, δ from $CFCl_3$): -61.15 (s). LR-ESI-MS (*m/z*): $[M\text{-}Et_4N]^-$ calcd for $SC_{15}H_{11}F_3O_2N$ (relative abundance), 326.0 (100.0), 327.0 (17.4), 328.0 (4.7); found, 325.8 (100.0), 326.8 (17.8), 324.8 (6.6). Mp 47 – 49 °C.

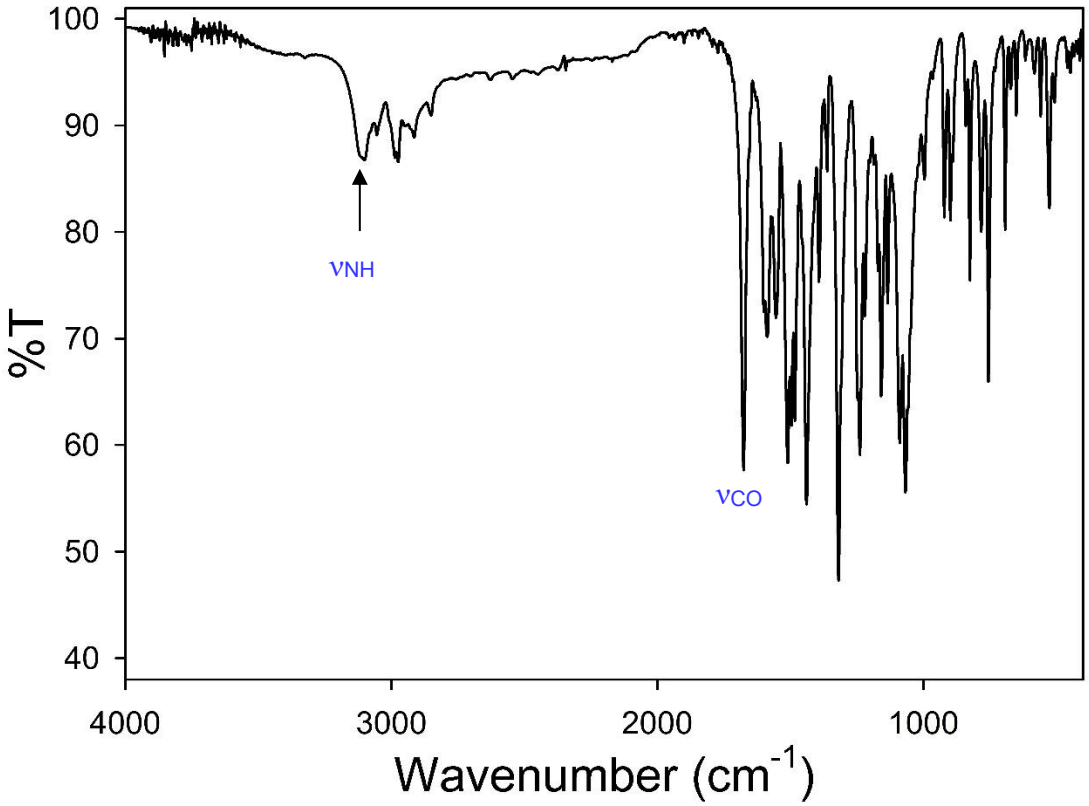

Figure S3.20. Solid-state FTIR spectrum of (Et_4N)(S-*o*-OPhCONH-*p*-CF_3-Ph) in a KBr matrix at RT.

^{1}H NMR (400 MHz, CD_3CN, RT) of **(Et_4N)(S-*o*-OPhCONH-*p*-CF_3-Ph)**

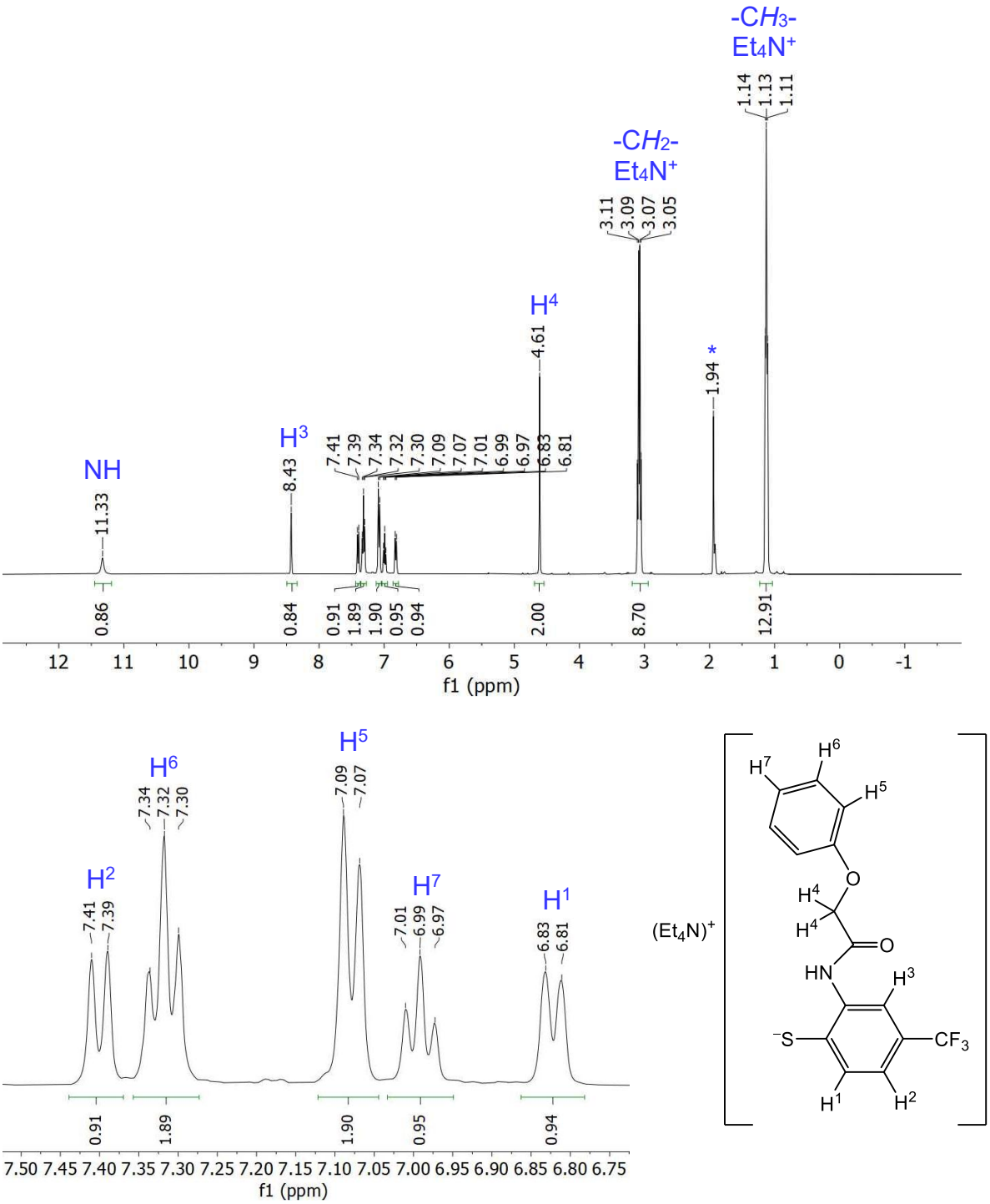

Figure S3.21. *Top:* ^{1}H NMR spectrum of (Et_4N)(S-*o*-OPhCONH-*p*-CF_3-Ph) in CD_3CN at RT (δ vs. protio signal). *Bottom:* expansion of 6 - 8 ppm region. Residual CH_3CN is observed at 1.94 ppm and is indicated with *.

^{13}C NMR (100 MHz, CD_3CN, RT) of **(Et_4N)(S-*o*-OPhCONH-*p*-CF_3-Ph)**

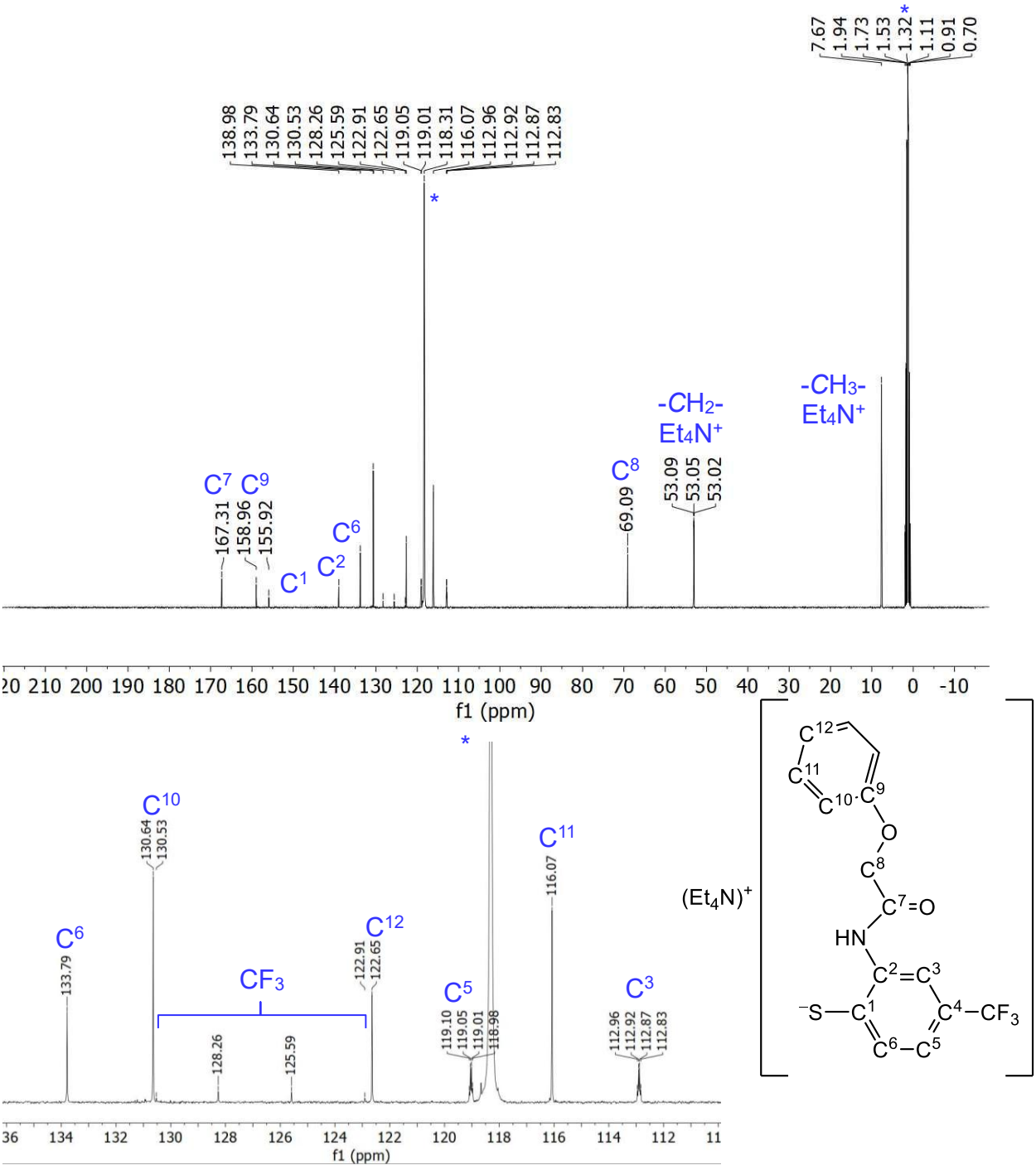

Figure S3.22. *Top:* ^{13}C NMR spectrum of (Et_4N)(S-*o*-OPhCONH-*p*-CF_3-Ph) in CD_3CN at RT (δ vs. protio signal). *Bottom:* expansion of 112 - 132 ppm region. Residual CH_3CN is observed at is indicated with *.

^{19}F NMR (376 MHz, CD_3CN, RT) of **(Et_4N)(S-*o*-OPhCONH-*p*-CF_3-Ph)**

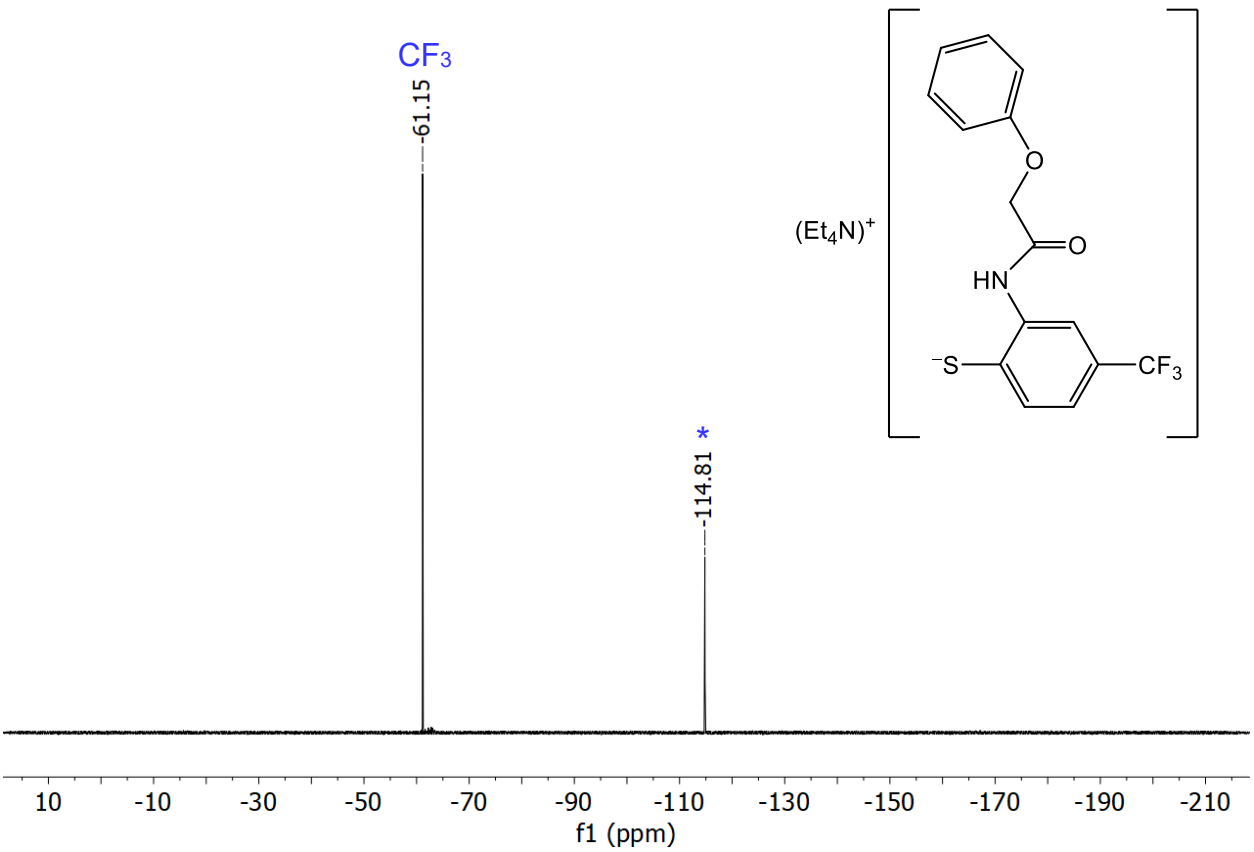

Figure S3.23. ^{19}F NMR spectrum of (Et_4N)(S-*o*-OPhCONH-*p*-CF_3-Ph) in CD_3CN at RT. The peak at -114.81 ppm is from PhF as an internal standard and is indicated with *.

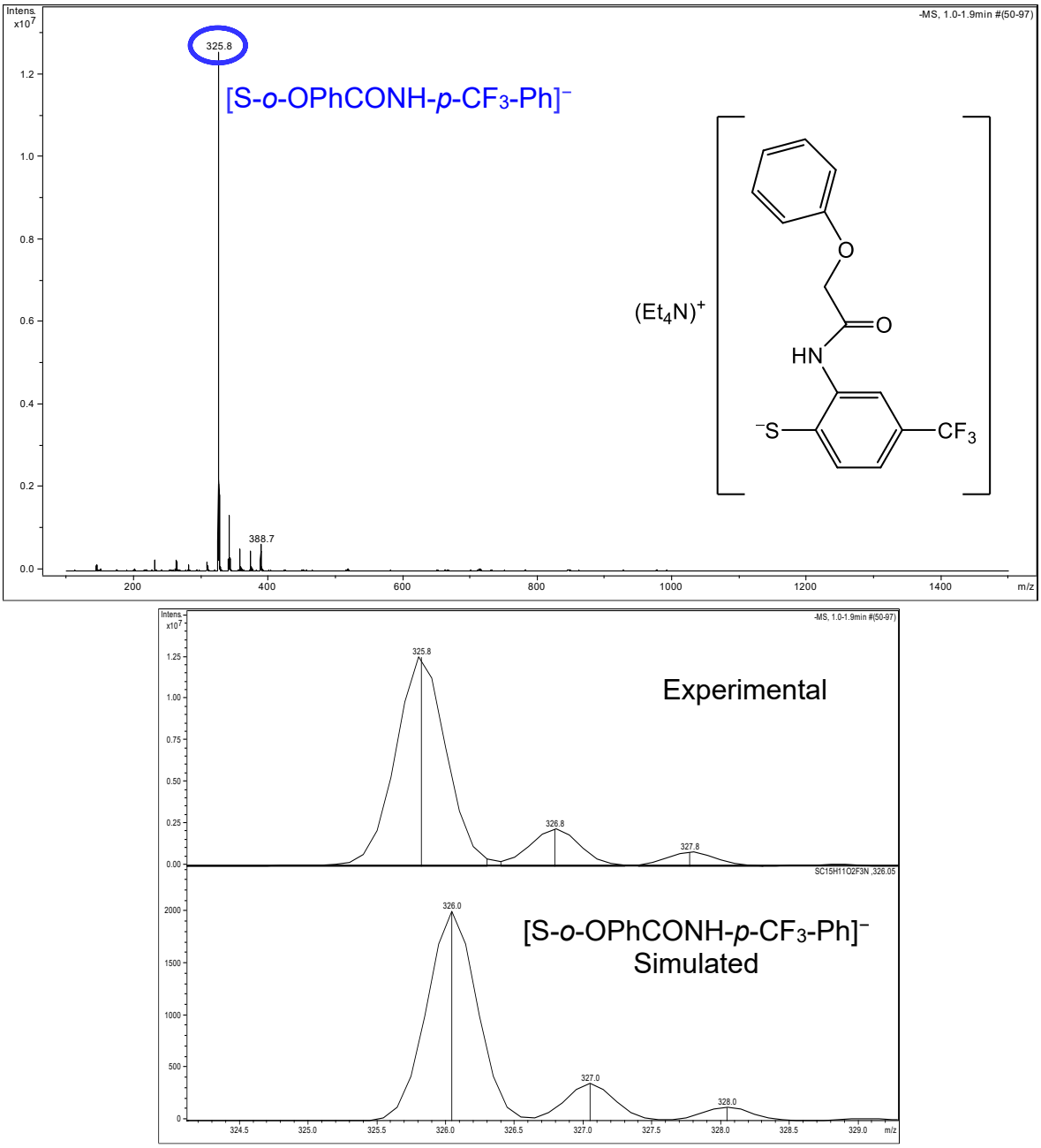

Figure S3.24. *Top:* Low-resolution ESI-MS(-) (negative mode) of (Et_4N)(S-*o*-OPhCONH-*p*-CF_3-Ph) in MeCN. *Bottom*: experimental and simulated theoretical isotopic distribution peak at *m/z*: 325.8 Other peaks have not been identified as reaction products.

$(Et_4N)_2[Ni(S\text{-}o\text{-}^{i}PrCONH\text{-}p\text{-}CF_3\text{-}Ph)_4]$ (1) To a yellow homogenous solution of $(Et_4N)(S\text{-}o\text{-}^{i}PrCONH\text{-}p\text{-}CF_3\text{-}Ph)$ (0.400 g, 1.02 mmol) in 2 mL of MeCN. To this, a blue slurry of $(Et_4N)_2[NiCl_4]$ (0.105 g, 0.227 mmol) in 4 mL of MeCN was added dropwise. Upon addition the solution immediately took on a red solution, becoming dark-red once all Ni salt was added with no change after 1 h of stirring. All MeCN was removed, after 1 h of stirring, affording a dark red/brown sticky solid. To this 3 mL of THF was added and stirred for 30 min taking on a dark reddish-brown color with white solid suspended in solution. The solution was filtered over a Celite packed frit and rinsed with an additional 2 mL of THF leaving behind a white precipitate. The reddish-brown filtrate was taken to dryness, leaving behind a sticky dark-red, almost black, solid. To this 7-8 mL of pentane was added and stirred for 3 hrs, leaving a black solid suspended in solution. The species was isolated, washed with 2 mL of pentane, and dried on a high vacuum line to afford green solid (0.270 g, 0.197 mmol, 86.9%). FTIR (KBr matrix), ν_{max} (cm^{-1}): 3269 (NH, w), 1675 (CO, m), 1327 (s, CF), 1107 (s, CF), 1078 (s, CF). FTIR (THF, ~10 mM), ν_{max} (cm^{-1}): 3252 (m, NH), 1684 (s, CO). ^1H NMR (400 MHz, CD_3CN, δ from residual protio solvent): 26.39 (s, 2H), 20.17 (s, 2H), 8.21 (s, H), 6.80 (s, H), 3.40 (s, 2H), 3.10 (q, 16H, J = 7.2 Hz), 1.29 (s, 10H), 1.15 (m, 38H), -12.28 (s, 2H). ^{19}F NMR (376 MHz, CD_3CN, δ from $CFCl_3$): -8.32 (s), -61.10 (s), -62.72 (s), -62.84 (s). UV-vis (MeCN, 25 °C. 50 mol-equiv. of $Et_4N(S\text{-}p\text{-}CF_3\text{-}o\text{-}NHC(O)^{i}Pr\text{-}Ph)$), λ_{max}, nm (ε, M^{-1} cm^{-1}): 480 (4100), 690 (570), 770 (460). Solution phase μ_{eff} = 1.86 BM and 2.32 BM (with 20 mol-equiv. of thiolate) at 25 °C from Evan's method in CD_3CN. LR-ESI-MS (*m/z*): $[M - (S\text{-}o\text{-}^{i}PrCONH\text{-}p\text{-}CF_3\text{-}Ph)]^-$ calcd for $C_{33}H_{33}F_9S_3N_3O_3Ni$ (relative abundance), 844.1 (100.0), 845.1 (39.7), 846.1 (60.4), 847.1 (23.4), 848.1 (16.3), 849.1 (5.4), 850.1 (3.4); found, 844.1 (100.0), 844.9 (80.3), 845.8 (55.9), 846.8 (21.7), 847.7 (9.4), 848.8 (3.1), 849.9 (8.8). $[M + Et_4N^+]^-$ calcd for $C_{52}H_{64}F_{12}S_4N_5O_4Ni$ (relative abundance); 1236.3 (100.0),

1237.3 (62.2), 1238.3 (76.4), 1239.3 (41.0), 1240.3 (26.5), 1241.3 (11.5), 1243.2 (2.5), 1244.3 (1.0), found, 1236.0 (100.0), 1237.0 (67.3), 1238.0 (72.7), 1238.9 (41.8), 1239.9 (41.8), 1241.0 (14.5). Anal. Calcd for $C_{64}H_{94}F_{12}N_{6.5}NiO_4S_4$: C, 53.63; H, 6.61; N, 6.35. Found: C, 53.70; H, 6.83; N, 6.49.

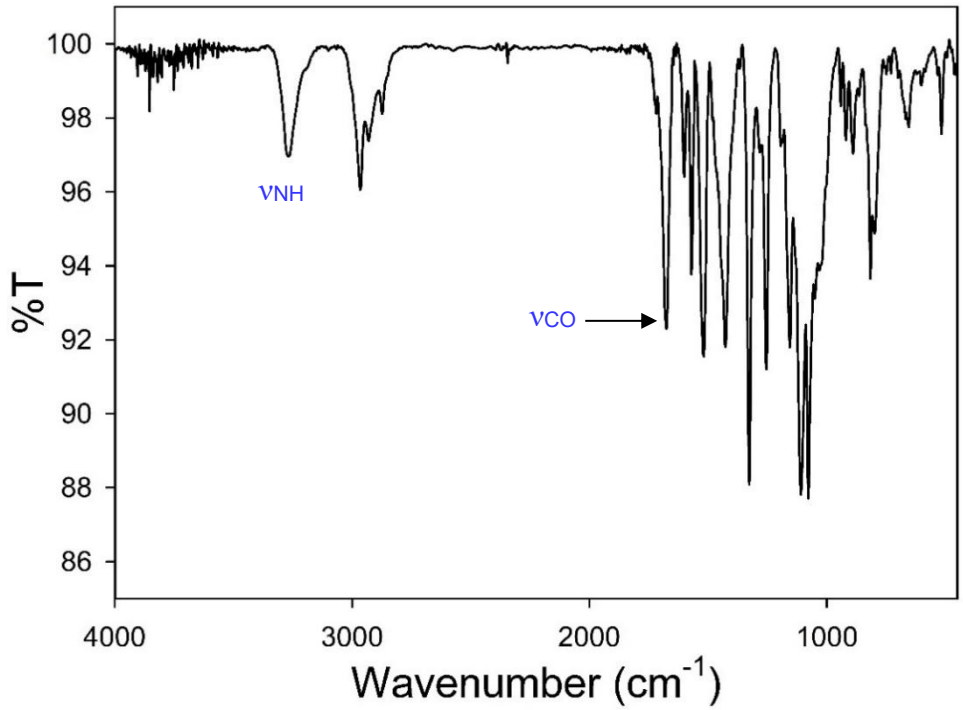

Figure S3.25. Solid-state FTIR spectrum of $(Et_4N)_2[Ni(S\text{-}o\text{-}^{i}PrCONH\text{-}p\text{-}CF_3\text{-}Ph)_4]$ (**1**) in a KBr matrix at RT.

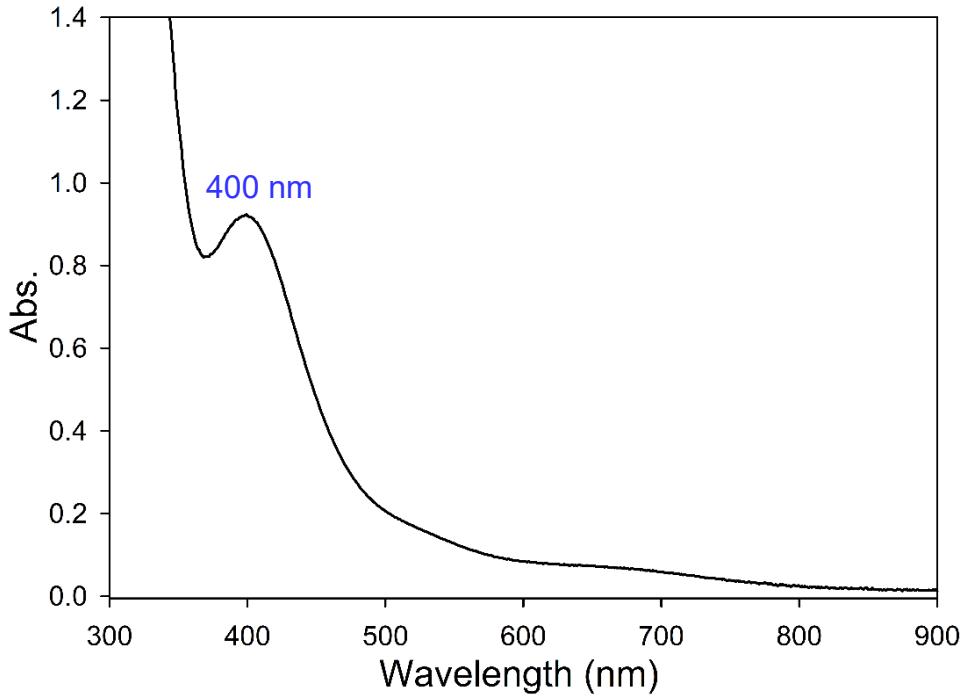

Figure S3.26. UV-vis spectrum of $(Et_4N)_2[Ni(S\text{-}o\text{-}^{i}PrCONH\text{-}p\text{-}CF_3\text{-}Ph)_4]$ (**1**) in MeCN at 25 ˚C.

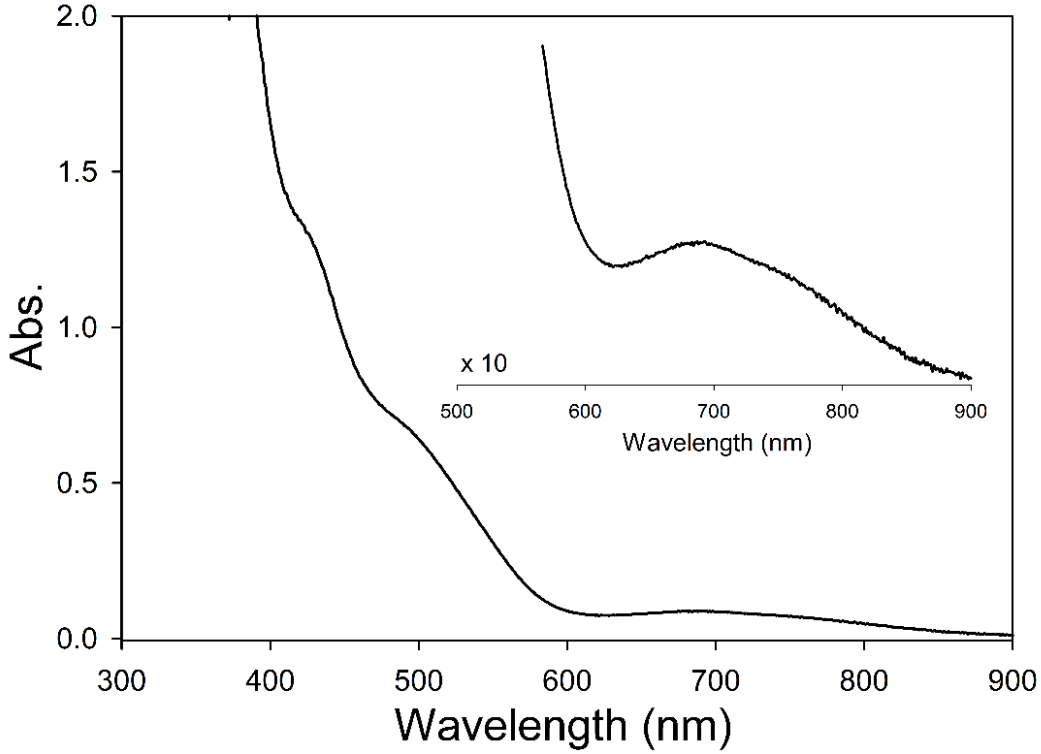

Figure S3.27. UV-vis spectrum of $(Et_4N)_2[Ni(S\text{-}o\text{-}^{i}PrCONH\text{-}p\text{-}CF_3\text{-}Ph)_4]$ (**1**) with 50 mol-equivalent of $(Et_4N)(S\text{-}o\text{-}^{i}PrCONH\text{-}p\text{-}CF_3\text{-}Ph)$ in MeCN at 25 ˚C.

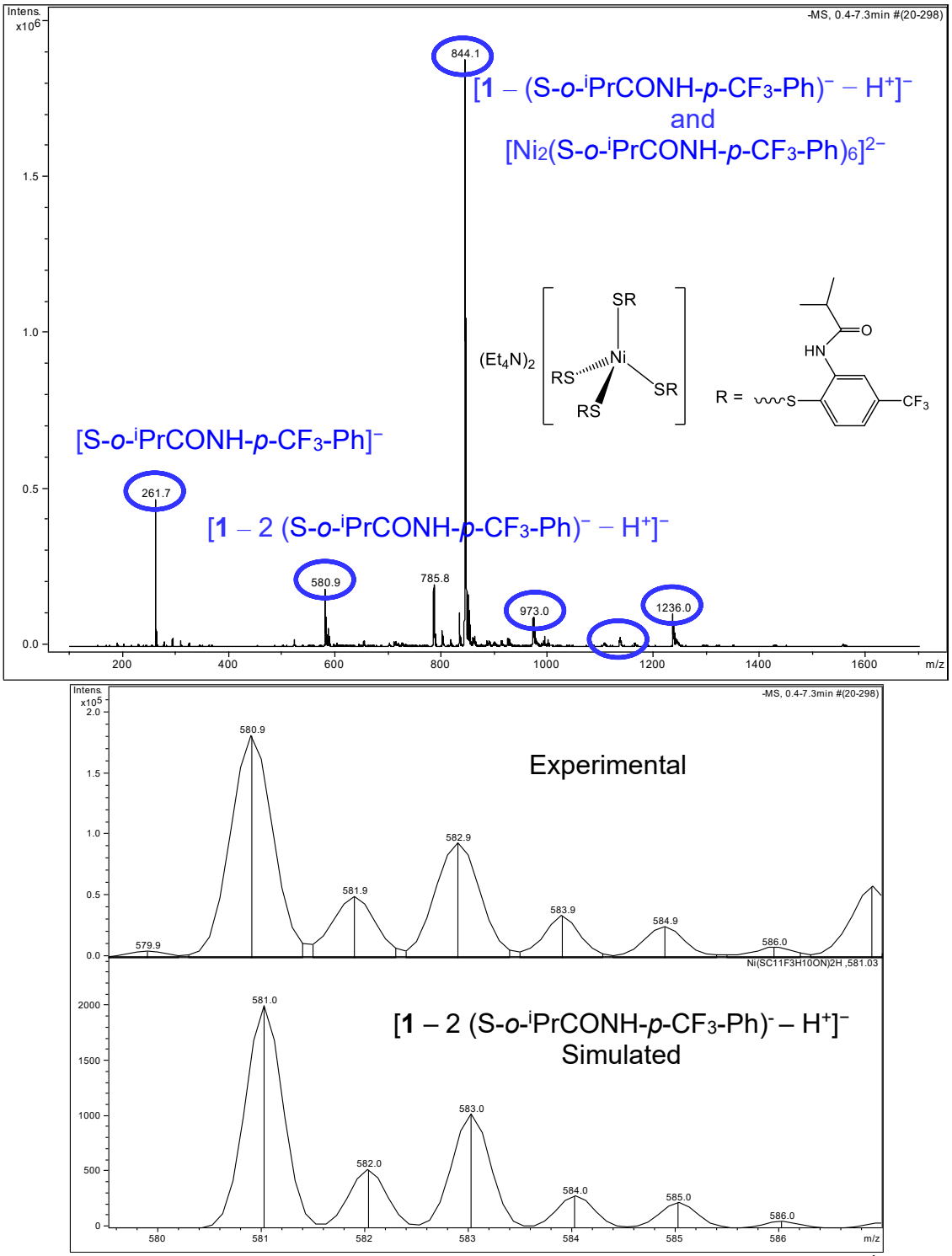

Figure S3.28. *Top:* Low-resolution ESI-MS(-) (negative mode) of $(Et_4N)_2$[Ni(S-*o*-^{i}PrCONH-*p*-CF_3-Ph)$_4$] (**1**) in MeCN. *Bottom*: experimental and simulated theoretical isotopic distribution peak at *m/z*: 580.9.

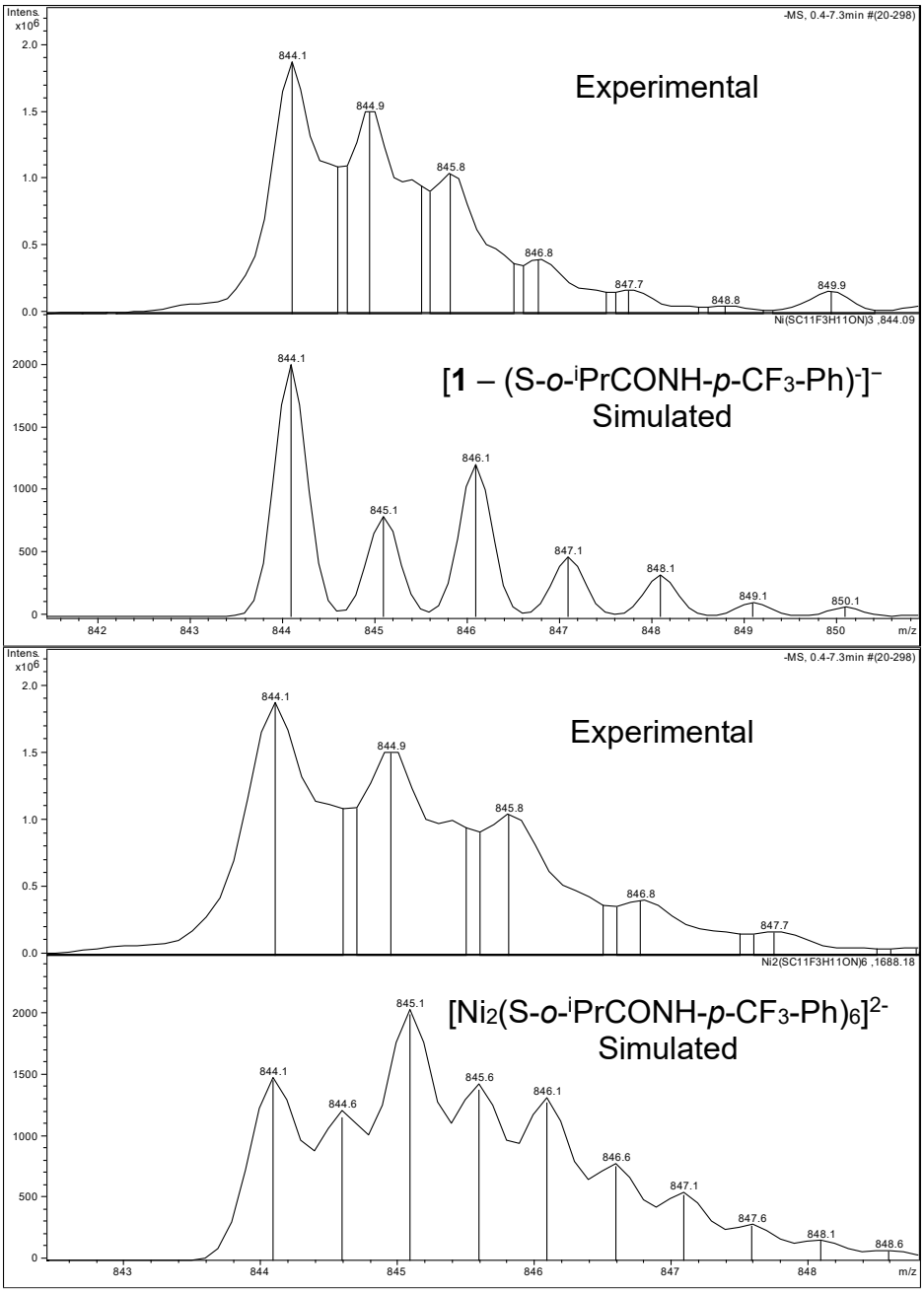

Figure S3.29. Experimental and simulated theoretical isotopic distribution of (*top*) [Ni(S-*o*-^{i}PrCONH-*p*-CF_3-Ph)$_3$]$^-$ and (*bottom*) [Ni_2(S-*o*-^{i}PrCONH-*p*-CF_3-Ph)$_6$]$^{2-}$ for peak at *m/z*: 844.1 corresponding to ESI-MS(-) of $(Et_4N)_2$[Ni(S-*o*-^{i}PrCONH-*p*-CF_3-Ph)$_4$] (**1**) in MeCN shown in Figure S3.28.

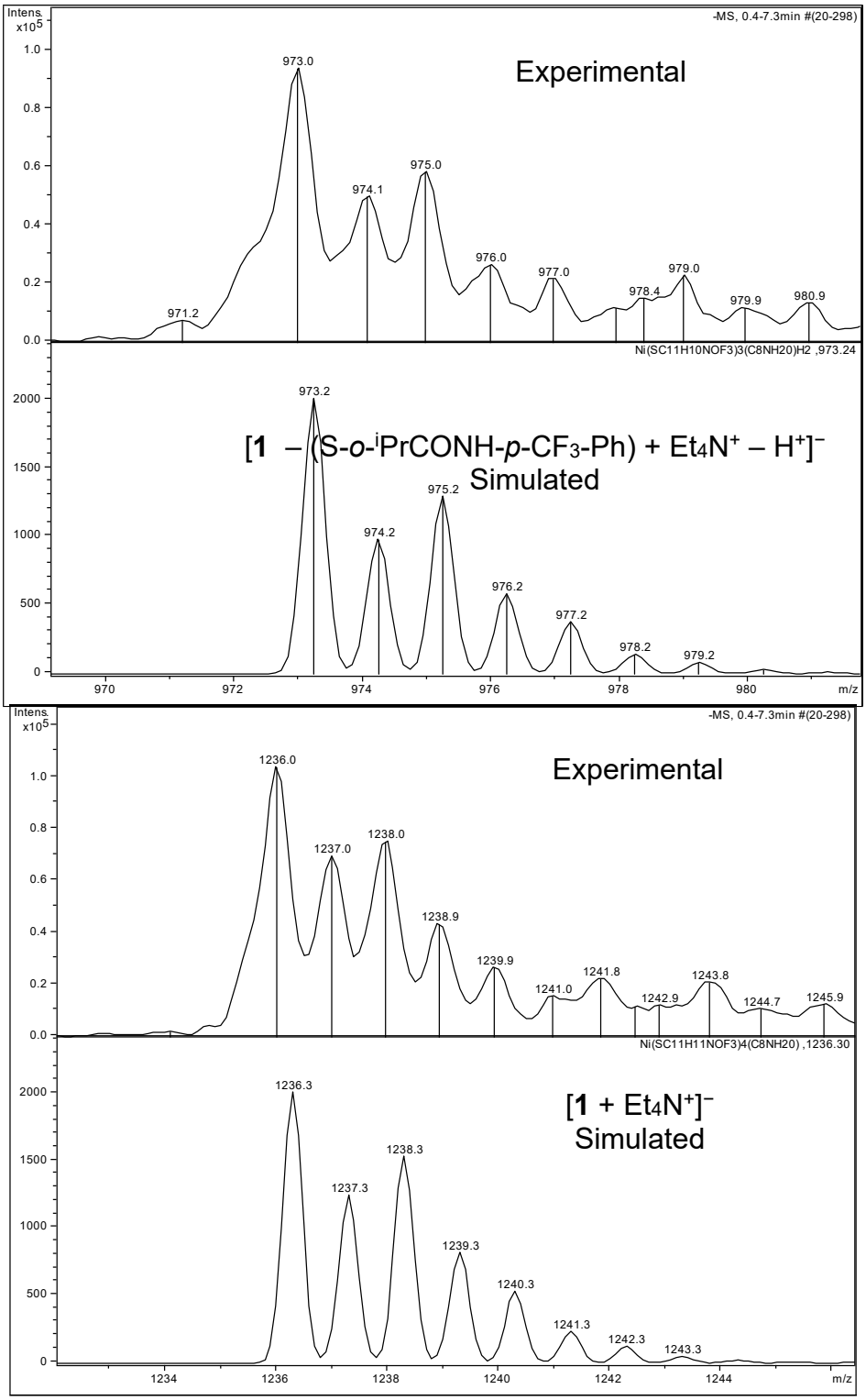

Figure S3.30. Experimental and simulated theoretical isotopic distribution of (*top*) [Ni(S-*o*-^{i}PrCONH-*p*-CF_3-Ph)$_3$ + Et_4N – H^+]$^-$ for peak at *m/z*: 973.0 and (*bottom*) [Ni(S-*o*-^{i}PrCONH-*p*-CF_3-Ph)$_3$ + 2.0 Et_4N]$^-$ for peak at *m/z*: 1236.0 corresponding to ESI-MS(-) of $(Et_4N)_2$[Ni(S-*o*-^{i}PrCONH-*p*-CF_3-Ph)$_4$] (**1**) in MeCN shown in Figure S3.28.

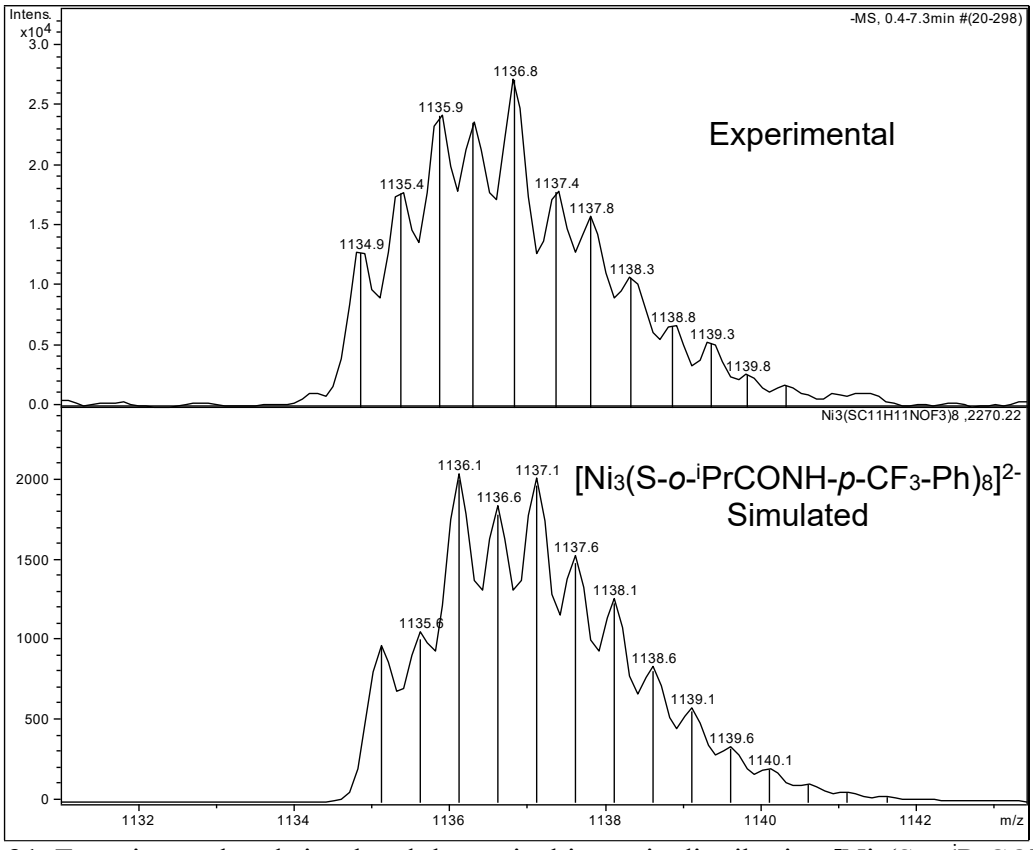

Figure S3.31. Experimental and simulated theoretical isotopic distribution $[Ni_3(S\text{-}o\text{-}^{i}PrCONH\text{-}p\text{-}CF_3\text{-}Ph)_8]^{2-}$ for peak at *m/z*: 1136.8 corresponding to ESI-MS(-) of $(Et_4N)_2[Ni(S\text{-}o\text{-}^{i}PrCONH\text{-}p\text{-}CF_3\text{-}Ph)_4]$ (**1**) in MeCN shown in Figure S3.28.

$(Et_4N)_2[Ni(S\text{-}o\text{-}OPhCONH\text{-}p\text{-}CF_3\text{-}Ph)_4]$ (2) To a yellow homogenous solution of $(Et_4N)(S\text{-}o\text{-}OPhCONH\text{-}p\text{-}CF_3\text{-}Ph)$ (0.169 g, 0.370 mmol) in ~2 mL of MeCN. To this, a blue slurry of $(Et_4N)_2[NiCl_4]$ (0.039 g, 0.084 mmol) in ~2 mL of MeCN was added dropwise. Upon addition the solution immediately took on a red solution, becoming dark-red once all Ni salt was added with no change after 1 h of stirring. All MeCN was removed, after 1 h of stirring, affording a dark red/brown sticky solid. To this ~3 mL of THF was added and stirred for 30 min taking on a dark reddish-brown color with white solid suspended in solution. The solution was filtered over a Celite packed frit and rinsed with an additional ~2 mL of THF leaving behind an off-white precipitate. The reddish-brown filtrate was taken to dryness, leaving behind a sticky dark-red, almost black,

solid. To this ~5 mL of pentane was added and stirred for 2 hr, leaving a black solid suspended in solution. The species was isolated, washed with 2 mL of pentane, and dried on a high vacuum line to afford a reddish-orange solid (0.124 g, 0.076 mmol, 90.9%). FTIR (KBr matrix), ν_{max} (cm^{-1}): 3254 (NH, w), 1686 (CO, m), 1325 (CF, vs), 1105 (s, CF), 1078 (s. CF). FTIR (THF, ~10 mM), ν_{max} (cm^{-1}): 3264 (m, ν_{NH}), 1690 (s, ν_{CO}). UV-vis (MeCN, 25 °C), λ_{max}, nm (ε, M^{-1} cm^{-1}):. ^{1}H NMR (400 MHz, CD_3CN, δ from residual protio solvent): 29.81 (s, 2H), 20.17 (s, 2H), 3.09 (q, 16H, *J* = 7.4 Hz), 1.16 (t, 25H, *J* = 8.3 Hz), -9.09 (s, 1H). ^{19}F NMR (376 MHz, CD_3CN, δ from $CFCl_3$): -10.34 (s), -62.41 (s). LR-ESI-MS (*m/z*): LR-ESI-MS (*m/z*): [M – (S-*o*-OPhCONH-*p*-CF_3-Ph)$_2$ + H^+]$^-$ calcd for $C_{30}H_{21}F_6S_2N_2O_4Ni$ (relative abundance), 709.0 (100.0), 710.0 (35.2), 711.0 (54.4), 712.0 (19.3), 713.0 (13.0), 714.0 (3.9), 715.0 (2.7); found, 709.1 (100.0), 709.9 (27.1), 710.9 (37.6), 711.8 (12.9), 712.8 (8.5), 714.0 (4.4), 715.0 (6.0). Solution phase μ_{eff} = 1.95 BM and 2.23 BM (with 10 mol-equiv of thiolate) at 25 °C from Evan's method in CD_3CN. Anal. Calcd for $C_{76}H_{84}F_{12}N_6S_4O_8Ni$: C, 56.19; H, 5.21; N, 5.71. Found: C, 53.43; H, 5.07; N, 5.02.

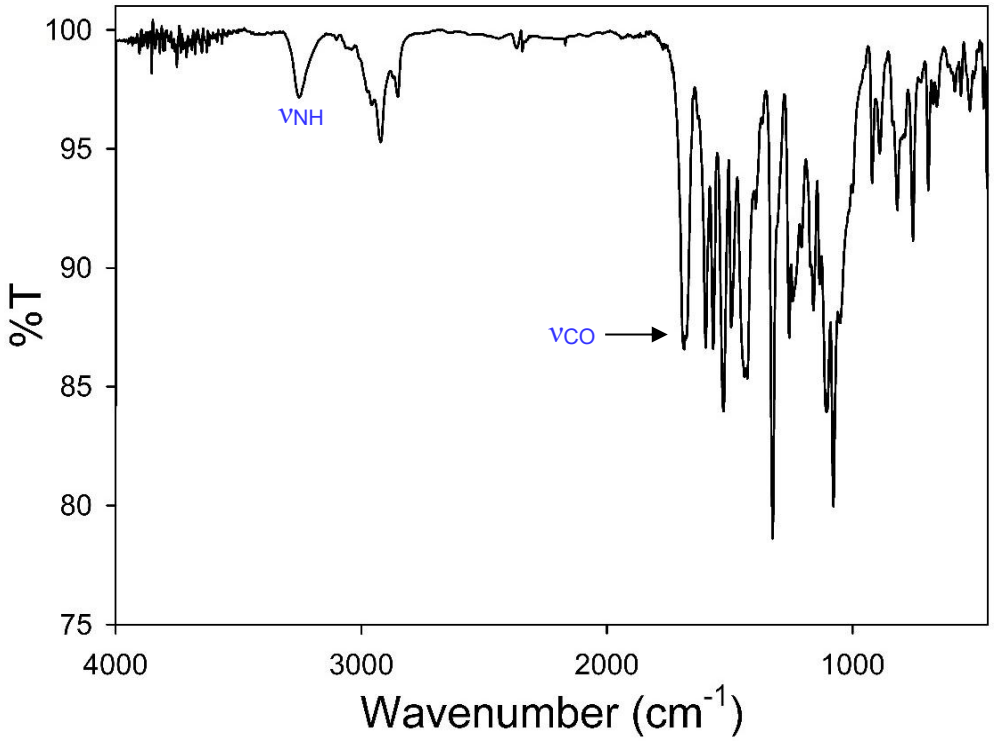

Figure S3.32. Solid-state FTIR spectrum of $(Et_4N)_2[Ni(S\text{-}o\text{-}OPhCONH\text{-}p\text{-}CF_3\text{-}Ph)_4]$ (**2**) in a KBr matrix at RT.

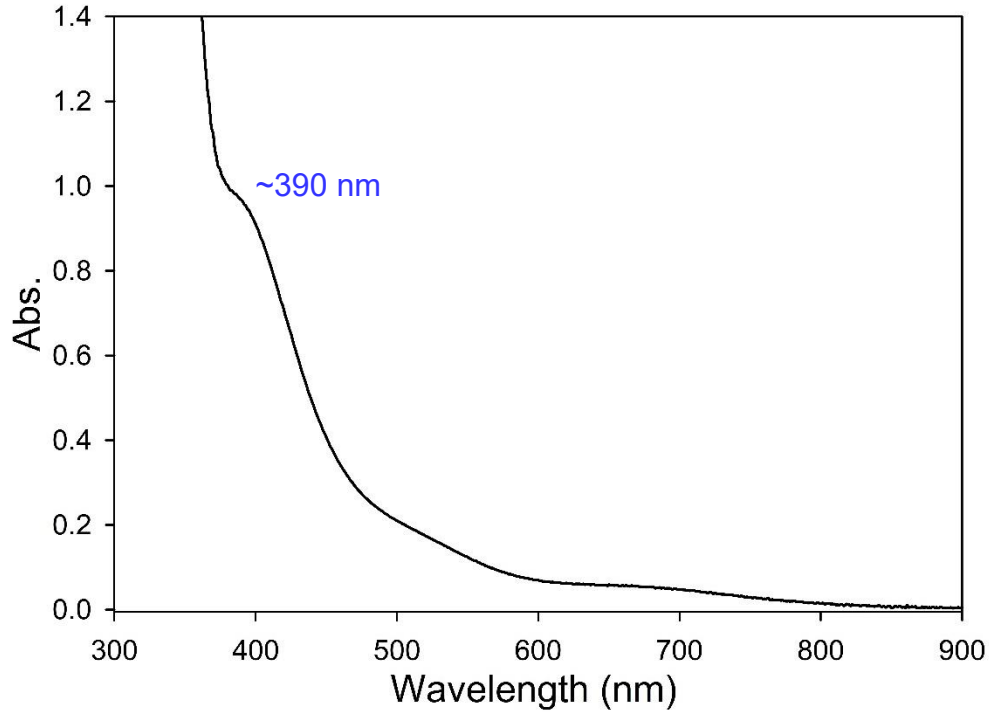

Figure S3.33. UV-vis spectrum of $(Et_4N)_2[Ni(S\text{-}o\text{-}OPhCONH\text{-}p\text{-}CF_3\text{-}Ph)_4]$ (**2**) in MeCN at 25 ˚C.

^{1}H NMR (400 MHz, CD_3CN, RT) of **$(Et_4N)_2$[Ni(S-*o*-OPhCONH-*p*-CF_3-Ph)$_4$]** (**2**)

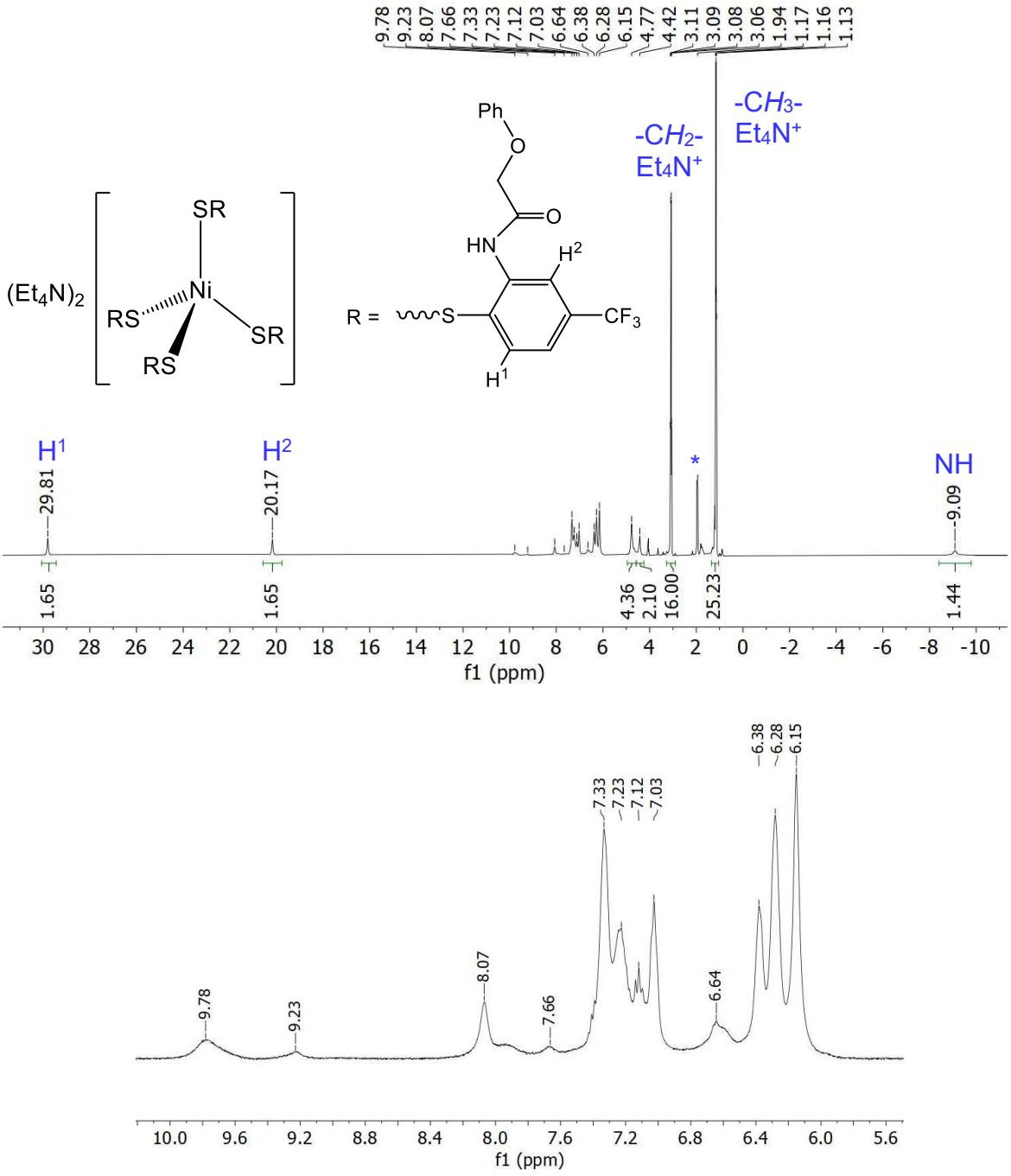

Figure S3.34. *Top:* ^{1}H NMR spectrum of $(Et_4N)_2$[Ni(S-*o*-OPhCONH-*p*-CF_3-Ph)$_4$] (**2**) in CD_3CN at RT (δ vs. protio signal). *Bottom:* expansion of 5 - 10 ppm region. Residual CH_3CN is observed at 1.94 ppm and is indicated with *.

^{19}F NMR (376 MHz, CD_3CN, RT) **$(Et_4N)_2$[Ni(S-*o*-OPhCONH-*p*-CF_3-Ph)$_4$]** (**2**)

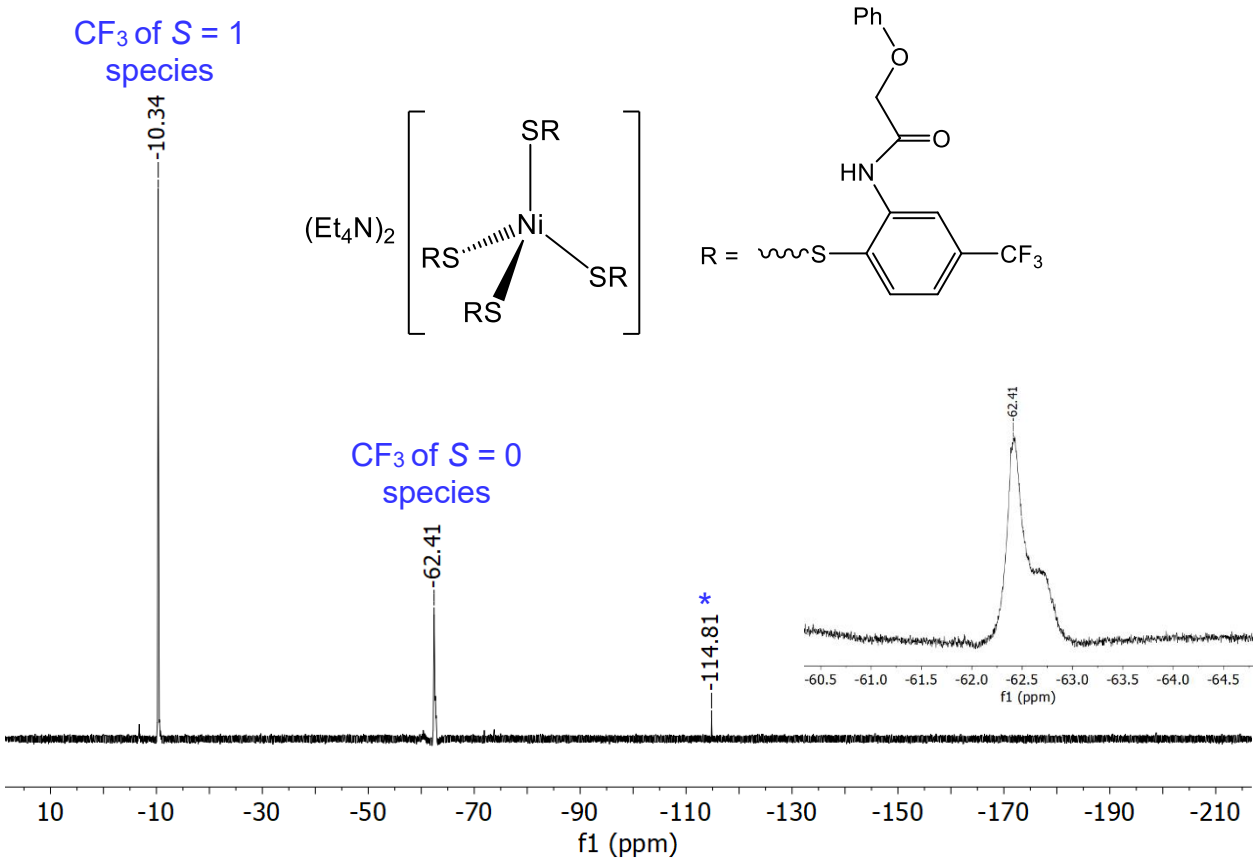

Figure S3.35. ^{19}F NMR spectrum of $(Et_4N)_2$[Ni(S-*o*-OPhCONH-*p*-CF_3-Ph)$_4$] (**2**) in CD_3CN at RT. The peak at -114.81 ppm is from PhF as an internal standard and is indicated with *. *Inset*: zoom-in of diamagnetic region of spectrum.

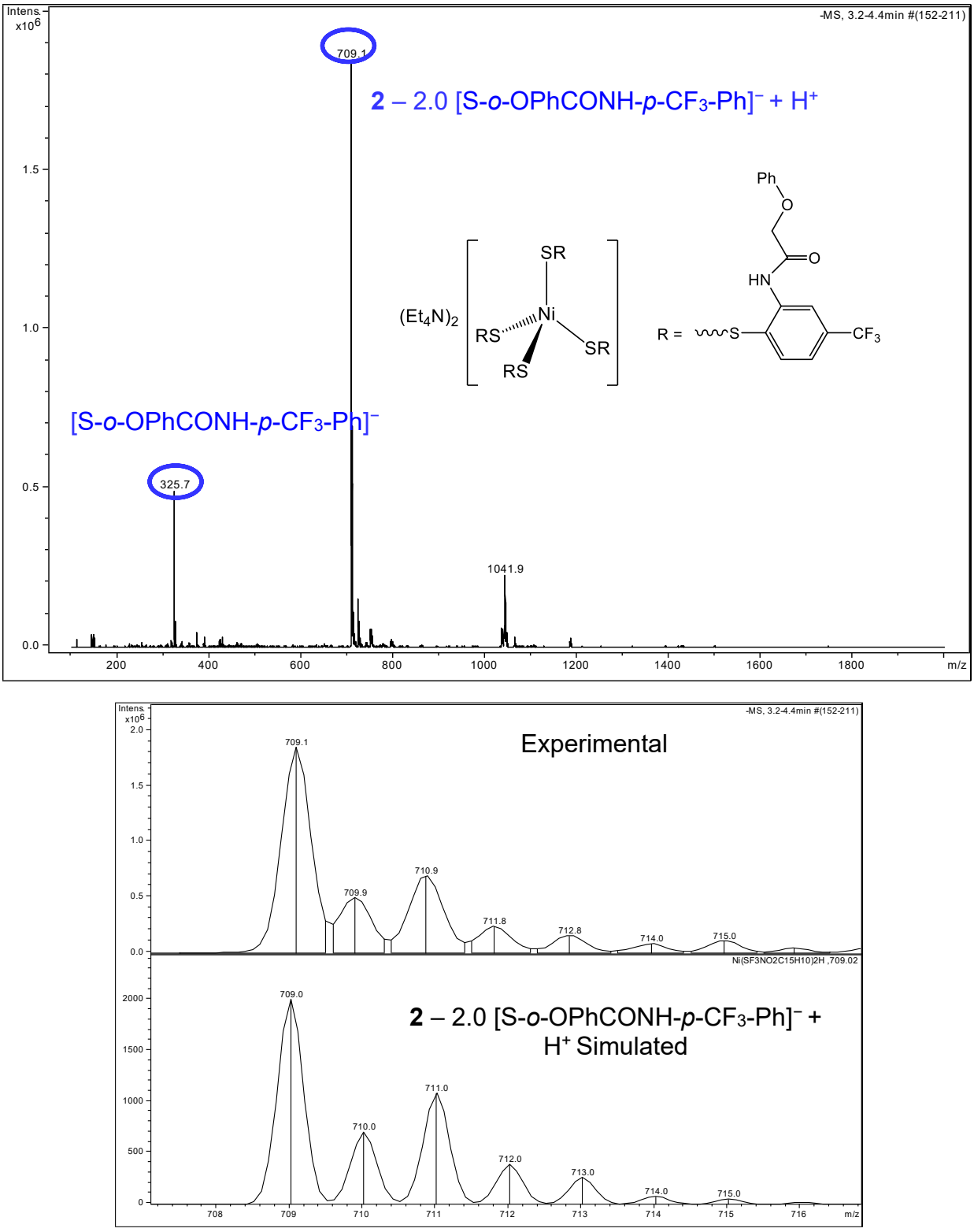

Figure S3.36. *Top:* Low-resolution ESI-MS(-) (negative mode) of $(Et_4N)_2$[Ni(S-*o*-OPhCONH-*p*-CF_3-Ph)$_4$] (**2**) in MeCN. *Bottom*: experimental and simulated theoretical isotopic distribution peak at *m/z*: 709.1. Other peaks have not been identified as reaction products.

$(Et_4N)_2$[Zn(S-*o*-^{i}PrCONH-*p*-CF_3-Ph)$_4$] (4) To a yellow solution of (S-*o*-^{i}PrCONH-*p*-CF_3-Ph)$_2$ (0.147 g, 0.281 mmol) in 2 mL of THF, a slight-yellow solution of $(Et_4N)_2$[Zn(S-*p*-CF_3-Ph)$_4$] (0.132 g, 0.128 mmol) in 2 mL of THF was added dropwise. Upon addition, the solution took on a yellow color and was stirred for 20 h. The solution was taken to dryness leaving behind a sticky yellow solid. To this 5 mL of Et_2O was added and stirred for 30 min picking up a light-yellow color with the solid left behind. The solution was decanted off. This was repeated a total of three times. The solid was dried under vacuum, leaving behind an off-white foam. To this pentane (3 mL) was added and after 30 min of stirring, the resulting solid was isolated by vacuum filtration on a glass-frit, washed with pentane (3 x 2 mL), and dried using a high vacuum line to afford the desired complex (0.110 g, 0.0800 mmol, 62.7%) as an off-white solid. FTIR (KBr matrix), ν_{max} (cm^{-1}): 3269 (NH, m), 1676 (CO, s), 1327 (CF, s), 1109 (s, CF), 1083 (s, CF). ^{1}H NMR (400 MHz, CD_3CN, δ from residual deuterated solvent): 9.29 (s, 4H), 8.40 (s, 3H), 7.52 (d, 4H, *J* = 7.84 Hz), 6.80 (d, 4H, *J* = 7.64 Hz), 3.11 (q, 15H, *J* = 7.24 Hz), 2.52 (sept, 4H, *J* = 6.43 Hz) 1.17 (m, 47H). ^{19}F NMR (376 MHz, CD_3CN, δ from residual deuterated solvent): -62.01 (s). LR-ESI-MS (*m/z*): [M – S-*p*-CF_3-*o*-NHC(O)^{i}Pr-Ph]$^-$ calcd for $C_{33}H_{33}F_9S_3N_3O_3Zn$ (relative abundance), 850.1 (100.0), 851.0 (39.7), 852.1 (79.7), 853.1 (37.7), 854.1 (56.3), 855.1 (21.3), 456.1 (11.4), 857.1 (3.1); found, 850.1 (100.0), 851.0 (39.0), 852.0 (69.6), 853.0 (36.9), 853.9 (52.4), 854.9 (19.3), 855.9 (9.4), 856.9 (3.3). [M – S-*p*-CF_3-*o*-NHC(O)^{i}Pr-Ph]$^-$ calcd for $C_{44}H_{44}F_{12}S_4N_4O_4Zn$ + $C_8H_{20}N$ (relative abundance), 1242.3 (100), 1243.3 (62.2), 1244.3 (95.3), 1245.3 (59.5), 1246.3 (71.1), 1247.3 (37.3), 1248.3 (20.8), 1249.3 (8.2), 1250 (3.0); found, 1242.1 (100.0), 1243.0 (58.0), 1244.0 (88.9), 1244.9 (51.8), 1245.9 (70.4), 1246.9 (32.1), 1247.8 (21.0), 169.0 (6.2).

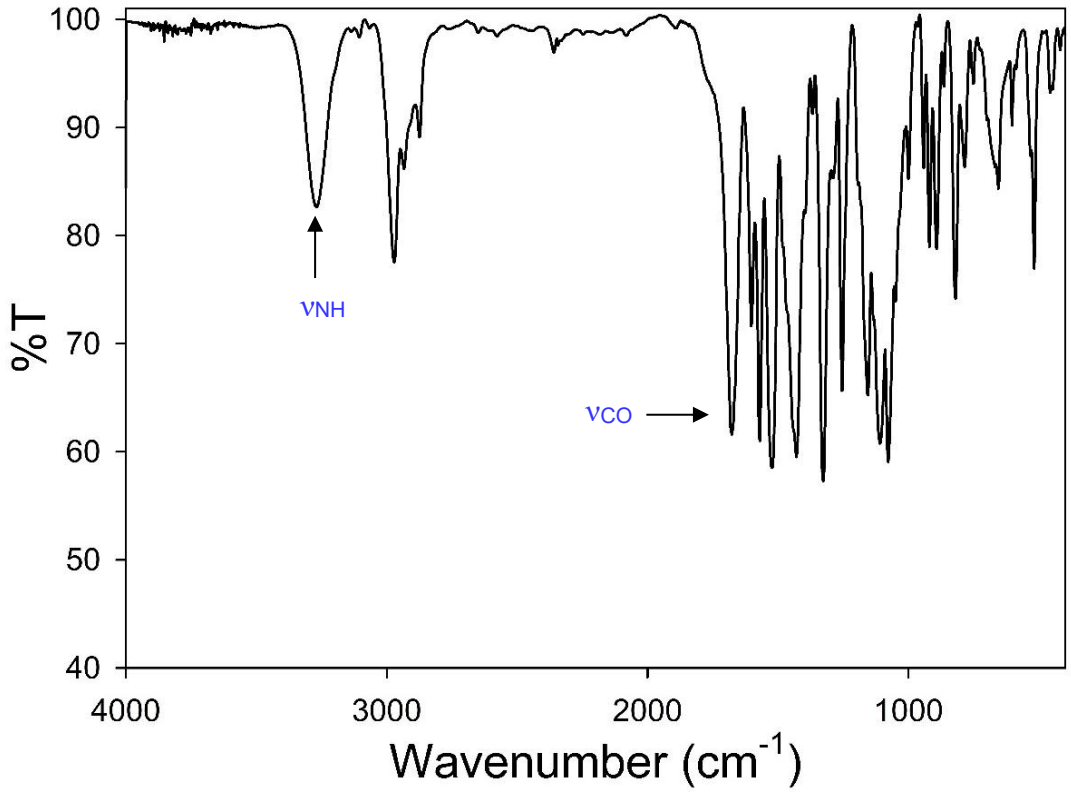

Figure S3.37. Solid-state FTIR spectrum of $(Et_4N)_2[Zn(S\text{-}o\text{-}^{i}PrCONH\text{-}p\text{-}CF_3\text{-}Ph)_4]$ (**4**) in a KBr matrix at RT.

^{1}H NMR (400 MHz, CD_3CN, RT) of **$(Et_4N)_2$[Zn(S-*o*-^{i}PrCONH-*p*-CF_3-Ph)$_4$] (4)**

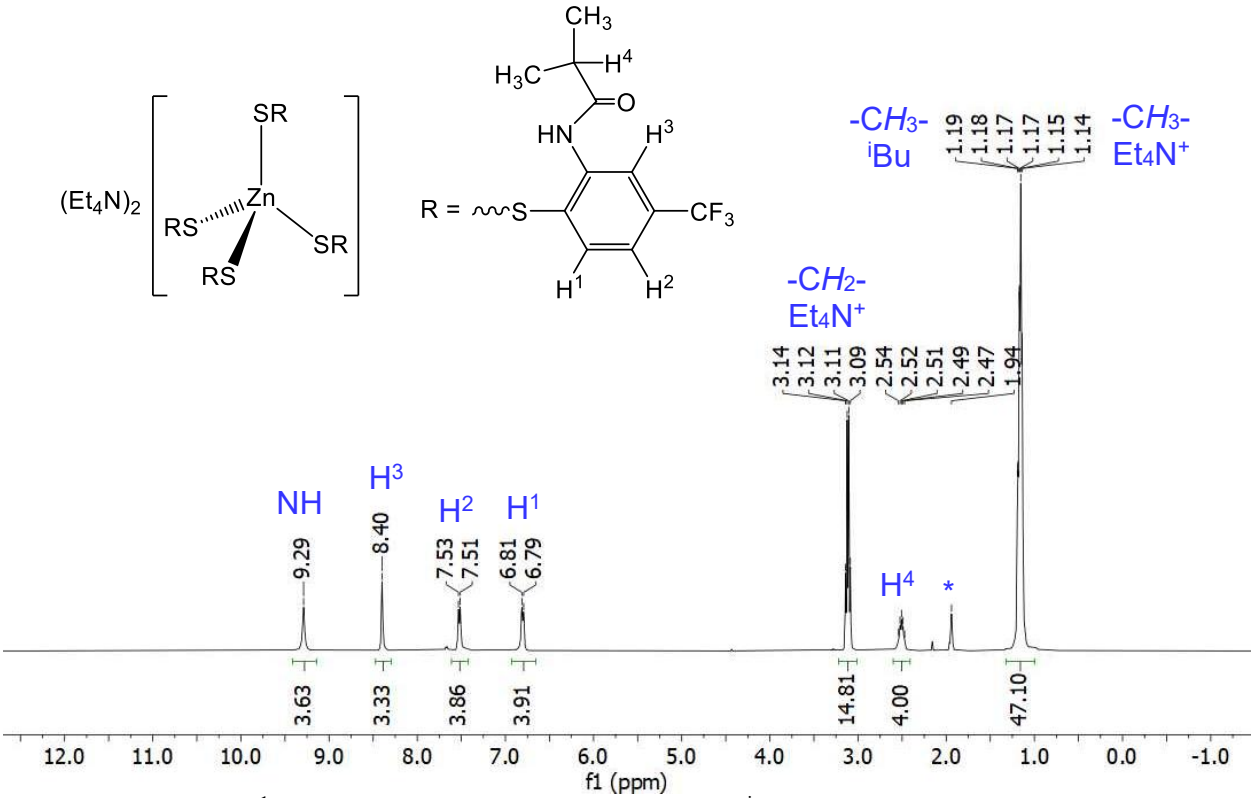

Figure S3.38. *Top:* ^{1}H NMR spectrum of $(Et_4N)_2$[Zn(S-*o*-^{i}PrCONH-*p*-CF_3-Ph)$_4$] (**4**) in CD_3CN at RT (δ vs. protio signal).

^{19}F NMR (376 MHz, CD_3CN, RT) of **$(Et_4N)_2$[Zn(S-*o*-^{i}PrCONH-*p*-CF_3-Ph)$_4$]** (**4**)

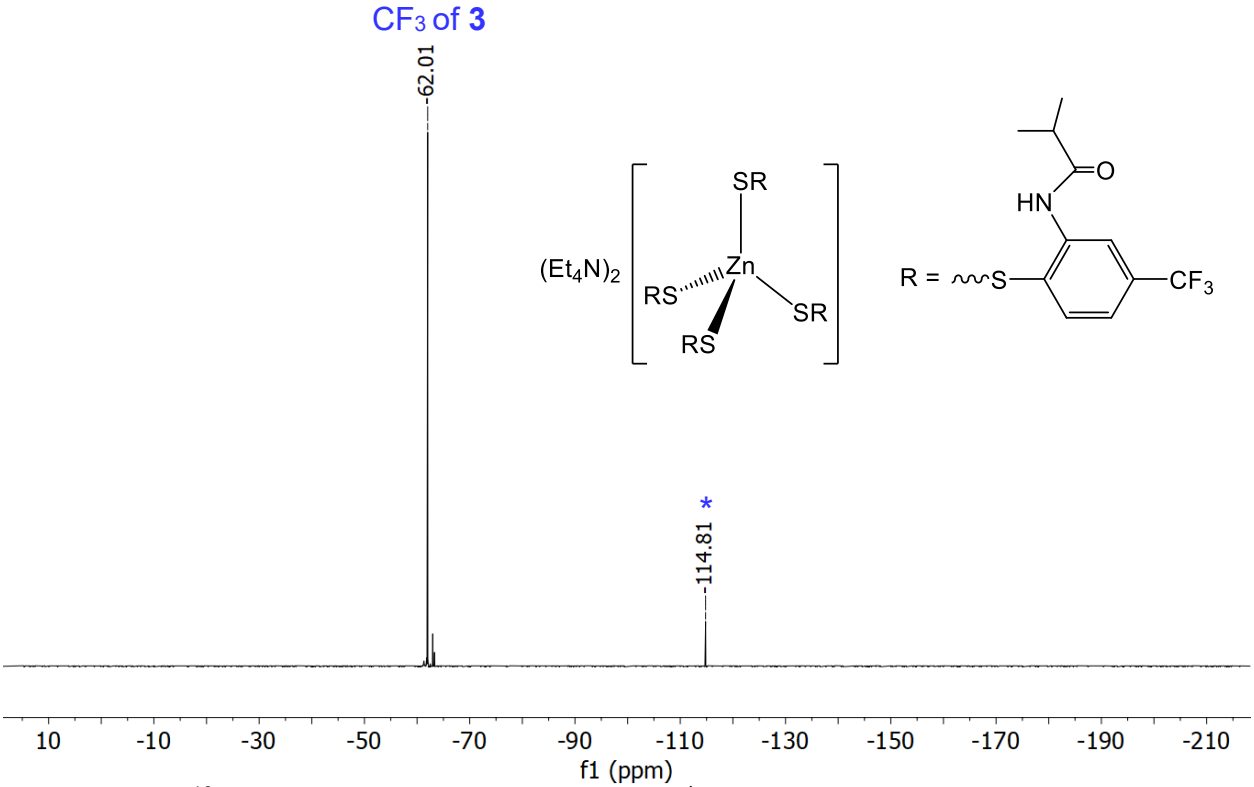

Figure S3.39. ^{19}F NMR spectrum of $(Et_4N)_2$[Zn(S-*o*-^{i}PrCONH-*p*-CF_3-Ph)$_4$] (**3**) in CD_3CN at RT. The peak at -114.81 ppm is from PhF as an internal standard and is indicated with *.

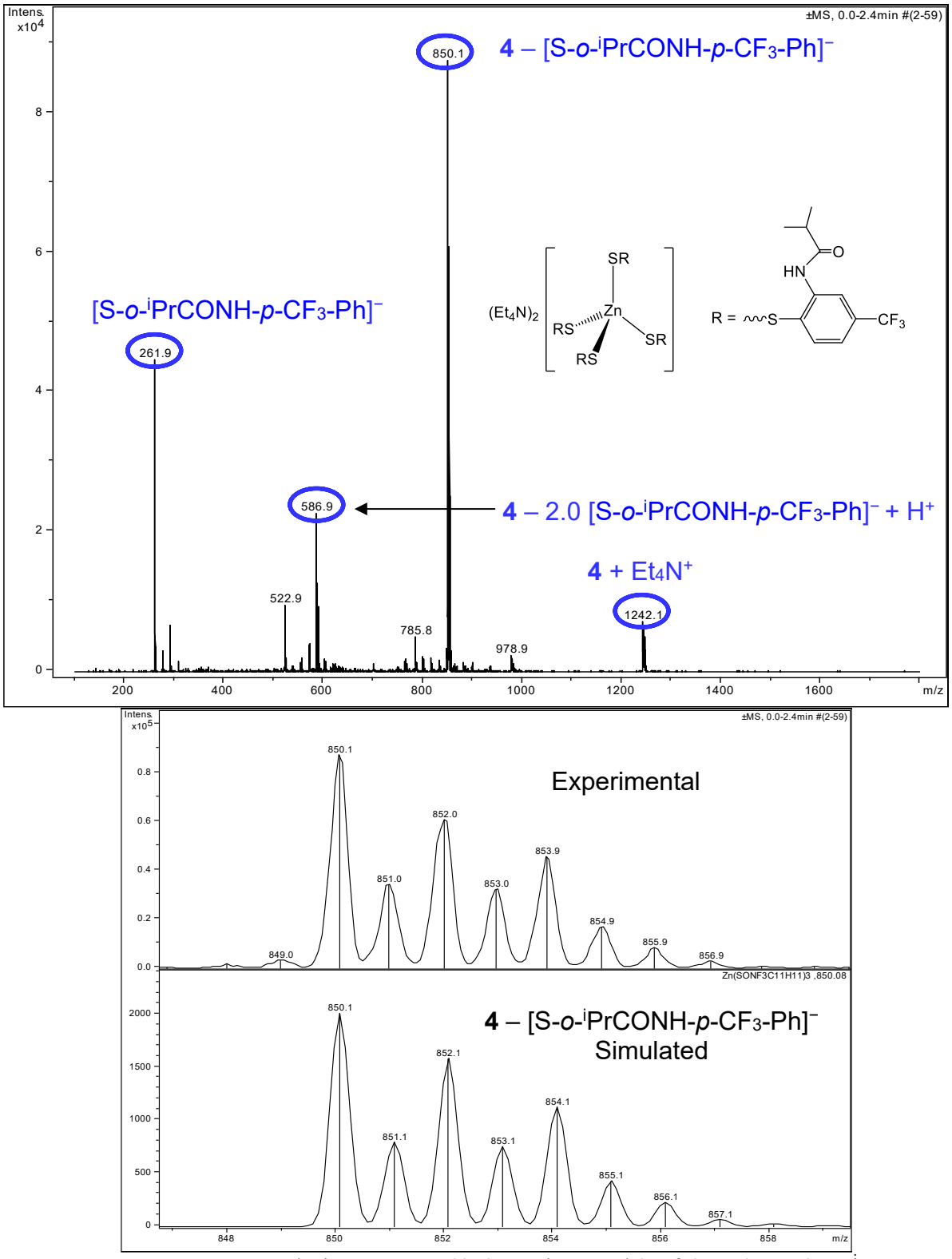

Figure S3.40. *Top:* Low-resolution ESI-MS(-) (negative mode) of $(Et_4N)_2[Zn(S\text{-}o\text{-}^{i}PrCONH\text{-}p\text{-}CF_3\text{-}Ph)_4]$ (**4**) in MeCN. *Bottom*: experimental and simulated theoretical isotopic distribution peak at *m/z*: 850.1. Other peaks have not been identified as reaction products.

3.7 Physical Measurements

X-ray Absorption Spectroscopy (XAS). XAS data of **1** was collected at the Standford Synchrotron Radiation Lightsource (SSRL) beamline 7-3, which utilizes a Si[220] double-crystal monochromator with an inline mirror for X-ray focusing and for harmonic rejection. Duplicate independent samples were prepared anaerobically inside an MBraun glove box, with solid samples diluted 3:1 with inert Boron Nitride, then wrapped in Kaption tape. During data collection, samples were maintained at 10.8 K using a liquid He continuous flow cryostat. Transmission spectra were measured in 0.25 eV increments in the edge region (8325-8370 eV) and 0.05 $Å^{-1}$ increments in the extended X-ray absorption fine structure (EXAFS) region (out to k = 13.3 $Å^{-1}$), integrating from 1 to 25 s in a k^3-weighted manner for a total scan length of approximately 50 min. Data represents the average of three scans. X-ray energy scans were individually calibrated by collecting a Ni-foil absorption spectrum simultaneously with the compound; the first inflection point of the Ni-foil spectrum was assigned to 8,333 eV. The pre-edge features were investigated by normalizing the edge data using the EDG_FIT program (R-29). For analysis of the 1s→3d transition, data was fit with an arctan background + a pseudo-Voigt peak to model the rising edge and 1s→3d peak, XAS spectra were processed using the Macintosh OSX version of the EXAFSPAK program suite[114] integrated with the Feff v8 software for theoretical model generation.[115] XAS simulations followed a pre-existing published strategy[116]

X-ray Crystallographic Data Collection and Structure Solution and Refinement. Green crystals of **1** were obtained from slow diffusion of Pentane into a saturated solution of **1** (with Me_4N counterion) in ethyl acetate at -20 °C. The data was collected at 273 K on the goniometer head of a Bruker D8 diffractometer equipped with a Bruker ApexII CCD detector. Data were collected with the use of Mo Kα (λ = 0.71073 Å) fine-focus sealed tube. A multi-scan absorption

correction was applied with the program SADABS.[117] The structure was solved by the dual space method, (SHELXT)[118] and refined by full-matrix least-squares on F2 (SHELXL-2017) [119].

Electrochemistry and Electrocatalysis. Cyclic voltammetry (CV) measurements were performed with a WaveDriver 40 bipotentiostat/galvanostat from Pine Research Instrumentation using an Ag/Ag^+ reference electrode, Pt-wire counter electrode (immersed directly into solution), and a stationary glassy carbon working electrode (3 mm outer diameter). The potentiostat was interfaced with a PC using the Aftermath software. Measurements were collected at ambient temperature using ~2.0 mM analyte in MeCN containing 0.25 M $^n Bu_4NPF_6$ as the supporting electrolyte in an inert N_2 atmosphere. Analyte potentials were referenced against a 5 mM MeCN solution of ferrocene as an internal standard under identical conditions. Purity of the electrolyte medium was confirmed over the available electrochemical window through scans taken prior to addition of external reference. The acid titration experiments were performed by addition of MeCN alliqouts of a acetic acid solution (pK_a = 23.6; MeCN).[80] The solution was stirred for 20 s and undisturbed for an additional 30 s prior to measurement. The working electrode was cleaned between scans by washing with solvent, polishing with 0.3-micron Alumina suspension from Allied High ech Products, and sonicating in DI water. Rinse tests were performed at the end the acid titration experiment by removing working electrode, rinsing with solvent medium, placing working electrode into fresh solution of electrolyte and acid, and performing the CV. All spectra are graphed corresponding to the US convention.

Surface analysis sample preparation. Electrolyzed samples of **1** were prepared on a stationary glassy carbon working electrode (3 mm outer diameter). The surface of the electrode was polished using 0.3-micron Alumina suspension from Allied High Tech Product and rinsed and sonicated with MiliQ water for 1 min. After repeating two more times, the working electrode was

sonicated in MiliQ water for 20 minutes to thoroughly remove polishing material. SEM-EDS measurements were taken of the surface of the working electrode with a radiation power of 20 kV utilizing a Hitachi SU3900 coupled to an Oxford EDS system. Electrolyzed samples were produced using the same set-up as described for the electrochemical experiments. To the solution of **1** (1.7 mM), 24.6 mol-equivalents of acid were added, and a complete scan was taken to determine E_{cat}. Afterwards, the working electrode was removed and rinsed with acetone and IPA, polished, rinsed and sonicated with MiliQ water for 5 minutes, and dried. To the solution with catalyst and acid, a potential at the E_{cat} (-2.11 V vs Fc/Fc^{+}) was applied for 0.5 h. After electrolysis, samples were removed from solution, rinsed with MeCN, blotted dry, and placed under vacuum for 15 min. SEM samples were exposed to atmosphere briefly (3 min) when transferred to instrument. SEM-EDS measurement of the electrolyzed materials was taken of the working electrode with a radiation power of 20 kV utilizing a Hitachi SU3900 coupled to an Oxford EDS system.

3.8 Reactivity Studies

^{1}H NMR Titration Experiments with AcOD-d_4. For **1**, a 46.1 mM solution (0.0290 g, 0.021 mmol) was made in 0.46 mL of CD_3CN, was placed in a J-young tube, capped with a rubber septum, taped, wrapped with parafilm, and further sealed with a copper wire. The solution was prepared under N_2 atmosphere. The ^{1}H and ^{19}F NMR were recorded at 25 C° with 64 scans. After the NMR was recorded of **1**, a 12 uL aliquot of AcOD-d_4 was added to the J-young tube, via an air-tight syringe, solution shaken and stood for 1 minute prior to running the sample. This was repeated until no change in significant change in the spectrum was observed. The stability of **1** is measured by the loss of the intensity of the peaks at ~26 ppm, ~20 ppm, and ~−12 ppm with all integration relative to anticipated protons of from two counterions (Et_4N^{+}).

For **2**, a 5.29 mM solution (0.0110 g, 0.0068 mmol) was made in 1.28 mL of CD_3CN and 0.46 mL of this solution was placed in a J-young tube, capped with a rubber septum, taped, wrapped with parafilm, and further sealed with a copper wire. A separate solution of 8.74 M AcOD-d4 (2.00 mL, 2.24 mL, 0.035 mol) and 2.00 mL of MeCN was made an sealed with a screw cap septa. Both solutions were prepared under N_2 atmosphere. The ^1H and ^{19}F NMR were recorded at 25 C° with 64 scans. After the NMR was recorded of **2**, a 14 uL aliquot of AcOD-d_4 was added to the J-young tube, via an air-tight syringe, solution shaken and stood for 1 minute prior to running the sample. This was repeated until no change in significant change in the spectrum was observed. The stability of **2** is measured by the loss of the intensity of the peaks at 30 ppm, ~20 ppm, and ~−9 ppm with all integration relative to anticipated protons of from two counterions (Et_4N^+).

UV-vis Titration Experiment with Thiolate. For **1**, a 7.4 mM stock solution of **1** (0.010 g, 0.0074 mmol) was made in 1.0 mL of MeCN and 50 µL was added to a cuvette containing 2.00 mL of MeCN and sealed with a cap. A separate 38 mM stock solution of (Et_4N)(S-*o*-^{i}PrCONH-*p*-CF_3-Ph) (0.015 g, 0.038 mmol) was made in 1.00 mL of MeCN. After the spectrum of **1** was recorded, 40 µL of (Et_4N)(S-*o*-^{i}PrCONH-*p*-CF_3-Ph) was added to the cuvette containing **1**, stirred, and the spectra was recorded after roughly a minute at room temperature. Titrations were repeated in the same manner until no change in the spectra was observed. All stock solutions and titrations were made and performed in a MBraun Unilab glovebox under N_2 atmosphere.

For **2**, a 7.4 mM stock solution of **2** (0.012 g, 0.0074 mmol) was made in 1.0 mL of MeCN and 40 µL was added to a cuvette containing 2.00 mL of MeCN and sealed with a cap. A separate 30 mM stock solution of (Et_4N)(S-*o*-OPhCONH-*p*-CF_3-Ph) (0.014 g, 0.030 mmol) was made in 1.00 mL of MeCN. After the spectrum of **2** was recorded, 60 µL of (Et_4N)(S-*o*-OPhCONH-*p*-CF_3-Ph) was added to the cuvette containing **2**, stirred, and the spectra was recorded after roughly a minute

at room temperature. Titrations were repeated in the same manner until no change in the spectra was observed. All stock solutions and titrations were made and performed in a MBraun Unilab glovebox under N_2 atmosphere.

Chemical Oxidation of 1 with $FcBF_4$. A small batch of **1** (0.033 g, 0.024 mmol) was dissolved in minimal MeCN resulting in a dark red color and $FcBF_4$ (0.007 g, 0.024 mmol) was added dropwise in a blue solution of MeCN. Immediately, upon addition of oxidant the solution took on a brown color and darkened as more was added. After the solution was stirred for 1 h, MeCN was completely removed, and ~3 mL of 2-Me-THF was added. The solvent took on a brown, slight-reddish color, with an insoluble suspended in solution. The solution was filtered over a Celite packed frit and rinsed with an additional ~2 mL of 2-Me-THF leaving behind an off-white precipitate. The brown filtrate was taken to dryness, ~5 mL of Et_2O, stirred for 20 min, picking up an amber color, and decanted leaving behind a dark-brown oil. This was repeated for a total of three times. To the oily product left behind ~5 mL of pentane was added and after 30 min of stirring, the resulting solid was isolated by vacuum filtration on a glass-frit, washed with pentane (3 x 2 mL), and dried using a high vacuum line to a dark-brown complex (0.017 g). The Et_2O soluble portion was taken to dryness to yield an orange-brown and white solid (0.014 g) determined to be a mixture of disulfide, Fc, and bridged complex $^{1}H/^{19}F$ NMR and FTIR.

3.9 Supplementary Information

Table S3.1. Summary of Crystal Data and Intensity Collection and Structure Refinement Parameters for $(Et_4N)_2[Ni(S\text{-}o\text{-}^iPrCONH\text{-}p\text{-}CF_3\text{-}Ph)_4]$ (**1**) and $(Et_4N)_2[Ni(S\text{-}o\text{-}OPhCONH\text{-}p\text{-}CF_3\text{-}Ph)_4]$ (**2**).

Parameters	**1**
Formula	$2(C_{22}H_{22}F_6N_2Ni_{0.5}O_2S_2)\cdot 2(C_4H_{12}N)\cdot C_4H_8O$
MW	1344.17
Crystal system	Triclinic
Space group	*P*1
Crystal color, habit	green, needle
a, Å	10.6810(9)
b, Å	17.3590(14)
c, Å	18.5262(15)
α, deg	86.155(2)
β, deg	75.965(2)
γ, deg	89.381(2)
V, Å^3	3324.9(5)
Z	2
$\rho_{calcd,}$ g/cm^3	1.327
T, K	273
abs coeff, μ (Mo Kα), mm^{-1}	0.50
θ limits, deg	2.5 – 25.4
total no. of data	46990
no. of unique data	12025
no. of parameters	822
GOF of F^2	1.14
R_1,[a]	0.123
wR_2,[b]	0.400
max, min peaks, e/Å^3	2.87, -0.58

[a] $R_1 = \Sigma| |F_o| - |F_c| | / \Sigma |F_o|$; [b] $wR_2 = \{\Sigma[w(F_o^2 - F_c^2)^2]/\Sigma[w(F_o^2)^2]\}^{1/2}$

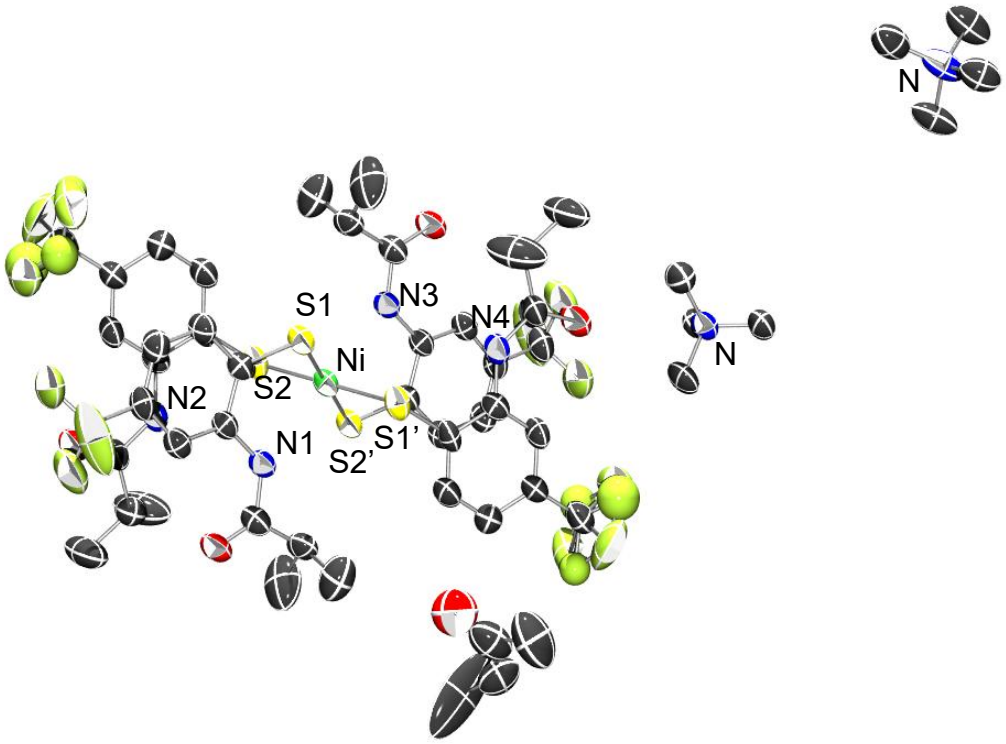

Figure S3.41. ORTEP diagram of $[Ni(S\text{-}o\text{-}^{i}PrCONH\text{-}p\text{-}CF_3\text{-}Ph)_4]^{2-}$ (**1**) at 50% thermal probability ellipsoids. H atoms and counter anions are omitted for clarity. Disorder in one of the trifluoromethyl groups consisting of atoms (F1-F3 and F10-F12) is shown.

Table S3.2. Selected bond distances (Å) and bond angles (deg) for $[Ni(S\text{-}o\text{-}^{i}PrCONH\text{-}p\text{-}CF_3\text{-}Ph)_4]^{2-}$ (**1**) (Figure S3.41).

Atoms	Bond Distance (Å)	Atoms	Angle
$Ni\text{-}S_1$	2.236	$S_1\text{-}Ni\text{-}S_2$	94.2˚
$Ni\text{-}S_2$	2.207	$S_1\text{-}Ni\text{-}S_3$	180.0˚
$Ni\text{-}S_3$	2.236	$S_1\text{-}Ni\text{-}S_4$	86.2˚
$Ni\text{-}S_4$	2.214	$S_2\text{-}Ni\text{-}S_3$	85.8˚
$S_1\text{-}N_1$	2.923	$S_2\text{-}Ni\text{-}S_4$	178.8˚
$S_2\text{-}N_2$	3.045	$S_3\text{-}Ni\text{-}S_4$	93.8˚
$S_3\text{-}N_3$	2.923		
$S_4\text{-}N_4$	3.006		
Atoms	**Angle**	**<Ar-(Ni-S)**	**Angle**
$Ni\text{-}S_1\text{-}C_{\alpha 1}$	106.9˚	$Ar_1\text{-}(Ni\text{-}S_1)$	36.4˚
$Ni\text{-}S_2\text{-}C_{\alpha 2}$	114.7˚	$Ar_2\text{-}(Ni\text{-}S_2)$	74.1˚
$Ni\text{-}S_3\text{-}C_{\alpha 3}$	106.9˚	$Ar_3\text{-}(Ni\text{-}S_3)$	31.9˚
$Ni\text{-}S_4\text{-}C_{\alpha 4}$	112.8˚	$Ar_4\text{-}(Ni\text{-}S_4)$	81.8˚

Table S3.3. Selected bond distances (Å) and angles (deg) for $[Ni(S\text{-}o\text{-}^{i}PrCONH\text{-}p\text{-}CF_3\text{-}Ph)_4]^{2-}$ (**1**) (Figure S3.41).

Atoms	Angle	Ar-Ar	Distance of Centroids (Å)	<Ar-Ar
$C_{\alpha1}$-$C_{\beta1}$-N_1-C_1(O)	158.0˚	Ar_1---Ar_2	4.126	8.2˚
$C_{\alpha2}$-$C_{\beta2}$-N_2-C_2(O)	162.2˚	Ar_3---Ar_4	4.126	8.2˚
$C_{\alpha3}$-$C_{\beta3}$-N_3-C_3(O)	158.0˚			
$C_{\alpha4}$-$C_{\beta4}$-N_4-C_4(O)	162.2˚			

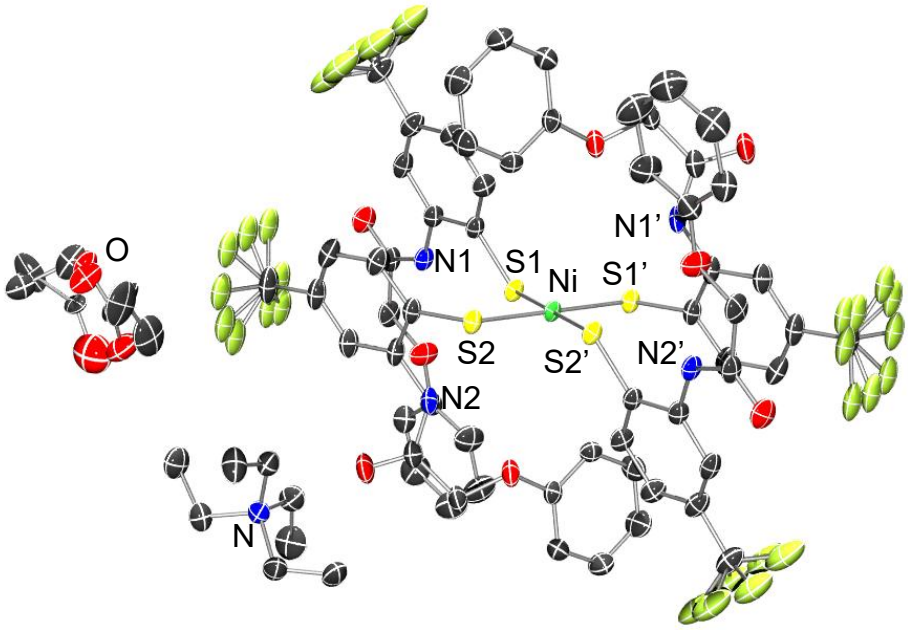

Figure S3.42. ORTEP diagram of $[Ni(S\text{-}o\text{-}OPhCONH\text{-}p\text{-}CF_3\text{-}Ph)_4]^{2-}$ (**2**) at 50% thermal probability ellipsoids, from *preliminary data*. H atoms and counter anions are omitted for clarity.

Table S3.4. Selected bond distances (Å) and bond angles (deg) $[Ni(S\text{-}o\text{-}OPhCONH\text{-}p\text{-}CF_3\text{-}Ph)_4]^{2-}$ (**2**) (Figure S3.42).

Atoms	Bond Distance (Å)	Atoms	Angle
$Ni\text{-}S_1$	2.224	$S_1\text{-}Ni\text{-}S_2$	97.0˚
$Ni\text{-}S_2$	2.223	$S_1\text{-}Ni\text{-}S_{1'}$	180.0˚
$Ni\text{-}S_{1'}$	2.224	$S_1\text{-}Ni\text{-}S_{2'}$	83.0˚
$Ni\text{-}S_{2'}$	2.223	$S_2\text{-}Ni\text{-}S_{1'}$	83.0˚
$S_1\text{-}N_1$	2.930	$S_2\text{-}Ni\text{-}S_{2'}$	180.0˚
$S_2\text{-}N_2$	3.017	$S_3\text{-}Ni\text{-}S_{2'}$	97.0˚
$S_3\text{-}N_{1'}$	2.930		
$S_4\text{-}N_{2'}$	3.017		
Atoms	**Angle**	**<Ar-(Ni-S)**	**Angle**
$Ni\text{-}S_1\text{-}C_{\alpha1}$	108.5˚	$Ar_1\text{-}(Ni\text{-}S_1)$	21.8˚
$Ni\text{-}S_2\text{-}C_{\alpha2}$	114.3˚	$Ar_2\text{-}(Ni\text{-}S_2)$	69.4˚
$Ni\text{-}S_{1'}\text{-}C_{\alpha3}$	108.5˚	$Ar_{1'}\text{-}(Ni\text{-}S_{1'})$	21.8˚
$Ni\text{-}S_{2'}\text{-}C_{\alpha2'}$	114.3˚	$Ar_{2'}\text{-}(Ni\text{-}S_{2'})$	69.4˚

Atoms	Angle	Ar-Ar	Distance of Centroids (Å)	<Ar-Ar
$C_{\alpha1}\text{-}C_{\beta1}\text{-}N_1\text{-}C_1(O)$	147.6˚	$Ar_1\text{---}Ar_2$	3.665	10.65
$C_{\alpha2}\text{-}C_{\beta2}\text{-}N_2\text{-}C_2(O)$	176.0˚	$Ar_{1'}\text{---}Ar_{2'}$	3.665	10.65
$C_{\alpha3}\text{-}C_{\beta3}\text{-}N_{1'}\text{-}C_{1'}$ (O)	147.6˚			
$C_{\alpha4}\text{-}C_{\beta4}\text{-}N_{2'}\text{-}C_{2'}$ (O)	176.0˚			

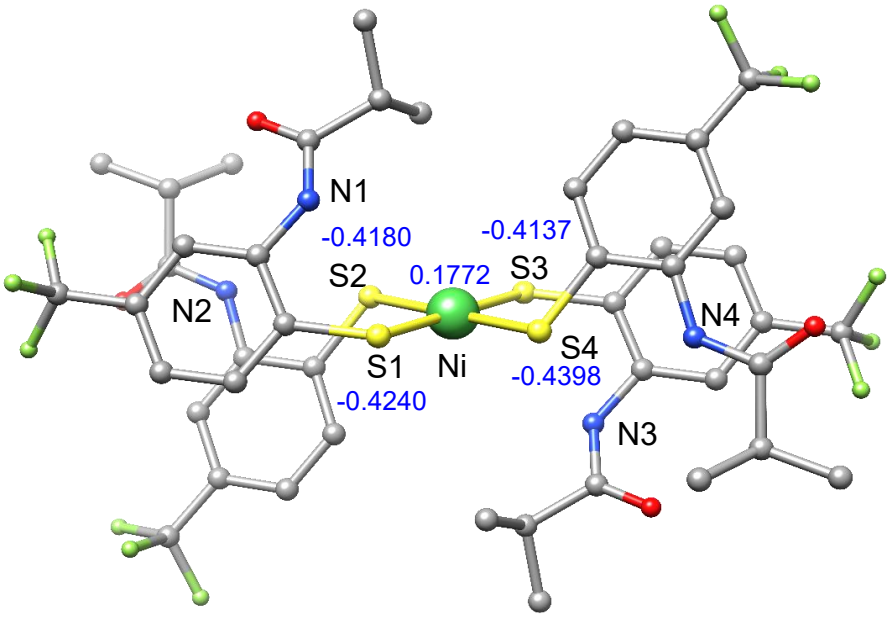

Figure S3.43. Geometry-optimized structure of the square-planar ($S = 0$) dianion of **1** in the gas phase with Mulliken atomic charges. H atoms are omitted for clarity. Input coordinates taken from the X-ray crystal structure of **1**.

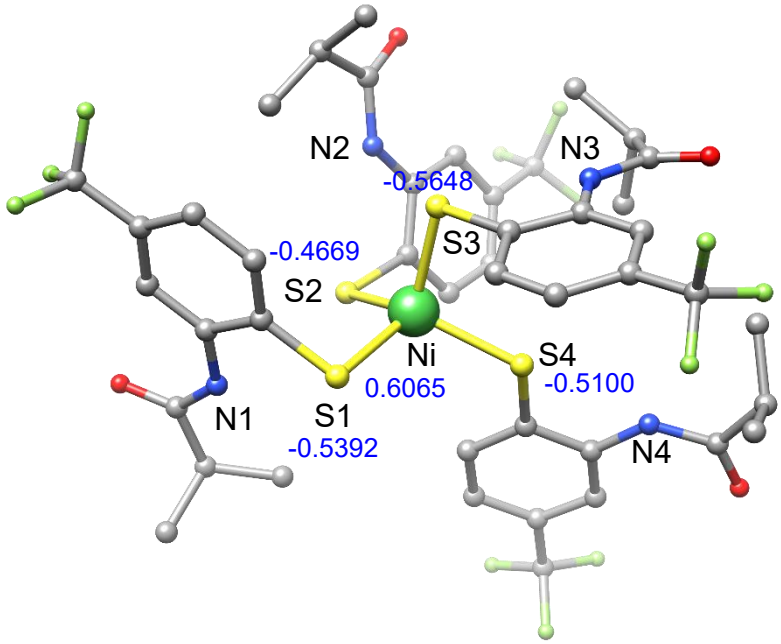

Figure S3.44. Geometry-optimized structure of the tetrahedral ($S = 1$) dianion of **1** in the gas phase with Mulliken atomic charges. H atoms are omitted for clarity.

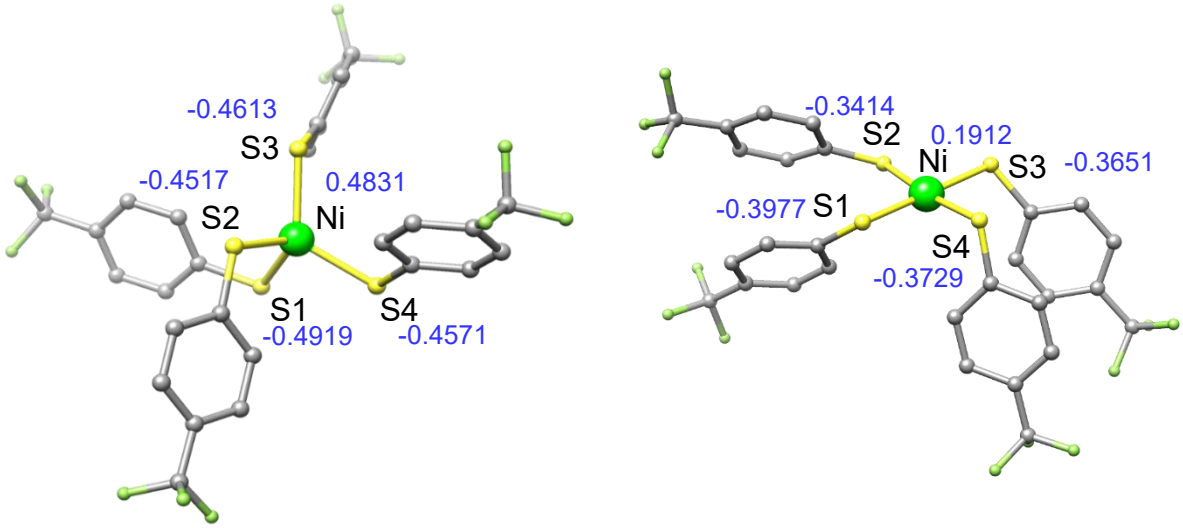

Figure S3.45. Geometry-optimized structures of the tetrahedral ($S = 1$) (*left*) and square-planar ($S = 0$) (*right*) dianion of **3** in the gas-phase with Mulliken atomic charges. Input coordinates taken from the X-ray crystal structure of **3**.

Table S3.5. Selected bond distances (Å) and bond angles (deg) for geometry-optimized structures of the dianion of **1*** and **3*** in tetrahedral and square-planar geometry.

	1(T$_d$) (S = 1)	**1(SqPl)** (S = 0)	**3(T$_d$)** (S = 1)	**3(SqPl)** (S = 0)
	Bond Distance (Å)			
Ni-S$_1$	2.334	2.235	2.323	2.248
Ni-S$_2$	2.307	2.213	2.335	2.269
Ni-S$_3$	2.316	2.235	2.332	2.280
Ni-S$_4$	2.307	2.214	2.320	2.301
S$_1$-N$_1$	2.959	2.957		
S$_2$-N$_2$	2.949	2.895		
S$_3$-N$_3$	2.940	2.956		
S$_4$-N$_4$	2.894	2.895		
	Angle (°)			
S$_1$-Ni-S$_2$	102.6	97.5	119.5	97.8
S$_1$-Ni-S$_3$	104.9	180.0	118.6	177.1
S$_1$-Ni-S$_4$	104.6	82.5	94.4	88.2
S$_2$-Ni-S$_3$	112.4	82.5	90.1	84.3
S$_2$-Ni-S$_4$	131.0	180.0	129.2	173.5
S$_3$-Ni-S$_4$	99.0	97.5	118.6	89.5
	τ_4			
	0.79	0.00	0.79	0.06
<Ar-(Ni-S)	**Angle (°)**			
Ar$_1$-(Ni-S$_1$)	85.6˚	64.2	23.6	42.8
Ar$_2$-(Ni-S$_2$)	86.7˚	24.8	11.2	35.7
Ar$_3$-(Ni-S$_3$)	75.9˚	64.2	26.4	27.8
Ar$_4$-(Ni-S$_4$)	17.6˚	24.8	23.6	42.2
<Ni-S-C$_{Ph}$(α)*	**Angle (°)**			
Ni-S$_1$-C	100.2	113.1	104.5	111.0
Ni-S$_2$-C	99.2	109.5	108.0	111.6
Ni-S$_3$-C	102.3	113.1	110.3	106.0
Ni-S$_4$-C	107.4	109.5	106.9	108.5

*C$_{Ph}$(α) = phenyl carbon directly bonded to S-atom

Table S3.6. M-S and N_{amide}---S bond distances (Å) and τ_4 values of monomeric complexes containing aryl thiolate containing an *ortho*-carboxamide group.

Complex	$(M\text{-}S)_{avg}$ (Å)	$N_{amide}\text{---}S_{avg}$ (Å)	τ_4	ref
1	2.222	2.974	0.01	TW
2	2.224	2.974	0.00	TW
$(Et_4N)_2[Fe(S\text{-}o\text{-}^tBuCONHPh)_4]$	2.329	2.930	0.89	[40]
$(Et_4N)_2[Co(S\text{-}o\text{-}^tBuCONHPh)_4]$	2.296	2.915	0.87	[40]
$[Ni(HpyS)_4](NO_3)_2$	2.212	2.858*	0.05	[52]
$[Pt(bpy)(S\text{-}o\text{-}^tBuCCONHPh)_2]$	2.284	3.086	0.00	[41]
$[Pt(bpy)(S\text{-}o\text{-}PH_3CCONHPh)_2]$	2.287	2.984	0.00	[41]
$[Pt(PPh_3)_2(S\text{-}o\text{-}PhCONHPh)_2]$	2.36	2.94	0.08	[120]
$[Ni(dppe)Me(S\text{-}o\text{-}^tBuCONHPh)]$	2.144	2.973	0.07	[49]
$(Et_4N)[Ni(nmp)(S\text{-}o\text{-}PhCONHPh)]$	2.194	2.954	0.09	[27]
$[(L1)Zn(S\text{-}o\text{-}CF_3CONHC_6H_4)]^-$	2.241	2.922	0.81	[35]

*H-bond engagement to NO_3^-; nmp = *N*-(2-mercaptoethyl)picolinamide; L1= bis(5-tert-bityl-3-methylpyrazol-2-yl)acetate

Table S3.7. Computed Gibbs free energy (B3LYP/def2-TZVPP) with CPCMC(MeCN) of the dianion of **1** and **3** in tetrahedral and square-planar geometry.

Complex	Gibbs Free Energy (Eh)	ΔG (Eh)	ΔG (kcal/mol)
1*(SqPl)	-6520.067081	-0.008116	-5.1
1*(T_d)	-6520.075197		
3*(SqPl)	-5375.787262	-0.022509	-14.1
3*(T_d)	-5375.809771		

$\Delta G = G(T_d) - G(SqPl)$

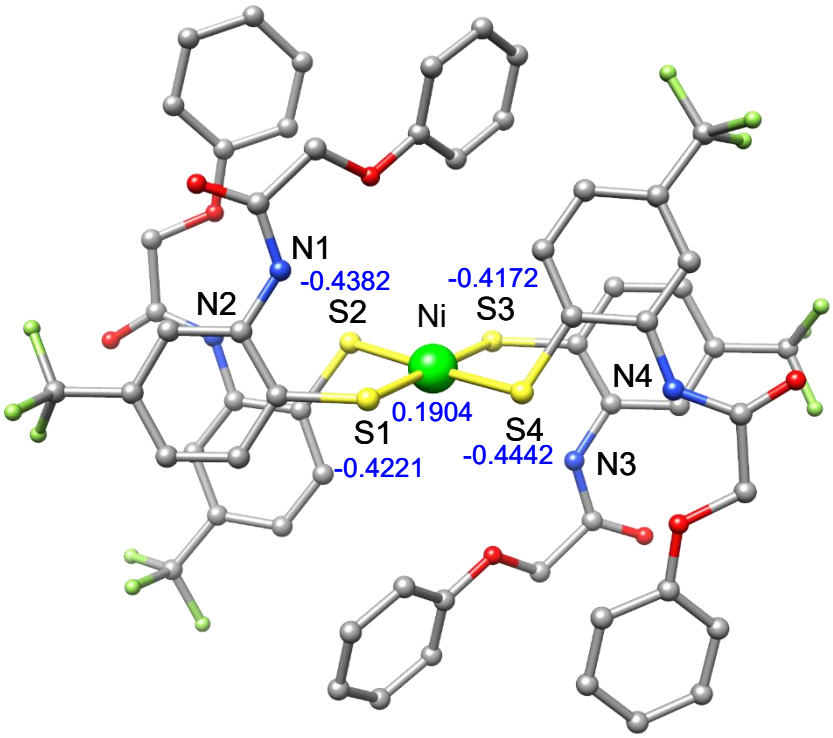

Figure S3.46. Geometry-optimized structure of the square-planar (S = 0) dianion of **2** in the gas phase with Mulliken reduced orbital charges. H atoms are omitted for clarity. Input coordinates taken from the X-ray crystal structure of **2**.

Table S3.8. Selected bond distances (Å) and bond angles (deg) for geometry-optimized structure of $[Ni(S\text{-}o\text{-}OPhCONH\text{-}p\text{-}CF_3\text{-}Ph)_4]^{2-}$ (**2***) in the gas phase (Figure SX).

Atoms	Bond Distance (Å)	Atoms	Angle
$Ni\text{-}S_1$	2.258	$S_1\text{-}Ni\text{-}S_2$	97.4˚
$Ni\text{-}S_2$	2.250	$S_1\text{-}Ni\text{-}S_3$	179.5˚
$Ni\text{-}S_3$	2.260	$S_1\text{-}Ni\text{-}S_4$	82.9˚
$Ni\text{-}S_4$	2.253	$S_2\text{-}Ni\text{-}S_3$	82.5˚
$S_1\text{-}N_1$	3.013	$S_2\text{-}Ni\text{-}S_4$	178.1˚
$S_2\text{-}N_2$	2.905	$S_3\text{-}Ni\text{-}S_4$	82.9˚
$S_3\text{-}N_3$	3.010		
$S_4\text{-}N_4$	2.902		

Table S3.9. Summary of best fit simulation of EXAFS of **1** and **2** as solids.

	Nearest-Neighbor Ligand Environment [a]				
Sample	**Atom [c]**	**R(Å) [d]**	**C.N. [e]**	**σ^{2} [f]**	**F' [g]**
1 (solid)	S	2.22	4	3.76	1.05
2 (solid)					

[a/b] - Independent metal-ligand scattering environments.
[c] - Scattering atoms: N (nitrogen), O (oxygen), C (carbon).
[d] - Metal-ligand bond length.
[e] - Metal-ligand coordination number.
[f] - Debye-Waller factor (Å x 10^3).
[g] - Number of degrees of freedom weighted mean square deviation between data and fit.

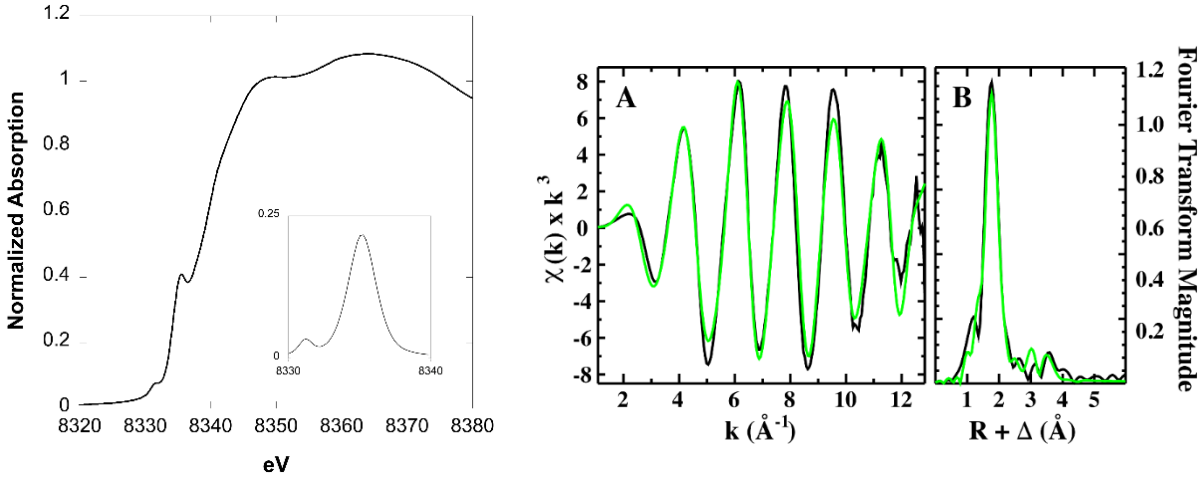

Figure S3.47. *Left*: Ni K-edge XANES for **1** from as-isolated material. Inset contains zoom-in of pre-edge region. *Right*: Raw k^3-weighted EXAFS data (panel A; black) and phase shifted Fourier transform EXAFS (panel B; black) of **1** with best-fit simulation (green).

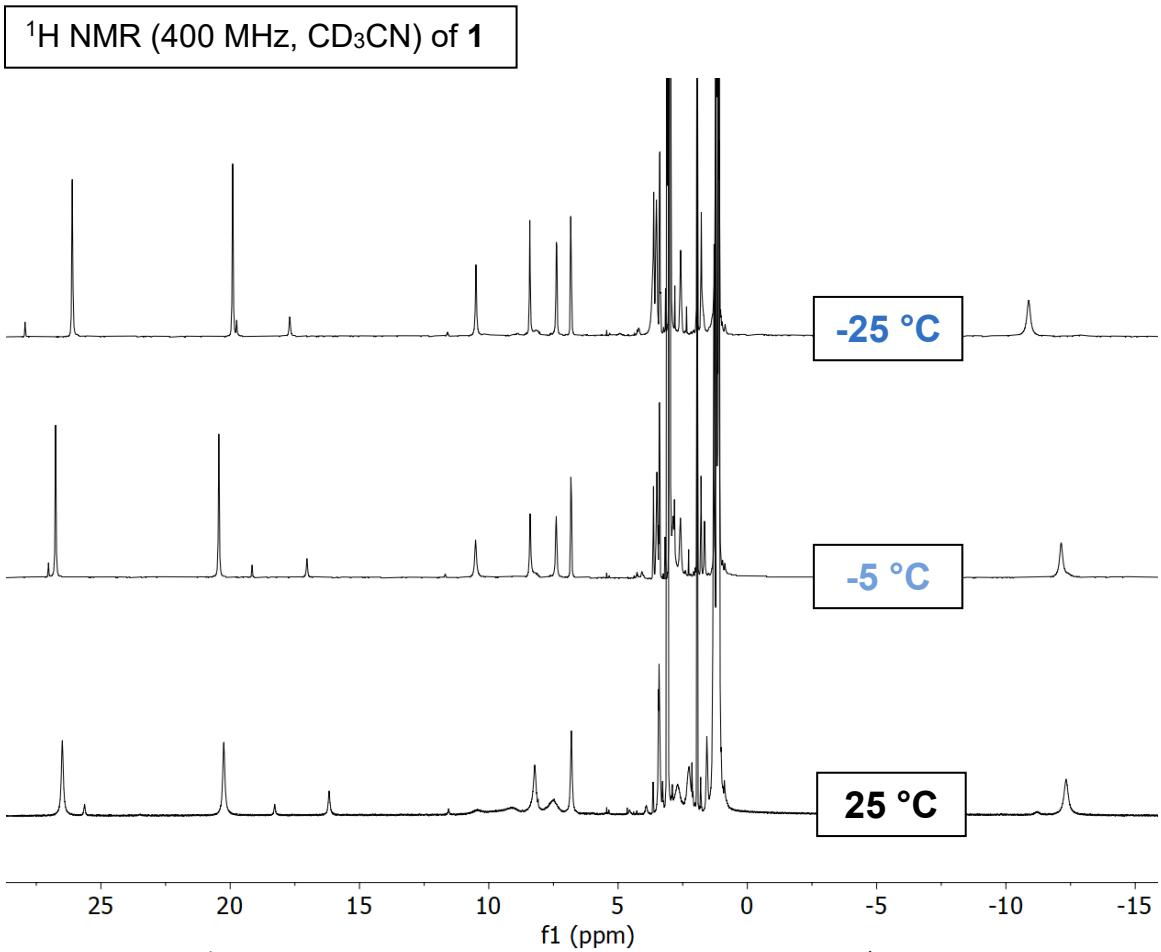

Figure S3.49. ^{1}H NMR (400 MHz, CD_3CN) of $(Et_4N)_2$[Ni(S-*o*-^{i}BuCONH-*p*-CF_3-Ph)$_4$] (**1**) at various temperatures. Residual CH_3CN is observed at 1.94 ppm.

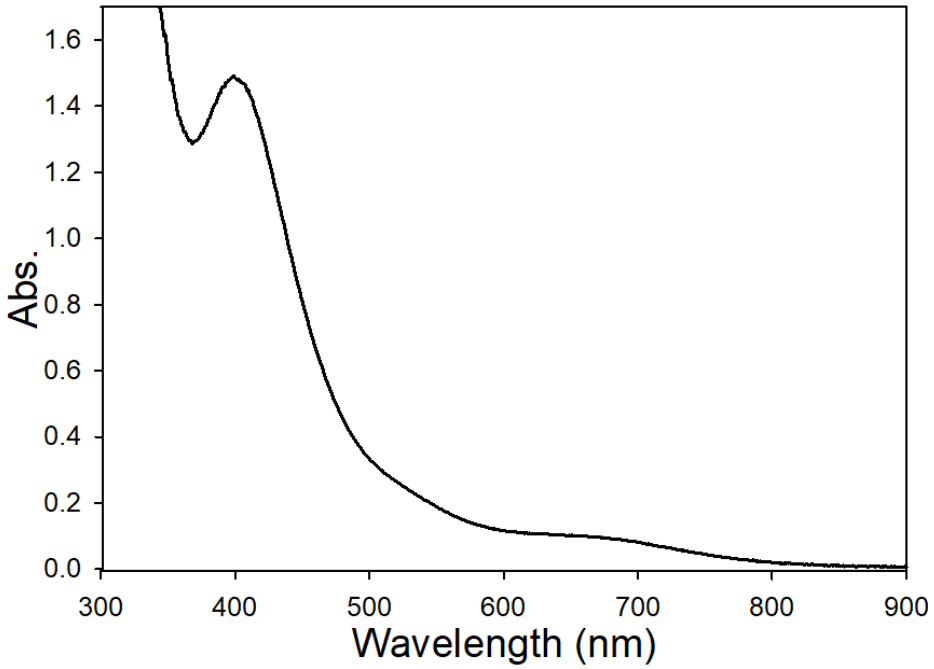

Figure S3.50. UV-vis spectrum of Et_2O insoluble product from reaction of **1** with $FcBF_4$ in MeCN at 25 ˚C.

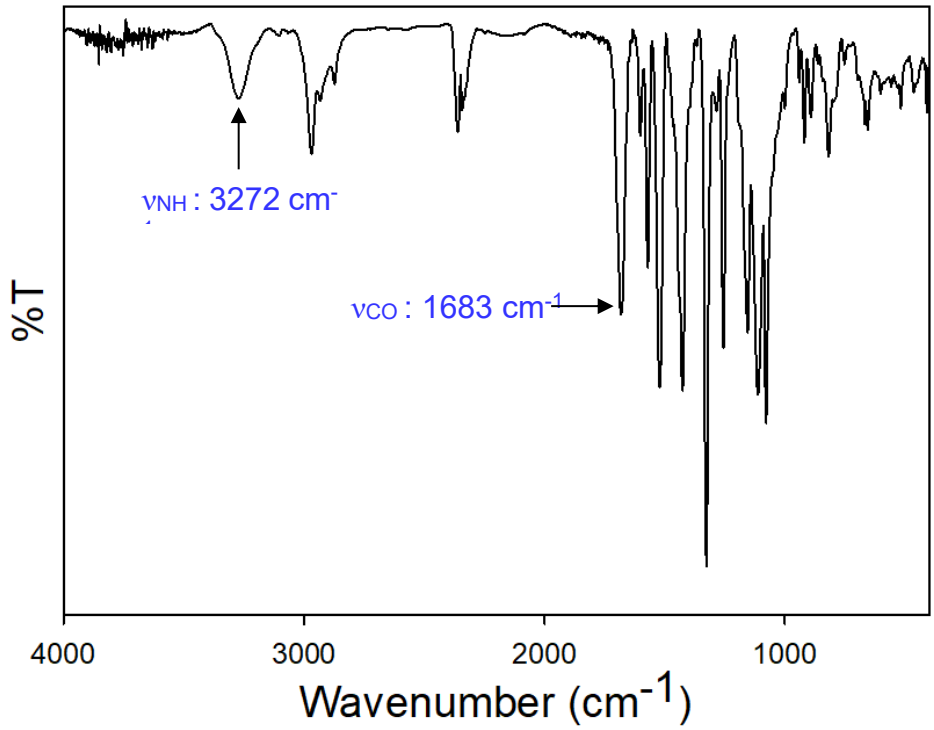

Figure S3.51. Solid-state FTIR spectrum of Et_2O insoluble product from reaction of **1** with $FcBF_4$ in a KBr matrix at RT.

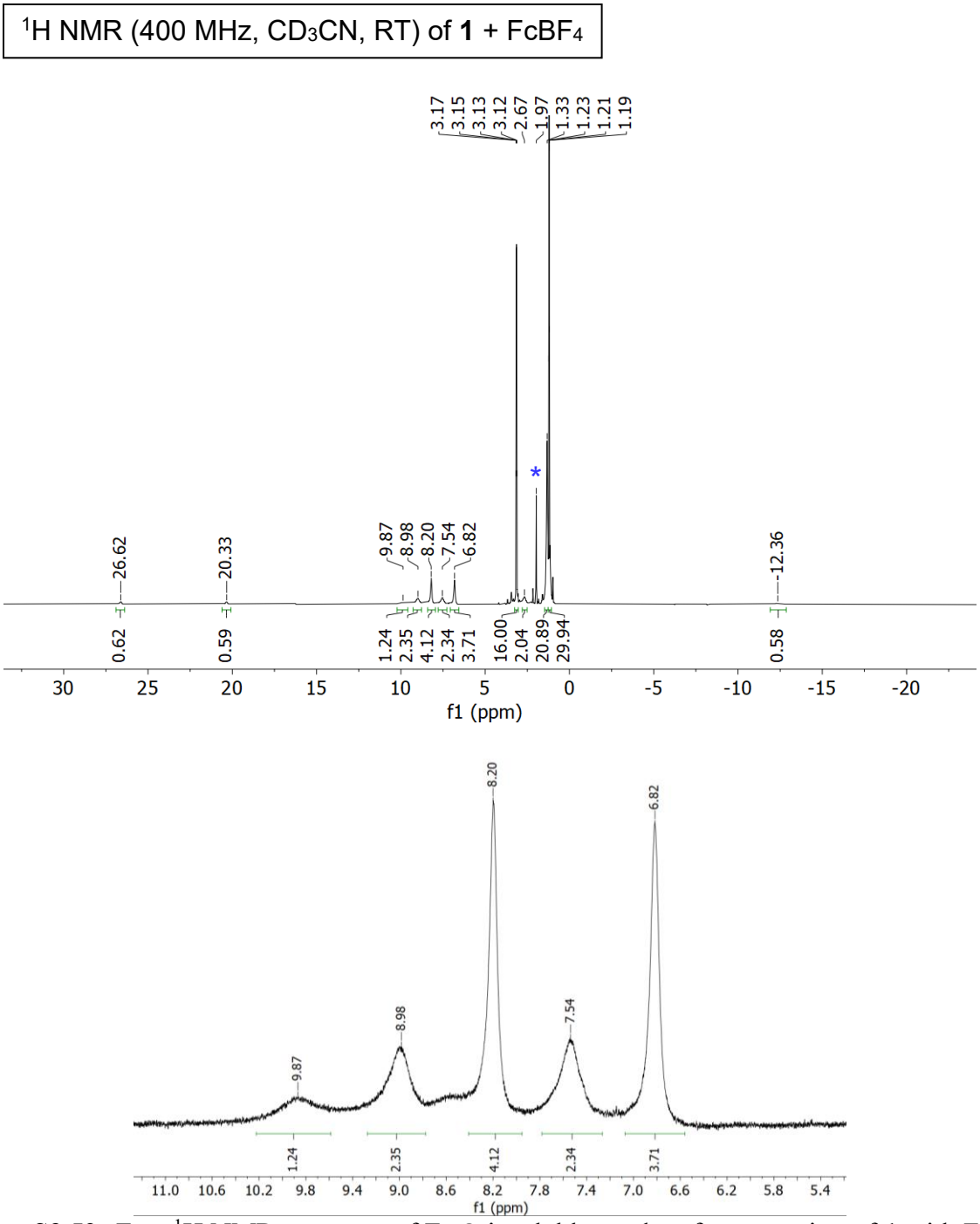

Figure S3.52. *Top:* ^{1}H NMR spectrum of Et_2O insoluble product from reaction of **1** with $FcBF_4$ in CD_3CN at RT (δ vs. protio signal). *Bottom:* expansion of 5 - 11 ppm region. Residual CH_3CN is observed at 1.94 ppm and is indicated with *.

^{1}H NMR (400 MHz, CD_3CN, RT)

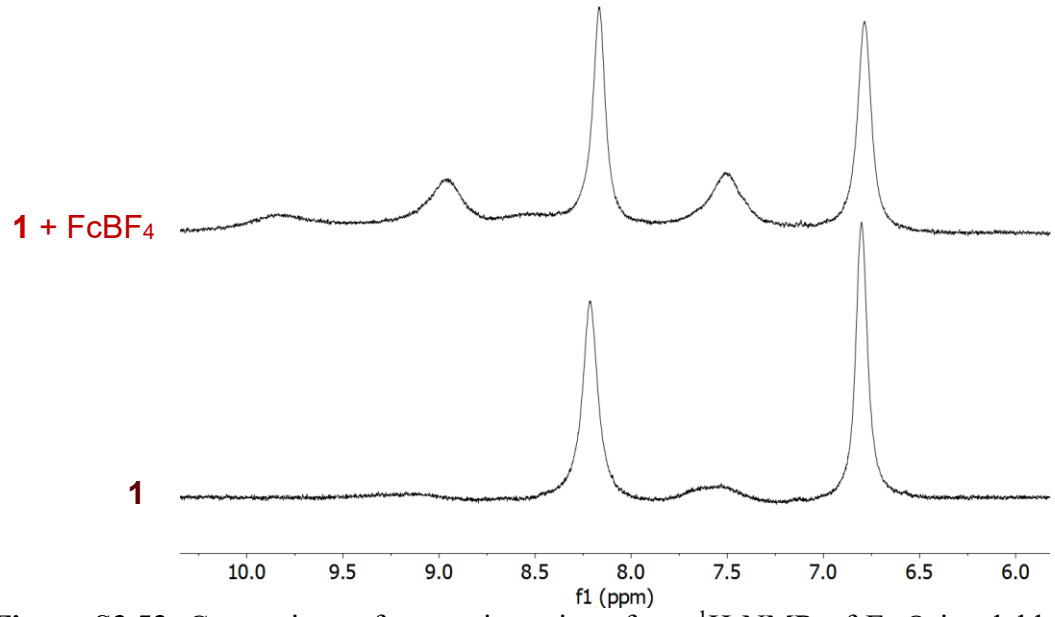

Figure S3.53. Comparison of aromatic regions from ^{1}H NMR of Et_2O insoluble product from reaction of **1** with $FcBF_4$ (*top*) and **1** (bottom) in CD_3CN at RT (δ vs. protio signal).

^{19}F NMR (376 MHz, CD_3CN, RT) of **1** + $FcBF_4$

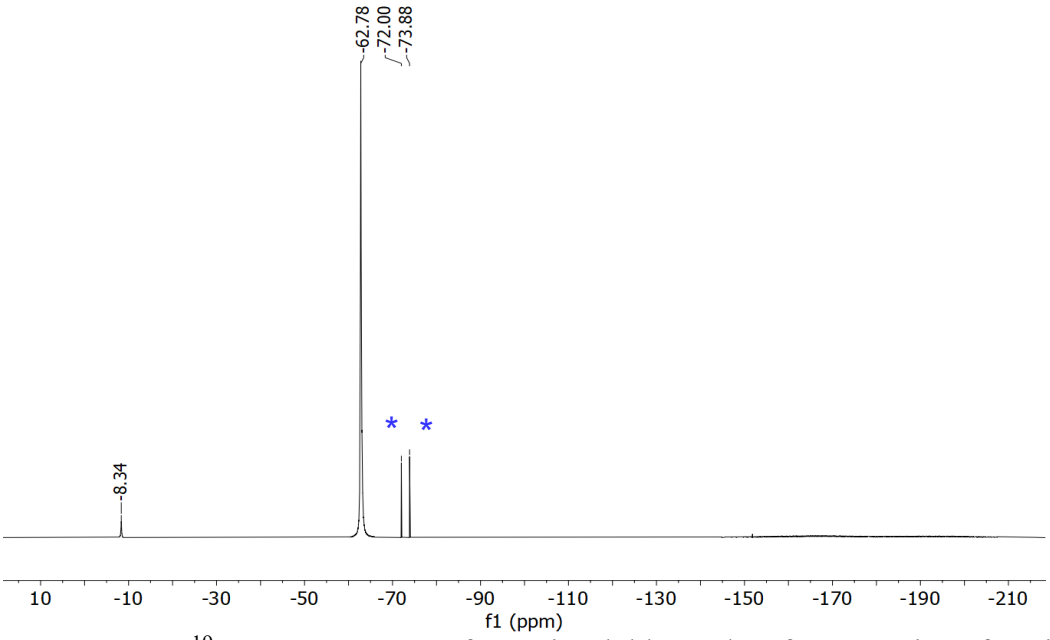

Figure S3.54. ^{19}F NMR spectrum of Et_2O insoluble product from reaction of **1** with $FcBF_4$ in CD_3CN at RT. The peaks at -72.00 and -73.88 ppm are from BF_4 and are indicated with *.

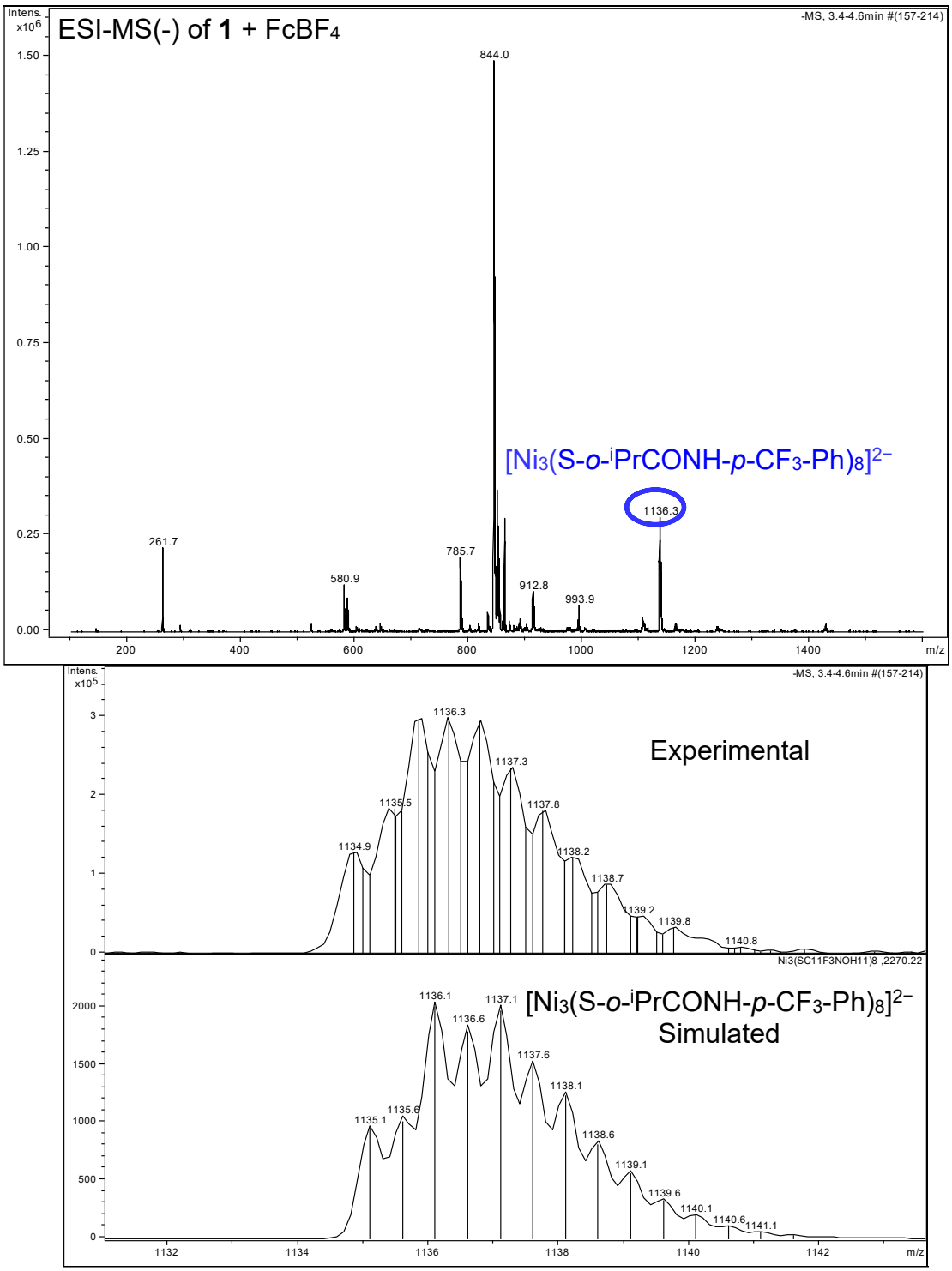

Figure S3.55. *Top:* Low-resolution ESI-MS(-) (negative mode) of Et_2O insoluble product from reaction of **1** with $FcBF_4$ in MeCN. *Bottom*: experimental and simulated theoretical isotopic distribution peak at *m/z*: 1136.6.

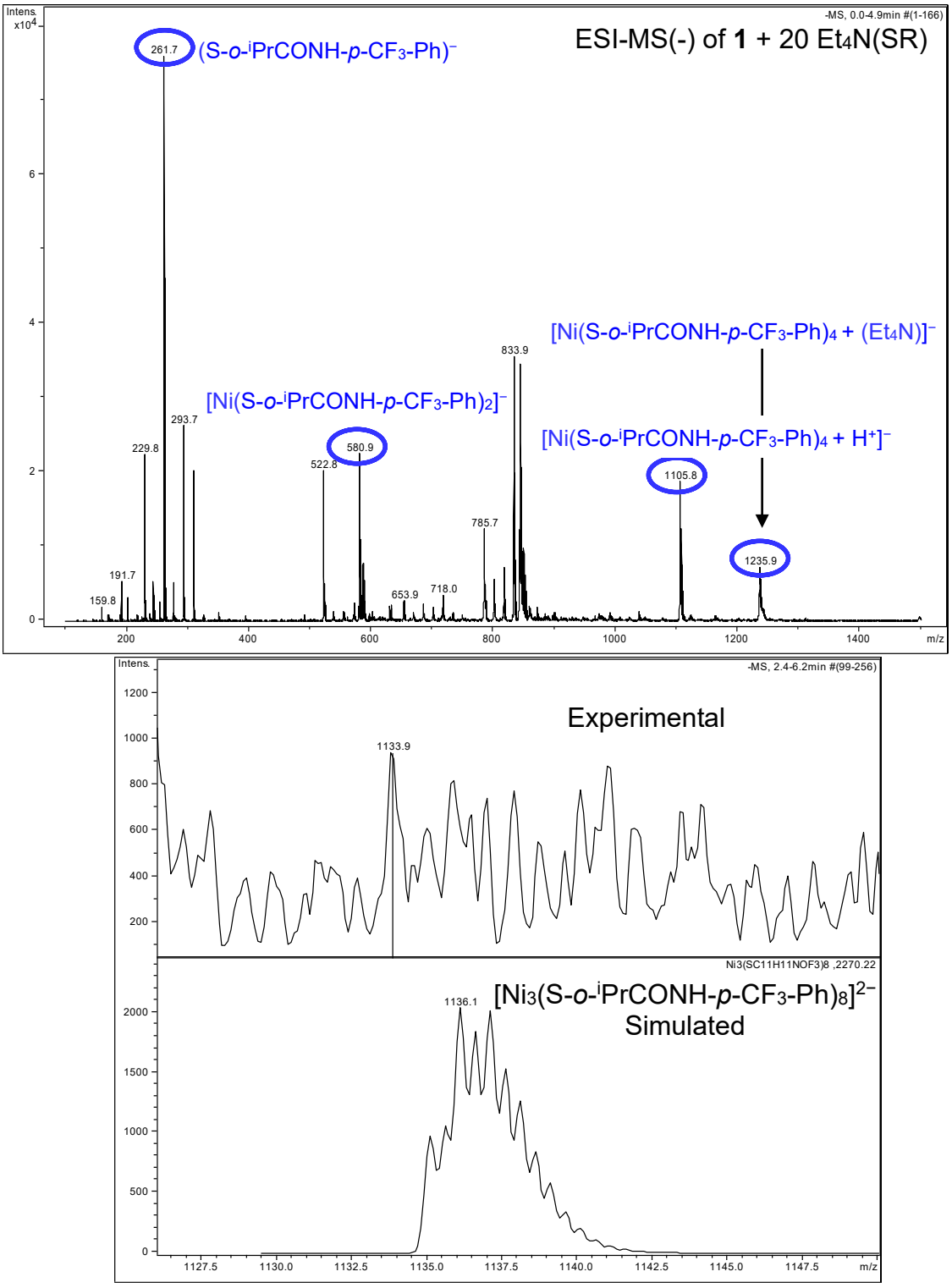

Figure S3.56. *Top:* Low-resolution ESI-MS(-) (negative mode) of $(Et_4N)_2$[Ni(S-*o*-^{i}PrCONH-*p*-CF_3-Ph)$_4$] (**1**) with 20 mol-equiv. of (Et_4N)(S-*o*-^{i}PrCONH-*p*-CF_3-Ph) in MeCN. *Bottom*: experimental and simulated theoretical isotopic distribution peak at *m/z*: 1136.1.

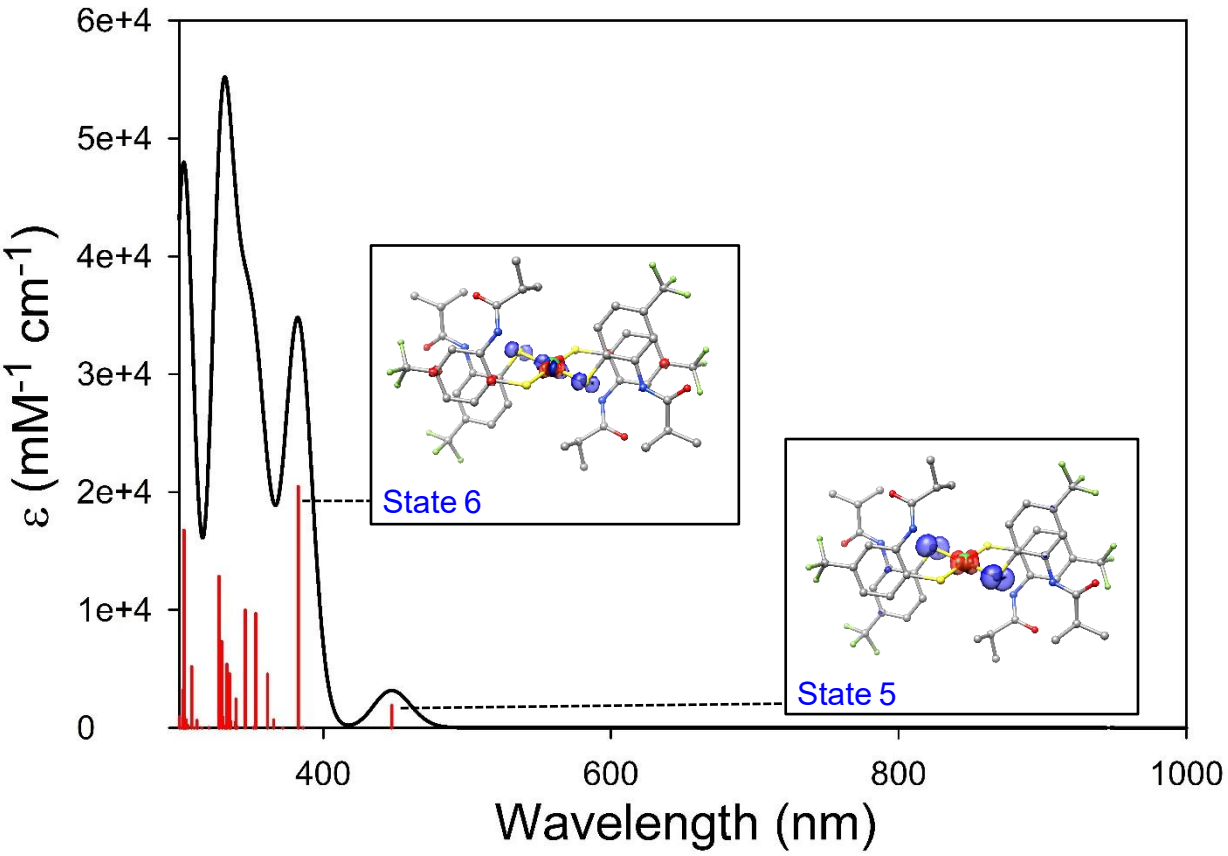

Figure S3.57. TD-DFT calculated optical absorption spectrum of **1(SqPl)*** with gaussian distribution (black line) and optical transitions (red ticks). (*Insets*) Electron difference densities for select transitions, blue lobes reflect loss of electron density, while red lobes reflect increased electron density in the transitions.

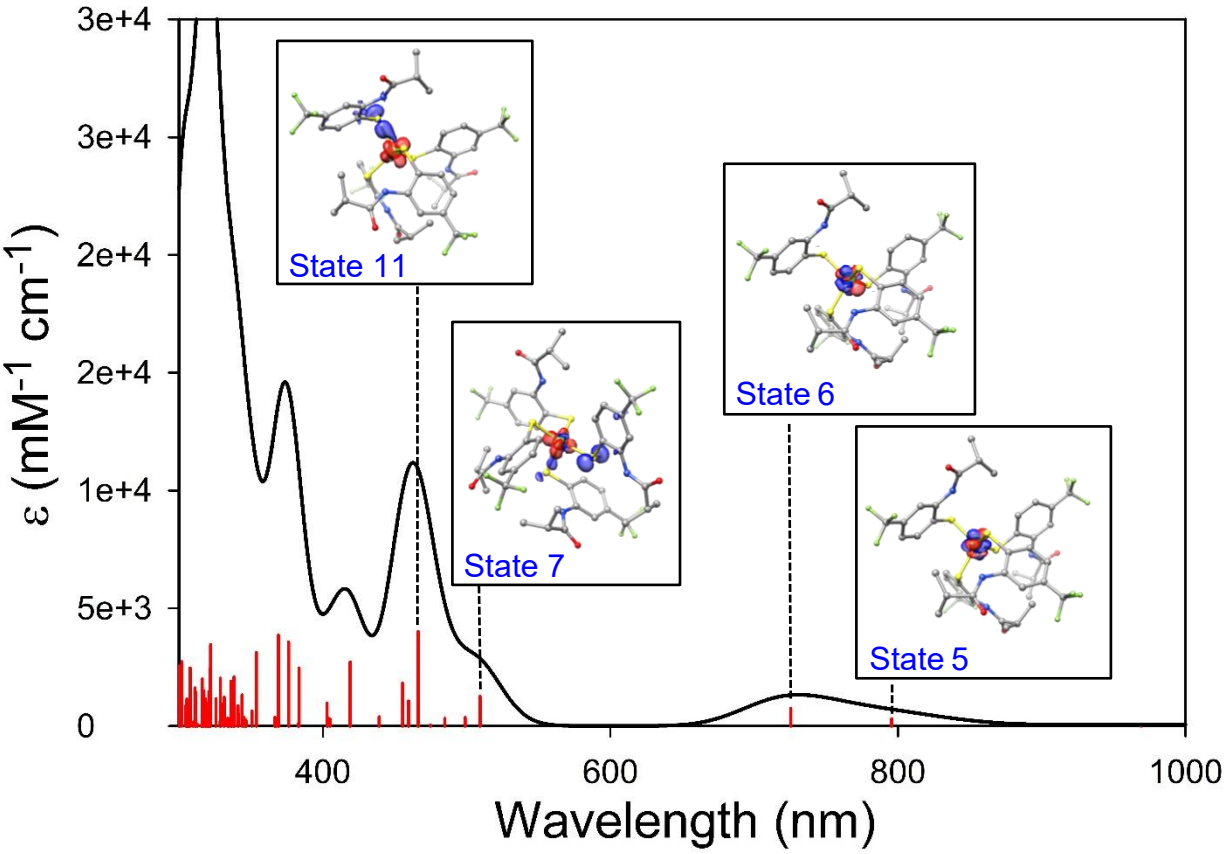

Figure S3.58. TD-DFT calculated optical absorption spectrum of **1(T_d)*** with gaussian distribution (black line) and optical transitions (red ticks). (*Insets*) Electron difference densities for select transitions, blue lobes reflect loss of electron density, while red lobes reflect increased electron density in the transitions.

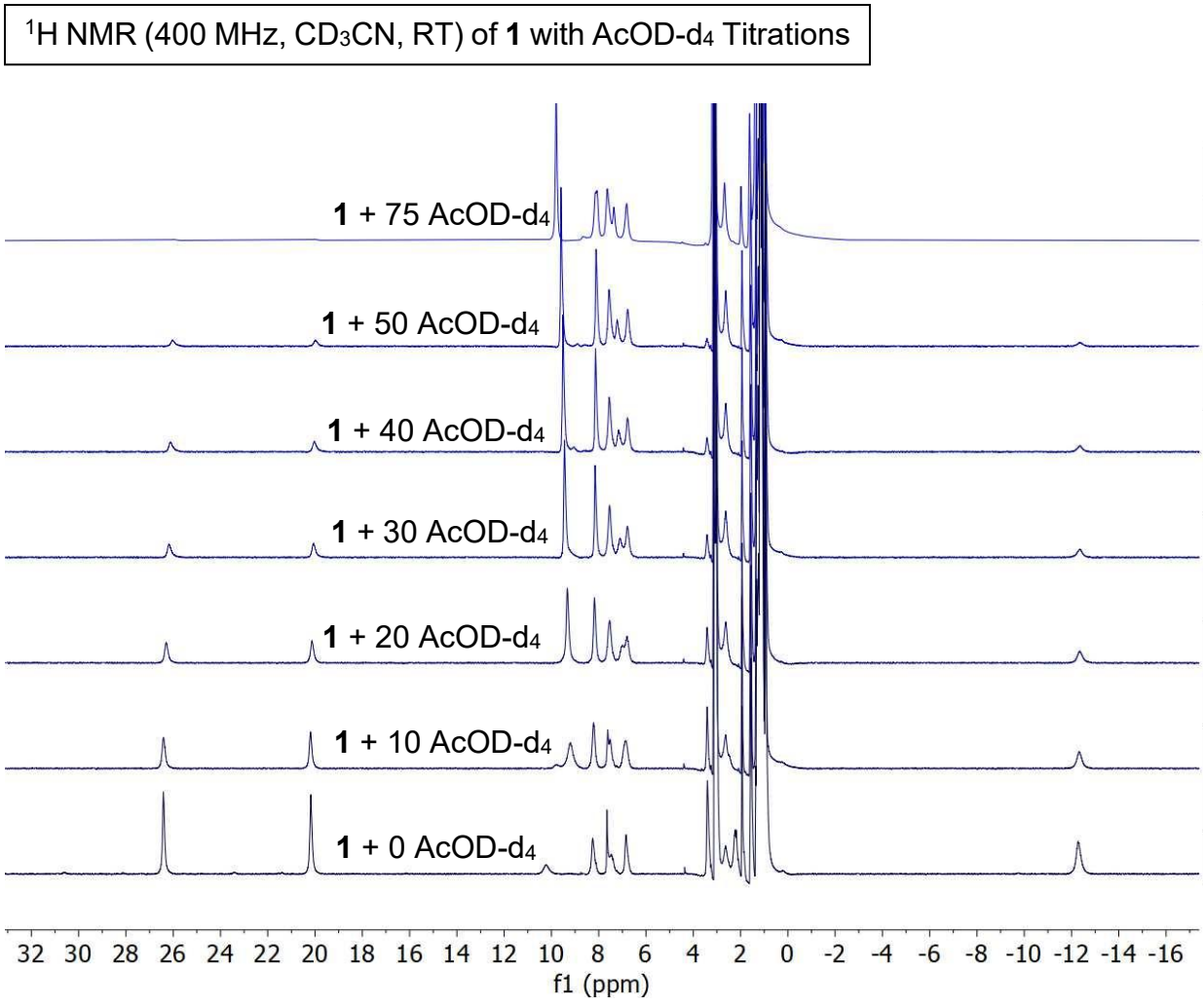

Figure S3.59. ^{1}H NMR (400 MHz, CD_3CN, RT) of $(Et_4N)_2$[Ni(S-*o*-^{i}PrCONH-*p*-CF_3-Ph)$_4$] (**1**) with addition of various equivalents of AcOD-d_4. Residual CH_3CN is observed at 1.94 ppm.

Table S3.10. Number of protons from the integration of the peaks associated with tetrahedral monomer of **1** obtained from the addition of AcOD-d$_4$ into solutions **1** (Figure S3.59). Integrations are relative to the expected number of protons for the peak at ~3 ppm of the Et_4N^+ salt.

Equivalents of AcOD-d$_4$	Integration of H$^+$ (~26 ppm)	Integration of H$^+$ (~20 ppm)	Integration of H$^+$ (~ -12 ppm)	Integration of H$^+$ (Aromatic)
0.0	2.22	2.25	1.91	4.87
10.0	1.43	1.39	1.21	7.31
20.0	1.05	1.04	0.89	10.04
30.0	0.75	0.73	0.62	10.51
40.0	0.58	0.59	0.45	11.33
50.0	0.38	0.35	0.28	12.06
75.0	0.13	0.14	0.10	13.24

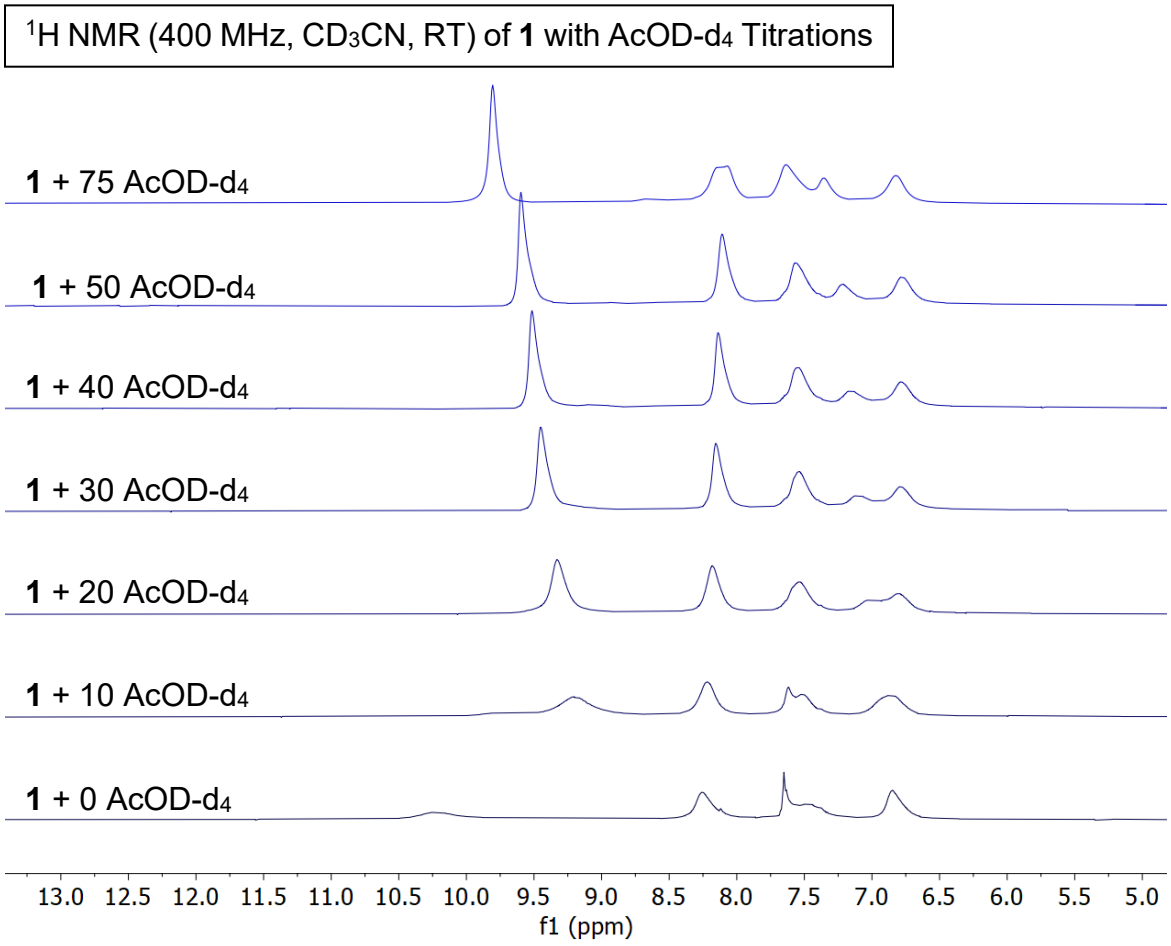

Figure S3.60. Magnified region of the ^{1}H NMR of $(Et_4N)_2$[Ni(S-*o*-^{i}PrCONH-*p*-CF_3-Ph)$_4$] (**1**) with addition of various equivalents of AcOD-d$_4$. Residual CH_3CN is observed at 1.94 ppm.

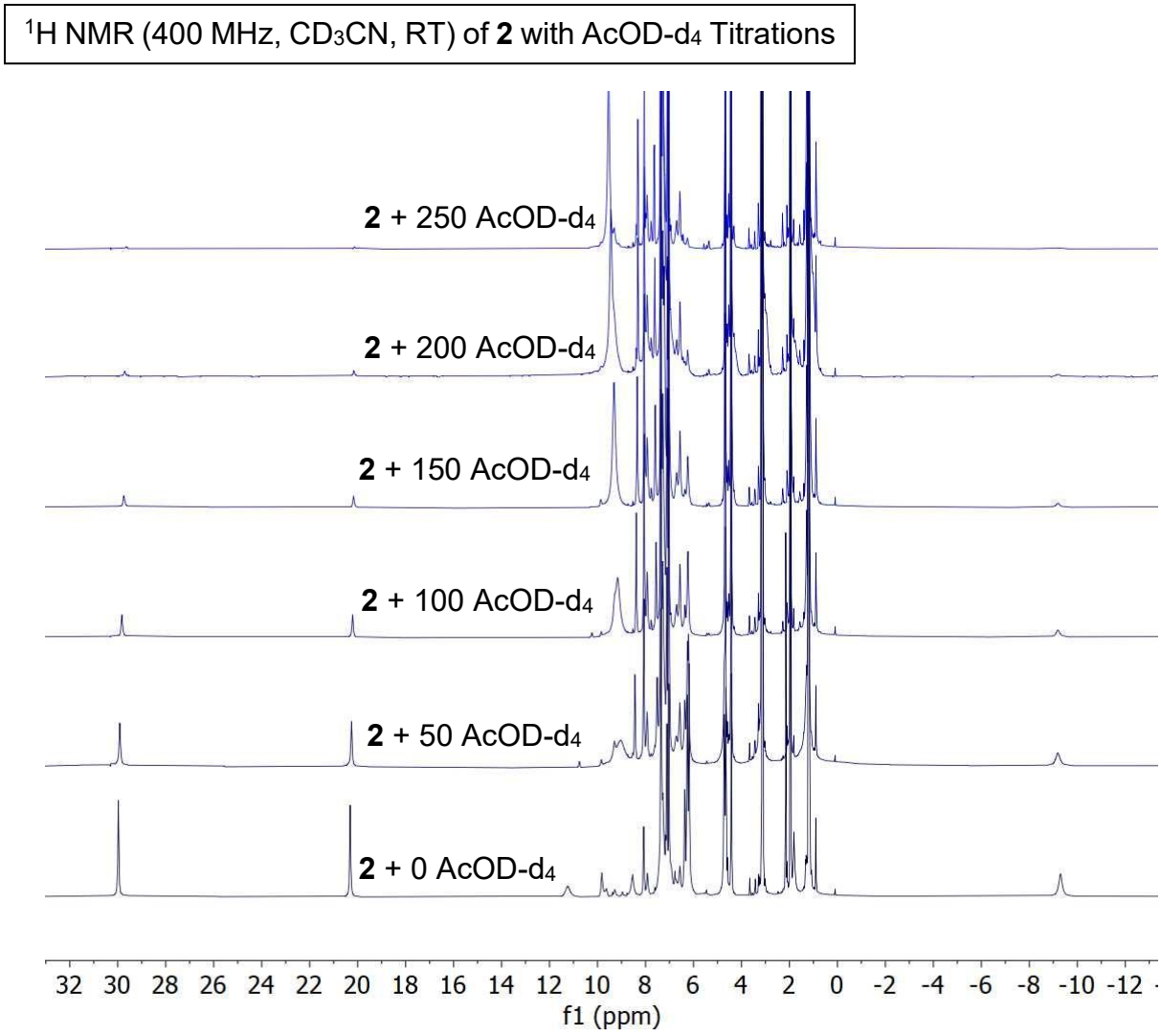

Figure S3.61. ^{1}H NMR (400 MHz, CD_3CN, RT) of $(Et_4N)_2$[Ni(S-*o*-OPhCONH-*p*-CF_3-Ph)$_4$] (**2**) with addition of various equivalents of AcOD-d_4. Residual CH_3CN is observed at 1.94 ppm.

Table S3.11. Number of protons from the integration of the peaks associated with tetrahedral monomer of **1** obtained from the addition of AcOD-d_4 into solutions **1** (Figure S3.61). Integrations are relative to the expected number of protons for the peak at ~3 ppm of the Et_4N^+ salt.

Equiv. of AcOD-d_4	Integration of H^+ (~30 ppm)	Integration of H^+ (~20 ppm)	Integration of H^+ (~ -9 ppm)
0.0	1.88	1.86	1.53
50.0	1.25	1.18	0.86
100.0	0.56	0.60	0.41
150.0	0.29	0.32	0.05
200.0	0.11	0.12	0.02
250.0	0.06	0.07	0.00

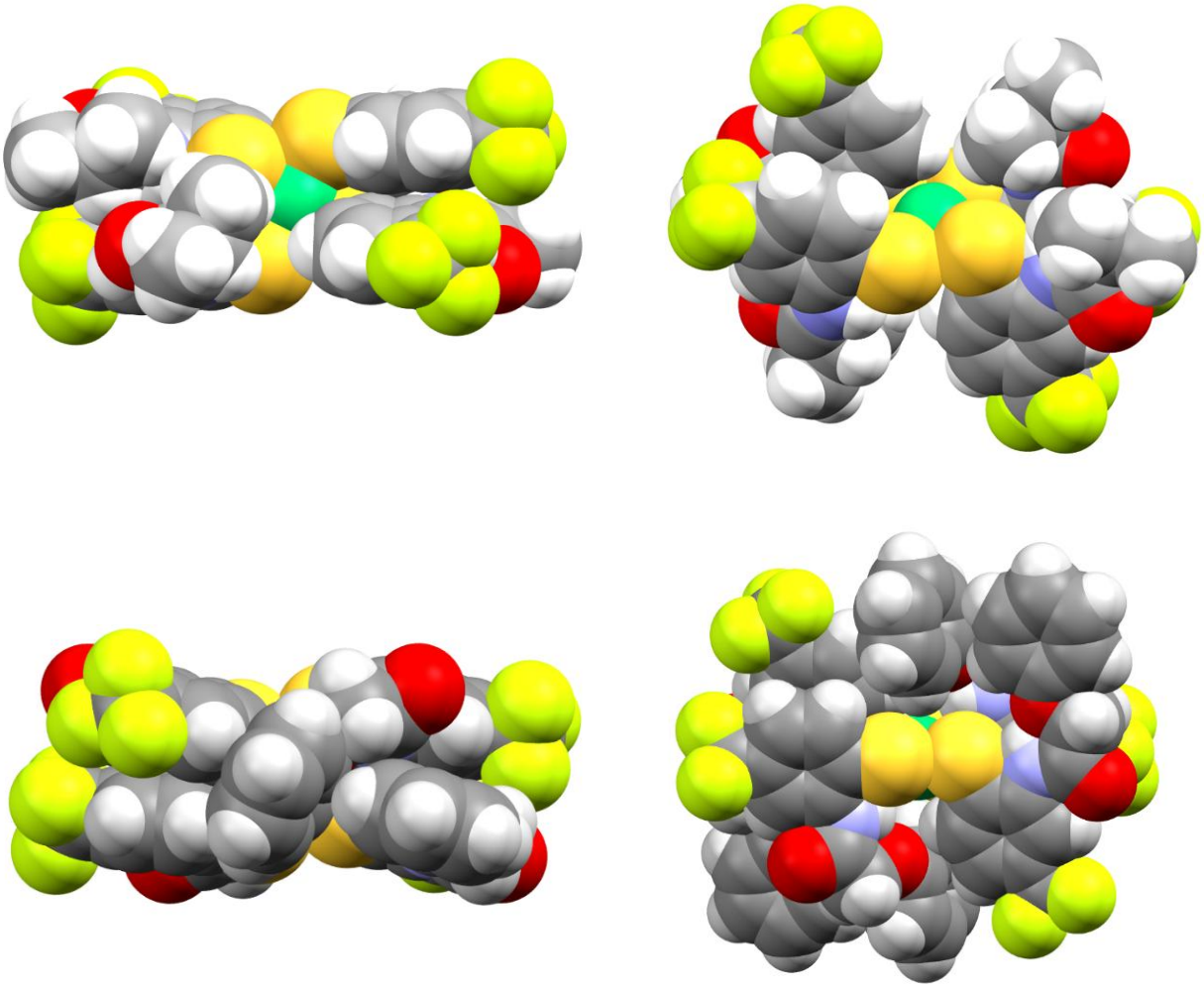

Figure S3.62. Space filling model from a (*left*) top-down view and (*right*) side view of (*top*) [Ni(S-*o*-^{i}PrCONH-*p*-CF_3-Ph)$_4$]$^{2-}$ (**1**) and (*bottom*) [Ni(S-*o*-OPhCONH-*p*-CF_3-Ph)$_4$]$^{2-}$ (**2**) gotten from the XRD crystal structure.

Electrochemistry

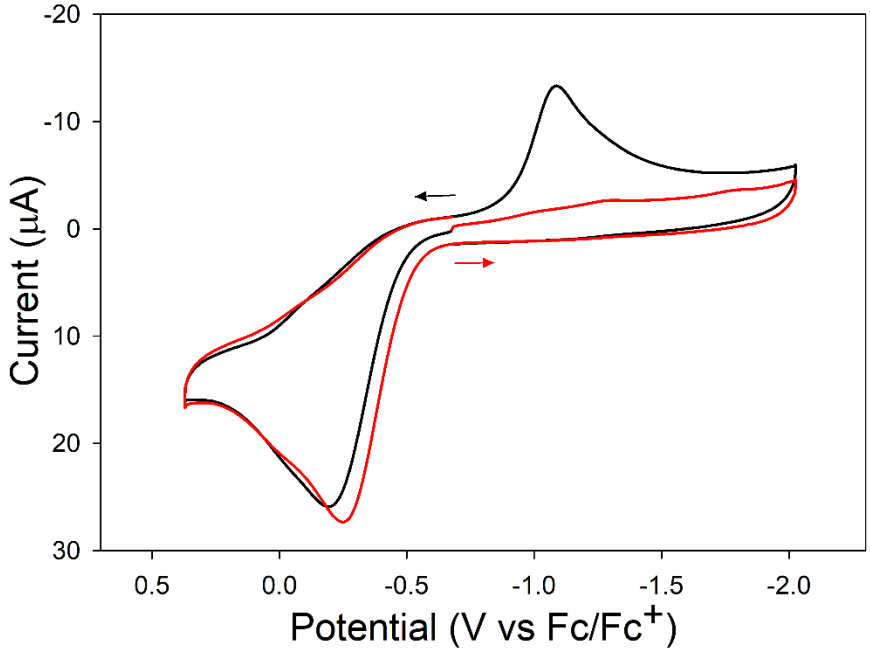

Figure S3.63. CVs' of (Et_4N)(S-*o*-^{i}PrCONH-*p*-CF_3-Ph) in MeCN at RT (0.25 M $^{n}Bu_4NPF_6$ supporting electrolyte, glassy carbon working electrode, 100 mV/s scan rate). Arrow shows direction of scan.

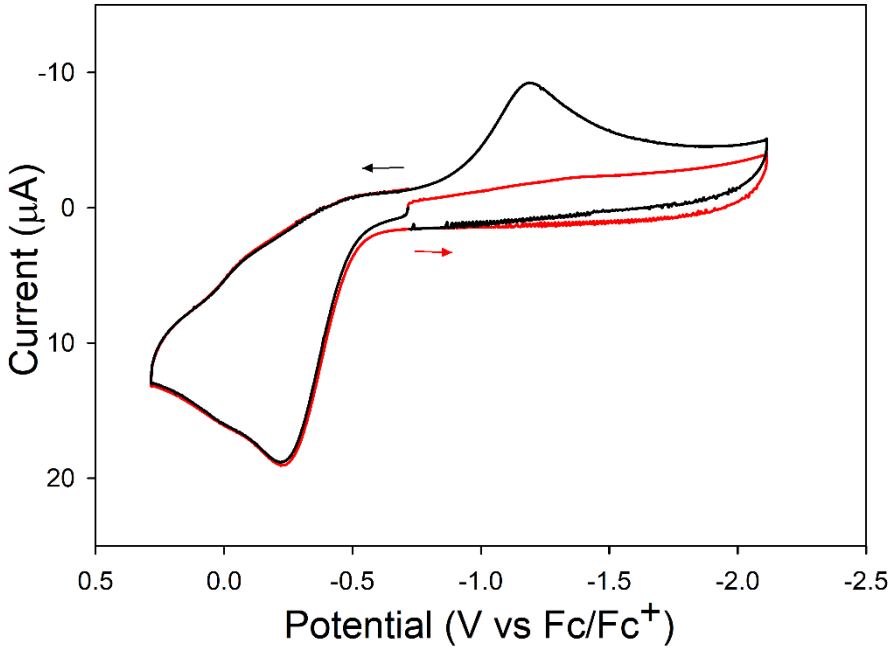

Figure S3.64. CVs' of (Et_4N)(S-*o*-OPhCONH-*p*-CF_3-Ph) in MeCN at RT (0.25 M $^{n}Bu_4NPF_6$ supporting electrolyte, glassy carbon working electrode, 100 mV/s scan rate). Arrow shows direction of scan.

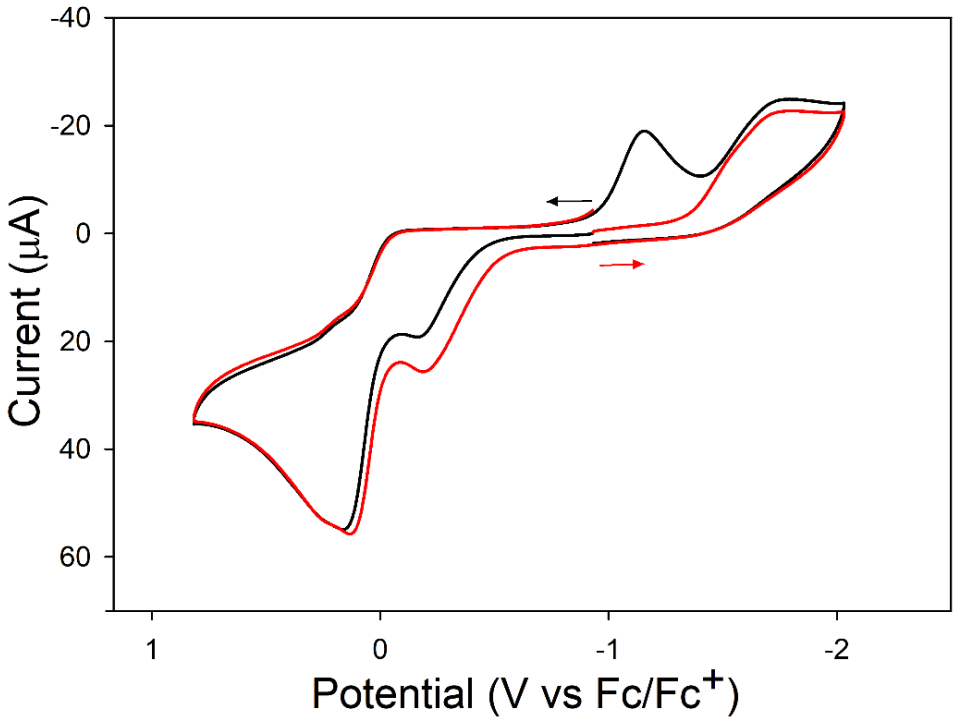

Figure S3.65. CVs' of $(Et_4N)_2$[Ni(S-*o*-OPhCONH-*p*-CF_3-Ph)$_4$] (**2**) in MeCN at RT (0.25 M $^nBu_4NPF_6$ supporting electrolyte, glassy carbon working electrode, 100 mV/s scan rate). Arrow shows direction of scan.

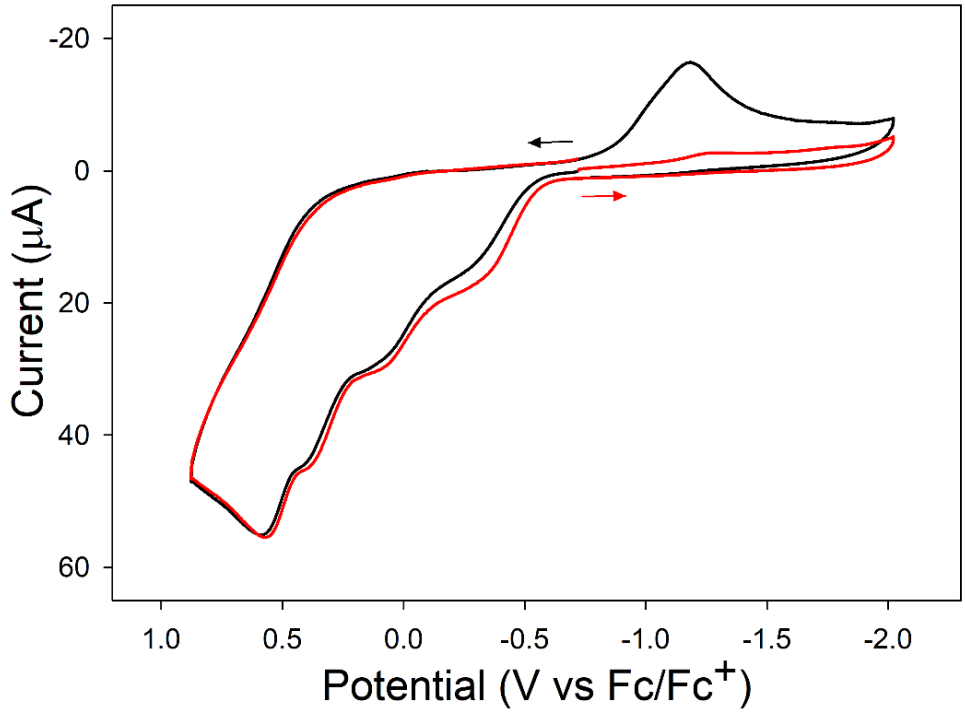

Figure S3.66. CVs' of $(Et_4N)_2$[Zn(S-*o*-^{i}PrCONH-*p*-CF_3-Ph)$_4$] (**4**) in MeCN at RT (0.25 M $^nBu_4NPF_6$ supporting electrolyte, glassy carbon working electrode, 100 mV/s scan rate). Arrow shows direction of scan.

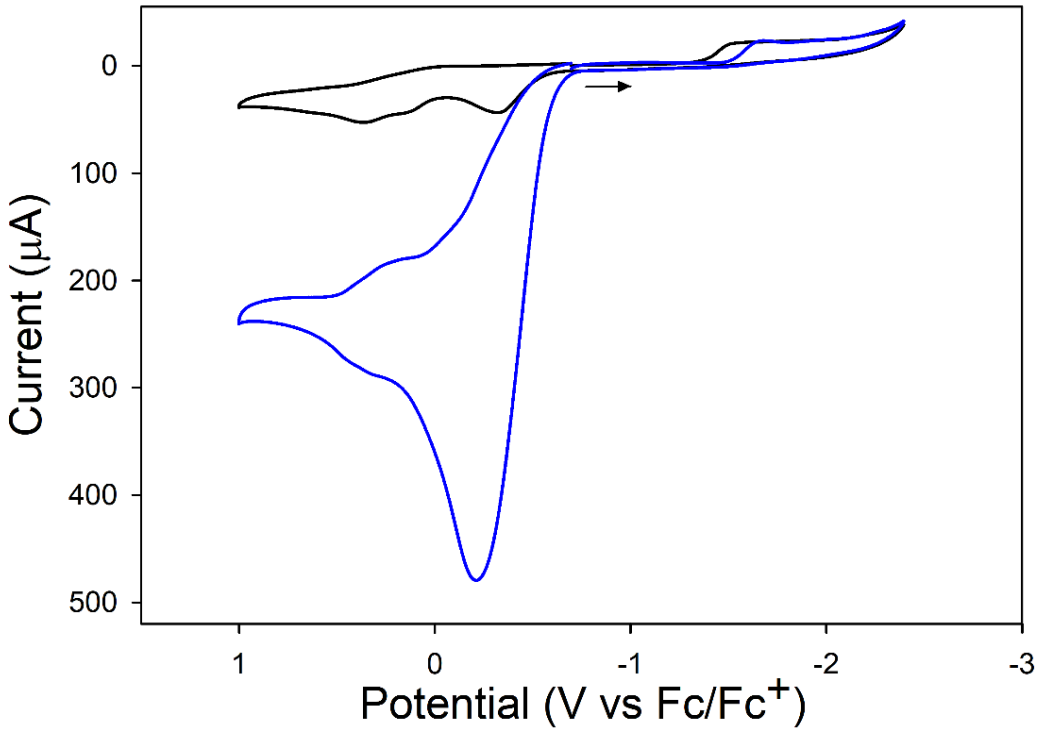

Figure S3.67. CVs' of $(Et_4N)_2[Ni(S\text{-}o\text{-}^{i}PrCONH\text{-}p\text{-}CF_3\text{-}Ph)_4]$ (**1**) (black) and with 20 mol-equiv. $(Et_4N)(S\text{-}o\text{-}^{i}PrCONH\text{-}p\text{-}CF_3\text{-}Ph)$ (blue) in MeCN at RT (0.25 M $^{n}Bu_4NPF_6$ supporting electrolyte, glassy carbon working electrode, 100 mV/s scan rate). Arrow shows direction of scan.

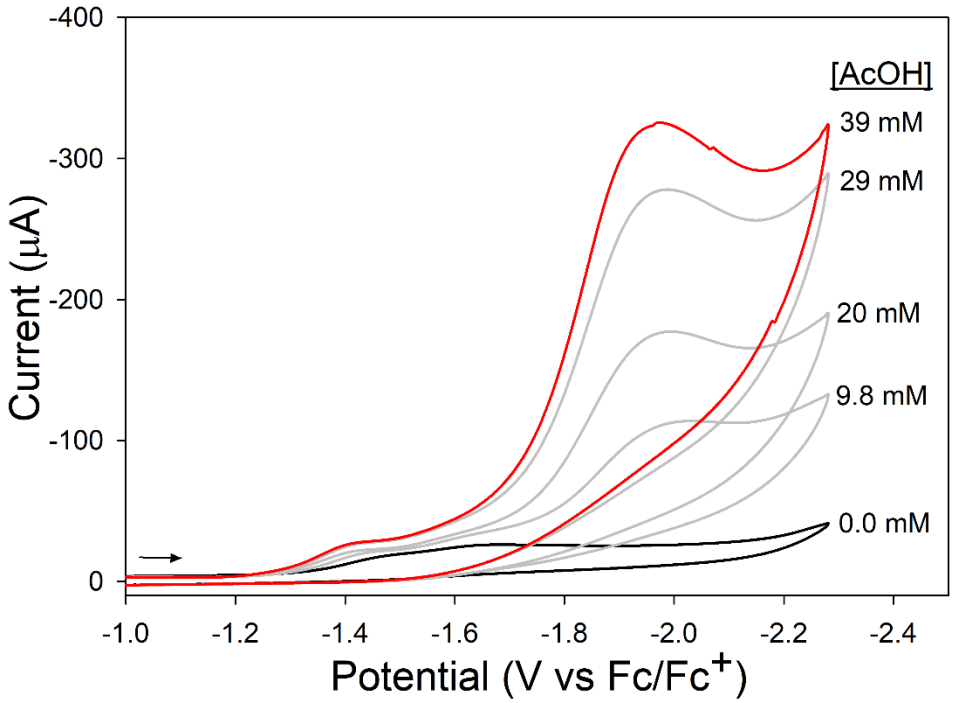

Figure S3.68. CV of $(Et_4N)_2[Ni(S\text{-}o\text{-}OPhCONH\text{-}p\text{-}CF_3\text{-}Ph)_4]$ (**2**) after titrating with AcOH in in MeCN at RT (0.25 M $^nBu_4NPF_6$ supporting electrolyte, glassy carbon working electrode, 100 mV/s scan rate). Arrow shows direction of scan.

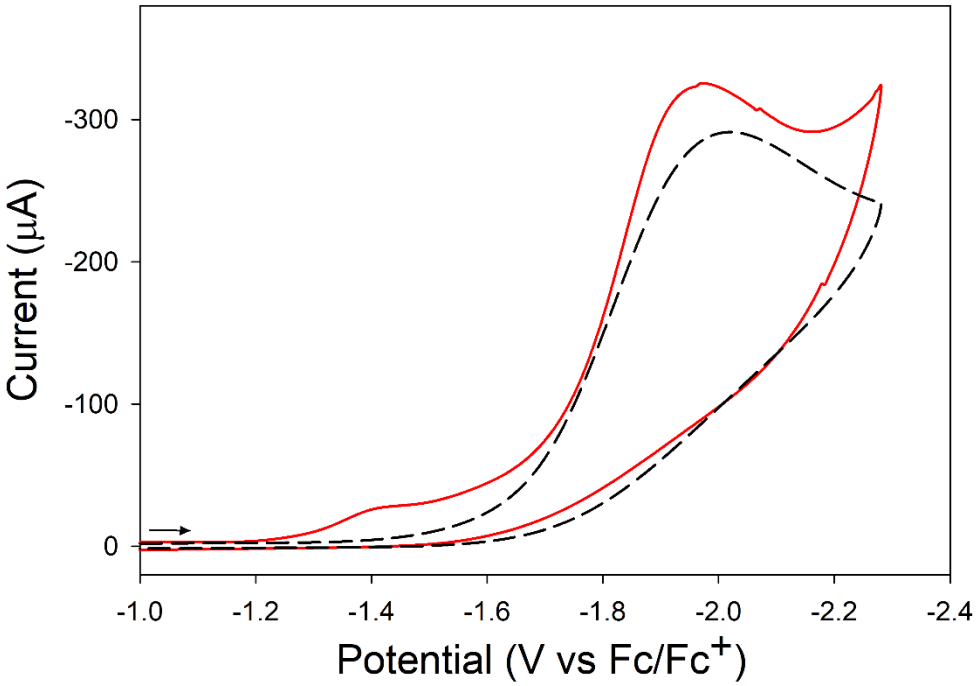

Figure S3.69. CV of $(Et_4N)_2[Ni(S\text{-}o\text{-}OPhCONH\text{-}p\text{-}CF_3\text{-}Ph)_4]$ (**2**) (red) and rinse test experiment (black-dashed) both with AcOH (39 mM) in MeCN at RT (0.25 M $^nBu_4NPF_6$ supporting electrolyte, glassy carbon working electrode, 100 mV/s scan rate). Arrow shows direction of scan.

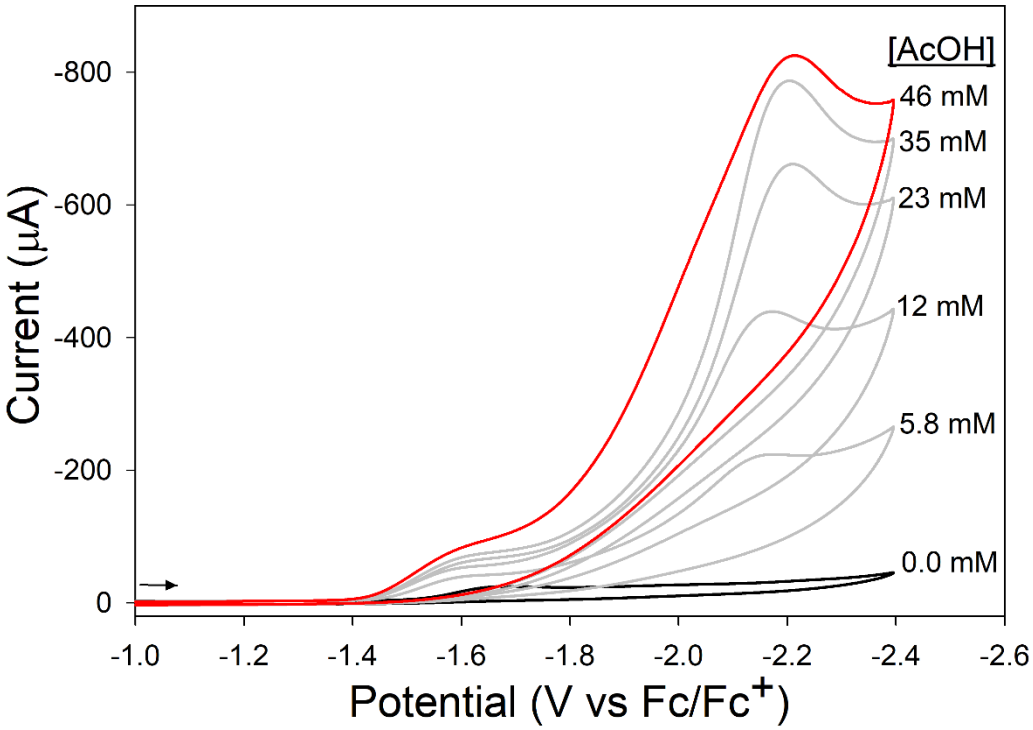

Figure S3.70. CV of $(Et_4N)_2$[Ni(S-*o*-^{i}PrCONH-*p*-CF_3-Ph)$_4$] (**1**) (black) with 20 mol-equiv. (Et_4N)(S-*o*-^{i}PrCONH-*p*-CF_3-Ph) after titrating AcOH in MeCN at RT (0.25 M ^{n}Bu$_4$NPF$_6$ supporting electrolyte, glassy carbon working electrode, 100 mV/s scan rate). Arrow shows direction of scan.

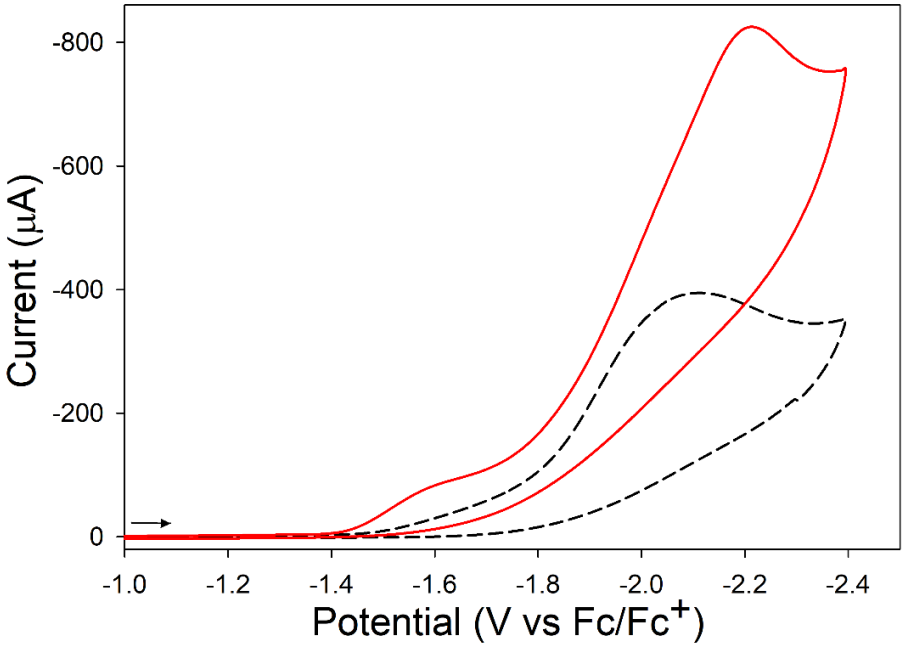

Figure S3.71. CV of $(Et_4N)_2$[Ni(S-*o*-^{i}PrCONH-*p*-CF_3-Ph)$_4$] (**1**) (red) and rinse test experiment (black-dashed) both with AcOH (46 mM) and 20 mol-equiv. (Et_4N)(S-*o*-^{i}PrCONH-*p*-CF_3-Ph) in MeCN at RT with (0.25 M ^{n}Bu$_4$NPF$_6$ supporting electrolyte, glassy carbon working electrode, 100 mV/s scan rate). Arrow shows direction of scan.

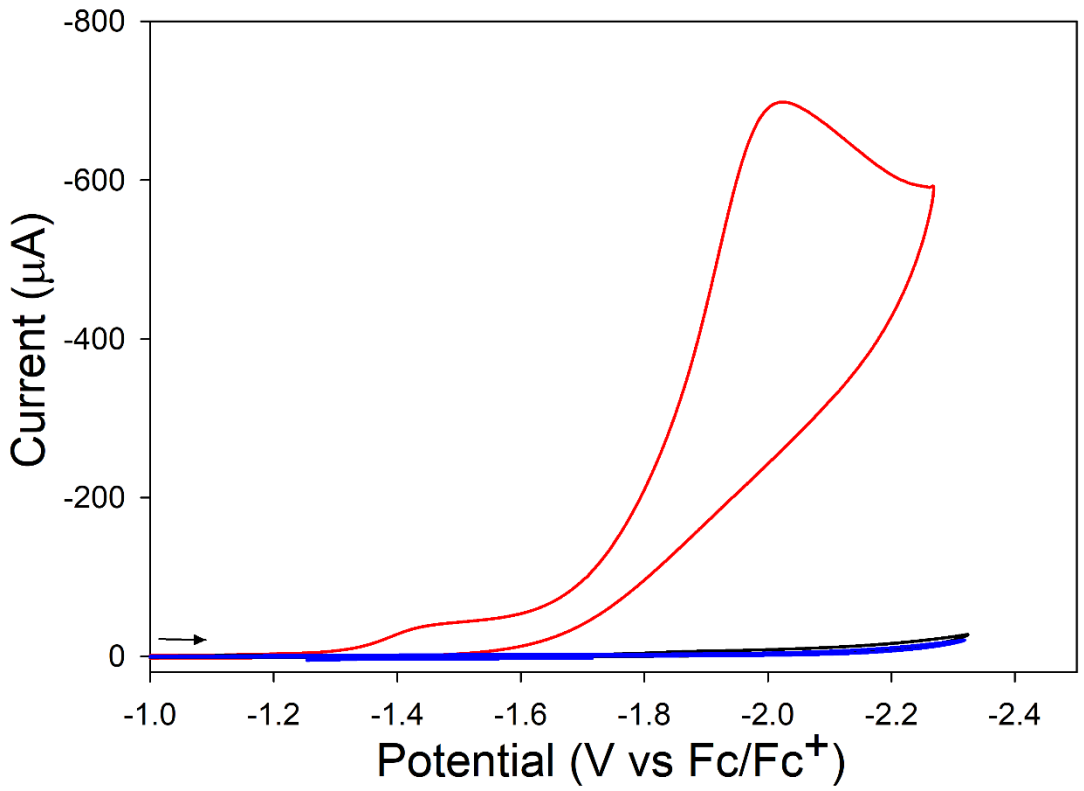

Figure S3.72. Control experiments of CV's of $(Et_4N)_2[Ni(S\text{-}o\text{-}^{i}PrCONH\text{-}p\text{-}CF_3\text{-}Ph)_4]$ (**1**) (red), $(Et_4N)[Zn(S\text{-}o\text{-}^{i}PrCONH\text{-}p\text{-}CF_3\text{-}Ph)_4]$ (**4**) (blue), and $(Et_4N)(S\text{-}o\text{-}^{i}PrCONH\text{-}p\text{-}CF_3\text{-}Ph)$ (black) with ~46 mM AcOH in MeCN at RT with (0.25 M $^{n}Bu_4NPF_6$ supporting electrolyte, glassy carbon working electrode, 100 mV/s scan rate). Arrow shows direction of scan.

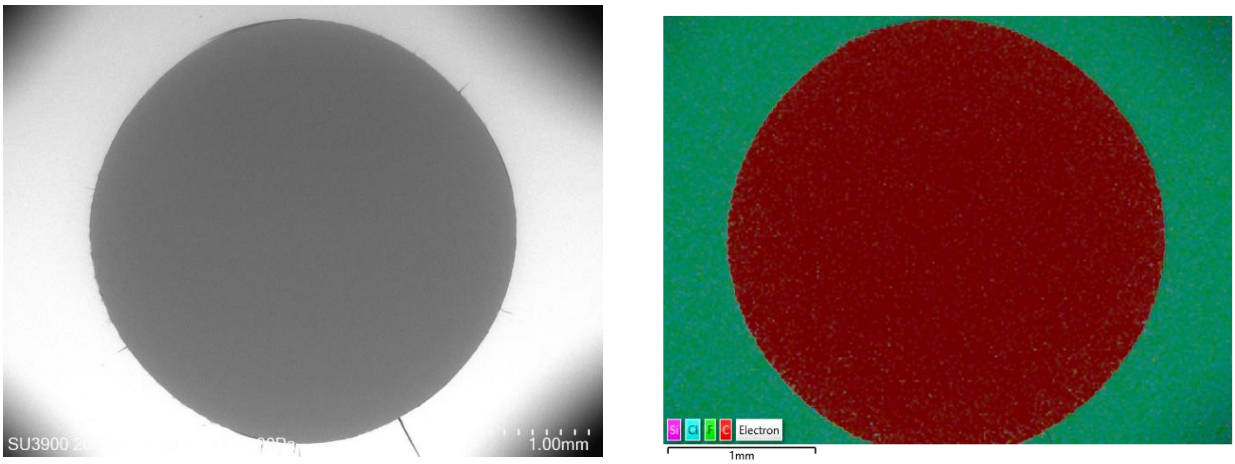

Figure S3.73. Full (*left*) SEM image and (*right*) EDS image of the glassy carbon working electrode prior to electrolyzed material being deposited.

Table S3.12. EDS elemental analysis results for the bare glassy carbon working electrode from image shown in Figure S3.75.

Element	Weight%	Weight% Sigma
C	82.1	0.1
F	12.9	0.1
Cl	5.0	0.0

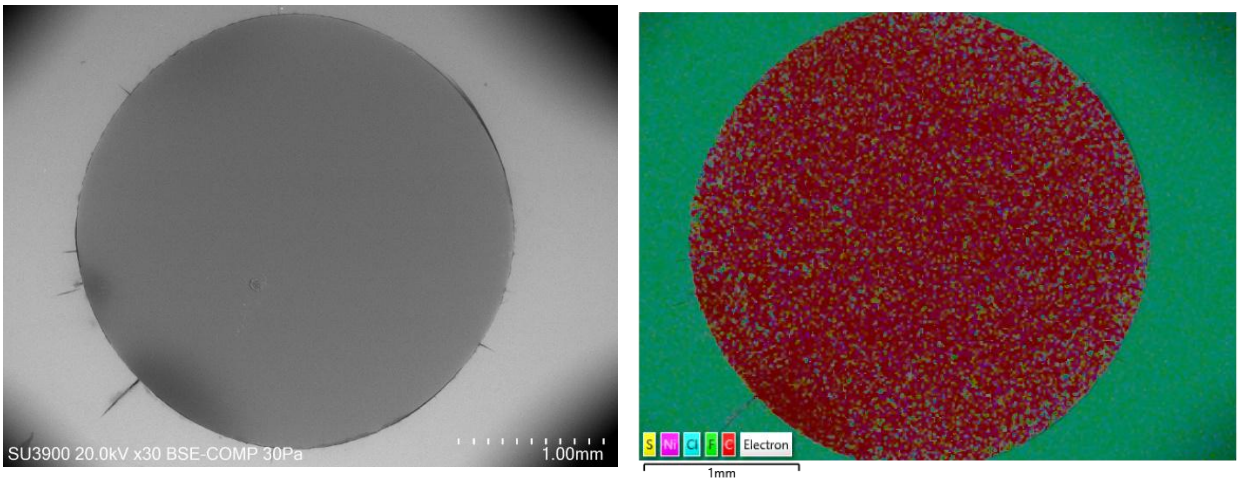

Figure S3.74. Full (left) SEM image and (right) EDS image of electrolyzed glassy carbon working from 1.7 mM solution of **1** and 24.6 mol-equiv. for 0.5 h.

Table S3.13. EDS elemental analysis results for the bare glassy carbon working electrode from image shown in Figure S3.76.

Element	Weight%	Weight% Sigma
C	0.0	0.0
F	48.5	0.3
Cl	35.9	0.2
Ni	14.8	0.2
S	0.8	0.1

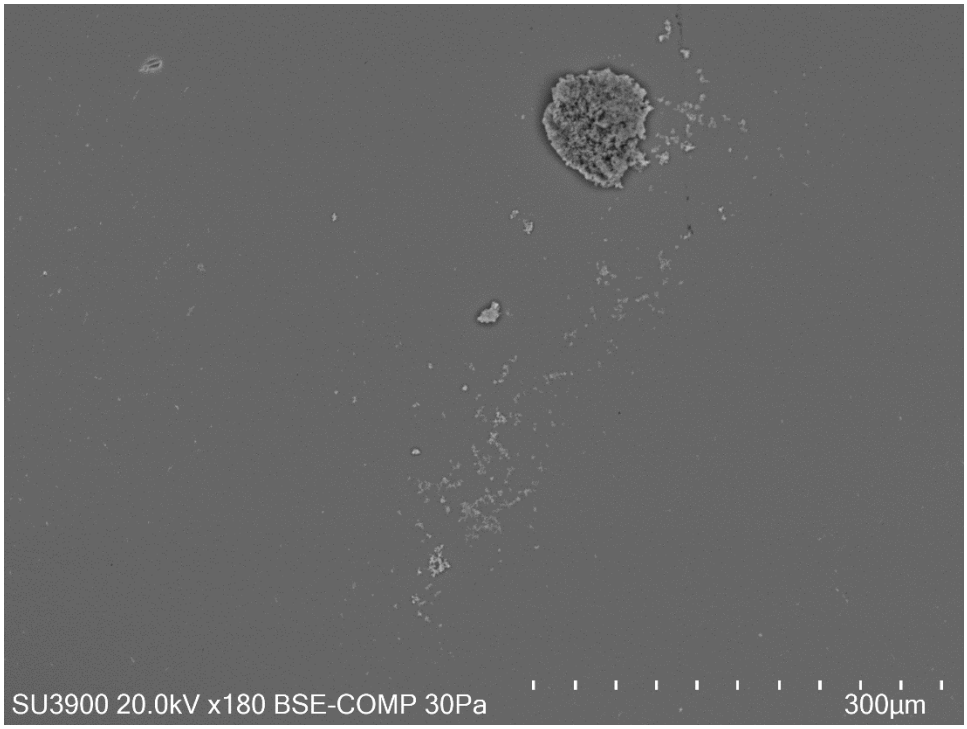

Figure S3.75. Zoom-in of SEM image of electrolyzed glassy carbon working from 1.7 mM solution of **1** and 24.6 mol-equiv. for 0.5 h.

Table S3.14. EDS elemental analysis results for the bare glassy carbon working electrode from image shown in Figure S3.77.

Element	Weight%	Weight% Sigma
C	0.0	0.0
F	0.0	0.0
Cl	3.1	0.2
Ni	**89.6**	**0.3**
S	**6.6**	**0.2**
K	0.6	0.2

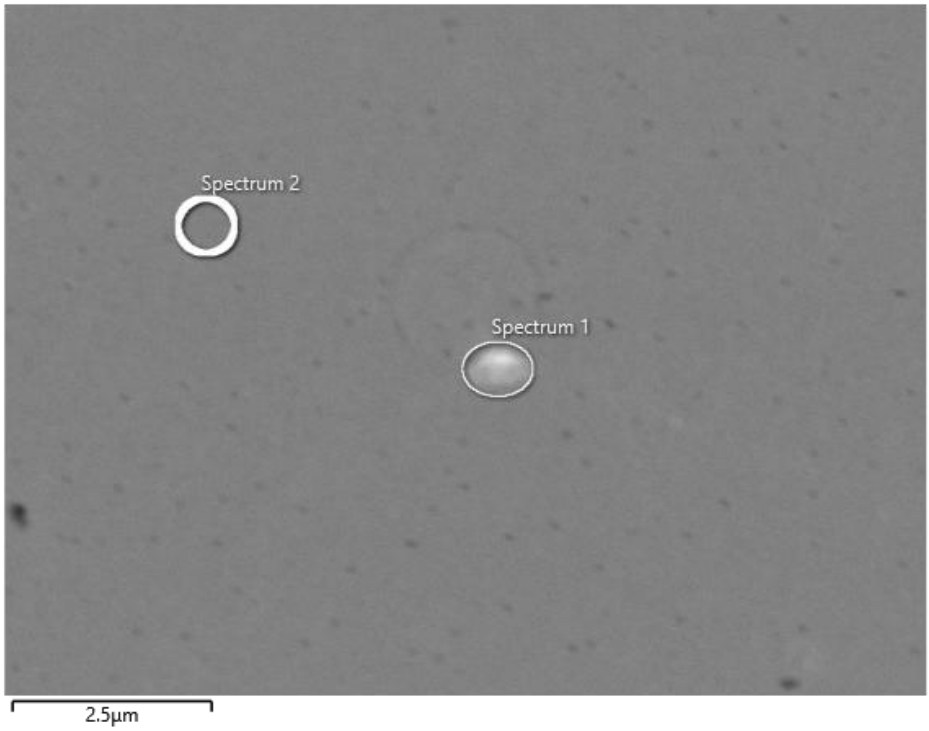

Figure S3.76. Zoom-in of particle from SEM image of electrolyzed glassy carbon working from 1.7 mM solution of **1** and 24.6 mol-equiv. for 0.5 h.

Table S3.15. EDS elemental analysis results for the bare glassy carbon working electrode from image shown in Figure S3.78. Spectra 1 and 2 are from the film and particle deposits.

	Atomic%	
Element	**Spectrum 1**	**Spectrum 2**
C	0.0	0.0
F	0.0	0.0
Cl	3.4	5.3
Ni	**85.4**	**83.1**
S	**11.2**	**11.6**
K	0.0	0.0

Table S3.16. Reported Ni-S containing precatalysts for electrocatalytically active heterogeneous Ni/S films/particles formed under protic and reducing conditions.

Catalyst	Decomposition Product	Decomposition Product Composition[a]	Ref
1	Ni/S film with embedded Ni/S nanoparticles	Ni:S (8:1)	TW
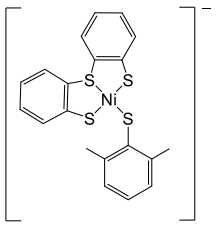	Ni/S nanoparticles	Unknown	95
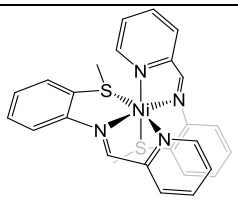	Ni/S film with embedded Ni/S nanoparticles	Ni:S (18:1)	89
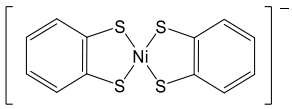	Ni/S film	Ni:S (2:1)	91
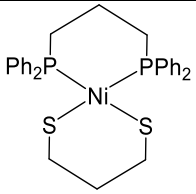	Ni/S containing film	Ni:S (1:1)	90

[a]Composition ratio from atomic percent.

Table S3.17. Löwdin population analysis derived from the DFT calculations (B3LYP/def2-TZVPP) for selected MOs of **1(SqPl)*** ($S = 0$), with an MeCN solvent model using CPCMC. Only s and p contributions were tabulated for S-atoms.

Orbitals	MO#	Energy (eV)	%Ni	%S
LUMO + 3	289	-0.7107	2.6	3.6
LUMO + 2	288	-0.8106	0.5	4.2
LUMO + 1	287	-0.9067	2.8	4.9
LUMO	286	-1.6319	38.9	22.0
HOMO	285	-4.8963	17.6	43.3
HOMO - 1	284	-5.0739	36.3	43.9
HOMO - 2	283	-5.1185	0.4	51.3
HOMO - 3	282	-5.4891	3.0	40.1

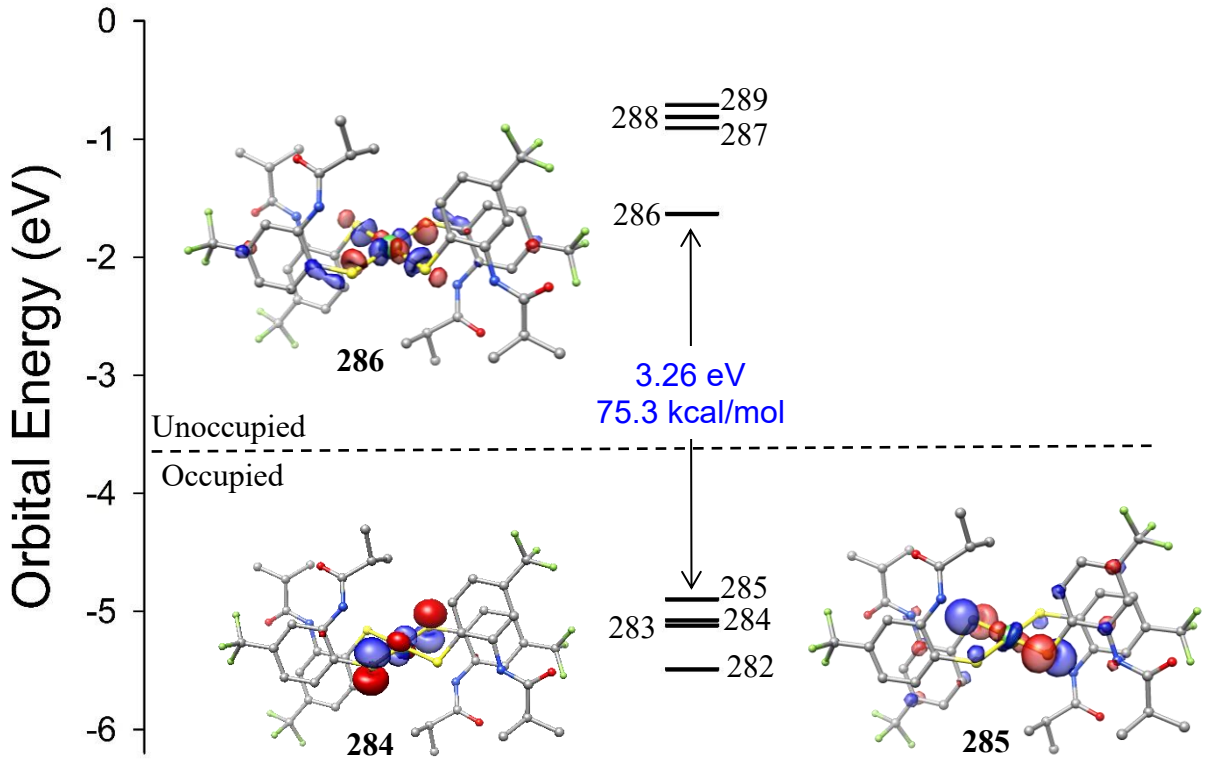

Figure S3.77. DFT-computed (B3LYP/def2-TZVPP) orbital energies of **1(SqPl)*** ($S = 0$), with an MeCN solvent model using CPCMC. The dashed line indicates the level below which MOs are occupied. See Table S3.17 for contributions.

Table S3.18. Löwdin population analysis derived from the DFT calculations (B3LYP/def2-TZVPP) for selected MOs of **1(T$_d$)*** (*S* = 1) , with an MeCN solvent model using CPCMC. Only s and p contributions were tabulated for S-atoms.

	Orbitals (α)				Orbitals (β)			
	MO#	**Energy (eV)**	**%Ni**	**%S**	**MO#**	**Energy (eV)**	**%Ni**	**%S**
LUMO + 3	290	-0.6494	1.7	4.5	288	-0.7075	1.9	3.0
LUMO + 2	289	-0.6828	1.0	5.3	287	-0.7775	2.0	1.8
LUMO + 1	288	-0.7316	2.1	3.1	286	-2.0075	65.1	13.7
LUMO	287	-0.8109	1.7	2.0	285	-2.1098	63.1	13.8
HOMO	286	-4.9959	7.8	51.1	284	-5.0902	8.7	51.1
HOMO - 1	285	-5.0706	12.9	47.3	283	-5.1903	19.9	52.8
HOMO - 2	284	-5.3449	8.1	51.9	282	-5.5889	5.8	45.6
HOMO - 3	283	-5.4899	9.3	60.9	281	-5.6240	9.0	38.3

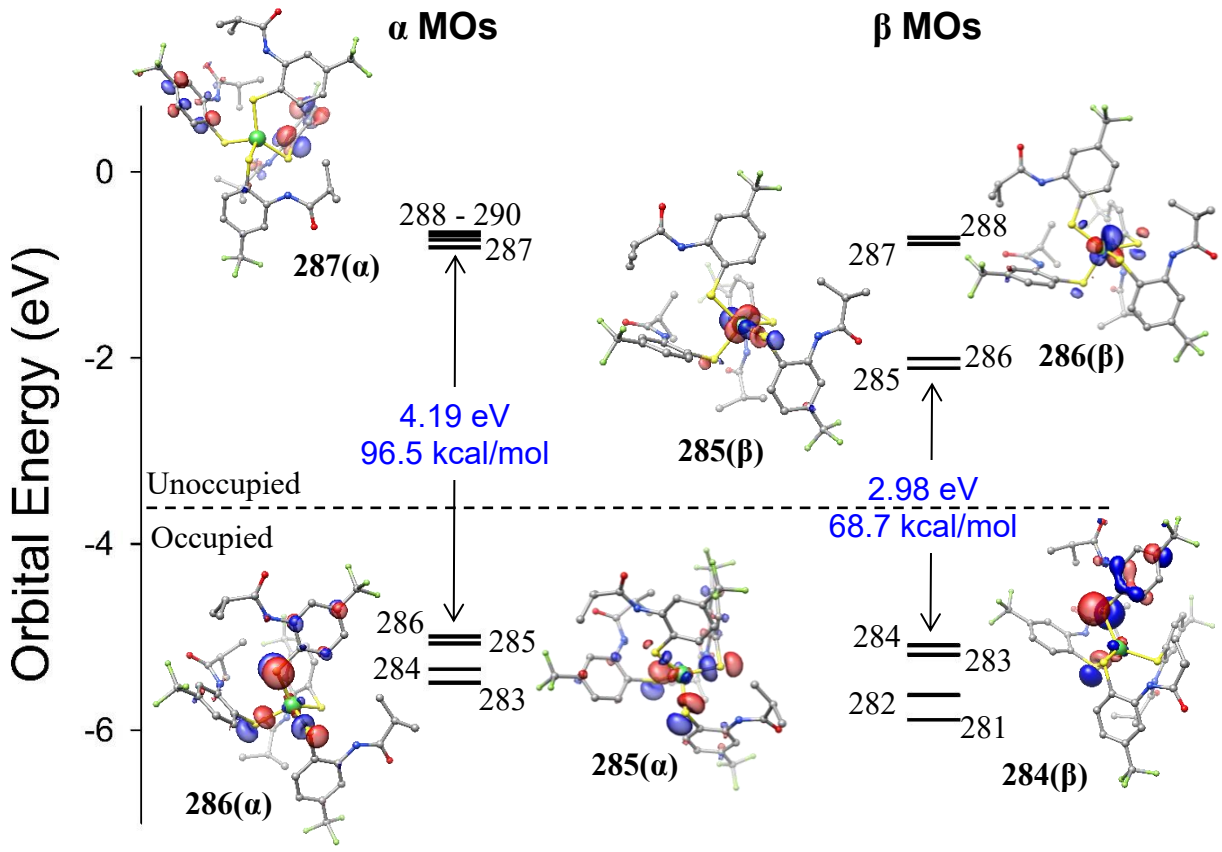

Figure S3.78. DFT-computed (B3LYP/def2-TZVPP) of **1(T$_d$)*** (*S* = 1) with an MeCN solvent model using CPCMC. The dashed line indicates the level below which MOs are occupied. Spin-up (α) MOs (*left*); spin-down (β) MOs (*right*). See Table S3.18 for contributions.

Table S3.19. Löwdin population analysis derived from the DFT computations (B3LYP/def2-TZVPP) for selected MOs of **3** ($S = 1$), with a MeCN solvent model using CPCMC. Only s and p contributions were tabulated for S-atoms.

	Orbitals (α)				Orbitals (β)			
	MO#	**Energy (eV)**	**%Ni**	**%S**	**MO#**	**Energy (eV)**	**%Ni**	**%S**
LUMO + 3	198	-0.5305	0.4	6.1	196	-0.4938	1.1	9.3
LUMO + 2	197	-0.6036	1.0	6.2	195	-0.7033	16.2	4.8
LUMO + 1	196	-0.6363	1.2	5.7	194	-1.8772	70.2	18.0
LUMO	195	-0.7468	2.1	3.5	193	-1.9242	63.3	13.6
HOMO	194	-4.9573	10.6	55.1	192	-4.8433	11.9	51.5
HOMO - 1	193	-5.0063	9.6	55.2	191	-5.1047	1.4	60.4
HOMO - 2	192	-5.2089	8.3	60.7	190	-5.2702	24.5	51.9
HOMO - 3	191	-5.2154	2.3	64.5	189	-5.4739	7.3	45.8

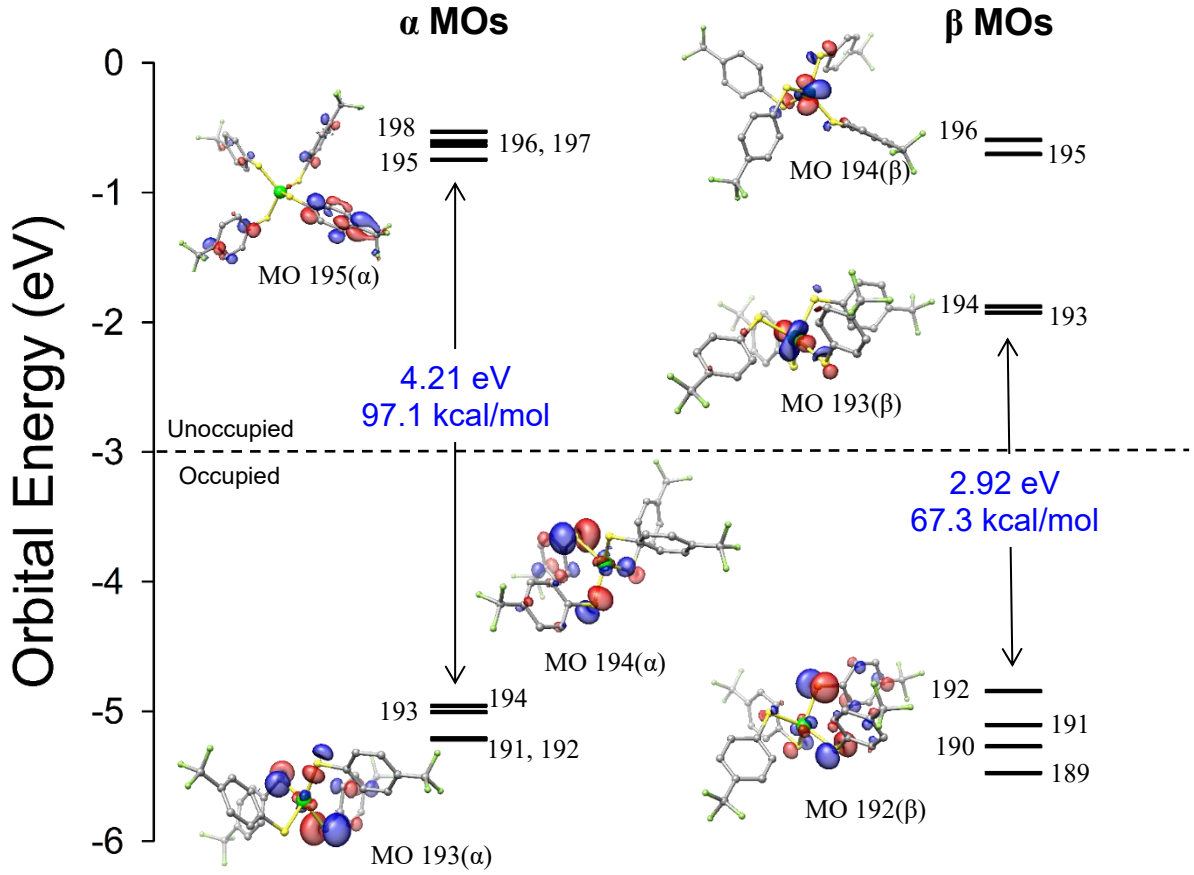

Figure S3.79. DFT-generated isosurface plots of the frontier MOs for tetrahedral ($S = 1$) **3** using CPCMC to model MeCN. The dashed line indicates the level below which MOs are occupied. Spin-up (α) MOs (*left*); spin-down (β) MOs (*right*). See Table S3.19 for contributions.

Table S3.20. Löwdin population analysis derived from the DFT computations (B3LYP/def2-TZVPP) for selected MOs of square-planar **3** ($S = 0$), with an MeCN solvent model using CPCMC. Only s and p contributions were tabulated for S-atoms.

Orbitals	MO#	Energy (eV)	%Ni	%S
LUMO + 3	197	-0.3373	1.2	5.3
LUMO + 2	196	-0.4232	0.8	4.5
LUMO + 1	195	-0.5161	3.2	5.0
LUMO	194	-1.2968	39.2	23.9
HOMO	193	-4.5471	34.7	52.2
HOMO - 1	192	-4.6915	17.7	52.9
HOMO - 2	191	-4.8444	8.6	65.4
HOMO - 3	190	-5.1671	83.8	12.8

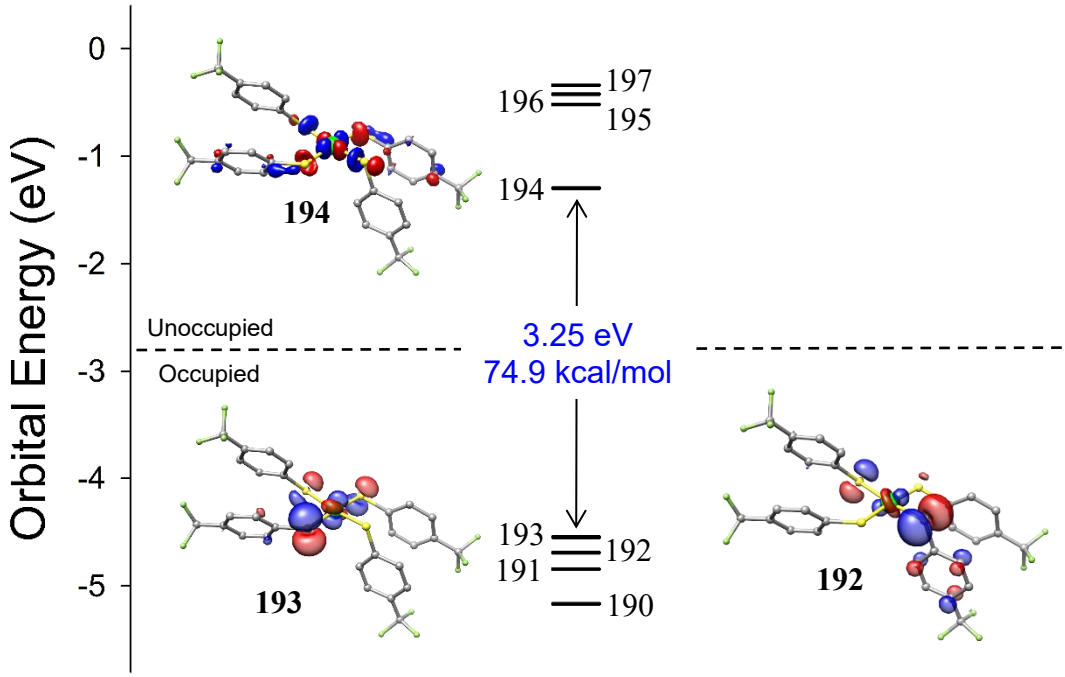

Figure S3.80. DFT-computed (B3LYP/def2-TZVPP) orbital energies of **3(SqPl)*** ($S = 0$), with a MeCN solvent model using CPCMC. The dashed line indicates the level below which MOs are occupied. See Table S3.20 for contributions.

Table S3.21. Löwdin population analysis derived from the DFT (B3LYP/def2-TZVPP) calculations for selected MOs of **2*** ($S = 0$) with an MeCN solvent model using CPCMC. Only s and p contributions were tabulated for S-atoms.

Orbitals	MO#	Energy (eV)	%Ni	%S
LUMO + 3	352	-0.6012	1.5	1.9
LUMO + 2	351	-0.7575	0.4	2.5
LUMO + 1	350	-0.8533	2.9	3.3
LUMO	349	-1.6146	40.2	22.5
HOMO	348	-4.8714	33.6	49.6
HOMO - 1	347	-4.9036	25.4	49.7
HOMO - 2	346	-5.0829	1.0	59.1
HOMO - 3	345	-5.4588	69.9	14.5

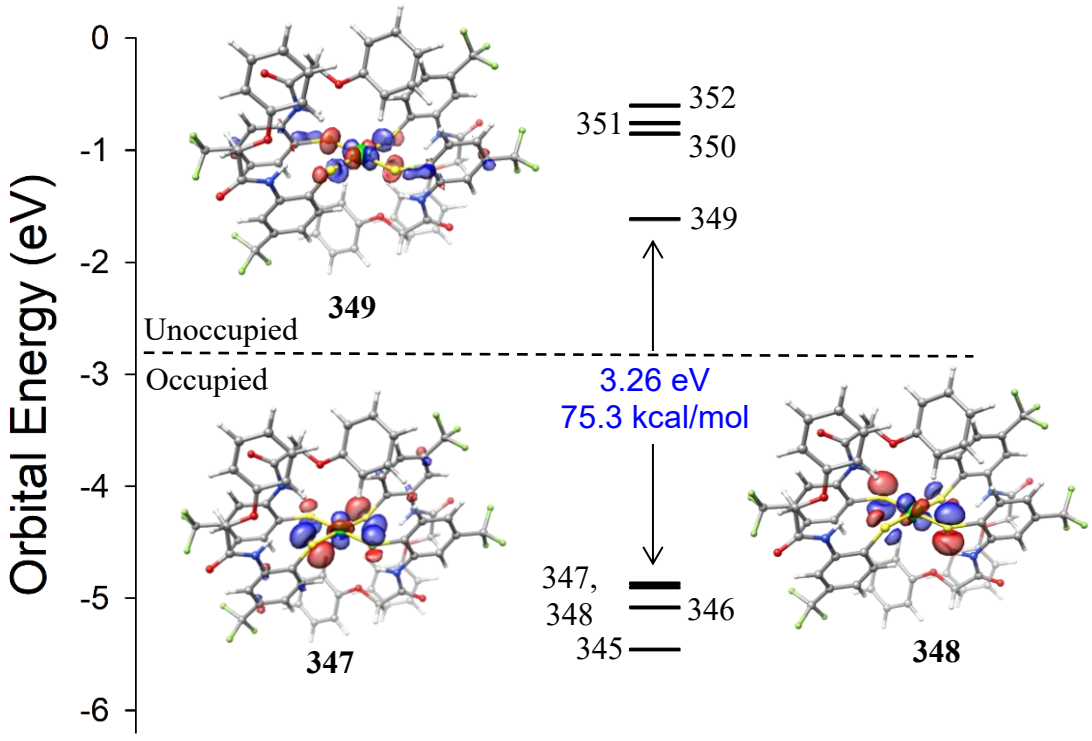

Figure S3.81. DFT-computed (B3LYP/def2-TZVPP) orbital energies of **2*** (S = 0), with an MeCN solvent model using CPCMC. The dashed line indicates the level below which MOs are occupied. See Table S3.21 for contributions.

Table S3.22. Cartesian coordinates for DFT-optimizes **1(T$_d$)*** (*S* = 1, B3LYP, def2-TZVPP, Gas).

Ni	-0.31217240881845	0.34409070575906	-1.54793332909081
S	-1.89949032065221	1.92719392480521	-2.21236034627270
S	0.27545831108956	0.65534143371445	0.65872313953394
O	-5.89222712472404	1.72204320248003	1.14856936318938
O	-0.26773862487383	2.75959277326252	5.38463400335240
N	-3.99247557804833	1.77962590500771	-0.13409399021427
N	0.13694678905881	1.67996066958938	3.40074532569029
C	-3.26876165718855	0.81200396069538	-2.20222710796281
C	-4.23836193616641	0.86441370782479	-1.15728948581958
C	-5.33637893213880	-0.00645405687674	-1.15744629128778
C	-5.46630510534743	-0.95625681401081	-2.17630799549536
C	-4.51144609736760	-1.04112508352903	-3.20119172762113
C	-3.43208204082654	-0.16331799580104	-3.20437781972812
C	-4.74437977866043	2.11294611036414	0.95428999574889
C	-4.00662229276418	2.98076130291674	1.97995824458288
C	0.35686960920568	2.34808865128883	1.09417084816760
C	0.27116431140265	2.72067680489628	2.47400019177817
C	0.33383389610133	4.06142146549915	2.85393802750324
C	0.49472679203350	5.05843678078717	1.88138699800244
C	0.58975601433406	4.71455158601714	0.52840485239661
C	0.52029562386990	3.37495262610025	0.14743872127054
C	-0.13199053838546	1.72435893424957	4.73743571963073
C	-0.28861100837187	0.34969559019999	5.39404510169174
C	-3.09858840603065	4.05767129408283	1.37530932223881
C	-3.22772947625397	2.04974765359595	2.92521934605780
H	-4.81083539926491	3.46911959201135	2.55444004477400
H	-0.22835829806509	0.56985365923865	6.47196727962737
C	0.82881708198630	-0.62854725031622	5.02398516398301
C	-1.67664054907053	-0.23800344660171	5.09449395675773
H	-3.07909172580598	2.21614847627170	-0.24105567642886
H	0.15642171243805	0.76636150363719	2.95793409956511
H	-6.06021696518962	0.06042511582323	-0.34915719615963
C	-6.62407884814110	-1.90512625260478	-2.18655526618915
H	-4.60416443142898	-1.79978526988281	-3.98143759300696
H	-2.67156201742351	-0.23412181704975	-3.98376794505200
H	0.25097015531432	4.31142810397372	3.90905100524678
C	0.62990458609440	6.47459816646497	2.33903586543931
H	0.72122850234417	5.48767170657542	-0.22983930198250
H	0.60020569332748	3.10124127055361	-0.90543817576646
H	-2.22881059608058	3.62714786083249	0.85466994702403
H	-3.64411285019776	4.69514198568275	0.66112193703744
H	-2.68973927738053	4.69859546055677	2.17081946315107
H	-3.90002589202759	1.32344233719590	3.40517340104308
H	-2.46026313279983	1.48698243651002	2.37197027255511
H	-2.71722031046957	2.62979197872598	3.70961291126865

H	0.73168067177631	-1.56231393326657	5.59786166115502
H	0.79426237808061	-0.92438695027793	3.96524029824067
H	1.82267521026350	-0.19730111835449	5.22552350073180
H	-1.82799012598080	-1.16855686517318	5.66255476789295
H	-2.47686793558724	0.46524662379691	5.36728740613890
H	-1.78801442445594	-0.48242619407669	4.02683463726348
S	-0.33127559431648	-1.99971555040741	-1.56399030373836
S	1.28627618018717	0.97681372408615	-3.11521218802563
C	-1.29224088369060	-2.29787484092092	-0.10507515519305
C	2.81291246063696	0.26267173096902	-2.60665769796682
C	-0.66350449193000	-2.70913576840810	1.10565846515205
C	-2.68421594193836	-2.11736875512820	-0.09125642376767
C	3.51085365633172	-0.64403376132834	-3.45997658067031
C	3.41111320550658	0.59055296438026	-1.37574782567103
N	0.72710832365716	-2.81411883982920	1.06259603468841
C	-1.41668827821507	-2.94472334310943	2.26231860738510
C	-3.43783151553805	-2.32488882365524	1.06028230997183
H	-3.17199385880647	-1.79504430611210	-1.00804075193051
N	2.88409102854317	-0.97962470326656	-4.66931794128431
C	4.74293301483415	-1.18276712308785	-3.07980307654692
C	4.64504995339156	0.06589228628804	-0.99880913485920
H	2.87762417891308	1.26682293600283	-0.70654543543880
C	1.62847062055526	-3.04214477740960	2.05276737001024
H	1.07969088278988	-2.53226800068870	0.14931108332211
C	-2.80255657173683	-2.75060389524410	2.23540831965332
H	-0.90578216881747	-3.26972981397696	3.16481943059168
H	-4.51615548012231	-2.15371326522466	1.04100383196036
C	3.38017715906606	-1.64423943910395	-5.74646642398937
H	1.93731736890269	-0.60395099993646	-4.71425162338984
C	5.30883414072356	-0.82607510061980	-1.85022711299515
H	5.24604248811924	-1.87734575883190	-3.74811765658904
H	5.08039762130795	0.33983492299586	-0.03773781043715
O	1.33748908819538	-3.39987307938822	3.19318865321411
C	3.07890303006383	-2.74492421476487	1.65866635065177
C	-3.63900314553810	-3.01560353428687	3.45001312672837
O	4.53337971007192	-2.05539674213771	-5.84894561936780
C	2.34494194784433	-1.90577899321087	-6.84924258430749
C	6.63816546714261	-1.40570626878096	-1.48411587353504
C	3.40026770817833	-1.29212009666539	2.06010996412854
C	3.41230737181409	-3.01910640900824	0.18749483454561
H	3.67725440313302	-3.41726796088181	2.29456536385326
H	1.50434910254782	-1.20362061666365	-6.71549602986807
C	1.80710702359697	-3.33905978984548	-6.69828145310191
C	2.96559150339488	-1.69484990884289	-8.23207940964615
H	2.78210701584234	-0.58252632450898	1.48775423987566
H	3.20262354155254	-1.12922585259551	3.13036582822851

H	4.45997420746232	-1.06353913532899	1.86589243067975
H	3.09810905850672	-4.02815298291623	-0.12383638087359
H	2.93690677931474	-2.29144581719575	-0.48835738116010
H	4.49556548634132	-2.93519001406367	0.02088016925918
H	1.02431488525613	-3.54143070171503	-7.44748880769364
H	2.62190723820551	-4.06554873477319	-6.84826123579862
H	1.37278965831942	-3.50629236981624	-5.70025716268451
H	2.23307230253114	-1.93092314448871	-9.02179037609670
H	3.30937600972273	-0.65711127065001	-8.37039564369485
H	3.83937648673507	-2.35211709881903	-8.35558795413215
F	-6.23531784628745	-3.21236332948999	-2.20186540467397
F	-7.40805897815618	-1.75679068785849	-3.29964089883787
F	-7.44567953283862	-1.76154544566659	-1.12210968970919
F	6.76709663886065	-2.70429784682420	-1.86981163060797
F	6.87992724628184	-1.37267144838108	-0.14632461499380
F	7.69089063995426	-0.75097118559864	-2.06544815727051
F	-2.92112172364945	-3.44371098631695	4.51909383917186
F	-4.58868892211525	-3.97460103258364	3.22575738793131
F	-4.32894337420023	-1.91644738939967	3.86576834207321
F	0.54943708462662	7.37376353037655	1.32379492384253
F	1.82849545944301	6.71595593676158	2.95813903887834
F	-0.31906330324109	6.83704093473139	3.24757193309716

Table S3.23. Cartesian coordinates for DFT-optimizes **1(SqPl)*** (*S* = 0, B3LYP, def2-TZVPP, Gas).

Ni	5.60913554659462	8.51064610947849	0.05010790870178
S	5.87459602174046	9.73675627634984	-1.81929904493439
S	7.33564424852974	9.31027796390742	1.28600145685634
O	9.34411304653007	8.36467543770363	-3.34661347637238
N	7.58307175072096	11.62424295497729	-3.29714228080008
H	7.57020624661375	10.61163618456261	-3.22572014799571
O	8.27645811148422	13.37247905855892	-4.60670773279336
N	8.86472441238218	8.42439842196483	-1.10837356213300
H	8.24418318643067	8.01507958629091	-0.41131338785426
C	6.94447678590464	12.24350253394655	-2.21931253893838
C	6.15584968452441	11.40830634913080	-1.37414626717285
C	10.07137328697141	10.53559303833778	-1.48417689114097
H	10.58225200443852	10.10763960540831	-2.34223173720044
C	10.28420173910258	11.86773297544621	-1.10922057949004
C	6.53377403306125	14.13863994970673	-0.76800875670749
C	8.79693119262759	7.88101614134596	-2.35922454611458
F	6.68870146645105	16.39831236026630	-1.50343762222461
C	9.16336434210284	9.75022579798316	-0.76813645330609
C	8.46362820633535	10.29019760072750	0.34828809035230
C	7.12036340255469	13.59631404112220	-1.91882361736943
H	7.73125325679769	14.20560986900905	-2.58185038529665

C	8.73692142926784	11.61565951077573	0.72283758886874
H	8.18568610503125	12.03727864575903	1.56486135850923
C	5.60123462030133	11.98503473494586	-0.21942865850467
H	5.04591816608924	11.34239089927606	0.45743896946651
F	11.46545937654731	12.26763552514288	-3.14093835733215
C	9.62824104701853	12.40756155132928	0.00407494197569
H	9.78562296493008	13.45031555927899	0.28461927611936
C	8.22739652299170	12.16963894916321	-4.36673008307092
C	5.78258749084721	13.32724848913747	0.09191039409316
H	5.34054863765338	13.74180223411238	0.99936089325028
C	8.89034620719532	11.11069093100534	-5.25722065043724
H	9.48857591848881	10.46789430956915	-4.59069292866324
C	11.23610823326075	12.72564481932103	-1.88457719297750
C	7.95651712530798	6.59897513409558	-2.41085793656157
H	7.03648263797318	6.80849236358168	-1.83705894623337
F	5.93859129457166	16.05065422244303	0.51453941134763
F	8.05161600508899	15.78075125392184	0.06889174879414
C	6.79333949033412	15.56876998895292	-0.42985403647596
F	10.81215794997064	14.00748753203880	-2.00543547262252
C	7.83549055591618	10.21093870139880	-5.92135583813749
H	7.21134076755660	9.68912071881301	-5.18061117359702
H	8.33053061080262	9.43980672521378	-6.53334231943254
H	7.17191502326859	10.80336404251551	-6.57475477093465
C	8.67354687417961	5.42397974978082	-1.72631055810842
H	8.02208841813431	4.53526903426078	-1.72517908623623
H	8.93107183569589	5.65004386050022	-0.67974428109013
H	9.60492344551847	5.16563462164050	-2.25834483727953
C	9.80995920711608	11.76743867968328	-6.28151675553392
H	9.23650152515432	12.41159995301866	-6.96676170195813
H	10.33109781988720	10.99794778823411	-6.87512001581604
H	10.56031060242904	12.40064440459577	-5.78617504173035
F	12.46982069122645	12.80682737605078	-1.28787001605234
C	7.55433144156761	6.26632446127464	-3.84584620637550
H	8.43804370844741	6.03361992712093	-4.46093118582210
H	7.03485303194670	7.11559105954848	-4.31175209798720
H	6.87466177039792	5.39947453332075	-3.85915028565354
S	4.99066642624978	7.64746357097129	2.04081761250392
S	4.24327653675999	7.21633775363489	-1.22621079913778
O	0.92879861849434	9.23989949898345	2.26294608736814
N	3.16685910686917	5.94039556646190	3.53725568494014
H	3.20531614698789	6.92418019920960	3.28491563707327
O	2.11129601491006	4.41778738441060	4.88259962371259
N	2.18173836454626	8.61211993738460	0.44689610807818
H	2.94799514251256	8.90652521996543	-0.15338712667509
C	4.06071313032258	5.17348636932751	2.78200305699038
C	4.98950985870645	5.90355870636660	1.98026169148240

C	0.93028577365377	6.60485024007930	1.07805331000206
H	0.22330870630209	7.21857268649568	1.63048091179565
C	0.79926052077429	5.21085796260529	1.03787322473356
C	4.91049696275404	3.08784664516663	1.89059341301264
C	1.75673798033447	9.49660493333561	1.39048820031350
F	4.68286037267273	0.96068760287428	2.95694989092461
C	1.99449554553642	7.22627761149621	0.42006246890454
C	2.94381031085888	6.45639291694221	-0.31628652323128
C	4.03113455824070	3.77811482978598	2.73991492839537
H	3.29718182871345	3.25131077051178	3.34610480735895
C	2.77254894565480	5.06290890560563	-0.34085372786892
H	3.51673015253060	4.46344537631855	-0.86608740722808
C	5.86507172542095	5.17948564846346	1.15541279897029
H	6.56925946863358	5.73570418847270	0.53870239316219
F	-0.63461617277092	5.13009166723411	2.93955779176911
C	1.72068161086530	4.43593292757250	0.32626119658888
H	1.63993650542783	3.34840712918877	0.32182107974299
C	2.27501713776811	5.57129289676047	4.49828215416045
C	5.82669509654899	3.79026964033811	1.09676652606605
H	6.50711985163549	3.25362935767103	0.43440773772212
C	1.51067291047839	6.76864045447999	5.08804386151016
H	1.13453209670744	7.36580664677984	4.23827192530989
C	-0.37531642139850	4.58350869264526	1.72270875498963
C	2.43677861993096	10.86227072673725	1.30463491662543
H	3.03972658552327	10.89437661317376	0.38380878726856
F	5.83341510264367	1.03413029755396	1.10892760013490
F	3.66738074196264	1.23288841162774	1.05838364719855
C	4.78288009717737	1.60479448377362	1.76222004222216
F	-0.23517784868620	3.25174335405231	1.91604959282493
C	2.46410765422488	7.66227692384649	5.90315450011241
H	3.27311659693280	8.07824369623475	5.28391527721709
H	1.91049199062760	8.50826424296870	6.34299366814748
H	2.92660088295957	7.08979859593808	6.72548871800692
C	1.40765568421900	11.99325571644366	1.24805765782020
H	1.92503359758423	12.96398720911140	1.17206260155110
H	0.73951641956884	11.88962265416342	0.37780942706131
H	0.78487145013207	11.99313369895564	2.15634088542707
C	0.32737736865926	6.29866895288055	5.93118507062688
H	0.67354066073479	5.70423770614991	6.79152659226216
H	-0.23821723871964	7.16653080620881	6.30978041811514
H	-0.35118101079793	5.66500431126966	5.34428629054746
F	-1.53734342540894	4.73220122670083	1.00511397860835
C	3.37225149607709	11.01127729337862	2.51357610831604
H	2.79868254379890	10.88561841235706	3.44616627086265
H	4.17316217510038	10.25819767019940	2.49741623696139
H	3.84141451803348	12.00851851167877	2.51984184277489

Table S3.24. Cartesian coordinates for DFT-optimizes **2*** (*S* = 0, B3LYP, def2-TZVPP, Gas).

Ni	-0.01826664065976	0.02949138291788	0.07099869135076
S	-0.16362086544442	0.56427707659006	-2.12017255035451
S	1.98914239189789	-0.76649829907205	-0.56078248191809
S	-2.05895977766631	0.76453017717051	0.67886669087077
S	0.14101690904121	-0.48965748545238	2.26271300054163
N	-1.14040424457464	3.32955917391652	-1.44189533465547
N	-4.61555712086677	1.81906595274217	-0.20115972043007
N	4.53405972943352	-1.95560543425523	0.17909957654711
N	1.12373486440384	-3.25823488066361	1.59543976185265
O	-1.65702444918101	5.53437965238361	-1.83880210022250
O	3.96264274385141	-4.17449111123880	-1.02619565585760
O	-6.75282183245456	2.46382213792907	-0.78447574344233
O	-0.24850173218897	-3.93701039527499	-0.57171773140446
O	0.25012119025530	4.02953422134395	0.70626922726677
O	6.66670066381293	-2.68932354349782	0.66766150229916
O	-4.10226858513207	4.09691907687674	0.87925898884981
O	1.72786000121004	-5.45610257136505	1.90842735581839
C	-2.42489081028696	-4.52982534903087	-4.07045108440258
C	-5.25489483012405	3.15881919181561	-4.20705637262155
C	-3.75363143950339	1.17452078992946	-3.92962727130665
C	-1.60835879457170	-3.40365936925289	-3.89135693099340
C	-4.03046685251037	2.51476188004972	-3.62914104727630
C	-2.59837454094123	0.58533928992413	-3.42341851376281
C	-2.52114401809623	-5.47272203725328	-3.04623667883737
C	-3.15737425875731	3.25097834700913	-2.82349795742900
C	1.78720885827084	-7.47030254920634	-2.33039818167053
C	-1.69686349914942	1.29267783535467	-2.60758147787831
C	-6.10599528435663	-2.11438917651535	-2.80149136396327
C	-0.89173853738749	-3.22287220124139	-2.71075933396613
C	1.50706623550545	-6.17403907265265	-2.78717959061693
C	-2.01040832998102	2.64412895748999	-2.30024428624467
C	2.81023566027211	-7.66111621103503	-1.39919588371873
C	-1.80487821356238	-5.30976250327536	-1.85353075099303
C	-5.13052482131876	-1.46243363722892	-1.87530198938980
C	2.24660219317311	-5.08941735283725	-2.32516141411694
C	-1.02703400459072	4.65974718732041	-1.25020038434760
C	3.56551738031723	-6.58088606515355	-0.92866941493369
C	-3.93599746904642	-2.10036752256581	-1.51992333145838
C	-0.98517100268417	-4.18464025258567	-1.69278584253522
C	3.28416752429230	-5.29323821410620	-1.40124760944822
C	-5.40700679825542	-0.16568841751083	-1.41417486208948
C	-3.01165621371064	-1.43896076218209	-0.71431377540365
C	0.03163914811726	5.07174920276741	-0.23112115523714
C	-4.47133520924603	0.49240561838965	-0.61725731597418
C	5.06419237843140	-4.27247423711460	-0.13720417166590

C	-3.23561588323424	-0.12984635886733	-0.26090384578298
C	-5.62813268401615	2.69430541460952	-0.35297556993148
C	5.52115726328362	-2.86904742675048	0.26773964349612
C	-5.23445813949204	4.12488665547449	0.02608702991412
C	3.24709740363975	0.05623533267509	0.33494427737008
C	4.46878906457923	-0.62873592109991	0.61475359456573
C	0.01255732630741	-5.00171955297665	0.32818519915124
C	3.11605754022992	1.37111673307981	0.81241369596238
C	-3.48616557755386	5.25393540371007	1.24373393545961
C	-3.86208620603385	6.52340340922333	0.78859357960073
C	5.48824109575585	-0.01895610432465	1.34431377171428
C	1.05325289594958	4.26409248344722	1.78296187562239
C	4.12611632317459	1.98549706182795	1.54927802816654
C	-2.41175596716668	5.11058034436358	2.13604990973478
C	-3.16209263513153	7.64705453899458	1.24235525512412
C	5.31603757159233	1.29204578915471	1.81176115468362
C	1.05964954229850	-4.58421154246283	1.35723087729260
C	1.89213893909857	5.38100727755279	1.90517612931600
C	-1.73027935994900	6.23846428183479	2.58426766259384
C	-2.10255719808468	7.51676437522599	2.14257069078384
C	6.38845732155330	1.89775154020526	2.65866230360169
C	2.00082499475114	-2.55953327982835	2.43673897775573
C	1.00912752537614	3.29612470739807	2.80006920482574
C	1.68368537109639	-1.20747131827633	2.73746604038389
C	3.16367794056615	-3.15114420972551	2.94233527749805
C	2.68260760829385	5.52448364573624	3.05313256743293
C	2.59636773972764	-0.48545480469841	3.52835095142305
C	4.04682119118812	-2.40055773533368	3.72224932391546
C	1.80004541768738	3.45867758862705	3.93503058154061
C	5.28618455887653	-3.03553062341209	4.27671016439593
C	3.76676403717461	-1.05962638523977	4.01620012593756
C	2.64082692742850	4.57274891528910	4.07266273602212
H	-2.99304944843438	-4.66353261922753	-4.99376506332007
H	-4.44989071666430	0.59046111136267	-4.53410550282315
H	-1.53568338516245	-2.64642728730005	-4.67626653651548
H	-2.38157896542150	-0.46100682273396	-3.63852772281334
H	-3.16782742973825	-6.34614583923292	-3.16718029669223
H	1.19874612249465	-8.31784077551078	-2.69023912724350
H	0.69069781803805	-5.99760825899998	-3.49117764597413
H	-3.35090887265373	4.29412584414546	-2.59215908824062
H	3.03085642783869	-8.66138066320249	-1.01489049342268
H	-0.28465592410916	-2.32885642931529	-2.54607455474714
H	-3.72152611964155	-3.10328610338355	-1.88606731020479
H	2.02590277121462	-4.07143325353139	-2.64997506942920
H	-6.31761178256382	0.35547367632327	-1.70640225982953
H	4.34568560141751	-6.74720175477562	-0.18693094830577

H	-1.89617927275202	-6.05279541009810	-1.06123121130641
H	5.91047381373158	-4.79976881159261	-0.60782576928888
H	0.96141146725989	5.31415409778867	-0.78038376168829
H	-0.51001452938130	2.72029532587968	-0.92741087354239
H	-5.00406110290685	4.66252104250896	-0.91057621434232
H	-2.07569511564012	-1.92327221528552	-0.43937868280830
H	-0.33145180271703	5.98253725231592	0.26719491431213
H	3.65504309229305	-2.27802232380859	-0.22404380374811
H	0.40782265908090	-5.87975106470486	-0.20384659432009
H	-3.76289034198041	2.18656793990359	0.22064535982054
H	4.77447050872599	-4.80696449682755	0.78519735074978
H	-4.67641732263603	6.64331333751053	0.07480796759881
H	2.18806944713208	1.90170303471158	0.60311254260585
H	-6.09305429582635	4.61275113976051	0.51727080962122
H	1.94547480018492	6.13087941706950	1.11588060126330
H	-0.90484744277706	-5.30022792964133	0.87097368184933
H	0.47497804421971	-2.65570453812324	1.09581657188399
H	6.39346786163076	-0.58165035147451	1.56428795378702
H	-2.12001989041957	4.10610188328290	2.44677896816153
H	-3.45558720111823	8.63318095500625	0.87014975578979
H	3.98532882828852	2.99940505816683	1.92552822751923
H	0.38307204830873	2.40945044914625	2.66699654504258
H	-1.55934866336094	8.39821647268699	2.49260276604403
H	-0.88649109965335	6.11105061638445	3.26650116988347
H	3.36376168056382	-4.19394888127337	2.71555330385358
H	3.34186504185505	6.39254177423387	3.14200652328106
H	2.37526185416051	0.56065251818571	3.73869192153491
H	1.76578488292394	2.69642969545813	4.71774933619405
H	4.47118702294030	-0.46407923506922	4.59958877820036
H	3.26507625322003	4.69153203580949	4.96122953686401
F	-5.13443689251413	3.39163402000927	-5.55269536808600
F	-6.36305514265503	2.39332577783634	-4.07403283112394
F	-5.74319849138201	-3.37154295251920	-3.16550478161827
F	-6.27265243854901	-1.42185010836429	-3.96932055118161
F	-5.53978861224744	4.36560926188881	-3.65155553328569
F	-7.35931288581432	-2.22012580799569	-2.27003853466734
F	7.64145855916490	1.56815543116888	2.24199077032329
F	6.33830191751201	3.25697954927905	2.69344119323300
F	5.57959335265351	-4.22828324195958	3.69982956605402
F	6.32832118715328	1.49897313607512	3.96924415240436
F	5.18508416811417	-3.28827572326844	5.62151719307622
F	6.38231831159509	-2.25171769046525	4.14298803521695

Table S3.25. Cartesian coordinates for DFT-optimizes **3*(T$_d$)** (*S* = 1, B3LYP, def2-TZVPP, Gas).

Ni	0.46465529578580	-0.20143422215947	-0.04916990634501
S	-0.58184403872915	-1.12296462462491	-1.90315724370788
S	2.01431931367600	-1.92013521098563	0.15429566557847
S	1.13813005152755	2.00353942120657	0.32317853554982
S	-1.17904767294548	0.01742080072735	1.59034709393560
C	-5.28964333156493	2.37236410677879	-3.49110918101067
C	3.72172030496825	4.34968283327966	-4.63914116522548
C	-3.98455726032746	0.23995169635479	-3.58559140194731
C	-4.14481563079221	1.52989807866247	-3.05332724941286
C	-2.89678804597837	-0.53880259195763	-3.21913120756092
C	2.22416450600880	2.64366073349962	-3.54060615806805
C	-3.17845206646349	2.01493265184597	-2.15326681380428
C	3.11140761499444	3.72559523802001	-3.43450194816569
C	-1.91963428278885	-0.07615998918796	-2.30269048108518
C	-2.08992643548557	1.23242280144433	-1.78562493089247
C	1.65389099810031	2.07598544703933	-2.40660350818342
C	3.44989624168318	4.20490355340712	-2.15539091478997
C	1.94859751446931	2.57048456606994	-1.11358257905256
C	2.88041222042463	3.63754036286650	-1.02350765990853
C	-1.51535038270100	-2.73883258737955	1.32916076152213
C	-2.19662609853675	-3.92557367269026	1.56965463734696
C	2.78610239344400	-1.63116866739279	1.69479414321024
C	4.08063161196145	-2.14180057809536	1.95607502976137
C	-1.98047690892468	-1.50719478608651	1.84972943527410
C	-3.37429170337043	-3.93619375410584	2.33375872772639
C	-4.13052598202399	-5.18691986989997	2.59770092558447
C	2.15970063254318	-0.90204690689919	2.73520743754444
C	4.72072213150450	-1.92156436280794	3.17154454838283
C	-3.16601992615332	-1.53965182120776	2.63013450800485
C	-3.84477772245093	-2.72468418041290	2.87224372762015
C	2.79964597968751	-0.67140371246791	3.94204070678929
C	4.09102300241193	-1.17550450896157	4.17956637223463
C	4.76407608424307	-0.87041434383149	5.46903951839726
H	-4.72843699716033	-0.15557464777406	-4.28155155798106
H	1.94914678717836	2.25575203923376	-4.52464402964683
H	-2.78237300804639	-1.54277671127559	-3.63458213488761
H	-3.28337186754514	3.01623593599172	-1.72708236336305
H	0.95338638870162	1.24470700650014	-2.51502664903048
H	-1.35815030034026	1.63146432201882	-1.07903547310997
H	4.15052018055555	5.03854245367726	-2.05490308132659
H	3.13456725448621	4.02511508753655	-0.03380827935879
H	-0.60052534299331	-2.74881691876238	0.73559889267105
H	-1.81446576411174	-4.85553329315853	1.14305178045610
H	4.58333524518187	-2.71493439835040	1.17194531207409
H	1.14935110862718	-0.51926772384718	2.57981457165056

H	5.72052110658447	-2.32819753415986	3.34009604086010
H	-3.54752939155978	-0.59988832032518	3.03800831392246
H	-4.76221721444051	-2.71456650523020	3.46798757516556
H	2.28813741755491	-0.09508254680319	4.71797364221134
F	-5.05960529462144	3.05752292185870	-4.66098697171032
F	3.04391624584609	4.07522607736407	-5.78467044795965
F	-6.41524861068647	1.63833160359621	-3.73437439582070
F	3.78222038872094	5.71309513677835	-4.55580576140894
F	-5.64625390161354	3.32218857863732	-2.58471413609072
F	5.01974381430779	3.95949137527703	-4.86778817666046
F	-3.62688096081151	-6.27380022293331	1.95916304839497
F	-5.44570516261180	-5.10900115846959	2.22250126538024
F	-4.17669612747478	-5.52143926188720	3.93049568203505
F	5.09448440960713	0.45478908812772	5.60532214781806
F	5.92142595040723	-1.56676580243333	5.65113071928395
F	3.97939523806037	-1.13752848123544	6.55663504112891

Table S3.26. Cartesian coordinates for DFT-optimizes **3*(SqPl)** (*S* = 0, B3LYP, def2-TZVPP, Gas).

Ni	-0.71116725539616	1.64185942766516	-1.15379336295201
S	-1.35991113880822	0.15932310037687	-2.74418478996227
S	0.05046754367483	3.28400368111378	0.26613542239010
S	0.83049301663284	2.28662350275295	-2.70444186906385
S	-2.25051491234381	1.11569057876739	0.39765515254793
C	-7.15724112374735	-1.44516408318577	-1.89180959112847
C	6.25407453597298	2.25232032680092	0.04012005363619
C	-4.78751650661646	-2.00186262213848	-2.54721003267803
C	-5.75893706831372	-1.04738506618114	-2.21486998064735
C	-3.46008591605875	-1.61706936657136	-2.72112318078464
C	3.98995702796432	1.22203027489643	-0.37031008479958
C	-5.37752654441962	0.30249965953834	-2.09862651298010
C	4.90712875532592	2.26238446906825	-0.59490747949746
C	-3.05023420989135	-0.27455780893705	-2.57207332525005
C	-4.05483590014881	0.68037702835265	-2.28490059418294
C	2.75290386080871	1.23092616354621	-1.00356438364861
C	4.55340534233102	3.30578905306545	-1.46625213968858
C	2.37273053138103	2.27337224689064	-1.88279269015746
C	3.31365467185250	3.30993567711162	-2.09526834669476
C	-1.56866842549877	-1.56190832297610	0.09529925520845
C	-1.84377926886712	-2.92051432683127	0.14811075872909
C	1.14038010599885	2.56086013746644	1.41258662234558
C	0.99105604289063	1.24810975763919	1.93310625758024
C	-2.55698373314729	-0.59879008851272	0.41777023909817
C	-3.11576529547803	-3.37934703820603	0.53658649852090
C	-3.40861207268284	-4.83707311422936	0.54152127383636
C	2.26961749089953	3.29972344611065	1.84381081901134

C	1.92238594870934	0.71326434626687	2.81216311848003
C	-3.83007991861376	-1.08021246914243	0.80437384737684
C	-4.10923740975272	-2.44032041497692	0.85892814237239
C	3.20875270798394	2.76077089180859	2.71198517657015
C	3.05206152419279	1.45731223551087	3.20807399300711
C	4.07795051059759	0.84769138813055	4.09546950728141
H	-5.06404021795902	-3.05377432352595	-2.63522195109694
H	4.23644494749221	0.41813305254176	0.32517432598176
H	-2.70117336106737	-2.37130267711225	-2.93505870984248
H	-6.12621995506124	1.05792843791856	-1.84752661664609
H	2.04034063506755	0.42718632905540	-0.81393972808641
H	-3.76101462900692	1.72483959304866	-2.18384674393280
H	5.25495541325465	4.12715515671630	-1.63666158459137
H	3.03521553307704	4.13817870714773	-2.75055291598138
H	-0.58528846682186	-1.21488600264860	-0.21871470737758
H	-1.06268360311087	-3.63897151795798	-0.11278840181002
H	0.11636757540449	0.66928109173155	1.63221676199038
H	2.42704264015059	4.29617736908580	1.42742816460617
H	1.77489856264264	-0.29814476006410	3.20066058319379
H	-4.61445964322271	-0.35589260103347	1.03315953823830
H	-5.11012430930210	-2.77794804260507	1.13727123171364
H	4.08789765833859	3.34409762994263	2.99199212090035
F	-8.09121972077039	-0.61176902700146	-2.44654885508561
F	6.31059078619384	1.51983237973498	1.17672502876973
F	-7.47823059664778	-2.69964863589623	-2.30772891747822
F	7.23406972499473	1.73129542747355	-0.77776429748177
F	-7.43423440236867	-1.42670081522572	-0.54725697677878
F	6.70565125016391	3.50503472880841	0.35563893361817
F	-3.77333581233298	-5.32802696608878	-0.68799606579421
F	-4.42485661867219	-5.17888928924234	1.38236186646159
F	-2.33834624137344	-5.59944227638293	0.91584820593967
F	4.80847512314308	-0.15006780398927	3.50306017491323
F	3.54036664712279	0.26176112922635	5.21078034854153
F	4.99462816323976	1.74721103535113	4.54241141323919

3.10 References

(1) Reece, S. Y.; Nocera, D. G. Proton-Coupled Electron Transfer in Biology: Results from Synergistic Studies in Natural and Model Systems. *Annu. Rev. Biochem.* **2009**, *78*, 673. DOI: 10.1146/annurev.biochem.78.080207.092132.

(2) Huynh, M. H. V.; Meyer, T. J. Proton-Coupled Electron Transfer. *Chem. Rev.* **2007**, *107*, 5004. DOI: 10.1021/cr0500030.

(3) Turner, J. A. Sustainable Hydrogen Production. *Science* **2004**, *305*, 972. DOI: 10.1126/science.1103197.

(4) Gray, H. B. Powering the planet with solar fuel. *Nat. Chem.* **2009**, *1*, 7. DOI: 10.1038/nchem.141.

(5) Fontecilla-Camps, J. C.; Amara, P.; Cavazza, C.; Nicolet, Y.; Volbeda, A. Structure–function relationships of anaerobic gas-processing metalloenzymes. *Nature* **2009**, *460*, 814. DOI: 10.1038/nature08299.

(6) Fontecilla-Camps, J. C.; Volbeda, A.; Cavazza, C.; Nicolet, Y. Structure/Function Relationships of [NiFe]- and [FeFe]-Hydrogenases. *Chem. Rev.* **2007**, *107*, 4273. DOI: 10.1021/cr050195z.

(7) Shima, S.; Pilak, O.; Vogt, S.; Schick, M.; Stagni, M. S.; Meyer-Klaucke, W.; Warkentin, E.; Thauer, R. K.; Ermler, U. The Crystal Structure of [Fe]-Hydrogenase Reveals the Geometry of the Active Site. *Science* **2008**, *321*, 572. DOI: 10.1126/science.1158978.

(8) Fontecilla-Camps, J. C.; Volbeda, A.; Cavazza, C.; Nicolet, Y. Structure/Function Relationships of [NiFe]- and [FeFe]-Hydrogenases. (Chem. Rev. 2007, 107, 4273−4303. Published on the Web September 13, 2007.). *Chem. Rev.* **2007**, *107*, 5411. DOI: 10.1021/cr078107t.

(9) Darensbourg, M. Y.; Lyon, E. J.; Zhao, X.; Georgakaki, I. P. The organometallic active site of [Fe]hydrogenase: Models and entatic states. *Proc. Natl. Acad. Sci. U.S.A.* **2003**, *100*, 3683. DOI: 10.1073/pnas.0536955100.

(10) Silakov, A.; Wenk, B.; Reijerse, E.; Lubitz, W. ^{14}N HYSCORE investigation of the H-cluster of [FeFe] hydrogenase: evidence for a nitrogen in the dithiol bridge. *Phys. Chem. Chem. Phys.* **2009**, *11*, 6592. DOI: 10.1039/B905841A.

(11) Duan, J.; Mebs, S.; Laun, K.; Wittkamp, F.; Heberle, J.; Happe, T.; Hofmann, E.; Apfel, U.-P.; Winkler, M.; Senger, M.; et al. Geometry of the Catalytic Active Site in [FeFe]-Hydrogenase Is Determined by Hydrogen Bonding and Proton Transfer. *ACS Catal.* **2019**, *9*, 9140. DOI: 10.1021/acscatal.9b02203.

(12) Dementin, S.; Burlat, B.; De Lacey, A. L.; Pardo, A.; Adryanczyk-Perrier, G.; Guigliarelli, B.; Fernandez, V. M.; Rousset, M. A Glutamate Is the Essential Proton Transfer Gate during the

Catalytic Cycle of the [NiFe] Hydrogenase. *J. Biol. Chem.* **2004**, *279*, 10508. DOI: 10.1074/jbc.M312716200.

(13) De Lacey, A. L.; Fernández, V. M.; Rousset, M.; Cammack, R. Activation and Inactivation of Hydrogenase Function and the Catalytic Cycle: Spectroelectrochemical Studies. *Chem. Rev.* **2007**, *107*, 4304. DOI: 10.1021/cr0501947.

(14) Ogata, H.; Nishikawa, K.; Lubitz, W. Hydrogens detected by subatomic resolution protein crystallography in a [NiFe] hydrogenase. *Nature* **2015**, *520*, 571. DOI: 10.1038/nature14110.

(15) Senger, M.; Eichmann, V.; Laun, K.; Duan, J.; Wittkamp, F.; Knör, G.; Apfel, U.-P.; Happe, T.; Winkler, M.; Heberle, J.; et al. How [FeFe]-Hydrogenase Facilitates Bidirectional Proton Transfer. *J. Am. Chem. Soc.* **2019**, *141*, 17394. DOI: 10.1021/jacs.9b09225.

(16) Chongdar, N.; Rodríguez-Maciá, P.; Reijerse, E. J.; Lubitz, W.; Ogata, H.; Birrell, J. A. Redox tuning of the H-cluster by second coordination sphere amino acids in the sensory [FeFe] hydrogenase from *Thermotoga maritima*. *Chem. Sci.* **2023**, *14*, 3682. DOI: 10.1039/D2SC06432D.

(17) Ogata, H.; Lubitz, W.; Higuchi, Y. Structure and function of [NiFe] hydrogenases. *J. Biochem.* **2016**, *160*, 251. DOI: 10.1093/jb/mvw048.

(18) Lubitz, W.; Ogata, H.; Rüdiger, O.; Reijerse, E. Hydrogenases. *Chem. Rev.* **2014**, *114*, 4081. DOI: 10.1021/cr4005814.

(19) Qiu, S.; Azofra, L. M.; MacFarlane, D. R.; Sun, C. Hydrogen bonding effect between active site and protein environment on catalysis performance in H_2-producing [NiFe] hydrogenases. *Phys. Chem. Chem. Phys.* **2018**, *20*, 6735. DOI: 10.1039/C7CP07685A.

(20) Agrawal, A. G.; van Gastel, M.; Gärtner, W.; Lubitz, W. Hydrogen Bonding Affects the [NiFe] Active Site of *Desulfovibrio vulgaris* Miyazaki F Hydrogenase: A Hyperfine Sublevel Correlation Spectroscopy and Density Functional Theory Study. *J. Phys. Chem. B* **2006**, *110*, 8142. DOI: 10.1021/jp0573902.

(21) Ogata, H.; Hirota, S.; Nakahara, A.; Komori, H.; Shibata, N.; Kato, T.; Kano, K.; Higuchi, Y. Activation Process of [NiFe] Hydrogenase Elucidated by High-Resolution X-Ray Analyses: Conversion of the Ready to the Unready State. *Structure* **2005**, *13*, 1635. DOI: 10.1016/j.str.2005.07.018.

(22) Barondeau, D. P.; Kassmann, C. J.; Bruns, C. K.; Tainer, J. A.; Getzoff, E. D. Nickel Superoxide Dismutase Structure and Mechanism. *Biochemistry* **2004**, *43*, 8038. DOI: 10.1021/bi0496081.

(23) Xia, B.; Wilkens, S. J.; Westler, W. M.; Markley, J. L. Amplification of One-Bond 1H/2H Isotope Effects on 15N Chemical Shifts in Clostridium pasteurianum Rubredoxin by Fermi-Contact Effects through Hydrogen Bonds. *J. Am. Chem. Soc.* **1998**, *120*, 4893. DOI: 10.1021/ja974167c.

(24) Bougault, C. M.; Eidsness, M. K.; Prestegard, J. H. Hydrogen Bonds in Rubredoxins from Mesophilic and Hyperthermophilic Organisms. *Biochemistry* **2003**, *42*, 4357. DOI: 10.1021/bi027264d.

(25) Deng, T.-j.; Macdonald, I. D. G.; Simianu, M. C.; Sykora, M.; Kincaid, J. R.; Sligar, S. G. Hydrogen-Bonding Interactions in the Active Sites of Cytochrome P450cam and Its Site-Directed Mutants. *J. Am. Chem. Soc.* **2001**, *123*, 269. DOI: 10.1021/ja001517d.

(26) Dey, A.; Green, K. N.; Jenkins, R. M.; Jeffrey, S. P.; Darensbourg, M.; Hodgson, K. O.; Hedman, B.; Solomon, E. I. S K-Edge XAS and DFT Calculations on Square-Planar Ni^{II}−Thiolate Complexes: Effects of Active and Passive H-Bonding. *Inorg. Chem.* **2007**, *46*, 9655. DOI: 10.1021/ic7006292.

(27) Gale, E. M.; Narendrapurapu, B. S.; Simmonett, A. C.; Schaefer, H. F., III; Harrop, T. C. Exploring the Effects of H-Bonding in Synthetic Analogues of Nickel Superoxide Dismutase (Ni-SOD): Experimental and Theoretical Implications for Protection of the Ni−SCys Bond. *Inorg. Chem.* **2010**, *49*, 7080. DOI: 10.1021/ic1009187.

(28) Steiner, R. A.; Dzul, S. P.; Stemmler, T. L.; Harrop, T. C. Synthesis and Speciation-Dependent Properties of a Multimetallic Model Complex of NiSOD That Exhibits Unique Hydrogen-Bonding. *Inorg. Chem.* **2017**, *56*, 2849. DOI: 10.1021/acs.inorgchem.6b02997.

(29) Lin, I.-J.; Gebel, E. B.; Machonkin, T. E.; Westler, W. M.; Markley, J. L. Changes in hydrogen-bond strengths explain reduction potentials in 10 rubredoxin variants. *Proc. Natl. Acad. Sci. U.S.A.* **2005**, *102*, 14581. DOI: 10.1073/pnas.0505521102.

(30) Slater, J. W.; Marguet, S. C.; Gray, M. E.; Monaco, H. A.; Sotomayor, M.; Shafaat, H. S. Power of the Secondary Sphere: Modulating Hydrogenase Activity in Nickel-Substituted Rubredoxin. *ACS Catal.* **2019**, *9*, 8928. DOI: 10.1021/acscatal.9b01720.

(31) Dey, A.; Okamura, T.-a.; Ueyama, N.; Hedman, B.; Hodgson, K. O.; Solomon, E. I. Sulfur K-Edge XAS and DFT Calculations on P450 Model Complexes: Effects of Hydrogen Bonding on Electronic Structure and Redox Potentials. *J. Am. Chem. Soc.* **2005**, *127*, 12046. DOI: 10.1021/ja0519031.

(32) Slater, J. W.; Marguet, S. C.; Monaco, H. A.; Shafaat, H. S. Going beyond Structure: Nickel-Substituted Rubredoxin as a Mechanistic Model for the [NiFe] Hydrogenases. *J. Am. Chem. Soc.* **2018**, *140*, 10250. DOI: 10.1021/jacs.8b05194.

(33) Bhattacharjee, A.; Brown, D. S. V.; Virca, C. N.; Ethridge, T. E.; Mendez Galue, O.; Pham, U. T.; McCormick, T. M. Computational investigation into intramolecular hydrogen bonding controlling the isomer formation and pK_a of octahedral nickel(II) proton reduction catalysts. *Dalton Trans.* **2022**, *51*, 3676. DOI: 10.1039/D2DT00043A.

(34) Roos, G.; Foloppe, N.; Messens, J. Understanding the pK_a of Redox Cysteines: The Key Role of Hydrogen Bonding. *Antioxidants & Redox Signaling* **2013**, *18*, 94. DOI: 10.1089/ars.2012.4521.

(35) Smith, J. N.; Hoffman, J. T.; Shirin, Z.; Carrano, C. J. H-Bonding Interactions and Control of Thiolate Nucleophilicity and Specificity in Model Complexes of Zinc Metalloproteins. *Inorg. Chem.* **2005**, *44*, 2012. DOI: 10.1021/ic048630f.

(36) Smith, J. N.; Shirin, Z.; Carrano, C. J. Control of Thiolate Nucleophilicity and Specificity in Zinc Metalloproteins by Hydrogen Bonding: Lessons from Model Compound Studies. *J. Am. Chem. Soc.* **2003**, *125*, 868. DOI: 10.1021/ja029418i.

(37) Chiou, S.-J.; Riordan, C. G.; Rheingold, A. L. Synthetic modeling of zinc thiolates: Quantitative assessment of hydrogen bonding in modulating sulfur alkylation rates. *Proc. Natl. Acad. Sci. U.S.A.* **2003**, *100*, 3695. DOI: 10.1073/pnas.0637221100.

(38) Yamamura, T.; Miyamae, H.; Katayama, Y.; Sasaki, Y. Nickel Thiolates. Simple Synthesis, the Behaivor Upon Protolysis and Oxidation Potentials. *Chem. Lett.* **1985**, *14*, 269. DOI: 10.1246/cl.1985.269.

(39) Rosenfield, S. G.; Armstrong, W. H.; Mascharak, P. K. Convenient Synthesis and Properties of $(R_4N)_2[Ni(SAr)_4]$ (Ar = C_6H_5, *p*-C_6H_4Cl, *p*-$C_6H_4CH_3$, and *m*-C_6H_4Cl) and the Structure of Tetraethylammonium Tetrakis(*p*-chlorobenzenethiolato)nickelate(II). *Inorg. Chem.* **1986**, *25*, 3014. DOI: 10.1021/ic00237a018.

(40) Okamura, T.-a.; Takamizawa, S.; Ueyama, N.; Nakamura, A. Novel Rubredoxin Model Tetrathiolato Iron(II) and Cobalt(II) Complexes Containing Intramolecular Single and Double NH···S Hydrogen Bonds. *Inorg. Chem.* **1998**, *37*, 18. DOI: 10.1021/ic970640b.

(41) Kato, M.; Okamura, T.-a.; Yamamoto, H.; Ueyama, N. Effects of the Intramolecular NH···S Hydrogen Bond in Mononuclear Platinum(II) and Palladium(II) Complexes with 2,2‘-Bipyridine and Benzenethiol Derivatives. *Inorg. Chem.* **2005**, *44*, 1966. DOI: 10.1021/ic0490167.

(42) Ueyama, N.; Yamada, Y.; Okamura, T.-a.; Kimura, S.; Nakamura, A. Structure and Properties of $[Fe_4S_4\{2,6\text{-bis(acylamino)benzenethiolato-}S\}_4]2-$ and $[Fe_2S_2\{2,6\text{-bis(acylamino)benzenethiolato-}S\}_4]^{2-}$: Protection of the Fe−S Bond by Double NH···S Hydrogen Bonds. *Inorg. Chem.* **1996**, *35*, 6473. DOI: 10.1021/ic9604324.

(43) Yang, L.; Powell, D. R.; Houser, R. P. Structural variation in copper(I) complexes with pyridylmethylamide ligands: structural analysis with a new four-coordinate geometry index, τ_4. *Dalton Trans.* **2007**, 955. DOI: 10.1039/B617136B.

(44) Colpas, G. J.; Maroney, M. J.; Bagyinka, C.; Kumar, M.; Willis, W. S.; Suib, S. L.; Mascharak, P. K.; Baidya, N. X-ray Spectroscopic Studies of Nickel Complexes, with Application to the Structure of Nickel Sites in Hydrogenases. *Inorg. Chem.* **1991**, *30*, 920. DOI: 10.1021/ic00005a010.

(45) Swenson, D.; Baenziger, N. C.; Coucouvanis, D. Tetrahedral Mercaptide Complexes. Crystal and Molecular Structures of $[(C_6H_5)_4P]_2M(SC_6H_5)_4$ Complexes (M = Cd(II), Zn(II), Ni(II), Co(II), and Mn(II)). *J. Am. Chem. Soc.* **1978**, *100*, 1932. DOI: 10.1021/ja00474a053.

(46) Rheingold, A. L.; Beall, K. S.; Riggs, P. J.; Groh, S. E. Bis(tetraethylammonium) Nickel Tetrakisthiophenolate: a New Polymorph. *Acta Cryst. C* **1993**, *49*, DOI: 10.1107/S0108270192007704.

(47) Queen, M. S.; Towey, B. D.; Murray, K. A.; Veldkamp, B. S.; Byker, H. J.; Szilagyi, R. K. Electronic structure of [Ni(II)S_4] complexes from S K-edge X-ray absorption spectroscopy. *Coord. Chem. Rev.* **2013**, *257*, 564. DOI: doi.org/10.1016/j.ccr.2012.07.020.

(48) Adman, E.; Watenpaugh, K. D.; Jensen, L. H. NH---S hydrogen bonds in *Peptococcus aerogenes* ferredoxin, *Clostridium pasteurianum* rubredoxin, and *Chromatium* high potential iron protein. *Proc. Natl. Acad. Sci. U.S.A.* **1975**, *72*, 4854. DOI: 10.1073/pnas.72.12.4854.

(49) Ariyananda, P. W. G.; Kieber-Emmons, M. T.; Yap, G. P. A.; Riordan, C. G. Synthetic analogs for evaluating the influence of N–H···S hydrogen bonds on the formation of thioester in acetyl coenzyme a synthase. *Dalton Trans.* **2009**, 4359. DOI: 10.1039/B901192G.

(50) Ueyama, N.; Nishikawa, N.; Yamada, Y.; Okamura, T.-a.; Nakamura, A. Cytochrome P-450 Model (Porphinato)(thiolato)iron(III) Complexes with Single and Double NH···S Hydrogen Bonds at the Thiolate Site. *J. Am. Chem. Soc.* **1996**, *118*, 12826. DOI: 10.1021/ja9622970.

(51) Kato, M.; Okamura, T.; Yamamoto, H.; Ueyama, N. Effects of the Intramolecular NH···S Hydrogen Bond in Mononuclear Platinum(II) and Palladium(II) Complexes with 2,2‘-Bipyridine and Benzenethiol Derivatives. *Inorg. Chem.* **2005**, *44*, 1966. DOI: 10.1021/ic0490167.

(52) Han, Z.; Shen, L.; Brennessel, W. W.; Holland, P. L.; Eisenberg, R. Nickel Pyridinethiolate Complexes as Catalysts for the Light-Driven Production of Hydrogen from Aqueous Solutions in Noble-Metal-Free Systems. *J. Am. Chem. Soc.* **2013**, *135*, 14659. DOI: 10.1021/ja405257s.

(53) Baidya, N.; Mascharak, P. K.; Stephan, D. W.; Campagna, C. F. Mononuclear nickel(II) thiolates of square-planar geometry: syntheses, spectral and redox properties of $[Ni(SCH_2CH_2S)_2]^{2-}$ and $[Ni(SCH(CH_3)CH(CH_3)S)_2]^{2-}$ and the structure of $(Ph_4P)_2[Ni(SCH_2CH_2S)_2]\cdot 4H_2O$. *Inorg. Chim. Acta* **1990**, *177*, 233. DOI: 10.1016/S0020-1693(00)85981-2.

(54) Erkizia, E.; Conry, R. R. Synthesis and Characterization of Square Planar Nickel(II)−Arylthiolate Complexes with the Biphenyl-2,2'-dithiolate Ligand. *Inorg. Chem.* **2000**, *39*, 1674. DOI: 10.1021/ic990931f.

(55) Silver, A.; Koch, S. A.; Millar, M. X-ray crystal structures of a series of $[M^{II}(SR)_4]^{2-}$ complexes (M - Mn, Fe, Co, Ni, Zn, Cd and Hg) with S_4 crystallographic symmetry. *Inorg. Chim. Acta* **1993**, *205*, 9. DOI: 10.1016/S0020-1693(00)87348-X.

(56) Williams, K. R.; Hedman, B.; Hodgson, K. O.; Solomon, E. I. Ligand K-edge X-ray absorption spectroscopic studies: metal-ligand covalency in transition metal tetrathiolates. *Inorg. Chim. Acta* **1997**, *263*, 315. DOI: 10.1016/S0020-1693(97)05663-6.

(57) Van Heuvelen, K. M.; Cho, J.; Dingee, T.; Riordan, C. G.; Brunold, T. C. Spectroscopic and Computational Studies of a Series of High-Spin Ni(II) Thiolate Complexes. *Inorg. Chem.* **2010**, *49*, 6535. DOI: 10.1021/ic100362q.

(58) Janiak, C. A critical account on π–π stacking in metal complexes with aromatic nitrogen-containing ligands. *J. Chem. Soc., Dalton Trans.* **2000**, 3885. DOI: 10.1039/B003010O.

(59) Barone, V.; Cossi, M. Quantum Calculation of Molecular Energies and Energy Gradients in Solution by a Conductor Solvent Model. *J. Phys. Chem. A* **1998**, *102*, 1995. DOI: 10.1021/jp9716997.

(60) Fiedler, A. T.; Bryngelson, P. A.; Maroney, M. J.; Brunold, T. C. Spectroscopic and Computational Studies of Ni Superoxide Dismutase: Electronic Structure Contributions to Enzymatic Function. *J. Am. Chem. Soc.* **2005**, *127*, 5449. DOI: 10.1021/ja042521i.

(61) Grapperhaus, C. A.; Darensbourg, M. Y. Oxygen Capture by Sulfur in Nickel Thiolates. *Acc. Chem. Res.* **1998**, *31*, 451. DOI: 10.1021/ar950048v.

(62) Grapperhaus, C. A.; Mullins, C. S.; Kozlowski, P. M.; Mashuta, M. S. Synthesis and Oxygenation of a Nickel(II) and Zinc(II) Dithiolate: An Experimental and Theoretical Comparison. *Inorg. Chem.* **2004**, *43*, 2859. DOI: 10.1021/ic035205y.

(63) Mullins, C. S.; Grapperhaus, C. A.; Kozlowski, P. M. Density functional theory investigations of NiN_2S_2 reactivity as a function of nitrogen donor type and N–H···S hydrogen bonding inspired by nickel-containing superoxide dismutase. *J. Biol. Inorg. Chem.* **2006**, *11*, 617. DOI: 10.1007/s00775-006-0109-6.

(64) Perdew, J. P.; Levy, M. Comment on "Significance of the highest occupied Kohn-Sham eigenvalue". *Phys. Rev. B* **1997**, *56*, 16021. DOI: 10.1103/PhysRevB.56.16021.

(65) Ueyama, N.; Okamura, T.-A.; Nakamura, A. Intramolecular NH ··· S Hydrogen Bond in *o*-Acylamino Substituted Benzenethiolate Iron(II) and Cobalt(II) Complexes. *J. Chem. Soc., Chem. Commun.* **1992**, 1019. DOI: 10.1039/C39920001019.

(66) Jha, N. N.; Ray, I. P. Magnetic studies on Co(II) and Ni(II) complexes of hydroxamic acid. *Asian Journal of Chemistry* **2000**, *12*, 703.

(67) Yamamura, T.; Arai, H. Tetrakis(thiolato)nickelate(II), $[Ni(RS)_4]^{2-}$; Ligand Dissociation and Electronic Spectra. *Bull. Chem. Soc. Jpn.* **1992**, *65*, 1799. DOI: 10.1246/bcsj.65.1799.

(68) Colpas, G. J.; Kumar, M.; Day, R. O.; Maroney, M. J. Structural Investigations of Nickel Complexes with Nitrogen and Sulfur Donor Ligands. *Inorg. Chem.* **1990**, *29*, 4779. DOI: 10.1021/ic00348a037.

(69) Kowal, A. T.; Zambrano, I. C.; Moura, I.; Moura, J. J. G.; LeGall, J.; Johnson, M. K. Electronic and magnetic properties of nickel-substituted rubredoxin: a variable-temperature magnetic circular dichroism study. *Inorg. Chem.* **1988**, *27*, 1162. DOI: 10.1021/ic00280a015.

(70) Huang, Y. H.; Moura, I.; Moura, J. J. G.; LeGall, J.; Park, J. B.; Adams, M. W. W.; Johnson, M. K. Resonance Raman Studies of Nickel Tetrathiolates and Nickel-Substituted Rubredoxins and Desulforedoxin. *Inorg. Chem.* **1993**, *32*, 406. DOI: 10.1021/ic00056a012.

(71) Slater, J. W.; Marguet, S. C.; Cirino, S. L.; Maugeri, P. T.; Shafaat, H. S. Experimental and DFT Investigations Reveal the Influence of the Outer Coordination Sphere on the Vibrational Spectra of Nickel-Substituted Rubredoxin, a Model Hydrogenase Enzyme. *Inorg. Chem.* **2017**, *56*, 3926. DOI: 10.1021/acs.inorgchem.6b02934.

(72) Watson, A. D.; Rao, C. P.; Dorfman, J. R.; Holm, R. H. Systematic Stereochemistry of Metal(II) Thiolates: Synthesis and Structures of $[M_2(SC2H5)_6]^{2-}$ (M = Mn(II), Ni(II), Zn(II), Cd(II)). *Inorg. Chem.* **1985**, *24*, 2820. DOI: 10.1021/ic00212a024.

(73) Nicholson, J. R.; Christou, G.; Huffman, J. C.; Folting, K. The synthesis, structure and spectroscopic properties of the di- and tri-nuclear Ni(II) thiolate complexes. *Polyhedron* **1987**, *6*, 863. DOI: 10.1016/S0277-5387(00)80927-4.

(74) Tremel, W.; Kriege, M.; Krebs, B.; Henkel, G. Nickel-Thiolate Chemistry Based on Chelating Ligands: Controlling the Course of Self-Assembly Reactions via Ligand Bite Distances. Synthesis, Structures, and Properties of the Homoleptic Complexes $[Ni_3(SCH_2C_6H_4CH_2S)_4]^{2-}$, $[Ni_3(SCH_2CH_2S)_4]^{2-}$, and $[Ni_6(SCH_2CH_2CH_2S)_7]^{2-}$. *Inorg. Chem.* **1988**, *27*, 3886. DOI: 10.1021/ic00295a004.

(75) Walters, M. A.; Dewan, J. C.; Min, C.; Pinto, S. Models of Amide-Cysteine Hydrogen Bonding in Rubredoxin: Hydrogen Bonding between Amide and Benzenethiolate in $[(CH_3)_3NCH_2CONH_2]_2[Co(SC_6H_5)_4]1/2CH_3CN$ and $[(CH_3)_3NCH_2CONH_2][SC_6H_5]$. *Inorg. Chem.* **1991**, *30*, 2656. DOI: 10.1021/ic00012a018.

(76) Steiner, T. The Hydrogen Bond in the Solid State. *Angew. Chem. Int. Ed.* **2002**, *41*, 48. DOI: 10.1002/1521-3773(20020104)41:1<48::AID-ANIE48>3.0.CO;2-U.

(77) Ueyama, N.; Okamura, T.-a.; Yamada, Y.; Nakamura, A. Crystal and Solution Structures of Novel Bulky Bis[2,6-bis(acylamino)phenyl] Disulfides. Absence of Covalent NH···S Hydrogen Bond between Amide NH and Neighboring Disulfide in Bis[2,6-bis(pivaloylamino)phenyl] Disulfide. *J. Org. Chem.* **1995**, *60*, 4893. DOI: 10.1021/jo00120a037.

(78) Ueyama, N.; Okamura, T.; Nakamura, A. Structure and Properties of Molybdenum(IV,V) Arenethiolates with a Neighboring Amide Group. Significant Contribution of NH···S HydrogenBond to the PositivevShift of Redox Potential of Mo(V)/Mo(IV). *J. Am. Chem. Soc.* **1992**, *114*, 8129. DOI: 10.1021/ja00047a022.

(79) Okamura, T.-A.; Ueyama, N.; Nakamura, A.; Ainscough, E. W.; Brodie, A. M.; Waters, J. M. The effect of strong NH ⋯ S hydrogen bonds in the copper(I) thiolate complex,(NEt4)2[Cu(o-pabt)3](o-pabt =o-pivaloylaminobenzenethiolato). *J. Chem. Soc., Chem. Commun.* **1993**, 1658. DOI: 10.1039/C39930001658.

(80) Kütt, A.; Tshepelevitsh, S.; Saame, J.; Lõkov, M.; Kaljurand, I.; Selberg, S.; Leito, I. Strengths of Acids in Acetonitrile. *Eur. J. Org. Chem.* **2021**, *2021*, 1407. DOI: 10.1002/ejoc.202001649.

(81) Poater, A.; Cosenza, B.; Correa, A.; Giudice, S.; Ragone, F.; Scarano, V.; Cavallo, L. SambVca: A Web Application for the Calculation of the Buried Volume of N-Heterocyclic Carbene Ligands. *Eur. J. Inorg. Chem.* **2009**, *2009*, 1759. DOI: 10.1002/ejic.200801160.

(82) Falivene, L.; Cao, Z.; Petta, A.; Serra, L.; Poater, A.; Oliva, R.; Scarano, V.; Cavallo, L. Towards the online computer-aided design of catalytic pockets. *Nat. Chem.* **2019**, *11*, 872. DOI: 10.1038/s41557-019-0319-5.

(83) Carter, C. W. New stereochemical analogies between iron-sulfur electron transport proteins. *J. Biol. Chem.* **1977**, *252*, 7802. DOI: 10.1016/S0021-9258(17)41038-6.

(84) Baba, K.; Okamura, T.-a.; Yamamoto, H.; Yamamoto, T.; Ueyama, N. Zinc, Cadmium, and Mercury 1,2-Benzenedithiolates with Intramolecular NH···S Hydrogen Bonds. *Inorg. Chem.* **2008**, *47*, 2837. DOI: 10.1021/ic702037k.

(85) Hagen, K. S.; Reynolds, J. G.; Holm, R. H. Definition of reaction sequences resulting in self-assembly of $[Fe_4S_4(SR)_4]^{2-}$ clusters from simple reactants. *J. Am. Chem. Soc.* **1981**, *103*, 4054. DOI: 10.1021/ja00404a013.

(86) Lee, K. J.; McCarthy, B. D.; Dempsey, J. L. On decomposition, degradation, and voltammetric deviation: the electrochemist's field guide to identifying precatalyst transformation. *Chem. Soc. Rev.* **2019**, *48*, 2927. DOI: 10.1039/C8CS00851E.

(87) Anxolabéhère-Mallart, E.; Costentin, C.; Fournier, M.; Robert, M. Cobalt-Bisglyoximato Diphenyl Complex as a Precatalyst for Electrocatalytic H_2 Evolution. *J. Phys. Chem. C* **2014**, *118*, 13377. DOI: 10.1021/jp500813r.

(88) Kaeffer, N.; Morozan, A.; Fize, J.; Martinez, E.; Guetaz, L.; Artero, V. The Dark Side of Molecular Catalysis: Diimine–Dioxime Cobalt Complexes Are Not the Actual Hydrogen Evolution Electrocatalyst in Acidic Aqueous Solutions. *ACS Catal.* **2016**, *6*, 3727. DOI: 10.1021/acscatal.6b00378.

(89) Martin, D. J.; McCarthy, B. D.; Donley, C. L.; Dempsey, J. L. Electrochemical hydrogenation of a homogeneous nickel complex to form a surface adsorbed hydrogen-evolving species. *Chem. Commun.* **2015**, *51*, 5290. DOI: 10.1039/C4CC08662G.

(90) McCarthy, B. D.; Donley, C. L.; Dempsey, J. L. Electrode initiated proton-coupled electron transfer to promote degradation of a nickel(II) coordination complex. *Chem. Sci.* **2015**, *6*, 2827. DOI: 10.1039/C5SC00476D.

(91) Fang, M.; Engelhard, M. H.; Zhu, Z.; Helm, M. L.; Roberts, J. A. S. Electrodeposition from Acidic Solutions of Nickel Bis(benzenedithiolate) Produces a Hydrogen-Evolving Ni–S Film on Glassy Carbon. *ACS Catal.* **2014**, *4*, 90. DOI: 10.1021/cs400675u.

(92) Artero, V.; Fontecave, M. Solar fuels generation and molecular systems: is it homogeneous or heterogeneous catalysis? *Chem. Soc. Rev.* **2013**, *42*, 2338. DOI: 10.1039/C2CS35334B.

(93) Cherdo, S.; Ghachtouli, S. E.; Sircoglou, M.; Brisset, F.; Orio, M.; Aukauloo, A. A nickel dimethyl glyoximato complex to form nickel based nanoparticles for electrocatalytic H_2 production. *Chem. Commun.* **2014**, *50*, 13514. DOI: 10.1039/C4CC05355A.

(94) Anxolabéhère-Mallart, E.; Costentin, C.; Fournier, M.; Nowak, S.; Robert, M.; Savéant, J.-M. Boron-Capped Tris(glyoximato) Cobalt Clathrochelate as a Precursor for the Electrodeposition of Nanoparticles Catalyzing H_2 Evolution in Water. *J. Am. Chem. Soc.* **2012**, *134*, 6104. DOI: 10.1021/ja301134e.

(95) Wombwell, C.; Reisner, E. Synthesis, structure and reactivity of Ni site models of [NiFeSe] hydrogenases. *Dalton Trans.* **2014**, *43*, 4483. DOI: 10.1039/C3DT52967C.

(96) Vicic, D. A.; Jones, W. D. Room-Temperature Desulfurization of Dibenzothiophene Mediated by $[(i\text{-}Pr_2PCH_2)_2NiH]_2$. *J. Am. Chem. Soc.* **1997**, *119*, 10855. DOI: 10.1021/ja972544f.

(97) Torres-Nieto, J.; Brennessel, W. W.; Jones, W. D.; García, J. J. Mechanistic Insights on the Hydrodesulfurization of Biphenyl-2-thiol with Nickel Compounds. *J. Am. Chem. Soc.* **2009**, *131*, 4120. DOI: 10.1021/ja809457s.

(98) Eisch, J. J.; Hallenbeck, L. E.; Han, K. I. Organic chemistry of subvalent transition metal complexes. Part 7. Desulfurization of dibenzothiophene by nickel(0) complexes: evidence for electron transfer in oxidative additions. *J. Org. Chem.* **1983**, *48*, 2963. DOI: 10.1021/jo00166a005.

(99) Gill, N. S. 680. Complex Halides of the Transition Metals. Part II. Tetrahedral Iron Complexes. *J. Am. Chem. Soc.* **1961**, 3512. DOI: 10.1039/JR9610003512.

(100) Fulmer, G. R.; Miller, A. J. M.; Sherden, N. H.; Gottlieb, H. E.; Nudelman, A.; Stoltz, B. M.; Bercaw, J. E.; Goldberg, K. I. NMR Chemical Shifts of Trace Impurities: Common Laboratory Solvents, Organics, and Gases in Deuterated Solvents Relevant to the Organometallic Chemist. *Organometallics* **2010**, *29*, 2176. DOI: 10.1021/om100106e.

(101) Rosenau, C. P.; Jelier, B. J.; Gossert, A. D.; Togni, A. Exposing the Origins of Irreproducibility in Fluorine NMR Spectroscopy. *Angew. Chem. Int. Ed.* **2018**, *57*, 9528. DOI: 10.1002/anie.201802620.

(102) Loliger, J.; Scheffold, R. Paramagnetic moment measurements by nmr. A micro technique. *J. Chem. Educ.* **1972**, *49*, 646. DOI: 10.1021/ed049p646.

(103) Bain, G. A.; Berry, J. F. Diamagnetic Corrections and Pascal's Constants. *J. Chem. Educ.* **2008**, *85*, 532. DOI: 10.1021/ed085p532.

(104) Becke, A. D. Density-functional thermochemistry. III. The role of exact exchange. *J. Chem. Phys.* **1993**, *98*, 5648. DOI: 10.1063/1.464913.

(105) Lee, C.; Yang, W.; Parr, R. G. Development of the Colle-Salvetti correlation-energy formula into a functional of the electron density. *Phys. Rev. B* **1988**, *37*, 785. DOI: 10.1103/PhysRevB.37.785.

(106) Kossmann, S.; Neese, F. Efficient Structure Optimization with Second-Order Many-Body Perturbation Theory: The RIJCOSX-MP2 Method. *J. Chem. Theory Comput.* **2010**, *6*, 2325. DOI: 10.1021/ct100199k.

(107) Grimme, S.; Antony, J.; Ehrlich, S.; Krieg, H. A consistent and accurate ab initio parametrization of density functional dispersion correction (DFT-D) for the 94 elements H-Pu. *J. Chem. Phys.* **2010**, *132*, 154104. DOI: 10.1063/1.3382344.

(108) Grimme, S.; Ehrlich, S.; Goerigk, L. Effect of the damping function in dispersion corrected density functional theory. *J. Comput. Chem.* **2011**, *32*, 1456. DOI: 10.1002/jcc.21759.

(109) Weigend, F.; Ahlrichs, R. Balanced basis sets of split valence, triple zeta valence and quadruple zeta valence quality for H to Rn: Design and assessment of accuracy. *Phys. Chem. Chem. Phys.* **2005**, *7*, 3297. DOI: 10.1039/B508541A.

(110) Schäfer, A.; Horn, H.; Ahlrichs, R. Fully optimized contracted Gaussian basis sets for atoms Li to Kr. *J. Chem. Phys.* **1992**, *97*, 2571. DOI: 10.1063/1.463096.

(111) Pettersen, E. F.; Goddard, T. D.; Huang, C. C.; Couch, G. S.; Greenblatt, D. M.; Meng, E. C.; Ferrin, T. E. UCSF Chimera—A Visualization System for Exploratory Research and Analysis. *J. Comput. Chem.* **2004**, *25*, 1605. DOI: 10.1002/jcc.20084.

(112) Petrenko, T.; Kossmann, S.; Neese, F. Efficient time-dependent density functional theory approximations for hybrid density functionals: Analytical gradients and parallelization. *J. Chem. Phys.* **2011**, *134*, 054116. DOI: 10.1063/1.3533441.

(113) Neese, F.; Olbrich, G. Efficient use of the resolution of the identity approximation in time-dependent density functional calculations with hybrid density functionals. *Chem. Phys. Lett.* **2002**, *362*, 170. DOI: 10.1016/S0009-2614(02)01053-9.

(114) *EXAFSPAK*; Stanford Synchotron Radiation Lightsource: Menlo Park, CA,, 2001. (accessed.

(115) Rehr, J. J.; Ankudinov, A. L. Progress and challenges in the theory and interpretation of X-ray spectra. *J. Synchrotron Rad.* **2001**, *8*, 61. DOI: 10.1107/S0909049500016423.

(116) Riggs-Gelasco, P. J.; Stemmler, T. L.; Penner-Hahn, J. E. XAFS of dinuclear metal sites in proteins and model compounds. *Coord. Chem. Rev.* **1995**, *144*, 245. DOI: 10.1016/0010-8545(95)01144-E.

(117) Krause, L.; Herbst-Irmer, R.; Sheldrick, G. M.; Stalke, D. Comparison of silver and molybdenum microfocus X-ray sources for single-crystal structure determination. *J. Appl. Cryst.* **2015**, *48*, 3. DOI: 10.1107/S1600576714022985.

(118) Sheldrick, G. SHELXT - Integrated space-group and crystal-structure determination. *Acta Cryst. A* **2015**, *71*, 3. DOI: 10.1107/S2053273314026370.

(119) Sheldrick, G. Crystal structure refinement with SHELXL. *Acta Cryst. C* **2015**, *71*, 3. DOI: 10.1107/S2053229614024218.

(120) Kawamoto, T.; Suzuki, S.; Konno, T. Synthesis and characterization of cyclometallated palladium(II) and platinum(II) complexes with amide-thiolate ligands. *J. Organomet. Chem.* **2007**, *692*, 257. DOI: 10.1016/j.jorganchem.2006.08.051.

CHAPTER 4

LIGAND-ASSISTED HYDROGEN EVOLUTION BY AN ELECTRON RICH NONHEME IRON-THIOLATE COMPLEX

Benjamin A. Yosen, Indranil Chakraborty, Jack H. Lin, and Todd C. Harrop. To be submitted to *Dalon Transaction*.

4.1 Abstract

Mitigating the use of fossil fuels requires clean, renewable alternatives such as hydrogen gas (H_2). Hydrogenases, which use earth-abundant metals like Fe and Ni, efficiently catalyzing H_2 production. In this work, we report a nonheme Fe-containing electrocatalyst for H_2 evolution utilizing an electron-rich mixed thiolate-S and carboxamide-N donor set, (Et_4N)[Fe(PyPS-*p*-CF_3)] (**1**) (fully deprotonated $PyPSH_4$-*p*-CF_3 = *N*,*N*'-bis(2-mercaptophenyl-5-triflouromethyl)pyridine-2,6-dicarboxamide). Although H_2 evolution was evidenced by the catalytic current response in cyclic voltammograms (CVs) upon H^+ titration with weak acids, rinse tests confirmed electrocatalysis arises from deposits on the surface of the electrode. Spectroscopic analysis of the homogeneous complex under acidic conditions suggests the formation of a tetrathiolate-Fe complex, via carboxamide-N protonation and ligand rearrangement, resulting in the release of free Fe which leads to the observed deposition. However, altering solvents conditions from MeCN to DMF diminishes deposition by hindering N-protonation and subsequent Fe-N bond cleavage, likely through solvent interaction with the protonated ligand frame. This, in turn, enables the evaluation of the electrocatalytic performance of homogenous **1**. Catalytic proton titration experiments with the redox-inert Zn(II) analog, and supporting DFT computations, suggest the redox-active ligand plays a key role in the catalytic cycle as an additional electron storage site. Furthermore, we propose the hemilabile thiolate serves a proton relay to facilitate H_2 evolution at moderate rates (~1200 s^{-1}) and overpotentials (~900 mV) through a proposed E(CECE) mechanism.

4.2 Introduction

The world's increasing demand for energy, currently provided by limited sources of fossil fuels, has led to a shift towards sustainable resources such as molecular hydrogen (H_2).[1] Combustion and/or splitting of H_2 generates energy without byproducts that contribute to the growing amount of greenhouse gases in earth's atmosphere. However, current electrochemical production of H_2 relies on Pt- and Pd- based catalysts necessitating the development of cheaper means to generate H_2. Nature utilizes Hydrogenase (H_2ase) enzymes that manage the interconversion of protons to H_2 relaying on earth-abundant metals, Ni and Fe. These enzymes have inspired the generation of low-molecular weight synthetic electrocatalysts to mimic the structure and function of the enzymatic active site.[2] Of the three classes of enzymes ([NiFe], [FeFe], and [Fe]-only) the [FeFe]-H_2ase is the most active catalyzing reversible reduction of protons at high rates, up to ~10^4 molecules of H_2 per second, and close to the thermodynamic minimum potential.[3] The active site of [FeFe]-H_2ase, shown in Figure 4.1, referred to as the H-cluster, consists of a $[4Fe\text{-}S4]^{2+}$ cluster covalently linked to the proximal Fe (Fe_p) of a [2Fe] cluster that is coordinated to CO, CN^-, and a unique azadithioalte ligand.[4] Although the $[4Fe\text{-}S4]^{2+}$ cluster is a common redox cofactor found in nature, involved in electron transfer, it is not typically bound to the active site and is proposed to play a key role by storing and later providing electrons to the active site during turnover. Another important feature in the enzyme is a azadithiolate (adt^{2-}) moiety, forming a bridge between the two low-spin Fe centers. This moiety is proposed to function as proton relay, shuttling protons to and from the distal Fe (Fe_d), believed to contribute to the high turnover frequencies (TOFs) observed.[5]

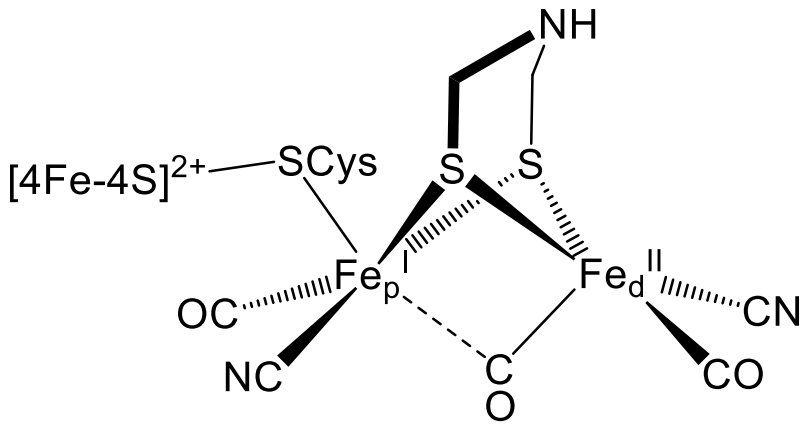

Figure 4.1. Depiction of the active site of [FeFe]-H_2ase in its most oxidized state (H_{ox}), proposed to be catalytically ready state.

Numerous synthetic and functional models of the di-iron active site have been studied for their electrocatalytic proton reduction activity with some possessing TOF values comparable to the native enzyme, albeit with overpotentials in excess of 0.5 V.[2, 6] Although much of the focus has been placed on di-iron mimics, the proposed mechanism of HER in [FeFe]-H_2ase involves only Fe_d as the site for terminal hydride formation and proton coupling suggesting mononuclear Fe complexes could be viable HER electrocatalysts. There are only a handful of mononuclear Fe electrocatalysts, shown in Scheme 4.1, possessing a wide range of overpotentials (η: 0.3 to 1.0 V) and turnover frequencies (TOF: 5 to 3300 s^{-1}), see Table 4.3.[7-14] Incorporation of pendant bases has been demonstrated to increase TOF values synthetic catalysts proposed to act as a proton relay, akin to the adt^{2-} moiety in the native enzyme. For example, Dey and coworkers found incorporation of a pendent pyridine group to Fe(TPP) doubled the reaction rate for HER.[7] In addition, hemilabile ligands such as thiolates in $(PMe_3)_2Fe(CO)_2(bdt)$[8] (bdt = 1,2-benzene ditihiolate) and phenoxide of $FeCl_2(N(Py)_2PhO)$[9], $(N(Py)_2PhO$ = N-(2-phenoxide)-N,N-bis(2-pyridylmethyl)amine) can serve as bases for proton relay yielding high TOF values, 240 and 3300 s^{-1} respectively. These electrocatalysts exhibit a common trend, wherein overpotential is predominantly governed by the

Fe(II/I) redox couple associated with the generation of the Fe(III)-H hydride intermediate. For example, McNamara and coworkers reported incorporation of a NO_2 group *para* to the phenolate donor in $FeCl_2(N(Py)_2(PhO))$ decreases overpotential by ~0.4 V due to a ~0.2 V positive shift in the Fe(III/II) couple.[15] These findings underscore the potential of mononuclear Fe complexes as tunable platforms for HER, where strategic ligand design can enhance catalytic performance.

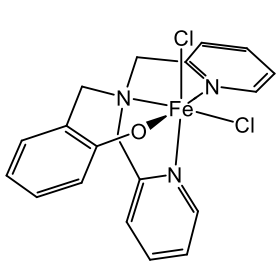

[$FeCl_2(N(Py)_2(PhO)$]

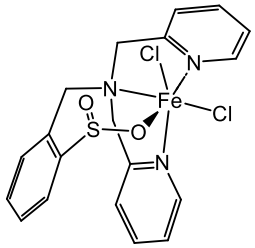

[$FeCl_2(N(Py)_2(PhSO_2)$]

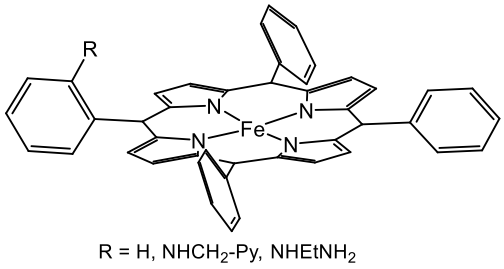

[Fe(TPP)]

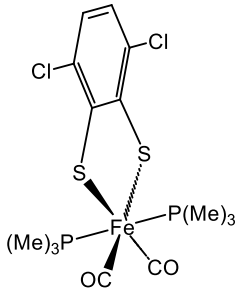

[Fe(bdt-3,6-Cl_2)$(CO)_2(PPh_3)_2$]

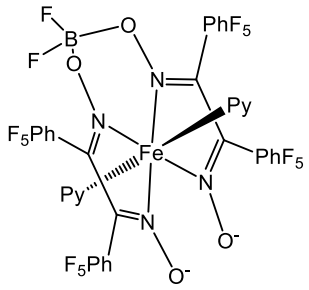

[$Fe(Py)_2(^dAr_{g2}H\text{-}BF_2)$]

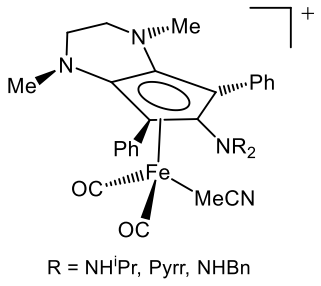

[$Fe(^{en}Cp^{Br})(CO)_2(MeCN)]^+$

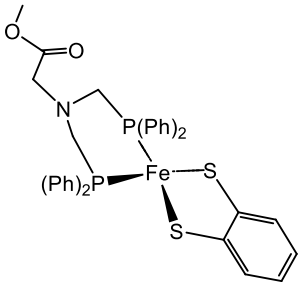

[Fe(κ^2-NP_2)CO(κ^2-bdt)]

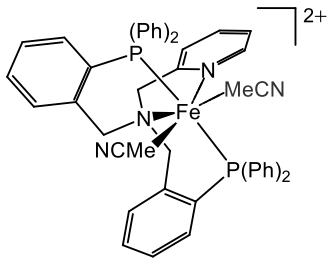

[$Fe(N_2P_2)(MeCN)_2]^{2+}$

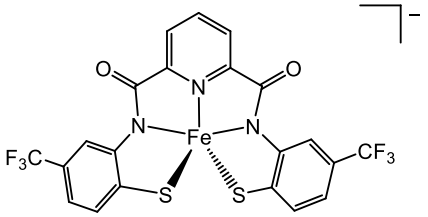

[Fe(PyPS-*p*-CF_3)]$^-$ (1)

Chart 4.1. Mononuclear Fe HER electrocatalysts including the catalyst studied in this work, (Et_4N)[Fe(PyPS-*p*-CF_3)] (**1**).

While previous studies have reported metal-centered reactivity, recent attention has been given to leveraging non-innocent ligands as a complimentary strategy for proton reduction, having recently been the subject of reviews by Mitsopoluo[16] and Zhang[17]. Redox-active ligands provide an additional site of electron storage rather than solely relying on the metal, similar to the role of the covalently bound $[4Fe\text{-}4S]^{2+}$-cluster and Fe_p in [FeFe]- H_2ase. The additional site of reduction provides an alternative pathway to generating a more thermodynamically demanding low-valent metal, i.e. Fe(I), often needed to generate the metal-hydride intermediate. Despite the growing number of ligand-assisted metal HER electrocatalysts, this strategy has not been employed for mononuclear Fe-based catalysts. To exploit this motif, we synthesized (Et_4N)[Fe(PyPS-*p*-CF_3)] (**1**) (fully deprotonated $PyPSH_4$-*p*-CF_3 = *N*,*N*'-bis(2-mercaptophenyl-5-triflouromethyl)pyridine-2,6-dicarboxamide), shown in chart 4.1, containing a redox active pyridine-2,6-dicarboxamide-based ligand featuring two *p*-CF_3-benzene thiolate rings. A similar ligand frame has been utilized by the Mascharak[18] group as models of nitrile hydratase, and Tsui [19, 20] to investigate the oxidative reactivity and sulfur insertion of Zn-thiolate bonds. This five-coordinate ligand forms a stable N_3 pincer cavity consisting of a N_{Py} group and four anionic atoms, two N_{amide} atoms and two S-atoms. The ligand frame provides several features making it an attractive target for electrocatalytic hydrogen evolution including: an open coordination site for hydride to bind, thiolates that can serve as hemilabile proton relays, and a redox-active pyridine-2,6-dicarboxamide moiety. Together, these features position complex **1** as a promising platform for investigating ligand-assisted electrocatalytic HER.

Herein, we report on the electrocatalytic activity of (Et_4N)[Fe(PyPS-*p*-CF_3)] (**1**) in MeCN and DMF. We found the electrocatalyst of **1** in MeCN arises from heterogenous material deposited on the surface of the electrode due to formation of a tetrathiolate-Fe complex, via carboxamide-N

protonation and ligand rearrangement, and free Fe. However, deposition under protic and reducing conditions can be suppressed by utilizing DMF as the solvent medium allowing the homogenous catalytic properties of **1** to be assessed. Proton titration experiments with the redox-inert Zn(II) analog, and supporting DFT computations, suggest the redox-active ligand plays an important role in the catalytic cycle and a hemilabile thiolate serves as a proton relay group to facilitate H_2 evolution at moderate rates (~1200 s^{-1}) and overpotentials (~900 mV) through a proposed E(CECE) mechanism.

4.3 Results and Discussion

Synthesis. The mixed carboxamide-thiolate ligand $PyPSH_4$ ($PyPSH_4$ = *N*,*N*'-bis(2-mercaptophenyl)pyridine-2,6-dicarboxamide) has previously been utilized as a ligand for Co(III)[21] and Fe(III/II)[18] to investigate the chemistry of the M(III) site of Nitrile Hydratase and for Zn(II) to study sulfur insertion into the Zn thiolate bond.[19] In this work, a slightly modified version of this ligand was synthesized to incorporate *p*-CF_3 groups ($PyPSH_4$-*p*-CF_3), ($PyPSH_4$-*p*-CF_3 = *N*,*N*'-bis(2-mercaptophenyl-5-triflouromethyl)pyridine-2,6-dicarboxamide). We propose that this modification will positively shift the reduction potentials, thus decrease overpotentials, and provide an additional spectroscopic handle for identification of catalytic intermediates. The ligand was synthesized according to the published procedure,[18] i.e. deprotonation with NaH, in MeCN or DMF, and then *in-situ* treated with $Et_4N[FeCl_4]$, $FeCl_2$, or $(Et_4N)_2[ZnCl_4]$ to produce (Et_4N)[Fe(PyPS-*p*-CF_3)] (**1**), $(Et_4N)_2$[Fe(PyPS-*p*-CF_3)] (**2**), and $(Et_4N)_2$[Zn(PyPS-*p*-CF_3)] (**3**), respectively, at modest to high yields (50.0 – 85.4%).

Solid and Solution-state characterization of 1, 2, and 3. Single-crystal XRD confirmed coordination of the pentadentate ligand to Zn(II) (**3**), shown in Figure 4.2, grown from slow diffusion of Et_2O into solutions of MeCN at −20 °C, in a distorted square pyramidal geometry (τ_5

= 0.33); τ_5 of 0 is square pyramidal and of 1 trigonal planar.[22] The average Zn-S (2.369 Å) and Zn-N_{amide} (2.136 Å) bond distances of **3** are on par with a similar $[Zn(PyPS)]^{2-}$ complex, lacking *p*-CF_3 moieties, (τ_5 = 0.22; Zn-S_{avg} = 3.365 Å; Zn-N_{amide} = 2.134 Å) reported by Tsui.[19] However, the Zn-N_{Py} bond of **3** is slightly shorter (2.101 Å) than the Tsui complex (Zn-N_{Py} = 2.117 Å) likely due the electron deficiency of the thiolate donors imparted by the *p*-CF_3 groups of **3**. Attempts to grow single crystals of **1** and **2** were unsuccessful, however, the theoretical structures were computed using density functional theory (DFT) employed at the B3LYP/def2-TZVPP level of theory, shown in Figure S4.75. The structures of **1*** and **2***, where asterisk denotes computed compounds, were optimized utilizing coordinates of $[Fe(III/II)(PyPS)]^{-/2-}$, reported by Noveron[18], with the addition of the trifluoromethyl groups para to the S-atoms. The computed structures of **1*** and **2*** agree well with the structures of $[Fe(III/II)(PyPS)]^{-/2-}$, see Table 4.1. Computations predict a distorted square pyramidal geometry for **1*** (τ_5 = 0.42) which becomes less distorted upon its reduction, **2*** (τ_5 = 0.23). This change is accompanied by the elongation of the Fe-S (~0.1 Å), Fe-N_{amide} (~0.15 Å), and Fe-N_{Py} (~0.06 Å) bond lengths. A similar reduction in distortion and increase in bond lengths is observed upon the oxidation state change of $[Fe(III)(PyPS)]^{-}$.

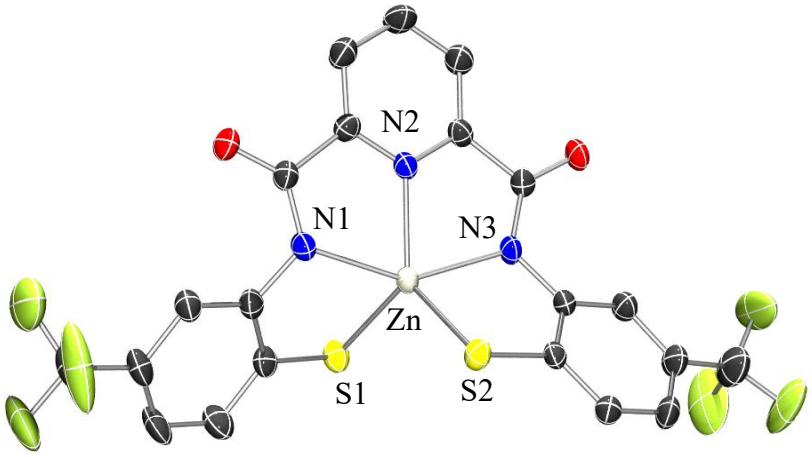

Figure 4.2. ORTEP diagram of the dianion of $(Et_4N)_2[Zn(PyPS\text{-}p\text{-}CF_3)]$ (**3**) at 50% thermal probability ellipsoids. H atoms and counter anions are omitted for clarity. Color code: tan, zinc; yellow, sulfur; nitrogen, blue; oxygen, red; gray, carbon; and green, fluorine.

Table 4.1. Select bond distances, structural parameters, and electronic absorption transitions of Fe(III), Fe(II), and Zn(II) five-coordinate PyPS-*p*-CF_3 complexes. Optimized structures of **1*** (*S* = 5/2), **2*** (*S* = 2), and **3*** (*S* = 0) (B3LYP, def2-TVZPP, gas-phase) were utilized for select bond distances and structural parameters.

Complex	**M-S (Å)**	**M-N_{amide} (Å)**	**M-N_{py} (Å)**	τ_5	**λ (nm) (ε (M^{-1} cm^{-1}))**	**Ref**
$[Fe(PyPS\text{-}p\text{-}CF_3)]^{-}$ (**1***)	2.312, 2.334	2.060, 2.045	2.111	0.42	617 (3400), 529 (3700), 407 (5000)[a]	TW
$[Fe(PyPS\text{-}p\text{-}CF_3)]^{2-}$ (**2***)	2.431, 2.408	2.184, 2.218	2.172	0.23	620 (sh, 2400)[a]	TW
(Et_4N)[Fe(PyPS)]	2.315, 2.314	2.035, 2.041	2.099	0.40	650 (3700), 540 (3600), 420 (4400)[b]	[18]
$(Et_4N)_2$[Fe(PyPS)]	2.409, 2.378	2.160, 2.179	2.129	0.30	680 (sh)[b]	[18]
$(Et_4N)_2[Zn(PyPS\text{-}p\text{-}CF_3)]$ (**3**)	2.352, 2.385	2.151, 2.122	2.101	0.33	*n.r.*	TW
$(Et_4N)_2[Zn(PyPS\text{-}p\text{-}CF_3)]$ (**3***)	2.417, 2.401	2.160, 2.163	2.144	0.37	*n.r.*	TW
$(Et_4N)_2$[Zn(PyPS)]	2.353, 2.377	2.140, 2.129	2.117	0.22	*n.r.*	[19]

[a]MeCN, [b]DMF, *n.r.* is not reported

Coordination of the deprotonated ligand is further substantiated by spectroscopic signatures in FTIR, UV-vis, and EPR. Coordination to the Fe(III) center of **1** is supported by the lack of amide N-H stretching frequencies and a red-shift of the carbonyl stretching frequency (ν_{CO}) of free ligand (ν_{CO} = 1687 cm^{-1}) to 1629 cm^{-1} and further shifted to 1571 cm^{-1} upon coordination to Fe(II) of **2**, shown in Figures S4.19 and S4.26. An almost identical ν_{CO} of 1570 cm^{-1} is observed for the Zn(II) analog (**3**). Similar red-shifting has been observed for Fe(III),[18, 23] Fe(II),[18] and Zn(II)[19] complexes coordinated with anionic carboxamide nitrogen. The electronic absorption of **1** in MeCN consists of three bands at 617 (ε = 3400 M^{-1} cm^{-1}), 529 (ε = 3700 M^{-1} cm^{-1}), 407 (ε = 5000 M^{-1} cm^{-1}) nm, shown in Figure S4.20, and are slightly blue-shifted compared to (Et_4N)[Fe(PyPS)] (λ = 650, 540, and 420 nm), reported by Noveron.[18] The observed bands are proposed to arise form thiolate-to-Fe(III) charge-transfer (CT) transitions. The blue-shifting of these CT bands are consistent with the electron-withdrawing *p*-CF_3 substituents, which lower the energy of the sulfur-based orbital involved in the transition. On the other hand, the electronic absorption spectra of **2** in MeCN only possess a broad shoulder near 620 nm, consistent with the UV-vis of $(Et_4N)_2$[Fe(PyPS)] (λ = 680 nm, sh) reported by Noveron.[18] Solution state magnetic moment of **1** (μ_{eff} = 5.8 BM; CD_3CN) and a broad EPR spectrum with g = 8.91, 5.18, 4.28. and 2.19 in DMF at 10 K, shown in Figure S4.25, confirm a high-spin Fe(III) (*S* = 5/2), consistent with (Et_4N)[Fe(PyPS)].[18, 24] Although **2** is EPR silent (*S* = 2), as measured by X-band, solution state magnetic moment measurement (μ_{eff} = 4.3 BM; CD_3CN) indicates a high-spin ferrous complex (*S* = 2). All spectra point to the anticipated pentacoordinate high-spin Fe(III) and Fe(II) complexes.

Electrochemistry and HER Electrocatalysis of 1 in MeCN. The electrochemical properties of **1** were first investigated by cyclic voltammetry (CV) experiments in MeCN using 0.25 M $^{n}Bu_4NPF_6$ supporting electrolyte and a glassy carbon working electrode; all potentials are reported

versus an externally referenced to ferrocenium (Fc/Fc^+) couple. During the cathodic sweep of **1**, shown in Figure S4.44, a reversible peak at −0.90 V appears, assigned to the Fe(III/II) couple, along with an irreversible peak at E_{ox} = 0.03 V. The more electron deficient thiolate donors in **1** results in a ~+0.2 V shift in the Fe(III/II) compared to $(Et_4N)[Fe(PyPS)]$[23] (Fe(III/II) = −0.64 V vs SCE, ~−1.09 vs Fc/Fc^+ in DMF[25]). Comparing the CV of **1** to its Zn(II) analog **3** (E_{ox} = −0.12 V, ~−0.3 V (sh)), shown in Figure S4.47, suggests the irreversible wave observed for **1** (E_{ox} = 0.03 V) likely corresponds to metal-bound thiolate oxidation. The absence of a corresponding redox event upon reversing the direction of the scan, i.e. oxidation of the disulfide formed at the electrode surface, is not particularly surprising given the irreversible-complex downstream products that form upon oxidation of these complexes. For example, Tsui reported that chemical oxidation of $[Zn(PyPS)]^{2-}$ using $FcBF_4$ (0.00 V vs Fc/Fc^+ in MeCN) yields an intractable mixture of products.[19] However, utilization of a milder chemical oxidation (I_2 = −0.14 V vs Fc/Fc^+ in MeCN)[25] at low temperature chemical results in a bimetallic disulfide-bridged complex $[(L^{SS}L)Zn_2]^{2-}$, in which one of the coordinated thiolates oxidized to from a disulfide bridge, with a corresponding arrangement at Zn (5-coordinate to 4-coordinate).[19] Although no electrochemistry of this complex is reported, **3** likely forms a similar bimetallic disulfide-bridged complex upon oxidation, which is further oxidized to an intractable mixture of products leading to a lack of a cathodic peak during the return wave in the CV of **3**.

Next, the electrocatalytic H^+ reduction of **1** was investigated by acquiring CV measurements after titration of H^+ equivalents using the weak Brønsted acid acetic acid (AcOH; pK_a = 23.5 in MeCN[26]) into MeCN solutions of **1** (0.25 M $^nBu_4NPF_6$ electrolyte, glassy carbon working electrode, scan rate = 100 mV/s), seen in Figure 4.3. Upon increasing equivalents of AcOH an irreversible current enhancement is observed (E_{cat} ~ −2.2 V), consistent with electrocatalytic

proton reduction. As the acid concentration is increased a positive shift in the E_{cat} is observed. This anodic shift of E_{cat} has been attributed to protonation of the catalyst, known as a C-step, occurring prior to reduction (E-step) or a coupling of an E- and C-step.[27, 28]

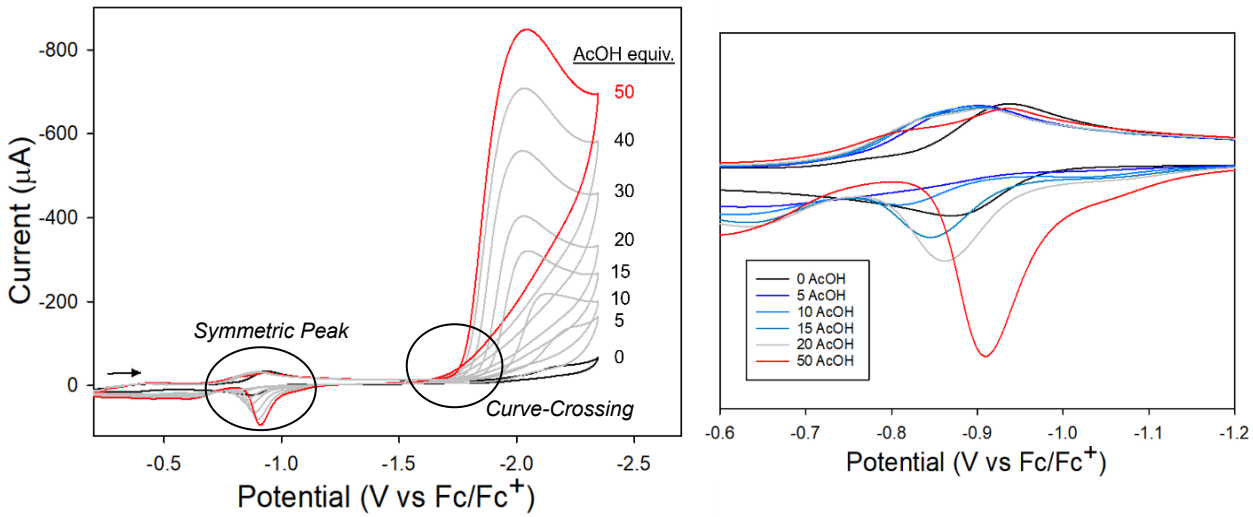

Figure 4.3. (*left*) CV **1** (1 mM) in MeCN with increasing mol-equivalents of AcOH at RT (0.25 M $^{n}Bu_4NPF_6$ supporting electrolyte, glassy carbon working electrode, 100 mV/s scan rate). Arrow shows direction of scan. (*right*) Zoom-in of return wave from the CV of **1** with AcOH.

Closer inspection of the Fe(III/II) couple reveals that immediately upon addition of acid (5 mol-equiv) its reversibility is lost and the reduction event of **1** is anodically shifted by ~30 mV. This positive shift in potential can indicate protonation of complex prior to reduction; however, loss of peak reversibility suggests **1** does not return to its initial form post-catalysis. A potential structural/chemical change under electrocatalytic conditions is further indicated by "curve-crossing", where the current on the return wave is higher than the forward scan, stemming from an increasing concentration of a new active catalyst or long-lived intermediate. For example, curve-crossing was observed in catalytic acid titration experiments of (μ-pdt)[$Fe(CO)_2$(PTA-H)]$_2(PF_6)_2$ (pdt = propanedithiolate; PTA = 1,3,5-triaza-7-phosphaadamantane) ascribed to the formation of a new catalytic species, a protonated Fe(I)Fe(0) complex, formed during trunover.[29]

However, this feature can also indicate presence of catalytic heterogenous material adsorbed on the electrode surface as seen by formation of heterogenous Ni-S films from $(Bu_4N)_2[Ni(bdt)]$ (bdt = benzene-1,2-dithiolate) under electrocatalytic conditions.[30] The build-up of a novel redox-active species/intermediate is further exhibited by the emergence of an additional anodic peak at ~−0.9 V during the return wave, the intensity of which increases proportionally with the concentration of AcOH. This unexpected symmetric peak can arise from a build-up of a novel homogenous species, including catalytic intermediates, or oxidation of a surface-adsorbed species, known as anodic stripping.[31] To determine if these features and HER activity are due to a heterogenous material deposited on the electrode surface, a rinse test was conducted. When the rinse test is performed under conditions that preclude anodic stripping, i.e., by terminating the reverse scan at a more positive potential than the stripping potential (~−0.9 V), thereby preserving heterogenous material, a catalytic wave is observed, see Figure 4.4. These results suggest the observed electrocatalytic activity arises from deposited material rather than homogenous complex.

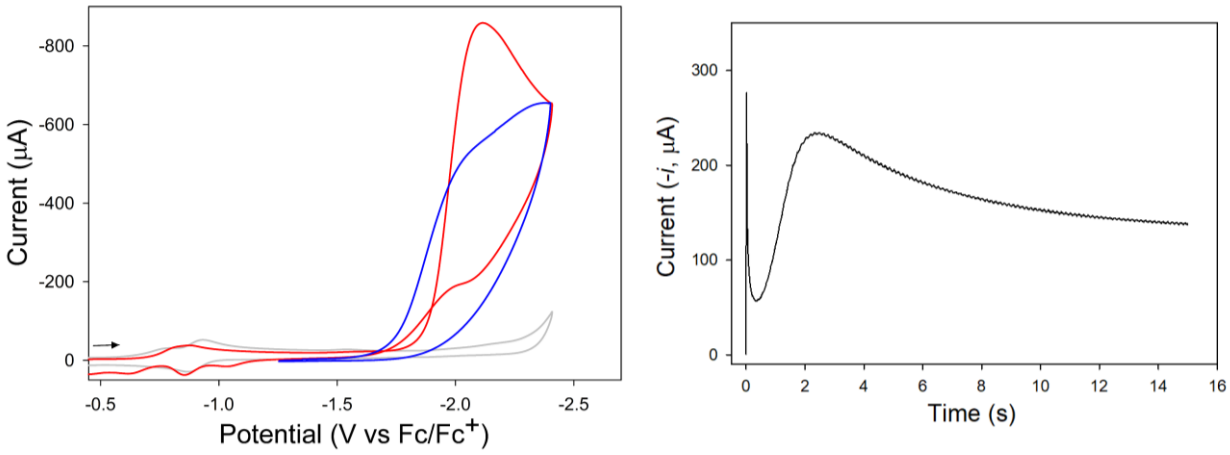

Figure 4.4. (*left*) CV **1** (grey), **1** and 50 mol-equiv. of AcOH with return wave stopped at -1.75 V (red), and rinse test with 50 mol-equiv. of AcOH stopping at −1.75 V (blue) in MeCN at RT (0.25 M $^nBu_4NPF_6$ supporting electrolyte, glassy carbon working electrode, 100 mV/s scan rate). Arrow shows direction of scan. (*right*) Chronoamperogram of **1** with 50 mol-equiv. of AcOH with a step voltage of −0.32 to −1.87 V (vs Fc/Fc^+).

To gain mechanistic insight into the formation of the deposited material, a chronoamperometry (CA) experiment was performed, in which the applied potential is stepped from a potential devoid of redox activity to a potential along the catalytic curve, measured as a function of time. If there Is an initial build-up of current then this suggests that the active catalyst is generated *in-situ* over time, i.e., a precatalytic transformation is taking place.[31] The CA experiment was performed for **1** by jumping from −0.32 to −1.87 V ($E_{cat/2}$) in the presence of AcOH (50 mol-equiv), resulting in Figure 4.4. The CA shows an initial spike of current followed by a gradual build-up of the catalytic current response indicative of a pre-catalytic transformation likely because of the adsorbed surface material accumulating over time. After the current peaks, there is a gradual decay due to substrate depletion. This result strongly suggests that **1** is a pre-catalyst to a surface-adsorbed electrocatalytic material. The increase in current associated with the anodic stripping peak suggests that deposition arises from the acid-induced instability of **1**, underscoring the necessity of mitigation this pathway to maintain homogeneous catalytic behavior.

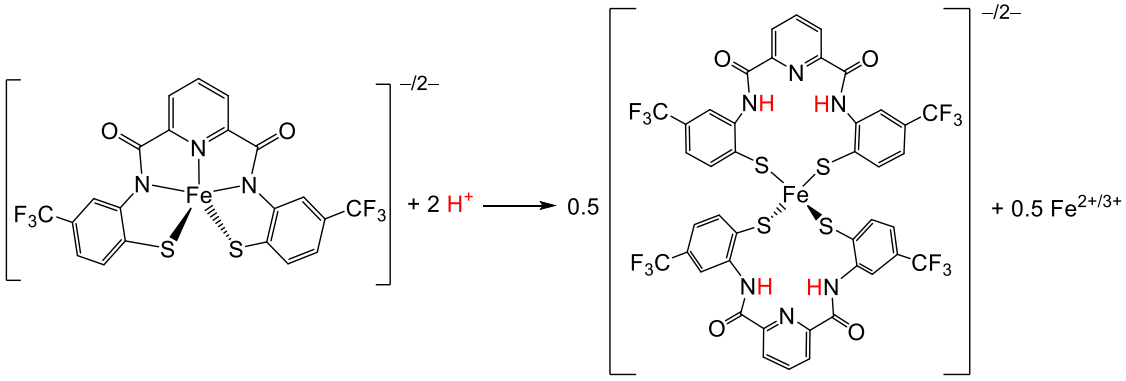

Scheme 4.1. Proposed fate of **1** and **2** upon protonation.

Protonation Studies of 1 and 2 in MeCN. To determine the fate of **1** and **2** upon protonation, bulk protonation experiments were conducted by treating each complex with AcOH, 5 mol-equiv, in MeCN. Three sites of protonation are likely: (i) S-atoms of the coordinated thiolates, (ii) N-atoms of the carboxamide groups (N_{am}), or (iii) N-atom of the pyridine ring (N_{py}). Analysis of the product from these bulk protonation experiments reveal that both **1** and **2** undergo protonation at the N-atoms of the carboxamide groups, evidenced by the appearance of new ν_{NH} and ν_{CO} stretching bands in their FTIR spectra. Upon protonation of **1** a new broad stretching frequency is observed ~3320 cm^{-1}, assigned to a NH stretch by isotopic labeling (ν_{ND} = 2480 cm^{-1}), and a new ν_{CO} frequency at 1686 cm^{-1}, shown in Figure S4.49. These stretching frequencies are in-line with free carboxamide (PyH_4PS-*p*-CF_3), i.e., not engaged in hydrogen bonding, see FTIR shown in Figure S4.1. The formation of ligand is attributed to auto-oxidation of the reaction product, discussed in detail below. Protonation of **2** yields appearance of lower energy ν_{NH} and ν_{CO} of 3220 cm^{-1} and 1676 cm^{-1}, shown in Figure S4.50, consistent with protonation of N_{am}. Red-shifting of these frequencies, relative to free ligand, is attributed to intramolecular H-bonding. To identify the complex formed upon protonation of N_{am} of **1** and **2**, electrospray ionization mass spectrometry (ESI-MS) was employed, shown in Figures S4.51 and S4.52. The ESI-MS(-) analysis reveals an intense peak at a *m/z* of 1085.9, not observed for either **1** and **2**, and simulates well to $[Fe(PyPSCF_3)_2 + 4H^+]^-$. Based on these spectroscopic results, we propose that protonation of **1** and **2** produces $[Fe(PyH_2PS\text{-}p\text{-}CF_3)_2]^{-/2-}$ and free $Fe^{2+/3+}$, resulting from protonation that results in Fe-N_{am} bond cleavage and subsequent ligand rearrangement, as described in Scheme 4.1.

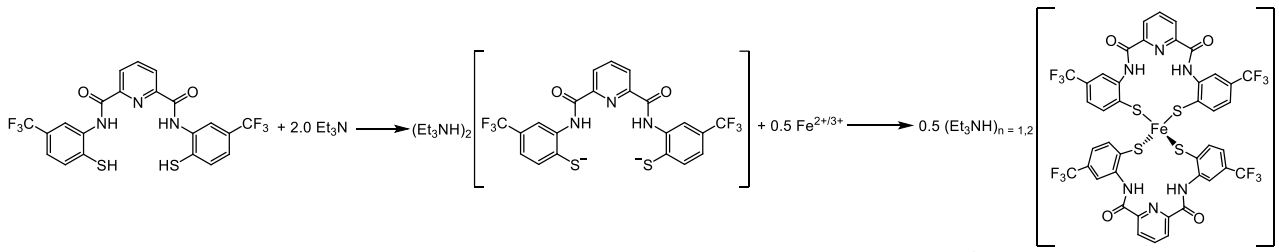

Scheme 4.2. Synthesis of $(Et_3NH)_2(PyPH_2S\text{-}p\text{-}CF_3)$ and $[Fe(III/II)(SR)_4]^{-/2-}$ complexes.

Synthesis and Characterization of 4. To confirm formation of $[Fe(PyH_2PS\text{-}p\text{-}CF_3)_2]^{-/2-}$ upon protonation of **1** or **2**, we attempted to synthesize of authentic $[Fe(III/II)(SR)_4]^{-/2-}$ complexes, described in Scheme 4.2. We found that the thiols of $PyH_4PS\text{-}p\text{-}CF_3$ can be selectively deprotonated using TEA (pK_a = 18.82 in MeCN)[32] and utilized in slight excess to coordinate to Fe(III) or Fe(II) salts in a 2:1 ratio. Attempts to isolate $[Fe(PyH_2PS\text{-}p\text{-}CF_3)_2]^-$ were unsuccessful due to auto-oxidation, commonly observed for $[Fe(SR)_4]^-$ systems ($2Fe^{3+} + 2RS^- \rightarrow 2Fe^{2+} + RSSR$).[33, 34] Nevertheless, UV-vis time course experiments, shown in Figure S4.54, reveal the *in-situ* generated putative intermediate is sufficiently long-lived to be spectroscopically probed. The initial spectrum (t = 0 h) reveals an absorbance band at 490 nm, which undergoes a ~50% decrease in intensity within the first hour. This absorbance band is consistent with other tetrahedral Fe(III) tetrathiolate complexes, for example, $[Fe(SEt)_4]^-$ (λ = 496 nm, DMF)[35], $[Fe(S\text{-}2,3,6\text{-}^iPr_3\text{-}C_6H_2)_4]^-$ (λ = 470 nm, MeCN)[34], assigned as S(σ)-to-metal charge transfer transitions,[36] and oxidized rubredoxin (Rb_{ox}, $[Fe(III)(SCys)_4]$) (λ = 490 nm, H_2O).[37] Further evidence for the formation an $[Fe(III)(SR)_4]^-$ complex is provided by the EPR spectrum of *in-situ* generated material, shown in Figure S4.55, exhibiting resonances at g = 10.68, 6.37, and 4.29, similar to those observed for the tetrahedral (τ_4 = 0.96) $[Fe(S_2\text{-}o\text{-}xyl)_2]^-$ (S_2-*o*-xyl = bis(*o*-xylyl-α,α'-dithiolate) (g = 8.4, 5.3, and 4.3 in a DMF/DCM glass at 6 K)[38], the small resonance at 2.01 is attributed to unreacted $[Fe(III)Cl_4]^-$. We propose that protonation of **1** generates a transient $[Fe(SR)_4]^-$ complex, which undergoes autooxidation to yield Fe(L) and RSSR (R = $PyPCF_3$). Formation of a disulfide is

consistent with the comparable ν_{NH}/ν_{CO} frequencies observed between isolated material of **1** + 5 AcOH (ν_{NH} = ~3320 cm^{-1}) and PyH_4PS-*p*-CF_3 (ν_{NH} = ~3330 cm^{-1}), *vide supra*.

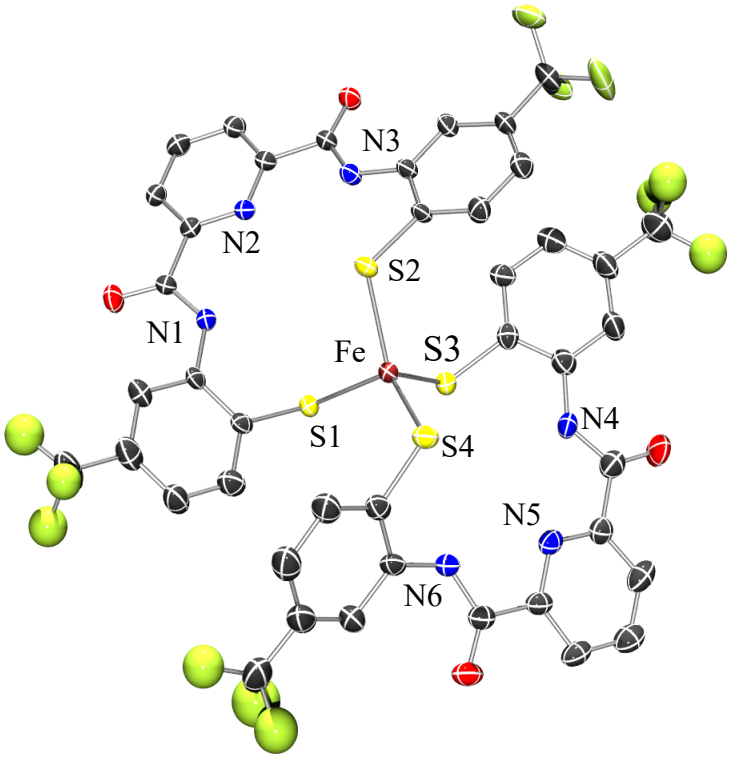

Figure 4.5. ORTEP diagram dianion $(Et_3NH)_2[Fe(PyH_2PS\text{-}p\text{-}CF_3)_2]$ (**4**) at 50% thermal probability ellipsoids. H atoms and counter anions are omitted for clarity. Color code: red, iron; yellow, sulfur; nitrogen, blue; oxygen, red; gray, carbon; and green, fluorine.

Due to an inability to isolate a stable $[Fe(SR)_4]^-$ complex, the ferrous complex $(Et_3NH)_2[Fe(PyH_2PS\text{-}p\text{-}CF_3)_2]$ (**4**) was synthesized, as described in Scheme 4.2, at high yields (94%). Diffraction quality crystals of **4**, seen in Figure 4.5, grown from pentane diffusion into a THF solutions at −20 ˚C, reveals the anticipated four coordinate complex possessing a distorted tetrahedral geometry (τ_4 = 0.85) with an average Fe-S bond length of 2.358 Å, comparable with bond lengths of tetrahedral Fe(II) tetrathiolate containing complexes, see Table 4.2. To accommodate the tetrahedral coordination geometry, the ligand undergoes a conformational twist about the N_{amide}-$C_{aryl\text{-}ring}$ bond, while maintaining an unbound N_3 pincer cavity. This ligand

distortion resembles the pentacoordinate ligand in **3**. The crystal structure reveals the *ortho*-carboxamide groups are positioned to serve as intramolecular H-bond donors to the coordinated S-atoms. Solid-state intramolecular H-bonding interactions are confirmed by an average N_{amide}--S bond distance of 2.968 Å that are well below the sum of the van der Waal's radii of N and S (3.55 Å).[39, 40] These bond distances are comparable to those observed in other M-SR (M = Ni[41, 42], Zn[43], Fe[44, 45], Pt[40]) complexes with similarly positioned carboxamide-NH functionalities on aryl thiolate ligands. In addition to these H-bonds, both Et_3NH^+ counterions are weakly involved in the intermolecular H-bonding carbonyl oxygen, possessing an N---O distance of 3.016 Å, slightly shorter than the sum of the van der Waal's radii of N and O (3.07 Å). This intermolecular H-bonding does not significantly influence the strength of the intramolecular H-bond between the N_{amide} and S.

Table 4.2. Select bond distances, structural parameters, and Fe(II/I) couples of Fe(II) tetrathiolate complexes.

Complex	**M-S (Å) (Avg)**	**M-N_{amide} (Å)**	**τ_4**	**Fe(III/II) (V vs Fc/Fc^+)**	**Ref**
$(Et_3NH)_2[Fe(PyH_2PS\text{-}p\text{-}CF_3)_2]$ (**4**)	2.379, 2.338, 2.379, 2.337 (2.358)	2.980, 2.953, 2.987, 2.953	0.85	-0.46 V[a]	TW
$(Et_4N)_2[Fe(S\text{-}o\text{-}t\text{-}BuCONHPh)_4]$	2.322, 2.336, (2.329)	2.92, 2.94	0.89	-0.67 V[a,b]	44
$(Et_4N)_2[Fe(S\text{-}o\text{-}CF_3CONHPh)_4]$	*n.r.*	*n.r.*	*n.r.*	-0.51 V[a,b]	44
$(Et_4N)_2[Fe(SPh)_4]$	2.359, 2.360, 2.338, 2.355 (2.353)	*n.a.*	0.89	-0.91 V[a,b]	44
$(Me_4N)_2[Fe(S_2\text{-}o\text{-}xyl)_2]$[c]	2.265, 2.258, 2.268, 2.278	*n.a.*	0.96	-1.43 V[a,d]	46

[a]MeCN, [b]Redox couples converted from SCE to Fc/Fc^+.[47] [c]S_2-*o*-xyl = bis(*o*-xylyl-α,α'-dithiolato. [d]DMF. *n.r.* is not reported. *n.a.* is not applicable.

To determine whether the tetrahedral coordination sphere of **4** is retained in solution, we measured the electronic absorption and NMR spectra of **4** in MeCN. Although the electronic absorption spectrum of **4** is largely featureless, see Figure S4.35, this is characteristic of $[Fe(SPh)_4]^{2-}$ complexes, wherein transitions of the phenyl groups mask the UV region.[48, 49] The tetrahedral geometry of **4** (S = 2) is best observed by by $^1H/^{19}F$ NMR and magnetic moment measurements. The ^1H NMR spectrum of **4**, shown in Figure S4.36, reveals three contact-shifted protons (δ_H = 27.16, 22.77, and −33.97 ppm) which align with reported Fe(II) tetrathiolate complexes containing ortho-carboxamide groups.[44, 50] These complexes typically show two downfield peaks at ~20 ppm and ~14 ppm, assigned to *meta*-H^+, and an up field peak near −13 ppm, assigned to N-H^+ of the carboxamide group. The downfield shifted peak at 15.78 ppm in the ^{19}F NMR of **4**, shown in Figure S4.37, provides additional evidence of its paramagnetic nature, whereas diamagnetic Zn(II) analog (**5**) exhibits a δ_F = −62.05 ppm. The paramagnetic nature of **4** is further confirmed by the solution state magnetic moment of 4.47 B.M., consistent with a high-spin S = 2 ferrous complex. In order to confirm presence of intramolecular H-bonding in **4**, changes in the ν_{NH} and ν_{CO} stretching frequencies of complexed ligand to free, via $PyPSH_4$-*p*-CF_3, were monitored. In a matrix of KBr, two ν_{NH} for $PyPSH_4$-*p*-CF_3 appear at 3342 and 3306 cm^{-1} whereas the ν_{NH} of **4** appears red-shifted at 3266 cm^{-1} indicating H-bonding is intact in the solution state, a 40 to 76 cm^{-1} shift. This ~100 cm^{-1} shift in ν_{NH} ($\Delta\nu_{NH}$) is similar to shifts seen in H-bonded synthetic Fe-S clusters[51], square-planar $[Pt(N_2S_2)]$[40], $[Ni(N_2S_2)]$[42], and [Ni(dppe)(SPh)Me][41] (dppe = 1,2-bis(dipheylphosphino)ethane) complexes bearing *ortho*-carboxamide aryl thiolate donors, suggestive of intramolecular H-bonding.

Bulk protonation studies of **1** and **2** suggest protonation of amide-groups results in the formation of $[Fe(PyPSH_2\text{-}p\text{-}CF_3)_2]^{-/2-}$, as depicted in Scheme 4.1. To validate this proposed result,

spectroscopic results from bulk protonation experiments of **2**, hereafter referred to as $\mathbf{2^{H+}}$, were compared to independently synthesized **4**. The FTIR spectra of **4** and $\mathbf{2^{H+}}$, shown in Figure 4.6, exhibit similar ν_{NH} ($\mathbf{2^{H+}}$= 3220 cm^{-1}; **4** = 3266 cm^{-1}) and ν_{CO} ($\mathbf{2^{H+}}$ = 1676 cm^{-1}; **4** = 1683 cm^{-1}) stretching frequencies, the latter showing a slight blue shit. Further confirmation of formation of the tetrathiolate Fe(II) complex is exhibited by the ^{1}H NMR of $\mathbf{2^{H+}}$, shown in Figure S4.53, possessing the same paramagnetically shifted peaks (δ_H = 27.18, and 22.83 ppm) as **4**. Lastly, the ESI-MS(−) of both **4** and $\mathbf{2^{H+}}$ reveal a monoanion flying at an *m/z* of 1085, shown in Figures S4.38 and S4.52, simulating well for $[Fe(PyPSCF_3)_2 + 4H^+]^-$. Collectively, these spectroscopic results strongly support **2**, and by proxy **1**, undergoes protonation of carboxamide nitrogen under protic conditions, leading to formation of $[Fe(PyPSH_2\text{-}p\text{-}CF_3)_2]^{-/2-}$.

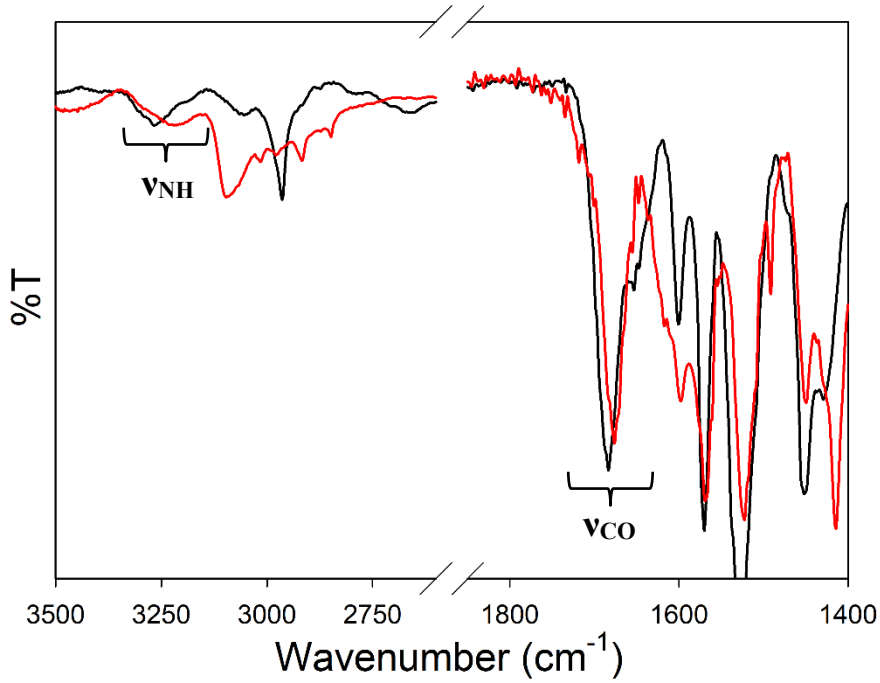

Figure 4.6. FTIR spectrum of $\mathbf{2^{H+}}$ (red) and $(Et_3NH)_2[Fe(PyPSH_2\text{-}p\text{-}CF_3)_2]$ (**4**) (black) in KBr matrix at RT.

Electrochemistry and HER Electrocatalysis of 4. To determine if **4**, the *in-situ* product upon protonation of starting complex, is responsible for deposited material observed in electrocatalytic titration experiments, *vide supra*, its electrochemistry and electrocatalytic behavior was investigated in MeCN solutions with 0.25 M $^{n}Bu_4NPF_6$ supporting electrolyte using a glassy carbon working electrode. Upon sweeping cathodically, the CV of **4**, see Figure S4.57, shows a reversible couple at −0.46 V, assigned to the Fe(III/II) couple, and an irreversible oxidation peak at E_{ox} = 0.49 V, assigned to oxidation of coordinated thiolate. Importantly, if the oxidation event at 0.49 V is accessed the Fe(III/II) couple loses its reversibility, indicating that this event results in a chemical transformation of **4**. This observation is consistent with the oxidative modification of coordinated thiolate. Indeed, the formation of disulfide is observed during the return wave of **4** in which an irreversible reductive peak arises at E_{red} = −0.91 V, consistent with the free ligand's E_{red} = −1.06 V appearing during the anodic sweep, shown in Figure S4.60. The oxidation of coordinated thiolate is further validated by comparison to its Zn(II) analog, $(Et_3NH)_2[Zn(PyH_2PS\text{-}p\text{-}CF_3)_2]$ (**5**), Figure S4.59, which possesses two E_{ox} events at 0.11 and 0.36 V. Lastly, we note that the Fe(III/II) redox couple is consistent with other $[Fe(II)(SR)_4]^{2-}$ rubredoxin model complexes bearing *ortho*-carboxamide groups (Fe(III/II) = −0.53 to −0.72 V vs Fc/Fc^{+}) reported by Nakamura.[44]

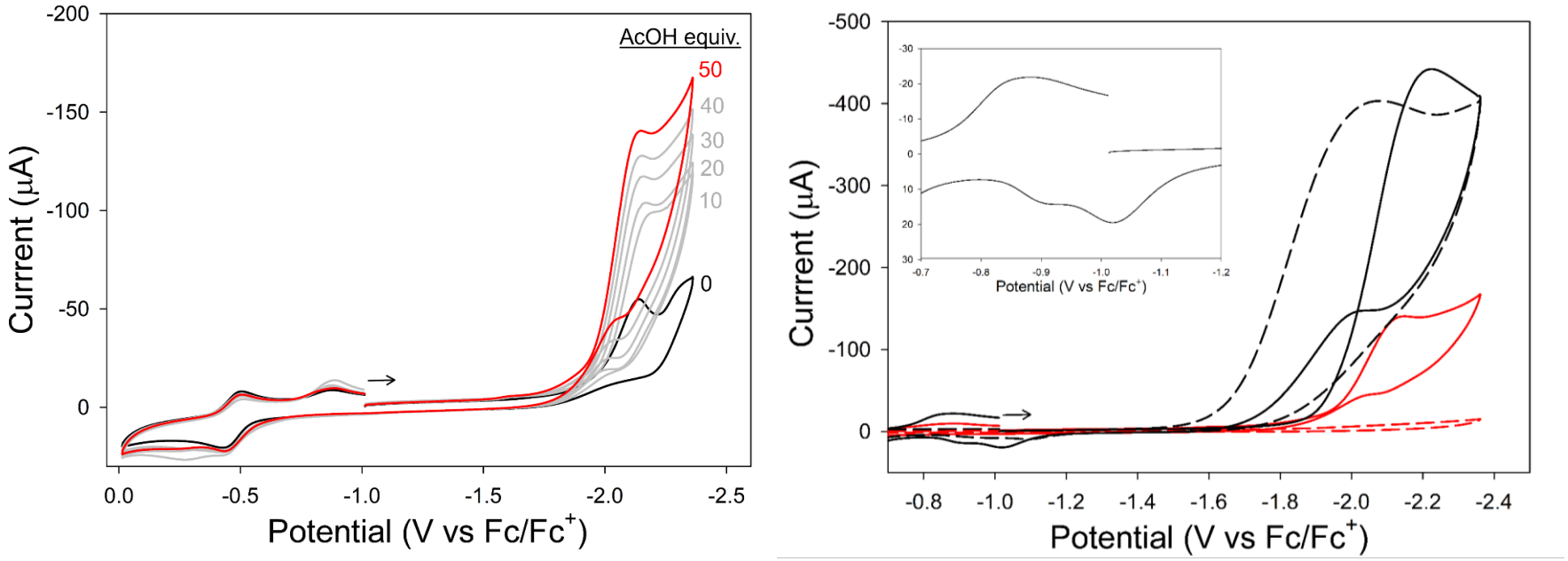

Figure 4.7. (*left*) CV of **4** with incremental addition of AcOH. (*right*) CV of **4** with 50 mol-equiv. of AcOH (red-solid), along with subsequent rinse test (red-dashed); CV of **4** and $(Et_4N)_2[FeCl_4]$ with 50 mol-equiv. of AcOH (black-solid), along with subsequent rinse test (black-dashed. *Right inset:* Zoom-in of return wave of **4** and $(Et_4N)_2[FeCl_4]$ with 50 mol-equiv. of AcOH. All CVs were recorded in MeCN at RT (0.25 M $^nBu_4NPF_6$ supporting electrolyte, glassy carbon working electrode, 100 mV/s scan rate). Arrow shows direction of scan.

Addition of AcOH to solutions of **4** results in a modest increase of irreversible current (E_{cat} = −2.15 V) upon acquiring the CV, Figure 4.7. However, unlike the electrocatalytic response observed for **1**, neither a symmetric peak on the return wave nor curve-crossing was detected, initially indicating the absence of electrocatalytically active deposits. This initial assessment was confirmed by the lack of catalytic current from the subsequent rinse test, shown in Figure 4.7 (dashed red trace), indicating **4** alone does not generate HER-active deposited material. According to scheme 4.2 protonation of **2** form both **4** and free Fe(II). To determine whether free Fe(II) is responsible for the observed catalytic deposits, the activity of $(Et_4N)_2[FeCl_4]$ alone was evaluated, shown in Figure S4.61, revealing negligible catalytic activity. However, when an equimolar amount of $(Et_4N)_2[FeCl_4]$ was introduced to a CV cell containing **4** and 50 mol-equivalents of AcOH, a pronounced catalytic current was observed (E_{cat} = −2.22 V), shown in Figure 4.7 (black trace). Notably, the voltammogram displays both curve-crossing and a symmetric return wave, features associated with deposited material from the CV acid titration experiments of **1**. A subsequent rinse test from this mixture (**4** and $[FeCl_4]^{2-}$), shown in Figure 4.7 (dashed black), confirms that the catalytic activity originates from material deposited on the electrode surface. These results strongly support that HER-active surface deposits observed for 1 originate from *in-situ* generation of Fe-tetrathiolate complex (**4**) and free Fe.

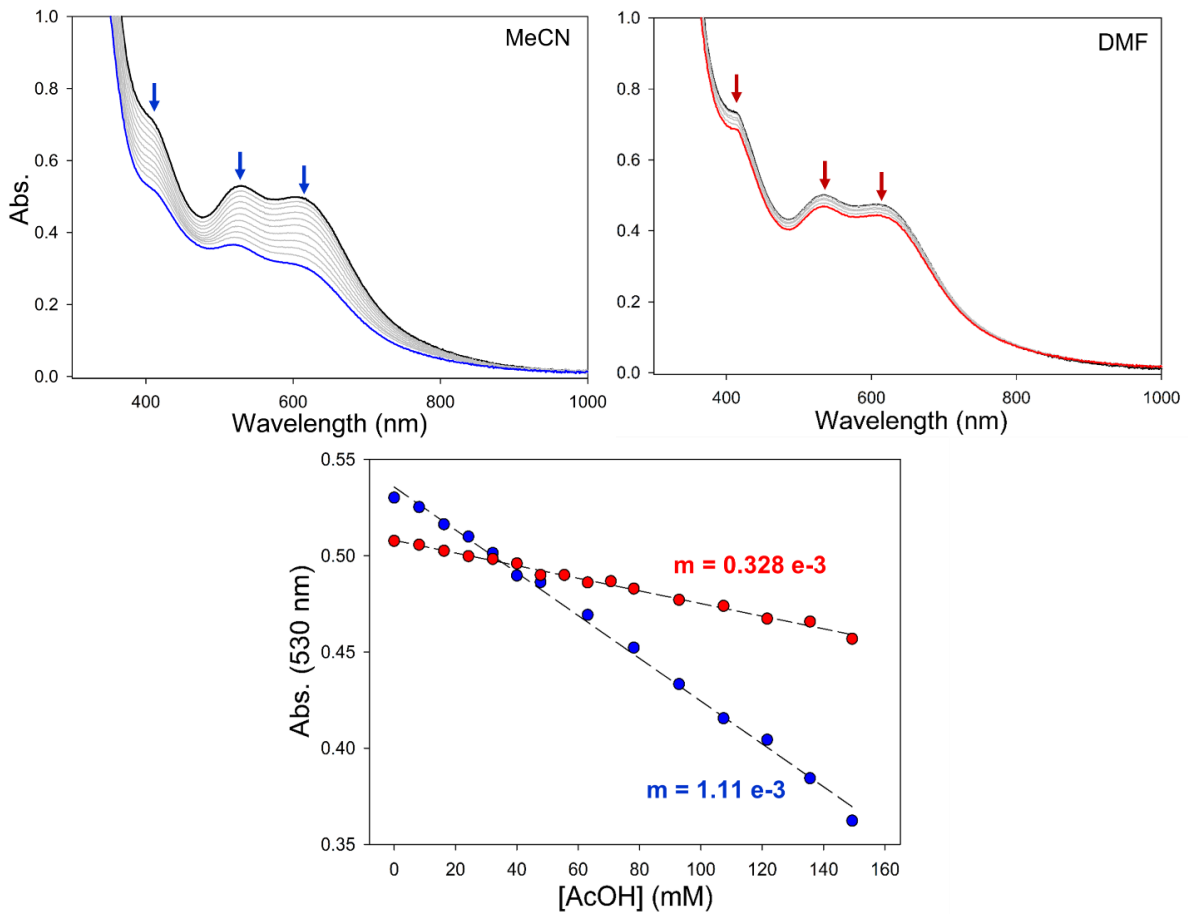

Figure 4.8. *Top:* UV-vis acid titration experiments of **1** (0.16 mM) upon the addition of AcOH in MeCN (*top left*, blue) and DMF (*top right*, red) at 0 equiv. (black) to 100 equiv. (blue or red) of AcOH, measured at 23.0 °C. *Bottom:* Protic stability of **1** assessed by the absorbance of the band at 530 nm versus AcOH concentration from UV-vis acid titration experiments in DMF (red) and MeCN (blue).

Protonation Studies of 1 and 2 in DMF. To prevent formation of deposits on the electrode, generation of **4** and free iron under protic conditions needs to be suppressed. We found that utilization of DMF as a solvent medium enhances the protic stability of **1** and **2**. This increased stability was assessed by monitoring the electronic absorbance spectra of **1** and **2** in MeCN and DMF as a function of AcOH (pK_a = 13.5; DMF[52]), specifically their electronic absorbance at 530 and 620 nm, respectively. In both solvents, incremental addition of AcOH results in a decrease in

all absorbance bands for both **1** and **2**, shown in Figure 4.8. The absence isosbestic points, coupled with the uniform decrease in all absorbance bands, indicate that no discrete, spectroscopically identifiable protonated complex is formed. However, the extent of absorbance loss reveals that **1** is approximately threefold more stable in DMF than in MeCN, highlighting the solvent's role in mitigating decomposition under acidic conditions. Indeed, repeating the bulk acid (5 mol-equiv. AcOH) addition to **1** in DMF results in no detectable protonated complex. Complex **2** is likewise more stable in DMF, exhibited by a similar UV-vis titration experiment, shown in Figure S4.65, with no detectable protonated species from under bulk acid conditions. The enhanced protic stability of **1** and **2** in DMF may be attributed to a stabilizing intermolecular hydrogen-bonding interaction between DMF and protonated ligand frame, depicted in Figure 4.9, which likely suppresses ligand rearrangement. Similar behavior has been reported for CuL (L = diacetyl-bis(*N*-4-methyl-3-thiosemicarbazonato), where intermolecular hydrogen-bonding between DMF and protonated ligand has been implicated in slowing down proton tautomerization across the ligand frame resulting in reduced TOF.[53] Although DMF appears to impede decomposition, attempts to experimentally probe the initial site of protonation of **1** and **2** in DMF were unsuccessful.

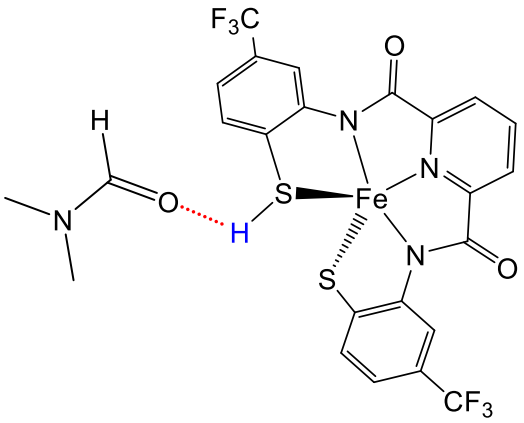

Figure 4.9. Proposed stabilizing interaction between DMF and protonated **1** (**1,SH**) preventing tautomerization to N_{amide}.

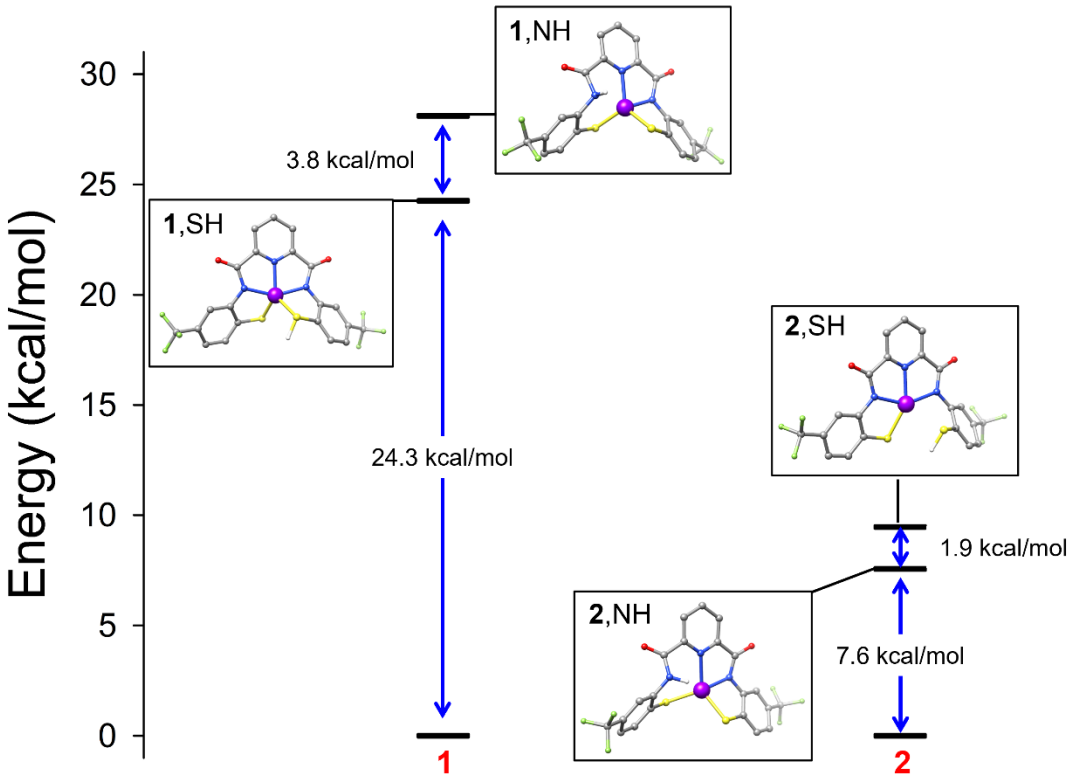

Figure 4.10. Computed (B3LYP, def2-TZVPP) energetic stability of protonated species of **1** (S = 5/2) and **2** (S = 2) using the solvent continuum model CPCMC(DMF).

In turn, computations were used to investigate the likely site of initial protonation. All parent and proposed protonated complexes of **1** and **2** were assessed using DFT employed at the B3LYP/def2-TZVPP level of theory with solvent effects accounted for by utilizing the conductor-like screening model CPCMC for DMF. We first evaluated the thermodynamics of a single protonation event at either S-thiolate or N-carboxamide of **1** and performed the same analysis for **2**. The computational results are shown in Figure 4.10. Protonation at either site was found to be thermodynamically unfavorable for both **1** (ΔG > ~24.0 kcal/mol) and **2** (ΔG > ~8.0 kcal/mol), although protonation of **2** is comparably more favorable, by ~16 kcal/mol, as anticipated due to its increased negative charge. Computed free energies suggest the thiolate protonated complex of **1**

(**1**,SH) (ΔG = 24.3 kcal/mol) is thermodynamically preferred, lying ~4 kcal/mol lower than its carboxamide protonated counterpart (**1**,NH) (ΔG = 28.1 kcal/mol). However, one-electron reduction impacts the site of protonation. For **2**, the carboxamide protonated complex (**2**,NH) (ΔG = 7.6 kcal/mol) is slightly favored, lying only ~2 kcal/mol lower in energy than the thiolate protonated complex (**2**,SH) (ΔG = 9.5 kcal/mol). These computations suggest that initial protonation of **1** occurs at the coordinated thiolate and, upon its reduction, the proton can transfer to the N-carboxamide of **2**, given the low barrier of isomerization (~2 kcal/mol), resulting in cleavage of the Fe-N_{amide} bond and formation of **4** and free iron. However, we propose that this process is hindered by the intermolecular hydrogen-bonding interaction between DMF and Fe(III)-SH, which impedes proton migration to N-carboxamide upon reduction resulting in the deposited material, *vide supra*.

Electrochemistry of 1 in DMF. Given the enhanced protic stability of **1** in DMF, its electrochemical properties and electrocatalytic activity were evaluated under identical conditions used in MeCN. While the CV of **1** in DMF, shown in Figure S4.67, is largely unchanged in comparison to MeCN as a solvent medium, two additional peaks are observed in DMF: an irreversible oxidation peak at E_{ox} = 0.32 V and a quasi-reversible peak at $E_{1/2}$ = −2.49 V. To help assign these new peaks, the CV of the Zn(II) analog **3** was recorded in DMF, shown in Figure S4.69, and found to be largely consistent with its electrochemical response in MeCN. However, in DMF, **3** exhibits a quasi-reversible peak at $E_{1/2}$ = −2.71 V, assigned to the reduction of the pryidne-2,6-dicarboxamide moiety (2,6-Py). Although this moiety is not typically considered non-innocent, its redox activity has been observed in [Fe(pydioneN_5)Cl(H_2O)](MeOH), reported by Korendovych[54], and [H_2LFe^{III}–(μ-O)–$Fe^{III}LH_2$] (H_2L = N^2,N^6-bis(4,5-dihydrothiazol-2-yl)pyridine-2,6-dicarboxamide), reported by Kumar,[55] with quasi-reversible peaks at ~−2.5 V and

~−1.8 V (vs Fc/Fc^+) respectively. Reduction of the ligand is further confirmed via the computed one electron reduced analog of **2** (**2^R**). Reduction of **2** was computed to be −2.89 V (vs Fc/Fc+), within modest agreement with the experimental value, and results in the elongation of Fe-S and Fe-N_{am} bonds, by ~0.08 Å and ~0.04 Å, respectively, along with the contraction of Fe-N_{py} by 0.14 Å, shown in Figure S4.78 and Table S4.5. This contraction in bond length is consistent with the population of the computed LUMO(β) of **2** possessing $N_{py}(p\pi)$-$Fe(d_{xy}\pi)$ bonding character, shown in Figure S4.81. Further inspection of this orbital reveals significant contribution from the 2,6-Py moiety (53.9%) with a minor Fe (14.8%) contribution, the full MO contributions are shown in Table S4.8. Furthermore, the spin-density plot of **2^R** reveals substantial spin localized on the 2,6-Py moiety, shown in Figure 4.81, further supporting this ligand-based reduction event. A comparable analysis of the reduced form of **3** (**3^R**), with a computed reduction potential of −3.11 V (vs Fc/Fc^+), reveals significant spin density delocalized across the 2,6-Py unit further reinforcing ligand non-innocence, shown in Figure S4.84. These results are consistent with a proposed ligand-based reduction event in the CV of **1**.

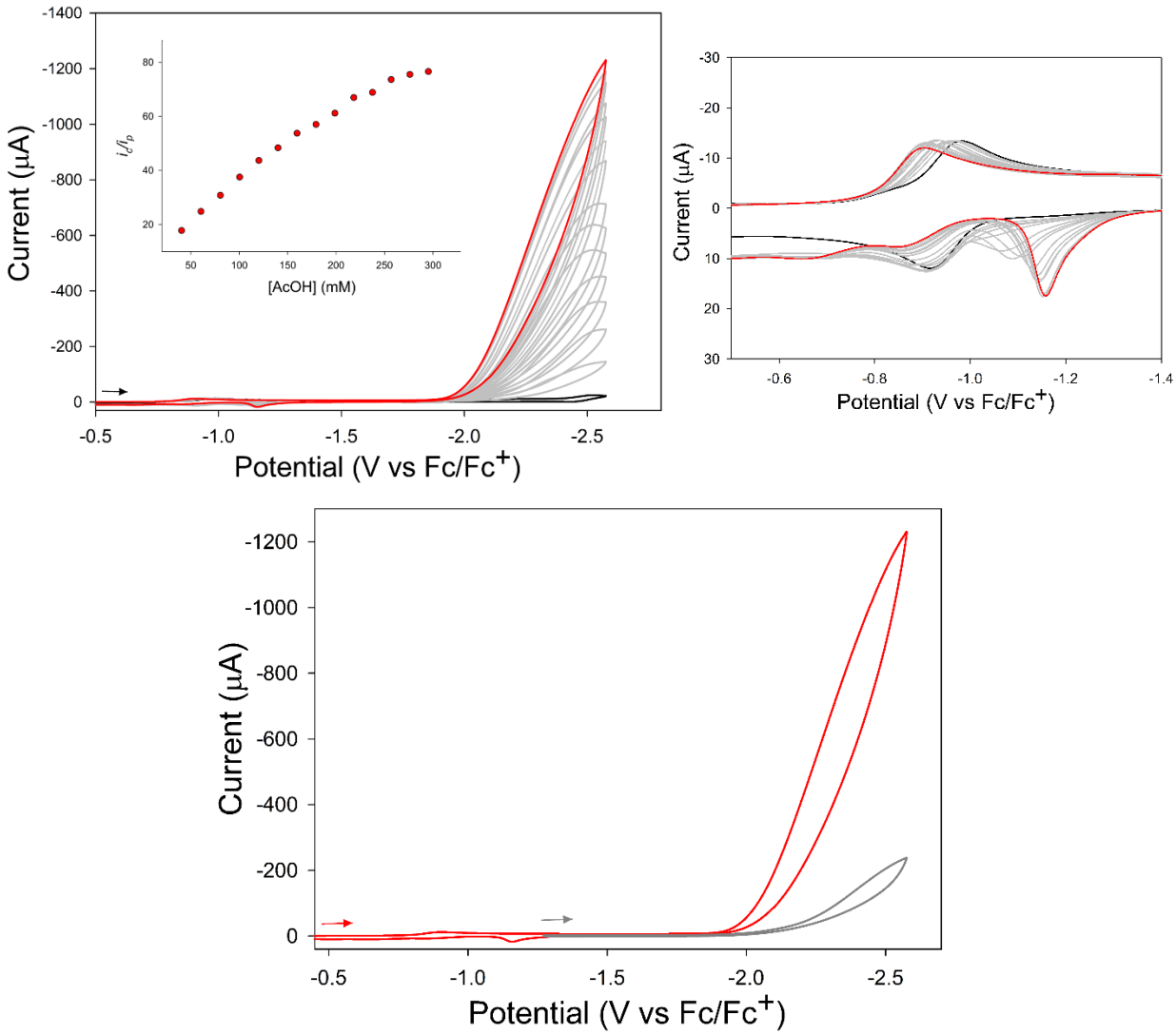

Figure 4.11. *Top left*: CV **1** (1 mM) in DMF with increasing mol-equiv. of AcOH from 0 (black) to 300 mol-equiv (red) with every scan in between (grey) 20 mol-equiv *Inset*: normalized current density versus concentration of AcOH from titration experiment. T*op right*: zoom-in of return wave from the CV of **1** with AcOH. *Bottom:* CV of **1** (1 mM) with 300 mol-equiv. AcOH (red) and subsequent rinse test with 300 mol-equiv. of AcOH (grey) in DMF. All spectra were recorded at RT (0.25 M $^{n}Bu_4NPF_6$ supporting electrolyte, glassy carbon working electrode, 100 mV/s scan rate). Arrow shows direction of scan.

HER Electrocatalysis of 1 in DMF. Upon addition of AcOH (pK_a = 13.5; DMF)[52] to a solution of **1** in DMF, a current enhancement is observed consistent with electrocatalytic H^+ reduction to H_2 (g), shown in Figure 4.11. The intensity of the catalytic wave increases progressively with higher equivalents of AcOH, reaching a plateau current (i_c/i_p ~ 75; i_c = catalytic current at E_{cat}; i_p = peak current of Fe(III/II) couple) at ~275 mol-equiv. of AcOH (~0.28 M) at an E_{cat} of ~−2.5 V. Concurrently, starting at 80 mol-equiv. of AcOH, the Fe(III/II) couple gradually losses its reversibility. As the reversibility diminishes, a symmetric peak arises at ~−1.1 and shifts cathodically with further addition of AcOH; however, no curve crossing is observed. To evaluate whether the observed activity arises from deposited heterogeneous catalyst, a rinse test was performed under conditions to prevent stripping of surface-bound material, *vide supra*, shown in Figure 4.11. In contrast to the behavior of **1** in MeCN, the rinse test in DMF shows limited activity from deposited material indicating DMF suppresses formation of active heterogenous catalyst on the electrode surface. The relative difference in amount of material deposited on the electrode between each solvent can be determined by the relative current response of the symmetric peak as a function of acid-equivalency. In DMF, the symmetric peak reaches a current of 15.9 μA at 300 mol-equiv of AcOH. By contrast, in MeCN, a comparable current (16.8 μA) is achieved at 10 mol-equiv. of AcOH, highlighting the suppressive effect of DMF on deposited material.

By suppressing formation of deposited material utilizing DMF, one can better assess the electrocatalytic activity for homogenous **1**. From these results, the overpotential of HER catalyzed by **1** was found to be 0.94 ± 0.04 V using a standard method that accounts for AcOH homoconjugation,[56] with a turnover frequency (TOF; solve for k_{obs} in eq. ii) of 1.2 ± 0.3 * 10^3 s^{-1}, obtained from the i_c/i_p value at ~275 mol-equiv. of AcOH (~0.28 M) under saturating conditions, i.e. addition of acid results in no more significant current enhancement. The TOF and overpotential

of **1** are comparable to previously reported mononuclear Fe-based electrocatalysts for HER, Table 4.3. To confirm electrocatalytic production of H_2 (g) by **1** in DMF bulk electrolysis experiments were performed by at ~ –2.8 V in the presence of 270 equiv. of AcOH for 80 min. The presence and amount of H_2 (g) in the headspace of the electrochemical cell were confirmed by ^{1}H NMR. Although this technique has been utilized for *in-situ*, stochiometric H_2 quantification, we modified the experimental approach for electrocatalytic H_2 detection, see SI for details.[57-59] Following electrolysis, 0.5 mL of headspace gas was injected into a J-young NMR tube containing C_6D_6 resulting in a signal at 4.47 ppm, see Figures S4.76-77, consistent with dissolved H_2.[60] Electrolytic production of H_2 from **1** was confirmed with a faradaic yield of 70% and 3.4 turnover number (TON).

Table 4.3. Figures of merit of select Fe-based electrocatalyst for hydrogen evolution reaction, see Chart 4.1 for chemical structures.

Catalyst	**TOF (s^{-1})**	**η (V)**	**TON**	**FE%**	**Acid Source/Solvent**	**Ref.**
1	1200	0.94	3.4 (1.3 h)	70	AcOH/DMF	TW
$FeCl_2(N(Py)_2(PhSO_2))$[a]	3300	0.80	*n.r.*	98	TFA/MeCN	10
$FeCl_2(N(Py)_2(PhO))$[a]	1000	0.66	*n.r.*	98	TFA/MeCN	9
$[Fe(^{en}Cp^{Bn})(CO)_3](PF_6)$[b]	45	0.98	*n.r.*	64	Tos_2NH/MeCN	11
Fe(TPP)[c]	4.9	*n.r.*	*n.r.*	*n.r.*	BA-H^+/MeCN[i]	7
$[Fe(N_2P_2)(MeCN)_2](BF_4)_2$[g]	29	0.49	2.2 (0.8 h)	93	Et_3NH^+/MeCN	12
$(\kappa^2\text{-}NP_2)Fe(CO)(\kappa^2\text{-}bdt)$[d,h]	240	0.43	*n.r.*	96	AcOH/THF	8
$(PMe_3)_2(CO)_2Fe(bdt\text{-}3,6\text{-}Cl_2)$[d]	*n.r.*	0.30	*n.r.*	*n.r.*	TFA/MeCN	13
$[(dAr^Fg_2H\text{-}BF_2)_2Fe(py)_2]$[f]	200	0.30	*n.r.*	82	TFA/DCM	14

[a]Py =pridine. [b] $^{en}Cp^{Bn}$ =1,4-dimethyl-5,7-diphenyl-1,2,3,4-tetrahydro-6Hcyclopenta[b]pyrazin-6-one. [c]TPP = tetraphenylporphrin. [d]bdt = benzene dithiolate. [e]bpy = 2,2-Bipyridine. [f]dAr^FgBF_2 = 1,2-bis(perfluorophenyl)ethane-1,2-dionedioxime. [g]N_2P_2 = N,N-bis(2-(diphenylphosphino)benzyl)-1-(pyridin-2-yl)methanamine. [h]NP_2 = methyl-2-{bis(diphenylphosphinomethyl)amino}-acetate. [i]BA-H^+ = *p*-bromoanilinium tosylate. *n.r.* is not reported.

Additional kinetic parameters for the **1**-catalyzed HER were obtained from plots of the catalytic current (i_c) or ratio of i_c to the reduction peak current of **1** in the absence of acid (i_p), i.e., i_c/i_p with

respect to various conditions. For instance, i_c/i_p exhibits a linear dependence on $\sqrt{[H^+]}$ until the acid-independent region is reached at ~0.28 M (280 mol-equiv.) of AcOH and a maximum i_c/i_p ratio of ~70. The linear plot of i_c/i_p versus $\sqrt{[H^+]}$ indicates a first-order dependence on $[H^+]$ for the rate of HER by **1**, shown in Figure S4.73.[61] Similarly, i_c plotted against [**1**], see Figure S4.74, is also linear indicating a first-order dependence of the catalytic rate on the concentration of **1**. Hence, the results obtained correspond to the overall rate expression: rate = k[**1**][H^+] using AcOH as the H^+ source. Addition of acid to the Zn analog (**3**) in DMF results in a slight current enhancement, shown in Figure S4.71, but does not increase upon further addition of AcOH indicating Fe is necessary for catalysis. Comparison of **1** to **3** and free AcOH, shown in Figure S4.72, under the same conditions confirm **1** is solely responsible for catalysis. Lastly, attempts to obtain a KIE value for **1** in DMF, utilizing AcOD-d_4, were unsuccessful due to curve-crossing in the electrocatalytic response.

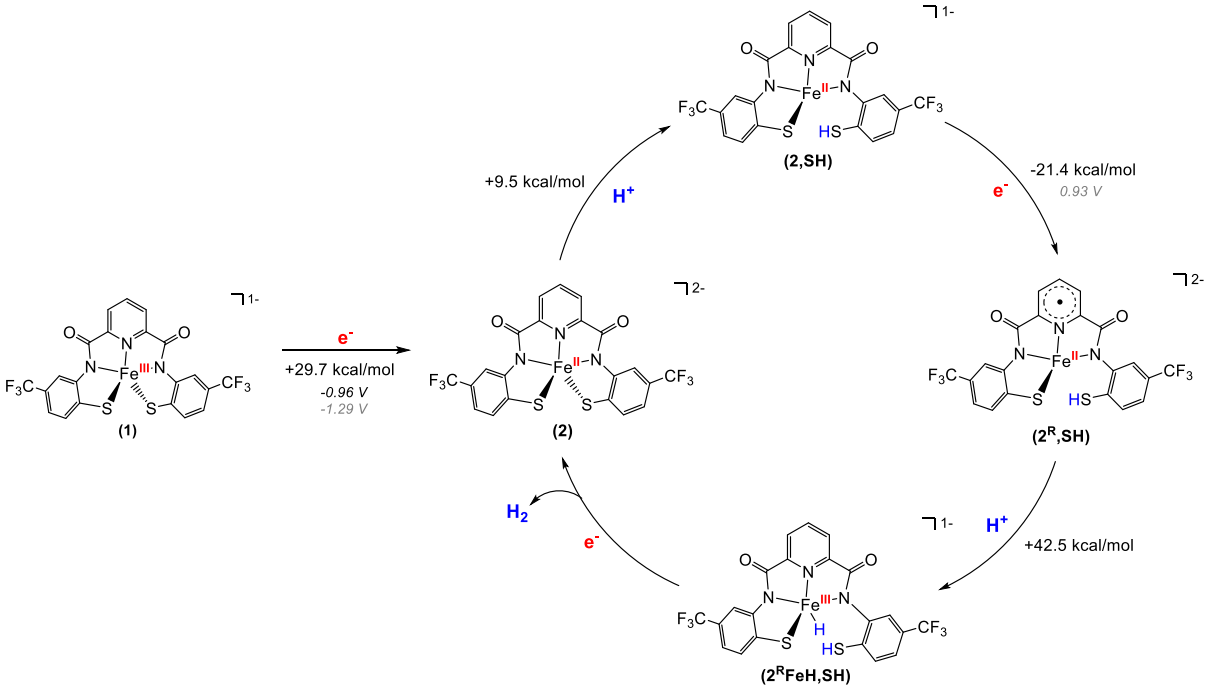

Scheme 4.3. Proposed electrocatalytic E(CECE) HER mechanism for **1** in DMF. Experimental (black) and computed (grey) redox potentials are referenced to Fc/Fc^+.

Proposed Mechanism of HER by 1 in DMF. A mixture of experimental results and computations were utilized to elucidate the catalytic HER mechanism of **1** in DMF, shown in Scheme 4.3. Initial UV-vis and bulk protonation experiments of **1** in DMF, see above, indicate that protonation of **1** is suppressed in DMF suggesting the likely first step in the catalytic cycle is reduction of **1** resulting in **2**, referred to as an E-step. After formation of **2**, we propose the next step is protonation. A sequential E-step is not required to initiate catalysis as seen from the more positive catalytic onset potential (~−2.00 V) than the **2**/**2**$^{\mathbf{R}}$ couple ($E_{1/2}$ = −2.49 V). Further insight into the catalytic mechanism is gathered from DFT calculations using a def-2/TZVPP level of theory with B3LYP in DMF using the conductor-like screening model (CPCMC). Stepwise electron- and proton-transfers can be analyzed to determine the more thermodynamically favorable step. For example, a second reduction event following formation of **2** (**2**/**2**$^{\mathbf{R}}$) was found to be ~55 kcal/mol more challenging than protonation with a computed redox potential of −2.89 V (vs Fc/Fc^{+}), in reasonable agreement with the experimental value (−2.49 V vs Fc/Fc^{+}). In turn, two sites of protonation were considered, at thiolate (**2**,**SH**) or N_{amide} (**2**,**NH**). Both proton transfer steps (C-steps) are nearly isoenergetic, with **2**,**NH** slightly favored by ~2 kcal/mol. However, formation of **2**,**NH** presents two challenges. First, experimental evidence indicates protonation at N_{amide} yields formation of **4** and free iron yielding deposited material. Second, deprotonation of a primary amide (BDE_{NH} = ~104 kcal/mol)[62] is more difficult than an aromatic thiol (BDE_{PhS-H} = 79.0 kcal/mol),[63] thus, making it thermodynamically challenging to heterolytically couple with Fe-hydride. Considering this, we propose the most likely protonated intermediate following reduction is **2**,**SH**. Protonation induces cleavage of the Fe-S bond, affording a four-coordinate complex with a see-saw geometry (τ_4 = 0.44, τ_4' = 0.57), see Figure S4.85 and Table S4.13. This transformation

is accompanied by a contraction in the remaining Fe-N/S bonds (~0.06 Å), consistent with the decreased coordination number.

Subsequent reduction of **2**,**SH** was found to be exothermic with a computed free energy change of −21.4 kcal/mol yielding the reduced $\mathbf{2^R}$,**SH** intermediate. As anticipated, reduction leads to an elongation of the Fe-S/N_{amide} bond lengths with little change in geometry (τ_4 = 0.41) and a slight contraction of the Fe-N_{py} bond (~0.02 Å), see Figure S4.86 and Table S4.15. Like $\mathbf{2^R}$, the protonated form exhibits significant spin density delocalized over the 2,6-Py unit, shown in Figure S4.84, consistent with a ligand-centered reduction. Next, we considered formation of a Fe(III)-H intermediate ($\mathbf{2^R}$**FeH,SH**) via oxidative addition of a free proton, corresponding to the most endergonic step (+42.5 kcal/mol) in the catalytic pathway. Although this is a costly step, further reduction of $\mathbf{2^R}$**,SH** was calculated to be at a potential of −4.10 V (vs Fc/Fc^+), far lower than the experimentally obtained catalytic redox window. The spin-density of $\mathbf{2^R}$**FeH,SH**, depicted in Figure S4.87, is primarily Fe-centered, with negligible residual spin on the 2,6-Py unit, indicating the two electrons necessary to generate the hydride-containing intermediate are derived from the ligand and metal center. Oxidative addition of H^+ affords a square-pyramidal (τ_5 = 0.09) complex featuring a Fe(III)-H bond length of 1.677 Å, see Figure S4.86 and Table S4.15. This values is in line with other high-spin Fe(II)/Fe(I)-H complexes (Fe-H = 1.74/1.68 Å)[64, 65] as well as a recently reported isoelectronic high-spin (S = 5/2) Mn(II)-H complex (Mn-H = 1.68 Å)[66], although these complexes possess lower coordination numbers. Moreover, formation of $\mathbf{2^R}$FeH,SH induces a rotation of the protonated aryl thiolate, repositioning it to serve as a proton-relay site that facilitates coupling with the coordinated hydride (H---H = 1.697 Å).

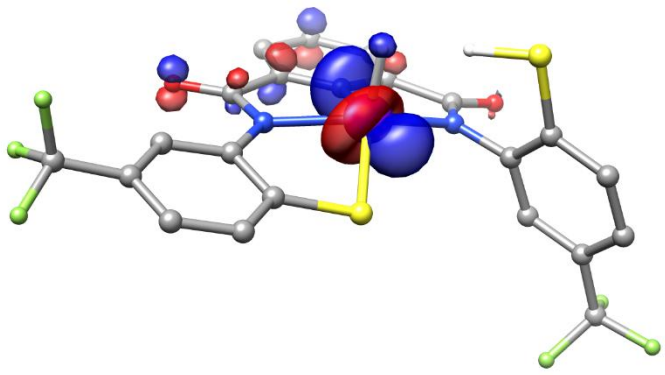

Figure 4.12. DFT-generated (B3LYP, def2-TVZPP) isodurface plot of the LUMO(β) of **2^{R}**FeH,SH using CPCMC(DMF). Color scheme: Fe, Purple; S, yellow; N, blue; F, green-yellow; C, gray. H-atoms are omitted for clarity.

To investigate the transition state associated with heterolytic H-H bond coupling, a potential energy scan was performed starting from the **2^{R}FeH,SH** intermediate, see Figure S4.85. However, the reaction coordinate profile does not exhibit a clear local maximum followed by a minimum as would be expected for H-H coupling. Instead, the energy increases continuously as the H-atoms are brought closer together, suggesting that heterolytic coupling of the metal bound hydride and proximal proton is unfavorable from the **2^{R}FeH,SH** intermediate. Closer examination of structures along the reaction coordinate reveals that the Fe(III)-H bond remains intact, indicating that it is too stable to undergo coupling with the proton. To overcome this, further reduction of **2^{R}FeH,SH** was considered. This reduction is anticipated to weaken the Fe-H bond, thereby promoting coupling with the nearby proton. This is supported by the LUMO(β) of **2^{R}FeH,SH**, shown in Figure 4.12, which is primarily Fe-based (71.8%) and characterized by an anti-bonding interaction between Fe(dz^2) and H(s-σ). Optimization of the one-electron reduced **2^{R}FeH,SH** intermediate (**2^{R2}FeH,SH**), minimized to **2** and free H_2 diatom (H-H = 0.762 Å) closing the cycle. Although the associated reduction potential and energy barrier associated with this final step could not be

explicitly computed, these values are expected to be comparable to those of the initial reduction event (i.e reduction of **1** to **2**) given a similar overall change, coordination environment, geometry, and energies of their respective LUMOs'. Based on these findings, we propose that **1** in DMF catalyzes H_2 evolution through an E(CECE) mechanism wherein the redox-active ligand and hemilabile aryl thiolate serve as key elements in electron and proton transfer, respectively.

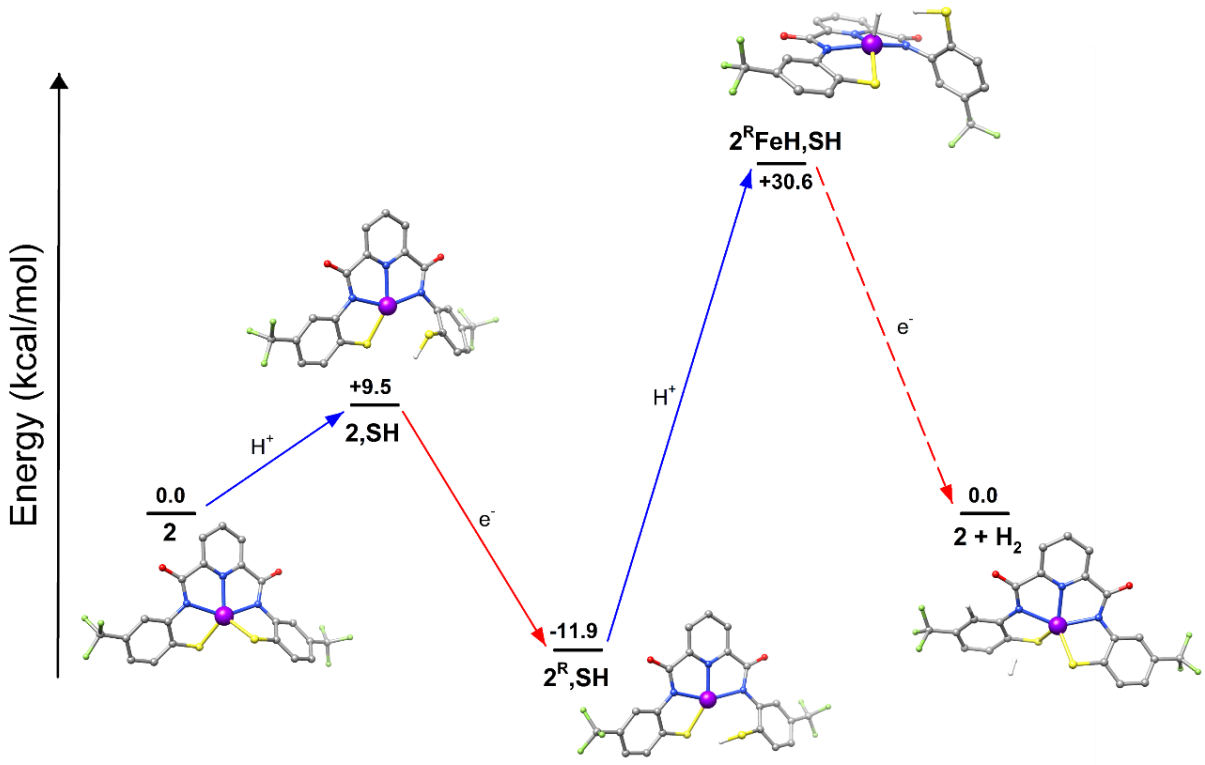

Figure 4.13. Computed free energy profile and optimized intermediates for an E(CECE) HER mechanism catalyzed by **1** in DMF. Color scheme: Fe, Purple; S, yellow; N, blue; F, green-yellow; C, gray. H-atoms are omitted for clarity.

4.4 Conclusion

This work demonstrates that the electron-rich non-heme iron complex **1** serves as a competent hydrogen evolution electrocatalysts in DMF, achieving a TOF of 1200 s^{-1} despite operating a relatively high overpotentials, 0.94 V. Analysis of the homogeneous complex under acidic conditions suggests **1** is protonated at carboxamide-N resulting in Fe-N bond cleavage, ligand rearrangement, and release of Fe to produce the tetrathiolate-Fe complex, **4**. The resulting mixture yields electrocatalytically active deposits in MeCN. However, the stability of **1** under acidic conditions is enhanced in DMF proposed to be due to H-bonding interaction between protonated ligand (**1,SH**) and solvent impeding intramolecular proton transfer to carboxamide-N. Enhanced stability diminishes deposition under electrocatalytic conditions, allowing for a reliable assessment of the electrocatalysis behavior of homogenous **1**. Computational analysis of a catalytic mechanism suggests **1** catalyzes H_2 evolution by an E(CECE) pathway, with a hemilabile thiolate group facilitating proton transfer. These studies further reveal the non-innocent nature of the ligand, which serves as an additional site of reduction, thereby circumventing the formation of a more thermodynamically unfavorable Fe(I) intermediate. However, the significantly negative potential required for ligand reduction likely contributes to the large overpotential of **1**. Overall, this study highlights the potential of combining hemilabile thiolates and redox-active ligands as an effective platform for proton reduction electrocatalysts.

4.5 Materials and Methods

General Information. All reagents were procured from commercial suppliers and used as received unless otherwise noted. Acetonitrile (MeCN), tetrahydrofuran (THF), and diethyl ether (Et_2O) were purified by passage through activated alumina columns using an MBraun solvent purification system (MB-SPS). Dimethylformide (DMF) was degassed by purging with N_2 for 1 h. All solvents were stored over 3 Å molecular sieves in an anaerobic glovebox three days before use. The metal salts $(Et_4N)[FeCl_4]$, $(Et_4N)_2[FeCl_4]$, and $(Et_4N)_2[ZnCl_4]$ were synthesized according to the published procedure.[67] All reactions were performed under an inert atmosphere of N_2 using Schlenk-line techniques or in an MBraun Unilab glovebox.

Physical Methods. FTIR spectra were collected with a ThermoNicolet 6700 spectrophotometer running the OMNIC software. Solid-state samples were prepared as KBr pellets in a glovebox under N_2 atmosphere and run in ambient conditions. UV-vis spectra were recorded at 25 °C using a Cary-50 spectrophotometer containing a Quantum Northwest TC 125 temperature control unit. All UV-vis samples were prepared in gastight/screw-cap quartz cells with an optical pathlength of 1 cm. NMR spectra were recorded in the reported solvent on a 400 MHz Bruker BZH 400/52 NMR spectrometer and 600 MHz Varian Unity INOVA NMR RT with chemical shifts referenced to residual protio signal of the deuterated solvent.[60] ^{19}F NMR spectra are referenced to $CFCl_3$ by employing a fluorobenzene internal standard (δ = -114.81 ppm vs. $CFCl_3$).[68] Magnetic susceptibility measurements were recorded in CD_3CN at 25 °C using the Evans method on a 600 MHz NMR spectrometer.[69] Pascal's constants for diamagnetic corrections are taken from the literature.[70] Low resolution electrospray ionization mass spectrometry (LR-ESI-MS) data were collected using a PerkinElmer Sciex APII Plus quadrupole mass spectrometer or a Bruker Esquire 3000 plus ion trap mass spectrometer. X-band (9.35 GHz) EPR spectra were obtained using a

Bruker EMXplus EPR spectrometer controlled with a Bruker microwave bridge. The EPR was equipped with a closed loop helium gas flow with re-circulator (Bruker Cold Edge) and temperature controller.

Computational Details. Density functional theory (DFT) calculations were performed with the ORCA electronic structure package, version 4.2.1. Geometry optimization, frequency analysis, and single point energy of all models were performed using the B3LYP functional[71, 72] employing the RIJCOSX aproximation[73] and Grimme's D3(BJ) dispersion correction[74, 75] using coordinates from the crystal structures of $(Et_4N)[Fe^{III}(PyP)]$[18] with the incorporation of *p*-CF_3 groups and the crystal structure of **3**. The def2-SVP basis set was used for all atoms except for Fe, S, N, O, and F for which the triple-ζ basis set def2-TZVPP[76, 77] was used for geometry optimization frequency analysis, and single point energy calculations with an automatically constructed auxiliary basis set on all atoms. The conductor-like polarizable continuum model (CPCMC)[78] was used with MeCN ($\varepsilon = 37.5$) or DMF ($\varepsilon = 36.7$) for single point energy calculations and frequency analysis with no imaginary frequencies found. UCSF Chimera[79] was used to generate model structure to visualize isosurface plots of MOs and spin density plots with isodensity values of 0.05 a.u. and 0.005 a.u., respectively.

4.6 Synthesis and Characterization:

Tritylated Aminothiophenol A batch of triphenylmethanol (5.516 g, 21.19 mmol) was partially dissolved in ~10 mL TFA resulting in a yellow-brown heterogenous solution. To this 3-amino-4-(trifluoromethyl)benzenethiol hydrochloride (4.865 g, 21.18 mmol) was added and stirred overnight resulting in a bright-yellow color. All TFA was removed resulting in an amber oil and ~100 mL DCM to afford a dark-yellow solution. To this, ~100 mL of H_2O, turning the solution to a bright yellow color, was added to wash orange/yellow filtrate and K_2CO_3 was added until solution was basic (~pH 9). Three additional washes of saturated $NaHCO_3$ (x2) and NaCl solutions were performed. To the isolated DCM layer, $MgSO_4$ was stirred in, filtered over filter paper, and rinsed with ~10 mL of DCM. The yellow filtrate was taken to dryness to afford a dark-yellow color and ~50 mL of hexane was added. The solution was stirred for 2 hr and placed in the freezer for 12 hrs. The precipitate was isolated by vacuum filtration on a glass-frit, washed with hexane (3 x 5 mL), and dried on a high vacuum line to afford the desired product as a white solid (5.973 g, 13.71 mmol, 64.7%). FTIR (KBr matrix), ν_{max} (cm^{-1}): 3457 (w, NH), 3360 (w, NH), 1340 (s, CF), 1114 (s, CF), 1082 (s, CF). ^1H NMR (400 MHz, $CDCl_3$, δ from residual deuterated solvent): 7.36 (m, 6H), 7.23 (m, 10H, residual solvent underneath), 7.05 (d, 1H, J = 8.1 Hz), 6.66 (s, 1H), 6.60 (d, 1H, J = 8.10 Hz), 3.90 (s, 2H). ^{19}F NMR (376 MHz, $CDCl_3$, δ from C_6H_5F): -65.00 (s). $^{13}C\{H\}$ NMR (100 MHz, $CDCl_3$, RT): 151.0 (s), 144.3 (s), 137.9 (s), 132.4 (q, J = 32.1 Hz), 130.0 (s), 128.1 (s), 127.9 (s), 127.1 (s), 124.0 (q, J = 272.5 Hz), 120.4 (s), 113.9 (q, J = 3.7 Hz), 111.3 (q, J = 3.9 Hz), 71.7 (s). Mp: 115 - 117 °C.

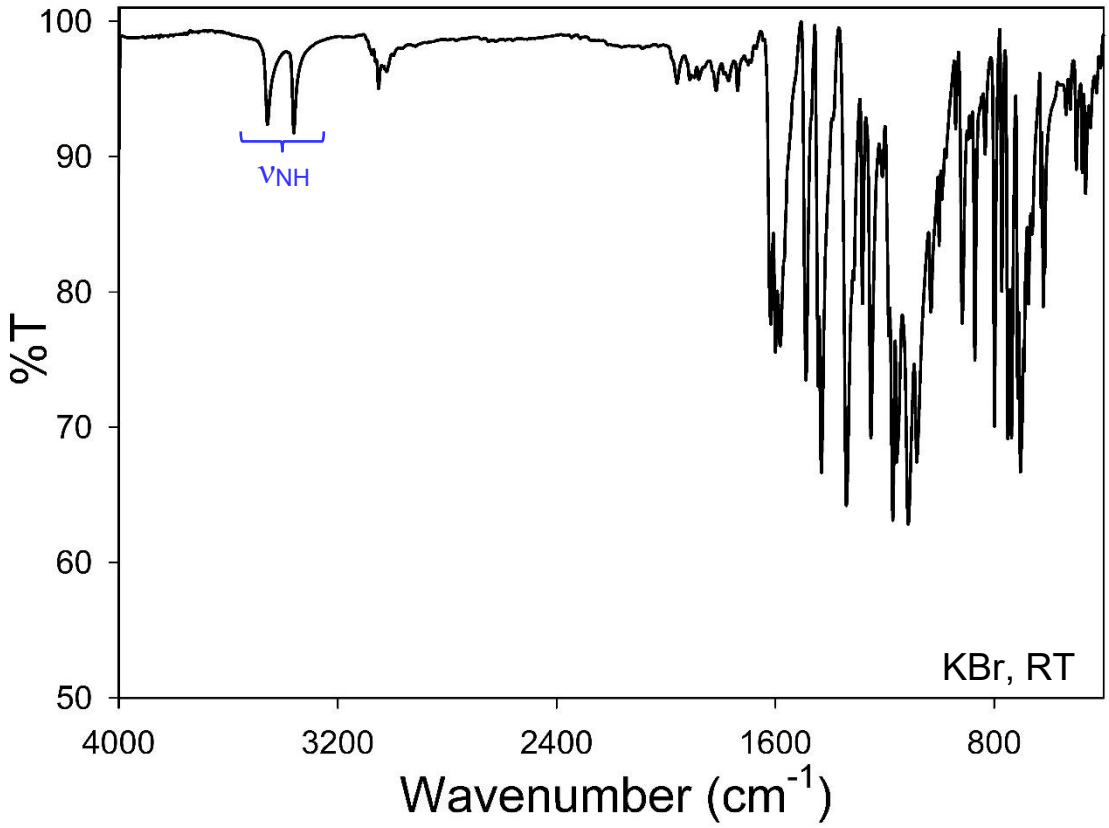

Figure S4.1. Solid-state FTIR spectrum of S(CPh_3)-*o*-NH_2-*p*-CF_3-Ph in a KBr matrix at RT.

^{1}H NMR (400 MHz, $CDCl_3$, RT) of **S(CPh$_3$)-*o*-NH$_2$-*p*-CF$_3$-Ph**

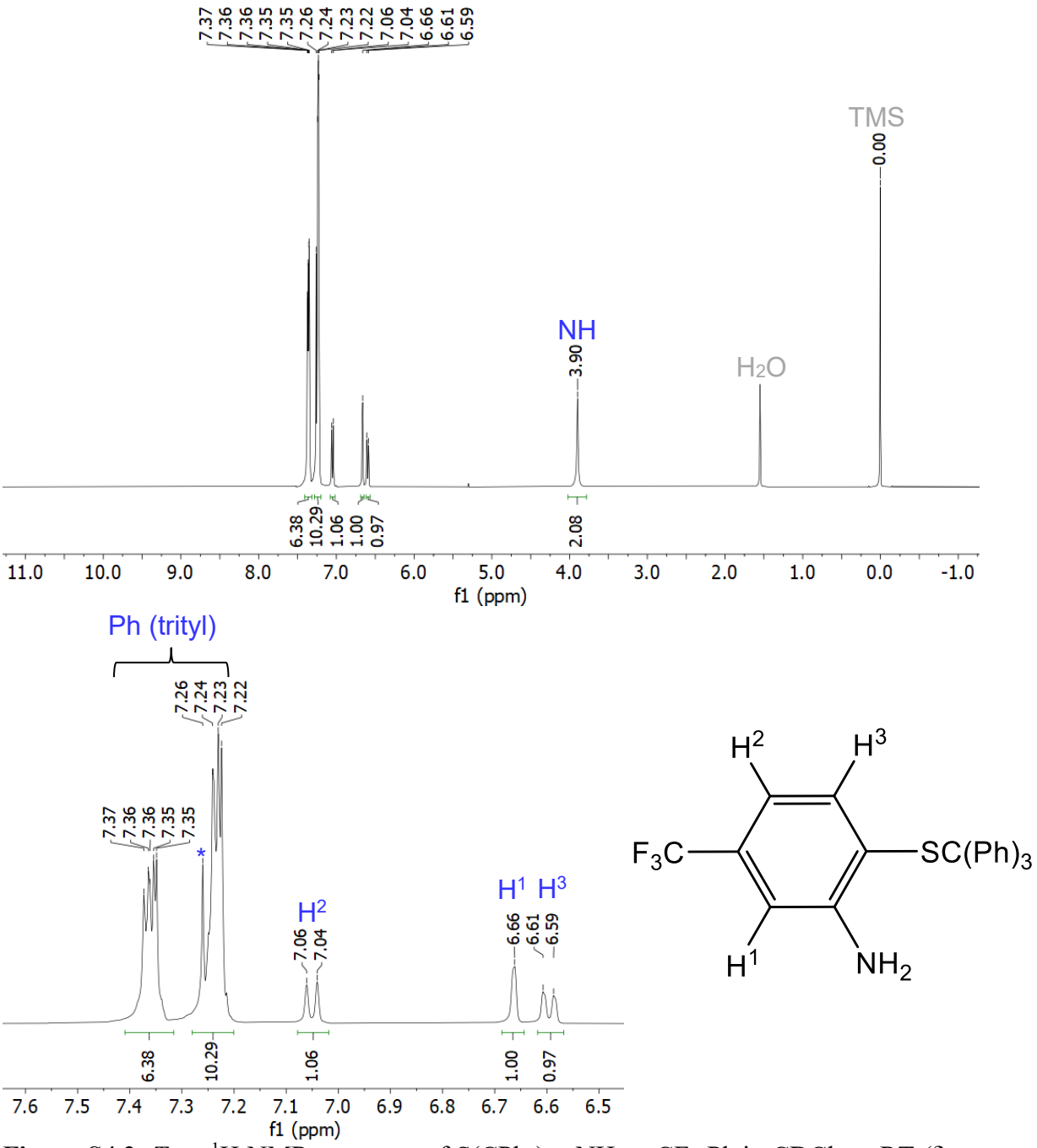

Figure S4.2. *Top:* ^{1}H NMR spectrum of S(CPh$_3$)-*o*-NH$_2$-*p*-CF$_3$-Ph in $CDCl_3$ at RT (δ vs. protio signal), peak at 1.5 ppm is due to water. *Bottom:* expansion of 6 – 8 ppm region. Residual $CHCl_3$ is observed at 7.26 ppm and is indicated with *.

^{13}C NMR (100 MHz, $CDCl_3$, RT) of **S(CPh$_3$)-*o*-NH$_2$-*p*-CF$_3$-Ph**

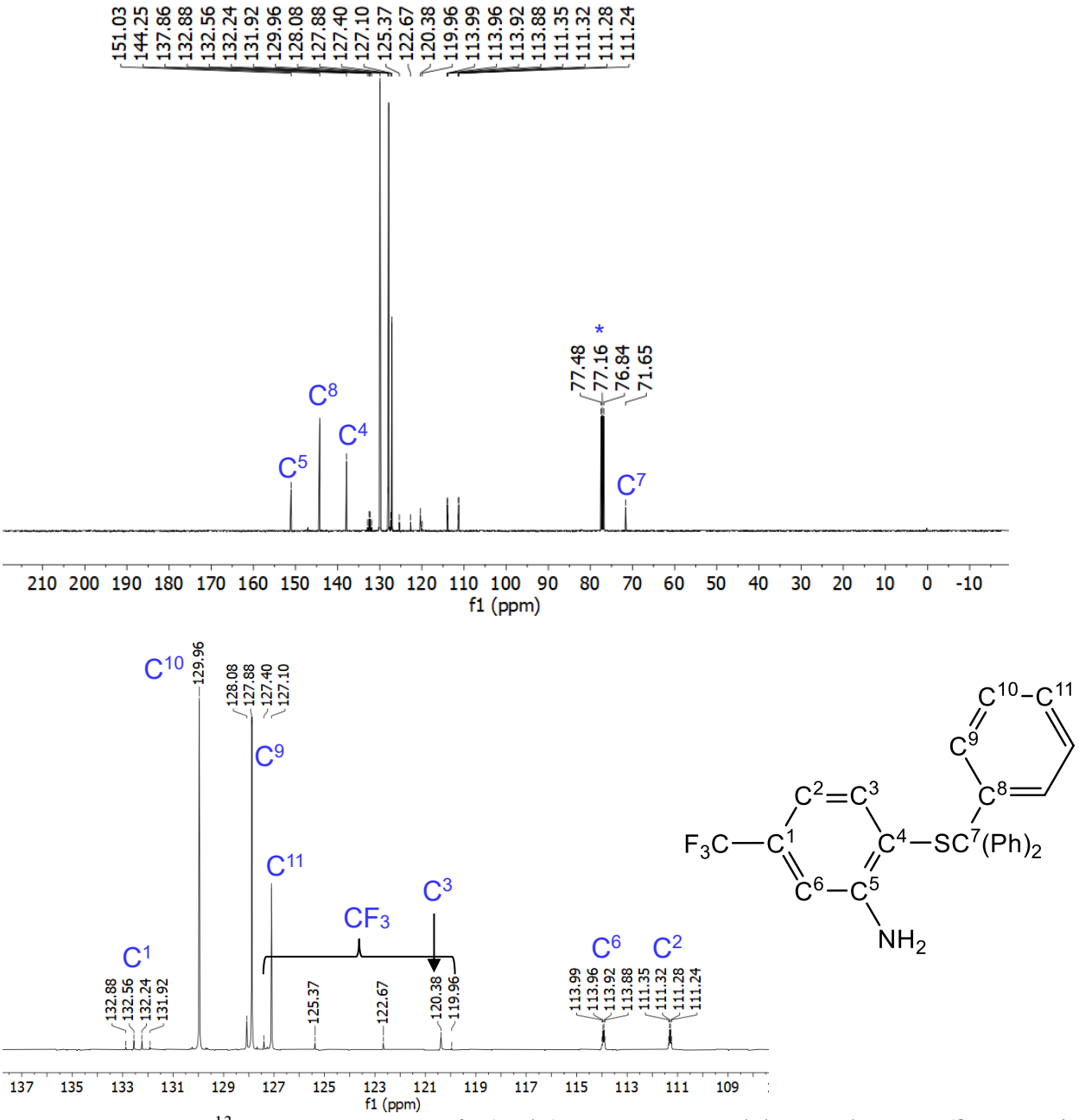

Figure S4.3. *Top:* ^{13}C NMR spectrum of S(CPh$_3$)-*o*-NH$_2$-*p*-CF$_3$-Ph in $CDCl_3$ at RT (δ vs. protio signal. *Bottom:* expansion of 108 - 137 ppm region. Residual $CHCl_3$ is observed at 77.16 ppm and is indicated with *.

^{19}F NMR (376 MHz, $CDCl_3$, RT) of **S(CPh_3)-*o*-NH_2-*p*-CF_3-Ph**

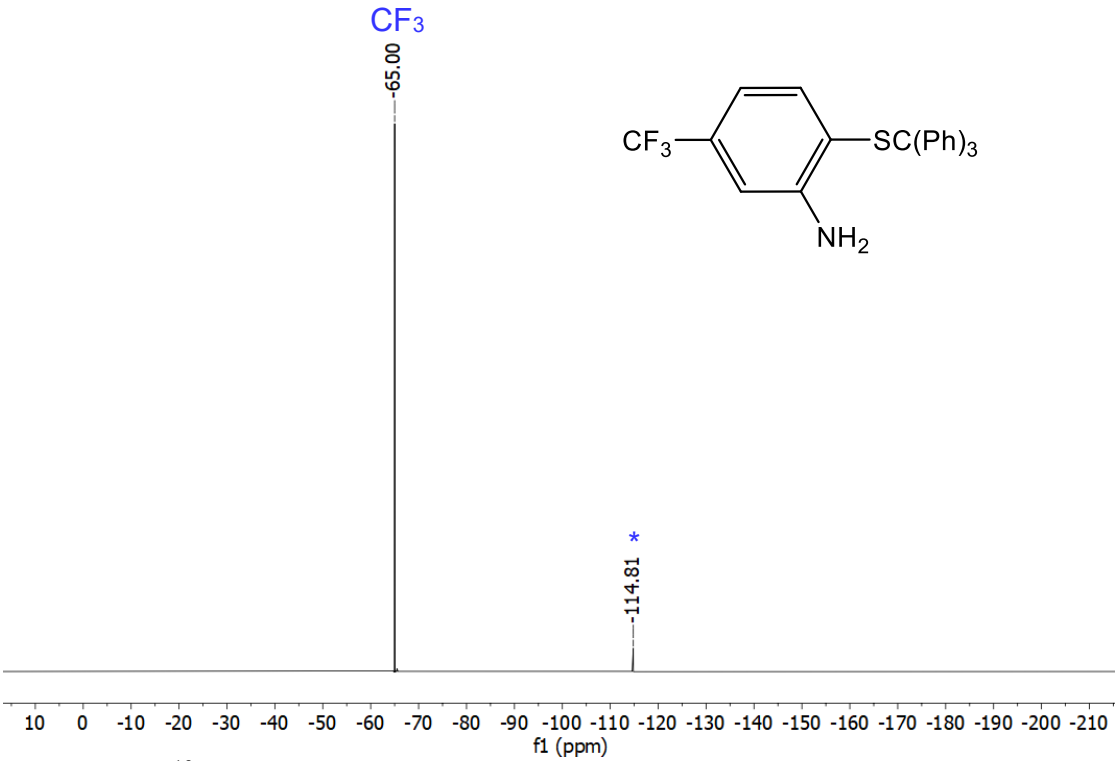

Figure S4.4. ^{19}F NMR spectrum of S(CPh_3)-*o*-NH_2-*p*-CF_3-Ph in $CDCl_3$ at RT. The peak at -114.81 ppm is from PhF as an internal standard and is indicated with *.

PyPS-Try-*p*-CF_3 To a light-yellow solution of trytilated aminothiphenol (1.632 g, 3.747 mmol) in ~20 mL of DCM, triethylamine (1.548 g, 15.30 mmol) was added and let stir for 5 min, no color change was observed. To this 2,6-pyridinedicarbonyl dichloride (0.383 g, 1.88 mmol) under N_2 atmosphere and stirred for ~12 hr. The resulting white precipitate was isolated by vacuum filtration on a glass-frit, washed with cold MeOH (3 x 5 mL), and dried on a high vacuum line to afford the desired product as a white solid (1.530 g, 1.527 mmol, 81.3%). FTIR (KBr matrix), ν_{max} (cm^{-1}): 3290 (m, NH), 1689 (s, CO), 1328 (s, CF), 1129 (s, CF), 1084 (s, CF). ^{1}H NMR (400 MHz, $CDCl_3$, δ from residual deuterated solvent): 10.65 (s, 2H), 8.91 (s, 2H), 8.24 (d, 2H, J = 7.6 Hz), 8.09 (t, H, J = 8.4 Hz), 7.64 (d, 2H, J = 8.2 Hz), 7.27 (d, 4H, residual solvent underneath), 7.10 (d, 12H, J

= 8.2 Hz), 6.95 (6H, t, J = 7.2 Hz), 6.77 (t, 12H, J = 7.5 Hz). ^{19}F NMR (376 MHz, $CDCl_3$, δ from C_6H_5F): -64.74 (s). ^{13}C{H} NMR (100 MHz, $CDCl_3$, RT): 161.0 (s), 148.7 (s), 143.1 (s), 142.9 (s), 139.2 (s), 138.5 (s), 133.4 (q, J = 34.0 Hz), 129.5 (s), 127.6 (s), 127.4 (s), 125.9 (s), 125.3 (s), 123.8 (q, J = 272.0 Hz), 120.2 (q, J = 3.6 Hz), 116.7 (q, J = 3.4 Hz), 72.9 (s). Decomposes at 230 °C.

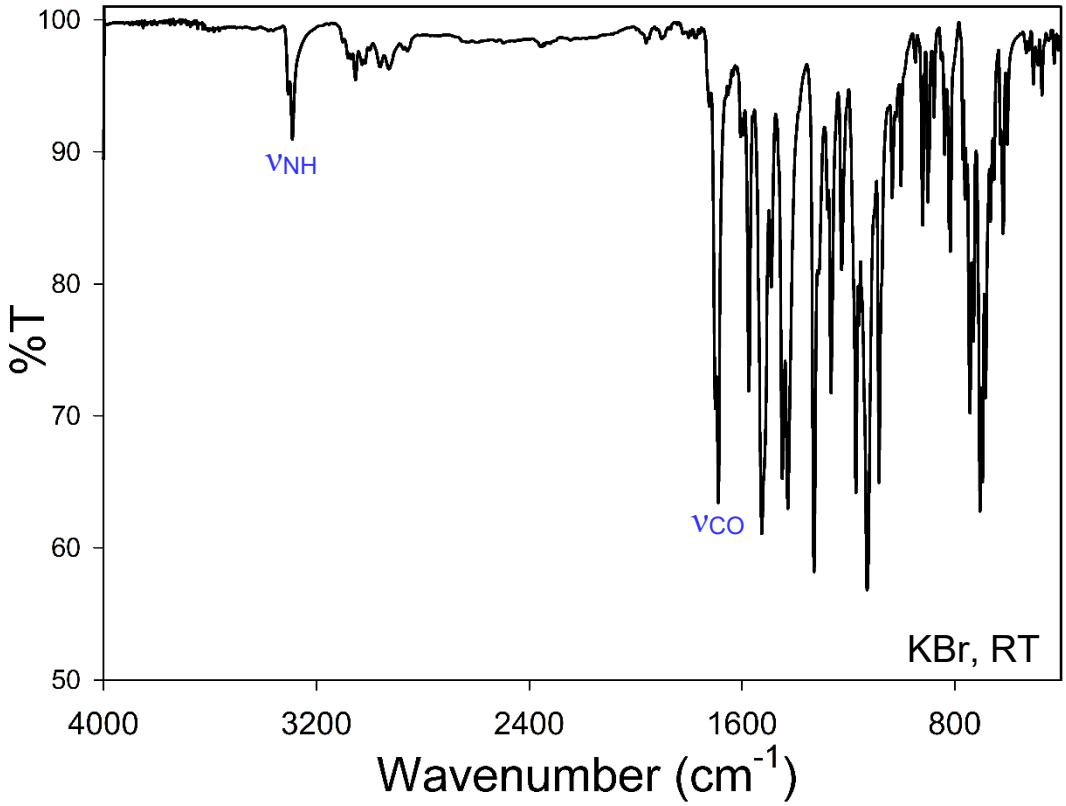

Figure S4.5. Solid-state FTIR spectrum of PyPS-Try-*p*-CF_3 in a KBr matrix at RT.

^{1}H NMR (400 MHz, $CDCl_3$, RT) of **PyPS-Try-*p*-CF_3**

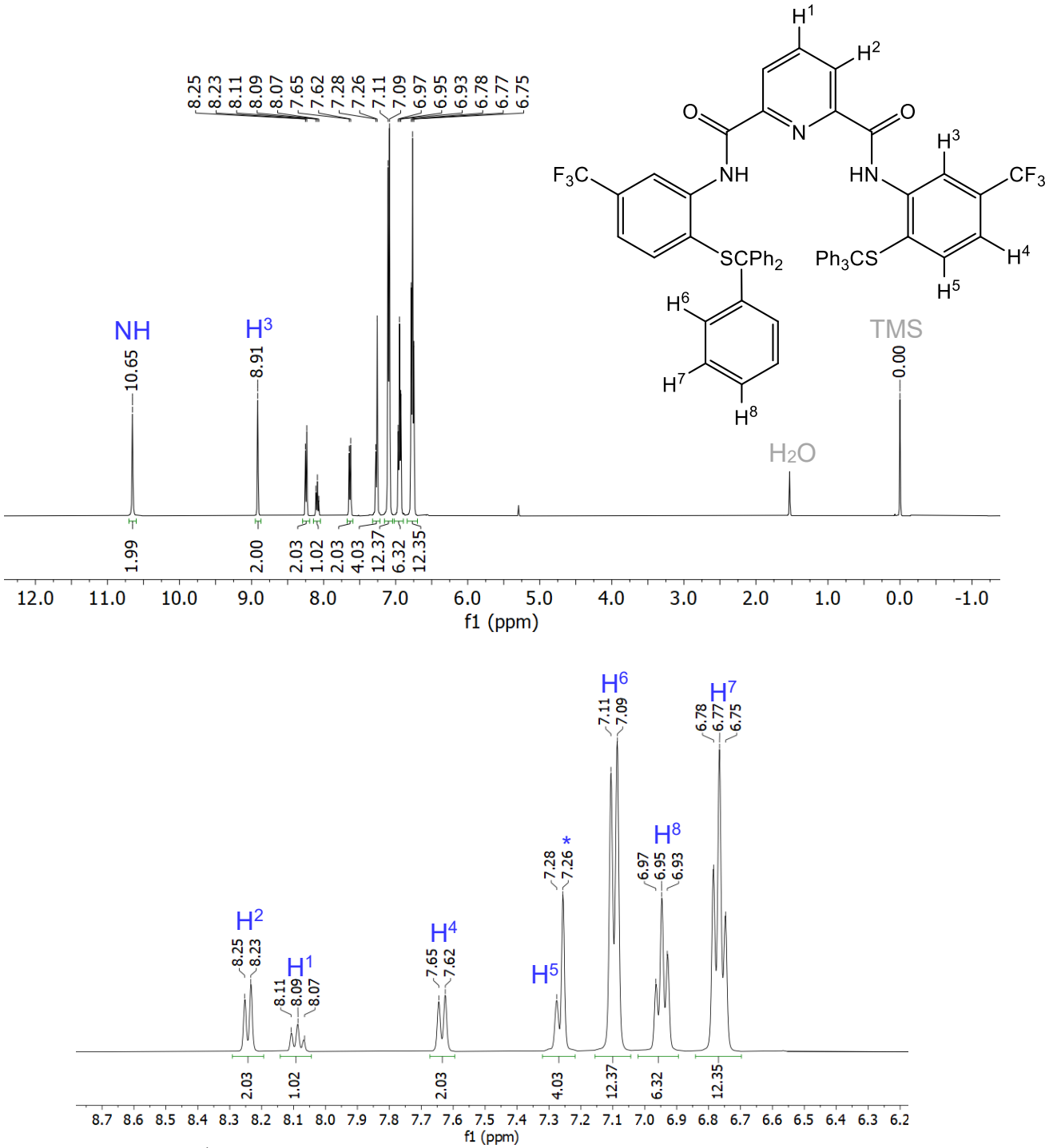

Figure S4.6. *Top:* ^{1}H NMR spectrum of PyPS-Try-*p*-CF_3 in $CDCl_3$ at RT (δ vs. protio signal), peak at 1.5 ppm is due to water. *Bottom:* expansion of 6 – 8 ppm region. Residual $CHCl_3$ is observed at 7.26 ppm and is indicated with *.

^{13}C NMR (100 MHz, $CDCl_3$, RT) of **PyPS-Try-*p*-CF_3**

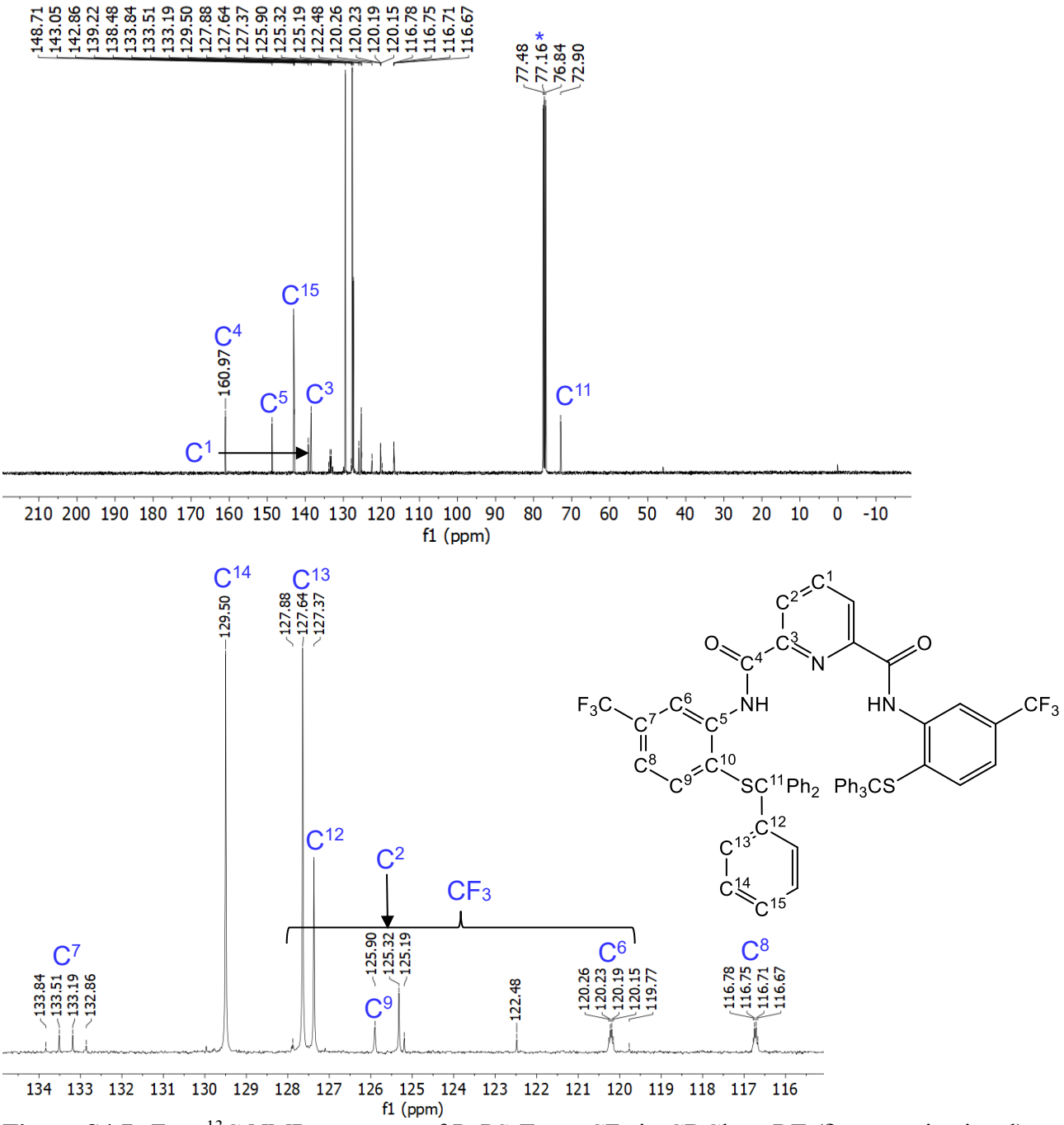

Figure S4.7. *Top:* ^{13}C NMR spectrum of PyPS-Try-*p*-CF_3 in $CDCl_3$ at RT (δ vs. protio signal). *Bottom:* expansion of 6 – 8 ppm region. Residual $CHCl_3$ is observed at 77.16 ppm and is indicated with *.

^{19}F NMR (376 MHz, $CDCl_3$, RT) of **PyPS-Try-*p*-CF_3**

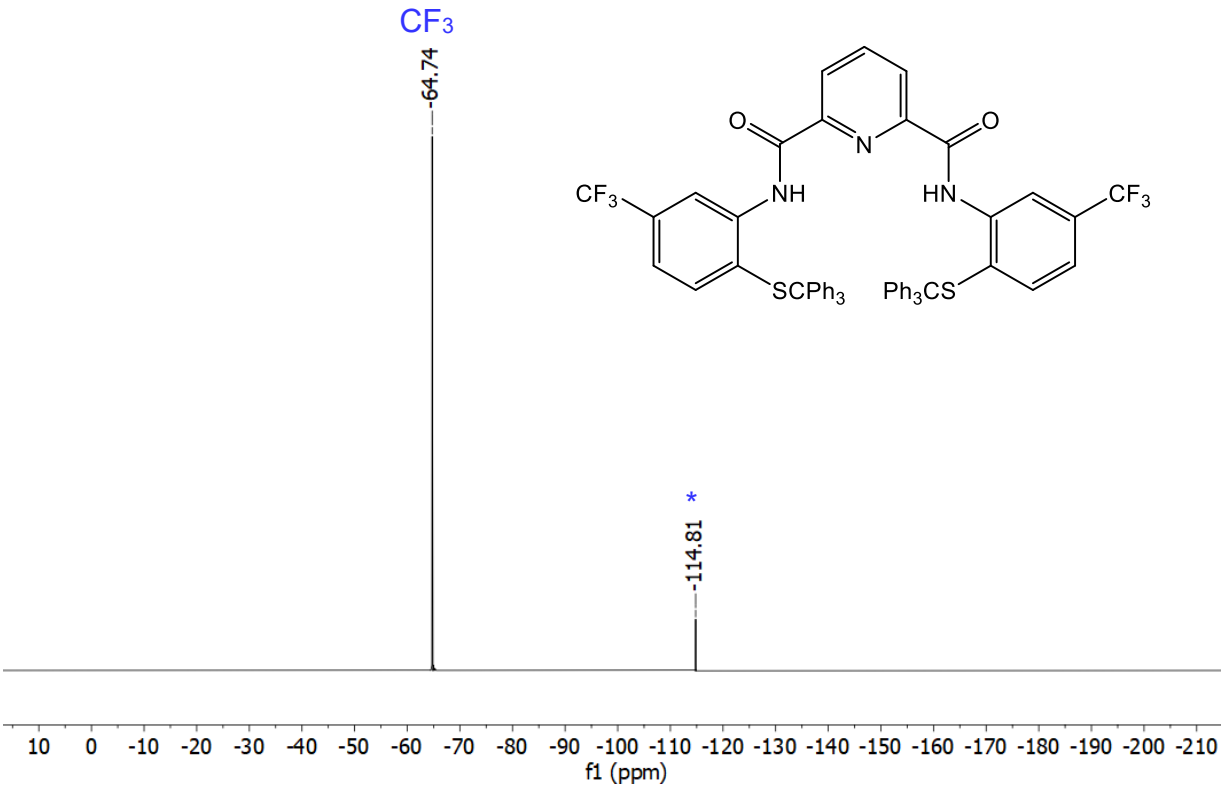

Figure S4.8. ^{19}F NMR spectrum of PyPS-Try-*p*-CF_3 in $CDCl_3$ at RT. The peak at -114.81 ppm is from PhF as an internal standard.

PyPSH_4-*p*-CF_3 A batch of PyPS-Try-*p*-CF_3 (1.527 g, 1.525 mmol) was dissolved in a 1:1 mixture (5 mL:5 mL) of TFA and DCM to form a dark-yellow homogenous solution. To this solution triethylsilane (0.369 g, 3.173 mmol) was added and the solution instantly took on a light-yellow color upon addition. The solution was stirred for 1 h and was concentrated to half on the initial volume resulting in a white precipitate. The precipitate was filtered off and rinsed with ~3 mL of TFA. The TFA was completed removed from the yellow filtrate resulting in a light-yellow precipitate. To this ~10 mL of cold Et_2O was added and stirred for 30 min. The precipitate was isolated by vacuum filtration on a glass-frit, washed with Et_2O (3 x 5 mL), and dried on a high vacuum line to afford the desired product as an off-white solid (0.567 g, 1.10 mmol, 72.1%). FTIR

(KBr matrix), ν_{max} (cm^{-1}): 3342 (w, NH), 3306 (w, NH), 2553 (w, SH), 1686 (s, CO), 1331 (s, CF), 1115 (s, CF), 1085 (s, CF), ^{1}H NMR (400 MHz, $CDCl_3$, δ from residual deuterated solvent): 10.39 (s, 2H), 8.69 (s, 2H), 8.57 (d, 2H, J = 7.8 Hz), 8.24 (t, 1H, J = 7.7 Hz), 7.65 (d, 2H, J = 8.1 Hz), 7.37 (d, 2H, J = 8.1 Hz), 3.52 (s, 2H). ^{19}F NMR (376 MHz, $CDCl_3$, δ from C_6H_5F): -64.52 (s). $^{13}C\{H\}$ NMR (100 MHz, $CDCl_3$, RT): 161.4 (s), 148.8 (s), 140.2 (s), 137.7 (s), 134.4 (s), 131.3 (q, J = 32.9 Hz), 126.5 (s), 124.2 (s), 123.8 (q, J = 272.4 Hz), 121.9 (q, J = 3.7 Hz), 119.3 (q, J = 3.9 Hz). Mp: 149 - 151 °C.

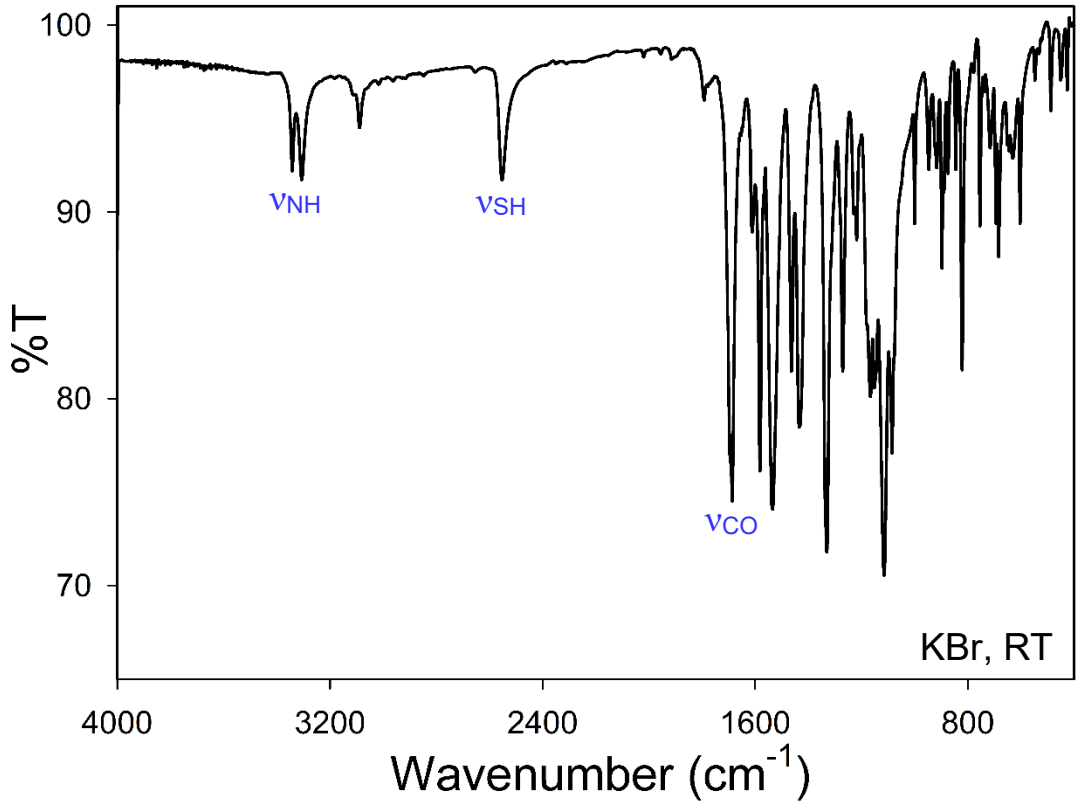

Figure S4.9. Solid-state FTIR spectrum of $PyPSH_4$-*p*-CF_3 in a KBr matrix at RT.

^{1}H NMR (400 MHz, $CDCl_3$, RT) of **$PyPSH_4$-*p*-CF_3**

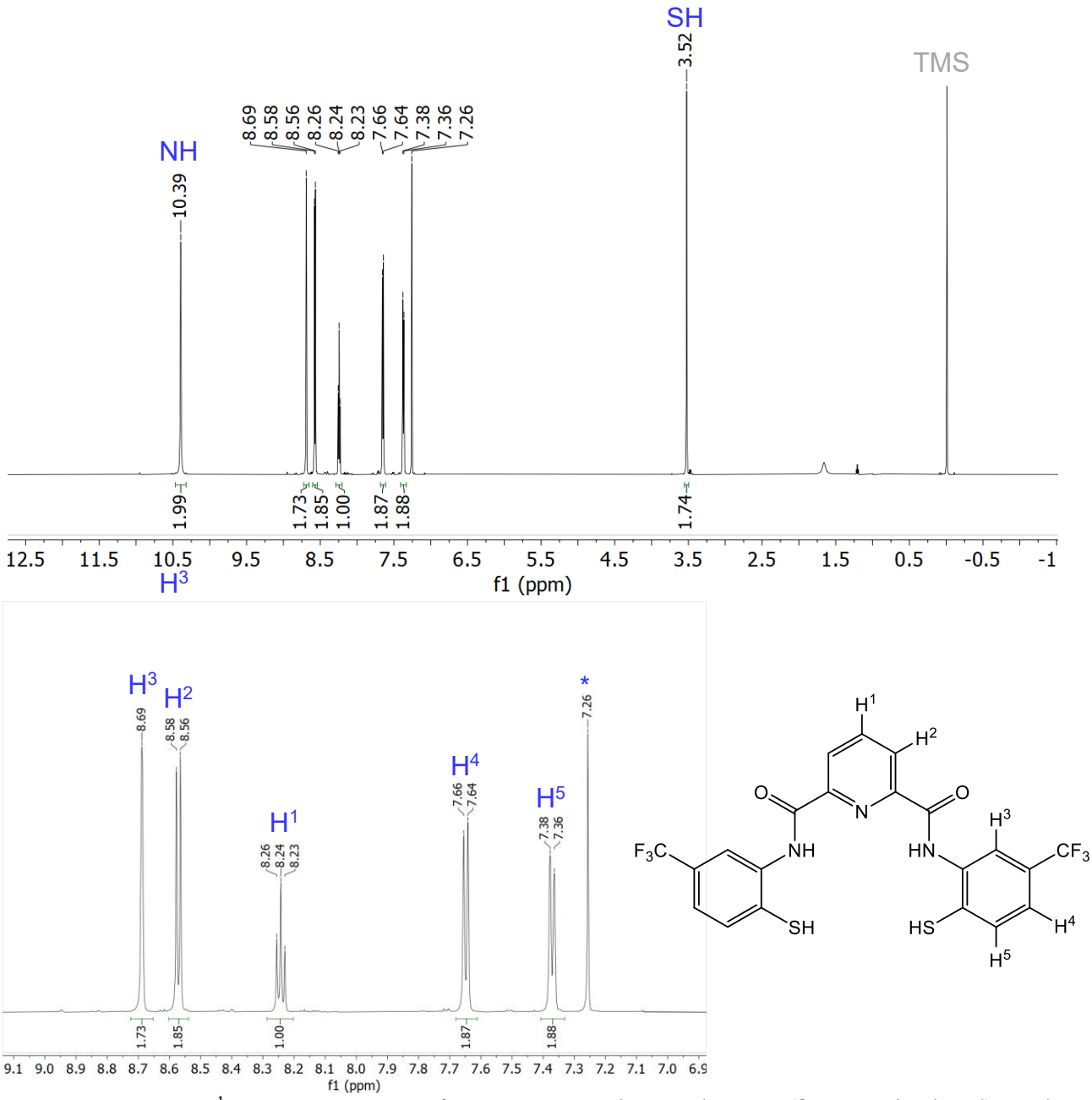

Figure S4.10. *Top:* ^{1}H NMR spectrum of $PyPSH_4$-*p*-CF_3 in $CDCl_3$ at RT (δ vs. protio signal), peak at 1.5 ppm is due to water. *Bottom:* expansion of 7 – 9 ppm region. Residual $CHCl_3$ is observed at 7.26 ppm and is indicated with *.

^{13}C NMR (100 MHz, $CDCl_3$, RT) of **$PyPSH_4$-*p*-CF_3**

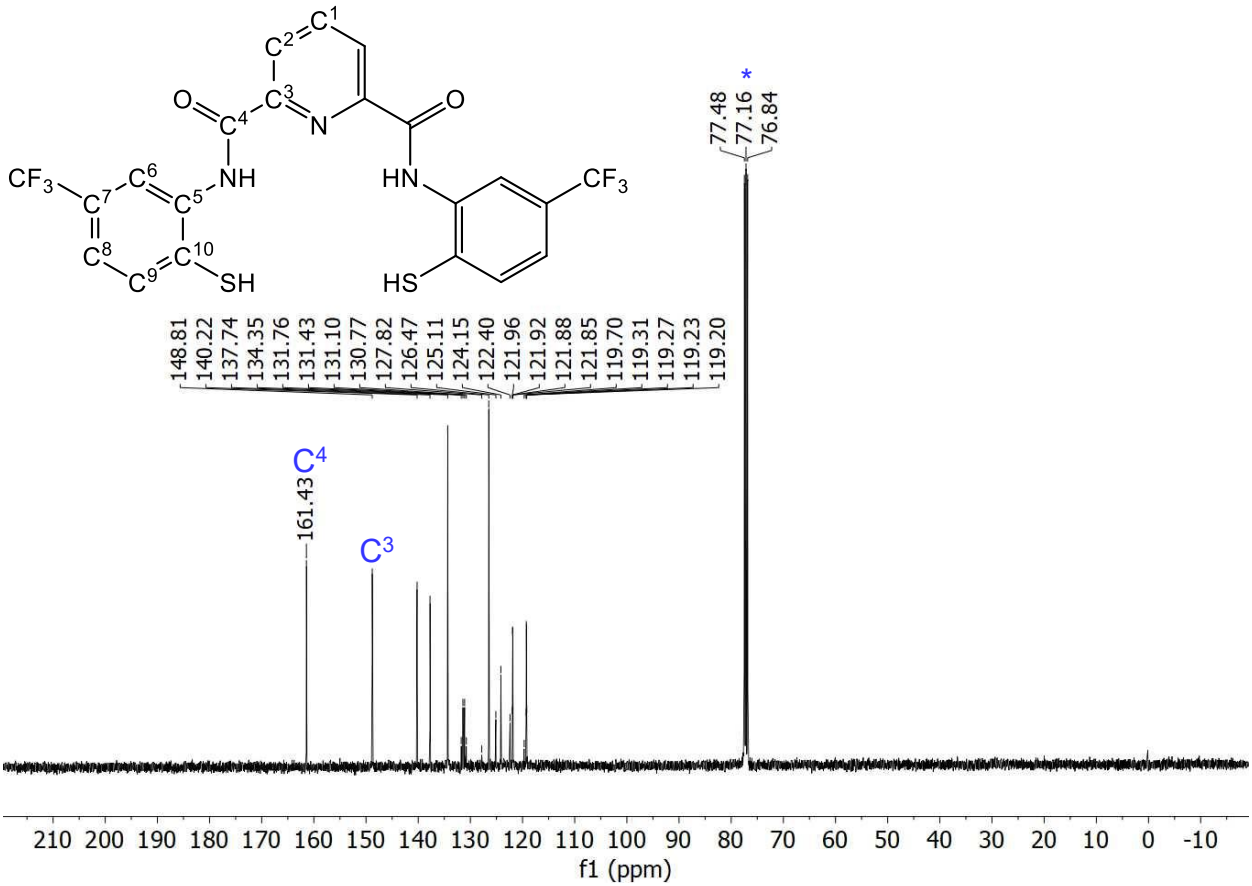

Figure S4.11. ^{13}C NMR spectrum of $PyPSH_4$-*p*-CF_3 in $CDCl_3$ at RT (δ vs. protio signal). Residual $CHCl_3$ is observed at 7.26 ppm and is indicated with *. Zoom-in of 118 to 141 ppm region shown in Figure S4.12.

^{13}C NMR (100 MHz, $CDCl_3$, RT) of **$PyPSH_4$-*p*-CF_3**

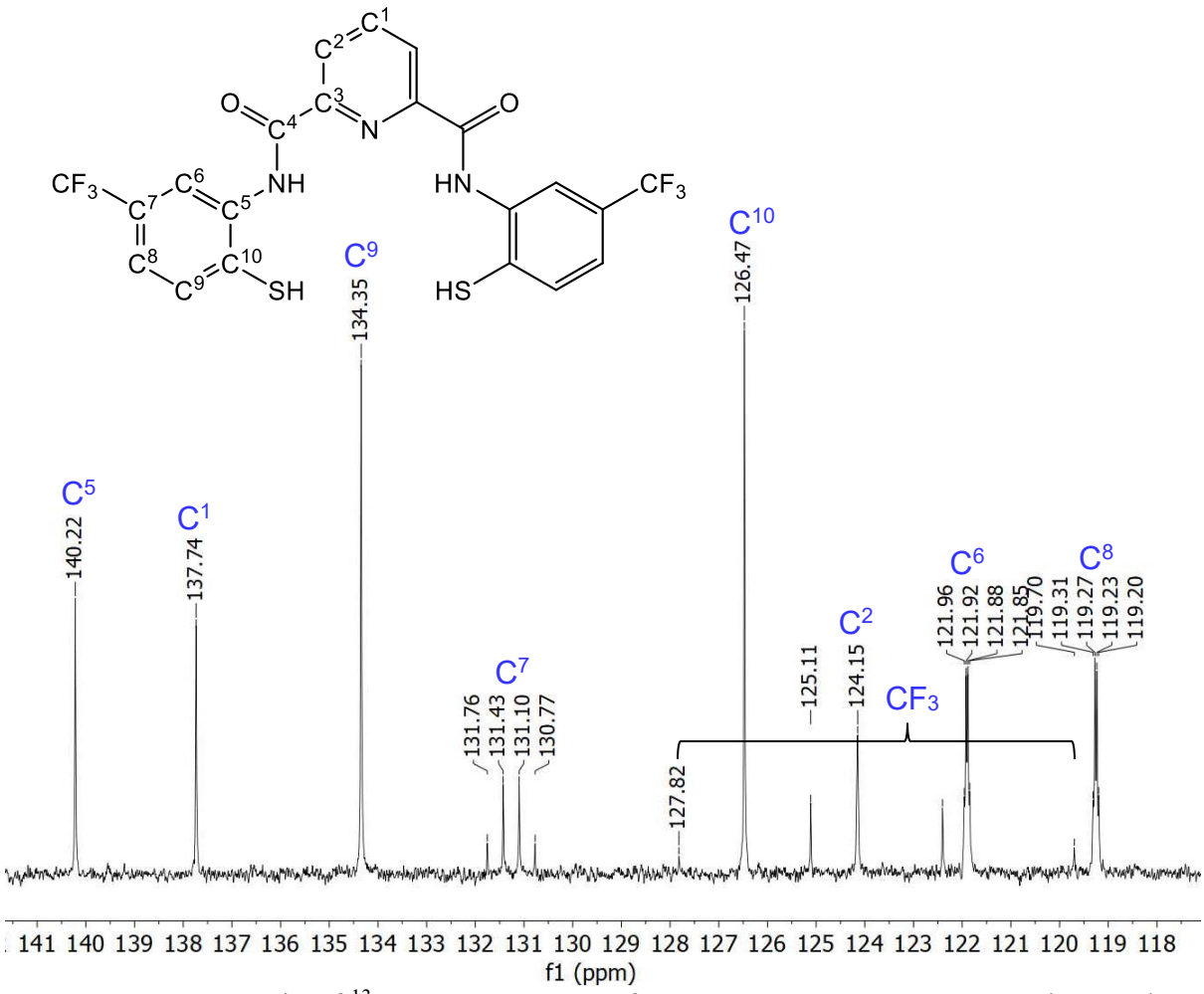

Figure S4.12. Zoom-in of ^{13}C NMR spectrum of $PyPSH_4$-*p*-CF_3 **(Figure S4.11)** in $CDCl_3$ at RT (δ vs. protio signal).

^{19}F NMR (376 MHz, $CDCl_3$, RT) of **$PyPSH_4$-*p*-CF_3**

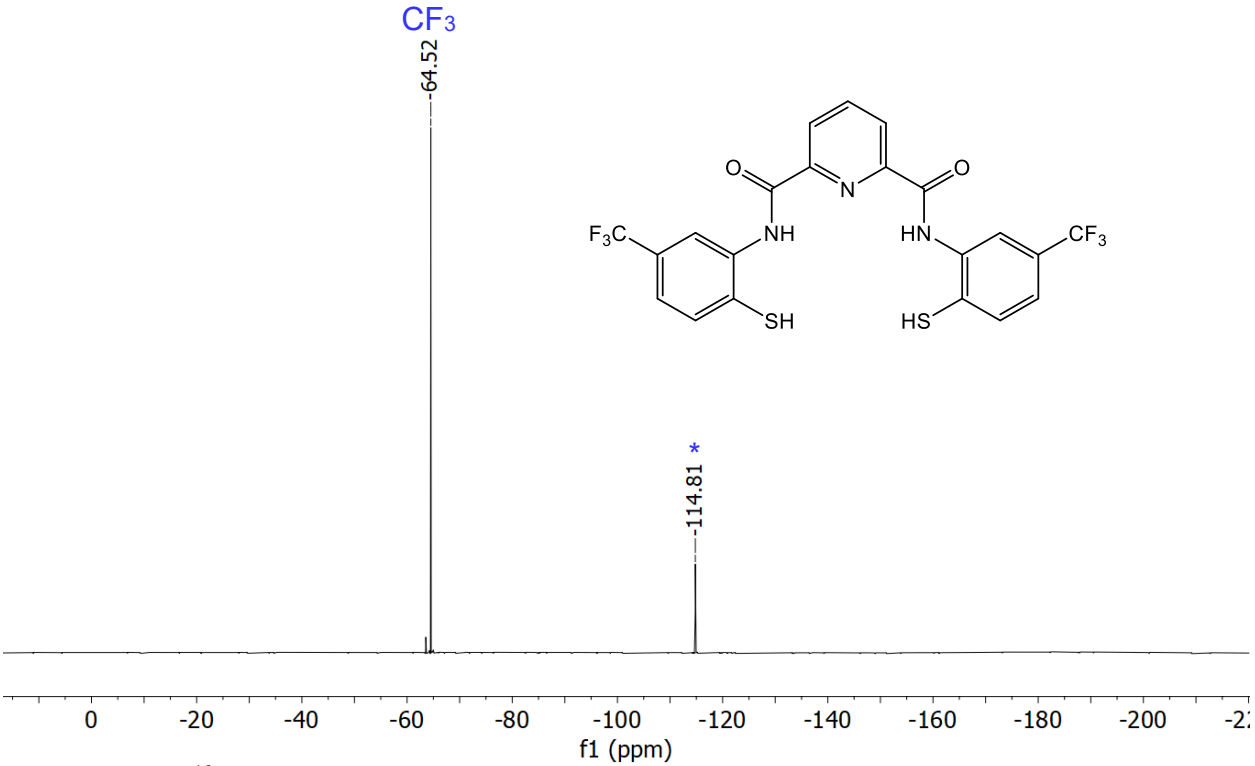

Figure S4.13. ^{19}F NMR spectrum of $PyPSH_4$-*p*-CF_3 in $CDCl_3$ at RT. The peak at -114.81 ppm is from PhF as an internal standard and is indicated with *.

$(Et_3NH)_2(PyH_2PS$-*p*-$CF_3)$ A slight yellow solution of $PyPSH_4$-*p*-CF_3 (0.099 g, 0.19 mmol) was made in ~2 mL of THF and placed in a freezer (~ −20 ˚C) for 15 min. To this solution triethylamine (0.044 g, 0.43 mmol) was added dropwise and stirred for 30 min, allowing the solution to warm up to RT. Immediately upon addition of triethylamine, the solution took on a darker yellow color and became an orange-yellow color within 1 min. After 30 min, THF was removed, ~4 mL of Et_2O was added, and allowed to stir for 30 min. The resulting precipitate was isolated by vacuum filtration on a glass-frit, washed with Et_2O (3 x 3 mL), and dried on a high vacuum line to afford the desired product as a light-yellow solid (0.120 g, 0.166 mmol, 87.4%). FTIR (KBr matrix), ν_{max} (cm^{-1}): 3189 (w, NH), 2578 (w, NH), 2345 (w, NH), 1672 (s, CO), 1324 (s, CF), 1106 (s, CF), 1075 (s, CF). ^{1}H NMR (400 MHz, CD_3CN, δ from residual deuterated solvent): 11.68 (s, 2H), 8.50

(s, 2H), 8.35 (d, 2H, J = 7.8 Hz), 8.19 (t, H, J = 7.8 Hz), 7.53 (d, 2H, J = 8.2 Hz), 7.03 (d, 2H, J = 8.6 Hz), 2.98 (q, 13H, J = 7.3 Hz), 1.09 (t, 19H, J = 7.3 Hz). ^{19}F NMR (376 MHz, CD_3CN, δ from C_6H_5F): -60.99 (s). ^{13}C{H} NMR (100 MHz, $CDCl_3$, RT): 163.2 (s), 151.8 (s), 151.2 (s), 140.5 (s), 139.4 (s), 134.7 (s), 126.5 (q, J = 269.7 Hz), 125.9 (s), 121.4 (q, J = 31.6 Hz), 120.1 (q, J = 3.9 Hz), 115.8 (q, J = 4.3 Hz), 46.9 (s), 9.0 (s). LR-ESI-MS (*m/z*): $[N_3S_2RH_2]^-$ calcd for $C_{21}H_{12}F_6N_3O_2S_2$ (relative abundance), 516.0 (100.0), 517.0 (25.6), 518.0 (12.6), 519.0 (2.6); Found: 515.8 (100.0), 516.6 (23.7), 517.7 (13.6), 518.6 (2.3). Decomposes at 125 °C.

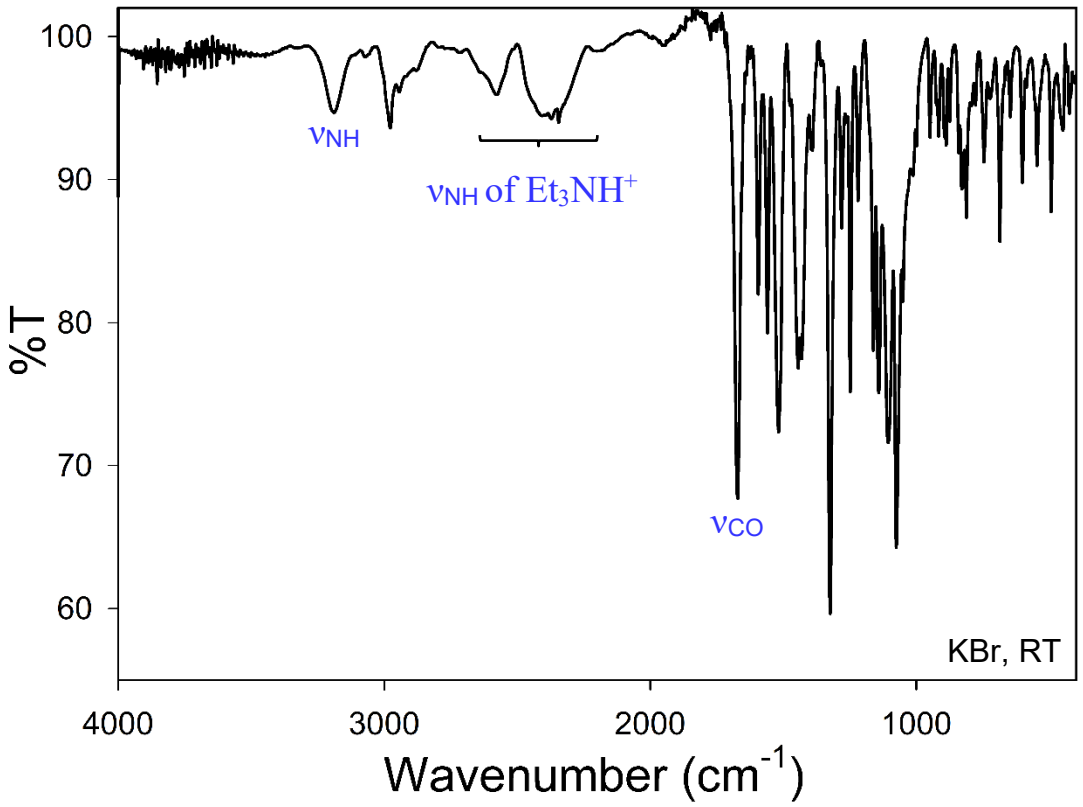

Figure S15. Solid-state FTIR spectrum of $(Et_3NH)_2(PyH_2PS\text{-}p\text{-}CF_3)$ in a KBr matrix at RT.

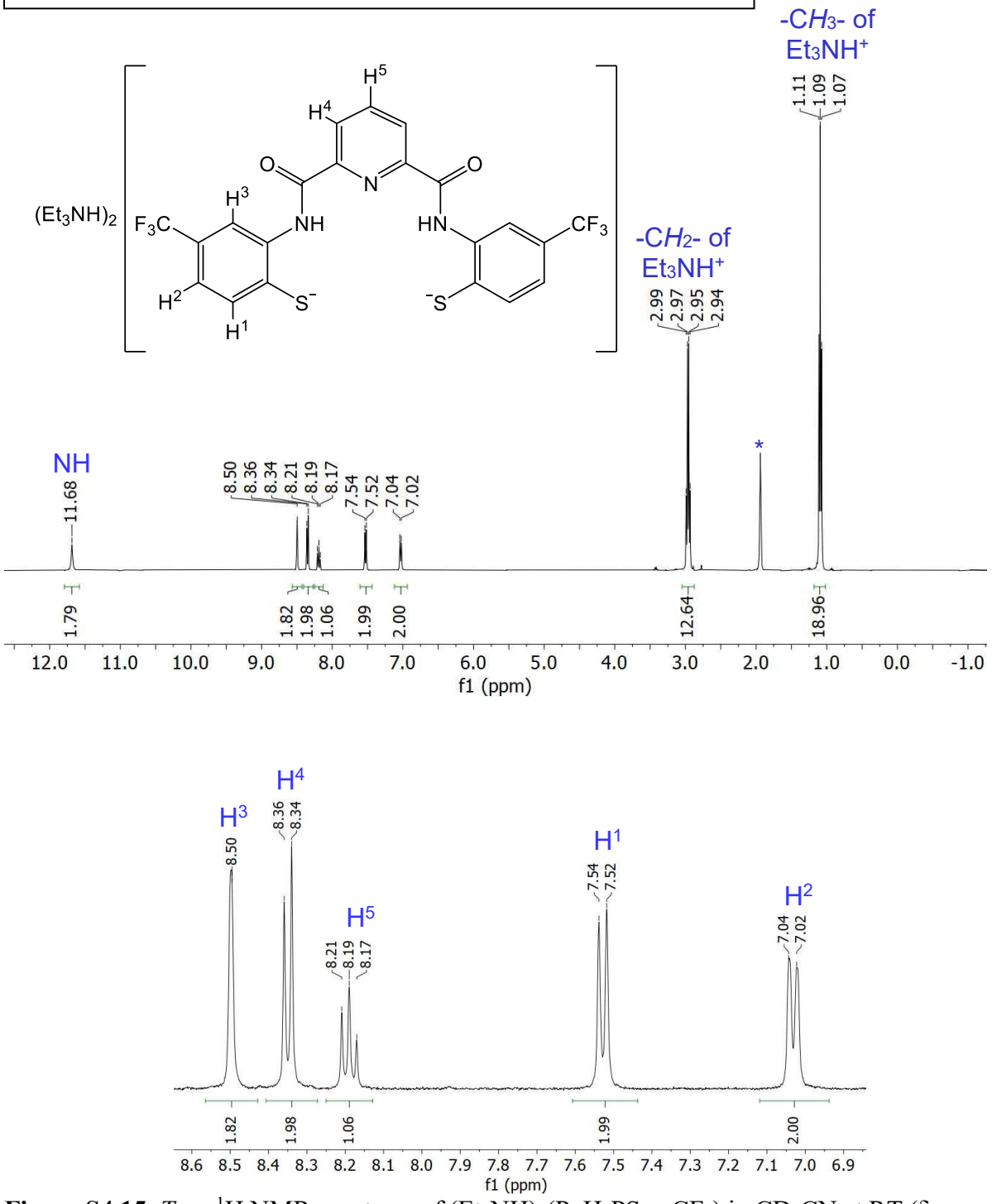

Figure S4.15. *Top:* ^{1}H NMR spectrum of $(Et_3NH)_2(PyH_2PS\text{-}p\text{-}CF_3)$ in CD_3CN at RT (δ vs. protio signal). *Bottom:* expansion of 7-9 ppm region. Residual CH_3CN is observed at 1.94 ppm and is indicated with *.

^{19}F NMR (376 MHz, CD_3CN, RT) of **$(Et_3NH)_2(PyH_2PS\text{-}p\text{-}CF_3)$**

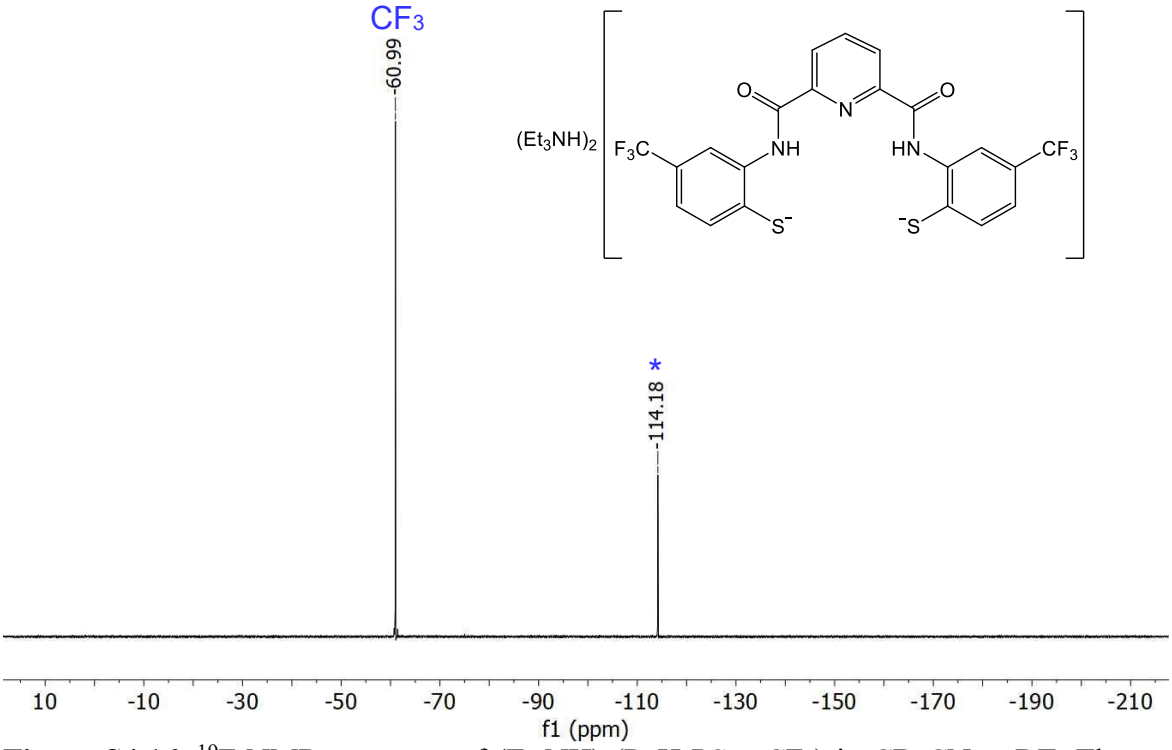

Figure S4.16. ^{19}F NMR spectrum of $(Et_3NH)_2(PyH_2PS\text{-}p\text{-}CF_3)$ in CD_3CN at RT. The peak at -114.18 ppm is from PhF as an internal standard and is indicated with *.

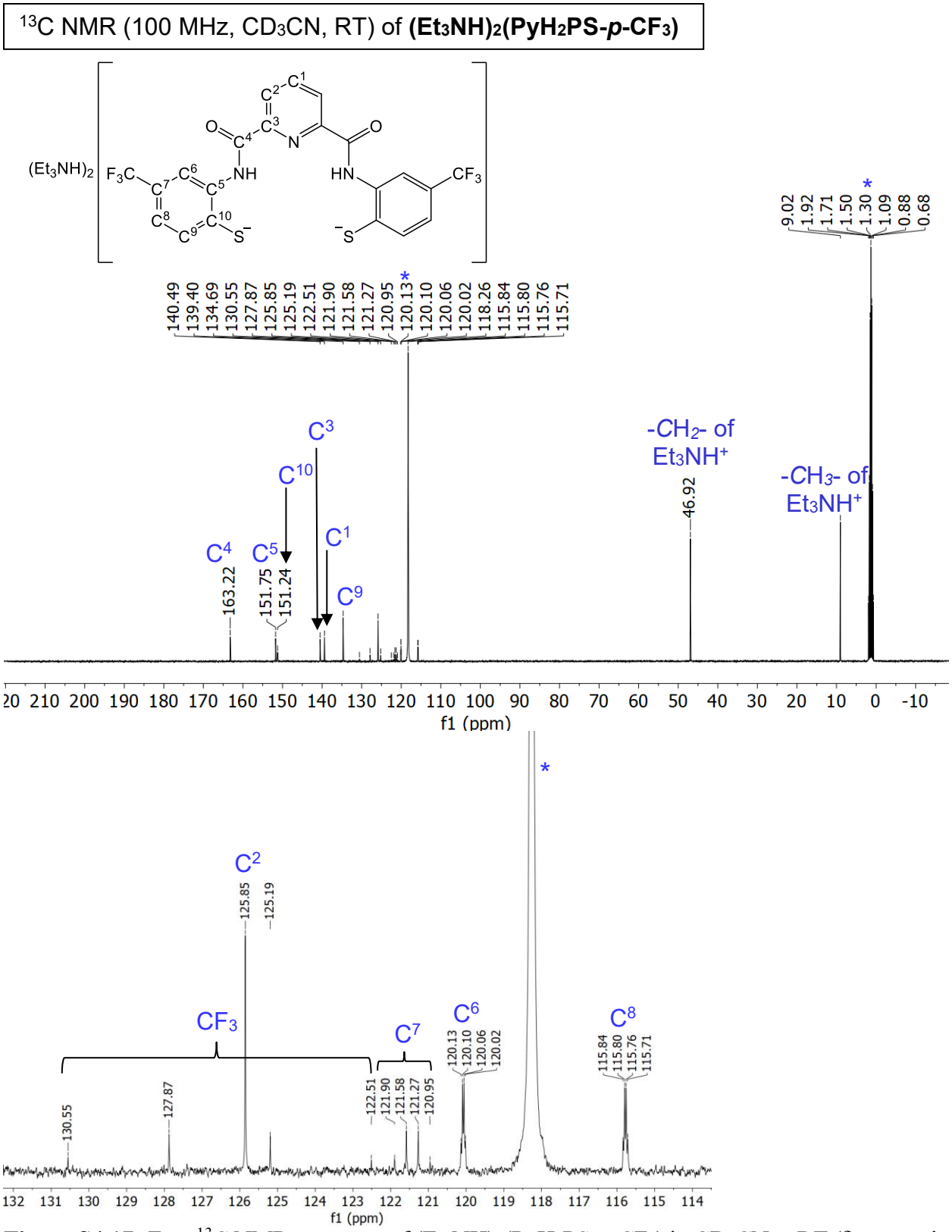

Figure S4.17. *Top:* ^{13}C NMR spectrum of $(Et_3NH)_2(PyH_2PS\text{-}p\text{-}CF_3)$ in CD_3CN at RT (δ vs. protio signal). *Bottom:* expansion of 6 – 8 ppm region. Residual $CHCl_3$ is observed at 118.26 and 1.30 ppm and is indicated with *.

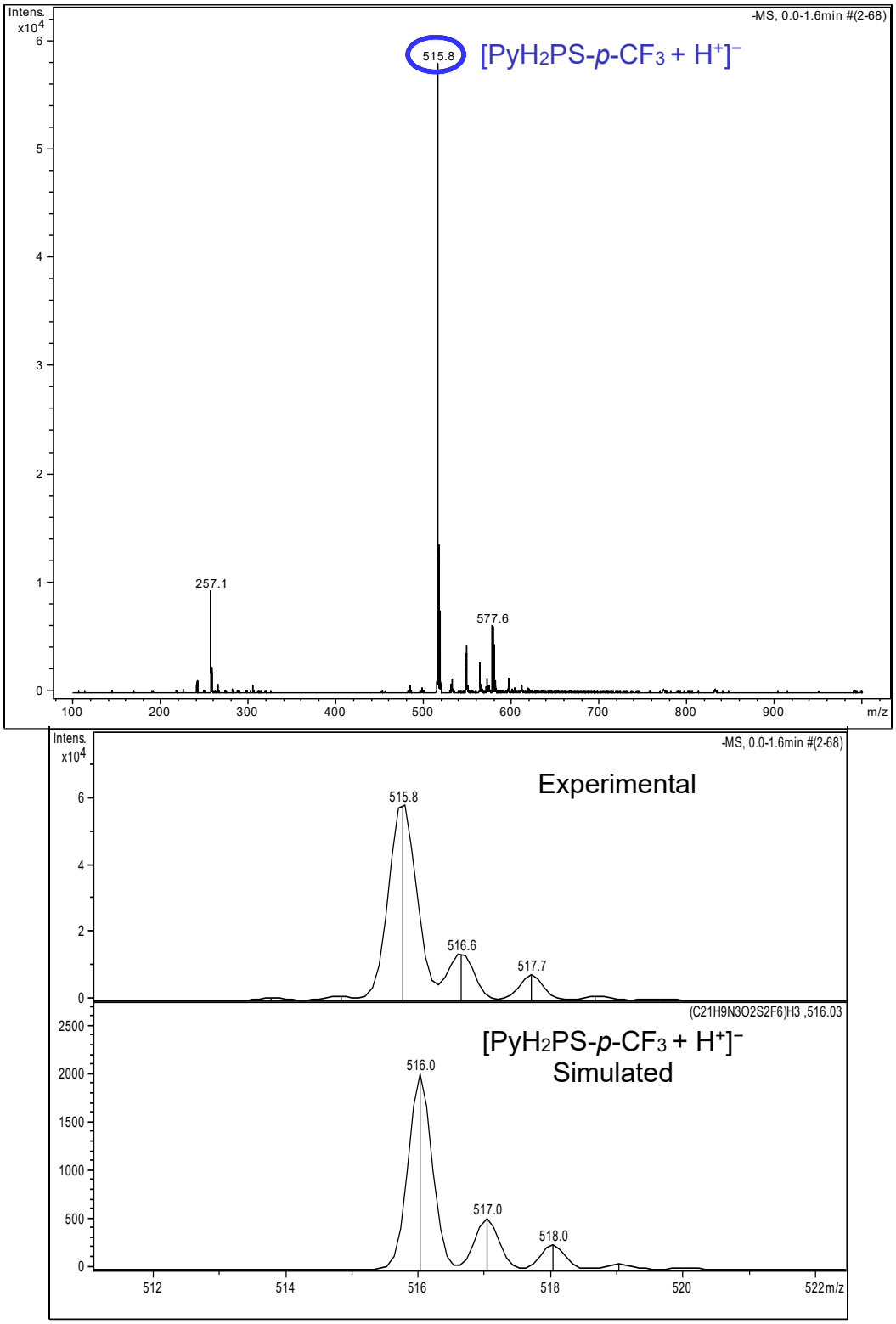

Figure S4.18. *Top:* Low-resolution ESI-MS(-) (negative mode) of $(Et_3NH)_2(PyH_2PS\text{-}p\text{-}CF_3)$in MeCN. *Bottom*: experimental and simulated theoretical isotopic distribution peak at *m/z*: 515.8 Other peaks have not been identified as reaction products.

(Et_4N)[Fe(PyPS-*p*-CF_3)] (1) Cold MeCN (~ 0 °C, 2 mL) was added to a batch of $PyPSH_4$-*p*-CF_3 (0.173 g, 0.335 mmol) resulting in a heterogenous mixture. To this NaH (0.034 g, 1.4 mmol) was added and the solution immediately took on a yellow color with gas evolving. The solution was stirred for 15 min resulting in a yellow-orange homogenous mixture, while pulling vacuum occasionally. The solution was frozen and $Et_4N[FeCl_4]$ (0.109 g, 0.332 mmol) was added dropwise in ~2 mL of MeCN. The solution was allowed to warm up to RT and stirred for 1 h taking on a black-dark blue color. After stirring for 1 h, the solution was concentrated to half of its initial volume, placed in a freezer (-20 ˚C) for 15 min, and filtered over a Celite packed frit. The resulting black-dark blue filtrate was taken down to dryness and ~2 ml of Et_2O was added. The precipitate was isolated by vacuum filtration on a glass-frit, washed with Et_2O (3 x 5 mL), and dried on a high vacuum line to afford the desired product as a black-blue solid (0.160 g, 0.229 mmol, 68.4%). FTIR (KBr matrix), ν_{max} (cm^{-1}): 1629 (m, CO), 1327 (s, CF), 1114 (s, CF), 1074 (s, CF). UV-vis (MeCN, 25 °C), λ_{max}, nm (ε, M^{-1} cm^{-1}): 617 (3400), 529 (3700), 407 (5000). UV-vis (DMF, 25 °C), λ_{max}, nm (ε, M^{-1} cm^{-1}): 617 (2600), 529 (2800), 407 (4400). LR-ESI-MS (*m/z*): $[M\text{-}N_3S_2R]^-$ calcd for $C_{21}H_9F_6N_3O_2S_2Fe$ (relative abundance), 566.9 (6.3), 567.9 (1.6), 568.9 (100.0), 569.9 (27.9), 570.9 (13.4), 571.4 (2.9); Found: 567.0 (5.1), 568.1 (1.3), 569.0 (100.0), 569.9 (24.2), 570.9 (11.3), 571.9 (3.1). μ_{eff} (solution, CD_3CN, 298 K): 5.80 μ_B.

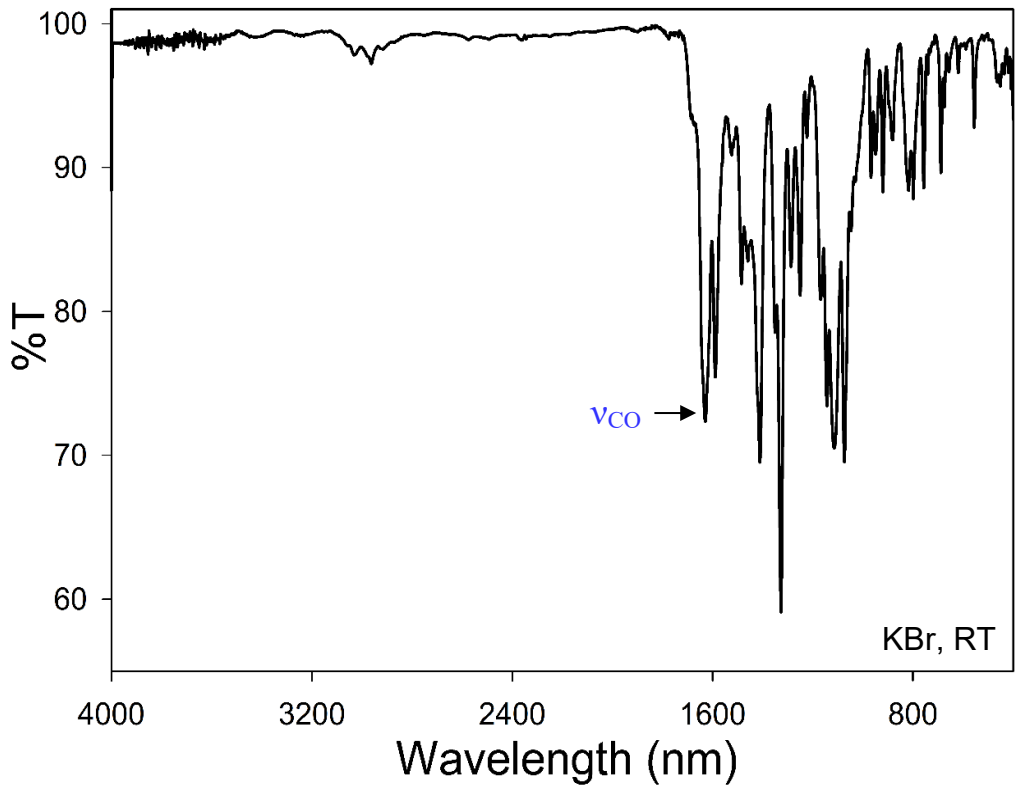

Figure S19. Solid-state FTIR spectrum of $(Et_4N)[Fe(PyPS\text{-}p\text{-}CF_3)]$ (**1**) in a KBr matrix at RT

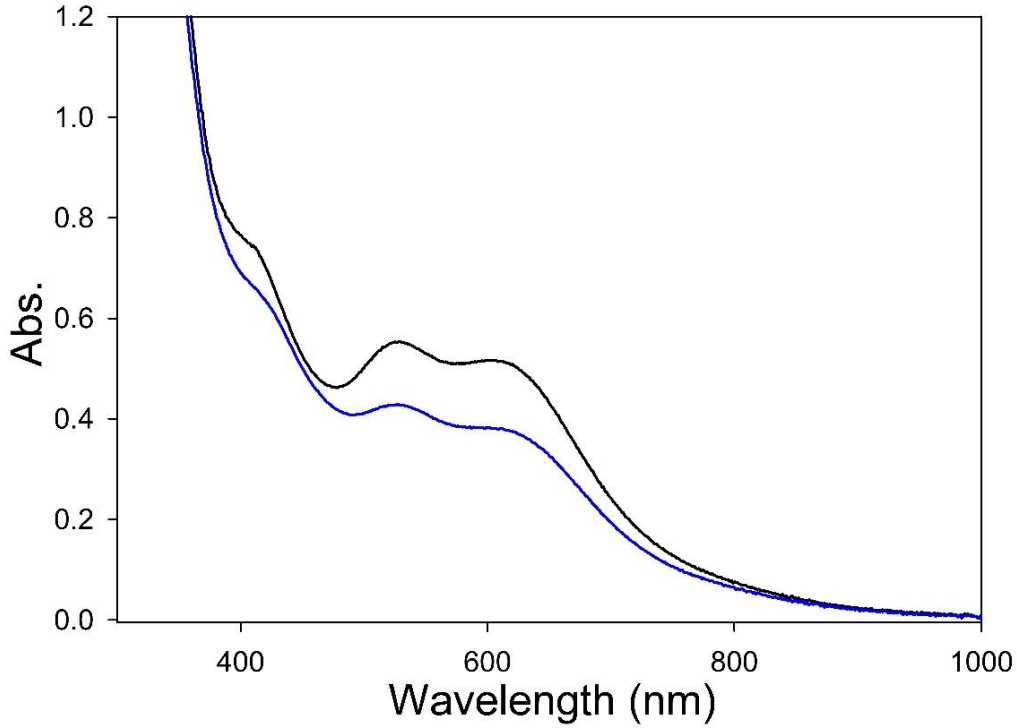

Figure S4.20. UV-vis spectrum of $(Et_4N)[Fe(PyPS\text{-}p\text{-}CF_3)]$ (**1**) in MeCN (black) and DMF (blue) at 25 ˚C.

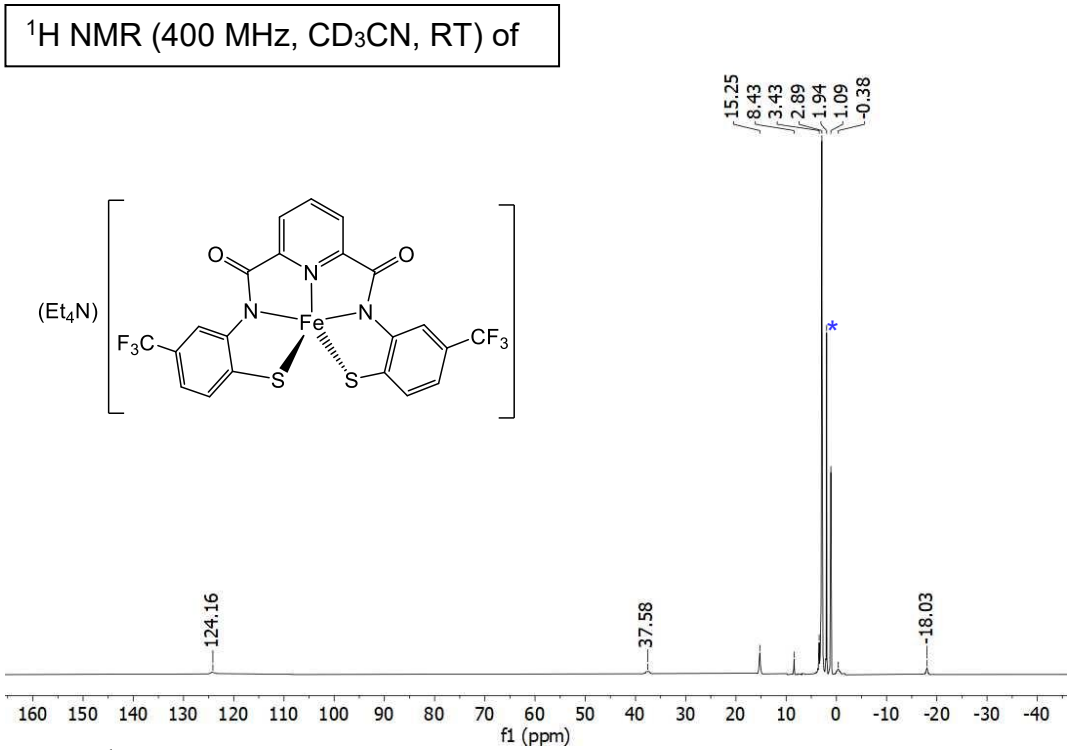

Figure S4.21. ^{1}H NMR spectrum of (Et$_4$N)[Fe(PyPS-*p*-CF$_3$)] (**1**) in CD$_3$CN at RT (δ vs. protio signal). Residual CH$_3$CN is observed at 1.94 ppm and is indicated with *.

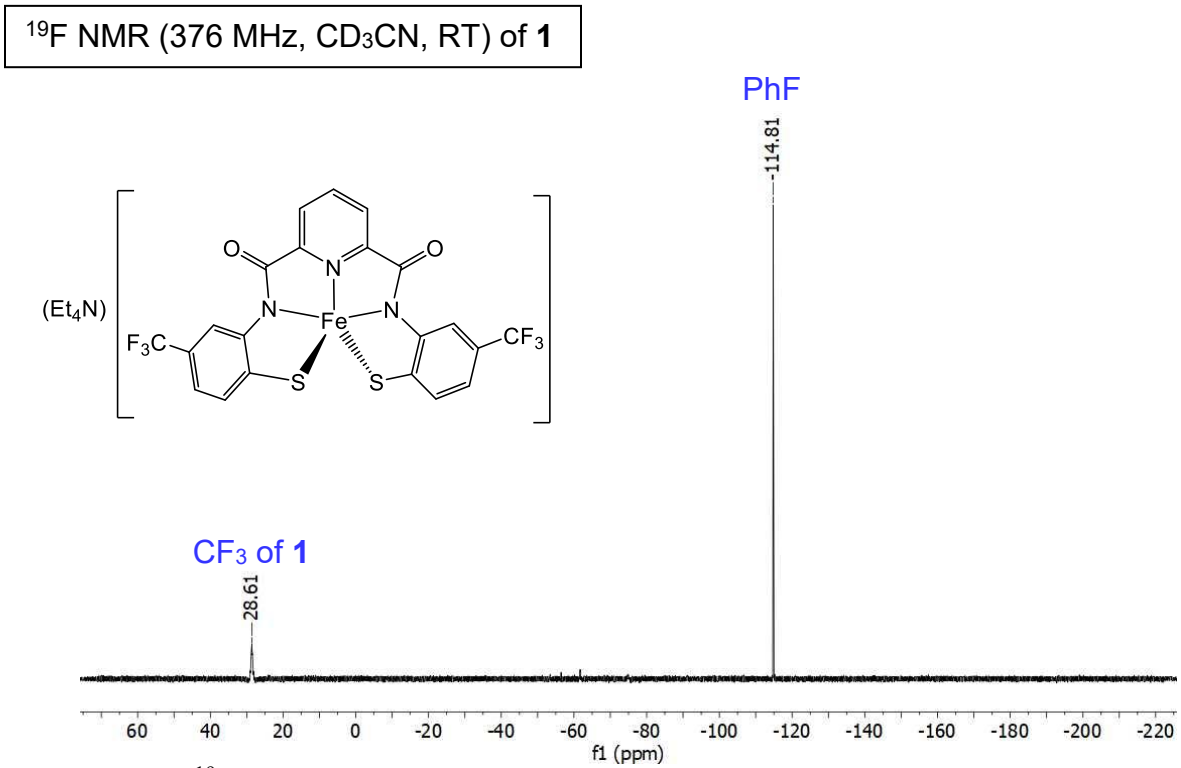

Figure S4.22. ^{19}F NMR spectrum of (Et$_4$N)[Fe(PyPS-*p*-CF$_3$)] (**1**) in CD$_3$CN at RT. The peak at -114.81 ppm is from PhF as an internal standard.

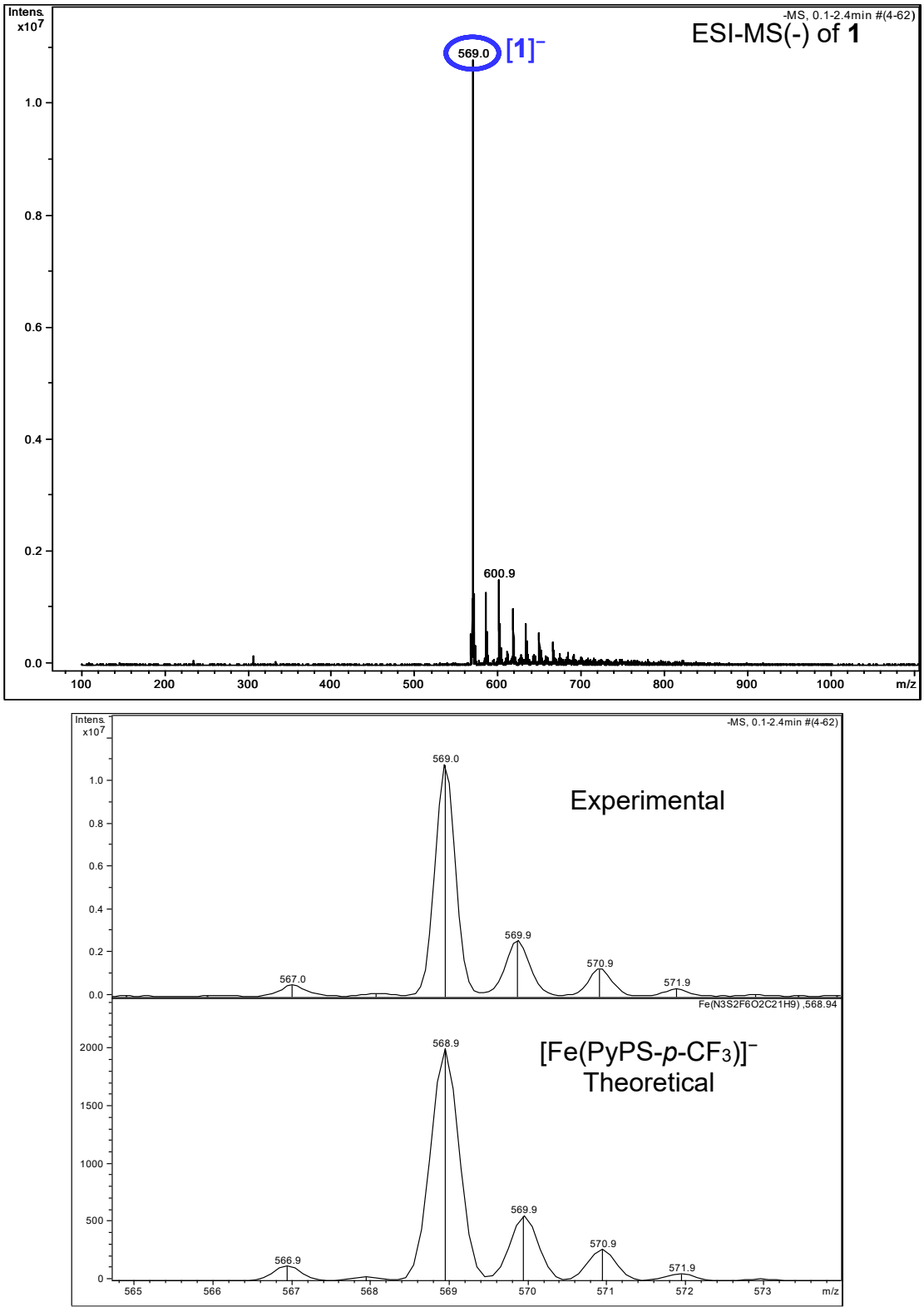

Figure S4.23. *Top*: Low-resolution ESI-MS(-) of (Et_4N)[Fe(PyPS-*p*-CF_3)] (**1**) in MeCN. *Bottom*: experimental and simulated theoretical isotopic distribution peak at *m/z*: 569.0

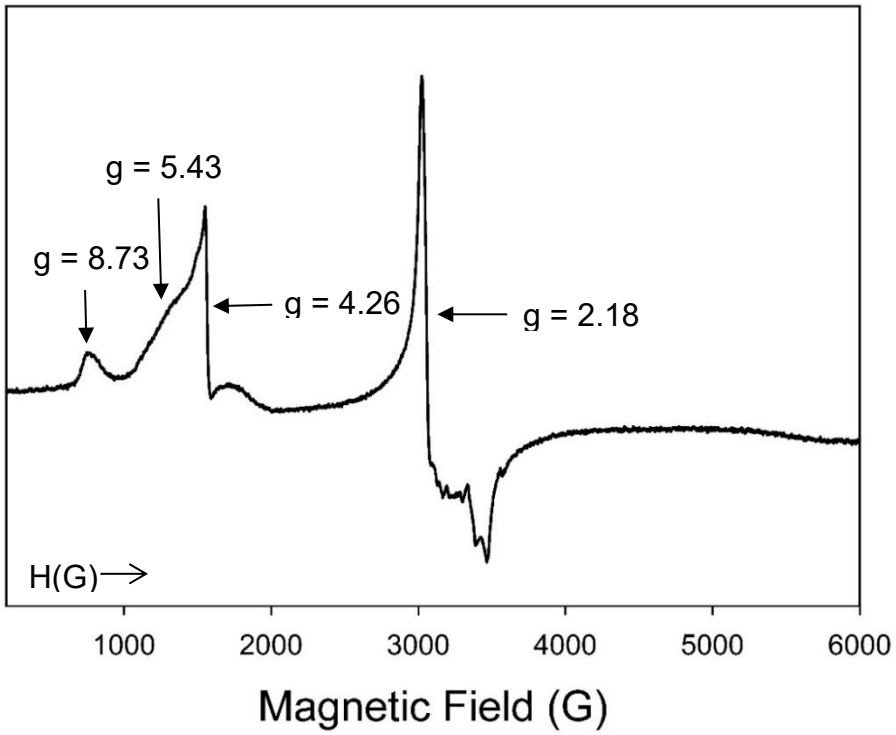

Figure S4.24. X-band (9.35 GHz) EPR spectrum of **1** in a MeCN/toluene (1:1 v/v) glass at 10 K. Spectrometer settings: microwave power, 2.0 mW; modulation frequency, 100 kHz; modulation amplitude, 4.00 G.

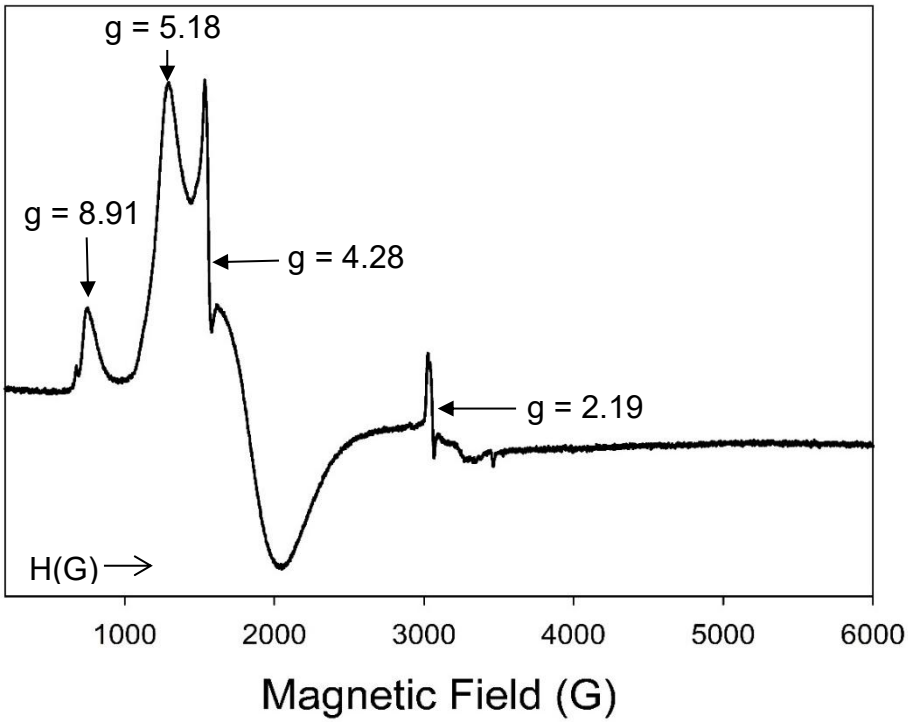

Figure S4.25. X-band (9.35 GHz) EPR spectrum of **1** in DMF at 10 K. Spectrometer settings: microwave power, 10.0 mW; modulation frequency, 100 kHz; modulation amplitude, 2.00 G.

$(Et_4N)_2$[Fe(PyPS-*p*-CF_3)] (2) Cold MeCN (~ 0 °C, ~2 mL) was added to a batch of $PyPSH_4$-*p*-CF_3 (0.160 g, 0.310 mmol) resulting in a heterogenous mixture. To this NaH (0.032 g, 1.3 mmol) was added and the solution immediately took on a yellow color with gas evolving. The solution was stirred for 15 min resulting in a yellow homogenous mixture. To this $FeCl_2$ (0.039 g, 0.31 mmol) was added dropwise in a solution of ~2 mL of MeCN immediately taking on a green color and darkened over time. After stirring for 1 h, Et_4NCl (0.103 g, 0.622 mmol) was added and a white solid immediately appeared in solution. After stirring for 30 min, the solution was concentrated to half of its initial volume and filtered over a Celite packed frit. The resulting dark-green filtrate was taken down to dryness and ~2 ml of Et_2O was added. The precipitate was isolated by vacuum filtration on a glass-frit, washed with Et_2O (3 x 5 mL), and dried on a high vacuum line to afford the desired product as a green solid (0.115 g, 0.139 mmol, 44.7%). FTIR (KBr matrix), ν_{max} (cm^{-1}): 1571 (s, CO), 1322 (s, CF), 1098 (m, CF), 1073 (s, CF). UV-vis (MeCN, 25 °C), λ_{max}, nm (ε, M^{-1} cm^{-1}) 620 (sh, 2400). μ_{eff} (solution, CD_3CN, 298 K): 4.29 μ_B.

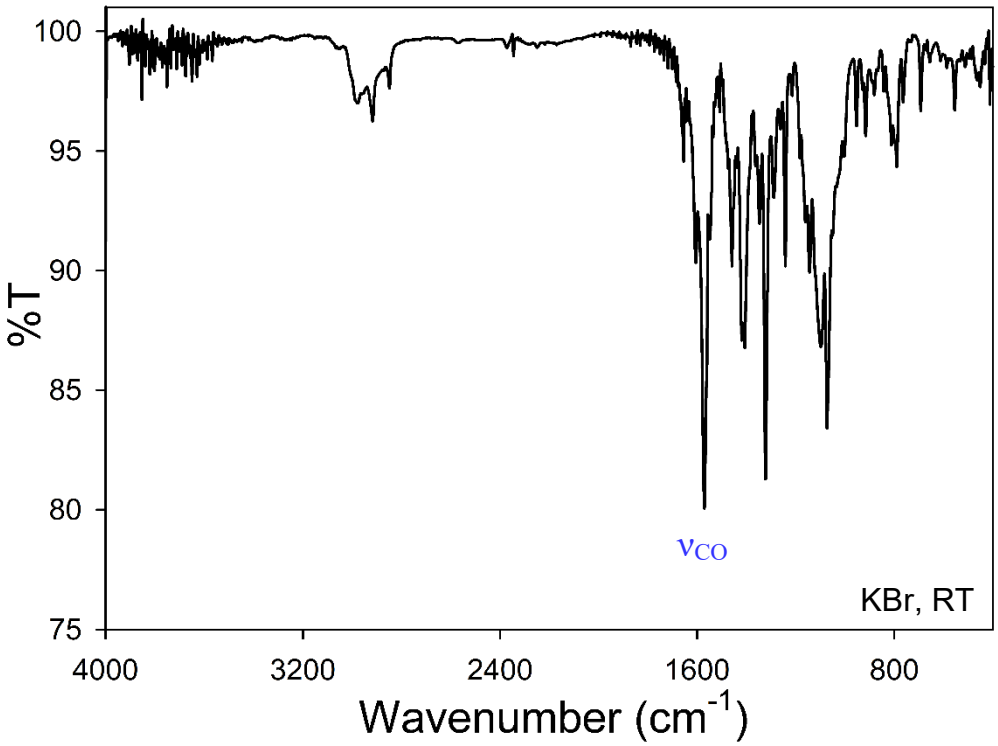

Figure S4.26. Solid-state FTIR spectrum of $(Et_4N)_2$[Fe(PyPS-*p*-CF_3)] (**2**) in a KBr matrix at RT.

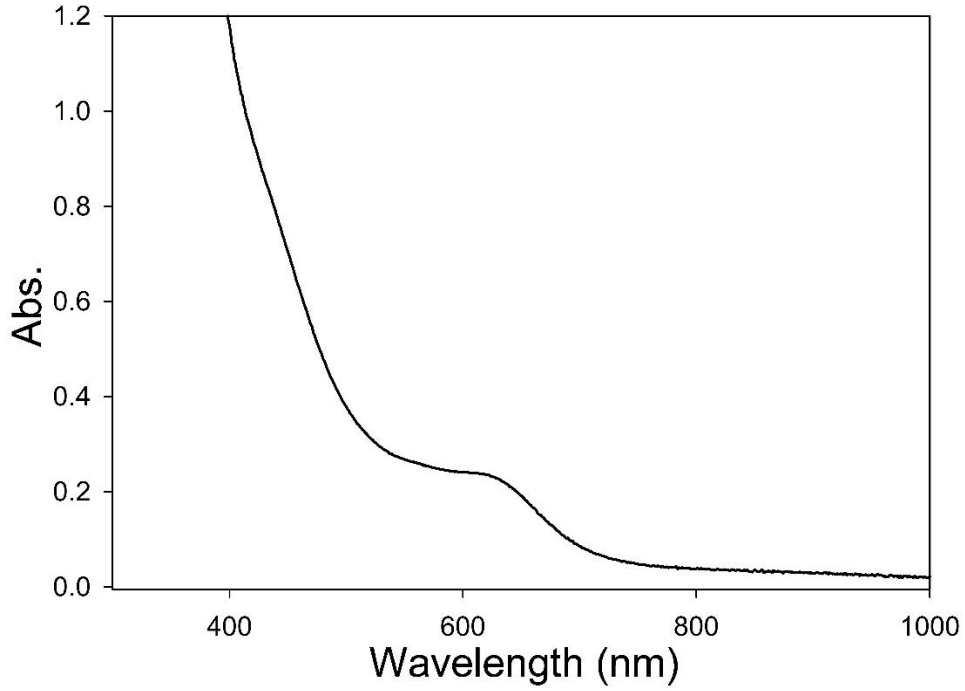

Figure S4.27. UV-vis spectrum of $(Et_4N)_2$[Fe(PyPS-*p*-CF_3)] (**2**) in MeCN at 25 ˚C.

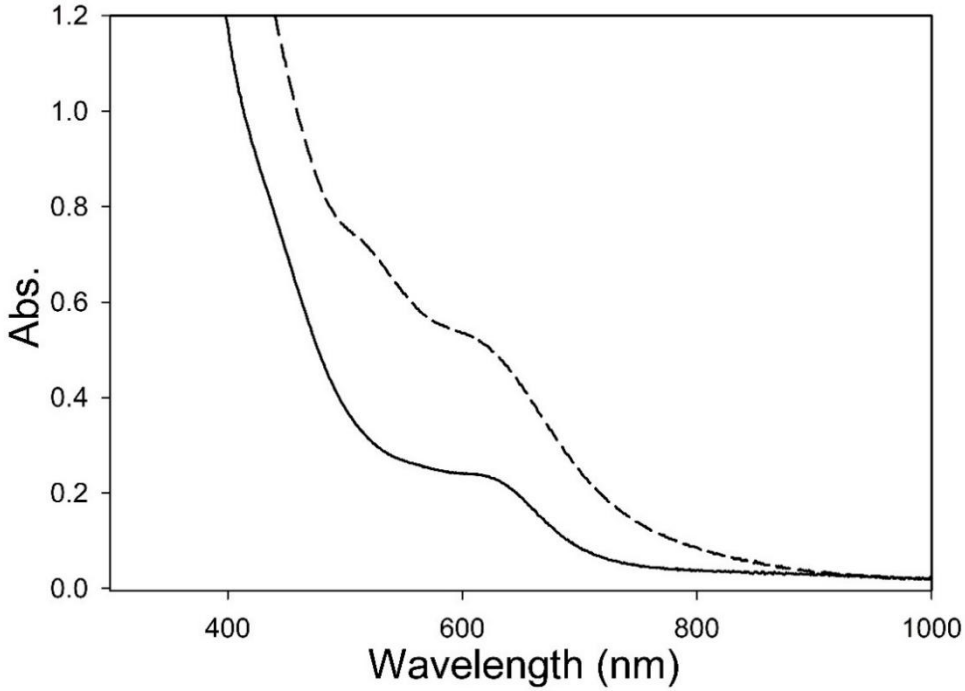

Figure S4.28. UV-vis spectrum of $(Et_4N)_2$[Fe(PyPS-*p*-CF_3)] (**2**) (solid line) and upon exposure to air (dashed line) in MeCN at 25 ˚C.

$(Et_4N)_2$[Zn(PyPS-*p*-CF_3)] (3) Cold MeCN (~ 0 °C, ~2 mL) was added to a batch of $PyPSH_4$-*p*-CF_3 (0.105 g, 0.203 mmol) resulting in a heterogenous mixture. To this NaH (0.021 g, 0.88 mmol) was added and the solution immediately took on a yellow color with gas evolving. The solution was stirred for 30 min resulting in a yellow homogenous mixture. To this $(Et_4N)_2[ZnCl_4]$ (0.094 g, 0.20 mmol) was added dropwise in a solution of ~2 mL of MeCN with a white solid appearing in solution. After stirring for 1 h, the solution was taken to dryness and 3 mL of THF was added taking on a yellow-orange color with a white solid in solution. After 30 min of stirring, the solution was filtered over a Celite packed frit. The resulting yellow-orange filtrate was taken down to dryness and ~2 ml of Et_2O was added. The precipitate was isolated by vacuum filtration on a glass-frit, washed with Et_2O (3 x 5 mL), and dried on a high vacuum line to afford the desired product as a yellow-orange solid (0.144 g, 0.171 mmol, 85.4%). FTIR (KBr matrix), ν_{max} (cm^{-1}): 1570 (s, CO), 1322 (s, CF), 1096 (m, CF), 1073 (s, CF). ^{1}H NMR (400 MHz, CD_3CN, δ from

residual deuterated solvent): 8.10 (m, 3H) 7.95 (s, 2H), 7.41 (d, 2H, J = 8.0 Hz), 6.85 (d, 2H, J = 8.2 Hz), 3.06 (q, 17H, J = 7.3 Hz), 1.10 (m, 25H). $^{13}C\{H\}$ NMR (100 MHz, $CDCl_3$, RT): 163.6 (s), 153.2 (s), 152.1(s), 148.5 (s), 141.9 (s), 132.0 (s), 126.9 (q, J = 267.0 Hz), 122.0 (s), 121.5 (q, J = 31.0 Hz), 119.4 (q, J = 3.9 Hz), 117.4 (q, J = 4.2 Hz), 53.0 (t, J = 3.1 Hz), 7.6 (s). ^{19}F NMR (376 MHz, CD_3CN, δ from C_6H_5F): -61.09 (s). LR-ESI-MS (*m/z*): $[M-(N_3S_2R)_2]^-$ calcd for $C_{42}H_{22}F_{12}N_6O_4S_4Fe$ (relative abundance), 707.1 (100.0), 708.1 (34.9), 709.1 (72.7), 710.1 (32.3), 711.1 (51.2), 712.1 (17.1), 713.1 (8.0); Found: 706.9 (100), 707.8 (34.7), 708.9 (68.1), 709.9 (31.3), 710.8 (44.3), 711.8 (15.9), 712.8 (10.2), 713.8 (3.4).

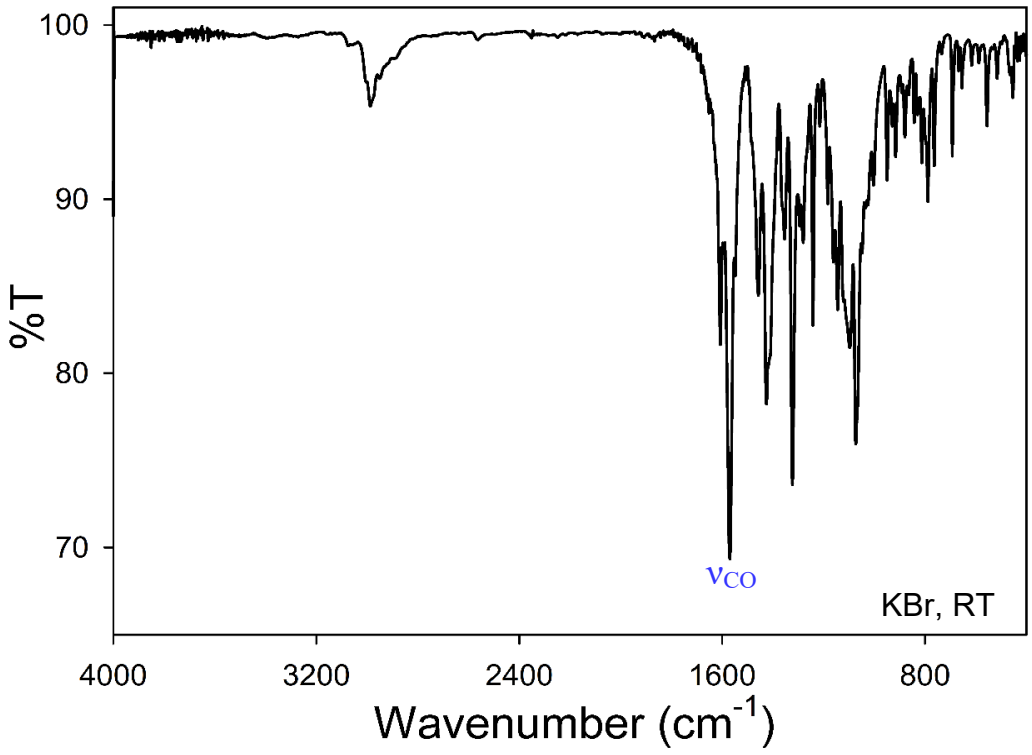

Figure S4.29. Solid-state FTIR spectrum of $(Et_4N)_2[Zn(PyPS\text{-}p\text{-}CF_3)]$ (**3**) in a KBr matrix at RT.

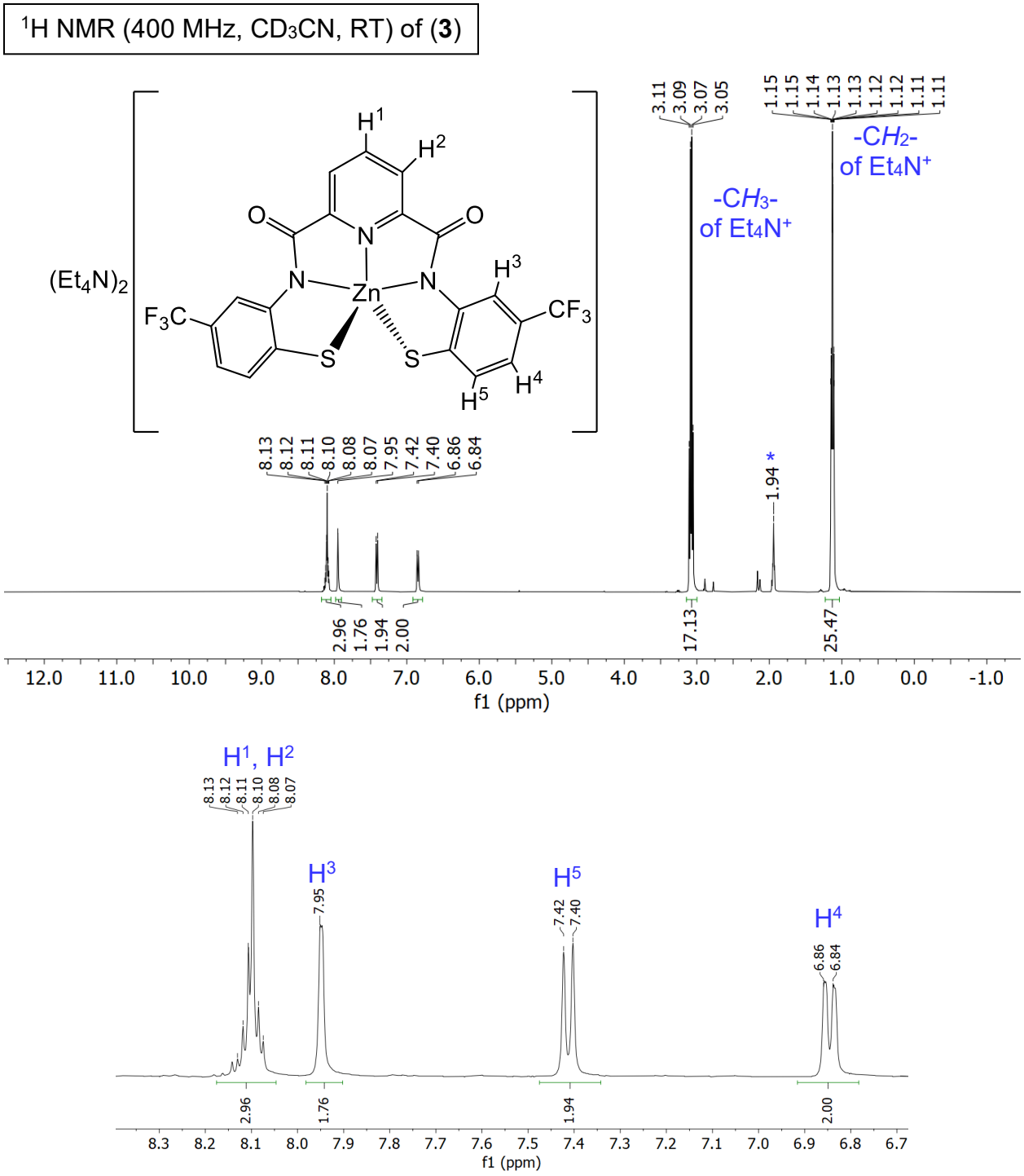

Figure S4.30. *Top:* $(Et_4N)_2$[Zn(PyPS-*p*-CF_3)] (**3**) in CD_3CN at RT (δ vs. protio signal). *Bottom:* expansion of 6 – 9 ppm region. Residual CH_3CN is observed at 1.94 ppm and is indicated with *.

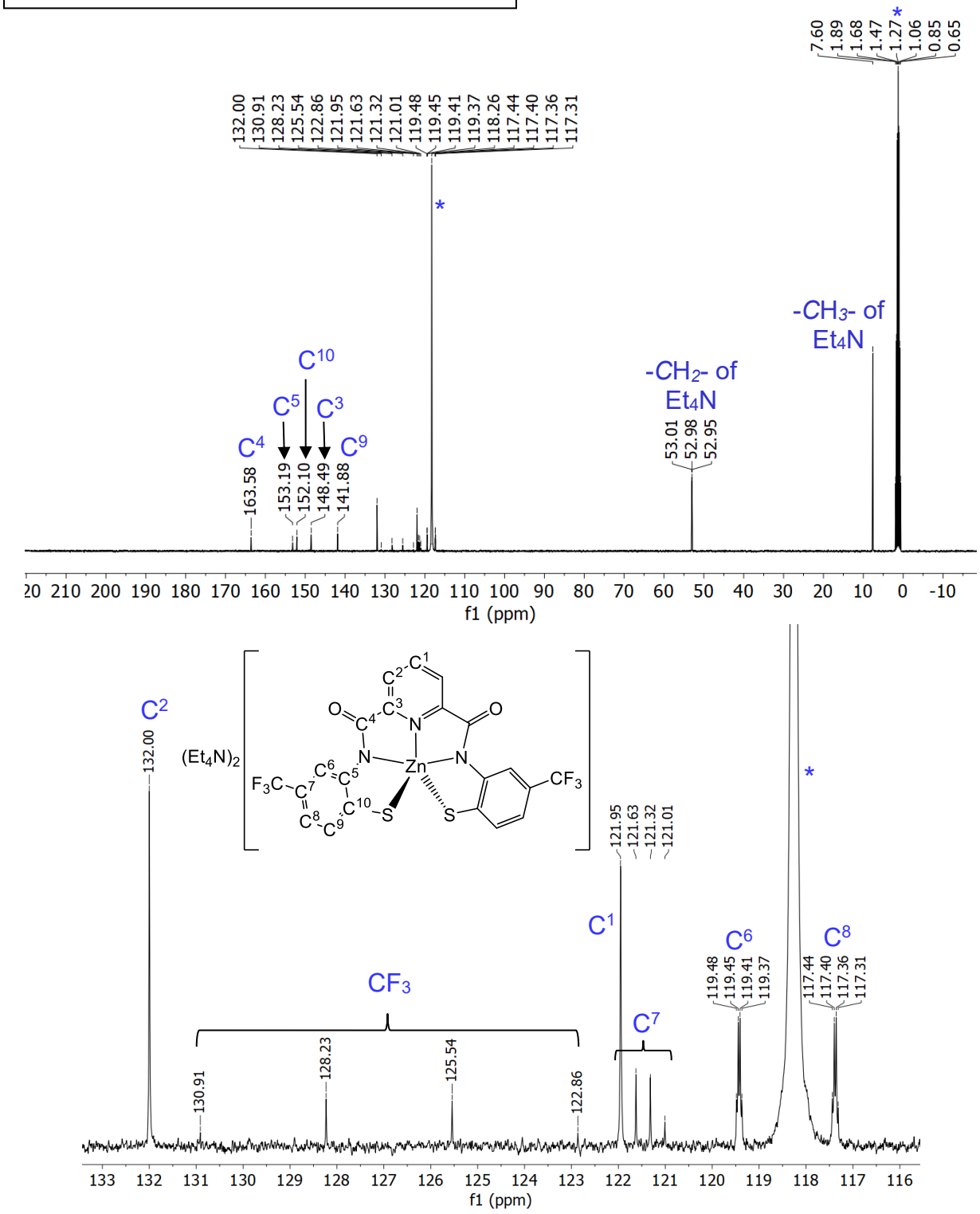

Figure SX. *Top:* ^{13}C NMR spectrum of $(Et_4N)_2$[Zn(PyPS-*p*-CF_3)] (**3**) in CD_3CN at RT (δ vs. protio signal). *Bottom:* expansion of 116 – 133 ppm region. Residual CH_3CN is observed at 118.26 and 1.27 ppm and is indicated with *

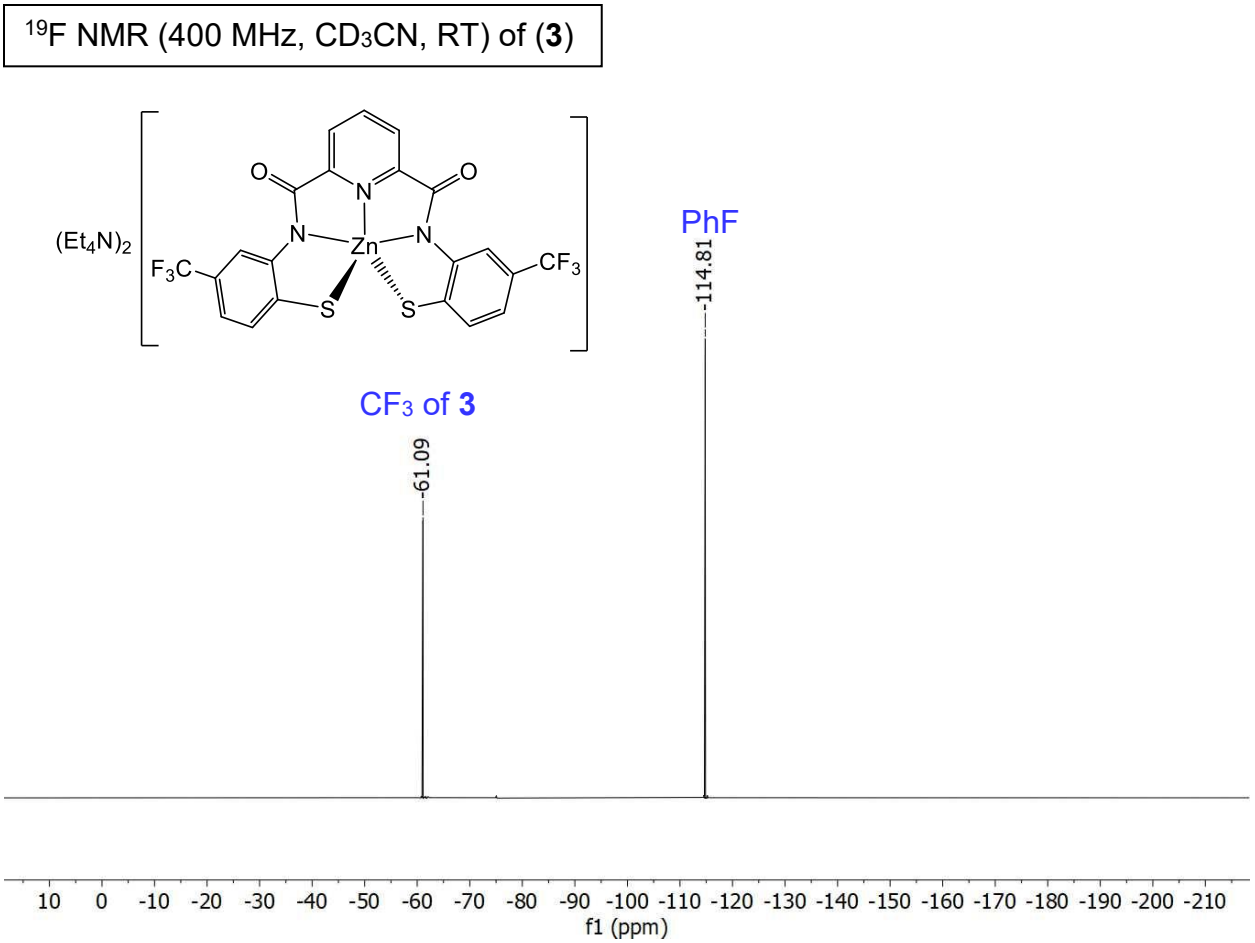

Figure S4.31. ^{19}F NMR spectrum of $(Et_4N)_2[Zn(PyPS\text{-}p\text{-}CF_3)]$ in (**3**) CD_3CN at RT. The peak at -114.81 ppm is from PhF as an internal standard.

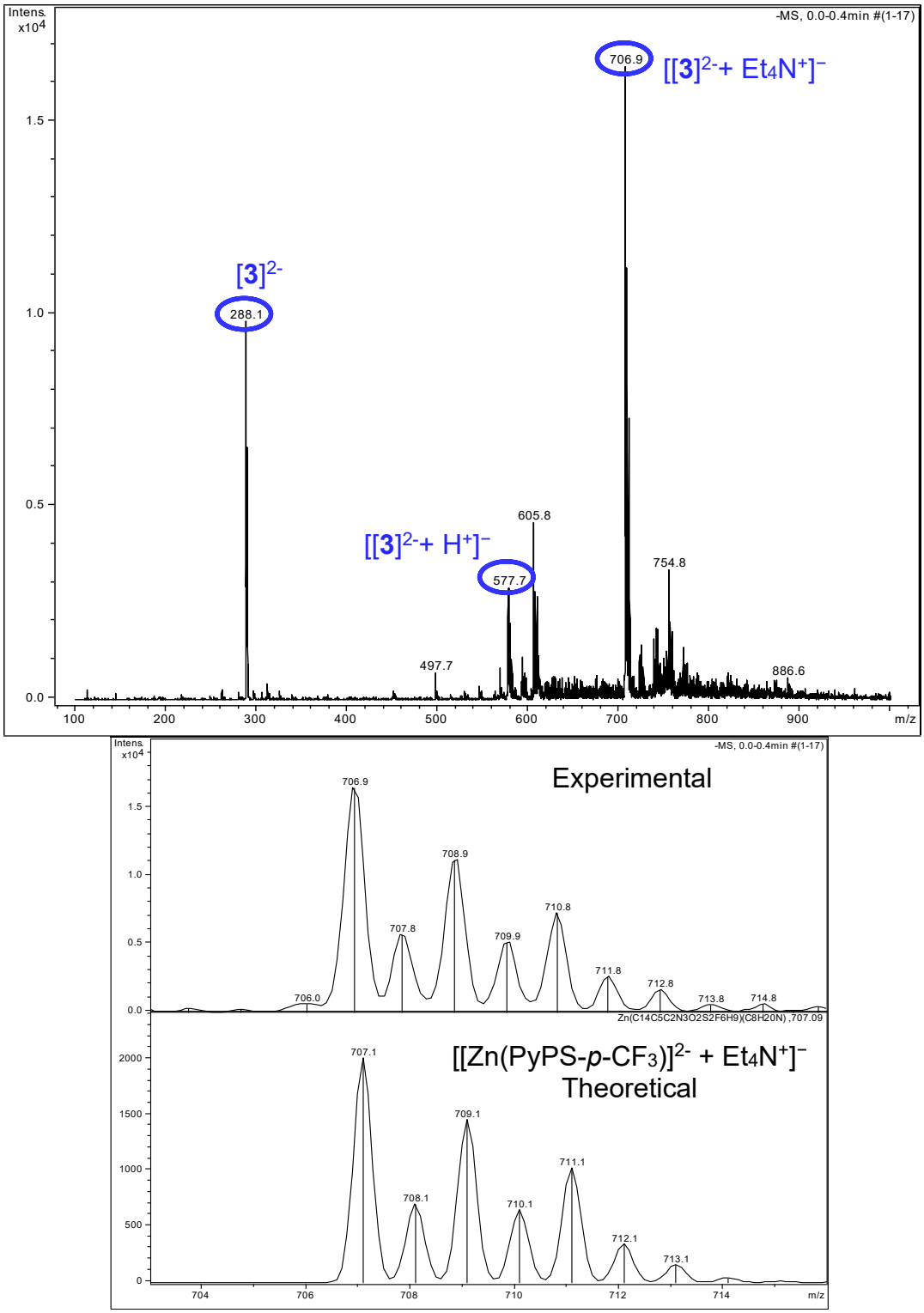

Figure S4.32. *Top*: Low-resolution ESI-MS(-) of $(Et_4N)_2[Zn(PyPS\text{-}p\text{-}CF_3)]$ (**3**) in MeCN. *Bottom*: experimental and simulated theoretical isotopic distribution peak at *m/z*: 706.9.

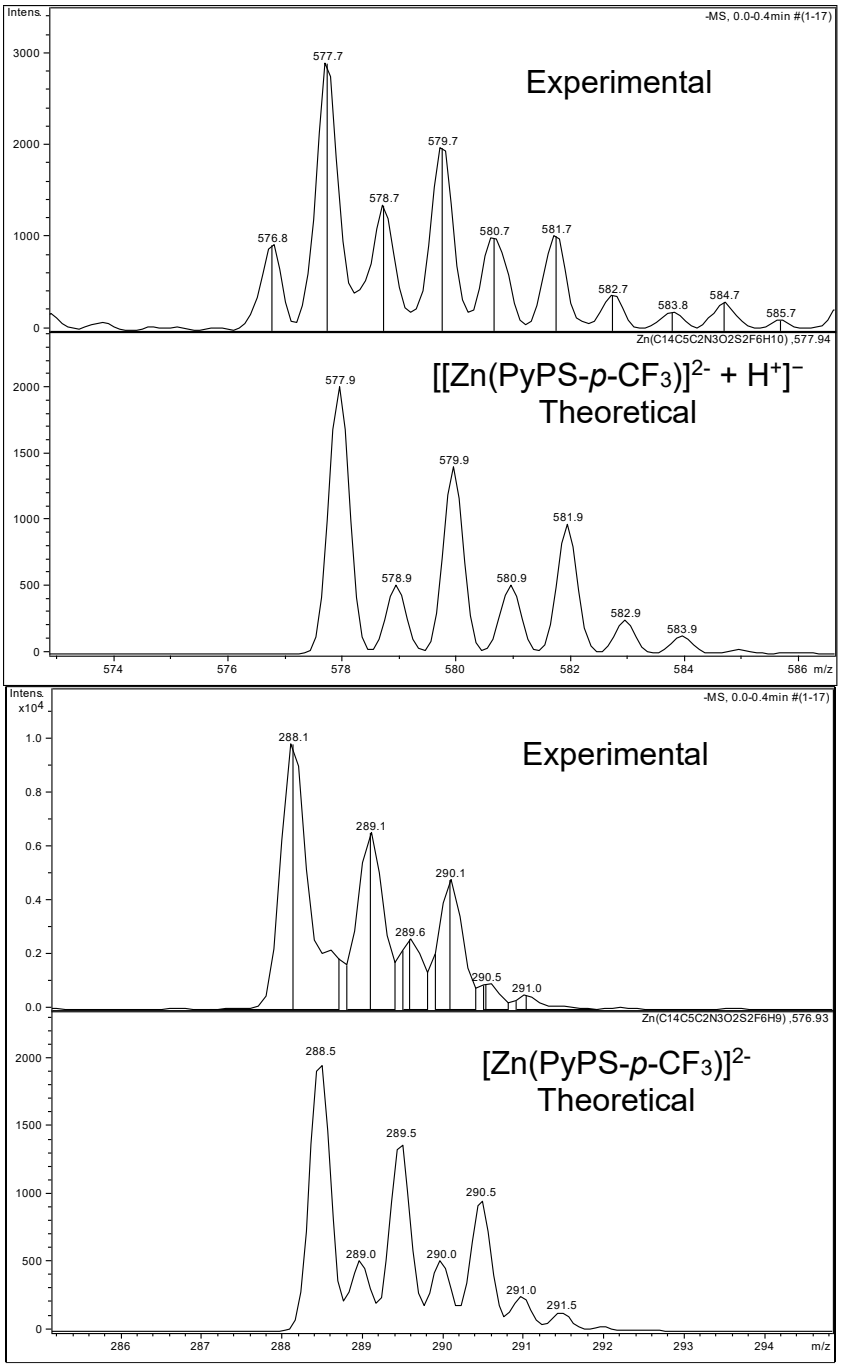

Figure S4.33. Experimental and simulated simulated theoretical isotopic distribution peak at *m/z*: (*top*) 706.9 and (*bottom*) 288.1 from low-resolution ESI-MS(-) of $(Et_4N)_2$[Zn(PyPS-*p*-CF_3)] (**3**) in MeCN, shown in Figure S4.32.

$(Et_3NH)_2[Fe(PyH_2PS\text{-}p\text{-}CF_3)_2]$ (4) A batch of $(Et_3NH)_2(PyH_2PS\text{-}p\text{-}CF_3)$ (0.122 g, 0.169 mmol) was dissolved in ~2 mL MeCN resulting in a yellow/orange solution. To this solution, $FeCl_2$ (0.009 g, 0.07 mmol) was added as a slurry in ~2 mL of MeCN and stirred for 1 h. Upon the addition of $FeCl_2$, the solution took an orange color, darkening over time, and turned an orange-red color after ~20 min with no change afterwards. Once MeCN was removed, 3 mL of THF was added resulting in a red-orange solution with a solid suspended in solution. The mixture was stirred for 20 min, placed in a freezer (~ −20 ˚C) for 10 min, and filtered over a Celite packed frit leaving behind an off-white solid. After the red-orange filtrate was taken to dryness, ~4 mL of Et_2O was added and allowed to stir for 30 min. The resulting precipitate was isolated by vacuum filtration on a glass-frit, washed with Et_2O (3 x 3 mL), and dried on a high vacuum line to afford the desired product as a light-orange solid (0.090 g, 0.070 mmol, 94.4%). FTIR (KBr matrix), ν_{max} (cm^{-1}): 3266 (w, NH), 2655 (w, NH), 2493 (w, NH), 1683 (m, CO), 1328 (s, CF), 1107 (s, CF), 1078 (s, CF). ^1H NMR (400 MHz, CD_3CN, δ from residual deuterated solvent): 27.16 (s, 4H), 22.77 (s, 4H), 10.20 (s, 2H), 9.84 (s, 4H), 6.98 (s, br, 3H), 3.03 (s, 12H), 1.19 (s, 19H). ^{19}F NMR (376 MHz, CD_3CN, δ from C_6H_5F): -15.14 (s). LR-ESI-MS (*m/z*): $[M\text{-}(N_3S_2R)_2 + H^+]^-$ calcd for $C_{42}H_{22}F_{12}N_6O_4S_4Fe$ (relative abundance), 1084.0 (6.2), 1085.0 (3.2), 1086.0 (100.0), 1087.0 (53.2), 1088.0 (32.9), 1089.0 (12.4), 1090.0 (4.4); Found: 1084.0 (7.4), 1085.0 (5.3), 1085.9 (100.0), 1086.8 (54.7), 1087.9 (35.0), 1088.9 (14.8), 1089.9 (5.6). μ_{eff} (solution, CD_3CN, 298 K): 4.47 μ_B.

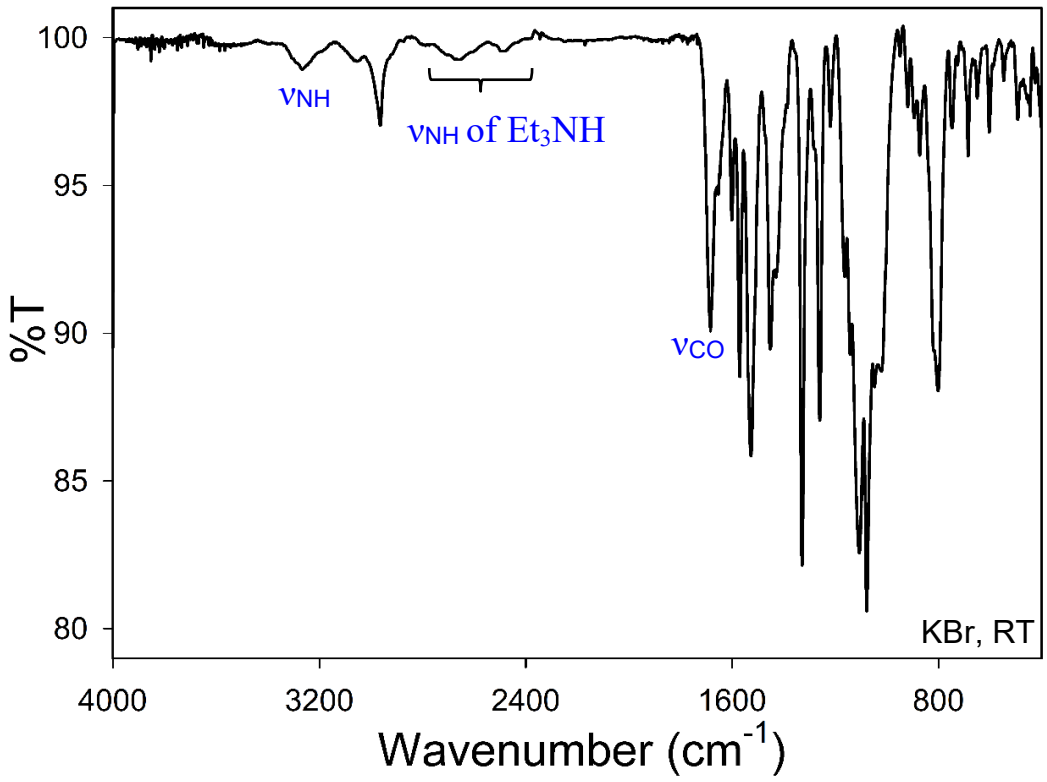

Figure S4.34. Solid-state FTIR spectrum of $(Et_3NH)_2[Fe(PyH_2PS\text{-}p\text{-}CF_3)_2]$ (**4**) in a KBr matrix at RT.

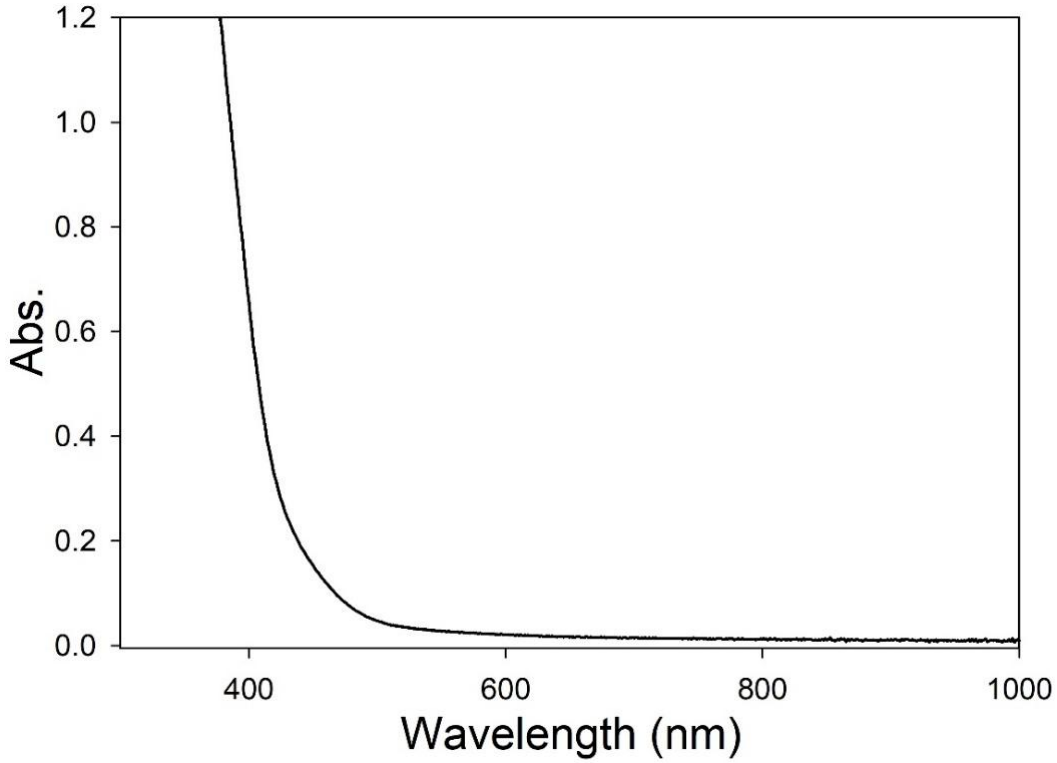

Figure S4.35. UV-vis spectrum $(Et_3NH)_2[Fe(PyH_2PS\text{-}p\text{-}CF_3)_2]$ (**4**) in MeCN at 25 ˚C.

^{1}H NMR (400 MHz, CD_3CN, RT) of

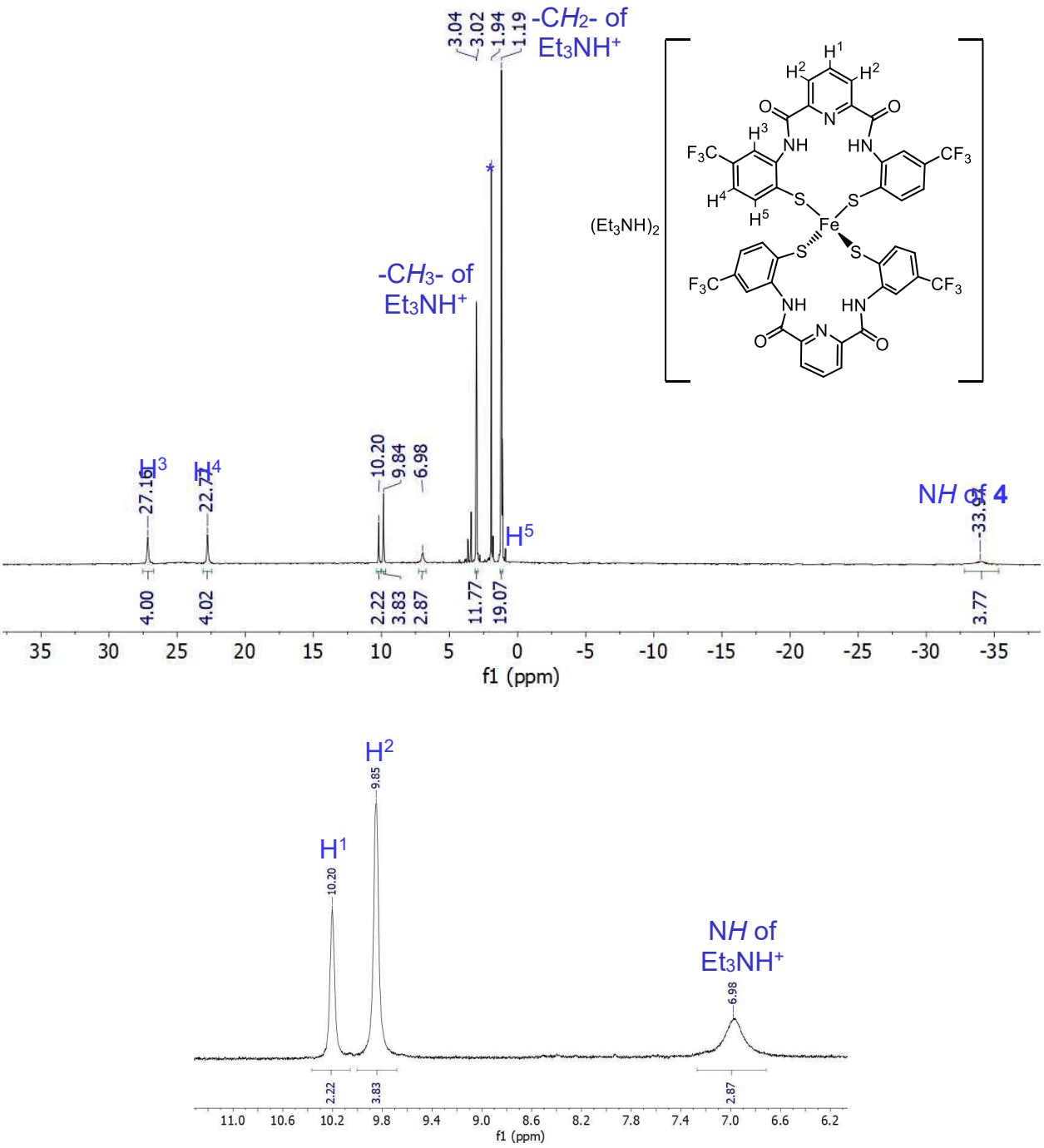

Figure S4.36. *Top:* ^{1}H NMR spectrum of $(Et_3NH)_2[Fe(PyH_2PS\text{-}p\text{-}CF_3)_2]$ (**4**) in CD_3CN at RT (δ vs. protio signal). *Bottom:* expansion of 6-12 ppm region. Residual CH_3CN is observed at 1.94 ppm and is indicated with *.

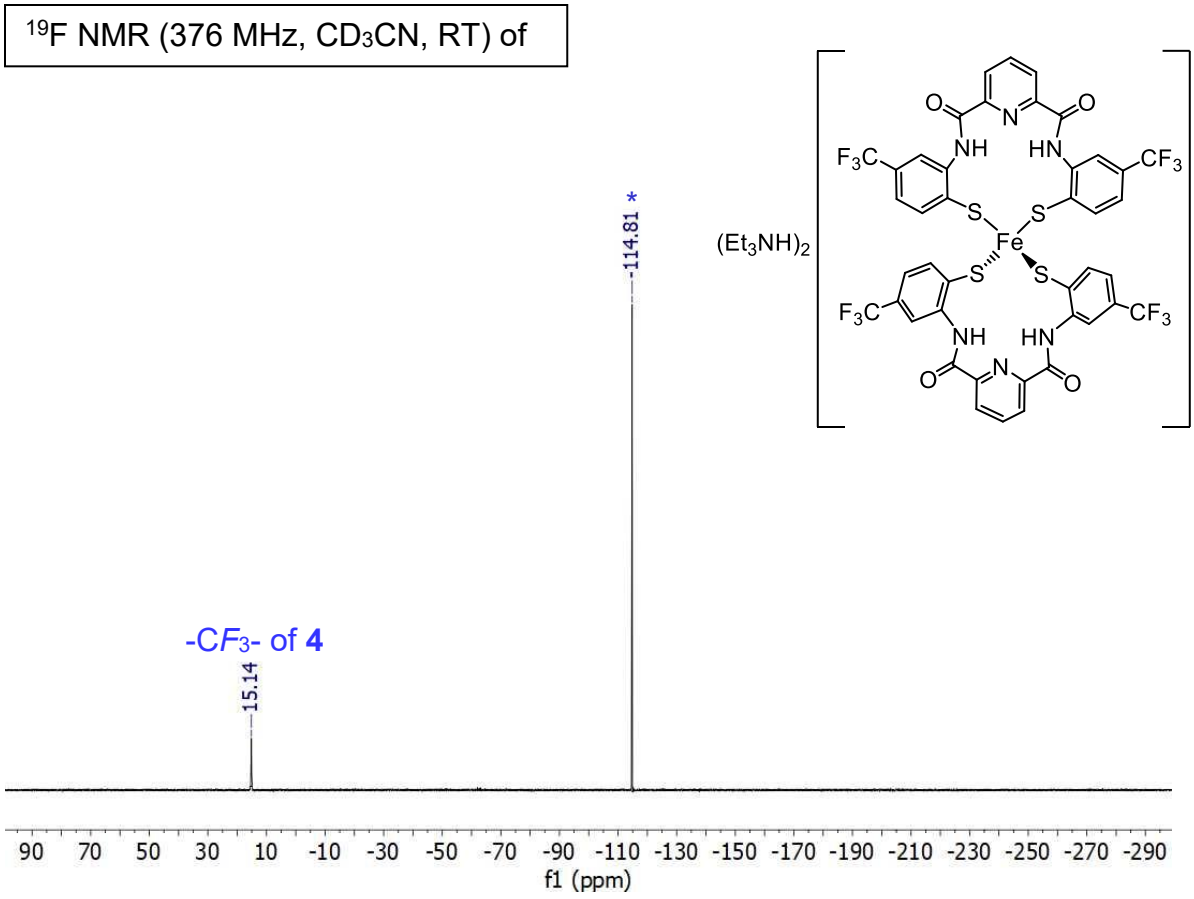

Figure S4.37. ^{19}F NMR spectrum of $(Et_3NH)_2[Fe(PyH_2PS\text{-}p\text{-}CF_3)_2]$ (**4**) in CD_3CN at RT. The peak at -114.81 ppm is from PhF as an internal standard.

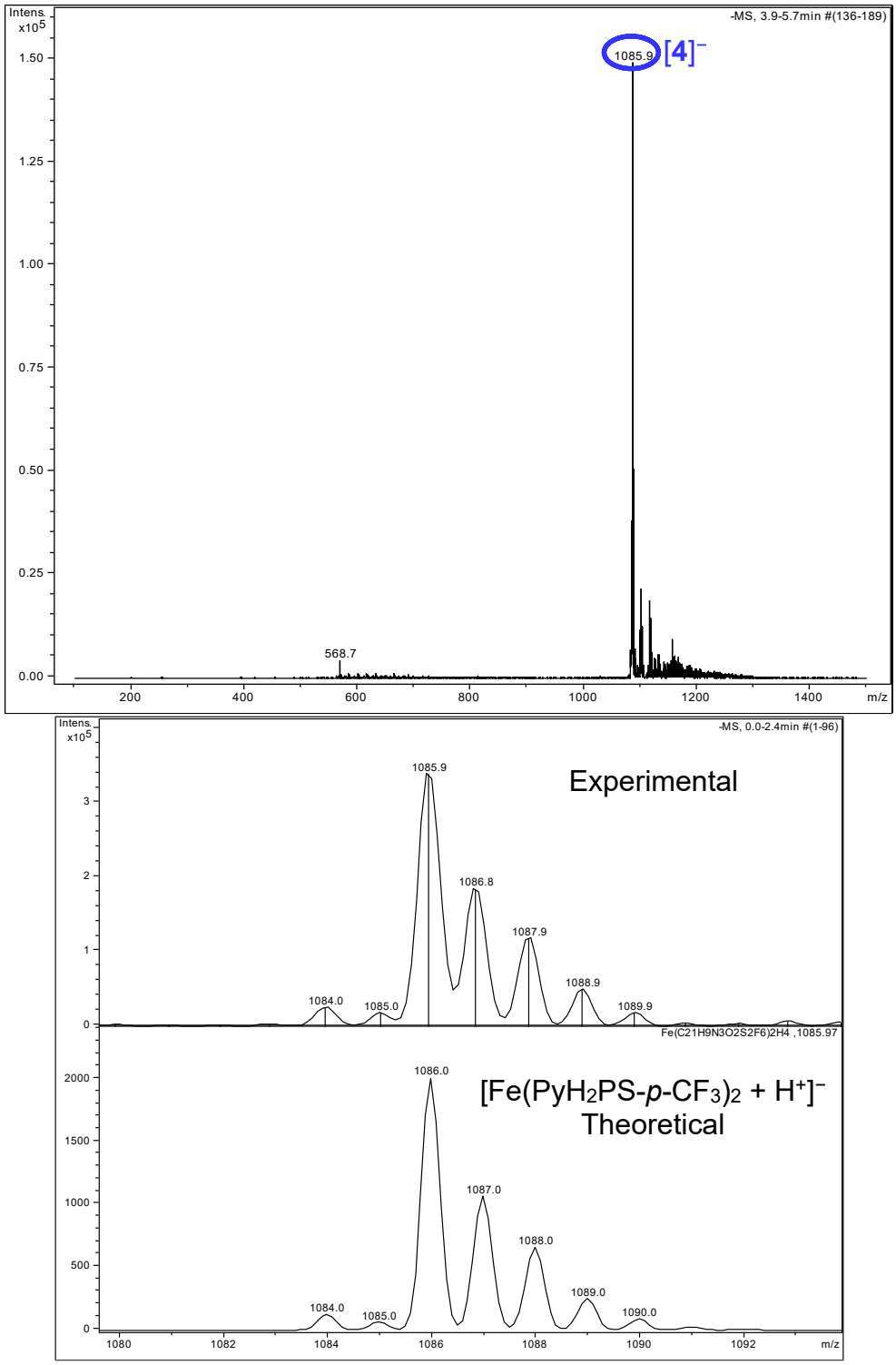

Figure S4.38. *Top*: Low-resolution ESI-MS(-) of $(Et_4N)[Fe(PyH_2PS\text{-}p\text{-}CF_3)]$ (**4**) in MeCN. *Bottom*: experimental and simulated theoretical isotopic distribution peak at *m/z*: 1085.9.

$(Et_3NH)_2[Zn(PyH_2PS\text{-}p\text{-}CF_3)_2]$ (5): A batch of $(Et_3NH)_2(PyH_2PS\text{-}p\text{-}CF_3)$ (0.101 g, 0.140 mmol) was dissolved in ~2 mL THF resulting in a yellow/orange solution. To this solution, $ZnCl_2$ (0.009 g, 0.07 mmol) was added as a slurry in ~2 mL of THF and stirred for 1 h. Upon addition of $ZnCl_2$, the solution took a yellow color, lightening over time, and turned a pale yellow after ~20 min with a solid suspended in solution. The solution was placed in a freezer (~ −20 ˚C) for 10 min and filtered over a Celite packed frit leaving behind an off-white solid. After the pale-yellow filtrate was taken to dryness, ~4 mL of Et_2O was added and allowed to stir for 30 min. The resulting precipitate was isolated by vacuum filtration on a glass-frit, washed with Et_2O (3 x 3 mL), and dried on a high vacuum line to afford the desired product as a pale yellow solid (0.077 g, 0.059 mmol, 84.3%). FTIR (KBr matrix), ν_{max} (cm^{-1}): 3286 (w, NH), 3195 (w, NH), 2603 (w, NH), 2485 (w, NH), 1683 (m, CO), 1328 (s, CF), 1112 (s, CF), 1078 (s, CF). ^1H NMR (400 MHz, CD_3CN, δ from residual deuterated solvent): 12.02 (s, 4H), 8.55 (s, 3H), 8.38 (d, 3H, J = 7.8 Hz), 8.25 (t, 2H, J = 7.7 Hz), 7.91 (br, 2H), 7.26 (d, 4H, J = 8.1 Hz), 6.94 (d, 4H, J = 8.3 Hz), 3.06 (q, 14H, J = 7.3 Hz), 1.21 (t, 19H, J = 7.3 Hz). $^{13}C\{H\}$ NMR (100 MHz, $CDCl_3$, RT): 162.4 (s), 150.5 (s), 143.2 (s), 141.0 (s), 140.8 (s), 137.9(s), 126.1 (q, J = 270.6 Hz), 125.5 (s), 124.9 (q, J = 31.7 Hz), 119.6 (q, J = 4.0 Hz), 115.1 (q, J = 4.1 Hz), 47.6 (s), 9.1 (s). ^{19}F NMR (376 MHz, CD_3CN, δ from C_6H_5F): -62.05 (s). LR-ESI-MS (*m/z*): $[M\text{-}(N_3S_2R)_2 + H^+]^-$ calcd for $C_{42}H_{22}F_{12}N_6O_4S_4Zn$ (relative abundance), 1095.0 (100.0), 1096.0 (51.3), 1097.0 (89.3), 1098.0 (49.5), 1099.0 (65.2), 1100.0 (30.3), 1101.0 (17.1); Found: 1094.9 (100.0), 1095.9 (51.0), 1096.7 (50.6), 1098.6 (59.4), 1099.6 (27.6), 1100.6 (16.4), 1101.6 (5.4).

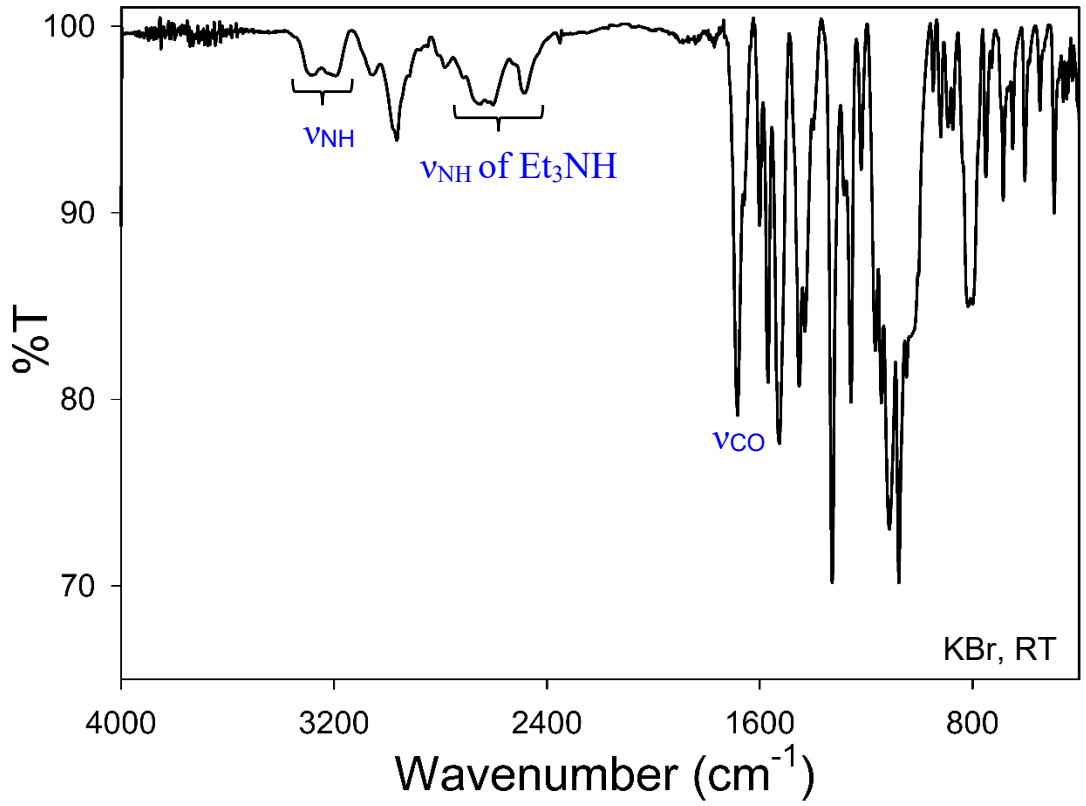

Figure S4.39. Solid-state FTIR spectrum of $(Et_3NH)_2[Zn(PyH_2PS\text{-}p\text{-}CF_3)_2]$ (**5**) in a KBr matrix at RT.

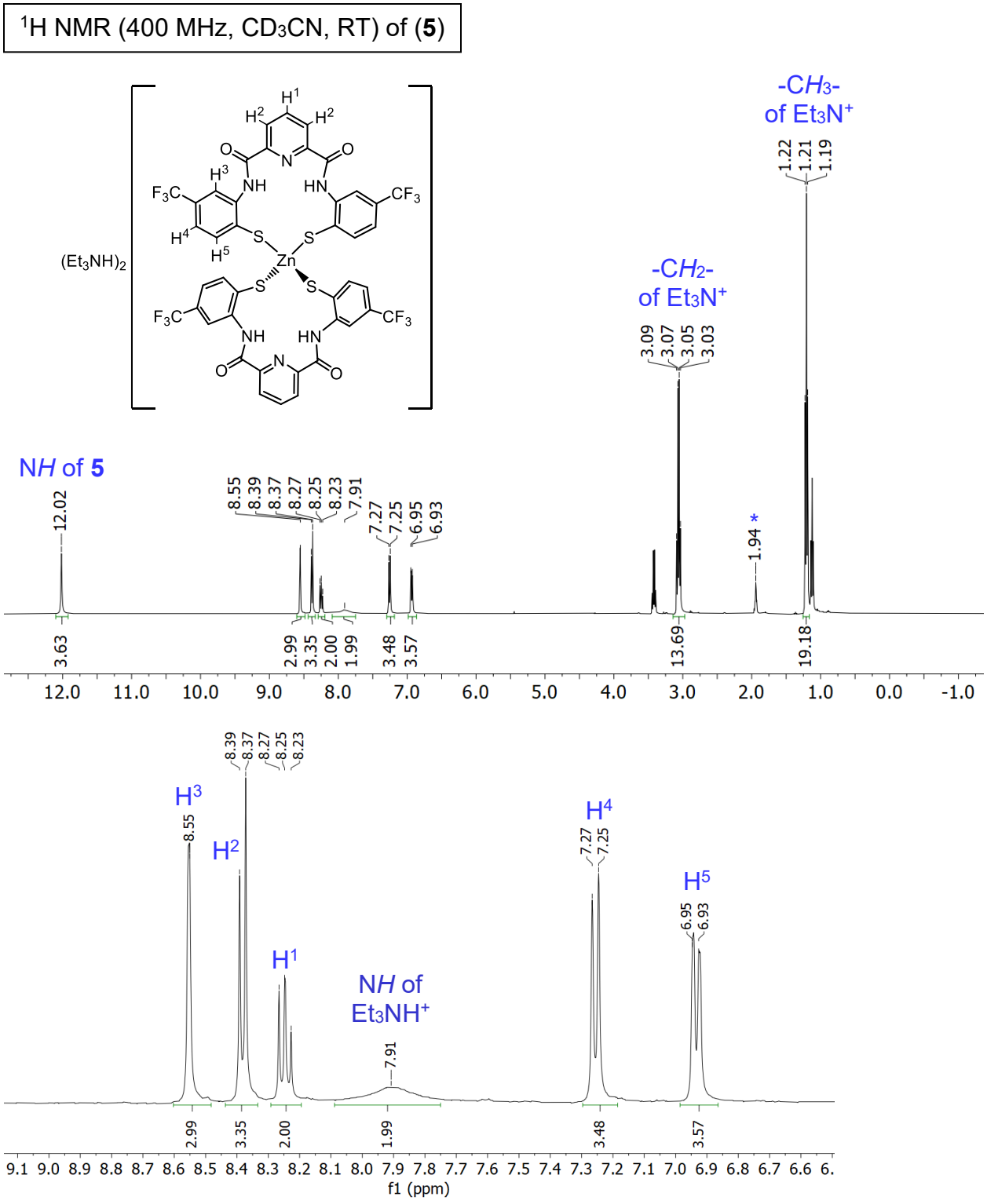

Figure S4.40. *Top:* ^{1}H NMR spectrum of $(Et_3NH)_2[Zn(PyH_2PS\text{-}p\text{-}CF_3)_2]$ (**5**) in CD_3CN at RT (δ vs. protio signal). *Bottom:* expansion of 6 – 9 ppm region. Residual CH_3CN is observed at 1.94 ppm and is indicated with *.

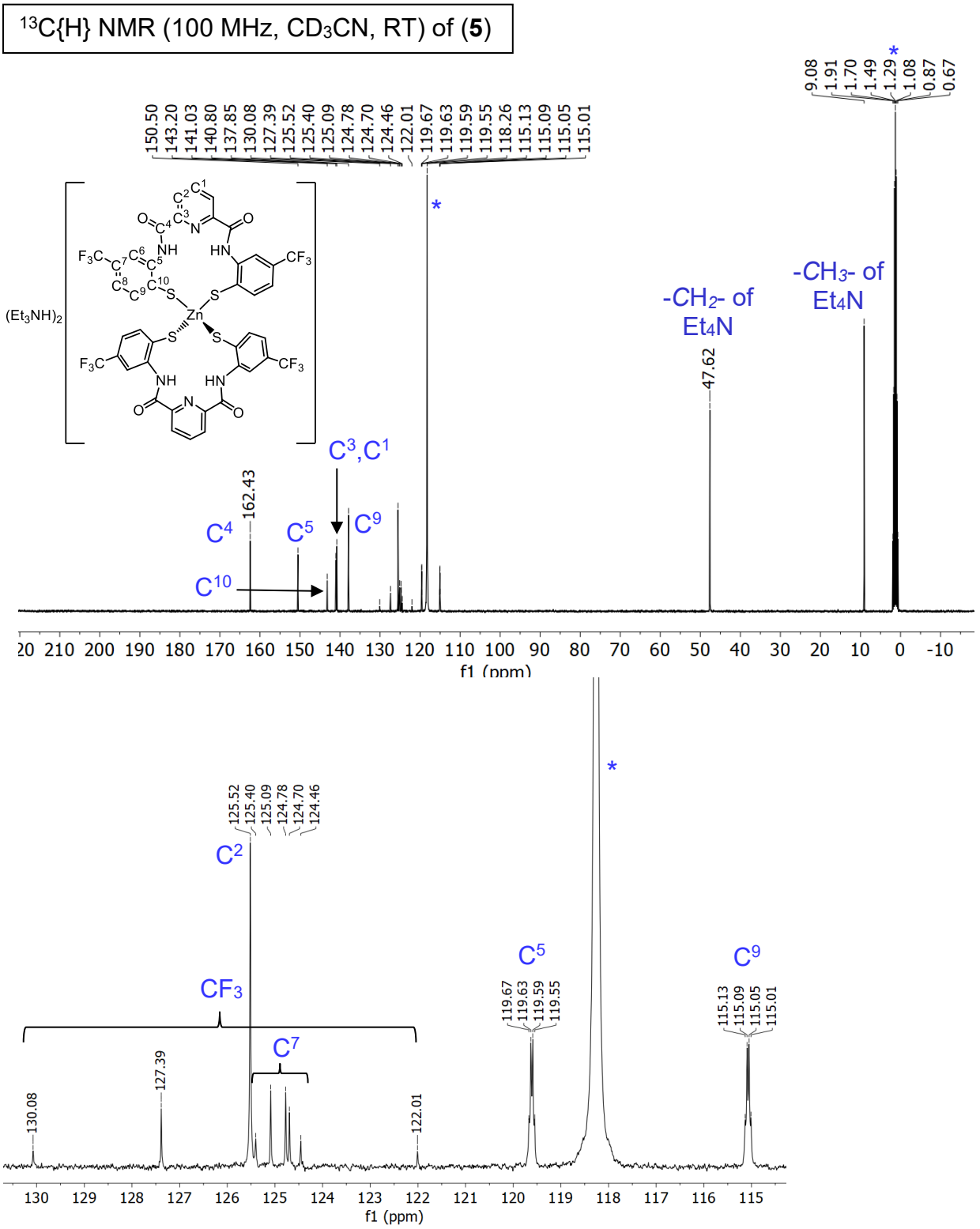

Figure SX. *Top:* ^{13}C NMR spectrum of $(Et_3NH)_2[Zn(PyH_2PS\text{-}p\text{-}CF_3)_2]$ (**5**) in CD_3CN at RT (δ vs. protio signal). *Bottom:* expansion of 116 – 133 ppm region. Residual CH_3CN is observed at 118.26 and 1.29 ppm and is indicated with *

^{19}F NMR (400 MHz, CD_3CN, RT) of (**5**)

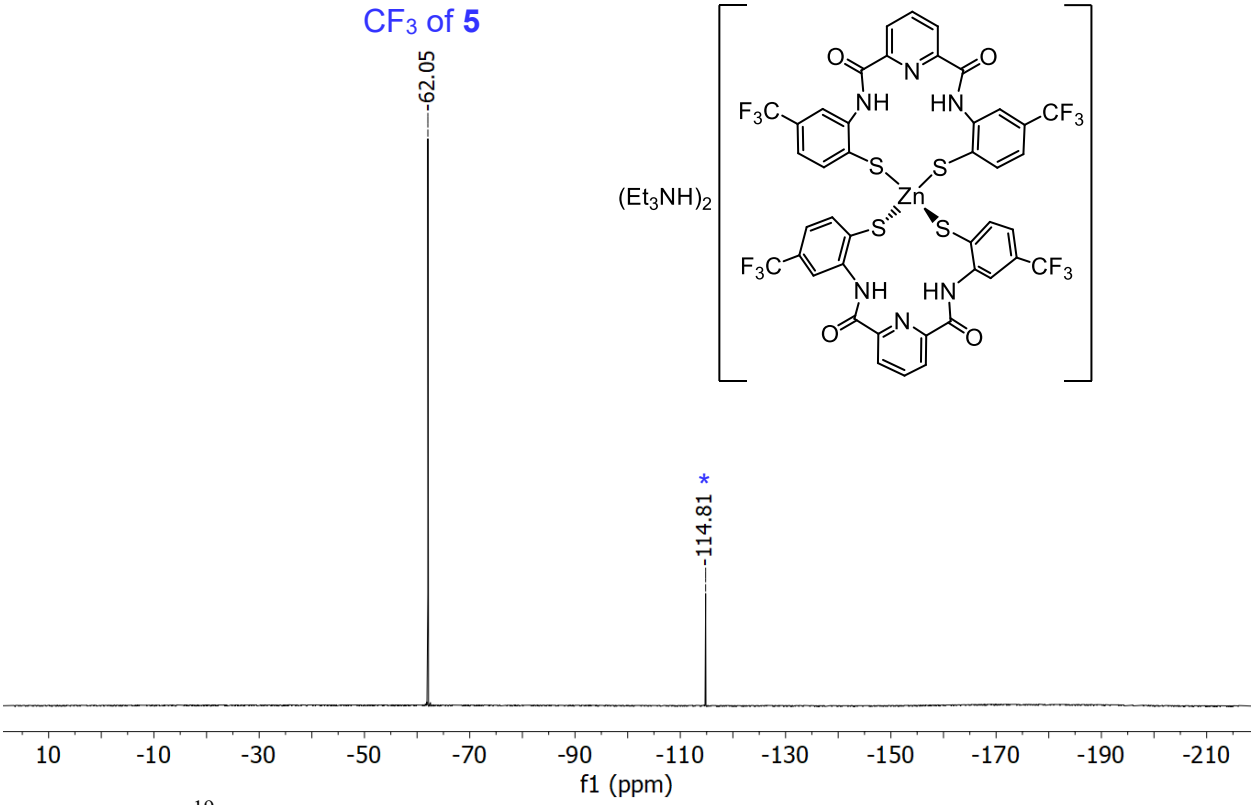

Figure S4.41. ^{19}F NMR spectrum of $(Et_3NH)_2[Zn(PyH_2PS\text{-}p\text{-}CF_3)_2]$ (**5**) CD_3CN at RT. The peak at -114.81 ppm is from PhF as an internal standard.

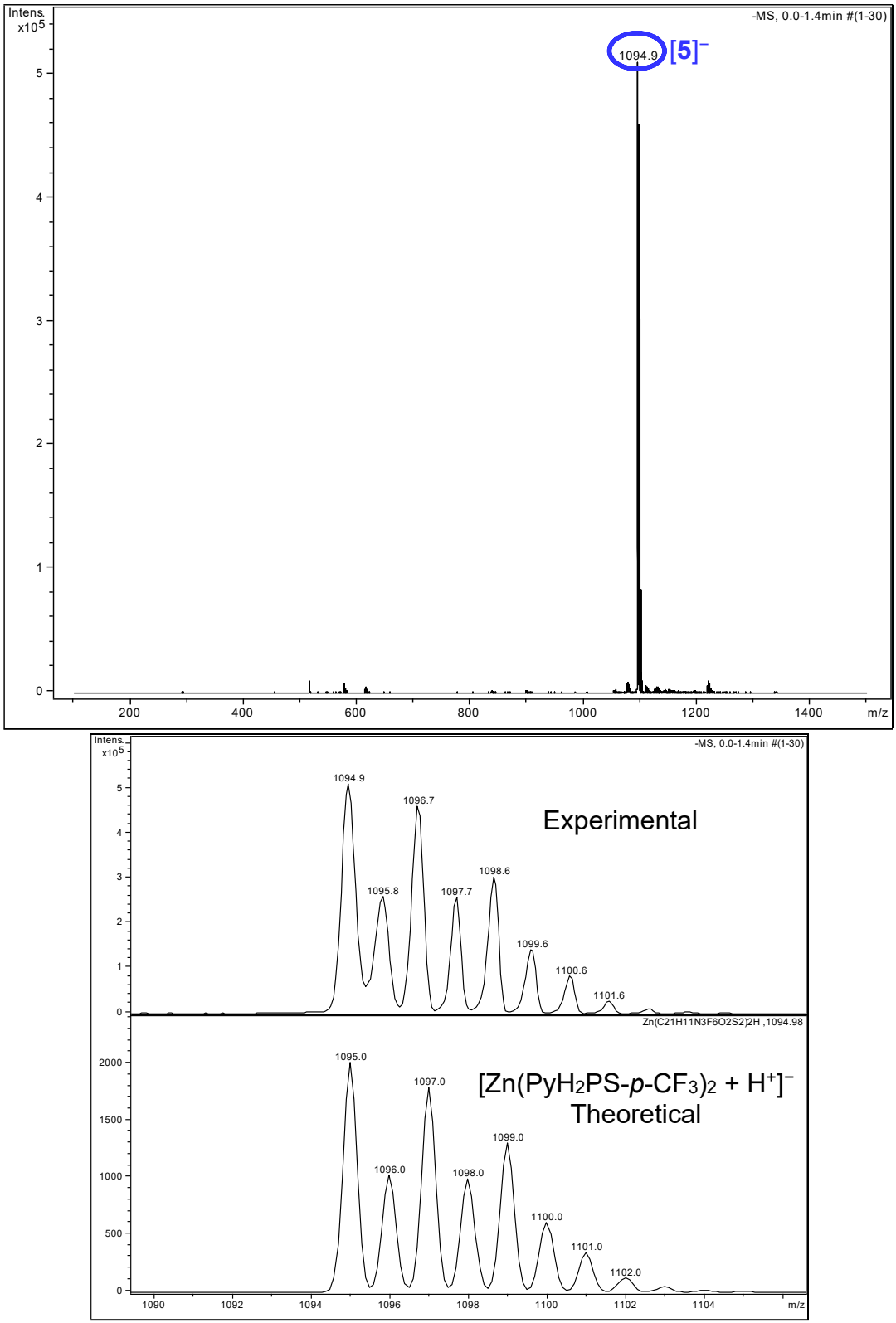

Figure S4.42. *Top*: Low-resolution ESI-MS(-) of $(Et_3NH)_2[Zn(PyH_2PS\text{-}p\text{-}CF_3)_2]$ (**5**) in MeCN. *Bottom*: experimental and simulated theoretical isotopic distribution peak at *m/z*: 1094.9.

4.7 X-ray Diffraction

X-ray Crystallographic Data Collection and Structure Solution and Refinement. Yellow crystals of **3** were obtained from slow diffusion of Et_2O into a saturated solution of **3** in MeCN at -20 °C. The data was collected at 170 K on the goniometer head of a Bruker D8 Quest diffractometer equipped with a Bruker PHOTON III detector. Data were collected with the use of Mo Kα (λ = 0.71073 Å) fine-focus sealed tube. A multi-scan absorption correction was applied with the program SADABS.[80] The structure was solved by the dual space method, (SHELXT)[81] and refined by full-matrix least-squares on F2 (SHELXL-2017).[82] The fluorine's (F4-6) of one of the CF_3 group of **3** were located in two positions with ratios of 70:30. Orange crystals of **4** were obtained from slow diffusion of pentane into a saturated solution of **4** in THF at -20 °C. The data was collected at 150 K on the goniometer head of a Bruker Kappa diffractometer equipped with a Bruker PHOTON III detector. Data were collected with the use of Mo Kα (λ = 0.71073 Å) fine-focus sealed tube. A multi-scan absorption correction was applied with the program SADABS.[80] The structure was solved by the dual space method, (SHELXT 2014/5)[83] and refined by full-matrix least-squares on F2 (SHELXL-2016/6).[82] The fluorine's (F1-9) from three of the CF_3 group of **4** were located in three positions with ratios of 40:30:30.

4.8 Reactivity Studies

Bulk Protonation of 1 and 2 with AcOH. A batch of **1** (0.014 g, 0.020 mmol) was dissolved in ~2 mL of MeCN resulting in dark blue almost black solution. To this solution, AcOH (6.0 μL, 0.006 g, 0.10 mmol) was added and stirred for 30 min. Within a minute from the addition of acid, the solution took on a brown color, turning a slight red-hue after 0.5 h. The solution was taken to dryness and DCM was stirred in for 30 min. After stirring, the solution was filtered over a Celite packed frit and rinsed with DCM. After the reddish-brown filtrate was taken to dryness, Et_2O was

added and allowed to stir until a solid was suspended in solution. The resulting precipitate was isolated by vacuum filtration on a glass-frit, washed with Et_2O, and dried on a high vacuum line to afford a reddish-brown solid (0.009 g). This procedure and workup were repeated for **2** (0.020 g, 0.024 mmol) with AcOH (7.0 μL, 0.007 g, 0.12 mmol) yielding a similar result; however, the solution and powder isolated (0.016 g) was redder in color.

UV-vis titration of AcOH into solutions of 1 and 2. A 6.72 mM stock solution of **1** (0.009 g, 0.013 mmol) in 2.00 mL of MeCN was made, 50 uL of stock was added to cuvette containing 2.0 mL of MeCN (creating a 0.16 mM solution), and sealed with a septum cap. A 1.68 M stock solution of AcOH (0.48 mL, 0.504 g, 8.39 mmol) was made with 4.52 mL of MeCN in a septum sealed vial. After the spectra of **1** alone was recorded an alliqout of AcOH stock was added to cuvette containing **1** via an air-tight syringe, stirred for 20 s, left undisturbed for 10 s, and the spectra was recorded. The following aliquots were performed in the same manner. This was repeated under identical conditions for **1** using DMF. Preparation of stock solutions and titrations were done in a glovebox, and spectra were recorded at 23 ˚C.

A similar titration experiment was performed with a 14.5 mM stock solution of **2** (0.012 g, 0.014 mmol) in 1.0 mL of MeCN. An aliquot of 120 uL of **2** stock was added to cuvette containing 2.00 mL of MeCN (creating a 0.82 mM solution), and sealed with a gas-tight screw cap. A 0.17 M stock solution of AcOH (0.050 mL, 0.053 g, 0.87 mmol) was made with 4.95 mL of MeCN. After the spectra of **2** alone was recorded, an alliqout of AcOH stock was added to cuvette containing **2**, shaken, and recorded after ~1 min. The following aliquots were performed in the same manner. This was repeated under identical conditions for **2** using DMF. Preparation of stock solutions and titrations were done in a glovebox, and spectra were recorded at 23 ˚C.

4.9 Electrochemical Measurements

Electrochemistry and catalysis. Cyclic voltammetry (CV) measurements were performed with a WaveDriver 40 bipotentiostat/galvanostat from Pine Research Instrumentation using an Ag/Ag^+ reference electrode, Pt-wire counter electrode, and a stationary glassy carbon working electrode (3 mm outer diameter). The potentiostat was interfaced with a PC using the Aftermath software. Measurements were collected at ambient temperature using ~1.0 mM analyte in MeCN or DMF containing 0.25 M $^n Bu_4NPF_6$ as the supporting electrolyte in an inert N_2 atmosphere. Analyte potentials were referenced against a 5 mM MeCN or DMF solution of ferrocene as an internal standard under identical conditions. Purity of the electrolyte medium was confirmed over the available electrochemical window through scans taken prior to addition of external reference. The acid titration experiments were performed by addition of MeCN aliquots of acetic acid (pK_a = 23.5 in MeCN[26]; 13.5 in DMF[52]). AcOH was added in 10-20 μL aliquots, stirred with for 20 s, and sat undisturbed for an additional 10 s prior to measurement. The working electrode was cleaned between scans by washing with solvent, polishing on a felt cloth with a 0.3 um alumina suspension from Allied High-Tech Products, and sonicating for 30 s in DI water. Rinse tests were performed at the end the acid titration experiment by removing working electrode, rinsing with solvent medium, placing working electrode into fresh solution of electrolyte and acid, and performing the CV. All spectra are graphed corresponding to the US convention.

Determination of Overpotential. The overpotential (η) was calculated using eq. i, which was developed for homogenous electrocatalysis of the HER.[84]

$$\eta = |E^{\circ}_{H^+/H_2} - E_{cat/2}| \quad \text{(i)}$$

$E°_{H+}$ is the standard reduction potential for the $2H^+/H_2$ couple of AcOH in DMF taking into account homoconjugation.[52] $E°_{H+}$ was calculated to be -1.34 V vs. Fc^+/Fc in DMF. $E_{cat/2}$ is the

potential for the HER catalyzed by the reported complexes at half the maximum of the catalytic current (i_c).[84]

Determination of k_{obs}. Observed rate constants (k_{obs}) for HER electrocatalysis were calculated under pseudo first-order conditions where the [H^+] is high enough that it is not depleted during catalysis, i.e., the acid-independent regime. Under our experimental conditions, we define k_{obs} as being equivalent to maximum TOF or TOF_{max}. that is estimated according to eq. ii.

$$\frac{i_c}{i_p} = \frac{n}{0.4463}\sqrt{\frac{RTk_{obs}}{Fv}} \quad \text{(ii)}$$

In eq. ii i_c is the current under catalytic conditions, i_p is the current in the absence of acid, T is temperature (298 K), n is number of electrons per catalytic process (n = 2 for HER), v is the scan rate (0.1 V/s), R is the gas constant, and F is the Faraday constant.

Quantification of H_2. The amount of H_2 (g) produced from bulk electrolysis was quantified utilizing ^{1}H NMR with an internal standard, 1,3,5-trimethoxybenzene, of a known concentration (0.18 M) in C_6D_6. ^{1}H NMR detection and quantification of H_2 has been utilized for *in-situ*, stochiometric H_2 generation.[57-59] In order to utilize this technique for electrocatalytic H_2 evolution, bulk electrolysis experiments of **1** (2.2 mM in a 0.25 M ^{n}Bu$_4$NPF$_6$ solution of DMF) were performed in a low volume H-Cell (Figure S4.75) from Pine Research (part number: RRPG255), separated by an ACE fritted glass disc, porosity E (4 – 8 μm) utilizing the same electrodes as in the CV experiments. Bulk electrolysis was performed by applying a potential at the E_{cat} (~ −2.8 V vs Fc/Fc$^+$, determined by an external Fc/Fc+ reference post-electrolysis) for 80 min in the presence of 270 mol-equiv. of AcOH while stirring the solution. Once complete, a septa-capped J-young tube containing 2.75 mL of C_6D_6 and 50 μL of the internal standard stock, resulting in ~0.4 mL of headspace with an internal standard concentration of 3.1 mM, was prepared under inert conditions. Then, a sample of the headspace from the working electrode compartment (0.5 mL) was collected

using an airtight syringe and injected into a septa-capped J-young tube (Figure S4.76). The solution was inverted every ~30 s for 10 min to equilibrate dissolved gas and sat undisturbed for 0.5 h. ^{1}H NMR (600 MHz, RT) was run for a total of ~30 min (256 scans; relaxation delay (T_1) = 5.0 s, T = 298 K).

To quantify the amount of solubilized H_2 in the J-young tube ($n_{H2(l)}$), eq. iii was utilized:

$$n_{H2(l)} = \frac{\int \delta_{H\sim 4.46\ ppm}}{2} \times [IS] \quad \text{(iii)}$$

where $\int \delta_{H\sim 4.46\ ppm}$ is the integration of the peak corresponding to dissolved H_2 referenced to the *Me*O-Ph of 1,3,5-trimethoxybenzene, i.e. $\int\delta_H = 9.00$) and *[IS]* is concentration (M) of 1,3,5-trimethoxybenzene in the J-young tube (0.00315 M).

To calculate the total mols of H_2 in the headspace of the J-young tube ($n_{H2(g)}$), eq. iv was utilized:

$$n_{H2(g)} = \frac{\left(\frac{n_{H2(l)}}{V_{tube}}\right) \times V_{HS-tube}}{K_H \times R \times T} \quad \text{(iv)}$$

where V_{tube} is the volume (L) of C_6H_6 in the J-young tube, $V_{HS-tube}$ is the volume (L) of headspace in the J-young tube, K_H is the Henry's constant ($3.9655*10^3$ M*atm^{-1})[85], R is the gas constant, and T is the temperature.

To determine the mols of H_2 in the headspace of the H-cell produced by **1**, eq. v was utilized:

$$\left(n_{H2(l)} + n_{H2(g)}\right) \times \frac{V_{HS(f)}}{V_{injected}} \times \frac{(V_{HS(f)} - V_{HS(i)})}{V_{HS(f)}} \quad \text{(v)}$$

where $V_{HS(f)}$ is the volume of headspace remaining in the H-cell post electrolysis, $V_{HS(i)}$ is the volume of the headspace pre-electrolysis, and $V_{injected}$ is the volume of gas injected in the J-young tube. The amount of H_2 quantified by this method is most likely an under-estimate of actual gas produced.

Determination of Faradaic Efficiency and Turnover Number. Faradaic Efficiency (FE) was calculated utilizing eq vi:

$$FE = \frac{Mols\ of\ H_2\ Produced}{Theorhetical\ Mols\ of\ H_2\ Produced} \times 100\% \quad \text{(vi)}$$

where the $Theorhetical\ Mols\ of\ H_2\ Produced$ was calculated utilizing eq vii:

$$\left|\frac{Q_{cat} - Q_{blank}}{2 \times F}\right| \quad \text{(vii)}$$

where Q_{cat} is the charge passed for bulk electrolysis, Q_{blank} (-0.23 C) is the charge passed for electrolyte alone, and F is Faradaic constant (96,485 C/mol).

Turnover numbers (TON) were calculated utilizing eq viii:

$$TON = \frac{Mols\ of\ H_2\ Produced}{Mols\ of\ Catalyst} \quad \text{(viii)}$$

Catalyst Concentration Dependence. A 0.030 M stock solution of **1** (0.010 g, 0.015 mmol) was made in a 0.25 M $^{n}Bu_4NPF_6$ solution of DMF. An aliquot of this stock solution (100 uL) and 50 uL of glacial AcOH was added to the CV cell containing 9.50 mL of 0.25 M $^{n}Bu_4NPF_6$ solution in DMF, ~290 mol-equiv of AcOH with respect to **1.** The solution was stirred for 30 s and sat undisturbed for 10 s prior to measurement. This procedure was repeated, totaling five aliquots. The working electrode was cleaned between each scan as described prior. A linear relationship between i_c and [**1**] is indicative of a first-order dependence based on eq ix.[86, 87]

$$i_c = nFA[cat]\sqrt{D(k[H^+])} \quad \text{(ix)}$$

AcOH Concentration Dependence. The order with respect to AcOH was calculated utilizing eq. iii. A linear relationship between i_c and √[AcOH] is indicative of a first-order dependence, where i_c was taken at non-saturating conditions (less than ~270 mM AcOH) from the electrochemical AcOH titration experiments.

4.10 Mechanism Computations

DFT calculated protonation energy. For mechanistic considerations, all intermediates were computed utilizing the same level of theory as previously described for **1**. The geometry optimizations were performed in the gas phase with FREQ and SPE calculated with CPCMC to model the solvent environment of DMF. The Gibbs free energy of the protonation step ($\Delta G_{C\text{-}step}$) was calculated with eq. x utilizing the Gibbs free energy of Et_3NH^+ as H^+ donor and its conjugate base Et_3N:

$$\Delta G_{C-step} = \Delta G(AH + Et_3N) - \Delta G(A^- + Et_3NH^+) \qquad \text{(x)}$$

Both acid and conjugate base were optimized under the same level of theory as for **1** and frequency analysis was done with CPCMC (DMF).

DFT-calculated redox potential. DFT methods were utilized to provide an estimate of the redox potential of the proposed intermediates for the catalytic cycle of **1** (Figure SX). DFT methods have been used to calculate the one-electron redox potentials of several transition metal complexes and metalloenzymes. The redox potential (E°) is related to the Gibbs free energy difference in solution (ΔG_{soln}) given by eq. xi:

$$E^\circ = -\frac{\Delta G_{soln}}{nF} \quad \text{(xi)}$$

Where F is Faraday's constant (23.06 kcal mol^{-1} V^{-1}) and n is the number of electrons transferred (n = 1). ΔG_{soln} can be determined from eq. x using the thermodynamic cycle depicted in Scheme S4.1:

$$\Delta G_{soln} = \Delta G_{gas} + \Delta G(\mathbf{2})_{solv} - \Delta G(\mathbf{1})_{solv} \quad \text{(xii)}$$

where ΔG_{gas} is the Gibbs free energy difference in the gas phase, and the $\Delta G(\mathbf{1})_{solv}$ and $\Delta G(\mathbf{2})_{solv}$ are the solvation energies in DMF.

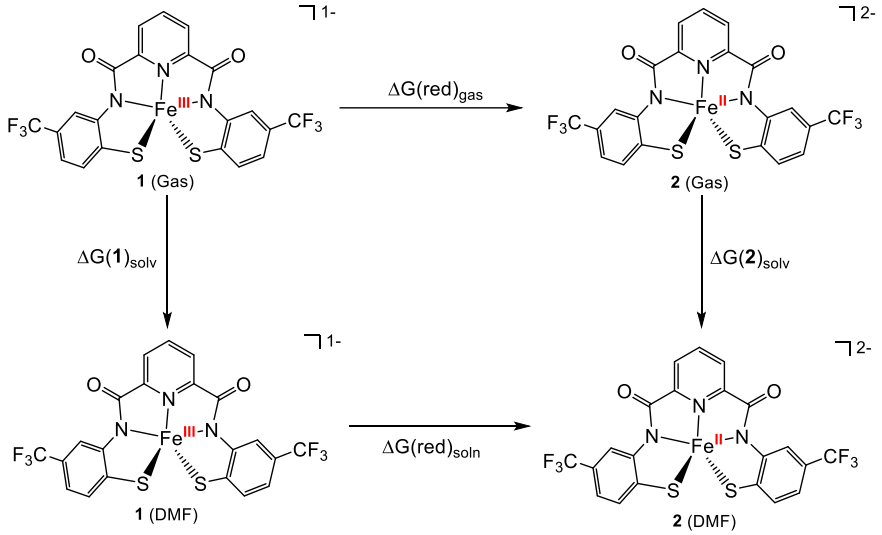

Scheme S4.1. Thermodynamic cycle that is used to calculate redox potential for **1/2** couple.

The difference of the gas-phase Gibbs free energies of **1** and **2** yields $\Delta G(red)_{gas}$, and the difference of the Gibbs free energies of **1** and **2** using the conductor-like screening model (CPCMC) for DMF yields $\Delta G(red)_{soln}$. Solvation energies (ΔG_{solv}) were obtained from the difference of single point energies, from single point energy calculations, of the intermediate in the absence and presence of the solvation model. The absolute potential for Fc/Fc^{+} was calculated at the same level of theory under an identical procedure to properly reference the redox couples. The results of the redox calculations for **1**/**2** are presented in Table S4.1.

Table S4.1. Redox Potential calculations for **1**/**2** and Fc^+/Fc in DMF. [a]

	Fc^+	**Fc**	**1**	**2**
Gibbs free energy (G)	-1649.83178	-1650.08528	-3778.56123	-3778.55453
ΔG (gas)	-0.25351		0.00670	
Single Point Energy (gas)	-1650.00834	-1650.26308	-3778.77305	-3778.76408
Single Point Energy (soln.)	-1650.08356	-1650.26877	-3778.84143	-3778.97581
Solvation Energy	-0.07526	-0.00569	-0.06838	-0.21172
ΔΔG (solv.)[b]	0.06957		-0.14334	
ΔG (soln.)[c]	-0.18394		-0.13664	
ΔG (soln.) (kcal/mol)	-115.420		-85.746	
E˚ (V)[d]	5.005		3.718	
E˚ (V) (vs Fc+/Fc)	**0.000**		**-1.287**	

[a] Energies are in hartrees (E_h) unless noted otherwise. [b] Difference in solvation energies. [c] Calculated according to equation 2. [d] Calculated according to eq. v.

The energy of each reduction step ($\Delta G°$) was calculated according to eq. xiii:

$$\Delta G^{\circ} = -23.06(n)(E½) \qquad \text{(xiii)}$$

where n is the number of electrons transferred (n = 1) and $E½$ is the compound reduction potential. Transition state calculations were performed utilizing a relaxed surface scan (ScanTS), under the same level of theory as for **1** utilizing CPCMC (MeCN), to scan the distances between hydride and proton on coordinated thiolate (1.697-to-0.400 Å in 20 steps). UCSF Chimera[79] was used to generate model intermediates.

4.11. Supplementary Information

Table S4.2. Summary of Crystal Data and Intensity Collection and Structure Refinement Parameters for $(Et_4N)_2[Zn(PyPS\text{-}p\text{-}CF_3)]$ (**3**).

Parameters	**3**
Formula	$C_{21}H_9F_6ZnN_3O_2S_2$ $2(C_8H_{20}N)$
MW	839.32
Crystal system	Monoclinic
Space group	$P2_1/n$
Crystal color, habit	Yellow, block
a, Å	12.1702
b, Å	12.361
c, Å	26.485
α, deg	---
β, deg	96.409
γ, deg	----
V, Å^3	3959.2
Z	4
$\rho_{calcd,}$ g/cm^3	1.408
T, K	170
abs coeff, μ (Mo Kα), mm^{-1}	0.79
θ limits, deg	25.3, 2.4
total no. of data	14954
no. of unique data	7097
no. of parameters	514
GOF of F^2	1.03
R_1,[a]	0.052
wR_2,[b]	0.128
max, min peaks, e/Å^3	0.53, -0.50

[a] $R_1 = \Sigma| |F_o| - |F_c| | / \Sigma |F_o|$; [b] $wR_2 = \{\Sigma[w(F_o^2 - F_c^2)^2]/\Sigma[w(F_o^2)^2]\}^{1/2}$

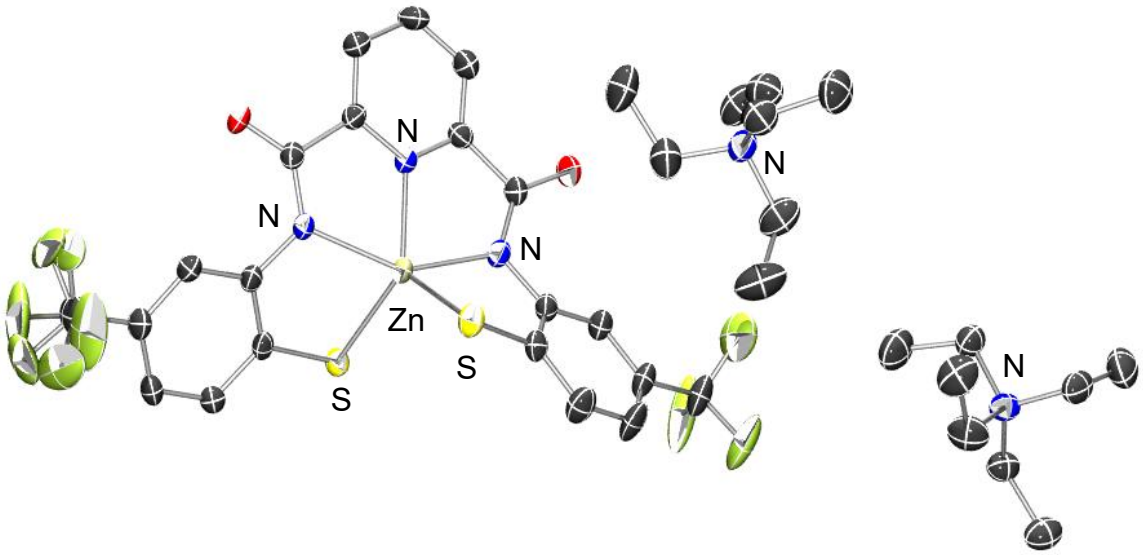

Figure S4.43. ORTEP diagram of $[Zn(PyPS\text{-}p\text{-}CF_3)]^{2-}$ at 50% thermal probability ellipsoids. H atoms are omitted for clarity. Disorder in one of the trifluoromethyl groups consisting of atoms (F4-F6) is shown.

Table S4.3. Select bond distances (Å) and angles (deg) of $(Et_4N)_2[Zn(PyPS\text{-}p\text{-}CF_3)]$ (**3**).

	3 (M = Zn)
Atoms	**Bond Distances (Å)**
$M\text{-}S_1$	2.352
$M\text{-}S_2$	2.385
$M\text{-}N_1$	2.151
$M\text{-}N_2$	2.101
$M\text{-}N_3$	2.122
	Bond Angles (deg)
$S_1\text{-}M\text{-}S_2$	109.4
$S_1\text{-}M\text{-}N_1$	82.7
$S_1\text{-}M\text{-}N_2$	128.6
$S_1\text{-}M\text{-}N_3$	116.0
$S_2\text{-}M\text{-}N_1$	117.9
$S_2\text{-}M\text{-}N_2$	122.0
$S_2\text{-}M\text{-}N_3$	81.4
$N_1\text{-}M\text{-}N_2$	74.1
$N_1\text{-}M\text{-}N_3$	148.4
$N_2\text{-}M\text{-}N_3$	74.3
τ_5	0.33

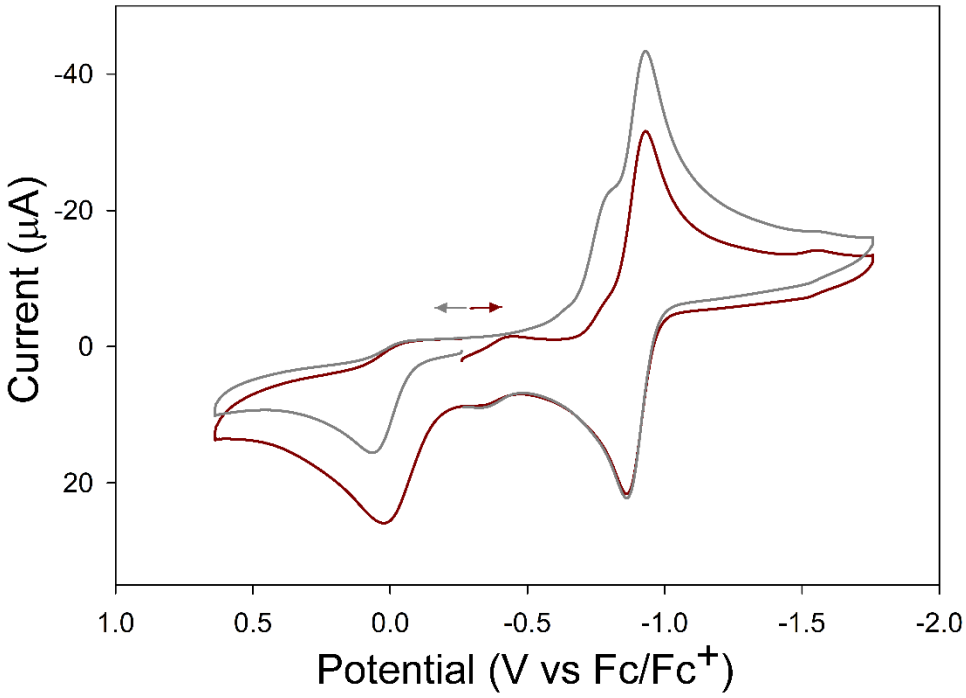

Figure S4.44. CV of **1** (1 mM) in MeCN at RT (0.25 M $^{n}Bu_4NPF_6$ supporting electrolyte, glassy carbon working electrode, 100 mV/s scan rate). Arrow shows direction of scan.

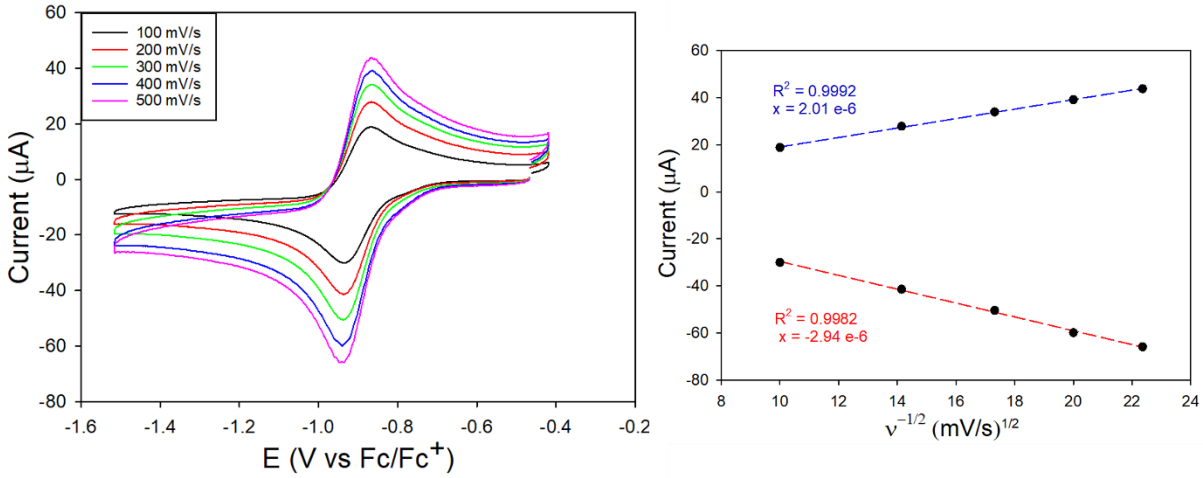

Figure S4.45. Scan speed dependency of Fe(III/II) couple of **1** (1 mM) in MeCN at RT (0.25 M $^{n}Bu_4NPF_6$ supporting electrolyte, glassy carbon working electrode, 100 mV/s scan rate).

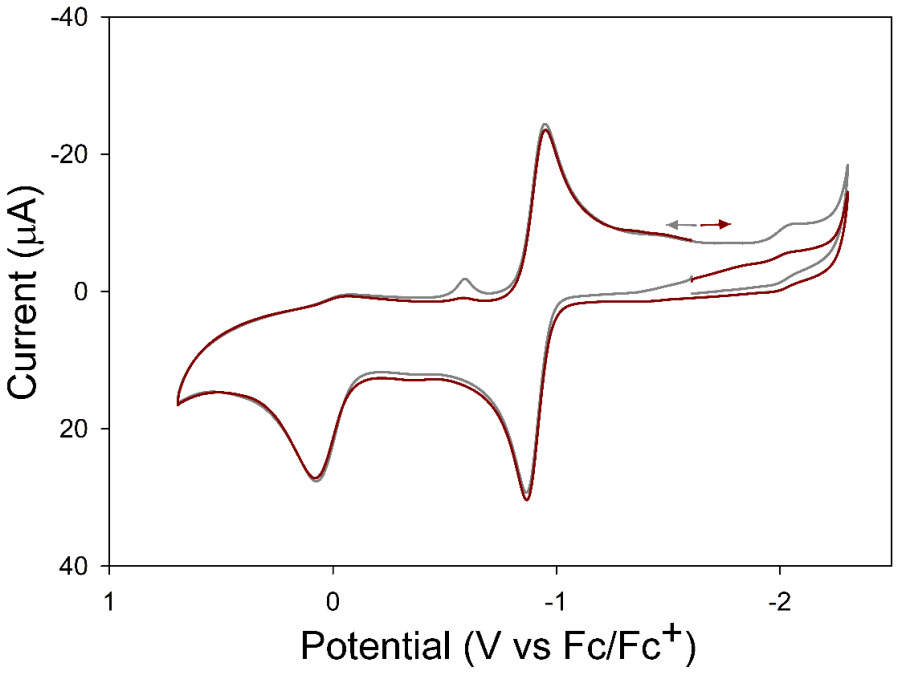

Figure S4.46. CV of **2** (1 mM) in MeCN at RT (0.25 M $^{n}Bu_4NPF_6$ supporting electrolyte, glassy carbon working electrode, 100 mV/s scan rate). Arrow shows direction of scan.

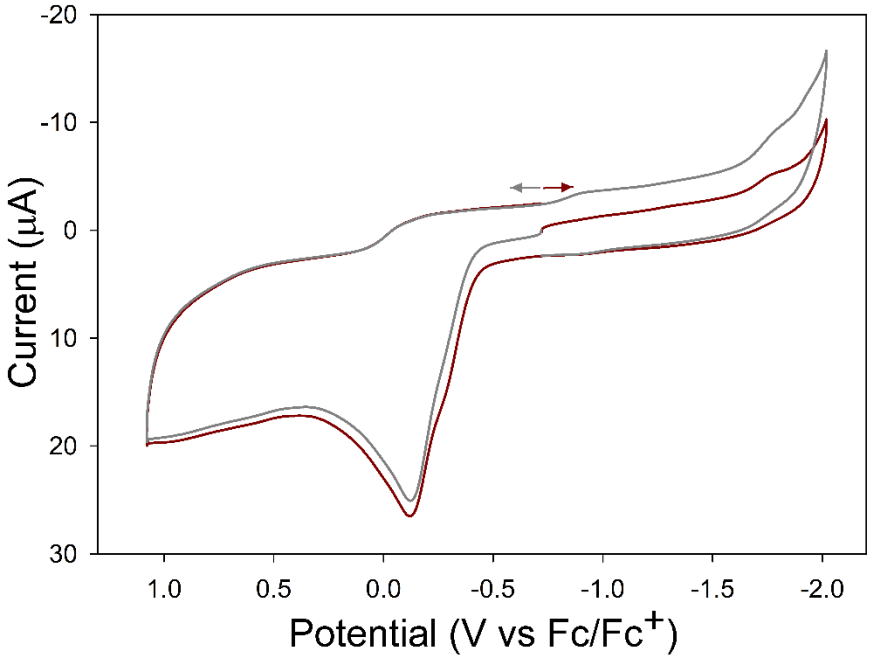

Figure S4.47. CV of **3** (1 mM) in MeCN at RT (0.25 M $^{n}Bu_4NPF_6$ supporting electrolyte, glassy carbon working electrode, 100 mV/s scan rate). Arrow shows direction of scan.

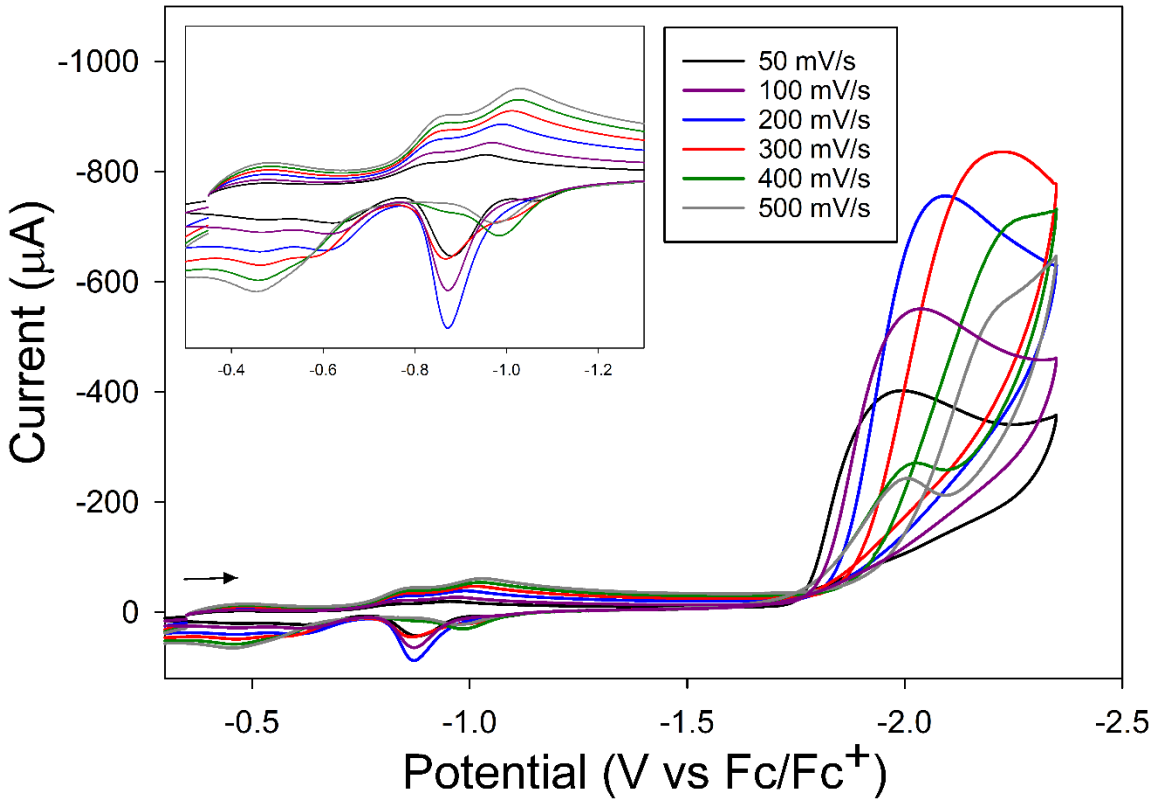

Figure S4.48. CV of **1** (1 mM) with 30 mol-equiv. of AcOH in MeCN at various scan rate (0.25 M $^{n}Bu_4NPF_6$ supporting electrolyte, glassy carbon working electrode, RT). Arrow shows direction of scan. *Inset*: zoom-in of region showing the symmetric peak.

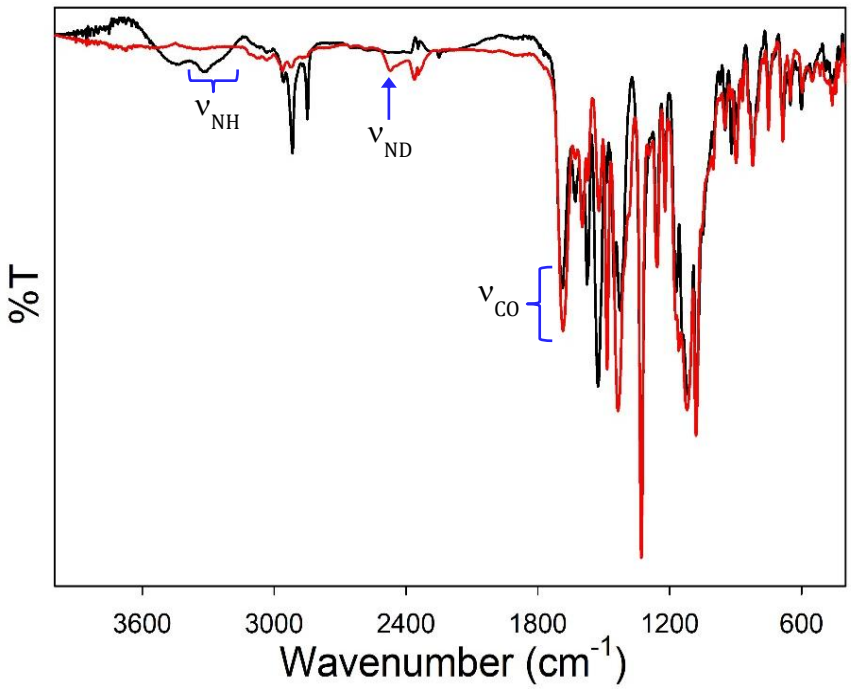

Figure S4.49. Solid-state FTIR spectrum of isolated material form (Et_4N)[Fe(PyPS-*p*-CF_3)] (**1**) + 5.0 mol-equiv. AcOH (black) and AcOD-d_4 (red) in a KBr matrix at RT.

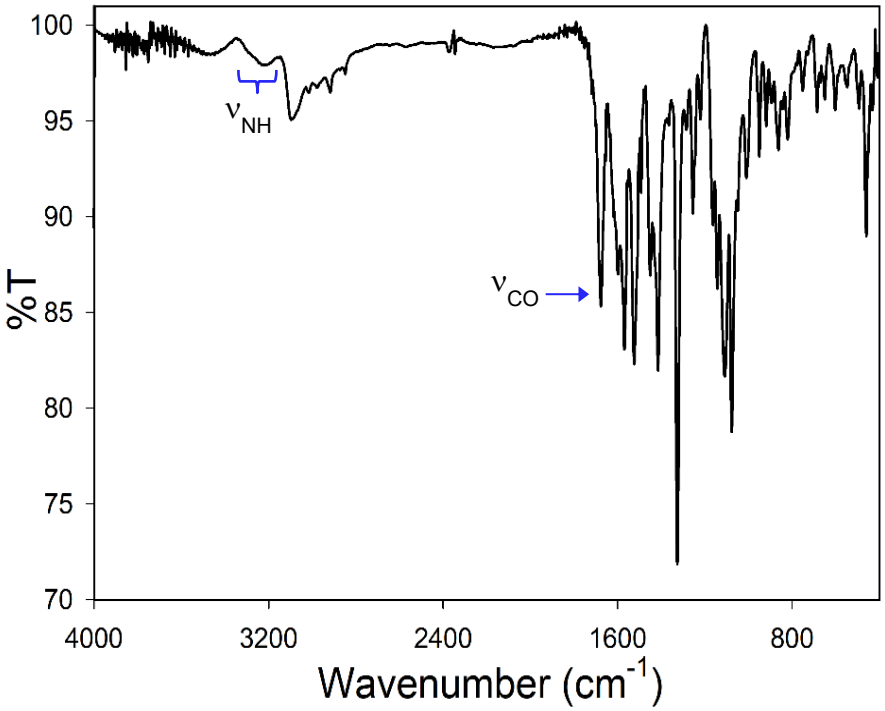

Figure S4.50. Solid-state FTIR spectrum of isolated material from (Et_4N)[Fe(PyPS-*p*-CF_3)] (**2**) + 5.0 mol-equiv. AcOH in a KBr matrix at RT.

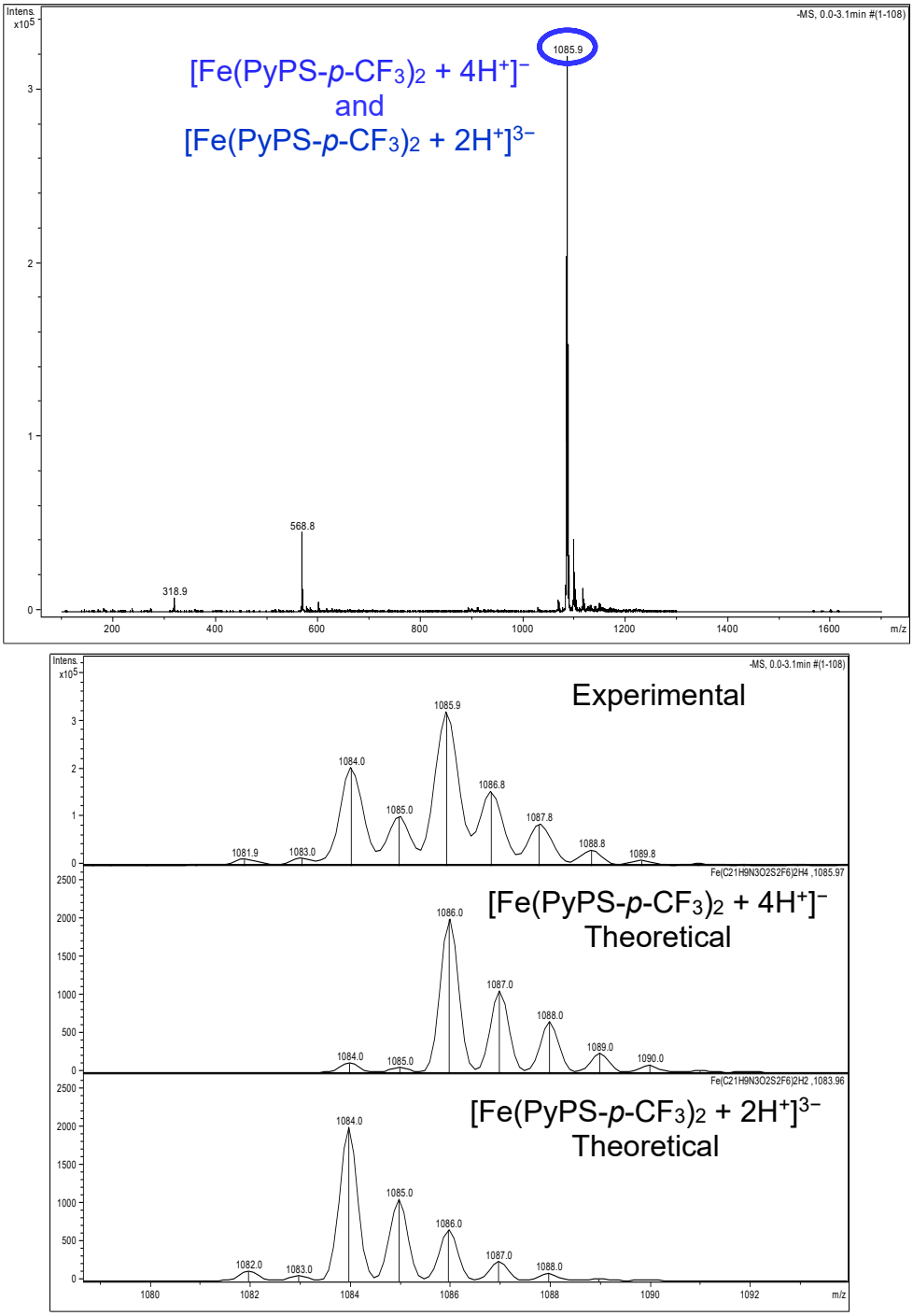

Figure S4.51. *Top*: Low-resolution ESI-MS(-) of isolated material from (Et_4N)[Fe(PyPS-*p*-CF_3)] (**1**) + 5.0 mol-equiv. AcOH in MeCN. *Bottom*: experimental and simulated theoretical isotopic distribution peak at *m/z*: 1085.9.

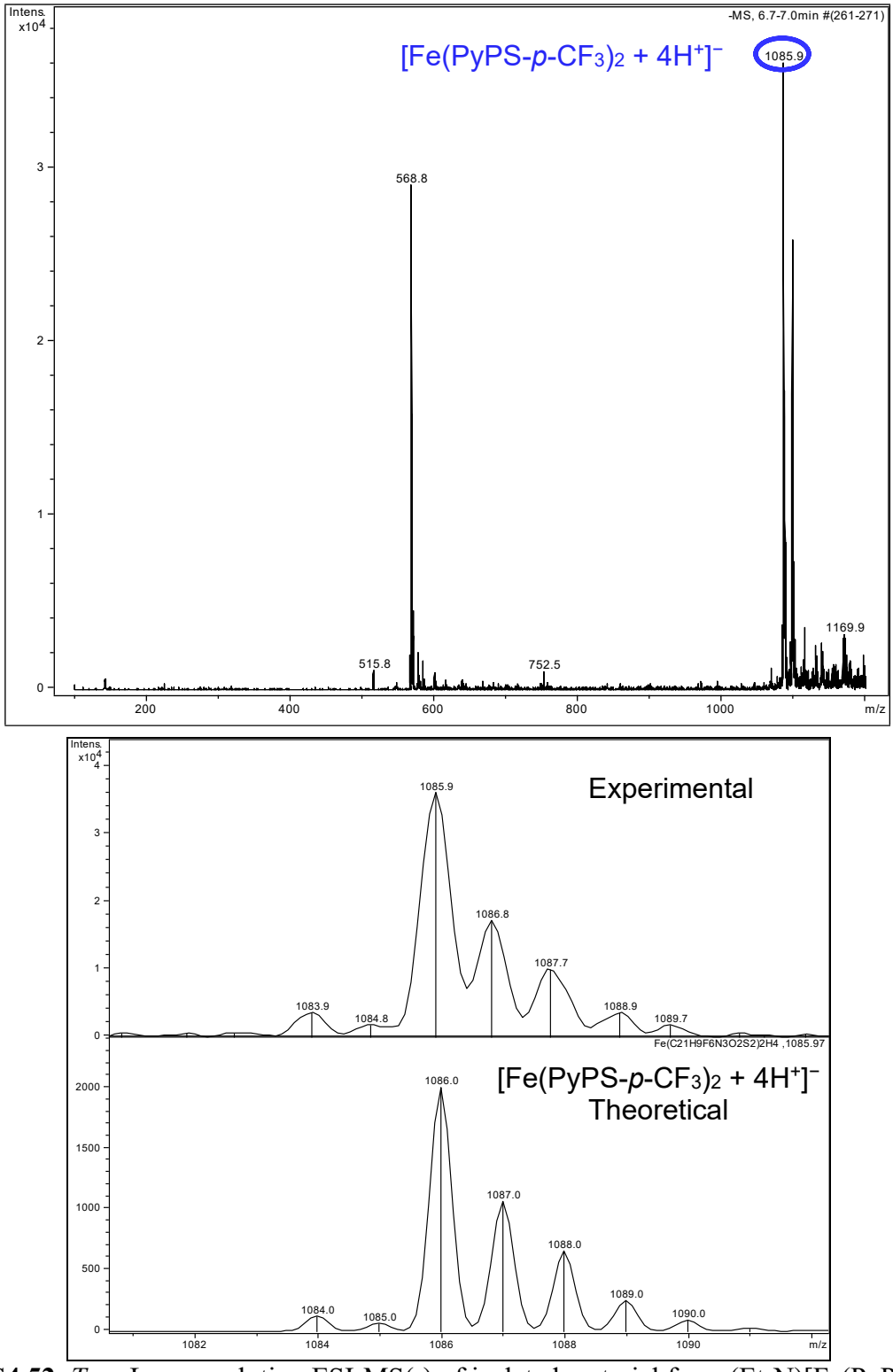

Figure S4.52. *Top*: Low-resolution ESI-MS(-) of isolated material from (Et_4N)[Fe(PyPS-*p*-CF_3)] (**2**) + 5.0 mol-equiv. AcOH in MeCN. *Bottom*: experimental and simulated theoretical isotopic distribution peak at *m/z*: 1085.9.

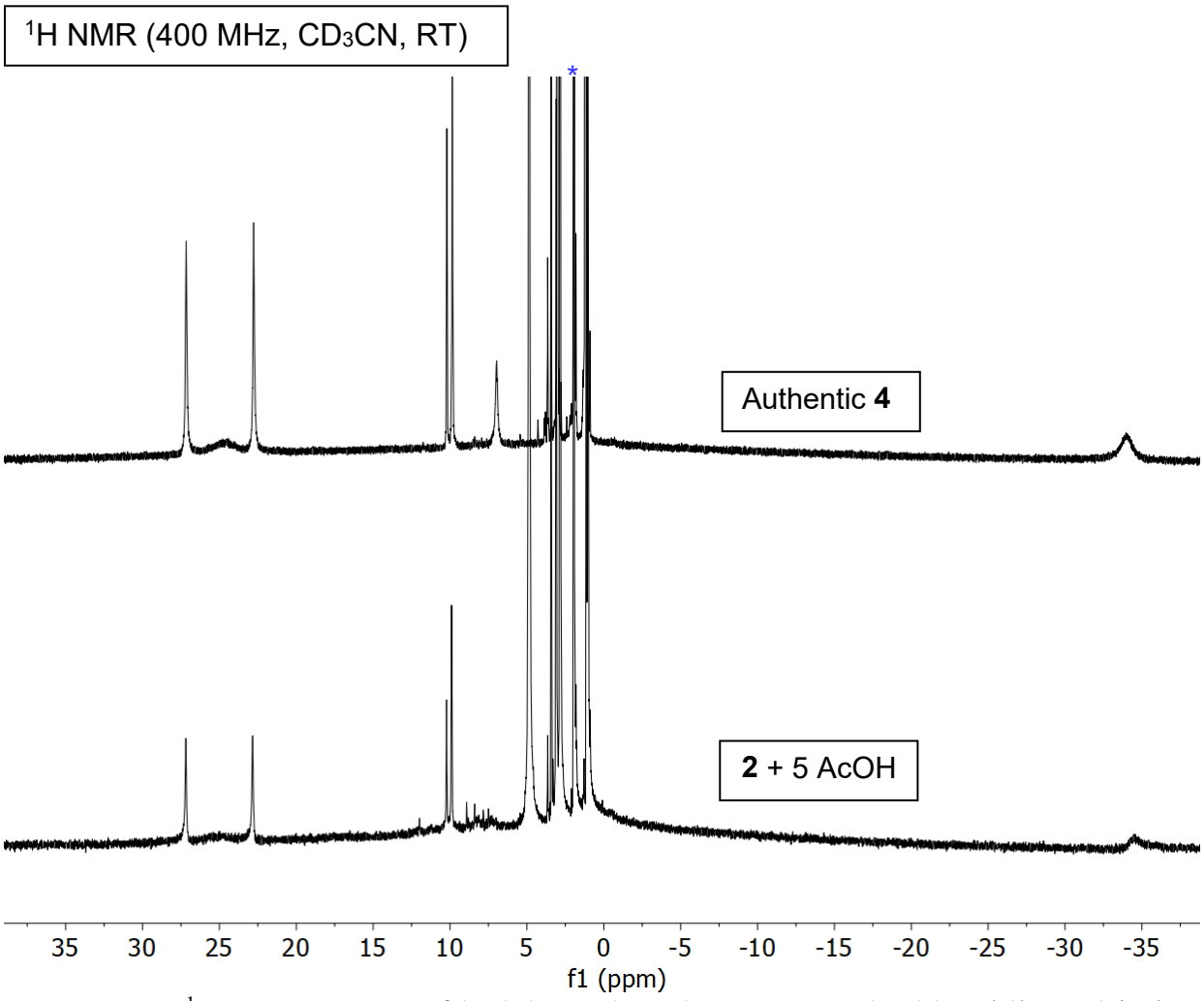

Figure S4.53. ^{1}H NMR spectrum of (*top*) $(Et_3NH)_2[Fe(PyH_2PS\text{-}p\text{-}CF_3)_2]$ (**4**) and (*bottom*) isolated material from **2** + 5.0 mol-equiv. AcOH in CD_3CN at RT (δ vs. protio signal).

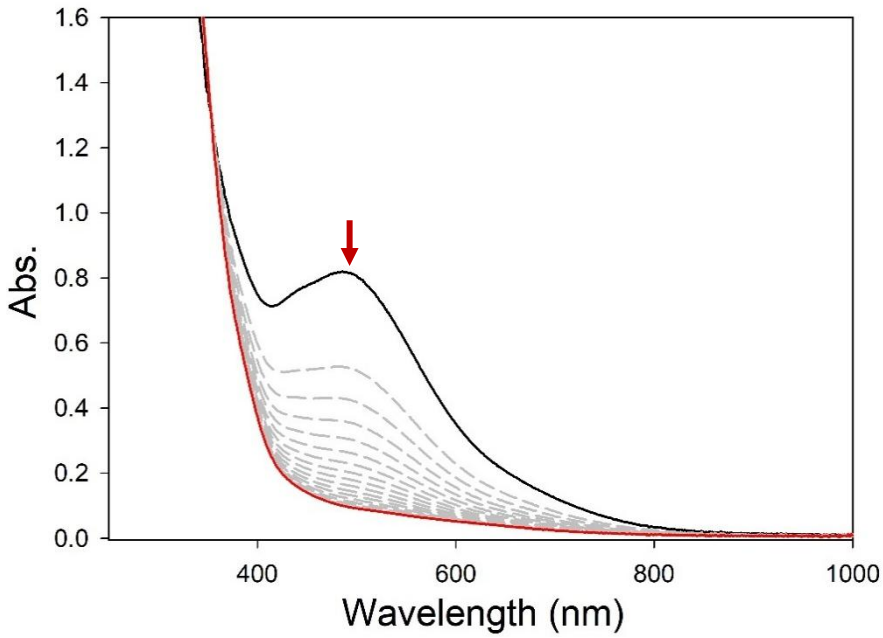

Figure S4.54. Time monitored UV-vis spectrum of *in-situ* generated $[Fe(PyH_2PS\text{-}p\text{-}CF_3)_2]^-$ at t = 0 h (back) until t = 8 h (red), recorded every 0.5 h (grey) in MeCN at 25 ˚C.

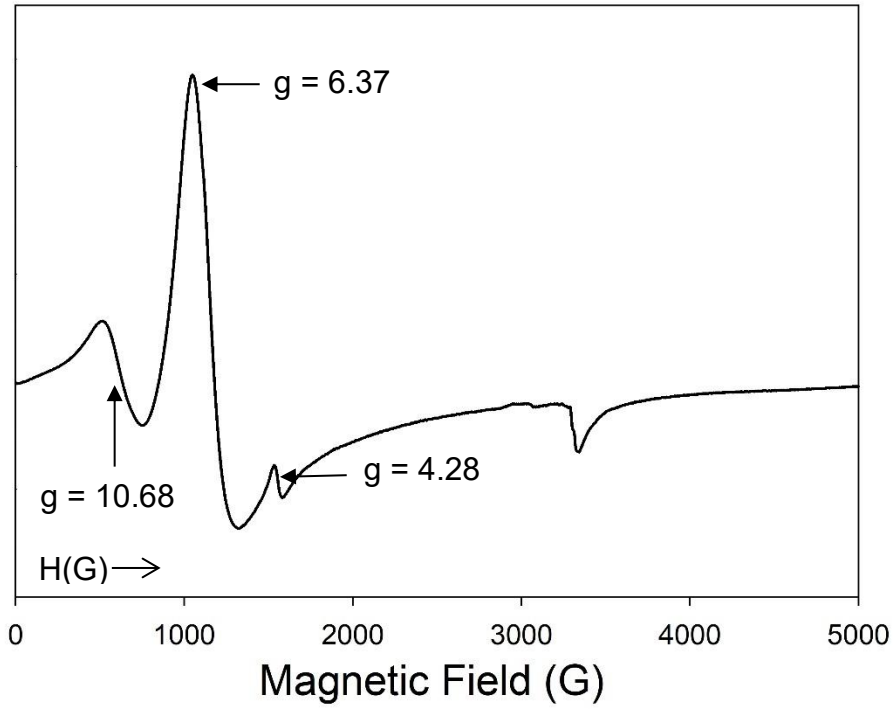

Figure S4.55. X-band (9.35 GHz) EPR spectrum of *in-situ* generated $[Fe(PyH_2PS\text{-}p\text{-}CF_3)_2]^-$ in MeCN:Tol (1:1) at 10 K. Spectromete settings: microwave power, 10.0 mW; modulation frequency, 100 kHz; modultation amplitude, 2.00 G.

Table S4.4. Table SX. Summary of Crystal Data and Intensity Collection and Structure Refinement Parameters for $(Et_4N)_2[Fe(PyH_2PS\text{-}p\text{-}CF_3)_2]$ (**4**).

Parameters	**4**
Formula	$C_{42}H_{22}F_{12}FeN_6O_4S_4 \bullet 2(C_6NH_{16}) \bullet 1.5(C_4OH_8)$
MW	1399.29
Crystal system	Triclinic
Space group	P1
Crystal color, habit	Orange, Block
a, Å	10.471
b, Å	17.004
c, Å	20.382
α, deg	78.173
β, deg	83.145
γ, deg	75.990
V, Å^3	3437.0
Z	2
$\rho_{calcd,}$ g/cm^3	1.276
T, K	150
abs coeff, μ (Mo Kα), mm^{-1}	0.43
θ limits, deg	27.7, 1.5
total no. of data	93179
no. of unique data	15906
no. of parameters	826
GOF of F^2	1.06
R_1,[a]	0.076
wR_2,[b]	0.236
max, min peaks, e/Å^3	1.04, -1.04

[a] $R_1 = \Sigma| |F_o| - |F_c| | / \Sigma |F_o|$; [b] $wR_2 = \{\Sigma[w(F_o^2 - F_c^2)^2]/\Sigma[w(F_o^2)^2]\}^{1/2}$

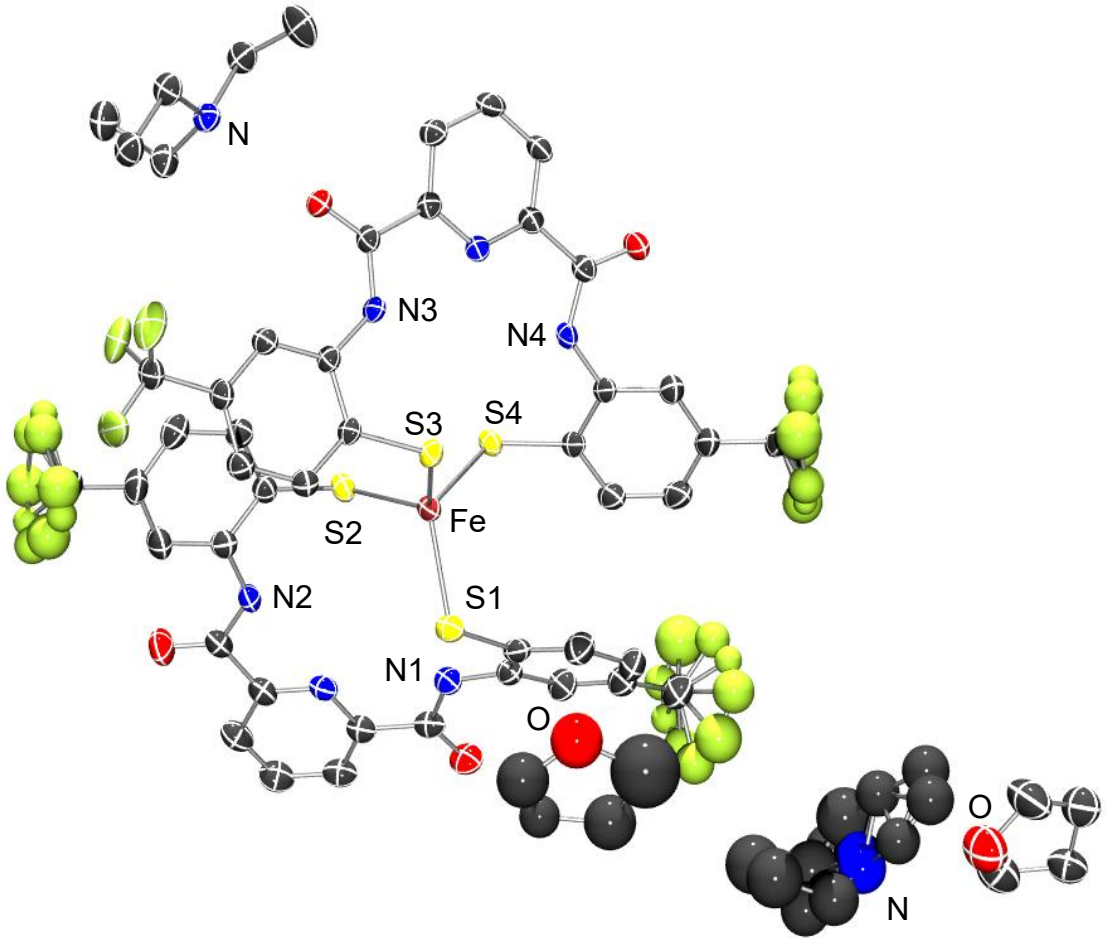

Figure SX. ORTEP diagram of $[Fe(PyH_2PS\text{-}p\text{-}CF_3)_2]^{2-}$ at 50% thermal probability ellipsoids. H atoms are omitted for clarity. Disorder in three of the trifluoromethyl groups consisting of atoms (F1-F9) is shown.

Table S4.4. Select bond distances (Å) and angles (deg) of $[Fe(PyH_2PS\text{-}p\text{-}CF_3)_2]^{2-}$ (**4**).

	4
Atoms	**Bond Distances (Å)**
$Fe\text{-}S_1$	2.379
$Fe\text{-}S_2$	2.337
$Fe\text{-}S_3$	2.379
$Fe\text{-}S_4$	2.336
$S_1\text{-}N_1$	2.980
$S_2\text{-}N_2$	2.953
$S_3\text{-}N_3$	2.953
$S_4\text{-}N_4$	2.987
	Bond Angles (°)
$S_1\text{-}Fe\text{-}S_2$	112.6
$S_1\text{-}Fe\text{-}S_3$	108.4
$S_1\text{-}Fe\text{-}S_4$	121.1
$S_2\text{-}Fe\text{-}S_3$	119.2
$S_2\text{-}Fe\text{-}S_4$	86.9
$S_3\text{-}Fe\text{-}S_4$	108.0
τ_4	0.85

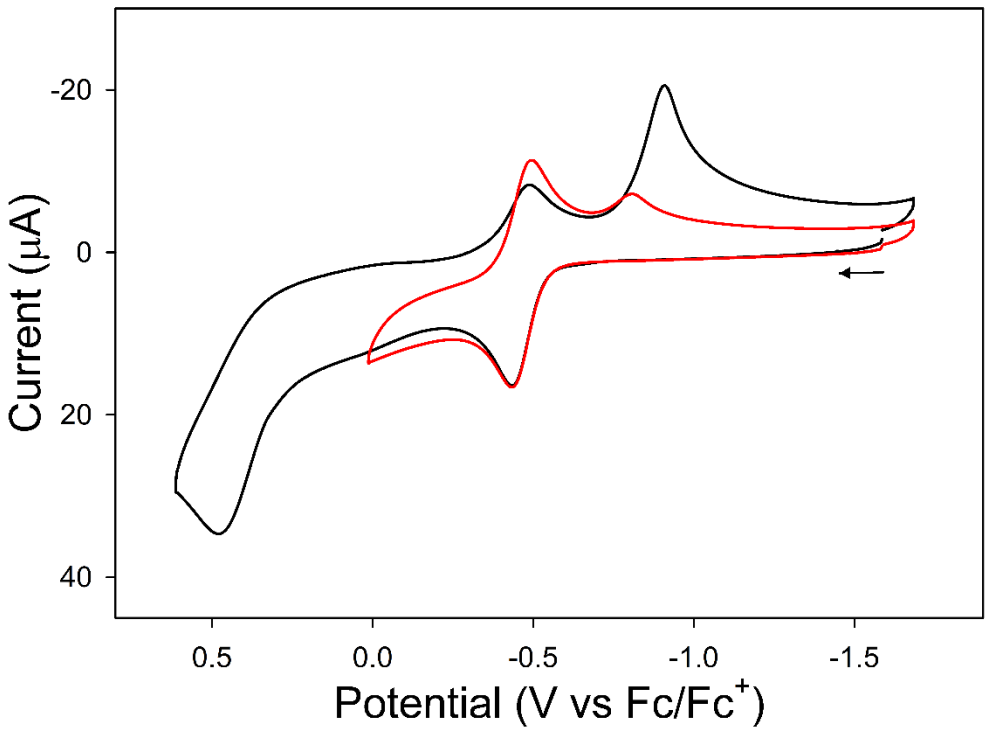

Figure S4.57. CV of **4** (1 mM) in MeCN at RT (0.25 M $^{n}Bu_4NPF_6$ supporting electrolyte, glassy carbon working electrode, 100 mV/s scan rate). Arrow shows direction of scan.

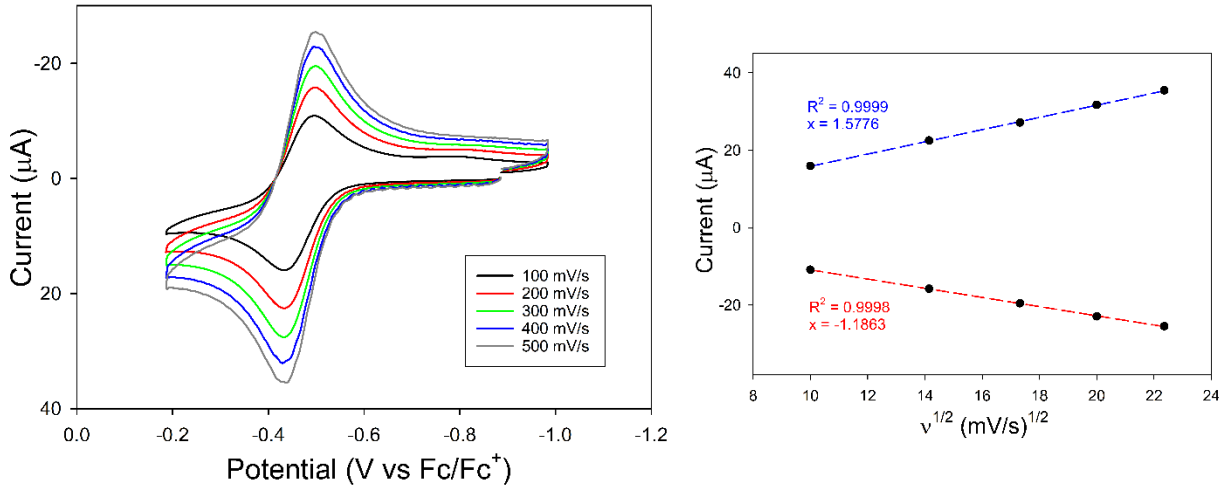

Figure S4.58. Scan speed dependency of Fe(III/II) couple of **4** (1 mM) in MeCN at RT (0.25 M $^{n}Bu_4NPF_6$ supporting electrolyte, glassy carbon working electrode, 100 mV/s scan rate).

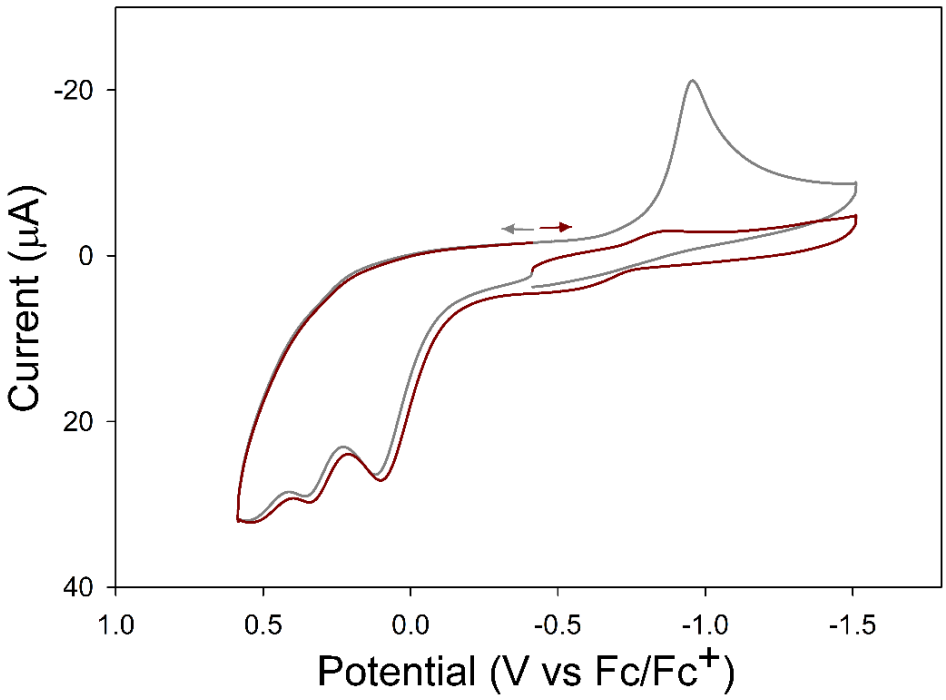

Figure S4.59. CV of **5** (1 mM) in MeCN at RT (0.25 M $^{n}Bu_4NPF_6$ supporting electrolyte, glassy carbon working electrode, 100 mV/s scan rate). Arrow shows direction of scan.

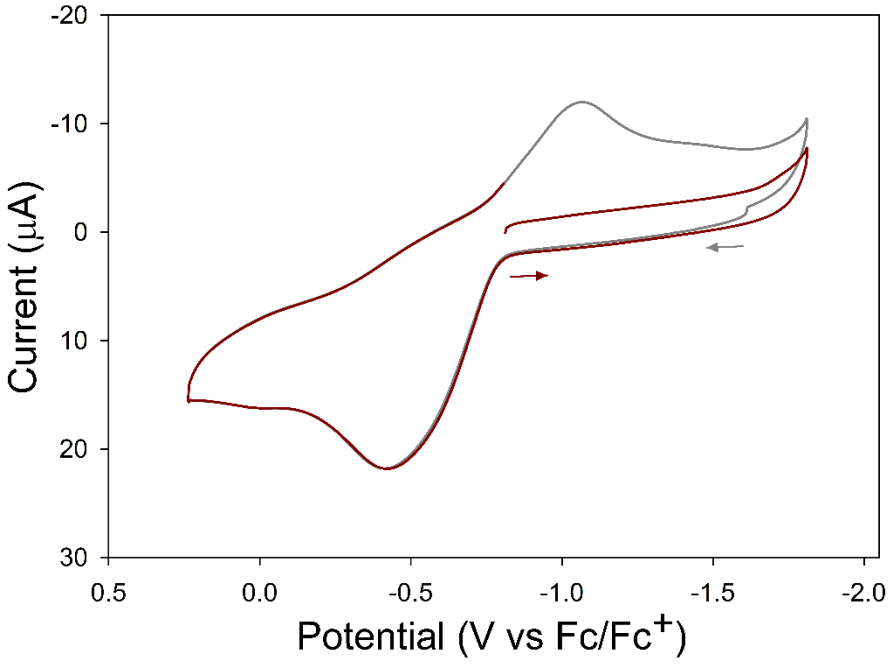

Figure S4.60. CV of $(Et_3NH)_2(PyPH_2S\text{-}p\text{-}CF_3)$ (1 mM) in MeCN at RT (0.25 M $^{n}Bu_4NPF_6$ supporting electrolyte, glassy carbon working electrode, 100 mV/s scan rate). Arrow shows direction of scan.

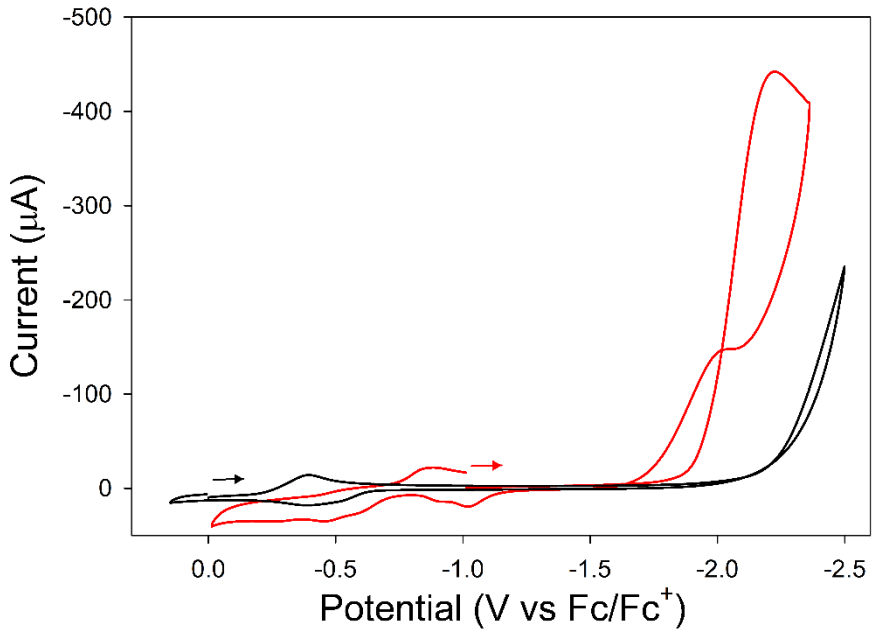

Figure S4.61. CV of $(Et_4N)_2[FeCl_4]$ alone (black) and with equal-molar **4** (red). Both spectra are recorded with 50 mol-equiv. of AcOH in MeCN at RT (0.25 M $^nBu_4NPF_6$ supporting electrolyte, glassy carbon working electrode, 100 mV/s scan rate). Arrow shows direction of scan.

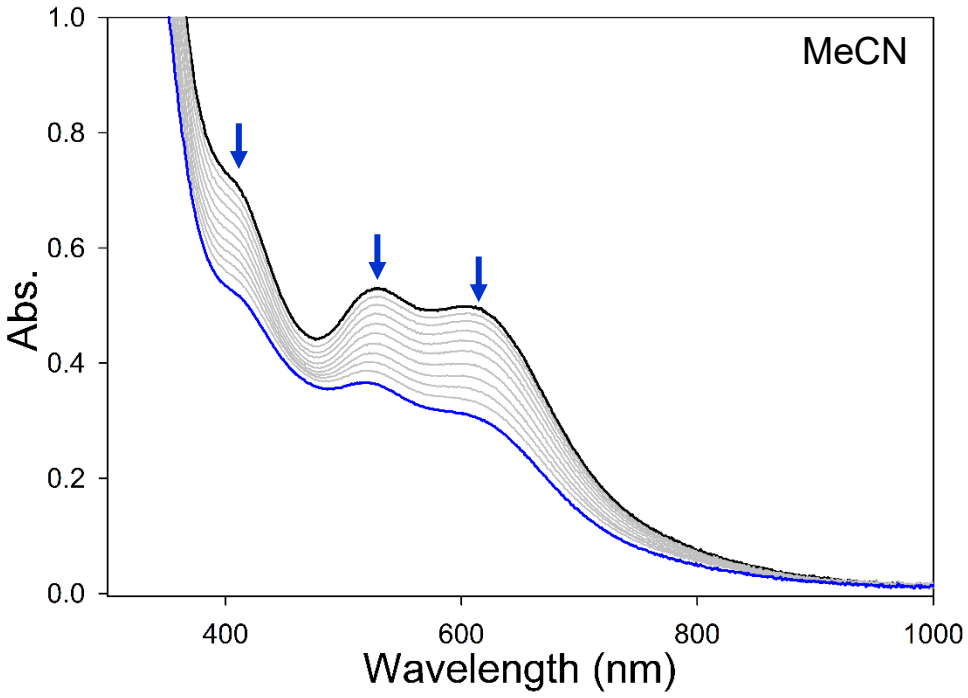

Figure S4.62. UV-vis spectrum of **1** (black) with addition of 50 mol-equiv. of AcOH (grey) up to 1000 mol-equiv of AcOH (red) in *MeCN* at 23 ˚C.

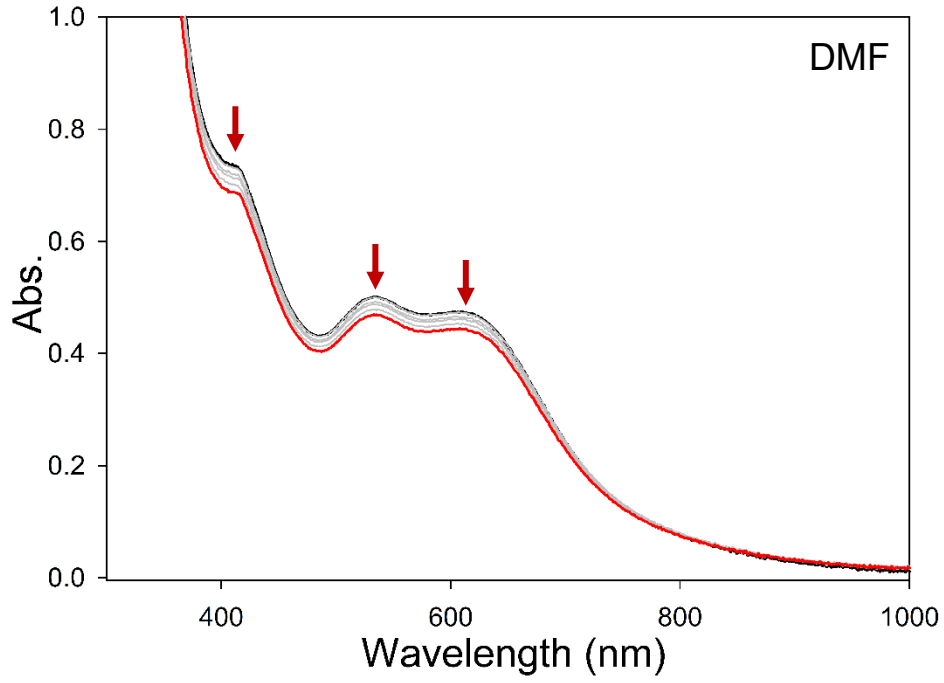

Figure S4.63. UV-vis spectrum of **1** (black) with addition of 200 mol-equiv. of AcOH (grey) up to 1000 mol-equiv of AcOH (red) in *DMF* at 23 ˚C.

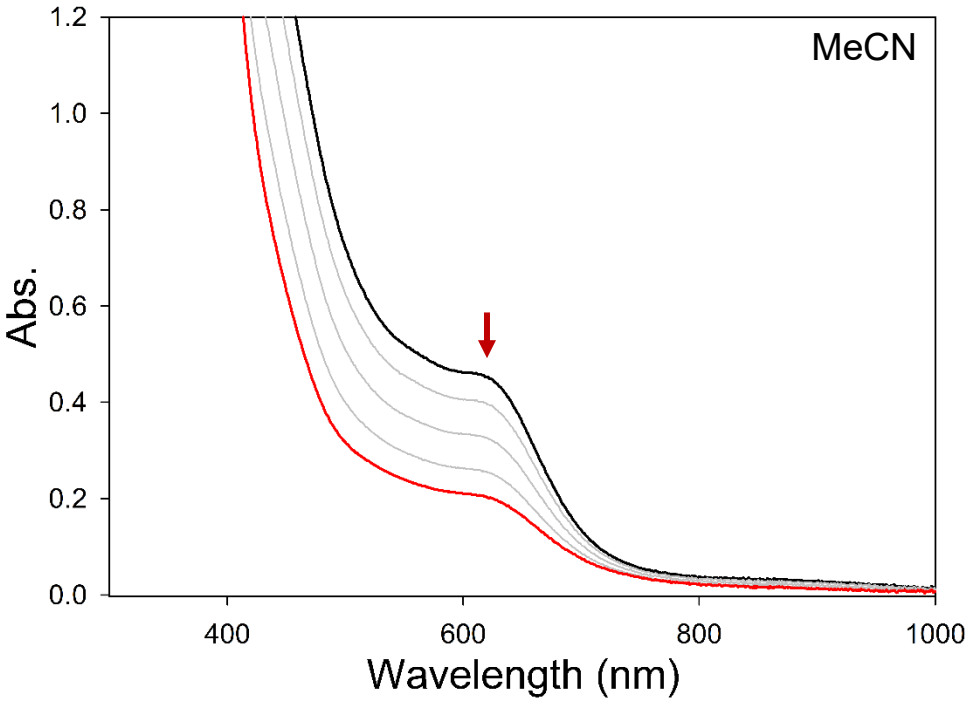

Figure S4.64. UV-vis spectrum of **2** (black) with addition of 1 mol-equiv. of AcOH (grey) up to 4 mol-equiv of AcOH (red) in *MeCN* at 23 ˚C.

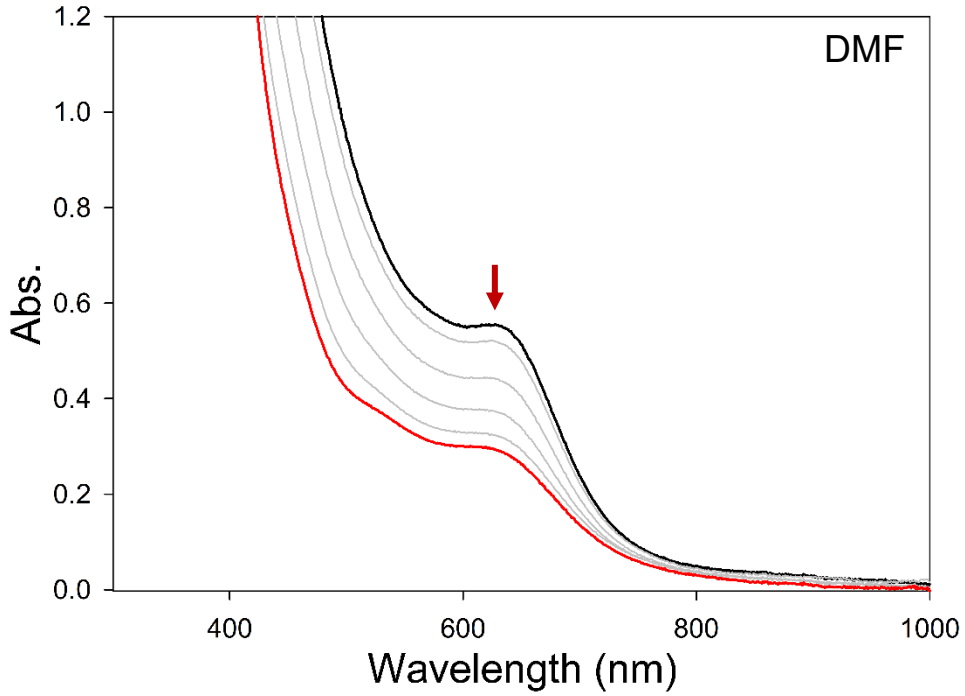

Figure S4.65. UV-vis spectrum of **2** (black) with addition of 10 mol-equiv. of AcOH (grey) up to 50 mol-equiv of AcOH (red) in *DMF* at 23 ˚C.

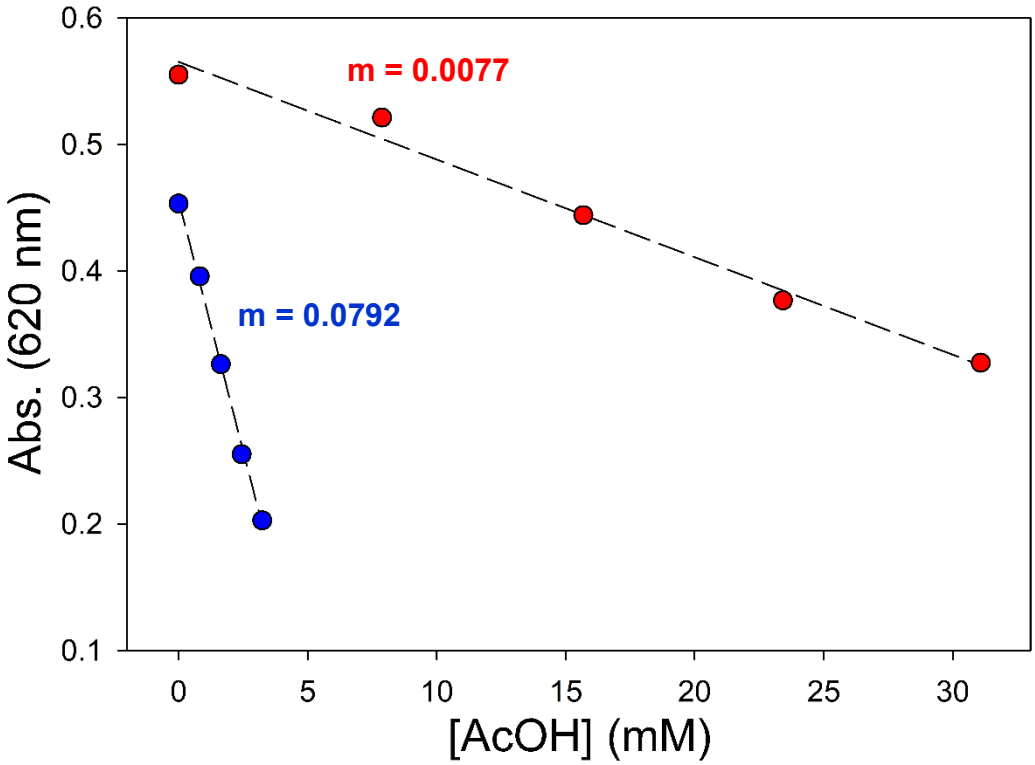

Figure S4.66. Protic stability of **2** assessed by the absorbance 620 nm versus AcOH concentration from UV-vis acid titration experiments, Figures S4.65 and S4.65.

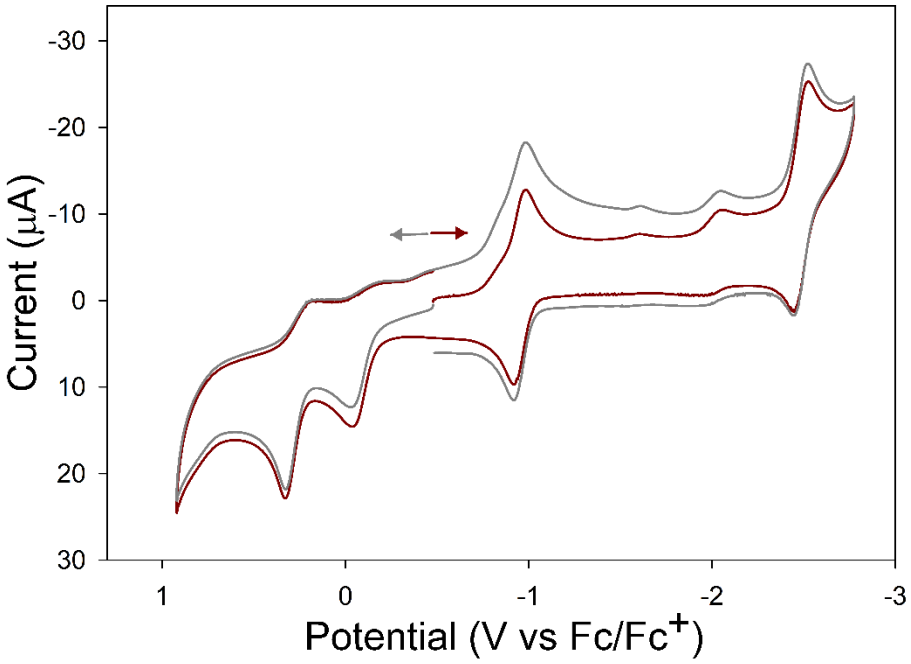

Figure S4.67. CV of **1** (1 mM) in DMF at RT (0.25 M $^{n}Bu_4NPF_6$ supporting electrolyte, glassy carbon working electrode, 100 mV/s scan rate). Arrow shows direction of scan.

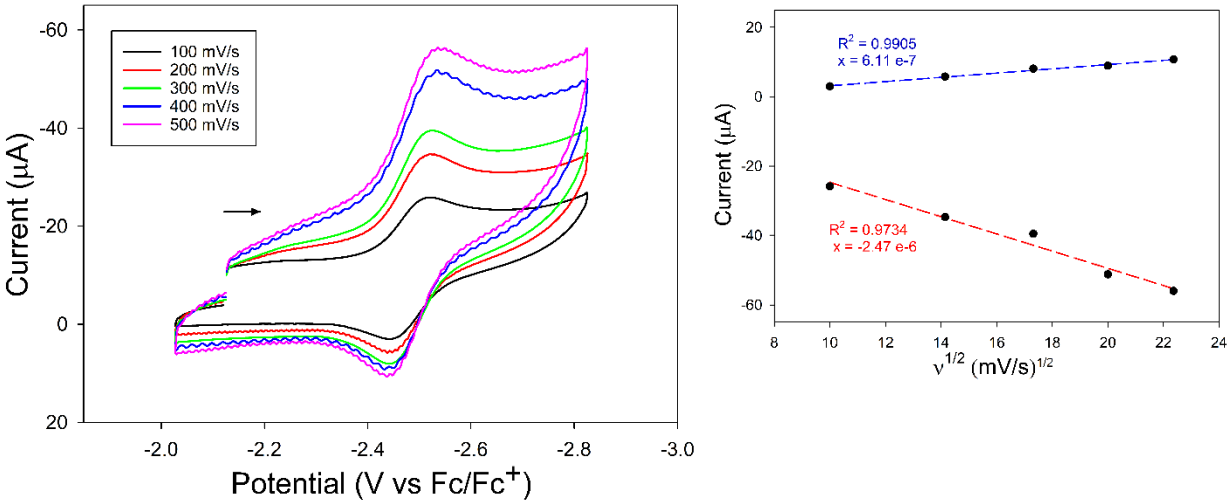

Figure S4.68. Scan speed dependency of $E_{1/2}$ = -2.49 V couple of **1** (1 mM) in DMF at RT (0.25 M $^{n}Bu_4NPF_6$ supporting electrolyte, glassy carbon working electrode, 100 mV/s scan rate).

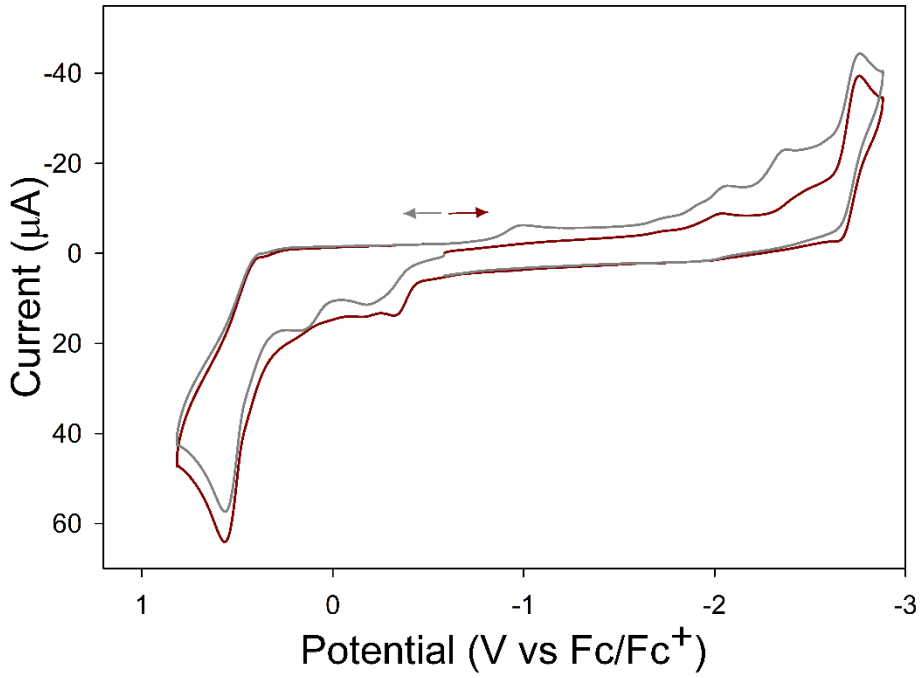

Figure S4.69. Full CV of **3** (1 mM) scan in DMF at RT (0.25 M $^{n}Bu_4NPF_6$ supporting electrolyte, glassy carbon working electrode, 100 mV/s scan rate). Arrow shows direction of scan.

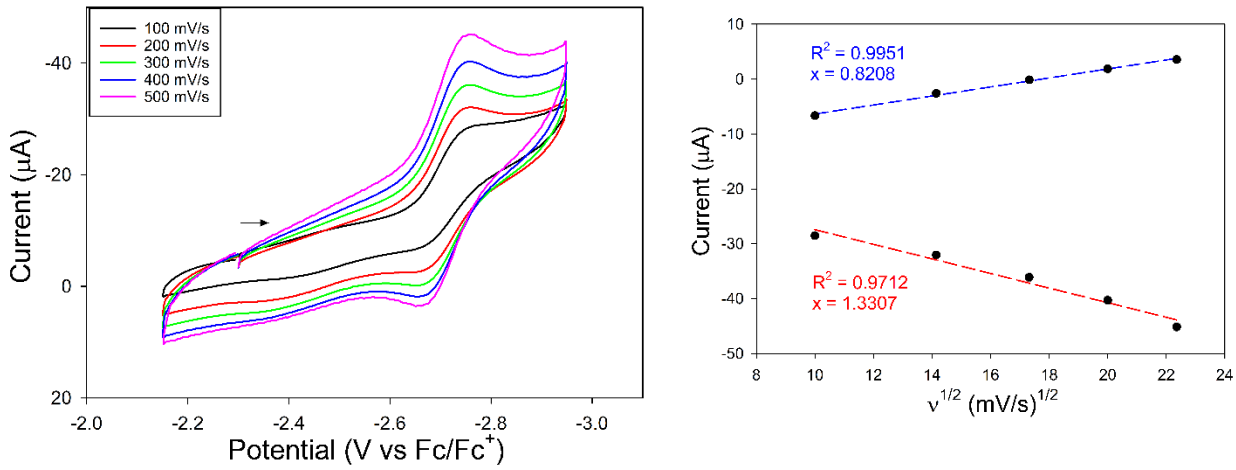

Figure S4.70. Scan speed dependency of $E_{1/2}$ = -2.71 V couple of **3** (1 mM) in DMF at RT (0.25 M $^{n}Bu_4NPF_6$ supporting electrolyte, glassy carbon working electrode, 100 mV/s scan rate).

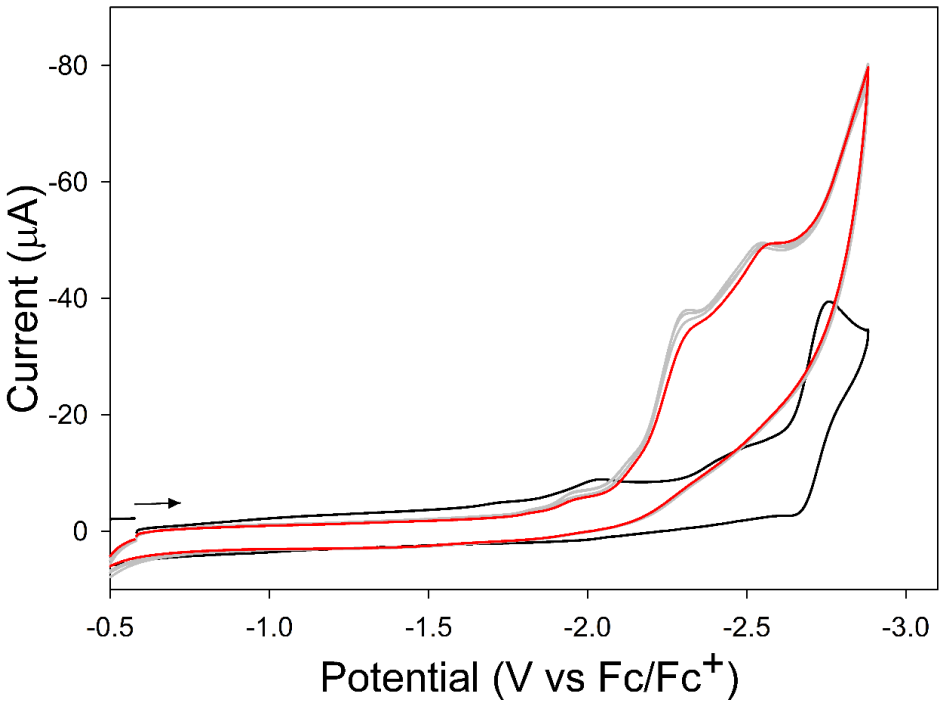

Figure S4.71. CV **3** (1 mM) in DMF with increasing mol-equivalents of AcOH from 0 (black) to 50 mol-equiv (red) with every scan in between (grey) 10 mol-equiv at RT (0.25 M $^{n}Bu_4NPF_6$ supporting electrolyte, glassy carbon working electrode, 100 mV/s scan rate). Arrow shows direction of scan.

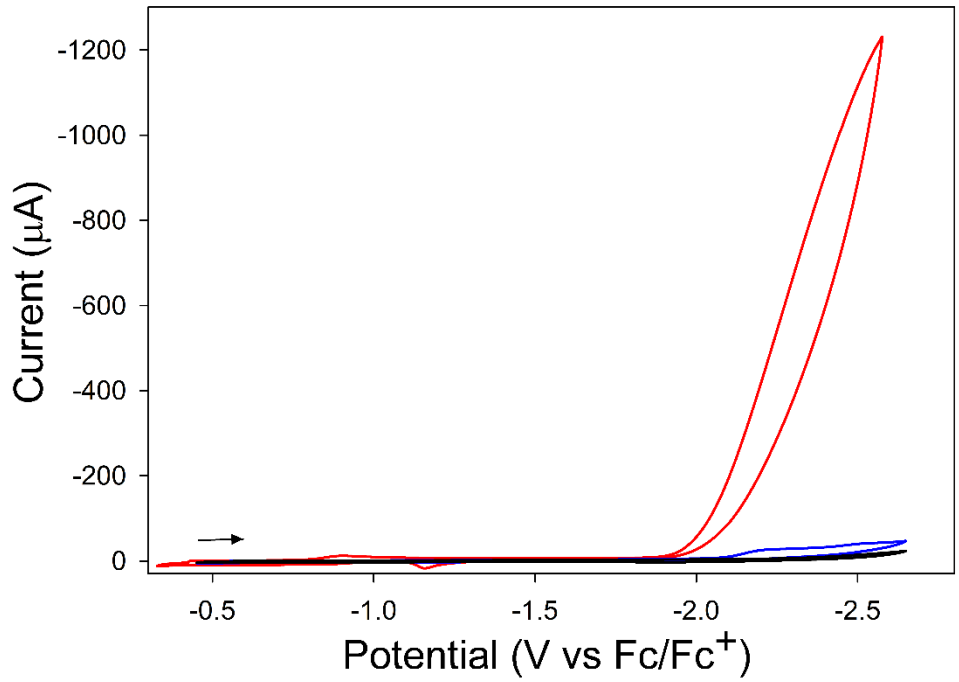

Figure S4.72. CV of **1** (1 mM, red), **3** (1 mM, blue), and electrolyte (black) with 0.30 M of AcOH in DMF at RT (0.25 M $^{n}Bu_4NPF_6$ supporting electrolyte, glassy carbon working electrode, 100 mV/s scan rate). Arrow shows direction of scan.

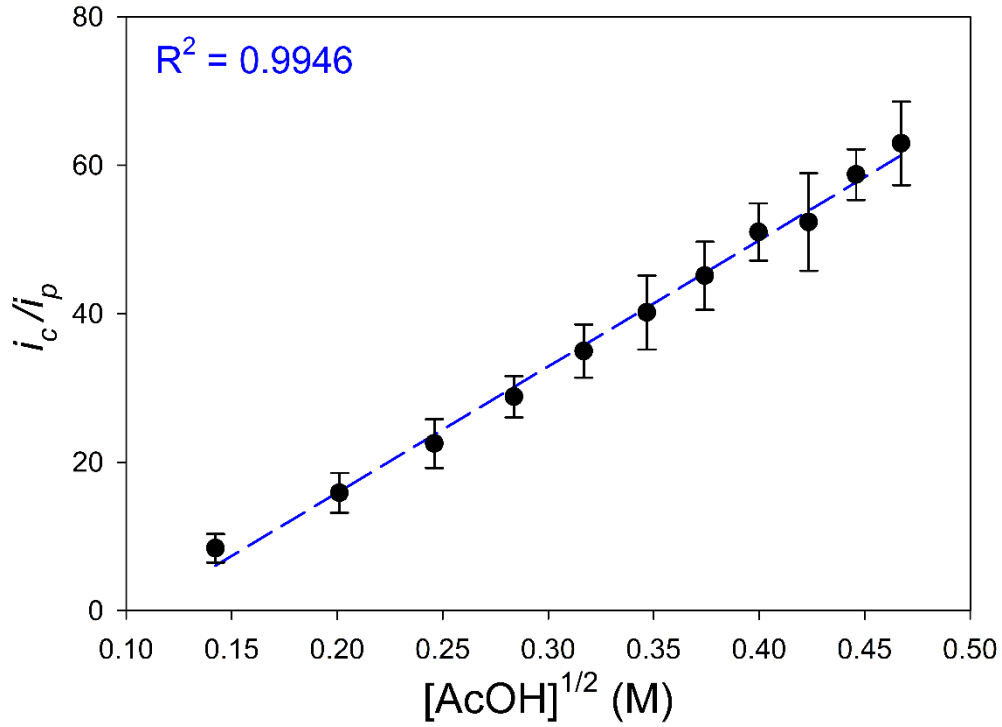

Figure S4.73. Normalized catalytic current (i_c/i_p) dependency on the square-root of AcOH concentration.

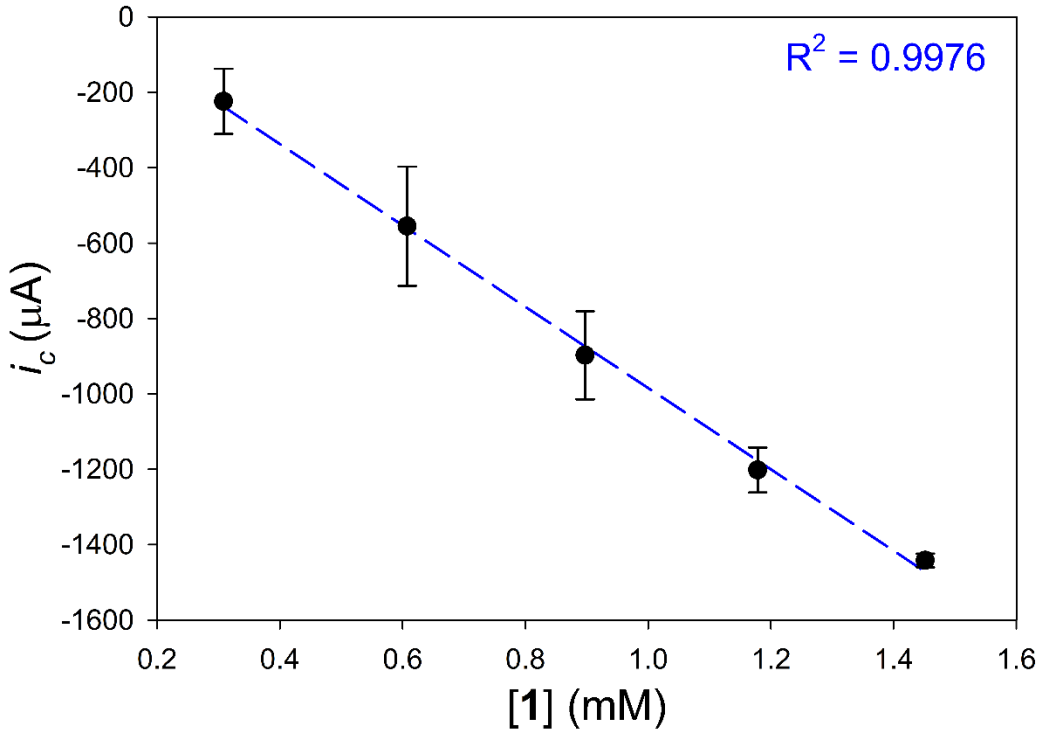

Figure S4.74. Catalytic current, at E_{cat} (~−2.7 V vs Fc/Fc^+), dependency on the concentration of **1**.

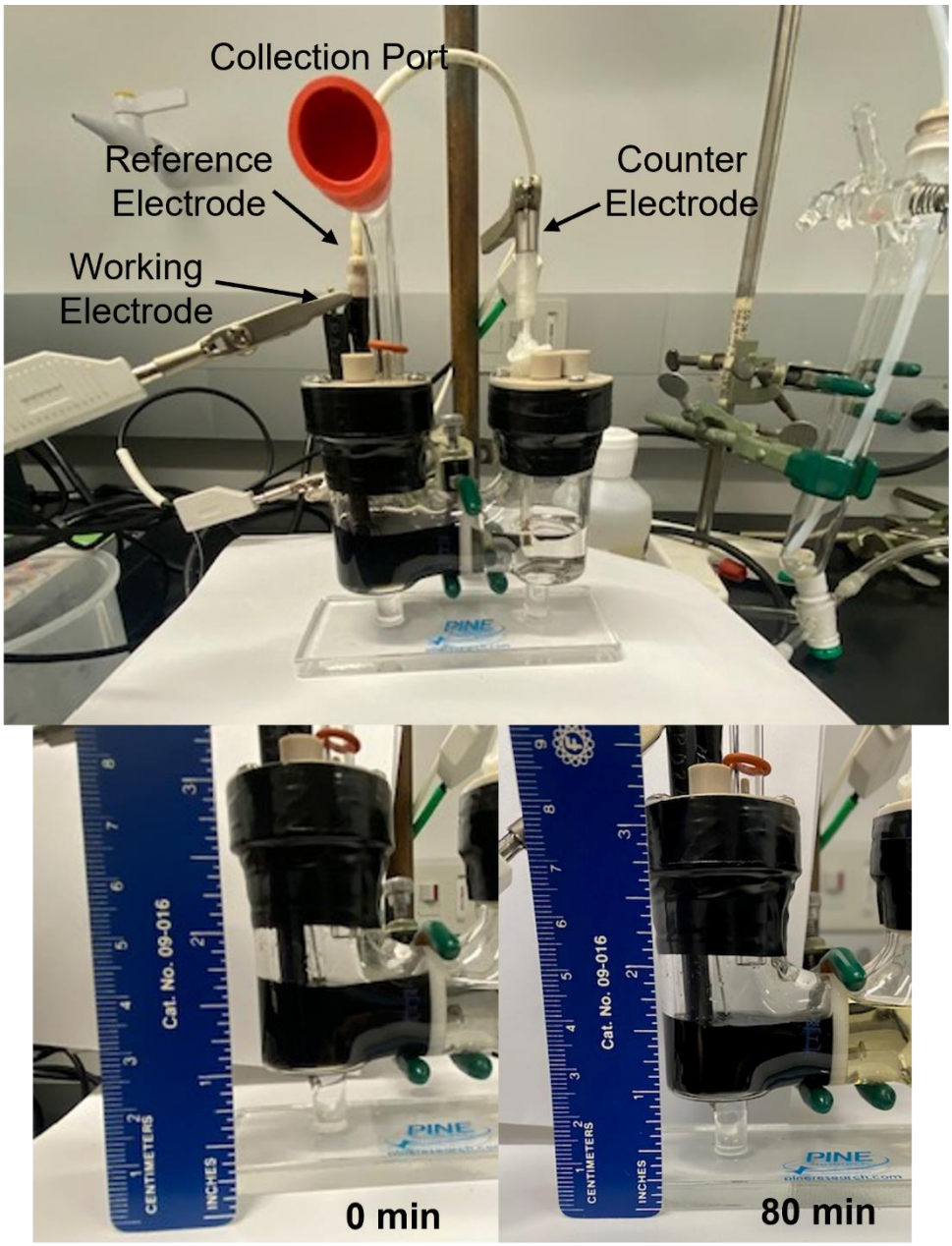

Figure S4.75. *Top*: experimental set-up for bulk-electrolysis experiments of **1** with 270 mol-equiv of AcOH. *Bottom*: zoom-in of the working electrode compartment during the experiment at (*left*) 0 and (*right*) 80 min.

^{1}H NMR (600 MHz, C_6D_6, 25 °C) from Headspace Post-Electrolysis

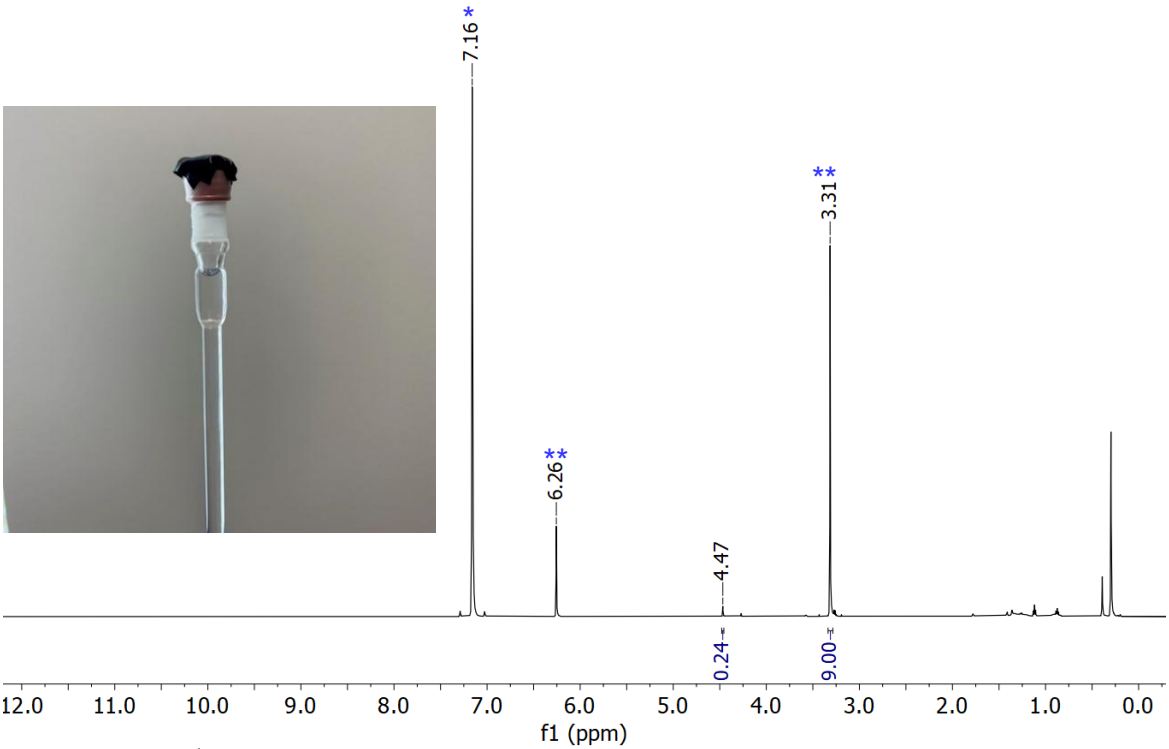

Figure S4.76. ^{1}H NMR spectrum of 0.5 mL of headspace of the working electrode compartment post-electrolysis with 1,3,5-trimethoxybenzene as the internal standard (observed at 6.26 and 3.31 pm and is indicated with **) in C_6D_6 at 25 °C (δ vs. protio signal). Residual C_6H_6 is observed at 7.16 ppm and is indicated with *. *Inset*: J-young tube post-injection of headspace.

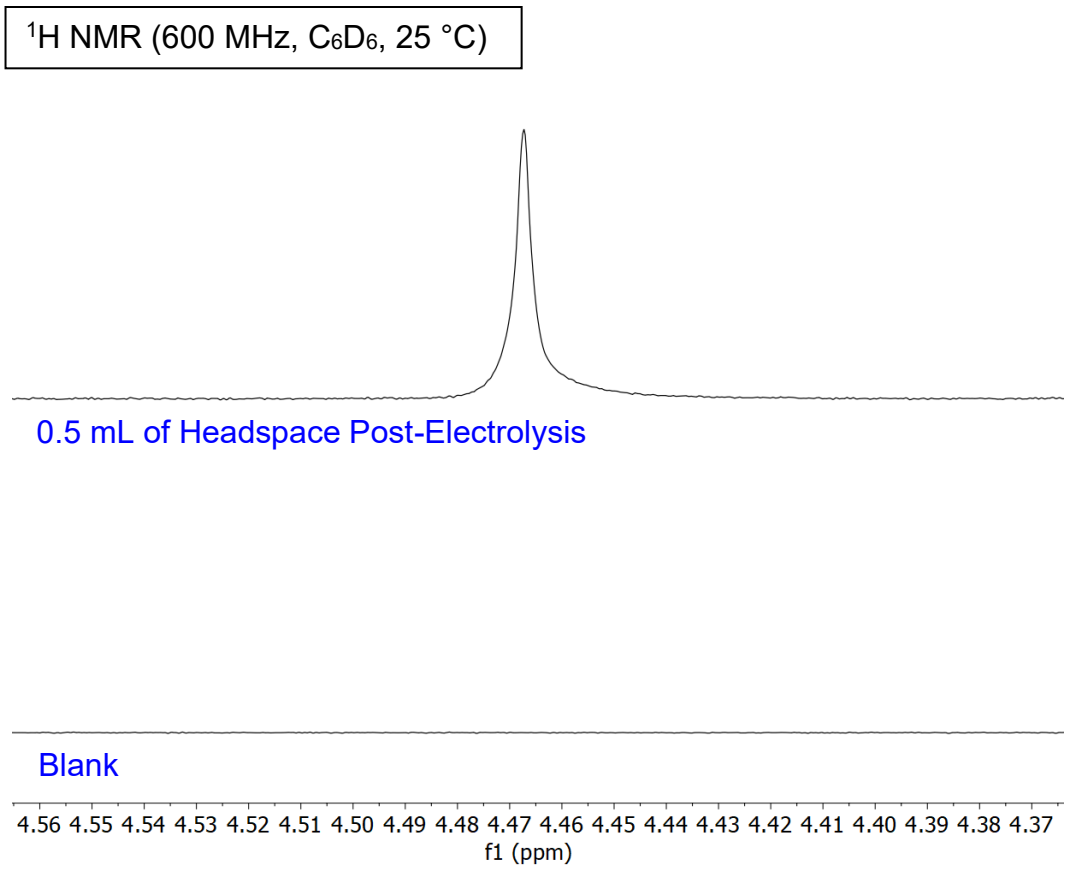

Figure S4.77. *Top***:** expansion of the ^{1}H NMR spectrum in Figure S4.76. *Bottom*: expansion of the ^{1}H NMR spectrum prior to injection of 0.5 mL of the working electrode compartment in C_6D_6 at 25 °C (δ vs. protio signal). Residual C_6H_6 is observed at 7.16 ppm and is indicated with *.

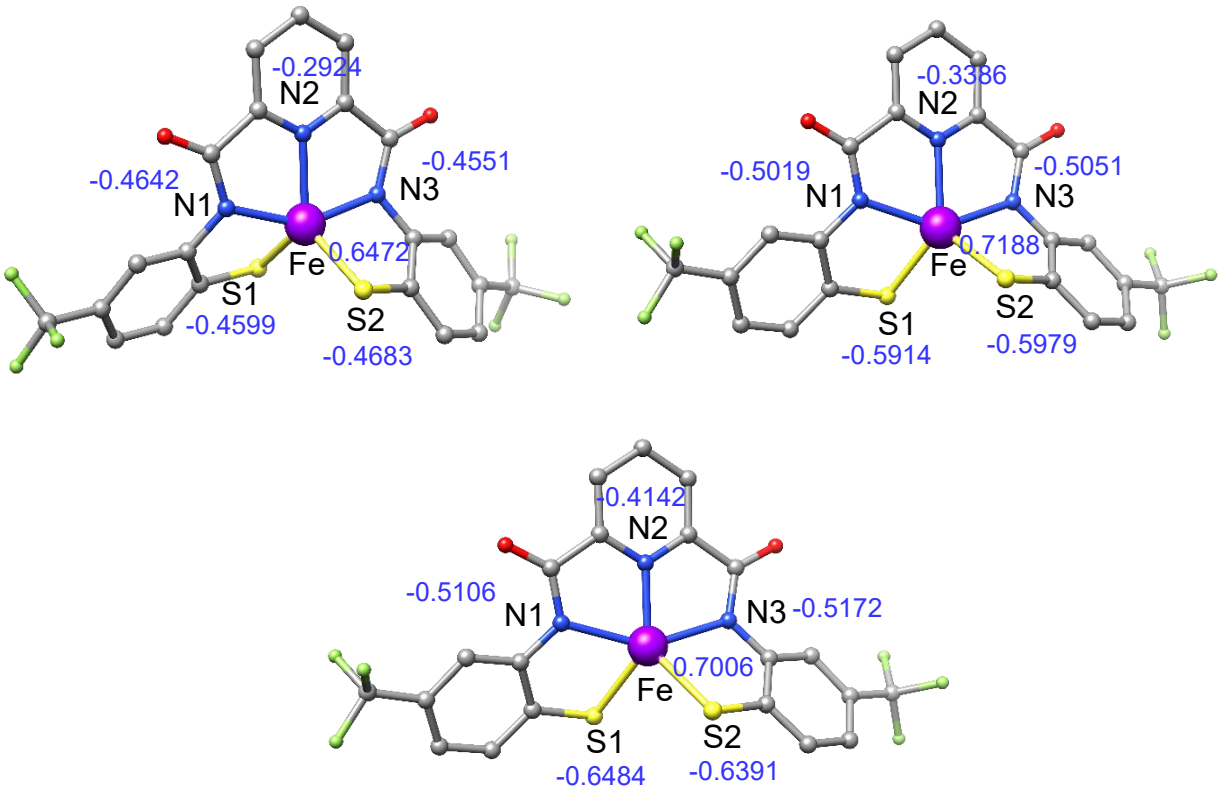

Figure S4.78. Optimized structures of **1** (S = 5/2) (*top left*), **2** (S = 2) (*top right*), $\mathbf{2^R}$ (S = 3/2) (*bottom*) in the gas-phase (B3LYP, def2-TZVPP). H atoms are omitted; purple = Fe; yellow = S; blue = N; red = O; yellow-green = F; gray = C.

Table S4.5. Select bond distances (Å) and angles (deg) of optimized structures (B3LYP/def2-TZVPP) of **1**, **2**, and $\mathbf{2^R}$ in the gas-phase.

	1 ($S = 5/2$)	**2** ($S = 2$)	$\mathbf{2^R}$ ($S = 3/2$)
Fe-S_1	2.312	2.431	2.492
Fe-S_2	2.334	2.408	2.519
Fe-N_1	2.060	2.184	2.243
Fe-N_2	2.111	2.172	2.028
Fe-N_3	2.045	2.218	2.224
S_1-Fe-S_2	112.0	104.6	97.5
S_1-Fe-N_1	84.4	79.7	77.8
S_1-Fe-N_2	123.1	124.2	132.5
S_1-Fe-N_3	108.3	124.7	122.4
S_2-Fe-N_1	117.5	121.4	126.8
S_2-Fe-N_2	124.7	131.2	129.9
S_2-Fe-N_3	83.9	80.1	77.1
N_1-Fe-N_2	75.1	72.6	74.6
N_1-Fe-N_3	149.8	144.8	149.1
N_2-Fe-N_3	75.0	72.4	74.7
τ_5	0.42	0.23	0.28

Table S4.6. Löwdin population analysis derived from the DFT calculations (B3LYP/def2-TZVPP) for selected MOs of **1*** (*S* = 5/2) with CPCMC(DMF). Only s and p contributions were tabulated for S, C, O, and N-atoms.

α Orbitals	**MO#**	**Energy (eV)**	**%Fe**	**%S**	**%2,6-Py***
LUMO + 3	149	-0.7295	0.3	3.6	-
LUMO + 2	148	-0.8212	1.5	4.8	-
LUMO + 1	147	-1.7860	0.6	0.2	31.8
LUMO	146	-1.9073	2.3	1.0	65.9
HOMO	145	-5.4804	5.2	44.5	0.6
HOMO - 1	144	-5.6438	7.7	36.7	6.2
HOMO - 2	143	-6.0050	18.6	26.0	-
HOMO - 3	142	-6.3436	1.9	36.9	-

β Orbitals	**MO#**	**Energy (eV)**	**%Fe**	**%S**	**%2,6-Py**
LUMO + 3	144	-2.3594	70.7	14.5	4.1
LUMO + 2	143	-2.5732	14.8	3.7	5.1
LUMO + 1	142	-2.7723	77.6	1.3	4.2
LUMO	141	-2.9278	54.9	12.8	1.3
HOMO	140	-5.7117	12.5	47.4	6.3
HOMO - 1	139	-5.8576	12.1	25.0	5.6
HOMO - 2	138	-6.2118	1.8	13.8	4.9
HOMO - 3	137	-6.4741	7.4	16.5	2.2

*2,6-Py = pyridine-2,6-diamide

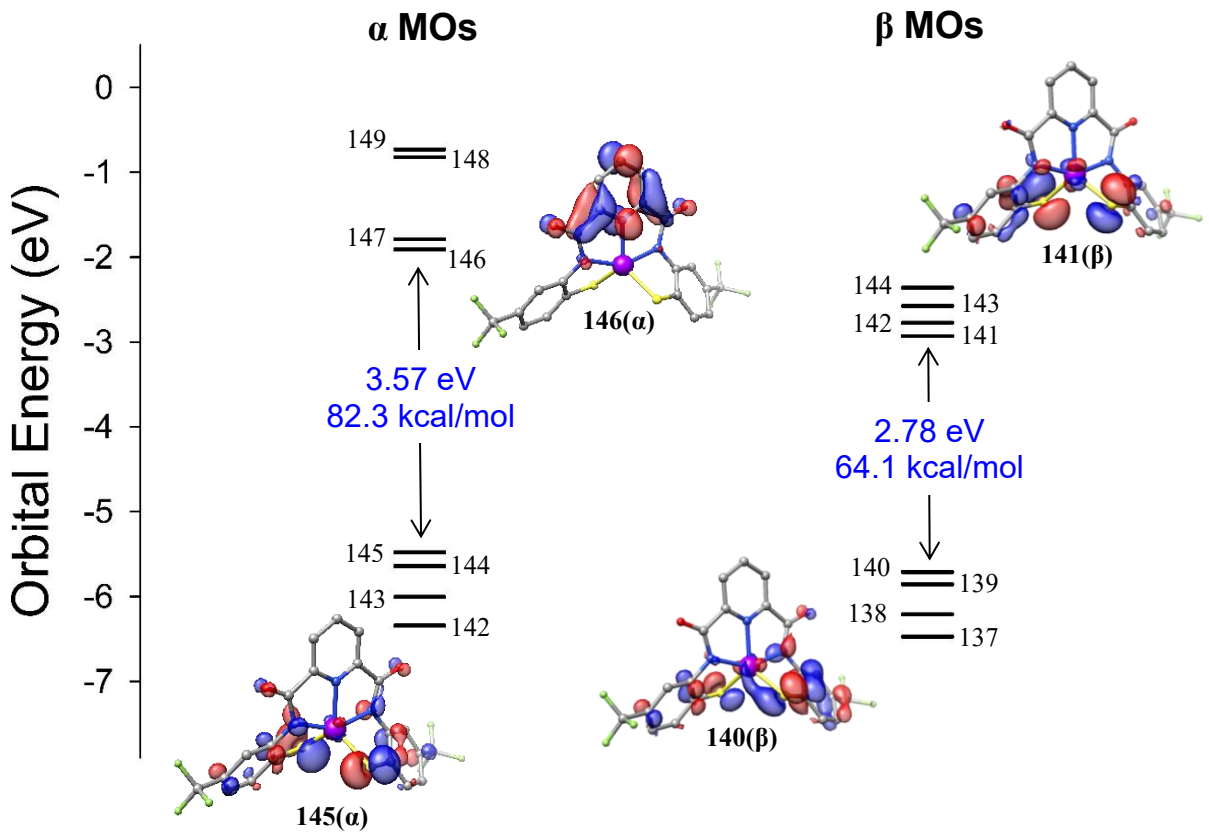

Figure S4.79. DFT-generated isosurface plots (B3LYP/def2-TZVPP) with CPCMC(DMF) of the frontier MOs of **1*** (S = 5/2) (from *gas-phase* geometry optimization). Spin-up (α) MOs (*left*); spin-down (β) MOs (*right*).

Table S4.7. Löwdin population analysis derived from the DFT calculations for selected MOs of **2*** (*S* = 2) B3LYP/def2-TZVPP with CPCMC(DMF). Only s and p contributions were tabulated for S, C, O, and N-atoms.

α Orbitals	**MO#**	**Energy (eV)**	**%Fe**	**%S**	**%2,6-Py***
LUMO + 3	149	-0.3571	0.7	6.3	-
LUMO + 2	148	-0.3886	0.7	5.1	-
LUMO + 1	147	-1.2885	0.7	0.7	34.2
LUMO	146	-1.3810	2.7	1.0	64.7
HOMO	145	-4.6077	7.3	49.2	3.9
HOMO - 1	144	-4.8576	13.1	39.7	1.8
HOMO - 2	143	-5.2226	23.6	16.5	-
HOMO - 3	142	-5.4129	14.7	63.6	-

β Orbitals	**MO#**	**Energy (eV)**	**%Fe**	**%S**	**%2,6-Py***
LUMO + 3	145	-0.4828	22.1	0.7	-
LUMO + 2	144	-0.5642	65.5	3.6	-
LUMO + 1	143	-1.3265	4.4	0.1	32.9
LUMO	142	-1.6145	14.8	0.7	53.9
HOMO	141	-4.4705	83.3	1.3	0.4
HOMO - 1	140	-4.8169	4.2	48.7	0.7
HOMO - 2	139	-5.1610	8.8	32.1	-
HOMO - 3	138	-5.6965	1.9	21.5	-

*2,6-Py = pyridine-2,6-diamide

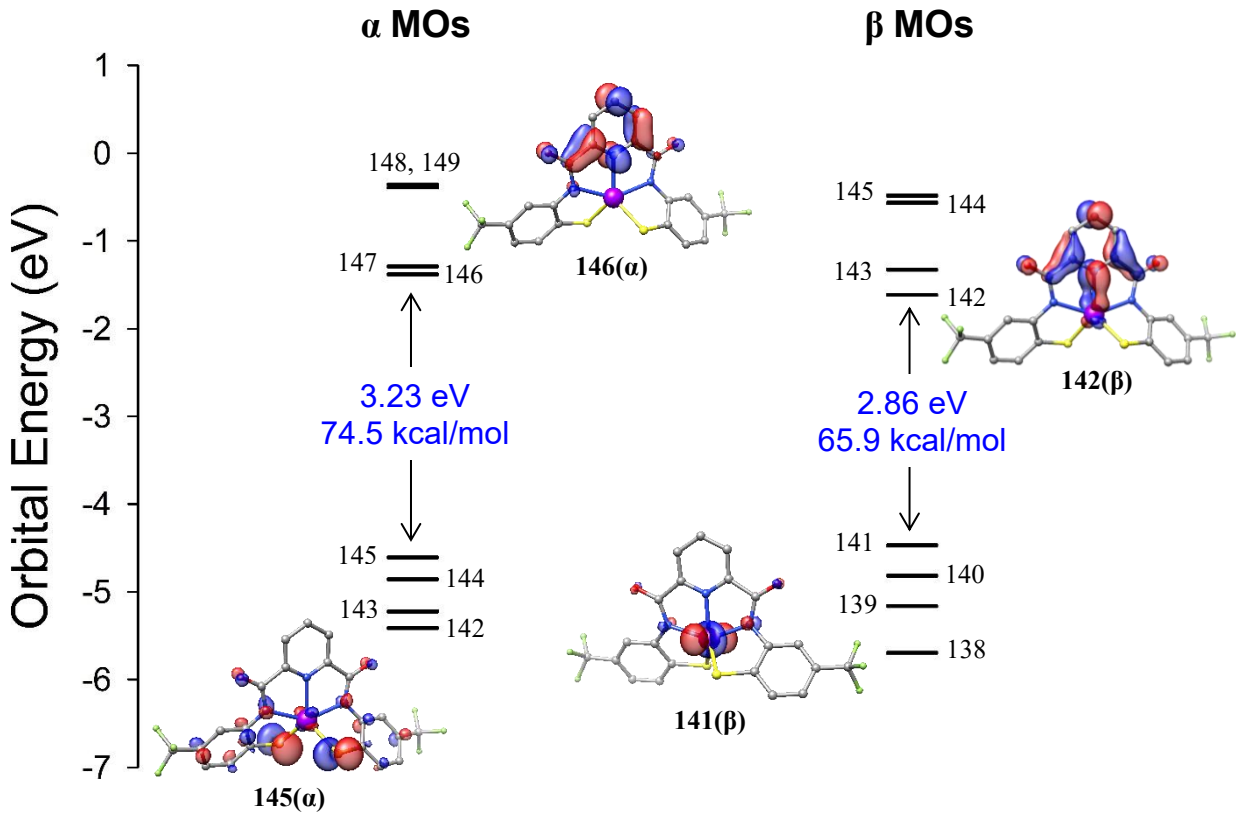

Figure S4.80. DFT-generated isosurface plots (B3LYP/def2-TZVPP) with CPCMC(DMF) of the frontier MOs of **2*** ($S = 2$) (from *gas-phase* geometry optimization). Spin-up (α) MOs (*left*); spin-down (β) MOs (*right*).

Table S4.8. Gibbs free energies from frequency calculations (B3LYP/def2-TZVPP with CPCMC(DMF)) of $\mathbf{2^R}$ at different spin states.

Complex	Spin	Gibbs Free Energy (Eh)	ΔG (kcal/mol)
$[Fe(PyPS\text{-}p\text{-}CF_3)]^{3-}$	3/2	-3778.84255988	0.0
$[Fe(PyPS\text{-}p\text{-}CF_3)]^{3-}$	5/2	-3778.82972368	7.9

Table S4.9. Löwdin population analysis derived from the DFT calculations for selected MOs of $\mathbf{2^R}$ (S = 3/2) (B3LYP/def2-TZVPP) with CPCMC(DMF). Only s and p contributions were tabulated for S, C, O, and N-atoms.

α Orbitals	MO#	Energy (eV)	%Fe	%S	%2,6-Py*
LUMO + 3	149	-0.0964	0.6	4.2	12.5
LUMO + 2	148	-0.1310	0.3	4.0	10.7
LUMO + 1	147	-0.4620	2.7	1.7	44.0
LUMO	146	-0.5852	0.8	1.2	45.8
HOMO	145	-4.1494	8.1	44.2	7.7
HOMO - 1	144	-4.3163	28.7	15.8	40.7
HOMO - 2	143	-4.4825	11.8	25.2	6.7
HOMO - 3	142	-4.8649	18.0	57.3	6.9

β Orbitals	MO#	Energy (eV)	%Fe	%S	%2,6-Py*
LUMO + 3	146	0.0828	52.3	1.1	4.7
LUMO + 2	145	-0.1323	1.9	4.8	13.1
LUMO + 1	144	-0.1565	1.9	2.1	10.1
LUMO	143	-0.7353	4.0	0.6	42.6
HOMO	142	-2.4411	13.3	0.4	59.1
HOMO - 1	141	-3.7279	87.2	1.1	0.5
HOMO - 2	140	-4.3498	3.2	44.1	1.6
HOMO - 3	139	-4.6978	7.4	24.4	2.0

*2,6-Py = pyridine-2,6-diamide

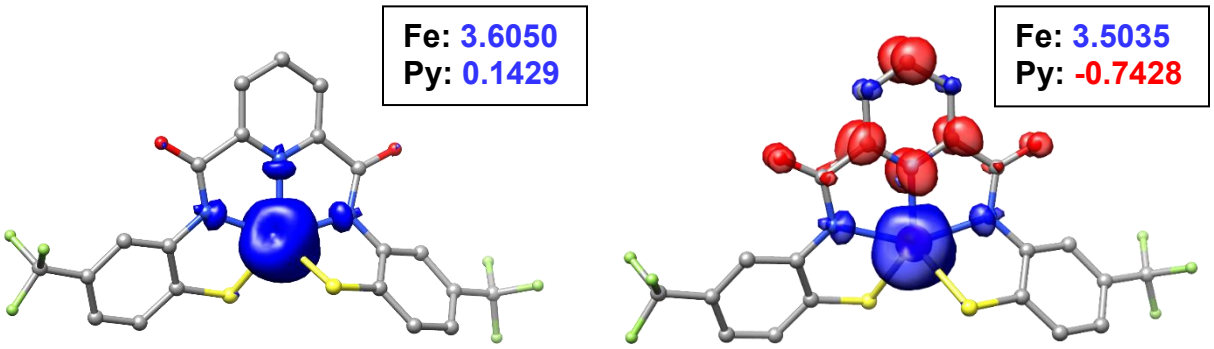

Figure S4.81. DFT-generated Löwdin spin density plot of **2*** (S = 2) (*left*) and $\mathbf{2^R}$ (S = 3/2) (*right*) (blue = positive spin density; red = negative spin density).

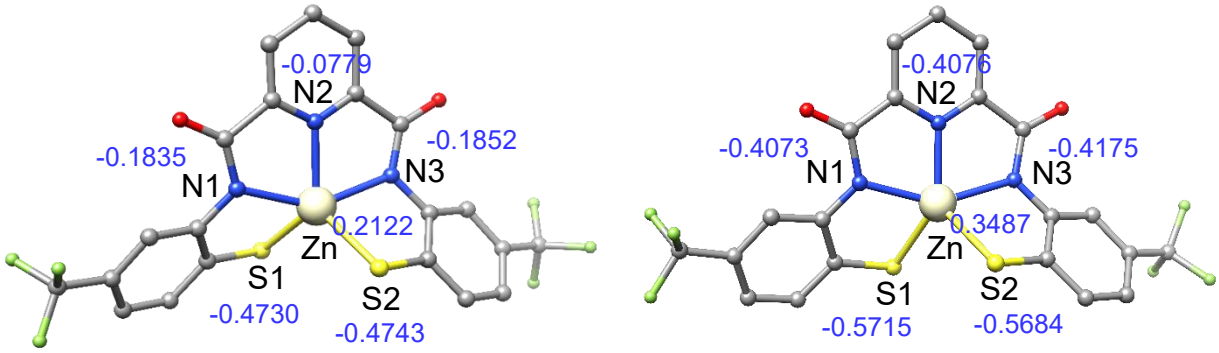

Figure S4.82. Optimized structures of **3** (S = 0) (*left*) and **3^{R}** (S = 1/2) (*right*) in the gas-phase (B3LYP, def2-TZVPP). H atoms are omitted; white = Zn; yellow = S; blue = N; red = O; yellow-green = F; gray = C.

Table S4.10. Select bond distances (Å) and angles (deg) of optimized structure of **3** and **3^{R}** in the gas-phase (B3LYP, def2-TZVPP).

	3 (S = 0.0)	**3^{R}** (S = 1/2)
Zn-S_1	2.417	2.541
Zn-S_2	2.401	2.454
Zn-N_1	2.160	2.218
Zn-N_2	2.144	2.049
Zn-N_3	2.163	2.166
S_1-Zn-S_2	110.8	100.0
S_1-Zn-N_1	81.1	77.3
S_1-Zn-N_2	123.8	124.3
S_1-Zn-N_3	119.2	122.8
S_2-Zn-N_1	116.8	118.5
S_2-Zn-N_2	125.4	135.7
S_2-Zn-N_3	81.7	81.2
N_1-Zn-N_2	73.5	74.6
N_1-Zn-N_3	147.3	150.9
N_2-Zn-N_3	73.8	76.5
τ_5	0.37	0.25

Table S4.11. Löwdin population analysis derived from the DFT calculations (B3LYP/def2-TZVPP) for selected MOs of **3*** with CPCMC(DMF). Only s and p contributions were tabulated for S, C, O, and N-atoms.

Orbitals	MO#	Energy (eV)	%Zn	%S	%2,6-Py*
LUMO + 3	149	-0.3290	0.7	3.9	--
LUMO + 2	148	-0.3722	1.1	6.4	--
LUMO + 1	147	-1.2235	0.6	0.4	64.2
LUMO	146	-1.2996	2.4	0.8	84.0
HOMO	145	-4.7775	3.2	42.7	11.9
HOMO - 1	144	-5.0278	5.0	34.6	12.0
HOMO - 2	143	-5.6327	5.0	33.1	--
HOMO - 3	142	-5.6501	4.1	38.8	--

*2,6-Py = pyridine-2,6-diamide

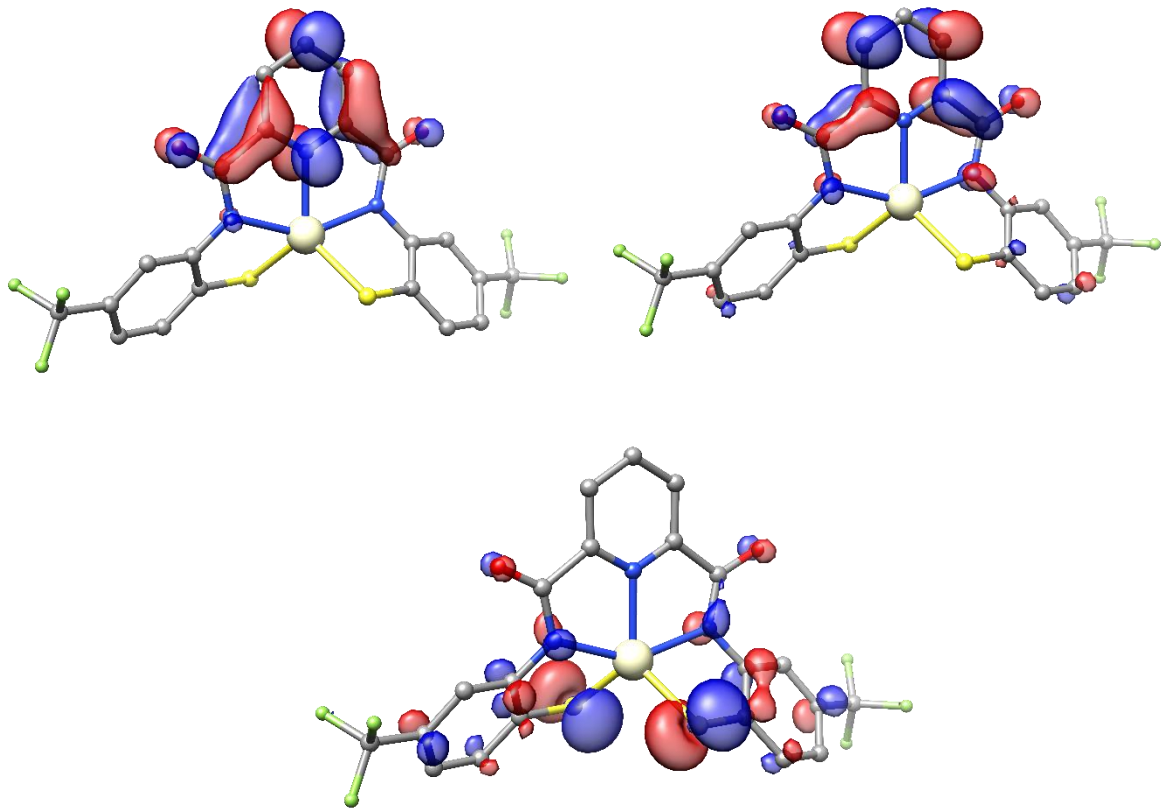

Figure S4.83. DFT-generated isosurface plots (B3LYP/def2-TZVPP) of the frontier MOs of **3*** (*S* = 0) (from *gas-phase* geometry optimization). LUMO (*top left*); LUMO + 1 *(top right*); HOMO (*bot*).

Table S4.12. Löwdin population analysis derived from the DFT calculations for selected MOs of $\mathbf{3^R}$ (S = 1/2) (B3LYP/def2-TZVPP) with CPCMC(DMF). Only s and p contributions were tabulated for S, C, O, and N-atoms.

α Orbitals	MO#	Energy (eV)	%Zn	%S	%2,6-Py*
LUMO + 3	150	0.3825	2.0	0.0	8.3
LUMO + 2	149	-0.0395	0.5	4.6	2.9
LUMO + 1	148	-0.1374	0.9	6.8	4.1
LUMO	147	-0.5709	1.1	1.1	57.9
HOMO	146	-2.1269	2.6	11.0	79.3
HOMO - 1	145	-4.3108	2.6	44.0	15.7
HOMO - 2	144	-4.6103	4.3	32.8	14.3
HOMO - 3	141	-4.9899	8.3	20.9	54.7

β Orbitals	MO#	Energy (eV)	%Zn	%S	%2,6-Py*
LUMO + 3	149	0.0076	0.7	4.5	5.8
LUMO + 2	148	-0.1180	0.9	4.9	6.1
LUMO + 1	147	-0.3562	3.3	1.8	64.9
LUMO	146	-0.4865	0.8	1.4	50.8
HOMO	145	-4.2404	2.7	39.0	20.1
HOMO - 1	144	-4.5800	3.9	31.5	18.1
HOMO - 2	143	-4.9286	8.7	21.4	54.3
HOMO - 3	142	-5.1865	3.1	40.9	30.7

*2,6-Py = pyridine-2,6-diamide

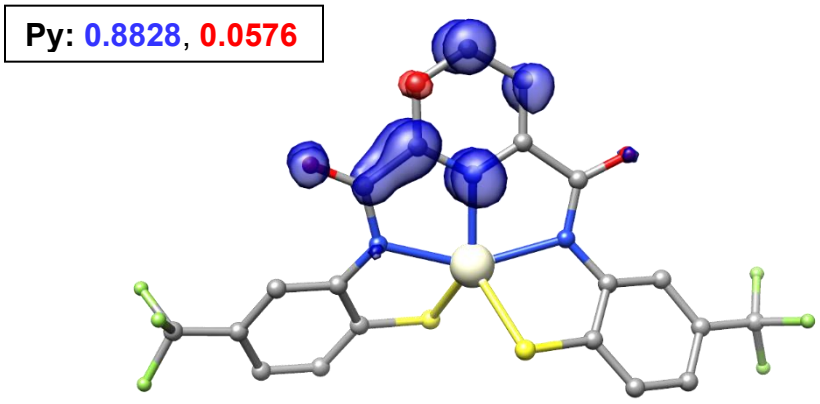

Figure S4.84. DFT-generated Löwdin spin density plot of $\mathbf{3^R}$ (S = 1/2) (blue = positive spin density; red = negative spin density).

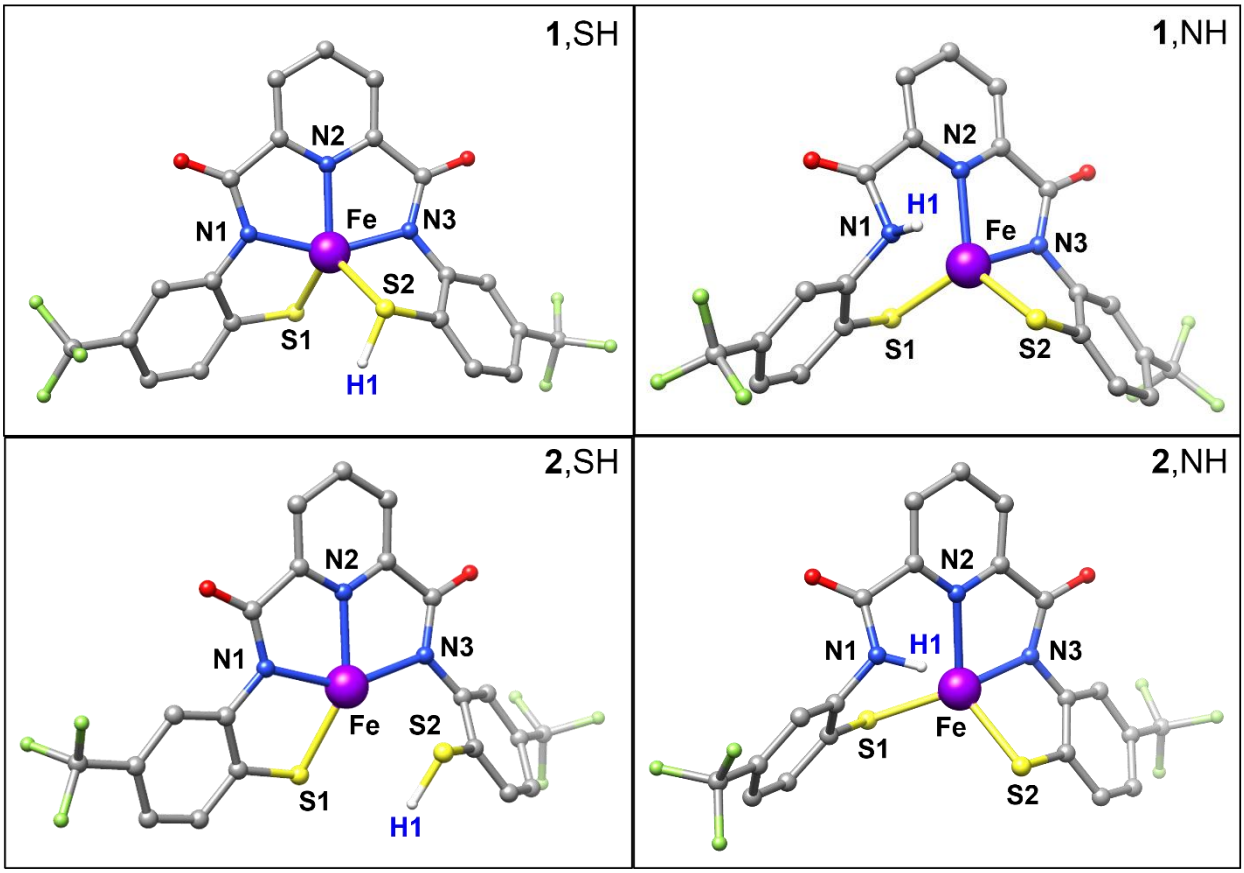

Figure S4.85. DFT-optimized structures of proposed protonated complexes of **1** and **2** in the as phase (B3LYP/TZVPP), see Table S4.13 for structural metrics**.**

Table S4.13. Select bond distances (Å) and angles (deg) of optimized structure of protonated intermediates of **1** and **2** in the gas-phase (B3LYP, def2-TZVPP), see Figure S4.86 for structures.

	1,SH	**1**,NH	**2**,SH	**2**,NH
Fe-S_1 (Å)	2.271	2.300	2.353	2.334
Fe-S_2 (Å)	2.507	2.260	2.772	2.352
Fe-N_1 (Å)	2.010	2.945	2.120	2.905
Fe-N_2 (Å)	2.075	2.164	2.121	2.239
Fe-N_3 (Å)	2.028	1.954	2.150	2.019
S_2-H_1 (Å)	1.349	---	1.349	---
N_1-H_1 (Å)	---	1.015	---	1.015
τ_5	0.44	---	---	---
τ_4	---	0.74	0.44	0.64

Table S4.14. Charge, multiplicity (2S + 1), and Gibbs free energy of each DFT computed intermediate utilizing CPCMC(DMF).

Compound	Charge	Multiplicity	Gibbs Free Energy (Eh)
1	-1	6	-3778.630003
1,SH	0	6	-3779.045638
1,NH	0	6	-3779.039648
2	-2	5	-3778.637502
2,SH	-1	5	-3779.076705
2,NH	-1	5	-3779.07974
Et_3N	0	1	-291.9124992
Et_3NH	+1	1	-292.3667916

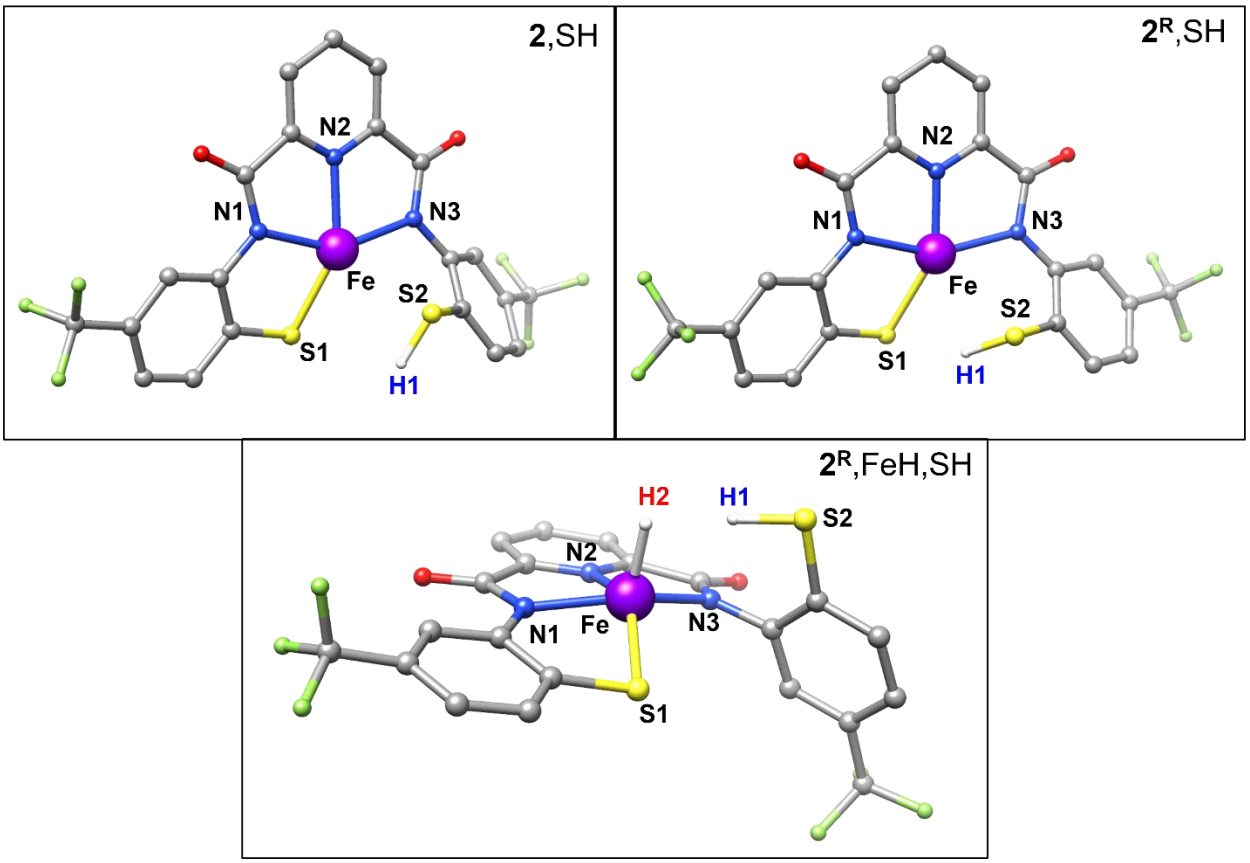

Figure S4.86. DFT-optimized structures (B3LYP, def2-TVZPP, gas-phase) of proposed intermediates for E(CECE) mechanism of HER of **1**, see Table S4.15 for structural metrics**.**

Table S4.15. Structural and geometric metrics of DFT-optimized structures of proposed intermediates for E(CECE) mechanism of HER of **1,** see Figure S4.86 for structures.

	2,SH	**2^{R}**,SH	**2^{R}**FeH,SH	**2^{R2}**FeH,SH
Fe-S_1 (Å)	2.353	2.429	2.313	2.410
Fe-S_2 (Å)	2.772	2.922	3.767	2.431
Fe-N_1 (Å)	2.120	2.145	2.083	2.234
Fe-N_2 (Å)	2.121	1.982	2.105	2.177
Fe-N_3 (Å)	2.150	2.158	2.083	2.199
S_2-H_1 (Å)	1.349	1.349	1.368	---
Fe-H_2 (Å)	---	---	1.677	---
H_1-H_2	---	---	1.697	0.762
τ_5	---	---	0.09	0.24
τ_4	0.44	0.41	---	---

Table S4.16. Charge, multiplicity, and Gibbs free energy of each DFT computed intermediate utilizing CPCMC(DMF).

Compound	**Charge**	**Multiplicity**	**Gibbs Free Energy (Eh)**
1	-1	6	-3778.630003
2	-2	5	-3778.637502
2^{R}	-3	4	-3778.84256
3	-2	1	-4294.407366
3^{R}	-3	2	-4294.482649
Et_3N	0	1	-291.9124992
Et_3NH	+1	1	-292.3667916
2,SH	-1	5	-3779.076705
2^{R},SH	-2	4	-3779.296499
2^{R}FeH,SH	-1	6	-3779.683066

Table S4.17. Gibbs free energies from frequency calculations (B3LYP/def2-TZVPP with CPCMC(DMF)) of **2^{R},SH** at different spin states.

Spin	**Gibbs Free Energy (Eh)**	**ΔG (kcal/mol)**
2	-3779.296499	0.0
6	-3779.289600	4.3

Table S4.18. Löwdin population analysis derived from the DFT calculations for selected MOs of **2**$^{\mathbf{R}}$FeH,SH (*S* = 5/2) **(**B3LYP/def2-TZVPP) with CPCMC(DMF). Only s and p contributions were tabulated for S, C, O, and N-atoms.

α Orbitals	**MO#**	**Energy (eV)**	**Fe%**	**%S**	**%2,6-Py***
LUMO + 3	150	-0.7125	1.0	4.0	0.1
LUMO + 2	149	-0.9409	0.6	3.4	0.7
LUMO + 1	148	-1.7584	0.4	0.2	71.7
LUMO	147	-1.9001	2.2	0.6	74.8
HOMO	146	-5.3491	15.1	30.2	14.8
HOMO - 1	145	-5.8221	7.2	26.6	29.3
HOMO - 2	144	-6.2414	12.3	42.4	8.1
HOMO - 3	143	-6.3412	8.8	10.4	29.3

β Orbitals	**MO#**	**Energy (eV)**	**%Fe**	**%S**	**%2,6-Py***
LUMO + 3	145	-2.4148	66.7	9.1	7.0
LUMO + 2	144	-2.5537	79.0	1.1	8.7
LUMO + 1	143	-2.7028	67.5	6.3	14.8
LUMO	142	-2.7703	71.8	1.5	15.6
HOMO	141	-5.7221	12.9	25.0	13.0
HOMO - 1	140	-6.0898	3.5	40.9	9.4
HOMO - 2	139	-6.2944	3.5	22.1	22.2
HOMO - 3	138	-6.6142	4.2	11.8	27.2

*2,6-Py = pyridine-2,6-diamide

Table S4.19. Löwdin population analysis derived from the DFT calculations for selected MOs of $\mathbf{2^R}$,SH (*S* = 5/2) **(**B3LYP/def2-TZVPP) using CPCMC(DMF). Only s and p contributions were tabulated for S, C, O, and N-atoms.

α Orbitals	**MO#**	**Energy (eV)**	**Fe%**	**%S**	**%2,6-Py***
LUMO + 3	149	-0.3827	0.7	4.2	1.2
LUMO + 2	148	-0.6680	1.0	0.4	7.9
LUMO + 1	147	-0.8816	3.2	0.7	72.2
LUMO	146	-1.0824	0.4	0.7	44.9
HOMO	145	-4.4800	33.5	13.4	37.8
HOMO - 1	144	-4.9019	6.0	29.7	17.5
HOMO - 2	143	-5.2950	5.3	1.7	70.4
HOMO - 3	142	-5.6725	10.6	31.0	48.4

β Orbitals	**MO#**	**Energy (eV)**	**%Fe**	**%S**	**%2,6-Py***
LUMO + 3	146	-0.4174	14.9	2.5	0.8
LUMO + 2	145	-0.5970	58.7	4.6	2.9
LUMO + 1	144	-0.7739	13.9	1.6	1.9
LUMO	143	-1.1492	3.2	0.4	47.2
HOMO	142	-2.8182	16.1	0.6	66.7
HOMO - 1	141	-4.3210	87.4	2.9	4.6
HOMO - 2	140	-4.9781	4.2	30.0	20.5
HOMO - 3	139	-5.4855	5.2	0.8	60.2

*2,6-Py = pyridine-2,6-diamide

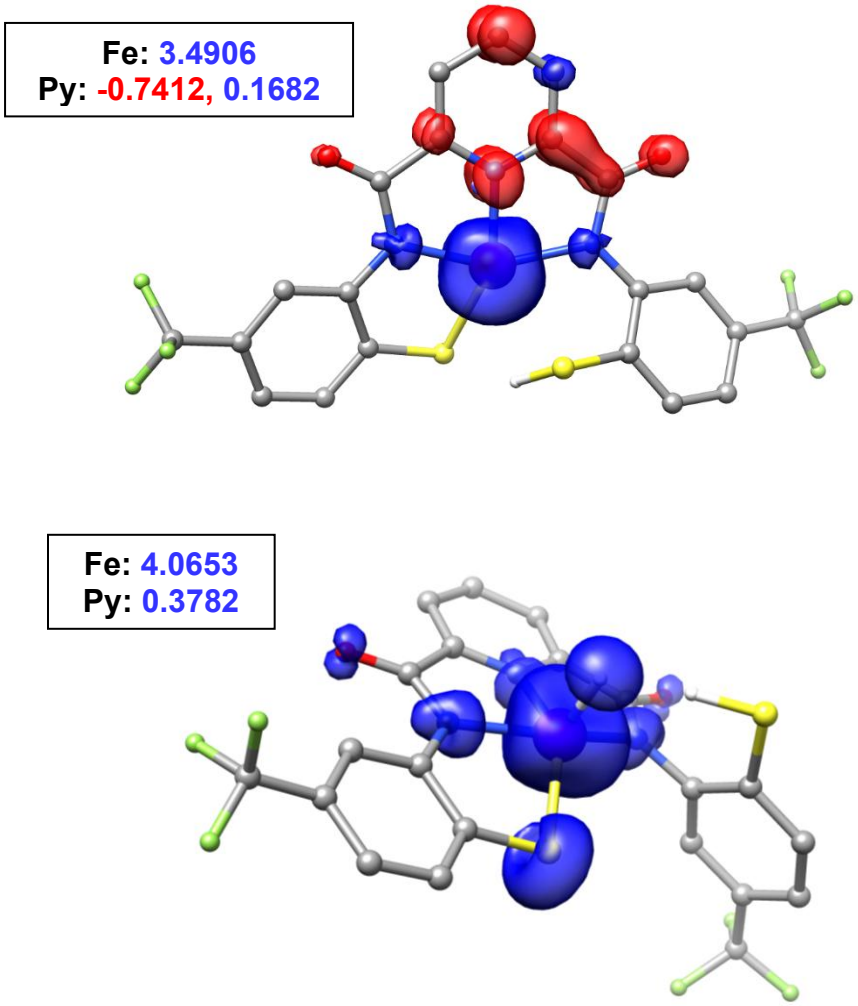

Figure S4.87. DFT-generated Löwdin spin density plot of $\mathbf{2^R}$,SH (S = 3/2) (*top*) and $\mathbf{2^R}$FeH,SH (S = 5/2) (*bottom*) (blue = positive spin density; red = negative spin density).

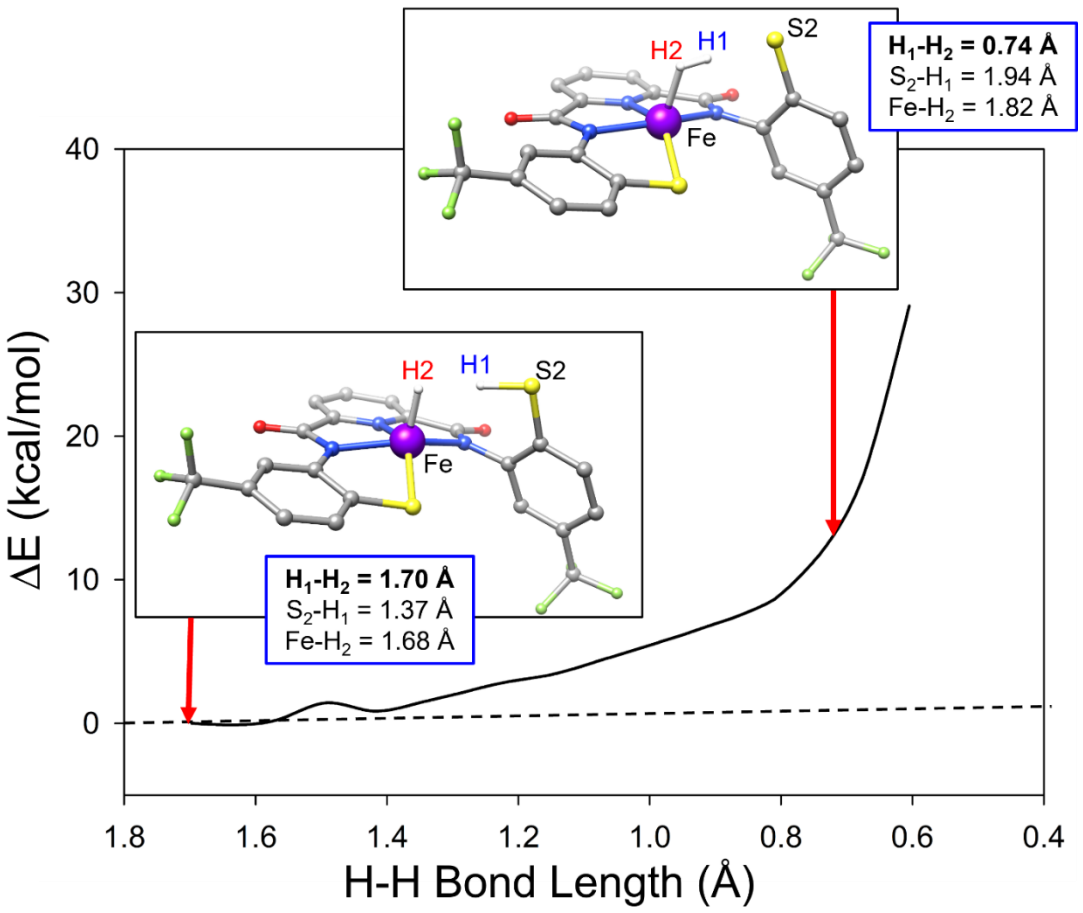

Figure S4.88. Potential energy scan of H-H coupling from **2**^{R}FeH,SH (S = 5/2).

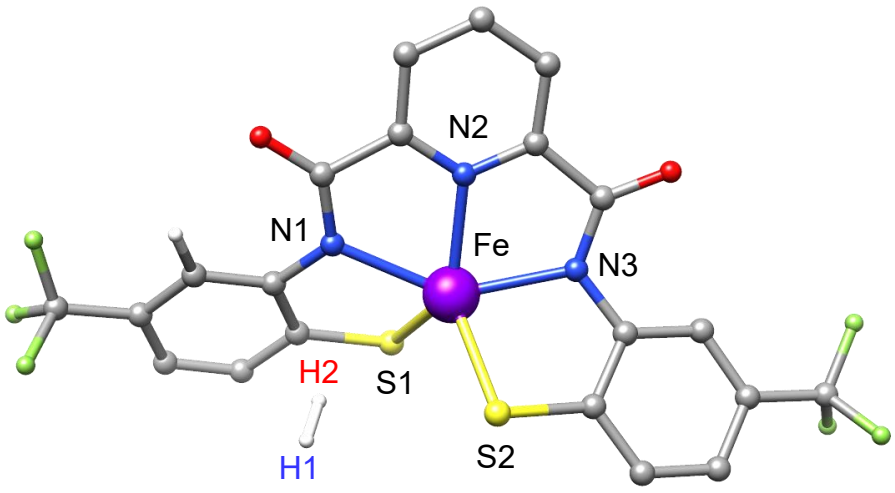

Figure S4.89. Optimized structures of **2**^{R2}FeH,SH (S = 2) in the gas-phase (B3LYP, def2-TZVPP).

Table S4.20. Cartesian coordinates for DFT-optimized **1** (*S* = 5/2, B3LYP, def2-TZVPP, Gas).

Fe	-3.89459051323624	-3.03062728981015	0.09491392029543
S	-5.50019308829696	-2.52637983169435	-1.49028693574709
S	-4.65920690904390	-4.59828729387323	1.64641937702387
O	-0.65263156903747	-5.32828631055720	-1.25166880975428
O	-2.88225751922483	0.92089932933837	1.09618655101174
N	-2.77310542387488	-4.59197776887933	-0.60212892616085
N	-1.91994062270843	-2.29001305117639	0.01080836718858
N	-4.05573276043316	-1.03908964526788	0.59676820970837
C	-3.33197101617463	-6.82851633894636	-1.50042145081736
C	-4.14722406824541	-7.96183766494822	-1.42101839230254
C	-7.43653452013927	-0.68857899232625	-0.82145078924267
C	-3.47870689088129	-5.79312286430960	-0.56530947091266
C	-5.09315689685094	-8.08702689930480	-0.38977744282790
C	-1.44863275099267	-4.48022016397756	-0.84364717998539
C	-6.14025695028510	-1.16390231023737	-0.57397365484692
C	-0.96711822776811	-3.09014710802206	-0.45744911799217
C	0.35123241796478	-2.63582952778949	-0.52933112257433
C	-7.94422170441074	0.41113812496620	-0.13150783210015
C	-4.45356932765522	-5.90264541769347	0.47229669414315
C	-5.23905053690868	-7.06658275045679	0.54400440395340
C	0.62384393678872	-1.33545144634184	-0.08532016579676
C	-5.33367753825136	-0.50757204427391	0.40767624781813
C	-1.70073467018822	-1.04348096893028	0.41765743409122
C	-0.40728598850611	-0.51942009793887	0.39593110176196
C	-2.95696681851644	-0.26776200689228	0.77897576006139
C	-7.15050083496860	1.04976513918239	0.82930815020143
C	-5.84936337731026	0.59893654750748	1.09303032838024
H	-2.59102764407914	-6.72300800988322	-2.29094092405756
H	-8.04685847427040	-1.19653715931164	-1.57135518931518
H	-5.71836719813681	-8.98030546272223	-0.32537328549982
H	1.12268871848849	-3.29892765301632	-0.92212300074766
H	-8.95229151399709	0.77088360567272	-0.34218415980981
H	1.64650298457696	-0.94957854608007	-0.12208478918407
H	-5.97942370744934	-7.15450223119131	1.34176815471438
H	-0.24058191445067	0.50188000516446	0.74115271324960
H	-5.22362500939188	1.10043420606177	1.82948604373619
C	-4.08770351497278	-9.03105460524780	-2.47030068181933
F	-3.10928181575549	-8.83163950574412	-3.38244060836414
F	-5.25625872081879	-9.12321709187148	-3.17082235575843
F	-3.88832263029004	-10.27649416752491	-1.94852871668910
C	-7.67150956461057	2.21430643750411	1.61619075883269
F	-8.94006346985450	2.56041400180612	1.27590270202839
F	-6.91312269832086	3.33371727229408	1.46223013478939
F	-7.69134965751155	1.96694755674315	2.95733794931663

Table S4.21. Cartesian coordinates for DFT-optimized **1**,SH (*S* = 5/2, B3LYP, def2-TZVPP, Gas).

Fe	-3.79795011552644	-2.91746194096646	-0.01317184659085
S	-5.44242459638869	-2.55055821831975	-1.53531954845670
S	-4.63248181895802	-4.55587264276244	1.69094258344153
O	-0.63383728663541	-5.39576732969504	-1.06584247854273
O	-2.84002999853107	1.04425711315607	0.71232881258685
N	-2.72326619855512	-4.58116693980938	-0.44704717959295
N	-1.84273071758175	-2.22989463112135	-0.10442276887715
N	-3.97450704236427	-0.97184298491298	0.45821337078068
C	-3.32218607073083	-6.78650813842505	-1.42412292050635
C	-4.19270389404395	-7.87762188706844	-1.40251949024747
C	-7.44353753096564	-0.80403304325621	-0.77745298442342
C	-3.46285232668411	-5.76435764984043	-0.46927065296137
C	-5.19354654764699	-7.99497186156100	-0.42515214659040
C	-1.39150574105055	-4.49588241210200	-0.70248928645580
C	-6.10876873777867	-1.19467281081363	-0.60581495170240
C	-0.88382740638684	-3.09482483936407	-0.42047589945634
C	0.44855627653868	-2.68363199298485	-0.42445792410168
C	-7.96976286883774	0.26239168955389	-0.04830110622083
C	-4.49366330554033	-5.88147179121823	0.49332197280561
C	-5.34015766287741	-6.99162505914397	0.53016652056499
C	0.72647924069398	-1.35438468797990	-0.07808163202423
C	-5.28133824744180	-0.49281773342817	0.32147547010582
C	-1.61575997049553	-0.96458292839792	0.23760678798265
C	-0.31018555524753	-0.47509908163499	0.26113843952098
C	-2.87714929067438	-0.17286652022498	0.52295266488853
C	-7.15649487406325	0.94153601836668	0.86779955648290
C	-5.81782473343789	0.57404832965926	1.05088962147279
H	-2.55604181474978	-6.69483511474390	-2.19122584810524
H	-8.07456325674229	-1.34319597042852	-1.48685725824935
H	-5.85756477532257	-8.86099386473573	-0.40764443056848
H	1.24025719094148	-3.38582706068246	-0.68668975923730
H	-9.00928270543045	0.55798510797106	-0.19433690064930
H	1.75943319742570	-0.99967717058182	-0.06883189736728
H	-6.11376217520709	-7.07296877160962	1.29569670036375
H	-0.11578594171247	0.56057770772541	0.54155735656250
H	-5.18895875593782	1.09644898540817	1.77063092860250
C	-4.11035253244076	-8.93980884946565	-2.46892007761542
F	-3.14852993483765	-8.69115434041367	-3.38419348318907
F	-5.28244463141955	-9.05215321277178	-3.14781271764937
F	-3.86025762457286	-10.17230559888616	-1.95380060157827
C	-7.70735677120203	2.04864011769931	1.72197740545624
F	-8.97732480988246	2.38332703468334	1.40357056860581
F	-6.96845601758246	3.18681384246313	1.63543346191037
F	-7.71490269581219	1.70928808332751	3.04325597795811

H	-5.97646892430299	-4.43663695066310	1.68106759086716

Table S4.22. Cartesian coordinates for DFT-optimized **1**,NH (*S* = 5/2, B3LYP, def2-TZVPP, Gas).

Fe	-4.06023478919614	-2.93862608555574	-0.63607832727509
S	-5.35360722023413	-1.72503757054204	-2.10000683514240
S	-5.32491984096954	-4.21517706350706	0.73499253047080
O	-0.81572244522722	-5.27101152880391	-1.40065215946425
O	-2.81780854249749	0.56579232056336	1.76018397814089
N	-2.98827286416082	-4.52320942062255	-1.03473681847284
N	-2.08242226444359	-2.15025061606335	-0.24770629879138
N	-3.83121701947545	-0.03099641197302	-0.22482072030033
C	-3.28734473056024	-6.94771108031300	-1.51714253845075
C	-4.03959495636362	-8.10289845667098	-1.29048109922039
C	-7.43973259908728	-0.54365794635306	-0.71244323079560
C	-3.67557209140065	-5.73913225913570	-0.91526121217995
C	-5.18198266859624	-8.06970170451877	-0.47582463464237
C	-1.62951890369212	-4.41176379171823	-1.09405251412819
C	-6.05216962352385	-0.64430905803733	-0.87477116858337
C	-1.15035228603729	-3.05356274714688	-0.60601005468057
C	0.21065787003179	-2.79178128180687	-0.44398878241196
C	-7.98445479174524	0.30274446828605	0.25266770960310
C	-4.83424176779093	-5.70414769481023	-0.08518206955659
C	-5.58040234224769	-6.87595557994634	0.11311472680788
C	0.60195105858954	-1.58729260963160	0.14489709447265
C	-5.21320609575190	0.14723888337456	-0.04429428459828
C	-1.71290325245845	-0.97883648561456	0.30247270953435
C	-0.37424393940503	-0.67151637076419	0.54191666514769
C	-2.82884775320193	-0.04035981559034	0.70720597191172
C	-7.14166172498979	1.07098589275161	1.06192824046879
C	-5.75149721266519	1.00122153739820	0.91656526419757
H	-2.39609135613633	-6.97229648263237	-2.14005935772219
H	-8.08995305897429	-1.15247555928688	-1.34246052011036
H	-5.75253270781922	-8.98295749351150	-0.29763537147934
H	0.92469811760256	-3.55267275031836	-0.76139078017891
H	-9.06614365005393	0.36326320212602	0.37929382238278
H	1.65967224130423	-1.36352431629066	0.30382114235336
H	-6.46469797042870	-6.84189616242260	0.75170098986282
H	-0.12466873881166	0.27213627036072	1.02862047766996
H	-5.08727115868861	1.59668752278131	1.54087229754572
C	-3.66510992193597	-9.42283513226177	-1.91826643694505
F	-2.49188948763085	-9.38055605446845	-2.57916785965762
F	-4.60665500247759	-9.83623777260627	-2.80668931865721
F	-3.56790261578912	-10.40483780396054	-0.98530145994001
C	-7.72041827699586	1.94450069088004	2.14591805948381

F	-8.98787120882223	2.32765350527850	1.87319422461649
F	-6.99047623511670	3.06663958739189	2.33399150976464
F	-7.75764658637439	1.29747981652853	3.33700723832884
H	-3.61621958575086	-0.45603859083558	-1.12086079937886

Table S4.23. Cartesian coordinates for DFT-optimized **2** (*S* = 2, B3LYP, def2-TZVPP, Gas).

Fe	-4.21060025416712	-3.11260680277094	-0.01621180559144
S	-6.15167922282211	-2.42469721195836	-1.26483271459824
S	-5.00116525138705	-4.93317298553771	1.38816983447725
O	-0.74005707447426	-5.33122335651066	-1.33522003150957
O	-2.95277030661052	0.86899823384470	1.17834555025780
N	-2.92528551855871	-4.73353099630000	-0.71519401624006
N	-2.16977068797062	-2.36873962798583	-0.01891865150554
N	-4.28030962784202	-0.96592064562252	0.53892289744622
C	-3.18380718317981	-7.02302280465382	-1.60555706789233
C	-3.85389051202254	-8.25537459112193	-1.55643043975816
C	-7.74734211145419	-0.31613873777384	-0.53661403526560
C	-3.52616328666071	-5.98481066734817	-0.72544623758370
C	-4.85944373933653	-8.46899497993935	-0.59831173369712
C	-1.61804520686270	-4.54828414283891	-0.91792385903335
C	-6.49522310501467	-0.94999383978011	-0.39562759105355
C	-1.19520821600626	-3.16406573626290	-0.45910333491005
C	0.13813945042257	-2.74071752368560	-0.43206928497870
C	-8.04695981529787	0.88691054086856	0.09724079466246
C	-4.56339795010311	-6.18929063213413	0.24821807483627
C	-5.20093010707101	-7.44793009732777	0.28165234505036
C	0.42018418006065	-1.47539919188425	0.09311450144321
C	-5.50804519715293	-0.32449792081711	0.44564300400299
C	-1.93072197298936	-1.14690245620150	0.45464324214858
C	-0.62100893929591	-0.66161307426050	0.54605913261877
C	-3.14437777370299	-0.30561670533177	0.79700852638725
C	-7.07977622162387	1.49239020068555	0.91297955792917
C	-5.82192081620408	0.88952391290422	1.07873987000513
H	-2.38560967018435	-6.84884125260142	-2.32423108038106
H	-8.49347204496605	-0.79571498549989	-1.17518104601405
H	-5.37589846851471	-9.43140511258170	-0.54892466966265
H	0.90665498634568	-3.41568813823460	-0.81016825278133
H	-9.02608193179434	1.35132596957649	-0.03904775445900
H	1.45432702402274	-1.11798486214111	0.14673688324144
H	-5.98582768133713	-7.60815358416231	1.02472682985373
H	-0.46444322619550	0.33615024089396	0.95789205282746
H	-5.05783100820993	1.36101502601802	1.69246244287475
C	-3.50300975227109	-9.36005611661973	-2.48781624879993
F	-2.67350327914213	-8.98745377240740	-3.49331397282518
F	-4.60086807121175	-9.92519415489197	-3.09335278470610

F	-2.88201753961630	-10.42373051414619	-1.86831527235213
C	-7.33738036474832	2.80648440650588	1.55943684589897
F	-8.66754289615354	3.11538899707741	1.64286904257365
F	-6.77042042706106	3.87469585965313	0.90128183327724
F	-6.84970918163425	2.89119383330625	2.83023862378614

Table S4.24. Cartesian coordinates for DFT-optimized **2**,SH (*S* = 2, B3LYP, def2-TZVPP, Gas).

Fe	-4.02881017394783	-3.03181856116561	0.03021297781422
S	-6.23382412995006	-2.80589376417100	-0.75803832980091
S	-4.85672675965030	-5.08055915104829	1.70330841581392
O	-0.65311922409538	-5.46381121364921	-0.91747011779486
O	-2.90155532535319	0.97203462147539	0.82250015646482
N	-2.81030984571589	-4.76314869422406	-0.34433702611778
N	-2.02412510364798	-2.34075435269793	-0.01152120248792
N	-4.18231425289695	-0.95364168775415	0.41961554373378
C	-3.16502790759696	-6.92863582662384	-1.48906261120791
C	-3.93892438908470	-8.08208115566703	-1.61865728290593
C	-7.81268636776415	-0.64794467237210	-0.18158401113889
C	-3.45530779919973	-5.97973313952369	-0.48344676936037
C	-4.99279365026147	-8.35200959751624	-0.73144015506804
C	-1.48420205478495	-4.61808944769766	-0.56646005266327
C	-6.51322975594950	-1.18124071914155	-0.13506155346762
C	-1.03903677500790	-3.20176275759288	-0.25500176050937
C	0.29344002914390	-2.78975277248230	-0.18473543612637
C	-8.09780008225813	0.62861528637146	0.29386059062469
C	-4.52691906693003	-6.26313294658256	0.40371018558594
C	-5.27218818588128	-7.44011632357361	0.28367299385539
C	0.55118909425160	-1.45718062528354	0.15768437407115
C	-5.45504526706803	-0.38434532298857	0.40839270247602
C	-1.81100503847266	-1.07072116169019	0.32211853080285
C	-0.50583215362086	-0.57860644358535	0.41597219169931
C	-3.05319039825484	-0.23012230113912	0.56284674886104
C	-7.06386378425805	1.40269213316432	0.83643144689778
C	-5.75654841077049	0.90547838354417	0.88567628777745
H	-2.34380534541460	-6.72702982930746	-2.17359617242440
H	-8.60865371408430	-1.26340747005062	-0.60643537723486
H	-5.58577658129095	-9.26152420843060	-0.83598931726547
H	1.08522458437308	-3.51018733497210	-0.39275112581917
H	-9.11593243739254	1.02004067942019	0.24908019945613
H	1.58285721709482	-1.10003510675022	0.22890388495779
H	-6.07759028001750	-7.64112137598191	0.99309071433691
H	-0.35484085791179	0.46497718317680	0.69434271318899
H	-4.95021859003813	1.50849120016303	1.29375099469774
C	-3.63128159945466	-9.08034935521777	-2.70371855032437
F	-2.93850759390024	-8.54332433419004	-3.73296472621081
F	-4.75947652502886	-9.62538622732815	-3.23425150958441

F	-2.89722387746898	-10.13365190294494	-2.24614960873985
C	-7.34994429299552	2.79419731465047	1.30843286005814
F	-8.60781743732460	2.92417090198096	1.81888054662005
F	-7.27042984250669	3.72466381032837	0.30611665654800
F	-6.49916950805194	3.21837528515468	2.27549485100267
H	-6.14333653956044	-4.82723701608530	1.38599612890779

Table S4.25. Cartesian coordinates for DFT-optimized **2**,NH (*S* = 2, B3LYP, def2-TZVPP, Gas).

Fe	-4.16310286118865	-3.21119205482800	-0.32792526393247
S	-5.46464249115289	-1.78428645443193	-1.63769438188583
S	-5.44523312445931	-4.68612117212072	0.98074658003436
O	-0.71607165617466	-5.53864487928051	-0.56768242293491
O	-2.80926115271028	1.11468795262205	-0.04463028967244
N	-2.92244956012650	-4.78034841862045	-0.60229784035239
N	-2.13158540893592	-2.31838254760958	-0.02850476112335
N	-4.06026819335774	-0.57018151987123	0.87658891816836
C	-3.15183534363996	-7.09836922697429	-1.39621680140182
C	-3.91640851406096	-8.26713270356257	-1.46058700551066
C	-7.36312017622920	-0.02587706222147	-0.75317033418011
C	-3.59421454514340	-6.00425422879962	-0.64371631551677
C	-5.10374805295169	-8.37087768533898	-0.71939492747623
C	-1.59154456642905	-4.66600485538773	-0.51013658553339
C	-6.07627989816030	-0.56969424688661	-0.52583115233313
C	-1.17050168667456	-3.22753226542189	-0.26032865335370
C	0.18137419324032	-2.87224584273428	-0.26164721155044
C	-7.89491960839133	0.96197305062410	0.06369397967588
C	-4.82777519475097	-6.07600139288175	0.07306899062819
C	-5.54768849201522	-7.28533668067286	0.03030183327178
C	0.53155270930374	-1.53740452550674	-0.06286404136180
C	-5.36062195038874	-0.06192004218355	0.59029806817086
C	-1.80202864291174	-1.03332067998420	0.16160304363991
C	-0.47685078215070	-0.59346005258484	0.13361437667883
C	-2.92951993378155	-0.04316088592101	0.32037140495093
C	-7.16110207111531	1.44976994654456	1.15758763773079
C	-5.88892335152490	0.93237384264496	1.40886250231077
H	-2.21947365313557	-7.01125081222321	-1.95047006989355
H	-7.94109700217450	-0.41276426912084	-1.59437809505256
H	-5.69133505349776	-9.29092203924200	-0.74935606942103
H	0.91389313172021	-3.66135184256895	-0.43473037551988
H	-8.89264768322761	1.35773128538674	-0.14050112536940
H	1.58069610111997	-1.22963216185917	-0.07203262223314
H	-6.48424916411538	-7.35558743042825	0.58719480023242
H	-0.27027456979760	0.46875015357340	0.26655372398070
H	-5.29007726932998	1.29528322079804	2.24387107173969
C	-3.46909232431527	-9.40898170284305	-2.31697478264692

F	-2.59725580002835	-9.03199280934645	-3.28516966174759
F	-4.50960316634610	-10.02179846208996	-2.95181295303742
F	-2.84518350383472	-10.39703154166588	-1.60877698245177
C	-7.73960905754576	2.52187386832386	2.02563745982861
F	-8.99335233643717	2.21691280357294	2.46489979570501
F	-7.86435073240650	3.71637761261086	1.37858369960175
F	-6.98889103734161	2.76093851687572	3.12652385937827
H	-4.00458652342367	-1.53247975836385	1.19476897976566

Table S4.26. Cartesian coordinates for DFT-optimized $\mathbf{2^R}$ (S = 3/2, B3LYP, def2-TZVPP, Gas).

Fe	-4.18052145010004	-3.08239898442850	0.00939818746265
S	-6.22946556724484	-2.35059932276065	-1.20532804369880
S	-5.20684690219810	-5.02277492469993	1.24548738658591
O	-0.77085459417496	-5.38853898058715	-1.32546359751161
O	-2.96610312783979	0.91297311086307	1.18728271015095
N	-2.94950190857666	-4.80737584578205	-0.66435436514829
N	-2.26803198628308	-2.40665759896533	0.00382791552434
N	-4.31415420243402	-0.91392468464234	0.56715443309825
C	-3.11109811328347	-7.10416461070542	-1.55844705973676
C	-3.76911234755874	-8.34883624911274	-1.55922180319365
C	-7.78533413874663	-0.21792830475293	-0.46166112327836
C	-3.52657031644081	-6.05292919992618	-0.71605458389910
C	-4.84399794751517	-8.57645678190412	-0.67848583356361
C	-1.63397104732387	-4.58106744845552	-0.88975999169046
C	-6.53860753868214	-0.87063164064027	-0.34266730909018
C	-1.24371939871902	-3.20238302140116	-0.46104635647261
C	0.06989852923748	-2.76357864055747	-0.47292042561906
C	-8.06454092917024	0.99619184038600	0.16411963059356
C	-4.64858367392600	-6.27672107738429	0.17247937571312
C	-5.26471868271787	-7.54818457746686	0.16021773240499
C	0.39255683116693	-1.47579734500086	0.02237665214393
C	-5.51604772417019	-0.25332000940052	0.48168864106452
C	-1.97222452788614	-1.13498492245723	0.45073195488233
C	-0.66786661840235	-0.66618580691491	0.48660369288326
C	-3.13832711958778	-0.27498108227081	0.80256807937920
C	-7.07045101549389	1.59823641285999	0.95514318932988
C	-5.81347915793796	0.97806286653936	1.10170484521633
H	-2.25686575114561	-6.92122944161719	-2.20671179089566
H	-8.54773839320033	-0.69416664400060	-1.08555697207523
H	-5.35049808401698	-9.54654266735341	-0.66033542259519
H	0.82669512733336	-3.44907555095238	-0.86281751520675
H	-9.04197797693014	1.47014197549944	0.04059434892021
H	1.42658653083856	-1.11200212853477	0.03469319440514
H	-6.10417787183693	-7.71206172637495	0.84231611616741
H	-0.50835648059174	0.34574819354903	0.86897697036792

H	-5.02437029060079	1.44443467057035	1.68817789741202
C	-3.33530478257992	-9.44380816842517	-2.45169350168319
F	-2.45669063975658	-9.07356062890879	-3.41946324184719
F	-4.37990193541535	-10.06081830098557	-3.12039662311157
F	-2.71989099721534	-10.50775248808769	-1.79952584373716
C	-7.30266847090723	2.91427544497727	1.58763736795488
F	-8.63378609193004	3.24949187847996	1.69335952215222
F	-6.74332259881880	3.99318993894614	0.91811220826359
F	-6.79821661721666	3.02600247278725	2.85579935197780

Table S4.27. Cartesian coordinates for DFT-optimized **2^{R}**,SH (*S* = 3/2, B3LYP, def2-TZVPP, Gas).

Fe	-4.01397434445540	-3.02849829147231	-0.03635219204321
S	-6.18623577446376	-2.08424591057819	-1.74723236183812
S	-5.63899056026172	-4.68294261248617	0.68791619814731
O	-0.72208650346106	-5.47976227394477	-1.06775974835678
O	-2.95690715285697	0.97591666534399	0.88549466635361
N	-2.90987296775792	-4.78501061621838	-0.58086192359515
N	-2.14079176909029	-2.38205732777457	-0.02277127127898
N	-4.23677508373401	-0.90187838644187	0.25538998597162
C	-3.06844502172517	-7.13551221893956	-1.34519426506108
C	-3.83157314115550	-8.30919534333823	-1.45379057100415
C	-7.80107380298810	-0.25460483026178	-0.49475428219160
C	-3.58123844573104	-5.98209852065023	-0.71379277013325
C	-5.12714844931210	-8.36655052610836	-0.92367652666869
C	-1.56735946839833	-4.63190428408846	-0.71995708371998
C	-6.51697999691152	-0.80586121142875	-0.54379312674642
C	-1.13060506020454	-3.23297846656960	-0.34605901954609
C	0.18845719050293	-2.83125901657762	-0.30256446542595
C	-8.09661074082407	0.84260534248862	0.31305359818126
C	-4.91326744780174	-6.04637544190629	-0.16463960264362
C	-5.64483548738600	-7.23915162102092	-0.28842148581836
C	0.49207016823808	-1.49493524104769	0.09817494430564
C	-5.45148047554207	-0.28172932567712	0.26630814055416
C	-1.87930978614113	-1.07666912901555	0.32829604390055
C	-0.55532233762558	-0.62796451116076	0.40751787258023
C	-3.05898499458381	-0.22538559469038	0.54154370427994
C	-7.05241851452856	1.40223659110845	1.07076066256597
C	-5.76676989179668	0.86811408337294	1.05054152844245
H	-2.05663254765390	-7.08457429031618	-1.74249394617760
H	-8.57789296005696	-0.69980936377753	-1.12122664302877
H	-5.72205247621825	-9.27791612933349	-1.00536706627274
H	0.96227746469643	-3.55075926610416	-0.57545076043705
H	-9.10137296528881	1.26575856661205	0.34555187622366
H	1.53017449785486	-1.15223234273200	0.15251039065236

H	-6.64848609396888	-7.27102672518216	0.14333852958019
H	-0.38331434366670	0.40840254051141	0.70828776554544
H	-4.96095347892864	1.31798569891249	1.62581318676383
C	-3.27252334497558	-9.48283437416624	-2.18554243049446
F	-3.25185104377171	-9.31915776358219	-3.54999682005995
F	-3.98764399785910	-10.63100576507096	-1.97918690095955
F	-1.98586228414338	-9.78225077060984	-1.85082891604509
C	-7.30915474456982	2.65795253829465	1.84725875886165
F	-8.62132518316997	2.80129429896764	2.20414687765351
F	-7.01097580473409	3.78847879599480	1.13316465850163
F	-6.59376672159148	2.75174783880261	2.99626632128806
H	-6.34689131095740	-3.18900074713696	-0.94304123780639

Table S4.28. Cartesian coordinates for DFT-optimized **2**$^{\mathbf{R}}$FeH,SH (*S* = 5/2, B3LYP, def2-TZVPP, Gas).

Fe	-4.01665848667558	-2.84850744318120	-0.91968895678511
S	-6.22317404754235	-0.54592957170554	-2.92436751586992
S	-5.75799585939114	-4.03996343837879	0.02875611219202
O	-0.71572219613567	-5.43832431557992	-0.61805172070837
O	-3.05622113436496	1.13176127933434	0.03667016231621
N	-2.90173500076145	-4.58517206660850	-0.63928840624785
N	-2.05781849739034	-2.18757882471984	-0.51620646953076
N	-4.21976298937067	-0.82330467191683	-0.47852732345002
C	-3.11404915687972	-7.04321628023437	-0.81425354719597
C	-3.93987267936761	-8.17061600561599	-0.77846411452764
C	-7.75981540575769	0.31078522756555	-0.86392064797512
C	-3.64335366591377	-5.75975604067088	-0.59269737796530
C	-5.30926635617263	-8.03923756381215	-0.51252523197754
C	-1.55065452426593	-4.52746423597689	-0.61747237915771
C	-6.48701659437238	-0.16995599312334	-1.21679894982006
C	-1.08131390824160	-3.08970449925786	-0.53255687218546
C	0.24889394499014	-2.68016936860109	-0.42275777789410
C	-8.05126969699580	0.72132392974606	0.43374046209855
C	-5.03901416643635	-5.62081990110384	-0.30815878247315
C	-5.84201575091945	-6.77240408065414	-0.28100939924595
C	0.50658923715343	-1.31104404195734	-0.28466060986030
C	-5.48386505408433	-0.26449166907021	-0.21828840036876
C	-1.84947232885851	-0.88601123473190	-0.35890028615847
C	-0.54952392560019	-0.39252803355346	-0.23917870196148
C	-3.11743200398900	-0.06400950093322	-0.25364356548495
C	-7.05476699224598	0.64563821455519	1.41311758358628
C	-5.79117968721618	0.15327560969199	1.08322621525125
H	-2.05036480023957	-7.13775786338992	-1.01778419281365
H	-8.53451659795546	0.35509182935941	-1.63273013053703
H	-5.95209031373321	-8.92065904913663	-0.48264624318796

H	1.03870291239767	-3.43240142851478	-0.43681563529584
H	-9.04490218976579	1.09282272611408	0.68638963565617
H	1.53732907375575	-0.95673635759231	-0.19518931817867
H	-6.90662156308023	-6.65959563270059	-0.06451781465885
H	-0.39603464781419	0.67817905068608	-0.09994425897792
H	-5.01323144464018	0.07959928338650	1.84448048348669
C	-3.35888986523454	-9.51327863342225	-1.10881687480020
F	-3.35585994053002	-9.76328327427710	-2.45380674168908
F	-4.05437668014099	-10.53801743892278	-0.54558860279317
F	-2.07241504668549	-9.65416304989145	-0.70510655172155
C	-7.32220147074943	1.04571386264222	2.83348805328934
F	-8.55892947144802	1.57725208567516	3.00402199688219
F	-6.43641869208759	1.97104274785980	3.29064645169801
F	-7.23538943718135	-0.00843668798559	3.69087177425139
H	-5.25614719257770	-1.50269708519957	-2.77821860797041
H	-4.27805570548294	-2.87462056419531	-2.57582692123975

Table S4.29. Cartesian coordinates for DFT-optimized **2^{R2}**FeH,SH (*S* = 5/2, B3LYP, def2-TZVPP, Gas).

Fe	-4.29164141214224	-2.91661024496989	-0.14728151519504
S	-6.08696075073826	-2.00308524811272	-1.50848386068399
S	-5.36781988207178	-4.73426490413031	1.01337498917770
O	-0.79171393016877	-5.16412334079237	-1.43499090487145
O	-2.97552046546742	0.96810797013842	1.25608361496395
N	-2.98021856859903	-4.61832165270828	-0.76035087824091
N	-2.22707541008176	-2.22847002756701	-0.07551289664271
N	-4.31395947393271	-0.83704014949488	0.56701803116076
C	-3.03763449281585	-6.99983190375615	-1.44827601099510
C	-3.65444056428719	-8.25876699395782	-1.35375455655156
C	-7.73727250185812	-0.03378320866489	-0.52652828653441
C	-3.54672347479802	-5.88674027350956	-0.75358666036031
C	-4.80077365154424	-8.41879885745623	-0.55872286592109
C	-1.68025021542764	-4.40341732003743	-0.99648719905649
C	-6.48602877504902	-0.68106167828210	-0.43583300805324
C	-1.26231942769980	-3.01814728011617	-0.54436556115188
C	0.07216699617786	-2.59371295887626	-0.54478066298080
C	-8.06934193967233	1.04722123626313	0.28329779619473
C	-4.71728937279818	-6.05036866100866	0.06865813815211
C	-5.31511656856751	-7.32622870360856	0.13051539213752
C	0.36851689963258	-1.33968914856385	-0.00393897619061
C	-5.54091582755959	-0.18786896455565	0.52761008281003
C	-1.97156899683557	-1.02008010776057	0.42636587867696
C	-0.66012856166437	-0.53876601973816	0.49918859720066
C	-3.17367788602637	-0.18902546681371	0.82928806857286
C	-7.13914520855263	1.52165639238609	1.22350470628303

C	-5.88371877010166	0.90641595422861	1.33845553253658
H	-2.13941636968037	-6.86337145152103	-2.04575638429143
H	-8.45368962243685	-0.40330779728854	-1.26434660118857
H	-5.28392403076580	-9.39553145365567	-0.47821826486546
H	0.82945754940931	-3.26315566989033	-0.95372750543168
H	-9.04587186483876	1.52870371977085	0.18530159826977
H	1.40358472792391	-0.98227053414009	0.02616541814327
H	-6.20291553361008	-7.44437175269509	0.75651940960405
H	-0.49263166314602	0.44729418805257	0.93420470515897
H	-5.14315633830884	1.27625893968852	2.04359842028567
C	-3.14180552231360	-9.41849458101461	-2.13507162701934
F	-3.76369060565298	-9.58450497719710	-3.35555774242843
F	-3.32869076428691	-10.61795280898639	-1.49494980294272
F	-1.81565289976778	-9.35246149641383	-2.42428785668401
C	-7.52568645574489	2.64275217920878	2.12014060015177
F	-8.15325875867890	3.66929337317962	1.45738496005944
F	-6.48429691440842	3.20637732566433	2.78192323031106
F	-8.42625290375583	2.27547655606156	3.09785203050324
H	-5.57296498957645	-4.64514940968792	-3.52381301334963
H	-5.09646480770896	-4.53015278766905	-2.94082855872318

Table S4.30. Cartesian coordinates for DFT-optimized **3** (*S* = 0, B3LYP, def2-TZVPP, Gas).

Zn	-4.10217399313188	-3.02277028761309	-0.08592327486063
S	-5.79375023293610	-2.26218541581513	-1.60995137580431
S	-4.97594629751287	-4.73122650212994	1.38310227246074
O	-0.70794530067114	-5.33613096556327	-1.31847330956733
O	-2.87667005053488	0.89724984262412	1.13890702426212
N	-2.87923777285381	-4.68034027030019	-0.73746330617208
N	-2.07173807944030	-2.33465450625882	-0.04195213519040
N	-4.17843799675741	-0.95325131852439	0.53944511454063
C	-3.23724592085076	-6.97350723293705	-1.54147926760557
C	-3.95374003681440	-8.16691583199310	-1.45595742596002
C	-7.55784746324093	-0.35096583188774	-0.74794612863265
C	-3.52785266701208	-5.90072340817595	-0.69591897705949
C	-4.96215247153695	-8.30551049307038	-0.49944196509198
C	-1.57137363015967	-4.52818434650697	-0.92895029210426
C	-6.28681282478063	-0.92373768955865	-0.59071145361785
C	-1.11974682771844	-3.14162651642405	-0.49240576115833
C	0.20896772387505	-2.72386807247548	-0.48955449289434
C	-7.97342936491084	0.74326640295853	-0.00651174318675
C	-4.56950433211549	-6.02787608251523	0.27769509771843
C	-5.25538610113807	-7.25084251225500	0.34538318845946
C	0.49662250170789	-1.45910114104492	0.01660517101883
C	-5.41707077242807	-0.35401162015221	0.39591387990810
C	-1.83147342083170	-1.11604761269512	0.42406009511353

C	-0.52524751113872	-0.63819018792424	0.48402944192012
C	-3.05327469175244	-0.28029567350271	0.77567472463421
C	-7.11718133060984	1.29584503508463	0.94690043229195
C	-5.84492396257513	0.75175639067981	1.13450541202774
H	-2.43699559403643	-6.85881985139679	-2.25409338423252
H	-8.22363049051270	-0.78885043047939	-1.48003678418286
H	-5.51798734522838	-9.23206449977678	-0.42574495707625
H	0.96849484487832	-3.39073718170799	-0.87030764839763
H	-8.96124228884481	1.15871695395210	-0.15862498670827
H	1.52233333491119	-1.10789942519116	0.04436895744224
H	-6.04225727267546	-7.35371493718616	1.08039402409901
H	-0.34742512486598	0.35154430900574	0.87883806454302
H	-5.16080825867708	1.18220808139889	1.84743269831875
C	-3.68477463242396	-9.29312893336441	-2.38103057026927
F	-2.72758857797504	-9.03335076487641	-3.29840977314772
F	-4.79103153382438	-9.67779866828769	-3.09583282409625
F	-3.28992331291373	-10.44230269632756	-1.73966736033670
C	-7.53254059794695	2.50094588759696	1.70682175325463
F	-8.86925579111657	2.52329010225245	1.99497043488008
F	-7.31323914875562	3.68158411751266	1.03743721001105
F	-6.88971538212266	2.64155378485215	2.89246420044888

Table S4.31. Cartesian coordinates for DFT-optimized $\mathbf{3^R}$ (S = 1/2, B3LYP, def2-TZVPP, Gas).

Zn	-4.15445110164102	-3.00284312979501	-0.09716994170060
S	-6.21603576561435	-2.41073348964077	-1.28877902704624
S	-5.00895939817365	-4.91857486915161	1.33657399694937
O	-0.80183192440528	-5.33003743438335	-1.47442222998752
O	-2.97557239488843	0.90928985314693	1.17885012063326
N	-2.96789734339611	-4.72856063782231	-0.82895177371504
N	-2.21043090533802	-2.35621820472257	-0.12018793536166
N	-4.30295449555460	-0.92800883845457	0.50786208585350
C	-3.18885026126164	-7.04963517872886	-1.62460571472335
C	-3.80821302735761	-8.31165022507376	-1.51059777702254
C	-7.78246105255246	-0.29588234562701	-0.52369277539772
C	-3.54045581236995	-5.97777405759248	-0.78651584862398
C	-4.80305512214804	-8.51147225642570	-0.53741477568809
C	-1.65687643799482	-4.51995412004939	-1.04621040464143
C	-6.52941958023405	-0.92927628032708	-0.40881426655144
C	-1.22434025825282	-3.13033199683330	-0.59785526043269
C	0.10005079739344	-2.71820856486981	-0.61300148899005
C	-8.08579972516848	0.91271999694257	0.10985816747178
C	-4.56141417138654	-6.18088389744395	0.22367691414037
C	-5.15999164263294	-7.45987580046373	0.30394848178462
C	0.41054847580254	-1.42617060626858	-0.05692698351372
C	-5.51028362802075	-0.30202824064476	0.42095386091948

C	-1.95448324776206	-1.08654255799431	0.37729694300961
C	-0.62167266774425	-0.63533360940778	0.43296502114926
C	-3.11573868096454	-0.27573338003201	0.75344022280724
C	-7.09868249443211	1.52415809575733	0.90201522805835
C	-5.83445819217138	0.92495389785718	1.04767641802411
H	-2.39883875421270	-6.88135984610956	-2.35461153754699
H	-8.53811888255919	-0.77784017846686	-1.15185998605372
H	-5.29000653944037	-9.48540381192670	-0.43504707759953
H	0.86032495790069	-3.38804058062725	-1.01727587105355
H	-9.07109183852266	1.37044286157664	-0.01061419366945
H	1.44791730832055	-1.07022201353752	-0.01682300540830
H	-5.92380621372080	-7.61653616080358	1.07121408194460
H	-0.44124819693302	0.35291380674804	0.86624547008651
H	-5.05106343357916	1.39860793292586	1.63665261274687
C	-3.48275040499965	-9.38069916115852	-2.47970997110213
F	-2.16973118862115	-9.43185860757298	-2.85637673198312
F	-4.17068410099917	-9.28531708511775	-3.68249698500738
F	-3.78166669328690	-10.64783234349736	-2.03080149265086
C	-7.34854652214611	2.83458294207493	1.54334659508029
F	-8.68396460636290	3.15241085560854	1.65018622699417
F	-6.80262622508079	3.92358630822511	0.88062868316914
F	-6.84808860748622	2.94508295970796	2.81294192464862

4.12 References

(1) Lewis, N. S.; Nocera, D. G. Powering the planet: Chemical challenges in solar energy utilization. *Proc. Natl. Acad. Sci. U.S.A.* **2006**, *103*, 15729. DOI: 10.1073/pnas.0603395103.

(2) Schilter, D.; Camara, J. M.; Huynh, M. T.; Hammes-Schiffer, S.; Rauchfuss, T. B. Hydrogenase Enzymes and Their Synthetic Models: The Role of Metal Hydrides. *Chem. Rev.* **2016**, *116*, 8693. DOI: 10.1021/acs.chemrev.6b00180.

(3) Adams, M. W. W. The structure and mechanism of iron-hydrogenases. *Biochimica et Biophysica Acta (BBA) - Bioenergetics* **1990**, *1020*, 115. DOI: 10.1016/0005-2728(90)90044-5.

(4) Pandey, A. S.; Harris, T. V.; Giles, L. J.; Peters, J. W.; Szilagyi, R. K. Dithiomethylether as a Ligand in the Hydrogenase H-Cluster. *J. Am. Chem. Soc.* **2008**, *130*, 4533. DOI: 10.1021/ja711187e.

(5) Lubitz, W.; Ogata, H.; Rüdiger, O.; Reijerse, E. Hydrogenases. *Chem. Rev.* **2014**, *114*, 4081. DOI: 10.1021/cr4005814.

(6) Felton, G. A. N.; Mebi, C. A.; Petro, B. J.; Vannucci, A. K.; Evans, D. H.; Glass, R. S.; Lichtenberger, D. L. Review of electrochemical studies of complexes containing the Fe_2S_2 core characteristic of [FeFe]-hydrogenases including catalysis by these complexes of the reduction of acids to form dihydrogen. *J. Organomet. Chem.* **2009**, *694*, 2681. DOI: 10.1016/j.jorganchem.2009.03.017.

(7) Bhunia, S.; Rana, A.; Hematian, S.; Karlin, K. D.; Dey, A. Proton Relay in Iron Porphyrins for Hydrogen Evolution Reaction. *Inorg. Chem.* **2021**, *60*, 13876. DOI: 10.1021/acs.inorgchem.1c01079.

(8) Roy, S.; Mazinani, S. K. S.; Groy, T. L.; Gan, L.; Tarakeshwar, P.; Mujica, V.; Jones, A. K. Catalytic Hydrogen Evolution by Fe(II) Carbonyls Featuring a Dithiolate and a Chelating Phosphine. *Inorg. Chem.* **2014**, *53*, 8919. DOI: 10.1021/ic5012988.

(9) Connor, G. P.; Mayer, K. J.; Tribble, C. S.; McNamara, W. R. Hydrogen Evolution Catalyzed by an Iron Polypyridyl Complex in Aqueous Solutions. *Inorg. Chem.* **2014**, *53*, 5408. DOI: 10.1021/ic500069c.

(10) Cavell, A. C.; Hartley, C. L.; Liu, D.; Tribble, C. S.; McNamara, W. R. Sulfinato Iron(III) Complex for Electrocatalytic Proton Reduction. *Inorg. Chem.* **2015**, *54*, 3325. DOI: 10.1021/ic5030394.

(11) Sánchez, P.; Goel, B.; Neugebauer, H.; Lalancette, R. A.; Grimme, S.; Hansen, A.; Prokopchuk, D. E. Ligand Protonation at Carbon, not Nitrogen, during H_2 Production with

Amine-Rich Iron Electrocatalysts. *Inorg. Chem.* **2021**, *60*, 17407. DOI: 10.1021/acs.inorgchem.1c03142.

(12) Huang, D.; He, B.; Zhao, Y.; Liu, M.; Wang, L. Homogeneous electrocatalytic hydrogen evolution by a $N_2P_2Fe(II)$ complex: Structural characterization of iron-hydride intermediate. *J. Mol. Struct.* **2025**, *1325*, 141021. DOI: 10.1016/j.molstruc.2024.141021.

(13) Kaur-Ghumaan, S.; Schwartz, L.; Lomoth, R.; Stein, M.; Ott, S. Catalytic Hydrogen Evolution from Mononuclear Iron(II) Carbonyl Complexes as Minimal Functional Models of the [FeFe] Hydrogenase Active Site. *Angew. Chem. Int. Ed.* **2010**, *49*, 8033. DOI: 10.1002/anie.201002719.

(14) Rose, M. J.; Gray, H. B.; Winkler, J. R. Hydrogen Generation Catalyzed by Fluorinated Diglyoxime–Iron Complexes at Low Overpotentials. *J. Am. Chem. Soc.* **2012**, *134*, 8310. DOI: 10.1021/ja300534r.

(15) Hartley, C. L.; DiRisio, R. J.; Chang, T. Y.; Zhang, W.; McNamara, W. R. Electrocatalytic hydrogen evolution by an iron complex containing a nitro-functionalized polypyridyl ligand. *Polyhedron* **2016**, *114*, 133. DOI: 10.1016/j.poly.2015.11.023.

(16) Drosou, M.; Kamatsos, F.; Mitsopoulou, C. A. Recent advances in the mechanisms of the hydrogen evolution reaction by non-innocent sulfur-coordinating metal complexes. *Inorg. Chem. Front.* **2020**, *7*, 37. DOI: 10.1039/C9QI01113G.

(17) Luo, G.-G.; Zhang, H.-L.; Tao, Y.-W.; Wu, Q.-Y.; Tian, D.; Zhang, Q. Recent progress in ligand-centered homogeneous electrocatalysts for hydrogen evolution reaction. *Inorg. Chem. Front.* **2019**, *6*, 343. DOI: 10.1039/C8QI01220B.

(18) Noveron, J. C.; Olmstead, M. M.; Mascharak, P. K. A Synthetic Analogue of the Active Site of Fe-Containing Nitrile Hydratase with Carboxamido N and Thiolato S as Donors: Synthesis, Structure, and Reactivities. *J. Am. Chem. Soc.* **2001**, *123*, 3247. DOI: 10.1021/ja001253v.

(19) Ballesteros, M., II; Tsui, E. Y. Reactivity of Zinc Thiolate Bonds: Oxidative Organopolysulfide Formation and S_3 Insertion. *Inorg. Chem.* **2019**, *58*, 10501. DOI: 10.1021/acs.inorgchem.9b01074.

(20) Seo, W. T. M.; Ballesteros, M., II; Tsui, E. Y. Sulfane Decreases the Nucleophilic Reactivity of Zinc Thiolates: Implications for Biological Reactive Sulfur Species. *J. Am. Chem. Soc.* **2022**, *144*, 20630. DOI: 10.1021/jacs.2c07380.

(21) Noveron, J. C.; Olmstead, M. M.; Mascharak, P. K. Co(III) Complexes with Carboxamido N and Thiolato S Donor Centers: Models for the Active Site of Co-Containing Nitrile Hydratases. *J. Am. Chem. Soc.* **1999**, *121*, 3553. DOI: 10.1021/ja9833523.

(22) Addison, A. W.; Rao, T. N.; Reedijk, J.; van Rijn, J.; Verschoor, G. C. Synthesis, Structure, and Spectroscopic Properties of Copper(II) Compounds Containing Nitrogen–Sulphur Donor Ligands; the Crystal and Molecular Structure of Aqua[1,7-bis(*N*-methylbenzimidazol-2′-yl)-2,6-dithiaheptane]copper(II) Perchlorate. *J. Chem. Soc., Dalton Trans.* **1984**, 1349. DOI: 10.1039/DT9840001349.

(23) Noveron, J. C.; Olmstead, M. M.; Mascharak, P. K. Effect of Carboxamido N Coordination to Iron on the Redox Potential of Low-Spin Non-Heme Iron Centers with N,S Coordination: Relevance to the Iron Site of Nitrile Hydratase. *Inorg. Chem.* **1998**, *37*, 1138. DOI: 10.1021/ic971388a.

(24) Drago, R. *Physical Methods for Chemist*; 1977.

(25) Connelly, N. G.; Geiger, W. E. Chemical Redox Agents for Organometallic Chemistry. *Chem. Rev.* **1996**, *96*, 877. DOI: 10.1021/cr940053x.

(26) Kütt, A.; Tshepelevitsh, S.; Saame, J.; Lõkov, M.; Kaljurand, I.; Selberg, S.; Leito, I. Strengths of Acids in Acetonitrile. *Eur. J. Org. Chem.* **2021**, *2021*, 1407. DOI: 10.1002/ejoc.202001649.

(27) Brands, M. B.; Reek, J. N. H. Mechanistic Insights into Electrocatalytic Hydrogen Evolution by an Exceptionally Stable Cobalt Complex. *Inorg. Chem.* **2024**, *63*, 8484. DOI: 10.1021/acs.inorgchem.4c01043.

(28) Queyriaux, N.; Sun, D.; Fize, J.; Pécaut, J.; Field, M. J.; Chavarot-Kerlidou, M.; Artero, V. Electrocatalytic Hydrogen Evolution with a Cobalt Complex Bearing Pendant Proton Relays: Acid Strength and Applied Potential Govern Mechanism and Stability. *J. Am. Chem. Soc.* **2020**, *142*, 274. DOI: 10.1021/jacs.9b10407.

(29) Mejia-Rodriguez, R.; Chong, D.; Reibenspies, J. H.; Soriaga, M. P.; Darensbourg, M. Y. The Hydrophilic Phosphatriazaadamantane Ligand in the Development of H_2 Production Electrocatalysts: Iron Hydrogenase Model Complexes. *J. Am. Chem. Soc.* **2004**, *126*, 12004. DOI: 10.1021/ja039394v.

(30) Fang, M.; Engelhard, M. H.; Zhu, Z.; Helm, M. L.; Roberts, J. A. S. Electrodeposition from Acidic Solutions of Nickel Bis(benzenedithiolate) Produces a Hydrogen-Evolving Ni–S Film on Glassy Carbon. *ACS Catal.* **2014**, *4*, 90. DOI: 10.1021/cs400675u.

(31) Lee, K. J.; McCarthy, B. D.; Dempsey, J. L. On decomposition, degradation, and voltammetric deviation: the electrochemist's field guide to identifying precatalyst transformation. *Chem. Soc. Rev.* **2019**, *48*, 2927. DOI: 10.1039/C8CS00851E.

(32) Kaljurand, I.; Kütt, A.; Sooväli, L.; Rodima, T.; Mäemets, V.; Leito, I.; Koppel, I. A. Extension of the Self-Consistent Spectrophotometric Basicity Scale in Acetonitrile to a Full Span of 28 pK_a Units: Unification of Different Basicity Scales. *J. Org. Chem.* **2005**, *70*, 1019. DOI: 10.1021/jo048252w.

(33) Ellis, K. J.; Lappin, A. G.; McAuley, A. Metal-Ion Oxidations in Solution. Part XV.[1] Rate-Determining Dimerisations in Redox Reactions of Iron(III) with Some α-Mercaptocarboxylic Acids. *J. Chem. Soc., Dalton Trans.* **1975**, 1930. DOI: 10.1039/DT9750001930.

(34) Millar, M.; Koch, S. A.; Fikar, R. The Reactions of Fe(III) with Sterically Hindered Thiolate Ligands. *Inorg. Chim. Acta* **1984**, *88*, L15. DOI: 10.1016/S0020-1693(00)83582-3.

(35) Maelia, L. E.; Millar, M.; Koch, S. A. General Synthesis of Iron(III) Tetrathiolate Complexes. Structural and Spectroscopic Models for the [Fe(Cys-*S*)$_4$] Center in Oxidized Rubredoxin. *Inorg. Chem.* **1992**, *31*, 4594. DOI: 10.1021/ic00048a029.

(36) Deaton, J. C.; Gebhard, M. S.; Koch, S. A.; Millar, M.; Solomon, E. I. Ligand Field Transitions and the Origin of Zero Field Splitting in [PPh$_4$][FeCl$_4$] and [NEt$_4$][Fe(SR)$_4$] (R = 2,3,5,6-Me$_4$C$_6$H): A Model for the High-Spin Fe(III) Site in Rubredoxin. *J. Am. Chem. Soc.* **1988**, *110*, 6241. DOI: 10.1021/ja00226a047.

(37) Lovenberg, W.; Sobel, B. E. Rubredoxin: A New Electron Transfer Protein from *Colstridium pasteurianum*. *Proc. Natl. Acad. Sci. U.S.A.* **1965**, *54*, 193. DOI: 10.1073/pnas.54.1.193.

(38) Millar, M.; Lee, J. F.; O'Sullivan, T.; Koch, S. A.; Fikar, R. Models for the iron-sulfur protein rubredoxin: the use of sterically hindered thiolate ligands to stabilize [Fe(SR)$_4$]$^{1-}$ complexes; some considerations of the structure of the [Fe(S-Cys)$_4$] centers in oxidized rubredoxins. *Inorg. Chim. Acta* **1996**, *243*, 333. DOI: 10.1016/0020-1693(96)04924-9.

(39) Adman, E.; Watenpaugh, K. D.; Jensen, L. H. NH---S hydrogen bonds in *Peptococcus aerogenes* ferredoxin, *Clostridium pasteurianum* rubredoxin, and *Chromatium* high potential iron protein. *Proc. Natl. Acad. Sci. U.S.A.* **1975**, *72*, 4854. DOI: 10.1073/pnas.72.12.4854.

(40) Kato, M.; Okamura, T.-a.; Yamamoto, H.; Ueyama, N. Effects of the Intramolecular NH···S Hydrogen Bond in Mononuclear Platinum(II) and Palladium(II) Complexes with 2,2‘-Bipyridine and Benzenethiol Derivatives. *Inorg. Chem.* **2005**, *44*, 1966. DOI: 10.1021/ic0490167.

(41) Ariyananda, P. W. G.; Kieber-Emmons, M. T.; Yap, G. P. A.; Riordan, C. G. Synthetic analogs for evaluating the influence of N–H···S hydrogen bonds on the formation of thioester in acetyl coenzyme a synthase. *Dalton Trans.* **2009**, 4359. DOI: 10.1039/B901192G.

(42) Gale, E. M.; Narendrapurapu, B. S.; Simmonett, A. C.; Schaefer, H. F., III; Harrop, T. C. Exploring the Effects of H-Bonding in Synthetic Analogues of Nickel Superoxide Dismutase (Ni-SOD): Experimental and Theoretical Implications for Protection of the Ni−SCys Bond. *Inorg. Chem.* **2010**, *49*, 7080. DOI: 10.1021/ic1009187.

(43) Smith, J. N.; Hoffman, J. T.; Shirin, Z.; Carrano, C. J. H-Bonding Interactions and Control of Thiolate Nucleophilicity and Specificity in Model Complexes of Zinc Metalloproteins. *Inorg. Chem.* **2005**, *44*, 2012. DOI: 10.1021/ic048630f.

(44) Okamura, T.-a.; Takamizawa, S.; Ueyama, N.; Nakamura, A. Novel Rubredoxin Model Tetrathiolato Iron(II) and Cobalt(II) Complexes Containing Intramolecular Single and Double NH···S Hydrogen Bonds. *Inorg. Chem.* **1998**, *37*, 18. DOI: 10.1021/ic970640b.

(45) Ueyama, N.; Nishikawa, N.; Yamada, Y.; Okamura, T.-a.; Nakamura, A. Cytochrome P-450 Model (Porphinato)(thiolato)iron(III) Complexes with Single and Double NH···S Hydrogen Bonds at the Thiolate Site. *J. Am. Chem. Soc.* **1996**, *118*, 12826. DOI: 10.1021/ja9622970.

(46) Lane, R. W.; Ibers, J. A.; Frankel, R. B.; Papaefthymiou, G. C.; Holm, R. H. Synthetic Analogs of the Active Sites of Iron-Sulfur Proteins. 14. Synthesis, Properties, and Structures of Bis(*o*-xylyl-α,α'-dithiolato)ferrate(II,III) Anions, Analogs of Oxidized and Reduced Rubredoxin Sites. *J. Am. Chem. Soc.* **1977**, *99*, 84. DOI: 10.1021/ja00443a017.

(47) Pavlishchuk, V. V.; Addison, A. W. Conversion constants for redox potentials measured versus different reference electrodes in acetonitrile solutions at 25 °C. *Inorg. Chim. Acta* **2000**, *298*, 97. DOI: 10.1016/S0020-1693(99)00407-7.

(48) Coucouvanis, D.; Swenson, D.; Baenziger, N. C.; Murphy, C.; Holah, D. G.; Sfarnas, N.; Simopoulos, A.; Kostikas, A. Tetrahedral Complexes Containing the $Fe^{II}S_4$ core. The Syntheses, Ground-State Electronic Structures and Crystal and Molecular Structures of the $[P(C_6H_5)_4]_2Fe(SC_6H_5)_4$ and $[P(C_6H_5)_4]_2Fe(S_2C_4O_2)_2$ Complexes. An Analogue for the Active Site in Reduced Rubredoxins (Rd_{red}). *J. Am. Chem. Soc.* **1981**, *103*, 3350. DOI: 10.1021/ja00402a020.

(49) Holah, D. G.; Coucouvanis, D. Synthesis and Characterization of a New Series of First Row Element Tetrahedral Mercaptide Complexes. *J. Am. Chem. Soc.* **1975**, *97*, 6917. DOI: 10.1021/ja00856a079.

(50) Ueyama, N.; Okamura, T.-A.; Nakamura, A. Intramolecular NH ⋯ S Hydrogen Bond in *o*-Acylamino Substituted Benzenethiolate Iron(II) and Cobalt(II) Complexes. *J. Chem. Soc., Chem. Commun.* **1992**, 1019. DOI: 10.1039/C39920001019.

(51) Ueyama, N.; Yamada, Y.; Okamura, T.-a.; Kimura, S.; Nakamura, A. Structure and Properties of $[Fe_4S_4\{2,6\text{-bis(acylamino)benzenethiolato-}S\}_4]2-$ and $[Fe_2S_2\{2,6\text{-}$

bis(acylamino)benzenethiolato-*S*}$_4$]$^{2-}$: Protection of the Fe−S Bond by Double NH···S Hydrogen Bonds. *Inorg. Chem.* **1996**, *35*, 6473. DOI: 10.1021/ic9604324.

(52) Fourmond, V.; Jacques, P.-A.; Fontecave, M.; Artero, V. H_2 Evolution and Molecular Electrocatalysts: Determination of Overpotentials and Effect of Homoconjugation. *Inorg. Chem.* **2010**, *49*, 10338. DOI: 10.1021/ic101187v.

(53) Haddad, A. Z.; Cronin, S. P.; Mashuta, M. S.; Buchanan, R. M.; Grapperhaus, C. A. Metal-Assisted Ligand-Centered Electrocatalytic Hydrogen Evolution upon Reduction of a Bis(thiosemicarbazonato)Cu(II) Complex. *Inorg. Chem.* **2017**, *56*, 11254. DOI: 10.1021/acs.inorgchem.7b01608.

(54) Korendovych, I. V.; Staples, R. J.; Reiff, W. M.; Rybak-Akimova, E. V. A New High-Spin Iron(III) Complex with a Pentadentate Macrocyclic Amidopyridine Ligand: A Change from Slow Single-Ion Paramagnetic Relaxation to Long-Range Antiferromagnetic Order in a Hydrogen-Bonded Network. *Inorg. Chem.* **2004**, *43*, 3930. DOI: 10.1021/ic0351601.

(55) Kumar, P.; M, B.; Rasool, A.; Demeshko, S.; Bommakanti, S.; Mukhopadhyay, N.; Gupta, R.; Dar, M. A.; Ghosh, M. Bioinspired Diiron Complex with Proton Shuttling and Redox-Active Ligand for Electrocatalytic Hydrogen Evolution. *Inorg. Chem.* **2024**, *63*, 16146. DOI: 10.1021/acs.inorgchem.4c01112.

(56) Fourmond, V.; Jacques, P.-A.; Fontecave, M.; Artero, V. H2 Evolution and Molecular Electrocatalysts: Determination of Overpotentials and Effect of Homoconjugation. *Inorganic Chemistry* **2010**, *49*, 10338. DOI: 10.1021/ic101187v.

(57) Kiernicki, J. J.; Shanahan, J. P.; Zeller, M.; Szymczak, N. K. Tuning ligand field strength with pendent Lewis acids: access to high spin iron hydrides. *Chem. Sci.* **2019**, *10*, 5539. DOI: 10.1039/C9SC00561G.

(58) Waldie, K. M.; Flajslik, K. R.; McLoughlin, E.; Chidsey, C. E. D.; Waymouth, R. M. Electrocatalytic Alcohol Oxidation with Ruthenium Transfer Hydrogenation Catalysts. *J. Am. Chem. Soc.* **2017**, *139*, 738. DOI: 10.1021/jacs.6b09705.

(59) Ramakrishnan, S.; Chakraborty, S.; Brennessel, W. W.; Chidsey, C. E. D.; Jones, W. D. Rapid oxidative hydrogen evolution from a family of square-planar nickel hydride complexes. *Chem. Sci.* **2016**, *7*, 117. DOI: 10.1039/C5SC03189C.

(60) Fulmer, G. R.; Miller, A. J. M.; Sherden, N. H.; Gottlieb, H. E.; Nudelman, A.; Stoltz, B. M.; Bercaw, J. E.; Goldberg, K. I. NMR Chemical Shifts of Trace Impurities: Common Laboratory Solvents, Organics, and Gases in Deuterated Solvents Relevant to the Organometallic Chemist. *Organometallics* **2010**, *29*, 2176. DOI: 10.1021/om100106e.

(61) Rountree, E. S.; McCarthy, B. D.; Eisenhart, T. T.; Dempsey, J. L. Evaluation of Homogeneous Electrocatalysts by Cyclic Voltammetry. *Inorg. Chem.* **2014**, *53*, 9983. DOI: 10.1021/ic500658x.

(62) Bordwell, F. G.; Harrelson, J. A., Jr.; Lynch, T. Y. Homolytic Bond Dissociation Energies for the Cleavage of *a*-N-H Bonds in Carboxamides, Sulfonamides, and Their Derivatives. The Question of Synergism in Nitrogen-Centered Radicals. *J. Org. Chem.* **1990**, *55*, 3337. DOI: 10.1021/jo00297a064.

(63) Fu, Y.; Lin, B.-L.; Song, K.-S.; Liu, L.; Guo, Q.-X. Substituent effects on the S–H bond dissociation energies of thiophenols. *J. Chem. Soc., Perkin Trans. 2* **2002**, 1223. DOI: 10.1039/B201003H.

(64) Smith, J. M.; Lachicotte, R. J.; Holland, P. L. N=N Bond Cleavage by a Low-Coordinate Iron(II) Hydride Complex. *J. Am. Chem. Soc.* **2003**, *125*, 15752. DOI: 10.1021/ja038152s.

(65) Chiang, K. P.; Scarborough, C. C.; Horitani, M.; Lees, N. S.; Ding, K.; Dugan, T. R.; Brennessel, W. W.; Bill, E.; Hoffman, B. M.; Holland, P. L. Characterization of the Fe-H Bond in a Three-Coordinate Terminal Hydride Complex of Iron(I). *Angew. Chem. Int. Ed.* **2012**, *51*, 3658. DOI: 10.1002/anie.201109204.

(66) Drena, A.; Fraker, A.; Thompson, N. B.; Doan, P. E.; Hoffman, B. M.; McSkimming, A. Terminal Hydride Complex of High-Spin Mn. *J. Am. Chem. Soc.* **2024**, *146*, 18370. DOI: 10.1021/jacs.4c03310.

(67) Gill, N. S. 680. Complex Halides of the Transition Metals. Part II. Tetrahedral Iron Complexes. *J. Am. Chem. Soc.* **1961**, 3512. DOI: 10.1039/JR9610003512.

(68) Rosenau, C. P.; Jelier, B. J.; Gossert, A. D.; Togni, A. Exposing the Origins of Irreproducibility in Fluorine NMR Spectroscopy. *Angew. Chem. Int. Ed.* **2018**, *57*, 9528. DOI: 10.1002/anie.201802620.

(69) Loliger, J.; Scheffold, R. Paramagnetic moment measurements by nmr. A micro technique. *J. Chem. Educ.* **1972**, *49*, 646. DOI: 10.1021/ed049p646.

(70) Bain, G. A.; Berry, J. F. Diamagnetic Corrections and Pascal's Constants. *J. Chem. Educ.* **2008**, *85*, 532. DOI: 10.1021/ed085p532.

(71) Becke, A. D. Density-functional thermochemistry. III. The role of exact exchange. *J. Chem. Phys.* **1993**, *98*, 5648. DOI: 10.1063/1.464913.

(72) Lee, C.; Yang, W.; Parr, R. G. Development of the Colle-Salvetti correlation-energy formula into a functional of the electron density. *Phys. Rev. B* **1988**, *37*, 785. DOI: 10.1103/PhysRevB.37.785.

(73) Kossmann, S.; Neese, F. Efficient Structure Optimization with Second-Order Many-Body Perturbation Theory: The RIJCOSX-MP2 Method. *J. Chem. Theory Comput.* **2010**, *6*, 2325. DOI: 10.1021/ct100199k.

(74) Grimme, S.; Antony, J.; Ehrlich, S.; Krieg, H. A consistent and accurate ab initio parametrization of density functional dispersion correction (DFT-D) for the 94 elements H-Pu. *J. Chem. Phys.* **2010**, *132*, 154104. DOI: 10.1063/1.3382344.

(75) Grimme, S.; Ehrlich, S.; Goerigk, L. Effect of the damping function in dispersion corrected density functional theory. *J. Comput. Chem.* **2011**, *32*, 1456. DOI: 10.1002/jcc.21759.

(76) Weigend, F.; Ahlrichs, R. Balanced basis sets of split valence, triple zeta valence and quadruple zeta valence quality for H to Rn: Design and assessment of accuracy. *Phys. Chem. Chem. Phys.* **2005**, *7*, 3297. DOI: 10.1039/B508541A.

(77) Schäfer, A.; Horn, H.; Ahlrichs, R. Fully optimized contracted Gaussian basis sets for atoms Li to Kr. *J. Chem. Phys.* **1992**, *97*, 2571. DOI: 10.1063/1.463096.

(78) Barone, V.; Cossi, M. Quantum Calculation of Molecular Energies and Energy Gradients in Solution by a Conductor Solvent Model. *J. Phys. Chem. A* **1998**, *102*, 1995. DOI: 10.1021/jp9716997.

(79) Pettersen, E. F.; Goddard, T. D.; Huang, C. C.; Couch, G. S.; Greenblatt, D. M.; Meng, E. C.; Ferrin, T. E. UCSF Chimera—A Visualization System for Exploratory Research and Analysis. *J. Comput. Chem.* **2004**, *25*, 1605. DOI: 10.1002/jcc.20084.

(80) Krause, L.; Herbst-Irmer, R.; Sheldrick, G. M.; Stalke, D. Comparison of silver and molybdenum microfocus X-ray sources for single-crystal structure determination. *J. Appl. Cryst.* **2015**, *48*, 3. DOI: 10.1107/S1600576714022985.

(81) Sheldrick, G. SHELXT - Integrated space-group and crystal-structure determination. *Acta Cryst. A* **2015**, *71*, 3. DOI: 10.1107/S2053273314026370.

(82) Sheldrick, G. Crystal structure refinement with SHELXL. *Acta Cryst. C* **2015**, *71*, 3. DOI: 10.1107/S2053229614024218.

(83) Sheldrick, G. *SHELXT* - Integrated space-group and crystal-structure determination. *Acta Crystallogr. A* **2015**, *71*, 3. DOI: 10.1107/S2053273314026370.

(84) Appel, A. M.; Helm, M. L. Determining the Overpotential for a Molecular Electrocatalyst. *ACS Catal.* **2014**, *4*, 630. DOI: 10.1021/cs401013v.

(85) Zhou, Z.; Cheng, Z.; Yang, D.; Zhou, X.; Yuan, W. Solubility of Hydrogen in Pyrolysis Gasoline. *J. Chem. Eng. Data* **2006**, *51*, 972. DOI: 10.1021/je050478o.

(86) Nicholson, R. S.; Shain, I. Theory of Stantionary Electrode Pology raphy. Single Scan and Cyclic Methods Applied to Reversible, Irreversible, and Kinetic Systems. *Anal. Chem.* **1964**, *36*, 706. DOI: 10.1021/ac60210a007.

(87) Saveant, J. M.; Vianello, E. Potential-Sweep Chronoamperometry: Kinetic Currents for First-Order Cheimcal Reaction Parallel to Electron-Transfer Process (Catalytic Currents). *Electrochim. Acta* **1965**, *10*, 905. DOI: 10.1016/0013-4686(65)80003-2.

CHAPTER 5

CONCLUSIONS

Overall, this work focused on the development and mechanistic investigation of electron-rich transition metal-thiolate electrocatalysts for hydrogen evolution. We have successfully synthesized and characterized Ni tetra-aryl thiolate electrocatalysts for hydrogen evolution as low-molecular-weight (LMW) synthetic models of the Ni-site in [NiFe]-hydrogenase (H_2ase). Additionally, we investigated electrocatalytic hydrogen evolution using a thiolate-containing electron-rich, non-heme synthetic analog of nitrile hydratase. The electron-rich ligand platforms in these complexes are important for promoting formation of metal-hydrides, a crucial intermediate in H_2 evolution, from relatively weak acids in organic solvents. Furthermore, coordinated thiolates play a key role by providing a proximal protonation site that facilitates heterolytic coupling to a metal bound hydride to generate H_2. While thiolates are prone to oxidative modification and often form bridging complexes upon coordination to transition metals, our work demonstrates that these challenges can be overcome, allowing thiolate-rich complexes to serve as effective hydrogen evolution electrocatalysts.

To mimic the tetrahedral $Ni(SCys)_4$ site in [NiFe]-H_2ase, we employed aryl thiolates due to their unique ability to stabilize mononuclear $[Ni(SPh)_4]^{2-}$ complexes in a tetrahedral geometry. In contrast, alkyl thiolates or chelating dithiolate ligands afford exclusively square-planar complexes that tend to form multimers of the general form $[(SPh)Ni(\mu\text{-}SPh)_2Ni(SPh)]_n$. Despite the structural similarity between the native enzyme $[Ni(SPh)_4]^{2-}$, these complexes were never

tested as HER electrocatalysts due to their ill-defined speciation upon dissolution and tendency to form intractable oligomers under protic conditions. To address these limitations, we initially explored $[Ni(S\text{-}p\text{-}CF_3\text{-}Ph)_4]^{2-}$ as a model system. We found that catalytic inefficiencies stem from the dissociation of coordinated thiolate to form putative $[Ni(SPh)_3(solv)]^-$ intermediates that undergo polymerization. Despite these shortcomings, we found utilization of excess thiolate suppresses the formation of bridging complexes allowing electrocatalytic activity to be assessed. $[Ni(S\text{-}p\text{-}CF_3\text{-}Ph)_4]^{2-}$ was found to catalyze proton reduction with turnover frequencies of 14 s^{-1} at overpotentials of 0.72 V, following an ECCE mechanism. This catalyst exhibits structural and mechanistic parallels to [NiFe]-H_2ase, including formation of a Ni(III)-H intermediate via oxidative addition and involvement of a protonated thiolate functioning as a proton relay.

To enhance the stability of the homoleptic Ni(II)-aryl thiolates and improve overpotentials, by positively shifting the Ni(II/I) redox couple, we incorporated *ortho*-carboxamide substituents capable of intramolecular hydrogen-bonding to the coordinated thiolates in $(Et_4N)_2[Ni(S\text{-}o\text{-}^i PrCONH\text{-}p\text{-}CF_3\text{-}Ph)_4]$ (where S-*o*-^{i}PrCONH-*p*-CF_3-Ph = thiolate of *o*-isopropylamide-*p*-trifluoromethyl-phenyl thiol) and $(Et_4N)_2[Ni(S\text{-}o\text{-}OPhCONH\text{-}p\text{-}CF_3\text{-}Ph)_4]$ (where S-*o*-OPhCONH-*p*-CF_3-Ph = thiolate of *o*-phenoxyacetamide-*p*-trifluoromethyl-phenyl thiol). Although the modified complexes exhibited improved stability under protic conditions and shifted the Ni(II/I) by ~+0.2 V, the complexes form HER active Ni:S films with embedded nanoparticles on the electrode surface. Unexpectedly, the introduction of *ortho*-carboxamide moieties resulted in the presence of square-planar monomeric $[Ni(SR)_4]^{2-}$ complexes. In solution we found that a mixture of monomeric tetrahedral and square-planar Ni tetrathiolates are present. We propose that hydrogen-bonding interaction with the thiolate increases the ligand field strength by reducing their π-donor capacity, leading to the stabilization of the square-planar

geometry. These findings shed light on the delicate balance required to maintain a tetrahedral geometry in homoleptic tetrathiolate Ni(II) complexes and avenues to further improve stability of Ni(II) thiolate complexes in protic conditions.

Lastly, we investigated the electrocatalytic activity of an electron-rich non-heme Fe-thiolate complex supported by a tetra-anionic pentadentate ligand, complex (Et_4N)[Fe(PyPS-*p*-CF_3)] (fully deprotonated $PyPSH_4$-*p*-CF_3 = *N*,*N*'-bis(2-mercaptophenyl-5-triflouromethyl)pyridine-2,6-dicarboxamide). In MeCN, the complex decomposed under electrocatalytic conditions, forming HER active deposits. However, this decomposition was mitigated in DMF enabling the activity of the homogenous catalysis to be determined. We propose that deposition results in protonation of carboxamide-nitrogen resulting in Fe-N cleavage, and ligand arrangement to form $[Fe(SR)_4]^-$ and free Fe. We propose DMF forms a stabilizing H-bonding interaction with the protonated ligand frame impeding its decomposition. Catalytic proton titration experiments with the redox-inert Zn(II) analog, and supporting DFT computations, suggest the redox-active ligand participates as an additional electron storage site and as a proton relay via a hemilabile thiolate. These factors facilitate H_2 evolution at moderate rates (~1200 s^{-1}) and overpotentials (0.94 V) through a proposed E(CECE) mechanism.

In summary, this work offers insights into the design and function of thiolate-coordinated Ni(II) and Fe(III) electrocatalysts for hydrogen evolution. These electron-rich synthetic analogs of [NiFe]-H_2ase provide a valuable platform to elucidate the dual role of thiolates/CysS in modulating the electron density at the metal and in mediating proton relay. Although the challenges of creating and testing these thiolate-rich complexes are apparent through this work, we have developed effective strategies for stabilizing these complexes under catalytically relevant conditions. Ultimately, our work provides a foundation for developing synthetic mimics

that more accurately reflect the structural features of native enzyme active, offering deeper insights in the structure-to-function relationships that underpin of hydrogenases activity. Future efforts will focus on the design of modifiable thiolate-rich ligand constructs that rigidly hold Ni in a tetrahedral geometry, further enhancing both stability and catalytic activity in biomimetic hydrogen evolution systems.

APPENDIX A

DIVERGENT BEHAIVOR OF NICKEL(II) TETRATHIOLATE ORTHO-CARBOXAMIDE COMPLEXES IN EXCESS THIOLATE CONDITIONS

A.1. Results and Discussion

The complexes $(Et_4N)_2[Ni(S\text{-}o\text{-}^t BuCONH\text{-}p\text{-}CF_3\text{-}Ph)_4]$ (**1**) and $(Et_4N)_2[Ni(S\text{-}o\text{-}OPhCONH\text{-}p\text{-}CF_3\text{-}Ph)_4]$ (**2**) were prepared to probe the effects of S-directed hydrogen-bonding on acid-stability and electrocatalysis of homoleptic Ni(II) tetrathiolate complexes. Both complexes were crystallographically characterized and probed by XAS/EXAFS revealing a square-planar homoleptic $[Ni(SR)_4]^{2-}$ coordination environment, Chapter 3 contains a detailed structural description. Upon solvation of **1** and **2**, their NMR spectra are consistent with a tetrahedral (S = 1) $[Ni(SR)_4]^{2-}$ complexes. Furthermore, **1** was determined to be in equilibrium with a S,S-bridged multimer, Scheme A.1, that can be pushed back to its monomeric complex by addition of thiolate. This equilibrium was established by increased solution-state magnetic moment values and change in the electronic absorption profile of **1** upon addition of thiolate, see Chapter 3 for a more detailed discussion. Given the structural and spectral similarities between **1** and **2**, we anticipate **2** would exhibit a similar equilibrium as shown in Scheme A.1. However, under excess thiolate conditions, **2** exhibits divergent behavior.

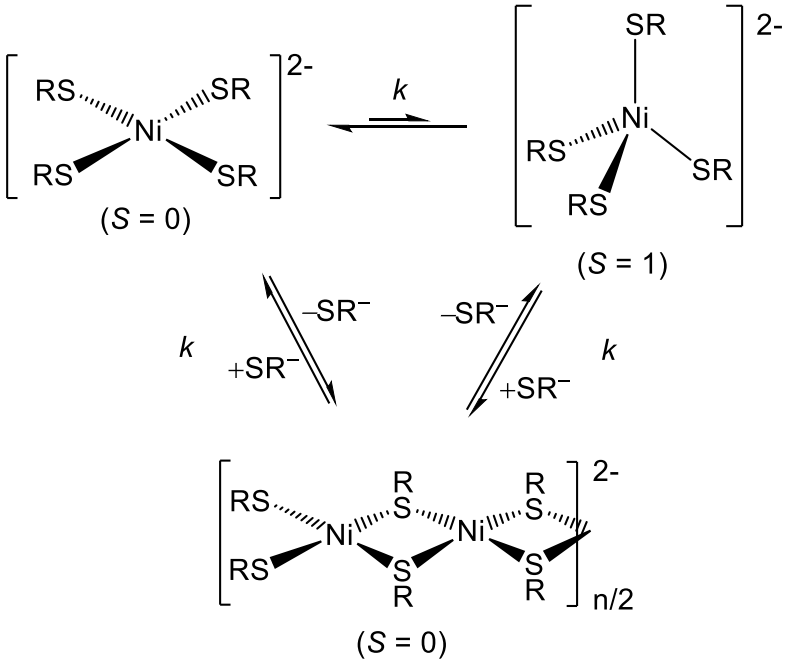

Scheme A.1. Proposed ligand dissociation equilibrium between Ni-tetrathiolate monomer and S,S-bridged Ni multimer.

The NMR (^{1}H/^{19}F) of **2** are consistent with a mixture of $S = 1$ and $S = 0$ complexes, discussed in Chapter 3, with three paramagnetically shifted peaks, assigned to tetrahedral ($S = 1$) monomer and several peaks in the aromatic region of the ^{1}H NMR. A mixture of paramagnetic and diamagnetic complexes in solutions of **2** are further indicated by the low solution state magnetic moment ($\mu_{eff} = 1.95$ BM) compared to other tetrahedral Ni(II) complexes ($\mu_{eff} = 3.5$-4.2 BM). Measuring the magnetic moment of **2** in the presence of 10 mol-equivalents increases the amount of paramagnetic material ($\mu_{eff} = 2.23$ BM), presumably monomeric tetrahedral complex, consistent with the ligand dissociation equilibrium presented in Scheme A.1 and behavior of **1** under excess thiolate conditions. To further validate this equilibrium, the electronic absorption spectrum of **2** was monitored as increasing equivalents of (Et_4N)(S-*o*-OPhCONH-*p*-CF_3-Ph) were added, shown in Figure A.1. The UV-vis of **2** alone is nearly featureless consisting of a broad band at ~680 nm and shoulder at 390 nm. Upon addition of just 4.0 mol-equiv. of thiolate,

the shoulder at 390 nm disappears, the broad band at 680 nm becomes more distinct, and a new band arises at 510 nm. As thiolate concentration is increased the solution begins to bleach and all absorption bands decrease in intensity with only the 510 nm band remaining at 20 mol-equiv. of (Et_4N)(S-*o*-OPhCONH-*p*-CF_3-Ph). These results suggest that a new complex is formed; however, the electronic absorption profile does not resemble those of reported tetrahedral Ni(II) terta-aryl thiolate complexes, with two distinct charge-transfer bands (~500 and ~450 nm) and two broad ligand field bands, centered around 700 nm. The electronic absorption of **2** with excess thiolate resembles the spectra in DMF, shown in Figure A.2. Computational and sulfur K-edge XAS spectroscopy of a similar Ni-tetrathiolate complex, $[Ni(HpyS)_4]^{2-}$, indicates the thiolate ligand dissociates upon dissolution of DMF yielding $[Ni(DMF)_6]^{2+}$ complexes.[1] Although counterintuitive, these results suggest that the addition of thiolate to **2** results in the formation of $[Ni(MeCN)_4]^{2+}$ or a mixed thiolate-solvato Ni(II) complex.

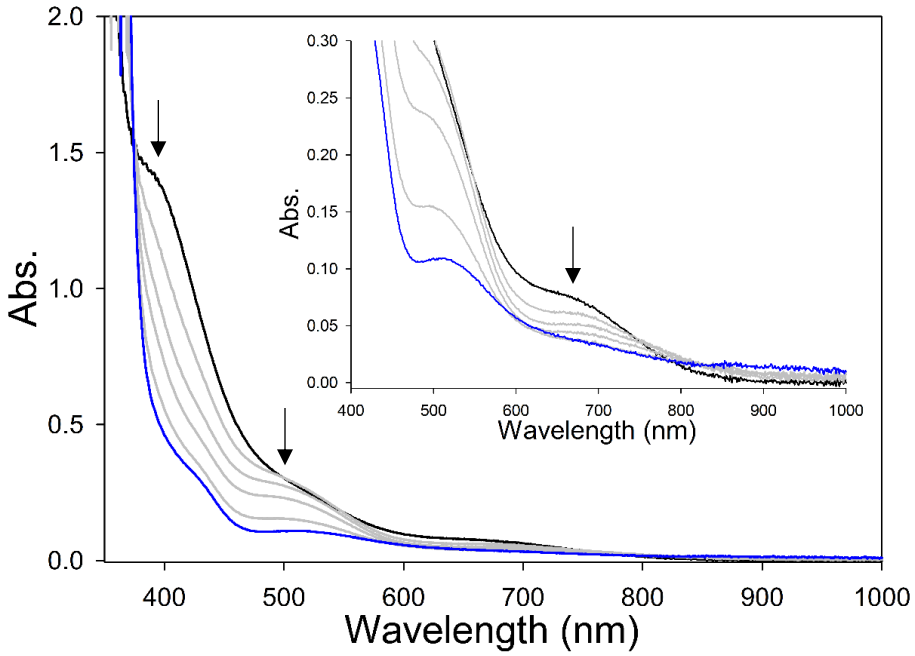

Figure A.1. UV-vis of **2** (black) and addition of (Et_4N)(S-*o*-OPhCONH-*p*-CF_3-Ph) up to 20 mol-equivalents (blue) with each scan in-between representing addition of 4.0 mol-equiv. of thiolate (grey) in MeCN at 25 °C. *Inset:* zoom-in of 400-1000 nm region of spectra.

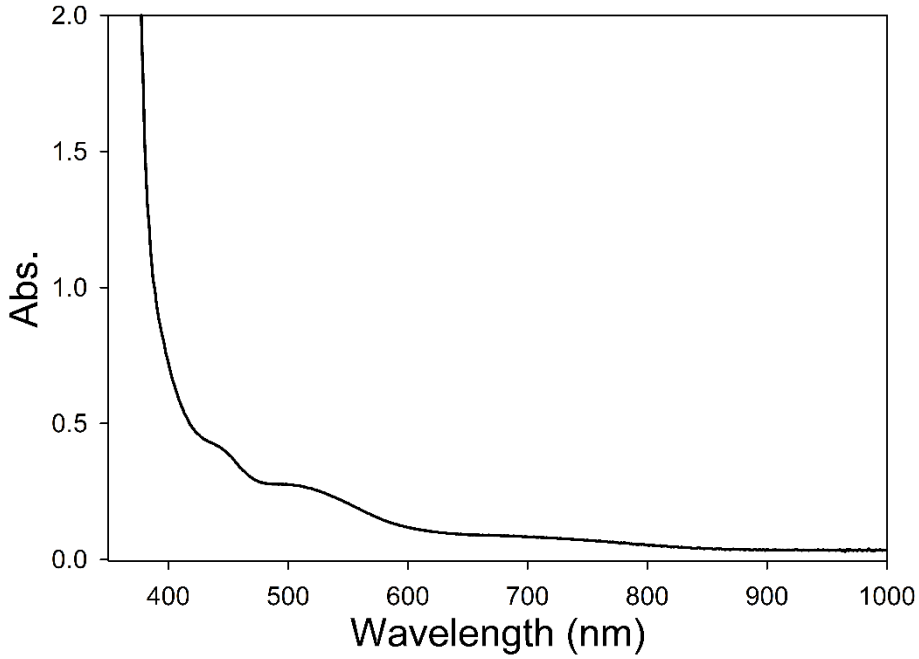

Figure A.1. UV-vis of **2** in DMF at 25 °C.

A.2. Synthesis and Reactivity

UV-vis Titration Experiment with Thiolate. For **2**, a 7.4 mM stock solution of **2** (0.012 g, 0.0074 mmol) was made in 1.0 mL of MeCN and 40 μL was added to a cuvette containing 2.00 mL of MeCN and sealed with a cap. A separate 30 mM stock solution of (Et_4N)(S-*o*-OPhCONH-*p*-CF_3-Ph) (0.014 g, 0.030 mmol) was made in 1.00 mL of MeCN. After the spectrum of **2** was recorded, 60 μL of (Et_4N)(S-*o*-OPhCONH-*p*-CF_3-Ph) was added to the cuvette containing **2**, stirred, and the spectra was recorded after roughly a minute at room temperature. Titrations were repeated in the same manner until no change in the spectra was observed. All stock solutions and titrations were made and performed in a MBraun Unilab glovebox under N_2 atmosphere.

A.3. References

(1) Ledbetter, K.; Larsen, C. B.; Lim, H.; Zoric, M. R.; Koroidov, S.; Pemmaraju, C. D.; Gaffney, K. J.; Cordones, A. A. Dissociation of Pyridinethiolate Ligands during Hydrogen Evolution Reactions of Ni-Based Catalysts: Evidence from X-ray Absorption Spectroscopy. *Inorg. Chem.* **2022**, *61*, 9868. DOI: 10.1021/acs.inorgchem.2c00167.